

MATERIALS  
RESEARCH  
SOCIETY  
SYMPOSIUM PROCEEDINGS

VOLUME 369

# Solid State Ionics IV

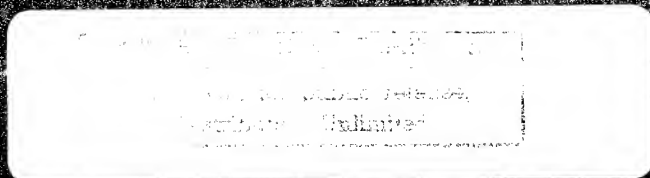


EDITORS

Gholam-Abbas Nazri

Jean-Marie Tarascon

Martha Schreiber



MRS

**Solid State Ionics IV**



19950720 081

**DISTRIBUTION STATEMENT A**  
**Approved for public release;**  
**Distribution Unlimited**

**DTIC QUALITY INSPECTED 5**



## Solid State Ionics IV

Symposium held November 28–December 1, 1994, Boston, Massachusetts, U.S.A.

EDITORS:

**Gholam-Abbas Nazri**

GM NAO R&D Center  
Warren, Michigan

**Jean-Marie Tarascon**

Bell Communication Research  
Red Bank, New Jersey

**Martha Schreiber**

Daimler-Benz AG  
Ulm, Germany

Accession For	
NTIS	CRA&I <input checked="" type="checkbox"/>
DTIC	TAB <input type="checkbox"/>
Unannounced <input type="checkbox"/>	
Justification _____	
By _____	
Distribution /	
Availability Codes	
Dist	Avail and/or Special
A-1	

**MRS**

MATERIALS RESEARCH SOCIETY  
Pittsburgh, Pennsylvania

This work was supported in part by the Office of Naval Research under Grant Number N00014-95-1-0140. The United States Government has a royalty-free license throughout the world in all copyrightable material contained herein.

Single article reprints from this publication are available through  
University Microfilms Inc., 300 North Zeeb Road, Ann Arbor, Michigan 48106

CODEN: MRSPDH

Copyright 1995 by Materials Research Society.  
All rights reserved.

This book has been registered with Copyright Clearance Center, Inc. For further information, please contact the Copyright Clearance Center, Salem, Massachusetts.

Published by:

Materials Research Society  
9800 McKnight Road  
Pittsburgh, Pennsylvania 15237  
Telephone (412) 367-3003  
Fax (412) 367-4373

Library of Congress Cataloging in Publication Data

Solid State Ionics IV: symposium held November 28-December 1, 1994, Boston, Massachusetts, U.S.A. / editors Gholam-Abbas Nazri, Jean-Marie Tarascon, Martha Schreiber;  
p. cm.—(Materials Research Society symposium proceedings,  
ISSN 0272-9172; v. 369)  
Includes bibliographical references and index.  
ISBN 1-55899-271-5 (hardcover : acid-free paper)

Manufactured in the United States of America

## Contents

PREFACE .....	xiii
MATERIALS RESEARCH SOCIETY SYMPOSIUM PROCEEDINGS .....	xiv

### PART I: INSERTION COMPOUNDS

*PULSE APPLICATIONS OF ELECTROCHEMICAL CELLS CONTAINING INSERTION REACTION ELECTRODES .....	3
Robert A. Huggins	
*TRANSITION METAL OXIDES FOR ROCKING-CHAIR CELLS .....	17
M.M. Thackeray, E. Ferg, R.J. Gummow, and A. de Kock	
*A COMPARATIVE STUDY OF $\text{LiMn}_2\text{O}_4$ FROM VARIOUS SOURCES .....	29
B. Ouyang, S.G. Greenbaum, M. den Boer, A. Massucco, M. McLin, J. Shi, and D. Fauteux	
*DEFECT SPINELS IN THE SYSTEM Li-Mn-O. CHEMISTRY AND LITHIUM INSERTION .....	39
F. Le Cras, D. Bloch, M. Anne, and P. Strobel	
*SYNTHESIS AND LITHIUM INTERCALATION PROPERTIES OF A LAYERED LITHIATED MANGANESE OXIDE WITH RANCIEITE TYPE .....	47
F. Leroux, D. Guyomard, and Y. Piffard	
*LITHIUM-7 NMR STUDIES OF $\text{Li}_{1-x}\text{CoO}_2$ BATTERY CATHODES .....	59
B. Ouyang, X. Cao, H.W. Lin, S. Slane, S. Kostov, M. denBoer, and S.G. Greenbaum	
*LITHIUM INTERCALATION FROM AQUEOUS SOLUTIONS .....	69
W. Li, J.R. Dahn, and J.H. Root	
CRYSTAL CHEMISTRY AND ELECTROCHEMICAL BEHAVIOR OF NEW MANGANESE SUBSTITUTED NICKEL HYDROXIDES .....	81
L. Guerlou-Demourgues and C. Delmas	
*ELECTROCHEMICAL ACTIVITY OF NATURAL AND SYNTHETIC MANGANESE DIOXIDES .....	87
J.M. Amarilla, L.A.H. MacLean, F. Tedjar, F. Le Cras, P. Strobel, and C. Poinson	
*PROTON INTERCALATION IN $\gamma\text{-MnO}_2$ FROM RAMSDELLITE TO GROUTITE THROUGH GROUTELLITE .....	97
Yves Chabre and Jean Pannetier	
*DISSOLUTION-RECRYSTALLIZATION PROCESSES OF NICKEL HYDROXIDE, THE ACTIVE MATERIAL OF THE Ni/Cd AND Ni/ $\text{H}_2$ CELLS .....	107
A. Delahaye-Vidal, N. Sac-Epee, F. Portemer, B. Beaudoin, M. Figlarz, and T. Jamin	
EFFECT OF THE HEAT TREATMENT ON THE LITHIUM INSERTION PROCESS IN $\text{MoO}_3$ .....	119
B. Yebka and C. Julien	

\*Invited Paper

ROUGHNESS EFFECT ON THE LITHIUM DIFFUSIVITY IN WO <sub>3</sub> THIN FILMS . . . . .	125
M. Maaza, A. Gorenstein, C. Sella, F. Bridou, B. Pardo, J. Corno, G. Roger, O. Bohnke, and C. Julien	
ELECTROCHEMICAL STUDY, SYNTHESIS AND MICROSTRUCTURAL CHARACTERIZATION OF LITHIUM AND SODIUM INSERTED W <sub>18</sub> O <sub>49</sub> . . . . .	131
A. Martínez de la Cruz, Leticia M. Torres-Martínez, F. García-Alvarado, E. Moran, and M.A. Alario-Franco	
*PROPERTIES OF A CARBON NEGATIVE ELECTRODE IN COMPLETELY INORGANIC THIN FILM Li-ION BATTERIES WITH A LiCoO <sub>2</sub> POSITIVE ELECTRODE . . . . .	137
R.B. Goldner, S. Slaven, T.Y. Liu, T.E. Haas, F.O. Arntz, and P. Zerigian	
CHEMISTRY OF ELECTROCHROMIC IrO <sub>x</sub> FILMS DEPOSITED UNDER VARIABLE REDOX CONDITIONS . . . . .	149
J.D. Klein and S.L. Clauson	
*SYNTHESIS OF GRAPHITE INTERCALATION COMPOUNDS WITH DONOR SPECIES . . . . .	155
Daniel Guérard and Vera A. Nalimova	
*THE CARBON-LITHIUM NEGATIVE ELECTRODE FOR LITHIUM-ION BATTERIES IN POLYMER ELECTROLYTE . . . . .	165
R. Yazami and M. Deschamps	

## PART II: SOL-GEL PROCESS

*VANADIUM PENTOXIDE GELS FROM LIQUID CRYSTALS TO LITHIUM BATTERIES . . . . .	179
J. Livage, N. Baffier, J.P. Pereira-Ramos, and P. Davidson	
*SOL GEL INTERCALATION MATERIALS FOR LITHIUM BATTERIES . . . . .	191
J.P. Pereira-Ramos, S. Bach, J. Farcy, and N. Baffier	
*PROPERTIES OF LiV <sub>3</sub> O <sub>8</sub> CATHODE MATERIALS PREPARED FROM GELS BY SPRAY-DRYING . . . . .	201
M.Y. Saidi, I.I. Olsen, R. Koksang, J. Barker, R. Pynenburg, K. West, B. Zachau-Christiansen, and S. Skaarup	
*MORPHOLOGY AND PROPERTIES OF VANADIUM OXIDE XEROGELS AND AEROGELS . . . . .	211
B. Katz, W. Liu, K. Salloux, F. Chaput, B. Dunn, and G.C. Farrington	

## PART III: THEORY OF ION CONDUCTION IN SOLIDS

*MONTE CARLO STUDY OF DISPERSIVE TRANSPORT IN GLASSY ELECTROLYTES . . . . .	225
D. Knödler, P. Pendzig, and W. Dieterich	
*COMPLETE CONDUCTIVITY SPECTRA OF CRYSTALLINE AND GLASSY FAST ION CONDUCTORS UP TO FAR INFRARED FREQUENCIES . . . . .	233
C. Cramer, R. Graeber, M.D. Ingram, T. Saatkamp, D. Wilmer, and K. Funke	

\*Invited Paper

*THE MECHANISM AND MODELING OF CONDUCTIVITY IN POLYMER ELECTROLYTES .....	245
Mark C. Lonergan, Duward F. Shriver, Abraham Nitzan, and Mark A. Ratner	
MASS TRANSPORT AND DC ELECTROMOTIVE FORCE INDUCED IN IONIC CRYSTALS BY HIGH-FREQUENCY ELECTRIC FIELD .....	263
K.I. Rybakov and V.E. Semenov	

#### PART IV: DEFECT CHEMISTRY

*APPLICATION OF DEFECT MODELING TO MATERIALS DESIGN .....	271
Marlene A. Spears and H.L. Tuller	
POINT DEFECTS AND PROTONIC CONDUCTION IN $A_3B'B''_2O_9$ COMPOUNDS .....	289
Yang Du and A.S. Nowick	
FAILURE OF THE FRENKEL DEFECT MODEL TO EXPLAIN THE TREND IN ANIONIC CONDUCTIVITY IN THE $MF_2$ FLUORITE STRUCTURE AND RELATED $MSnF_4$ MATERIALS .....	295
Georges Denes	
POINT DEFECTS AND CATION DIFFUSION IN COBALTOUS OXIDE .....	301
Sanjeev Aggarwal and Rüdiger Dieckmann	
NON-STOICHIOMETRY AND CATION TRACER DIFFUSION STUDIES IN THE MAGNETITE-ULVÖSPINEL SOLUTION, $(Fe,Ti)_{3-3}O_4$ .....	307
Sanjeev Aggarwal and Rüdiger Dieckmann	
NONSTOICHIOMETRY AND POINT DEFECT STRUCTURE OF OLIVINES, $(Fe_xMg_{1-x})_2SiO_4$ .....	313
Tse-Lun Tsai and R. Dieckmann	
POINT DEFECTS AND CATION TRACER DIFFUSION IN $(Cr_xFe_{1-x})_{3-3}O_4$ SPINELS .....	319
J. Töpfer and R. Dieckmann	
CALCULATION OF DEFECT FORMATION ENERGY FROM THE THERMAL EXPANSION DATA FOR LEAD FLUORIDE .....	325
Brenda J. Schuler, T.S. Aurora, D.O. Pederson, and S.M. Day	

#### PART V: SOLID ELECTROLYTES

*IMPROVED OXIDE ION ELECTROLYTES .....	333
Man Feng and John B. Goodenough	
PEROVSKITES AS OXIDE-ION ELECTROLYTES .....	343
Man Feng and John B. Goodenough	
ELECTROCHEMICAL STUDIES OF PERVOSKITE MIXED CONDUCTORS .....	349
Eric L. Brosha, Brandon W. Chung, and Fernando H. Garzon	
* $Bi_2Sr_2M'M''O_{11.5}[(M' = Nb, Ta) \text{ AND } (M'' = Al, Ga)]$ , SYNTHESIS AND CHARACTERIZATION OF OXYGEN-DEFICIENT AURIVILLIUS PHASES .....	355
Kurt R. Kendall, Carlos J. Navas, and Hans-Conrad Zur Loye	

\*Invited Paper



*CATION CONDUCTIVITY IN MIXED SULFATE-BASED AND MIXED IODIDE-BASED SOLIDS WITH PHASE TRANSITIONS . . . . .	361
E.A. Secco	
ELECTRICAL CONDUCTIVITY IN $(\text{Gd}_{1-x}\text{Ca}_x)_2\text{Sn}_2\text{O}_{7+\delta}$ PYROCHLORE SYSTEM . . . . .	371
Tae-Hwan Yu and Harry L. Tuller	
OXYGEN PERMEABILITY OF STRONTIUM-DOPED $\text{LaCoO}_{3-\delta}$ PEROVSKITES . . . . .	377
René H.E. Van Doorn, H. Kruidhof, H.J.M. Bouwmeester, and A.J. Burggraaf	
OXYGEN PERMEATION STUDIES OF $\text{SrCo}_{0.8}\text{Fe}_{0.2}\text{O}_{3-\delta}$ . . . . .	383
Y.L. Yang, T.H. Lee, L. Qiu, L. Liu, and A.J. Jacobson	
A STUDY OF THE ELECTROCATALYTIC PROPERTIES OF $\text{SrCo}_{0.8}\text{Fe}_{0.2}\text{O}_{3-\delta}$ BY IMPEDANCE SPECTROSCOPY . . . . .	389
Ai Quoc Pham and Allan J. Jacobson	
PROCESSING AND ELECTROCHEMICAL PROPERTIES OF MIXED CONDUCTING $\text{La}_{1-x}\text{A}_x\text{Co}_{1-y}\text{Fe}_y\text{O}_{3-\delta}$ (A = Sr, Ca) . . . . .	395
W.J. Weber, J.W. Stevenson, T.R. Armstrong, L.R. Pederson, and J.J. Kingsley	
STRUCTURAL, ELECTRICAL AND OPTICAL PROPERTIES OF LASER DEPOSITED THIN FILMS OF $\text{SrCo}_{0.8}\text{Fe}_{0.2}\text{O}_{3-\delta}$ . . . . .	401
C. Zhang, H. Deng, J. Varon, B. Abeles, Y. Yang, A.Q. Pham, and A.J. Jacobson	
MEASUREMENT OF PARTIAL CONDUCTIVITIES IN MIXED CONDUCTORS USING BLOCKING ELECTRODES . . . . .	409
Ai Quoc Pham and Allan J. Jacobson	
DIFFUSION-REACTION IN MIXED IONIC ELECTRONIC CONDUCTOR SOLID OXIDE MEMBRANES WITH POROUS ELECTRODES . . . . .	415
Huiming Deng, Minyau Zhou, and Benjamin Abeles	
STUDY OF AC CONDUCTIVITY IN DILUTE $\text{CeO}_2\text{:Y}^{3+}$ CERAMICS . . . . .	421
A.V. Vaysleyb, B.S. Lim, and A.S. Nowick	
WATER UPTAKE AND CONDUCTION IN STRONTIUM YTTERBIUM CERATE . . . . .	427
G.W. Coffey, L.R. Pederson, and W.J. Weber	
*MICROSTRUCTURE-CONDUCTIVITY RELATIONSHIPS IN SOLID ANISOTROPIC IONICALLY CONDUCTING MATERIALS . . . . .	433
E. Butcherit, J. Schoonman, H.W. Zandbergen, C. Lutz-Elsner, M. Schreiber, and P. Wang	
*IONIC CONDUCTIVITIES OF LITHIUM PHOSPHORUS OXYNITRIDE GLASSES, POLYCRYSTALS AND THIN FILMS . . . . .	445
B. Wang, J.B. Bates, B.C. Chakoumakos, B.C. Sales, B.W. Kwak, R.A. Zuhr, and J.D. Robertson	
STRUCTURAL CHEMISTRY OF ALKALINE EARTH HEXA-ALUMINATES . . . . .	457
Jae-Gwan Park and A.N. Cormack	
STRAIN DRIVEN TWO-DIMENSIONAL PHASE TRANSITION IN $\text{PbSnF}_4$ SUPERIONIC CONDUCTOR . . . . .	463
Georges Denes, M.C. Madamba, and J.M. Parris	

\*Invited Paper

ELECTRICAL CONDUCTIVITY AND RAMAN STUDIES OF B <sub>2</sub> O <sub>3</sub> -Na <sub>2</sub> O-NaI GLASS . . . . .	469
Byoung-Koo Choi, Kyoung-Hee Shin, and Hyo-Kyoung Lee	
SPECTROFLUORIMETRIC CHARACTERIZATION OF AN IONIC CONDUCTOR: SODIUM SULFATE HIGH-TEMPERATURE PHASES DOPED WITH EUROPIUM(III) . . . . .	475
Lowell R. Matthews, Edward T. Knobbe, Gamini Dharmasena, Renée Cole, and Roger Frech	
SYNTHESIS, CHARACTERIZATION AND ELECTROCHEMICAL STUDY OF THE SOLID SOLUTION Li <sub>x</sub> Na <sub>0.875-x</sub> Fe <sub>0.875</sub> Ti <sub>1.125</sub> O <sub>4</sub> (0 ≤ δ ≤ 0.4, x ≥ 0) . . . . .	481
Alois Kuhn, F. Garcia-Alvarado, E. Moran, and M.A. Alario-Franco	
MONITORING OF PROCESS OF ION TRANSPORT IN NONSTOICHIOMETRIC FLUORIDES WITH THE LaF <sub>3</sub> STRUCTURE . . . . .	487
Nikolay I. Sorokin and Boris P. Sobolev	

#### PART VI: POLYMER ELECTROLYTES AND ELECTRODES

*NEW CONCEPTS IN PRIMARY AND RECHARGEABLE SOLID STATE LITHIUM POLYMER BATTERIES . . . . .	495
Gianni Appetecchi, Fausto Croce, Furio Gerace, Stefania Panero, Stefano Passerini, Eraldo Spila, and Bruno Scrosati	
NON-CRYSTALLIZING MOLTEN SALT AND IONIC RUBBER ELECTROLYTES WITH WIDE ELECTROCHEMICAL WINDOWS . . . . .	505
K. Xu and C.A. Angell	
ELECTRICAL PROPERTIES OF HIGH ION CONDUCTIVE POLYMER COMPLEXES CONTAINING ROOM TEMPERATURE MOLTEN SALT . . . . .	511
Norio Aoshima, Masahiro Rikukawa, Kohei Sanui, and Naoya Ogata	
CHARACTERIZATION OF PLASTICIZED POLYETHER-URETHANE SOLID POLYMER ELECTROLYTES . . . . .	517
M. Forsyth, P. Meakin, D.R. MacFarlane, and A.J. Hill	
*IONIC ASSOCIATION OF LITHIUM TRIFLATE IN GLYMES, MODEL SOLVENTS, AND HIGH MOLECULAR WEIGHT POLY(ETHYLENE OXIDE) . . . . .	523
R. Frech, W. Huang, and M.A.K.L. Dissanayake	
CONDUCTIVITY IN POLY(ETHYLENE OXIDE) COMPLEXED WITH MIXED ALKALI METAL SALTS . . . . .	535
Byoung-Koo Choi and Young-Wan Kim	
POLYMER BLENDS BASED ON POLY(ETHYLENE OXIDE) AS MATRICES OF SOLID STATE IONICS . . . . .	541
Anna I. Suvorova and Irina S. Tujkova	
*XAFS STUDIES OF POLYMER ELECTROLYTES . . . . .	547
H.M.N. Bandara, R.G. Linford, R.J. Latham, and W.S. Schlindwein	
XAS STUDIES OF PEO BASED POLYMER ELECTROLYTES . . . . .	559
J. McBreen, X.Q. Yang, H.S. Lee, and Y. Okamoto	
POLYANILINE: INFLUENCE OF POLYMERIZATION CURRENT DENSITY . . . . .	565
Steen Skaarup, L.M.W.K. Gunaratne, Keld West, and Birgit Zachau-Christiansen	

\*Invited Paper

INTERLAYER INTERACTIONS IN SELF-ASSEMBLED POLY(PHENYLENE VINYLENE) MULTILAYER HETEROSTRUCTURES, IMPLICATIONS FOR LIGHT-EMITTING PHOTOELECTRIC DIODES . . . . .	575
A.C. Fou, O. Onitsuka, M. Ferreira, M.F. Rubner, and B.R. Hsieh	
PREPARATION AND CHARACTERIZATION OF POLYANILINE-PALLADIUM COMPOSITE FILMS . . . . .	581
Hongshi Li, D.R. Baer, M.H. Engelhard, J. Janata, and M. Josowicz	
MOLECULAR LAYER PROCESSING OF POLYANILINE VIA THE USE OF HYDROGEN BONDING INTERACTIONS . . . . .	587
William B. Stockton and Michael F. Rubner	

#### PART VII: IONIC DEVICES

*THE Li-ION TECHNOLOGY: ITS EVOLUTION FROM LIQUID TO PLASTIC . . . . .	595
J.M. Tarascon, C. Schmutz, A.S. Gozdz, P.C. Warren, and F.K. Shokoohi	
*PERFORMANCE OF POLYMER-BASED SUPERCAPACITORS . . . . .	605
Catia Arbizzani, Marina Mastragostino, and Luca Meneghello	
*SENSORS FOR ACID-BASE-ACTIVE GASES . . . . .	613
Joachim Maier, Michael Holzinger, and Werner Sitte	
VAPOR DEPOSITION OF THIN-FILM Y-DOPED ZrO <sub>2</sub> FOR ELECTRO-CHEMICAL DEVICE APPLICATIONS . . . . .	623
Brandon W. Chung, Eric L. Brosha, David R. Brown, and Fernando H. Garzon	
*IONIC CURRENT INDUCED MIGRATION OF A HOT SPOT IN GdBa <sub>2</sub> Cu <sub>3</sub> O <sub>7-δ</sub> CERAMICS . . . . .	629
T. Okamoto, B. Huybrechts, and M. Takata	
*FABRICATION OF V <sub>2</sub> O <sub>5</sub> THIN FILMS AND THEIR ELECTRO-CHEMICAL PROPERTIES IN LITHIUM MICROBATTERIES . . . . .	639
C. Julien, A. Gorenstein, A. Khelifa, J.P. Guesdon, and I. Ivanov	
EFFECT OF THE CRYSTALLINITY OF V <sub>6</sub> O <sub>13</sub> FILMS ON THE ELECTROCHEMICAL BEHAVIOR OF LITHIUM MICROBATTERIES . . . . .	649
A. Gorenstein, A. Khelifa, J.P. Guesdon, and C. Julien	
ELECTROCHROMISM AND PHOTOCHROMISM OF WO <sub>3</sub> THIN FILMS . . . . .	657
C. Lefrou, O. Marrot, and F. Garot	
HIGH RATE DEPOSITION OF NICKEL OXIDE ELECTROCHROMIC THIN FILMS BY REACTIVE DC MAGNETRON SPUTTERING . . . . .	663
Kazuki Yoshimura, T. Miki, and S. Tanemura	
*THIN FILM FUEL CELLS . . . . .	669
V.E.J. Van Dieten, J.P. Dekker, and J. Schoonman	
*THIN-FILM ELECTROLYTES FOR REDUCED TEMPERATURE SOLID OXIDE FUEL CELLS . . . . .	683
Steven J. Visco, Li-Shun Wang, Selmar Souza, and Lutgard C. De Jonghe	

\*Invited Paper

NANOSTRUCTURED ORGANIC/INORGANIC FILMS FROM POLY (D-LYSINE HYDROBROMIDE) OR POLY(N-METHYL-4-VINYL PYRIDINIUM BROMIDE) AND HECTORITE . . . . .	697
Elaine R. Kleinfeld and Gregory S. Ferguson	
ELECTRICAL PROPERTIES OF DONOR AND ACCEPTOR DOPED $Gd_2Ti_2O_7$ . . . . .	703
Igor Kosacki and Harry L. Tuller	
AUTHOR INDEX . . . . .	709
SUBJECT INDEX . . . . .	713

## Preface

This symposium proceedings on Solid State Ionics includes invited and contributed papers presented at the 1994 MRS Fall Meeting. The field of solid state ionics is enjoying significant activity due to several breakthroughs in materials aspects of rechargeable batteries, supercapacitors, sensors, electrochromics, catalysis, and ion exchange materials. Solid state chemistry and physics, materials science, and electrochemistry are the main contributors to the field of ionics. Material designers have shown capability of synthesizing materials with desired ionic-electronic properties, tailored surface area, crystal structure, and design porosity in terms of cavity size and geometry through templating action for specific applications in solid state ionic devices. Atomic and molecular simulation of large systems are also becoming a reality, which may help material designers to fine tune their synthetic approach and to prepare new materials. This proceedings volume features activities on solid state ionics with a stronger emphasis on materials aspects of rechargeable lithium batteries.

The first part of the proceedings deals with the chemistry and physics of insertion materials, mostly from the viewpoint of applications as cathode materials for rechargeable lithium batteries, Ni/Cd, and Ni/metal hydride systems. Crystal chemistry and electrochemical properties of potential oxide cathodes are discussed. The second part of the proceedings deals with the sol-gel process for preparation of cathode materials for lithium batteries and other applications. Novel synthetic methods for preparation of high surface area transition metal oxides are presented. The third part deals with theory of ion conduction in solids, as well as mechanisms of ion conduction in glassy and polymeric materials. Monte Carlo study of dispersive transport and high-frequency conductivity of crystalline and glassy solids are treated. Part four deals with defect chemistry in solid electrolytes and the role of defects on ionic conductivity of ceramic electrolytes. The fifth part of the proceedings deals with polymer electrolytes and electrodes. Synthesis, characterization and performance of various polymer electrolytes and electrodes are discussed. The sixth part of the proceedings deals with characteristics and materials aspects of ionic devices. This includes advanced solid state batteries, sensors, electrochromic devices, fuel cells, and the dynamics of ion exchange in  $\text{Hf-T}_c$  superconductors.

We would like to acknowledge the great contribution of participants, session chairs and students for making this symposium possible. Financial support from Department of Energy, Office of Naval Research, Bell Communication Research, and M. Braun Inc. are also acknowledged.

Gholam-Abbas Nazri  
Jean-Marie Tarascon  
Martha Schreiber

May 1995



---

## MATERIALS RESEARCH SOCIETY SYMPOSIUM PROCEEDINGS

---

- Volume 336—Amorphous Silicon Technology-1994, E.A. Schiff, A. Matsuda, M. Hack, M.J. Powell, A. Madan, 1994, ISBN: 1-55899-236-7
- Volume 337—Advanced Metallization for Devices and Circuits—Science, Technology, and Manufacturability III, S.P. Murarka, K.N. Tu, A. Katz, K. Maex, 1994, ISBN: 1-55899-237-5
- Volume 338—Materials Reliability in Microelectronics IV, P. Børgesen, W. Filter, J.E. Sanchez, Jr., K.P. Rodbell, J.C. Coburn, 1994, ISBN: 1-55899-238-3
- Volume 339—Diamond, SiC and Nitride-Wide-Bandgap Semiconductors, C.H. Carter, Jr., G. Gildenblat, S. Nakamura, R.J. Nemanich, 1994, ISBN: 1-55899-239-1
- Volume 340—Compound Semiconductor Epitaxy, C.W. Tu, L.A. Kolodziejski, V.R. McCrary, 1994, ISBN: 1-55899-240-5
- Volume 341—Epitaxial Oxide Thin Films and Heterostructures, D.K. Fork, J.M. Phillips, R. Ramesh, R.M. Wolf, 1994, ISBN: 1-55899-241-3
- Volume 342—Rapid Thermal and Integrated Processing III, J.J. Wortman, J.C. Gelpey, M.L. Green, S.R.J. Brueck, F. Roozeboom, 1994, ISBN: 1-55899-242-1
- Volume 343—Polycrystalline Thin Films—Structure, Texture, Properties and Applications, M. Parker, K. Barmak, R. Sinclair, D.A. Smith, J. Floro, 1994, ISBN: 1-55899-243-X
- Volume 344—Materials and Processes for Environmental Protection, C. Adkins, P.N. Gadgil, L.M. Quick, K.E. Voss, 1994, ISBN: 1-55899-244-8
- Volume 345—Flat Panel Display Materials, J. Batey, A. Chiang, P. Holloway, 1994, ISBN: 1-55899-245-6
- Volume 346—Better Ceramics Through Chemistry VI, C. Sanchez, M.L. Mecartney, C.J. Brinker, A. Cheetham, 1994, ISBN: 1-55899-246-4
- Volume 347—Microwave Processing of Materials IV, M.F. Iskander, R.J. Lauf, W.H. Sutton, 1994, ISBN: 1-55899-247-2
- Volume 348—Scintillator and Phosphor Materials, M.J. Weber, P. Lecoq, R.C. Ruchti, C. Woody, W.M. Yen, R.-Y. Zhu, 1994, ISBN: 1-55899-248-0
- Volume 349—Novel Forms of Carbon II, C.L. Renschler, D. Cox, J. Pouch, Y. Achiba, 1994, ISBN: 1-55899-249-9
- Volume 350—Intermetallic Matrix Composites III, J.A. Graves, R.R. Bowman, J.J. Lewandowski, 1994, ISBN: 1-55899-250-2
- Volume 351—Molecularly Designed Ultrafine/Nanostructured Materials, K.E. Gonsalves, G.-M. Chow, T.D. Xiao, R.C. Cammarata, 1994, ISBN: 1-55899-251-0
- Volume 352—Materials Issues in Art and Archaeology IV, P.B. Vandiver, J.R. Druzik, J.L. Galvan Madrid, I.C. Freestone, G.S. Wheeler, 1995, ISBN: 1-55899-252-9
- Volume 353—Scientific Basis for Nuclear Waste Management XVIII, T. Murakami, R.C. Ewing, 1995, ISBN: 1-55899-253-7
- Volume 354—Beam-Solid Interactions for Materials Synthesis and Characterization, D.E. Luzzi, T.F. Heinz, M. Iwaki, D.C. Jacobson, 1995, ISBN: 1-55899-255-3
- Volume 355—Evolution of Thin-Film and Surface Structure and Morphology, B.G. Demczyk, E.D. Williams, E. Garfunkel, B.M. Clemens, J.E. Cuomo, 1995, ISBN: 1-55899-256-1
- Volume 356—Thin Films: Stresses and Mechanical Properties V, S.P. Baker, P. Børgesen, P.H. Townsend, C.A. Ross, C.A. Volkert, 1995, ISBN: 1-55899-257-X
- Volume 357—Structure and Properties of Interfaces in Ceramics, D.A. Bonnell, U. Chowdhry, M. Rühle, 1995, ISBN: 1-55899-258-8

---

## MATERIALS RESEARCH SOCIETY SYMPOSIUM PROCEEDINGS

---

- Volume 358—Microcrystalline and Nanocrystalline Semiconductors, R.W. Collins, C.C. Tsai, M. Hirose, F. Koch, L. Brus, 1995, ISBN: 1-55899-259-6
- Volume 359—Science and Technology of Fullerene Materials, P. Bernier, D.S. Bethune, L.Y. Chiang, T.W. Ebbesen, R.M. Metzger, J.W. Mintmire, 1995, ISBN: 1-55899-260-X
- Volume 360—Materials for Smart Systems, E.P. George, S. Takahashi, S. Trolrier-McKinstry, K. Uchino, M. Wun-Fogle, 1995, ISBN: 1-55899-261-8
- Volume 361—Ferroelectric Thin Films IV, S.B. Desu, B.A. Tuttle, R. Ramesh, T. Shiosaki, 1995, ISBN: 1-55899-262-6
- Volume 362—Grain-Size and Mechanical Properties—Fundamentals and Applications, N.J. Grant, R.W. Armstrong, M.A. Ootoni, T.N. Baker, K. Ishizaki, 1995, ISBN: 1-55899-263-4
- Volume 363—Chemical Vapor Deposition of Refractory Metals and Ceramics III, W.Y. Lee, B.M. Gallois, M.A. Pickering, 1995, ISBN: 1-55899-264-2
- Volume 364—High-Temperature Ordered Intermetallic Alloys VI, J. Horton, I. Baker, S. Hanada, R.D. Noebe, D. Schwartz, 1995, ISBN: 1-55899-265-0
- Volume 365—Ceramic Matrix Composites—Advanced High-Temperature Structural Materials, R.A. Lowden, J.R. Hellmann, M.K. Ferber, S.G. DiPietro, K.K. Chawla, 1995, ISBN: 1-55899-266-9
- Volume 366—Dynamics in Small Confining Systems II, J.M. Drake, S.M. Troian, J. Klafter, R. Kopelman, 1995, ISBN: 1-55899-267-7
- Volume 367—Fractal Aspects of Materials, F. Family, B. Sapoval, P. Meakin, R. Wool, 1995, ISBN: 1-55899-268-5
- Volume 368—Synthesis and Properties of Advanced Catalytic Materials, E. Iglesia, P. Lednor, D. Nagaki, L. Thompson, 1995, ISBN: 1-55899-270-7
- Volume 369—Solid State Ionics IV, G-A. Nazri, J-M. Tarascon, M. Schreiber, 1995, ISBN: 1-55899-271-5
- Volume 370—Microstructure of Cement Based Systems/Bonding and Interfaces in Cementitious Materials, S. Diamond, S. Mindess, F.P. Glasser, L.W. Roberts, J.P. Skalny, L.D. Wakeley, 1995, ISBN: 1-55899-272-3
- Volume 371—Advances in Porous Materials, S. Komarneni, D.M. Smith, J.S. Beck, 1995, ISBN: 1-55899-273-1
- Volume 372—Hollow and Solid Spheres and Microspheres—Science and Technology Associated with their Fabrication and Application, M. Berg, T. Bernat, D.L. Wilcox, Sr., J.K. Cochran, Jr., D. Kellerman, 1995, ISBN: 1-55899-274-X
- Volume 373—Microstructure of Irradiated Materials, I.M. Robertson, L.E. Rehn, S.J. Zinkle, W.J. Phythian, 1995, ISBN: 1-55899-275-8
- Volume 374—Materials for Optical Limiting, R. Crane, K. Lewis, E.V. Stryland, M. Khoshnevisan, 1995, ISBN: 1-55899-276-6
- Volume 375—Applications of Synchrotron Radiation Techniques to Materials Science II, L.J. Terminello, N.D. Shinn, G.E. Ice, K.L. D'Amico, D.L. Perry, 1995, ISBN: 1-55899-277-4
- Volume 376—Neutron Scattering in Materials Science II, D.A. Neumann, T.P. Russell, B.J. Wuensch, 1995, ISBN: 1-55899-278-2

*Prior Materials Research Society Symposium Proceedings  
available by contacting Materials Research Society*

---

## PART I

---

### Insertion Compounds

## PULSE APPLICATIONS OF ELECTROCHEMICAL CELLS CONTAINING INSERTION REACTION ELECTRODES

ROBERT A. HUGGINS

Center for Solar Energy and Hydrogen Research, Helmholtzstr. 8, D-89081 Ulm, Germany

### ABSTRACT

There is a rapidly increasing interest in energy sources optimized to provide electrical energy at high power levels for short times. Applications include very short pulses for digital electronic devices, the somewhat longer power pulse demands of some implantable medical devices, and the much larger transient power needs in connection with vehicle traction.

Several mechanisms can be used to provide short term energy, with fundamentally different characteristics and applicability to different types of transient output requirements.

Four different electrochemical methods can be used to evaluate the critical materials parameters in insertion reaction materials that might be applicable to such applications, and spreadsheet techniques can be used to model the transient transport behavior of such electrodes under various conditions. LaPlace transform methods can then be used to convert information about the physical mechanisms and parameters of individual components into the dynamic response of an electrochemical system.

### INTRODUCTION

There is increasing interest in the use of electrochemical systems under conditions in which the electrical power demand is highly time - dependent, often in the form of short term pulses. This has led to efforts to develop electrical devices that are optimized in terms of their short-term power output, rather than total energy content.

Because of the general observation that capacitors can be used to provide short electrical pulses, attention has been focussed upon the concept of electrochemical systems that exhibit capacitor-like characteristics. These can typically store much more charge than the conventional type of physical dielectric capacitor.

The range of both current and potential future requirements and applications is very broad. Typical examples that are now highly visible include digital communication devices that require pulses in the millisecond range, implanted medical devices, that require pulses with characteristic times of the order of seconds, and vehicle traction applications, where the high power demand can extend from seconds up to minutes.

These all require output characteristics that are different from those that are normally considered for electrochemical systems, which are typically more oriented toward energy storage and output at lower power levels.

A typical pulse output requirement for a digital communication device has a number of millisecond-length pulses with currents of 2.5 A, on top of a 15 millisecond square wave at 2 A. This is followed by a "recovery period" of 75 milliseconds at a much lower current, only 0.25 A.

The test procedure that is now used for batteries that are to be used for subcutaneous heart defibrillators has a group of four 10-second pulses with current densities of 20 mA/cm<sup>2</sup>, scaled to the macroscopic surface area of the battery electrodes, is repeated every 30 minutes.

The characteristics needed to meet the requirements for electric vehicles have been formulated in terms of several different types of duty cycles that are assumed to simulate typical usage demands. They require significant amounts of power over longer times, of the order of minutes.

Because of the great variation in the requirements for transient power sources, it is unrealistic to assume that any one type of device, or any one design, will be able to optimally fulfill them all.

It is now quite common to think in terms of hybrid systems that include components that can meet two different types of needs, a primary energy source, and a supplemental source that can meet the transient needs for higher power levels than can be handled by the primary source. This

combination can be represented schematically in terms of the commonly - used Ragone type of diagram, in which the specific power is plotted versus the specific energy, both on logarithmic scales, as shown in Fig. 1.

A possible strategy is to use a high energy system that operates at a relatively high voltage when the power demand is low. The output voltage of such energy sources typically falls off as the output current is increased. If a second high-power, but lower-energy source that operates at a lower voltage is placed in parallel, it will take over under the conditions that drive the output voltage of the primary high-energy system down into its range of operating voltage, and meet the high-power demand for a short period. When this demand is no longer present, the voltage will again rise, and the high-power component of the system will be recharged by the higher-energy component. This combination is also shown schematically in Fig. 1.

The way that the properties of batteries are typically described, such as by a graphical display of the discharge (voltage vs. state of charge) curves at different constant current densities, or in terms of the change of extractable capacity as a function of the number of discharge cycles, cannot be considered to provide a satisfactory description of behavior in these very different types of applications. Likewise, the value of the capacitance at a single frequency is also certainly not a satisfactory description of the behavior of a capacitor over such a wide range of potential uses.

In order to approach the development of useful devices for this type of application one should consider the several types of charge storage mechanisms that can be employed, their thermodynamic and kinetic characteristics, and the basic properties of candidate materials, as well as the relationships that determine system performance.

## ELECTROCHEMICAL CHARGE STORAGE MECHANISMS

There are four basic types of charge storage mechanisms in electrochemical systems.

### A. The storage of charge in the electrical double-layer within the electrolyte in the vicinity of the electrolyte/electrode interface.

In this approach the electrode is considered to be chemically inert. The amount of charge that can be stored is of the order of 15-40 microfarads per  $\text{cm}^2$  of interface [1,2]. Thus one tries to optimize the amount of interface in the device microstructure. Techniques have been devised to produce various types of carbon, as well as some other electronically conducting, but chemically inert, materials in very highly dispersed form, leading to very large interfacial areas.

A device in which this is the dominant charge storage mechanism will behave like a pure capacitor in series with its internal resistance. Although there is some confusion in the literature about terminology, devices of this type that have been developed with large values of such capacitance are generally called either EDLC devices [3], or "ultracapacitors" [1,2].

Ultracapacitor devices utilizing the storage of charge in the electrochemical double layer have been developed and produced in large numbers in Japan for a considerable period of time [3]. These are primarily used for semiconductor memory backup purposes, as well as for several types of small actuators.

### B. Underpotential Faradaic two-dimensional adsorption on the surface of a solid electrode.

Due to the characteristics of the electrolyte/electrode surface structure and its related thermodynamics, it is often found that modest amounts of Faradaic electrodeposition can occur at potentials somewhat removed from those needed for the bulk deposition of a new phase. This results in the occupation of specific crystallographic surface sites. This mechanism typically results in only partial surface coverage, and thus the production of an "adsorption pseudocapacitance" of some 200-400  $\text{mF/cm}^2$  of interface [2]. This is significantly larger than the amount of charge stored per unit area in the electrochemical double layer.



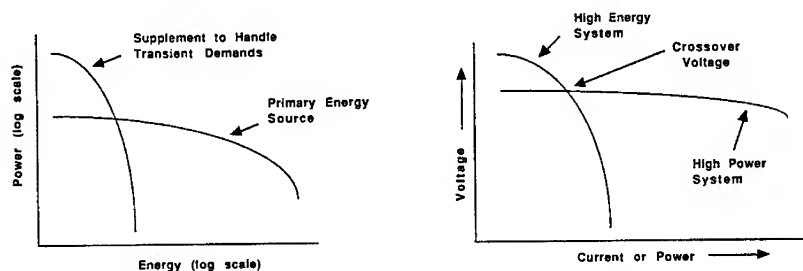


Figure 1. Typical hybrid system characteristics (left), and schematic representation of possible hybrid system strategy (right).

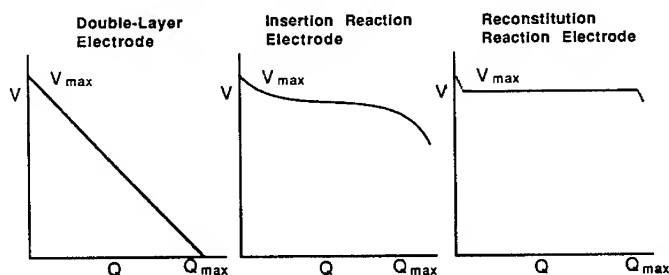


Figure 2. Comparison between different types of energy storage mechanisms. Left, double-layer electrode, Middle, insertion reaction electrode, and Right, reconstitution reaction electrode.

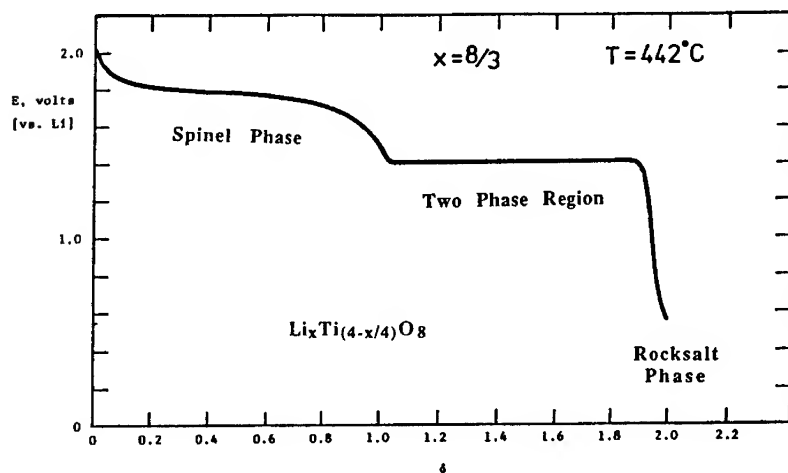


Figure 3. Discharge curve of a composition in the Li-Ti-O ternary system showing the occurrence of both insertion and reconstitution reactions in lithium cell.

C. Faradaic deposition that results in the three-dimensional absorption of the electroactive species into the bulk solid electrode material by an insertion reaction.

Many materials are now known that can act as solid solution electrodes. In such cases, the electroactive species diffuses into the interior of the crystal structure of the solid electrode. Since the amount of energy stored is proportional to the amount of the electroactive species that can be absorbed by the electrode, this bulk storage mechanism can lead to much higher values of energy storage per unit volume of electrode structure than can any surface-related process. Because it makes no sense to express this bulk phenomenon in terms of the capacitance per unit interfacial area, values are generally given as Farads per gram.

This mechanism has been called "redox pseudo-capacitance" by the Conway group [1,2], who also first started the use of the term "supercapacitors" to describe devices utilizing this type of charge storage. In this way, bulk storage "supercapacitors" can be distinguished from double-layer storage "ultracapacitors".

The bulk storage "supercapacitor" mechanism is utilized in the devices that are most interesting for energy-sensitive pulse applications. Since the kinetic behavior of such devices is related to the electrolyte/electrode area, it is useful to have very fine microstructures in such devices.

In contrast to the Japanese development and production of "ultracapacitors" shown in Table 1, work on the development of bulk-storage "supercapacitors" has been much less visible. It started in Canada about 1975, the key players being D.R. Craig [4,5] and B.E. Conway. This soon evolved into a proprietary development program at the Continental Group, Inc. laboratory in California, which subsequently was taken over by Pinnacle Research Institute. The products that were developed and manufactured were all oriented toward the military market. This orientation is changing now, and a joint activity is being undertaken with the Westinghouse Electric Corp. to produce these products for the civilian market. Activities in this area have also been initiated more recently in Europe.

D. Faradaically-driven reconstitution reactions.

The electrodes in many battery systems undergo reconstitution reactions, in which different phases form and others are consumed. In accordance with the Gibbs Phase Rule, this often results in an open-circuit electrode potential that is independent of the state of charge. The amount of charge storage is determined by the characteristics of the related phase diagram, and can be quite large. Some reactions of this type can also have relatively rapid kinetics. However, there is a potential difficulty in the use of this type of reaction in applications that require many repeatable cycles, for they generally involve microstructural changes that are not entirely reversible. Thus the possibility of a cycle-life limitation must be kept in mind.

A special strategy whereby this microstructural irreversibility may be avoided in certain cases has been proposed [6]. This involves the use of an all-solid electrode in which a mixed-conducting solid matrix phase with a very high chemical diffusion coefficient surrounds the reactant phases.

## COMPARATIVE MAGNITUDES OF ENERGY STORAGE

The maximum amount of energy that can be stored in any device is the integral of its voltage-charge product, and cannot exceed the product of its maximum voltage and the maximum amount of charge it can store. On this basis, we can make a simple comparison between these different types of energy storage mechanisms.

The results are shown schematically in Fig. 2, in which the relationship between the potential and the amount of charge delivered is plotted for three different types of systems, a double-layer electrode, an insertion reaction electrode, and a reconstitution reaction electrode. Electrodes that involve two-dimensional Faradaic underpotential deposition are not included, as they do not constitute a practical alternative.

In the case of a true capacitor, the amount of charge stored is a linear function of the applied voltage. Thus, as shown on the left side of Fig. 2, the voltage falls off linearly with the amount of charge delivered.

A single phase solid solution insertion-reaction type of electrode characteristically has a potential-charge relation of the type shown in the middle. The thermodynamic basis for this shape, in which the potential is composition-dependent, and thus state of charge-dependent, will be discussed below.

The characteristic behavior of a reconstitution-reaction electrode system is shown on the right side. In this case, it is assumed that the number of components is equal to the number of phases, so that from a thermodynamic point of view there are no degrees of freedom. This means that all of the intensive variables, including the electrode potential, are independent of the overall composition, and thus independent of the amount of charge delivered. Thus the discharge characteristic consists of a voltage plateau.

The maximum amount of energy that is available in each case is the area under the  $V/Q$  curve. It is seen that the maximum amount of energy that can be stored in an electrode that behaves as a capacitor is  $1/2 (V_{\max})(Q_{\max})$ . The actual amount of available energy will, of course, depend upon the power level, due to unavoidable losses, such as that due to the inevitable internal resistance of the system.

The features and parameters that determine the values of  $V_{\max}$  and  $Q_{\max}$ , as well as the maximum amount of energy that can be stored by these three mechanisms are shown in Table 1.

Table 1.

**Parameters That Determine the Values of Maximum Potential, Maximum Charge, and Maximum Energy Stored**

Type of Electrode	$V_{\max}$ Determined By
Double-layer capacitor	The electrolyte stability window
Insertion reaction	Thermodynamics of guest-host phase
Reconstitution reaction	Thermodynamics of phase reactions
Type of Electrode	$Q_{\max}$ Determined By
Double-layer capacitor	Electrode microstructure, electrolyte
Insertion reaction	Mass of electrode, thermodynamics
Reconstitution reaction	Mass of electrode, thermodynamics
Type of Electrode	Maximum energy stored
Double-layer capacitor	50 % of $(V_{\max})(Q_{\max})$
Insertion reaction	About 80 % of $(V_{\max})(Q_{\max})$
Reconstitution reaction	About 90% of $(V_{\max})(Q_{\max})$

## THE CONCEPT OF ENERGY QUALITY

The quality of heat is a commonly used concept in engineering thermodynamics. High temperature heat is generally much more useful than low temperature heat. Thus, in considering a practical thermal system one has to consider both the amount of heat and its quality (the temperature at which it is available).

We can consider an analogous situation in the application of energy storage devices and systems. In such cases, in addition to the total amount of energy that can be stored, one also should consider the voltage at which it is available. Thus it is useful to introduce the concept of

energy quality. We can make a rough scale, with high quality energy being that which is available over 2 V, medium quality energy that which is available between 1 and 2 V, and low quality energy that which is available at less than 1 V.

If we take this factor into account, we see an additional difference between systems that utilize electrodes that operate by these three different mechanisms. This is indicated in Table 2, in which the amount of higher value energy available in the different cases is compared, using the simple criterion that energy at a potential above  $V_{\max}/2$  is considered to be high value energy

**Table 2.**

**Maximum Amount of High Value Energy Available**

Type of Electrode	High Value Energy ( $V > V_{\max}/2$ )
Double-layer capacitor	12.5 %
Insertion reaction	About 30 %
Reconstitution reaction	About 40 %

**EXAMPLES OF SYSTEMS WITH BOTH INSERTION REACTION AND RECONSTITUTION REACTIONS**

In some cases, the insertion of species into an electrode can result in both insertion and reconstitution reactions. This is the case for the insertion of hydrogen into  $MnO_2$  in the common  $Zn/MnO_2$  cell. In that case, approximately half a mol of hydrogen can enter the  $MnO_2$  structure by insertion. Further reaction requires the formation of a new phase, and is much slower. This second, reconstitution, reaction is not used in practical applications.

Another example is the reaction of lithium with materials in the lithium-titanium-oxygen system [7]. A number of phases can form in different composition regions within this ternary system.

It has been found that if one starts at the lithium - poor end of the spinel phase stability region, about one mol of lithium can be added by insertion into the host spinel structure. The addition of further lithium results in the nucleation and growth of a new phase with a much higher lithium content that has the rocksalt structure. The resulting discharge curve, shown in Fig. 3, clearly indicates the effect of these two mechanisms upon the composition - dependence of the electrode potential.

**THE INFLUENCE OF COMPOSITION ON THE POTENTIAL OF INSERTION REACTION ELECTRODES**

It has been shown that materials in which the charge is stored by the use of solid state insertion reactions are most useful for applications in which both the amount of energy stored and the cycle life are important. Thus it is worthwhile to consider what is known about the composition dependence of the potential of such materials. If this is measured under open circuit conditions, it is commonly known as the coulometric titration curve.

In such cases, the electrode potential is determined by the electrochemical potential of the electroactive guest species in the solid, which can be formally divided into two components, the contribution due to the electron energy band structure of the host material, and that due to the enthalpy and entropy values of the guest ions.

In the case of a random solid solution the two major contributions are the contribution from the Fermi level of the degenerate electron gas that is characteristic of such mixed conductors, and that due to the configurational entropy of the guest ions in the host crystal lattice [8].

If we assume that the electrons can be treated as fully degenerate, the chemical potential of the electrons is directly related to the Fermi level,  $E_F$ , which can be written as

$$E_F = (\text{Constant}) ((x)^{2/3} / m^*)$$

where  $m^*$  is the effective mass of the electrons.

The configurational entropy of guest ions, assuming random mixing, and a concentration  $x$ , statistically distributed among  $x^0$  lattice sites of equal energy, is

$$S = -R \ln [x/(x^0 - x)]$$

Thus the electrode potential can be written in general form as

$$E = (\text{Constant}) (x^{2/3}) - (RT/nF) \ln (x/(1-x))$$

Thus the value of the electron effective mass influences the general slope of the composition-dependent open circuit electrode potential. Larger effective masses make the potential less composition - dependent.

#### EXPERIMENTAL DETERMINATION OF THE CRITICAL PROPERTIES OF POTENTIAL ELECTRODE MATERIALS

In order to determine the response of electrodes to different requirements one needs to have basic information about the relevant parameters of the electrochemically active materials involved. The most important properties of electrode materials are:

1. the potential, and its dependence upon the state of charge,
2. the capacity, i.e. the maximum amount of charge that can be stored or supplied, and
3. the kinetic behavior under various conditions.

The actual behavior of electrodes may deviate from the properties of their electrochemically active components, of course. This may be due to non-uniform reaction under dynamic conditions or microstructural inaccessibility of the active material due to the presence of blocking constituents, for example. Thus information about the basic properties of the electroactive components themselves represents the limiting case. Actual performance may be less attractive.

Several electrochemical methods have been developed by which information about insertion reaction electro-active components can be obtained. These include:

1. the Galvanostatic Intermittent Titration Method (GITT) [9],
2. the Potentiostatic Intermittent Titration Method (PITT) [10]
3. the Faradaic Intermittent Titration Method (FITT) [10], and
4. the Alternating Current (Wechselstrom) Intermittent Titration Method (WITT) [11].

In each case, stepwise measurement of the electrochemical titration curve is accompanied by an evaluation of the kinetic behavior after each step. Thus one can simultaneously obtain both thermodynamic and kinetic information as a function of electrode composition (the extent of reaction).

The kinetic measurement parts of these four methods have been discussed in detail elsewhere [10,12], and can be represented schematically as shown in Fig. 4 [12], in which the controlled (independent) variables, and the type of response of the relevant dependent variables are shown.

The design of these different methods and the analysis of the data obtained are both based upon the analytical solution of the diffusion equations under various relevant initial and boundary conditions.

The most important parameter relating to the transient behavior of a solid material that operates by an insertion reaction mechanism is the chemical diffusion coefficient. This quantity can be much greater than the self, or component, diffusion coefficient that is often evaluated by the use of radiotracer or nuclear magnetic measurement techniques because of the enhancement factor  $W$ . This factor results from the influence of a concentration gradient upon the interaction between the different particle fluxes involved in the mass transport process in the solid. This will not be



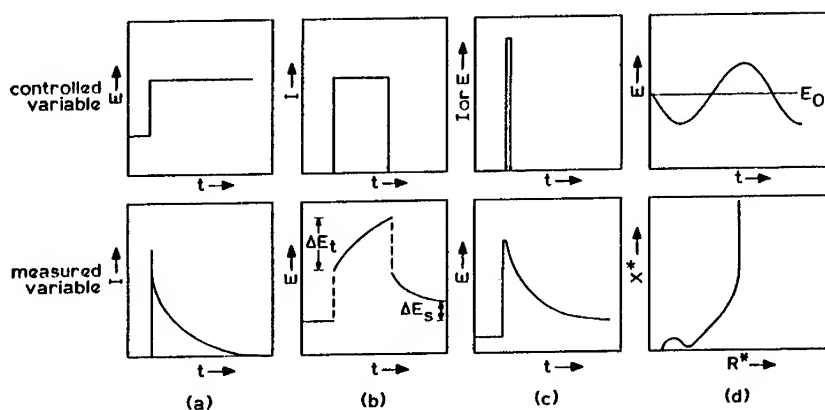


Figure 4. Schematic representation of four experimental methods that can be used to determine the chemical diffusion coefficient in mixed-conducting electrode materials. (a) potential jump, (b) current pulse, (c) relaxation after Faradaic pulse, (d) steady state AC.

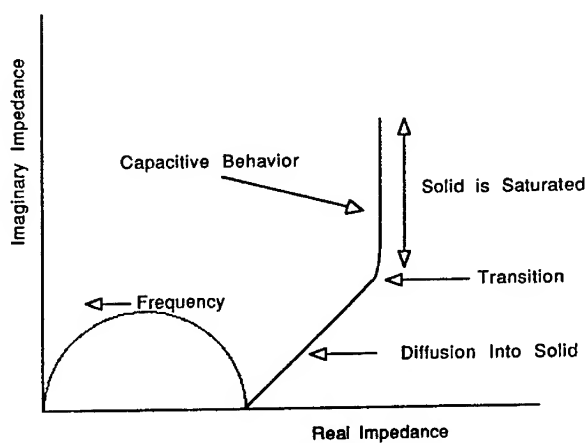


Figure 5. Schematic representation of the frequency dependence of the complex impedance of an insertion reaction electrode.

discussed here, as it can readily be found elsewhere [9,13] The important point is, however, that  $W$  can be very large in some mixed conductors, so that one has to be careful about using data obtained by the use of experimental methods that do not employ concentration gradients. In one example, it was shown to reach values of about 70,000 [9].

In the GITT method, the time dependence of the potential after a current step can be expressed as

$$\frac{dE}{dt^{1/2}} = \left[ \frac{2 I V_m}{z F S D^{1/2} p^{1/2}} \right] \left[ \frac{dE}{dy} \right] \quad \text{if } t \ll (x^2/D)$$

Here,  $V_m$  is the molar volume,  $z$  the charge carried by the electroactive species,  $F$  the Faraday constant,  $y$  the stoichiometric parameter, and  $S$  the surface area.

Alternatively,  $D$  may be evaluated from an experiment in which a current step of finite length is applied, using the simplified expression

$$D = \left[ \frac{4 x^2}{p t} \right] \left[ \frac{DE_s}{DE_t} \right]^2 \quad \text{if } t \ll (x^2/D)$$

where  $t$  is the time duration of the current step,  $DE_s$  is the change in the equilibrium open circuit voltage resulting from the current pulse, and  $DE_t$  is the total transient voltage change, after eliminating the IR drop.

For a fixed value of  $(dE/dy)$ , the dependence of  $E$  on  $t$  will be linear at long times and the diffusion coefficient can be evaluated from

$$E - E(t=0) = \frac{I V_m}{z F S} \frac{x}{3 D} \left[ \frac{dE}{dy} \right] \quad \text{if } t \gg (x^2/D)$$

In the case of the PITT method, the current varies with time after the imposition of a potential step. At short times, the time dependence of the current can be approximated by

$$I = \frac{Q D^{1/2}}{2 x p^{1/2}} [t^{-1/2}] \quad \text{if } t \ll x^2/D$$

where  $Q$  is the total charge passed following the potential step, and  $x$  is the distance parameter into the solid.

At long times it becomes

$$I = \frac{2 Q D}{x^2} \exp \left[ -\frac{p^2 D t}{4 x^2} \right] \quad \text{if } t \gg (x^2/D)$$

In the FITT method, a given amount of electroactive solute material is deposited onto, or into, the surface of the electrode material. As it diffuses into (or out of) the underlying bulk material under open circuit conditions, the surface composition will gradually approach the value characteristic of a uniform solute distribution. The time dependence of the potential is thus

$$\frac{dE}{d(1/t^{1/2})} = \frac{Q V_m}{z F S D^{1/2} p^{1/2}} \left[ \frac{dE}{dy} \right] \quad \text{if } t \ll (x^2/D)$$

The WITT method involves the use of small signal alternating current methods to evaluate diffusion in a solid. Without going into the details of the method, which can be found elsewhere [11,12], the type of result that is obtained is illustrated in Fig. 5. Under ideal conditions and one-dimensional diffusion into a semi-infinite solid, the response is dominated by the diffusional admittance at low frequencies. In the case of thin films, the range of frequency in which diffusion

dominates the observed behavior can be limited. At even lower frequencies, below a critical value given by

$$\omega = 2 D/x^2$$

where  $D$  is the chemical diffusion coefficient, and  $x$  the dimensional parameter, there is sufficient time for the solid composition to stay saturated at the value related to the time-varying imposed potential. When that is the case, the sample electrode has the characteristics of a capacitor, for its composition varies with the applied potential.

The analytical solution to this problem has been obtained for two important cases, one-dimensional diffusion in a slab whose thickness is large compared to the depth of penetration of the diffusion profile, i.e.  $x^2 \gg D/\omega$ , and one-dimensional diffusion into a thin layer of material under conditions that compositional saturation is achieved, i.e.  $x^2 \ll D/\omega$ .

In the first (thick layer) case, the phase difference between the current and the potential is independent of the frequency, and is equal to  $45^\circ$ . The impedance related to diffusion of the electroactive species is then

$$|Z| = \left| \frac{V_m}{z F S D^{1/2}} \frac{dE}{dy} (\omega^{-1/2}) \right|$$

In the thin layer case the current is  $90^\circ$  out of phase with the potential, and is independent of the diffusion coefficient. The real part of the complex impedance ( $R$ ) is

$$R = \frac{|Z| \omega x^2}{3 D S}$$

and the imaginary part ( $X$ ) is

$$X = |Z| = \left| \frac{V_m}{z F \omega x S} \frac{dE}{dy} \right|$$

The limiting low frequency capacitance  $C_l$  and resistance  $R_l$  are given by

$$C_l = \omega X = \omega |Z|$$

and

$$R_l = \left| \frac{V_m}{z F S} \frac{1}{3 D} \frac{dE}{dy} \right|$$

The good correspondence obtained by the use of these four different methods is shown in Fig. 6, in which the composition dependence of the measured values of the chemical diffusion coefficient in the phase "LiAl" is plotted. Also shown is the data point of L'vov et al. [14].

## THE USE OF SPREADSHEET METHODS TO MODEL THE TRANSIENT BEHAVIOR OF INSERTION REACTION ELECTRODES

It is relatively simple to use the common personal computer spreadsheets, such as EXCEL, to numerically solve differential equations by a type of finite element method. An example is the solution of the diffusion equation under various initial and boundary conditions. Thus if one has information about the chemical diffusion coefficient, one can readily obtain the time evolution of the concentration profile within a solid solution electrode material, and also obtain the time dependence of the current, the total charge, or the interfacial potential.

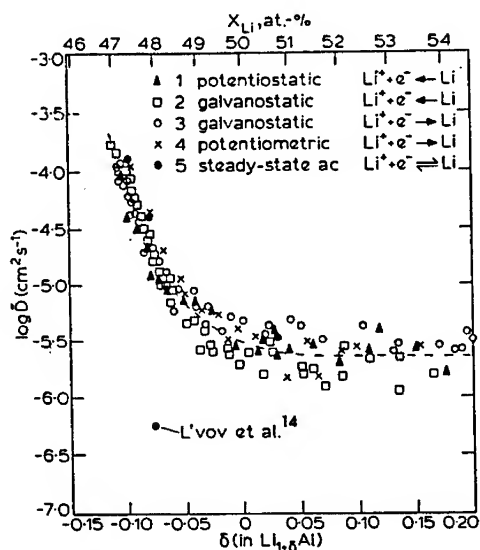


Figure 6. Composition dependence of the chemical diffusion coefficient evaluated by the use of the four different methods.

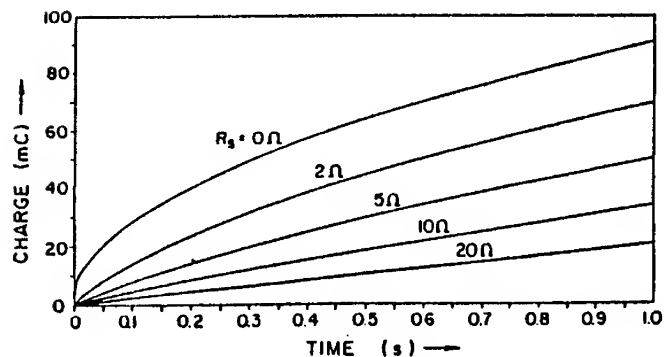


Figure 7. The influence of the value of series resistance on the time dependence of the current after the imposition of a potential step.

In that case, the values in the individual cells indicate the local values of the concentration of the electroactive species. The different rows indicate the distance each cell is from the electrolyte/electrode interface, and the columns contain data at different times.

One inserts the initial conditions, e.g. the values of the starting composition as a function of distance, into the first column. The boundary conditions are put into the first row. Fick's first law is then put into each cell in order to determine the relationship between its local composition and the compositions of its neighboring cells. This is essentially a calculation of the local composition change due to the difference between the incoming and outgoing particle fluxes.

One can then use the plotting facilities of the spreadsheet program to obtain the time and distance dependence of the composition under various initial and boundary conditions.

The time dependence of the concentration profile following the imposition of a current step, instead of a potential step, can also be determined. We can change the values of the related constants, and take values out of the spreadsheet to see how this time dependence varies with the magnitude of the current or the diffusion coefficient.

Another common situation in pulse applications is that the energy storage device is given a rest period, during which it is required to supply very little, or perhaps no, power. In the latter case this means that no current crosses the electrolyte/electrode interface. One can easily introduce this boundary condition into the spreadsheet at any time after a prior composition profile has developed as the result of current that has flowed through the system. Following this, the existing composition profile in the solid gradually relaxes, and the solute becomes more uniformly distributed throughout the bulk material. As this happens, the composition adjacent to the surface gradually shifts, causing a resulting time-dependent change in the potential.

## MODELLING THE SYSTEM BEHAVIOR

Several electrochemical methods that have been developed in order to experimentally determine the critical parameters of materials that might be employed in energy storage systems used to supply pulse power have already been discussed. In addition, it has been shown that one can use spreadsheet methods to determine the behavior of components containing these materials under various different imposed initial and boundary conditions.

The quantitative understanding of the application of these components in actual devices requires knowledge of the relationship between component properties and system behavior, for systems typically involve more than one component. As an example, in addition to the electrode impedances, there are almost always resistive impedances present, both relating to internal phenomena and to external factors.

A useful way to handle this problem in electrochemical systems is to follow the lead of the electrical engineering community, which is based upon the general concept of a relation between a driving force and the response of a device or system to it [15]. This relation can be written very generally as:

$$\text{Driving Function} = (\text{Transfer Function}) * (\text{Response Function})$$

The driving function represents the demands imposed by the application, and the response function is the output of the energy source subject to these demands. The key element of this approach is the determination of the (time-dependent) transfer function of the device or system, for that determines the relationship between application demand and system output.

The general method that has been developed for device and circuit analysis involves the use of Laplace transform techniques. There are several general steps in this analysis. They involve:

- the determination of the transfer function of the individual components,
- the calculation of the transfer function of the total system,
- the introduction of the driving function determined by the application, and finally,
- the calculation of the system (energy source) output.

Some readers of this paper may not be familiar with LaPlace transform methods. They can be readily understood by the use of an analogy. Consider the use of logarithms to multiply two numbers, e.g. A and B. The general procedure is to find the logarithms (transforms) of both A and B, to add them together, and then to use antilogarithms to reconvert the sum of the logarithms (transforms) into a normal number.

The response of insertion reaction electrodes and simple systems under various conditions by the use of this approach have been presented in [16].

The time dependence of the current after the imposition of a step potential of  $F_0$  for the case of a resistance in series with an insertion reaction electrode was found to be

$$i(t) = (F_0/R) \exp \left[ \left( \frac{Q_2}{R} \right) t \right] \operatorname{erfc} \left[ \frac{Q t^{1/2}}{R} \right]$$

and the charge accumulated (or produced) in the case of this combination was found to be

$$q(t) = \frac{F_0 R}{Q^{1/2}} \left[ \exp \left[ \left( \frac{Q}{R} \right)^2 t \right] \operatorname{erfc} \left[ \frac{Q t^{1/2}}{R} \right] - 1 \right] + \frac{2 F_0}{Q} \left( \frac{t}{p} \right)^{1/2}$$

The influence of the value of the series resistance can readily be seen in Fig. 7.

This LaPlace transform procedure is thus an alternative to the more conventional analytical approach. Its real value becomes clearer, however, under more complex conditions, such as when more than one component is present, and in which the normal analytical procedures become quite cumbersome.

## SUMMARY

The use of electrochemical devices and systems under conditions that require pulse output imposes requirements that are quite different from those typical of other, more traditional, applications.

Consideration has been given to the question of the most appropriate general strategy to follow to select and evaluate materials for this type of application. It was shown that there are three principal choices, materials that act as double-layer capacitors, materials that undergo insertion reactions, and reconstitution reaction systems.

Those that act as double-layer capacitors represent a relatively unattractive option for applications that require a substantial energy output. Reconstitution reactions, which involve a change in the phase constitution of the microstructure, may present problems in applications in which a long cycle life is required. Insertion reaction materials thus represent the best general approach, and are used in the devices based upon materials with the  $\text{SnO}_2$  type of crystal structure that presently show the best transient performance.

The critical materials properties include the thermodynamic parameters that determine the potentials and capacities, evaluated experimentally in terms of the coulometric titration curve, and kinetic parameters, the most important of which is the chemical diffusion coefficient. In a number of cases the analytical solutions to the diffusion equation also require information about the local slope of the titration curve.

Four different types of experimental methods have been developed to obtain quantitative data about these basic properties of potential materials. A series of investigations has demonstrated the very consistent results that can be obtained from these different techniques, as well as their good correspondence with theoretical expectations.

If one has information about the chemical diffusion coefficient for a given material, its kinetic properties as an electrode reactant can be calculated using the appropriate analytic solution of the diffusion equation. Alternatively, one can use computer spreadsheet methods to obtain numerical solutions under various initial and boundary conditions.

Actual devices, however, generally consist of several components, and the overall kinetic behavior is dependent upon their interaction. LaPlace transform methods can be utilized for this

purpose. In order to do this, one needs to know both the driving function imposed by the application and the system transfer function. The latter can be obtained from the proper combination of the transfer functions of the individual components.

The system behavior has been calculated for several situations by use of this method, and it has been shown that the results are consistent with those obtained by the analytical solution of the diffusion equation for individual components. In addition, this methodology has been employed to evaluate the system behavior in a more cumbersome case, the time dependence of the current after the imposition of a voltage step when a resistance is in series with an insertion reaction electrode.

## REFERENCES

- [1] B. E. Conway, "Transition From 'Supercapacitor' to 'Battery' Behavior in Electrochemical Energy Storage", *J. Electrochem. Soc.* **138**, 1539 (1991).
- [2] B. E. Conway, "Origin and Significance of "Redox Supercapacitance" and its Manifestation at Various Inorganic Materials", in Proceedings of Symposium on New Sealed Rechargeable Batteries and Supercapacitors, B. M. Barnett, E. Dowgiallo, G. Halpert, Y. Matsuda and Z. Takeharas, Eds., The Electrochemical Society (1993), p. 15.
- [3] A. Nishino, "Development and Current Status of Electric Double Layer Capacitors", in Proceedings of Symposium on New Sealed Rechargeable Batteries and Supercapacitors, B. M. Barnett, E. Dowgiallo, G. Halpert, Y. Matsuda and Z. Takeharas, Eds. The Electrochemical Society (1993), p. 1.
- [4] D. R. Craig, Canadian Patent 1,196,683 (1985).
- [5] D. R. Craig, "Electric Energy Storage Devices", European Patent Application 82,109,061.0, submitted 30 September, 1982, Publication No. 0 078 404, 11 May 1983.
- [6] B. A. Boukamp, G. C. Lesh and R. A. Huggins, "All-Solid Lithium Electrodes with Mixed-Conductor Matrix", *J. Electrochem. Soc.* **128**, 725 (1981).
- [7] B. E. Liebert, W. Weppner and R. A. Huggins, "Evaluation of Lithium Titanates as Cathode Material", in Proceedings of Symposium on Electrode Materials and Processes for Energy Conversion and Storage, J.D.E. MacIntyre, S. Srinivasan, F. G. Will, Eds. Electrochem. Soc. (1977), p. 821.
- [8] I. D. Raistrick, A. J. Mark and R. A. Huggins, "Thermodynamics and Kinetics of the Electrochemical Insertion of Lithium Into Tungsten Bronzes", *Solid State Ionics* **5**, 351 (1981).
- [9] W. Weppner, and R. A. Huggins, "Determination of the Kinetic Parameters of Mixed-Conducting Electrodes and Application to the System  $\text{Li}_3\text{Sb}$ ", *J. Electrochem. Soc.* **124**, 1569 (1977).
- [10] W. Weppner and R. A. Huggins, "Electrochemical Methods for Determining Kinetic Properties of Solids" in Annual Review of Materials Science, R. A. Huggins, Ed. Annual Reviews, Inc. (1978), p. 269.
- [11] C. Ho, I. D. Raistrick and R. A. Huggins, "Application of AC Techniques to the Study of Lithium Diffusion in Tungsten Trioxide Films", *J. Electrochem. Soc.* **127**, 343 (1980).
- [12] C. J. Wen, C. Ho, B.A. Boukamp, I.D. Raistrick, W. Weppner, and R.A. Huggins, "Use of Electrochemical Methods to Determine Chemical Diffusion Coefficients in Alloys: Application to 'LiAl'", *International Metals Reviews* **5**, 253 (1981).
- [13] C. Wagner, "Investigations on Silver Sulphide", *J. Chem. Phys.* **21**, 1819 (1953).
- [14] A. L. L'vov, et al., *Elektrokhimiya* **11**, 1322 (1975).
- [15] I. D. Raistrick and R. A. Huggins, "The Transient Response of Electrochemical Systems Containing Insertion Reaction Electrodes", *Solid State Ionics* **7**, 213 (1982).
- [16] I. D. Raistrick and R. J. Sherman, "Electrical Response of Electrochemical Capacitors Based on High Surface Area Ruthenium Oxide Electrodes", in Proceedings of Symposium on Electrode Materials and Processes for Energy Conversion and Storage, S. Srinivasan, S. Wagner, and H. Wroblowa, Eds. Electrochem. Soc. (1987), p. 582.

## TRANSITION METAL OXIDES FOR ROCKING-CHAIR CELLS

M. M. THACKERAY

Argonne National Laboratory, Electrochemical Technology Program, Argonne, Illinois, USA

E. FERG, R. J. GUMMOW, and A. de KOCK

CSIR, Division of Materials Science and Technology, Pretoria, South Africa

### ABSTRACT

Transition metal oxides have been evaluated extensively in the past as cathode materials for lithium cells. The major emphasis of recent research has been to develop lithium-ion or rocking-chair cells that are assembled in the discharged state with a lithiated transition metal oxide cathode and a carbon anode. Although these cells are significantly safer to use than lithium cells with metallic lithium anodes, the possibility of depositing lithium at the surface of the carbon particles at the top of charge or at high rates of charge cannot be discounted. This paper discusses some recent developments in fabricating rocking-chair cells with transition metal oxide host structures as both anode and cathode, the anode providing a relatively low voltage vs. lithium and the cathode a relatively high voltage vs. lithium. These cells avoid the reduction and oxidation of lithium during charge and discharge and, therefore, reduce the safety hazards of lithium cells. Improved safety is gained, however, at the expense of cell voltage and specific energy.

### INTRODUCTION

Lithium-ion technology makes use of insertion compounds at both the anode and cathode of electrochemical cells [1]. During discharge, lithium ions are released from an anode host structure and inserted into a cathode host with concomitant oxidation and reduction processes taking place at the anode and cathode. The reverse processes occur during charge. The name "rocking-chair cell" refers to the to-and-fro motion of the lithium ions during cell operation. The best known system that has recently been introduced into the battery market is  $\text{Li}_x\text{C}_6/\text{Li}_{1-x}\text{CoO}_2$  [2]. Cells are conveniently assembled in the discharged state with a carbon anode and a  $\text{LiCoO}_2$  cathode. The carbon can be either graphitic, i.e. with a well-crystallized lamellar structure, or characterized by turbostratic disorder, i.e., with a structure in which the carbon sheets are buckled and randomly rotated with respect to adjacent sheets [3]. Graphite anodes can accommodate one lithium per six carbon atoms ( $\text{LiC}_6$ ) and discharge most of their capacity at a voltage between 0 and 0.2 V vs. pure lithium, whereas disordered carbon electrodes can provide higher capacities, but typically over the range 0 to 1.2 V. The theoretical capacity of a charged  $\text{LiC}_6$  cathode is 339 mAh/g. High rechargeable capacities can be obtained from both graphitic and disordered carbon electrodes; their good rechargeability can undoubtedly be attributed to the stability of the host structures to lithium insertion and extraction. Because these electrodes reach full charge at the metallic lithium potential, there is the risk that metallic lithium may be deposited at the anode surface at the top of charge, particularly if high current rates are used. Therefore, if cell charging conditions are abused, there



is the possibility that the cell could become unsafe, for example, by a short circuit and subsequent self-heating and venting of the cell. Although lithium-ion cells produced today are protected from overcharging by sophisticated electronic circuitry, the design of new anode materials that chemically protect the cell during overcharge conditions is possible.

In this paper, transition metal oxides are discussed in terms of their suitability as anode and cathode materials for lithium-ion cells. Particular focus is placed on anode materials, on the family of spinel oxides, and on those compounds that offer the greatest structural stability to electrochemical cycling.

## DISCUSSION

Table I lists examples of materials that have been considered as anodes for rechargeable lithium cells [4]. The materials range from metallic lithium, which offers the highest theoretical capacity (3863 mAh/g), through metallic alloys such as  $\text{Li}_{4.4}\text{Si}$  (2012 mAh/g) and  $\text{LiAl}$  (790 mAh/g), to insertion compounds such as lithium-carbon  $\text{LiC}_6$  (339 mAh/g), metal oxides such as  $\text{LiWO}_2$  (120 mAh/g),  $\text{LiMoO}_2$  (199 mAh/g) and " $\text{Li}_6\text{Fe}_2\text{O}_3$ " (799 mAh/g), and metal sulfides, for example,  $\text{LiTiS}_2$  (228 mAh/g). More recently, lithium spinels, such as  $\text{Li}_{4+x}\text{Ti}_5\text{O}_{12}$ , have been investigated as possible anode materials [5].

**Table I. Theoretical Capacities of Various Anode Materials, Calculated from the Masses of Fully Charged Electrodes and for Full Utilization of Lithium.**

Material	Theoretical Capacity (mAh/g)	Average Voltage vs Li (V)
Li	3863	0
<i>Alloys</i>		
LiAl	790	0.36
$\text{Li}_{4.4}\text{Si}$	2012	0.2
<i>Insertion Compounds</i>		
$\text{LiC}_6$	339	0.5
$\text{LiWO}_2$	120	0.75
" $\text{Li}_6\text{Fe}_2\text{O}_3$ " ( $3\text{Li}_2\text{O} \cdot 2\text{Fe}$ )	799	0.9
$\text{LiMoO}_2$	199	1.5
$\text{Li}_7\text{Ti}_5\text{O}_{12}$ *	168*	1.56
$\text{LiTiS}_2$	225	2.2

\*Note: based on the compositional range  $\text{Li}_{4+x}\text{Ti}_5\text{O}_{12}$  ( $0 \leq x \leq 3$ ).

At the top of charge and at high current rates, when the voltage of lithium-alloy and lithium-carbon electrodes approaches that of metallic lithium, the risk of depositing finely divided and highly reactive lithium at the anode surface is greatly enhanced. It would therefore be advantageous to engineer alternative anode materials that provide a greater safety voltage window for lithium cells. For example, if a stable transition metal oxide or sulfide insertion electrode could be fabricated that offered a constant 1 V against lithium, then such an electrode could be coupled with a suitable 4-V insertion cathode, such as  $\text{LiCoO}_2$ ,  $\text{LiNiO}_2$ , or  $\text{LiMn}_2\text{O}_4$  (Table II), to provide a 3 V cell. In this type of lithium-ion cell, the cell potential is obtained from differences in the oxidation states of the transition metals in the anode and cathode host structures; the lithium ions transfer charge from one electrode to the other and do not take part in the redox process at any stage. Oxides are preferred to sulfides because oxygen is lighter than sulfur, and because oxide materials are, in general, easier to synthesize and handle. From a safety viewpoint, metal oxides and sulfides are also attractive, because at the top of charge when the insertion electrode is fully lithiated, overcharge will reduce the transition metal ions rather than lithium ions to the metallic state.

**Table II: Properties of "4 V" Cathode Materials.**

Material	Theoretical Capacity (mAh/g)	Average Voltage vs Li (V)	Symmetry
$\text{Li}_{1-x}\text{CoO}_2$	274	3.9	Trigonal $c/a = 4.93$
$\text{Li}_{1-x}\text{NiO}_2$	275	3.8	Trigonal $c/a = 4.99$
$\text{Li}_{1-x}\text{Mn}_2\text{O}_4$	148	4.0	Cubic $c/a = 4.90$

#### Structural Considerations of Metal Oxide Insertion Electrodes

Most transition metal oxide insertion electrodes that are of interest today have close-packed structures; those with a cubic-close-packed oxygen array are more stable to electrochemical cycling than hexagonal-close-packed structures [6]. Insertion electrodes will, in general, be tolerant to cycling if the host framework undergoes minimal structural modifications during cell operation. In particular, there should be as little distortion of the oxygen array as possible and a minimum displacement of the transition metal cations within the host. Electrodes with a stable transition metal oxide host framework are expected to offer excellent rechargeability if they have cubic crystallographic symmetry and can expand and contract isotropically during lithium insertion/extraction with minimum change to the unit cell volume.

#### Anode Materials

Relatively few metal oxides have been investigated in the past as anode materials for lithium-ion cells. Murphy and coworkers have evaluated  $\text{WO}_2$ ,  $\text{MoO}_2$ , and  $\text{RuO}_2$  electrodes with a rutile-type structure [7]. Although  $\text{WO}_2$ , in particular, provides an attractively low average voltage vs lithium (0.75 V), it has a low theoretical capacity (120 mAh/g). Like  $\text{MoO}_2$  and  $\text{RuO}_2$ ,  $\text{WO}_2$  is

unstable to prolonged electrochemical cycling. These rutile-type structures are, therefore, unlikely to find practical use as electrodes in rechargeable battery applications.

" $\text{Li}_6\text{Fe}_2\text{O}_3$ " was proposed as an anode for lithium-ion cells by Morzilli and coworkers [8]. This electrode is prepared by lithiation of  $\alpha\text{-Fe}_2\text{O}_3$ ; it offers a theoretical capacity of 799 mAh/g and discharges most of its capacity just below 1 V. Note, however, that this electrode represents the fully reduced state " $3\text{Li}_2\text{O}\cdot 2\text{Fe}$ ," in which metallic iron has been extruded from the close-packed oxygen framework. Strictly speaking, " $\text{Li}_6\text{Fe}_2\text{O}_3$ " is not an insertion electrode. Although the process of lithium insertion into, and iron extrusion from,  $\alpha\text{-Fe}_2\text{O}_3$  occurs reversibly in high temperature lithium cells [9], the kinetics are not sufficiently fast to permit good reversibility at room temperature.

The  $\text{Li}_{4+x}\text{Ti}_5\text{O}_{12}$  system provides a relatively low voltage vs lithium (1.56 V) and has recently been proposed as an anode material for lithium-ion cells [5,10]; it is a lithiated spinel with an ideal cubic-close-packed oxygen array. The  $\text{Li}_{4+x}\text{Ti}_5\text{O}_{12}$  system offers exceptional structural stability to lithium insertion/extraction and should provide excellent rechargeability over the compositional range  $0 \leq x \leq 3$ ; this electrode is discussed in greater detail in the following sections.

## Cathode Materials

Three 4 V cathode materials are of interest for lithium-ion battery applications:  $\text{Li}_{1-x}\text{CoO}_2$  (layered structure),  $\text{Li}_{1-x}\text{NiO}_2$  (layered structure), and  $\text{Li}_{1-x}\text{Mn}_2\text{O}_4$  (spinel structure) ( $0 \leq x \leq 1$ ); these materials have structures with ideal, or almost ideal, cubic-close-packed oxygen arrays. When synthesized in the correct way and cycled between carefully controlled voltage limits, these compounds are extremely tolerant to electrochemical cycling because the metal oxide framework is stable, and because lithium insertion and extraction reactions are accompanied by only a very gradual change in the unit cell parameters over a wide compositional range. The electrochemical and structural properties of these cathode materials have been comprehensively discussed in earlier papers [6,11-14].

## Spinel Electrodes for Lithium-ion Cells

The family of lithium spinels  $\text{Li}[\text{M}_2]\text{O}_4$  provides attractive electrode materials for lithium cells [5]; the  $[\text{M}_2]\text{O}_4$  spinel framework offers a three-dimensional interstitial space for lithium-ion diffusion and remains intact during lithium insertion/extraction. Many spinels have cubic symmetry, which is maintained on lithiating and delithiating their structures and thereby allows the electrodes to "breathe" isotropically during charge and discharge, sometimes with very little change to the "a" lattice parameter and to the unit cell volume. Moreover, the ability to vary the M cation on the octahedral sites of the  $\text{Li}[\text{M}_2]\text{O}_4$  spinel makes it possible to tailor the voltage of the spinel electrode, as demonstrated in Table III. For example, against a lithium metal reference electrode,  $\text{Li}_{1-x}[\text{Mn}_2]\text{O}_4$  provides 4 V [15];  $\text{Li}_{2-x}[\text{Co}_2]\text{O}_4$ , 3.4 V [6,16];  $\text{Li}_{4+x}[\text{Mn}_5]\text{O}_{12}$ , 2.8 V [17];  $\text{Li}_{1+x}[\text{V}_2]\text{O}_4$ , 2.3 V [18]; and  $\text{Li}_4[\text{Ti}_5]\text{O}_{12}$ , 1.5 V [19]. It is therefore possible to couple a low-voltage spinel with a high-voltage spinel to fabricate electrochemical cells that offer a wide range of voltages. Two examples of lithium-ion cells based on this type of configuration are described below.

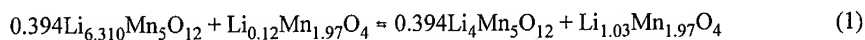
**Table III: Composition and Voltage of Various Lithium Metal Oxide Insertion Electrodes with the Spinel Structure.**

Cell Couple	$x_{\max}$	Approximate Operating Voltage (V)
Li/Li <sub>1+x</sub> Fe <sub>5</sub> O <sub>8</sub>	2	3.0-0.9
Li/Li <sub>4+x</sub> Ti <sub>5</sub> O <sub>12</sub>	3	1.5
Li/Li <sub>1+x</sub> V <sub>2</sub> O <sub>4</sub>	1	2.3-1.3 (two steps)
Li/Li <sub>1+x</sub> Mn <sub>2</sub> O <sub>4</sub>	1	2.8
Li/Li <sub>2+x</sub> Mn <sub>4</sub> O <sub>9</sub>	3	2.8
Li/Li <sub>4+x</sub> Mn <sub>5</sub> O <sub>12</sub>	3	2.8
Li/Li <sub>2-x</sub> Co <sub>2</sub> O <sub>4</sub>	~1	3.4
Li/Li <sub>1-x</sub> Mn <sub>2</sub> O <sub>4</sub>	~0.8	4.0

(i) **The Li<sub>4</sub>Mn<sub>5</sub>O<sub>12</sub>/Li<sub>1.03</sub>Mn<sub>1.97</sub>O<sub>4</sub> System [5].** It is now well known that spinels in the Li-Mn-O system deliver either 2.8 V or 4 V against lithium; the cell voltage is dependent on the composition of the spinel electrode. However, Li-Mn-O electrodes have the disadvantage that a Jahn-Teller distortion occurs in the crystal structure when the average manganese ion valency falls below 3.5, and this distortion reduces the crystal symmetry from cubic to tetragonal [20]. This effect is best known in the Li<sub>x</sub>Mn<sub>2</sub>O<sub>4</sub> system, which has a cubic configuration for the range 0 < x < 1, and provides 4 V against lithium. At x ≈ 1, the cell voltage drops to 2.8 V, and the onset of the Jahn-Teller distortion produces a two-phase electrode that delivers 2.8 V over the range 1 < x < 2. The anisotropic distortion of the crystal lattice, brought about by the Jahn-Teller effect, changes the c/a lattice parameter ratio by 16%, which is far too severe for the electrode to maintain its structural integrity on cycling; the cell loses capacity rapidly when cycled at 2.8 V. In general, lithium insertion into Li-Mn-O spinel electrodes should therefore be limited to avoid the Jahn-Teller effect by restricting the change in the manganese oxidation state, n<sup>+</sup>, to the range 3.5 < n<sup>+</sup> ≤ 4.0. However, even when LiMn<sub>2</sub>O<sub>4</sub> is used as a 4 V electrode, it is necessary to combat the onset of the Jahn-Teller effect towards the end of the cubic symmetry, 4-V region because distortion may still occur in localized regions on the surface of some spinel particles, even though the measured (average) cell voltage may be greater than 2.8 V. This phenomenon can be combated by using "stabilized" spinels such as Li<sub>1.03</sub>Mn<sub>1.97</sub>O<sub>4</sub> and LiZn<sub>0.025</sub>Mn<sub>1.95</sub>O<sub>4</sub>, in which a small fraction of the manganese ions is replaced by a monovalent or multivalent cation to keep the mean oxidation state of the manganese ions marginally above 3.5 at the end of discharge [21].

The stoichiometric spinel Li<sub>4</sub>Mn<sub>5</sub>O<sub>12</sub> (in spinel notation, Li[Li<sub>0.33</sub>Mn<sub>1.67</sub>]O<sub>4</sub>) is a cubic-symmetry, 2.8-V electrode [17]. Under ideal conditions, the symmetry remains cubic until the composition Li<sub>6.5</sub>Mn<sub>5</sub>O<sub>12</sub> (n<sup>+</sup> in Mn<sup>n+</sup> = 3.5) is reached; the unit cell expands by less than 1%. Therefore, by selection of the appropriate composition of Li-Mn-O spinel electrodes and the amount of anode and cathode material used in the cell, it is possible to design a 1.2 V lithium-ion cell based

on a manganese-manganese couple with electrodes that are structurally stable to electrochemical cycling. Such a configuration is demonstrated by the following ideal reaction of a  $\text{Li}_4\text{Mn}_5\text{O}_{12}/\text{Li}_{1.03}\text{Mn}_{1.97}\text{O}_4$  cell:



Note that, for this reaction, the manganese ions in the anode and cathode reach a minimum valence of 3.54 in the fully charged and fully discharged states, respectively, as shown in Table IV.

**Table IV. The Variation in the Oxidation State of Fully-Charged and Discharged Spinel Electrodes.**

Charged State	$\text{Mn}^{n+}$	Discharged State	$\text{Mn}^{n+}$
$\text{Li}_{6.31}\text{Mn}_5\text{O}_{12}$	3.54	$\text{Li}_4\text{Mn}_5\text{O}_{12}$	4.00
$\text{Li}_{0.12}\text{Mn}_{1.97}\text{O}_4$	4.00	$\text{Li}_{1.03}\text{Mn}_{1.97}\text{O}_4$	3.54

This type of cell is conveniently assembled in the discharged state from materials that are fairly easy to prepare. Figure 1 shows the electrochemical charge and discharge profiles of a typical  $\text{Li}_4\text{Mn}_5\text{O}_{12}/\text{Li}_{1.03}\text{Mn}_{1.97}\text{O}_4$  cell that was charged and discharged between upper and lower voltage limits of 1.6 V and 0.5 V, respectively, at a current density of  $0.15 \text{ mA/cm}^2$  [5]. It demonstrates the good cycling behavior that can be expected from this type of cell. Based on an average operating discharge voltage of 1.0 V and the masses of the electrode materials only, a balanced cell that fully utilizes the active electrodes provides an energy density of 66 Wh/kg.

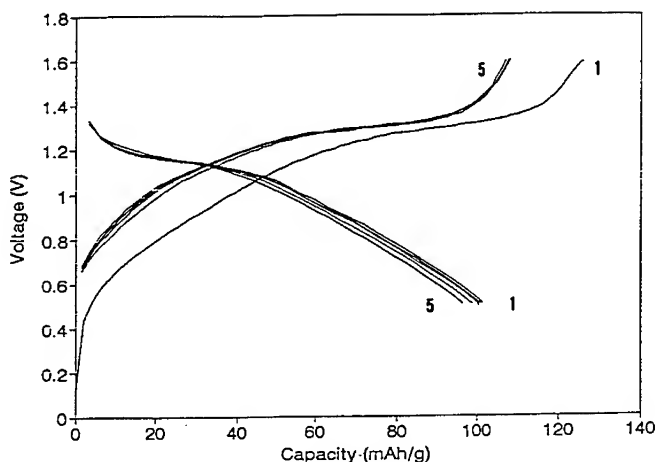
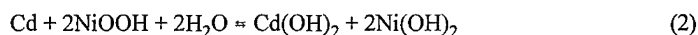


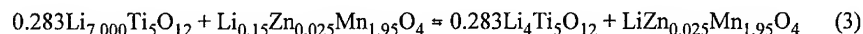
**Fig. 1. The Electrochemical Performance of a  $\text{Li}_4\text{Mn}_5\text{O}_{12}/\text{Li}_{1.03}\text{Mn}_{1.97}\text{O}_4$  Cell (from reference 5).**

Unfortunately, this value is too low for this particular cell to be used in practical applications. By comparison, the theoretical specific energy of a nickel-cadmium cell that operates at 1.2 V according to the reaction:



is significantly greater, namely, 192 Wh/kg.

(ii) **The  $\text{Li}_4\text{Ti}_5\text{O}_{12}/\text{LiZn}_{0.025}\text{Mn}_{1.95}\text{O}_4$  System**[5]. For several reasons  $\text{Li}_4\text{Ti}_5\text{O}_{12}$  is a more attractive anode material than  $\text{Li}_4\text{Mn}_5\text{O}_{12}$ . Firstly, lithium can be inserted into the cubic structure over the whole compositional range  $\text{Li}_{4+x}\text{Ti}_5\text{O}_{12}$  ( $0 \leq x \leq 3$ ) with hardly any change to the unit cell volume; the "a" lattice parameter only increases from 8.367 Å at  $x = 0$  to 8.37 Å at  $x = 3$  [18]. Secondly,  $\text{Li}_4\text{Ti}_5\text{O}_{12}$  delivers only 1.5 V against lithium and can therefore be coupled with a 4 V electrode to provide a 2.5 V cell which is twice that of a nickel-cadmium or nickel-metal hydride cell. With a zinc-stabilized spinel cathode,  $\text{LiZn}_{0.025}\text{Mn}_{1.95}\text{O}_4$ , and with full utilization of the available capacity from both electrodes, the reaction for a balanced cell is:



In this system, the manganese ions are reduced to a mean oxidation state of 3.56 on discharge. By contrast, the titanium cations in the anode can be reduced on charge to a minimum of 3.40, assuming that full lithiation of the  $\text{Li}_4\text{Ti}_5\text{O}_{12}$  spinel occurs on charge, as shown in Table V.

**Table V. The Variation in the Ti or Mn Oxidation States of Fully Charged and Discharged Spinel Electrodes.**

Charged State	$n^+$ in $\text{Ti}^{n+}$ or $\text{Mn}^{n+}$	$n^+$ in Discharged State	$\text{Ti}^{n+}$ or $\text{Mn}^{n+}$
$\text{Li}_{7.000}\text{Ti}_5\text{O}_{12}$	3.40	$\text{Li}_4\text{Ti}_5\text{O}_{12}$	4.00
$\text{Li}_{0.15}\text{Zn}_{0.025}\text{Mn}_{1.95}\text{O}_4$	4.00	$\text{LiZn}_{0.025}\text{Mn}_{1.95}\text{O}_4$	3.56

Based on an average discharge voltage of 2.45 V and the masses of the electrodes only, such a cell would provide a capacity of 180 Wh/kg. The excellent reversibility of this system is shown in Fig. 2; this figure also highlights the flat voltage response obtained at both electrodes against a metallic lithium reference electrode. Note the particularly flat response from the  $\text{Li}_{4+x}\text{Ti}_5\text{O}_{12}$  anode. This response results from a two-phase electrode consisting of the spinel phase  $\text{Li}_4\text{Ti}_5\text{O}_{12}$  and lithiated-spinel phase  $\text{Li}_7\text{Ti}_5\text{O}_{12}$ , which has a rock-salt-type structure.

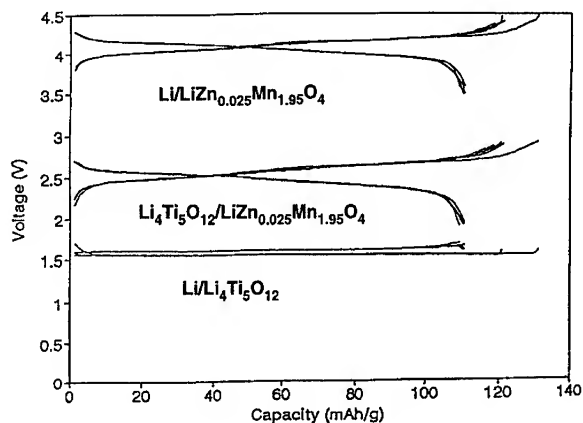
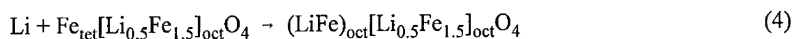
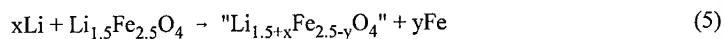


Fig. 2. The Electrochemical Performance of a  $\text{Li}_4\text{Ti}_5\text{O}_{12}/\text{LiZn}_{0.025}\text{Mn}_{1.95}\text{O}_4$  Cell (from Reference 5).

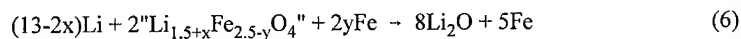
(iii) **The Lithium Iron Oxide Spinel,  $\text{LiFe}_5\text{O}_8$ .** The lithium iron oxide spinel,  $\text{LiFe}_5\text{O}_8$ , is an inverse spinel in which the tetrahedral sites are occupied by iron, and the octahedral sites are occupied by lithium and iron; it has the spinel notation  $\text{Fe}[\text{Li}_{0.5}\text{Fe}_{1.5}]\text{O}_4$ . Thus,  $\text{LiFe}_5\text{O}_8$  does not have the three-dimensional network of channels that accounts for good lithium-ion diffusion in  $\text{Li}[\text{M}_2]\text{O}_4$  spinels. Lithium insertion into  $\text{LiFe}_5\text{O}_8$  has been studied in both room temperature and high-temperature lithium cells [22]. At room temperature lithium insertion takes place until the rock salt stoichiometry is reached. The reaction in spinel notation is:



Further lithiation results in the extrusion of metallic iron from the oxygen lattice and can be represented by the generalized reaction:



and thereafter



Reaction (4) takes place in a single-phase process between 3 and 1 V (Fig. 3). The tetrahedrally coordinated iron cations are displaced into octahedral sites to yield a rock-salt phase in which the lithium and iron cations are almost evenly distributed over the two crystallographically independent sets of octahedral sites [represented by the round and square brackets in reaction 4].

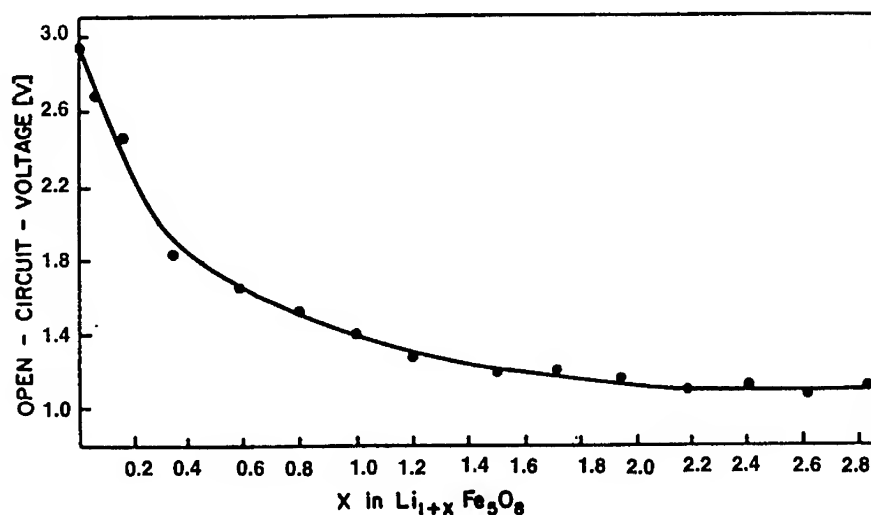
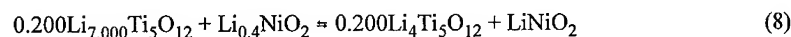
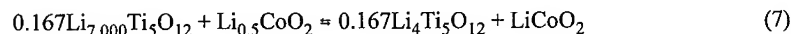


Fig. 3. Open-Circuit-Voltage Discharge Profile of a Li/Li<sub>1+x</sub>Fe<sub>5</sub>O<sub>8</sub> Cell (from reference 22).

Because lithium extraction from the lithiated spinel phase, (LiFe)<sub>oct</sub>[Li<sub>0.5</sub>Fe<sub>1.5</sub>]O<sub>4</sub>, is difficult, this electrode shows poor electrochemical reversibility. Reactions (5) and (6), which occur at about 1 V vs lithium, involve the extrusion of metallic iron and are not readily reversible at room temperature. This lithium spinel electrode, therefore, behaves in a similar manner to  $\alpha$ -Fe<sub>2</sub>O<sub>3</sub> [8]; it is unsuitable for lithium-ion battery applications.

(iv) **Alternative Lithium-Ion Couples.** The layered compounds LiCoO<sub>2</sub> and LiNiO<sub>2</sub> offer higher theoretical capacities, but slightly lower voltages, than LiMn<sub>2</sub>O<sub>4</sub> (Table II). If synthesized correctly, LiNiO<sub>2</sub> tends to yield a higher capacity than LiCoO<sub>2</sub> during cycling. For example, in Li<sub>1-x</sub>CoO<sub>2</sub>, good reversibility can be achieved for  $x_{\max}=0.5$  (which corresponds to a capacity of 137 mAh/g), whereas for Li<sub>1-x</sub>NiO<sub>2</sub>,  $x_{\max}$  can reach at least 0.6 (which corresponds to a capacity of 165 mAh/g). When coupled with Li<sub>4</sub>Ti<sub>5</sub>O<sub>12</sub> anodes, the balanced reactions for the two cells are:



Reactions (7) and (8) occur at an average discharge voltage of 2.3 and 2.1 V, respectively. Cells based on these configurations deliver specific energies of 177 Wh/kg and 178 Wh/kg,



respectively; these values approach the theoretical specific energy offered by the nickel-cadmium system (192 Wh/kg).

## CONCLUSIONS

The potential of lithium-ion cells fabricated with metal oxide anodes and cathodes has been discussed. Although the available capacity that can be delivered from these cells falls considerably short of the capacity delivered by lithium-ion cells that employ carbon anodes, those with  $\text{Li}_4\text{Ti}_5\text{O}_{12}$  anodes do offer comparable capacities to nickel-cadmium cells, at a voltage that is approximately twice that of the nickel-cadmium system. This type of non-aqueous lithium cell is expected to be inherently safe, and offer a superior shelf life to nickel-cadmium cells, which tend to self-discharge in a KOH electrolyte at a rate >20% per month [23]. Further research is required to identify alternative metal oxide anodes that are structurally stable and provide lower voltages against lithium, typically in the range 0.5 to 1.0 V. Such anodes would significantly improve the performance of metal-oxide rocking-chair cells.

## REFERENCES

1. G. Pistoia (ed.), *Lithium Batteries, New Materials, Developments and Perspectives*, Elsevier (Amsterdam), 1994.
2. T. Nagaura and K. Tozawa, *Progress in Batteries and Solar Cells*, **9**, 209 (1990).
3. J. R. Dahn, A. K. Sleight, Hang Shi, B. M. Way, W. J. Weydanz, J. N. Reimers, Q. Zhong, and U. von Sacken, in reference 1, p. 1.
4. D. Fauteaux and R. Koksang, *J. Appl. Electrochem.*, **23**, 1 (1993).
5. E. Ferg, R. J. Gummow, A. de Kock, and M. M. Thackeray, *J. Electrochem. Soc.*, **141**, L147, (1994).
6. M. M. Thackeray, *J. Electrochem. Soc.* (1994). In press.
7. D. W. Murphy, F. J. Di Salvo, J. N. Carides, and W. V. Waszczak, *Mat. Res. Bull.*, **13**, 1395 (1978).
8. S. Morzilli, B. Scrosati, and F. Sgarlatta, *Electrochim. Acta.*, **30**, 1271 (1985).
9. M. M. Thackeray, W. I. F. David, and J. B. Goodenough, *J. Solid State Chem.*, **55**, 280, (1984).
10. T. Ohzuku and A. Ueda, *Solid State Ionics*, **69**, 201 (1994).
11. J. N. Reimers, J. R. Dahn, and U. von Sacken, *J. Electrochem. Soc.*, **140**, 2752 (1993).
12. T. Ohzuku, A. Ueda, M. Nagayama, Y. Iwakoshi, and H. Komori, *Electrochim. Acta.*, **38**, 1159 (1993).
13. T. Ohzuku, A. Ueda, and M. Nagayama, *J. Electrochem. Soc.*, **140**, 1862 (1993).
14. W. Li, J. N. Reimers, and J. R. Dahn, *Solid State Ionics*, **67**, 123 (1993).
15. J. M. Tarascon, E. Wang, F. K. Shokoohi, W. R. McKinnon, and S. Colson, *J. Electrochem. Soc.*, **138**, 363 (1992).
16. R. J. Gummow, D. C. Liles, and M. M. Thackeray, *Mat. Res. Bull.*, **28**, 235 (1993).
17. M. M. Thackeray, A. de Kock, M. H. Rossouw, D. C. Liles, D. Hoge, and R. Bittihn, *J. Electrochem. Soc.*, **139**, 363 (1992).
18. L. A. de Picciotto and M. M. Thackeray, *Mat. Res. Bull.*, **20**, 1409 (1985).
19. K. M. Colbow, J. R. Dahn, and R. R. Haering, *J. Power Sources*, **26**, 397 (1989).

20. M. M. Thackeray, W. I. F. David, P. G. Bruce, and J. B. Goodenough, *Mat. Res. Bull.*, **18**, 461 (1983).
21. R. J. Gummow, A. de Kock, and M. M. Thackeray, *Solid State Ionics*, **69**, 59 (1994).
22. L. A. de Picciotto and M. M. Thackeray, *Mat. Res. Bull.*, **21**, 583 (1986).
23. K. Brandt, *Proc. 5th Int. Seminar on Lithium Battery Technology and Applications*, Deerfield Beach, Florida (March 4-6, 1991).

## A Comparative Study of $\text{LiMn}_2\text{O}_4$ From Various Sources

B. Oyang\*, S. G. Greenbaum\*, M. den Boer\*,  
A. Massucco<sup>+</sup>, M. McLin<sup>+</sup>, J. Shi<sup>+</sup>, and D. Fauteux<sup>+</sup>

\* The City University of New York, Hunter College, Physics Dept., New York, NY  
<sup>+</sup> Arthur D. Little, Cambridge, MA

### Abstract

A process recently developed at Arthur D. Little, Inc. has enabled the direct and rapid production of  $\text{LiMO}_x$  intercalation cathode materials having specific and controlled geometric and topographic attributes. Results of a comparative study of the electrochemical and spectroscopic characteristics of  $\text{LiMn}_2\text{O}_4$  from several commercial sources and  $\text{LiMn}_2\text{O}_4$  prepared using our process are reported. Improved electrochemical performance observed for the  $\text{LiMn}_2\text{O}_4$  cathode material produced using ADL's process are tentatively related to the small and uniform grain size and to the possible additional influence of electronic defects associated with surface states.

### Introduction

Successful commercialization of lithium and lithium-ion battery technologies will require the use of high voltage cathode materials. Much of the interest during the early phase of the lithium-ion battery technology development was focussed on the use of  $\text{LiCoO}_2$  as the cathode material of choice. More recently, alternative cathode materials, such as  $\text{LiNiO}_2$  and  $\text{LiMn}_2\text{O}_4$  have been suggested.

Within the context of a large scale production and a broad market penetration of the lithium-ion battery technology, abundant, economical, and non-toxic cathode materials will be required. Recently, research and development emphasis has been shifting toward the spinel  $\text{LiMn}_2\text{O}_4$  as a cathode material of choice. However, high specific capacity (mAh/g), high capacity retention during cycling, chemical, and electrochemical stability are also essential attributes to an optimal cathode material performance. In many instances, the spinel  $\text{LiMn}_2\text{O}_4$  cathode material has demonstrated lower specific capacity and lower capacity retention during cycling when compared to  $\text{LiCoO}_2$  and  $\text{LiNiO}_2$  cathode materials. Consequently, only an optimized  $\text{Li}_x\text{Mn}_2\text{O}_4$  cathode material having a highly reversible specific capacity ( $\geq 120$  mAh/g) and good capacity retention during cycling will represent a viable alternative to  $\text{LiCoO}_2$  and  $\text{LiNiO}_2$  cathode material.

Our work has been focussed on processing and manufacturing of  $\text{LiMO}_x$  ( $M = \text{Co, Ni, Mn}$ ) for the development of high performance composite cathode materials for lithium-polymer electrolyte rechargeable battery systems. Our approach is based on the development of a continuous manufacturing process for the production of cathode material particles of specific form factors, dimension, and narrow particle size distribution. These geometric attributes for the cathode material particle enable maximization of the particle surface area to volume ratio, the electrolyte-cathode material interfacial area, and the particle to particle utilization uniformity during cycling, consequently improving the performance of these cathode materials

when compared to "commercially" produced  $\text{LiMO}_x$  cathode materials. In order to produce cathode material particles having the attributes described above, a low temperature continuous process (Dynatrod) has been developed at Arthur D. Little. The Dynatrod process directly yields small and spherical  $\text{LiMO}_x$  particles of controlled particle size, controlled specific surface area, and controlled porosity, minimizing or eliminating the need of post-synthesis grinding and sizing of the cathode active material. A specific characteristic of the Dynatrod process is the very fast conversion kinetics of the precursor materials to the stoichiometric  $\text{LiMO}_x$  materials in less than 5 seconds. It is believed that this fast conversion kinetic has an effect on the crystallite grain size and microstrain and consequently on electrochemical performance characteristics of the cathode material.

Results of a comparative study of the electrochemical and spectroscopic characteristics of  $\text{LiMn}_2\text{O}_4$  from several "commercial" sources and of  $\text{LiMn}_2\text{O}_4$  produced using the Dynatrod process are reported. The paper will initially address crystalline structure, grain size and unit cell parameters. Electrochemical characterizations; specific capacity, rate capability, and cycle life performance, will be presented and discussed in relation with the geometric attributes of the tested  $\text{LiMn}_2\text{O}_4$  particles. Spectroscopic evaluation of the cathode materials include near edge x-ray absorption fine structure (NEXAFS), electron paramagnetic resonance (EPR), and  $^7\text{Li}$  nuclear magnetic resonance (NMR). These results will be discussed with the interest of gaining insight into the reasons for difference in electrochemical properties observed among the different cathode material samples.

## Experimental

"Commercial" samples of  $\text{LiMn}_2\text{O}_4$  were obtained from Cyprus Foote, Chemetals, and from IBA (lot #02-93 and 05-93). Dynatrod made  $\text{LiMn}_2\text{O}_4$  samples were produced between  $500^\circ\text{C}$  and  $1000^\circ\text{C}$ , samples produced at  $750^\circ\text{C}$  have been used for this study.

All samples were analyzed for phase content by means of powder x-ray diffraction techniques using a Rigaku diffractometer equipped with a rotating anode on  $\text{CuK}_{\alpha 1,2}$  radiation. For phase analysis, x-ray diffraction patterns were collected in the range of  $10^\circ$  to  $95^\circ$  ( $2\theta$ ) with a scan speed of  $5^\circ/\text{min}$  and step of  $0.02 - 0.03^\circ$  at  $60\text{kV}$  and  $300\text{ mA}$ . Cubic cell parameter for  $\text{LiMn}_2\text{O}_4$  was calculated by the least-square method using 10 or more peaks. The standard deviations were in the range of  $\pm 0.001$  to  $0.004\text{ \AA}$  (or  $0.01 - 0.05\%$  of cell parameter). For grain size and strain analysis, 3 to 8 peaks were deconvoluted to obtain full widths at half maximum of  $\alpha_1$  - components of the peak. Instrumental broadening was measured and compensated.

Particle size distribution was measured using a Microstat laser light scattering particle size analyzer (Fig. 1). Specific surface area was measured using a Micromeretic ASAP-2400 BET, particle porosity (Hg) was measured using a Micromeretic Autopore-II-9220, and specific density was measured using a Micromeretic Accupic-1330 helium pycnometer.

Electrochemical characterization was performed using 3 electrode cells, a liquid electrolyte (generally  $1\text{M LiClO}_4$  - Propylene Carbonate), and a Solartron ECI-1286 and FRA-1250. Electrode specific capacity, rate capability, and cycle life behavior were tested using 2 electrode cells and a Maccor battery cycling system.

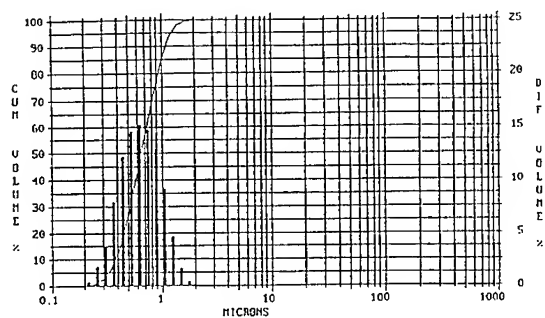


**Figure 1:** Particle size distribution of the Arthur D. Little made optimized  $\text{LiMn}_2\text{O}_4$  cathode material

NEXAFS absorption fine structure measurements were carried out in transition mode on powdered samples at Beamline X-23B of the National Synchrotron Light Source at Brookhaven National Laboratory. Both  $\text{MnO}$  and  $\text{MnO}_2$  were employed as reference standards and run concurrently with the lithiated samples in order to obtain improved energy calibration. Two different monochromator slit widths were utilized, 1mm and 2mm, the former giving a resolution of better than  $\pm 0.1$  eV. X-band EPR measurements were performed on powdered samples in

quartz EPR tubes, with an IBM/Bruker ER-220D spectrometer, utilizing 100kHz field modulation to record absorption first-derivative spectra. Wide line  $^7\text{Li}$  NMR spectra were obtained by Fourier transformation of either a single-pulse or solid-echo ( $90_x - 90_y$ ) sequence (the latter sequence utilized for very broad lines), with a typical  $90^\circ$  pulse length of 3  $\mu\text{s}$ , using a Chemagnetics CMX-300 spectrometer. The powdered samples were held in 5mm quartz tubes. Aqueous  $\text{LiCl}$  solution was employed as a chemical shift reference.

## Results

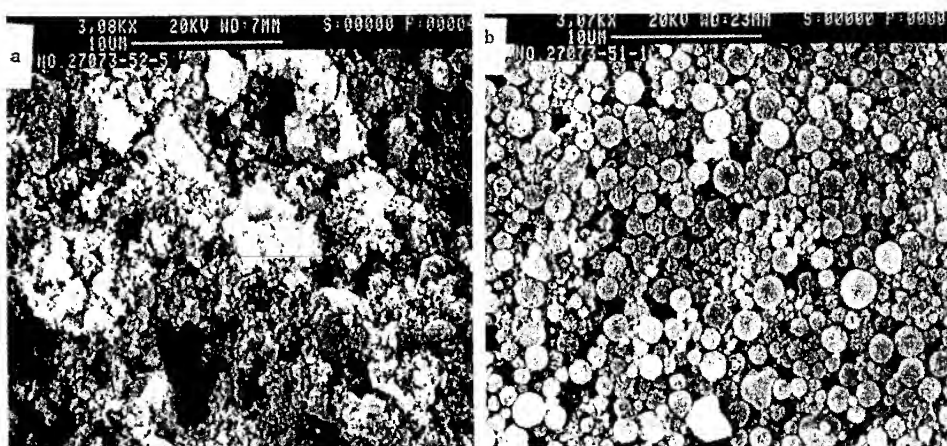


**Figure 2:** SEM photographs of a) commercial  $\text{LiMn}_2\text{O}_4$  and b) Arthur D. Little made  $\text{LiMn}_2\text{O}_4$  cathode materials ( bar scale 10  $\mu\text{m}$ )

SEM pictures presented in Figures 2a and 2b illustrate the geometric and topographic differences observed between a "commercially" produced  $\text{LiMn}_2\text{O}_4$  sample (Fig. 2a) and a

Dynatrod produced  $\text{LiMn}_2\text{O}_4$  sample (Fig. 2b). The latter sample has been produced at  $750^\circ\text{C}$  and illustrates well the following characteristic features of  $\text{LiMn}_2\text{O}_4$  samples:

- Spherical geometry of less than  $2\mu\text{m}$ ,
- High surface area ( $\sim 28\text{m}^2/\text{g}$ ),
- High porosity ( $0.24\text{ cm}^3/\text{g}$ )
- Narrow particle size distribution (Fig. 1)

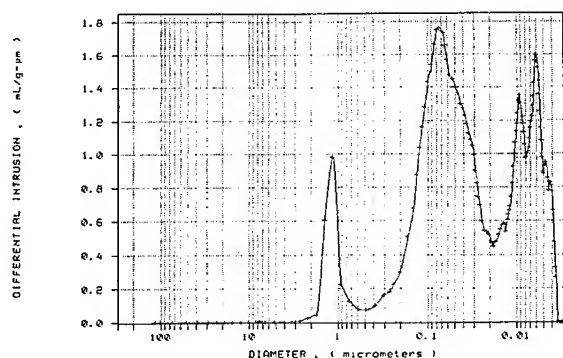


**Figure 3:** Differential mercury volume intrusion as function of pore opening diameter

Each of these features is related to at least one of the Dynatrod process controllable parameters which in turn, can be used to optimize specific attributes of the produced  $\text{LiMO}_x$  cathode material. In addition, a detailed analysis of the SEM pictures in connection with the pore size distribution (Fig. 3) reveals that the large  $\text{LiMn}_2\text{O}_4$  spherical aggregates ( $\sim 1\text{-}2\mu\text{m}$  in diameter) are made of smaller  $\text{LiMn}_2\text{O}_4$  spherical particles ( $0\text{-}0.5\mu\text{m}$  in diameter) within which the fine pore structure is included (pores less than  $0.01$  in diameter).

In Figure 4, the electrochemical performance characteristic of a "commercial"  $\text{LiMn}_2\text{O}_4$  sample is compared to the performance of a Dynatrod made  $\text{LiMn}_2\text{O}_4$  sample using slow scan cyclic voltammetry. The high voltage reaction ( $\text{Li}_1\text{Mn}_2\text{O}_4 \leftrightarrow \text{Li}_0\text{Mn}_2\text{O}_4$ ) region is characterized by a more reversible electrochemical behavior observed for the Dynatrod sample, although the specific capacity of the two samples is similar. For the lower voltage reaction ( $\text{Li}_1\text{Mn}_2\text{O}_4 \leftrightarrow \text{Li}_0\text{Mn}_2\text{O}_4$ ), the Dynatrod sample shows both an increased reversibility and increased specific capacity when compared to the commercial sample. The rate capability, during discharge, of the Dynatrod

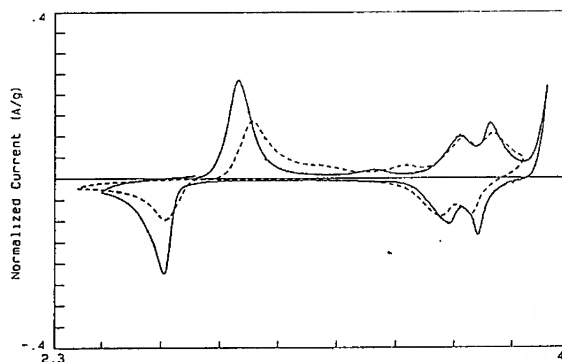


**Figure 4:** Slow scan cyclic voltammograms of  $\text{LiMn}_2\text{O}_4$  samples from a commercial (dot line) source and Arthur D. Little made (full line)

$\text{LiMn}_2\text{O}_4$  sample has been characterized in liquid electrolyte. Three observations are made from these results. First, for discharge rates ranging from 5 hours ( $C/5$  or  $20\text{ mA/g}$ ) to 30 minutes ( $2C$  or  $200\text{ mA/g}$ ) full utilization of the  $\text{LiMn}_2\text{O}_4$  is achieved. Second, the voltage profile during the initial part of the discharge does not depend on the discharge current density, and third, the voltage profile during the final part of the discharge does depend on the discharge current density.

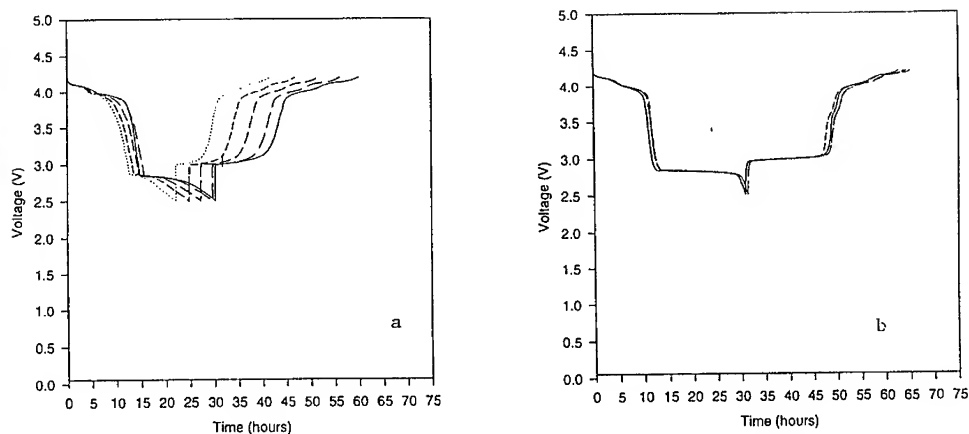


**Figure 5:** Voltage profile during discharge (C/30) of polymer electrolyte composite cathodes produced using a) a commercial and b) an Arthur D. Little made sample. Voltage versus time curves are presented for cycle 1, 5, 10, 15, and 20.

In Figures 5a and 5b, cycling behavior of a "commercial"  $\text{LiMn}_2\text{O}_4$  based polymer electrolyte composite electrode is compared to the behavior observed for an identical polymer electrolyte composite cathode fabricated using a Dynatrod made  $\text{LiMn}_2\text{O}_4$  cathode material. The cycling voltage limits were set between 4.2V and 2.5V in order to fully use the two lithium equivalents of the  $\text{LiMn}_2\text{O}_4$ . This is a very severe cycling condition since it forces the spinel  $\text{Li}_x\text{Mn}_2\text{O}_4$  to go through a phase transition (at  $x>1$ ) from cubic to tetragonal. In Figure 5a and 5b the 1<sup>st</sup>, 5<sup>th</sup>, 10<sup>th</sup>, 15<sup>th</sup> and 20<sup>th</sup> discharge voltage profiles are reported for the commercial and Dynatrod sample respectively. In Figure 5a, a progressive decay of the delivered capacity is observed associated mainly to the poor reversibility of the  $\text{Li}_2\text{Mn}_2\text{O}_4 \leftrightarrow \text{LiMn}_2\text{O}_4$  reaction (as seen in Figure 4). In Figure 5b an excellent reversibility and constant delivered capacity are observed for the polymer electrolyte composite cathode fabricated using the Dynatrod made  $\text{LiMn}_2\text{O}_4$ , confirming the electrochemical characterization results.

X-ray power diffraction results have not indicated any differences between the crystalline structure, as measured by the cell lattice parameters, of commercial and Dynatrod samples. However, significant differences were observed between these samples crystallite grain size and microstrain. The Dynatrod made  $\text{LiMn}_2\text{O}_4$  cathode material has an average grain size of approximately 180 Å, which is less than half the crystallite grain size of the commercial samples. In addition, if the x-ray diffraction line broadening is attributed to microstrain, then the Dynatrod made  $\text{LiMn}_2\text{O}_4$  cathode material has much higher microstrain value (approximately 0.4%) compared to the microstrain values observed for the commercial samples ( $\leq 0.2\%$ ).

The manganese K-edge x-ray absorption spectrum of the stoichiometric ADL sample is displayed in Fig. 6. The energy range from about 10 eV below the main absorption edge, usually referred to as the "white line", to about 20 eV above the edge is the NEXAFS region, which corresponds to dipole-allowed transitions of 1s-states into unoccupied 4p-states. The

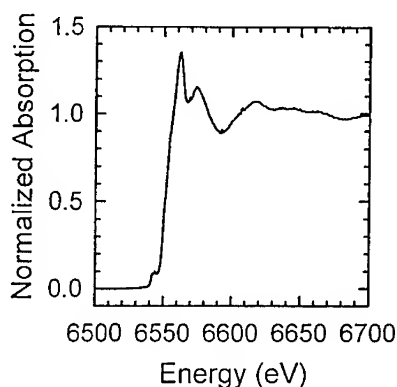


**Figure 6:** Manganese K-edge x-ray adsorption spectrum of the  $\text{Li}_1\text{Mn}_2\text{O}_4$  Arthur D. Little made sample

range from about 20 eV extending to ~100eV above the edge is referred to as the extended x-ray absorption fine structure (EXAFS) region, and corresponds to ionization of the core (1s) electrons. The EXAFS spectrum contains information that is often readily converted to nearest-neighbor coordination.<sup>1</sup>

The NEXAFS region also contains information, although interpretation in terms of specific electronic configurations or bonding arrangements is difficult. Nevertheless, trends observed in a series of similar materials, along with an appropriate choice of standard samples, can be quite useful.

Figure 7 shows NEXAFS spectra of stoichiometric  $\text{LiMn}_2\text{O}_4$  obtained from three different commercial sources and the ADL process. Also included are commercial  $\text{LiMnO}_2$  (Cyprus-Foote) and the Li-deficient material  $\text{Li}_{0.7}\text{Mn}_2\text{O}_4$  (prepared starting with the ADL stoichiometric material). The positions of the peak maxima are listed in Table 1. All of the stoichiometric  $\text{LiMn}_2\text{O}_4$  samples have broad peaks centered at about 6562.0 eV above the reference edge. Small differences in Table 1 are within experimental uncertainty ( $\pm 0.1\text{eV}$ ). The  $\text{LiMnO}_2$  sample exhibits a main peak at lower energy, but with a component shoulder at about the same position as in  $\text{LiMn}_2\text{O}_4$ . The presence of the higher energy shoulder suggests that this sample is not a single-phase material. These results can be understood simply in terms of the different nominal Mn valencies in the two materials,  $\text{Mn}^{+3}$  and  $\text{Mn}^{+3.5}$  in  $\text{LiMnO}_2$  and  $\text{LiMn}_2\text{O}_4$ , respectively. Of course the latter represents an average between  $\text{Mn}^{+3}$  and  $\text{Mn}^{+4}$ . These results are also consistent with those reported for a series of manganese oxides.<sup>2</sup>

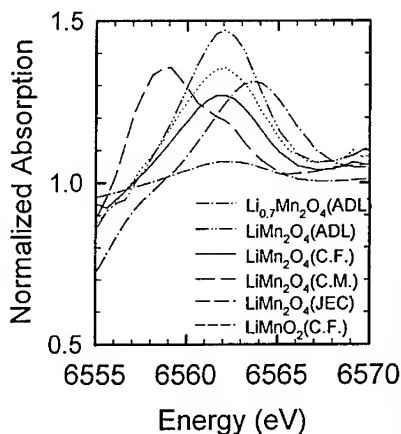


**Figure 7:** NEXAFS of stoichiometric  $\text{LiMn}_2\text{O}_4$  obtained from different sources



TABLE 1: NEXAFS peak maxima

Compound / source	NEXAFS PEAK (eV)
$\text{Li}_{0.7}\text{Mn}_2\text{O}_4$ (ADL)	6563.4
$\text{LiMn}_2\text{O}_4$ (CF)	6562.0
$\text{LiMn}_2\text{O}_4$ (CM)	6561.8
$\text{LiMn}_2\text{O}_4$ (IBA)	6561.6
$\text{LiMn}_2\text{O}_4$ (ADL)	6561.8
$\text{LiMnO}_2$ (CF)	6558.7

The NEXAFS spectrum of the Li-deficient material exhibits two interesting features. The first is the dramatic shift (about 1.5 eV) of the main peak to higher energy. This is attributed in part to the increase in charge on the Mn ion caused by the removal of compensating electronic charge associated with the lithium deficiency. This relatively large shift is consistent with the expectation that the compensating electrons come mostly from the Mn d-orbitals rather than from the generation of defect oxide species. The second feature of note is the clear low energy shoulder in the spectrum, occurring at about 6557 eV, which is attributed to the presence of  $\text{Mn}^{2+}$ . This assignment is based on published NEXAFS data for  $\text{MnO}$ ,<sup>1</sup> as well as EPR results to be discussed later.

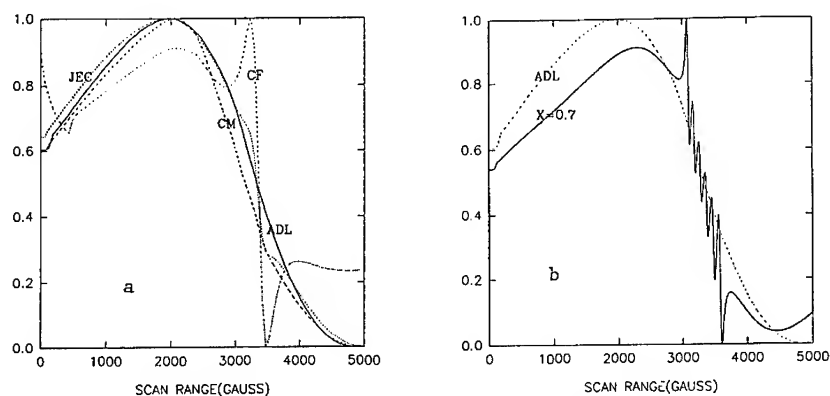


Figure 8: EPR first-derivative spectra of a) four different  $\text{LiMn}_2\text{O}_4$  samples and b) of Arthur D. Little's  $\text{Li}_{0.7}\text{Mn}_2\text{O}_4$  and  $\text{Li}_1\text{Mn}_2\text{O}_4$  samples

EPR first-derivative spectra of the four  $\text{LiMn}_2\text{O}_4$  samples are displayed in Fig.8a. As is typical of materials containing high concentrations of paramagnetic ions, the spectra are very

broad, due to magnetic dipole-dipole interactions, with no nuclear hyperfine structure revealed. However there are some differences between the samples, both in total integrated intensity and in specific features. For viewing purposes, spectra are displayed with normalized intensity, but differences were noted in the original data (i.e. receiver gain, microwave attenuation, etc.). Accurate intensity determinations for such broad lines are difficult because the spectrometer employed was not optimized for such a large magnetic field range, but relative intensity estimates are in rough agreement with NMR results to be discussed later. The CF sample exhibits a narrower line in addition to the broad resonance common to all the other samples. Comparison with solid  $\text{MnCl}_2$  and  $\text{MnO}_2$  (not shown) suggests that the narrower feature is attributable to  $\text{Mn}^{2+}$  and the broad line arises from  $\text{Mn}^{4+}$ ;  $\text{Mn}^{3+}$  cannot be detected by EPR because it is diamagnetic. The lack of a corresponding  $\text{Mn}^{2+}$  feature in the NEXAFS spectrum of the IBA (JEC) sample demonstrates that it is present only in relatively small quantity ( $\leq 10\%$ ).

Spectra of the stoichiometric and Li-deficient Dynatrod made samples are shown in Fig.8b. The Li-deficient material exhibits clear hyperfine structure due to the spin-5/2  $^{55}\text{Mn}$  nucleus. Comparison with results for  $\text{MnCl}_2$  in solution shows unambiguously that the source of this part of the signal is  $\text{Mn}^{2+}$ . The observation of hyperfine structure implies that the  $\text{Mn}^{2+}$  ions which gives rise to it are relatively well distributed (i.e. not clustered) in the sample. The existence of an associated  $\text{Mn}^{2+}$  feature in the NEXAFS spectrum (Fig.7) demonstrates that it is present in substantially more than impurity-level quantities ( $\geq 20\%$ ).

The room temperature  $^7\text{Li}$  NMR spectrum of a all the cathode material sample have been obtained. These spectra are characterized by both a very broad line and a large shift from the reference  $\text{LiCl}$  position. In view of the paramagnetic properties discussed above, both of these results are expected on the basis of the large magnetic interaction between spins localized on the  $\text{Mn}^{4+}$  (and to a lesser extent  $\text{Mn}^{2+}$ ) and the  $^7\text{Li}$  nuclei. Further evidence that paramagnetism completely dominates the NMR line positions and line shapes is clear from Figures 9a and 9b respectively, in which the temperature dependencies of the these two quantities are plotted. The increase of both quantities with decreasing temperature is typical of strongly paramagnetic systems.<sup>3</sup> Due to the very broad line of the Li-deficient sample, distortion of the line shape occurs when utilizing the single pulse measurement. Consequently this sample is not included in Fig.11. However, solid-echo measurements for several samples demonstrate that the Li-deficient material's line width is about 25% larger than that of the stoichiometric

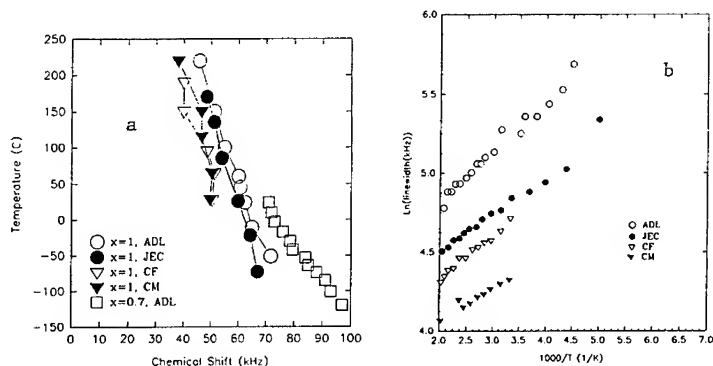


**Figure 9:** NMR line positions (a) at room temperature and line width (b) as a function of temperature for the  $\text{Li}_x\text{Mn}_2\text{O}_4$  cathode material samples

ADL sample, and has roughly the same temperature dependence. These results can be used to refine estimates of the relative spin densities obtained from the EPR data; as stated previously, they are in qualitative agreement. Thus the ADL sample has the highest spin density among the stoichiometric samples, and the spin density increases when Li is removed.

## Discussion

The apparent superiority of the ADL cathode by the electrochemical criteria described in this paper is attributable, in large part, to the small and uniform grain size, which leads to better interfacial properties as described in the Introduction. However, the possible additional influence of electronic defects associated with surface states cannot be dismissed at this time.

One likely mechanism of generating higher spin densities in these cathode materials is a disproportionation reaction:  $2 \text{Mn}^{3+} \rightarrow \text{Mn}^{2+} + \text{Mn}^{4+}$ .<sup>4</sup> This is most clearly evident in the case of the Li-deficient sample, which exhibits unambiguous NEXAFS and EPR  $\text{Mn}^{2+}$  signatures as well as the highest spin density among the samples. This mechanism can also provide a contribution to the white line shift to higher energy, in addition to that mentioned previously, concerning the removal of compensating electrons from Mn. In particular, given that the main white line peak is a superposition of  $\text{Mn}^{3+}$  and  $\text{Mn}^{4+}$  (corresponding to the nominal valence of 3.5), the conversion of a non-trivial fraction of the  $\text{Mn}^{3+}$  to  $\text{Mn}^{2+}$  and  $\text{Mn}^{4+}$  would shift the main peak to higher energy in addition to producing the low energy shoulder. That disproportion occurs upon electrochemical removal of Li has extremely important implications for battery operation because the cathode of a charged cell is prepared in a Li-deficient state. Further study of this phenomenon, involving samples with different levels of Li-deficiency and even cycled cathode material is clearly warranted.

Differences between stoichiometric samples from different sources are more subtle and less well-understood. In particular, the higher spin density of the ADL sample is not correlated with the presence of  $\text{Mn}^{2+}$ , for which spectroscopic evidence is lacking. One possibility is that additional paramagnetic entities are generated by the large number of surface defects associated with the small grain size of the ADL sample.

## References

1. M. Brown, R.E. Peirls and E.A. Stern, *Phys. Rev. B*, **15**, 738 (1977).
2. B.E. Conway, D.Qu and J. McBreen, in Synchrotron Techniques in Interfacial Chemistry, edited by C.A. Melendres and A. Tadjeddine (Kluwer Academic Publishers, Dordrecht, 1994), pp. 311-334.
3. A. Abragam, The Principles of Nuclear Magnetism, (Oxford University Press, 1961).
4. R.J. Gummow, A. de Kock and M.M. Thackeray, *Solid State Ionics*, **69**, 59 1994.

## DEFECT SPINELS IN THE SYSTEM Li-Mn-O. CHEMISTRY AND LITHIUM INSERTION

F. LE CRAS<sup>a,b</sup>, D. BLOCH<sup>b</sup>, M. ANNE<sup>a</sup> and P. STROBEL<sup>a</sup>,

<sup>a</sup>Lab. de Cristallographie, CNRS, BP 166, 38042 Grenoble Cedex 9, France

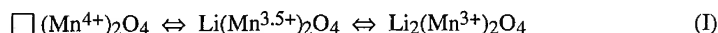
<sup>b</sup>Lab. d'Application de l'Electrochimie, CEA/CEREM, 38054 Grenoble Cedex 9, France

### ABSTRACT

Spinel phases Li-Mn-O with Li/Mn ratios between 0.35 and 0.8 were synthesized. The relationships between composition, manganese valence, vacancy fraction and electrochemical capacity are described using a new composition-valence phase diagram. Electrochemical performances in lithium batteries are compared. The best materials showed constant capacity > 140 Ah/kg in the range 3.5–2 V in liquid electrolyte batteries up to 20 cycles, without the usual capacity drop observed in stoichiometric  $\text{LiMn}_2\text{O}_4$ .

### INTRODUCTION

Spinel phases belonging to the Li-Mn-O system have been thoroughly studied as insertion electrodes materials for rechargeable lithium batteries. The classical intercalation reactions in this system are :



which occur at ca. 4.0 V and 3.0 V vs  $\text{Li/Li}^+$ , respectively <sup>1,2</sup>. The left-hand side reaction has been mostly studied in view of lithium-ion batteries, together with the development of liquid electrolytes stable at high potentials <sup>3</sup>. The 3 V reaction occurs entirely at average manganese valence < 3.5. As a consequence,  $\text{Li}_2\text{Mn}_2\text{O}_4$  is distorted due to the Jahn-Teller effect of the  $\text{d}^4$  ion  $\text{Mn}^{3+}$ . This cubic  $\leftrightarrow$  tetragonal phase transition is believed to be a major factor in the loss of capacity on cycling the 3V plateau of  $\text{Li}_x\text{Mn}_2\text{O}_4$  [4].

As shown by Thackeray et al.<sup>4-6</sup>, the range of Li-Mn-O spinel phase is not limited to the  $\text{Li}_x\text{Mn}_2\text{O}_4$  line. A wide range of spinels exists with general formula  $(\text{Li}_{1+x-\partial}\text{Mn}_{2-x})\text{O}_4$ , where  $x$  is the fraction of lithium atoms on octahedral sites, and  $\partial$  takes into account deviations from stoichiometry. This range includes for instance  $\text{Li}_4\text{Mn}_5\text{O}_{12}$  ( $x = 1/3$ ,  $\partial = 0$ ) and the defect compound  $\text{Li}_2\text{Mn}_4\text{O}_9$  [7] ( $x = 2/9$ ,  $\partial = 1/3$ ).

The crystal chemical relationships in the spinel phase range are best depicted using a new type of phase diagram<sup>8</sup> which will be briefly described here. We will then present the electrochemical properties of Li-Mn-O spinels with various stoichiometries and vacancy fractions in liquid-electrolyte lithium batteries in the voltage range 2–3.5 V.

### STOICHIOMETRY, VACANCIES AND THEORETICAL CAPACITY

Phase-compositions relations in ternary systems are usually represented in a triangular system with the elements Li, Mn and O at the corners<sup>4,9</sup>. We propose an alternate description of this system, using as coordinates two essential chemical parameters, namely the Li/Mn ratio and the average manganese valence  $V(\text{Mn})$ . This 'composition-valence diagram' is shown in Fig. 1 for  $0 \leq \text{Li/Mn} \leq 1.25$  and  $2.25 \leq V(\text{Mn}) \leq 4$ . In addition to an immediate reading of  $V(\text{Mn})$ , two important properties are easily displayed in this diagram :

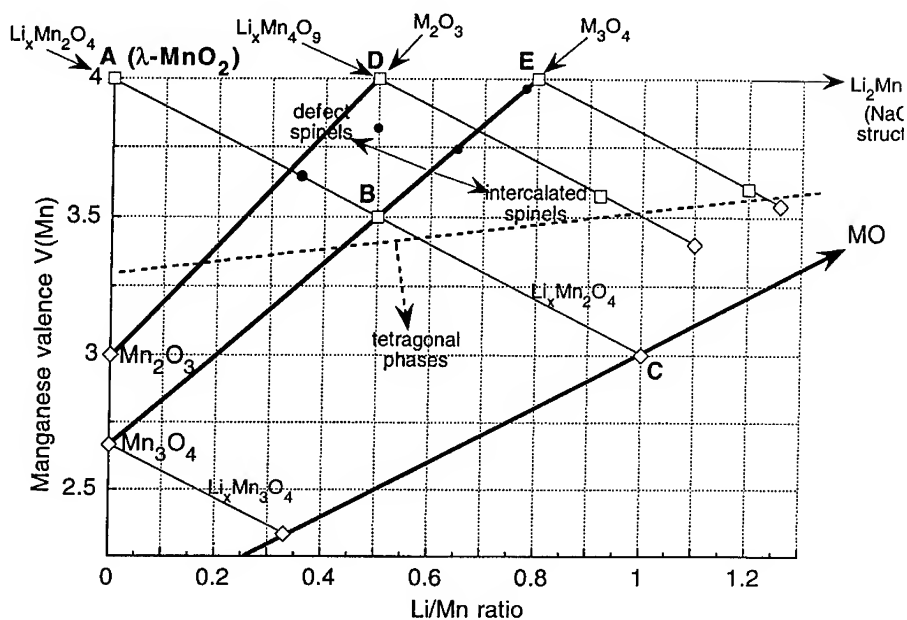


Fig. 1. Composition-valence diagram Li-Mn-O. B =  $\text{LiMn}_2\text{O}_4$ , C =  $\text{Li}_2\text{Mn}_2\text{O}_4$ , D =  $\text{Li}_2\text{Mn}_4\text{O}_9$ , E =  $\text{Li}_4\text{Mn}_5\text{O}_{12}$ . Black dots show the compositions studied here.

– constant cation/anion ratios (dashed lines in Fig. 1), which allow to easily distinguish stoichiometric ( $\text{M}_3\text{O}_4$  line), defective (upper left corner,  $\partial > 0$ ) and intercalated spinels (lower right corner,  $\partial < 0$ );

– intercalation lines (thin full lines in Fig. 1), which run from top left to bottom right in Fig. 1. The length of these intercalation lines is directly related to the theoretical capacity. It is longest along the  $\text{Li}_x\text{Mn}_2\text{O}_4$  line ABC, but this line should actually be considered as the sum of two separate segments AB and BC, corresponding to the two sides of equation (I). The composition-valence diagram also shows that capacities comparable to that of the BC line can be found, especially from points D or E in Fig. 1. Such compositions are attractive for several reasons :

- (i) they lie mostly above the tetragonal distortion limit,
- (ii) they have theoretical energy densities among the highest in 3 Volts spinel phases (120-180 Ah/kg according to Thackeray <sup>4</sup>),
- (iii) the low  $\text{Mn}^{3+}$  content of the active material not only prevents the Jahn-Teller distortion, but should also help preventing the dissolution of Mn in the electrolyte<sup>9</sup> and therefore limit cycling efficiency losses.

The theoretical capacity on the 3V plateau depends on the stoichiometry as follows. In the spinel formula unit  $(\text{Li}_{1+\partial}\text{Mn}_{2-\partial})\text{O}_4$ , the lithium intercalation capacity corresponds to the filling of the remaining cationic sites, i.e.  $1+\partial$  per formula unit. Structural determinations by Thackeray et al. showed that, in  $\text{Li}_2\text{Mn}_4\text{O}_9$  for instance, vacancies exist on both octahedral and tetrahedral sites<sup>5</sup>. The maximum specific capacity per mole  $\text{Q}_s$  is :

$$\text{Q}_s \text{ (in Ah / kg)} = \frac{\text{F}}{3.6} \cdot \frac{1+\partial}{\text{M}} = \frac{26800 (1+\partial)}{180.82 - 48x - 6.94\partial} \quad (2)$$

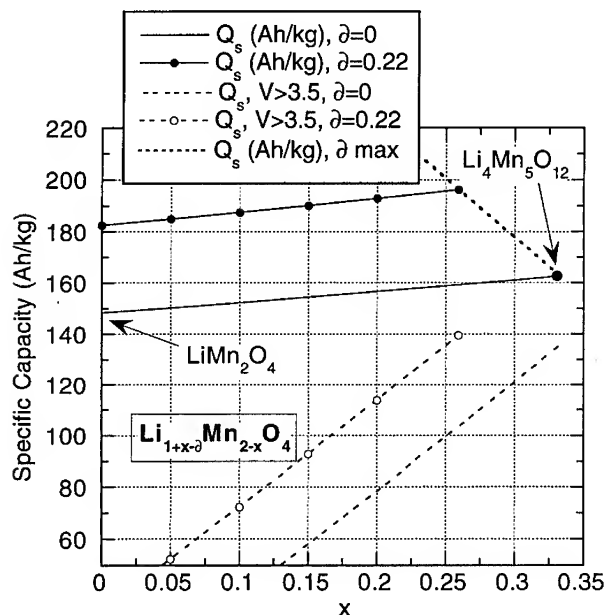


Fig. 2. Theoretical maximum capacity vs. stoichiometry and vacancy content

The usable capacity above the range of Jahn-Teller distortion is restricted to the site fraction with  $V(\text{Mn}) \geq 3.5$ . At  $V(\text{Mn}) = 3.5$ ,  $\partial = -2.5x$ , so that the number of sites available and the corresponding capacity are:

$$n_{>3.5} = 2.5x + \partial$$

$$Q_{>3.5} = \frac{26800 (2.5x + \partial)}{180.82 - 48x - 6.94\partial}$$

These capacities are shown in Fig. 2, where the value  $\partial = 0.22$  illustrates the  $\text{Li}_2\text{Mn}_4\text{O}_9$  case. The theoretical capacity  $Q_s$  increases slightly with  $x$ , while  $Q_{>3.5}$ , which is zero for  $\text{LiMn}_2\text{O}_4$  ( $x=0$ ), increases much more rapidly with  $x$ . The presence of 0.22 cation vacancies shifts both  $Q_s$  and  $Q_{>3.5}$  by more than 30 Ah/kg.

Note that the condition  $V(\text{Mn}) \leq 4$  also places a limit on the vacancy fraction  $\partial$ :

$$\partial \leq 1 - 3x$$

which reflects the decreasing length of lines parallel to AB when moving towards D in the ABD triangle in Fig. 1. This limit cuts the  $\partial = 0.22$  line in Fig. 2 for  $x > 0.259$ . From this figure, the maximum theoretical capacity is reached in the area  $0.2 \leq x \leq 0.26$  and high  $\partial$ . However, it should be kept in mind that the use of a defect spinel as a starting host for lithium intercalation does not guarantee that the guest Li atoms can be removed on charge from both "defect sites" and normal vacant sites at a suitable potential. The data in Fig. 2 must be considered as theoretical maxima.

## EXPERIMENTAL

Syntheses were carried out using either carbonates or reagent grade manganese dioxides, with the exception of sample R13, which was obtained by a new route in aqueous medium<sup>10</sup>. The preparation conditions are described in detail elsewhere<sup>8</sup> and summarized in Table I.

Electrochemical tests were carried out in 24-30 button-type batteries using a 1M solution of  $\text{LiClO}_4$  in PC:EC:DME as electrolyte. The batteries were tested at room temperature using a MacPile controller<sup>11</sup> working either in galvanostatic or in potentiostatic mode, in the latter case usually at 10 mV/h. Positive electrodes were made by mixing the oxide powder with 20% carbon black and 10% PTFE, pressed directly in the bottom of the button cell with an appropriate dye.

TABLE I  
Characteristics of typical spinel sample studied

sample #	preparation [8]	$\frac{\text{Li}}{\text{Mn}}$	V(Mn)	$x^*$	vacancy fraction $\delta^*$	cell parameter (Å)	impurities	theor. max. capacity (Ah/kg)
R13	aqueous oxidn. <sup>10</sup>	0.35	3.64	0	0.29	8.17	-	194 <sup>‡</sup>
C49	$\gamma/\text{Li}_2\text{CO}_3$ 850°C	0.5	3.51	0	0	8.24	-	148
F40b	carbonates 400°C	0.5 <sup>†</sup>	3.82 <sup>†</sup>	$\approx 0.15$	$\approx 0.22$	8.152	$\text{Li}_2\text{CO}_3$	190
F45	$\beta/\text{Li}_2\text{CO}_3$ 400°C	0.5 <sup>†</sup>	$\approx 3.8^{\dagger}$	ibid.		8.155	$\beta\text{-MnO}_2$	ibid.
C71	$\beta/\text{Li}_2\text{CO}_3$ 400°C	0.65 <sup>†</sup>	$\approx 3.75^{\dagger}$	0.18	0	8.158	$\beta\text{-MnO}_2$	$\approx 156$
C78	$\gamma/\text{Li}_2\text{CO}_3$ 400°C	0.8	3.91	1.33	$\approx 0$			163

\* formula  $(\text{Li}_{1+x-\delta}\text{Mn}_{2-x})\text{O}_4$

<sup>†</sup> nominal values

<sup>‡</sup> the fraction in excess of 148 Ah/kg is expected to involve tetrahedral vacancies, i.e. to occur at 4 Volts.

## RESULTS AND DISCUSSION

### Voltammetric behaviour

The cyclic voltammograms of samples C49 (stoichiometric  $\text{LiMn}_2\text{O}_4$ , included here as a reference), F40b and C78, recorded at 10 mV/h, are shown in Fig. 3. The main redox reversible current peak is sharpest for the stoichiometric compound, and it even becomes narrower on cycling. This is consistent with a two-phase reaction with equilibrium potential  $2.995 \pm 0.005$  V.

The current peaks in the defect spinel F40b are much broader, and they evolve considerably during the first three cycles (Fig. 3b): both oxidation and reduction peaks get narrower and the potential difference between decreases. This change is especially notable on charge, where two oxidation phenomena are visible. With cycling, the lower-potential one (resembling that of  $\text{LiMn}_2\text{O}_4$ ), seems to grow at the expense of the higher-potential peak. This trend is still visible at the 7th. vs. 11th. cycle (Fig. 3c), where a shoulder remains on the high-potential side of the main current peak both in reduction and oxidation. This shoulder can be ascribed to lithium intercalation / deintercalation involving vacant sites in this sample, which contains up to 0.22 vacancies per formula unit. The associated capacity, however, is difficult to compute because of the large overlap between both curves.

Sample C78 (Fig. 3d) is not a defect spinel, but it lies close to the spinel range limit in lithium content (high manganese valence,  $\text{Li}/\text{Mn} \approx 0.8$ , close to point E in Fig. 1). Like F40b, it shows a broad redox peak. At the low voltage scanning speed used (10 mV/h), the width of both oxidation and reduction peaks, as well as their overlap, indicates that the intercalation mechanism is probably single-phase, unlike  $\text{LiMn}_2\text{O}_4$ . This is consistent with an intercalation reaction beginning far above the cubic to tetragonal transition line (see Fig. 1). With increasing cycle number, the peaks sharpen, but the overlap between them remains.

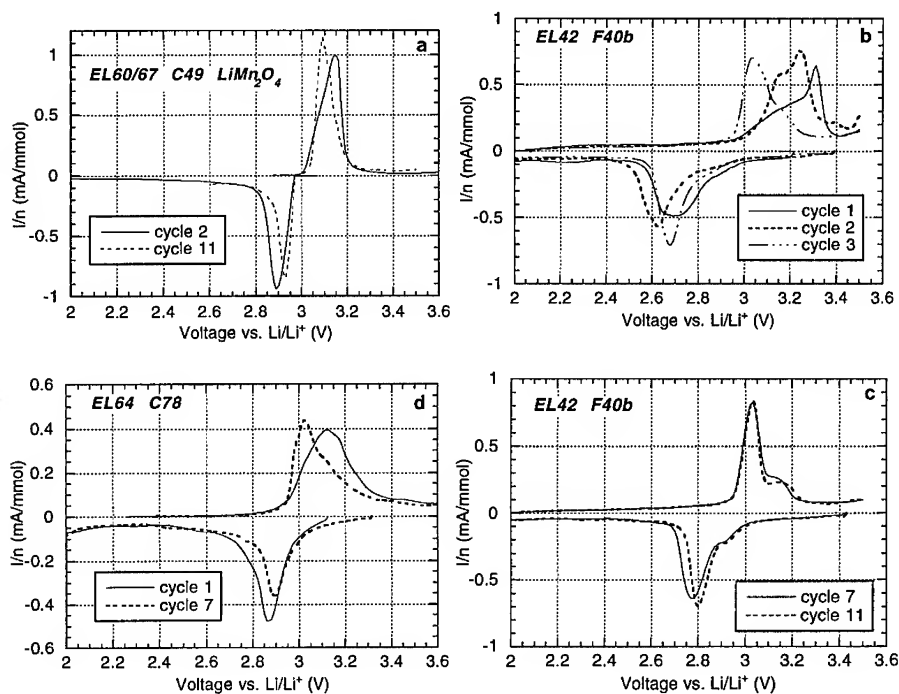


Fig. 3. Cyclic voltammograms at 10 mV/h of spinel samples (see characterization in Table I).

#### Capacity vs. cycling

The discharge curves and capacities for defect and stoichiometric spinels are compared in Fig. 4. The defect phase R13 (black dot on the AB line in Fig. 1) actually lies on the same intercalation line as  $\text{LiMn}_2\text{O}_4$ . It shows a fairly flat discharge plateau, but the capacity drops considerably with increasing cycle number (Fig. 4a). In spite of its defect structure, the available capacity on the first cycle does not exceed (but is exactly) 0.5 Li/Mn. This could be expected, because vacancies on the AB line are known to belong to the left-hand side of reaction I, i.e. to a 4 V reaction.

The defect spinel F40b, with a stoichiometry ca.  $\text{Li}_{0.93}\text{Mn}_{1.85}\text{O}_4$  (neglecting the secondary phases), shows a high initial capacity (0.67 Li/Mn) with 0.5 Li above 2.6 V (Fig. 4b). After the initial drop, the capacity remains larger than 0.5 Li/Mn for at least 10 cycles, which seems to indicate that some of the vacancies are active in the redox process at 3 Volts.

Sample C71 lies about mid-way along the BE line in Fig. 1, and has a negligible fraction of vacancies. Its discharge curve (Fig. 4c) is characterized by (i) a very flat plateau, (ii) an important step at 2.2 V, corresponding to about 35% of the capacity down to 2V. The capacity is remarkably constant after the initial drop in the first two cycles. The 2.2V step is not observed on charge. Its origin is not clear at the moment. This feature is also present, but to a lesser extent, on the new sample C63 (Fig. 4d). In this case the second plateau amounts to  $\approx 20\%$  of the total capacity (Fig. 4c).



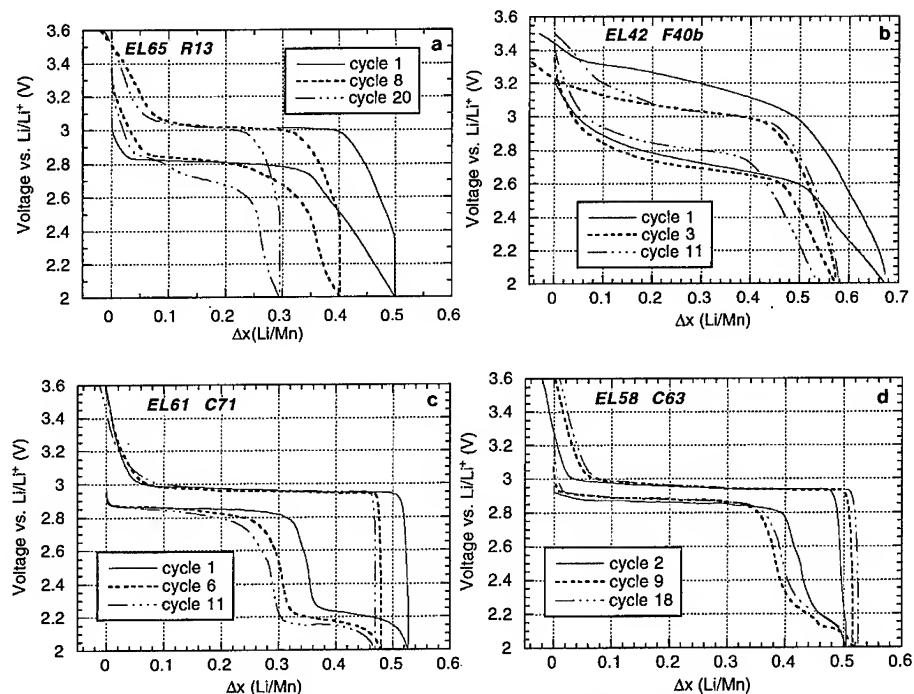


Fig. 4. Discharge curves of spinel samples  
(R13: C/25, F40b: potentiostatic, C71: C/50, C63: C/40)

The performances of these samples are summarized in Fig. 5 (the scales are identical on both figures for easy comparison). The figure on the left shows the performances of samples with  $\text{Li/Mn} \leq 0.5$ . Sample R13, which has a fairly high fraction of vacancies  $\delta$  and a low initial lithium content, does not bring any improvement with respect to  $\text{LiMn}_2\text{O}_4$ .

Sample F40b, a defect spinel with  $\text{Li/Mn} = 0.5$ , has much higher performances than the previous samples, and remains above the theoretical capacity of  $\text{LiMn}_2\text{O}_4$  (148 Ah/kg) after 11 cycles. Its vacancies act quite differently as those in sample R13, for instance. Its high capacity shows that the vacancies take part in the intercalation process at 3 V. It is likely that the active vacancies are located on the octahedral sites in this case. In addition, the X-ray powder diagram of sample F40b stopped at 2.5 V after 12 cycles in a lithium battery showed a general broadening of the reflections, but no trace of tetragonal phase (see Fig. 6). The cell parameter is  $\approx 8.186 \text{ \AA}$ , to be compared to 8.152 for the starting material.

The large discrepancy between samples F40b and F45, which have very close compositions and cation vacancies, shows that other parameters are important in controlling the rechargeable capacity.

On samples with higher Li contents (right-side figure), C78, with a composition close to that of the terminal phase  $\text{Li}_4\text{Mn}_5\text{O}_{12}$ , exhibits poor performances. Sample C71, with  $\text{Li/Mn} = 0.65$ , is better and shows an extremely constant capacity between the 3rd and 12th cycle, but an important fraction of its capacity lies below 2.5 V (see Fig. 4c). Finally, the new sample C63<sup>12</sup> shows both a high initial capacity and remarkably stable performances on cycling.

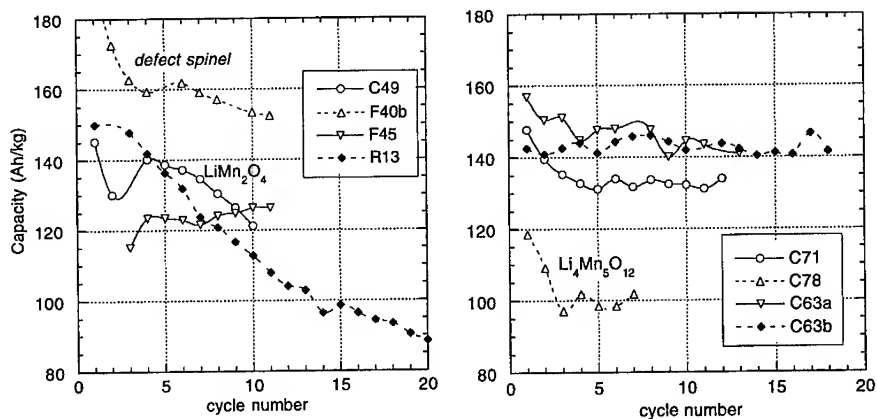


Fig. 5. Cycling performances of various spinel samples in the range 2-3.5 V.

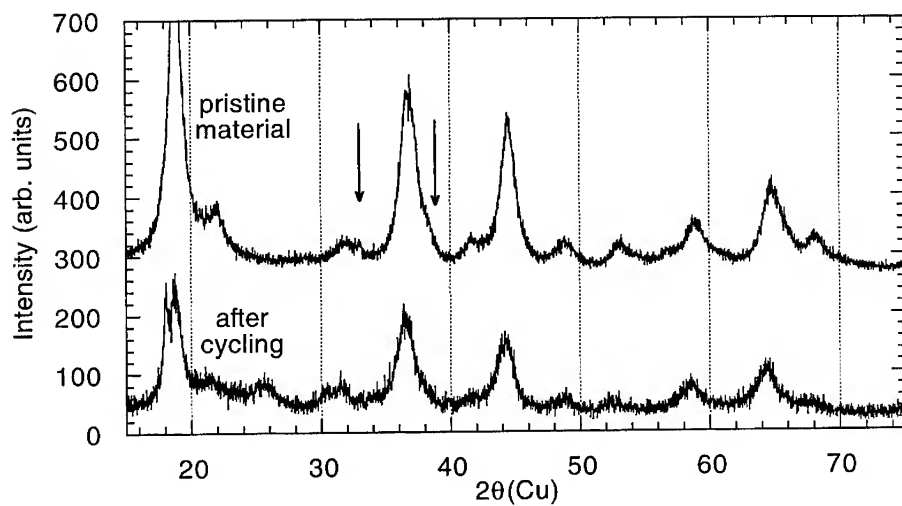


Fig. 6. Powder X-ray patterns of sample F40b as prepared (top) and after 12 cycles (bottom). Arrows show the positions of strong reflections of tetragonal  $\text{Li}_2\text{Mn}_2\text{O}_4$ .

## CONCLUSION

The comparison of the electrochemical cycling behaviour of various spinel phases Li-Mn-O in liquid electrolytes at ambient temperature shows that:

- a lithium-deficient composition derived from  $\text{LiMn}_2\text{O}_4$  (SR13) does not bring any improvement with respect to the stoichiometric composition;
- the end-member  $\text{Li}_4\text{Mn}_5\text{O}_{12}$ , characterized by a high initial manganese valence and a fairly high capacity without reaching the cubic-tetragonal phase transition, exhibits only a limited capacity;
- a defect spinel of composition close to  $\text{Li}_2\text{Mn}_4\text{O}_9$  (F40b) shows superior performances and probably cycles in a single-phase range;
- a new spinel (C63) recently synthesized<sup>12</sup>, has a constant capacity  $> 140 \text{ Ah/kg}$  in the range 2-3.5 V for more than 18 cycles.

Several results remain to be better understood: (i) the origin of the step at 2.2V, which can be fairly large and occurs only on reduction, (ii) important differences in the cycling performances between samples with very close compositions. The kinetic behaviour of the best samples is still under investigation.

## Acknowledgments

The authors wish to thank G. Lonchamp (CEA/CEREM). This work was carried out thanks to a grant from the Joule/CEE program. F. Le Cras is supported by CEA and Bolloré Technologies. The authors also thank J.C. Rousche and J.B. Soupart (Sedema) for supplying various manganese oxides.

## References

1. T. Ohzuku, M. Kitagawa and T. Hirai, *J. Electrochem. Soc.* **137**, 769 (1990).
2. J.M. Tarascon, E. Wang, F.K. Shokoohi, W.R. McKinnon and S. Colson, *J. Electrochem. Soc.* **138**, 2859 (1991).
3. J.M. Tarascon and D. Guyomard, *J. Electrochem. Soc.* **138**, 2864 (1991); .
4. M.M. Thackeray, A. de Kock, M.H. Rossouw, D. Liles, R. Bittihn and D. Hoge, *J. Electrochem. Soc.* **139**, 363 (1992).
5. M.H. Rossouw, A. de Kock, L.A. de Piccioto, M.M. Thackeray, W.I.F. David and R.M. Ibberson, *Mater. Res. Bull.* **25**, 173 (1990).
6. M.M. Thackeray, A. de Kock and W.I.F. David, *Mater. Res. Bull.* **28**, 1041 (1993).
7. A. de Kock, M.H. Rossouw, L.A. de Piccioto, M.M. Thackeray, W.I.F. David and R.M. Ibberson, *Mater. Res. Bull.* **25**, 657 (1990).
8. F. Le Cras, D. Bloch, P. Strobel, M. Anne, J.B. Soupart and J.C. Rousche, to be published.
9. R.J. Gummow and M.M. Thackeray, *J. Electrochem. Soc.* **141**, 1178 (1994); *Solid State Ionics* **69**, 59 (1994).
10. P. Strobel, S. Rohs, F. Le Cras and M. Anne, to be published.
11. C. Mouget and Y. Chabre, licensed from CNRS to Bio-Logic, Claix, France.
12. D. Bloch et al., to be patented.

## SYNTHESIS AND LITHIUM INTERCALATION PROPERTIES OF A LAYERED LITHIATED MANGANESE OXIDE WITH RANCIEITE TYPE

F. LEROUX, D. GUYOMARD AND Y. PIFFARD

Laboratoire de Chimie des Solides, Institut des Matériaux de Nantes, 2, rue de la Houssinière -  
44072 Nantes Cedex 03, France

### ABSTRACT

The 2D lithiated manganese oxide with Rancieite-type structure (lithium phyllomanganate), synthesized via a soft chemistry route ( $T \leq 60^\circ\text{C}$ ) is hydrated at room temperature and can be dehydrated progressively by a thermal treatment. This compound and a series of samples obtained after annealing at different temperatures were characterized and studied for their electrochemical lithium intercalation properties. They are poorly crystallized, with however the advantage of a manganese oxidation state very close to 4, a must to get high specific capacity. Their chemical characterization was achieved after gathering results obtained from complementary techniques such as AAS, redox titration, TGA and XPS measurements. Special care was taken for the chemical characterization of electrode compositions effectively used in the electrochemical cells.

Electrochemical lithium intercalation was systematically studied for the series of samples, when starting in charge or in discharge after assembly of the Li battery. The electrochemical behavior is discussed in relation with the manganese average oxidation state and the interlayer water content. Materials of the series showing the larger specific capacities were further examined on the application point of view, for their reversibility, cyclability and high rate capability upon Li intercalation.

This work shows that the anhydrous material which is obtained at  $300^\circ\text{C}$ , with the composition  $\text{Li}_{0.42}\text{Mn}^{\text{III}}_{0.20}\text{Mn}^{\text{IV}}_{0.80}\text{O}_{2.11}$ , is a promising rechargeable layered manganese dioxide material.

### INTRODUCTION

Layered transition metal sulphides and oxides present a suitable framework for reversible Li intercalation and, for that reason, have been extensively studied as electrode materials for Li batteries<sup>1,2</sup>. Oxides are now preferred because of their larger operating voltage<sup>3</sup>, and among oxides, manganese oxides present the advantages of a large theoretical specific capacity together with being wide-spread in nature, of low cost and non toxic.

Layered manganese oxides are known since a long time for their good ion-exchange properties<sup>4,5</sup> and their structural chemistry has been recently modeled and reviewed<sup>6,7</sup>. Since that time, intensive study of Li intercalation in such materials has been conducted world-wide, in order to try to design a layered manganese oxide suitable for the Li battery application.

2D-MnO<sub>2</sub>'s can be prepared by low temperature techniques such as air oxidation of Mn(OH)<sub>2</sub> in LiOH solution<sup>8</sup>, various aqueous oxidations, hydrothermal and molten salt reactions<sup>6,7</sup>, leaching of Li<sub>2</sub>O from 2D  $\alpha$ -Li<sub>2</sub>MnO<sub>3</sub><sup>9-11</sup>, or Na<sub>2</sub>O from sol-gel 2D  $\alpha$ -NaMnO<sub>2</sub><sup>12,13</sup> in acidic medium, or aqueous Na<sup>+</sup>/Li<sup>+</sup> ion-exchange from 2D  $\alpha$ -NaMnO<sub>2</sub><sup>14</sup>. To a certain extent, orthorhombic LiMnO<sub>2</sub>, synthesized either at low<sup>15,16</sup>, medium<sup>17</sup> or high temperature<sup>18</sup>, can be considered as a 2D-MnO<sub>2</sub>, as well. Some of these compounds contain interlayer Li<sup>+</sup> ions and/or interlayer water molecules. Most of these compounds intercalate Li reversibly<sup>8-13,19-21</sup> with capacities in the range of 200 mAh/g for some of them<sup>8,12,20</sup> at first discharge, but loose capacity very fast upon further cycling. Orthorhombic LiMnO<sub>2</sub> deintercalates Li but converts to spinel upon cycling<sup>15-18</sup>.

Work has then still to be done to improve the cycling performance of 2D-MnO<sub>2</sub>'s. Recently we have undertaken investigations on the synthesis, the chemical characterization and the Li intercalation properties of various phyllomanganates with the Rancieite-type structure<sup>22</sup>, containing different interlayer alkali cations or being alkali-free<sup>23,24</sup>. This kind of materials, whose

precursor was prepared from aqueous reduction of  $\text{KMnO}_4$ , have an average manganese oxidation state close to 4, favorable to even larger theoretical specific capacities than other  $2\text{D-MnO}_2$ 's. This paper will focus on the lithiated Rancieite-type manganese oxide, denoted Li-RMO (or 25-Li-RMO) in the text. It is hydrated at room temperature and can be dehydrated progressively by a thermal treatment leading to T-Li-RMO materials (T is the annealing temperature), which allows the study of the influence of water on the Li intercalation phenomena.

This paper will present the synthesis, the chemical characterization and results of electrochemical lithium intercalation in these compounds.

## EXPERIMENTAL

### Synthesis

The Rancieite-type layered manganic acid (H-RMO) has been prepared by a method derived from that already proposed by Tsuji et al.<sup>25</sup> and involving an aqueous reduction of  $\text{KMnO}_4$  at  $60^\circ\text{C}$  followed by an ion-exchange process in acidic medium<sup>23,24</sup>. AAS shows that H-RMO can be considered as an alkali-free material.

The Li-derivative of H-RMO (Li-RMO) was prepared by taking advantage of the ion-exchange properties<sup>23</sup>. A sample of the acid was equilibrated for 2 weeks with a large excess of an equimolar solution of 1M LiCl and 1M LiOH at room temperature (RT). The product was then washed with distilled water, freeze-dried and kept in the same conditions as the acid.

### Characterization of T-Li-RMO compounds

A combination of X-ray diffraction (XRD), chemical analyses, TGA and several spectroscopic techniques was used to characterize T-Li-RMO compounds. XRD patterns were recorded at various fixed temperatures on a Siemens D5000 diffractometer using  $\text{Cu K}\alpha$  radiation. The thermal analyses were performed on a Perkin-Elmer Model TGS-2 TGA system at a rate of  $1\text{K/min}$ . A Leybold LHS12 ESCA unit was used to record the XPS spectra (XPS mode, excitation  $\text{Mg K}\alpha$  :  $1253.6\text{ eV}$ ).

### Battery preparation and testing

Selected material were mixed with carbon black (Super-S from Chemetals Inc., Baltimore, MD, USA), 9% by weight, and PVDF binder, 4% by weight, to make a composite electrode on an aluminum disk, according to the technique designed at Bellcore<sup>26,27</sup>. Electrodes had a surface area of  $1\text{ cm}^2$  and contained about 5 mg of active material.

The electrolyte was a 1M solution of  $\text{LiClO}_4$  in a 2:1 volumic mixture of ethylene carbonate (EC) and dimethyl carbonate (DMC). The solvents have been purified and dried by double distillation and the salts have been vacuum dried for three days at  $150^\circ\text{C}$ , a procedure which leads to a water content of the electrolyte less than 40 ppm.

Swagelok test cells<sup>26,27</sup> were assembled in an argon-filled drybox with moisture and oxygen levels less than 1 ppm. Electrodes were vacuum dried at  $80^\circ\text{C}$  during one hour prior entering the antichamber, for materials annealed at  $T \geq 180^\circ\text{C}$ , while 25-Li-RMO was only evacuated in the antichamber. In the test cells, the composite electrode was separated from the lithium metal negative electrode by a 0.3mm thick glass fiber paper, soaked in the electrolyte. All cells use a Li metal anode, then voltages reported in the text are given vs Li.

Swagelok cells have been tested at RT using a Mac-Pile system in a galvanostatic mode. The Li composition of the materials is calculated from the elapsed time, the current, the active material mass and the formula weight, according to Faraday law, assuming that the experimental capacity is due to the intercalation-deintercalation reaction. For convenience, experimental capacities, even

due to mixed phenomena, will be reported in the text and figures as an equivalent number of Li per Mn atom, positively for discharge and negatively for charge.

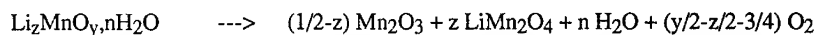
## RESULTS AND DISCUSSION

### Chemical characterization

The XRD patterns of H- and T-Li-RMO compounds are rather similar and show that they are not well crystallized. However, their similarity with that given by Tsuji et al. in ref.<sup>25</sup> clearly indicates that they are Rancieite type phases with an interlayer distance of  $\sim 7.4$  Å. Such patterns are quite different from that reported for birnessite<sup>28,29</sup>.

Li-RMO was analyzed for its alkali and manganese contents with use of AAS. A chemical analysis of the oxidation state of Mn was done according to the Vetter and Jaeger method<sup>30</sup>. At this level, if the chemical formula is written as  $\text{Li}_z\text{MnO}_y \cdot n\text{H}_2\text{O}$ ,  $z$  and  $y$  values are known.

The TG curve of Li-RMO is shown in Fig. 1a. The weight loss process is rather fast up to  $\sim 100^\circ\text{C}$  and becomes much slower at higher temperature. XRD patterns show that the lamellar character of the material is maintained up to  $\sim 400^\circ\text{C}$ , although diffraction peaks are getting weaker. Decomposition products were identified from their XRD patterns as  $\text{Mn}_2\text{O}_3$  (bixbyite) and  $\text{LiMn}_2\text{O}_4$  (3D spinel structure). Then, the thermal decomposition which occurs according to the following reaction:



allows to calculate the formula weight  $M$  (and then  $n$ ) per Mn atom of Li-RMO at ambient temperature.

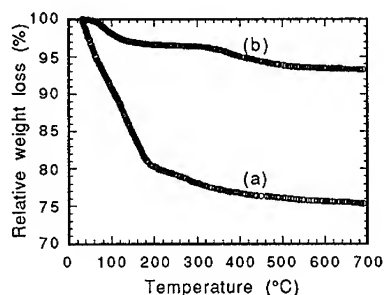


Fig. 1: TG curves of Li-RMO (a) and 300-Li-RMO (b).

upon a further heating up to  $100^\circ\text{C}$ , as shown on TG curves (Fig. 1b) where a plateau is now observed between  $\sim 100^\circ\text{C}$  and T.

In order to confirm the results of the chemical analyses, the T-Li-RMO compounds were examined by ESCA. The O 1s electron spectrum shows two peaks with slightly different binding energies (529.5 and 531.5 eV). According to the literature<sup>31,32</sup> the peak at 529.5 eV represents framework oxygen whereas the second peak is due to water. Furthermore, as the Mn 2p spectrum does not show satellite peaks at 5 eV to higher energies than the main peaks, we may conclude, as already mentioned<sup>33,34</sup> that no  $\text{Mn}^{2+}$  is present in the material at the level of detection possible with the ESCA satellite peaks and this is true also for samples of the manganic acid heated at various temperatures up to  $400^\circ\text{C}$ <sup>23</sup>.

Table I: Compositions of T-Li-RMO materials at RT, in open air, as a function of T

Temperature	Formulation
25°C	$\text{Li}_{0.42}\text{Mn}^{\text{III}}_{0.06}\text{Mn}^{\text{IV}}_{0.94}\text{O}_{2.18}$ ; 1.41 H <sub>2</sub> O
180°C	$\text{Li}_{0.42}\text{Mn}^{\text{III}}_{0.12}\text{Mn}^{\text{IV}}_{0.88}\text{O}_{2.15}$ ; 0.70 H <sub>2</sub> O
250°C	$\text{Li}_{0.42}\text{Mn}^{\text{III}}_{0.14}\text{Mn}^{\text{IV}}_{0.86}\text{O}_{2.14}$ ; 0.45 H <sub>2</sub> O
300°C	$\text{Li}_{0.42}\text{Mn}^{\text{III}}_{0.20}\text{Mn}^{\text{IV}}_{0.80}\text{O}_{2.11}$ ; 0.23 H <sub>2</sub> O
400°C	$\text{Li}_{0.42}\text{Mn}^{\text{III}}_{0.26}\text{Mn}^{\text{IV}}_{0.74}\text{O}_{2.08}$ ; 0.20 H <sub>2</sub> O

Table II: Compositions of T-Li-RMO materials at RT, cooled in dry atmosphere (25-Li-RMO was evacuated for 2 hrs), as a function of T (used as electrode materials).

Temperature	Formulation
25°C	$\text{Li}_{0.42}\text{Mn}^{\text{III}}_{0.06}\text{Mn}^{\text{IV}}_{0.94}\text{O}_{2.18}$ ; 1.06 H <sub>2</sub> O
180°C	$\text{Li}_{0.42}\text{Mn}^{\text{III}}_{0.12}\text{Mn}^{\text{IV}}_{0.88}\text{O}_{2.15}$ ; 0.12 H <sub>2</sub> O
250°C	$\text{Li}_{0.42}\text{Mn}^{\text{III}}_{0.14}\text{Mn}^{\text{IV}}_{0.86}\text{O}_{2.14}$ ; 0.04 H <sub>2</sub> O
300°C	$\text{Li}_{0.42}\text{Mn}^{\text{III}}_{0.20}\text{Mn}^{\text{IV}}_{0.80}\text{O}_{2.11}$ ; ε H <sub>2</sub> O
400°C	$\text{Li}_{0.42}\text{Mn}^{\text{III}}_{0.26}\text{Mn}^{\text{IV}}_{0.74}\text{O}_{2.08}$ ; ε H <sub>2</sub> O

#### Electrochemical study of first discharge

T-Li-RMO materials (Table II) were studied for their ability to intercalate reversibly Li in an electrochemical cell. On the one hand, according to the open character of the layered structure that should present available sites for guest atoms, and to the presence of reducible  $\text{Mn}^{4+}$  cations, Li intercalation should be possible in the starting materials. On the other hand, the chemical formulation of the electrode materials (Table II) shows the simultaneous presence of  $\text{Li}^+$  ions and oxidizable  $\text{Mn}^{3+}$  cations in the structure; then Li deintercalation should be possible in the starting materials, as well. Such chemistry has been widely used in the literature<sup>13,21,35</sup>, e.g. lithiated positive electrode materials ( $\text{LiMn}_2\text{O}_4$ ,  $\text{LiMO}_2$  (M=Ni, Co)) for rocking-chair lithium batteries behave as deintercalating cathodes, while non-lithiated positive electrodes ( $\text{TiS}_2$ ,  $\text{V}_2\text{O}_5$ , etc) are used as intercalating cathodes. In the following, the influence of a previous charge (Li deintercalation) on the first discharge (Li intercalation), will be examined.

#### a - Starting in discharge

According to literature, a discharge cut-off voltage of 2V should correspond to the end of the reduction step of  $\text{Mn}^{4+}$  to  $\text{Mn}^{3+}$ . Indeed, preliminary experiments on T-Li-RMO confirm that the main reduction step occurring at about 3V is finished at 2V vs Li.

The first Li intercalation in T-Li-RMO compounds, at a low rate corresponding to the intercalation of 1 Li per Mn in 80 hrs, is shown in Fig. 2a for the series of samples corresponding to different annealing temperatures. The amount of intercalated Li increases first with increasing annealing temperature, up to about 300°C, and then decreased at higher temperatures. An increase

of the annealing temperature resulted in a decrease of both the water and  $\text{Mn}^{4+}$  contents, as shown in Table II. To check for the influence of the  $\text{Mn}^{4+}$  initial concentration, the first discharge capacity was compared in Fig. 3 to the maximum theoretical capacity determined from the  $\text{Mn}^{4+}$  content, assuming that intercalation is finished when the whole Mn content is reduced to  $\text{Mn}^{3+}$ . Experimental capacity is closer to the theoretical value in thermally dehydrated materials, indicating a detrimental role of water on the effective capacity at first discharge.

Discharge V vs x curves show roughly a S-shape and not a plateau, which seems to indicate a topotactic single phase transformation. The average discharge voltage, calculated from curves in Fig 2a, remains roughly constant at 2.85V up to about 300°C and then decreases for higher annealing temperatures, consistent with a decrease of the initial amount of  $\text{Mn}^{4+}$  in the samples. As a matter of fact, lowering the manganese average oxidation state in a starting material with a given structure, is expected to lower both starting open circuit voltage, average discharge voltage and discharge capacity. Open circuit voltage after assembly of the cell was effectively lower for materials annealed at higher temperatures.

Li intercalation in 180-Li-RMO was investigated under open circuit conditions (see Fig. 2b), resulting from a relaxation of the voltage (to a variation less than 3mV/hr), after a current pulse. Both voltages, at the end of current pulse (close circuit voltage: CCV) and at the end of relaxation period (Open Circuit Voltage: OCV) are reported. The polarization, measured as the difference between CCV and OCV, remains low and constant during the first 2/3 of the intercalation range, and increases dramatically at high Li contents. The absence of a sharp decrease at the end of the OCV vs x curve shows that the intercalation process is not finished yet, even if the CCV reaches the discharge cut-off voltage of 2V, due to the increasing polarization. Relaxation data were fitted according to the model described by Basu and Worrell<sup>36</sup> to estimate a diffusion coefficient for  $\text{Li}^+$  ions. Results clearly show that the Li diffusion coefficient decreases at high Li content, by two orders of magnitude, compared to low or intermediate Li content (where the order of magnitude is  $10^{-10} \text{ cm}^2 \text{ s}^{-1}$ ). The kinetics limitation at large Li content explains why open circuit conditions allowed to intercalate more Li, compared to constant current conditions (Fig2b, curve 3), and explains partly why experimental maximum intercalation content is always smaller than the theoretical value. Such a limitation could be due to an almost full occupancy of  $\text{Li}^+$  sites at high Li content, indicating then an ionic limitation for Li intercalation and not an electronic one.

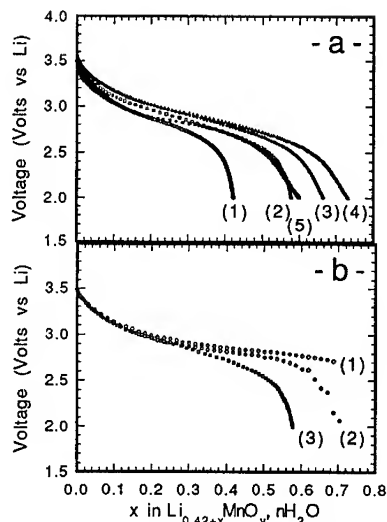


Fig. 2: a - First discharge of T-Li-RMO: (1) RT, (2) 180°C, (3) 250°C, (4) 300°C, (5) 400°C. b - First discharge of 180-Li-RMO under open circuit conditions ((1) OCV, (2) CCV), compared to constant current (3)

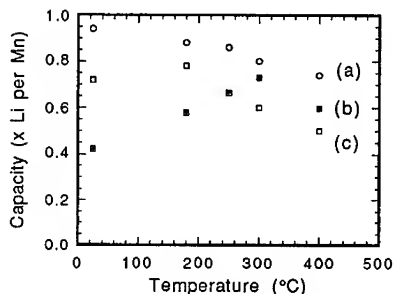
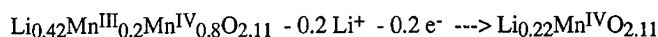


Fig. 3: Comparison of first discharge capacities for T-Li-RMO (a) theoretical discharge, (b) experimental initial discharge, (c) experimental discharge after an initial charge up to 4.3V.



### b - Starting in charge

According to the chemical formulation of the compounds, indicating a large  $\text{Li}^+$  ion content and a low  $\text{Mn}^{3+}$  content, the charge capacity should be theoretically limited by the electronic factor. For example, in the case of 300-Li-RMO, Li deintercalation at first charge, if possible, can be written on the following way:



Starting in charge after cell assembly should increase the following discharge capacity up to a theoretical value of 1 Li per Mn, if one assumes that the charge corresponds to the maximum reversible Li deintercalation up to a  $\text{Mn}^{4+}$  material, and that no spacial limitation occurs after that at the following Li intercalation down to a  $\text{Mn}^{3+}$  material. Assuming the same ionic limitation as during the first discharge, the experimental discharge capacity after an initial charge should be enhanced by the number of Li extracted during this first charge, compared to an initial discharge. The experimental discharge capacity after an initial charge is reported as a function of the annealing temperature in Fig. 3. Results show that the theoretical capacity is never reached. It should be noticed that much higher capacities than that measured at first discharge, are obtained at  $T \leq 180^\circ\text{C}$ , while  $T \geq 300^\circ\text{C}$  leads to lower values. This behavior was not expected, then special attention has been given to the V vs x behavior.

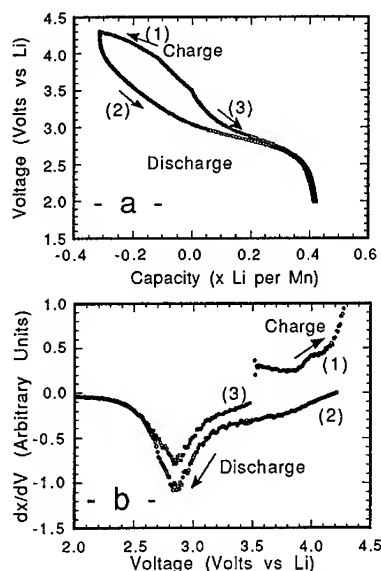


Fig. 4: a - First charge (1) and discharge (2) for 25-Li-RMO compared to an initial discharge (3). b - derivative  $dx/dV$  vs V curves of the previous curves.

water (interlayer water) oxidation and material oxidative degradation. If only electrolyte oxidation was occurring during the charge, the following discharge should be identical to the direct initial discharge, but shifted to lower x values by the charge capacity. Consequently, electrolyte oxidation is not the major contribution to the charge capacity in both compounds.

Voltage vs x curves for a discharge after an initial charge up to 4.3V vs Li, are shown, and compared to a direct initial discharge, in Fig. 4a for 25-Li-RMO and in Fig. 5a for 300-Li-RMO. For 25-Li-RMO, the observed initial charge capacity is equivalent to 0.32 Li per Mn, a high value compared to the theoretical one of 0.06 (see Table II). Upon the following discharge, a capacity corresponding to  $0.06 + 0.42 = 0.48$  Li per Mn (0.42 corresponding to the experimental capacity when starting in discharge) was expected, but a capacity of 0.74 Li per Mn was obtained, a value higher by 50%. On the contrary, the initial charge capacity was low in the case of 300-Li-RMO, 0.08 Li per Mn compared to the theoretical value of 0.2, while the following discharge capacity, equivalent to 0.6 Li per Mn, was lower than the experimental capacity when starting in discharge.

This effect of enhanced, or lowered, discharge capacity of 25-Li-RMO, or 300-Li-RMO, respectively, after an initial charge up to 4.3V, is not an experimental artefact because it can be reproduced for different intercalation rates and for both Na-RMO and Li-RMO<sup>24</sup>. This result shows that the presence or the absence of water plays a major role during the first charge.

The initial total charge capacity obtained at voltages higher than 4V may have several origins: Li deintercalation, electrolyte oxidation,

Figs. 4b and 5b which relate to 25-Li-RMO and 300-Li-RMO, respectively, allow to compare, for each material, the  $dx/dV$  vs  $V$  shape of the discharge curve after an initial charge, to that of a direct initial discharge. The  $dx/dV$  peaks have exactly the same shape in the 2.5V-3.4V range, in both cases. For 25-Li-RMO the intensity of the peak is larger after an initial charge whereas it is lower for 300-Li-RMO. This indicates the presence of the same sites, but with a different filling. It can then be concluded that no degradation occurs in both compounds during the first charge. For 25-Li-RMO, new sites for  $\text{Li}^+$  ions with an energy in the 3.4V-4V range appear after the oxidation treatment.

According to the previous analysis, the following mechanism is proposed to explain experimental data of Figs. 4 and 5. In 25-Li-RMO, both interlayer water is oxidized and Li is reversibly deintercalated during the charge, creating both new sites in the 3.4V-4V range and more pre-existing sites in the 2.5V-3.4V range, that can be used by  $\text{Li}^+$  ions at the following intercalation. In 300-Li-RMO, Li is irreversibly extracted from the structure, leading to less available  $\text{Li}^+$  sites at the following intercalation.

On the application point of view, an initial charge of the cell up to 4.3V vs Li was beneficial to the subsequent discharge capacity in the case of 25-Li-RMO, while it was detrimental in the case of 300-Li-RMO.

The first cycles obtained with RT-sample, when starting either in charge or in discharge, lead to a fast decrease of the capacity as a function of the cycle number, more drastic in the case of a start in charge, as shown in Fig. 6. For that reason, and because hydrated material are not suitable on a general point of view for Li batteries, except in special case<sup>12</sup>, RT samples were not studied further.

The following of the paper will then focus on 300-Li-RMO material.

#### Application-oriented electrochemical study of 300-Li-RMO

Reversibility and cyclability of Li intercalation in 300-Li-RMO will be studied over several tens of charge-discharge cycles, as a function of various experimental parameters: charge cut-off voltage, initial charge or discharge and C rate.

##### a - Optimization of the charge cut-off voltage

After an initial discharge, the influence of the charge cut-off voltage  $V_{\text{max}}$  on the next discharge

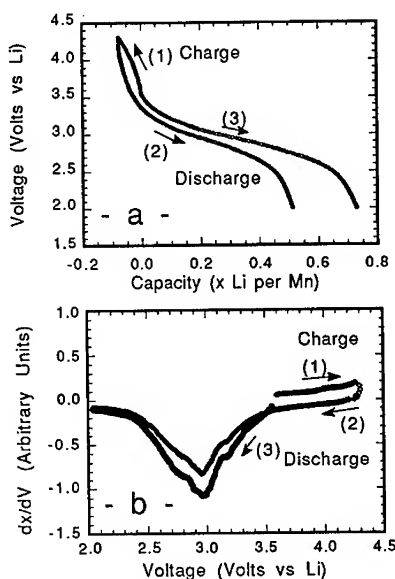


Fig. 5: a - First charge (1) and discharge (2) for 300-Li-RMO compared to an initial discharge (3). b - derivative  $dx/dV$  vs  $V$  curves of the previous curves.

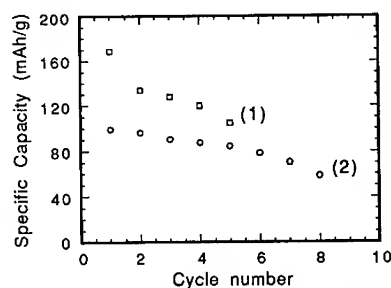


Fig. 6: Cycling behavior of RT-Li-RMO: (1) starting with an initial charge, (2) starting with an initial discharge.

capacity, has been examined by increasing  $V_{\max}$  by 0.1V at each cycle and measuring the subsequent discharge capacity. The capacity vs  $V_{\max}$  curve, reported in Fig. 7, shows three distinct ranges of behavior, first a low increase of the capacity for  $3.6V \leq V_{\max} \leq 4V$ , then a fast increase of the capacity for  $4V \leq V_{\max} \leq 4.3V$ , and finally a constant capacity after pushing the charge above 4.3V. Increasing  $V_{\max}$  from 3.6V to the optimized value of 4.3V lead to an increase of the capacity by 30%.  $V_{\max}$  values of 3.6V and 4.3V will then be selected for further studies.

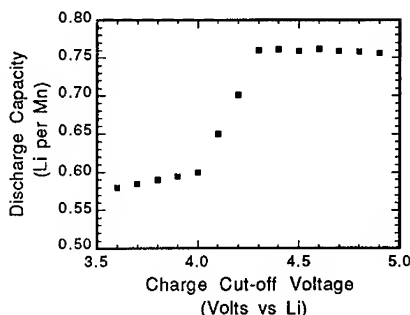


Fig. 7: Evolution of the discharge capacity of 300-Li-RMO with the charge cut-off voltage.

#### b - Reversibility at first cycles

The three first cycles obtained in both 2V-3.6V and 2V-4.3V ranges, after starting with an initial discharge, are shown in Figs. 8a and 8b, respectively. Cycling in the narrower voltage range was not enough to recover the whole first discharge capacity and lead to a faster decrease of the capacity. However, during a charge up to 4.3V, a larger capacity than the first discharge one, was recovered with a high reversibility on following discharge-charge cycles. It indicates that about 0.1 pre-existing chemical  $\text{Li}^+$  ions were reversibly electrochemically extracted during a charge following an initial discharge, while an initial charge up to the same  $V_{\max}$  had a completely different consequence, as seen above (Fig. 5).

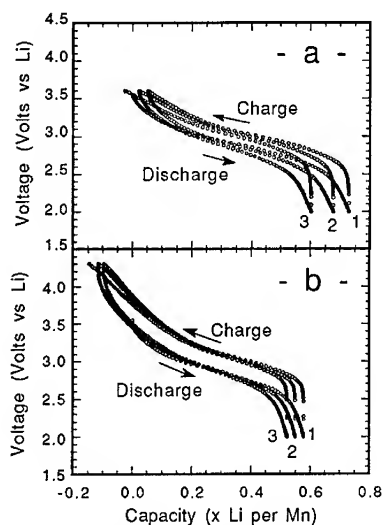


Fig. 8: Three first cycles of 300-Li-RMO when starting with an initial discharge: a - in the range 2V-3.6V at C/10, b - in the range 2V-4.3V at C/3.

faster capacity fading over the first 10 cycles. For the same cycling voltage range, starting in charge even at a fast rate of C/3, where the first charge lasts a few minutes, is readily detrimental to the further discharge capacities, which are shifted to lower values, but the rate of the capacity loss remains almost the same.

Voltage vs x curves show that Li intercalation is a fully reversible process with an extremely low voltage difference (about 0.2V), between charge and discharge (corresponding roughly to 2 times the polarization) even at fast rates such as C/3. Such a behavior is better than that reported in the literature<sup>12,13,20,21</sup>, where larger polarization occurs even with the use of larger carbon black content in the composite electrodes.

Voltage vs x curves do not show two processes, at about 4V and 3V, as it is the case in spinel lithium manganese oxide, indicating that the material structure, although not known, does not have a spinel character.

#### c - Cyclability over several tens of cycles

Results of cycling experiments performed under different conditions are reported in Figs. 9a and 9b. For initially discharged 300-Li-RMO, increasing the intercalation rate from C/15 to C/3 and to C/1.5, shifts the available capacity in the range 2V-4.3V without affecting the slope of the capacity vs cycle number decay, but limiting the voltage range to 2V-3.6V at the same rate (Fig. 9a, curves (1)-(2)) leads to a

Present results show that capacity retention of 300-Li-RMO is pretty good over several tens of cycles at various cycling rates. A capacity of 190mAh/g is still achieved after 20 cycles at C/15, with a composite electrode containing only 9% of carbon black. On the contrary, the best results reported in literature on the cycling behavior of phyllomanganates show that less than 150mAh/g was achieved after 20 cycles<sup>12</sup> at about the same rate, even when using 50% carbon mixed composite electrodes.

Close examination of the evolution of the shape of the discharge curve with the cycle number was achieved by calculating the  $dx/dV$  vs  $V$  variation at 2<sup>nd</sup> and 100<sup>th</sup> cycles from the corresponding discharge curves. Comparison of the two curves (Fig. 10) indicates the preservation of the general shape of the  $dx/dV$  peak. The slight shift of the peak voltage to lower voltages by about 0.1V is interpreted as a consequence of the polarization increase with the cycle number, which was observed for all cells. It seems then that the nature of the sites available for  $Li^+$  ions during intercalation, does not evolve during cycling, but their number decreases. Consequently, it can be assumed that the capacity fading upon cycling is not due to a degradation of the material but, at least in part, to a small fraction of  $Li^+$  ions that remains stuck in the interlayer space at each cycle.

Even after a large number of cycles, no evolution of the material to a spinel structure can be noticed, contrarily to what was observed when cycling orthorhombic  $LiMnO_2$ <sup>15-18</sup>.

#### d - High rate capability

The capability of 300-Li-RMO to sustain high discharge rates was studied by following the evolution of the discharge capacity with increasing discharge current at each cycle. The dependence of the discharge capacity on the cycling rate is depicted in Fig. 11. The capacity remains almost constant at rates lower than C/7, but decreases almost linearly with the logarithm of the current at rates larger than C/3 with a 3C rate corresponding to 50% utilization of the maximum capacity. After the high rate test, the cell was cycled again at low rates. The remaining capacity at a low rate of C/15 was slightly larger than that obtained after the same number of cycles at the constant rate of C/15. These results indicate the excellent ability of the material to handle high cycling rates without any memory effect.

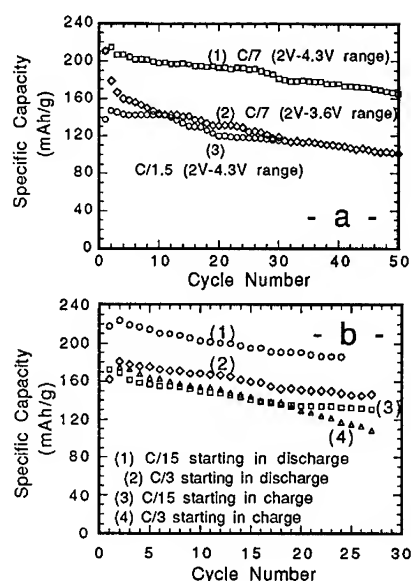


Fig. 9: Cycling behavior of 300-Li-RMO: **a** - as a function of the voltage range when starting with an initial discharge, **b** - as a function of the initial start in discharge or charge in the same voltage range, 2V-4.3V.

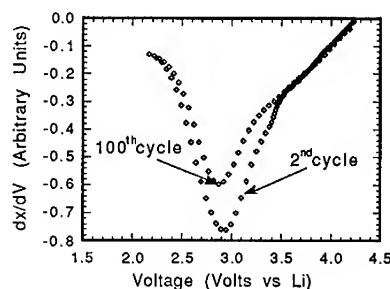


Fig. 10:  $dx/dV$  vs  $V$  representation of the 100<sup>th</sup> discharge compared to the 2<sup>nd</sup> discharge for a cycling at C/15 after a start in discharge in the 2V-4.3V range.

## CONCLUSION

Although Rancieite mineral is very poorly crystallized, as most naturally-occurring Birnessites, it is considered as an independent species<sup>22</sup>. Similarly, synthetic Rancieite materials such as T-Li-RMO's and H-RMO exhibit features and behaviors<sup>23-25</sup> that clearly differentiate them from Birnessites: a larger interlayer distance, for H-RMO a larger Li<sup>+</sup> exchange capacity, different thermal and electrochemical behaviors.

A careful chemical characterization of T-Li-RMO's used as electrode materials, allowed to study the role of interlayer water in the Li deintercalation/intercalation processes. This water strongly influences the Li intercalation at first cycle. A reversible Li extraction during the first charge creates new sites that can accommodate Li<sup>+</sup> ions at the next discharge which then leads to a larger capacity. However, long term cyclability is better with anhydrous 300-Li-RMO. This latter material shows:

- a high reversibility of the Li intercalation process, with low polarization even at high rates and for low carbon black content of the composite electrode,
  - a good cyclability at various rates and no degradation upon cycling,
  - a high rate capability with, however, a capacity divided by two at 3C compared to C/15.
- Such results make 300-Li-RMO a good candidate for 3V cathode of a Li battery.

## ACKNOWLEDGEMENTS

The authors would like to thank staff members of the laboratory, especially J.F. Berthelot, G. Billard, A. Bléteau, J.Y. Guilbaud and P. Molinié for their efficient help in the technical realizations needed in this work and in the set-up of the lab.

We are also grateful to M. Chabanel and D. Le Goff (Laboratoire de Spectrochimie des Ions, Nantes) for their scientific and technical help, respectively, in the distillation of the solvents used in our electrolytes.

This work is a part of a research program in collaboration with Hydroquebec, Canada and LIES, Grenoble, France.

## References

- <sup>1</sup> M. S. Wittingham, Prog. Solid State Chem. **12**, 41 (1978).
- <sup>2</sup> J. Desilvestro and O. Haas, J. Electrochem. Soc. **137**, 5C (1990).
- <sup>3</sup> C. Delmas, Lithium Batteries, Ed. G. Pistoia (Elsevier, Industrial Chemistry Library, 1994) Vol.5, p. 457.
- <sup>4</sup> D. C. Golden, J. B. Dixon and C. C. Chen, Clays and Clays Minerals, **34**, 511 (1986).
- <sup>5</sup> E. Paterson, J. L. Bunch and D. R. Clark, Clay Minerals, **21**, 949 (1986).
- <sup>6</sup> P. Strobel and J-C. Charenton, Rev. Chim. Min. **23**, 125 (1986).
- <sup>7</sup> P. Strobel, J-C. Charenton and M. Lenglet, Rev. Chim. Min. **24**, 199 (1987).

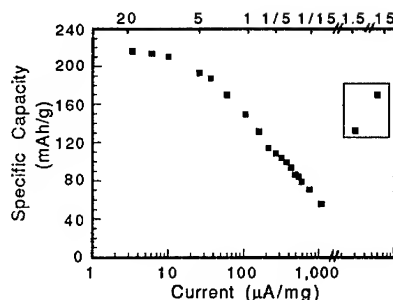


Fig. 11: Evolution of the capacity with the discharge current intensity, with increasing the constant current at each cycle.

- <sup>8</sup> T. Ohzuku, H. Fukuda and T. Hirai, *Chemistry Express* **2**, 543 (1987).
- <sup>9</sup> F. Lubin, A. Lecerf, M. Broussely and J. Labat, *J. Power Sources* **34**, 161 (1991).
- <sup>10</sup> M. H. Rossow and M. M. Thackeray, *Mat. Res. Bull.* **26**, 463 (1991).
- <sup>11</sup> M. H. Rossow, D. C. Liles and M. M. Thackeray, *J. Solid State Chem.*, **104**, 464 (1993).
- <sup>12</sup> S. Bach, J-P. Pereira-Ramos, N. Baffier and R. Messina, *Electrochim. Acta* **36**, 1595 (1991).
- <sup>13</sup> P. Le Goff, N. Baffier, S. Bach, J-P. Pereira-Ramos and R. Messina, *Solid State Ionics* **61**, 309 (1993).
- <sup>14</sup> F. Capitaine, P. Gravereau and C. Delmas, GFECI meeting (Montpellier, France, March 1994), **Abstract p.57**.
- <sup>15</sup> T. Ohzuku, A. Ueda and T. Hirai, *Chemistry Express* **7**, 193 (1992).
- <sup>16</sup> J. N. Reimers, E.W. Fuller, E. Rossen and J. R. Dahn, *J. Electrochem. Soc.* **140**, 3396 (1993).
- <sup>17</sup> R. J. Gummow, D.C. Liles and M. M. Thackeray, *Mat. Res. Bull.* **28**, 1249 (1993).
- <sup>18</sup> I. J. Davidson, R. S. MacMillan, and J. J. Murray, Proceedings of 7th International Meeting of Lithium Batteries (Boston, May 1994) **Abstract II-B-26**, p. 586, to be published.
- <sup>19</sup> P. Strobel, *Solid State Ionics III*, MRS Symposium Proceedings **Vol. 293**, p. 63 (1993).
- <sup>20</sup> P. Strobel and C. Mouget, *Mat. Res. Bull.* **28**, 93 (1993).
- <sup>21</sup> F. Le Cras, P. Strobel and M. Anne, Proceedings of 7th International Meeting of Lithium Batteries (Boston, May 1994) **Abstract II-A-40**, p. 480, to be published.
- <sup>22</sup> W. E. Richmond, M. Fleischer and M. E. Mrose, *Bull. Soc. fr. Minéral. Cristallogr.* **92**, 191 (1969).
- <sup>23</sup> F. Leroux, D. Guyomard and Y. Piffard, *Solid State Ionics*, *to be published*.
- <sup>24</sup> F. Leroux, D. Guyomard and Y. Piffard, *Solid State Ionics*, *to be published*.
- <sup>25</sup> M. Tsuji, S. Komarneni, Y. Tamaura and M. Abe, *Mat. Res. Bull.* **27**, 741 (1992).
- <sup>26</sup> D. Guyomard and J-M. Tarascon, *J. Electrochem. Soc.* **140**, 3071 (1993).
- <sup>27</sup> D. Guyomard and J-M. Tarascon, *Solid State Ionics* **69**, 222 (1994).
- <sup>28</sup> R. Giovanoli, E. Stähli and W. Feitknecht, *Helv. Chem. Acta* **53**, 209 (1970).
- <sup>29</sup> P. Le Goff, N. Baffier, S. Bach and J-P. Pereira-Ramos, *J. Mater. Chem.* **4**, 875 (1994).
- <sup>30</sup> K. J. Vetter and N. Jaeger, *Electrochimica Acta* **11**, 401 (1966).
- <sup>31</sup> X. M. Shen and A. Clearfield, *J. Solid State Chem.* **64**, 270 (1986).
- <sup>32</sup> M. Oku, K. Hirokawa and S. Ikeda, *J. Electron Spectrosc.* **7**, 465 (1975).
- <sup>33</sup> M. A. Baltanas, J. R. Katzer and A. B. Stiles, *Acta Chim. Acad. Sci. Hung.* **124**, 341 (1987).
- <sup>34</sup> M. I. Zaki and C. Kappenstein, *Zeitschrift für Physikalische Chemie* **176**, 97 (1992).

---

<sup>35</sup> M. N. Richard, E. W. Fuller and J. R. Dahn, *Solid State Ionics* **73**, 81 (1994).

<sup>36</sup> S. Basu and W. L. Worell, Fast Ion Transport in Solids, edited by P. Vashita, J. N. Mundy and G. K. Shenoy (Elsevier North-Holland, Amsterdam 1979), p. 149.

## LITHIUM-7 NMR STUDIES OF $\text{Li}_{1-x}\text{CoO}_2$ BATTERY CATHODES

B. Ouyang\*, X. Cao\*, H.W. Lin<sup>†</sup>, S. Slane\*\*, S. Kostov\*, M. denBoer\* and S.G. Greenbaum\*

\*Physics Department, Hunter College of CUNY, New York, NY 10021

<sup>†</sup>Alliant Techsystems, 104 Rock Road, Horsham, PA 19044

\*\*U.S. Army Research Lab (EPSCD), Ft. Monmouth, NJ 07703

### ABSTRACT

Lithium-deficient cathode materials  $\text{Li}_{1-x}\text{CoO}_2$ , where  $x = 0.1, 0.4$  and  $0.6$  were prepared electrochemically from the stoichiometric parent compound ( $x = 0.0$ ). The materials were observed to be air-stable, and x-ray diffraction characterization yielded good agreement with the *in situ* studies of Dahn and co-workers, regarding changes in lattice parameters. In addition to both static and magic angle spinning (MAS)  $^7\text{Li}$  NMR, measurements, the samples were investigated by EPR and cobalt K-edge NEXAFS. The removal of Li is accompanied by compensating electrons from the Co d-orbitals, as evidenced by both shifts in the NEXAFS peak and the observation of EPR signals due to spins localized on the Co ions. These spins, in turn, result in dramatic  $^7\text{Li}$  chemical shifts (89 ppm for  $x = 0.6$ ) and line broadening. Whereas MAS analysis of  $\text{Li}_{0.9}\text{CoO}_2$  indicates two magnetically inequivalent Li sites, the spectra become too broad to resolve different sites for higher values of  $x$ . Finally NMR linewidth and spin-lattice relaxation measurements as a function of temperature suggest a modest increase in  $\text{Li}^+$  ion mobility for Li-deficient samples as compared to the parent compound.

### INTRODUCTION

$\text{LiCoO}_2$  is one of the leading cathode materials in secondary lithium batteries, despite the relatively high cost of cobalt. Lithium ions can be electrochemically (and reversibly) deintercalated from the parent compound to form  $\text{Li}_{1-x}\text{CoO}_2$ , and cell voltages lie in the 3.5 - 4.5 V range as the value of  $x$  increases from 0.0.<sup>1,2</sup> Although there have been extensive electrochemical and structural studies of this cathode material, little is known about the local environment of the  $\text{Li}^+$  ions because of their extremely small x-ray scattering power. Neutron diffraction could certainly be of use in this regard although there have been no reports of neutron studies of Li-deficient cathode material. For this reason,  $^7\text{Li}$  nuclear magnetic resonance (NMR) studies were undertaken.  $^7\text{Li}$  NMR spectra can provide information about the local environment of the Li ion, through a variety of interactions. Among these are the nuclear quadrupole interaction, which is present when the site symmetry is low, and the chemical shift arising from either conduction electrons (Knight shift) or interactions with nearby paramagnetic ions. Both of these effects can lead to shifting and broadening of the resonance.

Supplementary measurements performed on these materials include x-ray diffraction, to verify that expected changes in the unit cell parameters occur as lithium is removed; electron paramagnetic resonance (EPR) to identify the main source of NMR broadening; and near edge x-ray absorption fine structure (NEXAFS), to provide supplementary information about the changes in the cobalt electronic structure which accompany Li-deintercalation.



## EXPERIMENTAL

$\text{Li}_{1-x}\text{CoO}_2$ , where  $x = 0.1, 0.4$  and  $0.6$ , was prepared using electrochemical titration of commercial  $\text{LiCoO}_2$  (as received, from FMC Corp.). The electrolyte solution was  $2.0\text{M LiAsF}_6 + 0.4\text{M LiBF}_4$  in methyl formate. The current density was  $0.2\text{ mA/cm}^2$ . After titration the powder was washed in methyl formate and then dried at room temperature under vacuum for 16 hours. Atomic absorption analyses on Li and Co concentrations revealed Li to Co mole ratios of 0.87, 0.58 and 0.52 for the expected compositions  $(1-x)$  of 0.9, 0.6 and 0.4, respectively. All samples were deemed air stable, by checking for reproducibility of selected x-ray, EPR and NMR measurements on samples exposed to ambient atmosphere, compared to samples sealed under argon. X-ray diffraction patterns of the  $\text{Li}_{1-x}\text{CoO}_2$  samples were obtained with a Phillips PW1840 powder diffractometer using  $\text{CuK}\alpha$  radiation. The lattice constants of the as-received (stoichiometric)  $\text{LiCoO}_2$  were  $a = 2.823(2)\text{ \AA}$  and  $c = 14.066(2)\text{ \AA}$ , which are in good agreement with literature values.<sup>3</sup>

NEXAFS measurements were carried out in transition mode on powdered samples at Beamline X-23B of the National Synchrotron Light Source at Brookhaven National Laboratory. CoO was employed as a reference standard and run concurrently with the lithiated samples in order to obtain improved energy calibration. Two different monochromator slit widths were utilized, 1mm and 2mm, the former giving a resolution of better than  $\pm 0.1\text{ eV}$ . X-band EPR measurements were performed on powdered samples in quartz EPR tubes, with an IBM/Bruker ER-220D spectrometer, utilizing 100kHz field modulation to record absorption first-derivative spectra. Both magic angle spinning (MAS) and wide line  $^7\text{Li}$  NMR spectra of packed powder samples were obtained by Fourier transformation of a single-pulse sequence, with a typical  $90^\circ$  pulse length of  $3\text{ }\mu\text{s}$ , using a Chemagnetics CMX-300 spectrometer. Spin-lattice relaxation times were measured by saturation recovery. Aqueous  $\text{LiCl}$  solution was employed as a chemical shift reference.

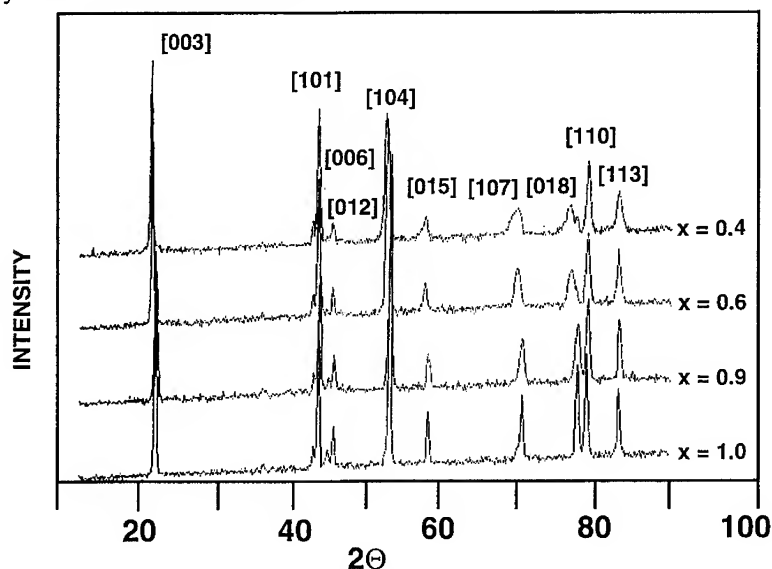


Figure 1a. X-ray diffraction results for  $\text{Li}_x\text{CoO}_2$ , indicating specific lattice reflections.

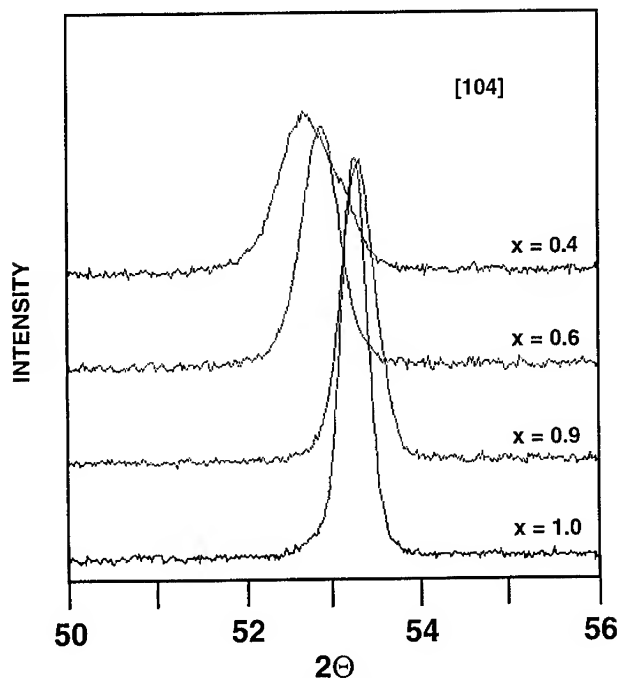


Figure 1b. Expanded scale diffraction, showing [104] reflection of  $\text{Li}_{1-x}\text{CoO}_2$

## RESULTS AND DISCUSSION

The x-ray patterns of the  $\text{Li}_{1-x}$  samples, shown in Fig. 1a, indicate evidence of a small quantity of  $\text{Co}_3\text{O}_4$  in the initial  $\text{LiCoO}_2$  material. The use of internal and external standard methods for measuring phase quantities yield an estimate of approximately 3 wt% of this impurity phase. It has been found by step potentiodynamic cyclic sweeps and overpotential measurements that insertion and de-insertion reactions of  $\text{Li}_{1-x}\text{CoO}_2$  proceed as single-phase reversible reactions over at least three phases for  $0.0 < x < 0.7$ .<sup>1</sup> These phases have been characterized by *in situ* x-ray diffraction studies, which revealed significant expansion of the c-lattice parameter from  $0.07 < x < 0.25$ , and a lattice distortion from hexagonal to monoclinic symmetry at  $x = 0.5$ .<sup>2</sup> Our x-ray results are in agreement with the more detailed *in situ* findings. In particular, shifts to lower Bragg angles for the [003], [104], [107] and [018] reflections are observed as well as splitting of the [018] peak. This agreement is significant in that it validates the use of *ex situ* spectroscopic studies of the ionic and electronic behavior of cathode materials.

The cobalt K-edge x-ray absorption spectrum of the stoichiometric sample is displayed in Fig. 2. The energy range from about 10 eV below the main absorption edge, usually referred to as the "white line", to about 20 eV above the edge is the NEXAFS region, which corresponds to dipole-allowed transitions of 1s-states into unoccupied 4p-states. The range from about 20 eV extending to  $\sim 1000\text{eV}$  above the edge is referred to as the extended x-ray absorption fine structure (EXAFS) region, and corresponds to ionization of the core (1s) electrons. The EXAFS spectrum contains information that is often readily converted to nearest-neighbor

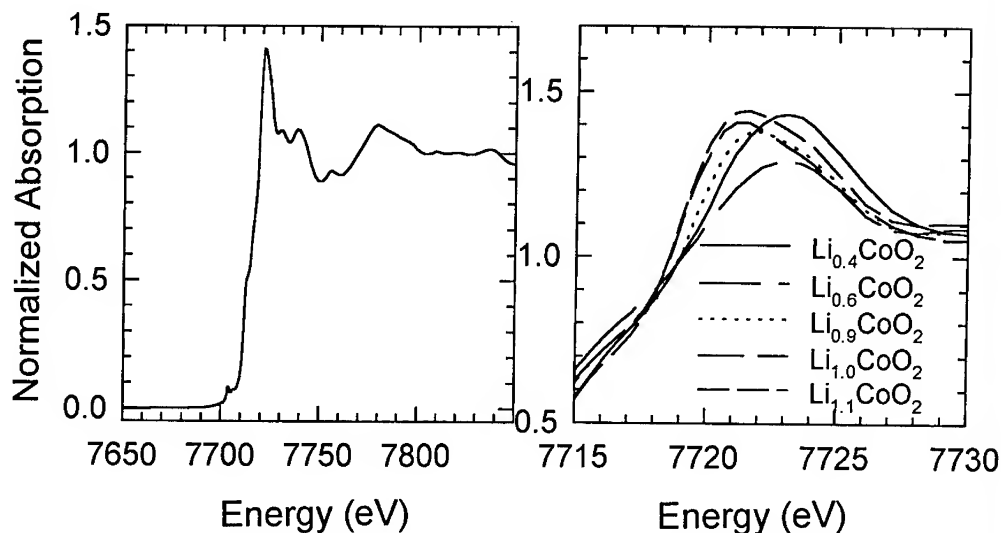


Figure 2. Cobalt K-edge NEXAFS spectra in  $\text{Li}_{1-x}\text{CoO}_2$  series.

Figure 3. Detailed view of NEXAFS white line spectra for  $\text{Li}_{1-x}\text{CoO}_2$  series.

coordination.<sup>4</sup> The NEXAFS region also contains information, although interpretation in terms of specific electronic configurations or bonding arrangements is difficult. Nevertheless, trends observed in a series of similar materials, in this case, insertion compounds with varying amounts of  $\text{Li}^+$  ions, can be quite useful. The x-ray absorption spectrum corresponding to the cobalt K-edge for stoichiometric  $\text{LiCoO}_2$  is shown in Fig. 2. The overall shape of the absorption is approximately the same in all samples, but there are some subtle differences discussed below.

The main peak (or white line) absorptions are shown in Fig. 3, and the peak values are listed in Table I. For the three samples with x-values 0.0 (stoichiometric), 0.1 and 0.4, the peak shifts to higher energy with decreasing Li content. This is attributed to the increase in charge on the Co ion caused by the removal of compensating electronic charge associated with the lithium deficiency. The relatively large shift (almost 2 eV over the entire range) is consistent with the expectation that the compensating electrons originate from the Co ions rather than from the generation of defect oxide species. There is no significant difference between the peak positions for the  $x = 0.4$  and 0.6 materials, which may be due to the actual Li contents of the two samples being closer to each other than the nominal Li contents, and the presence of the structural phase transition in the lowest Li content sample, which can also affect the edge position.

The integrated intensity of the small pre-edge feature occurring around 7704 eV (Fig. 2) is plotted in Fig. 4 as a function of Li-content. The weak pre-edge absorption is attributed to the dipole-forbidden  $1s \rightarrow 3d$  transition, and its intensity provides a measure of the degree of departure of the Co environment from octahedral coordination symmetry.<sup>5</sup> The trend of decreasing symmetry with decreasing Li content is monotonic, even including an excess Li sample ( $\text{Li}_{1.1}\text{CoO}_2$ ) prepared by sol-gel techniques. Departure from the trend is noted for the  $\text{Li}_{0.4}\text{CoO}_2$  sample, and is, again, attributed to the structural phase transition which occurs at the lower lithium content.

Table I. NEXAFS White Line Positions

COMPOUND	NEXAFS PEAK (eV)
$\text{Li}_{0.4}\text{CoO}_2$	7722.8
$\text{Li}_{0.6}\text{CoO}_2$	7722.8
$\text{Li}_{0.9}\text{CoO}_2$	7721.6
$\text{Li}_{1.0}\text{CoO}_2$	7721.0
$\text{Li}_{1.1}\text{CoO}_2$	7721.2

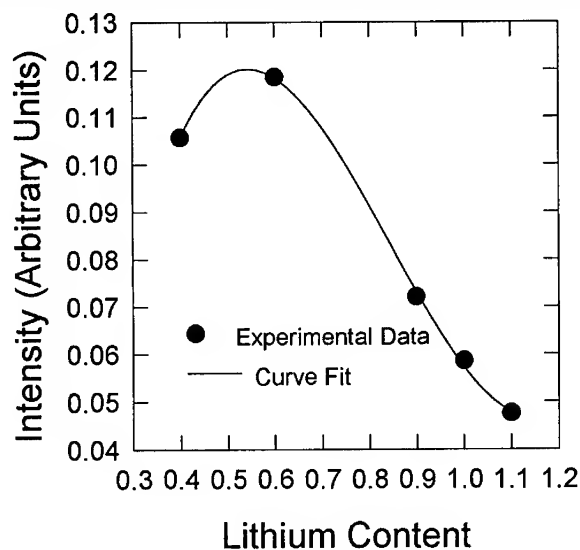


Figure 4. Plot of Co pre-edge integrated intensity vs. Li content.

The parent compound,  $\text{LiCoO}_2$  is expected to be diamagnetic because the nominal valence of Co is 3+. It is therefore also expected that the removal of d-electrons corresponding to charge neutrality in Li-deficient samples should yield paramagnetic material. The first derivative EPR spectrum of  $\text{LiCoO}_2$  is shown in Fig. 5a and spectra of the Li-deficient samples are displayed in Fig. 5b. The strong and relatively narrow resonance of the stoichiometric sample (5a) is attributed to the presence of the several percent  $\text{Co}_3\text{O}_4$  impurity which was detected by x-ray diffraction.  $\text{Co}_3\text{O}_4$  has inequivalent Co ions, two in the diamagnetic 3+ state and one in the paramagnetic 2+ state.<sup>6</sup> The EPR spectra of the Li-deficient samples are, however, quite broad due to magnetic dipole-dipole interactions between spins induced by the loss of the compensating d-electrons and localized on the Co sites.

Lithium-7 NMR absorption lineshapes under static (non-spinning) conditions for  $x = 0.0$ , 0.1 and 0.4 are displayed in Fig. 6. The parent compound is characterized by both a small chemical shift, ~5 ppm relative to aqueous LiCl solution, and a relatively narrow line width,

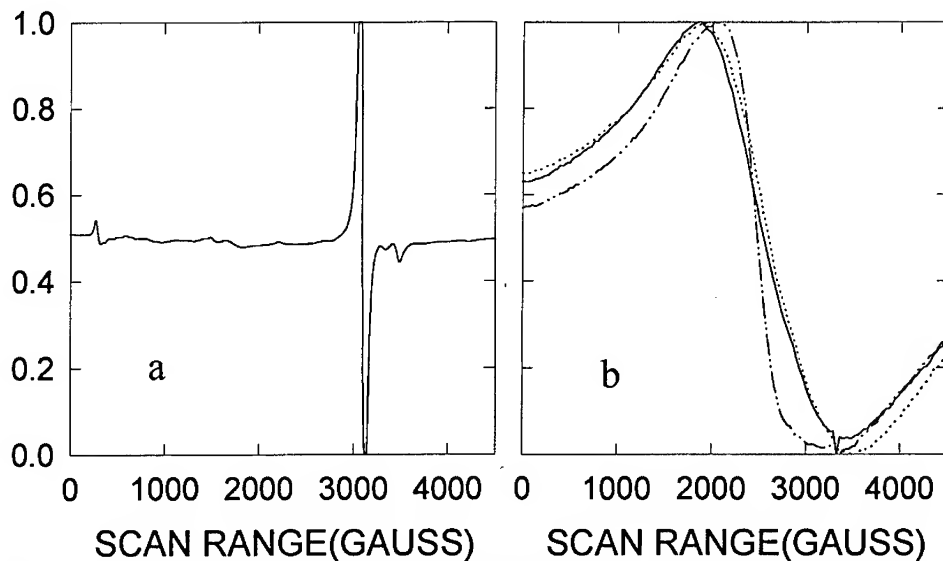


Figure 5. (a) EPR spectrum of  $\text{LiCoO}_2$ . (b) EPR spectra of  $\text{Li}_{1-x}\text{CoO}_2$ ;  $x = 0.1$  (dots),  $x = 0.4$  (solid),  $x = 0.6$  (chain links). The microwave frequency is 9.42 GHz

15 kHz (130 ppm) full width at half maximum. Similar NMR results for  $\text{LiCoO}_2$  have been reported recently.<sup>7</sup> The lack of observable quadrupole satellite transitions, coupled with very low ionic mobilities inferred from variable temperature studies (to be discussed later), indicate that the Li site symmetry is high. The removal of Li results in a dramatic increase in chemical shift, values listed in Table II, as well as an increase in line width. The large chemical shifts and increased line widths of the Li-deficient materials are attributed to localized spins on the Co sites, as evidenced by the EPR results. The line widths of all four samples (including  $x = 0.6$ ) are plotted as a function of temperature in Fig. 7. The parent ( $x = 0.0$ ) and  $x = 0.1$  compounds exhibit essentially no variation in line width over the very large temperature range between  $-100$  to  $+250^\circ\text{C}$ , while the line widths of the  $x = 0.4$  and  $0.6$  materials change by nearly a factor of two over the same temperature range.

Lithium ion mobilities in these cathode materials can be said to be fairly small compared to other intercalation cathodes such as  $\text{Li}_x\text{TiS}_2$ , in which much more significant motional line narrowing effects are observed.<sup>8</sup> Some of the line width temperature dependence of the Li-deficient materials could be attributed to motional effects, because there are more possible sites for  $\text{Li}^+$  to occupy than in the stoichiometric compound. However, the ordinary temperature dependence of the paramagnetic susceptibility would also yield line broadening at lower temperatures. Spin-lattice relaxation ( $T_1$ ) measurements were made in an attempt to distinguish between these two effects, and the results are plotted in Fig. 8. Again, the stoichiometric compound exhibits remarkably little variation over the large 350-degree range previously cited. The  $T_1$ 's of the  $x = 0.4$  and  $0.6$  samples do change by about a factor of four over the same temperature range, but the lack of observable  $T_1$  minima in the Li-deficient samples does not permit an estimate of motional correlation times. However, because almost no temperature variation of  $T_1$  was noted in the more magnetic  $\text{LiMn}_2\text{O}_4$  cathode system,<sup>9</sup> some  $\text{Li}^+$  ion motion can be deduced.

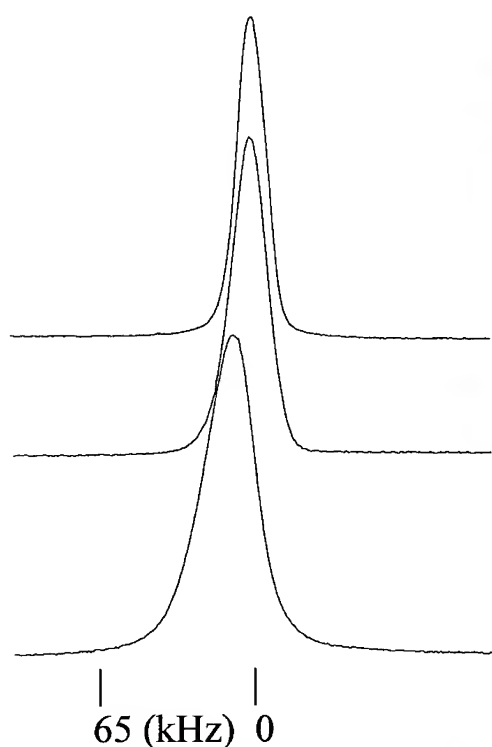


Table II. Chemical Shifts Relative to LiCl

Sample	$^7\text{Li}$ chemical shift (ppm)
$\text{Li}_{1.0}\text{CoO}_2$	5
$\text{Li}_{0.9}\text{CoO}_2$	7
$\text{Li}_{0.6}\text{CoO}_2$	75
$\text{Li}_{0.4}\text{CoO}_2$	89

Figure 6.  $^7\text{Li}$  NMR static spectra of  $\text{Li}_{1-x}\text{CoO}_2$  arranged from top to bottom:  $x = 0.0, 0.1$  and  $0.4$ .

Further information about the  $\text{Li}^+$  environment in these cathode materials can be obtained by magic angle spinning (MAS) techniques. The very broad lines characteristic of the  $x = 0.4$  and  $0.6$  samples, combined with the limited spinning rate of the current system ( $\sim 8$  kHz) made it difficult to extract structural detail for these samples. However, MAS spectra are displayed for the parent and  $x = 0.1$  samples in Fig. 9. While the  $x = 0.0$  compound exhibits only a single narrow peak (with attendant spinning sidebands), the  $x = 0.1$  sample shows two peaks: a major one in about the same position as that of the parent compound and a smaller one shifted about  $6.3$  kHz ( $\sim 55$  ppm) with respect to the main peak. Thus two magnetically inequivalent sites in  $\text{Li}_{0.9}\text{CoO}_2$  are resolved, although most of the  $\text{Li}^+$  ions experience an environment similar to that in the parent compound. MAS spectra for the  $x = 0.4$  and  $0.6$  samples (not shown) do not yield evidence for distinct sites in that the "center of masses" of the lines plus sidebands are shifted and thus provide little more information than the static spectra. The shifted component in  $\text{Li}_{0.9}\text{CoO}_2$  is attributed to proximity to paramagnetic cobalt ions, and the small intensity of the shifted peak relative to the main one implies that only a relatively small fraction of the cobalt ions are affected when  $x = 0.1$ . By the time  $x = 0.4$ , all of the Li ions and, by extension, all of the Co ions are affected. It certainly would have been of interest to examine intermediate-valued samples ( $\text{Li}_{0.8}\text{CoO}_2$  and  $\text{Li}_{0.7}\text{CoO}_2$ ), had they been available at the time of this investigation.

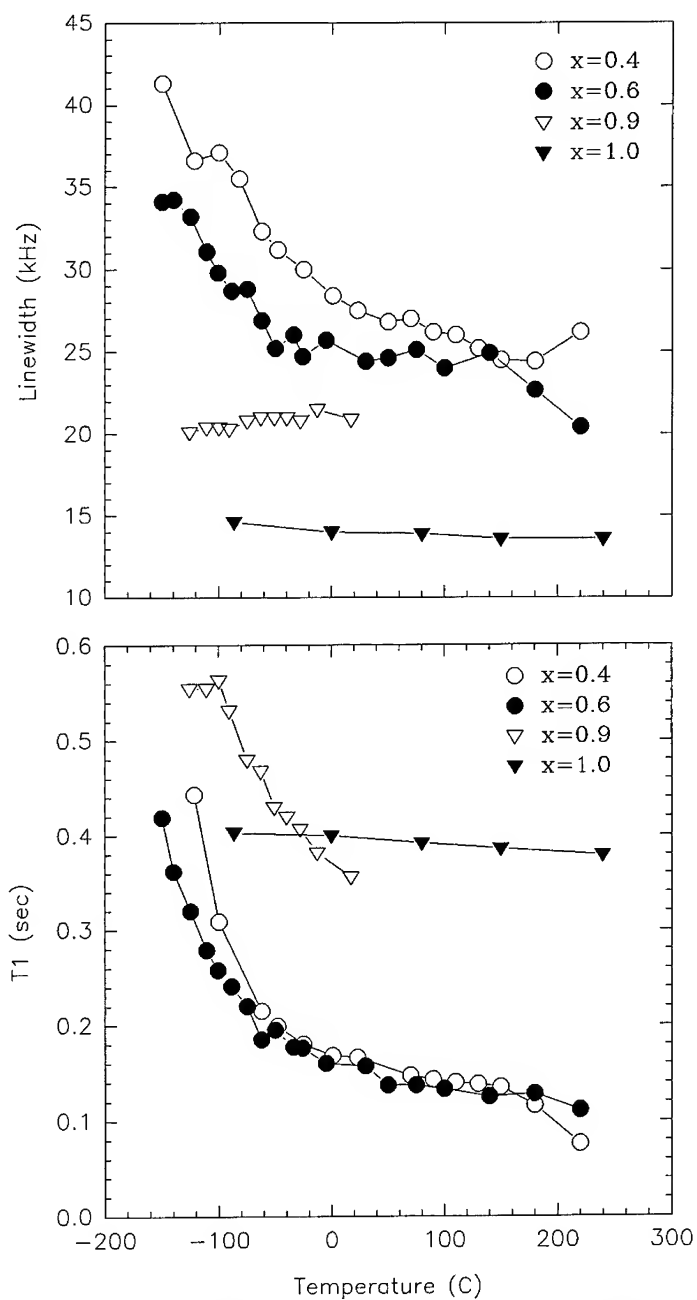


Figure 7 and 8.  $^7\text{Li}$  NMR line widths and  $T_1$  vs. temperature for  $\text{Li}_x\text{CoO}_2$  series.

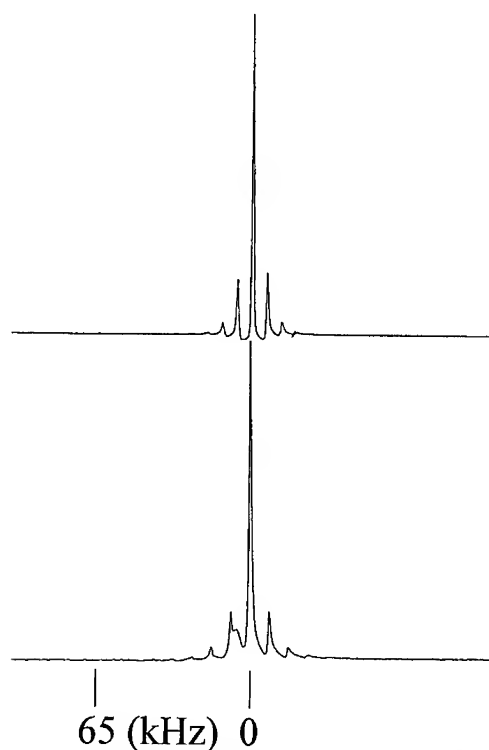


Figure 9.  ${}^7\text{Li}$  NMR magic angle spinning spectra of  $\text{Li}_{1-x}\text{CoO}_2$  arranged from top to bottom:  $x = 0.0$ ,  $x = 0.1$ .

## CONCLUSIONS

The preparation of air-stable cathodes ( $\text{Li}_{1-x}\text{CoO}_2$ ) with variable Li content was successfully achieved in order to carry out *ex situ* spectroscopic studies. The dependence of the *c*-lattice parameter on  $x$  and the observation a structural phase transition (at  $x \sim 0.5$ ) are in good agreement with the *in situ* results of Dahn and co-workers.<sup>2</sup> Cobalt K-edge NEXAFS and EPR measurements verify the expectation that compensating electrons associated with Li deintercalation originate from the Co d-orbitals. Static and MAS  ${}^7\text{Li}$  NMR spectra of  $\text{LiCoO}_2$  indicates high site symmetry for the  $\text{Li}^+$  ions (at least tetrahedral), through lack of quadrupole splitting, and essentially complete ionization, through lack of chemical shift. Spins localized on the Co ions in Li-deficient samples result in both broadening and shifting of the  ${}^7\text{Li}$  resonances. Magnetically inequivalent Li sites are resolvable in  $\text{Li}_{0.9}\text{CoO}_2$ , suggesting that only a relatively small fraction of the Co ions are paramagnetic in this sample.



## ACKNOWLEDGEMENTS

This work was supported, in part, by a grant from the U.S. Army Research Office. The NMR spectrometer employed in this investigation was purchased through an instrumentation grant from the Office of Naval Research. Dr. Fausto Croce (University of Rome) is acknowledged for providing the excess Li sample.

## REFERENCES

1. E.Plichta, S.Slane, M. Uchiyama, M. Salomon, D. Chua, W.B. Ebner and H.W. Lin, J. Electrochem. Soc. **136**, 1865 (1986).
2. J. Reimers and J.R. Dahn, *ibid.* **139**, 2091 (1992).
3. A.F. Wells, Structural Inorganic Chemistry (Clarendon, Oxford, 1984).
4. M. Brown, R.E. Pierls and E.A. Stern, Phys. Rev. B **15**, 738 (1977).
5. G. Sankar, P.R. Sarode and C.N.R. Rao, Chemical Physics **76**, 435 (1983).
6. J. van Elp, J.L. Wieland, H. Eskes, P. Kuiper and G.A. Sawatzky, Phys. Rev. B **44**, 6090 (1991).
7. M. Menetrier, A. Rougier and C. Delmas, Solid State Commun. **90**, 439 (1994).
8. B.G. Silbernagel and M.S. Whittingham, J. Chem. Phys. **64**, 3670 (1976).
9. D.G. Fauteux, A.A. Massucco, J. Shi, M.G. McLin, B. Ouyang, S. Kostov, M. denBoer and S.G. Greenbaum, Materials Research Society Symposium on Solid State Ionics, *this issue*.

## LITHIUM INTERCALATION FROM AQUEOUS SOLUTIONS

W. Li\*, J. R. Dahn\* and J. H. Root\*\*

\*Department of Physics, Simon Fraser University  
Burnaby, B. C. V5A 1S6 Canada

\*\*AECL Research, Chalk River Laboratories.  
Chalk River, Ontario  
K0J 1J0 Canada

### ABSTRACT

Lithium can be intercalated into a variety of materials using aqueous electrochemical methods, provided that certain criteria are met. The materials must be stable in concentrated  $\text{Li}^+$  aqueous solution and Li intercalation must take priority over hydrogen intercalation. We use X-ray and neutron diffraction, as well as electrochemical methods to investigate if lithium or hydrogen is intercalated into certain hosts. For example, spinel  $\text{Li}_2\text{Mn}_2\text{O}_4$  can be made from spinel  $\text{LiMn}_2\text{O}_4$  by intercalating one Li per mole in an electrochemical cell with 1 M  $\text{LiOH}$  electrolyte. If the electrochemical reduction is carried out further, beyond one electron per mole,  $\text{Mn}(\text{OH})_2$  is then formed, as we prove using neutron diffraction. By carefully selecting electrode materials and electrolyte composition it is possible to make rechargeable lithium-ion cells with aqueous electrolytes. For example,  $\text{LiMn}_2\text{O}_4/\gamma\text{-Li}_{0.36}\text{MnO}_2$  can be selected as an electrode couple, and 5 M  $\text{LiNO}_3$  in water as an electrolyte to make lithium-ion cells with aqueous electrolytes.

### Introduction:

Rechargeable lithium cells are attractive because of their high energy density and high voltage. Rechargeable lithium ion cells [1] are considered safer and simpler than those with lithium metal anodes because no lithium metal is used in the former. Therefore, rechargeable lithium batteries with non-aqueous electrolytes can be used for powering consumer electronics. However, it is more difficult to make a large rechargeable lithium battery which is safe using a non-aqueous electrolyte [2]. Furthermore, non-aqueous electrolytes usually have ion conductivity two orders of magnitude lower than aqueous electrolytes, so thin electrodes must be used in these cells in order to increase power. The salts and separators used in these cells are also very expensive. In a lithium-ion cell of the conventional construction, the cathode material is the only source of the lithium atoms needed for cell operation. Hence, using materials with more mobile lithium per formula unit leads to cells with larger capacity.

Recently, we showed how spinel  $\text{Li}_2\text{Mn}_2\text{O}_4$  could be prepared from spinel  $\text{LiMn}_2\text{O}_4$  using aqueous electrochemistry [3].  $\text{Li}_2\text{Mn}_2\text{O}_4$  prepared by this method can be used in rechargeable lithium cells and more lithium per Mn can be provided. Since lithium intercalation can appear in aqueous electrolytes, lithium-ion cells can be made with aqueous electrolytes by carefully selecting the

electrode materials and the electrolyte composition [4]. We showed that  $\text{LiMn}_2\text{O}_4/\text{VO}_2(\text{B})$  cells with 5 M  $\text{LiNO}_3$  in water as electrolyte have a specific energy which can compete with nickel cadmium and lead-acid batteries.

Here we consider the application of the same method to other  $\text{Li}_x\text{MnO}_2$  starting materials in an attempt to prepare materials with large Li:Mn ratios. We acknowledge that hydrogen may be involved in the electrochemical reactions as well as lithium and that hydrogen intercalation may dominate over lithium intercalation under certain conditions. For example, we show using neutron scattering that further electrochemical reduction of  $\text{Li}_2\text{Mn}_2\text{O}_4$  or  $\gamma\text{-LiMnO}_2$  results in the formation of  $\text{Mn}(\text{OH})_2$ . Furthermore, we use only Mn compounds as electrodes to prepare rechargeable lithium-ion cells with aqueous electrolytes and cells with reasonable specific energy are obtained.

## Experimental

$\gamma\text{-Li}_{0.36}\text{MnO}_2$  was prepared by thoroughly mixing stoichiometric ratios of  $\text{LiOH}$  and  $\gamma\text{-MnO}_2$  (EMD, Mitsui TAD 1 grade) as described in [5], followed by heating in air at  $375^\circ\text{C}$  for about 2 hours.  $\text{LiMn}_2\text{O}_4$  was prepared by heating stoichiometric mixtures of  $\text{Li}_2\text{CO}_3$  and  $\text{MnO}_2$  (Chemical Manganese Dioxide, Faradizer M, Sedema, Belgium) in air at  $750^\circ\text{C}$  for 24 hours.

We use an aqueous electrochemical cell to prepare  $\text{Li}_2\text{Mn}_2\text{O}_4$  [3] and  $\gamma\text{-LiMnO}_2$ . Typically, 1 M  $\text{LiOH}$  aqueous solution was used as the electrolyte. Carbon rods were used as the positive electrode and titanium plates for the negative electrode current collectors. The cell container was made of pyrex.  $\gamma\text{-Li}_{0.36}\text{MnO}_2$  was used as the starting material to prepare  $\gamma\text{-LiMnO}_2$  and  $\text{LiMn}_2\text{O}_4$  was used as the starting material to prepare  $\text{Li}_2\text{Mn}_2\text{O}_4$ .

Electrodes were pasted onto the titanium collectors. The paste was a mixture of the starting lithium manganese oxides with 10 % by weight carbon black, (Super S, MMM Carbon, Belgium) 3% by weight polyvinylidene fluoride (PVDF) and N-methyl pyrrolidinone (NMP) solvent (to prepare the samples used for neutron scattering experiments, we used  $\text{D}_2\text{O}$  instead of  $\text{H}_2\text{O}$  as the solvent in the electrolyte and Teflon as the binder instead of PVDF). The paste was spread on two titanium plates which were drilled with holes. Spreading the paste into the holes helps to make a good bond between the electrode ingredients and the Ti collector. The two titanium plates were then clamped together to make a Ti-(Li-Mn-O)-Ti sandwich. The paste was then dried by placing the assembly in a drying oven at  $105^\circ\text{C}$  in air while the NMP was evaporated. Typical electrodes used 4.0 grams of lithium manganese oxides and had an area of  $5.0 \times 3.5 \text{ cm}^2$ . The thickness of the starting material layer between the two titanium plates was about 3 mm.

The Li-Mn-O electrode sandwiched between the Ti plates and the carbon counter electrode were immersed to a depth of about 70 mm in the electrolyte in the pyrex beaker and the beaker was covered with a lucite lid. The distance between electrodes was typically about 25 mm. The beaker was then placed in a temperature controlled oil bath. Temperatures between  $17^\circ\text{C}$  and  $100^\circ\text{C}$  could be attained. A  $\text{Ag}/\text{AgCl}$  reference electrode was positioned roughly midway between

the two electrodes, and the voltage between Ag/AgCl and the correction to obtain the voltages versus the standard hydrogen electrode were applied (Ag/AgCl=+0.222 versus S.H.E.). The electrodes were connected to a current supply. Currents between 2 and 40 mA were applied to the cell. The constant currents were applied for between 24 hours and 240 hours, depending on the batch of material prepared. The number of electrons per manganese atom transferred between the two electrodes was calculated from the current, the mass of the lithium manganese oxide and the current duration. After the aqueous electrochemical reaction, the Ti sandwich electrode was disassembled and the reacted powder was rinsed in ethanol. The powder was then dried between 50°C and 110°C under vacuum.

A Philips powder diffractometer equipped with a copper target x-ray tube and a diffracted beam monochromator was used for the powder diffraction measurements. Neutron diffraction patterns were obtained with the DUALSPEC powder diffractometer, which is located at the NRU reactor at Chalk River Laboratories. Samples of about 5 grams were held in thin-walled vanadium cylindrical cans of 10 mm diameter. The DUALSPEC diffractometer has an 800-element multiwire position-sensitive detector that spans 80° of scattering angle in steps of 0.1°. The detector was moved 4 times to give data in steps of 0.05° from 5° to 120° in scattering angle. Typically, diffraction patterns were acquired in in 2 h. The wavelength of the neutron beam was 0.129902 nm (or 1.29902 Å).

Coin-type test cells using 1225 (12 mm diameter, 2.5 mm thickness) hardware were prepared with aqueous electrolytes. A 5.0 M LiNO<sub>3</sub> aqueous solution was used as the electrolyte. Tablet electrodes of 8 mm diameter and total mass 0.10 g were prepared from the desired materials. Carbon Black (10 % by weight) and EPDM (ethylene propylene diene monomer) binder (3% by weight) were added to the tablet mix to provide good electrical conductivity and good mechanical toughness. The mix was then pressed in 0.10 g allotments in a cylindrical die to the desired thickness (1.0 mm).

Coin-type test cells using 2325 hardware [6] were prepared with non-aqueous electrolytes. A 1.0 M solution of LiPF<sub>6</sub> in equal volumes of PC and EC (propylene carbonate and ethylene carbonate) was used as electrolyte. Li metal foil was used as the anode. Cathodes were prepared by mixing the active powder materials with Carbon Black (10 % by weight) and a (3 % by weight) binder solution of EPDM in cyclohexane, to make a slurry of the electrode powder mixture. The slurry was spread on Al foil and allowed to dry. Typical cathodes had a coverage of 20 mg/cm<sup>2</sup> and were 1.2x1.2 cm<sup>2</sup> in size.

## Results

Figure 1a shows the powder X-ray diffraction pattern of the  $\gamma$ -MnO<sub>2</sub> used as a starting material and figure 1b shows the X-ray pattern of  $\gamma$ -Li<sub>0.36</sub>MnO<sub>2</sub> made from it. The Bragg peaks in figure 1a are labelled by their Miller indices, assuming the  $\gamma$ -MnO<sub>2</sub> to be predominantly ramsdellite type MnO<sub>2</sub> [7].

The lattice constants are approximately  $a=4.40\pm0.02$  Å,  $b=9.55\pm0.02$  Å and  $c=2.81\pm0.02$  Å for  $\gamma$ -MnO<sub>2</sub>. When Li is added to make  $\gamma$ -Li<sub>0.36</sub>MnO<sub>2</sub>, the shortest

dimension of the 2x1 tunnels expands and the oxygen planes buckle leading to an increase in  $a$  as the major effect [7]. Therefore the 021 peak stays in about the same position and the shifts between the positions of the  $h21$  peaks in  $\gamma\text{-MnO}_2$  and in  $\gamma\text{-Li}_{0.36}\text{MnO}_2$  increase with  $h$ . The other Bragg peaks in these two compounds are substantially broadened due to the intermixing of regions of 1x1 tunnels into the predominantly 2x1 tunnel material as is well known [8,9,10]. The lattice constants are approximately  $a=4.89\pm0.02$ ,  $b=9.88\pm0.02$  and  $c=2.82\pm0.02$  for  $\gamma\text{-Li}_{0.36}\text{MnO}_2$ .

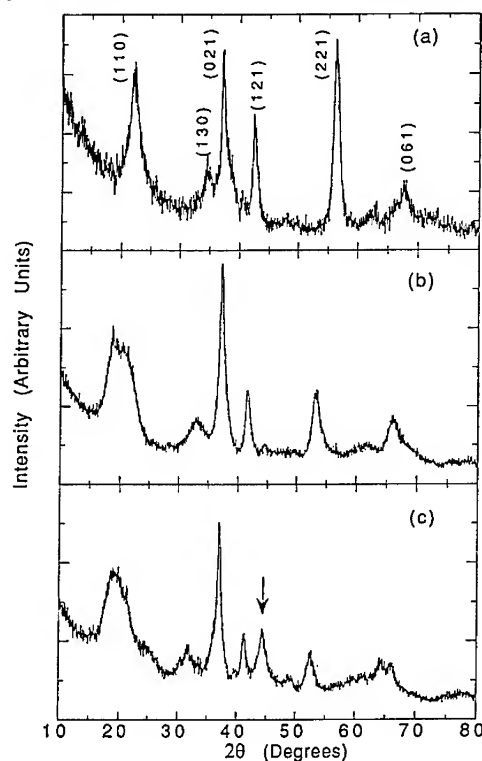


Figure 1. The X-ray diffraction patterns of (a)  $\gamma\text{-MnO}_2$ , (b)  $\gamma\text{-Li}_{0.36}\text{MnO}_2$  and (c) sample A made from  $\gamma\text{-Li}_{0.36}\text{MnO}_2$  followed by reduction with  $e/\text{Mn}=0.5$  in a 2.5 LiOH aqueous solution.

We used  $\gamma\text{-Li}_{0.36}\text{MnO}_2$  as a starting material in the aqueous cell, and the cell was operated at 17°C. The charge transferred from the carbon electrode to the  $\gamma\text{-Li}_{0.36}\text{MnO}_2$  during this experiment corresponded to 0.5  $e/\text{Mn}$ . After the electrochemical reaction, the Li-Mn-O powder was recovered as described above. This sample will be called sample A. Figure 1c shows the diffraction pattern of sample A, which closely resembles the ones shown in figure 1a and 1b, suggesting that the  $\gamma$ -type structure has been preserved. Only one peak shown in

figure 1c with an arrow is not obviously related to the peaks of the starting material. The lattice constants of Sample A are  $a=4.96\pm0.02\text{ \AA}$ ,  $b=10.14\pm0.02\text{ \AA}$  and  $c=2.77\pm0.02\text{ \AA}$ . Note that when lithium was inserted into the lattice, two lattice constants  $a$  and  $b$  increase while the other lattice constant,  $c$ , decreases. The dimensions  $a$  and  $b$  are perpendicular to the axis of the  $2\times1$  tunnels and are therefore expected to increase. The  $c$ -axis is parallel to the tunnel axis and parallel to the Mn atom chains in this material. Another tunnel compound,  $\text{Li}_x\text{MoO}_2$  has been shown to expand perpendicular to the tunnels and contract parallel to the tunnels as  $x$  is increased [11]. Furthermore, the lattice volumes for  $\gamma\text{-MnO}_2$ ,  $\gamma\text{-Li}_{0.36}\text{MnO}_2$  and Sample A are  $118\text{ \AA}^3$ ,  $136\text{ \AA}^3$  and  $139\text{ \AA}^3$  respectively, which means that the lattice volume increases when more lithium is in the lattice. The ramsdellite-related  $\text{Li}_x\text{MnO}_2$  compounds prepared by reacting  $\text{LiI}$  with ramsdellite  $\text{MnO}_2$  also have similar  $a$  and  $b$  expansion,  $c$  contraction and volume expansion as  $x$  is increased [7].

Figure 2 shows the  $\gamma\text{-Li}_{0.36}\text{MnO}_2/\text{Li}$  cell voltage with 1 M  $\text{LiPF}_6$  in PC/EC for

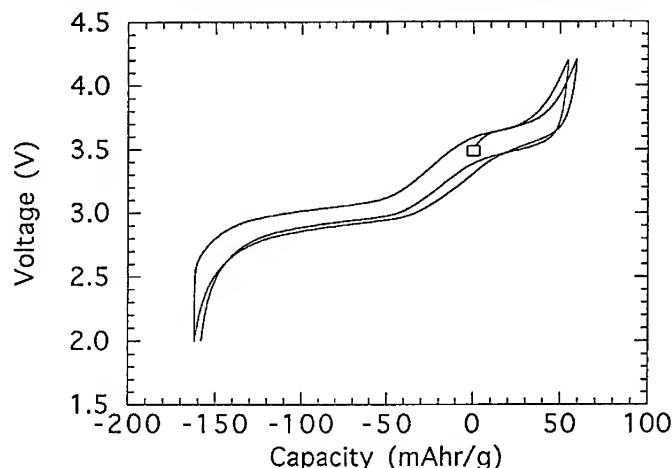


Figure 2. The voltage versus capacity of a non-aqueous  $\text{Li}/\gamma\text{-Li}_{0.36}\text{MnO}_2$  cell. The cell current was  $2.8\text{ mA/g}$ , and the temperature was  $30^\circ\text{C}$ . The square point designates the start of the experiment and the cell was initially charged.

the first few cycles. The square point in figure 2 indicates the starting point of the cell. Only about  $50\text{ mAh/g}$  capacity can be obtained during the first charge. After the first charge, there is about  $210\text{ mAh/g}$  reversible capacity. For regular Li-ion cells, the lithium source is provided only by the original cathode materials so  $\gamma\text{-Li}_{0.36}\text{MnO}_2$  is therefore not an effective cathode material to be used in Li-ion cells because of its low first charge capacity. Figure 3 shows the voltage of a Sample A/Li cell with 1 M  $\text{LiPF}_6$  in PC/EC electrolyte for the first two cycles. The first charge capacity is about  $230\text{ mAh/g}$  followed by a reversible capacity of  $170\text{ mAh/g}$ . The large first charge capacity also indicates that lithium had been intercalated from the aqueous solution to form  $\gamma\text{-LiMnO}_2$  type materials. The

charge and discharge features are slightly different between  $\gamma\text{-Li}_{0.36}\text{MnO}_2$  and Sample A. The difference is especially significant for the first charge. We do not yet understand the reasons for this difference.

We have shown that lithium intercalation can dominate over hydrogen intercalation reaction under certain conditions to form  $\text{Li}_2\text{Mn}_2\text{O}_4$  from spinel  $\text{LiMn}_2\text{O}_4$  in aqueous solutions [3]. Here, we suppose that  $e/\text{Mn}=0.64$  is needed to convert  $\gamma\text{-Li}_{0.36}\text{MnO}_2$  to  $\gamma\text{-LiMnO}_2$ . In order to further investigate if Li or H intercalates into  $\gamma\text{-Li}_{0.36}\text{MnO}_2$ , we made two identical cells but with 2.5 M KOH and 2.5 M LiOH aqueous electrolytes. Figure 4 shows the voltage profiles for these cells. The two voltage profiles are markedly different and the cell voltage using

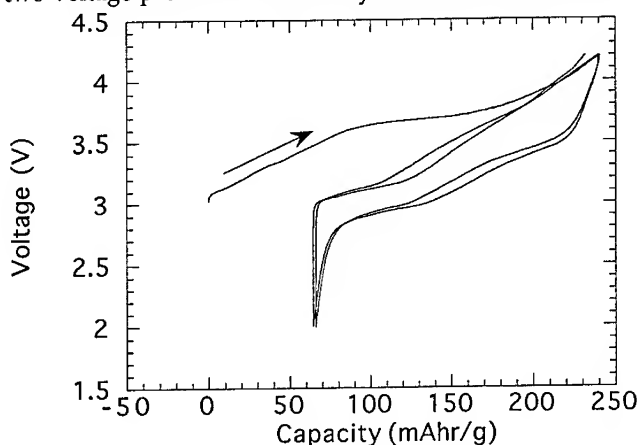


Figure 3. The voltage versus capacity of a non-aqueous Li/Sample A cell. The cell current was 2.8 mA/g and the temperature was 30°C.

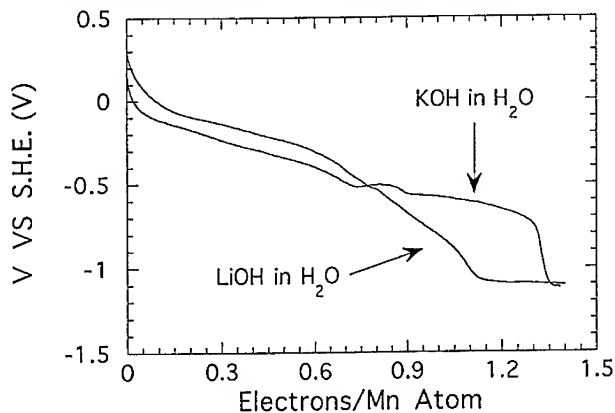


Figure 4. The voltage versus standard hydrogen electrode of two identical cells using  $\gamma\text{-Li}_{0.36}\text{MnO}_2$  as the starting material but with 2.5 M KOH and 2.5 M LiOH aqueous electrolytes, respectively.

the LiOH solution is higher than that using the KOH solution for  $e/\text{Mn} < 0.75$ . When  $e/\text{Mn} > 1.35$ , both cells reach the lower plateau and their voltage difference is much smaller than that for  $e/\text{Mn} < 0.60$ . This means that  $\text{H}_2$  evolution probably occurs in both cells at  $e/\text{Mn} > 1.35$  and the difference of voltage at  $e/\text{Mn} > 1.35$  may indicate the experimental error. Therefore, we believe that  $\text{Li}^+$  dominates over  $\text{H}^+$  during the intercalation into  $\gamma\text{-Li}_{0.36}\text{MnO}_2$  for  $e/\text{Mn} < 0.60$ , in 2.5 M LiOH solutions.

After we further treated the  $\gamma\text{-Li}_{0.36}\text{MnO}_2$  materials with a larger value of  $e/\text{Mn}$ , beyond the first plateau ( $e/\text{Mn} > 0.6$ ) shown in figure 4, the structure of the products changed from orthorhombic to hexagonal. Figure 5 shows the X-ray diffraction pattern of the product obtained from using the starting material  $\gamma\text{-Li}_{0.36}\text{MnO}_2$  followed by reduction with  $e/\text{Mn} = 0.98$  in 2.5 M LiOH. The products can be described by space group  $P\text{-}3\text{M}1$  with Mn atoms in 1a sites and O atoms in 2d sites, and with a hexagonal cell of lattice constants  $a = 3.32 \text{ \AA}$  and  $c = 4.74 \text{ \AA}$ , which is close to the values  $a = 3.34 \text{ \AA}$  and  $c = 4.68 \text{ \AA}$  for  $\text{Mn}(\text{OH})_2$ , and far from the values  $a = 3.195 \text{ \AA}$  and  $c = 5.303 \text{ \AA}$  in  $\text{Li}_2\text{MnO}_4$  [14]. These suggest the formation of  $\text{Mn}(\text{OH})_2$ . Further treating  $\text{LiMn}_2\text{O}_4$  beyond  $\text{Li}_2\text{Mn}_2\text{O}_4$  with values of  $e/\text{Mn} > 1$  in LiOH solution also have the similar results. The X-ray diffraction profiles shown in figure 6 suggest that the phase transitions are  $\text{LiMn}_2\text{O}_4 \rightarrow \text{spinel Li}_2\text{Mn}_2\text{O}_4 \rightarrow \text{Mn}(\text{OH})_2$  during treatment of the  $\text{LiMn}_2\text{O}_4$  materials with increasing of  $e/\text{Mn}$  in LiOH solution.

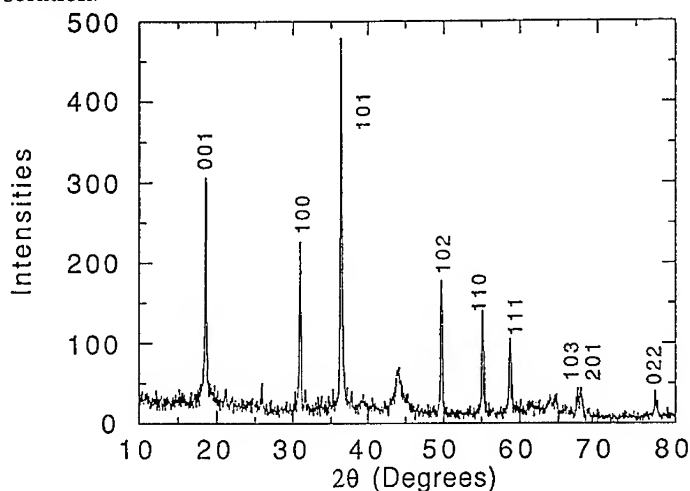


Figure 5. The X-ray diffraction profile of the product obtained from  $\gamma\text{-Li}_{0.36}\text{MnO}_2$  followed by reduction with  $e/\text{Mn} = 0.98$  in a 2.5 M LiOH aqueous solution.

In order to further investigate if H or Li is incorporated in these highly reduced materials, we used neutron diffraction to investigate the sample prepared by reducing  $\gamma\text{-Li}_{0.36}\text{MnO}_2$  with  $e/\text{Mn} = 0.98$ . We used  $\text{D}_2\text{O}$  and teflon binder  $[(-\text{CF}_2)_n]$  in order to minimize the H content in the sample and therefore the background



count rate of the neutron diffraction profile. In addition, because D has a positive scattering length and Li has a negative scattering length, their effect on the intensities of Bragg peaks is markedly different. Figure 7 shows the experimental neutron diffraction profile and the calculated profile from the Rietveld fitting program. The profiles shown in figure 7 (a), (b) and (c) are calculated by assuming  $\text{Mn}(\text{OD})_2$ ,  $\text{Mn}(\text{OLi}_x\text{D}_{1-x})_2$  and  $\text{Mn}(\text{OLi})_2$  respectively. We exclude two regions during the fit, from  $30.50^\circ$  to  $40.00^\circ$  and from  $57.00^\circ$  to  $67.00^\circ$ , because some strong broad peaks from an unknown impurity phase appear in those regions. This impurity phase did not appear in a similar sample measured by X-ray

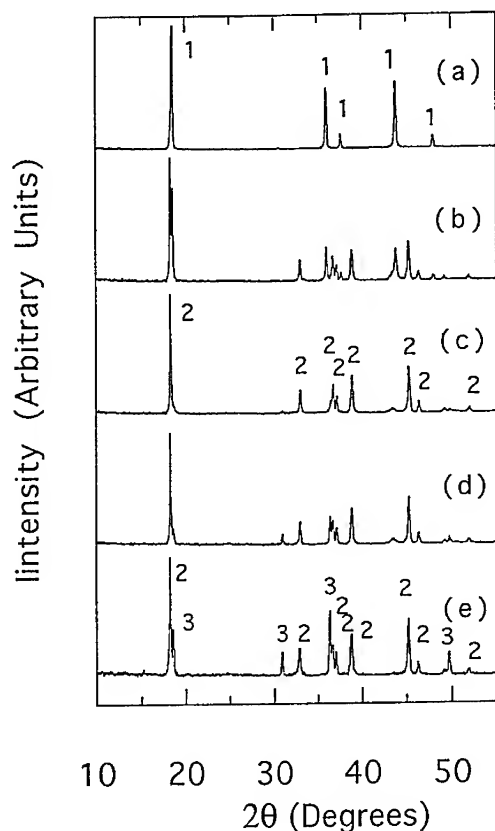


Figure 6. The X-ray diffraction profiles showing the phase transitions from spinel  $\text{LiMn}_2\text{O}_4$   $\rightarrow$  spinel  $\text{Li}_2\text{Mn}_2\text{O}_4$   $\rightarrow$   $\text{Mn}(\text{OH})_2$  in the aqueous cell. The numbers 1, 2 and 3 correspond to the Bragg peaks of  $\text{LiMn}_2\text{O}_4$ ,  $\text{Li}_2\text{Mn}_2\text{O}_4$  and  $\text{Mn}(\text{OH})_2$  respectively. a) The X-ray diffraction profile of spinel  $\text{LiMn}_2\text{O}_4$ . b) The X-ray diffraction profile when  $e/\text{Mn}=0.31$  showing both  $\text{LiMn}_2\text{O}_4$  and  $\text{Li}_2\text{Mn}_2\text{O}_4$ . c)  $e/\text{Mn}=0.63$ . d)  $e/\text{Mn}=0.75$ . e)  $e/\text{Mn}=1.61$ .

diffraction and we are unsure of its origin. The arrows in figure 7 (a) indicate the impurity phase. The best fit is obtained in figure 7 (b) with  $x=0.22$ . In order to clearly demonstrate the best fit in figure 7, we show the data between  $40^\circ$  and  $58^\circ$  in figure 8. Although we can not confirm the Li content because the samples are not pure enough, we can conclude that the sample is not  $\text{Mn}(\text{OLi})_2$  because of the poor fit for  $\text{Mn}(\text{OLi})_2$  shown in figure 7 (c) and figure 8 (c). The materials can

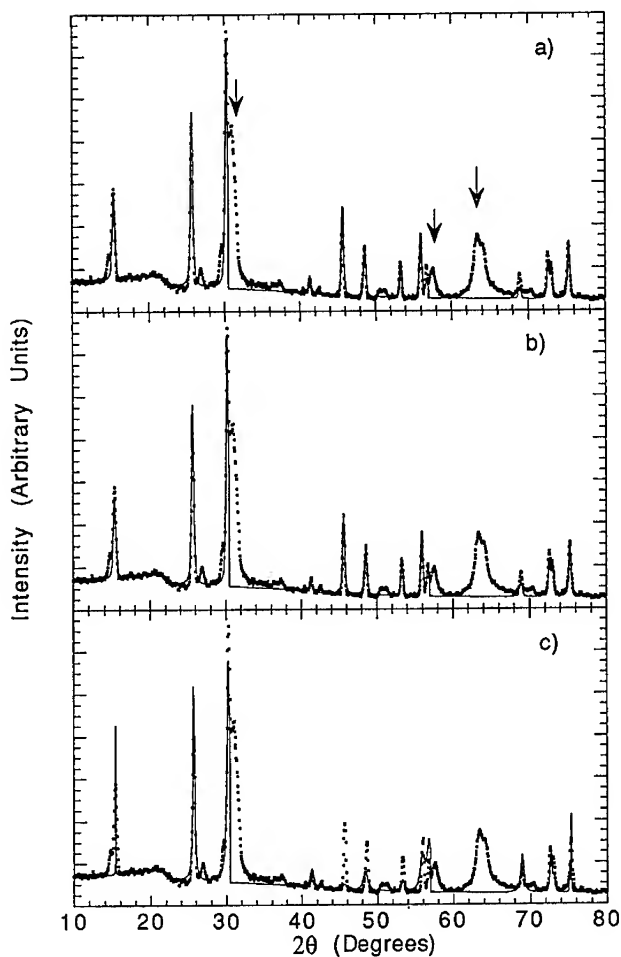


Figure 7. The neutron diffraction profile and the calculated results from the Rietveld fitting program. The data points are the experimental results. The lines in (a), (b) and (c) are the calculated results assuming  $\text{Mn}(\text{OD})_2$ ,  $\text{Mn}(\text{OLi}_x\text{D}_{1-x})_2$  and  $\text{Mn}(\text{OLi})_2$  respectively.

be written as  $\text{Mn}(\text{OLi}_x\text{D}_{1-x})_2$ , with the D content ( or  $1-x$  ) in the range between 0.5 and 1.0, and the Li content ( or  $x$  ) in the range between 0.5 and 0.0. Li was assumed to share the 2d sites in space group P -3M1 randomly with D. We can conclude that substantial D is in this material,  $\text{Mn}(\text{OLi}_x\text{D}_{1-x})_2$ , and that Li intercalation does not occur beyond  $\gamma\text{-LiMnO}_2$ . Instead, H(D) intercalation and ion exchange between  $\text{Li}^+$  and  $\text{H}^+(\text{D}^+)$  most likely occurs.

Rechargeable lithium-ion cells with aqueous electrolytes can be made by carefully selecting electrode materials and electrolyte composition. Here we used  $\text{LiMn}_2\text{O}_4$  as the positive electrode,  $\gamma\text{-Li}_{0.36}\text{MnO}_2$  as the negative electrode, and 5

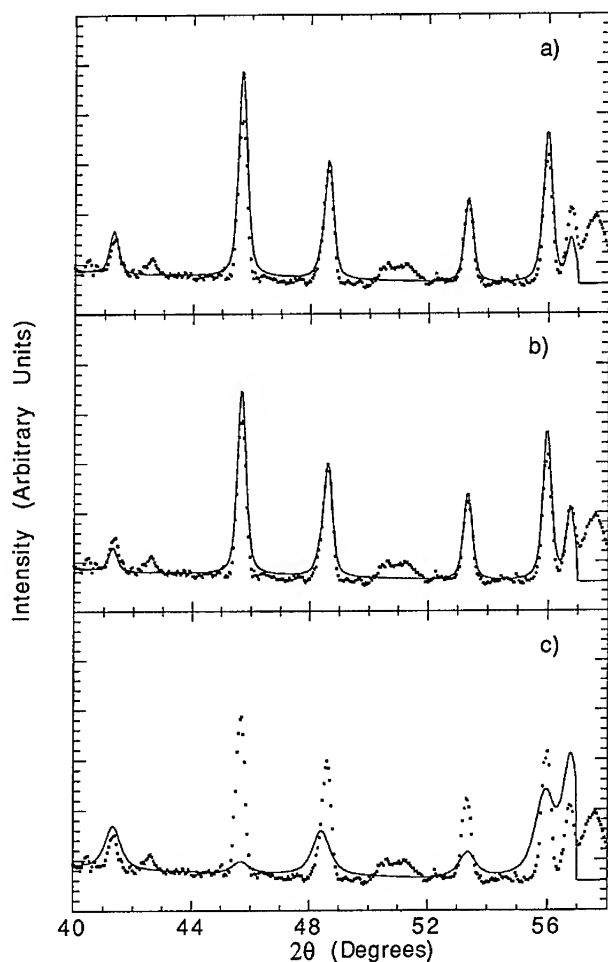


Figure 8. The neutron diffraction profile and the calculated results from the Rietveld fitting program. This is an expanded view of figure 7.

M  $\text{LiNO}_3$  in water as the electrolyte. During the charge of such a cell, lithium is extracted from  $\text{LiMn}_2\text{O}_4$ , making  $\text{Li}_{1-x}\text{Mn}_2\text{O}_4$ , and intercalated into  $\gamma\text{-Li}_{0.36}\text{MnO}_2$  making  $\gamma\text{-Li}_{0.36+x}\text{MnO}_2$ . Figure 9 shows the voltage profile during this charging and during the next few charge-discharge cycles all at currents of 1 mA. The cell shows good reversibility, an average voltage near 0.8 volts and a capacity of about 10 mAh. Since the total mass of the two electrodes is 0.2 g, the total energy is 8 mWh for this cell. The specific energy for the  $\text{LiMn}_2\text{O}_4/\gamma\text{-Li}_{0.36}\text{MnO}_2$  cell is about 40 mWhr/g if we only include the electrode weights in the calculation. Although the specific energy for this cell is less than that of the  $\text{LiMn}_2\text{O}_4/\text{VO}_2(\text{B})$  cells described in [4], it demonstrates that lithium-ion cells with aqueous electrolytes can be made using only manganese compounds as electrodes.

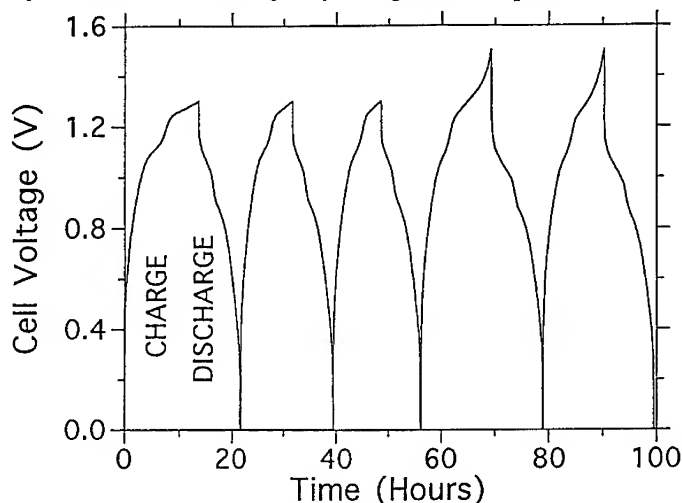


Figure 9. The voltage plotted versus time as a  $\text{LiMn}_2\text{O}_4/\gamma\text{-Li}_{0.36}\text{MnO}_2$  cell is repeatedly charged and discharged. The currents used were  $\pm 1$  mA. The cell test was carried out at  $30^\circ\text{C}$ .

## Conclusions

We showed that lithium intercalation from aqueous solutions can be used to make lithium-rich transition metal oxides which have a large first charge capacity. Therefore they can be used in lithium-ion cells to increase the specific energy. Using neutron diffraction, we showed that electrochemical reduction of  $\gamma\text{-Li}_{0.36}\text{MnO}_2$  beyond  $\gamma\text{-LiMnO}_2$ , and electrochemical reduction of  $\text{LiMn}_2\text{O}_4$  beyond  $\text{Li}_2\text{Mn}_2\text{O}_4$  in  $\text{LiOH}$  aqueous solutions results in the formation of  $\text{Mn}(\text{OH})_2$ . Furthermore, lithium-ion cells with aqueous electrolytes can be made by using only manganese compounds. These cells should be inexpensive and environmentally friendly.

# References:

- [1]. T. Nagaura and K. Tozawa, *Progress Batteries and Solar Cells*, **9**, 209 (1990).
- [2]. U. von Sacken, E. Nodwell, A. Sundher and J. R. Dahn, 7th International Meeting on Lithium Batteries, Boston, Massachusetts, U. S. A. May 15-20, page 12 (1994).
- [3]. W. Li, W. R. McKinnon and J. R. Dahn, *J. Electrochem. Soc.* **141**, 2310 (1994).
- [4]. W. Li, J. R. Dahn and D. S. Wainwright, *Science* **264**, 1115 (1994).
- [5]. J. R. Dahn and B. M. Way, U. S. Patent 4,959,282 (1990).
- [6]. J. R. Dahn, A. K. Sleight, Hang Shi, J. N. Reimers, Q. Zhong and B. Way, *Electrochimica Acta* **38**, 1179 (1993).
- [7]. M. M. Thackeray, M. H. Rossouw, R. J. Gummow, D. C. Liles, R. Pearce, A. De Kock, W. I. F. David, and S. Hull, *Electrochimica Acta* **38**, 1259 (1993).
- [8]. J. Pannetier, Presented at the 8th International Battery Materials Symposium, Brussels, Belgium, May 9-13 (1993); JEC Battery Newsletter No. 6, Nov-Dec. (1993) p. 64.
- [9]. Handbook of Manganese Dioxides Battery Grade, Editors: D. Glover, B. Schumm, Jr. and A. Kozawa, the Int'l Battery Ass'n (IBA, Inc. ) 1989.
- [10]. T. Ohzuku, M. Kitagawa and T. Hirai, *J. Electrochem. Soc.* **136**, 3169 (1989).
- [11]. J. R. Dahn and W. R. McKinnon, *Solid State Ionics* **23**, 1 (1987).
- [12]. J. R. Dahn, U. von Sacken, M. W. Juzkow, H. Al-Janaby, *J. Electrochem. Soc.* **138**, 2207 (1991).
- [13]. R. W. G. Wyckoff, *Crystal Structures* (2nd edn), Vol.2, p. 312 Interscience, New York (1964).
- [14]. W. I. F. David, J. B. Goodenough, M. M. Thackeray, M. G. S. R. Thomas, *Rev. Chim. Miner.* **20**, 636 (1983).

## CRYSTAL CHEMISTRY AND ELECTROCHEMICAL BEHAVIOR OF NEW MANGANESE SUBSTITUTED NICKEL HYDROXIDES.

L. GUERLOU-DEMOURGUES and C. DELMAS,  
Laboratoire de Chimie du Solide du CNRS and Ecole Nationale Supérieure de Chimie et  
Physique de Bordeaux, 351, cours de la Libération, 33405 Talence Cedex, FRANCE.

### ABSTRACT

Ageing of the manganese substituted nickel hydroxides in 5M-KOH electrolytic medium leads to a structure interstratification which is related to spontaneous oxidation of trivalent manganese ions to the tetravalent state. As far as the electrochemical behavior is concerned, the trend to interstratification has a positive influence on the stability of the capacity upon cycling. In addition, the chargeability is improved by the presence of manganese.

### INTRODUCTION

Previous works carried out in our laboratory have shown that partial substitution of cobalt or iron for nickel leads to a new family of mixed hydroxides containing interlamellar water [1-3], which are strongly appertained to the Layered Double Hydroxides (LDHs) [4]. These materials have been used as positive electrode materials in Ni//Cd batteries [5,6]. The cationic substitution turned out to be a way to monitor the cell potential as well as the oxygen evolution reaction, which both affect the electrode chargeability. As an example the cell potential increases with iron and decreases with cobalt [5-7]. As a consequence, the discharge capacity is improved by cobalt substitution whereas the opposite effect is observed for iron [5,6]. In order to further investigate the influence of cationic substitution on the electrochemical behavior of nickel hydroxide derivatives, the study of partial substitution of manganese for nickel has been undertaken.

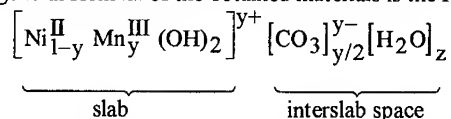
### RESULTS AND DISCUSSION

The crystal chemistry study of the manganese substituted nickel hydroxides, especially in ageing conditions in 5M-KOH electrolytic medium of the Ni//Cd battery, will be correlated to the electrochemical study.

#### Crystal chemistry of the freshly precipitated materials

The manganese substituted nickel hydroxides have been prepared by precipitation with 2M-NaOH from a divalent nickel and manganese sulfate solution in presence of hydrogen peroxide (5M-H<sub>2</sub>O<sub>2</sub>) which acts as an oxidizing agent of the manganese ions.

The general formula of the obtained materials is the following one :



Depending on the substitution amount (y), two types of material are obtained in accordance with the behavior already observed for the homologous cobalt or iron systems [1-3].

- For manganese amounts (y) higher than 0.2, the precipitation reaction leads to  $\alpha$  type phases, with interlamellar water molecules and carbonate ions statistically distributed in the interslab spaces.

• For  $y$  values smaller than 0.2, the amount of carbonate anions inserted as charge compensating species is not sufficient to lead to a homogeneous distribution of these ions within the interslab space. This behavior leads to segregation of the anions, which tend to regroup in  $\alpha$  type domains, giving rise to a structure constituted of a random packing of  $\alpha$  type interslab spaces (hydrated and carbonated domains) and  $\beta(\text{II})$  ones, as schematized in Fig 1.

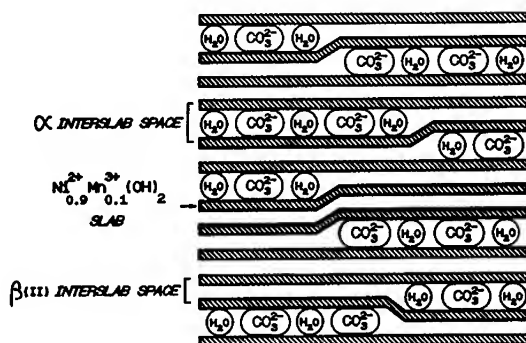


Fig. 1 Schematic representation of the interstratified structure.

The influence of interstratification on the X-ray diffraction patterns, reported elsewhere in detail [5], is illustrated in Fig 2, which allows to compare the X-ray diffraction patterns of the  $\alpha$ -( $y = 0.3$ ), interstratified I- ( $y = 0.1$ ) and  $\beta(\text{II})$  phases. The (003) and (006) lines (indexed in a hexagonal cell) observed for the  $\alpha$  phase (rhombohedral system SG: R3m) are replaced, for the  $y = 0.1$  composition, by two broader asymmetric lines that are no more multiple of one another. Such a behavior results from the disorder in the periodicity of the basal planes.

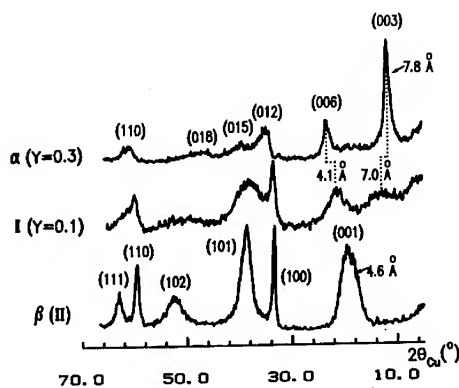


Fig. 2 Comparison of the X-ray diffraction patterns of the  $\alpha$ , interstratified and  $\beta(\text{II})$  phases.

### Ageing in concentrated KOH medium

Study of the ageing of the pristine materials in the electrolytic medium of the Ni//Cd cell turned out to be essential to understand the electrochemical behavior. As shown as an example for the  $y = 0.3$  composition in Fig. 3, structural modifications occur after staying in KOH medium: the (003) and (006) lines are indeed changed into one broad asymmetric line ( $d \approx 4.3 \text{ \AA}$ ) which is characteristic of a structure interstratification [9,10]. For an interstratified material, the profile of the diffracted intensity can be simulated according to the Hendricks and Teller method via a calculation that takes into account the values of both interslab distances as well as the molar ratio of both types of interslab spaces [8-10].

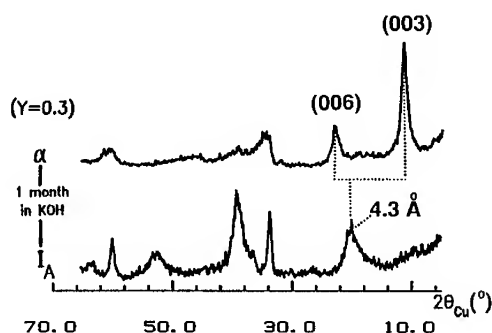


Fig. 3 Modifications of the X-ray diffraction patterns upon ageing.

Comparison of the position and shape of this line to theoretical diffraction line shapes calculated according to the Hendricks and Teller method suggests that the structure of the aged material (designated by  $I_A$ , A holds for Aged) is constituted of a random packing of  $\beta$  and  $\alpha$  type interslab spaces (ratio 3:1). In addition, the infrared spectroscopy study evidences the simultaneous presence of both  $\beta(II)$  and  $\alpha$  type interslab spaces in the  $I_A$  phase [9,10].

The chemical analysis and magnetic measurement results have shown the presence of trivalent manganese in the starting materials ( $(1-y)Ni^{2+}, yMn^{3+}$ ) and tetravalent manganese in the aged materials ( $(1-y)Ni^{2+}, yMn^{4+}$ ). The presence of  $Mn^{4+}$  ions in the  $I_A$  phases leads to further investigate the charge balance process. Indeed, previous studies have proved that, in the  $\alpha$  nickel hydroxides, 0.17  $CO_3^{2-}$  ions or 0.5  $OH^-$  ions per metal cation can be at most intercalated. As a consequence, in the  $I_A$  phases, the presence of  $Mn^{4+}$  ions entails that the charge balance cannot be totally performed by anionic insertion for  $y$  values higher than 0.25. The existence of proton deficiencies within the slab, and therefore of  $\beta(III)$  type interslab spaces has to be assumed. This hypothesis is fully confirmed by the chemical analysis results, which show that the H and  $CO_3$  amounts are significantly lower in the  $I_A$  phases than in the  $\alpha$  ones [10].

In conclusion, the overall results presented above suggest the coexistence of  $\beta(II)$ ,  $\beta(III)$  and  $\alpha$  type interslab spaces in the  $I_A$  interstratified phases. The distribution of these three domain types must be strongly related to that of the  $Mn^{4+}$  ions within the slab: the highly manganese concentrated domains exhibit the  $\beta(III)$  type, those containing exclusively  $Ni^{2+}$  ions exhibit the  $\beta(II)$  type and the intermediate manganese amounts give rise to  $\alpha$  type domains.



### Electrochemical behavior

The electrochemical behavior of the manganese substituted nickel hydroxides on cycling in Ni//Cd cells at the C/5 rate has been studied as a function of the manganese concentration.

#### Evolution of the discharge capacity

The variations with cycle number of the number of electron exchanged on discharge per metal (Ni + Mn) ion are gathered in Fig 4 for the various manganese compositions. The capacity values are very promising especially for low manganese amounts. The decrease of the capacity with increasing  $y$  is consistent with the difference in oxidation state between the charged and discharged materials : 3.5 and  $2 + 2y$  respectively, which leads to  $1.5 - 2y$  electron theoretically exchanged [11].

Whatever  $y$ , the remarkable stability of the capacity upon cycling has to be noticed. In order to identify the origin of this feature, the structural modifications of the electrode materials have been investigated by X-ray diffraction.

#### X-ray diffraction study of the electrode materials

The X-ray diffraction patterns of the electrode materials recovered after 100 cycles in charge and discharge successively can be compared in Fig 5 to that of the starting  $\alpha$  phase. The occurrence of lines with weak intensity at  $4.60 \text{ \AA}$  (in the discharged state) and  $4.70 \text{ \AA}$  (in the charged one) shows the presence of a small amount of  $\beta(\text{III})/\beta(\text{II})$  system. Nevertheless, the cycling is mainly performed between two materials with large interslab spaces. The  $\gamma$  phase (characterized by an interslab distance of  $6.90 \text{ \AA}$ ) is obtained after charge but the material recovered after discharge is not as expected an  $\alpha$  phase since the lines at  $7.25 \text{ \AA}$  and  $3.68 \text{ \AA}$  are significantly displaced in comparison with those of the starting  $\alpha$  phase ( $7.80 \text{ \AA}$  and  $3.90 \text{ \AA}$ ) and moreover, the larger reticular distance is not twice the smaller one.

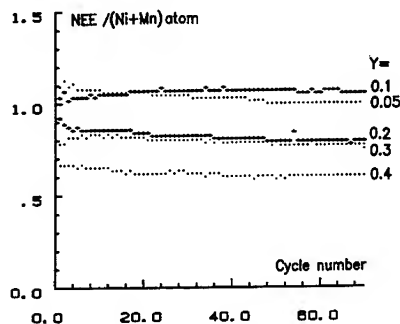


Fig. 4 Variations of the number of electron exchanged vs cycle number for various manganese amounts

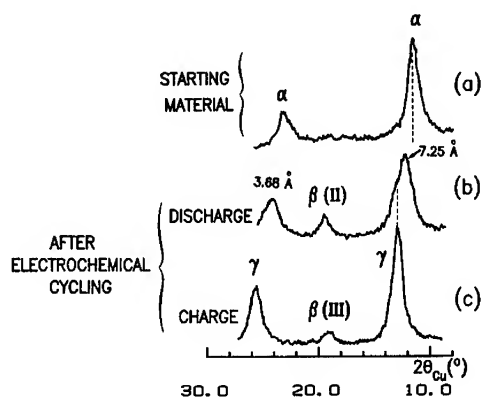


Fig. 5 Modifications of the X-ray diffraction patterns of the electrode materials upon cycling

Such a behavior, in addition to the line broadening, suggests an interstratified structure. Comparison of the X-ray pattern of the discharged material ( $I_E$ , E holds for Electrochemical) to the diffraction profiles calculated according to the Hendricks and Teller method has led to exclude unambiguously the occurrence of a  $\beta$ - $\alpha$  interstratification, as illustrated in Fig 6. The  $I_E$  discharged material appears to be constituted of an interstratified structure containing  $\gamma$  and  $\alpha$  type interslab spaces in the 3:2 ratio.

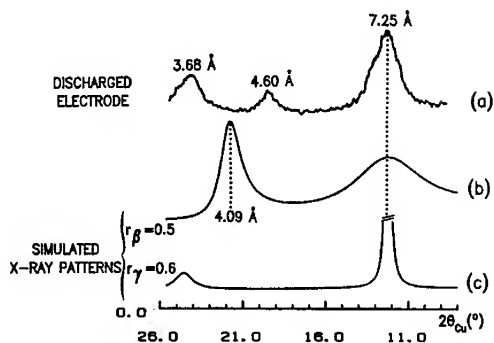


Fig. 6 Comparison of the experimental and calculated X-ray patterns of the discharged material.

Such a structure can be justified in terms of fluctuation of manganese distribution within the slab : as a result of the tetravalent state of manganese, the manganese rich domains will be very difficultly reduced to the  $\alpha$  form on discharging and will tend to retain the  $\gamma$  structure while the domains poor in manganese will be normally reduced to the  $\alpha$  form (13). It appears clearly that the average interslab distance of the  $I_E$  discharged material is very close to that of the  $\gamma$  phase, which decreases considerably the strains within the electrode and therefore improves the stability of the capacity upon cycling.

#### Modifications of the cycling curves upon cycling

The shapes of the discharge curves obtained at increasing cycle number for the  $\alpha$ -( $\gamma = 0.3$ ) manganese substituted nickel hydroxide are displayed in Fig 7. The discharge curves are gradually modified between the 3rd and 100th cycles. At the third cycle, only one plateau (rather « pseudo-plateau ») is present on the curves, corresponding to the  $\gamma/I_E$  system. At the 100th cycle, the occurrence of an additional plateau suggests that two redox systems are involved in the cycling : the plateau at the highest voltage (1.25 V) was shown to correspond to the  $\beta(III)/\beta(II)$  system [11] while the plateau at the lowest potential (1.17 V) has to be assigned to the  $\gamma/I_E$  system.

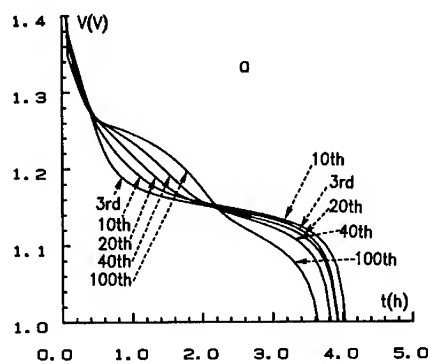


Fig. 7 Modifications of the cycling curve shapes upon cycling

Fig. 7 shows clearly a slow and partial transformation of the  $\gamma/I_E$  system to the  $\beta(III)/\beta(II)$  one, in accordance with the X-ray diffraction study reported above. This behavior is quite similar to the evolution of the  $\gamma/\alpha$  system to the  $\beta(III)/\beta(II)$  one, already observed in our lab respectively in the case of cobalt substituted nickel hydroxides and mixed 20 % cobalt - 5 % aluminum

substituted homologous phases[12]. This feature was attributed to removal of the cobalt from the structure, leading to demiction into two phases via a process of dissolution, nucleation and growth. Nevertheless, whereas the transformation  $\gamma/\alpha \rightarrow \beta(\text{III})/\beta(\text{II})$  was full in the latter two cases and induced a drop of the capacity, it is considerably slowed down in the manganese system presently studied and has actually no significant influence on the capacity.

#### Comparison of the cell potentials of the cobalt, iron and manganese systems

Fig 8 allows to compare the third cycle curves of the cobalt, iron and manganese substituted nickel hydroxides with  $y=0.3$ . Examination of the charge curves shows that the plateau corresponding to oxygen evolution is the highest in potential for the manganese system, which is in good agreement with the results claimed by Corrigan et al [13], and is the longest for the iron system. Moreover in the latter case, the potential of material oxidation is the highest, which leads to a strong competition between the oxygen evolution and the effective material oxidation. On the opposite, in the manganese or cobalt systems, both phenomena are well separated, which gives rise to a better chargeability.

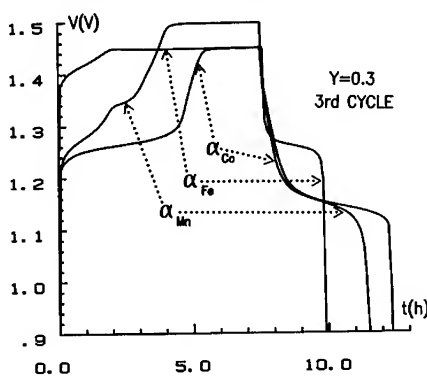


Fig. 8 Cycling curves of the cobalt, iron and manganese substituted nickel hydroxides.

The discharge potentials seem to be related to the difference in size between the substituting cations and the nickel ions in the  $\gamma$  phases [5,6]. The smaller size of the  $\text{Mn}^{4+}$  or  $\text{Co}^{3+}$  ions with regard to the  $\text{Ni}^{3+}$  ions and the larger size of the  $\text{Fe}^{3+/4+}$  ions are consistent with the variations of the potentials observed in Fig 8. We have already suggested that such a behavior may be related to the contribution of Madelung energy to the position of the Fermi level in the positive electrode material [5,6].

#### References

- [1] C. Delmas, J.J. Braconnier, Y. Borthomieu and P. Hagenmuller, *Mat. Res. Bull.*, **22**, (1987) 741.
- [2] C. Faure, C. Delmas and P. Willmann, *J. Power Sources*, **35**, 249 (1991).
- [3] L. Demourgues-Guerlou and C. Delmas, *J. Power Sources*, **45**, 281 (1993).
- [4] W.T. Reichle, *Solid State Ionics*, **22**, 135 (1986).
- [5] C. Delmas, C. Faure and Y. Borthomieu, *J. Mater. Science and Eng.*, **B13**, 89 (1992).
- [6] L. Demourgues-Guerlou and C. Delmas, *J. Electrochem. Soc.*, **141**, 713 (1994).
- [7] O. Glemser, J. Bauer, D. Duss, J. Harms And H. Low, *Proceedings of the 16th International Power Sources Symposium* (1988).
- [8] S.B. Hendricks and E. Teller, *J. Chem. Phys.*, **10**, 147 (1942).
- [9] L. Demourgues-Guerlou and C. Delmas, *J. Power Sources*, in press.
- [10] L. Demourgues-Guerlou and C. Delmas, *J. Power Sources*, in press.
- [11] L. Demourgues-Guerlou and C. Delmas, *J. Electrochem. Soc.*, submitted.
- [12] L. Gautier and C. Delmas, *J. Power Sources*, submitted.
- [13] D.A. Corrigan and R.M. Bendert, *J. Electrochem Soc.*, **136**, 723 (1989).

## ELECTROCHEMICAL ACTIVITY OF NATURAL AND SYNTHETIC MANGANESE DIOXIDES

J.M. Amarilla<sup>a,b</sup>, L.A.H MacLean<sup>a</sup>, F. Tedjar<sup>a,c</sup>, F. Le Cras<sup>d</sup>, P. Strobel<sup>d</sup> and C. Poinsignon<sup>a</sup>.

<sup>a</sup> Laboratoire d'Ionique et d'Electrochimie du Solide, ENSEEG -INP Grenoble BP 75, F-38402 Saint-Martin-d'Hères, France

<sup>b</sup> Instituto de Ciencia de Materiales Madrid, 28006 Madrid, Spain

<sup>c</sup> RECUPYL, 46 avenue F. Viallet, F- 38031 Grenoble Cedex, France

<sup>d</sup> Lab. de Cristallographie CNRS, BP 166, 38042 Grenoble Cedex 9, France

### ABSTRACT

Seven manganese dioxide (MD) forms including natural ramsdellite,  $\beta$ - $\text{MnO}_2$  and samples with structures intermediate between these two types, have been analyzed in terms of chemical and structural disorder. XRD and IR spectra show that natural ramsdellite contains groutellite,  $\text{MnO}_{1.5}(\text{OH})_{0.5}$ . The OH absorption band in the  $3400\text{cm}^{-1}$  region is sharp for groutellite, less intense on CMD spectrum, and superimposed to a broad and diffuse absorption ranging from  $3600$  to  $2000\text{cm}^{-1}$  in most  $\gamma$ - $\text{MnO}_2$ 's. The OH groups are associated with  $\text{Mn}^{3+}$  defects, while the broad and diffuse absorption band can be assigned to protons in empty  $\text{MnO}_6$  octahedra, and so related to instable manganese oxydation state between  $\text{Mn}^{3+}$  and  $\text{Mn}^{4+}$ .

A potentiostatic study in 1M and 7M KOH shows that the stoichiometric oxides, ramsdellite and  $\beta$ - $\text{MnO}_2$ , are not reduced, while CMD and EMD are reversibly reduced by  $\text{H}^+/\text{e}^-$  insertion. In 7M KOH, a reversible reduction occurs for both CMDs and EMDs until  $-0.2$  V, while a heterogeneous mechanism destroys the structure at lower potential (70% capacity loss after 3 redox cycles). Only ramsdellite and  $\beta$ - $\text{MnO}_2$  can be cycled reversibly below  $-0.37$  V, but the drained capacity is very low for  $\beta$ - $\text{MnO}_2$ .

The presence of  $\text{Mn}^{3+}$  and  $\text{Mn}^{4+}$  vacancies associated to structural disorder in synthetic MDs increases their reduction potential and completely modifies the chemical properties. This mixed valence state seems to be at the origin of the reduction properties by proton insertion in protonic electrolytes.

### INTRODUCTION

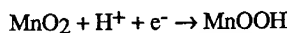
The structure of most allotropic forms of manganese dioxide (MD) can be described by different distributions of manganese in an approximately h.c.p. oxygen framework. These distributions are conveniently described by filled  $[\text{MnO}_6]$  octahedra forming infinite chains (by sharing octahedral edges) which can be linked to other octahedral chains by sharing octahedral corners or edges. In tetragonal, rutile-type  $\beta$ - $\text{MnO}_2$ , the filled octahedra form single chains running in the c direction, whereas orthorhombic ramsdellite contains double-octahedra chains.  $\gamma$ - $\text{MnO}_2$  was originally explained by de Wolff<sup>1</sup> as a random intergrowth of  $\beta$ - $\text{MnO}_2$  layers in a ramsdellite matrix (see ref. 13, fig1). Pannetier recently proposed a new structural model which explains the observed powder x-ray patterns of all forms of  $\gamma/\text{e}$ - $\text{MnO}_2$  in terms of two structural defects<sup>2</sup>: (i) a planar stacking disorder of R (Ramsdellite-type) and r (rutile-type) type layers as in the original de Wolff model, (ii) a microtwinning of the orthorhombic ramsdellite type lattice on the 021 and/or 061 planes. This model for the first time explains why battery active forms have an apparent hexagonal structure<sup>4</sup>.

The analysis of XRD patterns of various synthetic MDs allows to associate structural disorder and stoichiometric defects<sup>25</sup>: the presence of  $\text{Mn}^{3+}$  can be mainly associated to de Wolff

defects, whereas  $\text{Mn}^{4+}$  vacancies are mainly related to microtwinning. The charge defects produced by the presence of  $\text{Mn}^{3+}$  are compensated by OH groups, which can be identified on infrared spectra. The electrochemical activity of synthetic MDs is related to these stoichiometric defects ( $\text{Mn}^{3+}$  and  $\text{Mn}^{4+}$  vacancies), which increase the reduction potential by ca. 0.3 V compared to that in the stoichiometric, ordered MD forms, ramsdellite and  $\beta\text{-MnO}_2$ <sup>13</sup>. In the present study, we compare the electrochemical behaviour of natural ramsdellite,  $\beta\text{-MnO}_2$  and various CMDs, including new ones with a small fraction of de Wolff defects, in 1M and 7M KOH.

Obtaining pure ramsdellite is difficult as it is a rare mineral, which presumably accounts for the lack of study on this compound despite its popularity as a simplified structural model for explaining, in particular, the possible proton insertion sites in the reduction of battery-active  $\text{MnO}_2$ <sup>7,18</sup>. Several attempts have been made to synthesize it without success<sup>15,19, 20, 21</sup>. Recently, Rossouw et al.<sup>24</sup> have reported the synthesis of ramsdellite. However, their material still contains a notable fraction of De Wolff defects. In the present study, we use a synthetic ramsdellite, obtained by an improved procedure<sup>27</sup>.

I(V) curves obtained by the reduction of CMD/EMD in 1M and 7M KOH<sup>12</sup> from Ueq to -0.8V (vs. Hg/HgO) exhibit very different profiles below -0.2V. Referring to the work of Kozawa and Yeager<sup>9</sup>, we carried out a careful reduction/oxidation study in electrolytic KOH solutions of increasing concentration from 1 to 9M<sup>8</sup>. It led us to define the conditions of homogeneous and reversible reduction by proton insertion, which occurs in  $\text{KOH} < 1\text{M}$ , and corresponds to the simple reduction reaction :



A heterogenous process takes place when MDs are reduced in more concentrated KOH solutions. It is favoured by the increasing solubility of  $\text{Mn}^{3+}$  at increasing pH, leading after reduction to precipitation of  $\text{Mn}(\text{OH})_2$ <sup>9</sup>. This heterogenous reduction step irretrievably destroys the architecture of the starting material and is responsible for the irreversibility of MDs presently used in  $\text{MnO}_2$  primary batteries<sup>8</sup>. For that reason, it was interesting to compare the electrochemical and cycling behaviour of new samples close to ramsdellite in 1M and 7M KOH.

## EXPERIMENTAL

### Materials

Seven samples of  $\text{MnO}_2$  forms were examined :  $\beta\text{-MnO}_2$  (pyrolusite), obtained from thermal decomposition of manganese nitrate, natural ramsdellite from New Mexico, synthetic ramsdellite (F18) prepared by hot acid treatment of  $\text{LiMn}_2\text{O}_4$ <sup>15</sup>, a standard CMD (IBA no.11) from Kerr McGee prepared by oxidation with perchlorate solution of  $\text{Mn}^{2+}$ , exhibiting a low rate of pyrolusite intergrowth defect, an EMD (C8) prepared by electrodeposition from a  $\text{Mn}^{2+}$  sulfate solution under 0.2 A.dm<sup>2</sup> controlled current density<sup>25</sup>, and commercial samples from Sedema (CMD-WSA) and Tekkoshia (EMD). Each sample was characterized by X-ray diffraction, FTIR spectroscopy, chemical and thermogravimetric analysis.

### Characterization

XRD patterns were recorded using either a ( $\theta, 2\theta$ ) Philips (Fe  $\text{K}\alpha$ ) or a Siemens 5000 (Cu  $\text{K}\alpha$ ) diffractometer. Weight loss and thermal effects were recorded on heating with a TGA-DSC Netsch TG/TA apparatus, using a 10°/min heating rate. Samples were analyzed for total manganese and oxidation state using standard redox titrimetry.

The oxidation state of manganese and water contents are given in Table I. The natural ramsdellite sample was found to have an average oxidation state lower than four (see below). The

TABLE I. Composition and structural parameters of natural and synthetic samples

Sample	Mn/O H <sub>2</sub> O %	a (Å)	b (Å)	c (Å)	Tw (%)	P <sub>r</sub>	Ref.
Ramsdellite		4.533	9.27	2.866	0	0.00	Bystrom (1949)
Ramsdellite New Mexico	1.945 0.06	4.537	9.30	2.871	4	0.00	this work <sup>†</sup>
'synthetic rams.' (F18)	1.98±0.02 0.16	4.4785	9.3547	2.8537	20	0.20	this work <sup>††</sup>
'synthetic rams.' Rossouw <sup>24</sup>		4.499	9.3607	2.8459	25	0.27	Pannetier & Chabre (1994) <sup>ref 4</sup>
IBA 11	1.97 0.5	4.461	9.312	2.849	14	0.34	this work <sup>††</sup>
CMD WSA	1.97 1.9	4.463	9.403	2.834	35	0.45	Pannetier & Chabre (1994) <sup>ref 4</sup>
EMD C8	1.965 1.21	4.424	9.471	2.810	60	0.48	ref. 25

<sup>†</sup> refined using reflections (021), (200), (121), (140), (221) & (240)

<sup>††</sup> line (200) omitted because of overlap with reflection from KCl, used as internal standard.

synthetic ramsdellite F18 has MnO<sub>2</sub> stoichiometry within experimental errors, while IBA 11 and the commercial samples contain minor amounts of Mn<sup>3+</sup>.

IR spectra were recorded on a FTIR Nicolet 710, with an optical gain increased in reducing the mobile mirror velocity to 10 cm/mn, after accumulating 400 scans. Pelletized samples were obtained by pressing a mixture of 2.5mg MnO<sub>2</sub> and 100mg BrTI under 8 T/cm<sup>2</sup>.

#### Electrochemical measurements.

The electrochemical response of the MD samples was analyzed using a MacPile® computer-controlled system. For an accurate determination of I(V) and V(x) curves, composite electrodes made of 0.1g MnO<sub>2</sub> and graphite (3/1) were reduced in 1M and 7M KOH under potentiostatic control with a step scanning rate of 10 mV/2 hours. Cyclings were carried out in 7M KOH with a step scanning rate of 9 mV/0.1 h in the voltage range from V<sub>eq</sub> to -0.8V vs. Hg/HgO. The experimental cell is similar to the one used by McBreen and is described elsewhere<sup>10, 11</sup>.

## RESULTS

### Structural analysis

X-ray diffraction patterns of natural ramsdellite, sample F18 and  $\beta$ - $\text{MnO}_2$  are given in Fig. 1. Three phases have been identified in the natural 'ramsdellite' sample from New Mexico (USA) by comparison with the JCPDS cards: 39-375 (ramsdellite, or 43-1455), 42-1316 (given initially as ramsdellite, then as 'unnamed manganese oxide mineral' after we identified it as groutellite) and 24-735 ( $\beta$ - $\text{MnO}_2$ ). JCPDS card 42-1316 undoubtedly represents a naturally occurring 'groutellite'<sup>21</sup>, which appears to be isostructural to ramsdellite, but with an oxidation state intermediate between that of ramsdellite ( $\text{Mn}^{4+}$ ) and groutite ( $\text{Mn}^{3+}$ ). This natural 'groutellite' phase is nearly always found associated with ramsdellite, as stated by J. Post in this card.

The proportion of the three phases was estimated by the direct ratio of integrated intensities of well-separated peaks, yielding :

$$\begin{array}{ll} \text{groutellite} & 21 \pm 3 \% \\ \beta\text{-MnO}_2 & \approx 2\%. \end{array}$$

Neglecting the latter, the average Mn oxidation state corresponding to these proportions of ramsdellite ( $\text{Mn}^{4+}$ ) and groutellite ( $\text{Mn}^{3.5+}$ ) (23) would be  $\text{O/Mn} = 1.948$ , in good agreement with the experimental value 1.954.

The structural parameters of various samples are given in Table I.  $P_r$  is the fraction of rutile blocks in the ramsdellite matrix (de Wolff defects) and  $T_w$  the fraction of microtwinning, which are both deduced from the X-ray diagrams following Pannetier's method<sup>4</sup>. The ramsdellite data given by Byström<sup>17</sup> are used as a reference in which  $T_w$  is assumed to be zero.

Details of this analysis will be given elsewhere<sup>28</sup>. The results (Table II) show that the rate of de Wolff defects  $P_r$  increases in the series

natural ramsdellite < F18 < Rossouw < IBA 11 < CMD WSA < EMD C8

i.e. the new sample F18 has the lowest de Wolff defect rate ( $P_r=0.20$ ) among the synthetic samples. However, not any of the synthetic samples is pure ramsdellite.

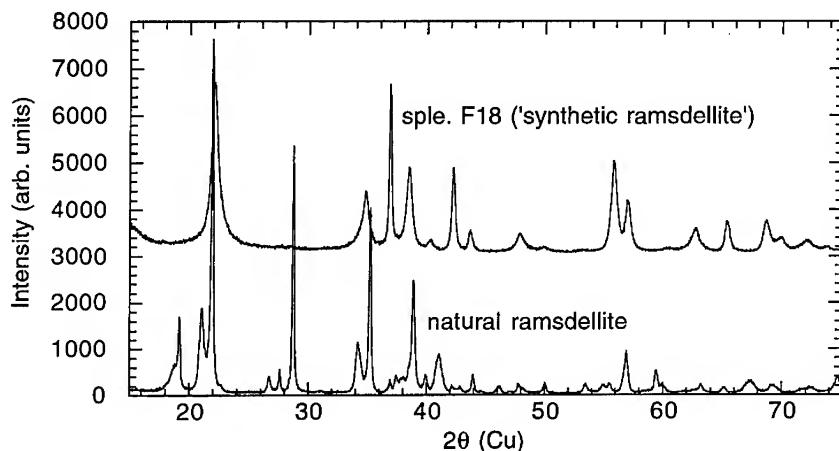


Fig. 1. – X-ray diffraction patterns of a) natural, b) 'synthetic ramsdellite'(sample F18) (Cu  $K\alpha$ ).

### IR spectra

The IR spectra of the samples studied are given in Fig. 2. The spectrum of New Mexico ramsdellite presents a well-resolved OH bending mode at  $3398\text{cm}^{-1}$ , assigned to the hydroxyl groups due to the groutellite phase. Note that this OH bending mode around  $3400\text{cm}^{-1}$  had been reported previously in New Mexico ramsdellite by Potter and Rossman<sup>22</sup>. However, these authors were unaware of the presence of groutellite, and logically stated the ramsdellite composition as ' $\text{MnO}_2 \cdot 0.06\text{H}_2\text{O}$ '.

The IR spectrum of sample F18 ('synthetic ramsdellite') also presents a resolved OH absorption band at  $3404\text{cm}^{-1}$ , superimposed to a wide and diffuse absorption band, ranging from  $3600$  to  $2000\text{cm}^{-1}$ , equally present in IBA11 and WSA spectra. The EMD C8 spectrum shows a wide and diffuse absorption band of low intensity between  $2000$  and  $3400\text{cm}^{-1}$ . Finally, the IR spectrum of  $\beta\text{-MnO}_2$  does not exhibit any absorption due to OH or water in the  $3000\text{cm}^{-1}$  range: it can be used as a base line reference for the other spectra. The analysis of the low frequency part, where the absorption bands of the Mn-O lattice appear, will be published in a forthcoming paper<sup>24</sup>.

### Electrochemical characterization: Potentiostatic reduction and cycling.

The first reduction voltammograms of natural ramsdellite, F18, IBA11 and CMD WSA in  $1\text{M KOH}$  under potentiostatic control at  $10\text{mV/h}$  are given in Fig. 3, and the results of cycling for pyrolusite, natural ramsdellite, CMD WSA and EMD Tekkosha (recorded under potentiostatic control at  $9\text{mV}/0.1\text{h}$ ) in Fig 4. The variation of the redox current intensity of natural and synthetic ramsdellite, is drawn versus time and potential in Fig. 5.

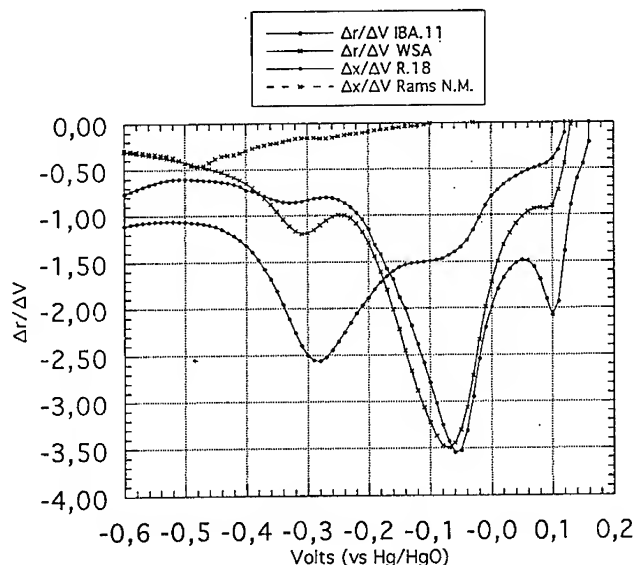


Fig. 2. – Voltammogram of the reduction of samples IBA11, WSA, F18 and in  $1\text{M KOH}$  at  $10\text{mV}/2\text{h}$ . (reference electrode  $\text{Hg}/\text{HgO}$ ).



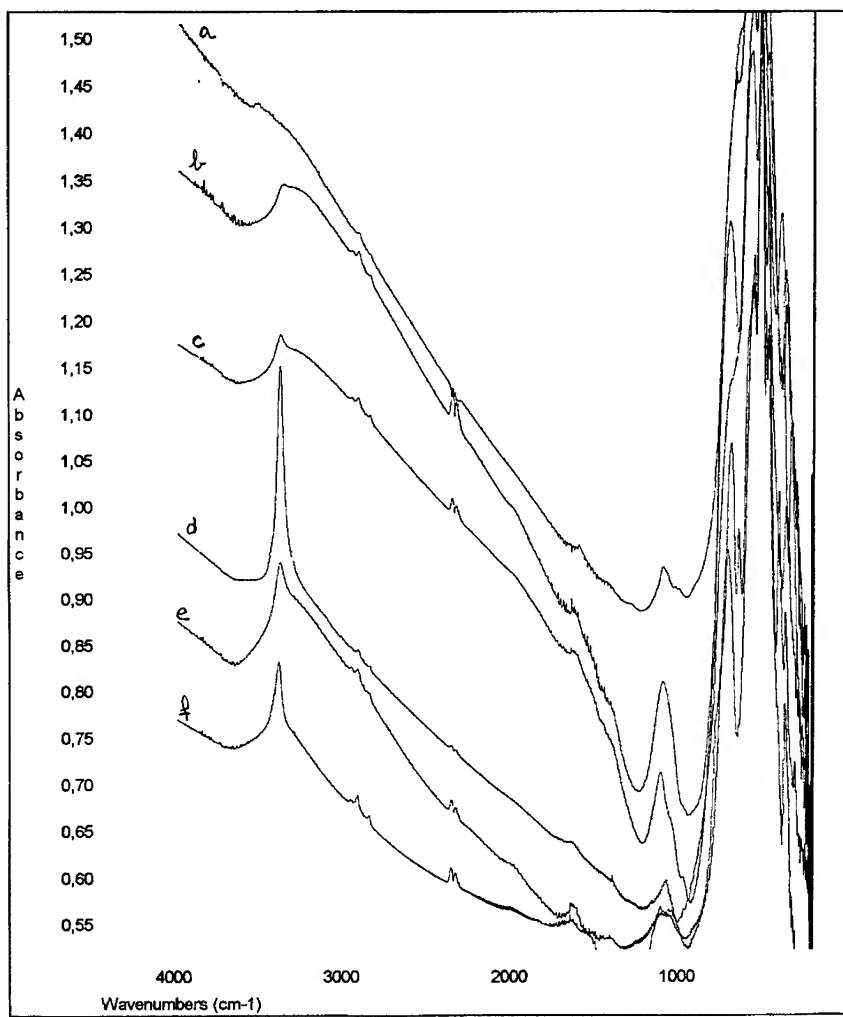


Fig. 2. – IR spectra : a)  $\beta$ -MnO<sub>2</sub>, b) EMD, c) IBA 11d ramsdellite, e) WSA, f) F18 ('synthetic ramsdellite').

Fig.3 shows an important observation : in molar KOH, IBA11 ( $\gamma$ - $\text{MnO}_2$ ), F18 and WSA samples start reducing above 0.10 V, ramsdellite at -0.11 V and  $\beta$ - $\text{MnO}_2$  at 0.04 V (for the latter, see fig. 3d in ref.13). The reduction peak of natural ramsdellite is weak (incremental capacity 0.5), broad and centered at -0.47 V, as that of  $\beta$ - $\text{MnO}_2$  (centered at -0.49 V). On the contrary, F18 and IBA11 reduction peaks are wide and extend to -0.460V, with a maximum incremental capacity equal to -1.5 and -3.5, respectively. Furthermore, 80% of IBA11 capacity is recovered above -0.35 V, but only 10% for ramsdellite and  $\beta$ - $\text{MnO}_2$ . The reduction peak of 'synthetic ramsdellite' F18 has a different shape from that of IBA11. It is actually double, with a first peak centered at -0.1 V, similarly to IBA11, and a second peak at -0.29 V, with a larger associated capacity (incremental capacities 0.5 and 2.6, respectively). These features are retained at different scanning rates (20, 40 mV/2 h and 90 mV/h on Fig 5).

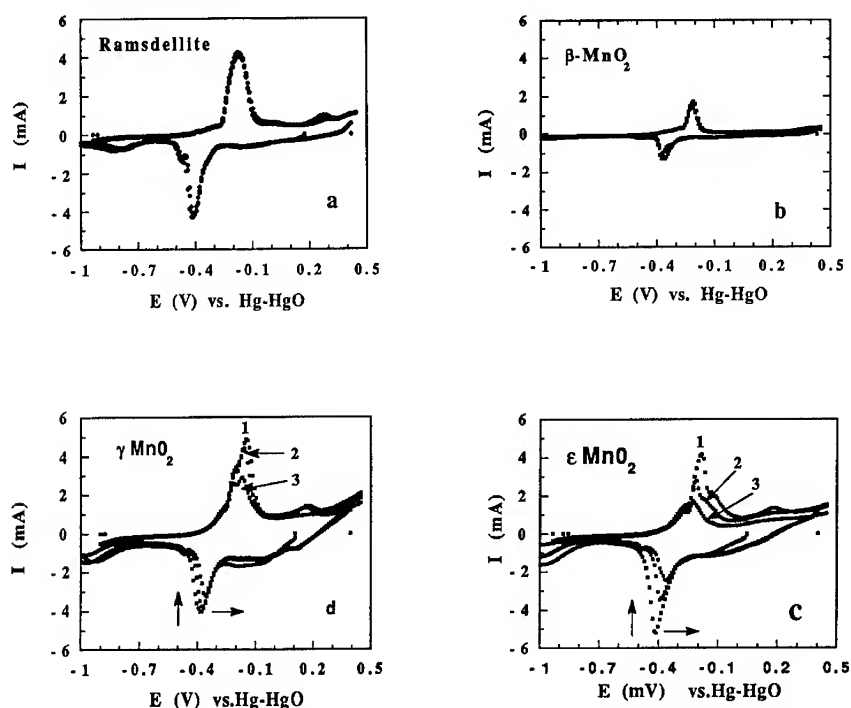


Fig. 4. - Potentiostatic cycling in 7M KOH (scan rate of 90mV/h). a)  $\beta$ - $\text{MnO}_2$ , b) natural ramsdellite, c) WSA, e) EMD Tekkosha (reference electrode Hg/HgO 7N).

This means that IBA11 behaves as a 'conventional'  $\gamma$ - $\text{MnO}_2$  and is reduced at higher potential than natural ramsdellite for the first peak, while 'synthetic ramsdellite' (F18) presents a specific behaviour, as if it contained two different kinds of Mn atoms, one with a ' $\gamma$ - $\text{MnO}_2$ -like' redox potential, and the other with a low redox potential.

Natural and 'synthetic' ramsdellite, as well as CMD (WSA) and EMD (C8) samples, were cycled in 7M KOH with a scan rate of 90mV/h. Figure 5 gives the evolution of reduction and oxidation current versus time during 3 cycles. The first cycle of natural ramsdellite redox voltammogram was described previously<sup>11</sup>. The second cycle shows only one current peak on

reduction and oxidation, with a peak maximum at -0.37 V and -0.175 V, respectively. On the contrary, sample F18 ('synthetic ramsdellite') exhibits on each cycle *two reversible peaks*, visible both on reduction and on oxidation.

CMD (Fig. 4d) starts reducing at 0.15 V. A broad maximum around -0.1 V is followed by a second cathodic peak at -0.43 V. On cycling, this peak is shifted to less negative potentials and its maximum peak current decreases, as indicated by the arrows on Fig.4d. The sweep reversal yields an oxidation current peak at -0.14– 0.18 V. For further cycles, a second oxidation peak begin to arise after the third cycle at - 0.22 V. The reduction of EMD (Fig. 4c) shows rather similar features on reduction. On oxidation, three anodic peaks are observed at -0.18 V, superimposed to a broad peak centered at -0.15V, and at 0.2 V.

Finally, the reduction of  $\beta$ -MnO<sub>2</sub> (Fig. 4a) begins at 0.035 V, with a current peak at -0.36 V. In the reverse sweep, only one anodic peak centered on -0.15V is detected.

Natural ramsdellite was cycled three times after the first cycle without losing any capacity, whereas CMD and EMD (fig 4c-d) lose 70% of their capacity after the third cycle, as well as 'synthetic ramsdellite'<sup>14</sup>.

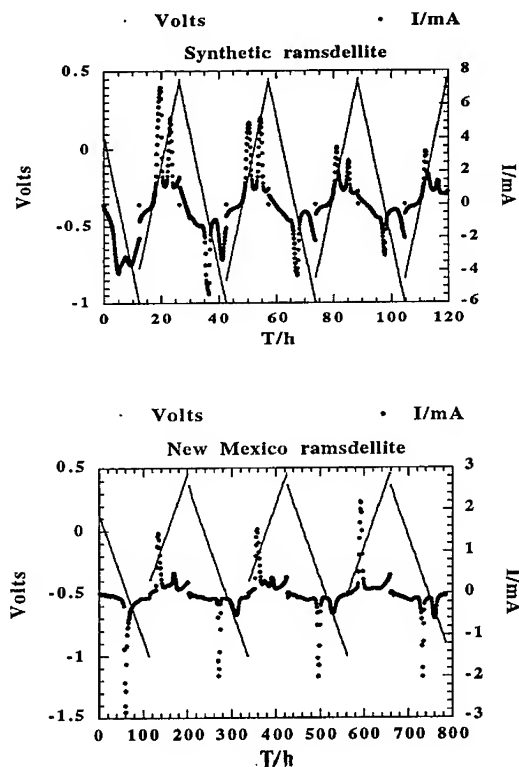


Fig. 5. – Variation of current with time for 3 cycles on 'synthetic' (top) and natural (bottom) ramsdellite.

## DISCUSSION

The structural analysis showed that natural ramsdellite (New Mexico sample) is a mixture of three phases, ramsdellite, pyrolusite and groutellite  $\text{MnO}_{1.5}(\text{OH})_{0.5}$ . Our 'synthetic ramsdellite' (F18) is the synthetic sample with structure closest to that of natural ramsdellite. The fraction of intergrown rutile-type blocks  $P_r$ , however, is still 0.20. But it is markedly different, both in rutile fraction and in rate of microtwinning, from the IBA11 standard.

The association of structural disorder and chemical nonstoichiometry in a given 'MnO<sub>2</sub>' (MD) phase appears to be related to the electrochemical activity. The high electrode potential value of sample IBA11 compared to ramsdellite confirms that structural and chemical disorder in synthetic MDs increases the energy of the Fermi level<sup>12-13</sup>. Nevertheless this conclusion is not so clear for synthetic ramsdellite.

The low  $\text{Mn}^{3+}$  content in this MD, the presence of a well-resolved OH bending mode at  $3404\text{ cm}^{-1}$  superimposed to a diffuse and weak absorption band in its IR spectrum seem to indicate that 'synthetic ramsdellite' does not behave like a mixed-valence dioxide as IBA11, but rather as an intermediate between groutellite and IBA11. The OH bending mode is superimposed to a diffuse absorption band in the IR spectrum of IBA11, and still present (but badly resolved) for EMD. In both cases the spectrum is dominated by a wide and diffuse absorption band from  $3600\text{ cm}^{-1}$  to  $2000\text{ cm}^{-1}$ . The OH bending peak maximum frequency is  $3407\text{ cm}^{-1}$  for groutite<sup>26</sup>,  $3404$  for groutellite,  $3398$  in CMD, not resolved for EMD. Can we relate the frequency shift to the variation of manganese oxidation state and the diffuse absorption band to instable electronic states.

The shape of the 'synthetic ramsdellite' reduction voltammograms (Fig. 3) presents two intense current peaks related to the insertion of the  $\text{H}^+/\text{e}^-$  couple as well as the  $I(V)$  curves of the others synthetic MD. The current peak of natural ramsdellite is very weak and is probably due to the reduction of groutellite. Natural ramsdellite and  $\beta\text{-MnO}_2$  are intensively reduced only in 7M KOH, corresponding to the heterogenous process proposed by Kozawa et al.<sup>11</sup>; it is representative of a second species electrode where the reduction involves a solubilization-precipitation process.

During cycling, New Mexico ramsdellite and  $\beta\text{-MnO}_2$  do not lose any capacity, while the other MDs lose up to 70% of their capacity after 3 cycles. This difference in electrochemical reactivity seems to be due to the different manganese 'oxidation states' in the material:  $\text{Mn}^{4+}$  in  $\beta\text{-MnO}_2$  and ramsdellite (after elimination of the groutellite phase during the first reduction)<sup>14</sup>, mixed valence in WSA, in IBA11 due predominantly to the presence of  $\text{Mn}^{3+}$  associated to a small number of  $\text{Mn}^{4+}$  vacancies and to a greater number of such vacancies in EMD. What is the manganese oxidation state in synthetic ramsdellite? This mixed valence state is probably responsible for the different behavior of both ramsdellite samples during cycling.

## CONCLUSION

The main conclusion of this study concerns the influence of  $P_r$ ,  $T_w$ , occurrence of  $\text{Mn}^{3+}$  and  $\text{Mn}^{4+}$  vacancy defects on the electrochemical activity of synthetic manganese dioxide. These defects modify the manganese oxidation state into an instable mixed valence state, which is very sensitive to the type of stoichiometric defects present in the material. It influences its chemical reactivity, as shown by the different electrochemical response given by the various MDs studied here. In  $\text{KOH} \leq 1\text{M}$ , synthetic MD reduction occurs by insertion of  $\text{H}^+/\text{e}^-$  couple in a reversible, homogenous process, whereas the stoichiometric polymorphs, ramsdellite and  $\beta\text{-MnO}_2$ , do not react. At higher KOH concentrations, a heterogenous process occurs during reduction: all MD react differently. Each type of disorder induces a specific response to the reduction process. Only the stoichiometric forms can be reversibly reoxidized, but at low potential value.

Chemical and structural disorders in  $\text{MnO}_2$  are necessary for electrochemical activity at high potential value in alkaline electrolytic solutions. This is well illustrated by the comparison of 'ramsdellite' samples. Except for the contribution of the groutellite fraction it contains, natural

ramsdellite does not manifest any electrochemical activity for  $H^+/e^-$  insertion in 1M KOH; it is reduced in 7M KOH below -0.35 V by a heterogenous process. The 'synthetic ramsdellite', on the other hand, has a low rate of rutile-type block intergrowth and stoichiometric defects in the same phase. As a consequence, it exhibits a good electrochemical activity during the first reduction in 1M KOH and behaves as an insertion material. In 7M KOH, natural ramsdellite behaves as a second species electrode and exhibits a good reproducibility during cycling which is not observed for 'synthetic ramsdellite'. In the latter, the low  $P_T$  value is correlated to a low  $Mn^{3+}$  and  $Mn^{4+}$  vacancies content (or a higher average oxidation degree than groutellite). The two current peaks on reduction (at -0.1 and -0.27 V) show that the rate of stoichiometric defects ( $Mn^{3+}$  and  $Mn^{4+}$  vacancies) is not high enough to increase the Fermi level energy to the value observed in IBA11, but is sufficient to allow reduction by  $H^+/e^-$  insertion. The different I(V) curves observed during cycling of natural and synthetic ramsdellite, CMD and EMD are electrochemical spectra which reveal that each type of synthetic material has a specific chemical reactivity, as well as it has a specific chemical formula, a specific XRD pattern and IR spectrum.

#### Aknowledgements.

The authors thank the Mineralogy Museum of the Paris Mining School for providing the New Mexico ramsdellite.

#### References

- 1 P.M. De Wolff, *Acta Crystallogr.*, 1959, **12**, 341.
- 2 J. Pannetier, *Progress in batteries and battery materials*, 1992, **11**, 51.
- 3 J. Pannetier, Y. Chabre, C. Poinsignon, *ISSI letters*, 1990, **1**, 2 5.
- 4 J. Pannetier, Y. Chabre, *Progr. in Solid State Chemistry*, 1995 to be published.
- 5 M. Ripert, C. Poinsignon, Y. Chabre & J. Pannetier, *Phase Transitions*, 1991, **2-4**, 205.
- 6 M. Ripert, C. Poinsignon, J. Pannetier, Y. Chabre *Mat. Res. Soc. Proc.*, 1991, **210**, 359.
- 7 W.C. Maskell, J.E. Shaw, F.L. Tye, *J. Applied Electroch.*, 1982, **12**, 101.
- 8 J.M. Amarilla, F. Tedjar, C. Poinsignon *Electrochem. Acta*, 1994, **39**, 15, 2321.
- 9 A. Kosawa, J.F. Yeager, *J. Electro Chem. Soc.*, 1968, **115**, 1003.
- 10 J. McBreen, *J. Power Sources*, 1975, **5**, 525.
- 11 C. Poinsignon, J.M. Amarilla, F. Tedjar, *Prog. in batt. battery materials*, 1994, **13**, 148.
- 12 C. Poinsignon, J.M. Amarilla, F. Tedjar, *Solid State Ionics*, 1994, **70/71**, 649.
- 13 C. Poinsignon, J.M. Amarilla, F. Tedjar, *J. Material Chemistry*, 1993, **3(12)** 1227.
- 14 F. Tedjar, J.M. Amarilla, C. Poinsignon, *Electrochem. Acta*, submitted.
- 15 M.M. Thackeray, M.H. Rossouw, R.J. Gummow, D.C. Lilies, K. Pearce, A. de Kock, W.I.F. David, S. Hull, *Electrochem. Acta*, 1993, **38**, 1259.
- 16 Y. Chabre, M. Ripert, *Mat. Res. Soc. Symp. Proc.*, 1991, **210**, 367.
- 17 A.M. Byström, *Acta Chem. Scand.*, 1949, **3**, 163.
- 18 M. Voinov, *Electrochem. Acta*, 1982, **7**, 833.
- 19 H. Bode, A. Schmier, *Die Naturwissenschaften*, 1962, **49-20**, 465.
- 20 T.E. Moore, M. Ellis, P.W. Selwood, *J. Am. Chem. Soc.*, 1950, **72**, 856.
- 21 O. Bricker, *Am. Miner.*, 1965, **50**, 1296.
- 22 R.M. Potter, G.R. Rossman *Am. Min.*, 1979, **64** 1199.
- 23 C. Klinsberg, R. Roy *Am. Min.*, 1959, **44** 819.
- 24 M.H. Rossouw, A. de Kock, D.C. Lilies, R.J. Gummow, M.M. Thackeray, *J. Mat Chem.*, 1992, **2** (11), 1211.
- 25 J.M. Amarilla, J. Pannetier, C. Poinsignon (1995) to be published
- 26 V.C. Farmer, *The Infrared Spectra of Minerals* (1974) The Mineralogical Society, London.
- 27 P. Strobel et al., to be published.
- 28 L.A.H. MacLean et al., to be published.

## PROTON INTERCALATION IN $\gamma$ -MnO<sub>2</sub> FROM RAMSDELLITE TO GROUTITE THROUGH GROUTELLITE

YVES CHABRE\* and JEAN PANNETIER\*\*

\*Laboratoire de Spectrométrie Physique, Université Joseph Fourier-Grenoble and CNRS  
BP 87 F-38402 Saint Martin d'Hères, France.

\*\*Institut Laue Langevin, BP 156 F-38042 Grenoble, France.

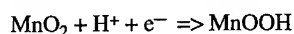
### ABSTRACT

This paper presents an investigation of electrochemical proton intercalation in two chemically prepared MDs containing low amounts of structural defects and in a natural MD containing 89% of highly crystalline ramsdellite. XRD examination of equilibrated partly reduced synthetic samples confirms the formation of groutite as a final reduction product and, before mid-reduction, suggests the formation of a solid solution between ramsdellite and groutellite H<sub>0.5</sub>MnO<sub>2</sub>. In contrast, electrochemical spectroscopy hint at a two-phase process with an equilibrium potential at -60 mV vs Hg/HgO. The implication of the structural defects on these observations are discussed.

### INTRODUCTION

The electroactive forms of manganese dioxides (MD) used in Leclanché and alkaline batteries have long been assumed to consist of an intergrowth of ramsdellite and pyrolusite units (De Wolff, 1959; Turner and Buseck, 1979), a defect for which we coined the name of De Wolff disorder. Recent investigations have shown that microtwinning is another prominent defect which has to be taken into account for explaining both the electrochemical and structural properties of MDs. Practical methods to analyse X-ray powder diffraction patterns of MDs and calculate the two defect concentrations (Tw for microtwinning and P<sub>r</sub> for De Wolff disorder) in real materials were developed by Pannetier (Ripert *et al.*, 1991; Pannetier, 1992, 1994, Chabre and Pannetier 1995) and led to a new classification of  $\gamma$ -MDs in a [Tw,P<sub>r</sub>] structural map. This model shows that  $\gamma$ - and  $\epsilon$ -MnO<sub>2</sub> are similar materials, both deriving from the ramsdellite structure, which differ only by the quantity of structural defects present, the so-called  $\epsilon$ -MnO<sub>2</sub> exhibiting much more microtwinning than  $\gamma$ -MnO<sub>2</sub> samples. Moreover it appears that only a small number of the possible members of the  $\gamma$ -MnO<sub>2</sub> structural family have been prepared up to now: P<sub>r</sub> is usually close to 0.3 for chemically prepared MDs and to 0.4 -0.5 for electrochemically prepared ones.

Concerning electrochemical properties, the overall reduction reaction in aqueous media is usually summarized by the following "chemical" equation:

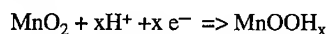


with groutite,  $\alpha$ -MnOOH, as the end product of the one electron reduction (Feitknecht *et al.*, 1960), a point that was firmly established by Coeffier and Brenet and Bell and Huber in 1964.

From the observation of a continuous increase of the cell parameters of MnO<sub>2</sub> at the beginning of the reduction, Brenet was the first to propose in 1956 that the so called "depolarizing effect" of

$\gamma$ -MnO<sub>2</sub> was taking place by capture of proton species by the MnO<sub>2</sub> structure. This was further confirmed by Brouillet *et al.* in 1963; using a thin-film electrode and working under galvanostatic and potentiostatic conditions they showed that the kinetics of reduction can be described by assuming a proton diffusion into the solid, ruled by Fick's law.

Besides, the fact that the potential of electrochemical cells decreases monotonically during reduction up to one electron per Mn led to the concept of a homogeneous phase reaction, partial reduction corresponding to the reaction



This suggests a monotonic evolution of properties during reduction, a point which is at variance from the early observation by the Brenet's school (1963) that several physical properties of the H/ $\gamma$ -MnO<sub>2</sub> system exhibit a discontinuity or a change of behavior in the vicinity of mid-reduction: a change of slope in the evolution of lattice parameters (Gabano *et al.*, 1965) and a step in the first part of the discharge curve (Bell and Huber, 1964; Kozawa and Powers, 1966).

To account for these observations Atlung (1975) proposed the existence of an intermediate compound, HMn<sub>2</sub>O<sub>4</sub> or "groutellite". Referring to De Wolff's work he also pointed out that "attention should here be drawn to the existence of alternate layers with  $\beta$  and  $\gamma$  structure", a first reference to the structural peculiarities of  $\gamma$ -MnO<sub>2</sub>.

Later on Tye and coworkers investigated the details of the reduction of  $\gamma$ -MnO<sub>2</sub> and attempted to model the proton-electron insertion process at the atomic level. Their work (Maskell *et al.*, 1981-1983), based on X-ray diffraction studies and OCV measurements of carefully chemically and electrochemically reduced  $\gamma$ -MnO<sub>2</sub>, led them to propose a structural interpretation of the two steps of the one e<sup>-</sup>/Mn reduction process: reduction first from MnO<sub>2</sub> to Mn<sub>2</sub>O<sub>3</sub>OH (noted MnO<sub>1.75</sub>) then to MnOOH (noted MnO<sub>1.5</sub>). The two processes involve protons occupying different locations within the [1x2] tunnels of the ramsdellite units of  $\gamma$ -MnO<sub>2</sub> structure and relate to the onset of a Jahn-Teller distortion of the [Mn<sup>3+</sup>O<sub>6</sub>] octahedra at mid-reduction.

Direct evidence of this two-step reduction of the ramsdellite layers of  $\gamma$ -MDs was obtained (Chabre, 1991; Chabre and Ripert, 1991) by using a potentiodynamic protocol of discharge, similar to the electrochemical potential spectroscopy previously proposed by Thompson (1979), i.e. a regular step-by-step potential scanning and systematic chronoamperometry.

The aim of the present work is to examine the first stages of reduction of  $\gamma$ -MnO<sub>2</sub> samples as close as possible to the ideal ramsdellite, i.e., samples containing low amounts of structural and chemical defects. In addition a natural sample of MD which appeared to contain essentially a very crystalline ramsdellite was also used. The main question we are addressing in this paper is the role played by defects in the mechanism of reduction/proton intercalation.

## EXPERIMENTAL

### Samples

Experiments were carried out with two  $\gamma$ -MD samples containing low amounts of defects, namely CMD IBA-11 (Glover *et al.*, 1989) and a non commercial ramsdellite-like CMD from Sedema, hereafter labelled RMD(RB); for the sake of comparison, a natural ramsdellite from Lake Valley, New Mexico, labelled NMD(LV) was also studied. Some characteristics of the  $\gamma$ -CMD samples are given in table I.

Table I. Characteristics of the  $\gamma$ -CMD samples used in this work.

Sample	%MnO <sub>2</sub>	O/Mn	BET area (m <sup>2</sup> /g)
RMD(RB) <sup>1</sup>	96.95	1.985	18.3
IBA-11 <sup>2,3</sup>	92.8	1.97	12.4

<sup>1</sup> Ramsdellite-like CMD, from Sedema.

<sup>2</sup> CMD from Kerr-McGee Corp., obtained by a chlorate process.

<sup>3</sup> Data from *The Handbook of Manganese Dioxides*, (Glover *et al.*, 1989)

To get proper powder averaging in XRD experiments, MD samples were grinded in an agate mortar. Scanning electron microscopy (SEM) observation of the powders showed that the 50  $\mu$ m spherical grains of IBA-11 had been broken to particles with a wide distribution of sizes, mainly in the range 5 to 10  $\mu$ m. RMD(RB) powder was observed to be made of aggregates of very small regular grains, with a narrow distribution around 0.1  $\mu$ m. The natural ramsdellite powder mainly contains elongated grains in the 1 to 10  $\mu$ m range. These powders were also used for the electrochemical measurements.

#### XRD measurements

XRD patterns of pristine samples were recorded with a Siemens D5000 diffractometer operating in Bragg-Brentano reflection geometry and using CuK $\alpha$  radiation, a graphite monochromator in the reflected beam and a single detector. High quality data were obtained by using a small scanning step (0.02° in 2 $\theta$ ) and a long counting time (40 s per point), thus requiring about two days of data collection per sample.

Reduced MD powders were recovered from the electrochemical cells and washed with outgassed distilled water. They were then transferred, still wet, into 0.5 mm diameter Lindemann tubes, by taking care to avoid direct contact with air. XRD patterns were collected with a Siemens D5000 diffractometer operating in transmission and equipped with a monochromator in the primary beam (CuK $\alpha$ 1 radiation) and a 1024-channel linear detector. Usual recording conditions were used with a 2 $\theta$  step of 0.016° and a total recording duration of 12h.

#### Electrochemical measurements

The electrochemical cells used in this work are similar to that presented in Chabre and Pannetier (1995). The working electrode is a mixture of MnO<sub>2</sub> powder (usually 100 mg but 20 mg only for NMD) with either graphite or carbon black or both. Measurements were performed in 1M KOH to avoid Mn<sup>3+</sup> solubility effects which occur in strongly alkaline media. Once assembled, the cell is loaded with the electrolyte and evacuated several times to ensure outgassing of the pores and thus a good impregnation of the composite electrode.

Electrochemical reductions were performed using step potential electrochemical spectroscopy (SPECS; Chabre, 1991) which is derived from the electrochemical spectroscopy previously proposed by Thompson (1979) for studying intercalation compounds. As diffusion coefficients in solids are low, typical conditions to study solid state redox processes are 10 mV steps every few hours. At each potential level the system we used (MacPile; Mouget and Chabre, 1991) performs a



chronocoulometry, thus enabling to follow the kinetics of the processes taking place in the sample at every redox level. This is of relevance for identifying the nature of the process, homogeneous single phase, two-phase equilibrium, etc...(Chabre 1992). By properly processing the data (e.g., calculating the average currents or the total charge at every potential level) one can obtain various representations of the process, such as the usual "dynamic" voltammograms (I vs V), incremental capacity  $\Delta Q/\Delta V$  (or  $\partial x/\partial V$  for an intercalation compound) vs V or x, etc. In this paper reduction degrees are reported as x in  $H_xMnO_2$ , referring to the amount of bare pristine  $MnO_2$ .

## RESULTS

### XRD analysis of the pristine materials

XRD patterns of the pristine materials are reported in fig.1. The natural sample NMD(LV) was found to be essentially a mixture of ramsdellite and pyrolusite<sup>1</sup>, the former phase containing little, if any, structural defects. The pattern of this sample could thereby be analyzed by the Rietveld technique. Using the program FullProf (Rodriguez-Carvajal, 1990) and assuming for ramsdellite the atomic coordinates given by Byström (1949) and for pyrolusite the structure refined by Baur (1976) we obtained reasonable figures of merit ( $R_{wp} = 21\%$ ,  $\chi^2 = 10.8$ ) and lattice parameters in good agreement with published values. Refinement of the scale factors led to a composition 89 %w ramsdellite and 11 %w pyrolusite.

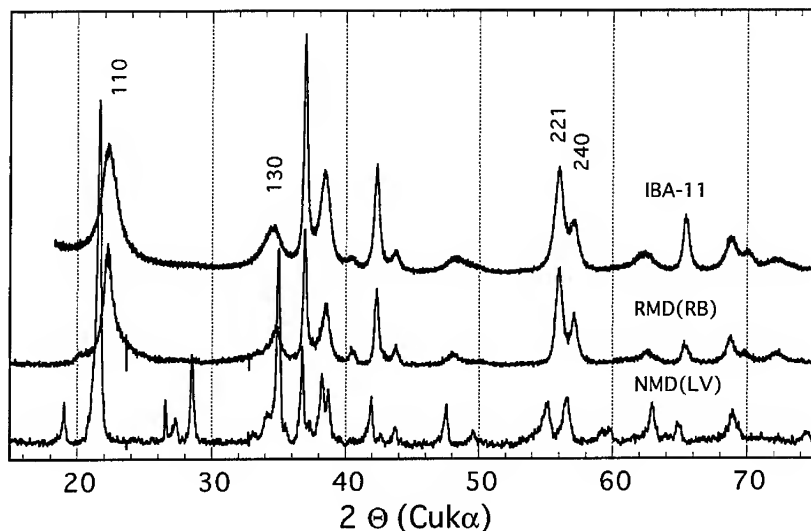


**Fig.1** X-ray diffraction patterns ( $CuK\alpha$ ) of NMD(LV), RMD(RB) and IBA-11 samples. Structural disorder is responsible for the large broadening and the shifts of most diffraction lines.

The patterns of synthetic samples were first analyzed with the program ABFit (Antoniadis *et*

<sup>1</sup> A few additional but unidentified lines are also observed (see for instance the weak line at  $2\theta \approx 26.5^\circ$ ). Whenever possible the corresponding angular ranges were excluded from the refinement. The presence of these spurious lines prevents refinement of atomic positions and explains the relatively high values of the goodness of fit and reliability factor.

The patterns of synthetic samples were first analyzed with the program ABFFit (Antoniadis *et al.*, 1990) and the results used to determine the values of the structural defect probabilities  $T_w$  and  $P_r$  according to the methods published by Chabre and Pannetier (1995). Briefly, the amount of microtwinning was deduced from the splitting of lines 221/240 or 002/061 pairs of lines and De Wolff disorder from the position of the line 110 or from the splitting of lines 110/130, assuming truly random De Wolff disorder.

The results are reported in Table II. Lattice parameters, labelled with the sub T index, are calculated using a limited set of lines (021, 200, 121, 140, 221 and 240 in Pbnm setting), selected to share equally well the line shifts due to microtwinning on the two directions **b** and **c** (Chabre and Pannetier, 1995). For the sake of comparison the values obtained for a usual  $\gamma$ -CMD (Sedema WSA) are also reported and one must bear in mind that most EMDs used in alkaline batteries exhibit almost 100% of microtwinning, with  $P_r$  values in the range 0.4 to 0.5.

Table II. Lattice parameters of the MD samples

Sample	$a_T$ (Å)	$b_T$ (Å)	$c_T$ (Å)	$b_T/2c_T$	$T_w$ (%)	$P_r$	Note.
Ramsdellite	4.533(5)	9.27(1)	2.866(5)	1.617	0	0	(1)
NMD(LV)	4.552(2)	9.270(4)	2.866(1)	1.617	0	0	(2)
RMD(RB)	4.449(2)	9.345(7)	2.847(2)	1.641	22	0.32	this work
CMD IBA-11	4.4549(8)	9.338(2)	2.8460(7)	1.640	20	0.32	(2)
Sedema WSA	4.463(5)	9.403(15)	2.834(5)	1.659	36	0.38	(2, 3).

(1) Byström, 1949; (2) Chabre and Pannetier, 1995; (3) commercial CMD for chloride batteries

#### Electrochemical spectroscopy

*Intercalation process:* figure 2 gives the results of the potentiodynamic reduction of the IBA-11 and RMD(RB) samples at -10mV/2h. Using such experimental conditions most  $\gamma$ -MDs used in batteries, after reduction of surface states (peak S at 0.1V vs Hg/HgO), exhibit a two-step process which is assigned to the reduction of ramsdellite blocks upon proton intercalation. These two steps (named A and B) show up as two maxima in the initial and final current values, that is, as maxima of the incremental capacity. They appear at about -50 and -150 mV vs Hg/HgO and have amplitudes of the same order of magnitude (Chabre 1991, Chabre and Pannetier, 1995).

These two steps, A and B, are well observed for sample IBA-11, although step B appears only as a broad shoulder on the low potential side of the A peak. With RMD(RB) the two peaks are also observed but at more reducing potentials, -170 and -330 mV. Initial currents at each potential step are also much lower, although the specific BET area of this MD is larger than that of IBA-11. This behavior indicates a slower kinetics of reduction, that is a slower proton intercalation. It is worth noting that both samples reached a similar reduction level at the potential of the A peak ( $x = 0.37$  and 0.33, respectively). The kinetics of reduction of natural ramsdellite appeared to be even slower. Reduction currents are one order of magnitude lower than for RMD(RB), in the  $\mu A$  range for 20 mg of active material; this explains the noisy aspect of the current curve in fig. 3 (right). In this experiment, starting from an initial open circuit potential (OCV) around 100 mV, the equilibrium OCV after reduction stabilizes at 70 ( $\pm 10$ ) mV.

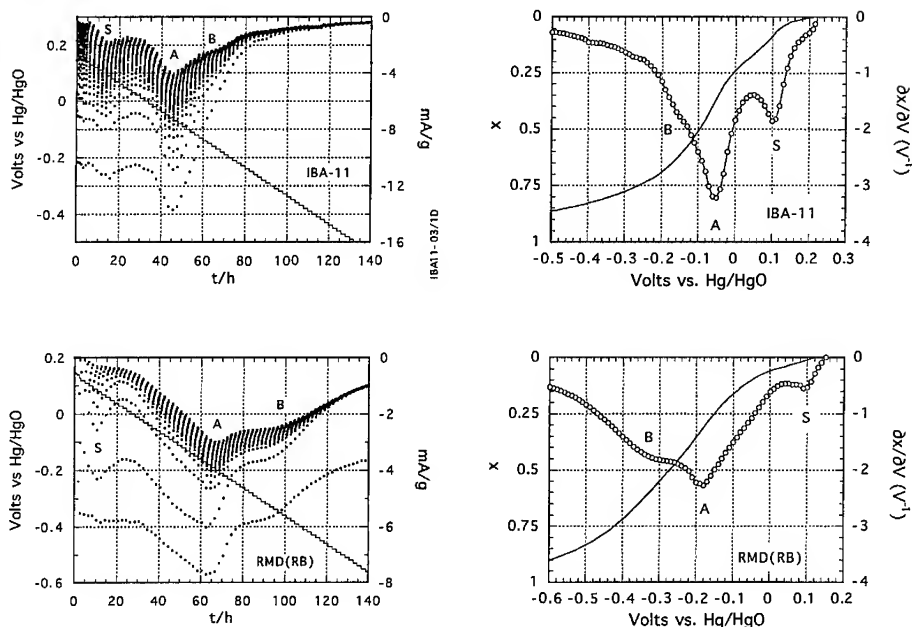


**Fig 2 left:** Chronoamperograms of potentiodynamic reduction with  $-10$  mV/2h steps for IBA-11 (top) and RMD(RB) (bottom). MDs are mixed with 50%w. carbon black in 1M KOH. **right:** Voltamperogram representations of incremental capacity (open dots) and reduction level  $x$ .

*Diffusion coefficient:* in a diffusion controlled intercalation process the initial relative charge increment, after applying a potential step from equilibrium, is a linear function of  $\sqrt{t}$ , with a slope proportional to  $S \cdot D^{1/2}$ ,  $S$  being the specific active surface area and  $D$  the diffusion coefficient. The precision of the diffusion coefficient determination is usually limited since the true active surface is a questionable notion. We previously discussed these points (Chabre and Pannetier, 1995): from determinations of  $S \cdot D^{1/2}$  close to  $5 \cdot 10^{-4} \text{ cm}^3 \cdot \text{s}^{-1/2} \cdot \text{g}^{-1}$  in usual MD samples in the homogeneous domain of ramsdellite reduction and by assuming an active surface area about one order of magnitude lower than the BET area, we concluded that proton diffusion coefficient is in the range  $10^{-15}$  to  $10^{-16} \text{ cm}^2 \cdot \text{s}^{-1}$ . The RMD(RB) sample has the peculiarity that its apparent geometrical surface area is very close to its BET area: assuming a spherical grain size of  $0.1 \mu\text{m}$  gives a geometrical surface area of  $13 \text{ m}^2/\text{g}$ , to be compared with the BET value of  $18.3$ . Thus it is reasonable to consider its BET area as its true geometrical area and, as intercalation is not isotropic but occurs through the **a,b** plane only (that is, along the axis **c** of the tunnels), the active surface should be taken at most as a third of the geometrical one, i.e. about  $6 \text{ m}^2/\text{g}$ . From preliminary measurements on this sample, after a potential step from  $+50$  mV to  $0$  V, we observed that the linear dependance of the charge increment holds for very long time (several hundred hours). This agrees with a one dimensional character of the intercalation and, from a measured  $S \cdot D^{1/2}$  value  $\approx 3.5 \cdot 10^{-4} \text{ cm}^3 \cdot \text{s}^{-1/2} \cdot \text{g}^{-1}$ , one gets a lower limit for the diffusion coefficient,  $D \approx 3.5 \cdot 10^{-17} \text{ cm}^2 \cdot \text{s}^{-1}$ .

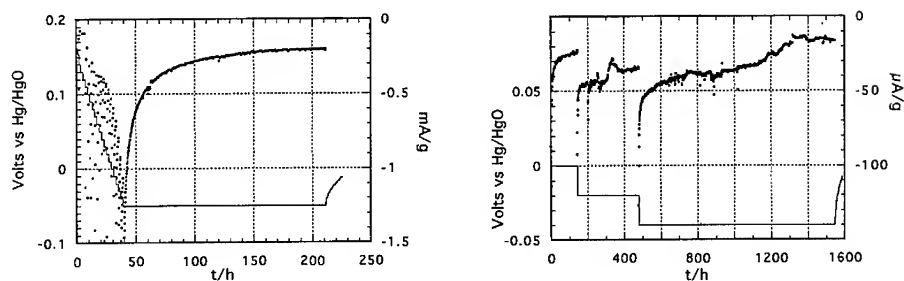


**Fig.3 left:** Chronoamperogram of potentiodynamic reduction with  $-10 \text{ mV}/2\text{h}$  steps down to a final plateau at  $-50 \text{ mV}$ . This protocol was used to prepare a partly reduced RMD(RB) in the (apparently) homogeneous domain of intercalation (final reduction degree  $x = 0.27$ ). **right:** similar protocol for natural ramsdellite, NMD(LV), leading to  $x = 0.17$  after 6 weeks at  $-40 \text{ mV}$ .

#### XRD of reduced samples

The XRD patterns of two reduced RMD(RB) samples are reported in fig 4. The pattern of the partly reduced sample exhibits the same set of lines as the pristine material, but shifted. Refinement of cell parameters (Table III) gives values intermediate between those of ramsdellite and groutellite, in agreement with the reduction degree. The (almost) fully reduced sample gives an apparently different pattern which corresponds to that of  $\alpha\text{-MnOOH}$  and gives cell constants slightly smaller than groutite, as expected from its average reduction degree  $x = 0.94$ .

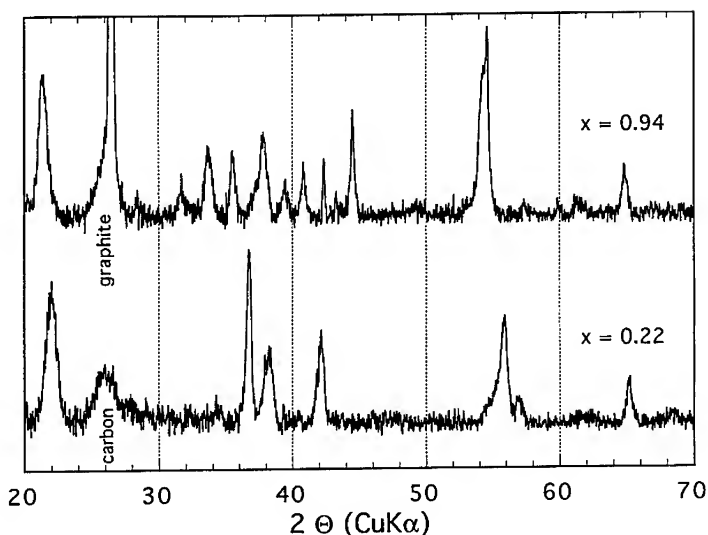
On the contrary the XRD pattern of the partly reduced NMD(LV) ( $x = 0.17$ ) differs very little from that of the pristine material, the main effect being a large asymmetric broadening of line 110 towards low angle. This suggests a limited and non-homogeneous proton intercalation into the sample.

Table III. Lattice parameters of reduced RMD(RB) samples

Reduction degree	$a_T(\text{\AA})$	$b_T(\text{\AA})$	$c_T(\text{\AA})$	$b_T/2c_T$	Volume ( $\text{\AA}^3$ )
0	4.449(2)	9.345(7)	2.847(2)	1.641	118.40
0.27	4.608(25)	9.373(26)	2.859(6)	1.639	123.48
0.94	4.513(6)	10.623(8)	2.872(2)	1.849	137.70
ramsdellite ( $x=0$ )	4.533	9.27	2.866	1.617	120.43
groutellite <sup>1</sup> ( $x=0.5$ )	4.700	9.531	2.8640	1.664	128.29
groutite <sup>2</sup> ( $x=1$ )	4.560	10.700	2.870	1.864	140.03

<sup>1</sup> JCPDS card 42-1316

<sup>2</sup> JCPDS card 24-713



**Fig.4** X-ray diffraction patterns ( $\text{CuK}\alpha$ ) of RMD(RB) at various reduction stages: **a**: partly reduced at  $-50$  mV vs Hg/HgO (reduction degree  $x = 0.27$ ) and **b**: fully reduced using  $-10$  mV/2h SPECS down to  $-0.7$  V vs Hg/HgO ( $x = 0.94$  and an equilibrium OCV of  $-0.310$  V vs Hg/HgO).

## DISCUSSION

The XRD results from reduced RMD(RB) samples are no surprise: the anisotropic expansion of the ramsdellite lattice upon reduction of  $\gamma\text{-MnO}_2$  in protonic media was observed earlier on by Gabano *et al.* (1965). Observation of groutite as the final product of the reduction was also proved long ago (Coeffier and Brenet, 1964; Bell and Huber, 1964). In this respect the specificity of the results presented here is that i) the pristine material was structurally well characterized and shown to exhibit only limited structural disorder, and ii) the electrochemical reduction was accurately controlled, at the potential value estimated for mid-reduction and occurrence of a cooperative Jahn-Teller distortion ( $V(\text{R} \rightarrow \text{G}) = -50$  mV vs Hg/HgO, Chabre and Pannetier, 1995). By identifying the mid reduction product groutellite  $\text{H}_{0.5}\text{MnO}_2$  to the unnamed natural mineral referred to in the JCPDS file (42-1316) and assuming a Vegard's law, the volume expansion of the partly reduced RMD(RB) leads to a  $x$  value close to 0.26 in good agreement with the value  $x = 0.27$  deduced by coulometric titration. This result hints at a homogeneous intercalation process up to mid-reduction, implying a continuous solid solution between ramsdellite and groutite.

However the electrochemical behavior of the RMD(RB) sample does not seem to support this hypothesis. Indeed, in the absence of ordering of an intercalated species, a homogeneous intercalation gives rise to a bell shaped incremental capacity curve (McKinnon and Hearing, 1983, Dahn *et al.*, 1985). In contrast a two phase process generates incremental capacity curves with a linear initial slope, if recorded with regular potential scanning conditions; the intercept of the line at zero current then corresponds to the two phase equilibrium potential (Chabre, 1993).

The data obtained for RMD(RB) clearly show a linear variation of  $dx/dV$  in the potential range 0 to  $-180$  mV (fig. 2). The intercept at null current yields a potential of  $+60$  mV (a value confirmed by other experiments currently in progress with the same compound at different scanning rate). It is worth noting that, although its curve is linear over a shorter potential range only, the initial slope of the A peak for IBA-11 also extrapolates to  $60$  mV for zero current. Likewise the equilibrium OCV observed for partly reduced natural ramsdellite is in this potential range.

The apparent difference in behavior of a same sample when examined by XRD and electrochemical techniques shows, as discussed by Chabre and Pannetier (1995), the importance of close or far-from-equilibrium conditions. XRD data were recorded after the sample had been allowed to intercalate slowly (the reduction current corresponded to a galvanostatic  $C/15000$  rate when it was interrupted) and to equilibrate in OCV for two weeks, whereas the voltamperograms, in the range of the linear slope, were obtained in less than 40 hours. The value  $+60$  mV is thus assigned to the equilibrium potential of pristine ramsdellite.

As IBA-11 and RMD(RB) apparently exhibit the same content of structural defects  $T_w$  and  $P_r$  (Table II), one expects them to behave similarly. However, they differ largely in their macroscopic kinetic behavior during reduction: fig. 2 shows that IBA-11, although it is made of coarser grains, reduces faster than RMD(RB). Careful examination of the XRD patterns of IBA-11 and RMD(RB) reveals that, although rather similar, they do exhibit a few subtle differences. Reflections 110 and 130 in IBA-11 pattern are fairly symmetrical with line widths in agreement with the values calculated for a true random stacking of the ramsdellite and pyrolusite layers in the structure of  $\gamma\text{-MnO}_2$ . In contrast the same lines in the pattern of RMD(RB) appear to be narrower but with asymmetric tails in between them (fig. 1)<sup>2</sup>. In addition, line 110 clearly exhibits on its low angle side a shoulder which is not visible in IBA-11 pattern and actually does not show up in most MD patterns. These observations suggest that the random model we developed to analyze the XRD patterns of MDs may not apply to RMD(RB). Preliminary additional simulations (based on the same model but varying the junction probability  $P_{r,r}$  which defines the probability of a pyrolusite layer  $r$  following another layer  $r$ ) hint that, although IBA-11 and RMD(RB) exhibit an similar average content of De Wolff disorder ( $P_r \approx 0.32$ ), the distribution of these defects into the lattice is different in the two samples. They are randomly distributed in IBA-11 but tend both to cluster in some parts of RMD(RB) and to get isolated in others. In the former case, individual ramsdellite and pyrolusite domains are larger in RMD(RB) than they are in IBA-11, a conclusion which could account for the different kinetic behavior of the two samples. Sample inhomogeneity is further supported by the asymmetry of lines 110 and 130 in the pattern of RMD(RB) which cannot be explained by a non-random sequence of ramsdellite and rutile layers only.

## CONCLUSION

Proton intercalation within the ramsdellite units of  $\gamma$ -MDs containing a limited amount of structural defects proceeds as observed previously with more faulted samples. Sample equilibration is very slow and, in the short time limit, reduction is seen as a two-phase process. The equilibrium potential of ramsdellite is found to be about  $+60$  mV vs  $\text{Hg/HgO}$ . After equilibration, samples with reduction degree less than 0.5 appear as a solid solution  $\text{MnO}_2\text{H}_x$  between ramsdellite and groutellite  $\text{MnO}_2\text{H}_{0.5}$ .

<sup>2</sup> Line 021 which is not affected by De Wolff disorder has the same width in the two patterns.

The macroscopic kinetics of the process appears to be very sensitive not only to the defect concentration, but also to their distribution within the structure as observed for sample RMD(RB).

Thus a precise determination of the diffusion coefficient of the proton in the solid solution range remains a challenge. Assuming the active surface area to be a tenth of the BET area, we previously reported values in the  $10^{-15}$  to  $10^{-16}$   $\text{cm}^2\text{s}^{-1}$  range for usual  $\gamma$ -MDs. The results presented in this paper tend to show that it is significantly lower, in the  $10^{-16}$  to  $10^{-17}$   $\text{cm}^2\text{s}^{-1}$  range, which explains the extreme difficulty to electrochemically reduce natural crystalline ramsdellite.

## ACKNOWLEDGEMENTS

We are grateful to B. Zachau-Christiansen (TU of Denmark, Lyngby) and to J.C. Rousche and R. Baldin from Sedema, for providing natural and ramsdellite like samples. Thanks are also due to M. Anne and P. Bordet (CNRS Grenoble) for XRD facilities.

## REFERENCES

- Antoniadis A., Berruyer J. and Filhol A. (1990) *Acta Cryst.*, **A46**, 692-711.
- Atlung S. (1975) *Proceedings of the Manganese Dioxide Symposium*, Cleveland, A. Kozawa and R.J. Brodd, eds., p. 47, I.C. Sample Office, Cleveland section of the Electrochem. Soc.
- Baur W. H. (1976) *Acta Cryst.*, **32**, 2200
- Bell G. S. and Huber R. (1964) *J. Electrochem. Soc.*, **111**, 1
- Brenet J.P., Malessan J. and Grund A. (1956) *C.R. Acad. Sci. Paris*, **242**, 111.
- Brouillet P., Grund A., Jolas F. and Mellet R. (1963) *C. R. Acad. Sc. Paris*, **257**, 3390
- Byström A.M. (1949) *Acta Chem. Scand.*, **3**, 163
- Chabre Y. (1991) *J. Electrochem. Soc.*, **138**, 329
- Chabre Y. (1993) *NATO ASI Series*, **B305**, 181
- Chabre Y. and Ripert M. (1991) *Mat. Res. Soc. Symp. Proc.*, **210**, 367
- Chabre Y. and Pannetier J. (1995) *Progress Solid State Chem.*, Vol. 23, No 1
- Coeffier G. and Brenet J. (1964) *Bull. Soc. Chim. France*, **11**, 2835
- Dahn J.R., Mc. Kinnon W.R. and Coleman S.T., 1985, *Phys Rev. B*, **33**, 5214
- De Wolff P.M. (1959) *Acta Crystallogr.*, **12**, 341
- Feitknecht W., Ostwald H. R. and Feitknecht-Steinmann U. (1960) *Helv. Chim. Acta*, **232**, 1947
- Gabano J.P., Morignat B., Fialdes E., Emery B. and Laurent J.F. (1965) *Z. Physik. Chem. Neue Folge*, **46**, 359
- Glover D., Schumm Jr. B. and Kozawa K., eds., 1989, *Handbook of Manganese Dioxide* IBA -JEC Press Inc,
- Kozawa A. and Powers R. (1966) *J. Electrochem. Soc.*, **113**, 870
- Maskell W.C., Shaw J.E.A. and Tye F.L. (1981) *Electrochim. Acta*, **26**, 1403; (1982a) *J. Appl. Electrochem.*, **12**, 101; (1982b) *J. Power Sources*, **8**, 113; (1983) *Electrochim. Acta*, **28**, 225 & 231
- McKinnon W.R. and Hearing R.R. (1983) in *Modern Aspects of Electrochemistry*, R.E. White, J.O. Bockris and B.E. Conway, eds., **15**, 235, Plenum Press, New York.
- Mouget C. and Chabre Y. (1991) Multichannel potentiostatic and galvanostatic system MacPile, licensed from CNRS and UJF Grenoble to Bio-Logic Corp., 1 Avenue de l'Europe, F-38640 Claix
- Pannetier J. (1992) *Progress in Batteries & Battery Materials*, **11**, 51, ITE-JEC Press Inc
- Pannetier J. (1994) *Progress in Batteries & Battery Materials*, **13**, 132, ITE-JEC Press Inc,
- Ripert M., Pannetier J., Chabre Y. and Poinçon C. (1991) *Mat. Res. Soc. Symp. Proceed. Series*, **210**, 359
- Rodriguez-Carvajal R. (1990) "FULLPROF: A Program for Rietveld Refinement and Pattern Matching Analysis", Satellite Meeting on Powder Diffraction of the XV Congress of the IUCr, p. 127, Toulouse, France
- Thompson A.H. (1979) *J. Electrochem. Soc.*, **126**, 603
- Turner S. and Buseck P.R. (1983) *Nature*, **304**, 143

## DISSOLUTION-RECRYSTALLIZATION PROCESSES OF NICKEL HYDROXIDE, THE ACTIVE MATERIAL OF THE Ni/Cd AND Ni/H<sub>2</sub> CELLS

A. DELAHAYE-VIDAL\*, N. SAC-EPEE\*, F. PORTEMER\*, B. BEAUDOIN\*,  
M. FIGLARZ\* and T. JAMIN\*\*

\*Laboratoire de Réactivité et de Chimie des Solides, URA CNRS 1211, 33 rue Saint-Leu,  
F-80039 Amiens Cedex, France

\*\*Centre National d'Etudes Spatiales (CNES), 18 Avenue Edouard Belin, F-31055 Toulouse  
Cedex, France

### ABSTRACT

Several examples of dissolution-recrystallization processes at the nickel hydroxide electrode are reviewed. Some of them are very well known and have been studied for a few years in the case of Ni/Cd cells. The cycling of the  $\alpha$ -type nickel hydroxide leads to the  $\alpha \rightarrow \beta$  transformation through dissolution of the  $\alpha$  phase in the electrolyte (KOH) and recrystallization of the  $\beta$  phase from the solution. Further cycling of the resulting  $\beta \rightarrow \alpha$  phase causes an ageing effect which occurs via the solution (Oswald ripening). More recently, a strong ripening phenomenon has been observed by studying the behavior of nickel hydroxides cycling in Ni/H<sub>2</sub> cells. By simulating the ageing of charged and discharged materials under hydrogen pressure in KOH media, it has been shown that in the absence of voltage, hydrogen cannot be responsible for the strong ripening effect. Synergetic effects between hydrogen and voltage have to be considered.

### INTRODUCTION

Nickel (II) hydroxides and their oxidation products constitute the active material of the positive electrode of Ni/H<sub>2</sub> and Ni/Cd alkaline cells. During cycling of these cells, two types of reactions may occur between the different phases involved at the positive electrode. The first one concerns the redox reactions which occur between the charged and discharged active material. It has been shown that these reactions take place in the solid state [1,2]. The other one involves mechanisms of dissolution-nucleation-growth of solid active material in the electrolyte [2,3]. The aim of this paper is to emphasize the role of these latter on the structural and textural changes at the positive plate during cycling or storage of the cells. The different phases which can be involved at the nickel hydroxide electrode are well described in the diagram of the figure 1. Initially proposed by Bode [4], this diagram has been improved from structural investigations [5-10]. The  $\alpha$ (II) and  $\beta$ (II) phases may be present at the positive electrode when the battery is in discharged state. The  $\beta$ (II) phase crystallizes in the hexagonal system with the brucite structural type. The definite structure determination has been made by Greaves and Thomas [11] with powder neutron diffraction.  $\beta$ (II) has a lamellar structure that can be simply described as Ni(OH)<sub>2</sub> layers stacked along the *c*-axis. These layers consist of hexagonal planar arrangements of Ni (II) ions with an octahedral coordination of oxygens, three oxygens lying above the nickel plane, three oxygens lying below. The interlamellar distance is 4.6Å. Contrary to the  $\beta$  phase, the  $\alpha$ (II) phase is poorly crystallized making its characterization rather difficult. It has already been shown for many years that such a phase consists of Ni(OH)<sub>2</sub> type layers stacked along the *c*-axis as in the  $\beta$ (II) phase. However, these layers are completely misoriented in relation with each other leading to a turbostratic structure. Water molecules are inserted between two consecutive layers. This model has been recently improved [9]. It has been clearly evidenced that anionic species are present in such  $\alpha$ -type phases. The anionic species can be nitrate, carbonate, sulfate or organic ions depending on the method of preparation. In order to compensate for the positive charge excess due to these species, hydroxyl vacancies have to be considered in the Ni(OH)<sub>2</sub> type layers. The presence of such vacancies is not really surprising in view of the very high divided state of the  $\alpha$  phases, evidenced by X-ray diffraction (XRD) and transmission electron microscopy (TEM)



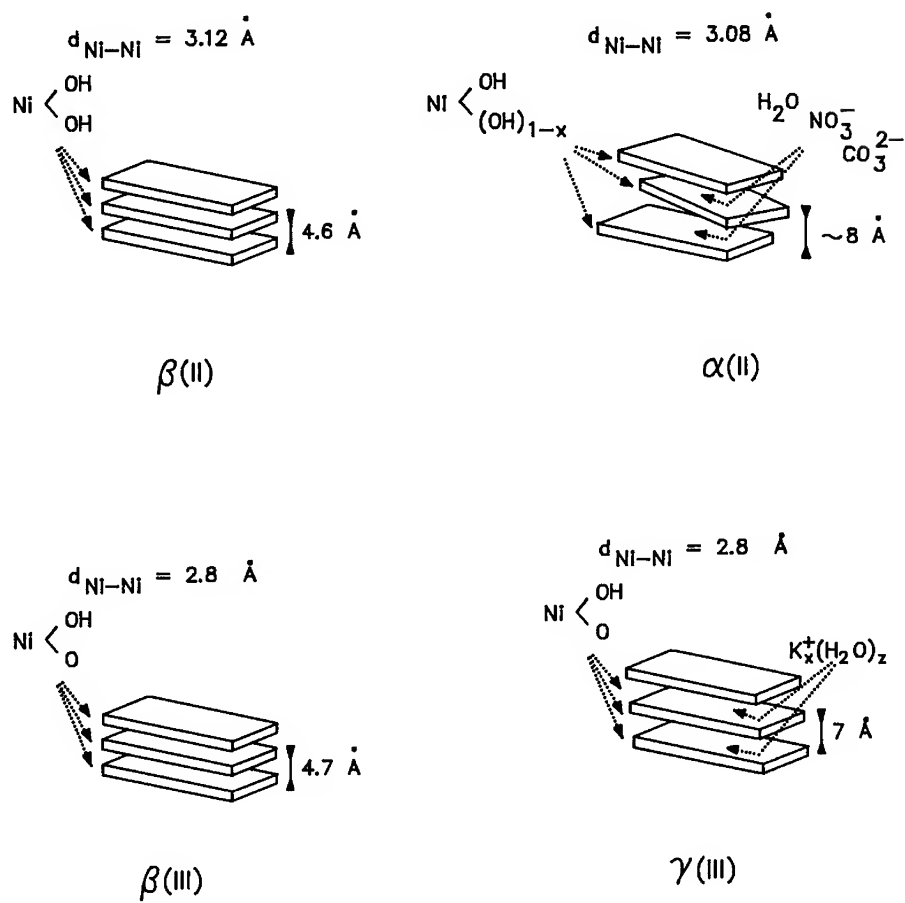


Figure 1 : Various structural types of the positive active material in the Ni/Cd and Ni/H<sub>2</sub> cells.

studies. Each plane behaves almost independently and may be regarded as a surface plane where non-stoichiometry is expected to occur. The oxidation of both the  $\alpha(\text{II})$  and  $\beta(\text{II})$  phases during the charge of the battery leads to nickel oxyhydroxides that can be  $\beta(\text{III})$  or  $\gamma(\text{III})$  (Fig. 1). The  $\beta(\text{III})$  phase has a nickel degree of oxidation which varies between 3 and 3.3 indicating that some nickel tetravalent ions are present in this phase. The structure of the  $\beta(\text{III})$  phase has never been solved but it can be regarded as deriving from that of  $\beta(\text{II})$  by direct removing of one proton and one electron. In fact, due to the small 4.7 Å intersheet distance, accommodation of electrostatic repulsions of adjacent oxygen planes is rather difficult to achieve. It is probably one of the reasons why the X-ray diffraction pattern of the  $\beta(\text{III})$  phase shows very broad lines. The  $\gamma(\text{III})$  phase has a larger intersheet distance than the  $\beta(\text{III})$  one. Hence, the accommodation of electrostatic repulsion is easier. In addition, alkaline ions in substitution for protons are located between the slabs with water molecules. The presence of such interlamellar species allows the structure to be stabilized.

In this system, schematically described in the figure 1, three examples of dissolution-recrystallization-processes will be reviewed. Among these three processes, two are already known because studied for a few years in the case of the Ni/Cd cells [2,3]. They are related to the  $\alpha \rightarrow \beta$  transformation and the ripening of the  $\beta(\text{II})$  phase. The last example concerns recent results related to the cycling of Ni/H<sub>2</sub> battery for spacecraft application.

## **I. $\alpha \rightarrow \beta$ TRANSFORMATION**

It is a well known fact that the  $\alpha$  nickel hydroxides are not stable in aqueous medium or KOH solutions and are converted into the  $\beta$  nickel hydroxide. Based on pure geometrical considerations, the reaction could be supposed to occur in the solid state with rotation and reorientation of the sheets while interlamellar species are removed from the Van der Waals space. From XRD and TEM studies, it has been shown that the  $\alpha \rightarrow \beta$  transformation occurs via the solution [3]. This result was obtained by studying the ageing in water of an  $\alpha$ -type phase prepared by chemical precipitation from a nitrate nickel solution with ammonia. The better evidence for a mechanism occurring via the solution was given by the TEM study. As shown in figure 2, the bright field images of samples removed during the course of the reaction clearly indicate that the ageing of  $\alpha$  phase in water produces important morphological modifications. The starting material consists of crumpled films as often observed for turbostratic phase whilst the final product shows monocrystalline large platelets with Bragg contours.

These observations prove that the reaction is biphasic and cannot proceed in the solid state. On the contrary, the reaction occurs via the solution involving the two following steps :

- dissolution of the  $\alpha$  phase
- nucleation and growth of the  $\beta$  phase from the solution.

A quite similar mechanism is involved when ageing is performed in alkaline solution instead of water. However, in alkaline medium the nucleation step is predominant in comparison with the growth step contrary to the situation in water. It results in the formation of smaller  $\beta$  platelets in KOH than in water. The knowledge of the  $\alpha \rightarrow \beta$  transformation mechanism allows to better understand the behavior of the nickel hydroxide electrode. For instance, during cycling of  $\alpha$ -type phases, anionic species such as nitrate or carbonate initially inserted in the Van der Waals space of the  $\alpha$  phase go towards the solution during the  $\alpha \rightarrow \beta$  transformation. This process may damage the cell because carbonates and nitrates are poisons for the negative electrode. It is then recommended to promote the  $\alpha \rightarrow \beta$  ageing before cycling when  $\alpha$ -type starting material have to be used for Ni/Cd or Ni/H<sub>2</sub> applications. This is generally done by electrochemical or chemical "cleaning" in KOH solutions.

## **II. OSWALD RIPENING OF THE $\beta$ PHASE**

The  $\beta(\text{II})$  phase is obtained with various textural features depending on the experimental preparation procedure. The most often observed morphology is platelets, which can show

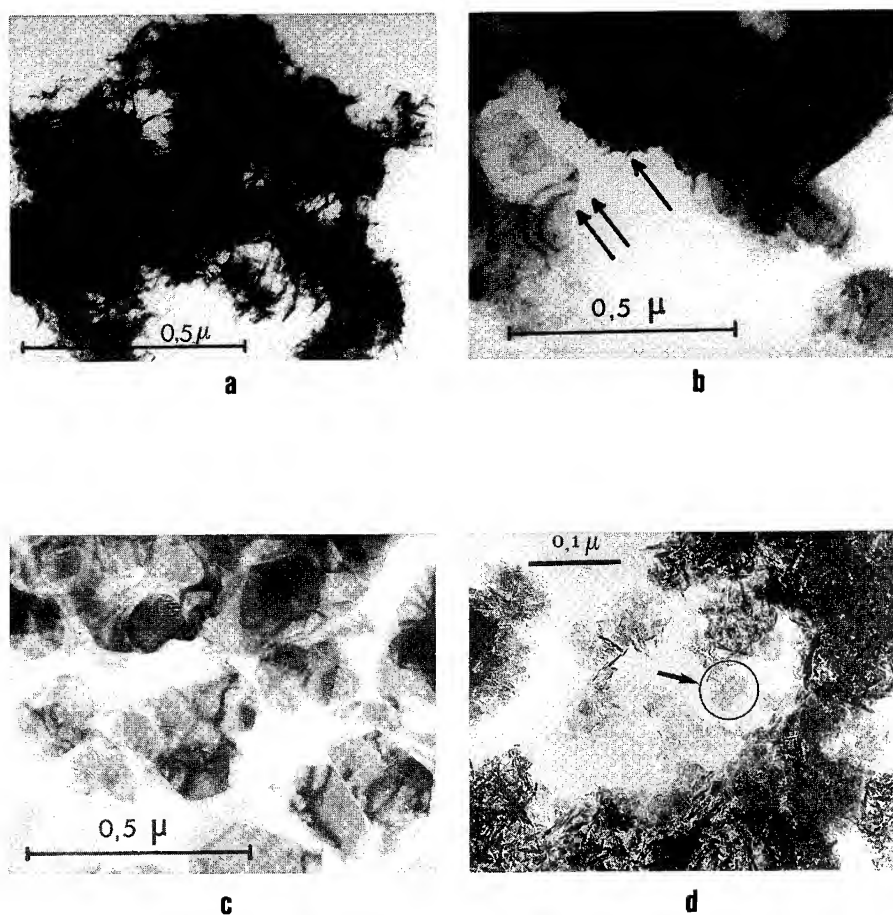
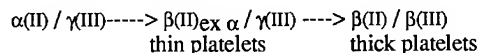


Figure 2 : TEM study of the  $\alpha \rightarrow \beta$  transformation occurring by ageing of  $\alpha$  in water or KOH solution : a) starting  $\alpha$  nickel hydroxide, b) sample removed during the course of the transformation in water : mixture of  $\alpha$  and  $\beta$  particles, c)  $\beta$   $\text{Ni}(\text{OH})_2$  platelets obtained at the end of the transformation in water, d)  $\beta$   $\text{Ni}(\text{OH})_2$  platelets obtained by ageing of  $\alpha$  in KOH solution.

different sizes (diameter in the range 100Å -5000Å and thickness in the range 50Å-500Å). The  $\beta(\text{II})$  hydroxide prepared by ageing of the  $\alpha$  phase in KOH solution (denoted as  $\beta_{\text{ex}\alpha}$ ) consist of very small and thin platelets (see section I). When this type of sample is subjected to cycling in KOH electrolytes, the thickness of the platelets is found to increase during the first cycles. Indeed, the comparison of the XRD patterns after one cycle and after five cycles clearly indicates that a narrowing of the 00l lines occurs (Fig. 3). This means that the number of  $\text{Ni}(\text{OH})_2$  layers in the  $[001]^*$  direction, *i.e.* the thickness of the  $\beta$  platelets, increases with cycling. The growth of the platelets in the  $[001]^*$  direction may be interpreted as Oswald ripening [12]. The thinnest particles dissolve in the solution whereas the thickest ones become thicker and thicker from the solution. It must be pointed out that such a ripening effect can induce a structural change of the active material during cycling with subsequent effects on the electrochemical performances of the battery. When the starting material is prepared by ageing of  $\alpha$ -type phase in electrolyte, two modes of oxidation compete for the resulting  $\beta_{\text{ex}} \alpha$  phase:

- (1)  $\beta(\text{II})_{\text{ex}} \alpha$  ( $c=4.6 \text{ \AA}$ )  $\rightarrow \gamma(\text{III})$  ( $c=7.0 \text{ \AA}$ )
- (2)  $\beta(\text{II})_{\text{ex}} \alpha$  ( $c=4.6 \text{ \AA}$ )  $\rightarrow \beta(\text{III})$  ( $c=4.7 \text{ \AA}$ )

Due to the large difference between the interlamellar distances of the  $\gamma(\text{III})$  and  $\beta(\text{III})$  phases, reaction (1) induces more strains than reaction (2). The strains are easily relaxed if the number of the involved hydroxide layers is small, *i.e.* the platelets are thin. For thicker platelets, the strains are no longer tolerable and then reaction (2) is favoured. This is the reason why the following sequence is observed during the cycling of  $\alpha$ -type phase in 4.5 KOH electrolytes [2] :



As the  $\gamma(\text{III})$  phase shows a higher degree of oxidation of nickel than the  $\beta(\text{III})$  phase, the shift from  $\beta(\text{II}) / \gamma(\text{III})$  to  $\beta(\text{II}) / \beta(\text{III})$  induces a decrease of the number of exchanged electrons *i.e.* a fall in capacity.

### III. RECRYSTALLIZATION OF THE $\beta(\text{II})$ PHASE IN $\text{Ni}/\text{H}_2$ CELLS

$\text{Ni}/\text{H}_2$  cells used in spacecraft are known to exhibit specific problems due to the interaction of hydrogen with the positive nickel hydroxide electrode : high self discharge rate, swelling in long life cycling, residual capacity at low voltages. The effects of storage conditions in  $\text{Ni}/\text{H}_2$  cells have been investigated by several authors [13-16]. The results emphasize that considerable care is necessary in handling  $\text{Ni}/\text{H}_2$  cells. A. H. Zimmerman has clearly described a number of processes resulting from the interaction of hydrogen with the nickel hydroxide electrode: segregation of cobalt additives initiated at low voltages and catalytic interaction of hydrogen with the sintered nickel matrix leading to the self discharge of the active material [17]. However, the effects of cycling under hydrogen pressure on the structural and textural characteristics of the active material of the positive electrode are not very well known. A study was undertaken in our laboratory in order to better understand the ageing of such cells from a structural and textural point of view.

From XRD and TEM studies of positive electrodes at various stages of cycling in the discharged state, a recrystallization process has been clearly evidenced. Cycling was performed by using standard  $\text{Ni}/\text{H}_2$  SAFT cells for GEO spacecraft applications. The starting uncycled active material is obtained by electrochemical impregnation of porous nickel sintered plates at 80°C. The electrodeposited phase corresponds to a crystallized nickel hydroxynitrate (HN) [18] that is converted into  $\beta(\text{II})$  phase in KOH solution as the  $\alpha$  phase. The active material recovered after ageing in KOH is denoted as  $\beta_{\text{ex}} \text{HN}$ . Before cycling, the  $\beta_{\text{ex}} \text{HN}$  phase shows very broad

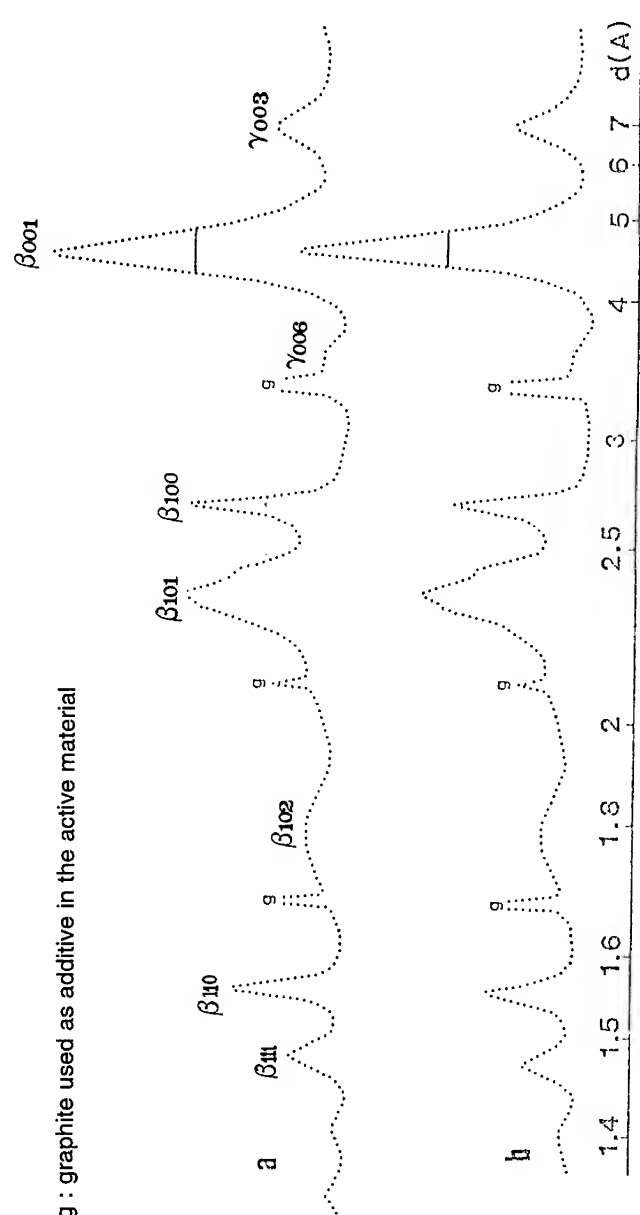


Figure 3 : XRD patterns of  $\beta_{ex\alpha}$  with small amount of  $\gamma(III)$ , obtained after a) 1 cycle, b) 5 cycles.

peaks (Fig. 4a). After 10 and 1000 cycles (Fig. 4c and 4d), a narrowing of the lines is observed. Table 1 allows the comparison of the crystallite size during cycling, calculated in the [100]\* direction by the Williamson and Hall's method [19]. A diminution is first noticed after 5 cycles but from 5 to 1000 cycles, the crystallite size slightly increases. The TEM study gives additional information: the platelet diameters of the uncycled active material does not exceed 200 Å and the dispersion is very difficult to achieve because of the high surface energy of the particles (Fig. 5a). After 5 cycles, the same morphology is observed (Fig. 5b) but the dispersion is easier. After 10 cycles, the diameter of platelets is found to be twice larger than that of the starting material (Fig. 5c and Table 2). Finally, after 1000 cycles, there is no doubt that the platelets have grown during cycling.

number of cycles	0	5	10	1000
crystallite size in the [100]* direction	125Å	90Å	120Å	150Å

Table I: Crystallite size of the positive discharged active material for different number of cycles.

number of cycles	0	5	10	1000
average diameter of the platelets	<200Å	200Å	400Å	570Å

Table II: Average diameter of the platelets characterizing the positive discharged active material for different numbers of cycles.

From the increase of the platelet diameter in cycling, it may be concluded that a strong ripening of the  $\beta_{\text{ex}}$  HN phase occurs in cycling. The slight decrease in the crystallite size noticed during the five first cycles can be explained by the change from a monolithic to a mosaic texture. This means that each uncycled  $\beta_{\text{ex}}$  HN platelet is made of one coherent diffraction domain whilst, after cycling, each one contains several crystallites slightly misoriented (Fig. 6).

Such phenomenon has been previously described in the case of Ni/Cd cells [1]. A model based on the pseudomorphous and topotactic characters of the redox reactions was used to explain the formation of the mosaic texture. The redox reactions which take place in the solid state by oriented growth of  $\beta(\text{II})$  or  $\gamma(\text{III})$  or  $\beta(\text{I})$  induce strains within the particles; they are due to the large difference in the nickel-nickel distances in both the oxidized and reduced phases. Strain relaxation brings about the formation of the mosaic structure during the first cycle. In the Ni/Cd cells, the mosaic texture is retained after the first cycle and no further textural change is noticed in long life cycling. In the case of Ni/H<sub>2</sub> cells, the mosaic texture is also retained in cycling. Indeed, the  $\beta(\text{II})$  phase recovered after 5, 10 and 1000 cycles always shows a number of crystallites smaller than the diameter of particles (see Tables I and II). However, as shown by the increase of the particle diameters, a dissolution-recrystallization process is also involved, which seems to characterize this type of cells. Hydrogen must have a strong influence.

In order to separate the effect of ageing in KOH under hydrogen pressure from that of applying a voltage in redox cycling, the behavior of various nickel hydroxides and oxyhydroxides was simulated in KOH solutions or in water medium under hydrogen pressure. For this purpose, samples of  $\beta(\text{II})$ ,  $\beta(\text{III})$  and  $\gamma(\text{III})$  phases with various morphologies were subjected to ageing in water or in KOH with sodium borohydride. In such conditions, reduction of water by sodium borohydride allows hydrogen at a pressure of about 20-30 bars to be evolved [20]. Other experiments were carried out by introducing the samples into a closed vessel with water or diluted KOH under hydrogen pressure.

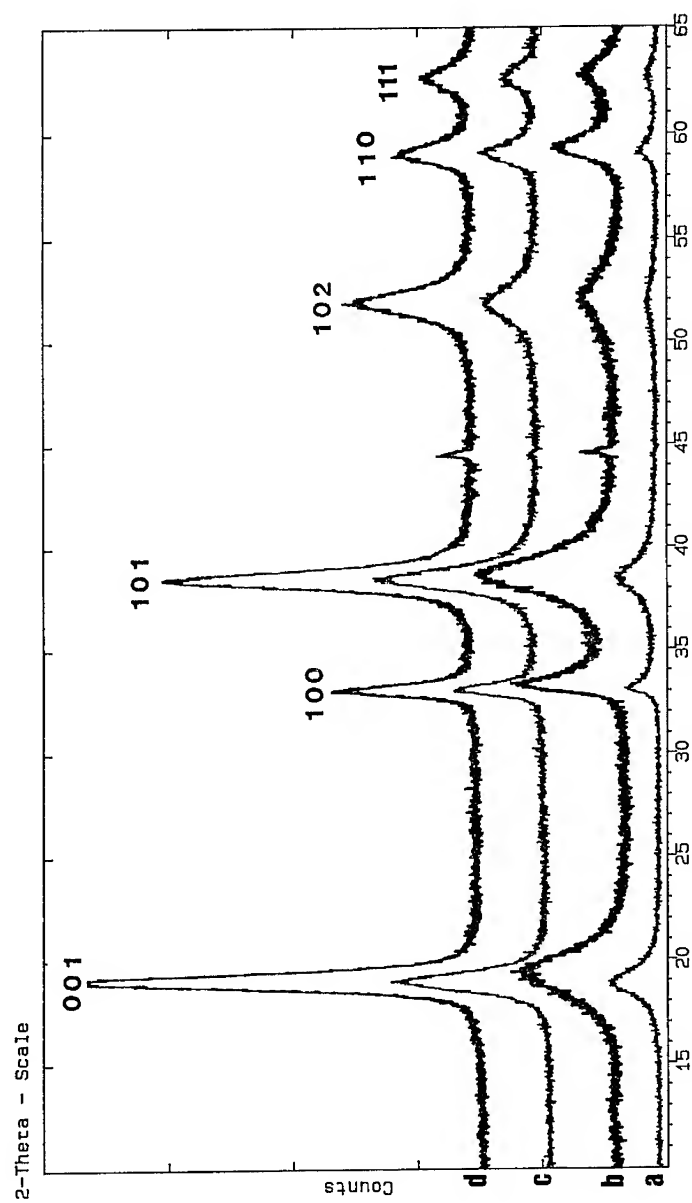
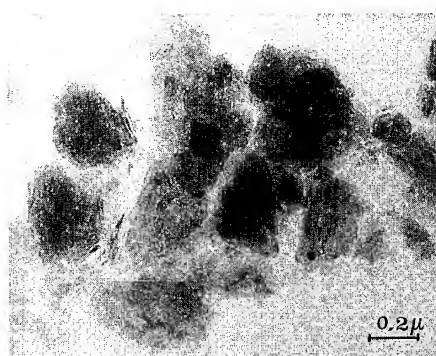
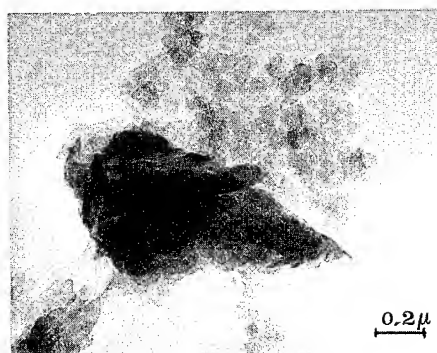


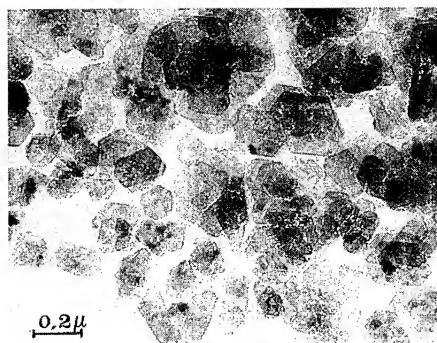
Figure 4 : XRD patterns of nickel hydroxides obtained : a) after electrochemical impregnation  $\beta_{exHN}$ , b) after 5 cycles, c) after 10 cycles, d) after 1000 cycles.



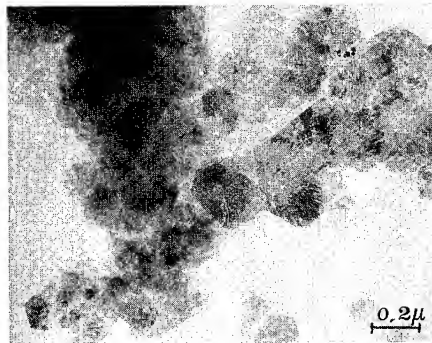
**a**



**b**



**c**



**d**

Figure 5 : TEM study of nickel hydroxides obtained : a) after electrochemical impregnation  $\beta_{\text{exHN}}$ , b) after 5 cycles, c) after 10 cycles, d) after 1000 cycles.



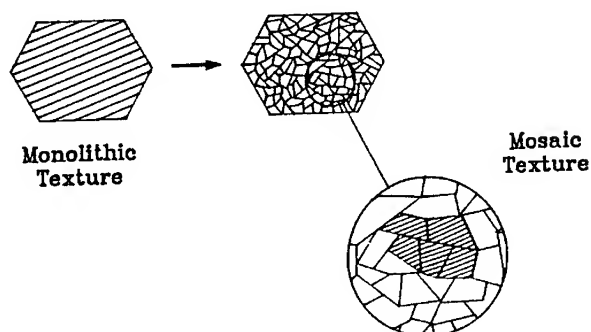


Figure 6 : Textural modifications occurring during the first cycle of  $\beta$  Ni(OH)<sub>2</sub>.

The preliminary results of the experiments simulating ageing in electrolytes under hydrogen pressure can be summarized as follows. Direct reduction into  $\beta$ (II) by hydrogen takes place for the  $\beta$ (III) and  $\gamma$ (III) phases. All  $\beta$ (II) samples are stable in water under hydrogen pressure. In KOH solutions, only a slight ripening in the [001]\* direction is observed for the thin  $\beta_{ex}$   $\alpha$  platelets (Oswald ripening described in section II). Above a critical value of the thickness of the platelets, no textural change occurs. These results indicate that synergetic effects between hydrogen pressure and voltage are certainly responsible for the large increase in the diameter of the particles observed for cycled positive  $\beta$ (II) materials. Further studies are now in progress to clarify the mechanism explaining the behavior of  $\beta_{ex}$  HN materials subjected to both hydrogen pressure and voltage cycles in KOH solutions.

The authors thank the Centre National d'Etudes Spatiales who sponsored this study and the SAFT for permission to publish this work.

#### References:

- [1] A. Delahaye-Vidal, B. Beaudoin and M. Figlarz, *React. Solids*, **2**, 223 (1986)
- [2] A. Delahaye-Vidal and M. Figlarz, *J. Appl. Electrochem.*, **17**, 589 (1987)
- [3] S. Le Bihan and M. Figlarz, *J. Cryst. Growth*, **13/14**, 458 (1972)
- [4] H. Bode, K. Dehmelt and J. Witte, *Electrochim. Acta*, **11**, 1079 (1966)
- [5] S. le Bihan J. Guenot and M. Figlarz, *C. R. Acad. Sci.*, **C 270**, 2131 (1970)
- [6] R. S. Mc Ewen, *J. Phys. Chem.*, **75**, 1782 (1971)
- [7] P. Oliva, J. Leonardi, J. F. Laurent, C. Delmas, J.J. Braconnier, M. Figlarz, F. Fievet and A. de Guibert, *J. Power Sources*, **8**, 229 (1982)
- [8] C. Delmas, Y. Borthemieu, C. Faure, A. Delahaye-Vidal and M. Figlarz, *Solid State*

- Ionics, **32/33**, 104 (1989)
- [9] P. Genin, A. Delahaye-Vidal, F. Portemer, K. Tekaia-Elhsissen and M. Figlarz, Eur. J. Solid State Inorg. Chem., **28**, 505 (1991)
- [10] J. Mc Breen, in Proceeding "Nickel hydroxide electrode", D. A. Corrigan and A. H. Zimmerman Eds, p.61, The Electrochemical Society Inc., Pennington, N. J. 1990
- [11] C. Greaves, M. A. Thomas, Acta Cryst. , **B42**, 51 (1986)
- [12] W. Oswald, Z. Phys. Chem., **34**, 495 (1900)
- [13] H.S. Lim and R. E. Doty, J. Power Sources, **50**, 57 (1994)
- [14] M. S. Suresh and A. Subrahmanyam, J. Power Sources, **50**, 383 (1994)
- [15] S. Aravamuthan, C. V. Annamma, N. R. Pillai and M. J. Nair, J. Power Sources, **50**, 81 (1994)
- [16] H. Vaidyanathan, NASA Aerospace Battery Workshop, p.247 (1992)
- [17] A. H. Zimmerman, in Proceeding "Nickel hydroxide electrode", D. A. Corrigan and A. H. Zimmerman Eds, p.311, The Electrochemical Society Inc., Pennington, N. J. 1990
- [18] F. Portemer, A. Delahaye-Vidal and M. Figlarz, J. Electrochem., **139** (3), 672 (1992)
- [19] G. K. Williamson and W. H. Hall, Acta Metall., **1**, p.22 (1953)
- [20] D. W. Murphy, S. M. Zahurak and B. Vyas et al., Chem. Mater., **5**, 767 (1993)

## EFFECT OF THE HEAT TREATMENT ON THE LITHIUM INSERTION PROCESS IN $\text{MoO}_3$

B. YEBKA AND C. JULIEN

Laboratoire de Physique des Solides, associé au CNRS, Université Pierre et Marie Curie  
4 place Jussieu, 75252 Paris Cedex 05, France.

### ABSTRACT

We have studied the electrochemical characteristics of  $\text{Li}/\text{MoO}_3$ -based batteries in relation with the morphology of the cathode-active material. The oxides and oxide-hydrates of molybdenum have been prepared with various degrees of heat treatment. The samples were characterized by X-ray diffraction, Raman spectroscopy, and conductivity measurements. The effect of the heat treatment on structural, optical and electrochemical properties are presented in this work. Thermodynamics and kinetics of lithium insertion were studied in  $\text{MoO}_3$  cathodes. Diffusion coefficients and enhancement factors were calculated as functions of the degree of lithium intercalation in the domain of the galvanic cell reversibility.

### 1. INTRODUCTION

Transition-metal oxides exhibiting topotactic insertion/extraction of lithium are of considerable interest. A variety of molybdenum oxides has been noted recently as active materials in secondary thin-film lithium batteries [1] and electrochromic devices [2]. The oxides and oxide-hydrates of molybdenum in its highest oxidation state display a variety of structural types involving linked  $\text{MoO}_6$  octahedra.  $\text{MoO}_3$  is such a host. Of the anhydrous  $\text{MoO}_3$ , the well-known orthorhombic form ( $\alpha$ - $\text{MoO}_3$ ) is the stable form at room temperature and possesses a layered structure [3]. Among the three stoichiometric solid hydrates of  $\text{MoO}_3$  or "molybdic acids", white  $\text{MoO}_3 \cdot \text{H}_2\text{O}$  has a structure closely related to that  $\alpha$ - $\text{MoO}_3$  [4], consisting of isolated double chains of edge-sharing  $\text{MoO}_6$  octahedra with each molybdenum atom bearing a coordinated water molecule.

Several studies have shown that  $\text{Li}^+$  ions can be reversibly incorporated in Mo-O compounds [5-13]. The  $\text{Li}/\text{MoO}_3$  system undergoes redox reactions with high reversibility, accommodating up to 1.5 Li per Mo atom and giving rise to a theoretical energy density of  $745 \text{ W h kg}^{-1}$  whereas the theoretical energy density of  $\text{MoO}_{2.765}$  ( $\sim 490 \text{ W h kg}^{-1}$ ) is comparable to that reported for  $\text{TiS}_2$ . Despite the apparent diversity of the structural types shown by the Mo(VI) oxides and molybdenum-oxide hydrates, it is evident that they possess a number of common features in their reactions with lithium.

The aim of this work is the comparison between the electrochemical features of the molybdenum-oxide hydrates with different degrees of dehydration. First, we report the structural and electrical characteristics of the compounds and then, electrochemical properties of oxide-hydrates of molybdenum and  $\alpha$ - $\text{MoO}_3$  are presented. Thermodynamics and kinetics of lithium-ion insertion in these host lattices are investigated and discussed in terms of a simple insertion model.

### 2. EXPERIMENTAL

Two types of raw materials have been used in the course of these studies: (1) A-samples of molybdenum-trioxide hydrate,  $\text{MoO}_3 \cdot 1\text{H}_2\text{O}$ , or molybdic acid (Prolabo) and (2) B-samples of commercially available Mo(VI) oxide (Alpha-Ventron). The various dehydrated A-samples were obtained by thermal annealing in a two-zone tube furnace with a  $50 \text{ cm}^3/\text{minute}$  argon flow. After 2 h purge, the furnace temperature was ramped from room temperature to the desired heat treatment over 1 h period. Samples were heat treated in the temperature range  $140$ - $750^\circ\text{C}$  for 48 h as determined from the onset of endothermal peaks of the differential thermal analysis (DTA) of molybdic acid. The raw  $\text{MoO}_3$  powder (B-sample) was also heat-treated using the above process at

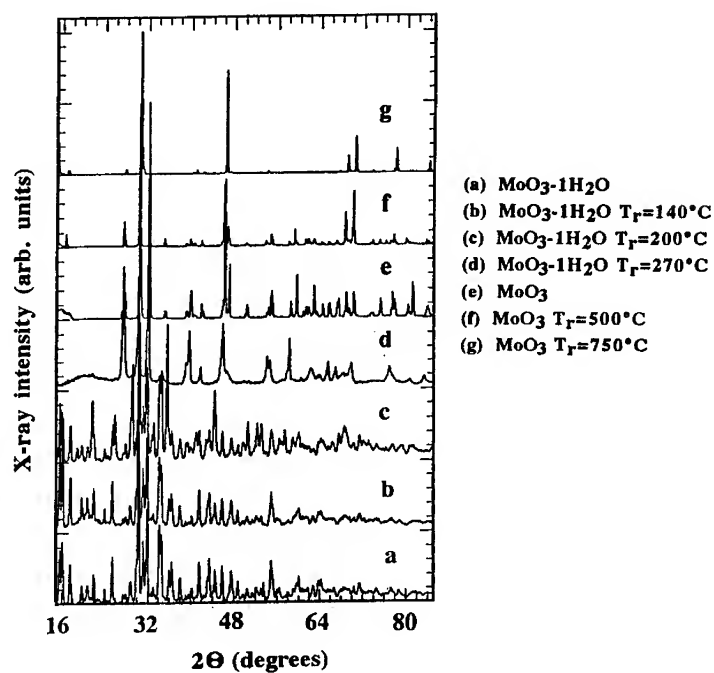


Fig. 1. X-ray diffraction diagrams of oxide-hydrates of molybdenum and  $\text{MoO}_3$  raw powder heat-treated at various temperatures in the range 140-750°C.

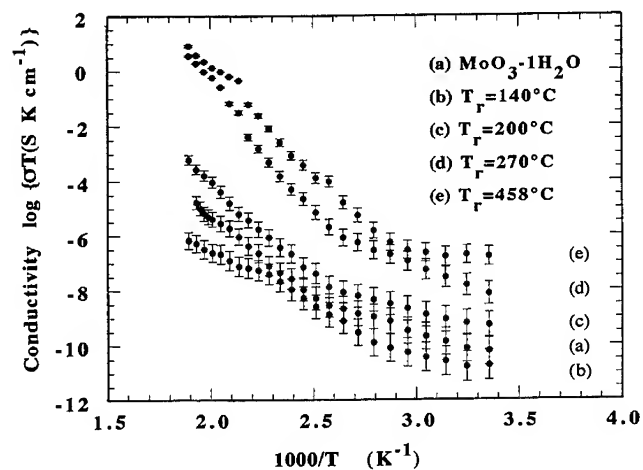


Fig. 2. Temperature dependence of the electrical conductivity of oxide-hydrates of molybdenum heat-treated at various temperatures in the range 140-458°C.

500 and 750°C (below the melting point of  $\text{MoO}_3$  at 820°C).

Structural properties were studied using X-ray diffraction (XRD) and Raman scattering (RS) experiments. XRD measurements were conducted using a Philips PX1820 diffractometer with a  $\text{Co K}\alpha$  radiation ( $\lambda=1.7899 \text{ \AA}$ ). RS spectra were recorded using a Jobin-Yvon U1000 spectrometer with a Ar-ion laser line at 514.5 nm. Electrical experiments were carried out in the same way as described in previous paper [14].

The non-aqueous cell assembly was of the type  $\text{Li}/1\text{M LiClO}_4\text{-propylene carbonate}/\text{MoO}_3$ . A cell was constituted by a pellet cathode pressed at  $0.5 \times 10^5 \text{ Pa}$  with an area of  $0.8 \text{ cm}^2$  cathode, a glass-fiber separator (Whatman GF/C), and a lithium-metal foil anode. This assembly were sandwiched between nickel foils as current collectors. Electrochemical titrations were carried out using a Mac-Pile system with current densities in the range  $100\text{-}150 \mu\text{A cm}^{-2}$ . Kinetics parameters have been determined by the GITT method from the variation of the cell voltage vs. time during the relaxation period following a long discharge or charge [15].

### 3. RESULTS AND DISCUSSION

Figure 1 shows the X-ray diffraction diagrams of oxide-hydrates of molybdenum and  $\text{MoO}_3$  raw powder heat-treated at various temperatures in the range 140-750°C. The main features of the XRD patterns of the A-samples (curves a-c) remain unchanged up to 200°C, indicating that the first dehydration step is a topotactic reaction with no significant structural modification. Therefore, the first dehydration step corresponds to the removal of interlamellar water which does not change the principal features of the  $\text{MoO}_6$  octahedra. Above 270°C, marked structural changes are observed in the second step of dehydration. The X-ray patterns coincide with the molybdenum oxides having infinite sheets of corner-shared  $\text{MoO}_6$  octahedra. These results are in agreement with those reported by Günter [16] who has proposed a structural model for the dehydration of molybdenum trioxide-monohydrate. This structure remains unchanged up to the onset of phase transformation around 500°C. The structural rearrangement at this stage indicates a monoclinic to orthorhombic phase transformation. Similar topotactic transformation occurs for the B-samples (curves e-g). The orthorhombic structure was formed above 500°C with lattice parameters  $a=3.962 \text{ \AA}$ ,  $b=13.858 \text{ \AA}$  and  $c=3.97 \text{ \AA}$ . This arrangement causes oxygen removal and formation of a multiple chain of vertex-shared  $\text{MoO}_6$  octahedra. Samples with a black color are formed at this stage, indicating an oxygen-deficient  $\text{MoO}_{3-x}$  structure.

Vibrational spectroscopy such as Raman scattering is a sensitive technique which can unambiguously distinguish interlamellar  $\text{MoO}_6$  octahedra from octahedra sharing two common edges. We have studied the RS spectra of  $\text{MoO}_3 \cdot \text{H}_2\text{O}$  and products after heat treatment. The RS spectrum of  $\text{MoO}_3$  can be discussed in terms of internal and external modes [17]. The highest stretching frequency at  $993 \text{ cm}^{-1}$  (the so-called molybdyl-mode) is attributed to the shortest Mo-O bond, whereas the next highest stretching frequency at  $817 \text{ cm}^{-1}$  is assigned to the intermediate bridging O-Mo-O bond. The bending modes are located in the medium frequency-range while the external modes appear at below  $200 \text{ cm}^{-1}$ . The RS results clearly shown the change in morphology of the molybdenum oxide materials upon annealing treatment. Here, the modifications of the crystallinity can be deduced using the shape and frequency of the three groups of peaks. At intermediate heat treatment we observed the bands attributed to the mixed phase during the transformation from  $\beta\text{-MoO}_3$  to  $\alpha\text{-MoO}_3$ .

Figure 2 shows the temperature dependence of the electrical conductivity,  $\sigma_{dc}$ , of oxide-hydrates of molybdenum heat-treated at various temperatures in the range 140-458°C. It is well known that transition-metal oxides can be non-stoichiometric.  $\text{MoO}_3$  is such a material.  $\text{Mo}^{5+}$  ions can be produced as a consequence of the formation of oxygen vacancies. The conduction process has been described as a carrier hopping mechanism between localized states [18]. Small polarons are formed around these ions, due to the highly polar structure of this oxide. A thermally activated electronic hopping between lower and higher valence states is responsible for the electric transport. Also, it has been pointed out that the amount of vacancies in  $\text{MoO}_3$  films is indicated by the color of the film [1]. The conductivity curves shown in Fig. 2 are typical of a hopping mechanism. The activation energies of the high-temperature regime are in the range 0.5-0.7 eV. The increase in  $\sigma_{dc}$  suggests a decrease of the O/Mo ratio due to the oxygen loss in annealed materials. The highly treated samples ( $T_f=458^\circ\text{C}$ ) have the highest electrical conductivity values.

Figure 3 shows the discharge curves of Li/MoO<sub>3</sub> cells using (a) MoO<sub>3</sub>-1H<sub>2</sub>O, (b) MoO<sub>3</sub> commercial powder, and (c) MoO<sub>3</sub> crystal formed by heating the B-sample at 750°C. The theoretical capacity of the cells is 10 mA h for an active-cathode mass of 40 mg. The discharge behaviour of molybdic-acid materials was compared with that of MoO<sub>3</sub> polycrystal. An initial voltage of 3.0 V was measured for all the samples. Comparing the discharge curves, we may remark that: (i) the cell voltage decreases from 3.0 to 1.5 V with the discharge capacity 1.5 e<sup>-</sup>/Mo atom, (ii) a stepwise discharge behaviour is observed including a plateau in the range 0 ≤ x ≤ 0.25, (iii) anhydrous MoO<sub>3</sub> (raw B-sample) gives a discharge capacity higher than that of molybdenum trioxide-monohydrate and MoO<sub>3</sub> single crystal, (iv) the capacity loss occurs mainly at high degree of lithium insertion (x > 0.8) and represents about 5% of the total capacity.

The discharge results of MoO<sub>3</sub> have been reported by several workers. The discharge capacities reported by Dampier [5], Margalit [6] and Besenhard et al. [7,9] are in the range from 1.3 to 1.6 e<sup>-</sup>/Mo in the potential range above 1.0 V vs. Li<sup>+</sup>/Li. The capacity of MoO<sub>3</sub> observed here is approximately in agreement with such previous results. Furthermore the discharge potential is higher than 1.5 V, probably due to the increase of the vacancy sites in the lattice. During the discharge, Li<sup>+</sup> ions could be easily incorporated in these sites because the dimension of the unit cell of the acid increases to a small extent as the water is removed. MoO<sub>3</sub>-1H<sub>2</sub>O has only a coordinated water molecule in the structure [19]. The structure consists of linear double rows of edge-sharing octahedra [MoO<sub>3</sub>(OH<sub>2</sub>)], and the octahedral double chains are linked to each other through possible hydrogen bonds only [19]. This open structure is favourable to the lithium insertion.

Kinetics of Li<sup>+</sup>-ions insertion in Li<sub>x</sub>MoO<sub>3</sub> have been studied in the composition 0 < x < 1.5. Figure 4 displays the chemical diffusion coefficients of (a) heat-treated molybdic acids and (b) raw MoO<sub>3</sub> powder, respectively. The compositional dependence of D in MoO<sub>3</sub>-1H<sub>2</sub>O is rather a quadratic function which is due to the nature of the empty sites in the host structure (Fig. 4a). The behaviour of the curves can be modeled using the relation  $D = x B (1-x)$  where B is an interaction parameter related to the repulsive interaction energy between alkali ions [20]. The maximum of D ( $D = 4 \times 10^{-9}$  cm<sup>2</sup> s<sup>-1</sup> in MoO<sub>3</sub>-1H<sub>2</sub>O annealed at 270°C) corresponds with the half-filling site number as shown in Fig. 4a.

The chemical diffusion coefficients of Li<sup>+</sup> in the raw MoO<sub>3</sub> powders exhibit different features: (i) values are slightly higher than for MoO<sub>3</sub>-1H<sub>2</sub>O, and (ii) D remains almost constant in the range 0 < x < 1.2 (Fig. 4b). Thus, the ideal lattice gas model can be applied in which the ion-ion interaction energy is negligible [21]. However, D decreases by three orders of magnitude for x > 1.2. This behaviour may be attributed to a blocking effect for the Li<sup>+</sup> diffusion.

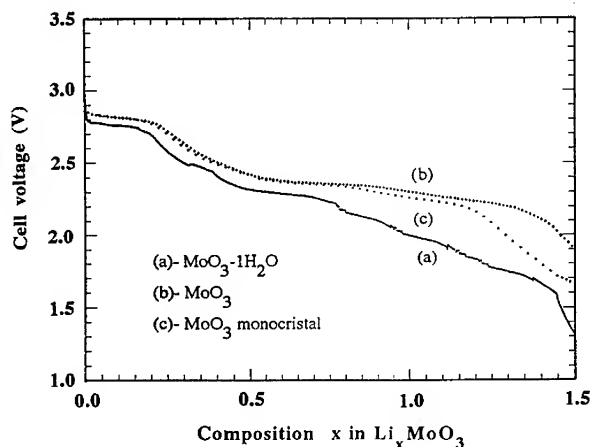


Fig. 3. Discharge curves of Li/MoO<sub>3</sub> cells using (a) MoO<sub>3</sub>-1H<sub>2</sub>O, (b) MoO<sub>3</sub> commercial powder, and (c) MoO<sub>3</sub> crystal.

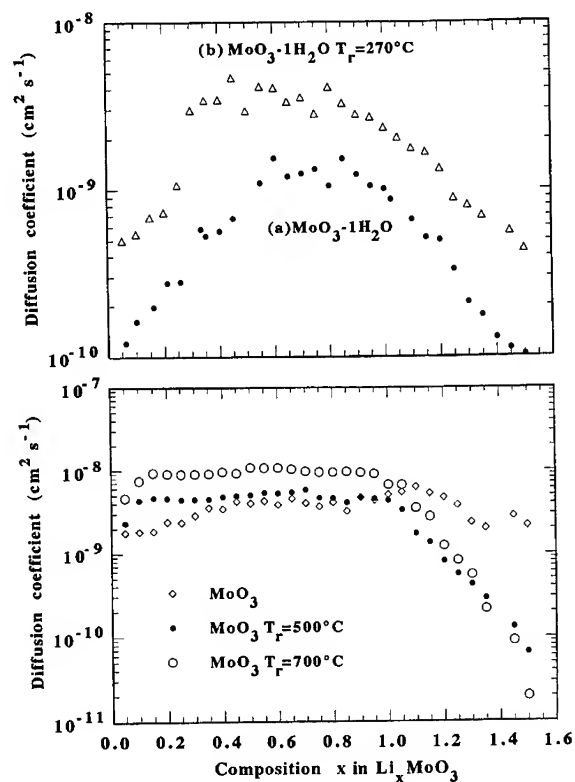


Fig. 4. (a) Chemical diffusion coefficients of  $\text{Li}^+$  ions in  $\text{MoO}_3-1\text{H}_2\text{O}$  and  $\text{MoO}_3-1\text{H}_2\text{O}$  heat-treated at  $270^\circ\text{C}$ . (b) Chemical diffusion coefficients of  $\text{Li}^+$  ions in  $\text{MoO}_3$  raw powder material,  $\text{MoO}_3$  heat-treated at  $500^\circ\text{C}$ , and  $\text{MoO}_3$  heat-treated at  $700^\circ\text{C}$ .

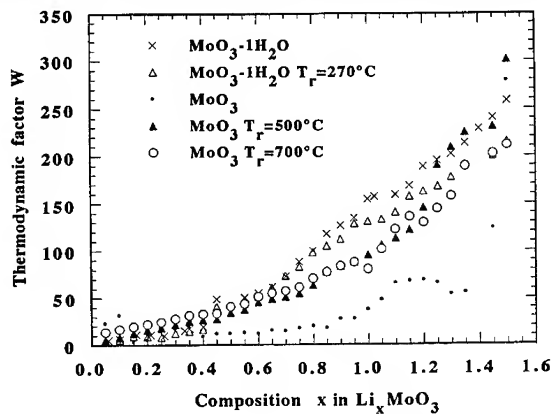


Fig. 5. Thermodynamic factor as a function of the degree of insertion in oxide-hydrates of molybdenum and in  $\text{MoO}_3$  raw materials heat-treated at various temperatures.

The thermodynamic factor is defined as  $W = \partial(\ln a^*) / \partial(\ln C^*)$  in which  $a^*$  is the activity of the intercalant species in the solid solution electrode.  $W$  is also expressed by the ratio  $W = D/D_0$ , between the chemical diffusion coefficient,  $D$ , and the component diffusion  $D_0$ . Figure 5 shows the compositional dependence of the thermodynamic factor in oxide-hydrates of molybdenum heat-treated at various temperatures and in  $\text{MoO}_3$  raw material. In the compositional range  $0 < x < 1.5$ ,  $W$  varies from 3 to 300, indicating a strong electronic contribution on the insertion reaction in  $\text{MoO}_3$  at high values of  $x$ .

#### 4. CONCLUSION

This work have shown a comparison between the electrochemical features of the molybdenum-oxide hydrates with different degrees of dehydration. The electrochemical properties of oxide-hydrates of molybdenum and  $\alpha\text{-MoO}_3$  can be related to their structural and electrical characteristics. Thermodynamics and kinetics of lithium-ion insertion are functions of the structural arrangement in these host lattices. Diffusion coefficient can be modeled using either a simple model for site occupancy or an ideal lattice gas model. The electronic contribution plays a role in the insertion process of  $\text{MoO}_3$  compounds. This study has demonstrated that the raw  $\text{MoO}_3$  heat-treated powder exhibits the highest conductivity and displays the best electrochemical features for Li-ion insertion.

#### REFERENCES

- [1] C. Julien, L. El-Farh, M. Balkanski, O.M. Hussain and G.A. Nazri, *Appl. Surf. Sci.* **65-66**, 325 (1993).
- [2] K. Hinokuma, A. Kishimoto and T. Kudo, *J. Electrochem. Soc.* **141**, 876 (1994).
- [3] L. Kihlberg, *Arkiv. Kemi* **21**, 357 (1963).
- [4] S. Crouch-Baker and P.G. Dickens, *Solid State Ionics* **32-33**, 219 (1989).
- [5] F.W. Dampier, *J. Electrochem. Soc.* **121**, 656 (1974).
- [6] N. Margalit, *J. Electrochem. Soc.* **121**, 1460 (1974).
- [7] J.O. Besenhard and R. Schollhorn, *J. Power Sources* **1**, 267 (1976/77).
- [8] P.A. Christian, J.N. Carides, F.J. DiSalvo and J.V. Waszczak, *J. Electrochem. Soc.* **127**, 2315 (1980).
- [9] J.O. Besenhard, J. Heydecke, E. Wudy, H.P. Fritz and W. Foag, *Solid State Ionics* **8**, 61 (1983).
- [10] N. Kumagal, N. Kumagai and K. Tanno, *Electrochim. Acta* **32**, 1521 (1987).
- [11] N. Kumagai, N. Kumagai and K. Tanno, *J. Appl. Electrochem.* **18**, 857 (1988).
- [12] M. Sugawara, Y. Kitada and K. Matsuki, *J. Power Sources* **26**, 373 (1989).
- [13] C. Julien and G.A. Nazri, *Solid State Ionics* **68**, 111 (1994).
- [14] C. Julien, A. Khelifa, J.P. Guesdon and A. Gorenstein, *Appl. Phys. A* **78**, 173 (1994).
- [15] W. Weppner and R.A. Huggins, *J. Electrochem. Soc.* **124**, 1569 (1977).
- [16] J.R. Günter, *J. Solid State Chem.* **5**, 354 (1972).
- [17] G.A. Nazri and C. Julien, *Solid State Ionics* **53-56**, 376 (1992).
- [18] M. Anwar and C.A. Hogarth, *Int. J. Electronics* **66**, 901 (1989).
- [19] H.R. Oswald, J.R. Günter and E. Dubler, *J. Solid State Chem.* **13**, 330 (1975).
- [20] S. Basu and W.L. Worrell, in *Fast Ion Transport in Solids*, edited by P. Vashishta, J.N. Mundy and G.K. Shenoy (North-Holland, Amsterdam, 1979), p. 149.
- [21] W.R. McKinnon and R.R. Hearing, in *Modern Aspects of Electrochemistry*, vol. 15, edited by R. White, J.O'M. Bockris and B.E. Conway (Plenum, New York, 1983), p. 235.



## ROUGHNESS EFFECT ON THE LITHIUM DIFFUSIVITY IN WO<sub>3</sub> THIN FILMS

M. MAAZA<sup>a</sup>, A. GORENSTEIN<sup>b</sup>, C. SELLA<sup>c</sup>, F. BRIDOU<sup>a</sup>, B. PARDO<sup>a</sup>, J. CORNO<sup>a</sup>,  
G. ROGER<sup>a</sup>, O. BOHNKE<sup>d</sup> AND C. JULIEN<sup>b</sup>

<sup>a</sup>Institut d'Optique Théorique et Appliquée, associé au CNRS, Bat. 503, 91405 Orsay, France

<sup>b</sup>Laboratoire de Physique des Solides, associé au CNRS, Université Pierre et Marie Curie  
4 place Jussieu, 75252 Paris Cedex 05, France

<sup>c</sup>Laboratoire de Physique des Matériaux du CNRS, 92195 Meudon Principal, France

<sup>d</sup>Laboratoire des Fluorures, Université du Maine, route de Laval, B.P.535  
72017 Le Mans Cedex, France

### ABSTRACT

In this work, we investigate the influence of surface roughness on the kinetics of Li<sup>+</sup> during the insertion process in the well-known electrochromic material WO<sub>3</sub>. Thin films 500 Å thick have been grown by rf-sputtering and annealed in the range of 25-350°C. Grazing angle X-ray reflectometry shows that the film roughness increases considerably with thermal treatment. These measurements are correlated with chemical diffusion investigations obtained by electrochemical titration in Li/WO<sub>3</sub> cells.

### 1. INTRODUCTION

The electrochromism is based on the property of certain compounds, mostly transition-metal oxides such as amorphous films of WO<sub>3</sub> to undergo colour changes when the oxidation state of the metal in the host lattice is changed [1]. Normally, alkali ions (such as Li<sup>+</sup> or Na<sup>+</sup>) from an electrolyte are inserted into the host during an electrochemical reaction. In WO<sub>3</sub>, the electrochromism has been described as a double injection of electrons and ions, according to the equation [2-6]



The optical performance of these electrochromic films are linked to the kinetics of the electrochemical reaction. The time response has been pointed out to depend on the diffusion coefficient of the alkali ions in the film [7]. To enhance this diffusion process without disturbing significantly the amorphous state of the electrochromic layer, one could increase the diffusion paths at the film-electrolyte interface by improving its roughness. This effect can be generated either by thermal treatment or by ionic irradiation. In this work, we are concerned with the thermal method. The aim of the paper is, first, to determine the thermal evolution of the interfacial roughness of WO<sub>3</sub> thin films using grazing angle X-ray reflectometry; second, to correlate this interfacial roughness with the film behaviour under lithium intercalation. The choice of the grazing angle reflectometry is justified due to the high sensitivity of this method for estimating the interfacial geometric defects at nanometric scale.

### 2. EXPERIMENTAL

WO<sub>3</sub> films were prepared by rf-sputtering from a target made of 99.97% pure WO<sub>3</sub> powder (Jonhson Matthey GmbH). The base pressure of the chamber before deposition was 4x10<sup>-6</sup> Torr. Sputtering was performed in atmosphere of Ar+5% O<sub>2</sub>. Either float-glass (FG) or indium-tin oxide (ITO) coated float glass (ICMC-France, sheet resistivity about 13 Ω cm<sup>-2</sup>) was used as substrates. The thicknesses of WO<sub>3</sub> and ITO films are 0.06 and 0.4 μm, respectively. The WO<sub>3</sub>/FG and WO<sub>3</sub>/ITO/FG samples were annealed in a cylindrical resistive annealing furnace at different temperatures (440, 560, and 621 K) during 3 hours under a pressure of the order of 10<sup>-7</sup>

Torr. The annealing temperature was limited to 621K in order to avoid the crystallisation of the amorphous  $\text{WO}_3$ .

X-ray diffraction experiments were performed in a conventional diffractometer using a  $\text{Cu K}\alpha$  source ( $\lambda=1.5405 \text{ \AA}$ ). The scanned angular range is between  $5^\circ$  and  $80^\circ$ . Grazing angle X-ray reflectometry measurements were performed only on  $\text{WO}_3/\text{FG}$  samples on a  $\theta$ - $2\theta$  reflectometer described in a previous paper [8]. It uses a sealed  $\text{Cu K}\alpha$  tube source. The reflectivity profiles were obtained by varying the grazing angle from 500 to 8000 sec of arcs with a step of 10 sec of arcs while tracking the reflected beam.

The electrochemical experiments were performed in an electrochemical cell in which the  $\text{WO}_3/\text{ITO}/\text{FG}$  samples are the working electrode and Li foils were the counter and reference electrodes. The electrolyte was  $1\text{M LiClO}_4$  in propylene carbonate (PC). All the experiments were performed inside a dry-box (Ar atmosphere) containing less than 2 ppm of water. Discharge/relaxation cycles at  $1.5 \mu\text{A cm}^{-2}$  were performed using a MacPile system. The kinetic parameters were evaluated using the method described in Ref. [9].

### 3. RESULTS AND DISCUSSION

#### 3.1. Thin-film structure

Figure 1 shows the X-ray diffractograms of annealed and non-annealed  $\text{WO}_3/\text{FG}$  and  $\text{WO}_3/\text{ITO}/\text{FG}$  samples. There are no discrete diffraction peaks in the patterns (a) and (b) at  $\theta > 15^\circ$ , arguing that  $\text{WO}_3$  films are amorphous ( $\text{a-WO}_3$ ) till an annealing temperature of  $T_a=621 \text{ K}$ . All the diffraction peaks in (c) and (d) for  $\theta > 15^\circ$  mark the crystalline structure of ITO films. Likewise, there is no significant difference between annealed and non-annealed samples. Thus,  $\text{WO}_3$  remain amorphous in the concerned temperature range.

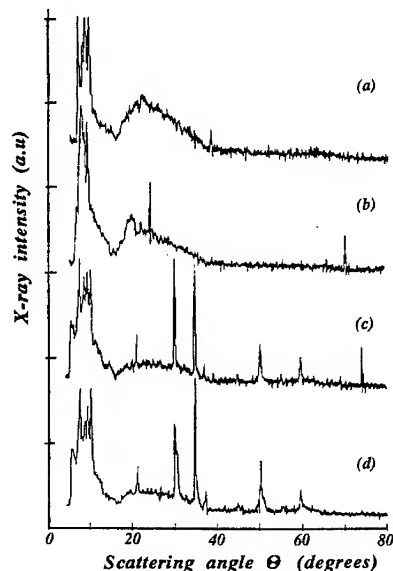


Figure 1. Diffraction patterns of (a) non-annealed  $\text{WO}_3/\text{FG}$ , (b)  $\text{WO}_3/\text{FG}$ , annealed at 621 K, (c) non-annealed  $\text{WO}_3/\text{ITO}/\text{FG}$  and (d)  $\text{WO}_3/\text{ITO}/\text{FG}$  annealed at 621 K.

#### 3.2. X-Ray reflectometry results

Before presenting the experimental results of grazing angle X-ray reflectometry, one can recall

briefly the principle of this surface analysis. It is well known that in the range of X-ray wavelength the refractive index  $n_x$  of condensed matter is less than unity and can be written as  $n_x = 1 - \delta - j\beta$ , where  $\delta = C\rho$  is essentially dependent on the density  $\rho$  [10].  $C$  is nearly a constant given approximately by  $C \approx (e^2 N f \lambda^2) / (2\pi M m c^2)$ , where  $\lambda$  is the wavelength,  $e^2/mc^2$  the classical electron radius,  $N$  the Avogadro constant, and  $M$  the molar mass.  $f$  is the atomic scattering factor which can be approximated by the atomic number  $Z$  since the reflection angle is small ( $\leq 5$  deg). The imaginary part of  $\beta$  is proportional to the linear absorption coefficient  $\mu$  ( $\beta = \mu\lambda/4\pi$ ) and expresses the absorption of X-rays in the medium. The theory of X-ray reflectivity is based upon Fresnel equations. The specular reflectivity of a stack of ideal layers can be computed with the optical theory of stratified media such as Abèles matrix calculus [11]. For a grazing angle lower than the critical angle  $\theta_c \approx \sqrt{2\delta}$ , the reflectivity  $R(\theta)$  is high ( $\approx 1$ , total reflection plateau). In the case of a very thin film on a bulk substrate, the X-ray beam is weakly absorbed for angles  $\theta$  greater than  $\theta_c$ , and then the so-called Kiessig fringes resulting from the interference between the films reflected at the two main interfaces (air-film and film-substrate) are observed. In practice, the interfaces between the various layers are neither sharp nor flat. For grazing incidence X-rays, the interfacial region appears like a transition layer [8, 12-13], in which the refractive index varies continuously with the depth  $z$  (Fig. 2). The interface is then divided into elementary layers where the refractive index  $n(z)$  will depend on the roughness distribution. Thus the measurement of the angular dependence of the reflectivity profile from a surface provides directly both the density, linear absorption coefficient, thickness and especially interfacial roughness at nanometric scale.

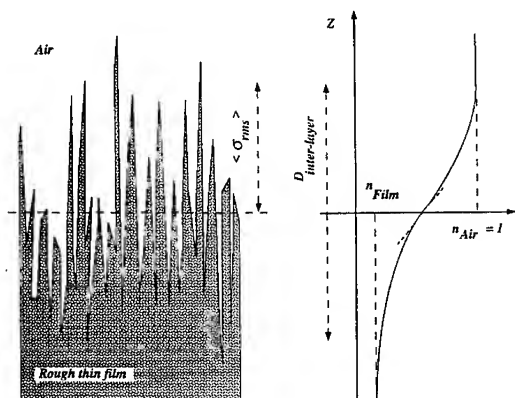


Figure 2. Schematic drawing of the rough between two homogeneous materials media (air and a thin film with an X-ray refractive index  $n_{\text{film}}$ ). If the roughness is randomly distributed, the refractive index profile  $n(z)$  along the  $z$ -axis normal to the surface, is an error function through the transition layer.

Typical experimental grazing angle X-ray reflectivity profiles versus  $\theta$  of simple layer of  $\text{WO}_3/\text{FG}$  samples, corresponding to non-treated (298 K) and annealed samples at 440, 560 and 621 K, are presented in Fig. 3, with their simulated curves. In each reflectivity profile, the total reflection plateau and Kiessig interference fringes are observed. The theoretical X-ray profile for which the electrochromic  $\text{WO}_3$  layers are expected to be fully pure and homogeneous, described by a step refractive index profile, is seriously different from the experimental one. An interfacial layer with a graded refractive index (error function type) located at the air- $\text{WO}_3$  interface is required to simulate the different curves [13]. The interfacial layer is characterized by its thickness  $D_{\text{int-layer}}$  and its refractive index (mainly  $\delta_{\text{int-layer}}$ ). A series of simulation is therefore carried out by varying thickness and refractive index of both  $\text{WO}_3$ , and this interfacial layer until a reasonable simulation with a good factor of merit is obtained. The simulation parameters are summarized in Table 1. According to these results (Fig. 4) the thickness of the interfacial layer  $D_{\text{int-layer}}$  is increasing with temperature, i.e., approximately by a factor of 3 from 298 to 621 K) and seems to

stabilize between 560 and 612 K. As it was emphasized before, this interfacial layer is analogous to a roughness whose distribution is assumed to be Gaussian-like with a rms roughness  $\langle \sigma_{\text{rms}} \rangle = D_{\text{int-layer}}/2$ . So, one can confirm that the annealing processing induces an enhancement of the roughness of the air-WO<sub>3</sub> interface and, in a first approximation, an extension of the effective diffusion surface at the electrolyte-WO<sub>3</sub> interface by a factor of the order of 3 in the concerned temperature range. Moreover, the simulated  $\delta_{\text{int-layer}}$  of the interfacial layer is almost constant ( $\approx 12 \times 10^{-6}$ ) whereas that of WO<sub>3</sub> varies. This last one increases with the temperature to reach approximately the theoretical value ( $\delta_{\text{WO}_3} \approx 18.25 \times 10^{-6}$ ). As the crystalline structure of WO<sub>3</sub> film does not change, this variation could be due to impurities or small local rearrangement [14].

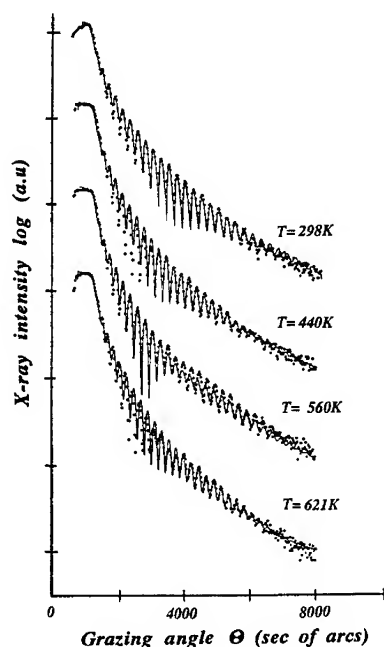


Figure 3. Measured (open circles) and calculated (solid lines) specular reflectivity  $R(\theta)$  (log scale) vs. grazing angle  $\theta$  given by the non-annealed (298 K) and annealed WO<sub>3</sub>/FG samples at 440, 560 and 621 K.

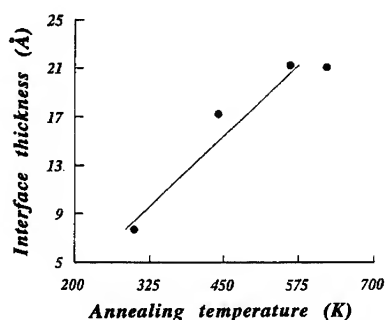


Figure 4. Temperature variation of the thickness  $D_{\text{int-layer}}$  of the interfacial layer.

Table 1. Theoretical and principal simulated values of the optical indices and thicknesses of WO<sub>3</sub> and interfacial layer (int-layer).

Parameters	Theoretical	293 K	440 K	560 K	621 K
Thickness of WO <sub>3</sub> layer (Å)	600	613	609	590	632
$\delta$ WO <sub>3</sub> (x10 <sup>6</sup> )	18.25	15.76	16.50	17.03	17.19
$\beta$ WO <sub>3</sub> (x10 <sup>6</sup> )	1.20	1.50	1.50	1.50	1.50
Thickness of in-layer (Å)	0	8	17	22	21
$\delta$ int-layer (x10 <sup>6</sup> )	0	12	11	12	12
$\beta$ int-layer (x10 <sup>6</sup> )	0	1	1	1	1

### 3.3. Electrochemical studies

Discharge/relaxation cycles in LiClO<sub>4</sub>-PC were performed using the as-grown and annealed WO<sub>3</sub>/ITO/FG samples. Figure 5 shows the open-circuit voltage (OCV) behaviour (near the thermodynamic equilibrium) as a function of the degree of Li<sup>+</sup> intercalation for as-grown and annealed films at 560 K. The OCV, for both samples remains greater than 2.6 V till a degree of lithium intercalation of 0.3 Li/W. The variations of the WO<sub>3</sub> electrode potential with the injected charge are in good agreement with the assumption of the formation of Li<sub>x</sub>WO<sub>3</sub> compounds. According to the reversible reaction (eq.1), the chemical potential of Li is varying continuously with x. This electrochemical behaviour has been reported in the literature [15-17]. It is interesting to notice that the variation in the OCV curves is almost the same for the two amorphous samples.

Chemical diffusion coefficients of Li<sup>+</sup> in a-WO<sub>3</sub> films shown in Fig. 6 have been measured on the same samples as in Fig. 5. It is found that D<sub>Li</sub> is a strong function of x. The values of D<sub>Li</sub> are in the range 10<sup>-14</sup>-10<sup>-17</sup> cm<sup>2</sup> s<sup>-1</sup>. Only a few data are available on the kinetics of ion insertion into WO<sub>3</sub> films. Nevertheless, our results are comparable with data concerning other amorphous compounds [18]; the chemical diffusion coefficient in films is always several orders of magnitude lower than that in crystals. A value of D<sub>Li</sub>=10<sup>-11</sup> cm<sup>2</sup> s<sup>-1</sup> is often reported in c-WO<sub>3</sub> [19].

Considering the features of D<sub>Li</sub> vs. x, we assume that the film roughness plays a role in the diffusion process. D<sub>Li</sub> of annealed film varies more slowly with x than D<sub>Li</sub> of as-grown a-WO<sub>3</sub>. Regarding the results of X-ray reflectometry, the interface is modified in heat-treated film, an extension of the effective diffusion surface by a factor of 3 occurs at the electrolyte-WO<sub>3</sub> interface. Thus a higher pathway for the ionic conduction should appear in this annealed film. We observe that D<sub>Li</sub> is enhanced by one order of magnitude near x=0.3.

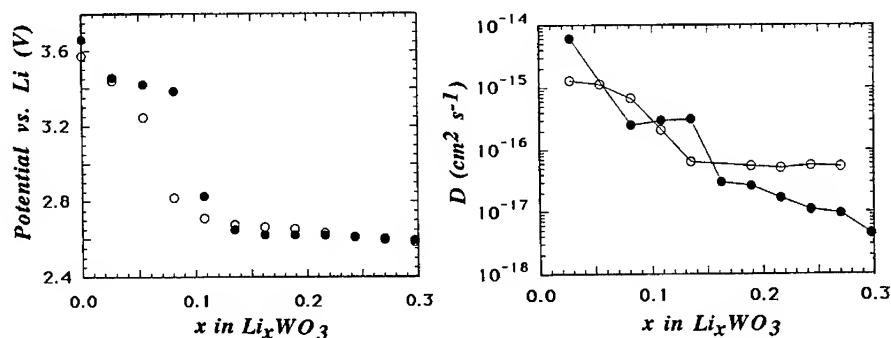


Figure 5. Equilibrium potential vs. x in Li<sub>x</sub>WO<sub>3</sub> for non-annealed samples (full circles) and annealed at 560 K (open circles).

Figure 6. Chemical diffusion coefficients vs. x in Li<sub>x</sub>WO<sub>3</sub> for non-annealed samples (full circles) and annealed at 560 K (open circles).

The electrolyte-electrode interface allows ions to migrate between two media. The interfacial impedance (expressed in  $\Omega \text{ cm}^2$ ) can be deduced experimentally from the variation of the transient cell voltage as [9]

$$Z_{o,i} = 3(E_0 - E_\infty)/i, \quad (2)$$

where  $E_0$  and  $E_\infty$  are the voltage at the beginning and at the end of the relaxation period after the application of a current pulse of intensity  $i$ . Values of  $Z_{o,i}$  are 650 and 432  $\text{k}\Omega \text{ cm}^2$  for as-grown and heat-treated a- $\text{WO}_3$  films, respectively. It is worth noting that the roughness influences the electrolyte-electrode interface in these materials.

#### 4. CONCLUDING REMARKS

In this work, we have determined the thermal evolution of the interfacial roughness of  $\text{WO}_3$  thin films using grazing angle X-ray reflectometry and this interfacial roughness has been correlated with the film behaviour under lithium intercalation. The choice of the grazing angle reflectometry has been justified due to the high sensitivity of this method for estimating the interfacial geometric defects at nanometric scale.

We can confirm that the annealing processing induces an enhancement of the roughness of the electrolyte- $\text{WO}_3$  interface and, in a first approximation, an extension of the effective diffusion surface at this interface by a factor of the order of 3 in the concerned temperature range. The interfacial impedance has been deduced experimentally. Values of  $Z_{o,i}$  are 650 and 432  $\text{k}\Omega \text{ cm}^2$  for as-grown and heat-treated a- $\text{WO}_3$  films, respectively. A satisfactory interface is difficult to obtain and the use of thin-film technology with appropriate film morphology can decrease the interfacial resistance.

#### REFERENCES

- [1] S.K. Deb, *Phil. Mag.* **27**, 801 (1973).
- [2] R.S. Crandall and B.W. Faughnan, *App. Phys. Lett.* **26**, 120 (1975).
- [3] W.C. Dautremont-Smith, M. Green and K.S. Kang, *Electrochim. Acta* **22**, 751 (1977).
- [4] S.K. Mohapatra, *J. Electrochem. Soc.* **125**, 284 (1978).
- [5] O. Bohnke, C. Bohnke and S. Amal, *Mat. Sci. Eng. B* **3**, 197 (1989).
- [6] S. Passerini, B. Scrosati, A. Gorenstein, A.M. Anderson and C.G. Granqvist, *J. Electrochem. Soc.* **136**, 3394 (1989).
- [7] C.G. Granqvist, in *Physics of Thin Films, Mechanic and Dielectric Properties*, vol. 17, edited by M.H. Francombe and J.L. Vossen (Academic Press, New York, 1993), p. 301.
- [8] F. Bridou and B. Pardo, *J. Optics* **21**, 183 (1990).
- [9] A. Honders, J.M. Der Kinderen, A.H. Van Heren, J.H.W. De Witt and G.H.J. Broers, *Solid State Ionics* **15**, 265 (1985).
- [10] P. Croce and B. Pardo, *Nouv. Rev. Opt. Appl.* **1**, 229 (1970).
- [11] F. Abelès, *Ann. Phys.* **12**, 596 (1950).
- [12] B. Pardo, T. Megademini and J.M. Andre, *Rev. Phys. Appl.* **23**, 1579 (1988).
- [13] L. Nevot, B. Pardo and J. Corno, *Rev. Phys. Appl.* **23**, 1675 (1988).
- [14] A. Agarwal and M. Habibi, *Thin Solid Films* **129**, 257 (1989).
- [15] O. Bohnke and G. Robert, *Solid State Ionics* **6**, 115 (1982).
- [16] J.P. Pereira-Ramos, R. Baddour-Hadjean, N. Kumagai and K. Tanno, *Electrochim. Acta* **38**, 431 (1993).
- [17] Q. Zhong, J.R. Dahn and K. Colbow, *J. Electrochem. Soc.* **139**, 2406 (1992).
- [18] C. Julien and G.A. Nazri, *Solid State Batteries: Materials Design and Optimization* (Kluwer, Boston, 1994), p. 513.
- [19] P.G. Dickens and G.J. Reynolds, *Solid State Ionics* **5**, 331 (1981).

# ELECTROCHEMICAL STUDY, SYNTHESIS AND MICROSTRUCTURAL CHARACTERIZATION OF LITHIUM AND SODIUM INSERTED $W_{18}O_{49}$ .

A. MARTINEZ DE LA CRUZ <sup>a,b</sup>, LETICIA M. TORRES-MARTINEZ<sup>b</sup>, F. GARCIA-ALVARADO<sup>a</sup>, E. MORAN<sup>a</sup> AND M. A. ALARIO-FRANCO<sup>a</sup>

<sup>a</sup>Departamento de Química Inorgánica, Facultad de Ciencias Químicas, Universidad Complutense, Madrid 28040, Spain.

<sup>b</sup>Facultad de Ciencias Químicas, Universidad Autónoma de Nuevo León, Apartado Postal 1864, Monterrey, México.

## ABSTRACT

The formation of lithium inserted  $W_{18}O_{49}$  phases has been studied by electrochemical methods. When lithium is inserted, several single phases  $Li_xW_{18}O_{49}$  are observed in the range  $0 \leq x \leq 40$  between 3 and 1 V. Nevertheless the reaction is reversible only for  $x \leq 22$ . Chemical reactions of  $W_{18}O_{49}$  with different quantities of n-butyllithium have been carried out to isolate and characterize some of these phases. For  $Li_{17}W_{18}O_{49}$ , this is ~1:1 Li/W ratio, electron diffraction experiments clearly indicate that lithium produces a periodicity change, doubling the *a*, *b* and *c* cell parameters. On the other hand, when sodium is inserted in  $W_{18}O_{49}$  two single phase regions  $Na_xW_{18}O_{49}$  are observed within the range  $0 \leq x \leq 1.2$  between 3 and 0.5 V.

## INTRODUCTION

The system  $WO_2$  -  $WO_3$  has been studied by several authors [ 1-3 ] and it is well known that many different phases can be found by reduction of  $WO_3$  to  $WO_2$ . These are 10n CS phases ( *n* = 1 and 2 ) as well as pentagonal column ( PC ) phases [ 4 ]. Nevertheless, the synthesis of the different members belonging to the corresponding homologous series is not easy since, due to the close structural relationship existing between CS-based phases, the formation of disordered intergrowths is frequent.

Within the range of existence of the PC-type phases a very stable and essentially stoichiometric phase with the composition  $W_{18}O_{49}$  exists [ 5 ]. The W-O framework, shown in Figure 1, forms a very open structure that can be described as PC's coupled in pairs by edge sharing octahedra. While in one direction these units are linked together by corner sharing, in the other direction the linking is made by additional octahedra. As a result three different types of tunnels are present ( hexagonal, quadrangular and triangular ).

$W_{18}O_{49}$  has already been used as a host compound in intercalation reactions mainly with lithium [ 6-7 ]. The structural consequences of alkali metal insertion in tungsten reduced oxides have been studied by several authors by X-Ray diffraction and, more recently, by electron microscopy [ 6-8 ]. We present in this paper a study of lithium insertion in  $W_{18}O_{49}$  by both chemical and electrochemical routes. Some experiments have also been performed with sodium in the electrochemical case. In addition, we report structural data for some of the single phases obtained.

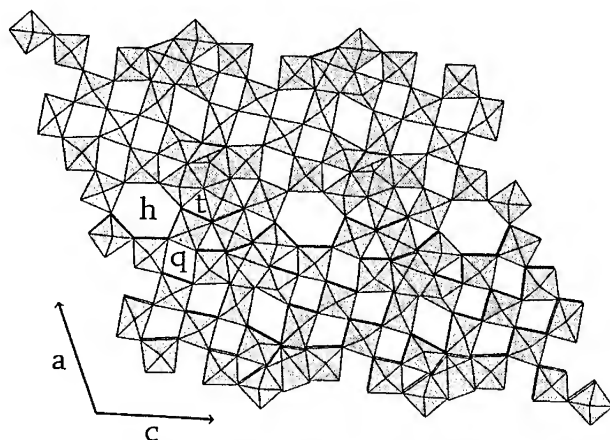


Figure 1.- Projection of the  $W_{18}O_{49}$  structure along the b-direction. Tunnels running along that direction are labeled as h ( hexagonal ), q ( quadrangular ) and t ( triangular ).

## EXPERIMENTAL

The synthesis of the parent oxide,  $W_{18}O_{49}$ , was carried out by solid state reaction of W and  $WO_3$  mixed in the appropriate stoichiometric ratio. The reactant  $WO_3$  was obtained by heating  $H_2WO_4$  at  $850^\circ C$  for 3 days. The mixture was ground and placed in a quartz tube that was evacuated, sealed and heated at  $1000^\circ C$  for 3 days.

The parent oxide and inserted phases were characterized by X - Ray diffraction using a SIEMENS D-5000 diffractometer with  $Cu K_\alpha$  ( $\lambda = 1.5418 \text{ \AA}$ ) radiation. For the microstructural characterization the electron microscopes JEOL 2000 FX and JEOL 4000 EX were used.

The electrochemical study of insertion in  $W_{18}O_{49}$  was carried out in a Swagelok type cell [ 9 ] with either lithium or sodium as the negative electrode. For the positive electrode a 5 mm pellet, obtained by pressing 25-30 mg of a mixture containing  $W_{18}O_{49}$ , carbon black and Ethylene - propylene - diene terpolymer ( EPDT ) in a 89:10:1 ratio, was used. When lithium was acting as the negative electrode, a 1 M solution of  $LiClO_4$  in a mixture of ethylene carbonate ( EC ) and diethoxy ethane ( DEE ) 50:50 was used as the electrolyte [ 10 ]. On the other hand, when sodium was to be inserted, a 1 M solution of  $NaClO_4$  in Propylene Carbonate ( PC ) was used as the electrolyte. All operations to assemble the cells were done into a glove box filled with argon. In a typical experiment a density current of  $0.15 \text{ mA cm}^{-2}$  was used to cycle the cell between the maximum limits 4 - 0.5 V.

Samples with composition  $Li_x W_{18}O_{49}$  were also prepared by a chemical indirect reaction. Several phases were synthesized by mixing, in an appropriate ratio,  $W_{18}O_{49}$  and n-butyllithium, which provides the alkaline metal. The mixture  $W_{18}O_{49}$  / organometallic reagent was stirred for seven days, the solvent was then extracted and the powder washed several times with the corresponding solvent.

To determine the extent of the reaction, lithium was extracted from  $W_{18}O_{49}$  by refluxing the samples with an acid solution for several hours. The remaining powder was then separated and washed, and the solution was analyzed. The lithium content was determined by Inductive Coupled Plasma Analysis using a JY-70 PLUS apparatus.



## RESULTS AND DISCUSSION

X-Ray diffraction confirms the formation of  $W_{18}O_{49}$  by the solid state high temperature reaction. When lithium is inserted in this phase using an electrochemical cell with the configuration  $Li / LiClO_4 \text{ 1 M + EC + DEE (50:50)} / W_{18}O_{49}$ , several single phase regions are detected. Figure 2 shows the evolution of the voltage during an open circuit voltage (OCV) experiment carried out between 3.3 and 0.8 V. On intercalation ( $I < 0$ ) five different regions labeled I, II, III, IV and V, can be seen. These regions correspond to the following approximate existence ranges:

I :  $W_{18}O_{49} - Li_{2.6}W_{18}O_{49}$ ; II :  $Li_{3.4}W_{18}O_{49} - Li_{10}W_{18}O_{49}$ ; III :  $Li_{11}W_{18}O_{49} - Li_{15}W_{18}O_{49}$ ;  
IV :  $Li_{15.5}W_{18}O_{49} - Li_{22}W_{18}O_{49}$  and V :  $Li_{37}W_{18}O_{49} - Li_{39.5}W_{18}O_{49}$

When lithium is being deintercalated ( $I > 0$ ) the corresponding curve is different with respect to the discharge. This indicates that the reaction is not reversible, so that only part of the lithium can be extracted from the structure. The origin of the irreversibility can be traced to the insertion of nearly 40 lithium per unit cell of  $W_{18}O_{49}$  producing an irreversible structural transformation. In order to know the limit of the transformation reaction we ran an OCV experiment where the minimum cut off voltage was limited to 1.3 V; the result is shown in Figure 3. At this voltage the maximum lithium content reached was 17.5 and the composition,  $Li_{17.5}W_{18}O_{49}$ , is within region IV, see Figure 2. In the plot shown in Figure 3, discharge and charge curves are perfectly underlaid showing that, up to this lithium content, the reaction occurs through a reversible intercalation reaction. Figure 4 shows a potentiostatic experiment limited to a voltage, 1.3 V, where the phases form by reversible intercalation reactions. The high reversibility of the reaction is also evident from this experiment. The maxima of the reductive current associated with the formation of single phases I and II are clearly seen at 2.35 and 2.07 V respectively. On the contrary, that corresponding to phase III is not well defined and two maxima, labeled III and III', are seen at 1.61 and 1.51 V. This seems to be evidence that two single phases form in region III. Besides, the peak corresponding to the formation of phase IV can be seen at 1.4 V.

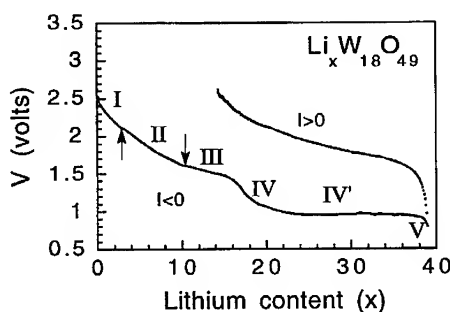


Figure 2.- Open circuit voltage-composition plot of a cell  $Li / LiClO_4 \text{ 1 M + EC + DEE (50:50)} / W_{18}O_{49}$  discharged and charged between 3.3 and 0.8 V.

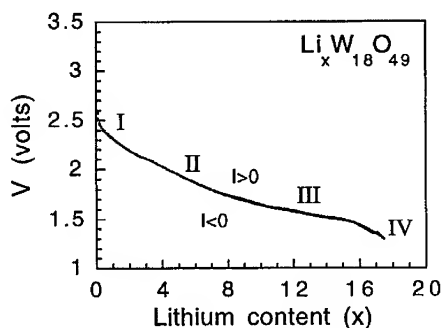


Figure 3.- Open circuit voltage-composition plot of a cell  $Li / LiClO_4 \text{ 1 M + EC + DEE (50:50)} / W_{18}O_{49}$  discharged and charged between 3.3 and 1.3 V.

In order to characterize these phases, some of them were prepared in sizeable amounts by chemical methods. The ICP analysis showed the formation of three phases with composition  $\text{Li}_x\text{W}_{18}\text{O}_{49}$  ( $x \sim 5, 17$  and  $40$ ) belonging to regions II, IV and V respectively. The X-Ray diffraction experiments showed that the  $\text{W}_{18}\text{O}_{49}$  framework seems to be maintained, although a certain loss of crystallinity is observed, for  $x \sim 5$  and  $17$ . Note that these samples belong to regions where reversible intercalation reaction occurs. Table I shows the cell parameters of  $\text{W}_{18}\text{O}_{49}$ ,  $\text{Li}_5\text{W}_{18}\text{O}_{49}$  and  $\text{Li}_{17}\text{W}_{18}\text{O}_{49}$ . A very marked expansion of the cell volume, amounting to 4.5 %, parallels the increase in the lithium content as observed in other systems [ 11 ].

When  $\text{Li}_{40}\text{W}_{18}\text{O}_{49}$  is formed, the X-Ray diffraction shows a very poorly crystallized phase which cannot be related to the parent phase. This is not surprising if one recalls that this composition was obtained through an irreversible reaction. A strong structural rearrangement of the W-O framework is then expected to occur. The broad diffraction peaks preclude further studies of this phase.

The microstructural study performed by means of electron diffraction reveals other interesting features. For phase  $\text{Li}_5\text{W}_{18}\text{O}_{49}$  the results are in agreement with those obtained by X-Ray diffraction. On the contrary for  $\text{Li}_{17}\text{W}_{18}\text{O}_{49}$ , this is  $\sim 1:1$  Li/W ratio, the electron diffraction patterns ( two of which are shown in Figure 5 ) cannot be indexed using the cell obtained from the X-Ray pattern ( Table I ). However a satisfactory indexing can be achieved with a new cell, obtained by doubling lattice parameters  $a$ ,  $b$  and  $c$  of the original  $\text{W}_{18}\text{O}_{49}$  cell. This new cell with  $a = 36.822 \text{ \AA}$ ,  $b = 7.772 \text{ \AA}$ ,  $c = 28.328 \text{ \AA}$  and  $\beta = 115.4^\circ$  has then be used to index the patterns shown in Figure 5.

The appearance of a double cell is likely to be related to the ordering of lithium in some of the different tunnels. The location of the inserted lithium in the different phases is not easy to predict due to the large number of available sites. As reported for other PC type-phases [12], monovalent cations larger than lithium ( $\text{Na}^+$  or  $\text{K}^+$ ) can only be lodged into the hexagonal sites. Other studies [ 13 ], based on the study of mixed hexagonal lithium and potassium bronzes  $\text{Li}_x\text{K}_y\text{WO}_3$  indicated that small cations can be accommodated in the trigonal tunnels.

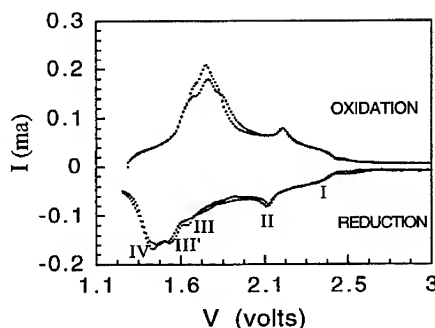


Figure 4.-Voltammogram of two consecutive discharge-charge cycles performed on  $\text{Li} / \text{W}_{18}\text{O}_{49}$ .

Table I. Lattice parameters of samples  $\text{Li}_x\text{W}_{18}\text{O}_{49}$ . All the parameters of lithiated samples are calculated on the basis of the  $\text{W}_{18}\text{O}_{49}$  unit cell.

	$a \text{ (}\text{\AA}\text{)}$	$b \text{ (}\text{\AA}\text{)}$	$c \text{ (}\text{\AA}\text{)}$	$\beta$	$V \text{ (}\text{\AA}^3\text{)}$	Color
$\text{W}_{18}\text{O}_{49}$	18.302(1)	3.7780(3)	14.014(1)	$115.205(2)^\circ$	876.8	violet
$\text{Li}_5\text{W}_{18}\text{O}_{49}$	18.387(4)	3.803(1)	14.061(3)	$115.27(2)^\circ$	889.0	dark red
$\text{Li}_{17}\text{W}_{18}\text{O}_{49}$	18.41(1)	3.886(2)	14.164(6)	$115.38(4)^\circ$	915.6	golden green

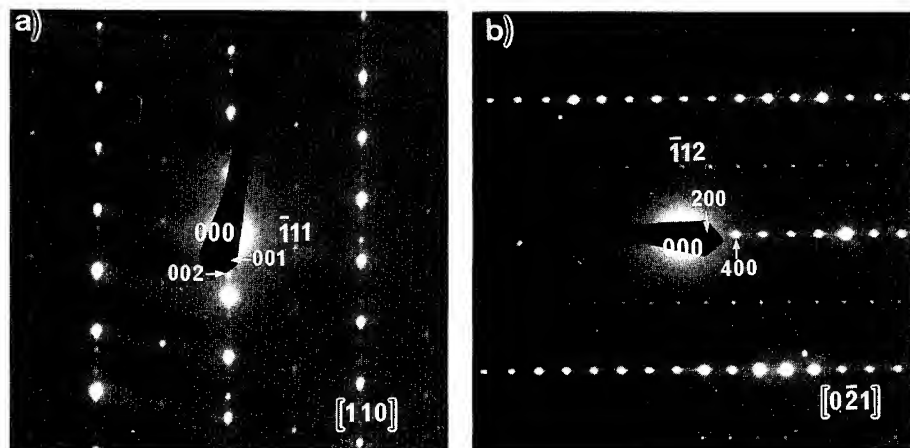


Figure 5.- Electron diffraction patterns of  $\text{Li}_{17}\text{W}_{18}\text{O}_{49}$  taken along a)  $[110]$  and b)  $[0\bar{2}1]$ . Both had to be indexed with a double cell ( $2a \times 2b \times 2c$ ) with respect to the corresponding to  $\text{W}_{18}\text{O}_{49}$ .

In the present case, with such a high degree of intercalation the situation could be similar. To study this we performed electrochemical insertion of sodium in  $\text{W}_{18}\text{O}_{49}$  using an electrochemical cell with the following configuration  $\text{Na} / \text{NaClO}_4 \text{ 1 M} + \text{PC} / \text{W}_{18}\text{O}_{49}$ . Figure 6 shows three consecutive charge-discharge cycles. It shows the existence of two single phases regions, labeled I and II:

- I :  $\text{Na}_{0.5}\text{W}_{18}\text{O}_{49} - \text{Na}_{0.57}\text{W}_{18}\text{O}_{49}$   
 II :  $\text{Na}_{0.84}\text{W}_{18}\text{O}_{49} - \text{Na}_{1.13}\text{W}_{18}\text{O}_{49}$

It should be appreciated that the quantity of inserted sodium is really small when compared with the lithium case, 1 to 22 atoms/cell. This seems to imply that due to its much smaller size ( for example for coordination VI  $r_{\text{Na}^+} = 1.02 \text{ \AA}$  and  $r_{\text{Li}^+} = 0.76 \text{ \AA}$  [ 14 ] ) lithium can also get into the smaller quadrangular and triangular tunnels existing in  $\text{W}_{18}\text{O}_{49}$  ( Figure 1 ).

Based on the actual data available we think that the ordering of lithium to form the highly lithiated phase  $\text{Li}_{17}\text{W}_{18}\text{O}_{49}$ , this is  $\sim 1:1$  Li/W ratio, is likely to be related to the occupancy of the smallest tunnels. Although we cannot proceed further at present with the structural characterization, a neutron diffraction experiment has been performed on  $\text{Li}_{17}\text{W}_{18}\text{O}_{49}$  and the data are being analyzed to determine the crystal structure.

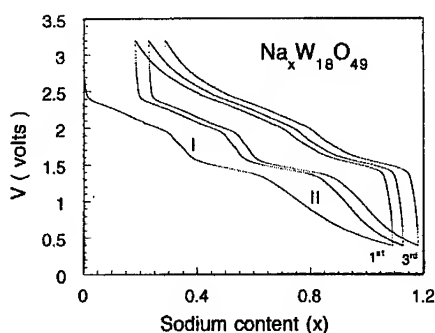


Figure 6.- Voltage - composition plot of a cell  $\text{Na} / \text{NaClO}_4 \text{ 1 M} + \text{PC} / \text{W}_{18}\text{O}_{49}$ . Three consecutive cycles are shown.

## CONCLUSIONS

During lithiation of  $W_{18}O_{49}$ , several single phase regions have been detected. These regions correspond to  $Li_xW_{18}O_{49}$  with  $x = 0-2$ ; 3.4-10; 11-15; 15.5-22 and 37-39.5. So the range of existence for  $Li_xW_{18}O_{49}$  corresponds to  $0 \leq x \leq 40$ . Nevertheless, only in the region between  $x = 0$  and  $x = 22$  are the phases formed by a reversible intercalation reaction.

Several compounds belonging to the single phase regions have been prepared. In some compounds the structural characterization indicates that lithium is occupying the tunnels of the  $W_{18}O_{49}$  structure in a disordered way. Nevertheless for a compound  $Li_{17}W_{18}O_{49}$ , which is a ~1:1 Li/W ratio, the situation is very different. Although the X-Ray diffraction only showed a shift of the peaks to lower angles, the electron diffraction data suggest the ordering of lithium in the tunnels. This produces the doubling of the unit cell, so that a new compound with the following cell parameters  $a = 36.822 \text{ \AA}$ ,  $b = 7.772 \text{ \AA}$ ,  $c = 28.328 \text{ \AA}$  and  $\beta = 115.4^\circ$  has been obtained.

When sodium is inserted in  $W_{18}O_{49}$  the situation is different and only 1.2 sodium can be inserted in the  $W_{18}O_{49}$  structure. This may be because, although lithium occupies all three types of tunnels, sodium is occupying only the largest tunnels.

## ACKNOWLEDGEMENTS

We would like to thank the " Centro de Microscopía Electrónica " ( UCM ) for technical assistance. We also thank CICYT ( SPAIN ) grant MAT92/0374 for financial support. One of us A.M.C. wants to thank CONACYT ( MEXICO ) for making possible the stay at Universidad Complutense.

## REFERENCES

1. R. Pickering and R.J.D. Tilley, *J. Solid State Chem.* **16**, 247 ( 1976 ).
2. J. Booth, T. Ekström, E. Iguchi and R.J.D. Tilley, *J. Solid State Chem.* **41**, 293 ( 1982 ).
3. L.A. Bursill, *J. Solid State Chem.* **48**, 256 ( 1983 ).
4. M.Lundberg, M.Sundberg and A. Magnéli, *J. Solid State Chem.* **44**, 32 ( 1982 ).
5. A. Magnéli, *Ark. Kemi* **1**, 213 ( 1949 ).
6. Kent H. Cheng and M. Stanley Whittingham, *Solid State Ionics* **1**, 151 ( 1980 ).
7. S.A. Kay, D. Phil. Thesis, University of Oxford ( 1986 ).
8. C. Rosique-Pérez, J. González- Calbet, M. Vallet-Regí and M.A. Alario-Franco, *J. Solid State Chem.* **76**, 313 (1988 ).
9. J.M.Tarascon, *J. Electrochem. Soc.*, **132**, 2089 ( 1985 ).
10. D. Guyomard and J.M.Tarascon, *J. Electrochem. Soc.* **139**, 937 (1992 ).
11. F. García-Alvarado, J.M.Tarascon and B.Wilkens, *J.Electrochem. Soc.* **139**, 3206 ( 1992 ).
12. K.H.Cheng, A.J.Jacobson and M.S.Whittingham, *Solid State Ionics* **5**, 355 ( 1981 ).
13. E.Banks and A.Goldstein, *Inorg. Chem.* **7**, 967 ( 1968 ).
14. R.D.Shannon, *Acta Cryst. A* **32**, 751 ( 1976 ).

## Properties of a Carbon Negative Electrode in Completely Inorganic Thin Film Li-Ion Batteries with a $\text{LiCoO}_2$ Positive Electrode

R.B.Goldner, S.Slaven, T.Y.Liu, T.E.Haas, F.O.Armzt, and P.Zerigian  
Tufts University, Electro-Optics Technology Center, Medford, MA 02155

### Abstract

Completely inorganic thin film lithium ion battery cells have been prepared by vapor deposition processes (vacuum evaporation and sputtering). The negative and positive electrodes were films of disordered carbon and lithium cobalt oxide, respectively. The results of battery charging/discharging and other measurements (e.g., in-situ lithium chemical diffusion constant measurements for the carbon films) indicate that disordered carbon films have a relatively high reversible charge capacity, ( $> 160 \text{ mC/cm}^2\text{-}\mu\text{m}$ , and possibly higher than  $360 \text{ mC/cm}^2\text{-}\mu\text{m}$ , or  $> 296$  and possibly  $667 \text{ mAh/g}$ , respectively, assuming the measured film density of  $1.5 \text{ g/cm}^3$ ), and a lithium chemical diffusion constant at room temperature  $\approx 10^{-9} \text{ cm}^2/\text{s}$ . These results suggest that disordered carbon films should be good substitutes for metallic lithium in thin film rechargeable batteries.

### Introduction

Currently, there exists a need for stable and affordable high energy and power density batteries for portable electrical and electronic equipment, and most importantly for powering electrical vehicles and for electrical power load leveling. Lithium-ion rocking-chair cells, that employ completely inorganic thin films, including thin film high voltage transition metal oxide positive electrodes (cathodes) are attractive candidates for rechargeable batteries. This is for several reasons among which are: (i) their potentially high energy and power densities (gravimetric and volumetric); (ii) the high probability for economically producing sequentially deposited bipolar stacks of series-connected cells, and thereby obtaining relatively high voltage batteries; and (iii) their potential to be stable for thousands of deep charge-discharge cycles, especially because of the proven or anticipated wide electrochemical stability range for thin film inorganic electrolytes [1,2].

For reasons of safety, materials availability, and practical manufacturing, it is desirable to use an insertion anode (negative electrode) rather than lithium metal. Carbon appears to be a good candidate. There are already available commercially  $\text{LiCoO}_2$  (cathode)/C (anode) bulk rechargeable batteries [3] and, recently, it has been reported that a type of bulk disordered carbon has a relatively high charge capacity (approximately  $680 \text{ mAh/g}$  or  $550 \text{ mC/cm}^2\text{-}\mu\text{m}$ , assuming a bulk density of  $2.25 \text{ g/cm}^3$ ) [4,5].

This paper is essentially a work-in-progress report on some of the properties of thin films of disordered carbon as employed in rocking-chair cells using a  $\text{LiCoO}_2$  cathode. Although other  $\text{LiMO}_2$  compounds ( $M = \text{one or more of the several 3d transition metals}$ ) are strong contenders for the cathode,  $\text{LiCoO}_2$  was chosen because of its being used commercially and because of our prior experience with it in electrochromic window cells [6]. The results to date suggest that disordered carbon films should be considered as good substitutes for lithium metal anodes in thin film batteries.

## **Experimental Details**

Lithium cobalt oxide (nominally  $\text{LiCoO}_2$ ) films were prepared by rf sputtering. The deposition conditions were: 5 inch diameter target of stoichiometric  $\text{LiCoO}_2$ , rf (13.56 MHz) power = 100 Watts, oxygen pressure = 10 mT, substrate to target distance = 7 cm, deposition rate = 130 nm/hr, and the substrates were at ambient temperature. The films were "Xray amorphous" and their density was approximately 3.7, as determined by a quartz crystal oscillator microbalance (mass) and a profilometer (thickness).

The electrolyte generally used was lithium phosphorous oxynitride (Lipon) [1]. It was prepared by reactive rf magnetron sputtering from a 2 inch target of  $\text{Li}_3\text{PO}_4$  in a nitrogen atmosphere. The deposition conditions were: rf power was either 100 Watts or 150 Watts, nitrogen pressure = 15 mT, substrate to target distance = 15 cm, deposition rate (@ 150 Watts)  $\approx$  75 nm/hr, and the substrates were at ambient temperature. The refractive index of the films was approximately 1.6 and their thicknesses were determined by both optical interference and profilometry measurements.

The carbon films were deposited by a controlled dc anodic arc process. Graphite electrodes were used for the anode and cathode, and the depositions were carried out in vacuum (pressure  $< 2 \times 10^{-5}$  Torr). The anode was machined from a high purity rod of graphite, with its evaporation end diameter = 2.5 mm; and the cathode was a dome shaped graphite rod of 2.5 cm diameter. The depositions were made using a dc lamp supply. The current was generally 35 A and the voltage was 20 V. The estimated current density at the anode during depositions was  $> 1000 \text{ A/cm}^2$ . Deposition rates exceeded 140 nm/s for substrate-anode distances of 5 cm and 35 nm/s for a 10 cm distance. The carbon film density was approximately 1.5, again determined by a quartz crystal oscillator microbalance (mass) and a profilometer (thickness). The films were nearly "Xray amorphous", with a broad peak at  $2\theta = 23^\circ$  and a much smaller one at  $42^\circ$  (Figure 1), similar to that reported recently for bulk disordered carbon [5]; and they exhibited a predominance of  $\text{sp}^2$  bonding as determined from Raman spectroscopy.

Metal films (Cr, Cu, Al, TiN) were deposited by thermal evaporation - either by electron beam heating (TiN) or by electrically heating a refractory metal boat (Cr, Cu, Al) - or by sputtering (TiN).

Three types of cells were prepared, but all three types were fabricated by sequential vacuum depositions, resulting in the structure: [(glass substrate)/(cathode metal current collector)/(positive electrode)/(electrolyte)/(negative electrode = carbon)/(anode metal current collector)]; and some cells were further sealed with a dielectric layer. The order of the depositions was purposely chosen to provide discharged cells and to avoid the problem of removing lithium from the carbon films before the  $\text{LiCoO}_2$  deposition.

One type of cell, Type 1, employed a Tufts  $\text{LiCoO}_2$  cathode followed by approximately 100 nm of sputter deposited  $\text{LiNbO}_3$  and then was sent to Eveready for completion by depositing their lithium oxy-sulfide electrolyte and a lithium metal anode. Characterizations were then done at Eveready in a controlled atmosphere chamber. Type 2 cells were basically the same as type 3 as regards composition - i.e., both were [(metal)/( $\text{LiCoO}_2$ )/(Lipon)/(C)/(metal)] cells. The major difference between the two types were that type 2 had unequal area electrodes, with the carbon electrodes being considerably smaller in area; this allowed us to deposit many anodes at once and insure that at least one cell was not shorted as a result of pinholes in the electrolyte.

Several type 3 cells employed secondary reference electrodes which were freshly deposited carbon layers on the Lipon electrolyte where it was covering only the glass substrate.

The carbon reference electrode was calibrated by measuring its potential ( $\approx +2.1$  V) vs freshly deposited Li.

### Measurements and Results

Shown in Table 1 is a summary of results from some of the measurements that were performed on  $\text{LiCoO}_2$  and carbon films. Some of the measurements were done on metal/electrode bilayers. Others were done in-situ, using type 2 or type 3 cells.

For reference potential measurements, a battery-powered electrometer, (Keithley 602, with input resistance  $\approx 10^{14} \Omega$ ), operating in a guarded mode, was utilized. The guarded mode allowed for stable, fast transient measurements). Galvanostatic and potentiostatic measurements were generally done using an EG&G PAR 263 potentiostat with computer control and data acquisition.

The chemical diffusion coefficient ( $\tilde{D}_{\text{Li}}$ ) measurements for  $\text{LiCoO}_2$  were made on bilayers in a wet cell using a non-aqueous electrolyte (lithium perchlorate in ethylene carbonate/propylene carbonate), and were done in-situ in the cells for carbon. Transient techniques similar to the GITT method [7,8] were utilized. In the case of carbon, an alternative technique was utilized: following a long low current charging/discharging current pulse (to obtain a quasi-equilibrium state of charge), a shorter but much higher current pulse was applied (short compared to the diffusion time,  $t_d \approx L_d^2/\tilde{D}_{\text{Li}}$ ,  $L_d$  = electrode thickness). For times shorter than  $t_d$  the electrode potential (relative to a reference electrode) should decay as  $t^{-0.5}$ , and for times  $\geq t_d$  it should decay as  $t^m$ , where  $m < 0.5$ , since the excess  $\text{Li}^+$  "reflects" from the electrode/metal boundary, slowing down the diffusion away from the electrode/electrolyte boundary. Thus, by monitoring the logarithm of the potential vs the logarithm of the time, one obtains a direct measure of  $t_d$ , namely where there is a breakpoint in the slope of the plot. This is illustrated in Figure 2. There is a breakpoint in the slope at approximately 220 ms after the onset of the pulse. The carbon layer was approximately 150 nm thick and therefore  $\tilde{D}_{\text{Li}} \approx 3 \times 10^{-10} \text{ cm}^2/\text{s}$ .

Type 1 cells ( $\text{LiCoO}_2/\text{Li}$ ) were used to obtain independent charging/discharging measurements for  $\text{LiCoO}_2$ . Out of 250 cycles, during the first 25 cycles plus during four other sets of 3 to 5 consecutive cycles, or during a total of 40 cycles, the  $\text{LiCoO}_2$  films exhibited reversible charging/discharging of approximately 6  $\mu\text{Ah}$ . Cycles 5, 6, and 7 are shown in Figure 3. The films were approximately 110 nm thick and the cell area was 1  $\text{cm}^2$ . The reversible charge capacity therefore corresponded to  $> 190 \text{ mC}/\text{cm}^2\text{-}\mu\text{m}$ , or assuming a density of  $3.7 \text{ g}/\text{cm}^3$  the capacity was  $> 140 \text{ mAh}/\text{g}$ .

Several type 2 cells ( $\text{LiCoO}_2/\text{C}$ ) had their electrolyte layer deposited under less energetic conditions than for type 3 cells (also  $\text{LiCoO}_2/\text{C}$ ). The second discharge and third charge half cycles are shown for one of the type 2 cells in Figure 4. The data were taken using a charging current density of  $1 \mu\text{A}/\text{cm}^2$ . The area of the carbon electrode was  $0.05 \text{ cm}^2$  and its thickness was between 180 and 280 nm. Using the latter thickness, the reversible charge capacity was  $> 160 \text{ mC}/\text{cm}^2\text{-}\mu\text{m}$  ( $> 295 \text{ mAh}/\text{g}$  for a density of  $1.5 \text{ g}/\text{cm}^3$ ), and for the former thickness, it was  $> 250 \text{ mC}/\text{cm}^2\text{-}\mu\text{m}$  ( $> 460 \text{ mAh}/\text{g}$  for a density of  $1.5 \text{ g}/\text{cm}^3$ ). Several type 2 and type 3 cells exhibited short circuit current densities  $> 1.0 \text{ mA}/\text{cm}^2$ , and on more than one occasion  $> 1.5 \text{ mA}/\text{cm}^2$ . The short circuit current density for one type 3 cell was  $> 500 \mu\text{A}/\text{cm}^2$  for longer than 5 seconds. These short circuit tests were done with charged cells open circuit potentials  $\geq 3 \text{ V}$ . One type 2 cell was first charged to  $400 \text{ mC}/\text{cm}^2\text{-}\mu\text{m}$  and  $360 \text{ mC}/\text{cm}^2\text{-}\mu\text{m}$  could be removed, but only with

Property	Lithium	Cobalt Oxide	Carbon	Measurement(s)
Li diffusion coefficient $\tilde{D}_L, (\text{cm}^2/\text{s})$	$\approx 10^{-12} - 10^{-11}$ (in bi-layer)		$\approx 10^{-10}$ or greater (in cell)	Transient
Charge capacity ( $\text{mC}/\text{cm}^2\text{-}\mu\text{m}$ )	$> 190$		$> 160$ (possibly $> 360$ )	$V(q)$ (galvanostatic)
Mass density ( $\text{g}/\text{cm}^3$ )	$\approx 3.7$		$\approx 1.5$	Quartz oscillator-mass Profilmeter-thick
$V(q)$ (V vs Li)	2.2 to 4.2 (type 1 cell)		$< 0.5$ to $> 2.0$ (cells)	3Galvanostat/Potentiostat Electrometer
Structure	Xray "amorphous"		$2\theta$ peaks @ $23^\circ$ & $42^\circ$ , with $\text{sp}^2$ bonding	Xray diffraction & Raman (for C)
Stress/Stress Change (GPa)	-3/less compressive ( $\approx +2$ ) with $[\text{Li}]\downarrow$		-0.8/changes not yet measured	Substrate curvature
$J_{sc}$ ( $\text{mA}/\text{cm}^2$ )	$\approx 1.5$		$\approx 1.5$	Cell @ $V_{oc} \approx 3.3\text{V}$

Table 1. Summary of some measured properties of films used in this study.



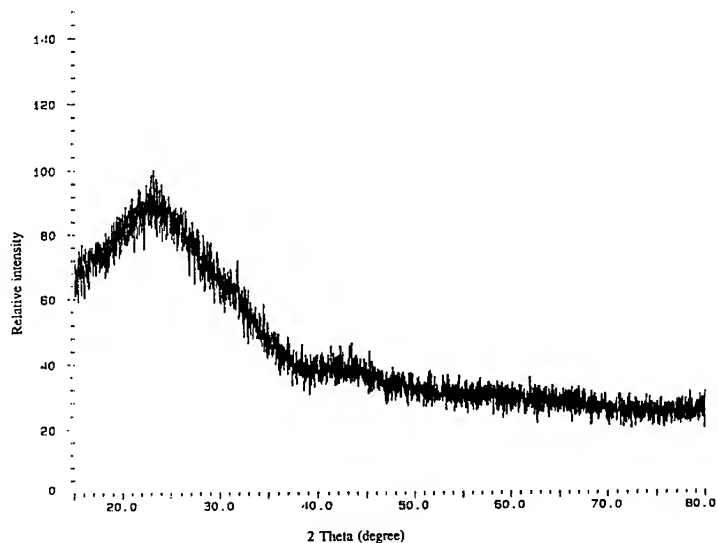


Figure 1. X-ray diffraction pattern (Cu target) for carbon film deposited by anodic arc deposition process.

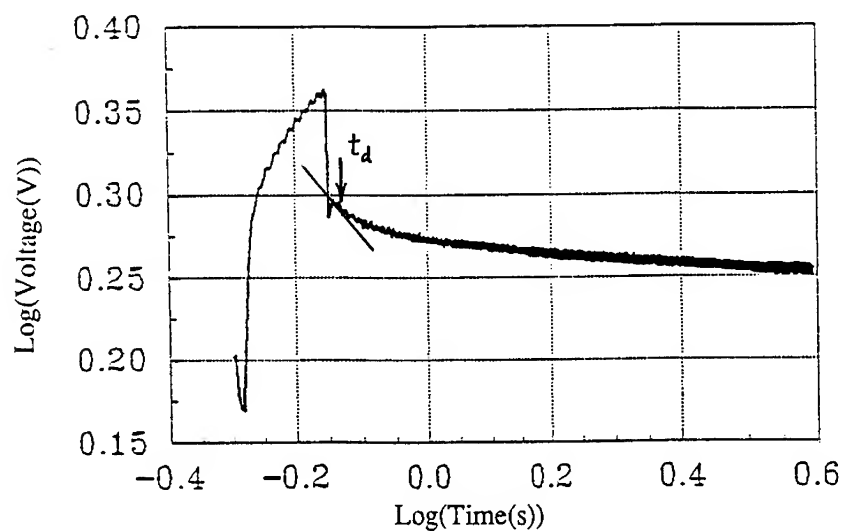


Figure 2. Carbon layer transient voltage compared to a carbon secondary reference electrode potential during and following a  $50 \mu\text{A}$  current pulse (of approximately 178 ms duration). Note the breakpoint in slope from  $-0.5$  to  $-m$  ( $m < 0.5$ ) at approximately 220 ms. Therefore,  $t_{\text{diffusion}} \approx 220 \text{ ms}$ , and since the layer is approximately 150 nm thick, the diffusion coefficient is approximately  $10^{-9} \text{ cm}^2/\text{s}$ .

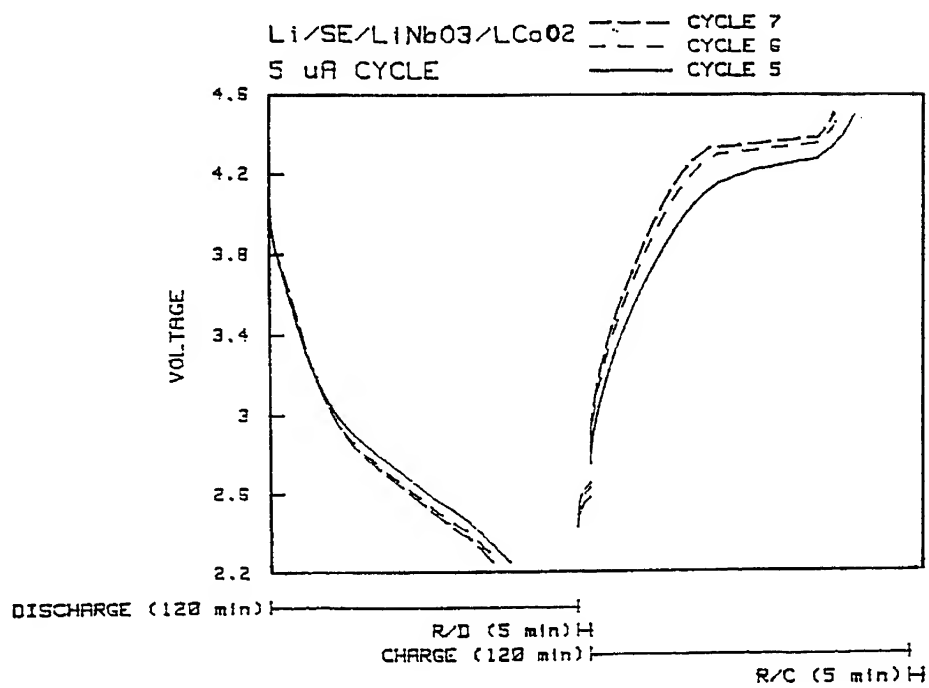
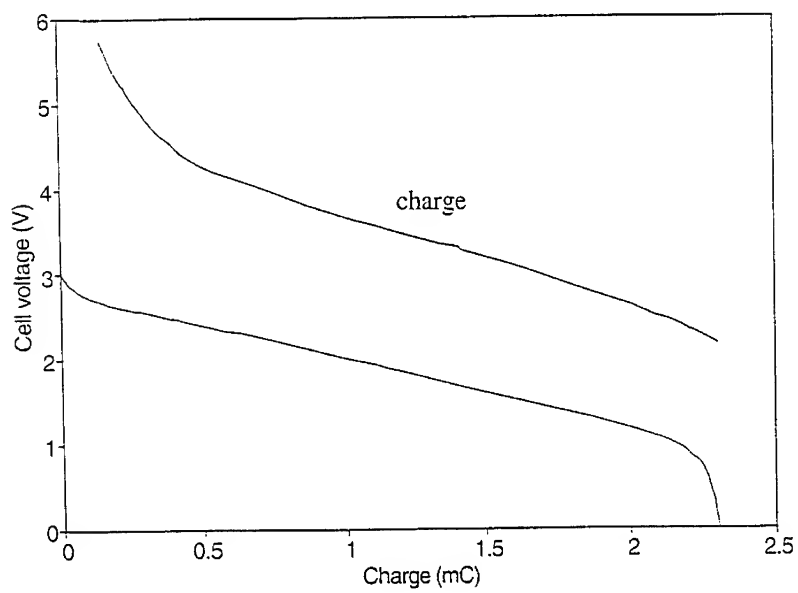


Figure 3. Charge and discharge cycles 5-7 for a type 1 cell (LiCoO<sub>2</sub>/solid electrolyte/Li). Area = 1 cm<sup>2</sup>. LiCoO<sub>2</sub> thickness  $\approx$  110 nm. Current density = 5  $\mu$ A/cm<sup>2</sup>.



**Figure 4.** Third charge-discharge cycle for a type 2 cell ( $\text{LiCoO}_2/\text{Lipon}/\text{C}$ ). C electrode area =  $0.05 \text{ cm}^2$ . Carbon layer thickness between 180 and 280 nm. Current density =  $1 \mu\text{A}/\text{cm}^2$ .

a high discharging voltage. On the second charge  $360 \text{ mC/cm}^2\text{-}\mu\text{m}$  could be reinserted into the carbon layer. This corresponds to a reversible charge capacity of  $> 660 \text{ mAh/g}$  assuming the measured density of  $1.5 \text{ g/cm}^3$  for the carbon films.

On a number of occasions large stress changes that occurred during charging/discharging led to stress-relief cracking of the top metal film. In previous studies of  $\text{LiCoO}_2$  films, we have measured changes of stress due to changes in lithiation as large as 2 to 4 GPa. As-deposited films generally exhibited an internal stress of approximately -2 GPa (compressive), and upon delithiation the stress became more tensile, sometimes reaching +2 GPa. To date only as-deposited stress measurements have been made on carbon films, and they exhibit a (compressive) stress of approximately -0.8 GPa. The internal stress measurements were made on films that were deposited on thin cover glass substrates, using an optical technique [9] to determine the induced substrate curvature.

#### **Further Discussion and Conclusions**

Although more research is needed on cells employing carbon film anodes and  $\text{LiMO}_2$  film cathodes ( $M = 3d$  transition metal(s)), the results to date suggest the following conclusions:

(i) The electrolyte deposition process probably adversely affects the kinetics of  $\text{LiCoO}_2/\text{C}$  cells. This is likely due to the formation of a very low electron and lithium ion conductivity region either within the  $\text{LiCoO}_2$  layer itself and/or between it and the electrolyte. This appears to be a process parameter effect, (principally sputter power density), and not an intrinsic  $\text{LiCoO}_2$  effect. The evidence for this is the difference between the charging/discharging behavior of type 3 cells (poor kinetics - very high overpotentials on discharge) compared to type 1 and 2 cells, both of which had a buffer electrolyte layer (100 nm of  $\text{LiNbO}_3$  for the type 1 cells and approximately 200 nm of a 100 W Lipon for the type 2 cells). One might speculate that there is a plasma induced reaction between Lipon and  $\text{LiCoO}_2$  which affects the transition region. This needs to be investigated further.

(ii) The electrolyte deposition also appears to cause a change in the density of states and/or a heavy lithiation (chemical reduction) of the underlying  $\text{LiCoO}_2$  layer since the chemical potential of the  $\text{LiCoO}_2$  is lowered considerably, from being  $> 2.5$  to 3.5 Volts (vs Li) for as-deposited films to  $< 2$  Volts after the electrolyte deposition. This may be directly associated with item (i), although the chemical potential has been found to be relatively low (2 to 2.5 V) for  $\text{LiCoO}_2$  in as-deposited type 2 cells, yet they exhibited satisfactory room temperature kinetics. This, too, is very likely a process parameter effect, associated with changes in the microstructure of disordered  $\text{LiCoO}_2$ .

(iii) In addition to items (i) and (ii), the high overpotentials associated with discharging some types 2 and 3 cells, and the origin of the often observed loss of first charge capacity in disordered carbon, might be due to difficulty with ionizing covalent lithium,  $\text{Li}_2$ , which Sato et al. proposed as being stored between carbon planes and thus served as the source of the high charge capacity they observed for their disordered carbon [4]. Alternatively, atomic or molecular lithium might be strongly bonding to carbon atoms at the ends of carbon planes that had been separated during lithium ion intercalation. It is also conceivable that some of the lithium in the carbon half cell might be irreversibly lost during the first charging by chemical reactions (e.g., by oxidation or alloying with the metal current collectors).

(iv) The carbon films are quite rough. Scanning tunneling microscope (STM) images of the films (Figure 5) indicate a peak to peak roughness of approximately 30nm with an rms

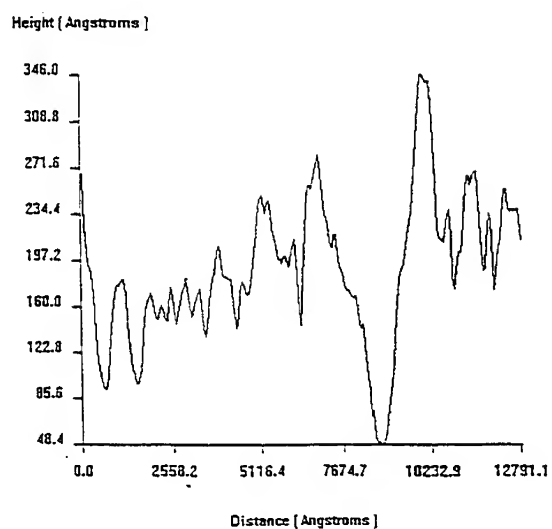
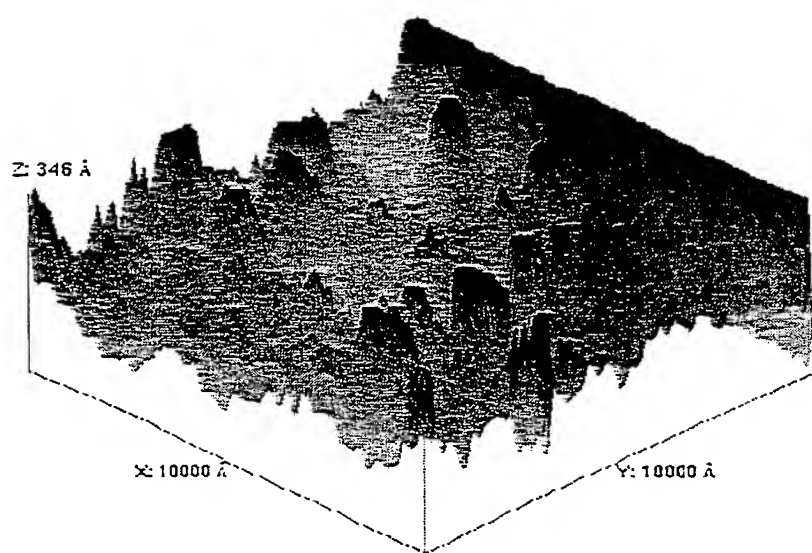


**Figure 5.** Scanning tunneling microscope image of anodic-arc deposited carbon film with diagonal cross-section. This image was obtained with a Burleigh Personal STM, using a Pt-Ir probe.

a high discharging voltage. On the second charge 360 mC/cm<sup>2</sup>-μm could be reinserted into the carbon layer. This corresponds to a reversible charge capacity of > 660 mAh/g assuming the measured density of 1.5 g/cm<sup>3</sup> for the carbon films.

On a number of occasions large stress changes that occurred during charging/discharging led to stress-relief cracking of the top metal film. In previous studies of LiCoO<sub>2</sub> films, we have measured changes of stress due to changes in lithiation as large as 2 to 4 GPa. As-deposited films generally exhibited an internal stress of approximately -2 GPa (compressive), and upon delithiation the stress became more tensile, sometimes reaching +2 GPa. To date only as-deposited stress measurements have been made on carbon films, and they exhibit a (compressive) stress of approximately -0.8 GPa. The internal stress measurements were made on films that were deposited on thin cover glass substrates, using an optical technique [9] to determine the induced substrate curvature.

#### **Further Discussion and Conclusions**

Although more research is needed on cells employing carbon film anodes and LiMO<sub>2</sub> film cathodes (M = 3d transition metal(s)), the results to date suggest the following conclusions:

(i) The electrolyte deposition process probably adversely affects the kinetics of LiCoO<sub>2</sub>/C cells. This is likely due to the formation of a very low electron and lithium ion conductivity region either within the LiCoO<sub>2</sub> layer itself and/or between it and the electrolyte. This appears to be a process parameter effect, (principally sputter power density), and not an intrinsic LiCoO<sub>2</sub> effect. The evidence for this is the difference between the charging/discharging behavior of type 3 cells (poor kinetics - very high overpotentials on discharge) compared to type 1 and 2 cells, both of which had a buffer electrolyte layer (100 nm of LiNbO<sub>3</sub> for the type 1 cells and approximately 200 nm of a 100 W Lipon for the type 2 cells). One might speculate that there is a plasma induced reaction between Lipon and LiCoO<sub>2</sub> which affects the transition region. This needs to be investigated further.

(ii) The electrolyte deposition also appears to cause a change in the density of states and/or a heavy lithiation (chemical reduction) of the underlying LiCoO<sub>2</sub> layer since the chemical potential of the LiCoO<sub>2</sub> is lowered considerably, from being > 2.5 to 3.5 Volts (vs Li) for as-deposited films to < 2 Volts after the electrolyte deposition. This may be directly associated with item (i), although the chemical potential has been found to be relatively low (2 to 2.5 V) for LiCoO<sub>2</sub> in as-deposited type 2 cells, yet they exhibited satisfactory room temperature kinetics. This, too, is very likely a process parameter effect, associated with changes in the microstructure of disordered LiCoO<sub>2</sub>.

(iii) In addition to items (i) and (ii), the high overpotentials associated with discharging some types 2 and 3 cells, and the origin of the often observed loss of first charge capacity in disordered carbon, might be due to difficulty with ionizing covalent lithium, Li<sub>2</sub>, which Sato et al. proposed as being stored between carbon planes and thus served as the source of the high charge capacity they observed for their disordered carbon [4]. It is also conceivable that some of the lithium in the carbon half cell might be irreversibly lost during the first charging by chemical reactions (e.g., by oxidation or alloying with the metal current collectors).

(iv) The carbon films are quite rough. Scanning tunneling microscope (STM) images of the films (Figure 5) indicate a peak to peak roughness of approximately 30nm with an rms roughness approximately 4-5 nm. Such roughness could adversely affect the integrity of subsequent sequentially deposited cells (especially as regards obtaining shorts-free electrolyte

layers) in high voltage batteries. Hence, for such batteries, it will be important to modify the deposition process so as to yield low roughness carbon layers.

(v) The reversible charge capacity of both  $\text{LiCoO}_2$  films ( $>190 \text{ mC/cm}^2\text{-}\mu\text{m}$ ) and C films, ( $>160 \text{ mC/cm}^2\text{-}\mu\text{m}$  and possibly  $> 360 \text{ mC/cm}^2\text{-}\mu\text{m}$ ), are satisfactory for high energy and power density batteries. However, there might be a significant amount of relatively low activity lithium in the carbon films, which could account for the high overpotential discharge characteristics of the cell which exhibited a reversible charge capacity of  $360 \text{ mC/cm}^2\text{-}\mu\text{m}$ .

(vi) Disordered carbon films have a useful lithium diffusion coefficient ( $\approx 10^{-9} \text{ cm}^2/\text{s}$ ) possibly because of orientational disorder (random orientation of transport planes); and this coupled with their apparently high charge capacity, their relatively low charge state voltage ( $< 0.5 \text{ V}$  vs lithium metal), the ready availability of carbon, and the relative ease with which one can rapidly and economically deposit them, make such films very attractive candidates for thin film anodes in rocking chair cells that employ  $\text{LiMO}_2$  cathodes ( $M = 3d$  transition metal, such as Co).

#### Acknowledgments

The authors should like to gratefully acknowledge the assistance of their colleagues at Tufts, including: D.Calef, K.Dickson, A.Gerouki, N.Tkachenko, S.Verma and K.Zhang. They should like to thank S.Jones and S. Humphreys of Eveready for valuable discussions and particularly the completion of and measurements on the type 1 cells; and they should like to acknowledge useful discussions with J.Bates and N.Dudney of Oak Ridge National Laboratory, with I.Licis of the E.P.A., and with A.Nazri of General Motors. This work has been supported, in part, by grants from DOE: DE-FG03-85SF15927 (Sec'y for Conservation & Renewable Energy) and DE-FG02-93ER14377 (Office of Basic Energy Sciences); and from Tufts Center for Environmental Management and the U.S. Environmental Protection Agency.

#### References

1. J.B.Bates, G.R.Gruzalski, N.J.Dudney, C.F.Luck, X.H.Yu, and S.D.Jones, *Solid State Technology*, p.59 (July 1993); and J.B.Bates, G.R.Gruzalski, N.J.Dudney, C.F.Luck, and X.Yu, *Solid State Ionics*, **70/71**, 619 (1994).
2. S.D.Jones and J.R.Akridge, *Solid State Ionics*, **53-56**, 628 (1992).
3. K.Ozawa and M.Yokokawa, 10th Intl. Seminar on Primary and Secondary Battery Technology and Application, Deerfield Beach, Florida (March 1993).
4. K.Sato, M.Noguchi, A.Demachi, N.Oki, and M.Endo, *Science* **264**, 556 (22 April 1994).
5. M.Alamgir, Q.Zuo, and K.M.Abraham, *J.Electrochem.Soc.* **141**, L143 (1994).
6. R.B.Goldner, F.O.Arntz, K.Dickson, M.A.Goldner, T.E.Haas, T.Y.Liu, S.Slaven, G.Wei, K.K.Wong, and P.Zerigian, *Solid State Ionics* **70/71**, 613 (1992).
7. W.Weppner and R.A.Huggins, *J.Electrochem.Soc.* **124**, 1569 (1977).
8. C.Julien and C.A.Nazri, *Solid State Batteries: Materials Design and Optimization*, Kluwer Academic Publishers, Boston (1994).
9. T.Aoki, Y.Nishikawa, and S.Kato, *Jap.J.Appl.Phys.* **28**, 299(1989).

## CHEMISTRY OF ELECTROCHROMIC IrO<sub>x</sub> FILMS DEPOSITED UNDER VARIABLE REDOX CONDITIONS

J. D. KLEIN AND S. L. CLAUSON  
EIC Laboratories, Norwood, MA 02062

### ABSTRACT

A thin film deposition technique is described whereby the oxidation condition of as-deposited iridium oxide thin films can be manipulated by varying deposition conditions. Iridium oxide thin films were deposited by reactive rf magnetron sputtering in a H<sub>2</sub>/O<sub>2</sub>/Ar gas blend. Optical emission spectroscopy, an *in-situ* process monitor, was employed to observe redox interactions in the deposition plasma. The plasma spectra exhibited characteristics normally observed in hydrogen flame spectroscopy. A competitive redox balance was found to exist between atomic O and atomic H emissions. Plasma redox conditions defined by the H-O emissions could be accessed by a variety of gas flow conditions. Electrochemical aspects of the IrO<sub>x</sub> films were examined by cyclic voltammetry. Electrochromic capabilities were demonstrated through optical transmittance.

### INTRODUCTION

Electrochemically active films can be more readily integrated into devices if they can be deposited within thin film stacks. If such a thin film device is to be completed *in vacuo*, the charge state of the constituent layers or at least that of the overall device must be determined by the deposition process. Iridium oxide thin films are employed in several electrochemical applications such as charge injection electrodes for neural stimulation [1] and optical switching layers in electrochromic devices [2]. The electrochemical properties of iridium oxide are sensitive to deposition conditions. Traditionally, a "wet" process using water additions has been employed to obtain the desired film properties [3,4]. However, the range of conditions afforded by such a technique is quite limited. The development of a "dry" process based on a H<sub>2</sub>/O<sub>2</sub> redox environment enhances process stability and extends the range of available properties. This is particularly true if the deposition technique provides sufficient latitude to accurately and consistently set the oxidation condition of the IrO<sub>x</sub> thin film.

Chemical reactions between oxygen and hydrogen are commonly discussed in the context of either a hydrogen flame [5,6] or an explosion vessel [7,8]. The operation of a sputter source in a continuously pumped chamber does not correspond exactly to either case. While the inlet gas blend is continuously fed to the combustion site as in the case of a hydrogen flame, the chamber walls may play an important role in reaction chain termination as in the case of explosions in sealed vessels. The discussion of a steady-state process such as magnetron sputtering requires consideration of the balance between chain propagating and chain terminating reactions. The chain propagation and branching steps are considered to be





in the discussion of explosion limits [7]. The three reactions provide a continuously branching chain. Avoidance of an explosion requires chain terminating reactions to consume free radicals such as O, H, and OH. One possible gas phase reaction is



where M denotes any third molecule that stabilizes the formation of  $HO_2$  [8]. Reaction 4 is chain terminating if  $HO_2$  is sufficiently stable to diffuse to the chamber wall for destruction. In addition, there will be other reactions leading to chain termination through conversion of O, H, and OH to stable species at the chamber wall [7]. Several additional reactions are possible if the water produced by these reactions accumulates in the chamber. In the present case of reactive sputter deposition from a metal target, reactions leading to the formation of the oxide film will also occur.

#### VARIABLE REDOX FILM DEPOSITION

All  $IrO_2$  sputter runs were performed in a Microscience IBEX-2000 deposition chamber evacuated by a cryopump after roughing by a mechanical pump. The commercially obtained 6.35 cm diameter Ir metal target was sputtered from an Ion Tech, Ltd. planar magnetron source at a pressure of 40 mTorr. The twelve  $H_2/O_2/Ar$  inlet gas flow conditions shown in Figure 1 were selected to reveal the effects of  $H_2$  and  $O_2$  flow variations. A rf power of 100 watts was applied at each sputter condition. The acquisition of  $IrO_x$  emission spectra was facilitated by a fiber optic cable, an Acton Research Spectra-Pro 275 spectrograph, and an EG&G Princeton Applied Research 1460/1463 diode array spectrophotometer. A collimator fitted to the collection end of the fiber optic cable allowed viewing of the sputter plasma through a quartz window of the deposition chamber.

One intent of the experiment was the definition of a "dry"  $H_2/O_2$  process to replace the "wet"  $H_2O$ -based deposition protocol previously employed. Three species were deemed essential to the examination of the  $H_2/O_2$  redox environment. Atomic

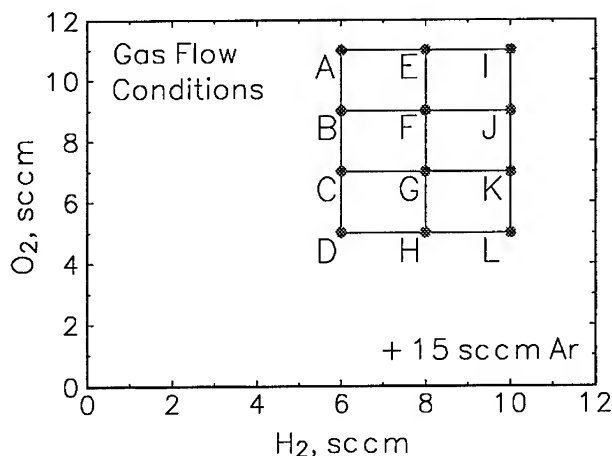


Fig. 1. Twelve  $Ar/H_2/O_2$  gas flow conditions used to reactively rf sputter an Ir metal target.

hydrogen was monitored by the 656.3 nm H I peak [10]. Atomic oxygen exhibits one readily observable peak, the 777 nm O I multiline peak. Since the  $O_2/H_2$  sputter plasma is in many ways a hydrogen flame, the spectra are similar to those observed in flame spectroscopy. In particular, the 306.4 nm molecular OH  $A^2\Sigma^+ - X^2\Pi$  band system [11] was evident whenever both  $O_2$  and  $H_2$  were present. Emission intensities noted are integrations with respect to wavelength of the chosen emission peaks normalized for detector exposure time. The emission characteristics of the reactive sputter plasma are dramatic in their simplicity. The intensity of the atomic O peak as a function of atomic H emission intensity is shown in Figure 2a.

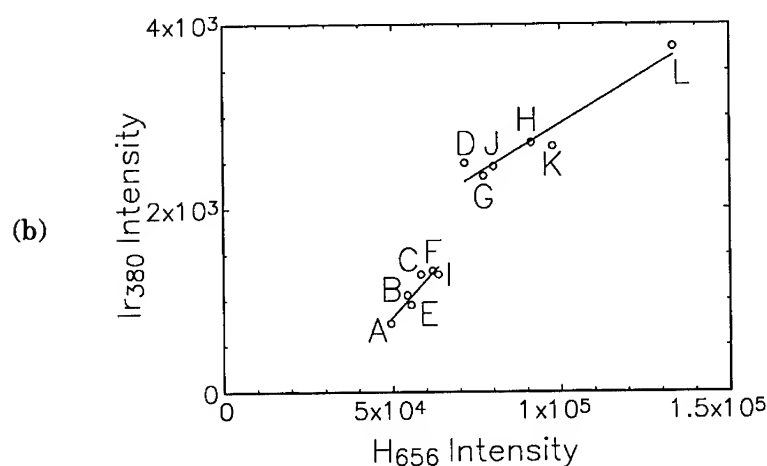
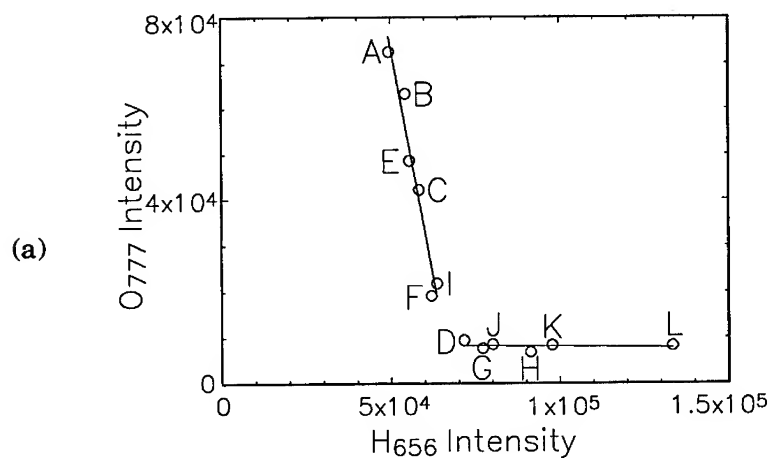


Fig. 2. Reactive  $IrO_2$  sputter conditions are shown in (a) H-O and (b) H-Ir emission intensity spaces.

All twelve deposition conditions fall on either of two lines in H-O emission space. The nearly vertical line defines a "lean" redox path in which O I emission drops rapidly with respect to increasing H I intensity. The horizontal line represents a "rich" path in which significant variations in H I intensity are observed with low O I emissions. The most important implication is that the redox characteristics are set by a tradeoff between  $H_2$  and  $O_2$  flows. The fact that similar plasma redox characteristics were obtained by more than one condition suggest that any observed redox point can be achieved by many different flow combinations.

The lean-rich transition evident in the oxygen-hydrogen emission tradeoffs has implications for the sputter target. Atomic Ir emission lines were identified, one at 351.364 and another at 380.012 nm [9]. The variation of Ir I emission intensity with respect to atomic H I emission intensity is shown in Figure 2b. Ir emissions increased as the plasma conditions became more reducing. However, a discontinuity is apparent at the same point at which the oxidizing-to-reducing shift occurs in the oxygen-hydrogen data of Figure 2a. It is suggested that the jump in Ir emissions is due to removal of oxide from the racetrack of the target and an associated increase in Ir sputter rate.

#### IrO<sub>x</sub> FILM PROPERTIES

Samples for electrochemistry were prepared by depositing iridium oxide atop ITO-coated Corning 7059 glass substrates. The electrochemical cell was configured using a 1 N  $H_2SO_4$  electrolyte with an iridium oxide working electrode, a saturated calomel reference electrode (SCE), and a Pt mesh counter electrode. Triangular wave cycling was performed at a sweep rate of 20 mV/sec between limits of -0.2 and 1.1 volts relative to the SCE. The cyclic voltammogram of a Condition J film is shown in Figure 3. The anodic and cathodic charges were well balanced, indicating good reversibility. Films deposited under conditions J, I, E, and A exhibited voltammograms of similar shape. However, there were some electrochemical differences which could not be explained by variations in film thickness.

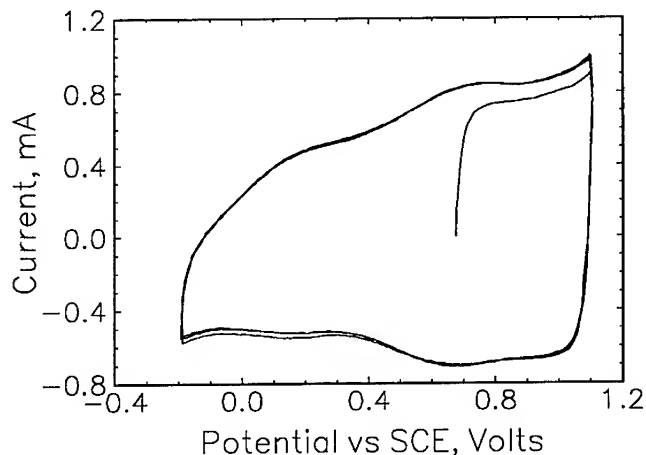


Fig. 3. The electrochemistry of IrO<sub>x</sub> films is indicated by cyclic voltammetry of a film deposited under condition J of Fig. 1.

The open-circuit potential provides an indication of the initial oxidation condition of a sample. As-deposited films placed in the electrochemical cell but protected from current flow will exhibit a potential difference relative to the SCE reference electrode. Shown in Figure 4 are the open circuit potentials of films deposited under conditions J, I, E, and A as a function of the intensity of the oxygen emission peak at the deposition condition. Higher potentials indicate a more oxidized condition. The monotonically increasing data clearly indicate that more oxidized films are associated with more oxidizing plasmas.

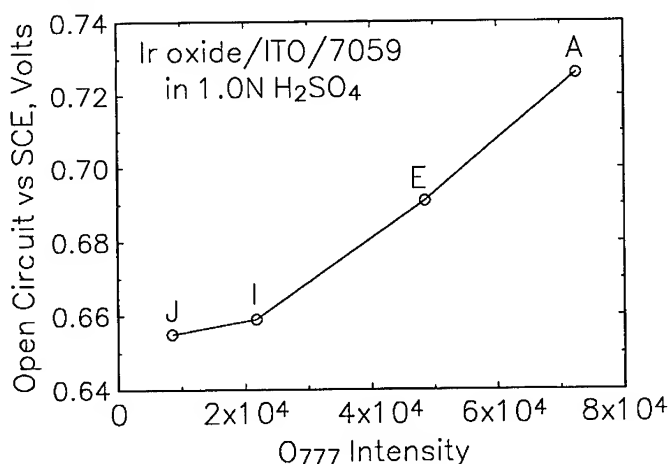
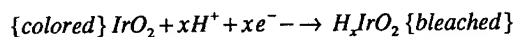


Fig. 4. The open circuit potential of films deposited under different sputter atmospheres vs SCE in 1 N H<sub>2</sub>SO<sub>4</sub>.

A significant application for iridium oxide films is as electrochromic layers in complementary electrochromic devices. Iridium is an anodically coloring material that optically switches according to



That is, iridium oxide is least transmissive when most oxidized. The electrochromic behavior of an IrO<sub>2</sub>/ITO/Corning 7059 sample is shown in Figure 5. Transmittance spectra are shown at the bleached (-0.2 volts vs SCE) and colored (1.1 volts vs SCE) limits of cycling as well as at intermediate potentials. A continuous range of optical properties can be accessed by adjusting the applied potential.

## CONCLUSION

Optical emission spectroscopy was found to be a sensitive *in-situ* monitor of the reduction/oxidation characteristics of Ar/O<sub>2</sub>/H<sub>2</sub> sputter environments. The sputter plasmas exhibited spectral characteristics similar to those encountered in hydrogen flame spectroscopy. Reactive rf sputtering of an Ir metal target in an Ar/O<sub>2</sub>/H<sub>2</sub> environment was performed at twelve distinct H<sub>2</sub>-O<sub>2</sub> flow combinations. Each of the twelve run condition lies along either of two lines in O-H emission intensity space. In the range of Ar/O<sub>2</sub>/H<sub>2</sub> flows examined, increasing H<sub>2</sub> flow reduced atomic oxygen emissions and increased molecular OH emissions.

Increasing  $O_2$  flow reduced both atomic hydrogen and OH emissions. The near coincidence of dissimilar run conditions in H-O emission space implies that any observed plasma redox condition could be accessed through a variety of deposition conditions. More oxidizing plasma conditions were found to produce more oxidized as-deposited films.

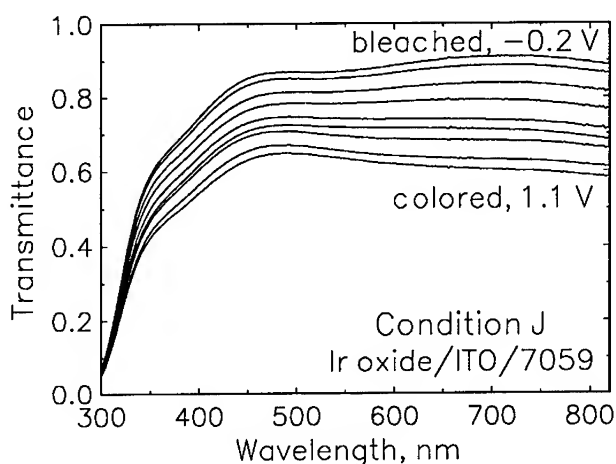


Fig. 5. Optical transmittance spectra for an  $IrO_x/ITO/glass$  sample at colored, bleached and intermediate potentials vs SCE.

#### REFERENCES

1. L.S. Robblee, J. Lefko, and S.B. Brummer, *J. Electrochem. Soc.* **130**, 731 (1983).
2. S.F. Cogan, T.D. Plante, R.S. McFadden, and R.D. Rauh, *Solar Energy Materials* **16**, 371 (1987).
3. J.D. Klein, S.L. Clauson, and S.F. Cogan, *J. Vac. Sci. Technol. A* **7**, 3043 (1989).
4. J.D. Klein, S.L. Clauson, and S.F. Cogan, *J. Mater. Res.* **4**, 1505 (1989).
5. E. Pungor and I. Cornides in *Flame Emission and Atomic Absorption Spectrometry* ed. by J.A. Dean and T.C. Rains, (Marcel Dekker, New York, 1969) p. 49.
6. A.G. Gaydon, *The Spectroscopy of Flames* (Chapman and Hall, London, 1974), p. 364.
7. N.N. Semonov, *Some Problems in Chemical Kinetics and Reactivity* Vol. 2, (Princeton University Press, Princeton, New Jersey, 1959).
8. B. Lewis and G. von Elbe, *Combustion, Flames, and Explosions of Gases* (Academic Press, Orlando, Florida, 1987).
9. *CRC Handbook of Chemistry and Physics*. 59th edition ed. by R.C. Weast (CRC Press, West Palm Beach, Florida 1978) pp. E-216-342.

## SYNTHESIS OF GRAPHITE INTERCALATION COMPOUNDS WITH DONOR SPECIES

DANIEL GUÉRARD\* AND VERA A. NALIMOVA\*,\*\*

\* Laboratoire de Chimie du Solide Minéral, URA 158, Université Henri Poincaré  
Nancy I, BP 239, 54506 Vandoeuvre Cedex, France

\*\* Department of High Pressure Chemistry, Moscow State University, Leninskie  
Gory, Moscow 119899, Russia

### ABSTRACT

For 15 years, the chemistry of the intercalation of donors species into graphite has been largely developed and a great number of new phases were discovered : over 100 if one takes into account the various stages and stacking, which involves different properties of the compounds for a given intercalate. Four new systems and synthesis methods were developed : intercalation of metallic alloys containing an alkali metal, ionic species (alkali metal hydrides, hydroxides and, even chlorides), alkali metals with oxygen (by addition to the metal of a small quantity of its peroxide  $M_2O_2$ ), intercalation under high pressure of the alkali metal. Those new syntheses, still in progress, lead to compounds in which the first stages exhibit a fairly high intercalate/carbon ratio : from  $LiC_2$  to  $MC_4$  ( $M = Na, K, Rb$  or  $Cs$ ) instead of  $LiC_6$  or  $MC_8$  obtained by classical methods.

The increase of this ratio confers them interesting properties and possibilities of application, especially in the field of new materials for primary or secondary batteries.

### INTRODUCTION

For more than 30 years, the intercalation into graphite of donor species was limited to the heavy alkali metals [1] then, sodium [2, 3] and lithium [4, 5] were also intercalated. Sodium leads to relatively high stages whose formulas are  $NaC_{8s}$  with  $s = 4$  to 8 [6].

The first stage compounds exhibit a composition  $LiC_6$  or  $MC_8$  (with  $M = K, Rb$  or  $Cs$ ). Those formulas were, up to the recent years, considered as the richer donor graphite intercalation compounds (GICs).

Since 15 years, many new GICs were obtained and described with a much larger M/C ratio in the first stage compounds :

- $MA_xC_4$  by intercalation of metallic alloys containing an alkali metal (M) and an other element unable to intercalate by itself (A) such as mercury [7], thallium [8], bismuth [9], antimony [10] or arsenic [11],
- $MH_{0.8}C_4$  from sodium [12], potassium [13], rubidium and cesium hydrides [14],
- superdense phases with alkali metals intercalated under high pressure :  $LiC_2$ - $LiC_4$ ,  $KC_4$ - $KC_6$ ,  $CsC_4$ - $CsC_6$  [15, 16] ;  $NaC_3$  [17] ;  $RbC_4$ - $RbC_6$  [18],
- compounds with KOH, NaOH e.g.  $Na(OH)_{0.9}C_{2.12}$  [19],  $LiCl$ - $KCl$  [20],
- ternary phases containing a small amount of oxygen, like  $KO_{0.07}C_{3.8}$  prepared from the alkali metal containing some traces of the alkali metal peroxide  $M_2O_2$  [21-24].

These compounds can be classified in :

- true ternary phases from alloys, hydrides, hydroxides or chlorides,
- true binaries obtained under high pressure,
- quasi-binaries with a small content of oxygen.

## TERNARY COMPOUNDS

Those syntheses were set up and developed at the LCSM in Nancy since 1980. They are performed in glass tubes sealed under vacuum and the transfers before and after the synthesis are made in a glove box under purified argon.

### From metal alloys containing an alkali metal

The preparation of  $MA_xC_{4s}$  where  $s$  represents the stage number which depends on the synthesis conditions (relative concentration of the metals) is done generally by reaction of a large excess of the molten alloy, at a temperature just above the melting point of the alloy, on graphite platelets : HOPG or single crystals. This method of intercalation is closely connected to the high boiling point of the third element (except mercury and arsenic) and to the difference of composition between the reactive alloy and the intercalated one [25].

These systems are very rich since, for instance, the M-As alloys lead to 15 different compounds among them 11 were isolated. All together, over 50 phases belong to this series [26].

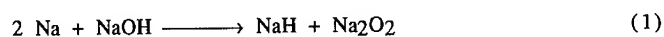
#### From alkali metal hydrides

The reaction is generally done with a large excess of the alkali metal hydride in powder form with HOPG or single crystals at a temperature high enough to provide a partial decomposition of the hydride. Then the intercalation starts by the formation of a binary compound with the alkali metal [27]. Lithium hydride is much more thermally stable than the others and, then, it is necessary to add 25 to 30% in weight of potassium. The first step of the intercalation is the formation of  $KC_8$  and the final compounds are quaternary ones whose general formula is  $K_2LiHC_{8s}$ ,  $s$  being the stage number which varies from 1 to 4 according to the reaction temperature (between 430 and 500°C) [28].

For the hydrides of rubidium and cesium, which are not commercialised, a preparation method was set up [29].

#### From alkali metal hydroxides

The intercalation can be obtained by chemical or electrochemical means. For the chemical intercalation, the presence of free sodium is required. It is added to the molten sodium hydroxide at 330°C. The "dissolution" is quite slow and leads to a blue liquid according to :



The liquid reacts readily with graphite and gives a blue first stage compound. The intercalate forms two planes containing both  $Na^+$  and  $OH^-$  and exhibits partly the quadratic structure of the free sodium hydroxide. By electrochemistry, the addition of metallic sodium is not necessary. The composition depends on the synthesis method :  $Na(OH)_{0.89}H_{0.045}C_{2.12}$  (chemical way) or  $Na(OH)_{0.94}H_{0.01}C_{2.26}$  (electrochemistry). Those last compounds seem thermally more stable than that obtained by chemical means [19].

#### From the eutectic LiCl-KCl

The electrolysis of the eutectic LiCl-KCl (58.5-41.5% mol.) whose melting point is close to 360°C. The liquid is added by around 5% of LiH in order to avoid the evolution of chlorine at the anode. when the electrolysis is performed at 365°C, the weight uptake as well as the thickness increase of the sample are quite important and both reach 250%. The X-ray analysis shows that there is formation of large



inclusions into the graphite of the chlorides, whose 100 planes are parallel to the graphene layers, while the intercalation of lithium occurs to lead to  $\text{LiC}_6$ . At higher reaction temperature ( $400^\circ\text{C}$ ), there is no formation of  $\text{LiC}_6$  anymore, but two quadratic phases are observed with  $a = b = 4.36 \text{ \AA}$  and  $c = 15.35$  and  $12 \text{ \AA}$  respectively. This suggests an intercalation compound which contains only  $\text{LiCl}$  and  $\text{KCl}$  (1:1). However, the simultaneous presence of inclusions of the chlorides prevents further analysis [20]

## BINARY PHASES SYNTHESIZED UNDER HIGH PRESSURES

For about 10 years, a new synthesis method was set up at the High Pressures Laboratory (HPL) at Moscow State University (MSU, Moscow) by compressing alkali metals and graphite under pressures comprised between 5 and 60 kbars. This type of reaction leads to compounds whose metal content is two ( $\text{MC}_4$  phases with potassium, rubidium or cesium) to three ( $\text{NaC}_3$ ,  $\text{LiC}_2$ ) times higher than in classical compounds. Among those new systems,  $\text{LiC}_2$  and  $\text{CsC}_4$  are stable enough under ambient conditions to allow some crystallographic and physical properties studies. The following table gathers the synthesis conditions for the different alkali metals.

Table 1- Highly saturated alkali metal GICs synthesis

Compound	Pressure (kbars)	Temperature ( $^\circ\text{C}$ )	Ref.
$\text{LiC}_2\text{-LiC}_4$	60	280	14-15
$\text{NaC}_3$	45	500	16-17
$\text{KC}_4\text{-KC}_6$	6-12	160-170	14-15
$\text{RbC}_4\text{-RbC}_6$	5-20	20-100	18
$\text{CsC}_4\text{-CsC}_6$	2-5	20	15

## PSEUDO-BINARY PHASES WITH PARTLY OXIDISED ALKALI METALS

This study is performed both at the LCSM (UHP, Nancy) and the HPL(MSU, Moscow). The presence of a third element A stabilises the high alkali metal M content in the ternary phases  $\text{MA}_x\text{C}_4$ s. Generally speaking, the value of x is decreasing as the electronegativity of A increases. If A presents a large electronegativity, like oxygen for instance, its amount can be small enough to consider the compound as a pseudo-binary one. This is true with the heavy alkali metals :  $\text{KO}_{0.07}\text{C}_4$  for instance. The reaction is done in liquid phase with potassium added by small quantities of the potassium peroxide  $\text{K}_2\text{O}_2$ . This system is particularly

rich since there are 11 different compounds : 5 which belong to stage 1 (and which are particularly stable towards air and water), 3 stage 2 and stages 3, 4 and 5 [22].

When the alkali metal is rubidium or cesium, the synthesis can be done in vapour phase since their oxides are not thermally stable and the oxygen pressure remains small compare to that of the alkali metal.

With sodium and sodium peroxide, the reaction leads to true ternary compounds (second stage) where the amount of oxygen becomes comparable to that of sodium :  $\text{NaO}_{0.35}\text{C}_{4.75}$ . Moreover, the structure of the intercalated layer is close to that of the free peroxide [21].

## STRUCTURAL CHARACTERISTICS

### In-plane structure

There are no general rules concerning the in-plane structure of the intercalated layers. For instance, the structure of the ternaries based on the alkali metal hydrides varies from one alkali to the other, as shown in the following table.

Table 2- In-plane parameters for the ternary compounds with alkali metal hydrides

Intercalate	System	a (Å)	b (Å)	Reference
NaH	Orthorhombic	9.84	12.78	[12]
KH	"	8.572	12.39	[11]
RbH	"	38.45	37.35	[14]
CsH	"	17.19	26.93	[14]
K + LiH	Hexagonal	4.951		[12]

In spite of a quite simple formula :  $\text{LiC}_2$  or  $\text{MC}_4$ , the compounds prepared by high pressure synthesis present large in-plane unit cells [30].

### Stacking along the c axis

There are two different situations :

- the true binary phases are characterised by a single intercalated layer, which can be more or less splitted as it appears for  $\text{CsC}_4$  in Figure 1 : a splitting of 0.4 Å of the cesium plane allows the residual factor to decrease from 18.2% to 4.7%. The presence of a single layer makes of those compounds highly saturated in alkali metal, which confers them a special behaviour.

From structural [30] and physical [31-33] properties, one knows that, in the lithium  $\text{LiC}_2$  compound, the concentration of lithium is 9% higher than in the free metal, in spite of the presence of the carbon atoms. This was also confirmed by electrochemistry : the potential of  $\text{LiC}_2$  vs.  $\text{Li}^0$  is negative [34]. This also gives a partial covalent character to the in-plane Li-Li bonding [35]. On the other hand, the in-plane Cs-Cs distances (less than a half of the  $\text{Cs}^+$  diameter), and the volume occupied by the cesium in  $\text{CsC}_4$  (around 30% of that of metallic cesium), confer probably to the intercalated cesium, which is metastable under ambient conditions, an electronic configuration close to that of the Cs V which is stable only at pressures over 100 kbars.

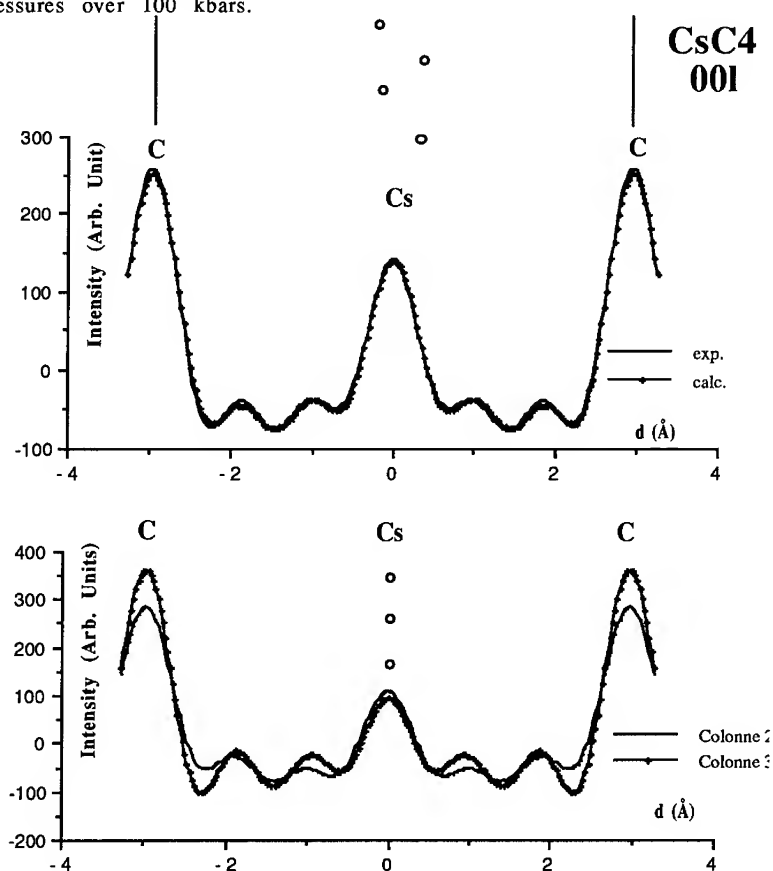


Figure 1- Electronic density along the c axis of the compound  $\text{CsC}_4$   
 Top : with a splitting of the cesium layer (0.4 Å),  $R = 0.047$   
 Below : without splitting,  $R = 0.182$

- the ternary and pseudo-binary compounds present, in general, three or more layers as shown in Figure 2. The stacking involves, in contact with the graphene layers, an alkali metal plane whereas the internal layer is made of the less electropositive element (as shown in Fig. 2 the compound  $\text{KHgC}_4$  presents the following stacking along the  $c$  axis :  $\text{C-K-Hg-K-C} \dots$ , the Hg layer is slightly splitted)), which, in some cases is splitted or mixed with a part of the alkali metal. This confers to the compounds a fairly high interplanar distance, much higher than that of the classical phases, typically 8 to 13 Å. Since there are, at least, two metal layers, for a  $\text{M/C}$  ratio close to  $1/4$ , the in-plane density of the alkali metal remains roughly the same as in the classical phases, however, the situation is quite more complicated in general and, once more, there is no general rule.

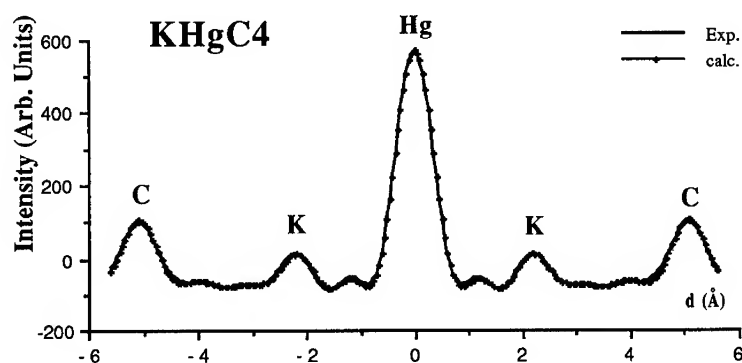


Figure 2- Electronic density along the  $c$  axis for the compound  $\text{KHgC}_4$  (1st stage)  
 $R = 0.035$

The compression at around 15 kbars of the pseudo-binary phase  $\text{KO}_{0.07}\text{C}_4$  leads to a partial transformation into a single layered compound with an interplanar distance of about 5.35 Å as in the classical  $\text{KC}_8$  or the superdense  $\text{KC}_4$ . This transition, accompanied by a large volume decrease, shows up that those compounds are comparable and, since the new phase obtained after compression was metastable enough to allow the structural study (the pure  $\text{KC}_4$  compound decomposes readily as the pressure is decreased), the presence of oxygen stabilises the high potassium content in those GICs.

## PROPERTIES

In the GICs, the oxidation for instance, but also other reactions, occurs at the edge of the graphite planes and the speed of the reaction depends on the mobility of the intercalate between the graphene layers and on the size of the crystallites. With the heavy alkali metals, the mobility of the intercalated layers is very high and, for instance, they burn in air when they are in powder form. With the ternary compounds, where the presence of the third element stabilises the multilayered intercalated plane, the mobility is much lower and prevents a rapid reaction at the edges. On the other hand, the metallic alloys, hydrides, hydroxides, halogenides are much less reactive than the corresponding free metals. At last, the bonding between the carbon layers through the intercalate is increased as the metal becomes more electropositive. The series of the compounds with the alkali metal hydrides is characteristic for this point of view :  $\text{KH}_{0.8}\text{C}_4$  burns in air and reacts violently with water, whereas  $\text{CsH}_x\text{C}_5$  is quite stable in the air and can stay in water for weeks without drastic transformations. This phenomenon, in contradiction to the respective reactivity of the free hydrides, was explained by a much stronger bonding between the graphene layers, which prevents a local exfoliation of the compound, due to the hydrogen evolving and which could favour the penetration of water molecules in the intercalated plane to react with the hydride inside the compound [36, 37].

## CONCLUSION

The chemistry of intercalation into graphite of electron donors is very active : for the last 15 years, over 100 new compounds were synthesized. Among them, 30 belong to the first stage and present a ratio alkali metal/carbon of 1/4, even more ( $\text{LiC}_2$ ).

Four different families of intercalates were discovered and the research in this domain is still in progress. On the other hand, the high value of the M/C ratio makes of these new phases good potential candidates as battery materials.

## ACKNOWLEDGEMENT

The research described in this publication was partly made possible through the Grant # MHF 000 from the International Science Foundation

## REFERENCES

- 1- K. Fredenhagen and G. Cadenbach, Z. anorg. allg. Chem. 158 (1926) 249
- 2- R.C. Asher and S.A. Wilson, Nature, London (1958) 181
- 3- A. Métrot and A. Hérold, C. R. Acad. Sc. Paris 264C (1967) 883
- 4- R. Juza and V. Wehle, Natw. 52 (1965) 560
- 5- M. Bagouin, D. Guérard and A. Hérold, C. R. Acad. Sc. Paris 262C (1966) 571
- 6- A. Métrot, D. Guérard, D. Billaud and A. Hérold, Synth. Met. 1-4 (1980) 363
- 7- M. El Makrini, P. Lagrange, D. Guérard and A. Hérold, Carbon 18 (1980) 211
- 8- M. El Makrini, P. Lagrange and A. Hérold, Carbon 18 (1980) 374
- 9- P. Lagrange, A. Bendriss-Rerhrhayé, J.F. Maréché and E. McRae, Synth. Met. 12 (1985) 201
- 10- A. Essaddek, J. Assouik and P. Lagrange, J. Mat. Res. 4 (1989) 244
- 11- J. Assouik and P. Lagrange, Carbon 28 (1990) 910
- 12- D. Guérard, N.E. Elalem, C. Takoudjou and F. Rousseaux, Synth. Met. 12 (1985) 195
- 13- D. Guérard, C. Takoudjou and F. Rousseaux, Synth. Met. 7 (1983) 43
- 14- D. Guérard, N.E. Elalem, L. Elansari, J.F. Maréché, E. McRae, H. Estrade-Szwarckopf, B. Rousseau, P. Lauginie and J. Conard, Z. Phys. Chem. N. F. 164 (1989) 1579
- 15- K.N. Semenenko, V.V. Avdeev and V.Z. Mordkovich Dokl. AN SSSR 6 (1983) 1402, in Russian ; and V.V. Avdeev, V.A. Nalimova and K.N. Semenenko, High Pressure Research 6 (1990) 11
- 16- I.T. Belash, A.D. Bronnikov, O.V. Zharikov and A.V. Pal'nichenko, Sol. St. Com. 64 (1987) 1445
- 17- V.V. Avdeev, V.A. Nalimova and K.N. Semenenko, Synth. Met. 39 (1990) 363
- 18- V.A. Nalimova, S.N. Chepurko, V.V. Avdeev and K.N. Semenenko, Synth. Met. 40 (1991) 267
- 19- A. Hérold, M. Lelaurain and J.F. Maréché, C. R. Acad. Sc. Paris 312 II (1991) 361
- 20- A. Hérold, M. Lelaurain and J.F. Maréché, Proc. Carbon'92 Essen 571
- 21- A. Hérold, M. Lelaurain, E. McRae and J.F. Maréché, Mat. Sc. For. 91-92 (1992) 89
- 22- M. El Gadi, C. Hérold and P. Lagrange, C. R. Acad. Sc. Paris 316 II (1993) 763
- 23- D. Sklovsky, C. Hérold, P. Lagrange, V. Nalimova and D. Guérard, to appear in Carbon
- 24- D.E. Sklovsky, P. Lagrange, C. Hérold, V.A. Nalimova, D. Guérard and K.N. Semenenko, to appear in Dokl. AN
- 25- P. Lagrange and R. Setton, Graphite Intercalation Compounds I, Springer Series in Mat. Sc. , Ed. S.A. Solin and H. Zabel, Springer publ. (1990) 283
- 26- P. Lagrange, Chemical Physics of Intercalation II, Plenum Press Ed., New York and London (1993) 303
- 27- D. Guérard and P. Lagrange NATO ASI Series 172B (1988) 205
- 28- D. Guérard and L. Elansari, Eur. J. Sol. St. Inorg. Chem. 29 (1993) 39
- 29- D. Guérard, N.E. Elalem, S. El Hadigui, L. Elansari, F. Rousseaux, H. Estrade-Szwarckopf J. Conard and P. Lauginie, J. Less Com. Met. 131 (1987) 173
- 30- D. Guérard and V.A. Nalimova, Mol. Cryst. Liq. Cryst. 244-245 (1994) 263
- 31- V.A. Nalimova, G.N. Bondarenko, V.L. Kofman, V.V. Avdeev and K.N. Semenenko, Carb. Conf. Santa Barbara (1991) 684
- 32- N.R. Gall, S.N. Mikailov, E.V. Rut'kov, A.Ya. Tontegode, V.A. Nalimova and V.V. Avdeev, Auger An. El. Str. Conf. Lund, Sweden (1991)
- 33- J. Conard, V.A. Nalimova and D. Guérard, Mol. Cryst. Liq. Cryst. 244-245 (1994) 427
- 34- R. Yazami, A. Cherigui, V.A. Nalimova and D. Guérard, Proc. 2nd Meeting Electroch. Soc. Toronto (1992)
- 35- V.A. Nalimova, J. Conard, D. Guérard, G.N. Bondarenko, K.N. Semenenko and V.V. Avdeev, GFECI, Bierville (1992) 32
- 36- D. Guérard, C. Takoudjou, N.E. Elalem and L. Elansari, Mat. Sc. For. 91 (1992) 85
- 37- D. Guérard, NATO ASI Series, Cond. Syst. of Low Dimensionality 69 (1990) 695.

## THE CARBON-LITHIUM NEGATIVE ELECTRODE FOR LITHIUM-ION BATTERIES IN POLYMER ELECTROLYTE

R. YAZAMI AND M. DESCHAMPS

Laboratoire d'Ionique et d'Electrochimie du Solide de Grenoble - URA CNRS 1213 -  
Institut National Polytechnique de Grenoble -  
BP75 - 38402 St Martin d'Hères - France

### ABSTRACT

Several types of carbonaceous materials are evaluated as negative electrodes for lithium storage in polymer electrolyte based cells operated at 100°C. The corresponding faradaic efficiencies of the spherical cycle and the achieved reversible first capacity and rate capacity will be given. A meso carbon yielded a higher capacity than the theoretical 372 mAh/g. This is tentatively explained by the necessary enhancement of the carbon/polymer interfacial properties through the formation of C-Li-O bonding at the carbon surface and by the possible formation of multilayers of lithium on the external a,b planes of disordered carbons. The formation of the passivating layer on the carbon surface will be described.

A lithium-ion type battery using coke and  $\text{LiNiO}_2$  as the negative and positive leads and POE- $\text{LiClO}_4$  was operated at 100°C and cycled galvanostatically. Good reversible capacity was attained with the  $\text{LiNiO}_2$  electrode.

### INTRODUCTION

The successful utilization of carbonaceous material as a host structure for lithium reversible electrochemical storage in the so called "lithium-ion" batteries in liquid electrolytes results from the successive improvement of the operation characteristics of this electrode such as the reversible capacity, the cycle life and the safety [1, 2]. The latter aspect is in relation with the reduction of the dendrite growth of metallic lithium during the cathodic process. To avoid the formation of dendritic lithium, several models have been so far proposed including the formation of intercalated lithium with the staging phenomenon [3, 4] and the preferential deposit of lithium in the micropores [5] or cavities [6] present in disordered carbons.

The formation of dendrites on metallic lithium was also reported in solid polymer electrolytes particularly when high current density ( $\text{mA}/\text{cm}^2$ ) or high surface capacity ( $\text{mAh}/\text{cm}^2$ ) are required [7]. Therefore the use of carbonaceous materials as a substitute to metallic lithium or to lithium alloys may also be considered in order to enhance the safety of the polymers or gels electrolytes based lithium-ion cells.

In this study we have evaluated several kinds of carbonaceous materials as possible negative electrodes in  $\text{Li}/\text{P}(\text{OE})_8\text{LiClO}_4$  /carbon cells. The formation of the passivation film which is at the origin of the low coulombic efficiency during the first

lithiation/de-lithiation of carbon is observed here by SEM. In addition, the excess capacity found in a spherical meso carbon is discussed using a multilayers model. The observed enhancement of the interfacial properties between the two solids: lithiated carbon and the PEO, will be discussed by the introduction of the "zipper" model.

Preliminary galvanostatic cycling tests on Li/POE-LiClO<sub>4</sub>/LiNiO<sub>2</sub> and Carbon/POE/LiNiO<sub>2</sub> cells will also be shown.

## EXPERIMENTAL

The carbonaceous materials used in this study are 1) acetylene black (AB) typically entered as electrical conductivity additive in composite electrodes, 2) natural graphite from Madagascar (20  $\mu\text{m}$  in average grain size), 3) coke powder from Carbone Lorraine (France) (HTT à 1100°C) and grinded to c.a. 8  $\mu\text{m}$ , 4) Meso Carbon Micro Breads (MCMB) with two heat treatments : 1000°C (MCMB 6-10) and 2800° (graphitized MCMB 6-28) : grain size ~ 6  $\mu\text{m}$  from Osaka Gas (Japan) . Carbon fibers derived from a petroleum pitch mesophase and heat treated to 2600°C were used for the chemical lithiation and the SEM observation of the passivation film.

For the electrochemical tests, dried carbon powders were dispersed into an acetonitrile solution of polyethylene oxide (POE), then sprayed on a stainless steel disc of 16 mm in diameter. The mixture was then evacuated at ambient temperature then at 120°C for several hours . The average weight of the obtained composite electrode is c. a. 5 mg and the volume composition is 40 % POE and 60% carbon (10% NA + 50% carbon) .

A fine powder of LiNiO<sub>2</sub> compound was prepared using a conventional method at high temperature [8] and used as the positive composite electrode.

For the evaluation of the carbon electrodes, button type (RC 2430) cells were mounted in a dry argon filled box using POE-LiClO<sub>4</sub> film as electrolyte and metallic lithium as the reference and the counter electrode. The cells were operated at 100°C under a C/20 galvanostatic regimes (LiC<sub>6</sub> reached in 20 hours) between 1.2 V and 5 mV as potential limits. Rate capability tests were performed with MCMB 6-10-10 in the C/10 to C/1 range. Complex impedance was also used in order to characterize the interfacial phenomena observed during the first cathodic reduction of carbon.

For the LiNiO<sub>2</sub> based electrodes, similar button cells were mounted with either lithium or coke as the negative and POE/LiClO<sub>4</sub> as electrolyte. The cells were cycled under C/20 regime. Cells using carbon negative were anode limited.



## RESULTS AND DISCUSSION

### Carbon Electrode

#### - TEM Observation of the passivation film :

Dried carbon fibers (CFs) were immersed into molten lithium at 220°C under high purity dry argon atmosphere for several hours. The color turned from black-grey to reddish indicating the formation of stage 1 intercalation compound. At this stage of reaction different CFs from the same tuft could be easily separated from each others. CFs were then introduced into the electrolyte (EC(1):PC(1):DME(2), 1M LiBF<sub>4</sub>) and stirred for several hours at the room temperature. The fibers were then separated from the electrolyte, washed with acetonitrile and dried at the ambient temperature under argon and at 100°C under primary vacuum for several hours. At this step of reaction, it was observed that the CFs became sticky each others. They were then transferred into TEM chamber using home made container which prevents from any direct exposure to air.

Figure 1 shows the resulting morphology of a CF tuft of same fibers after the successive treatments and figure 2 gives a larger magnification of the tuft. It can be easily observed the formation of a film which covers the CFs and makes them stick together. On the other hand, RAMAN spectrometry performed on virgin, lithiated and reacted with electrolyte CFs showed clearly the de-intercalation of lithium after reaction with electrolyte. Such observation led us to conclude that the film formed at the surface of the CFs results from the chemical reduction of the electrolytes by de-intercalated lithium. Such a film should be of the same nature than that formed during the first electrochemical reduction of carbonaceous materials in lithium/liquid electrolyte cells as reported by previous authors [9]. The in-situ EDX analysis of the film showed the presence of O, B and F besides the C element. Therefore, the chemical reduction of the electrolyte leads to polymeric like film which contains most constituent of the electrolyte. Further investigations are needed to better characterize the structure and the transport properties of the passivation film.

#### - Galvanostatic cycling :

For the Li/POE/Carbon cells, table I summarizes the main characteristics of cycling curves (not presented here) such as  $\gamma_1$  = coulombic yield of the first cycle,  $e_d$  and  $e_c$  = average discharge and charge voltage after the first cycle,  $Q_r$  = reversible specific capacity and  $x$  the reversible amount of lithium in Li<sub>x</sub>C<sub>6</sub>. The  $\gamma_1$  values are rather lower than those observed with the same carbons in EC:PC:DME-LiClO<sub>4</sub> solution [5]. This should be due to poorer interfacial properties between the two solids carbon and polymer. However, as will be discussed in the following section, the interfacial properties improve with increased amount of transferred lithium to the carbon electrode.

The average discharge and charge voltage ( $e_c$  and  $e_d$ ) also depends on the carbon nature. The trends observed in liquid electrolytes that  $e_c$  and  $e_d$  decrease

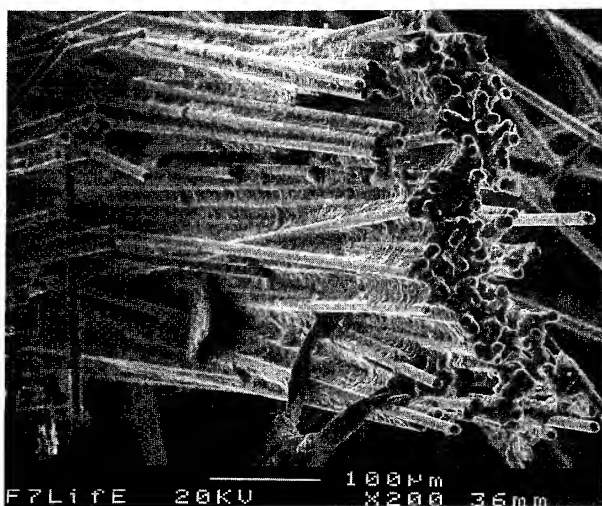


Figure 1 : SEM observation of lithiated carbon fibers after reaction with the electrolyte : the fibers are sticking to each other due to the formation of passivation film.

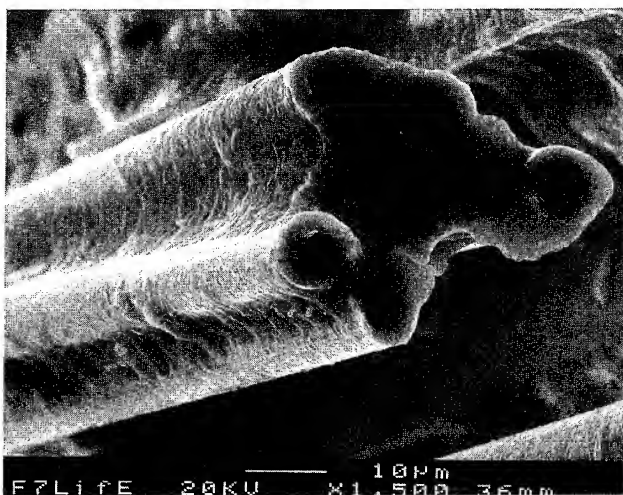


Figure 2 : magnification of figure 1 showing the morphology of the passivation film on the external surface of the carbon fibers.

with increasing degree of graphitization in soft carbons is also obtained with the polymer electrolytes. These potential values are in relation with the electronic Fermi level in lithiated carbon which depends on the extend of the charge transfer in  $\text{Li}_x\text{C}_6$ . An increased crystallinity of the carbon host yields higher negative charge bore by each carbon atom. As a consequence the Nernst potential is lower in graphite than in less well ordered carbons. Natural graphite and MCMB 6-28 yield the lowest  $e_c$  value which is in interest in practical lithium-ion cells as the carbon-lithium electrode is subjected to lithium deintercalation (anodic oxidation) during the complete cell discharge. Recently, we showed using slow scanning rate voltammetry that the lithium de-intercalation has a more "collective" character than the intercalation step. The latter is controlled mainly by the stage transitions [10], whereas the de-intercalation is not sensitive to staging, all the carbon layers being equivalent.

The most striking result showed in table I is the occurrence of a reversible capacity  $Q_r$  higher than the theoretical 372 mAh/g as for the MCMB 6-10 sample which yields 410 mAh/g. MCMB 6-10 consists on spherical particles of disordered carbon layers. In liquid electrolytes, Mabuchi et al showed recently that MCMB heat treated at 700°C gives even a higher reversible capacity of 750 mAh/g [6]. These authors attributed such an excess capacity to the contribution of the cavities formed between the carbon crystallites in the lithium reversible storage. We also had proposed a similar mechanism in microporous carbons such as activated cokes [5]. Another model has been suggested by Sato et al. [11] to deal with higher reversible capacity reached with a disordered carbon which involves the formation of superdense lithium phases between the carbon layers such as in  $\text{LiC}_2$ . We have showed by cyclic voltammetry that superdense lithium-graphite intercalation compounds do not have a fully reversible behaviour reversible due to the fact that under the normal pressure,  $\text{LiC}_2$  spontaneously releases metallic lithium in an irreversible manner [12]. Therefore the model of superdense lithium layers could hardly account for a reversible capacity exceeding 372 mAh/g.

Carbon	$\gamma$ %	$e_d$ (mV)	$e_c$ (mV)	$Q_r$ (mAh/g)	x in $\text{Li}_x\text{C}_6$
AB	17	262	506	190	0.52
N. Graphite	30	124	194	280	0.75
Coke	40	306	507	325	0.85
MCMB 6-28	30	168	237	355	0.95
MCMB 6-10	60	267	543	410	1.1

**Table I :** Comparative performances of different carbonaceous materials during the C/20 galvanostatic cycling. The Li/PEO-LiClO<sub>4</sub>/carbon cells were operated at 100°C.

- The multilayers model :

The specific surface area of a carbon crystallite based on a geometrical consideration can be expressed by the following equation :

$$\sigma = k \left( \frac{1}{L_c} + \frac{2}{L_a} \right) \text{ where } k = \frac{N_a}{12} \times d_{002} \times a^2 \sqrt{3} \quad (1)$$

and  $N_a$  = Avogadro number,  $d_{002}$  = the interlayers spacing,  $a$  = lattice parameter of the carbon unit cell. ( $\sigma$  would be in  $\text{m}^2/\text{g}$  if, for example,  $d_{002}$ ,  $L_a$  and  $L_c$  are expressed in  $\text{\AA}$  and  $a$  in meter).

The number of lithium atoms needed to form  $\text{LiC}_6$  monolayers on the two a,b plans is given by :

$$n_{\text{Li}} = \frac{N_a}{36} \times \frac{d_{002}}{L_c} = \frac{N_a}{36} \times \frac{1}{v_c} \quad (2)$$

( $v_c = \frac{L_c}{d_{002}}$  = number of coherent stacking carbon layers in the crystallite)

The excess capacity associated with the formation of one monolayer on each surface is therefore:

$$q_1 = n_{\text{Li}} e = \frac{F}{36 v_c} \quad (3)$$

( $e$  = electron charge and  $F$  = Faraday number =  $N_a e$ )

When converted to  $\text{mAh/g}$ ,  $q_1$  is expressed by :

$$q_1 = \frac{F}{3.6 \times 36 v_c} = \frac{743}{v_c} \quad (\text{mAh/g}) \quad (4)$$

In natural graphite  $v_c$  is close to 300 ( $L_c \sim 1000 \text{ \AA}$  and  $d_{002} = 3,35 \text{ \AA}$ ) which yields  $q_1 \sim 2,5 \text{ mAh/g}$ . Such a low value cannot be measured with a good accuracy since it would represent less than 1 % of the theoretical capacity of  $372 \text{ mAh/g}$ . In disordered carbons,  $v_c$  is much more lower (several layers), therefore the theoretical  $q_1$  may exceed several hundreds of  $\text{mAh/g}$ .

It has been shown that the maximum amount of chemically intercalated lithium into layered type carbons depends on the carbon precursor and on the heat treatment temperature [13, 14]. Stage-1  $\text{LiC}_6$  is obtained only with highly

graphitized carbons while more disordered ones yield lower amounts of intercalated lithium ( $\text{Li}_x\text{C}_6$ ,  $x < 1$ ).

The excess specific capacity due to non-intercalated lithium is given by :

$$q_{\text{exc}} = Q_r - 372x \quad (5)$$

The number of lithium layers that should be formed on each a,b faces of the carbon crystallite is given by :

$$n_{\text{Layers}} = \frac{q_{\text{exc}}}{2q_1} \quad (6)$$

Taking eq. (4) et (5) into account :

$$n_{\text{Layers}} = \frac{Q_r - 372x}{2 \times 743} v_c \quad (7)$$

Eq. (7) can be used to calculate the number of stacking lithium layers in the case of MCMB heat treated at 700°C from the data given by Mabuchi et al.[6]. In such carbon,  $L_c=26 \text{ \AA}$  and  $d_{002}= 3.44 \text{ \AA}$ , which yields  $v_c = \frac{26}{3.44} = 7.56$  layers. Assuming the capacity due to intercalated lithium is  $372x = 225 \text{ mAh/g}$  and  $Q_r= 750 \text{ mAh/g}$  one obtain  $n_{\text{Layers}} = 2.67$ . This result suggests that each a, b face of the carbon crystallite may be covered by several layers of lithium which contributes to the excess reversible capacity. Since the stability of the carbon-lithium lattice is controlled by the coulombic attraction between the host carbon and the guest lithium resulting from the charge transfer, the most likely type of stacking of the lithium layers should be reached when the first lithium layer occupy the  $\alpha$  sites of the hexal structure, the second and third layers occupy the  $\beta$  and  $\gamma$  sites respectively as showed in the insert of figure 3. In such arrangement the possibility of charge transfer with the adjacent carbon hexagons still exists and accordingly, a partial ionic character of the C-Li bonding should be preserved. Should any additional lithium layer be platted above the  $\alpha$ ,  $\beta$ ,  $\gamma$  layers, the character of the Li-Li bonding within this layer would be metallic due to the screening of the carbon substrate. The appearance of such metallic character would increase the possibility of lithium dendritic growth which is known to hinder the reversibility of the electrode reaction.

A schematic drawing of the multilayers model is given in figure 3. Note that the formation of molecular multilayers on the graphene a, b faces has been previously reported by several authors [15-17].

Further investigations including local studies such as high resolution  $^7\text{Li}$  NMR are needed to assess the validity of this model.

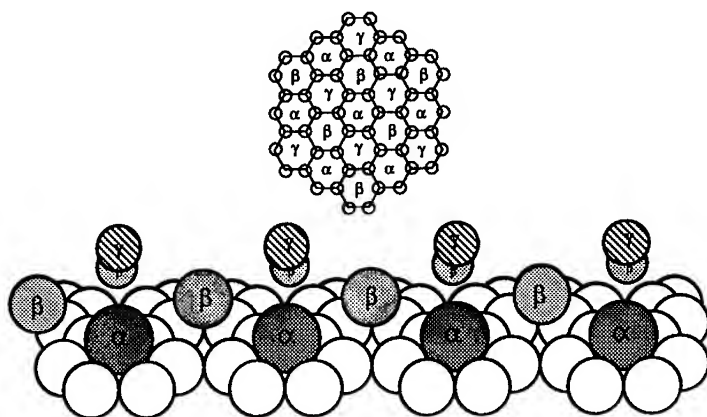


Figure 3: Model of lithium multilayers stacking on the graphite a, b face  
insert : Planar model showing the a, b, g sites of the hexal structure.

- Rate capability :

A Li/polymer/MCMB 6-10 cell was subjected to galvanostatic cycling in the 1.5 V - 5 mV range under increasing operating current regimes. In figure 4 the rate capacity curve is given after several cycles and stabilization of specific capability under a determined regime. Noteworthy is that the specific capacity value remains higher than the theoretical 372 mAh/g for cycling regime up to C/1.65 . Under C/1.18 regime the attained capacity is 340 mAh/g. Such results indicate a good kinetical feature of the coke based electrode.

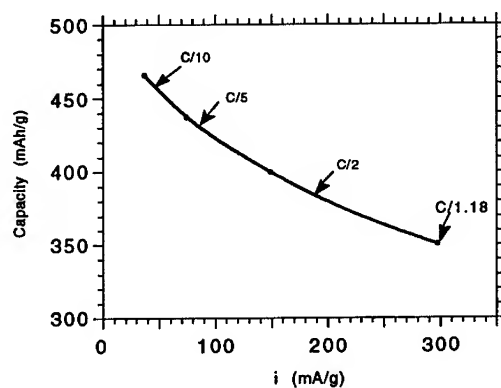


Figure 4: Rate capability curve of the Li/ P(OE)<sub>8</sub>-LiClO<sub>4</sub>/MCMB 6-10 cell.

# - Impedance measurements : the "zipper" model

We have used the impedance spectrometry as an appropriate technique to study the evolution of the interfacial properties of lithiated carbon and PEO during the first reduction scanning ( $0 < x < 2$  in  $\text{Li}_x\text{C}_6$ ).

Figure 5 gives the composition dependence of the double layer and the total impedance. The former decreases monotonously for  $0 < x < 0.75$ , then tends to stabilize. This enhancement of the interfacial properties with the amount of lithium transferred to the carbon host may result from the increase of the wetting factor between two solids: POE and carbon. Ideally, POE should cover the edges of the carbon layers to achieve a full wetting of the diffusion active surface. Due to differences in the surface properties between carbon and PEO, the wetting factor should be lower than the unity. At fixed temperature and internal pressure into the cell, one possible mechanism yielding an improvement of the wetting factor is chemically driven polymer chains motion towards the carbon electrode. A freshly reduced lithium may either be intercalated between the carbon sheets or be adsorbed on their edges. These two forms of lithium are designed  $\text{Int}(\text{Li})$  and  $\text{Ads}(\text{Li})$  respectively. Due to strong attraction between the  $\text{Ads}(\text{Li})$  and the ether group of PEO, the polymer chains should move closer to the carbon layers edges. This may result in the formation of a  $\text{C-Ads}(\text{Li})\text{-O}$  bridging bond which fixes the PEO close to the carbon surface. A such mechanism is sketched in figure 6 and schematized as the "zipper" model. As a direct consequence of this model,  $\text{Ads}(\text{Li})$  involved in the  $\text{C-Ads}(\text{Li})\text{-O}$  bonding accounts for the loss of capacity during the first discharge/charge cycle. In the present case, the relative amount of  $\text{Ads}(\text{Li})$  is c. a.  $0.75 \text{ Li/C}_6$  as suggested in figure 5 .

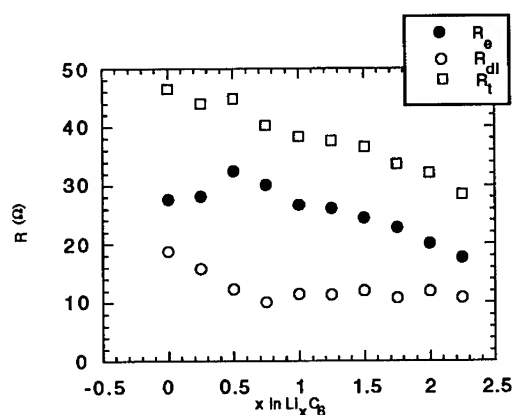


Figure 5: Composition dependence of ohmic ( $R_e$ ), the double layer ( $R_{dl}$ ) and the total ( $R_t$ ) impedance into a  $\text{Li/PEO-LiClO}_4/\text{Li}_x\text{C}_6$  (coke) cell.

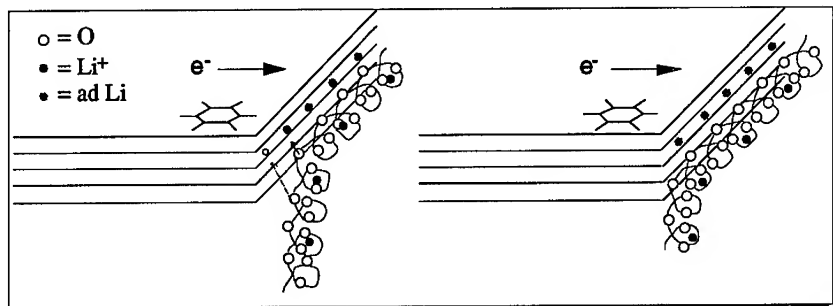


Figure 6: Schematic drawing of the mechanism of enhancement of the carbon/polymer interface properties via C-O-Li bonding formation called the "zipper" model.

#### Li or carbon/polymer/LiNiO<sub>2</sub> cells.

LiNiO<sub>2</sub> has been selected as appropriate positive electrode in polymer electrolyte because of its lower re-oxidation potential compared to LiCoO<sub>2</sub>. The cycle performances of a Li/P(OE)<sub>8</sub>LiClO<sub>4</sub>/LiNiO<sub>2</sub> cell are presented in figure 7. It shows that after five cycles, the specific capacity under C/20 regime stabilizes at 100 mAh/g with a charge/discharge yield close to unity. This value is lower than that achieved in liquid electrolyte due to the limitation of the highest recharge voltage (3.9 V in POE and 4.15 V in liquid electrolyte).

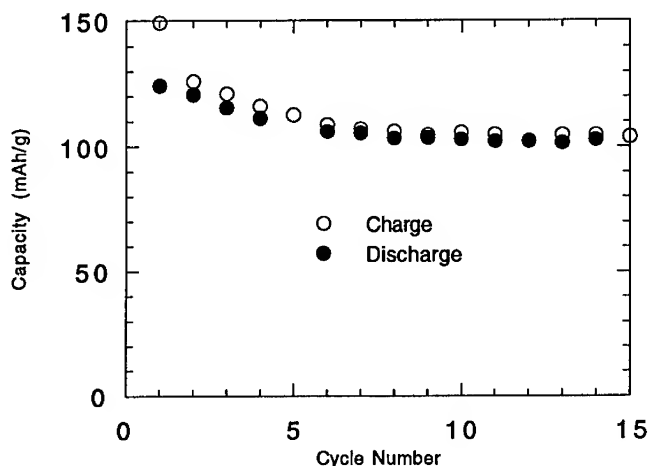


Figure 7: Cycle performance of the Li/PEO-LiClO<sub>4</sub>/LiNiO<sub>2</sub> cell.



Preliminary tests of a complete cell based on MCMB as the negative and lamellar  $\text{LiNiO}_2$  as positive have been carried out in the 3.9 V - 2.5 V range. The cell was cathode limited. Figure 8 shows the two first charge/discharge cycles. Note that the faradaic yield of the first cycle is 38 % which is mainly due to the low cycling efficiency of the carbon electrode.

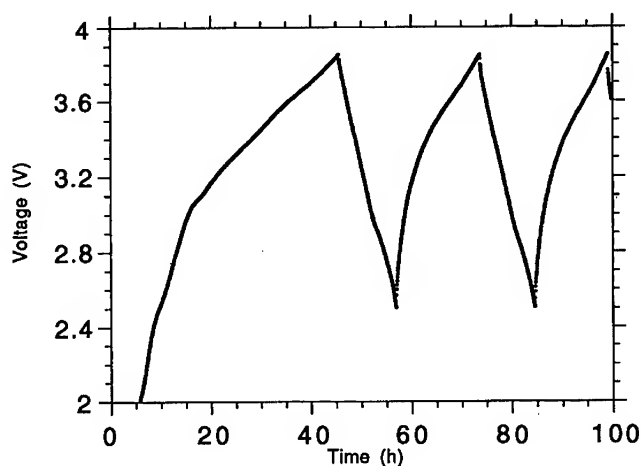


Figure 8: Two first galvanostatic cycles of the lithium-ion type cell: MCMB 6-10/  $\text{P}(\text{EO})_8\text{LiClO}_4/\text{LiNiO}_2$ .

## CONCLUSION

Carbon-lithium can be used as a reversible negative electrode for "lithium-ion" type batteries operated with polymer electrolyte. A disordered carbon such as MCMB heat treated at  $1000^\circ\text{C}$  shows a high specific reversible capacity of 410 mAh/g. In addition, lithiated carbon and PEO are compatible solids since their interfacial properties are enhanced during the first carbon cathodic lithiation.

The excess capacity may result from the formation of multilayers of lithium on the a, b faces of the carbon external sheets. The stabilization of such a construction should involve charge transfer between the lithium layers and carbon.

The observed decrease of the interfacial impedance during the first cathodic scanning is tentatively related to the enhancement of the wetting factor between the PEO and the carbon. A "zipper" model is showed to illustrate the mechanism of the polymer chains motion and fixation on the carbon surface.

Preliminary tests on complete cell (MCMB/POE/ $\text{LiNiO}_2$ ) showed relatively good performance of the positive electrode even though the limitation due to low

faradaic yield of the carbon electrode and the electrochemical stability of the POE above 3.9 V should be solved.

### References

1. T. Nagaura and K. Tozawa, *Progress in Batteries and Solar Cells* **9**, 209 (1990)
2. K. Ozawa and M. Yokokawa, in *Proc. 10<sup>th</sup> International Seminar on Primary and Secondary Battery Technology and Applications*, 1993, March 1-4, Deerfield Beach, U.S.A.
3. R. Yazami and Ph. Touzain, *J. Power Sources* **9**, 365 (1983)
4. D. Billaud, F. X. Henry and P. Willmann, *Molec. Cryst. and Liq. Cryst.* **245**, 159 (1994).
5. R. Yazami, K. Zaghib and M. Deschamps, *Molec. Cryst. and Liq. Cryst.* **245**, 165 (1994).
6. A. Mabuchi, K. Tokomitsu, H. Fujimoto and T. Kasuh in *Extended Abst. of 7th Intern. Meeting on Lithium Batteries*, Boston, May 15-20, 1994, p. 212.
7. M. Gauthier, D. Fauteux, G. Vassart, A. Bélanger, M. Duval, P. Ricoux, J. M. Chabagno, D. Muller, and P. Rigaud, M. B. Armand and D. Deroo, *J. Electrochem. Soc.* **122**, 1333 (1985).
8. K. Mizushima, P. C. Jones, P. J. Wiseman and J. B. Goodenough, *Mater. Res. Bull.* **15**, 783 (1980).
9. R. Fong, U. von Sacken and J. R. Dahn, *J. Electrochem. Soc.* **137**, 2009 (1990).
10. R. Yazami and M. Deschamps, *J. Power Sources* (to be published)
11. K. Sato, M. Noguchi, A. Demachi, N. Oki and M. Endo, *Science* **264**, 556 (1994)
12. R. Yazami, A. Cherigui, V. Nalimova and D. Guérard in *Proc. Lithium Batteries*, *Electrochem. Soc.* **93-24**, 1 (1993).
13. D. Guérard, Ph.D. Thesis, University of Nancy (France), 1974
14. R. Yazami and D. Guérard, *J. Power Sources* **43-44**, 39 (1993).
15. J. Menancourt, A. Thomy and X. Duval, *J. Physique (France)* **38-C4**, 194 (1977)
16. Y. Khatir, M. Coulon et L. Bonnetain, *J. Chim. Phys.* **75**, 789 (1978)
17. J. C. Delachaume, M. Coulon and L. Bonnetain *Surface Sci.* **133**, 365 (1983)

---

## PART II

---

### **Sol-Gel Process**

## VANADIUM PENTOXIDE GELS FROM LIQUID CRYSTALS TO LITHIUM BATTERIES

J. LIVAGE\*, N. BAFFIER\*, J.P. PEREIRA-RAMOS\*\* AND P. DAVIDSON\*\*\*

\* Chimie de la Matière Condensée, Université P.M. Curie, 75252 Paris - France

\*\* LECSO/CNRS, 2 rue Henri Dunant, 94320 Thiais - France

\*\*\* Physique des Solides, Université Paris Sud, 91405 Orsay - France

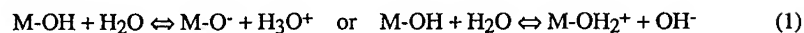
### ABSTRACT

Vanadium pentoxide gels  $V_2O_5 \cdot nH_2O$  are formed via the condensation of vanadic acid in aqueous solutions. They exhibit both ionic and electronic conductivity and could therefore be used as cathode materials in lithium batteries or electrochromic display devices. The polymerization process leads to ribbon-like vanadium pentoxide particles. In a given range of concentration, sols and gels exhibit a homogeneous lyotropic nematic phase in which the ribbons align in the same direction. Ordered fluid phases are thus obtained leading to oriented films when deposited onto flat substrates. Moreover, mixed oxides  $M_xV_2O_5$  ( $M = Na^+, K^+, Ba^{2+}, Al^{3+}, Fe^{3+}, \dots$ ) exhibiting some preferred orientation are obtained via ion exchange. These compounds exhibit improved electrochemical properties (specific capacity, cycling properties) compared to usual mixed oxides prepared via solid state reactions.

### INTRODUCTION

Transition metal oxide gels are known to exhibit ionic and electronic properties that make them good candidates for solid state ionics.<sup>1,2</sup> Their structure and microstructure can be optimized via the chemical control of polymerization reactions.<sup>3</sup> Amorphous oxides or metastable phases can be obtained at low temperature which exhibit improved ionic properties. Sol-gel materials can be easily designed into the desired shape such as thin films or thick coatings.<sup>4</sup>

Sol-gel chemistry actually leads to the formation of hydrous oxide gels  $MO_x \cdot nH_2O$  that can be described as nanocomposite materials. They are made of a solvent (water molecules) trapped within a solid framework (oxide). They exhibit a very open microstructure and ionic species can diffuse easily through the pores of the gel. Moreover, because of the high surface/volume ratio, a large oxide-solution interface is formed.<sup>5</sup> This leads to fully hydroxylated oxide particles which exhibit acid or basic properties as follows :



Vanadium oxide gels  $\text{V}_2\text{O}_5 \cdot n\text{H}_2\text{O}$  have been studied extensively because of their potential application as antistatic coatings in the photographic industry, humidity sensors, rechargeable cathodes in lithium batteries or counter electrodes in electrochromic display devices.<sup>6</sup> They are known to exhibit both electronic and ionic conduction. Vanadium pentoxide can be easily reduced and electronic properties involve electron hopping between vanadium ions in different valence states, namely  $\text{V}^{4+}$  and  $\text{V}^{5+}$ .<sup>7</sup> Ionic properties arise from the acid dissociation of surface V-OH groups so that these gels could also be described as polyvanadic acids  $\text{H}_x\text{V}_2\text{O}_5 \cdot n\text{H}_2\text{O}$  ( $x \approx 0.3$ ).<sup>8</sup>

This paper reports on the formation of lyotropic nematic phases in vanadium pentoxide suspensions, the formation of oriented films when colloidal solutions or gels are deposited onto flat substrates and their electrochemical properties as rechargeable cathodes in lithium batteries.

## SYNTHESIS AND STRUCTURE OF VANADIUM PENTOXIDE SOLS

### Chemical synthesis

Vanadium pentoxide sols were prepared via the acidification of sodium metavanadate solutions  $\text{NaVO}_3$  through a proton exchange resin (Dowex 50W-X2, 50-100 mesh). A yellow solution of decavanadic acid is first obtained that polymerizes slowly into a dark red gel. Depending on vanadium concentration, viscous gels or colloidal solutions can be obtained. The sol-gel transition occurs for a vanadium concentration  $[\text{V}_2\text{O}_5] \approx 0.2 \text{ mol.l}^{-1}$ , that is a composition close to  $\text{V}_2\text{O}_5 \cdot 250\text{H}_2\text{O}$ .<sup>9</sup>

The formation of vanadium pentoxide gels occurs around the point of zero charge ( $\text{pH} \approx 2$ ) from the neutral precursor  $\text{H}_3\text{VO}_4$  in which  $\text{V}^{\text{V}}$  is fourfold coordinated. It can be described as follows (Fig.1):<sup>3,6</sup>

- Coordination expansion first occurs via the nucleophilic addition of two water molecules. This gives hexacoordinated species  $[\text{VO}(\text{OH})_3(\text{OH}_2)_2]^0$  in which one water molecule lies along the z axis opposite to the short  $\text{V}=\text{O}$  double bond while the second one is in the equatorial plane opposite to an OH group. One  $\text{V-OH}_2$  and three  $\text{V-OH}$  bonds are formed in this plane so that x and y directions are not equivalent.
- Fast oxolation reactions, along the  $\text{HO-V-OH}_2$  direction (b axis) give rise to oxolated corner sharing chain polymers.
- Slower oxolation reactions, along the  $\text{HO-V-OH}$  direction (a axis) then link these chains together leading to the formation of edge sharing double chains.

This mechanism provides an explanation for the structure of vanadium pentoxide gels which have been shown to be made of flat ribbons about  $1\mu\text{m}$  long,  $100\text{\AA}$  large and  $10\text{\AA}$  thick. The internal structure of these ribbons was studied by electron and X-ray diffraction. It appears to be close to that observed in the ab planes of orthorhombic  $\text{V}_2\text{O}_5$ .<sup>10,11</sup>

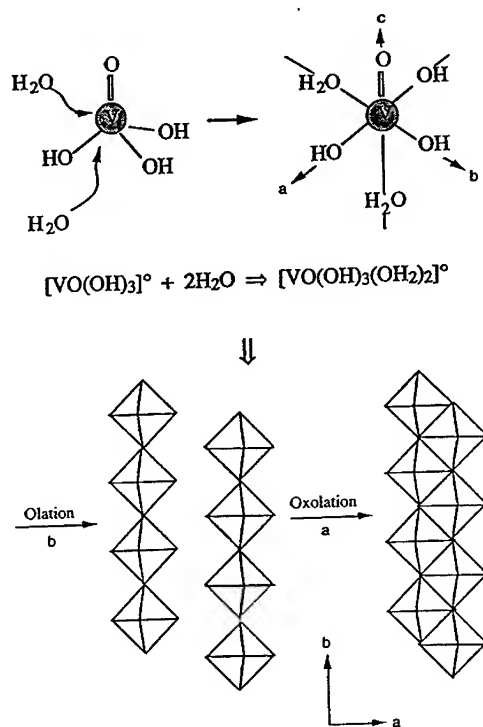


Figure 1. Formation of vanadium pentoxide gels via the condensation of neutral precursors  $[\text{H}_3\text{VO}_4]^0$

#### Formation of lyotropic nematic phases

When observed by optical microscopy, between crossed polarizers, vanadium pentoxide gels are not dark (Fig.2). This shows that the material is not isotropic otherwise no light should go through the crossed polarizer and analyzer system. Vanadium pentoxide gels and sols are anisotropic and optically birefringent. The photograph of figure 2 displays broad dark fringes, which arise from topological defects of the director field, the so-called disclination lines, commonly found in the textures of nematic phases. Since this phase is obtained by the action of

a solvent (water), a lyotropic nematic phase is observed. This points out that vanadium pentoxide sols or gels behave like "liquid crystals" giving rise to nematic phases where  $V_2O_5$  ribbons tend to be parallel to a common axis.<sup>12</sup> The entire sample actually shows the same type of nematic texture, suggesting that we have a homogeneous lyotropic nematic phase and not only 'spindle-like tactoids' as observed by H. Zocher.<sup>13</sup> At low vanadium content, sols become isotropic and nematic phases are only found for vanadium concentrations larger than  $0.1 \text{ mol.l}^{-1}$  ( $V_2O_5 \cdot 500H_2O$ ). The optical birefringence of  $V_2O_5 \cdot 200H_2O$  gels was evaluated using a crystalline slab compensator. A value  $\Delta n \approx 0.01$  was obtained, comparable with values already reported for lyotropic nematic phases of stiff organic polymers ( $\Delta n \approx 0.003$  for Tobacco Mosaic Virus).<sup>14</sup> It should be stressed here that the deposition of well oriented vanadium pentoxide films should be related to the existence of such a nematic phase characterized by large cooperative alignment of the ribbons.

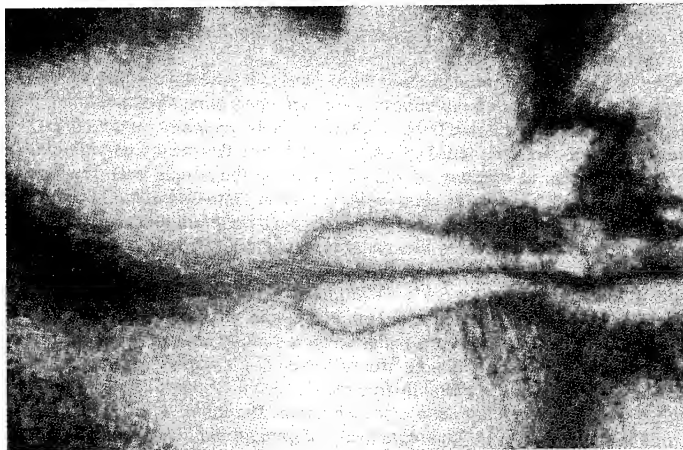


Figure 2. Texture photograph of a  $V_2O_5 \cdot 300H_2O$  sol observed by optical microscopy between crossed polarizers (magnification 250)

#### Deposition of oriented $V_2O_5 \cdot nH_2O$ films

Vanadium pentoxide films or sols can be easily deposited onto flat substrates. Upon drying under ambient conditions, they give rise to xerogels corresponding to the composition  $V_2O_5 \cdot 1.8H_2O$ .<sup>15</sup> Reflection X-ray diffraction spectra of these films give  $00l$  patterns typical of the 1D order of a lamellar compound (Fig.3a). They show that the preferred orientation of these

films is due to the turbostratic stacking of  $V_2O_5$  ribbons along a direction perpendicular to the substrate. The anisotropy of these films has been evidenced by several techniques such as IR-Raman spectroscopy,<sup>16</sup> ESR<sup>17</sup> or XANES.<sup>18</sup> The basal spacing ( $d=11.5\text{\AA}$ ) suggests that one water layer is intercalated between the vanadium pentoxide ribbons. It depends on the water content and increases by steps of about  $2.8\text{\AA}$  corresponding to the intercalation of one water layer, up to  $d=17.7\text{\AA}$  ( $V_2O_5 \cdot 6H_2O$ ). Beyond this value, a continuous swelling is observed. The  $d$  spacing becomes inversely proportional to the solid volume fraction in agreement with the 1-D swelling of lamellar particles (Fig.3b).<sup>19,20</sup>

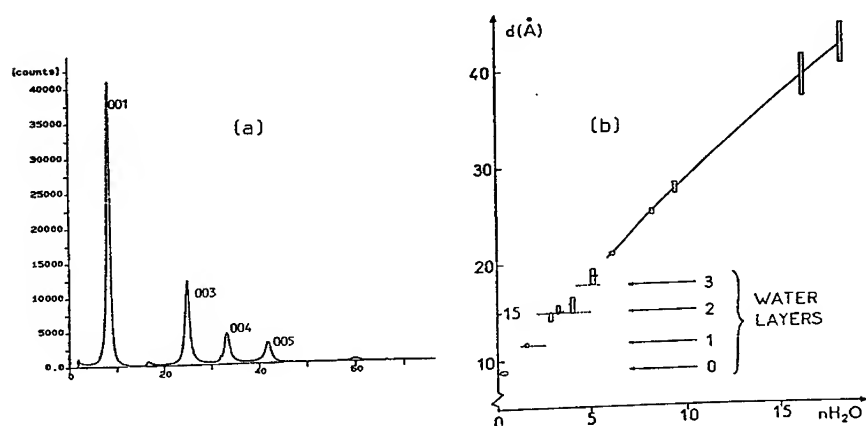


Figure 3. Layered structure of  $V_2O_5 \cdot nH_2O$  films  
a) X-ray diffraction pattern showing the  $00l$  peaks ( $n=1.8$ )  
b) variation of the basal spacing  $d$  with the amount of water  $n$

#### Intercalation properties of $V_2O_5 \cdot nH_2O$ gels.

Vanadium pentoxide gels are able to intercalate a wide variety of inorganic and organic guest species.<sup>21</sup> Intercalation in  $V_2O_5$  gels is much easier than with usual crystalline layered compounds. It occurs readily at room temperature within a few minutes when the gel is dipped into an aqueous solution of ionic salts. The internal structure of the oxide network and the 1-D stacking of the  $V_2O_5$  ribbons are not destroyed. The basal distance increases and intercalation can be easily followed by X-ray diffraction. Intercalation mainly involves ion exchange reactions with the acidic protons of the gel but redox reactions also occur leading to the formation of  $V^{4+}$  ions in the  $V_2O_5$  matrix.<sup>6</sup> Chemical titrations show that the exchange capacity



of vanadium pentoxide gels for monovalent metal cations  $M^+$  is close to 1.75 meq/g, i.e. 0.3 eq/ $V_2O_5$ .<sup>22</sup> This value corresponds to the number of acid protons previously measured by protometric titration. Large monovalent metal cations are intercalated with one water layer ( $d \approx 11 \text{ \AA}$ ) whereas smaller polyvalent cations are intercalated with two water layers ( $d \approx 13.6 \text{ \AA}$ ).<sup>21,23,24</sup> A wide range of other ionic or molecular species, including organic polymers can be intercalated within the layered structure of  $V_2O_5 \cdot nH_2O$  gels.<sup>6</sup>

## ELECTROCHEMICAL PROPERTIES OF VANADIUM PENTOXIDE GELS

Vanadium pentoxide  $V_2O_5$  would be one of the promising candidates as reversible cathode for lithium batteries. Its redox potential is higher than 3 Volts with reference to lithium and specific capacities as high as 125 Ah/kg could be obtained. Discharge curves of crystalline  $V_2O_5$  exhibit several steps corresponding to the formation of different  $Li_xV_2O_5$  phases (Fig.4a).<sup>25</sup> However, despite its layered structure, this oxide behaves as a 3-D framework rather than a Van der Waals host and reversible lithium insertion becomes difficult beyond the first two steps ( $x < 1$ ).<sup>26</sup> Better results are obtained with amorphous vanadium oxides and gels.

### Electrochemical insertion of $Li^+$ in $V_2O_5$ gels

Amorphous vanadium pentoxide is made by splat-cooling from the melt. A black powder is obtained that does not contain water when kept in a dry atmosphere. This amorphous oxide also exhibits a fibrous structure but without any preferred orientation. A swelling process is observed when water is added giving rise to  $V_2O_5 \cdot nH_2O$  gels which are quite similar to those obtained via the condensation of vanadic acid.<sup>27</sup> The electrochemical insertion of  $Li^+$  in the dried amorphous oxide was carried out with the following cell:  $Li/LiAsF_6$  (1M) in cyclic ether/a- $V_2O_5$ . The open circuit voltage (OCV) decreases continuously from 3.85 V (vs.  $Li/Li^+$ ) down to 2 V (Fig.4b).<sup>28</sup>

Vanadium pentoxide gels are deposited onto a platinum disk (working electrode) and dipped into a solution of  $LiClO_4$  (0.5M) in propylene carbonate (PC). Interlayer water molecules and acidic protons are then exchanged by PC and  $Li^+$  ions increasing the basal distance up to  $d = 21.6 \text{ \AA}$ . Chronopotentiometric measurements were performed using the following cell  $Li/LiClO_4$  (1M) in PC/ $Li_xV_2O_5$ . One main process is observed between 3.5 V and 2 V (vs.  $Li/Li^+$ ). Lithium insertion into the xerogel gives rise to a single large plateau around 3.1 V (Fig.4c).<sup>29</sup> It is interesting to point out that the shape of the OCV curve of the oriented gel is intermediate between that of amorphous and crystalline  $V_2O_5$ . As for the

amorphous oxide, a faradaic yield close to  $1.8 \text{ e/V}_2\text{O}_5$  is obtained at  $2\text{V}$  corresponding to the reduction of all  $\text{V}^{5+}$  ions into  $\text{V}^{4+}$ . This leads to a capacity close to  $250 \text{ Ah kg}^{-1}$ . Cycling experiments show a good reversibility, about 70% of the initial capacity is recovered after 30 cycles for a current density  $j=0.05 \text{ mA/cm}^2$ . Entropy measurements and X-ray diffraction experiments show that the electrochemical insertion of  $\text{Li}^+$  into the vanadium oxide gel first leads to the removal of PC from the inter-layer space. The basal spacing decreases down to  $d=10.6\text{\AA}$  ( $x \leq 0.2$ ). The internal structure of  $\text{V}_2\text{O}_5$  ribbons does not change suggesting that all  $\text{Li}^+$  ions are intercalated between rather than in the channels as for crystalline  $\text{V}_2\text{O}_5$ . This could explain the good reversibility of the process.<sup>30</sup>

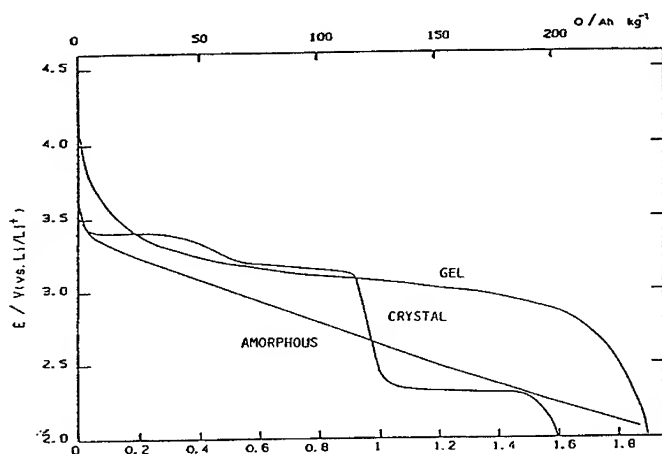


Figure 4. Emf vs. composition curve at  $20^\circ\text{C}$  for electroformed crystalline  $\text{Li}_x\text{V}_2\text{O}_5$ , non oriented amorphous  $\text{Li}_x\text{V}_2\text{O}_5$  and oriented  $\text{Li}_x\text{V}_2\text{O}_5$  gel layer

## SOL-GEL DERIVED MIXED OXIDES

### Electrochemical properties of sodium vanadium bronzes $\beta\text{-Na}_{0.33}\text{V}_2\text{O}_5$

Monovalent cations can be easily exchanged with the acid protons of vanadium pentoxide gels. Sodium intercalation for example leads to  $\text{Na}_{0.33}\text{V}_2\text{O}_5 \cdot 1.5\text{H}_2\text{O}$  compounds. The layered structure is preserved with a basal distance  $d \approx 11\text{\AA}$ . This ordered stacking is not only preserved upon intercalation of metal cations but also during a thermal treatment. Anisotropic coatings of vanadium bronzes  $\beta\text{-Na}_{0.33}\text{V}_2\text{O}_5$  in which about 16% of the vanadium ions are in the reduced  $\text{V}^{4+}$  valence state were made upon heating  $\text{Na}_{0.33}\text{V}_2\text{O}_5 \cdot 1.6\text{H}_2\text{O}$  gels.

These sol-gel bronzes crystallize around 350°C and exhibit the same monoclinic structure as the usual vanadium bronzes obtained via conventional solid state reactions at 700°C. However X-ray diffraction (Fig.5a) suggests that (a,c) planes are preferentially oriented parallel to the substrate while the tunnels of the bronze structure remain perpendicular to the substrate (Fig.5b).<sup>22</sup> The electrical conductivity of such layers is highly anisotropic ( $\sigma_{//} \approx 2\Omega^{-1}\text{cm}^{-1}$ ,  $\sigma_{\perp} \approx 2 \times 10^{-3}\Omega^{-1}\text{cm}^{-1}$ ).<sup>31</sup>

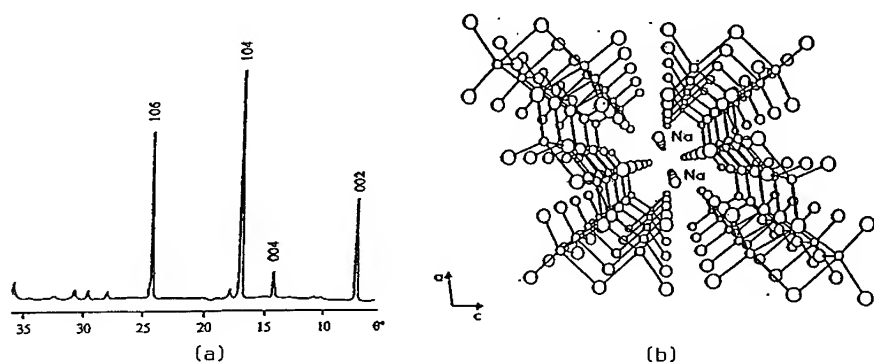


Figure 5. (a) X-ray diffraction diagram of  $\beta\text{-Na}_{0.33}\text{V}_2\text{O}_5$  layers deposited from gels  
(b) the tunnels of the bronze structure are perpendicular to the substrate.

Vanadium bronzes are known to be potentially attractive positive electrodes for Li cells. The preferred orientation of sol-gel layers could even enhance the diffusion of  $\text{Li}^+$  ions into the host lattice.<sup>32</sup> The electrochemical insertion of  $\text{Li}^+$  was studied using  $\text{LiClO}_4$  (1M) in PC as an electrolyte. It takes place in the potential range 3.5-2.4 V (vs.  $\text{Li}/\text{Li}^+$ ). Three well defined steps are observed corresponding to the filling of the different crystallographic sites of the bronze structure. The influence of current density on the discharge curve clearly points out the better electrochemical performance of the sol-gel materials compared to the corresponding bronze prepared via solid-state reactions at 700°C (Fig.6). Whatever the current density, the faradaic yield is about twice larger, about 0.8 instead of 0.5  $\text{Li}^+$  per mole of bronze can be reversibly inserted into the sol-gel materials (Fig.6). This is probably due to the faster lithium diffusion through the oriented sol-gel film. The chemical diffusion coefficient of lithium ( $D_{\text{Li}} \approx 10^{-10} \text{ cm}^2\text{s}^{-1}$  for  $0 < x < 0.3$ ) is almost two orders of magnitude larger than in the solid state derived bronze. The reversibility remains good in the potential range 3.8-1.8 V. A capacity of about  $120 \text{ Ahkg}^{-1}$  is still recovered after 50 cycles, twice the capacity obtained for solid state bronzes.<sup>33,34</sup>

### Electrochemical properties of potassium vanadium bronzes $\beta\text{-K}_{0.25}\text{V}_2\text{O}_5$

Ion exchange of a vanadium pentoxide gel in an aqueous solution of KCl (0.1M) leads to a  $\text{K}_{0.25}\text{V}_2\text{O}_5 \cdot 1.3\text{H}_2\text{O}$  layer without destroying the stacking of the vanadium pentoxide ribbons. Heating this compound at  $550^\circ\text{C}$  leads to the crystallization of the monoclinic  $\beta\text{-K}_{0.25}\text{V}_2\text{O}_5$  phase. As for the sodium compound, a preferred orientation is preserved and only the 002, 104 and 106 Bragg's peaks have noticeable intensities. Electrochemical  $\text{Li}^+$  insertion at low constant current density ( $20\mu\text{A}/\text{cm}^2$ ) involves three main steps in the potential window 3.7-2 V separated by sharp potential drops for  $x=0.4$  and  $x=0.8$  (Fig.7). This leads to a theoretical specific capacity of 240 Ah/kg. A comparison of the discharge curves of the sol-gel bronze and the corresponding solid state bronze emphasizes the better electrochemical performances of the first one (Fig.7).<sup>35</sup>

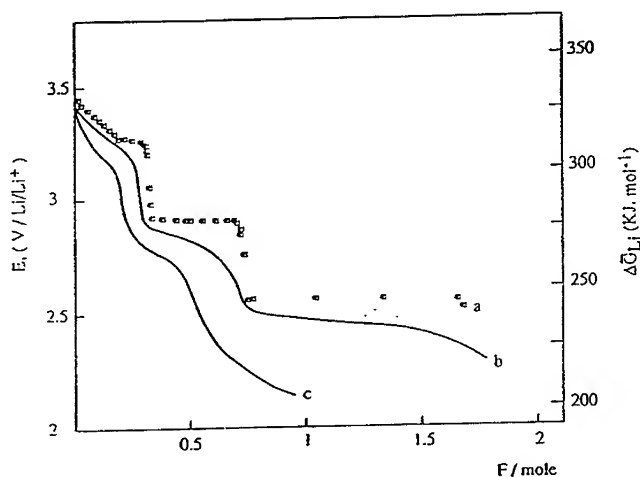


Figure 6. Chronopotentiometric curves for the reduction of  $\beta\text{-Na}_{0.33}\text{V}_2\text{O}_5$  bronzes  
(a) OCV curve, (b) sol-gel bronze, (c) solid state bronze  
(current density  $0.1\text{ mA}/\text{cm}^2$ , electrolyte  $\text{LiClO}_4$  (1M)/PC,  $T=20^\circ\text{C}$ )

### Electrochemical properties of iron vanadium mixed oxide $\text{Fe}_{0.12}\text{V}_2\text{O}_{5.16}$

A new  $\text{Fe}_{0.12}\text{V}_2\text{O}_{5.16}$  mixed oxide has been recently synthesized via the intercalation of  $\text{Fe}^{3+}$  ions into the layered structure of vanadium pentoxide gels. Its structure, determined by the Rietveld method, is built from the  $\text{V}_2\text{O}_5$  ribbons linked together via apex sharing  $[\text{FeO}_6]$

octahedra. Layers synthesized from oriented vanadium pentoxide gels only exhibit the 001 and 002 Bragg's peaks showing that the preferred orientation has been preserved.<sup>36</sup> Three reversible reduction steps are observed between 3.8 and 2V, at 20°C, using LiClO<sub>4</sub> (1M in PC) as an electrolyte (Fig.8). They correspond to a faradaic yield as high as 2.5F per mole. The presence of Fe<sup>3+</sup> ions in the vanadium pentoxide matrix provides improved cycling properties at high discharge-charge rates (C/4). A specific capacity of 200 Ah/kg is recovered after 40 cycles in the 3.8-2V window.<sup>37</sup>

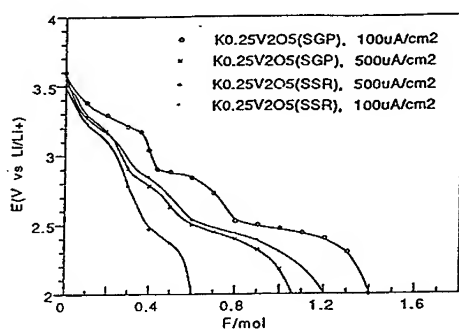


Figure 7. Discharge curves of  $\beta$ -K<sub>0.25</sub>V<sub>2</sub>O<sub>5</sub> bronzes derived from gels or solid state reactions

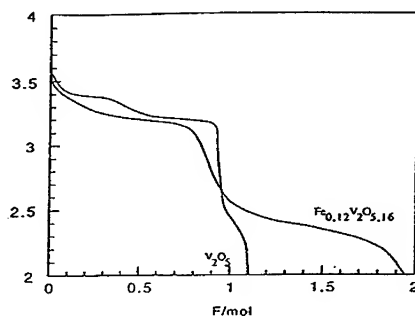


Figure 8. Discharge curve of V<sub>2</sub>O<sub>5</sub> and Fe<sub>0.12</sub>V<sub>2</sub>O<sub>5.16</sub> (low current density, 20 μA/cm<sup>2</sup>)

## CONCLUSION

The sol-gel process provides new routes for the synthesis of ionic materials. The design of molecular precursors provides a chemical control of condensation reactions allowing the synthesis of tailor made materials. Moreover, hybrid organic-inorganic gels can now be synthesized. They exhibit new properties and could be used for the fabrication of "all gel" micro-ionic devices such as electrochromic displays.<sup>38</sup>

This paper shows that improved electrochemical properties can be obtained via the orientation of sol-gel derived thin films. This appears to be very specific of vanadium pentoxide gels. We have shown how the chemical process leads to a ribbon-like structure. Colloidal solutions and gels then exhibit optical birefringence and behave like liquid crystals. Lyotropic nematic phases are formed in which all the ribbons are aligned along the same direction. This spontaneous and cooperative orientation can be preserved upon drying leading to anisotropic films made of the turbostratic stacking of the ribbons. A wide range of new materials was

synthesized from these oriented vanadium pentoxide films. They exhibit improved electrochemical properties as rechargeable cathode for lithium batteries, mainly in terms of faradaic capacity and cycling behaviour.

**ACKNOWLEDGMENTS.** Authors gratefully acknowledge the following students who have been working on vanadium pentoxide gels: S. Bach, R. Baddour-Hadjean, A. Garreau, S. Maingot and L. Schoutteten.

## REFERENCES

1. J. Livage, *Solid State Ionics*, **50** (307 (1992)
2. J. Livage, *Mat. Res. Soc. Symp. Proc.*, **293**, 261 (1993)
3. M. Henry, J.P. Jolivet, J. Livage, *Structure and Bonding*, **77**, 155 (1992)
4. *Sol-Gel Technology*, Edited by L. Klein, Noyes Pub., Park Ridge (1988)
5. C.J. Brinker and G.W. Scherer, *Sol-Gel Science*, Academic Press, San Diego (1990)
6. J. Livage, *Chem. Mater.*, **3**, 578 (1991) and references therein
7. C. Sanchez, F. Babonneau, R. Morineau, J. Livage, J. Bullot, *Phil. Mag. B*, **47**, 279 (1983)
8. N. Gharbi, C. Sanchez, J. Livage, J. Lemerle, L. Nejtem, J. Lefebvre, *Inorg. Chem.*, **21**, 2758 (1982)
9. J. Lemerle, L. Nejtem, J. Lefebvre, *J. Chem. Res.*, 301 (1978)
10. J.J. Legendre, J. Livage, *J. Colloids Interface Sci.*, **94**, 75 (1983)
11. J.J. Legendre, P. Aldebert, N. Baffier, J. Livage, *J. Colloids Interface Sci.*, **94**, 84 (1983)
12. P. Davidson, A. Garreau, J. Livage, *Liquid Crystals*, **16**, 905 (1994)
13. H. Zocher, *Z. Anorg. Allg. Chem.*, **147**, 91 (1925)
14. R. Oldenburg, X. Wen, R.B. Meyer, D.L.D. Caspar, *Phys. Rev. Lett.*, **61**, 1851 (1988)
15. P. Aldebert, N. Baffier, N. Gharbi, J. Livage, *Mat. Res. Bull.*, **16**, 669 (1981)
16. M.T. Vandenborre, R. Prost, E. Huard, J. Livage, *Mat. Res. Bul.*, **18**, 1133 (1983)
17. P. Barboux, D. Gourier, J. Livage, *J. Colloids Surf.*, **11**, 119 (1984)
18. S. Stizza, G. Mancini, M. Benfatto, C.R. Natoli, J. Garcia, A. Bianconi, *Phys. Rev. B*, **40**, 229 (1989)
19. P. Aldebert, H.W. Haesslin, N. Baffier, J. Livage, *J. Colloids Interface Sci.*, **98**, 478 (1984)
20. N. Baffier, P. Aldebert, J. Livage, H.W. Haesslin, *J. Colloids Interface Sci.*, **141**, 467 (1991)
21. A. Bouhaouss, P. Aldebert, N. Baffier, J. Livage, *Rev. Chim. Miner.*, **22**, 417 (1985)
22. L. Znaidi, N. Baffier, M. Huber, *Mat. Res. Bull.*, **24**, 1501 (1989)

23. S. Kittaka, N. Uchida, T. Kihara, T. Suetsugi, T. Sasaki, *Langmuir*, **8**, 245 (1992)
24. N. Baffier, L. Znaidi, J.C. Badot, *J. Chem. Soc. Faraday Trans.*, **86**, 2623 (1990)
25. K. West, B. Zachau-Christiansen, M.J.L. Ostergard, T. Jacobsen, *J. Power Sources*, **20**, 165 (1987)
26. C. Delmas, H. Cognac-Auradou, J.M. Cocciantelli, M. Ménétrier, J.P. Doumerc, *Solid State Ionics*, **69**, 257 (1994)
27. J. Livage, N. Gharbi, M.C. Leroy, M. Michaud, *Mat. Res. Bull.*, **13**, 1117 (1978)
28. M. Nabavi, C. Sanchez, F. Taulelle, J. Livage, *Solid State Ionics*, **28-30**, 1183 (1988)
29. R. Baddour, J.P. Pereira-Ramos, R. Messina, J. Perichon, *J. Electroanal. Chem.*, **277**, 359 (1990)
30. R. Baddour, J.P. Pereira-Ramos, R. Messina, J. Perichon, *J. Electroanal. Chem.*, **314**, 81 (1991)
31. J.C. Badot, D. Gourier, F. Bourdeau, N. Baffier, A. Tabuteau, *J. Solid State Chem.*, **92**, 8 (1991)
32. J.P. Pereira-Ramos, R. Messina, L. Znaidi, N. Baffier, *Solid State Ionics*, **28-30**, 886 (1988)
33. J.P. Pereira-Ramos, R. Messina, S. Bach, N. Baffier, *Solid State Ionics*, **40-41**, 970 (1990)
34. S. Bach, J.P. Pereira-Ramos, N. Baffier, R. Messina, *J. Electrochem. Soc.*, **137**, 1042 (1990)
35. S. Maingot, N. Baffier, J.P. Pereira-Ramos, P. Willmann, *Solid State Ionics*, **67**, 29 (1993)
36. S. Maingot, P. Deniard, N. Baffier, J.P. Pereira-Ramos, A. Kahn-Harari, R. Brec, *Mat. Sci. Forum*, **152-153**, 197 (1994)
37. S. Maingot, R. Baddour, J.P. Pereira-Ramos, N. Baffier, P. Willmann, *J. Electrochem. Soc.*, **140**, L158 (1993)
38. P. Judeinstein, J. Livage, A. Zarudiansky, R. Rose, *Solid State Ionics*, **28-30**, 1722 (1988)

## SOL GEL INTERCALATION MATERIALS FOR LITHIUM BATTERIES

J.P. PEREIRA-RAMOS<sup>1</sup>, S. BACH<sup>1</sup>, J. FARCY<sup>1</sup> and N. BAFFIER<sup>2</sup>

1. Laboratoire d'Electrochimie, Catalyse et Synthèse Organique, C.N.R.S., UMR 28, 2, rue Henri-Dunant 94320 Thiais, France.

2. Laboratoire de Chimie Appliquée de l'Etat Solide, C.N.R.S. URA 1466, ENSCP, 11, rue Pierre et Marie Curie 75231 Paris Cedex 05, France.

### ABSTRACT

This paper emphasizes the interest of sol-gel synthesis in obtaining high performance cathodic materials. New vanadium oxides, vanadium bronzes ( $M_xV_2O_5$ ) and manganese oxides ( $MnO_2$ ) are prepared via the sol-gel process using inorganic precursors in aqueous medium. Their electrochemical behaviour (working potential, specific capacity, kinetics of Li transport, rechargeability, cycle life) is investigated and discussed in relation with their specific structural, chemical and physical features. In particular, the results are compared to that achieved for the corresponding classical compounds prepared via a synthesis route involving solid state reactions or precipitation reactions.

### INTRODUCTION

Transition metal oxides usually investigated as lithium intercalation materials for secondary Li cells are prepared through solid state reactions at high temperature. Conversely, sol-gel chemistry is one of the various approaches offered by the "chimie douce" method to synthesize transition metal oxides at low temperature. Taking account for the influence of synthesis way upon the electrochemical properties of Li intercalation compounds, the sol-gel synthesis involving the formation of a solid in an aqueous or organic phase may afford significant progress in the field of rechargeable cathodic materials. Starting from molecular precursors, an oxide network is then obtained via inorganic polymerization reactions in solution [1].

A few years ago, our group started an evaluation of the sol-gel process in obtaining new cathodic materials, or in providing improvements to the electrochemical performance of the compounds already known. Our work is focused on two main groups of materials:  $V_2O_5$ - and  $MnO_2$ - based compounds. A wide variety of solids have been prepared:  $V_2O_5$  xerogel,  $V_2O_5$  oxide,  $\beta$  monoclinic bronzes  $M_xV_2O_5$  ( $M = Na, K, Ag$ ), mixed oxides  $M_yV_2O_{5+z}$  ( $M = Fe$ ) as well as spinel, layered and tunnel  $MnO_2$  phases.

In the present paper we briefly recall the most important results obtained with  $V_2O_5$  xerogel and vanadium bronzes with special emphasis on the synthesis and electrochemistry of a new mixed oxide  $Fe_{0.12}V_2O_{5.16}$  and  $MnO_2$  oxides.

#### 1-Sol-gel synthesis of $V_2O_5$ - and $MnO_2$ -based compounds

Sol-gel chemistry is based on inorganic polymerization reactions in solution. The starting molecular precursors containing hydroxyl groups undergo that polymerization that leads to colloidal entities and finally to a gel. The precursor used in our case is in aqueous solution. The reaction involves: i) hydroxylation of the inorganic precursor performed via pH modification for the vanadium system or via redox reactions in the case of manganese. ii) polycondensation reactions leading to the departure of water molecules, the bridging of oxygen atoms, and a hydrated oxide network is obtained.

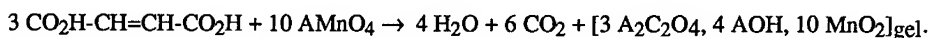


### *V<sub>2</sub>O<sub>5</sub>-based compounds*

The most important step is the preparation of the V<sub>2</sub>O<sub>5</sub> xerogel (V<sub>2</sub>O<sub>5</sub> 1,6H<sub>2</sub>O) obtained after departure of almost water molecules from the corresponding gel at RT: the latter is prepared upon the acidification of a NaVO<sub>3</sub> aqueous solution by passing the solution through a H<sup>+</sup>-exchanged resin. Indeed, due to the xerogel cationic exchange properties, various exchanged xerogel forms can be then obtained. Depending on the nature of cationic species, the corresponding vanadium bronzes (M<sub>x</sub>V<sub>2</sub>O<sub>5</sub>; M = Na<sup>+</sup>, K<sup>+</sup>, Ag<sup>+</sup> with x = 0.25/0.33) and mixed oxides (Fe<sub>0.12</sub>V<sub>2</sub>O<sub>5.16</sub>) are obtained after a heat-treatment near 550°C.

### *MnO<sub>2</sub>-based compounds*

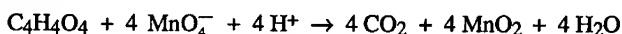
Contrary to the V<sub>2</sub>O<sub>5</sub> sol-gel synthesis, MnO<sub>2</sub> oxides are prepared via redox reactions because of the lack of stable Mn<sup>4+</sup> precursors in aqueous solution. The precursor is a soluble manganese salt in which the oxidation state of Mn = 7 : an aqueous permanganate solution AMnO<sub>4</sub> (A = Li, Na, K). Reduction of this Mn aqueous solution is made by the fumaric acid C<sub>4</sub>H<sub>4</sub>O<sub>4</sub> at a pH close to 7 with a molar ratio AMnO<sub>4</sub>/C<sub>4</sub>H<sub>4</sub>O<sub>4</sub> = 3 leading to hydroxylated Mn(IV) species. Condensation then occurs via ololation and oxolation. Under these conditions, gels are rapidly formed at room temperature following the overall reaction :



The mean oxidation state of Mn is ≈ 4. A<sup>+</sup> counter ions are not hydroxylated and remain trapped inside the gel network.

The kind of MnO<sub>2</sub> synthesized will depend on the nature of A<sup>+</sup> counterions used. Drying and calcination of the gels lead to the formation of trivalent Mn in LiMn<sub>2</sub>O<sub>4</sub>, Na<sub>0.7</sub>MnO<sub>2</sub> and K<sub>0.25</sub>MnO<sub>2</sub> at 600°C during 3/5 h. At 1000°C, all the counterions have reacted to form the corresponding ternary oxide AMnO<sub>2</sub>. By an appropriate sulphuric acid treatment (2.5 M) at RT, A<sup>+</sup> and Mn<sup>2+</sup> ions are released in the solution while the solid network progressively transforms into MnO<sub>2</sub>. Thus, λ MnO<sub>2</sub> (RT) and γ MnO<sub>2</sub> (90° C) are obtained from the LiMn<sub>2</sub>O<sub>4</sub> spinel oxide[2], and birnessite MnO<sub>1.84</sub>, 0.6 H<sub>2</sub>O from the layered Na and K mixed oxides [3].

The use of an excess of MnO<sub>4</sub><sup>-</sup> at pH 1 with a molar ratio of 4 for KMnO<sub>4</sub>/C<sub>4</sub>H<sub>4</sub>O<sub>4</sub> strengthens the oxidizing power of MnO<sub>4</sub><sup>-</sup> and ensures the quantitative oxidation of Mn<sup>2+</sup> to MnO<sub>2</sub>. In this way, a total consumption of C<sub>4</sub>H<sub>4</sub>O<sub>4</sub> and MnO<sub>4</sub><sup>-</sup> is observed according to the following reaction :



After washing and drying at 100° C, a long range disordered αMnO<sub>2</sub> oxide is obtained with only 0.06 K<sup>+</sup> ions per manganese and a high oxidation state for Mn : Z = 3.93.

## 2-Structural and Electrochemical properties

### *2-1 V<sub>2</sub>O<sub>5</sub>-based compounds*

Two kinds of sol-gel V<sub>2</sub>O<sub>5</sub>-based compounds are investigated : new compounds such as V<sub>2</sub>O<sub>5</sub> xerogel (VXG) or the mixed oxide Fe<sub>0.12</sub>V<sub>2</sub>O<sub>5.16</sub>, β Na<sub>0.33</sub>V<sub>2</sub>O<sub>5</sub>, K<sub>0.25</sub>V<sub>2</sub>O<sub>5</sub> and Ag<sub>0.33</sub>V<sub>2</sub>O<sub>5</sub> bronzes which exhibit a high preferred orientation in comparison to the corresponding bronzes prepared via solid state reactions.

Pure thin films of VXG (5 μm) on platinum can be used as positive electrode in 1 M LiClO<sub>4</sub> solution in propylene carbonate at RT. A preliminary ionic and molecular exchange procedure in electrolyte is required to use VXG containing only stable structural water. One of the most

striking features of VXG is that lithium insertion seems intermediate between that observed in the crystalline and amorphous  $V_2O_5$ . Indeed, only one single reduction step occurs located near 2.9 V and involves a massic capacity of 250 Ah/kg, ie, the quasi-quantitative reduction of  $V^{5+}$  into  $V^{4+}$ . Structural thermodynamic and kinetic measurements allowed to describe the complete Li insertion process which is accompanied by a turbostratic disorder and to outline interesting features : a high discharge capacity of 250 Ah/kg, a high kinetics for Li transport for  $0 < x < 1.3$  ( $D_{Li} > 5 \cdot 10^{-11} \text{ cm}^2\text{s}^{-1}$ ), a satisfactory reversibility. Nevertheless, due to its poor electronic conductivity ( $10^{-5} \Omega^{-1}\text{cm}^{-1}$ ), the cycle life of VXG is limited [4].

As explained in [5, 6], the sol gel vanadium bronzes  $M_xV_2O_5$  ( $Na_{0.33}V_2O_5$ ,  $Na_{0.25}V_2O_5$ ,  $K_{0.25}V_2O_5$ ,  $Ag_{0.33}V_2O_5$ ) exhibit a monoclinic tunnel structure. Their high preferred orientation, stemming from that of the parent oxide VXG (001), corresponds to the alignment of all the tunnels parallel to each other over large domains. Because of this preferred orientation, the sol-gel compounds behave as quasi-monocrystals also from the electronic view point. These specific features induce notable improvements of their electrochemical behaviour compared to usual materials prepared via solid state reactions (SSR).

Even when the same insertion steps at 3.3 V, 2.9 V and 2.55 V corresponding to the filling of specific crystallographic sites are evidenced for both SG and SSR materials, the kinetics of Li transport is found to be greatly enhanced by one order of magnitude for the sol gel bronze [6]. Thus, a higher massic capacity (120 Ah/kg), twice that of the classical bronze is achieved when cycling galvanostatic experiments are performed in the potential range 3.8/1.8 V at a C/6 rate (figure 1).

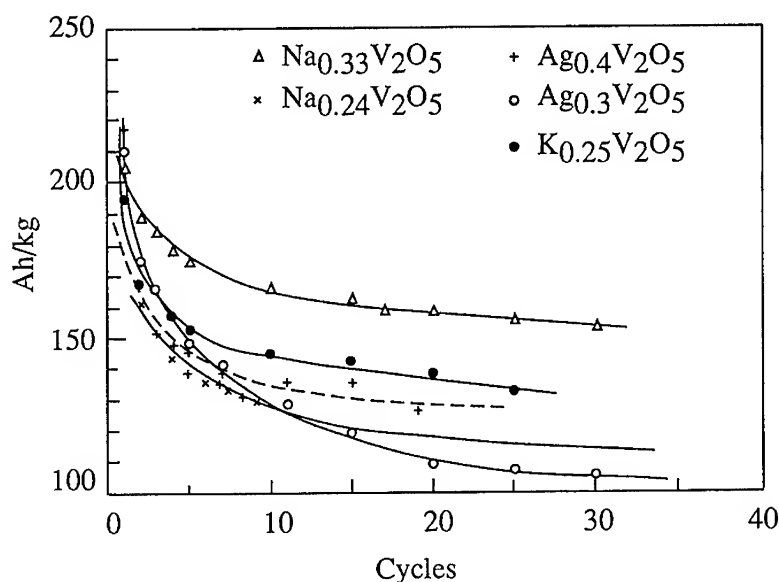


Figure 1: Evolution of the specific capacity as a function of the number of cycles for various  $\beta$  monoclinic  $M_xV_2O_5$  bronzes prepared via a sol-gel process (1M  $LiClO_4/PC$ ; C/6 discharge-charge rate)

Recent results on a new iron vanadium oxide  $\text{Fe}_{0.12}\text{V}_2\text{O}_{5.16}$  indicate an additional potentiality of the sol-gel technique. An ion exchange procedure performed in a 0.1 M  $\text{FeCl}_3$  aqueous solution allows for obtaining the corresponding iron xerogel. Heat treatment at  $520^\circ\text{C}$  in air gives rise to the formation of this oxide. Indeed, in contrast to what happened during the heat-treatment of Na, K or Ag-exchanged vanadium xerogels, no reduction process occurred and only 2%  $\text{V}^{4+}$  are evidenced through a redox chemical analysis.

X-ray powder diagrams (figure 2) show cell parameters which resemble those of orthorhombic  $\text{V}_2\text{O}_5$ :  $a = 11.54 \text{ \AA}$ ;  $b = 3.56 \text{ \AA}$ ;  $c = 4.36 \text{ \AA}$ . Rietveld calculation allows to suggest the introduction of  $\text{Fe}^{3+}$  ions in sites located between four oxygen atoms of the  $\text{V}_2\text{O}_5$  slabs with additional oxygen atoms along the  $c$  axis, above and below the iron site to complete the iron octahedral environment [7].

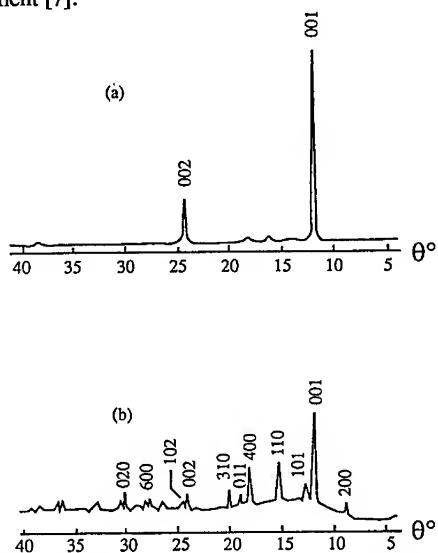


Figure 2: X-ray diffraction patterns (Co  $K\alpha$ ) from  $\text{Fe}_{0.12}\text{V}_2\text{O}_{5.16}$  bronze as thin layer (a) and previously ground (b).

The influence of the current density on the discharge curves of the oxide is reported in figure 3. Although the overall shape of discharge curves is close to that of orthorhombic  $\text{V}_2\text{O}_5$ , several features are evidenced: 1) for a 3 V cutoff voltage,  $x_{\text{max}} < 1$  probably due to the presence of additional interlayer oxygen atoms 2) an unusual extended third insertion step at 2.3 V ( $1 < x < 2$ ) always more important than for  $\text{V}_2\text{O}_5$ . These results are found by using graphite (20 % or 90 % by weight) or not, and a material ground or not. Moreover, these characteristics are of great interest since it is maintained even at high current densities. For the sake of comparison, a capacity of only 1.6 F/ mole is achieved at a 2.2V cutoff voltage when a current density of  $200 \mu\text{A}/\text{cm}^2$  is applied to a  $\text{V}_2\text{O}_5$  cathode. Contrary to the bronzes, these improvements do not stem from a preferred orientation but from unique structural properties and also a lower activation energy for the electronic conductivity (0.15 eV against 0.22 eV for  $\text{V}_2\text{O}_5$ ). This latter property could be explained by the role of the  $\text{Fe}^{3+}/\text{Fe}^{2+}$  couple during the redox Li insertion-extraction reaction. Impedance spectroscopy measurements (figure 4) indicate a high kinetics for Li transport. The values of  $D_{\text{Li}}$ , in the range  $10^{-10}$ - $10^{-11} \text{ cm}^2 \text{ s}^{-1}$  for  $0 < x < 1.35$ , are in good

accord with the influence of the current density. In addition, the evolution of the chemical diffusion coefficient  $D_{Li}$  as a function of the Li content accounts for the initial presence of ferric ions in the host lattice. Voltammetric, chronopotentiometric and structural studies have proved the rechargeability of the material in the potential 3.8/2 V for  $0 < x < 1.8$  [8, 9]. An initial massic capacity of  $\approx 300$  Ah/kg is available. The effect of ferric ions may be viewed as stabilizing the host structure during the Li intercalation process. In this way, extended one-phase regions are evidenced while the composition ranges for biphasic regions are narrower than for  $V_2O_5$ . A promising cycling behaviour in the potential range 3.8/2 V (C/4 discharge-charge rate) is observed with a high massic capacity of 200 Ah/kg after the fortieth cycle.

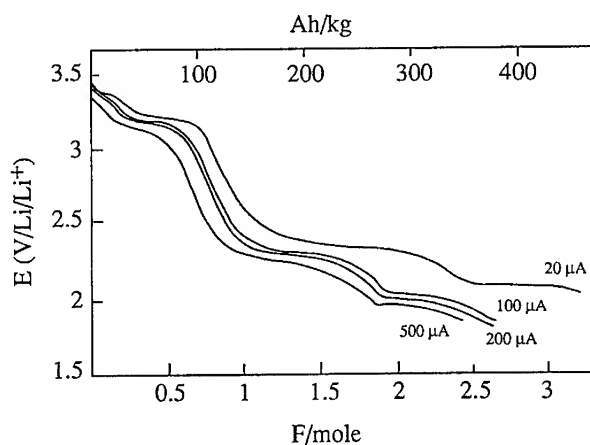


Figure 3: Influence of the current density on the discharge curves of  $Fe_{0.12}V_2O_{5.16}$  (90% weight graphite) in a 1M  $LiClO_4$  solution in PC at 20°C.

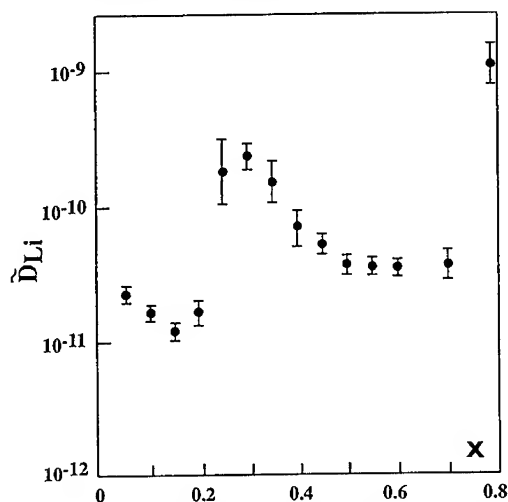


Figure 4: Evolution of the chemical diffusion coefficient of lithium as a function of  $x$  in  $Li_x Fe_{0.12}V_2O_{5.16}$

## 2.2 MnO<sub>2</sub>-based compounds

### LiMn<sub>2</sub>O<sub>4</sub>

A maximal extraction of 0.7 Li<sup>+</sup> from the host lattice LiMn<sub>2</sub>O<sub>4</sub> has been performed so that the spinel cubic compound Li<sub>0.3</sub>Mn<sub>2</sub>O<sub>4</sub> (*a* = 8.07 Å) was obtained. The OCV curve [10] indicated that the first two insertion steps are separated by a moderate potential change as in the case of V<sub>2</sub>O<sub>5</sub>. Afterwards, a sharp potential drop corresponds to the transformation of the cubic LiMn<sub>2</sub>O<sub>4</sub> phase (*a* = 8.24 Å) into a tetragonal phase (*a* = 5.66 Å ; *c* = 9.30 Å) which is maintained for 1 < *x* < 1.6. The rechargeability of the first two processes is very high while the third one reduces the cycle life of the material as often reported.

Acid treatment of LiMn<sub>2</sub>O<sub>4</sub> leads to the formation of the cubic spinel λMnO<sub>2</sub> (*a* = 8.02 Å). However, electrochemical lithiation is limited to a low composition range Δ*x* ≈ 0.3/Mn in the potential window 4/3.5 V. For higher depths of discharge we found a similar behaviour for the sol-gel and the classical materials [6].

### γMnO<sub>2</sub>

Cyclic voltammetric curves for MnO<sub>2</sub> (γ Mn<sub>1.92</sub>) are reported in [2]. Once again, we obtain an electrochemical behaviour which is very close to that found using other ways of synthesis. The Mn<sup>4+</sup>/Mn<sup>3+</sup> redox couple in γMnO<sub>2</sub> does not appear as a reversible system and is characterized by a low rechargeability which never exceed 60-70 % from the first cycles.

### MnO<sub>2</sub> birnessite

The sol-gel birnessite MnO<sub>1.84</sub> 0.6H<sub>2</sub>O constitutes the most promising compound both from the fundamental and practical viewpoints. The electrochemical behaviour of this cathodic material opens a new way of research in that the presence of structural water does not prejudice to its rechargeability. Secondly, the major advantage of the compound consists in an unusual high depth of discharge-charge of ≈ 0.9 F/Mn, available for Li intercalation between 4 and 2 V (figure 5).

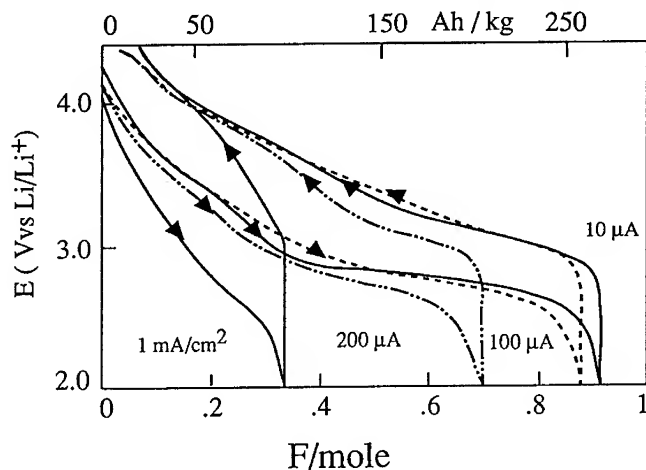


Figure 5: Influence of the current density on the cyclic chronopotentiograms for the sol-gel birnessite MnO<sub>1.84</sub>, 0.6H<sub>2</sub>O (20% weight graphite).

X-ray diffraction spectra of the sol-gel birnessite and ternary oxide  $\text{Na}_{0.7}\text{MnO}_2$  are shown in figure 6. The hexagonal symmetry ( $a = 2.85 \text{ \AA}$ ,  $c = 14.5 \text{ \AA}$ ) of the parent oxide is maintained after sulphuric treatment at RT as well as the high preferred orientation. The corresponding cells contain two consecutive layers as for  $\text{Na}_{0.7}\text{MnO}_2$  with trigonal prismatic (TP) sites. Conversely, for the corresponding classical birnessite obtained from the reaction of  $\text{KMnO}_4$  with  $\text{HCl}$  at  $90^\circ\text{C}$  the  $\text{MnO}_6$  octahedra are not superposable (figure 7). Thus, two types of sites appear: the trigonal antiprismatic (TAP) and the trigonal pyramidal (TPy) sites [11].

The thermal analysis of the sol-gel birnessite reveals a large endothermic peak originating from the departure of weakly bonded water molecules near  $120^\circ\text{C}$  while an endothermic peak at  $540^\circ\text{C}$  corresponds to the transformation of the compound into bixbyite  $\alpha\text{Mn}_2\text{O}_3$  [12].

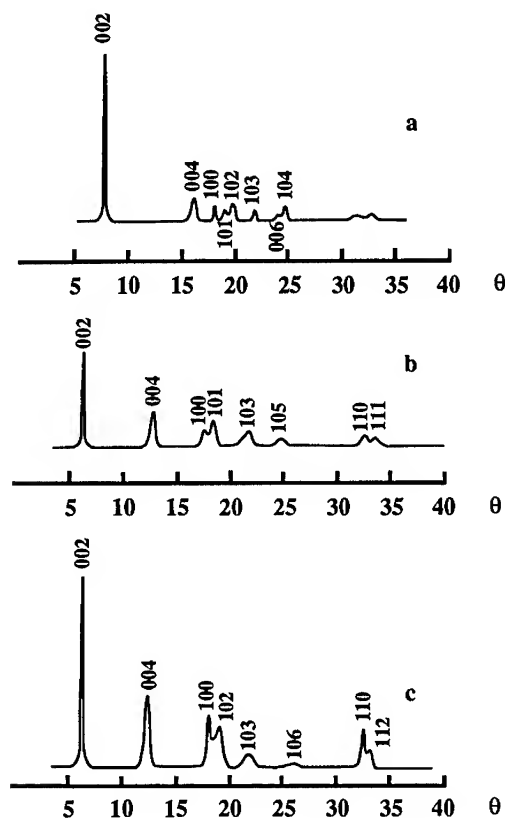


Figure 6: X-ray diffraction spectra of (a) the hexagonal ternary oxide  $\text{Na}_{0.7}\text{MnO}_2$ ; (b) the sol-gel synthesized hexagonal sodium compound  $\text{Na}_{0.45}\text{MnO}_{2.14} \cdot 0.76\text{H}_2\text{O}$ ; and (c) the sol-gel synthesized hexagonal sodium-free compound  $\text{MnO}_{1.84} \cdot 0.7\text{H}_2\text{O}$

A detailed structural and electrochemical investigation has been performed in order to elucidate the Li insertion process into sol gel birnessite [2, 3, 6, 11, 12]. Lithium easily enters trigonal prismatic sites in the potential range 4.2/2.85 V and then induces a monoclinic distortion from  $x = 0.05$  to lead to a closely related monoclinic phase ( $a = 5.15 \text{ \AA}$  ;  $b = 2.86 \text{ \AA}$  ;  $c = 14.29 \text{ \AA}$   $\beta = 102.1^\circ$ ) which is pure for  $x \geq 0.25$ . Such a structural change corresponds to a glide of the layers in the  $ab$  plane, one  $\text{MnO}_6$  layer relative to another, and is accompanied by a decrease of the interlayer spacing.

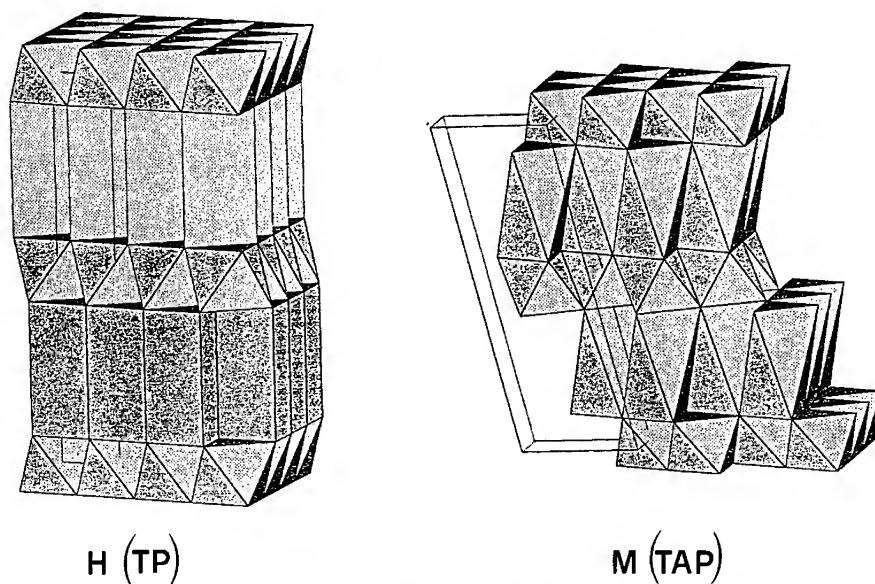


Figure 7: Hexagonal to monoclinic distortion of the sol-gel birnessite host lattice during Li insertion.

Therefore, from that value,  $\text{MnO}_6$  layers are no more superposable and further Li accommodation is more difficult, occurring in the trigonal antiprismatic sites of the monoclinic structure for  $0.25 < x < 0.9$  and a quasi-voltage plateau is observed around 2.9 V. The reversibility of the electrochemical Li insertion is possible because this hexagonal to monoclinic distortion is fully reversible. In addition, no water departure from the host lattice has been evidenced from X-ray and thermal analysis of lithiated compounds. Indeed, insertion of lithium ions induces a new localization of water, leading to the formation of more strongly bonded water. The lower the water content, the lower the capacity and the rechargeability. Then, the elasticity necessary to sustain repeated Li insertion-extraction cycles seems to be provided by interlayer water which ensures the remarkable cycling behaviour of the material. For instance, from an initial value of 200 Ah/kg, a specific capacity of  $\approx 150 \text{ Ah/kg}$  is still recovered after the fiftieth cycle at C/6 rate.

Conversely, the geometry of sites available for Li insertion in the classical birnessite is quite different. Although Li accommodation into TAP and TPy sites also induces a distortion into a final

monoclinic phase, this latter only appears close to the maximum Li content  $x \approx 0.5$ . The lower discharge capacity observed in this case could be also due to the low  $\text{Mn}^{\text{IV}}$  content available in the starting material, as shown by visible spectroscopy [10].

Another way to improve the cycle life of the layered material was investigated by maintaining some species able to limit the magnitude of the contraction-swelling process of the host lattice during the electrochemical reaction [6]. This point has been examined with the moderate oxidation treatment in aqueous solution of the sol-gel  $\alpha\text{Na}_{0.7}\text{MnO}_{2.14}$  at RT. The resulting product is  $\text{Na}_{0.45}\text{MnO}_{2.14}$ ,  $0.76 \text{ H}_2\text{O}$  in which  $Z_{\text{Mn}} = 3.83$ . An initial electrochemical oxidation at low current density allows to reach a higher maximum faradaic yield by removing  $0.12 \text{ Na}^+$  from the interlayer spacing and the true composition of the sol-gel sodium manganese dioxide is  $\text{Na}_{0.33} \text{Mn}^{\text{IV}}_{0.95} \text{Mn}^{\text{III}}_{0.05} \text{O}_{2.14}$ ,  $0.76 \text{ H}_2\text{O}$  ( $d$  interlayer =  $7.14 \text{ \AA}$ ). The pillaring effect of Na ions allows to reduce the magnitude of the electrostriction phenomenon from 7.5 % to only 4 %, and to make easier Li accommodation i.e. at a high potential ( $\approx 150 \text{ mV}$ ) than in the case of the sodium - free sample. A similar discharge capacity is achieved. Nevertheless, the presence of Na ions hinders a fast Li kinetics and then prevents the utilization of high current densities. For example, 0.8 against 0.55  $\text{Li}^+$  ions are inserted respectively into the sol-gel sodium free and sodium birnessite under a current density of  $100 \mu\text{A}/\text{cm}^2$ .

#### $\alpha \text{MnO}_2$

The interest of the disordered  $\alpha\text{MnO}_2$  form ( $\text{K}_{0.062}\text{MnO}_2$ ,  $0.43 \text{ H}_2\text{O}$ ) consists of the high oxidation state of Mn ( $Z = 3.93$ ) combined to a very low content of  $\text{K}^+$  ions within the channels of the structure. With a theoretical faradaic yield of 0.9 F/mole leading to a massic capacity of  $280 \text{ Ah/kg}$  available between 4.1 and 2.3 V, this material exhibits the best performances of  $\alpha\text{MnO}_2$  forms. The cycling behaviour is strongly dependent on the depth of discharge. For a d.o.d of  $\approx 0.6 \text{ F/mole}$ , and a C/20 discharge-charge rate, the specific capacity stabilizes near  $120 \text{ Ah/kg}$ . This study also emphasized the preponderant role of structural water for the rechargeability of the material [12].

## CONCLUSION

The sol-gel technique allows to synthesize a wide variety of  $\text{V}_2\text{O}_5$ - and  $\text{MnO}_2$ - based compounds usable as rechargeable cathodic materials. Some of them constitute new promising cathodic materials and outperform their analogs prepared via the classical way of synthesis.

Various parameters such as the morphology, the structure, the type of sites, the composition, the oxidation state of Mn or V can be modified using sol-gel synthesis. Besides these factors, the role of structural water in the case of  $\text{MnO}_2$  is of the utmost importance and seems to control the rechargeability of the Li insertion process.

#### Acknowledgements:

The authors would like to thank Professor J. Livage, Dr.R. Baddour, Dr P. Le Goff and Dr S. Maingot for helpful discussions. The financial support by the Direction des Recherches, Etudes et Techniques (DRET) and the Centre National d'Etudes Spatiales (CNES) is gratefully acknowledged.



## REFERENCES

1. J. Livage, Chem. Mater. **3**, 578 (1991).
2. S. Bach, Thesis, Paris VI University, 1991.
3. S. Bach, J. P. Pereira-Ramos, R. Messina and N. Baffier, Electrochim. Acta. **36**, 1595 (1991).
4. R. Baddour, J. P. Pereira-Ramos, R. Messina and J. Perichon, J. Electroanal. Chem. **314**, 81 (1991)
5. J. Livage, N. Baffier, J. P. Pereira-Ramos and P. Davidson, Mater. Res Soc. Proc., Boston, Ma, 1994, to be published.
6. J. P. Pereira-Ramos, N; Baffier and G. Pistoia, in *Lithium Batteries: New Materials, Developments and Perspectives*, edited by G. Pistoia (Elsevier Science Publishers, Amsterdam, 1994) p.281
7. S. Maingot, Ph. Deniard, N. Baffier, J. P. Pereira-Ramos, A. Kahn-Harari and R. Brec, in *Soft Chemistry Routes to New Materials*, edited by J. Rouxel, M; Tournoux and R. Brec (Materials Science Forum Volumes 152-153, Trans Tech Publication, Switzerland, 1994) p.297
8. S. Maingot, Thesis, Paris VI University, 1994
9. S. Maingot, R. Baddour, J. P. Pereira-Ramos, N. Baffier and P. Willmann, J. Electrochem. Soc. **140**, L158 (1993)
10. S. Bach, J. P. Pereira-Ramos, N. Baffier and R. Messina, Electrochim. Acta **37**, 1301 (1992)
11. P. Legoff, N. Baffier, S. Bach and J. P. Pereira-Ramos, J. Mater. Chem. **4**, 875 (1994)
12. P. Legoff, N. Baffier, S. Bach and J. P. Pereira-Ramos, J. Mater. Chem. **4**, 133 (1994)
13. S. Bach, J. P. Pereira-Ramos and N. Baffier , to be published.

## PROPERTIES OF $\text{LiV}_3\text{O}_8$ CATHODE MATERIALS PREPARED FROM GELS BY SPRAY-DRYING

M. Y. Saidi, I. I. Olsen, R. Koksang, J. Barker, R. Pynenburg  
Valence Technology, Inc., 6781 Via Del Oro, San Jose, CA 95119, USA

K. West, B. Zachau-Christiansen, S. Skaarup  
Department of Physical Chemistry, The Technical University of Denmark  
DK-2800 Lyngby, Denmark

### ABSTRACT

$\text{LiV}_3\text{O}_8$  powder has been prepared on a large scale by spray drying of an aqueous gel. The material was further dehydrated at 150 and 350°C. These materials were characterized by TGA, XRD and electrochemical methods. Materials dried at 150 and 350°C, showed an unusual high reversible capacity, close to 4 Li per formula unit, and cycle well. The material dried at 350°C is very similar to the crystalline  $\text{LiV}_3\text{O}_8$  prepared by conventional high temperature synthesis.

### INTRODUCTION

The layered trivanadate,  $\text{LiV}_3\text{O}_8$ , is able to accommodate relatively large amounts of lithium reversibly without major structural changes. The amount of lithium which may be inserted, and the mechanistic details, are strongly dependent on the method used for preparation of the oxide. In a previous publication [1] an alternative to the classic high temperature synthesis [5-6] of  $\text{LiV}_3\text{O}_8$  was presented. This method is a variation of the precipitation technique used by Pistoia et al to prepare totally amorphous lithium vanadate [2]. Our method is based on the dehydration of stable gels prepared from  $\text{LiOH}$  and  $\text{V}_2\text{O}_5$ . These gels are dehydrated to xerogels either by freeze drying [3] or by spray drying [4]. The xerogels are further dehydrated by a heat treatment. It was shown that xerogels prior to the heat treatment contain two types of water: The major part is loosely bound water that is removed when the xerogel is heated to 150 or 200°C, whereas a small part (2-4 %) is more strongly bound. By proper choice of the process conditions, the crystallinity and particle size of the product can be controlled very precisely. In this paper, results of the characterization of powders prepared from spray dried gels are presented.

### EXPERIMENTAL

An aqueous  $\text{LiV}_3\text{O}_8$  gel was prepared following the procedure described by Pistoia et al [2].  $\text{V}_2\text{O}_5$  powder was slowly added to a stirred  $\text{LiOH}$  solution, the resulting concentration of the two compounds being 0.75 M and 0.5 M, respectively. The mixture was then heated to 50°C and stirred overnight, whereupon a dark red gel gradually formed. This gel is stable, and does not convert to a sol or precipitate even when left for more than two years. A total amount of 14 l gel was dried using a centrifugal atomizer from Pasilac Anhydro A/S rotating at 50000 rpm. The inlet temperature of the dryer was set to 280°C, and the liquid feed rate was adjusted to give an outlet temperature of 120°C. The temperature of the material never exceeded the outlet temperature. The as-made xerogel contained approx. 2 % by weight of water, but re-absorbed water from humid air

on standing. The xerogel was further dehydrated in a heat treatment step either at 150°C or at 350°C overnight. Throughout this paper the resulting products are labeled with the heat treatment temperature: "LiV<sub>3</sub>O<sub>8</sub>-150" and "LiV<sub>3</sub>O<sub>8</sub>-350", respectively.

For comparison, LiV<sub>3</sub>O<sub>8</sub> was also prepared by the classical high temperature route ("LiV<sub>3</sub>O<sub>8</sub>-HT"). A melt containing Li<sub>2</sub>CO<sub>3</sub> and V<sub>2</sub>O<sub>5</sub> in the appropriate molar ratio, was heated to 700°C and quench cooled to room temperature. Chemical analysis of all products showed only traces of reduced vanadium and a ratio between Li and V close to 1:3.

Thermogravimetric analysis was carried out using a Perkin Elmer TGA7 with 5 - 10 mg samples and a scanning rate of 10°C/min.

The long range structural order/disorder was probed by powder XRD using a Siemens D5000 diffractometer (CuK<sub>α</sub> radiation).

The electrochemical characterization of the vanadates was performed in cells with metallic lithium as the negative electrode, a liquid organic electrolyte (LiPF<sub>6</sub> in a 50:50 ethylene carbonate, diethyl carbonate mixture) and porous polypropylene separators (Cellgard 2500). The cells were cycled galvanostatically between preset voltage limits. At the end of charge the cell was kept potentiostatically at the upper voltage limit until the current had decreased by 50 or 75 %. This was done to ensure that the electrodes were in well defined states at the start of each discharge. By numerical differentiation the corresponding "differential capacity", dx/dE, curves were obtained. For convenience the differential capacity during recharge is plotted as positive values. In this way curves similar to cyclic voltammograms are obtained. Pseudo OCV curves, and the associated differential capacity curves, were furthermore obtained by electrochemical voltage spectroscopy (EVS) as described in [9].

In order to determine the amount of lithium inserted per formula unit, the vanadium content of the cells was determined both by weighing of the electrodes prior to cell assembly and by spectrophotometric vanadium determination after completion of the cycling experiments. The conclusions in this paper are based on cells where the discrepancy between these two measurements is less than 5 %.

## RESULTS AND DISCUSSION

The as-made LiV<sub>3</sub>O<sub>8</sub> gel reabsorbed water after spray drying and generally contained about 15-20 % by weight of water after exposure to the atmosphere. Thermogravimetric data (Fig. 1) show that water is primarily lost in two steps. The largest fraction at temperatures below 200°C, while stronger bonded water (corresponding to 0.5 H<sub>2</sub>O per LiV<sub>3</sub>O<sub>8</sub> unit) is removed at higher temperatures. Accordingly, the gel LiV<sub>3</sub>O<sub>8</sub> used in the remaining experiments was heated in to 150 and 350°C, respectively.

Fig. 2 shows X-ray diffractograms of the spray dried material heat treated at 150°C and 350°C, compared with a diffractogram of LiV<sub>3</sub>O<sub>8</sub> prepared by the high-temperature route. The peak positions of the 350°C material coincides with the peak positions observed for the conventional high-temperature material, although the intensity distributions are quite different. The observed intensities for the high-temperature material are in good agreement with the findings of Wickham [5], while the observed intensities for the 350°C material are better in accordance with calculated intensities based on Wadsleys [6] structure data (compare Figure 1 with Figure 6 of reference 7), showing that this is a well crystallized material with isotropic, strain free crystallites. It is noteworthy that the (100) peak at 14° 2θ, which in LiV<sub>3</sub>O<sub>8</sub>-HT is much stronger than predicted, is too weak in LiV<sub>3</sub>O<sub>8</sub>-350.

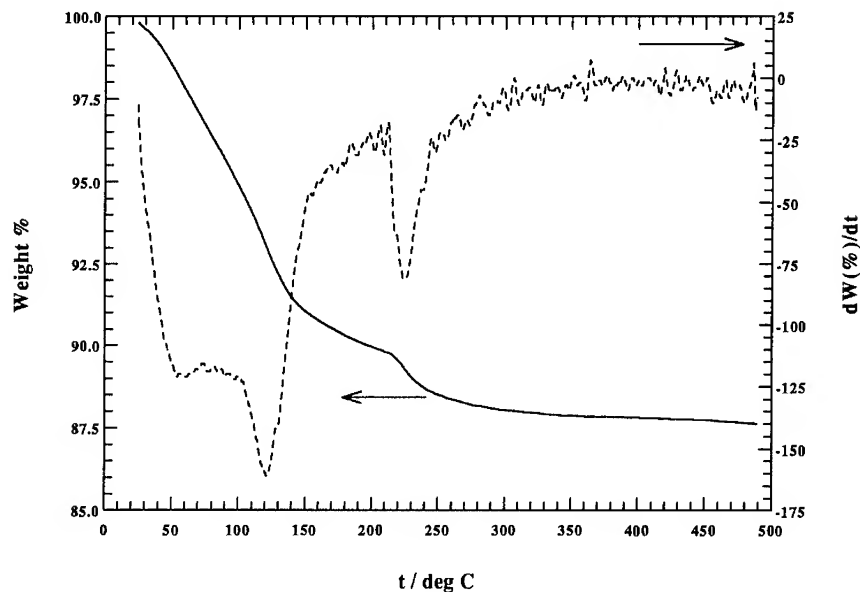


Fig. 1. Thermogravimetric analysis of spray dried  $\text{LiV}_3\text{O}_8$  gel. Scanning rate  $10^\circ\text{C}/\text{min}$ .

This indicates a difference in the aspect ratio of the crystallites of these materials. The high temperature material is prepared by crushing of large crystals, preferentially cleaved along the  $\{100\}$  planes corresponding to the layers of  $\text{VO}_n$  polyhedra. Consequently the dimensions of the crystallites in the directions in the  $\{100\}$  plane will be considerably larger than the out of plane dimensions, leading to relatively long diffusion paths for the lithium ions inserted between these planes. In contrast, the low temperature material is prepared in a micro-crystalline state that need not be further reduced by grinding.

The  $150^\circ\text{C}$  material is much less crystalline, with rather few broad peaks at positions that do not correspond to crystalline  $\text{LiV}_3\text{O}_8$ . The peak positions are consistent with the increase in interlayer spacing, from  $6.36$  to  $9.82 \text{ \AA}$ , resulting from uptake of water in the interlayer spacing between neighboring  $\text{V}_3\text{O}_8$  sheets reported by Schöllhorn et al [8]. The number of peaks is too small to make a positive identification of the structure of this material feasible.

Water is only released with difficulty. Both TGA and XRD indicate that relatively large amounts of water has been removed from the  $\text{LiV}_3\text{O}_8$  structure and that the compound heated to  $350^\circ\text{C}$  is free of water, but FT-IR spectra (not shown) indicate the presence of water even after heating to  $350^\circ\text{C}$  as evidenced by the infra red absorption bands at  $1600 \text{ cm}^{-1}$  and around  $3600 \text{ cm}^{-1}$ .

The voltage profile observed during low rate lithium insertion into electrodes made from  $\text{LiV}_3\text{O}_8\text{-350}$  (Fig. 3c) is very similar to the voltage curves previously published for  $\text{LiV}_3\text{O}_8\text{-HT}$  [10]. First a wide single phase region at low degrees of insertion with a characteristic inflection point at an intermediate composition, followed by two two-phase regions seen as voltage plateaus.

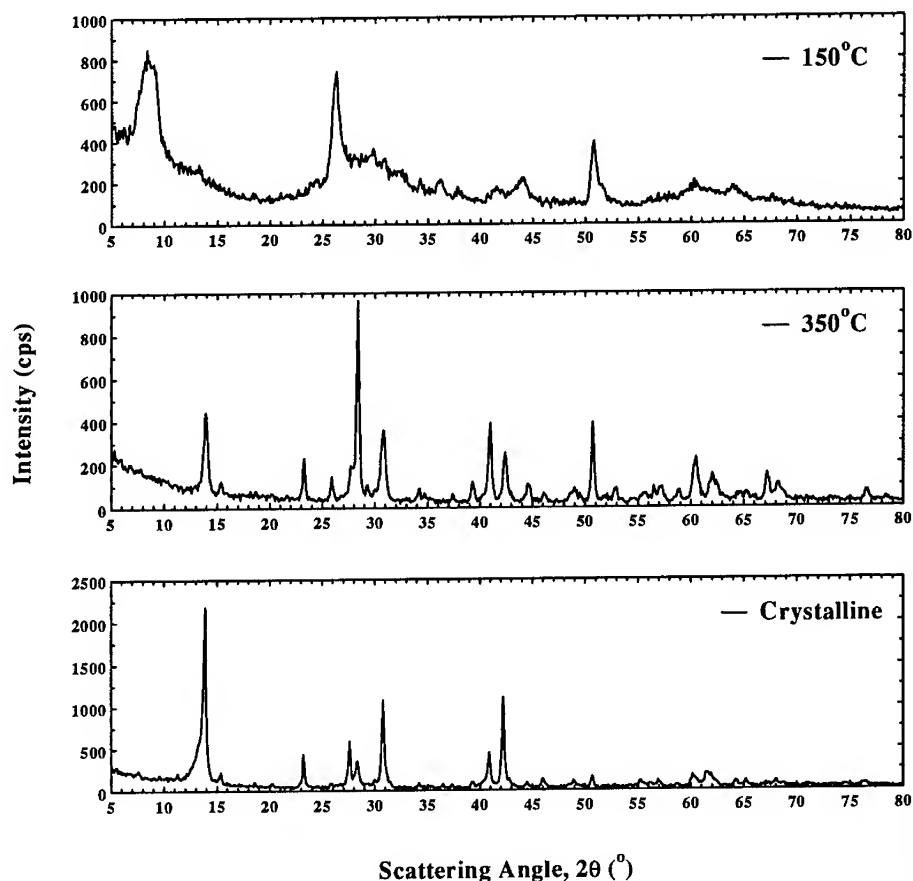


Fig. 2. Comparison of powder XRD of  $\text{LiV}_3\text{O}_8$  compounds.

A noticeable difference is that the capacity for lithium uptake by  $\text{LiV}_3\text{O}_8$ -350 is close to four additional lithium ions per formula unit, whereas values in the range 3 to 3.5 are most often cited for  $\text{LiV}_3\text{O}_8$ -HT. In a recent structural characterization of lithium inserted  $\text{LiV}_3\text{O}_8$ , de Picciotto et al [7] found that the multiplicity of the sites occupied by lithium in the fully intercalated trivanadate suggests a limiting composition  $\text{Li}_5\text{V}_3\text{O}_8$ . It is conceivable that crystal defects may block the diffusion paths for lithium in the two-dimensional interlayer space of the vanadate structure and thereby exclude parts of the crystal from participation in the insertion reaction. An explanation of the difference in lithium capacities could then be that the high temperature material is more prone to this limitation than  $\text{LiV}_3\text{O}_8$ -350 due to a flake-like crystallite morphology and to the defects induced by mechanical milling. The differences in X-ray diffraction peak intensities discussed above supports this assumption.

Fig. 3 shows the first three discharge/charge cycles of cells based on  $\text{LiV}_3\text{O}_8$ -350 cycled at different rates.

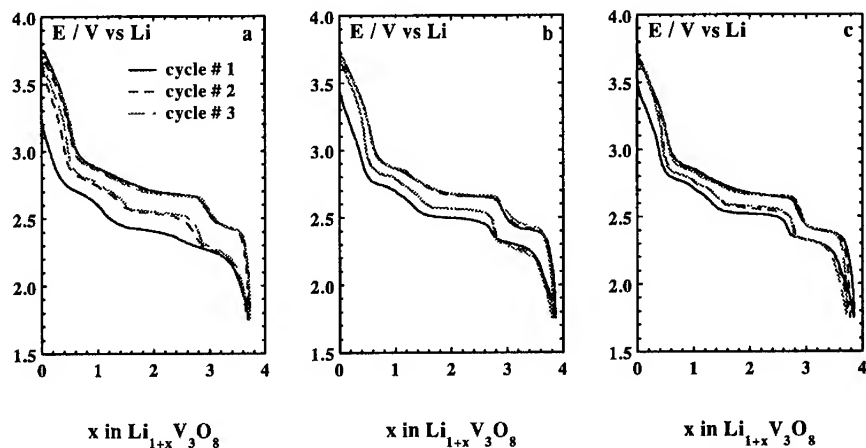


Fig. 3. Discharge/charge cycles of cells with  $\text{LiV}_3\text{O}_8$ -150 electrodes. a)  $200 \mu\text{A}/\text{cm}^2$  - 2 h/x, b)  $80 \mu\text{A}/\text{cm}^2$  - 5 h/x and c)  $20 \mu\text{A}/\text{cm}^2$  - 23 h/x.

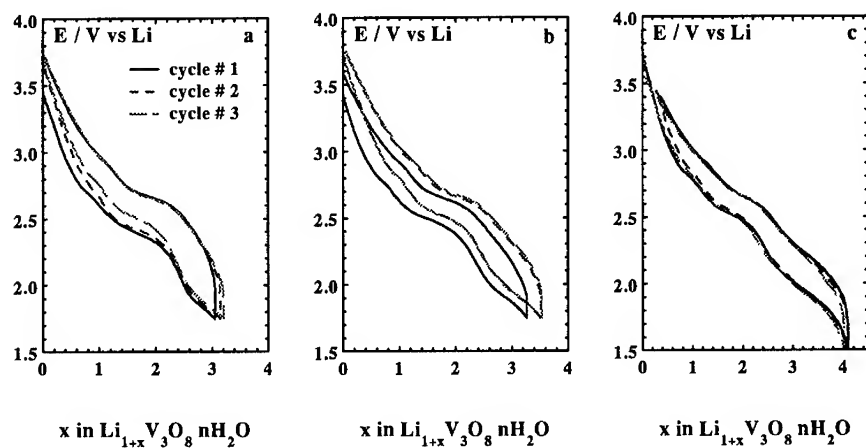


Fig. 4. Discharge/charge cycles of cells with  $\text{LiV}_3\text{O}_8$ -350 electrodes. a)  $200 \mu\text{A}/\text{cm}^2$  - 1.5 h/x, b)  $80 \mu\text{A}/\text{cm}^2$  - 5 h/x and c)  $40 \mu\text{A}/\text{cm}^2$  - 11 h/x.

At high rates, the first discharge is associated with a rather high overvoltage. At the composition corresponding to the last voltage plateau of the discharge curve, the overvoltage suddenly decreases, and this lower value is maintained throughout the rest of the cells cycle life. The nature of the transition leading to the decrease in overvoltage is not understood, but it is remarkable that it is not associated with a capacity decrease, as often seen with this type of effect.

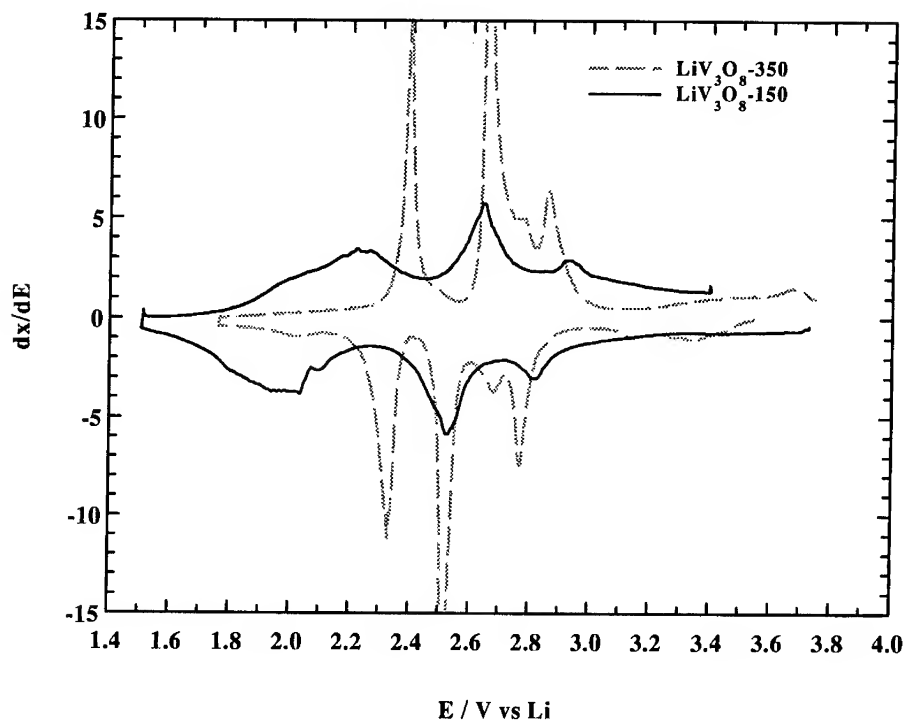


Fig. 5. Differential Capacity of first cycles of  $\text{LiV}_3\text{O}_8$ -150 and  $\text{LiV}_3\text{O}_8$ -350 (loads: 23 h/x and 11 h/x, respectively).

The voltage profile of  $\text{LiV}_3\text{O}_8$ -150 is different from  $\text{LiV}_3\text{O}_8$ -350 - see Fig. 4. The voltage plateaus indicating two phase transitions are absent, and the voltage range spanned is larger - discharge down to 1.5 V is necessary in order to reach the saturation composition corresponding to the insertion of four lithium per formula unit - see Fig. 4c. The rate capability of this system is fair, as a load corresponding to 2h/x generates an overvoltage less than 200 mV, decreasing slightly when the cell is cycled (Fig. 4a). The hysteresis is larger at deep discharge, and will limit the capacity at higher rates. Comparing the differential capacity curves of  $\text{LiV}_3\text{O}_8$ -150 and  $\text{LiV}_3\text{O}_8$ -350, (Fig. 5), it is seen that lithium insertion into these two materials apparently proceeds through the same number of steps, although the capacity peaks in  $\text{LiV}_3\text{O}_8$ -150 are much broader, and the long range interaction is too weak to cause phase separations. Again, this is consistent with the lower degree of crystallinity observed by XRD. The difference in peak positions reflects the differences in environment for the ions inserted: A change in interlayer distance, and presence of bound water in the interlayer space.

Both materials cycle well in laboratory cells, as illustrated in Fig. 6. It should be noted that these electrodes are not optimized for cycling, but the performance is slightly better than for  $\text{V}_6\text{O}_{13}$  electrodes prepared in the same way.

Similar results were obtained by the EVS technique (Figs. 7 and 8) for the  $\text{LiV}_3\text{O}_8$ -350 compound, i.e. close to 4 additional Li per formula unit and a structured voltage trace.

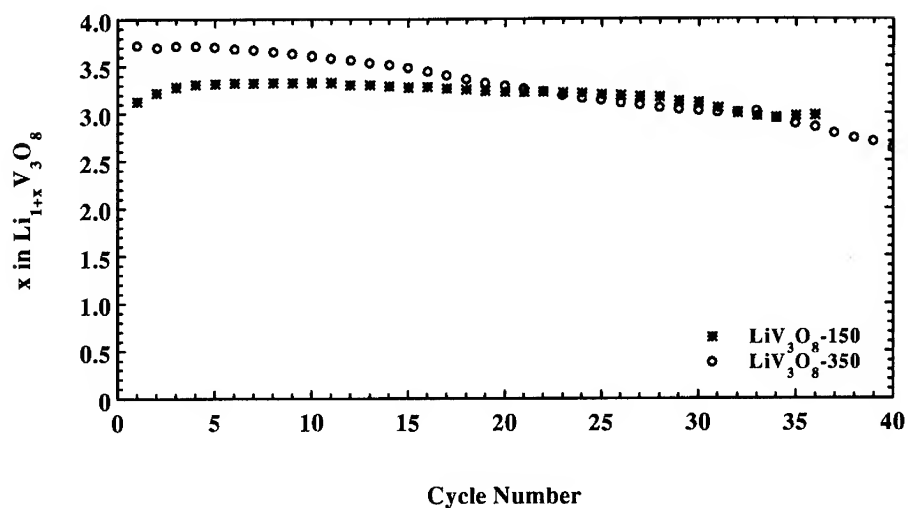


Fig. 6. Cycling of cells with LiV<sub>3</sub>O<sub>8</sub>-150 and LiV<sub>3</sub>O<sub>8</sub>-350 (200 $\mu$ A/cm<sup>2</sup>).

However, the LiV<sub>3</sub>O<sub>8</sub>-150 material behaves differently. Although the same featureless voltage curves are observed, a significantly lower capacity is observed.

This is due to the fact that the critical current used during these experiments was somewhat higher than those used during the constant current cycling, limiting the capacity at low voltages.

## CONCLUSION

LiV<sub>3</sub>O<sub>8</sub> has been prepared from an aqueous gel and dehydrated under controlled conditions. The materials were characterized by TGA, XRD and electrochemical methods. Materials dried at 150 and 350°C showed an unusual high reversible capacity and cycle well. The material dried at 350°C is very similar to the crystalline LiV<sub>3</sub>O<sub>8</sub> prepared by conventional high temperature synthesis, whereas the material dried at 150°C contains structurally bound water, and is less crystalline. The stoichiometric energy density calculated for the insertion of 4 Li per LiV<sub>3</sub>O<sub>8</sub> unit is 800 Wh/l for LiV<sub>3</sub>O<sub>8</sub>-150 and 850 Wh/l for LiV<sub>3</sub>O<sub>8</sub>-350.



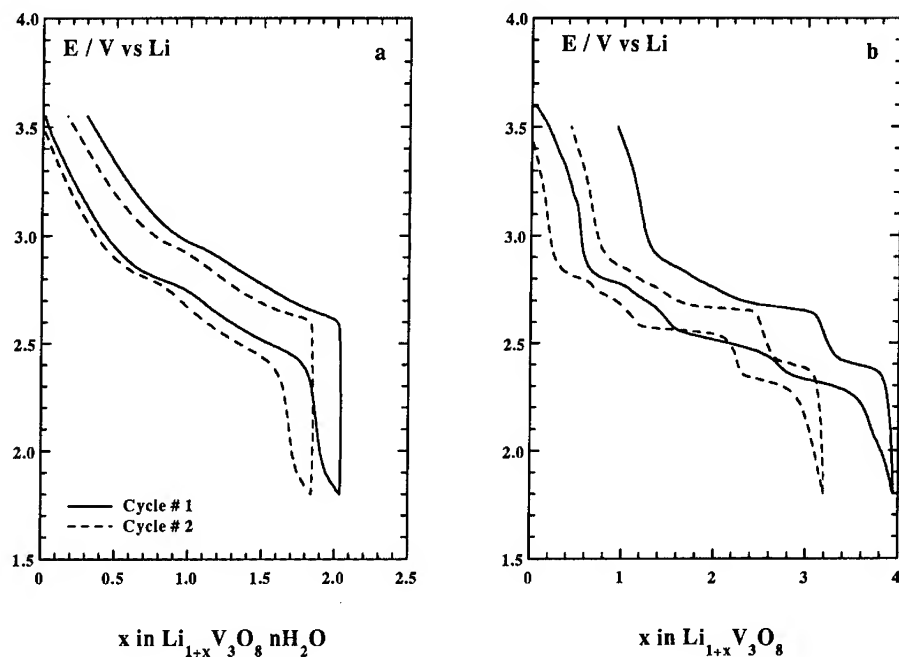


Fig. 7. EVS traces of a) Li/LiV<sub>3</sub>O<sub>8</sub>-150 and b) Li/LiV<sub>3</sub>O<sub>8</sub>-350 laboratory cells.

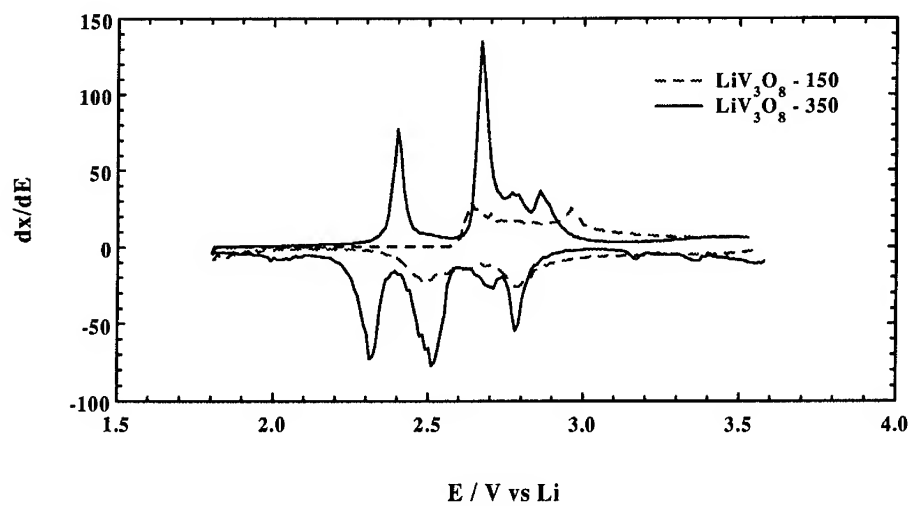


Fig. 8. Differential capacity traces corresponding to the EVS traces in Fig. 7.

## REFERENCES

1. K. West, Y. Saidi, J. Barker, B. Zachau-Christiansen, I. I. Olsen, R. Pynenburg, S. Skaarup, and R. Koksang, *Proc. Electrochem. Soc.* (1994), in press.
2. G. Pistoia, M. Pasquali, G. Wang, and L. Li, *J. Electrochem. Soc.*, **137**, 2365 (1990).
3. R. Koksang, US Patent, 5,334,334 (1994).
4. R. Koksang, US Patent, 5,326,545 (1994).
5. D. G. Wickham, *J. Inorg. Nucl. Chem.* **27**, 1939 (1965).
6. A. D. Wadsley, *Acta Cryst.* **10**, 261 (1957).
7. L. A. de Picciotto, K. T. Adendorff, D. C. Liles, M. M. Thackeray, *Solid State Ionics*, **62**, 297 (1993).
8. R. Schöllhorn, F. Klein-Reesink, and R. Reimold, *J. Chem. Soc. Chem. Comm.*, 398 (1979).
9. J. Barker, R. Pynenburg, R. Koksang, *J. Power Sources*, **52**, 185 (1994).
10. K. West, B. Zachau-Christiansen, M. J. Landeira, T. Jacobsen, in "Transport-Structure Relations in Fast Ion and Mixed Conductors", eds. F. W. Poulsen, N. Hessel Andersen, K. Klausen, S. Skaarup, O. Toft Sørensen, 6th Risø International Symposium on Metallurgy and Materials Science, Risø, Denmark, 1985, pp. 265.

## MORPHOLOGY AND PROPERTIES OF VANADIUM OXIDE XEROGELS AND AEROGELS

B. Katz#, W. Liu#, K. Salloux\*, F. Chaput\*, B. Dunn\* and G.C. Farrington#

#Department of Materials Science and Engineering  
University of Pennsylvania  
Philadelphia PA, 19104

\*Department of Materials Science and Engineering  
University of California  
Los Angeles CA 90024

### ABSTRACT

The high redox potential and ion insertion properties of vanadium pentoxide have made this material a viable cathode for secondary lithium batteries. The use of sol-gel methods to synthesize vanadium pentoxide and other transition metal oxides has been well studied as the technique represents a relatively simple approach for preparing thin films and powders. Although it is well known that sol-gel processing may be used to prepare high surface area aerogels, the research on transition metal oxides has been largely limited to xerogels. The present paper compares the properties, structures and morphologies of vanadate xerogels and aerogels.

### INTRODUCTION

The sol-gel process is a wet chemical technique often used to synthesize oxide powders and glasses. In most cases the final product is formed by heat treating a gelled mixture of reactants, which drives off the gelled solvent and converts the gel into the desired form and composition, which is typically quite dense. When compared to conventional synthetic routes, sol-gel processing often has advantages such as lower sintering temperature, higher degree of purity, and greater product homogeneity.

Interestingly, more gentle methods of removing the solvent from a gel, such as simple air drying at room temperature, freeze drying, or supercritical drying, can lead to quite intriguing new materials which have morphologies that not only retain the unusual gel microstructure but also possess their own distinctive characteristics. Air drying of gels generally produces hydrated oxide materials known as xerogels. Xerogels can be easily formed, via dipping or spinning methods, into thin film coatings having a variety of shapes and sizes. Supercritical drying of a gel can lead to the formation of aerogels, materials having exceptionally low densities, even lower than those of xerogels, and often formed as monoliths with extremely high surface areas.

The present paper compares and contrasts the microstructures, morphologies and properties of both xerogel and aerogel forms of vanadium oxides. The xerogels were prepared as thin films by the simple air drying of a vanadium oxide gel; whereas the aerogels were formed as monoliths by supercritical drying a vanadium oxide gel using CO<sub>2</sub>.

The sol-gel chemistry of vanadium oxide gels is well known [1-3]. In general there are two methods for preparing vanadate gels: the inorganic aqueous approach which makes use of proton exchange reactions with a sodium metavanadate solution and the organic alkoxide method [4]. In both cases the vanadate gel is comprised of a network of oxide fibers and water molecules. When the gel is dried in air, the oxide fibers tend to stack on top of each and prefer an orientation parallel to the substrate [5]. The xerogels thus formed are hydrous oxides; the amount of water present depends upon several factors such as humidity and the extent of reduced vanadium ions in the gel [6].

Vanadium oxide xerogels have a rich intercalation chemistry which includes reversible electrochemical lithium intercalation reactions. Lithium intercalation into the xerogels has been demonstrated by several groups [7-8]. However the chemistry of the intercalation is strongly dependent on the presence of solvent molecules between the layers and the age of the gel ( $V^{5+}/V^{4+}$  ratio). The high surface area and porosity of vanadium oxide aerogels makes them interesting candidates as high energy density battery electrodes [9]. Reversible electrochemical insertion of lithium ions into a vanadate aerogel is reported for the first time in this paper.

## EXPERIMENTAL PROCEDURES

### Method of Synthesis

Vanadium oxide gels were synthesized by both the widely-used ion exchange method and the alkoxide method [4]. Xerogel coatings were prepared by dip coating from gels derived by the ion exchange method. Monolithic vanadium oxide aerogels were prepared solely from alkoxide derived gels and were synthesized by supercritical drying with liquid  $CO_2$ . The aerogel synthesis has been described in detail elsewhere [9]. Typical aerogel samples were prepared in the form of rods, 1 cm in diameter by 3 cm in length.

### Characterization

Thermogravimetric analysis (TGA) was carried out using a DuPont 9900 Thermal Analysis System. The weight loss upon heating was measured from 25°C to temperatures as high as 500°C at heating rates of 5°C/min and 10°C/min in nitrogen.

X-ray diffraction patterns were obtained on a Rigaku diffractometer using  $Cu\ K\alpha$  radiation. Xerogel coatings were prepared on glass slides for reflection mode x-ray diffraction experiments and on cleaved mica for transmission mode x-ray diffraction experiments. Aerogel diffraction experiments (reflection mode geometry) were performed on large aerogel fragments and aerogel powders. Scanning electron microscopy (SEM) experiments were performed on aerogel fragments and xerogel coatings. An investigation of the cross section of a xerogel coating was also performed using the SEM. The cross sections were exposed by cracking a xerogel coated glass slide in liquid nitrogen. The SEM used in the study was a high resolution JEOL 6300FV.

Electrochemical cells were prepared inside an argon filled dry box. The electrolyte used was a 1M lithium perchlorate in propylene carbonate. The lithium perchlorate salt was first heated in a vacuum oven for 24 hours at 120°C. The propylene carbonate was dried over activated molecular sieves for 5 days. The xerogel samples were all prepared on platinum substrates. The vanadate aerogel samples were crushed into a powder, mixed with cyclopentanone and spun onto molybdenum-coated glass slides. Lithium foil was used for the counter and reference electrodes. Prior to electrochemical experiments the

xerogel coatings were placed in the electrolyte for at least 24 hours. The cyclic voltammetry experiments were performed at a scanning rate of 1mV/sec. The potentiostat used was a PAR 273A.

## RESULTS

### Chemical Properties

Vanadate aerogels had surface areas in the range of 300 to 400 m<sup>2</sup>/g and pore volumes as large as 1.5 cm<sup>3</sup>/g. The density of the aerogel was as low as 0.04 g/cm<sup>3</sup> to 0.1 g/cm<sup>3</sup>, which corresponds to a solid content of 1% to 3%.

Thermogravimetric analysis of xerogel coatings indicated the existence of at least 1.6 moles of water per mole of oxide (assuming V<sub>2</sub>O<sub>5</sub> as the solid phase). The weight change profile for the xerogel is characterized by a steep loss between room temperature and 100°C, followed by a more gradual weight loss up until 300°C, at which point there is a sharp 5% weight loss; see Figure 1a. In comparison, TGA results for the aerogel indicate at least 2.2 moles of water per mole of oxide (assuming V<sub>2</sub>O<sub>5</sub> as the solid phase). The weight change profile of the aerogel is analogous to that of the xerogel except that there is no indication of a sharp water loss at temperatures around 300°C, Figure 1b.

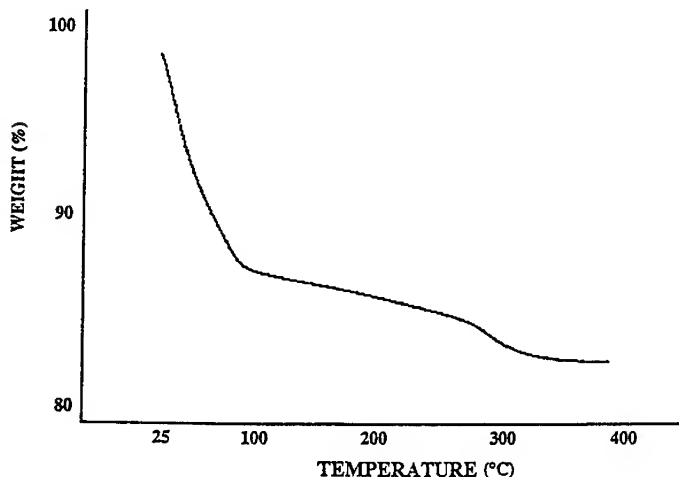


Figure 1a. TGA scan for xerogel. The sample was heated at a rate of 5°C per minute in a nitrogen atmosphere

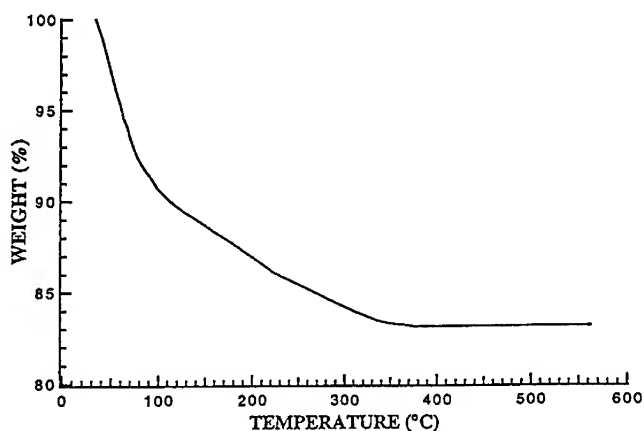


Figure 1b. TGA scan for aerogel. The sample was heated at a rate of 10°C per minute in a nitrogen atmosphere

### X-Ray Diffraction

The reflection mode x-ray diffraction pattern of a vanadium oxide xerogel coating is typical of a layered structure having a preferred orientation, Figure 2a. All the diffraction peaks can be indexed as 00l harmonics, the average inter-layer spacing being 11.6Å. The extent of the preferred orientation in the xerogel coating is illustrated by its rocking curve, Figure (3), the halfwidth of which is 17°. The transmission mode diffraction pattern of the xerogel coating is completely different from that of the corresponding reflection mode diffraction pattern, Figure 2b. Considering the turbostratic structure of the xerogel, all the peaks in the transmission pattern have been indexed as hk reflections [5].

All the peaks present in the reflection mode diffraction pattern of the aerogel are observed in the combined reflection and transmission mode diffraction patterns of a xerogel coating, Figure 2c. The peak position of the 001 reflection occurs at a  $2\theta$  angle greater than that of the xerogel, indicating a larger layered spacing for the aerogel. Moreover, the aerogel material does not show any degree of preferred orientation.

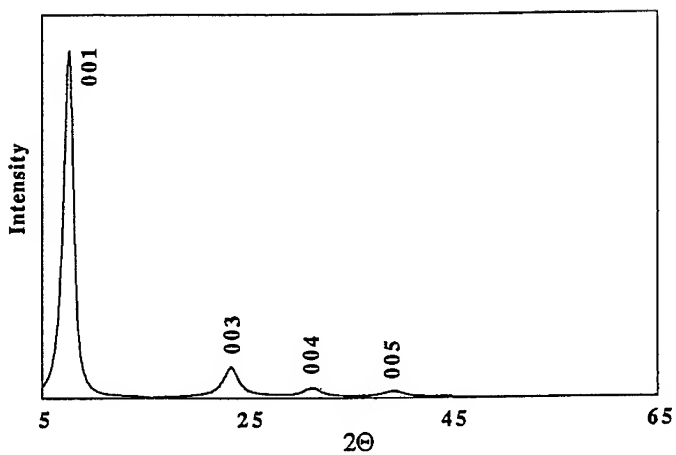


Figure 2a. Reflection mode X-ray diffraction pattern of a xerogel.

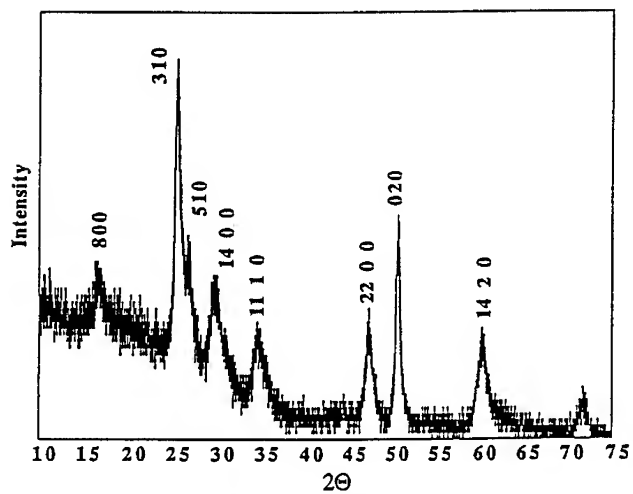


Figure 2b. Transmission mode X-ray diffraction pattern of a xerogel coating.

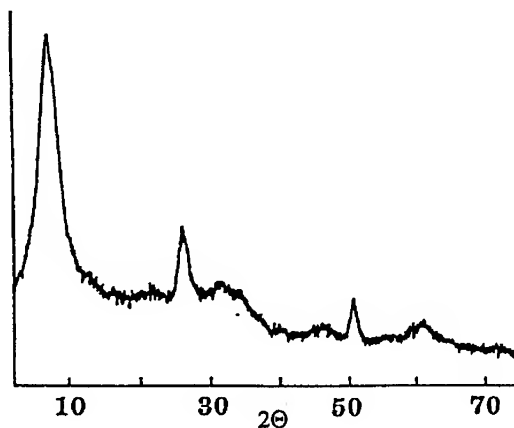


Figure 2c. Reflection mode X-ray diffraction pattern of an aerogel

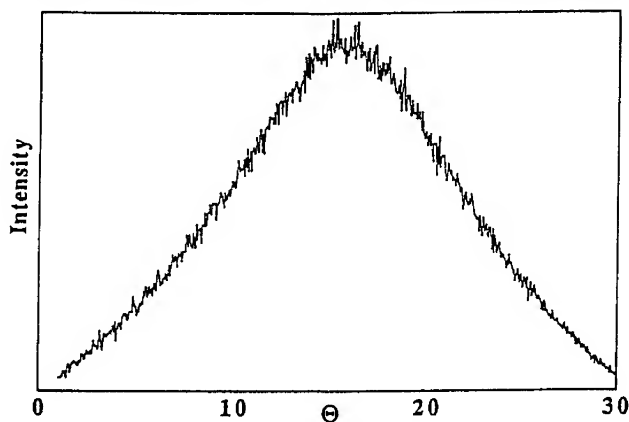


Figure 3. Rocking curve of a vanadate xerogel coating; less than 1  $\mu\text{m}$  thick.

#### Scanning Electron Microscopy

TEM investigations of the vanadate aerogel reveal the fibrous nature of its microstructure [9]. The ribbon-like structure of these fibers is similar to what is observed with vanadate xerogels [5].

An SEM micrograph of a dip coated xerogel is shown in Figure 4a. The texture of the coating shows evidence of a complex folding in what appears to be a homogeneous and corrugated morphology. The SEM micrograph in Figure 4b shows the cross section of a xerogel coating. The lamellar nature of the xerogel and its high porosity are evident in the micrograph. In comparison, the aerogel morphology appears to take the form of an interwoven network of oxide fibers, Figure 5. The low density and extremely high porosity of the aerogel are clearly seen in the micrograph.



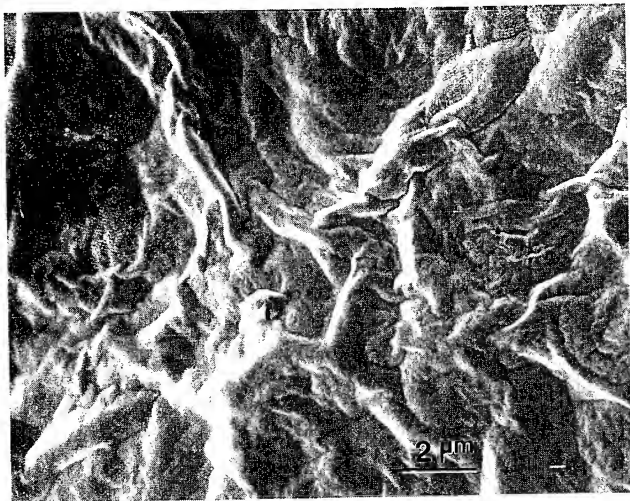


Figure 4a. SEM micrograph of the surface of a xerogel coating

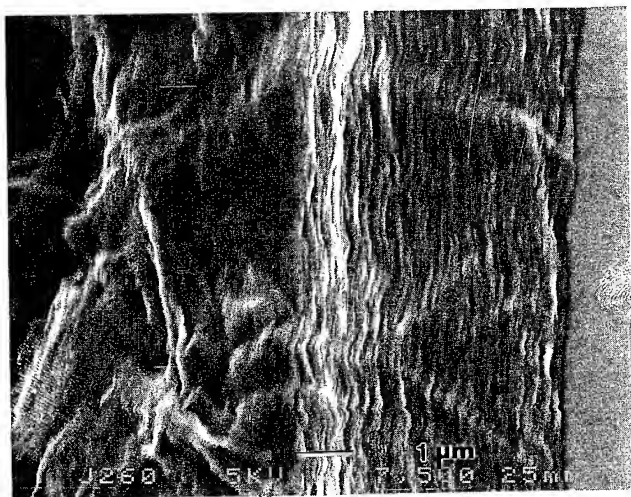


Figure 4b. SEM micrograph of a cross section of a xerogel coating

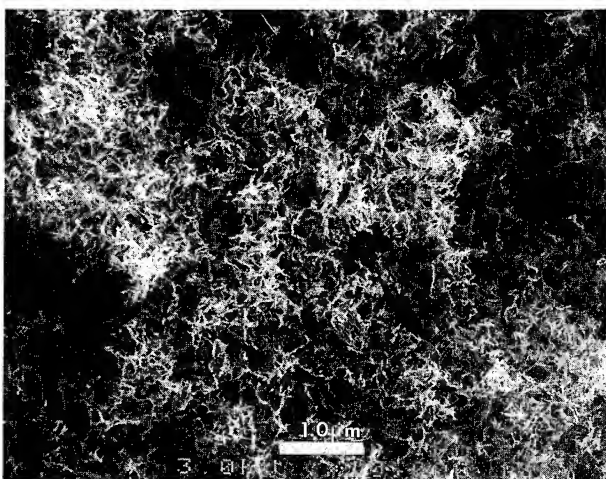


Figure 5. SEM micrograph of an aerogel fragment.

#### Electrochemical Lithium Intercalation

Figure 6a is a cyclic voltammogram of a xerogel coating (red in color) that, prior to electrochemical reduction, had undergone swelling of its layers by propylene carbonate molecules. The swelling was confirmed by x-ray diffraction experiments that showed the inter-layer distance increased from 11.6Å to 20.9Å. The cyclic voltammogram in Figure 6a exhibits a single broad cathodic and a single broad anodic peak centered around 2.8 volts and 3.4 volts respectively.

Figure 6b is a cyclic voltammogram of an aerogel that was crushed into powder form. In contrast to the broad reduction peaks observed with the red xerogel, the cyclic voltammogram of the aerogel exhibits two cathodic peaks around 2.9 volts and 2.4 volts. Moreover, both reduction peaks appear to ride on top of a single broad cathodic peak. The anodic wave of the cycle, corresponding to de-intercalation of lithium ions, gives rise to a single and relatively sharp peak at 3.5 volts.

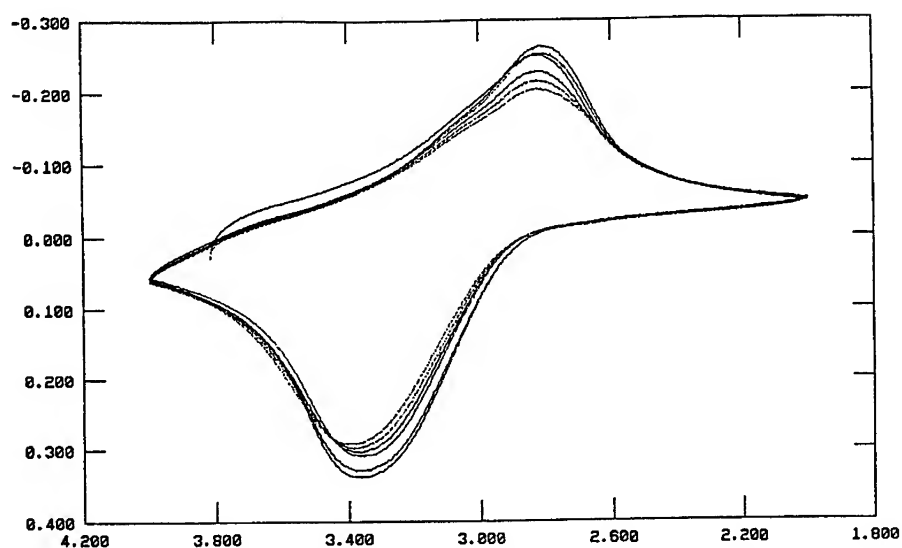


Figure 6a. Cyclic voltammogram of a fresh xerogel coating undergoing reversible lithium intercalation

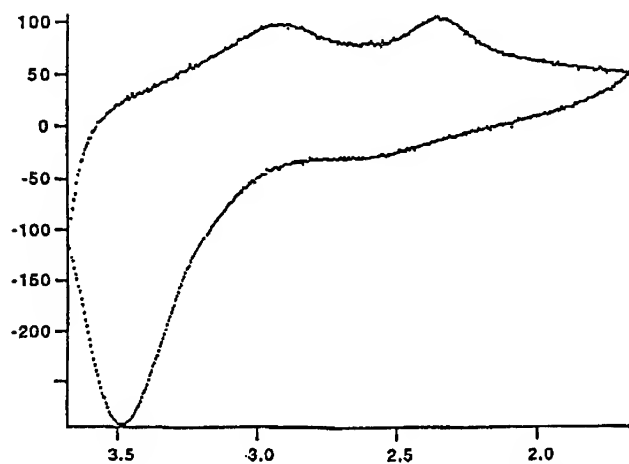


Figure 6b. Cyclic voltammogram of an aerogel undergoing reversible lithium intercalation

## DISCUSSION

The various techniques used to examine the structure of vanadate xerogel films prepared by dip coating and drying show that the films consist of ribbon-like vanadium oxide layers laid on top of each other with preferred orientation parallel to the substrate. Although the preferred orientation is not perfect, as shown by the rocking curve, it is complete enough to prevent the appearance of any reflections other than 001 in a reflection mode diffractogram. Thus, vanadium oxide xerogels have a random layer structure that arises from a stacking of the oxide layers parallel to one another but with mis-registry between the layers about the layer normal [5]. The absence of layer-to-layer registry prevents the appearance of general hkl reflections. However the individual layers diffract independently, giving rise to two dimensional hk reflections. As a result of the preferred orientation of the layers in a xerogel coating the only reflections observed in its transmission x-ray diffraction pattern are of the hk type. The hk reflections, which have been indexed based on the electron diffraction investigations of Kittaka et al. [10], do not correspond to any known vanadium oxides.

The x-ray diffraction pattern of an aerogel is quite similar to the combined reflection and transmission mode diffraction patterns of a xerogel coating. All the peak positions except the 001 are the same, indicating that there is no preferred orientation among the aerogel fibers and that the atomic structure of the individual layers in the aerogel is similar to that of the xerogel layers. The 001 peak in the aerogel diffractogram corresponds to a layer separation of about 12.7Å, compared to 11.6Å for the xerogel. The larger spacing is most likely the result of the increased level of hydration of the aerogel ( $n=2.2$ ) compared to that of the xerogel ( $n=1.6$ ). In fact it has previously been shown that the hydration state of xerogels strongly depends on their reduction state [5]. The aerogels, which are dark green in color, are partially reduced during synthesis. The larger degree of hydration of the aerogels may well be explained by the greater state of reduction as compared to that of a fresh xerogel. In addition, the absence of any 001 harmonics with  $n>1$  in the aerogel diffractogram is most likely due to low diffraction intensities resulting from both a lack of preferred orientation and small coherence lengths between diffracting layers.

The corrugated morphology of the xerogel coating as seen in the SEM micrograph of Figure 4a is most likely the result of shrinkage as the gel dries. Furthermore the lamellar nature of the xerogel, which is unmistakably evident in the cross section shown in Figure 4b, most probably arises because of the preferred stacking of the layers. In comparison, aerogel morphologies appear to resemble the oxide skeleton of the starting gel phase; see Figure 5. In this way the aerogel may be considered as the rigid oxide skeleton that corresponds to the solid matrix that exists in the hydrated gel. It appears that the supercritical drying process removes the solvent but leaves the solid relatively intact.

The TGA curves for xerogels and aerogels are quite similar, except for the amount of water per mole of oxide and the lack of any sharp weight loss for the aerogel around 300°C; see Figures 1a and 1b. It is well established that vanadate xerogels undergo a sharp weight loss of approximately 5% at 300°C prior to their transformation to crystalline  $V_2O_5$ . Curiously, there is no analogous weight loss from vanadate aerogels prior to the formation of crystalline  $V_2O_5$ . We are presently carrying out in-situ x-ray diffraction experiments as a function of temperature in an attempt to understand these differences. As mentioned earlier, the larger hydration state of the aerogel ( $n=2.2$ ) relative to that of a fresh xerogel ( $n=1.6$ ) is likely the result of a greater degree of reduction in the aerogel.

The electrochemistry of vanadate aerogels has been investigated in a number of laboratories over the last decade. The ease of sample preparation and fabrication into thin films, along with the high oxidation potential of the vanadate xerogels, are reasons why they are considered by some to be attractive electrode materials. Unfortunately, the complicated chemistry of the xerogel has made it difficult to characterize completely the lithium intercalation process.

It is clear that the  $\text{Li}^+$  intercalation chemistry of the vanadate xerogels is strongly affected by the presence or absence of neutral molecules (e.g. water, propylene carbonate, polymers) intercalated between the oxide layers [11]. Figure 6a shows a typical cyclic voltammogram of a xerogel coating in which propylene carbonate molecules had been intercalated into the lamellar spaces. It is characterized by broad cathodic and anodic peaks. In contrast we have shown previously that xerogels that do not undergo PC insertion prior to lithium intercalation have cyclic voltammograms exhibiting three intercalation and de-intercalation peaks, all of which ride on top of a broad peak [11].

Vanadate aerogels also undergo reversible lithium intercalation, as shown in the cyclic voltammogram in Figure 6b. The cathodic portion of the curve is somewhat similar to that of an aged xerogel, exhibiting two peaks riding on top of a rather broad peak. Curiously, the anodic portion of the cyclic voltammogram exhibits only a single sharp peak at 3.5 volts, indicating that the de-intercalation process occurs in a single step.

## CONCLUSIONS

The microstructure, morphology and properties of sol-gel derived vanadate xerogels and aerogels are quite intriguing. The fibrous nature of the vanadate gel phase is retained in both, though their respective morphologies are quite different. The slow drying of the gel during xerogel formation gives rise to a lamellar texture in which the oxide fibrils have a preferred orientation parallel to the substrate on which the xerogel is deposited. In contrast, the rapid supercritical drying process by which the aerogel is formed removes the solvent phase so quickly that the three-dimensional solid oxide matrix of the gel appears to be frozen in place. Vanadate aerogels undergo reversible  $\text{Li}^+$  intercalation by reactions that appear similar to those of an aged xerogel coating.

## ACKNOWLEDGEMENTS

This work was performed under financial support given by the Office of Naval Research through the grant DMR-14-90-5-1156 and the National Science Foundation, MRL program, under grant No.DMR 91-20668.

The authors would also like to thank K. Kowal for his assistance, as well as X.Q. Wang and Dr. R. Lakis for their help regarding the scanning electron microscopy studies.

## REFERENCES

1. J. Lemerle, L. Nejeh and J. Lefebvre, *J. Chem. Res., Miniprint*, **5**, 301 (1978).
2. J. Lemerle, L. Nejeh and J. Lefebvre, *J. Inorg. Nucl. Chem.* **42**, 17 (1980).
3. J. Livage, *Chem. Mater.* **3**, 578 (1991).
4. J. Livage, M. Henry and C. Sanchez, *Prog. Solid. St. Chem.* **18**, 259 (1988).
5. P. Aldebert, N. Baffier, N. Gharbi and J. Livage, *Mater. Res. Bull.* **16**, 669 (1981)
6. J. Livage, *Mater. Res. Bull.* **26**, 1173 (1991).
7. K. West, B. Zachau-Christiansen, T. Jacobsen and S. Skaarup. *Electrochim. Acta.* **38**, 1215 (1993)
8. R. Baddour, J.P. Pereira-Ramos, R. Messina and J. Perichon. *J. Electroanal. Chem.* **314**, 81 (1991)
9. F. Chaput, B. Dunn, P. Fuqua and K. Salloux. *J. Non-Crystal. Solids.*  
(to be published)
10. S. Kittaka, N. Uchida, H. Miyahara and Y. Yokota, *Mat. Res. Bull.* **26**, 391 (1991)
11. B. Katz, R. Huq and G.C. Farrington, *Solid State Ionics.* (to be published)

---

## PART III

---

### **Theory of Ion Conduction in Solids**

# MONTE CARLO STUDY OF DISPERSIVE TRANSPORT IN GLASSY ELECTROLYTES

D. Knödler, P. Pendzig and W. Dieterich

Fakultät für Physik, Universität Konstanz,  
Universitätsstr. 10, D-78434 Konstanz, Germany

## Abstract

A lattice-gas model is presented, where ions are diffusing in an energy landscape due to immobile, randomly placed counterions. All Coulombic interactions are taken into account. By Monte Carlo simulations we obtain the ac-conductivity, which shows strong dispersion in the form of power-laws. In a separate study we investigate a restricted model, where long-range diffusion is suppressed. These calculations suggest that the response at high frequencies can be interpreted in terms of highly correlated, local motions of dipolar character. Conductivity exponents  $n_1$  near unity or even exceeding unity are found in that regime. We discuss the relationship of these results to experiments on ionic transport in alkali-doped network glasses.

## 1 Introduction

Charge carrier motion in highly defective solids normally leads to slow, non-exponential relaxation processes which reflect themselves in an ac-response in the form of fractional power-laws in frequency [1]. An important class of materials that has widely been studied in this context are glassy electrolytes [2]. Their ac-conductivity commonly behaves as  $\sigma(\omega) \simeq \sigma(0) + A\omega^n$ , where the exponent  $n$  satisfies  $0 < n \lesssim 1$ . In recent years detailed experimental information has become available on conductivity spectra up to the GHz-regime and on their dependence on temperature and charge carrier concentration [3,4]. Despite of these efforts the question of the physical mechanism of ion migration in glasses is not really settled [5-8]. Model studies based on motions of charged particles in a random environment have suggested that both disorder and ion-ion interactions are important in understanding the experimentally observed conductivity spectra [9-11]. Specifically, for alkali-doped network glasses the "counterion model" seems promising as it simultaneously accounts for strong dispersive effects in various dynamical correlation functions and a strong increase of the dc-conductivity with carrier concentration [12]. This latter effect is a further characteristic feature of such glasses [2].

The basic idea of the counterion model is that diffusion of alkali ions in network glasses at low doping level may significantly be affected by the Coulomb-fields due to oppositely charged non-bridging oxygen ions. These are assumed to be fixed at random positions  $\mathbf{R}$ . All further effects of the disordered glassy network are ignored. This is of course an oversimplification in comparison with any real material. Nevertheless it turns out that transport and dynamical properties of ions under those simplifying assumptions show a rich behavior and exhibit several features in striking similarity with experimental observations on single-alkali glasses. Calculated activation energies and Haven ratios as a function of ion concentration as well as conductivity spectra and nuclear spin relaxation rates have



been discussed recently in comparison with experiments [12,13]. In this communication we shall first recall briefly the basic assumptions of the counterion model. New results on static ion-ion correlations are then presented, which indicate the existence of different time-scales in the dynamic properties. Different frequency regimes in the ac-conductivity are discussed on that basis. Secondly, we focus on the high-frequency response, which is due to highly correlated ionic motions of dipolar character. This yields an ac-conductivity of the form  $\sigma(\omega) \sim \omega^{n_1}$ , with  $n_1$  near unity. To support the conclusion that highly correlated dipolar motions give rise to a conductivity exponent  $n_1$  close to unity, we shall investigate in addition the ion dynamics in a restricted model which only contains dipolar degrees of freedom. Finally we add some remarks on the experimental high-frequency response of glasses.

## 2 Dispersive transport in the counterion model

Consider a three-dimensional simple-cubic lattice of spacing  $a$  and size  $L$  with periodic boundary conditions. A fraction  $c$  of unit cubes is selected at random, and the centers  $\mathbf{R}$  of these cubes are taken as fixed, singly-charged counterions (anions). Cations with the same concentration are distributed among the sites of the cubic substrate lattice and are moving via nearest-neighbour hops. The corresponding hopping probabilities are determined by Coulomb forces due to the instantaneous ionic configuration. The time evolution of configurations is obtained by using the Monte Carlo method. A detailed description of our model has been presented previously [10].

Fig. 1 shows simulation results for the real part of the dynamic conductivity, denoted by  $\sigma(\omega)$ , at low temperatures. Here, temperature is measured by the parameter  $V/k_B T$ , where  $V = e^2/a$  is a typical Coulomb energy. Clearly, the overall behavior of our data is in good qualitative agreement with conductivity spectra measured in alkali glasses [2].

Let us now interpret these results in terms of different ionic relaxation processes, which occur on different time scales. For that purpose it will be useful to investigate first some static properties. Consider a dilute system,  $c \ll 1$ , at low temperatures, where  $V/k_B T \gg 1$ . The majority of cations will then be trapped in Coulombic potential wells associated with the counterions. Fig. 2 shows the radial distribution function  $g_{-+}(r)$  among unlike ions at  $V/k_B T = 50$  and for  $c = 0.03$ . The distance of the first shell surrounding a counterion, i.e. the eight lattice sites next to it, is  $r_1 = a\sqrt{3}/2$ , and the value  $g_{-+}(r_1)$  reflects the enhanced occupation of the first shell. Complete association of cations and anions in the dilute limit would correspond to  $g_{-+}(r_1) = 1/8c$ . For example, for  $c = 0.03$  we find  $g_{-+}(r_1) \simeq 6.28$ , which is somewhat larger than that value because of overlap effects of first shells belonging to different counterions. Hops of cations among those eight binding sites and away from them are determined by two distinctly different hopping probabilities. This is directly evident from the two-peak structure in the distribution function  $p(\Delta H)$  shown in Fig. 3, where  $\Delta H$  denotes the energy difference between the final and the initial state in the attempted hops during our Monte Carlo runs. Data shown in Figs. 2 and 3 depend only weakly on temperature. However, by lowering the concentration the two-peak structure in  $p(\Delta H)$  becomes much more pronounced.

From these results on static ion-ion correlations it is clear that different time-scales will exist, which are connected with different dynamical processes. The shortest time-scale  $t_0$  is determined by the average hopping rate for hops among those binding sites. Within a range

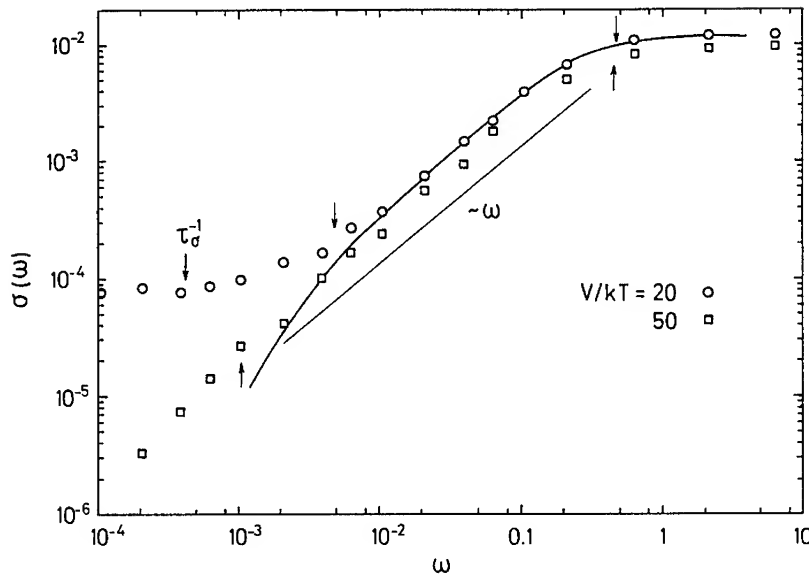


Figure 1: Monte Carlo results for the dynamic conductivity  $\sigma(\omega)$  at  $c = 0.03$  and for two different temperatures. Crossover frequencies  $t_0^{-1}$ ,  $t_1^{-1}$  and  $\tau_\sigma^{-1}$  (see text), obtained from independent simulations of the mean-square displacement  $\langle r^2(t) \rangle$  [10], are indicated by downward ( $V/k_B T = 20$ ) and upward ( $V/k_B T = 50$ ) pointing arrows. The slope of the straight line corresponds to an exponent  $n_1 = 1$ . The full curve is obtained from the dipolar model described in section 3, at  $V/k_B T = 50$ .

of times  $t_0 < t < t_1$  cations still remain bound to the counterions. Hence, for sufficiently small  $c$  the system can be regarded in a good approximation as an assembly of randomly placed localised dipoles, which reorient through ionic hopping events. Because of Coulomb interactions among different dipoles these reorientation processes show complex dynamical behavior. In particular, for frequencies  $t_1^{-1} < \omega < t_0^{-1}$  the ac-conductivity assumes a power-law with an exponent  $n_1$  close to unity, see Fig. 1. Strong correlations in the motion of different ions in that regime reflect themselves in the fact that  $n_1$  is distinctly larger than the exponent  $n_t$  characterizing the time-dependent mean-square displacement of a tracer ion,  $\langle r^2(t) \rangle \sim t^{1-n_t}$  [10]. In the case of our lowest temperature,  $V/k_B T = 50$ , the form  $\sigma(\omega) \sim \omega^1$  applies to about two decades in frequency. Additional calculations at lower concentrations indicate that  $n_1$  even can exceed unity. For example, at  $c = 0.01$  and  $V/k_B T = 50$ , the best fit is achieved with  $n_1 \simeq 1.3(\pm 0.1)$ . We shall return to the interpretation of this high-frequency regime in section 3, which contains a separate investigation of the dynamics of interacting dipoles.

The condition  $\langle r^2(t_1) \rangle \simeq a^2$  defines a characteristic time  $t_1$  beyond which ( $t > t_1$ ) a cation is able to leave the trapping sites next to a counterion and to explore the "Coulomb

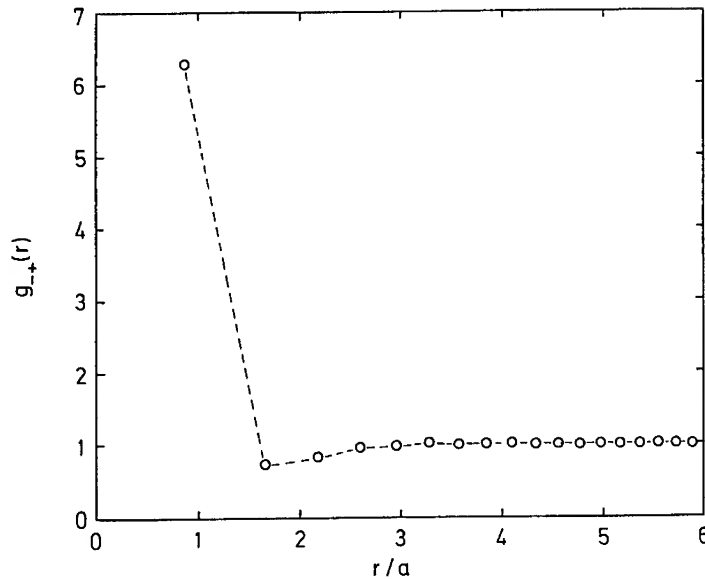


Figure 2: Radial distribution function  $g_{-+}(r)$  between unlike ions at  $V/k_B T = 50$  for  $c = 0.03$ .

basin" associated with it [10]. For  $\omega < t_1^{-1}$  there is still conductivity dispersion, see Fig. 1, due to both the spatial variation of site energies and Coulomb interactions. This situation resembles previous studies of disordered Coulomb lattice-gas models [9], where conductivity exponents  $n \simeq 0.6$  to  $0.7$ , typical of the Jonscher behavior [1], have been obtained. Finally, the condition  $\langle r^2(\tau_\sigma) \rangle \simeq r_s^2$ , where  $r_s = a(3/4\pi c)^{1/3}$ , determines another characteristic time of our model, the conductivity relaxation time  $\tau_\sigma$ , which gives the time-scale for escape of a cation out of a Coulombic center or for an effective hop to an adjacent center. Indeed, as shown before [12], its inverse  $\tau_\sigma^{-1}$  corresponds to a maximum in the electric modulus spectrum  $M''(\omega)$  calculated from our model. For  $\omega < \tau_\sigma^{-1}$  the ac-conductivity approaches the dc-plateau, see Fig. 1.

### 3 Dynamics of a random dipole system

After discussing the different types of motion in the counterion model and their respective time-scales, we investigate now in more detail the situation where dipolar reorientation steps are the dominant processes. For this purpose we study a restricted model, which differs from the model of section 2 by the fact that each immobile anion has exactly one cation in its first shell, and hops of a cation out of the first shell are forbidden. Anions are placed randomly, as before, apart from the additional condition that their first shells are non-overlapping. For  $c \ll 1$  this causes only a minor modification in the anion distribution. As in section

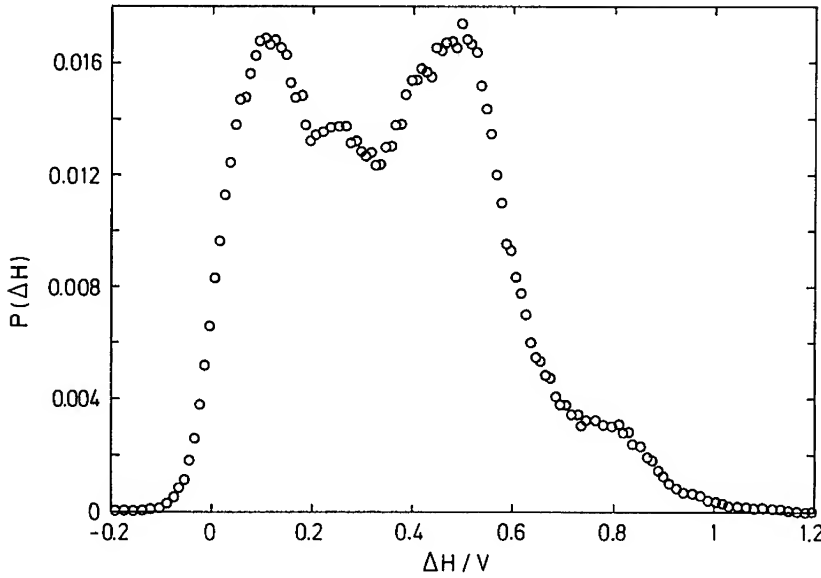


Figure 3: Distribution function  $p(\Delta H)$  at  $V/k_B T = 50$  for  $c = 0.03$ .

2, the hopping dynamics are governed by Coulomb-interactions among all ions. Yet we use the term "dipolar model" because dipole-dipole interactions represent the dominant contribution in the dilute limit.

In Fig. 4 we show a semilogarithmic plot of simulation results for the polarisation-autocorrelation function  $\langle \mathbf{P}(t)\mathbf{P}(0) \rangle$ . Obviously, the main relaxation is strongly non-exponential during a time interval that increases by lowering the temperature. From the data it appears that this non-exponential decay is followed by an exponential contribution. Assuming an exponential decay at long times, we can extrapolate our data and can calculate the dynamic conductivity

$$\sigma(\omega) = \frac{\omega^2}{3} \text{Re} \int_0^\infty dt e^{i\omega t} \langle \mathbf{P}(t)\mathbf{P}(0) \rangle \quad (1)$$

which is plotted in Fig. 5 for different temperatures. At intermediate frequencies there is clear evidence of a non-trivial power-law with an exponent  $n_1$  close to unity. Actual fits give exponents with even somewhat larger values, for example,  $n_1 \simeq 1.05$  for  $c = 0.03$  and  $V/k_B T = 50$ . At lower frequencies we observe a cross-over to the Debye-form  $\sigma(\omega) \sim \omega^2$ . However, because of uncertainties in the extrapolation of our data for  $\langle \mathbf{P}(t)\mathbf{P}(0) \rangle$  taken so far, the results in Fig. 5 for  $\omega \lesssim 10^{-2}$  should be regarded as preliminary.

Results for the case  $V/k_B T = 50$  shown in Fig. 5 are replotted in Fig. 1 by the full curve and agree well with the conductivity in the counterion model (section 2) at high frequencies,  $t_1^{-1} < \omega < t_0^{-1}$ . (There is a small discrepancy in the high-frequency plateau,  $\omega > t_0^{-1}$ , which may be due to the fact that the replacement of the counterion model by the dipolar model

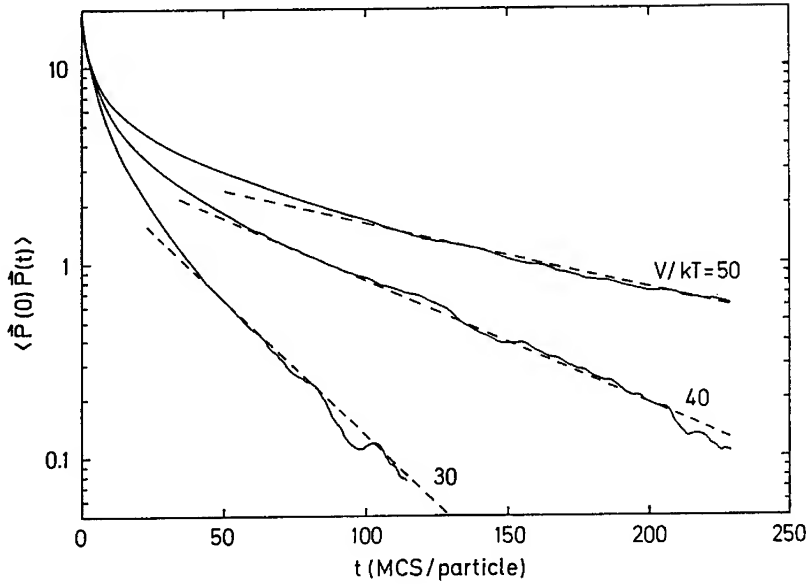


Figure 4: Semilogarithmic plot of the polarisation-autocorrelation function in the dipolar model at  $c = 0.03$  and for different temperatures.

becomes exact only in the limit  $c \rightarrow 0$  and  $T \rightarrow 0$ , keeping  $c/k_B T$  fixed.) Note that different algorithms have been used in both cases. Simulations in section 2 were carried out by a Monte Carlo procedure including an oscillating bias field, whereas in section 3 we analysed the polarisation fluctuations at equilibrium. To conclude, studying the present model, in which long-range diffusion is suppressed, confirms our interpretation of the high-frequency conductivity displayed in Fig. 1 in terms of dipolar processes. A more detailed investigation of the random dipole model by numerical and analytical techniques is in progress.

## 4 Concluding remarks

Conductivity dispersion in the counterion model at small concentrations originates from two different processes, whose frequency-scales separate at low temperatures. At small frequencies,  $\omega < t_1^{-1}$ , diffusion and escape processes in a smoothly varying energy landscape due to a distribution of "Coulombic traps" are dominant. On the other hand, at high frequencies,  $\omega > t_1^{-1}$ , correlated local motions of dipolar character prevail, whose relaxational properties are strongly affected by Coulomb-interactions. By a separate study we have shown that this last mechanism can lead to conductivity exponents even larger than unity at sufficiently low temperatures.

The distinction of two different processes appears interesting in view of double power-laws for the ac-conductivity of glasses proposed recently by Nowick [13] and Funke [14], consisting

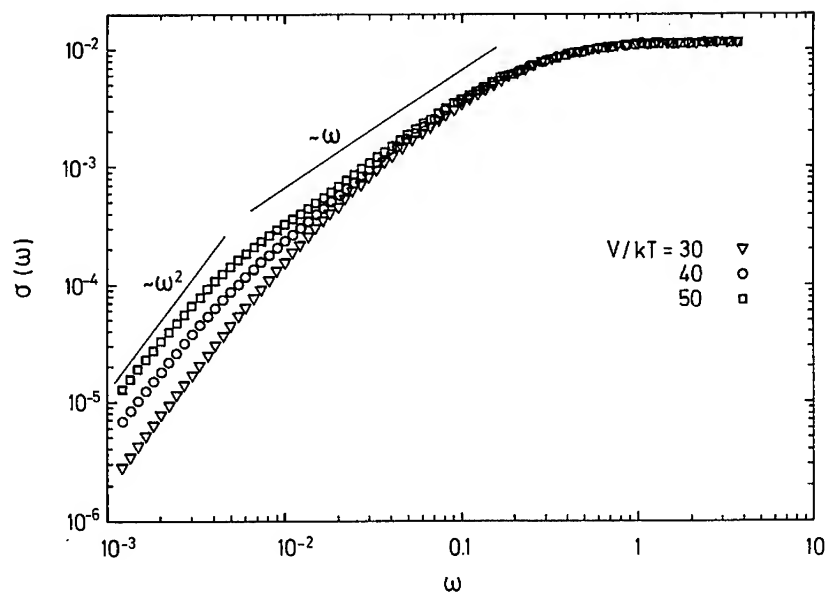


Figure 5: Dynamic conductivity in the dipolar model, derived from eq. (1), for the same set of parameters as in Fig. 4.

of a Jonscher-type contribution and a contribution proportional to  $\omega^1$ . The conventional interpretation of the latter is in terms of atomic double well potentials [15,16]. This, however, poses the problem of relating the required broad distribution of barrier heights to other material parameters. More research, both experimental and theoretical, seems necessary to clarify the physical origin of the high-frequency response of glassy electrolytes.

**Acknowledgements:** Helpful discussions with A. Bunde, K. Funke and K.L. Ngai are gratefully acknowledged. This work was supported in part by the Deutsche Forschungsgemeinschaft, SFB 306.

## References

- [1] A.K. Jonscher, *Nature* **267**, 673 (1977)
- [2] C. A. Angell, in: *High Conductivity Solid Ionic Conductors, Recent Trends and Applications*, ed. T. Takahashi (World Scientific, Singapore, 1989) p. 89;  
M. D. Ingram, *Phys. Chem. Glasses* **28**, 215 (1987)
- [3] K. Funke, *Prog. Solid St. Chem.* **22**, 111 (1993)

- 
- [4] W.K. Lee, J. F. Lin and A. S. Nowick, *Phys. Rev. Letters* **67**, 1559 (1991)
  - [5] S. R. Elliot and A. O. Owens, *Phil. Mag. B* **60**, 777 (1989)
  - [6] J. C. Dyre, *Phys. Rev.* **48**, 12511 (1993)
  - [7] A. Hunt, *J. Phys. Cond. Mat.* **4**, 5371 (1992)
  - [8] W. Schirmacher, *Solid State Ionics* **28-30**, 129 (1988)
  - [9] P. Maass, J. Petersen, A. Bunde, W. Dieterich and H. E. Roman, *Phys. Rev. Letters* **66**, 52 (1991)
  - [10] D. Knödler and W. Dieterich, *Physica A* **191**, 426 (1993)
  - [11] J. A. Puertolas and F. Falo, *J. Noncryst. Solids* **172-174**, 1202 (1994)
  - [12] D. Knödler, P. Pendzig and W. Dieterich, *Solid State Ionics* **70-71**, 356 (1994)
  - [13] A. S. Nowick, B. S. Lim and R. Vaysleyb, *J. Noncryst. Solids* **172-174**, 1243 (1994)
  - [14] C. Cramer, K. Funke, C. Vortkamp-Rückert and A. J. Dianoux, *Physica A* **191**, 358 (1992)
  - [15] A. R. Long, *Adv. Phys.* **31**, 553 (1982)
  - [16] S. R. Elliott, *Solid State Ionics* **70-71**, 27 (1994)

## COMPLETE CONDUCTIVITY SPECTRA OF CRYSTALLINE AND GLASSY FAST ION CONDUCTORS UP TO FAR INFRARED FREQUENCIES

C. CRAMER\*\*, R. GRAEBER\*, M.D. INGRAM†, T. SAATKAMP\*, D. WILMER\* AND K. FUNKE\*

\*Institut für Physikalische Chemie, Schlossplatz 4/7, 48149 Münster, Germany

\*\*Argonne National Laboratory, Materials Science Division, Building 223, 9700 South Cass Avenue, Argonne, IL 60439, USA

†Department of Chemistry, University of Aberdeen, Meston Walk, Aberdeen, AB9 2UE, Scotland, UK

### ABSTRACT

Complete conductivity spectra have been taken of a lithium ion conducting glass of composition  $B_2O_3 \cdot 0.56 Li_2O \cdot 0.45 LiBr$  and of lithium stabilized Na- $\beta''$ -alumina, at various temperatures. — In the glass, it has for the first time been possible to separate the hopping and vibrational contributions to the conductivity. The resulting hopping conductivity spectra display high-frequency plateaux similar to those known to exist in crystalline solid electrolytes like  $RbAg_4I_5$  and Na- $\beta$ -alumina. In the dispersive regime, the spectra are characterized by two different power-law exponents,  $p = 0.6$  and  $q = 1.3$ . The data are evaluated by combined application of the jump relaxation model and the dynamic structure model. — Na- $\beta''$ -alumina has pronounced high-frequency plateaux between about 200 GHz and 400 GHz. The hopping observed in the spectra can be decomposed into hops that are *a priori* unsuccessful and others that can be treated in terms of the jump relaxation model. The latter fraction is found to increase with increasing temperature.

### I INTRODUCTION

Frequency dependent ionic conductivities of solid electrolytes,  $\sigma(\omega)$ , contain valuable information on the dynamics of the elementary steps of hopping motion of the mobile ions in these materials. Measurement of complete conductivity spectra extending from dc to the far infrared does, however, require application of various experimental techniques which are not normally available in one laboratory. This may be the reason why complete spectra of  $\sigma(\omega)$  are still extremely rare.

Two well known examples are shown in Figs. 1a and 1b. In  $Na_2O \cdot 3SiO_2$  glass [1,2], there is a continuous increase of  $\log \sigma$  vs.  $\log \omega$ , and even of the slope of this function, until the vibrational regime is attained at about 1 THz, cf. Fig. 1a. — The situation is different in  $RbAg_4I_5$ , see Fig. 1b, where the increase of the hopping conductivity is restricted to a regime denoted by II in the figure. This regime is followed by the so-called high-frequency plateau, which is observed in regime I [3,4]. Note also that in regime II the slope,  $p$ , is always smaller than one, while in Fig. 1a the slope is found to exceed the value of one.

As pointed out earlier [3–5], the conductivity spectra of Fig. 1b are in general agreement with the predictions of the jump relaxation model [6]. By contrast, the spectra of Fig. 1a do not show the high-frequency plateaux predicted by this model. Moreover, power-law exponents larger than one cannot be explained in terms of jump relaxation, if only hops via equivalent sites are being considered [6].



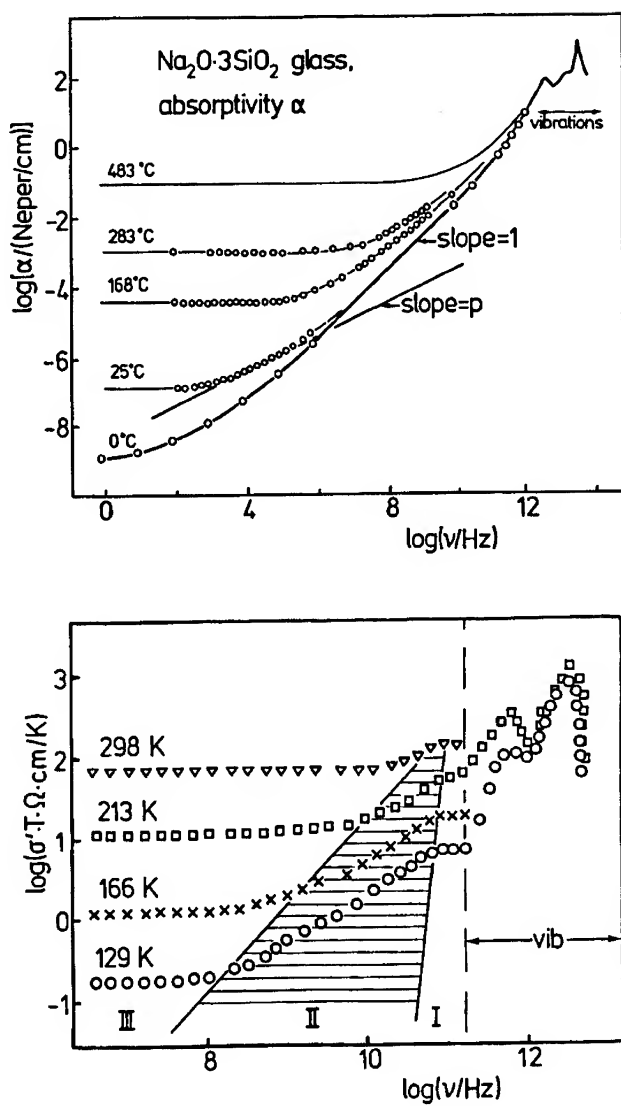


Figure 1: a) absorptivity/conductivity spectra of  $\text{Na}_2\text{O} - 3\text{SiO}_2$  glass at various temperatures, after [1] and [2]. 1 Neper  $\text{cm}^{-1}$  corresponds to  $3 \cdot 10^{-3} \Omega^{-1} \text{cm}^{-1}$ .  
b) Dynamic conductivity of the crystalline solid electrolyte  $\text{RbAg}_4\text{I}_5$  at temperatures between 129 K and 298 K, after [3].

In this paper we shall present complete conductivity spectra of glassy  $\text{B}_2\text{O}_3 \cdot 0.56 \text{Li}_2\text{O} \cdot 0.45 \text{LiBr}$  and of crystalline  $\text{Na-}\beta''\text{-alumina}$  (lithium stabilized). High-frequency plateaux of the hopping conductivity will clearly be identified in both cases. However, the shapes of the spectra call for an extension of the basic version of the jump relaxation model [6], to include the presence of non-equivalent sites and non-equivalent configurations of the immediate neighbourhoods of the hopping ions.

## II GLASSY $\text{B}_2\text{O}_3 \cdot 0.56 \text{Li}_2\text{O} \cdot 0.45 \text{LiBr}$

Complete ionic conductivity spectra of glassy  $\text{B}_2\text{O}_3 \cdot 0.56 \text{Li}_2\text{O} \cdot 0.45 \text{LiBr}$  have been taken at twelve temperatures, ranging from 173 K to 573 K. Examples are given in Figs. 2a and 2b, the experimental data being represented by squares. Evidently, the overall shape of the spectra is similar to Fig. 1a. In particular, a high-frequency plateau is not visible.

In the far infrared, the conductivity spectra are found to vary with frequency as  $\omega^2$ , the temperature dependence being rather small. This feature can be regarded as the low-frequency flank of the vibrational contribution to the conductivity. It is easily extrapolated to lower frequencies and taken out of the total spectra. The resulting frequency dependent conductivities are then interpreted in terms of the hopping motion of the mobile lithium ions.

In Figs. 2a and 2b, the resulting hopping-conductivity spectra,  $\sigma_{\text{hop}}(\omega)$ , are indicated by crosses (+). The most exciting feature is the appearance of high-frequency plateaux. With regard to their general shape, the spectra  $\sigma_{\text{hop}}(\omega)$  now resemble those of Fig. 1b.

However, closer inspection reveals systematic differences between these spectra  $\sigma_{\text{hop}}(\omega)$  and the predictions of the jump relaxation model. In Fig. 3, this is demonstrated for the 373 K spectrum. At all temperatures, like in Fig. 3, the low-frequency part is nicely fitted by

$$\sigma_1(\omega) = \sigma(0) \cdot [1 + (\omega t_2)^p] \quad \text{with } p = 0.6, \quad (1)$$

while the high-frequency part is close to

$$\sigma_2(\omega) = \sigma(\infty) \cdot [1 + (\omega t_1)^{-1}]^{-q} \quad \text{with } q = 1.3. \quad (2)$$

In Eqs. (1) and (2),  $\sigma(0)$  and  $\sigma(\infty)$  denote the low- and high-frequency plateau values of  $\sigma_{\text{hop}}(\omega)$ , while  $1/t_2$  and  $1/t_1$  are the angular crossover frequencies between the different power-law regimes. Both limiting cases are reminiscent of the jump relaxation model which predicts

$$\sigma_{\text{hop}}(\omega) \approx \sigma(0) + [\sigma(\infty) - \sigma(0)] \cdot [1 + (\omega t_1)^{-1}]^{-p} \quad \text{with } 0 < p < 1. \quad (3)$$

The only difference is that we now have  $q \neq p$  and even  $q > 1$ . The latter inequality is impossible in the original jump relaxation model, in which all hops are geometrically alike [6].

In fact, according to the dynamic structure model [7], we have to distinguish between at least two kinds of site in a single-alkali glass. These are the so-called  $\bar{A}$  sites which are optimally configured to meet the requirements of each mobile  $A^+$  ion (here:  $\text{Li}^+$ ), and the  $\bar{C}$  sites which provide less room and are less favourable. If an  $A^+$  ion leaves an  $\bar{A}$  site, this site is supposed to stay  $\bar{A}$  for some time and then to transform into a  $\bar{C}$  site. Correspondingly, if

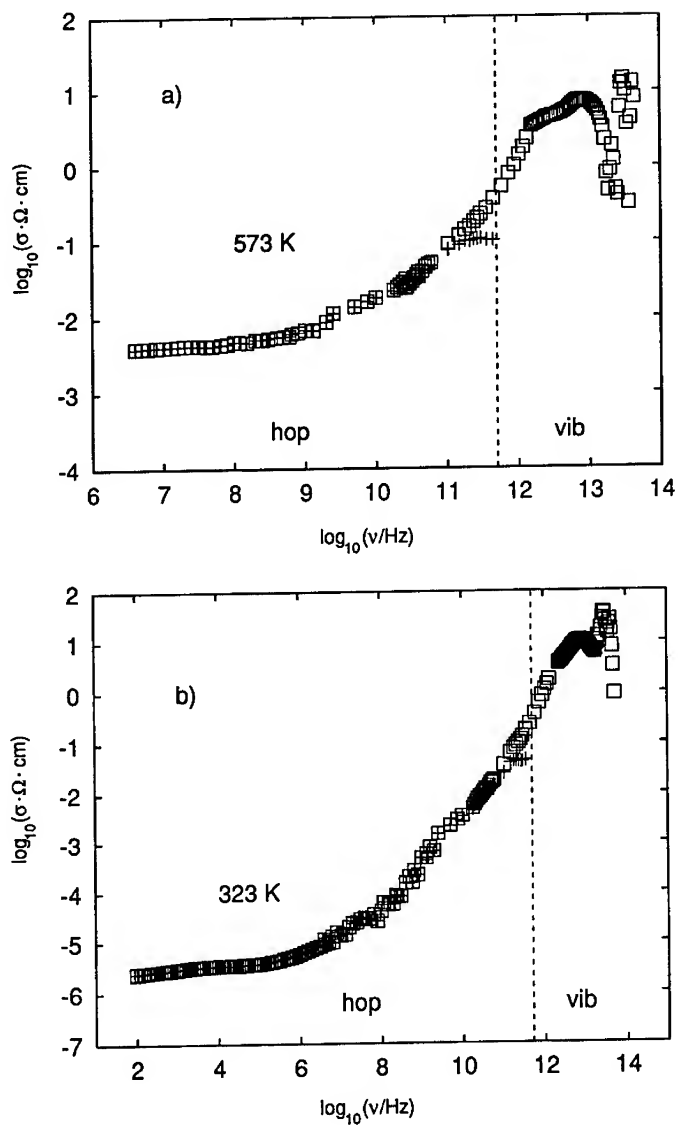


Figure 2: Total experimental conductivity spectra ( $\square$ ) and spectra obtained after removing vibrational contributions ( $+$ ), of glassy  $B_2O_3 \cdot 0.56Li_2O \cdot 0.45LiBr$  at a) 573 K and b) 323 K.

an  $A^+$  ion hops into a  $\bar{C}$  site and manages to stay, then the  $\bar{C}$  site is supposed to relax into an  $\bar{A}$  site.

There are thus two kinds of site relaxation:

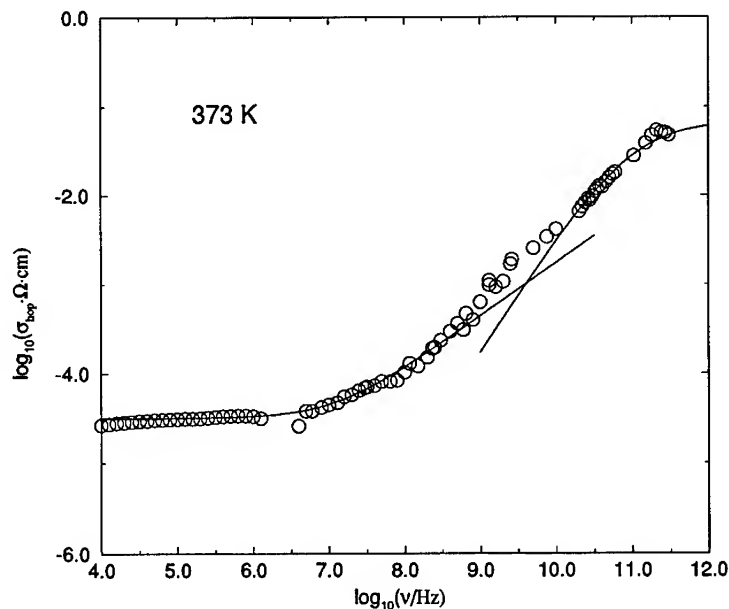


Figure 3: Hopping conductivity spectrum of  $B_2O_3 \cdot 0.56 Li_2O \cdot 0.45 LiBr$  glass at 373 K (o). Solid lines calculated via Eq. (1) (low frequency regime,  $p = 0.6$ ) and Eq. (2) (high frequency regime,  $q = 1.3$ ).

- (i) the shifting of the Coulomb cage as described by the jump relaxation model and
- (ii) the  $\bar{A}$  to  $\bar{C}$  and  $\bar{C}$  to  $\bar{A}$  relaxation as described by the dynamic structure model.

Effect (i) is achieved by the hopping of neighbouring mobile ions, while (ii) necessitates a restructuring of the glassy matrix. Therefore, (i) is assumed to be much faster than (ii).

Fig. 4 shows the difference between an  $\bar{A}$  to  $\bar{A}$  hop and an  $\bar{A}$  to  $\bar{C}$  hop, in terms of the single-particle potential felt by the mobile ion. Fig. 5 is applicable to both situations displayed in Fig. 4. This means that  $Y$  may be  $\bar{A}$  or  $\bar{C}$  while  $X$  is always  $\bar{A}$ .

Once the ion is at  $Y$ , a competition sets in between two ways of relaxation. The ion may hop back to  $X$  or the neighbourhood may relax with respect to  $Y$ . Either one of these competing ways of relaxation can be characterized by a time constant or by its inverse, the respective rate. The rates are denoted by

$$\frac{1}{t^*} := - \left( \frac{dW(t)}{dt} \right)_{t=0} = \text{initial back-hop rate}, \quad (4a)$$

$$\frac{1}{t_1} := \frac{1}{kT} \left( \frac{d\delta_{\text{back}}(t)}{dt} \right)_{t=0} = \text{initial site-relaxation rate}. \quad (4b)$$

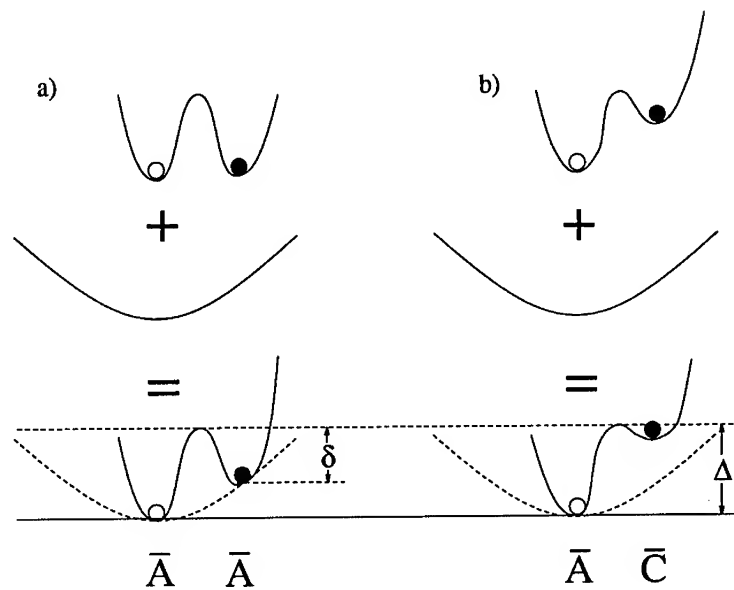


Figure 4: Typical single-particle potentials encountered by hopping ions (at  $t = 0$ ) in a)  $\bar{A}$  to  $\bar{A}$  and b)  $\bar{A}$  to  $\bar{C}$  hops. Each of the effective potentials constructed in a) and b) consists of two contributions: a site-sensitive potential (on top) and a *Coulomb cage* potential.

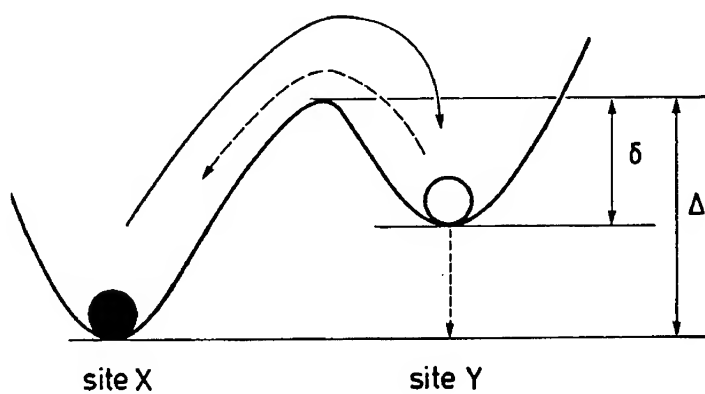


Figure 5: Effective single-particle potential of the *central* ion at the time of its *initial* hop from site  $X$  to site  $Y$ .

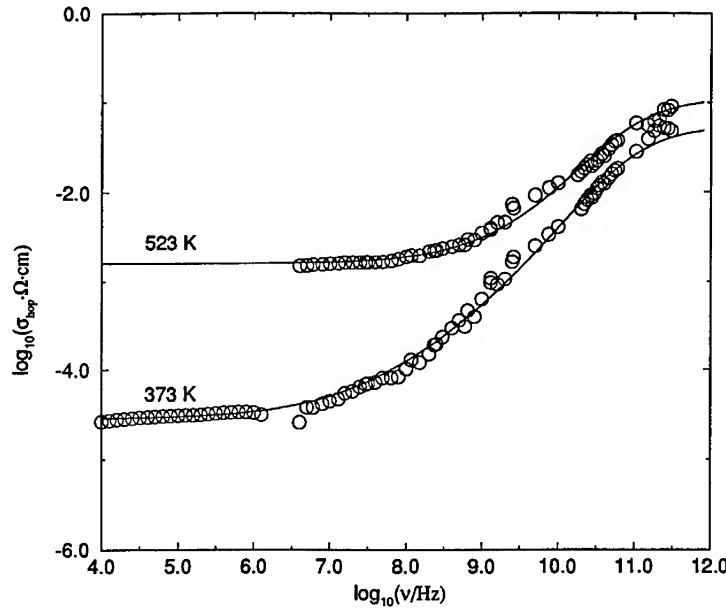


Figure 6: Hopping conductivity spectra of glassy  $B_2O_3 \cdot 0.56 Li_2O \cdot 0.45 LiBr$  (o). Solid lines result from our model construction.

In Eqs. (4a,b),  $W(t)$  is the probability for the correlated backward hop not to have occurred until time  $t$ , and  $\delta_{back}(t)$  is the time-dependent barrier height for that hop.

It is now easy to show that the ratio  $t_1/t^*$  determines the exponent ( $p$  or  $q$ ) in the frequency-dependent hopping conductivity. This is seen by considering the correlated back-hop rate,  $-\dot{W}(t)$ , and the rate of change of  $\delta_{back}(t)$ ,  $\dot{\delta}_{back}(t)$ , at sufficiently short times, when the site-relaxation process at  $Y$  is still far from being completed. Denoting the attempt frequency for a backward hop by  $\nu_0$ , we have

$$-\dot{W}(t) = W(t) \cdot \nu_0 \cdot \exp[-\delta_{back}(t)/kT]. \quad (5a)$$

On the other hand, numerical simulations [8] as well as the jump relaxation model show that

$$\dot{\delta}_{back}(t) = \frac{kT}{t + t_1} \quad (5b)$$

holds in the short-time regime. With the definition of Eq. (4a) and after a little algebra, we find

$$W(t) = \left(1 + \frac{t}{t_1}\right)^{-t_1/t^*}. \quad (6)$$

While  $W(t)$  is the probability for the  $X$  to  $Y$  hop still to be successful at time  $t$ , the ratio  $\sigma_2(\omega = 1/t)/\sigma(\infty)$  may be considered the corresponding probability on the angular frequency scale. This would imply

$$\sigma_2(\omega) = \sigma(\infty) \cdot [1 + (\omega t_1)^{-1}]^{-t_1/t^*}, \quad (7)$$

which is Eq. (2) with  $q = t_1/t^*$ .

Application of the linear response theory shows that Eq. (7) is, in fact, a very good approximation for  $\sigma_2(\omega)$  as long as  $t_1/t^*$  does not exceed the value of two [9]. The limiting case  $t_1/t^* \rightarrow \infty$  will be discussed in section III.

The experimental finding of a superposition of  $\sigma_1(\omega)$  and  $\sigma_2(\omega)$ , see Fig. 3, is now readily explained in terms of the two situations in Fig. 4. Hops via  $\bar{A}$  sites may be treated by the original jump relaxation model. As the Coulomb relaxation of the neighbourhood is essentially due to (successful)  $\bar{A}$  to  $\bar{A}$  hops of other ions, the model does, indeed, apply. In this case, the  $t_1/t^*$  ratio has a value of  $p < 1$ . The low-frequency conductivity, which is dominated by  $\bar{A}$  to  $\bar{A}$  hops, is thus well described by the low-frequency part of Eq. (3), which is Eq. (1).

Compared to an  $\bar{A}$  to  $\bar{A}$  hop, an  $\bar{A}$  to  $\bar{C}$  hop has a smaller backward barrier height. Therefore, the back-hop rate,  $1/t^*$ , is enhanced. As a consequence, the  $t_1/t^*$  ratio is now found to be larger, exceeding one. Neighbouring  $\bar{C}$  sites being quite common, there is frequent  $\bar{A}$  to  $\bar{C}$  hopping, mostly followed by a backward hop. This process is well described by Eqs. (2) and (7), with  $t_1/t^* = q = 1.3$ .

In Fig. 6 we show two experimental spectra,  $\sigma_{\text{hop}}(\omega)$ , along with numerical fits. The fits are essentially based on Eqs. (1) and (2). However, they also account for two additional features which become dominant at low temperatures and are described in ref. [9].

### III POLYCRYSTALLINE Na- $\beta''$ -ALUMINA

One of the classical examples of solid electrolytes exhibiting high-frequency conductivity plateaux is Na- $\beta$ -alumina [10–12]. On the other hand, Na- $\beta''$ -alumina, which contains a larger amount of mobile sodium ions and has a different stacking of the spinel blocks (see, e.g., [13]) has so far not been studied with regard to its high-frequency conductivity. In our present experiments we utilized lithium stabilized polycrystalline material supplied by Ceramatec Inc., containing 2.5 mol % of  $\text{Li}_2\text{O}$ , 13.4 mol % of  $\text{Na}_2\text{O}$ , and 84.1 mol % of  $\text{Al}_2\text{O}_3$ .

In Fig. 7 we present conductivity spectra up to 10 THz, taken at temperatures between 115 K and 473 K. As in Fig. 1b, the hopping and vibrational conductivity regimes are easy to distinguish. They join each other in the “high-frequency” plateaux, which are very well pronounced at each temperature, extending from about 200 GHz to about 400 GHz.

In the plateau regime, two differently activated contributions seem to be superimposed.

One of them dominates at relatively low temperatures and is characterized by a comparatively low activation energy of about 24 meV. At lower frequencies, it is found to vary in a simple Debye-type fashion,

$$\sigma_{\text{Debye}}(\omega) = \sigma_{\text{Debye}}(\infty) \cdot \frac{(\omega\tau)^2}{1 + (\omega\tau)^2}, \quad (8)$$

its relaxation time  $\tau$  being about 1.5 ps and rather temperature insensitive. This contribution is attributed to small reorientational displacements and will not be discussed any further.

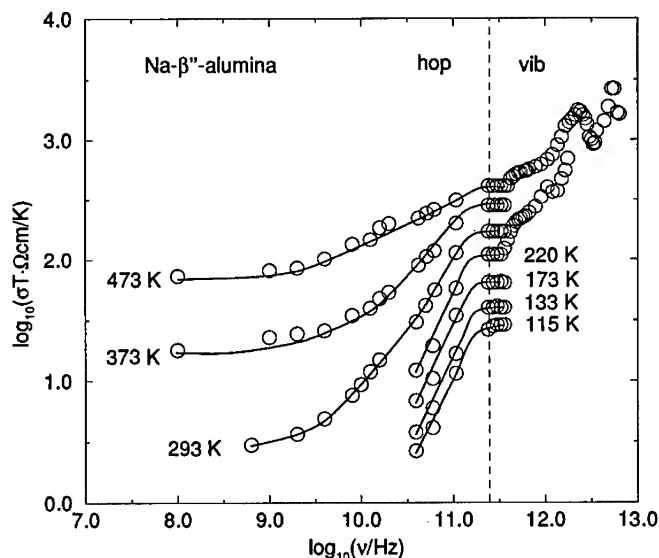


Figure 7: Conductivity spectra of Na- $\beta''$ -alumina (o). Solid lines are guides to the eye.

The other component is dominant at 293 K and above, its activation energy being about  $60 \text{ meV} \approx k \cdot 700 \text{ K}$ . Its dispersion is more clearly seen in Fig. 8, where  $\sigma_{\text{Debye}}(\omega)$  of Eq. (8) has been removed. In the following, the conductivities of Fig. 8 will be called  $\sigma_{\text{hop}}(\omega)$ .

Trying to describe the low-frequency part of  $\sigma_{\text{hop}}(\omega)$  in terms of Eq. (1), we may ask for the temperature dependences of  $\sigma_{\text{hop}}(0) \cdot T$  and of the crossover angular frequency,  $1/t_2$ . The latter quantity is the inverse time required for a hop to prove successful. In most solid electrolytes, the activation energies of  $\sigma_{\text{hop}}(0) \cdot T$  and  $1/t_2$  are found to be identical, which means that the dc conductivity increases with increasing temperature, because each ion performs more successful hops per unit time. In that case, the line in Fig. 8, which connects points where  $\sigma(\omega)$  equals  $2 \cdot \sigma(0)$ , would have to have a slope of one. However, the slope is found to be close to  $3/2$ . Interestingly, a similar behaviour was discovered earlier in Na- $\beta$ -alumina [14].

For an interpretation, one might first try to postulate a temperature dependent number of mobile ions. However, the number of sodium ions is, of course, constant. Rather, we have to assume that not all of those hops that contribute to the high-frequency plateau,  $\sigma_{\text{hop}}(\infty)$ , should be treated in terms of jump relaxation, but only a temperature dependent fraction of them. In fact, inspection of the 293 K spectrum of Fig. 8 shows that here jump relaxation and Debye relaxation are superimposed. This is indicated in the figure. At higher temperatures, however, the jump-relaxation component is found to contribute more significantly to  $\sigma_{\text{hop}}(\infty)$ .

The solid lines of Fig. 8, which fit the spectra very well, have been obtained on the basis



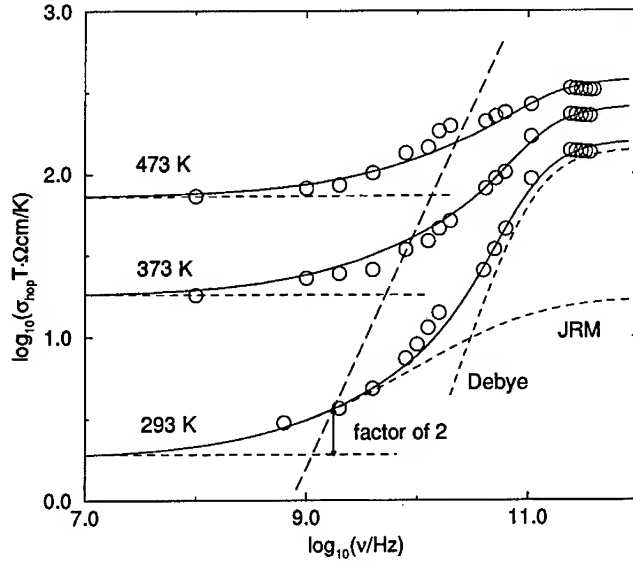


Figure 8: Hopping-conductivity spectra of Na- $\beta''$ -alumina ( $\circ$ ). Solid lines result from a model calculation based on Eq. (10). The 293 K spectrum is decomposed into its constituent parts, see Eq. (10).

of the following assumptions:

- (i) All hops are activated with  $\Delta = 0.060$  eV.
- (ii) A temperature dependent fraction,  $m(T)$ , of all hops, are *a priori* unsuccessful: the mobile ion immediately returns ("rolls back") to its previous position.
- (iii) In all other cases, the jump relaxation model can be applied.

The simultaneous existence of features (ii) and (iii) proves that the sodium ions do, indeed, encounter non-equivalent configurations of their environments.

Situations (ii) and (iii) resemble those sketched in Figs. 4b and 4a, respectively. In particular, for a treatment of (ii) we now assume that  $t_1/t^*$  tends to infinity. The right-hand side of Eq. (6) thus becomes  $\exp(-t/t_1)$ . By contrast, situation (iii) calls for use of the jump relaxation version of  $W(t)$ , which corresponds to Eq. (3):

$$W_{JR}(t) = W_{JR}(\infty) + [1 - W_{JR}(\infty)] \cdot \left(1 + \frac{t}{t_1}\right)^{-p}. \quad (9)$$

We thus have

$$W_{\text{total}}(t) = [1 - m(T)] \cdot W_{JR}(t) + m(T) \cdot \exp(-t/t_1), \quad (10)$$

where  $1 - m(T)$  is an increasing function of temperature.

A qualitative explanation of this temperature dependence is easily given. Evidently, the chances for finding a suitable site in a hop are dramatically increased as the neighbourhood becomes more mobile with increasing temperature. This is, of course, a highly cooperative effect. In a more detailed treatment of the dynamics, explicit allowance would have to be made for many-particle cross-terms. Consideration of the time-averaged structure [15] is necessary, but far from sufficient for such a treatment.

#### ACKNOWLEDGEMENTS

It is a pleasure to thank A. Bunde for fruitful discussions. He contributed essential views to our present paper. R. Holtwick helped with the preparation of the figures. The experimental and theoretical analysis of the frequency dependent ionic conductivity was funded by the Deutsche Forschungsgemeinschaft. Financial aid for our British-German collaboration is provided by the British Council and the DAAD in the framework of the ARC programme. Financial help by the Fonds der Chemischen Industrie is also gratefully acknowledged.

#### REFERENCES

- [1] J. Wong, C.A. Angell, *Glass, Structure by Spectroscopy*, Dekker, New York, 1976.
- [2] A. Burns, G.D. Chryssikos, E. Tombari, R.H. Cole, W.M. Risen Jr., *Phys. Chem. Glasses* **30**, 264 (1989).
- [3] R. Hoppe, T. Kloidt, K. Funke, *Ber. Bunsenges. Phys. Chem.* **95**, 1025 (1991).
- [4] K. Funke, T. Kloidt, D. Wilmer, C.J. Carlile, *Solid State Ionics* **53-56**, 947 (1992).
- [5] K. Funke, *Mat. Res. Soc. Symp. Proc.* **210**, 97 (1991).
- [6] K. Funke, *Prog. Solid St. Chem.* **22**, 111 (1993).
- [7] A. Bunde, M.D. Ingram, P. Maass, *J. Non-Cryst. Solids* **172-174**, 1222 (1994).
- [8] P. Maass, M. Meyer, A. Bunde, *Phys. Rev. B*, *in press* (1995).
- [9] C. Cramer, K. Funke, T. Saatkamp, D. Wilmer, M.D. Ingram, *Z. Naturforsch.*, *in press* (1995).
- [10] U. Strom, K.L. Ngai, *Solid State Ionics* **5**, 167 (1981).
- [11] U. Strom, K.L. Ngai, *J. Phys. (Paris)* **42**, C4-123 (1981).
- [12] K.L. Ngai, U. Strom, *Phys. Rev. B* **38**, 10350 (1988).
- [13] J.D. Jorgensen, F.J. Rotella, W.L. Roth, *Solid State Ionics* **5**, 143 (1981).
- [14] D.P. Almond, A.R. West, R.J. Grant, *Solid State Commun.* **44**, 1277 (1982).
- [15] B. Dunn, B.B. Schwarz, J.O. Thomas, P.E.D. Morgan, *Solid State Ionics* **28-30**, 301 (1988).



## The Mechanism and Modeling of Conductivity in Polymer Electrolytes

Mark C. Lonergan,<sup>†</sup> Duward F. Shriver, Abraham Nitzan,<sup>\*</sup> Mark A. Ratner  
Department of Chemistry and Materials Research Center, Northwestern University,  
2145 Sheridan Road, Evanston, IL 60208-3113.

### *Abstract*

The progress of dynamically disordered hopping (DDH) in modelling charge transport in polymer electrolytes is reviewed. The DDH model successfully describes many of the salient features of polymer electrolytes, most notably, the frequency and temperature dependence of the conductivity. Furthermore, analyses and simulations based on the DDH model provide rich mechanistic information. The general picture of charge transport that emerges from the DDH model is one in which two classes of charge carriers exist in thermal equilibrium: quasi-free and bound. The quasi-free carriers dominate the conductivity response and diffuse freely over short distances ( $\approx 1\text{\AA}$ ) with longer range diffusion requiring local segmental motions, renewal in the language of DDH, of the polymer solvent. The bound carriers, which are likely polymer solvated ion clusters, are immobile on the time-scale of renewal and contribute relatively little to the conductivity.

### *1. Introduction*

Uni-univalent polymer electrolyte systems are generally studied and utilized in the homogeneous amorphous phase; the ionic concentrations always exceed 0.01M. Under these conditions, conduction occurs in a dynamically-disordered immobile solvent, with strong coulomb correlations and extensive ion clustering.<sup>1</sup> This paper is devoted to modelling and mechanistic studies that examine the conductivity process in these materials. The overall picture that emerges shows that the conduction is dominated by motion of effectively-free ions in thermal equilibrium with clusters of

<sup>†</sup> Present Address: Department of Chemistry and Chemical Engineering, California Institute of Technology, Mail Code 127-72, Pasadena, CA 91125.

<sup>\*</sup> Perm. Address: School of Chemistry, Sackler Faculty of Science, Tel-Aviv University, Tel-Aviv Israel

various sizes; the mobility of the ions is dependent upon relaxation processes (segmental relaxation) of the host. Effectively, then, the ionic diffusion is dominated by the host segmental relaxation, so that the system is strongly "coupled".<sup>6,7</sup> This combined picture accounts well for the temperature, frequency and concentration dependencies of conductivity in neat polymer electrolytes.

The diffusion of ions in polymer electrolytes is modulated by relaxation modes of the strongly-coupled polymer solvent, and can be described by the dynamically disordered hopping (DDH) model.<sup>8-23</sup> In DDH, particle diffusion through a dynamic, percolative environment is considered. The percolative environment mimics the blocking of ion motion by the polymer solvent, and the dynamic redistribution (renewal) of percolation pathways within this environment mimics polymer segmental motion. With the DDH model, the diffusion coefficient for species in a renewing environment,  $D$ , can be calculated from knowledge of diffusion in the corresponding static system,  $D_o$ , according to:<sup>10</sup>

$$D(\omega) = D_o(\omega - i\lambda) = \frac{(\lambda + i\omega)^2}{6} \int_0^{\infty} g(t) \exp[-(\lambda + i\omega)t] dt \quad 1$$

where  $\lambda = 1/\tau_R$  with  $\tau_R$  the average renewal time for the redistribution of percolation pathways and  $g(t)$  is the average mean-squared displacement of a particle in the non-renewing, static system. In reference to polymer electrolytes,  $g(t)$  is the local displacement of an ion in the absence of segmental motion, and the renewal time is the characteristic time constant for these segmental motions (*vide infra*).

In this paper, we review the central predictions of the DDH model, the consistency of these predictions with current experimental data on polymer electrolytes, and the implications of these predictions with regard to the mechanism of charge transport in polymer electrolytes. Four major topics are addressed: the characteristic Vogel, Tammann, Fulcher (VTF) form<sup>24-26</sup> of the temperature-dependent dc conductivity, the frequency dependence, the nature of  $g(t)$ , and the importance of ion-ion interactions. These are the central mechanistic features that must be accounted for to understand conductivity in polymer electrolytes.

## II. Dc conductivity and the glass transition

From eq 1 and linear response theory, the dc diffusion coefficient is given by:<sup>10</sup>

$$D = \frac{\lambda^2}{6} \int_0^\infty g(t) \exp[-\lambda t] dt. \quad 2$$

Coupling eq 2 with the Nernst-Einstein equation gives the conductivity in the absence of collective particle correlations,

$$\sigma = \frac{\lambda^2 n q^2}{6 k_B T} \int_0^\infty g(t) \exp[-\lambda t] dt, \quad 3$$

where  $n$  and  $q$  are the carrier density and charge,  $k_B$  is the Boltzmann constant, and  $T$  is the temperature. In polymer electrolytes, the conductivity is dominated by the dynamics of the host, as described by models such as free volume<sup>27,28</sup> or configurational entropy,<sup>29-31</sup> and its temperature dependence follows the VTF form:

$$\sigma = A \exp \left[ \frac{-B}{(T - T_o)} \right] \quad 4$$

where  $A$ ,  $B$ , and  $T_o$  are fitting parameters with  $T_o$  empirically related to the glass transition temperature ( $T_o = T_g - (\approx 40\text{K})$ ). Below its glass transition temperature, the conductivity of a polymer electrolytes drops precipitously as the segmental motions necessary for ion transport are frozen out. Within a static percolation picture, this suggests that polymer electrolytes are below their percolation thresholds for ion diffusion in that long-ranged motion only occurs if the local percolation clusters are continually stirred or renewed by polymer segmental motion. Consequently,  $g(t)$  must saturate since it reflects the unstirred or static system (see Figure 1). Furthermore,  $g(t)$  must saturate on a time scale faster than for the renewal process. Otherwise, the dc conductivity response would be dominated by the intrinsic mobility of the ions rather than by the dynamics of the polymer solvent, as modeled by the renewal process (see Figure 1).<sup>16-18</sup> The quantitative statement of the renewal-limited regime is the following:

$$g(t) \rightarrow g(\infty), \quad t \ll \tau_r \quad 5$$

where  $g(\infty)$  is the saturation value of  $g(t)$ . In the renewal-limited regime, eqs 2 and 3 reduce to:<sup>16-18</sup>

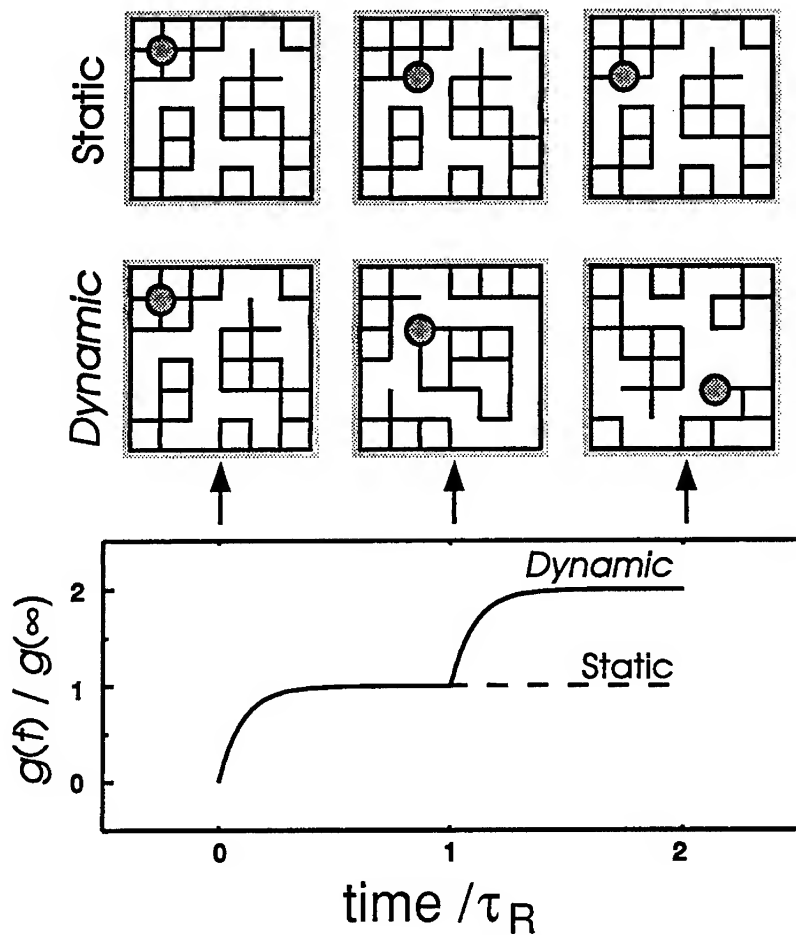


**Figure 1** - Schematic illustrating the dynamically disordered hopping model for an ion diffusing on a lattice. The lattice diagrams show the trajectory of a single diffuser for a static and dynamic system at  $t = 0$ ,  $\tau_R$ , and  $2\tau_R$ , and the graph shows the ensemble average mean-squared displacement,  $g(t)$ , for these two systems. The diffusion coefficient,  $D$ , is given by the long time slope of  $g(t)$ . In the static system, the motion is confined to a single percolation cluster resulting in  $D = 0$ . In the dynamic system, the percolation clusters are continually redefined allowing long-range transport. In this schematic, the dynamic system is shown in the renewal-limited regime where the maximum mean-squared displacement obtainable during a given renewal period is realized. In this limit,  $D$  is directly proportional to the renewal rate,  $\lambda = 1 / \tau_R$ .

$$D = \frac{g(\infty)}{6\tau_R}, \quad 6a$$

$$\sigma = \frac{nq^2 g(\infty)}{6k_B T \tau_R}. \quad 6b$$

Clearly,  $\tau_R$  is a central parameter determining the conductivity response.

Qualitatively, we have discussed the link between the renewal process and polymer segmental motion. There are, however, a wide range of polymer motions that may be coupled to ion diffusion. Although it is difficult to unambiguously assign one of these motions as facilitating ion transport in polymer electrolytes,<sup>32</sup> and hence to the renewal process in DDH, a striking correspondence between the conductivity of polymer electrolytes and their dielectric glass transition relaxation has been demonstrated (see Figure 2).<sup>38-40</sup> This strong correspondence has been used to argue that the time scale for the dielectric glass transition relaxation,  $\tau_{GTR} = 1/\omega_{GTR}$ , is a quantitative measure of  $\tau_R$ . Assuming  $g(\infty)$  to be weakly temperature dependent, a trivial result of assigning  $\tau_{GTR} = \tau_R$  is the recovery of VTF behavior from eq 6 since  $\omega_{GTR}$  exhibits VTF temperature dependence (see Figure 2).<sup>16-18</sup> Hence, in the renewal-limited regime, the DDH model is consistent with the observed temperature dependence of the dc conductivity of polymer electrolytes.

### III. Frequency Dependence

In applying the DDH model to the frequency dependence of the complex permittivity, the form of  $g(t)$  must be known. Typically, simple saturation behavior is assumed:<sup>11,16,17</sup>

$$g(t) = [1 - \exp(-\zeta t)]g(\infty) \quad 7$$

where  $\zeta$  is a filling rate describing the rate at which an ion fills the local percolation cluster that it resides in.<sup>41</sup> With the additional assumptions that the polymer and ionic response can be separated and that the collective correlations between ions can be neglected, the resulting form of the complex permittivity,  $\Sigma = \Sigma' - i\Sigma''$  is given by:



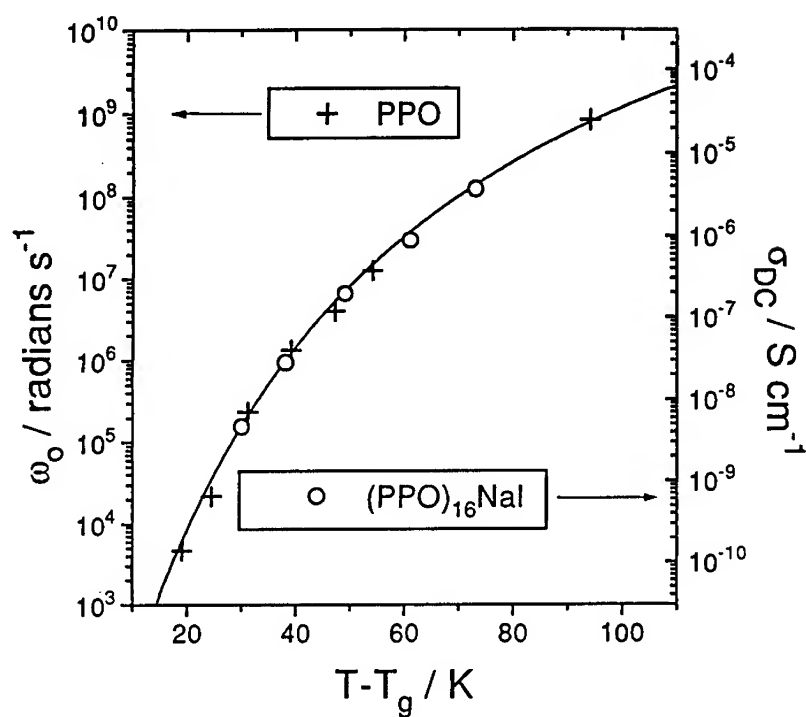


**Figure 2** - The characteristic frequency of the dielectric glass transition relaxation,  $\omega_0 = \omega_{GTR}$ , of PPO as a function of rescaled temperature,  $T - T_g$ , and the conductivity,  $\sigma$ , as a function of  $T - T_g$  for  $\text{PPO}_{16}\text{NaI}$ . The similar temperature dependencies of the dielectric data for PPO and the conductivity data for the salt complex is indicative of the correlation between ion transport in polymer electrolytes and the polymeric relaxations associated with the glass transition relaxation. This sort of correlation is the basis for the equation of  $\tau_R$  with  $\omega_{GTR}$ .

$$\epsilon_o \Sigma = \Sigma_{polymer} + \frac{\sigma_{dc} \zeta \tau}{\lambda} \left( \frac{1}{1 + \omega^2 \tau^2} - i \frac{\omega \tau}{1 + \omega^2 \tau^2} \right) - i \frac{\sigma_{dc}}{\omega} \quad 8$$

where  $\tau = 1 / (\lambda + \zeta)$ . The polymer response is left unspecified since the DDH model does not directly address the dielectric response of the polymer. Rather, it treats only the motion of ions and considers their response as being superimposed upon that of the polymers.<sup>42</sup> It is not to say, however, that the polymer response in the electrolyte is the same as that for the neat polymer. For instance, the characteristic frequency of the glass transition relaxation is shifted to lower frequencies after the addition of salt<sup>46,47</sup> due to the formation of virtual ion-dipole cross-links that also raise  $T_g$ .<sup>48-50</sup>

With the exception of the dc conduction term,  $\sigma_{dc} / \epsilon_o \omega$ , eq 8 predicts that the ionic contribution to the permittivity will be the same as the Debye response characteristic of the rotational motion of independent dipoles. The similarity between the ionic term and a typical dipolar response complicates the assignment of features in the dielectric spectrum of polymer electrolytes. Of course, the dipolar response of high polymers is not well characterized by the Debye equation arising from the exponential decay of the dipole-dipole correlation function. Dipolar relaxations of polymer segments are much broader than predicted by the Debye equation,<sup>43-45</sup> and they are characterized by empirical functions such as the Havriliak-Negami function.<sup>51</sup> The breadth of polymer relaxations does not necessarily simplify the assignment of dielectric relaxations since the ionic response may also be broad owing to a distribution of filling rates in eq 7.

As with the dc conduction process, appealing to the phenomenology of polymer electrolytes can greatly simplify the frequency dependent response, and allow for more unambiguous assignments to be made. If eq 8 is taken in the renewal-limited regime corresponding to  $\zeta \gg \lambda$  then it may be written as:<sup>16,17</sup>

$$\epsilon_o \Sigma = \Sigma_{polymer} + \frac{\sigma_{dc}}{\lambda} \left( \frac{1}{1 + \omega^2 \tau_\zeta^2} - i \frac{\omega \tau}{1 + \omega^2 \tau_\zeta^2} \right) - i \frac{\sigma_{dc}}{\omega} \quad 9$$

The ionic response is now centered about  $\omega = \zeta$  and may physically be described as arising from the polarization of ions in their local percolation clusters (of size  $g(\infty)$ ) as they wait for a renewal event to occur. Hence, it has been termed the ionic polarization relaxation (IPR). Furthermore, since  $\zeta \gg \lambda$ , the IPR is predicted to occur at frequencies higher than the GTR.

The IPR has not been directly observed, but the identification of its frequency range relative to the GTR has allowed for indirect verification of its presence. For long chain amorphous polyethers, such as PPO, under ambient conditions, the GTR is typically observed around 1-10GHz.<sup>40,52-54</sup> As salt is added, the GTR shifts to lower frequencies and eventually becomes overwhelmed by the dc conduction process and electrode effects which make it difficult to resolve.<sup>46,47,55</sup> To date, relaxations at higher frequencies than the GTR have not been observed in amorphous polymer electrolytes up to frequencies of approximately 20GHz. The presence of such high frequency relaxations, as would be the IPR, can be inferred from comparison of the optical dielectric constant obtained from the square of the refractive index,  $n_D^2$ , and the real component of the permittivity observed using high frequency dielectric response. Any difference suggests the presence of additional polarization mechanisms in the frequency range above the frequency of the dielectric measurement and below the frequency of the refractive index measurement. A comparison of  $\Sigma'(\approx 10\text{GHz})$  and  $n_D^2$  for PPO showed little disparity between these quantities.<sup>40</sup> In contrast, the salt complexes of PPO with NaI and  $\text{NH}_4\text{CF}_3\text{SO}_3$  showed significant disparity between  $\Sigma'(\approx 10\text{GHz})$  and  $n_D^2$  consistent with the presence of an IPR at frequencies greater than 10GHz.<sup>40</sup>

The DDH model consistently predicts both the standard dc conduction process ( $\sigma_{dc} / \epsilon_0\omega$ ) as well as explains the disparity between the optical dielectric constant and the real component of the high frequency ( $\approx 10\text{GHz}$ ). There is some evidence that additional features grow into the dielectric spectrum of polymers upon the addition of salt. In particular, several workers have reported the presence of an additional relaxation on the low frequency side of the GTR. It has been argued that this comes about from the rotational motion of ion clusters, but it has also been suggested that it is an artifact of the subtraction process used to deconvolute it from the  $\sigma_{dc} / \omega\epsilon_0$  contribution. To date, the DDH model has only been considered in the independent particle limit which cannot address the presence of such relaxations.

#### ***IV. Local Displacements***

The previous two sections have mainly discussed the evidence supporting the validity of the DDH model for diffusion; particularly, its consistency with both the dc and ac electrical response of polymer electrolytes. In this section, we summarize how the DDH model has been used to understand physically ion transport in polymer

electrolytes. We have already discussed the relevance of the renewal time and its relation to the segmental motions of the polymer host. From eq 6, it is apparent that  $g(\infty)$  is also important in the dc conduction process. Furthermore, an understanding of  $g(\infty)$  also provides microscopic information about the nature of ion motions in the absence of segmental motions.

Based on eq 6, the magnitude of  $g(\infty)^{1/2}$  has been estimated to be  $\approx 0.4\text{\AA}$  at slightly elevated temperatures (50-100°C) in PPO electrolytes.<sup>16,17</sup> The magnitude of  $g(\infty)$  suggests that ion motion in the absence of renewal is quite restricted and that ion hopping between many different coordination environments does not appear to occur in the absence of renewal. Given that amorphous polymer electrolytes are dense liquid-like continua, the calculated magnitude of  $g(\infty)$  is not surprising. The small displacements are consistent with a picture of ion-transport in which ions only exhibit small local motions within their coordination spheres, perhaps just vibrational displacements, with polymer segmental motion (renewal) facilitating long range transport through changes to these coordination environments. The physically reasonable values of  $g(\infty)$  also argue that the equation of  $\tau_R$  with  $\omega_{CTR}$  and the DDH model are valid.

The interpretation of  $g(\infty)$  is complicated by the fact that it is an ensemble average. Consequently, a small number of ions may exhibit large displacements in any given renewal period while the remainder of the ions exhibit only very small displacements. In fact, recent simulations<sup>17,18,56</sup> suggest that this may be the case as addressed in the next section in the context of ion-ion interactions. Even with a distribution of local displacements, the calculated  $g(\infty)$  suggests that these displacements are on the order of Angstroms.

## V. Ion-Ion Interactions

Extensive recent experimental work, particularly, Raman studies, have shown very clear effect of ion concentration, pairing and clustering on the dc conductivity.<sup>57-65</sup> In its original form, the DDH model did not attempt to grapple with the effects of ion-ion interactions on the diffusivity and conductivity of ions in polymer electrolytes. More recently, however, simulations have directed efforts to include ion-ion interactions into the DDH model.<sup>17,18,56</sup> The primary result of these simulations is that the diffusivity of ions can be altered by ion-ion interactions in a way that preserved renewal-limited ( $D \propto \lambda$ ) behavior (see Figure 3). This result demonstrates

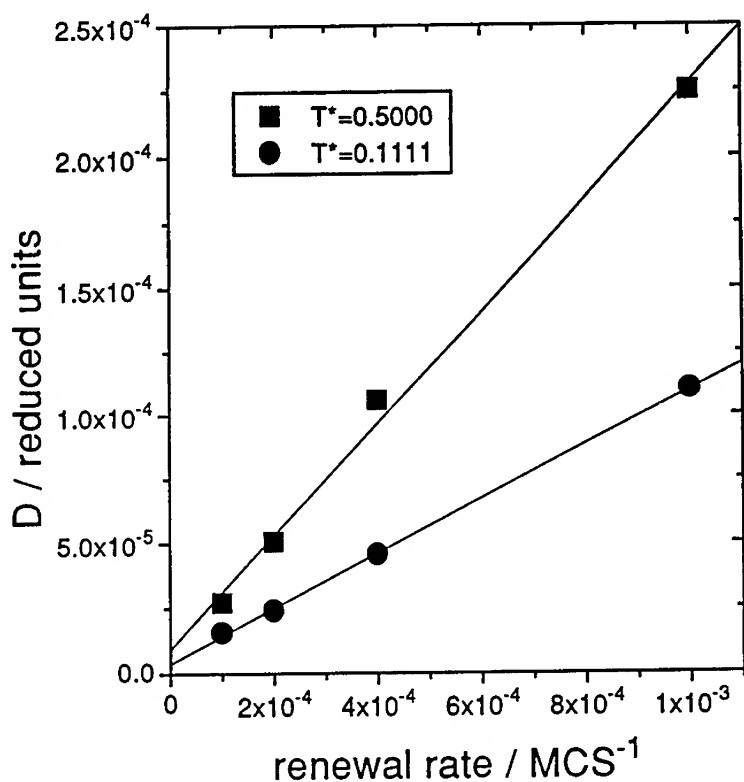


**Figure 3** - Diffusion coefficient as a function of renewal rate for Coulombically interacting particles diffusing on a renewing, percolative lattice at  $T^* = 0.5000$  and  $T^* = 0.1111$ . Here,  $T^* = k_B T / \epsilon_c$ , is a reduced temperature with  $\epsilon_c$  being the nearest neighbor Coulomb energy. In these simulations, increasing the dielectric constant of the media is equivalent to raising the temperature. Consequently, the two sets of data may be regarded as differing only in the strength of the Coulomb interactions between charge carriers with the host dynamics remaining constant. This graphic demonstrates that Coulomb interactions decrease the diffusion coefficient at any given value of the renewal rate, but that renewal-limited behavior ( $D \propto \lambda$ ) is still preserved. The implication of these results with regard to polymer electrolytes is that ion-ion interactions can alter the conductivity while preserving the VTF temperature dependence (a consequence of renewal-limited behavior).

that ion-ion interactions can alter the diffusivity of ions while preserving host controlled VTF behavior.

According to eq 6, the diffusivity of ions in the renewal-limited regime, the regime of physical relevance to polymer electrolytes since it recovers VTF behavior, depends only on  $g(\infty)$  and  $\tau_R$ . Various experiments have shown that ion-ion interactions can have order-of-magnitude effects on the equivalent conductivity ( $\sigma / n$ ).<sup>66</sup> These effects are separate from the large deviations caused by ion-polymer interactions that result in a shift in the glass transition temperature, the frequency of the GTR, and consequently  $\tau_R$ . In other words, order-of-magnitude variations in the equivalent conductivity are observed under conditions of essentially constant  $\tau_R$ . Within the DDH model, these variations can be explained either in terms of the  $g(\infty)$  term of eq 5 or the break down of the Nernst-Einstein equation relating the diffusivity to the conductivity. In polymer electrolytes, the Nernst-Einstein equation for independent particles has been shown to fail,<sup>67-73</sup> but it is unclear that the magnitude of the observed deviations are sufficient to explain completely the effects of ion-ion interactions on the conductivity. Since DDH is a diffusive model that does not directly address the failure of the Nernst-Einstein equation, we focus the relation between ion-ion interactions and diffusivity within the DDH model.

In the case where eq 7 characterizes each carrier individually, then  $g(\infty)$  also characterizes the local environment of each carrier. Recent simulations of Coulombically interacting ions diffusing on a renewing percolative lattice demonstrate that  $g(t)$  is more appropriately characterized by a double exponential,  $g_d(t)$ , rather than the single exponential eq 7 (see Figure 4):<sup>17,18,56</sup>

$$g_d(t) = g(\infty)[1 - C \exp(-\zeta_1 t) - (1 - C) \exp(-\zeta_2 t)] \quad 10$$

Physically, the two time-constant behavior may be described in terms of two classes of carriers: one that is strongly bound, say in a polymer solvated ion cluster, and relatively immobile, and one that is free. In the limit that the free carriers saturate their local environments on a time scale faster than renewal and the bound carriers do not ( $\zeta_2 \ll \lambda \ll \zeta_1$ ), eq 10 result in the following form for  $D$

$$D = \frac{Cg(\infty)}{6\tau_R} \quad 11$$

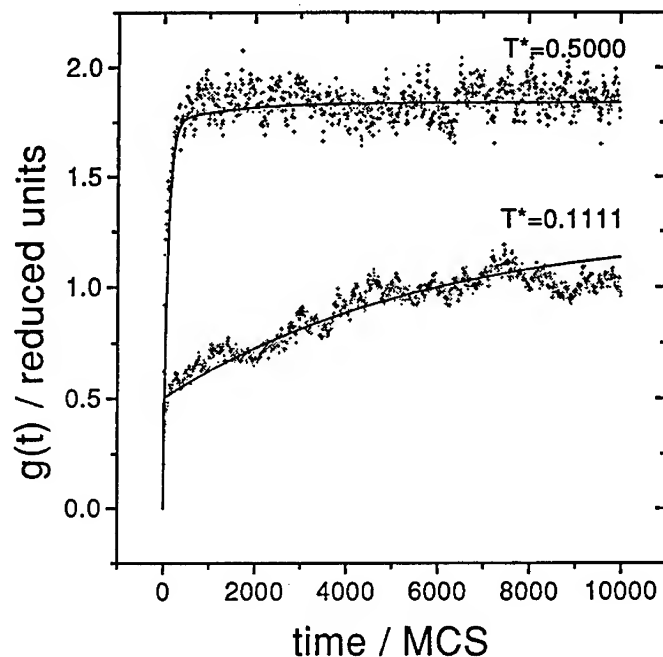


**Figure 4** - The average mean-squared displacement in the absence of renewal,  $g(t)$  for ions diffusing on the same percolative lattice as in Figure 3 at  $T^* = 0.5000$  and  $T^* = 0.1111$  ( $T^*$  is described in Figure 3). The lines represent fits of these data to the bi-exponential function eq 10. The parameters used for the fits are as follows with the value for  $T^* = 0.5000$  appearing first and the value for  $T^* = 0.1111$  appearing second (MCS = Monte Carlo steps per particle, the time unit of the simulations).  $g(\infty) = 1.8, 1.3$ ;  $C = 0.95; 0.4$ ;  $\zeta_1 = 0.011, 0.31 \text{ MCS}^{-1}$ ;  $\zeta_2 = 1.0 \times 10^{-4}, 1.7 \times 10^{-4} \text{ MCS}^{-1}$ . The presence of two processes may be interpreted in terms of two classes of carriers, quasi-free and bound (ion clustered), that are in thermal equilibrium. For the more weakly interacting system,  $T^* = 0.5000$ ,  $g(t)$  is well modeled by a single exponential ( $C = 0.95$ ) whereas the more strongly interacting system requires the bi-exponential form. This indicates that the majority of ions are free in the  $T^* = 0.5000$  system which is expected since  $k_B T$  approaches the nearest neighbor pairing energy. At  $T^* = 0.1111$ , however, only 40% of the carriers are free. Furthermore,  $g(\infty)$  is also reduced at the lower temperature. The combined effect of fewer free-carriers and smaller  $g(\infty)$  are responsible for the differences observed in Figure 3 while the separation in time scales between  $\zeta_1$  and  $\zeta_2$  preserves renewal-limited dynamics.

Eqs 6a and 11 are identical with the exception of the  $C$  coefficient in eq 11 that determines the fraction of free carriers.  $g(\infty)$  still characterizes the size of the local percolation cluster, but it cannot be directly extracted from  $D$  and  $\tau_R$  as described above. In the case where the motion of ions is described by eq 10, the value of  $g(\infty)$  calculated above according to eq 6 is an underestimate of the true  $g(\infty)$  since eq 6 assumes that each carrier fills its local percolation cluster faster than the time scale for renewal.

As with eq 6a, eq 11 is also renewal-limited in that  $D \propto 1 / \tau_R$ . Consequently, eq 11 preserves VTF behavior. In the case of eq 11, however, the diffusivity, and hence the conductivity, is reduced according to the number of free carriers. The double-exponential form of eq 10 also does not significantly alter the above form of the frequency dependent permittivity eq 9. The dielectric response is dominated by the free carriers, and it is only the free carriers that contribute to the IPR.

The double exponential-form of eq 10 and DDH theory allow for the effects of ion-ion interactions to be accounted for in a manner consistent with the phenomenology of polymer electrolytes and in a manner that does not rely solely on deviations from the Nernst-Einstein equation.

## VI. Remarks

Although many details of the ionic conductivity in polymer electrolytes remain beyond the scope of the simple dynamical percolation picture, still the dominant behavior of these materials can be very well characterized by this model.<sup>74</sup> This ionic conduction is due largely to the diffusion of quasi-free ions, whose effective concentration is determined by equilibration with clusters of various sizes (motion by larger clusters is insignificant). These ions diffuse freely only for very short distances, of the order of one Å. Longer diffusive motions, that determine the dc conductivity, require local segmental relaxation motion of the polymer; such motions are described by the VTF equation, so the conduction also follows this behavior.

These modeling studies show, in agreement with experiment, that the solvent relaxation and ionic diffusion processes are strongly coupled, and that one very effective way to increase conductivity is to increase segmental mobility - this is achieved by lowering  $T_g$ , and is responsible for the high conductivity of phosphazenes,<sup>79</sup> siloxanes<sup>80</sup> and a-PEO electrolytes.<sup>81</sup> Other mechanisms can also enhance the conduction - some of these (plasticisers<sup>82-85</sup>) can also be understood in



terms of increasing the renewal rate, while others (complexing agents<sup>86-89</sup>) increase the number of effectively free carriers. A third possibility, reducing the coupling between the ions and the host, is still largely unrealized, though the polymer-in-salt systems may be promising in this regard.<sup>90</sup>

### *Acknowledgments*

We are grateful to Roberto Olender, Stephen D. Druger and Austen Angell for helpful comments. This work has been generously supported by the ARO (Contract DAAL-03-09-G-0044), the NSF-MRC program through the Northwestern Materials Research Center (Award No. DMR-9120521), and the LBL-DOE (sub-contract # 4594110) program in advanced batteries.

### *Notes and References*

- 1) For a review of polymer electrolytes see ref 2-5.
- 2) MacCallum, J. R.; Vincent, C. A. *Polymer Electrolyte Reviews 1*; Elsevier: London, 1987.
- 3) Ratner, M. A.; Shriver, D. F. *Chem. Rev.* **1988**, *88*, 109-124.
- 4) MacCallum, J. R.; Vincent, C. A. *Polymer Electrolyte Reviews 2*; Elsevier: London, 1989.
- 5) Gray, F. M. *Solid Polymer Electrolytes*; VCH: New York, 1991.
- 6) Angell, C. A. *Solid State Ionics* **1983**, *9/10*, 3.
- 7) Angell, C. A. *Solid State Ionics* **1986**, *18 & 19*, 72-88.
- 8) Druger, S. D.; Nitzan, A.; Ratner, M. A. *J. Chem. Phys.* **1983**, *79*, 3133.
- 9) Druger, S. D.; Ratner, M. A.; Nitzan, A. *Solid State Ionics* **1983**, *9 & 10*, 1115-1120.
- 10) Druger, S. D.; Ratner, M. A.; Nitzan, A. *Phys. Rev. B* **1985**, *31*, 3939-3947.
- 11) Druger, S. D.; Ratner, M. A.; Nitzan, A. *Solid State Ionics* **1986**, *18&19*, 106-111.
- 12) Druger, S. D.; Ratner, M. A. *Phys. Rev. B* **1988**, *38*, 12589-12599.
- 13) Druger, S. D. *J. Chem. Phys.* **1991**, *95*, 2169-2177.
- 14) Druger, S. D. *J. Chem. Phys.* **1994**, *100*, 3979-3984.
- 15) Lonergan, M. C.; Nitzan, A.; Ratner, M. A. *J. Mol. Liq.* **1994**, *60*, 269-288.
- 16) Lonergan, M. C.; Nitzan, A.; Ratner, M. A.; Shriver, D. F. *J. Chem. Phys.*, *submitted*.
- 17) Lonergan, M. C. *Ion Transport in Polymer Electrolytes*; Ph.D. Thesis; Northwestern University, 1994

- 18) Lonergan, M. C.; Shriver, D. F.; Ratner, M. A. *Proceedings of the 4th Int. Symp. on Polymer Electrolytes, Electrochim. Acta* **1994**, in press.
- 19) Ratner, M. A.; Nitzan, A. *Discuss. Faraday Soc.* **1989**, *88*, 19-42.
- 20) Ratner, M. A.; Nitzan, A. *Solid State Ionics* **1988**, *28-30*, 3-33.
- 21) Nitzan, A.; Ratner, M. A. *J. Phys. Chem.* **1994**, *98*, 1765.
- 22) Granek, R.; Nitzan, A. *J. Chem. Phys.* **1989**, *90*, 3784.
- 23) Granek, R.; Nitzan, A.; Druger, S. D.; Ratner, M. A. *Solid State Ionics* **1988**, *28/30*, 120.
- 24) Vogel, H. *Phys. Z.* **1921**, *22*, 645.
- 25) Tammann, V. G.; Hesse, W. *Anorg. Allg. Chem.* **1926**, *156*, 245.
- 26) Fulcher, G. S. *J. Am. Ceram. Soc.* **1925**, *8*, 339.
- 27) Cohen, M. H.; Turnbull, D. *J. Chem. Phys.* **1959**, *31*, 1164-1169.
- 28) Cohen, M. H.; Grest, G. S. *Phys. Rev. B* **1980**, *B21*, 4113.
- 29) Gibbs, J. H.; DiMarzio, E. A. *J. Chem. Phys.* **1958**, *28*, 373-383.
- 30) Adam, G.; Gibbs, J. H. *J. Chem. Phys.* **1965**, *43*, 139.
- 31) Angell, C. A.; Sichina, W. *Ann. New York Acad. Sci.* **1976**, *279*, 53-67.
- 32) Recent Monte-Carlo and mean-field studies have shown that the segmental relaxation processes in the polymer host, that couple strongly and determine the renewal time, go over, in the limit of a small-molecule solvent, to the inertial relaxation time.<sup>33,34</sup> It is this latter time that is measured by time-dependent Stokes shift studies of chromophores in solution, and shows characteristic magnitudes of 100fsec or less<sup>35-37</sup>
- 33) Olender, R.; Nitzan, A. *J. Chem. Phys.* **1994**, *100*, 705-718.
- 34) Olender, R.; Nitzan, A. *J. Chem. Phys.* **1994**, *101*, 2338-2394.
- 35) Barbara, P. F.; Jarzeka, W. *Adv. Photochem.* **1990**, *15*, 1.
- 36) Kosower, E. M.; Huppert, D. *Annu. Rev. Phys. Chem.* **1986**, *37*, 127.
- 37) Maroncelli, M.; Fee, R. S.; Chapman, F.; Fleming, G. R. *J. Phys. Chem.* **1991**, *95*, 1012.
- 38) Wintersgill, M. C.; Fontanella, J. J. in *Polymer Electrolyte Reviews 2*; MacCallum, J. R. and Vincent, C. A., Ed.; Elsevier: London, 1989, pp 43-57.
- 39) Fontanella, J. J.; Wintersgill, M. C.; Calame, J. P.; Smith, M. K.; Andeen, C. G. *Solid State Ionics* **1986**, *18&19*, 253-257.
- 40) Tipton, A. L.; Lonergan, M. C.; Ratner, M. A.; Shriver, D. F.; Wong, T. T. Y.; Han, K. *J. Phys. Chem.* **1994**, *98*, 4148-4154.
- 41) With eq 7 for  $g(t)$ , the renewal limited regime corresponds to  $\zeta \gg \lambda$  in that eq 6 is recovered. In the case where  $\zeta \ll \lambda$ , however, eq 7 yields  $D = g(\infty)\zeta / 6$ . Hence, the parameter  $\zeta$  is related to the intrinsic particle mobility. Thereby,  $\zeta$  defines the

maximum diffusivity obtainable and is related to the so-called IR conductivity.<sup>7</sup> The limit  $\zeta \ll \lambda$  may be considered a decoupled regime where the diffusivity of particles does not depend on the dynamics of the media through which it diffuses. In contrast to decoupled, ionically conducting glasses<sup>7</sup> where host motion is very slow and the materials are presumably above their percolation thresholds for ion diffusion, eq 7 in the limit  $\zeta \ll \lambda$  characterizes a system below its static percolation threshold in the limit of very fast host renewal.

42) For a review of dielectric relaxation in high polymers see references 43-45.

43) McCrum, N. G.; Read, B. E.; Williams, G. *Anelastic and dielectric effects in polymeric solids*; John Wiley: London, 1967.

44) Ishida, Y. *J. Polym. Sci., Part A-2* **1969**, *7*, 1835-1861.

45) Jonscher, A. K. *Dielectric Relaxation in Solids*; Chelsea Dielectrics Press: London, 1983.

46) Fu, Y.; Pathmanathan, K.; Stevens, J. R. *J. Chem. Phys.* **1991**, *94*, 6323-6329.

47) Gray, F. M.; Vincent, C. A.; Kent, M. J. *Polym. Sci., Polym. Phys. Ed.* **1989**, *27*, 2011.

48) James, D. B.; Wetton, R. E.; Brown, D. S. *Polymer* **1979**, *20*, 187-195.

49) Torell, L. M.; Jacobsson, P.; Sidebottom, D.; Petersen, G. *Solid State Ionics* **1992**, *53-56*, 1037-1043.

50) Lemmon, J. P.; Kohnert, R. L.; Lerner, M. M. *Macromolecules* **1993**, *26*, 2767.

51) Havriliak, S.; Negami, S. *J. Polym. Sci., Part C* **1966**, *14*, 99-117.

52) Connor, T. M.; Read, B. E.; Williams, G. *J. Appl. Phys.* **1964**, *14*, 74-81.

53) Porter, C. H.; Boyd, R. H. *Macromolecules* **1971**, *4*, 589-594.

54) Yano, S.; Rahalkar, R. R.; Hunter, S. P.; Wang, C. H.; Boyd, R. H. *J. Polym. Sci., Polym. Phys. Ed.* **1976**, *14*, 1877-1890.

55) Technically, the dc conduction term only contributes to  $\Sigma''$ , and therefore, does not hamper the interrogation of  $\Sigma'$ . Dielectric measurements, however, are typically performed with ion-blocking electrodes. As a result, the mobility of ions gives rise to a space charge polarization that dominates the low frequency  $\Sigma'$ .

56) Lonergan, M. C.; Shriver, D. F.; Ratner, M. A., *manuscript in preparation*.

57) Papke, B. L.; Dupon, R.; Ratner, M. A.; Shriver, D. F. in *Fast Ionic Transport in Solids*; Bates, J. B. and Farrington, G. C., Ed.; North-Holland: Amsterdam, 1981, pp 685-688.

58) Dupon, R.; Papke, B. L.; Ratner, M. A.; Whitmore, D. H.; Shriver, D. F. *J. Am. Chem. Soc.* **1982**, *104*, 6247-6251.

59) Teeters, D.; Frech, R. *Solid State Ionics* **1986**, *18 & 19*, 271-276.

- 60) Schantz, S.; Sandahl, J.; Borjesson, L.; Torrel, L. M.; Stevens, J. R. *Solid State Ionics* **1988**, 28-30, 1047-1053.
- 61) Schantz, S.; Torell, L. M.; Stevens, J. R. *J. Appl. Phys.* **1988**, 64, 2038-2043.
- 62) Xu, W. Y.; Smid, J.; VanBeylen, M. *Solid State Ionics* **1992**, 57, 133-139.
- 63) MacCallum, J. R.; Tomlin, A. S.; Vincent, C. A. *Eur. Polym. J.* **1986**, 22, 787-791.
- 64) Gray, F. M. *Solid State Ionics* **1990**, 40/41, 637-640.
- 65) Gray, F. M. *J. Polym. Sci., Polym. Phys. Ed.* **1991**, 29, 1441-1445.
- 66) For a discussion of some of these effects see 18 and references therein.
- 67) Lonergan, M. C.; Perram, J. W.; Ratner, M. A.; Shriver, D. F. *J. Chem. Phys.* **1993**, 98, 4937.
- 68) Al-Mударis, A. A.; Chadwick, A. V. *Brit. Polym. J.* **1988**, 20, 213-217.
- 69) Bhattacharja, S.; Smoot, S. W.; Whitmore, D. H. *Solid State Ionics* **1986**, 18-19, 306-314.
- 70) Lindsey, S. E. Ph.D. Thesis; Northwestern University, 1989
- 71) Ward, I. M.; Boden, N.; Cruickshank, J.; Leng, S. E. *Proc. of the Fourth Int. Symp. on Polymer Electrolytes. Electrochim. Acta* **1994**, in press.
- 72) Boden, N.; Leng, S. A.; Ward, I. M. *Solid State Ionics* **1991**, 45, 261-270.
- 73) Vincent, C. A. *Proc. of the Fourth Int. Symp. on Polymer Electrolytes, Electrochim. Acta* **1994**, in press.
- 74) The aspects that go beyond the simple DDH scheme include clustering and its concentration dependence, ionic motion within clusters, effects of complexing agents and of multiply charged ions; several of these, notably those involving clustering, can be understood using molecular dynamics simulation,<sup>75-78</sup> and others, such as charge and chain lengths effects, can be well described by Monte-Carlo lattice models.<sup>33,34</sup>
- 75) Payne, V. A.; Forsyth, M.; Ratner, M. A.; Shriver, D. F.; deLeeuw, S. W. *J. Chem. Phys.* **1994**, 100, 5201-5210.
- 76) Mills, G. E.; Catlow, C. R. A. *J. Chem. Soc., Chem. Commun.* **1994**, 18, 2037-2039.
- 77) Neyertz, S.; Brown, D.; Thomas, J. O. *J. Chem. Phys.* in press.
- 78) Muller-Plathe, F. *Acta Polymer* **1994**, 45, 259.
- 79) Blonsky, P. M.; Shriver, D. F. *J. Am. Chem. Soc.* **1984**, 106, 6854-6855.
- 80) Smid, J.; Fish, D.; Khan, I. M.; Wu, E.; Zhou, G. *Advances in Chemistry Series* **1990**, 224, 113-124.
- 81) Craven, J. R.; Mobbs, R. H.; Booth, C. *Makrom. Chem. Rapid Commun.* **1986**, 7, 81.
- 82) Huq, R.; Koksang, R.; Tonder, P. E.; Farrington, G. C. *Electrochim. Acta* **1992**, 37, 1681-1684.
- 83) Munshi, M. Z. A.; Owens, B. B. *Solid State Ionics* **1988**, 26, 41.

- 
- 84) Cameron, G. G.; Ingram, M. D.; Sarmouk, K. *Polym. J.* **1990**, *26*, 1097-1101.
- 85) Sheldon, M. H.; Glasse, M. D.; Latham, R. J.; Linford, R. G. *Solid State Ionics* **1989**, *34*, 135-138.
- 86) Kaplan, M. L.; Rietman, E. A.; Cava, R. J.; Holt, L. K.; Chandross, E. A. *Solid State Ionics* **1987**, *25*, 37.
- 87) Chen, K.; Ganapathiappan, S.; Shriver, D. F. *Chem. Mater.* **1989**, *1*, 483.
- 88) Chen, K.; Shriver, D. F. *Chem. Mater.* **1991**, *3*.
- 89) Zhou, G.; Khan, I. M.; Smid, J. *Macromolecules* **1993**, *26*, 2202-2208.
- 90) Angell, C. A.; Liu, C.; Sanchez, E. *Nature* **1993**, *362*, 137-139.

## MASS TRANSPORT AND DC ELECTROMOTIVE FORCE INDUCED IN IONIC CRYSTALS BY HIGH-FREQUENCY ELECTRIC FIELD

K. I. RYBAKOV AND V. E. SEMENOV

Institute of Applied Physics, Russian Academy of Sciences  
46 Ulyanov St., Nizhny Novgorod 603600, Russia

### ABSTRACT

Results of the theoretical study of the effects produced on ionic crystals by high-frequency electric fields of moderate intensity are presented. The ponderomotive action of the electric field on the space charge induced by it in a thin layer within the crystal near its surface causes directional mass transport that leads to plastic deformation and induces a stationary distribution of electric potential. The analysis shows that the proposed effect (that appears to be equivalent to the action of mechanical stresses which exceed the electromagnetic pressure by many orders of magnitude) can influence the results of processing of ionic crystalline materials significantly.

According to numerous experiments, there is certain specificity in the course of mass transport processes in ionic crystalline materials when they experience action of high-frequency (HF) electromagnetic field even of very modest intensity. In particular, the apparent activation energy for diffusional transport in single crystals has been reported to lower by several tens of percents [1]. The kinetics of ceramics sintering and grain growth has been observed to be influenced drastically by the presence of microwave fields [2]. Finally, recent measurements have shown that high-frequency fields induce DC electric potentials and currents in ionic crystals [3].

These and similar experimental observations remained unexplained for a number of years. The main cause of theoretical difficulties was relative weakness of the electric field in all experiments. Many of the proposed ideas failed when the quantitative estimates were made. A successful attempt of explanation of these effects must show a mechanism of field action "amplification" to the extent necessary for influencing the mass transport processes in solid matter. Such mechanism based on the ponderomotive action of the HF field on the space charge induced by it near the crystal surface was proposed by us recently [4, 5]. It provided possibilities for quantitative explanation of microwave-enhanced mass transport phenomena in ionic crystals. In this paper, basic results of that model are reviewed and the formation of DC electric potentials in ionic crystals under high-frequency electric field exposure is explained.

As the subject of our theory, we consider a bounded ionic crystal with the vacancy mechanism of diffusion predominating [6]. In the presence of electric field, charged vacancies in the crystal participate in diffusional and drift currents, and the resulting flux of vacancies of each sort can be written as

$$\mathbf{J}_\alpha = -D_\alpha \nabla N_\alpha + D_\alpha N_\alpha \frac{e_\alpha}{kT} \mathbf{E}, \quad (1)$$

where  $D_\alpha$  is diffusivity,  $N_\alpha$  is concentration,  $e_\alpha$  is the electric charge of vacancies of sort  $\alpha$ , and  $\mathbf{E}$  is the vector of electric field (here the Nernst-Einstein relation was used to express the vacancy mobility).

The effects of plastic deformation of the crystal and of DC potential formation can be deduced from the quasistationary picture of vacancy flows which can be obtained by solving Fick's equations

$$\frac{\partial N_\alpha}{\partial t} + (\nabla \cdot \mathbf{J}_\alpha) = 0 \quad (2)$$

together with quasistatic Maxwell's equations (provided that the dimensions of the crystal are small compared with the electromagnetic wavelength)

$$\begin{aligned} \nabla \times \mathbf{E} &= 0, \\ \nabla \cdot \mathbf{E} &= \frac{4\pi}{\omega} \sum e_\alpha N_\alpha, \end{aligned} \quad (3)$$

Here  $\mathbf{E} = \mathcal{E} - \nabla\varphi$ ,  $\mathcal{E}$  is the HF field vector,  $\varphi$  is the slowly varying charge separation field potential,  $\omega$  is vacancy volume, summation is over the sorts of particles, and the lattice dielectric constant is assumed equal to unity for simplicity. We shall restrict our consideration to a crystal having two sorts of vacancies with the charges  $e_\alpha = \pm e$  and with the same equilibrium concentrations  $N_0$ . In this case, the following boundary conditions for Fick's equation can be written meaning that vacancy concentration at the crystal surface is equal to its equilibrium value,

$$\sum N_\alpha|_S = 2N_0, \quad (4)$$

and that there is no electric current through the surface,

$$\mathbf{n} \cdot \sum e_\alpha \mathbf{J}_\alpha|_S = 0 \quad (5)$$

(here  $\mathbf{n}$  is the outward unit normal to the surface). For Maxwell's equations, the boundary conditions at the crystal surface should correspond to continuity of the normal and tangential components of electric field, and the intensity of external field  $E_0$  should be specified.

Eqs. (1)-(3) can be solved by the perturbation method developed in [4]. The oscillating vacancy concentration perturbations  $\nu_\alpha$  and the HF electric field  $\mathcal{E}$  can be obtained from the first-order equations. Assuming that the diffusivities of vacancies of two sorts are proportional, i.e., the ratio  $D_+/D_-$  is constant throughout the crystal, we can link  $\nu_\alpha$  with the density of HF electric charge  $\rho = \sum e_\alpha \nu_\alpha / \omega$ :

$$\nu_\alpha = D_\alpha \rho \omega / e_\alpha \sum D_\beta. \quad (6)$$

If the scale length of inhomogeneity of diffusional properties of the crystal is much larger than the smaller of the Debye-Huckel radius  $\lambda = \sqrt{\omega kT / 8\pi e^2 N_0}$  and the characteristic diffusion length  $l = \sqrt{D/\Omega}$  ( $\Omega$  is the frequency of the applied electric field), then the diffusion parts of HF vacancy fluxes can be neglected, and  $\rho$  and  $\mathcal{E}$  can be obtained by solving Eqs.(1)-(3) in given geometry using standard methods of electrodymanics [7]. The complex dielectric permittivity  $\epsilon$  of the ionic crystal can be introduced in our approximation as

$$\epsilon = 1 + i4\pi G / \Omega, \quad (7)$$

where  $G = N_0 e^2 \sum D_\alpha / \omega k T$  is the ionic conductivity of crystal.

Inhomogeneity of diffusional properties of the crystal can be connected with the so-called amorphized layer that usually exists at the crystal surface. The vacancy diffusivity in such layers is known to exceed the bulk values by several orders of magnitude [8]. In this paper, we will assume that the vacancy diffusivity (and the imaginary part of  $\epsilon$ ) is inhomogeneous only in the near-surface layer whose thickness  $a$  is much smaller than the characteristic dimensions of the crystal. The analysis of the electrodynamic problem shows that if  $a \gg \lambda, l$  then the electric charge induced by the field is localized within this layer. In particular, for a spheric crystal of radius  $R$  ( $a \ll R$ ) the following solution of the quasielectrostatic problem can be obtained [5]:

$$\begin{aligned} \mathcal{E}_r &= \frac{3E_0 \cos \theta}{\tilde{\epsilon}(R) + 2} \cdot \frac{\tilde{\epsilon}(r)}{\epsilon(r)}; \quad \mathcal{E}_\theta = -\frac{3E_0 \sin \theta}{\tilde{\epsilon}(R) + 2}; \\ \rho &= \frac{1}{4\pi} \frac{3E_0 \cos \theta}{\tilde{\epsilon}(R) + 2} \left\{ \tilde{\epsilon}(r) \frac{\partial}{\partial r} \left[ \frac{1}{\epsilon(r)} \right] + \tilde{\epsilon}(R) \left[ 1 - \frac{1}{\epsilon(R)} \right] \delta(r - R) \right\} \end{aligned} \quad (8)$$

where  $\tilde{\epsilon}(r) = \epsilon_0 + (2/R) \int_{R-a}^r (\epsilon - \epsilon_0) dr$ ,  $\epsilon_0$  is the dielectric permittivity (7) in the bulk, and the integration starts from the inner boundary of the amorphized layer.

To obtain the quasistationary vacancy flows and DC potential distribution, it is necessary to solve Eqs.(1)-(3) in the second order of the perturbation theory. Eqs.(1)-(2) acquire the following form:

$$\begin{aligned} \nabla \cdot \mathbf{j}_\alpha &= 0, \\ \mathbf{j}_\alpha &= \frac{D_\alpha N_0}{kT} \left( -\nabla \mu_\alpha + \frac{e_\alpha}{N_0} \langle \nu_\alpha \mathcal{E} \rangle \right), \end{aligned} \quad (9)$$

where  $\mathbf{j}_\alpha \equiv \langle \mathbf{J}_\alpha \rangle$  is the quasistationary flux,  $\mu_\alpha = kT \eta_\alpha / N_0 + e_\alpha \varphi$  is the chemical potential,  $\eta_\alpha$  is the quasistationary perturbation of concentration of vacancies of sort  $\alpha$ , and the angular brackets  $\langle \rangle$  denote averaging over the period of HF field. As for the field equations (3), they can be written in the form of Poisson's equation

$$\Delta \varphi - \frac{1}{\lambda^2} \varphi = -\frac{4\pi N_0}{\omega k T} \sum e_\alpha \mu_\alpha. \quad (10)$$

The boundary conditions (4)-(5) rewrite as

$$\begin{aligned} \sum \mu_\alpha|_S &= 0; \\ \mathbf{n} \cdot \sum e_\alpha \mathbf{j}_\alpha|_S &= 0, \end{aligned} \quad (11)$$

and the boundary conditions for Poisson's equation remain standard electrostatic.

The quasistationary vacancy fluxes and chemical potentials that can be obtained by solving Eqs.(9) determine the velocity of plastic deformation at the surface of the crystal

$$\mathbf{V} = -\mathbf{n} \cdot (\mathbf{n} \cdot \sum \mathbf{j}_\alpha|_S) \quad (12)$$

and the distribution of the electric potential according to Eq.(10).



Solving Eqs.(9) can be facilitated by the following considerations. As follows from the above, the source term  $\langle \nu_\alpha \mathcal{E} \rangle$  in Eqs.(9) is localized within the thin amorphized layer. Therefore within this layer the equations can be integrated in one-dimensional geometry. At the same time, in the bulk the equations are uniform, and their solutions in the spheric geometry can be obtained easily. It can be shown that the action of the normal (to the surface) component of the electric field cannot lead to effects of sufficient strength [5] and therefore can be neglected, which also contributes to simplification of the solving procedure. In the spheric geometry we can then rewrite Eqs.(9) and the boundary conditions (11) as

$$\frac{\partial}{\partial r} \left( D_\alpha \frac{\partial}{\partial r} \mu_\alpha \right) = \frac{e_\alpha}{N_0} \frac{D_\alpha}{R \sin \theta} \frac{\partial}{\partial \theta} (\sin \theta \langle \nu_\alpha \mathcal{E}_\theta \rangle); \quad (13)$$

$$\sum \mu_\alpha|_R = 0; \quad \sum e_\alpha D_\alpha \frac{\partial}{\partial r} \mu_\alpha|_R = 0.$$

Integrating Eqs.(13) and using the relations (6) and (12), we obtain the velocity of plastic deformation under the ponderomotive action of the electromagnetic field:

$$V = \frac{\omega}{kT} \frac{2 \Pi D_\alpha}{(\sum D_\alpha)^2} \frac{1}{R \sin \theta} \int_{R-a}^R \sum D_\alpha \frac{\partial}{\partial \theta} (\sin \theta \langle \rho \mathcal{E}_\theta \rangle) dr. \quad (14)$$

Localization of the space charge within the amorphized layer leads to the fact that the value of the integral in Eq.(14) is determined by the diffusivity in the amorphized layer, i.e.,

$$V \simeq \frac{D_a}{R} \frac{\omega}{kT} \int_{R-a}^R \langle \rho \mathcal{E}_\theta \rangle dr, \quad (15)$$

where  $D_a$  is the characteristic value of the diffusivity in the amorphized layer (for this estimate we assumed that the diffusivities of vacancies of two sorts are not very different). It should be noted that  $\int_{R-a}^R \langle \rho \mathcal{E}_\theta \rangle dr$  can be interpreted as the pressure of the tangential component of the electric field. Let us compare this result with the velocity of deformation of the same crystal under the action of mechanical pressure  $p$ . This velocity can be estimated [9] as

$$V_m \simeq \left( D_0 + D_a \frac{a}{R} \right) \frac{N_0 p \omega}{R kT}, \quad (16)$$

where  $D_0$  is the characteristic value of the bulk diffusivity. We can see that the ponderomotive action of the electric field leads to the same deformation velocity as does mechanical pressure that is

$$[N_0(D_0/D_a + a/R)]^{-1} \quad (17)$$

times greater than the field pressure. This result shows that there can exist "amplification" of the field action, and the factor of this amplification reaches highly significant values. The presence of the factor  $N_0^{-1}$  in Eq.(17) can be understood easily if we realize that the electric field acts on the charged vacancies, i.e., directly on the atoms

neighbouring an empty node of the lattice – the only atoms that are able to move – whereas the mechanical pressure is applied to the whole crystal in which most of the atoms are fixed. As the equilibrium vacancy concentration  $N_0$  is a thermally-activated quantity, the observed reduction of the activation energy of diffusional transport [1] can be associated with this effect. The second factor of amplification in Eq.(17) is associated with the fact that under ponderomotive action of the tangential component of the field the vacancies are driven within the amorphized layer where their mobility is much higher than in the bulk.

In our opinion, one of the best ways to experimentally test this theory may lie in measuring DC electromotive forces and/or electric currents in external circuits [3] that are generated under the ponderomotive action of the field if the diffusivities of vacancies of two sorts are not equal. DC potentials originate due to cumulation of the electric charges of vacancies that are not compensated in the case of different diffusivities. The quasistationary distribution of DC potential can be obtained by solving Eq.(10). However, we can note that the condition  $\lambda \ll a$  that is assumed in this paper to be fulfilled means that the vacancy plasma is quasineutral, i.e.,

$$\varphi \approx \sum e_a \mu_a / 2e^2 \quad (18)$$

(this is equivalent to neglecting  $\Delta\varphi$  in Eq.(10)). Using the solution of Eqs.(13), we obtain:

$$\varphi|_R = \frac{\omega}{2eN_0 \sin \theta} \int_{R-a}^R (D_- - D_+) \frac{\partial}{\partial \theta} (\sin \theta \langle \rho \mathcal{E}_\theta \rangle) dr / \left( \sum D_{a0} + \frac{3}{R} \int_{R-a}^R \sum D_a dr \right), \quad (19)$$

where  $D_{a0}$  are the bulk diffusivities. The reasoning similar to that used when obtaining the estimate (15) leads to the following estimate for the maximal potential difference  $\delta\varphi$  on the crystal surface:

$$\delta\varphi \simeq [N_0(D_0/D_a + a/R)]^{-1} \omega \int_{R-a}^R \langle \rho \mathcal{E}_\theta \rangle dr / e. \quad (20)$$

As the diffusivities  $D_+$  and  $D_-$  are considered proportional, the results (14) and (19) contain integrals of the same type:

$$\frac{1}{\sin \theta} \int_{R-a}^R D_a \frac{\partial}{\partial \theta} (\sin \theta \langle \rho \mathcal{E}_\theta \rangle) dr.$$

Calculation of this integral with the use of the values of  $\rho$  and  $\mathcal{E}_\theta$  from Eqs.(8) gives

$$D_{aR} \frac{E_0^2}{8\pi} \frac{9(3 \cos^2 \theta - 1)}{|\tilde{\epsilon}(R) + 2|^2} \left[ \frac{\arctan \epsilon_R''}{\epsilon_R''} - 1 - \frac{\arctan \epsilon_0''}{\epsilon_R''} + \frac{\epsilon_0''}{\epsilon_R''} \left( 1 + \frac{1}{2} \ln \frac{1 + \epsilon_R''^2}{1 + \epsilon_0''^2} \right) \right], \quad (21)$$

where  $\epsilon_0'' \equiv \text{Im } \epsilon_0$  and  $\epsilon_R'' \equiv \text{Im } \epsilon(R)$  are the imaginary parts of the dielectric permittivity in the bulk and at the outer boundary of the amorphized layer, respectively, and  $D_{aR}$  are vacancy diffusivities at the outer boundary of the amorphized layer. This result allows to reveal the frequency dependence of the described effects. As follows from

Eq.(21), the effects vanish at high frequencies, when  $\Omega$  becomes much greater than  $4\pi G_R$ . At such high frequencies the HF field is not perturbed by the crystal, including its amorphized layer, and no electric charge is induced. In the low-frequency limit the effects disappear when  $\Omega \ll \max(4\pi G_0, 4\pi G_R a/R)$  because of the decrease in the tangential component of the electric field.

The quantitative estimates of the described ponderomotive effects require knowledge of experimental data on the thickness of the amorphized layer and on the vacancy diffusivity in it. These data vary greatly from one experiment to another, but for ionic crystals with dimensions in the micrometer range and higher it may be taken with sufficient reliability that  $D_0/D_a + a/R \leq 10^{-3}$  [8]. The equilibrium vacancy concentration  $N_0$  at temperatures still far enough from the melting point can be as high as  $10^{-5}$  [9]. Hence, if the frequency is within the above specified limits, the action of the electric field  $E_0 \simeq 1$  kV/cm (that can be considered as a typical value for technological systems of RF and microwave processing (see, e.g., [10])) whose own pressure is of order of 0.1 Pa can become equivalent to the action of mechanical stresses of  $10^7$  Pa. This opens prospects for electromagnetic control of mass transport in ionic crystalline materials which can have diverse applications in processing technologies.

## References

- [1] M.A.Janney and H.D.Kimrey, Mater. Res. Soc. Proc., **189**, 215 (1991).
- [2] R.W.Bruce, Mater. Res. Soc. Proc., **124**, 3 (1988).
- [3] S. Freeman, J. Booske, R. Cooper, and B. Meng, Mater. Res. Soc. Proc. **347**, 479 (1994)
- [4] K.I.Rybakov and V.E.Semenov, *Phys.Rev.B*, **49**, 64 (1994).
- [5] K.I.Rybakov and V.E.Semenov, *Plastic deformation of an ionic crystal due to ponderomotive action of high-frequency electric field*, preprint No. 357, Institute of Applied Physics, Nizhny Novgorod, Russia, 1994. To be published in *Phys. Rev. Lett.*
- [6] J.P.Stark, *Solid State Diffusion* (Wiley, New York, 1976).
- [7] L.D.Landau, E.M.Lifshits, and L.P.Pitaevskii, *Electrodynamics of Continuous Media*, 2nd ed. (Pergamon, New York, 1984).
- [8] I.Kaur, W.Gust, *Fundamentals of Grain and Interphase Boundary Diffusion* (Zieger Press, Stuttgart, 1989).
- [9] J.E.Geguzin, *Physics of Sintering* (in Russian) (Nauka, Moscow, 1984).
- [10] Y.V.Bykov, A.G.Eremeev, V.V.Holoptsev, Mater. Res. Soc. Proc. **347** (1994)

---

---

## PART IV

---

### Defect Chemistry

## APPLICATION OF DEFECT MODELING TO MATERIALS DESIGN

MARLENE A. SPEARS AND H.L. TULLER

Crystal Physics and Electroceramics Laboratory, Department of Materials Science and Engineering, Massachusetts Institute of Technology, Cambridge, MA 02139, U.S.A.

### ABSTRACT

Defect chemical models have been found to be useful in establishing defect generation and transport mechanisms, extracting thermodynamic data and deconvoluting contributions to the total electrical conductivity. In most cases, however, the utility of the approach has been limited due to the imposed simplifications made to make the analysis more tractable, e.g. the simplified neutrality relation and the elimination of defect associates. In this work, we treat more complex equilibria with the aid of numerical methods and illustrate how this approach can be used, not only to extract key thermodynamic and kinetic data, but also to assist in the design and optimization of materials. Some specific examples with application to solid state ionics will be used to illustrate this approach.

### INTRODUCTION

Defects in non-metallic systems often play a predominant role in controlling the electrical, optical, and mass transport properties of solids. The simplest of these, point defects, can be categorized into three groups, i.e. electronic, lattice, and impurity defects. We begin by describing these groups and their likely impact on properties. We briefly review how we treat the often complex interaction of these defects, in terms of defect chemical models, to gain insight into the mechanisms defining defect generation and transport. We conclude by illustrating the use of numerical methods, which allow for the treatment of more complex equilibria, to assist in the design and optimization of materials.

As is customary in describing semiconductors and insulators, electrons and holes, refer to the population of electronic states in the conduction and valence bands which are occupied and empty respectively. The density and mobility of these carriers obviously determine the electronic conductivity of these materials. Likewise the thermal and optical generation of electron-hole pairs across the band gap determine the intrinsic temperature dependence of the electronic conductivity and the wavelength dependence of photoconductivity and optical absorptivity.

The simplest lattice defects include vacancies and interstitials. Such defects are essential for providing diffusion pathways for the ions. The self-diffusivity of a given ion depends on the density of corresponding defects. Further, since the ions are charged, they also contribute to the ionic conductivity. In solid electrolytes, this form of conduction predominates over electronic conduction.

All materials contain impurities at some levels. Of particular import are those which have a net electrical charge relative to the ideal crystal. This results in the generation of electronic and/or ionic defects with opposite net charges to maintain overall charge neutrality. Impurities, like

lattice defects, often lead to the creation of energy levels in the band gap of the host crystal. These levels lead to extrinsic sources of absorption and emission, so important in, for example, high power ruby and Nd: YAG lasers. Deep levels, as is well known in conventional semiconductors, e.g. Au:Si, also play an essential role in the generation-recombination statistics which control the operation of devices driven away from equilibrium.

## DEFECT EQUILIBRIA

Obviously defects cannot be treated in isolation. The ionization of a neutral impurity leads to the formation of electronic and charged impurity defects. The reduction of an oxide by a gaseous reducing species, for example, leads to the generation of lattice (e.g. oxygen vacancies) and electronic (e.g. electrons) defects. We commonly treat such processes in the form of quasi chemical reactions. Table 1 summarizes the reactions

REACTION	EQUILIBRIUM
<b>Intrinsic</b>	
$O_o + V_o \rightleftharpoons V_o^+ + O_i^-$	$[V_o^+][O_i^-] = K_i = K_i^0 \exp\left(-\frac{E_i}{kT}\right)$
$V_o^{++} + e' \rightleftharpoons V_o^+$	$\frac{[V_o^+]}{[V_o^{++}] \cdot n} = K_{-1} = \frac{1}{N_c} \exp\left(-\frac{E_{-1}}{kT}\right)$
$O_i^- \rightleftharpoons O_i + e'$	$\frac{[O_i^-] \cdot n}{[O_i]} = K_{-2} = N_c \exp\left(-\frac{E_{-2} - E_f}{kT}\right)$
$\emptyset \rightleftharpoons e' + h'$	$np = K_{-3} = N_c N_v \exp\left(-\frac{E_g}{kT}\right)$
<b>Reduction</b>	
$O_o \rightleftharpoons \frac{1}{2} O_2(g) + V_o^+ + 2e'$	$p_{O_2}^{1/2} [V_o^+] n^2 = K_r = K_r^0 \exp\left(-\frac{E_r}{kT}\right)$
<b>Donor and Acceptor Deionization</b>	
$D' + e' \rightleftharpoons D^0$	$\frac{[D^0]}{[D'] \cdot n} = K_{d1} = \frac{1}{N_c} \exp\left(\frac{E_{d1}}{kT}\right)$
$A' \rightleftharpoons A^0 + e'$	$\frac{[A^0] \cdot n}{[A']} = K_{a1} = N_c \exp\left(\frac{E_{a1} - E_f}{kT}\right)$
<b>Donor and Acceptor Association</b>	
$D' + O_i^- \rightleftharpoons [D' \cdot O_i^-]$	$\frac{[D' \cdot O_i^-]}{[D'] \cdot [O_i^-]} = K_{a2} = \frac{n_0^2}{2} \exp\left(\frac{E_{a2}}{kT}\right)$
$A' + V_o^{++} \rightleftharpoons [A' \cdot V_o^{++}]$	$\frac{[A' \cdot V_o^{++}]}{[A'] \cdot [V_o^{++}]} = K_{a3} = \frac{3n_0^2}{8} \exp\left(\frac{E_{a3}}{kT}\right)$

Table 1. Defect reactions and mass action relations for an oxide with intrinsic frenkel disorder on the oxygen sublattice

relevant to an oxide whose intrinsic ionic disorder is controlled by frenkel equilibria on the oxygen sublattice. Also included are the vacancy and interstitial ionization, intrinsic electron-hole, gaseous reduction, donor and acceptor ionization, and donor and acceptor-lattice defect association reactions as well as the corresponding mass action equations. Charge neutrality must also be conserved as specified in the following equation:

$$\begin{aligned}
& 2 [O_i'] + [O_i'] + n + [A'] + [(D^\bullet \cdot O_i'')] \\
& = 2[V_O''] + [V_O'] + p + [D^\bullet] + [(A'V_O'')] \quad (1)
\end{aligned}$$

This neutrality relation which contains ten variables, combined with the nine relations in Table 1 can, in principle, be combined to solve for the ten unknowns. Using the above expressions one, for example, arrives at an eighth-order polynomial in  $n$  which cannot be solved analytically.

While such equations may be solved numerically, this approach, to which we return below, is rarely exercised. More commonly workers in the field revert to the Brouwer approximation [1] in which conditions (e.g.  $T$ ,  $P_{O_2}$ , dopants) are selected such that only one term predominates on either side of the neutrality relation. This allows a piecemeal solution of the overall problem often adequate for gaining insight into the predominant defect process i.e. nature, concentration and ionization state of the majority charged carriers or absorbing centers.

Kröger and Vink [2] further popularized the defect diagram in which the logarithm of defect density is plotted versus the logarithm of the partial pressure or activity of a key constituent of the solid, e.g.  $P_M$  or  $P_{O_2}$  for a metal oxide  $M_xO_y$ . The defect diagram is an important tool for visualization of the key defect regimes as set forth by the Brouwer approximation.

To illustrate the approach we select a simplified set of defect reactions with only four distinct defect species, i.e.

$$\text{Frenkel Disorder:} \quad [V_O''] [O_i'] = K_f \quad (2)$$

$$\text{Electronic Disorder} \quad n p = K_e \quad (3)$$

$$\text{Reduction} \quad [V_O''] n^2 P_{O_2}^{1/2} = K_r \quad (4)$$

$$\text{Electroneutrality} \quad 2[V_O''] + p = 2[O_i'] + n \quad (5)$$

We have simplified the equilibria described in Table 1 by assuming that contributions from impurities and singly ionized oxygen defect species can be ignored. If one further assumes that frenkel disorder is greater than electronic disorder i.e.  $K_f \gg K_e$ , then, near stoichiometry, Eq. 5 can be simplified to

$$[V_O''] = [O_i'] = K_f^{1/2} \quad (6)$$

which when substituted into Eqs. 3 and 4 provide the following expressions for  $n$  and  $p$ .

$$n = K_f^{1/4} K_r^{1/2} P_{O_2}^{1/4} \quad (7)$$

$$p = K_f^{1/4} K_r^{-1/2} K_e P_{O_2}^{1/4} \quad (8)$$

At sufficiently high and low  $P_{O_2}$ , simplified electroneutrality expressions given by  $p = 2[O_i']$  and  $n = 2[V_O'']$  apply respectively and it can be shown readily that  $p$  and  $[O_i']$  follow  $P_{O_2}^{1/6}$  and  $n$  and  $[V_O'']$  follow  $P_{O_2}^{-1/6}$  dependencies under those circumstances. These results, illustrated

schematically in Fig. (1), show the three defect regimes and the unrealistic sharp transition from one defect regime to the next. Also typical of such diagrams is the use of non-specific values for ordinate and abscissa resulting from inadequate knowledge of equilibrium constants.

An alternative diagram, with only the central region differing, is obtained if  $K_e$  is assumed to be much greater than  $K_f$  such that the neutrality relation becomes  $n = p$  with the consequence that  $[O_i'] \propto P_{O_2}^{1/2}$  and  $[V_O''] \propto P_{O_2}^{-1/2}$ . The measured power laws followed by specific defects can therefore be used as a means for distinguishing between different defect models.

#### The $Gd_2(Zr_xTi_{1-x})_2O_7$ System - An Example

As a practical illustration of the above approach, we refer to our studies on the  $Gd_2(Zr_xTi_{1-x})_2O_7$  (GZT) and related pyrochlore systems. Here, we found evidence for increasing disorder on the oxygen sublattice with increasing values of  $x$ . [4-7] This is evidenced, for example, as a 4-order of magnitude increase in the oxygen ion conductivity at 600C as  $x$  increases from 0 to 0.8. [7] The total conductivity of materials in this system are expected to follow the expression:

$$\begin{aligned}\sigma_{total} &= 2[V_O''] e\mu_i + nq\mu_e + pq\mu_h \\ &= \sigma_i^0 \exp(-E_i/kT) \\ &+ \sigma_A^0 \exp(-E_A/kT)P_{O_2}^{-1/4} \\ &+ \sigma_B^0 \exp(-E_B/kT)P_{O_2}^{+1/4}\end{aligned}\quad (9)$$

as follows from Eqs. (6-8) and the definition of electrical conductivity. The key feature to note is the different  $P_{O_2}$ -dependence exhibited by each of the three components (the mobility of  $O_i'$  was found to be much smaller than that of  $V_O''$  and was therefore ignored.[4]) A plot of the total conductivity of GZT with  $x=0.3$  is shown in Fig. (2) The data show  $\sigma$  to decrease with increasing  $P_{O_2}$  at low  $P_{O_2}$  followed successively by a  $P_{O_2}$ -insensitive regime at intermediate  $P_{O_2}$  and an increasing conductivity at high  $P_{O_2}$ . Fitting an expression of the form of Eq. (9) to the data (see solid curves through data points) shows that the data can indeed be deconvoluted at each isotherm into a  $\sigma_n \propto P_{O_2}^{-1/4}$ , a  $\sigma_{ion} \propto P_{O_2}^0$  and a  $\sigma_p \propto P_{O_2}^{+1/4}$  term consistent with predictions of Fig. (1) for the middle defect region.

A similar plot of  $\log \sigma$  vs.  $\log P_{O_2}$  for GZT with  $x=0.6$  is shown in Fig. (3). Note that the increase in  $x$  and corresponding increase in ionic disorder has resulted in the predominance of the  $P_{O_2}$ -independent ionic region for all temperatures below 1200C. From a practical standpoint, the increase in  $x$  resulted in the transformation of GZT from a mixed ionic-electronic conductor ( $x=0.3$ ) to a predominantly ionic conductor ( $x=0.6$ ) commonly referred to as a solid electrolyte.



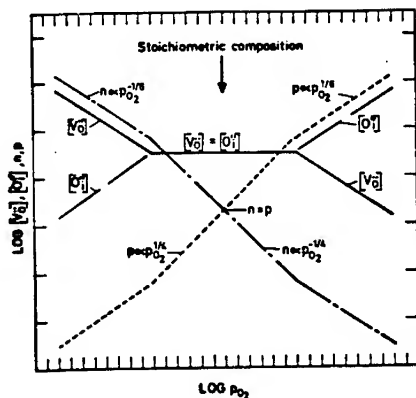


Fig. 1. Defect diagram showing the  $\text{Po}_2$ -dependence of the ionic and electronic defects in the three key defect regimes described in the text (from Kofstad[3]).

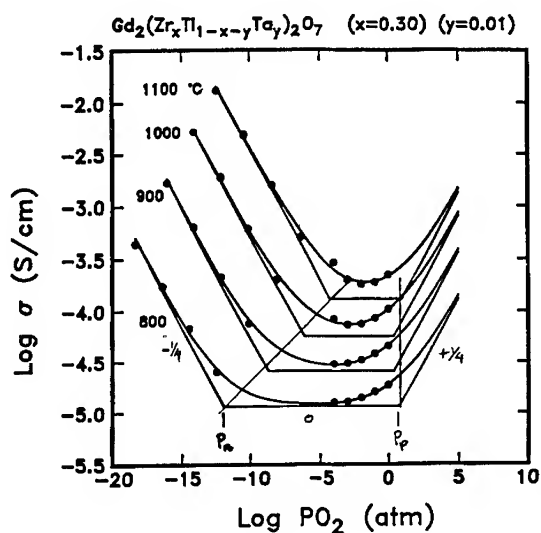


Fig. 2 The  $\text{Po}_2$  dependence of the conductivity of  $\text{Gd}_2(\text{Zr}_{0.3}\text{Ti}_{0.69}\text{Ta}_{0.01})_2\text{O}_7$  is shown for temperatures of 800-1000°C. The straight line segments correspond to the designated components  $\sigma_n$ ,  $\sigma_{\text{ion}}$ ,  $\sigma_p$  of the total conductivity which are represented by the smooth curves fit through the data points. Also shown are the electrolytic domain boundaries designated by  $P_n$  and  $P_p$  (from Ref. [22]).

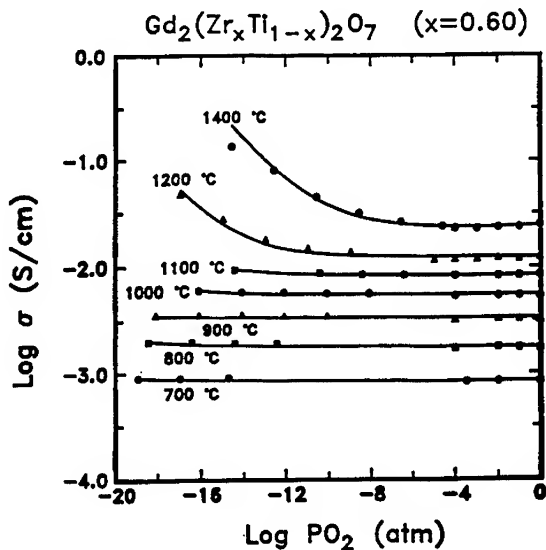


Fig. 3: Similar data as in Fig. (2) for the system  $\text{Gd}_2(\text{Zr}_{0.6}\text{Ti}_{0.4})_2\text{O}_7$ . (from Ref. [7]).

Practical application of solid electrolytes depends not only on the magnitude of ionic conductivity, which one obviously desires to be as high as possible, but also on the range of conditions over which it remains predominantly ionic. Referring back to Fig. (2), we have designated the  $\text{PO}_2$ 's at which the n and p conductivities become equal to the ionic conductivity by  $P_n$  and  $P_p$ , respectively. This region, bounded by  $P_n$  and  $P_p$ , is commonly referred to as the electrolytic domain. For GZT ( $x=0.3$ ) as well as for other solid electrolytes such as stabilized zirconia, the domain size shrinks with increasing temperature due to the more highly activated nature of the electronic conductivities. Comparing the data in Fig. (2) and (3), it is obvious that the electrolytic domain broadens dramatically as  $x$  increases from  $x=0.3$  to  $0.6$ . At  $1200^\circ\text{C}$ , for example,  $P_n$  has shifted from  $\sim 10^{-2}$  atm for  $x=0.3$  to  $\sim 10^{-16}$  atm for  $x=0.6$ . Indeed, after experimentally deriving the parameters of Eq. (9), it becomes a simple task [9] to predict the locations of  $P_n$  and  $P_p$  for any temperature of interest.

Following a similar approach, i.e. fitting experimental data to the defect model, values for  $K_f$ ,  $K_e$ ,  $K_r$ , as well as carrier mobilities were obtained for a number of compositions  $x$  in GZT. These are summarized in Table (2) for  $x=0$  and  $x=0.3$  and will be used later when we describe more complex equilibria.

#### The $\text{Ba}_{0.03}\text{Sr}_{0.97}\text{TiO}_3$ System-An Example:

The  $\text{BaTiO}_3$ - $\text{SrTiO}_3$  (BST) solid solution system represents another example where correlation of a defect model and experimental data can lead

a.

Mass action product	Defect relationship	Gd <sub>2</sub> Ti <sub>2</sub> O <sub>7</sub> value	Gd <sub>2</sub> (Zr <sub>0.3</sub> Ti <sub>0.7</sub> ) <sub>2</sub> O <sub>7</sub> value
K <sub>v</sub>	$[V_O^{\bullet}] \cdot n^2 \cdot p_{O_2}^{1/2}$	$5.1 \times 10^{68} \cdot \exp(-6.34/kT)$	$4.2 \times 10^{71} \cdot \exp(-6/kT)$
K <sub>i</sub>	$[V_O^{\bullet}] \cdot [O_i^{\bullet}]$	$10^{90} \cdot \exp(-5.25/kT)$	$10^{98} \cdot \exp(-0.24/kT)$
K <sub>n</sub>	$n \cdot p$	$2.53 \times 10^{45} \cdot \exp(-3.48/kT)$	$3.1 \times 10^{44} \cdot \exp(-3.9/kT)$

b.

Mass action product	Defect relationship	Parametric Form	Simulation Value
K <sub>v1</sub>	$\frac{[V_O^{\bullet}]}{[V_O^{\bullet}] \cdot n}$	$N_C^{-1} \cdot \exp(E_{v1}/kT)$	$6.59 \times 10^{-23} \cdot \exp(0.002/kT)$
K <sub>i1</sub>	$\frac{[O_i^{\bullet}] \cdot n}{[O_i^{\bullet}]}$	$N_C \cdot \exp((E_{i1} - E_F)/kT)$	$1.52 \times 10^{22} \cdot \exp(-3.479/kT)$
K <sub>d1</sub>	$\frac{[D^{\bullet}]}{[D^{\bullet}] \cdot n}$	$N_C^{-1} \cdot \exp(E_{d1}/kT)$	$6.59 \times 10^{-23} \cdot \exp(1.25/kT)$
K <sub>o1</sub>	$\frac{[D^{\bullet} \cdot O_i^{\bullet}]}{[D^{\bullet}] \cdot [O_i^{\bullet}]}$	$\frac{1}{2} a_s^1 \cdot \exp(E_{o1}/kT)$	$5.27 \times 10^{-22} \cdot \exp(0.95/kT)$
K <sub>d2</sub>	$\frac{[A^{\bullet}] \cdot n}{[A^{\bullet}]}$	$N_C \cdot \exp((E_{d2} - E_F)/kT)$	$1.52 \times 10^{22} \cdot \exp(-1.9/kT)$
K <sub>o2</sub>	$\frac{[A^{\bullet} \cdot V_O^{\bullet}]}{[A^{\bullet}] \cdot [V_O^{\bullet}]}$	$\frac{3}{8} a_s^2 \cdot \exp(E_{o2}/kT)$	$3.96 \times 10^{-22} \cdot \exp(0.95/kT)$

Table 2: Point defect formation parameters used to simulate defect concentrations (from Spears [8]). a) Values obtained for Gd<sub>2</sub>Ti<sub>2</sub>O<sub>7</sub> and Gd<sub>2</sub>(Zr<sub>0.3</sub>Ti<sub>0.7</sub>)<sub>2</sub>O<sub>7</sub> by fitting defect model to data; b) Parameters for Gd<sub>2</sub>Ti<sub>2</sub>O<sub>7</sub> estimated from a variety of sources.

to confirmation of the model and extraction of key thermodynamic defect parameters. It also represents a system with importance in applications as dielectrics, piezoelectrics and gas sensors, to name a few, and it is thus of interest to understand these systems as well as possible. Further, as we illustrate again below, knowledge of the defect equilibria can be used to predict performance under conditions not examined explicitly.

Unlike the GZT system, the BST system does not exhibit significant intrinsic ionic disorder. Under these circumstances, ionic defects form largely in response to aliovalent impurities either intentionally or non-intentionally added to the material during processing. Unintentional acceptor impurities commonly control the defect equilibria in these systems. As a consequence, the simplified neutrality relation at high and intermediate Po<sub>2</sub>, which commonly applies, (see Eq. (1)) is given by [10]

$$[A^{\bullet}] = 2[V_O^{\bullet}] \quad (10)$$

which like the previous case for GZT, results in a  $P_{O_2}$ -independent ionic conductivity. considering that Eqs. (3) and (4) still apply, the total conductivity is again expected to take the form of Eq. (9).

At low  $P_{O_2}$ , as in Fig. (1), one expects the defect equilibria to be controlled by the reduction process while, at sufficiently high  $P_{O_2}$ , acceptor compensation occurs by holes rather than by vacancies. In Table (3), we summarize the appropriate electroneutrality relations and expressions for the key charge carriers for the different defect regimes.

Region	Electroneutrality condition	$P_{O_2}$ range	Concentrations of key charge carriers
I	(5) $n = 2[V_O^{\bullet}]$	Low	(6) $n = (2K_s)^{1/2} P_{O_2}^{-1/6}$
II	(7) $2[V_O^{\bullet}] = [I']$	Intermediate	(8) $n = (2K_s/[I'])^{1/2} P_{O_2}^{-1/4}$ (9) $p = ([I']K_{ox}/2)^{1/2} P_{O_2}^{1/4}$
III	(10) $p = [I']$	High	$P_{O_2}$ , independent

Table 3: Electroneutrality conditions and concentrations of key charge carriers in each region for the case of acceptor doping as in  $(Ba_xSr_{1-x})TiO_3$  (from Choi and Tuller[10])

Examination of Fig. (4) which shows the  $P_{O_2}$ -dependence of the total conductivity measured for  $Ba_{0.03}Sr_{0.97}TiO_3$ [10] reveals that, except for the lowest  $P_{O_2}$ 's above 900C, the data follow a transition from a  $P_{O_2}^{-1/4}$  to a  $P_{O_2}^{+1/4}$  dependence as the  $P_{O_2}$  is increased as predicted for region II in Table (3). This implies that  $2[V_O^{\bullet}] = [A'] \gg n, p$ . No ionic conduction is, however, observed due to the fact that the minority electrons and holes possess mobilities far in excess of that of the oxygen vacancies unlike the situation in GZT. In the upper left hand quadrant of Fig. (4),  $\sigma$  begins to follow a  $P_{O_2}^{-1/6}$  dependence as predicted for region I in Table (3).

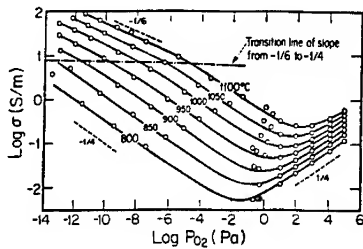


Fig. 4:  $P_{O_2}$ -dependent electrical conductivity of  $Ba_{0.03}Sr_{0.97}TiO_3$ . Circles are experimental data; curves are calculated values based on the defect model (from Choi and Tuller[10])

Fitting these electrical conductivity and corresponding thermoelectric power data to the defect model, enabled many of the key thermodynamic and kinetic parameters to be extracted.[10] These are listed in Table (4). Note that the acceptor density was determined to be  $\sim 100$ ppm.

With such parameters in hand, it becomes possible to predict the temperature and  $P_{O_2}$ 's for which each of the defect regimes will hold. This

Constant	Calculated values
$E_s^\circ$	$314 \pm 5 \text{ kJ/mol}$
$\beta$	$0.0482 \text{ kJ/(mol} \cdot \text{K)}$
$\Delta H_R$	$500 \pm 17 \text{ kJ/mol}$
$\Delta H_{Ox}$	$125 \pm 2 \text{ kJ/mol}$
$\mu_e$	$2.3 \times 10^{-5} \text{ m}^2/(\text{V} \cdot \text{s}) (T = 950^\circ\text{C})$
$\mu_h$	$10^{-5} \text{ m}^2/(\text{V} \cdot \text{s}) (T = 950^\circ\text{C})$
$K_R$	$(1.52 \pm 0.17) \times 10^{87} \text{ Pa}^{1/2} \cdot \text{m}^{-9}$
$K'_{Ox}$	$(2.45 \pm 0.18) \times 10^{25} \text{ Pa}^{-1/2} \cdot \text{m}^{-3}$
$[I']$	$(1.85 \pm 0.19) \times 10^{24} \text{ m}^{-3}$
	$= (1.15 \pm 0.12) \times 10^{-4} / \text{Ti} = 115 \pm 12 \text{ ppm of Ti}$
$K'_i$	$(7.67 \pm 0.57) \times 10^{34} \text{ m}^{-6}$

Table 4: Constants derived from experimental data for single-crystalline  $\text{Ba}_{0.03}\text{Sr}_{0.97}\text{TiO}_3$  (from Choi and Tuller[10])

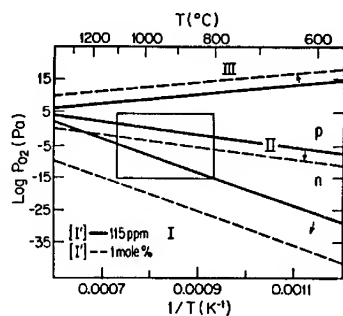


Fig. 5: Boundaries delineating different defect regimes of  $\text{Ba}_{0.03}\text{Sr}_{0.97}\text{TiO}_3$  for acceptor densities of 115ppm and 1 mol%. Rectangular box represents limits of experimental measurements (from Choi and Tuller[10]).

is illustrated in Fig. (5) with the acceptor dopant as a parameter. Higher values of  $[I'] \equiv [A']$  broaden region II at the expense of regions I and III. Note further that the position of the II-III boundary can be predicted even though no data in the vicinity of this boundary was obtained.

### COMPLEX DEFECT EQUILIBRIA

While the simplified approach for analyzing the defect equilibria is, at times, satisfactory in evaluating experimental data and extracting useful constants as illustrated above, it is often inadequate in dealing with systems in which many types of defect species, including associates or clusters, are important. Further, the Brouwer approximation cannot, under such circumstances, be applied, since a number of defect species of like charge may remain of comparable concentration over extended  $\text{P}_{\text{O}_2}$  ranges. Then, the simple  $\text{P}_{\text{O}_2}$  power laws will no longer apply. Rather, one finds curves with continuously changing slopes as the ratios of the defect concentrations in the neutrality relation change.

To overcome the limitations of the simple model, we have solved numerically, by the Newton-Raphson method,[8] the high order polynomials which come about during attempts to solve the simultaneous defect equations utilizing the complete electroneutrality equation (see Eq. (1)) as discussed above. Using constants derived and/or estimated for the GZT system (Tables 2a and b) we show a defect diagram in Fig. 6 appropriate for an acceptor doped GZT specimen characterized by strong oxygen vacancy-acceptor association. The vertical dashed lines indicate the boundaries of the various defect regimes based on the Brouwer approximation. Note that deviations from the linear curves occur over five or more orders of magnitude in  $P_{O_2}$  in the vicinity of these so-called boundaries. In the case of the defect regime centered at  $\sim \log P_{O_2} = -40$  the regime is sufficiently narrow so that no single slope is characteristic of this regime.

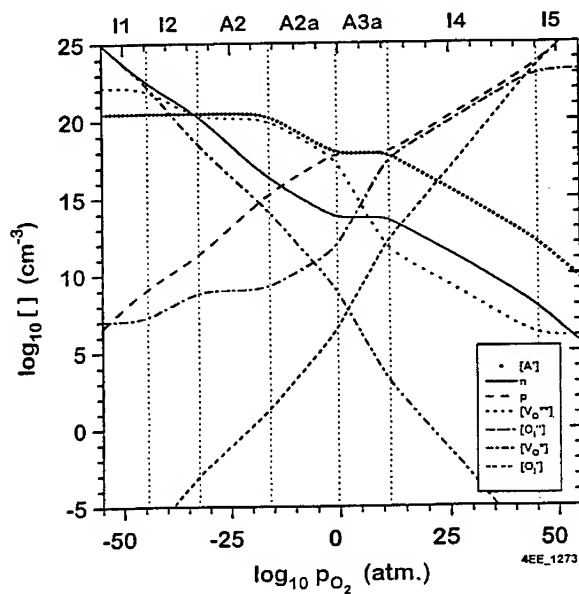


Fig. 6: Defect diagram for acceptor doped  $Gd_2Ti_2O_7$  with strong acceptor-oxygen vacancy association. For  $T=1273K$ ,  $[A']=0.02$  (from Spears [8]).

#### Mixed Conduction in $Gd_2(Zr_{0.3}Ti_{0.7})_2O_7$ : An Example

In the following, we illustrate the utility of the above approach in optimizing the desired properties of materials such as GZT. We begin by calculating the density of the four most mobile charge carriers in  $Gd_2(Zr_{0.3}Ti_{0.7})_2O_7$  since these will ultimately determine the conductivity under any specified conditions. The defect densities are plotted in Fig. (7)

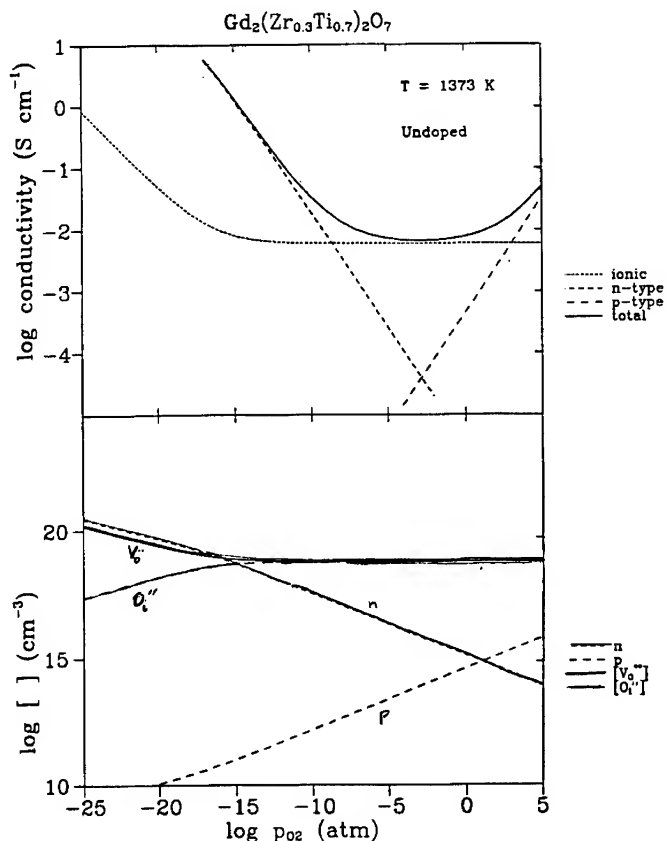


Fig. 7: The calculated  $P_{O_2}$ -dependencies at 1373 K of the predominant defect concentrations and their partial conductivities in undoped  $Gd_2(Zr_{0.3}Ti_{0.7})_2O_7$ . The solid curve in the upper diagram represents the total conductivity (from Ref. [7]).

for a temperature of 1373K and a  $P_{O_2}$  range of interest for sensor or fuel cell applications (a somewhat broader range is included to present the imminent transitions to other defect or conduction regimes). A transition from ionic disorder,  $[V_O''] = [O_i'']$  at high  $P_{O_2}$  to reduction control,  $n = 2[V_O'']$  occurs at  $\sim P_{O_2} = 10^{-15}$  atm. Note also the n-p transition at  $P_{O_2} \approx 10$  atm.

Since we have expressions for the carrier mobilities, [8], it is possible to calculate the ionic, n- and p-type partial conductivities as also illustrated in Fig. (7). Here, the electrolytic domain ranges from  $P_n \approx 10^{-9}$  atm to  $P_p \approx 10^3$  atm with an ionic conductivity of somewhat below  $10^{-2}$  S/cm.

One can now ask if this intrinsically disordered oxygen conductor could benefit further from addition of acceptor dopants. Fig. (8) shows the corresponding defect diagram for GZT,  $x=0.3$  doped with an acceptor at a

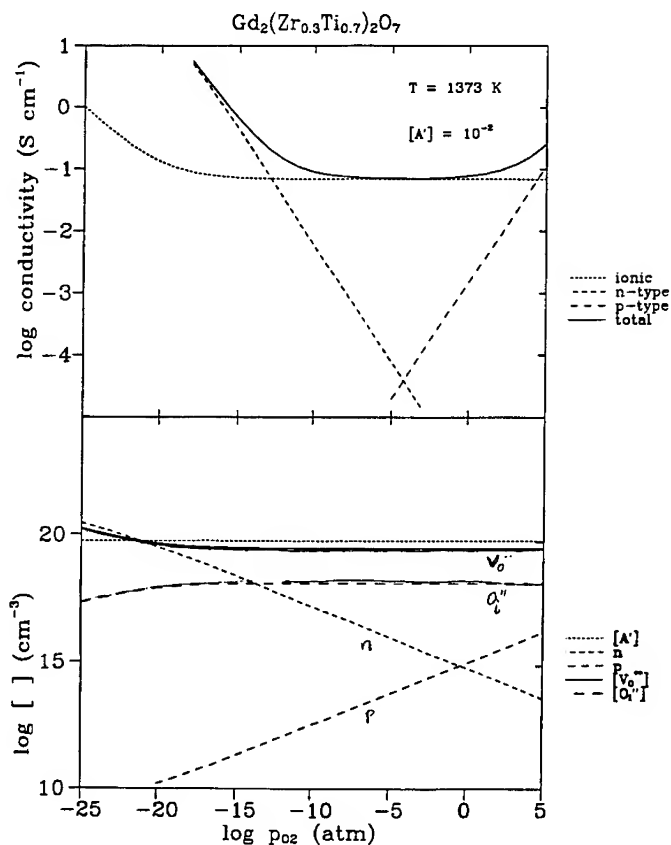


Fig. 8: As in Fig. (7) but with acceptor doping  $[A']$  with 1 atomic percent substitution on the Gd site (from Ref. [7]).

level of 1% substitution for Gd. As expected, the oxygen vacancy density is enhanced at the expense of the oxygen interstitial density (see Eq. (2)). Likewise the p-type conduction is increased at the expense of the n-type conduction. Note also the narrowing of the defect regime defined by  $n = 2[V_{\text{O}}^{\bullet}]$ .

The corresponding calculated conductivity data also shown in Fig. (8). The ionic conductivity has increased by about an order of magnitude while the electrolytic domain has broadened dramatically with  $P_{\text{N}} \approx 10^{-13}$  atm and  $P_{\text{P}} \approx 10^4$  atm making this a far better potential electrolyte. These features have been largely confirmed by doping experiments completed recently on both GZT with  $x=0$ [11] and  $x=0.3$ [4].

Similar calculations were performed on donor doped GZT ( $x=0.3$ ) with the reverse effect, i.e. a resultant decrease in ionic conduction, an increase in n-type conduction and a shrinking of the electrolytic domain to below



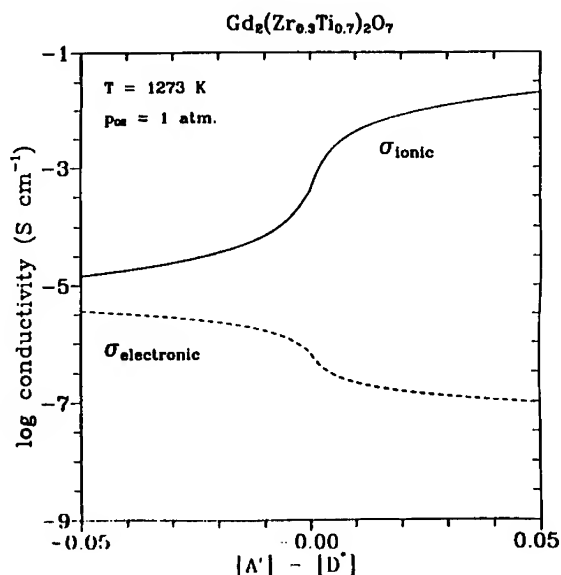


Fig. 9: Calculated ionic and electronic conductivities for the material of Fig. (7) obtained for  $T = 1273\text{K}$  and  $P_{\text{O}_2} = 1 \text{ atm}$  as a function of net acceptor fraction. Negative values of  $[\text{A}'] - [\text{D}^\bullet]$  correspond to net excess donor fraction (from Ref. [7]).

that found in undoped GZT,  $x=0.3$ . In Fig. (9), we plot the calculated ionic and electronic conductivities for this material as a function of net acceptor (+) or net donor (-) density for  $T = 1273 \text{ K}$  and  $P_{\text{O}_2} = 1 \text{ atm}$ . Under these conditions, the results show that it is possible to modify the  $\sigma_{\text{ionic}}/\sigma_{\text{electronic}}$  ratio from  $\approx 10^5$  for acceptor doped material to  $\approx 5$  for donor doped material. If we consider that  $\sigma_{\text{electronic}}$  would increase by a factor of  $\sim 10^4$  at  $P_{\text{O}_2} = 10^{-20} \text{ atm}$  (the  $P_{\text{O}_2}^{-1/4}$  dependence does not extend all the way down to  $P_{\text{O}_2}^{-20} \text{ atm}$ ) then the  $\sigma_{\text{ionic}}/\sigma_{\text{electronic}}$  ratio will drop even further to  $< 10^{-3}$ .

The above results show that it is possible to manipulate this material by control of dopant and  $P_{\text{O}_2}$  in such a way so as to achieve high and predominantly ionic conductivity at one extreme and predominantly electronic conductivity at the other extreme with any degree of mixed conduction at intermediate conditions. We are presently using this versatility to design compatible electrolytes and electrodes for solid oxide fuel cell (SOFC) applications.[12]

#### Ce<sub>1-x</sub>Gd<sub>x</sub>O<sub>2</sub> Solid Electrolytes: An Example

For cost and stability reasons, one would like to lower the operating temperatures of SOFC from above  $900^\circ\text{C}$  to below  $800^\circ\text{C}$ . [13] This is difficult with stabilized zirconia due to its rapidly decreasing ionic conductivity with

decreasing temperature.[14] Doped CeO<sub>2</sub> has long been known to possess a higher ionic conductivity at reduced temperatures [15,16] but has not been seriously considered as an alternative to zirconia due to its tendency to reduce at low P<sub>O2</sub>. In terms of our above discussion, doped ceria would require a more extended electrolytic domain, i.e. a reduced P<sub>N</sub>, to be of interest as the solid electrolyte in an SOFC.

Based on an expectation of one of the authors (HLT) that a variable valent element such as Pr<sup>3,4+</sup>, in the band gap of CeO<sub>2</sub>, might serve to trap excess electrons formed during reduction, experiments were performed which confirmed the efficacy of Pr (1 mol %) in extending the electrolytic domain of Ce<sub>0.8</sub>Gd<sub>0.2</sub>O<sub>2-y</sub> by approximately two orders of magnitude.[17]

To ascertain if this indeed would be expected based on defect chemical models we calculated the density of the four key defects at 973 K and 1273K for Ce<sub>0.98</sub>Gd<sub>0.02</sub>O<sub>2-y</sub> and Ce<sub>0.96</sub>Gd<sub>0.02</sub>Pr<sub>0.02</sub>O<sub>2-y</sub>. Since we do not know the position of the Pr level in the gap, we used this level as a parameter and made calculations assuming E<sub>Pr</sub> values of 1,2,3 and 4 eV below the conduction band. The other appropriate constants were obtained from the literature.[18] A representative plot for the case of E<sub>Pr</sub> = E<sub>C</sub>-2eV where E<sub>C</sub> is the conduction band edge is shown in Fig. (10). The figure does indeed show that the Pr<sup>4+</sup> level "soaks up" electrons due to reduction but that this process is complete at very high P<sub>O2</sub>'s. By the time one reaches P<sub>N</sub>, all the Pr is already in the trivalent state and should be equivalent to doubling the fixed valent Gd<sup>3+</sup> content.

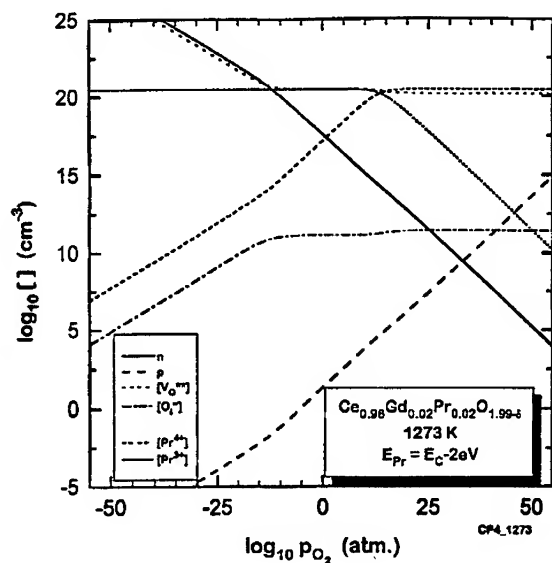


Fig .10: Calculated defect densities as a function of Po<sub>2</sub> for Ce<sub>0.96</sub>Gd<sub>0.02</sub>Pr<sub>0.02</sub>O<sub>1.99-d</sub> for T = 1273K and E<sub>Pr</sub> = E<sub>C</sub>-2eV.

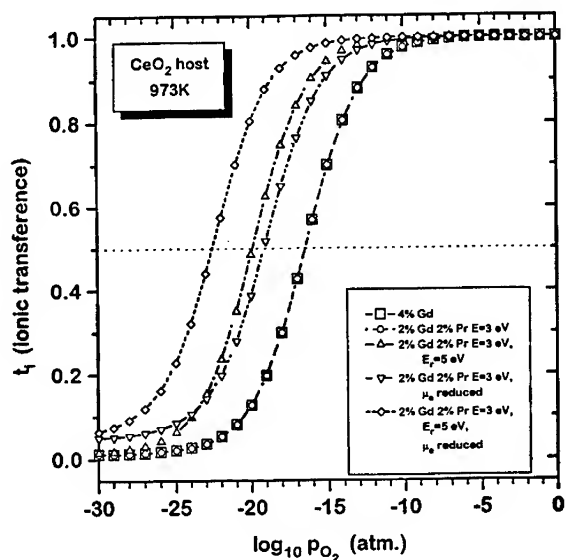


Fig. 11: Calculated ionic transference number  $t_i$  at  $T=973K$  as a fraction of  $P_{O_2}$  for  $CeO_2$  substituted with specified levels of Gd and Pr (see text for details).

This expectation is confirmed in Fig. (11) in which the calculated ionic transference number  $t_i = \frac{\sigma_{ionic}}{\sigma_{total}}$  is shown plotted as a function of  $P_{O_2}$  at 973K. Indeed, no difference is observed for  $CeO_2$  doped with 2% Gd + 2%Pr or 4% Gd. The question then arises why the experimental data confirmed praseodymium's ability to extend the electrolytic domain? A number of other possibilities were examined. First considered was an increase in the reduction energy  $E_r$  (see e.g. Eq. (4)) from the reported 4.7 eV in undoped  $CeO_2$  to 5.0eV. As shown in Fig. (11), this results in a shift of  $P_n$  of ~4 orders of magnitude to lower  $P_{O_2}$ . A similar effect is achieved if the mobility of electrons is reduced by a factor of ~3. If both were to occur simultaneously due to the Pr addition, the effect is roughly additive, as illustrated in Fig. (11). The determination of the actual source of the experimentally observed shift in  $P_n$  deserves further study.

The above results point to an obvious limitation of the dilute solution approximation in which defect interactions are ignored and all parameters are viewed as independent of defect concentration. Obviously, equilibrium constants do not remain constant when dopants or cation substitutions reach the percent or even fractions of a percent level.

Two features of our approach however, extend the utility of defect modeling to higher defect concentrations. First, defect associates and clusters can be incorporated into the models. Second, as illustrated above for solid solutions in which the thermodynamic or kinetic parameters vary

in some systematic manner, numerical estimates of the implications of these changes can be readily made.

## SUMMARY

A number of defect controlled properties, with the emphasis on ionic and electronic conduction in oxides, were reviewed. We have had good success in recent years in extending our understanding of the correlation between defect and optical properties as well.[19-21]

The traditional means for constructing defect chemical models and visualizing them via defect diagrams was outlined. The successful application of this approach for evaluating the key defects and their dependence on T,  $P_{O_2}$ , and dopant density was illustrated with examples representing intrinsically disordered pyrochlores  $Gd_2(Zr_xTi_{1-x})_2O_7$  and acceptor doped perovskites  $(Ba_xSr_{1-x})TiO_3$ .

The possibility of treating considerably more complex defect models numerically allowed for detailed analysis of mixed ionic-electronic conduction in  $Gd_2(Zr_{0.3}Ti_{0.7})_2O_7$ . We were able to show that it is possible to control the magnitude of the ionic transference number by nearly eight orders of magnitude by control of dopant type and density and  $P_{O_2}$ . This points to the possible design of compatible electrodes and electrolytes for SOFC and other solid state electrochemical devices.

The efficacy of extending the electrolytic domain at low  $P_{O_2}$  in ceria-gadolinia solid electrolytes by the addition of variable valent praseodymium was also examined in this manner. No change was predicted, in contrast to experimental evidence. We were able to demonstrate that relatively small increases in the reduction energy and/or reductions in the electron mobility could easily account for the experimental observations.

The ability to accommodate defect associates and clusters and to make numerical estimates of defect densities and corresponding physical properties significantly extends the utility of defect modeling to higher defect concentrations and, more importantly, for enabling the prediction and optimization of the performance of new materials.

## ACKNOWLEDGEMENTS

The authors thank the Basic Energy Sciences, Department of Energy under Contract # DE FG02 86ER45261 for support of this work. This paper is based, in part, on the dissertation submitted by M.A. Spears for the Doctoral degree at MIT, January 1995. Discussions with B.C.H. Steele and M. Kleitz stimulated the modeling of the  $Ce_{1-x}Gd_xPr_yO_2$  system.

## REFERENCES

1. G. Brouwer, Philips Res. Rep. **9**, 366 (1954)
2. F.A. Kröger and H.J. Vink, Solid State Physics **3**, 310 (1956).
3. P. Kofstand, *Nonstoichiometry, Diffusion and Electrical Conductivity in Binary Oxides*, (Wiley, NY, 1972), pg 40.

4. P.K. Moon and H.L. Tuller, *Sol. St. Ionics* **28-30**, 470-74 (1988).
5. P.K. Moon and H.L. Tuller, *Solid St. Ionics*, edited by G. Nazri, R.A. Huggins, and D.F. Shriver, (MRS Symp. Proc. Vol. **135**, Pittsburgh, PA, 1989), pp. 149-163.
6. H.L. Tuller, S. Kramer, and M.A. Spears, *High Temperature Electrochemical Behaviour of Fast Ion and Mixed Conductors*, editors F.W. Poulsen, J.J. Bentzen, T. Jacobsen, E. Skou and M.J.L. Ostergard, (Riso National Laboratory, Roskilde, Denmark, 1993), p151-73.
7. H.L. Tuller, *Solid State Ionics* **52**, 135-146 (1992).
8. M.A. Spears, PhD thesis, Massachusetts Institute of Technology, 1995.
9. S. Kramer, M. Spears, and H.L. Tuller, *Proceedings of the Third Intl. Symp. on Solid Oxide Fuel Cells*, editors S.C. Singhal and H. Iwahara, (The Electrochemical Society, Proc. Vol. **93-4**, Pennington, NJ, 1993), pgs. 119-128.
10. G.M. Choi and H.L. Tuller, *J. Am. Ceram. Soc.* **71**, 201 (1988).
11. S. Kramer, M. Spears, and H.L. Tuller, *Solid State Ionics* **72**, 59-66 (1994).
12. H.L. Tuller, S. Kramer, and M. Spears, U.S. Patent, Notice of Allowance received.
13. C. Milliken, S. Elangavan, and A.C. Khandkar, *Ionic and Mixed Conducting Ceramics*, editors. R.A. Ramanarayan, W.L. Worrell, and H.L. Tuller, (The Electrochem. Soc., Proc. Vol. **94-12**, Pennington, NJ, 1994), p. 466.
14. H.L. Tuller and P.K. Moon, *Mat. Sc. Eng.* **B1**, 171-91 (1988).
15. H. L. Tuller and A. S. Nowick, *J. Electrochem. Soc.* **122**, 255-259 (1975).
16. T. Kudo and H. Obayashi, *J. Electrochem. Soc.* **123**, 415 (1976).
17. H.L. Tuller, D.L. Maricle, and T.E. Swarr, "U.S. Patent No. 5,001,021, March 19, 1991.
18. H. L. Tuller, *Non-Stoichiometric Oxides*, ed. O.T. Sorensen, Academic Press, NY (1981), pp. 271-335.
19. S.R. Rotman, R.P. Tandon, and H.L. Tuller, *J. Appl. Phys.* **57**, 1951-55 (1985).

20. S.R. Rotman and H.L. Tuller, J. Appl. Phys. **62**, (1987) pp. 1305-1312.
21. S.R. Rotman, M. Roth, H.L. Tuller, and C. Warde, J. Appl. Phys. **66**, 1366-1369 (1989).
22. P.K. Moon, Ph.D. thesis, Massachusetts Institute of Technology, 1988.

## POINT DEFECTS AND PROTONIC CONDUCTION IN $A_3B'B''_2O_9$ COMPOUNDS

YANG DU AND A.S. NOWICK  
Materials Science, Columbia University, New York, NY 10027

### ABSTRACT

We have investigated the defect structure and protonic transport properties of nonstoichiometric complex perovskite-type compounds of the type  $A_3B'_{1-x}Nb_{2-x}O_{9.5}$  where A and B' are both divalent ions. Protons are incorporated by treatment in  $H_2O$  vapor and their presence is manifested by the appearance of an OH band in the IR spectra, as well as by the large increase in electrical conductivity to produce excellent protonic conductors, with lower activation energies. A non-classical isotope effect, in which the Arrhenius plots for  $D^+$  and  $H^+$  cross over, can be explained by a modification of the classical ART hopping theory.

### I. INTRODUCTION

The high temperature proton conductors (HTPCs) have drawn considerable interest in the last decade for their application in fuel cells, steam electrolyzers and other solid state electrochemical devices. Much attention has been paid to the  $ACeO_3$  perovskites,[1-5] particularly the  $M^{3+}$  (rare earth)-doped  $SrCeO_3$  and  $BaCeO_3$  because of their excellent proton conductivity of  $\sim 0.001 (\Omega \cdot cm)^{-1}$  at  $600^\circ C$ .

However, Ce-based perovskites suffer a degraded electrolytic quality upon exposure to severe atmosphere, e.g. they show considerable hole conduction under oxidizing gases[6] and are readily decomposed into  $ACO_3$  and  $CeO_2$  in  $CO_2$ -containing atmosphere.[7] The search for alternative compounds in  $A^{2+}B^{4+}O_3$  appears not very successful. For instance,  $SrZrO_3$  has been studied for its improved electrolytic stability, but with a lower proton conductivity;[7] attempts to replace  $A^{2+}B^{4+}O_3$  by  $A^{3+}B^{3+}O_3$  seem not too optimistic.[8]

On the other hand, HTPCs also exist in the wider class of complex perovskites. Some  $A_2B'B''O_6$  were found to show considerable proton conductivity when nonstoichiometric.[9] More recently, we demonstrated that  $Sr_2Sc_{1-x}Nb_{1-x}O_{6.5}$  and  $Ba_3Ca_{1.18}Nb_{1.82}O_{9.5}$  are proton conductors with conductivity comparable to Yb-doped  $SrCeO_3$  and Nd-doped  $BaCeO_3$ . [10] This finding suggests that excellent HTPCs can also be produced from the  $A_3B'B''_2O_9$  complex perovskites.

In  $A_3B'B''_2O_9$ , the two B ions, due to the large valence difference, are often distributed in an ordered manner, i.e. 1:1 and 1:2 order.[11] The chemical distribution in the structure depends on the type of order and microstructure that the material adopts.[12] Consequently, the defect distribution and the defect-related properties are, to a large degree, affected by the manner in which the B site is ordered. In this paper, we study the proton incorporation and conductivity in several  $A_3B'_{1-x}Nb_{2-x}O_{9.5}$  complex perovskite-type oxides. It will be shown that HTPCs comparable or superior to the Ce-based perovskites can be created in this class of complex compounds. Some interesting observations of the IR spectra and conductivity isotope effect will be given and their physical significance will be discussed.

### II. EXPERIMENTAL METHODS AND RESULTS

Ceramic  $A_3B'_{1-x}Nb_{2-x}O_{9.5}$  (A=Ba, Sr, Ca and B'=Sr, Ca, Mg) compounds were prepared from 99.995% purity carbonates and oxides. The raw materials were carefully weighed and well mixed by ball-milling for 2 hours in 200 proof ethyl alcohol. Calcination and sintering were carried out at  $1200^\circ C$  and  $1500^\circ C$ , respectively, each for 12 hours. Samples of 90% theoretical density have been routinely obtained by this preparation route.

The proton incorporation was studied by detecting the weight change after various high temperature pretreatments. Specifically, 900°C vacuum pretreatment for 10 hours serves to produce a "dry" sample. The sample weight  $W_0$  was taken as the proton-free reference. Keeping the sample at 500°C in  $H_2O$ -containing Ar for 12 hours, followed by a slow-cooling of 50°C/h, showed a weight gain,  $\Delta W$ . Such a weight change is attributed to high temperature water uptake through the following reaction (in Kröger-Vink notation):



In this study, we focus on  $Sr_3Ca_{1+x}Nb_{2-x}O_{9-\delta}$ . As will be revealed later, the oxygen vacancies are the charge compensators when  $x > 0$ . Then, Eq. (1) predicts the saturation limit of proton concentration  $[H]_s \approx x$ . Figure 1 shows the  $[H]$  (measured from weight change) as function of  $x$  for this compound. The proton concentration is found to obey approximately a linear relation with  $x$ . A notable result is that all experimental points fall in the vicinity of a line given by  $[H] = x/3$ . Similar results were also observed in other  $A_3B'_{1+x}Nb_{2-x}O_{9-\delta}$ , showing  $[H] = [H]_s/3$ . Such an early saturation is different from that observed in 5% Nd- or Gd-doped  $BaCeO_3$ , in which the actually absorbed proton concentration is as high as 80% of the theoretical limit.[13]

A direct, but qualitative evidence of proton absorption comes from IR spectra. The presence of protons is manifested by the presence of a sharp OH band at 3500  $cm^{-1}$  for isolated OH ions.[14] As revealed in Fig. 2, after the  $H_2O$ -vapor pretreatment, both  $Sr_3Ca_{1.18}Nb_{1.82}O_{9-\delta}$  (SCN18) and  $Ba_3Ca_{1.18}Nb_{1.82}O_{9-\delta}$  (BCN18) show broad OH bands at 3200 and 3300  $cm^{-1}$  respectively (curves c and d), in strong contrast to that after 900°C treatment in 1%CO+99%CO<sub>2</sub>. Moreover, an OD band at 2400  $cm^{-1}$  is found when the dried sample was annealed in  $D_2O$ -containing Ar. Similar OH bands at 3200  $cm^{-1}$  with a band width over nearly 500  $cm^{-1}$  have been observed in 5% Y-doped single-crystal  $SrCeO_3$  and  $SrZrO_3$ . [15]

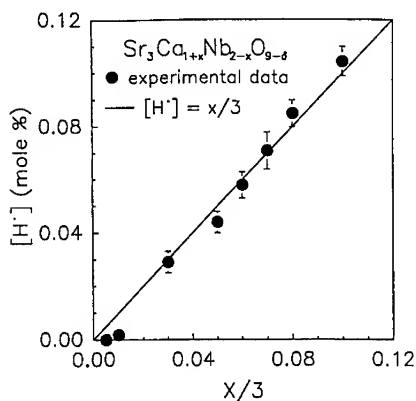


Fig. 1 Weight-change measurements show the proton concentration as function of nonstoichiometry,  $x$ .

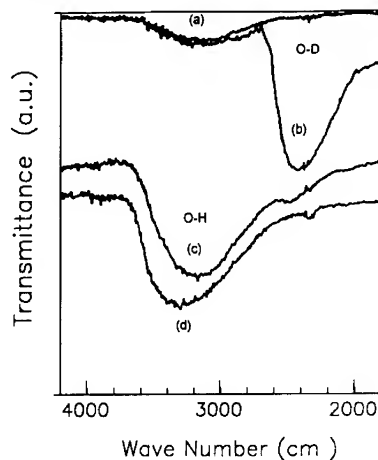


Fig. 2 IR spectra of SCN18 and BCN18 after various pretreatments: (a) SCN18 treated in 1%CO+99%CO<sub>2</sub> at 900°C; (b) SCN18 treated in  $D_2O$  at 500°C; (c) SCN18 treated in  $H_2O$  at 500°C; (d) BCN18 treated in  $H_2O$  at 500°C.

Electrical conductivity was measured by the impedance method in an automated Andeen capacitance bridge capable of detecting a capacitance range of  $10^{-5}$  to  $10^6$  pf and conductance range of  $10^{-12}$  to  $10^2$  mhos. The system can continuously measure 17 frequencies from 10 to  $10^5$  Hz and collect the impedance data in an interfacing IBM PC. All measurements were made at



temperatures below 400°C. Within this temperature range, the proton concentration is considered to be constant, or in a frozen-in state. In the following, dc conductivity is presented in Arrhenius plot by,

$$\sigma T = A \exp(-E_a/kT) \quad (2)$$

where  $E_a$  is the apparent activation energy. When the conductivity is due to nonassociated charge carriers,  $E_a$  represents the activation of motion  $E_m$ . [16]

We start with the proton-free samples. Introducing nonstoichiometry can produce oxygen vacancies and electron holes. The presence of electronic defects in such materials is manifested by a  $P_{O_2}$  dependence of conductivity. In this study,  $P_{O_2}$  was regulated over 18 orders of magnitude by 900°C pretreatments in various dry gases from dry air to 90%CO+10%CO<sub>2</sub> gas mixture. As revealed by the inset to Fig. 3, the conductivity for SCN18 is not appreciably affected by oxygen partial pressure, clearly excluding an electronic contribution. The activation energy fell in the neighborhood of 0.94 eV, close to that of Ca-stabilized ZrO<sub>2</sub> (1.0 eV) [17] with improved conductivity behavior.

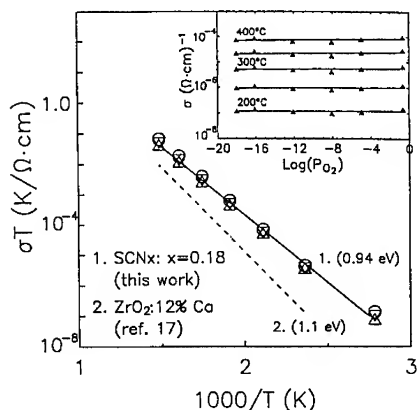


**Fig. 3** Conductivity Arrhenius plots for SCN18 after various dry-pretreatments at 900°C: O—dry air; Δ—1%CO+99%CO<sub>2</sub>; ▽—90%CO+10%CO<sub>2</sub>. The inserted figure gives the conductivity as function of  $P_{O_2}$ .

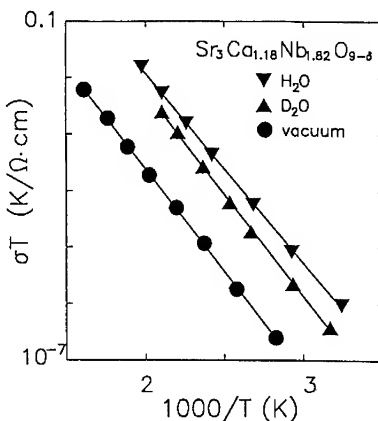


**Fig. 4** Comparison of Arrhenius plots for SCN18 after various pretreatments in H<sub>2</sub>O and D<sub>2</sub>O vapor at 500°C, and in 10<sup>-5</sup> atm. vacuum at 900°C.

Now, we turn to proton conduction. In Fig. 4, the proton-saturated sample shows a large conductivity increase compared to that of vacuum-pretreated SCN18 and an activation energy of 0.66 eV, which is clearly much lower than that of oxygen ion motion. Proton conduction is also manifested by the nonclassical isotope effect, showing an 0.054 eV increase in activation energy when protons are replaced by deuterons. Figure 5 shows the variation of the proton conductivity Arrhenius plots for 7 different degree of nonstoichiometry. We found a substantial drop of conductivity from  $x = 0.06$  to 0.03 and 0.015 with slightly increasing activation energy. This result is consistent with the observation that at  $x = 0.03$  and 0.015, the measured  $[H]$  is far less than  $x/3$  (also see Fig. 1).

Among the studied compounds,  $Sr_3Ca_{1+x}Nb_{2-x}O_{9.8}$  (SCNx) and  $Ba_3Ca_{1+x}Nb_{2-x}O_{9.8}$  (BCNx) are found to have proton conductivity compatible or even superior to that Yb-doped SrCeO<sub>3</sub> and Nd-doped BaCeO<sub>3</sub>, as presented in Fig. 6. The activation energies of SCNx and BCNx are 0.65 eV and 0.54 eV, practically the same as that in SrCeO<sub>3</sub> and BaCeO<sub>3</sub>. [4,5]

Table I summarizes the conductivity data for the five  $A_3B'_{1.18}Nb_{1.82}O_{9.8}$  compounds studied. Two points in the table are remarkable. Firstly, the ratio of the Arrhenius preexponentials (also

refer to Eq. 2) of deuteron and proton,  $A_D/A_H$  falls in the range of 1.0 to 2.0, different from the classical expectation of  $(m_H/m_D)^{1/2} = (1/2)^{1/2}$ . As a consequence, the Arrhenius plots of proton and deuteron conduction show a crossover (also see Fig. 7). Such an abnormal behavior has been attributed to the assumption inherent in the absolute rate theory (ART) that the interaction between the charge carriers and the crystal bath is efficient enough to allow a complete transfer of the carrier kinetic energy to the bath, which is not realistic for such light particles as protons.[13] Secondly, when B' was placed with smaller ions, e.g. from Sr (1.2 Å) to Ca (1 Å) and Mg (0.7 Å), the activation energy decreases. Moreover, replacing Sr by Ba at A-site always decreases the activation energy. These observations seem to suggest that the proton motion is significantly influenced by the lattice constant, or equivalently the O-O distance. Such a correlation was also proposed to exist in  $ABO_3$  perovskites.[2] It appears that further study in this aspect may provide some empirical rules for the selection of materials for proton conductors. This point is left for future investigation.

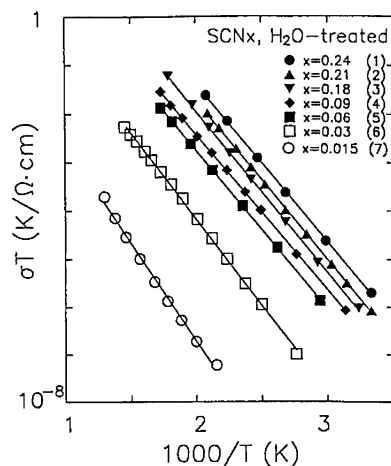


Fig. 5 Conductivity Arrhenius plots of  $SCN_x$  after pretreatment in  $H_2O$  vapor at  $500^\circ C$ .

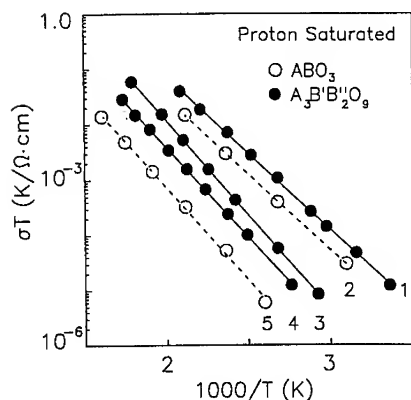


Fig. 6 Comparison of conductivity data for complex  $A_3B'B''O_9$  and simple  $ABO_3$  after pretreatment in  $H_2O$  vapor.

1) BCN18; 2)  $BaCeO_3$ : 5% Nd (ref. 5);  
3) SCN18; 5)  $SrCeO_3$ : 5% Yb (ref. 4).  
4) SCN9;

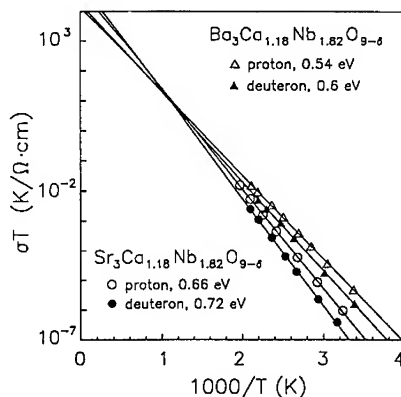


Fig. 7 Conductivity isotope effect in proton- and deuteron-saturated BCN18 and SCN18, showing the crossover of proton and deuteron conductivity Arrhenius plots.

Table I. Summary of proton conductivity and isotope effect for  $A_3(B'_{1.18}Nb_{1.82})O_{9.5}$  (AB'Nb18). The second last column shows that the isotope effect is nonclassical. The last column reveals  $A_D/A_H \sim \sqrt{2}$  with some scatter.

Formula	$E_H$ (eV)	$A_H$ ( $\times 10^4$ ) (K/ $\Omega$ -cm)	$E_D$ (eV)	$A_D$ ( $\times 10^4$ ) (K/ $\Omega$ -cm)	$E_H - E_D$ (eV)	$A_D/A_H$
BCN18	0.54	2.15	0.60	2.50	0.06	1.16
SMN18	0.61	0.02	0.64	0.038	0.03	1.90
SCN18	0.66	5.50	0.72	5.70	0.06	1.04
BSN18	0.83	9.43	0.88	17.86	0.05	1.89
SSN18	0.97	2.32	1.02	2.48	0.05	1.07

### III. DISCUSSION

The results presented above clearly establish that excellent proton conductors can be made from the complex  $A_3B'Nb_2O_9$  compounds when nonstoichiometry is introduced, allowing the incorporation of considerable protons. The presence of protonic conduction was manifested by the nearly two orders of magnitude increase in conductivity and an nonclassical isotope effect (see Fig. 3 and Table I). An additional advantage of these materials in comparison with the Ce-based perovskites is their extremely stable electrolytic character.

That the saturation proton concentration makes up only about 1/3 of the charge compensator can be explained if each excessive  $B'$  ion, e.g.  $Ca_{Nb}$ , tends to be bound with a  $V_O^{\bullet}$ , leaving one negative charge to be compensated by a proton. The fact that  $[H^+] \ll x/3$  in  $Sr_3Ca_{1+x}Nb_{2-x}O_{9.5}$  at  $x \leq 0.06$  is probably due to "misplacing" Ca in the A sites. On the other hand, TEM and x-ray microanalysis have revealed that the structure of these complex materials tended to be partitioned into domains or clusters of different structural order and chemical composition, e.g. Ca-rich 1-1 ordered clusters have been found to be present in  $A_3Ca_{1+x}Nb_{2-x}O_{9.5}$  ( $A=Ba$  or  $Sr$ ) at  $x \geq 0.06$ , [18] at which  $[H^+] \approx x/3$  is observed. Within these domains,  $V_O^{\bullet}$  are concentrated and may be ordered to become a part of the lattice structure. Consequently, they are not readily replaced by protons.[19]

Also, the OH band at  $3200-3300\text{ cm}^{-1}$  observed in IR spectra is much lower and broader than the very narrow band at  $3500\text{ cm}^{-1}$  for isolated OH groups. Similar broad OH band at  $3200\text{ cm}^{-1}$  was also observed in 5% Y-doped single crystal  $SrCeO_3$  and  $SrZrO_3$ . [15] These results suggest that significant interaction of the OH<sup>-</sup> ions with the surrounding crystal cage must be present in these fast proton conducting perovskite-type oxides.

To explain the presence of an cross-over in the isotope conductivity Arrhenius plots requires a theoretical modification of the ART hopping model. It has been suggested that, since the collision between a light charge carrier and heavier cage ions may eventually be elastic, a proper hopping model must take into account the efficiency of energy transfer in each collision event.[20] We have proposed a similar modification scheme to the proton conduction process and predicted that the modified ART should give an isotope effect of  $A_D/A_H = \sqrt{2}$ . [13] Our present results are in general agreement with this prediction. It is noteworthy that the cross-over described earlier has also been frequently observed in other perovskite-type oxides and therefore the modification applies universally.

### IV. CONCLUSION

1. Nonstoichiometric  $Ba_3Ca_{1+x}Nb_{2-x}O_{9.5}$  and  $Sr_3Ca_{1+x}Nb_{2-x}O_{9.5}$  are excellent proton conductors, with proton conductivity behavior comparable to the well-studied doped  $BaCeO_3$  and  $SrCeO_3$ .

2. Protons are strongly affected by the surrounding crystal environment, especially by the nearby charged defects. Such an effect, when comes to complex perovskites, is reflected by a proton concentration saturated at only 1/3 of the theoretical limit.

3. The modification of the "absolute rate theory" gives the ratio of the Arrhenius preexponentials  $A_D/A_H \sim \sqrt{2}$ .

#### ACKNOWLEDGMENT

The authors are grateful to the support by the U.S. Department of Energy for this study.

#### REFERENCES

- [1] H. Iwahara, T. Esaka, H. Uckida and N. Maeda, Solid State Ionics 3/4 (1981) 359.
- [2] A. Mitsui, M. Miyayama and H. Yanagida, Solid State Ionics 22 (1987) 213.
- [3] N. Bonanos, B. Ellis and M.N. Mahmood, Solid State Ionics 28/30 (1988) 579.
- [4] T. Scherban, W-K Lee and A.S. Nowick, Solid State Ionics 28/30 (1988) 585.
- [5] J.F. Liu and A.S. Nowick, Solid State Ionics 50 (1992) 131.
- [6] N. Bonanos, Solid State Ionics 53/56 (1992) 967.
- [7] T. Yajima, H. Suzuki, T. Yogo and H. Iwahara, Solid State Ionics 51 (1992) 101.
- [8] Y. Larring and T. Norby, Solid State Ionics 70/71 (1994) 305.
- [9] K.C. Liang and A.S. Nowick, Solid State Ionics 61 (1993) 77.
- [10] K.C. Liang, Yang Du and A.S. Nowick, Solid State Ionics 69 (1994) 117.
- [11] F.S. Galasso, "Perovskites and High  $T_c$  Superconductors" (Gordon and Breach Science, 1990).
- [12] M.P. Harmer, J. Chen, P. Peng, H.M. Chan and D.M. Smyth, Ferroelectrics Vol. 97 (1989) 263.
- [13] A.S. Nowick and Yang Du, Solid State Ionics in press (VII Intl. Conf. on Solid Proton Conductors, Germany, Sept., 1994).
- [14] S. Kapphan, J. Koppitz and G. Weber, Ferroelectrics 25 (1980) 585.
- [15] S. Shin, H.H. Huang, M. Ishigame and H. Iwahara, Solid State Ionics 40/41 (1990) 910.
- [16] A.S. Nowick, W-K Lee and H. Jain, Solid State Ionics 28/30 (1988) 89.
- [17] T.H. Etsell and S.N. Flangas, Chem. Rev. 70 (1970) 339.
- [18] Yang Du and A.S. Nowick, to be published.
- [19] Yang Du, Doctoral Thesis, Columbia University (1994).
- [20] G. Iche and J. Nozieres, J. Physique 37 (1876) 1313.

# FAILURE OF THE FRENKEL DEFECT MODEL TO EXPLAIN THE TREND IN ANIONIC CONDUCTIVITY IN THE MF<sub>2</sub> FLUORITE STRUCTURE AND RELATED MSnF<sub>4</sub> MATERIALS

GEORGES DENES

Concordia University, Laboratory of Solid State Chemistry and Mössbauer Spectroscopy, Laboratories for Inorganic Materials, Department of Chemistry and Biochemistry, 1455 De Maisonneuve Blvd. W., Montreal, Quebec, H3G 1M8, Canada

## ABSTRACT

The high fluoride ion conductivity of fluorite type MF<sub>2</sub> has been attributed to the fact that half of the F<sub>8</sub> cubes present in this structure are empty and therefore, are potential vacant sites for interstitial fluoride ions in the formation of Frenkel defects. However, the model of long range ion motion through Frenkel defects by use of empty F<sub>8</sub> cubes is in contradiction with: (i) the little difference between the conductivities of CaF<sub>2</sub> and BaF<sub>2</sub>, (ii) the conductivity of  $\beta$ -PbF<sub>2</sub> being much larger than that of BaF<sub>2</sub>, and (iii) the much higher performance of MSnF<sub>4</sub> even though there is no empty cube to form Frenkel defects in the MSnF<sub>4</sub> structures.

## INTRODUCTION

The highest performance fluoride ion conductors known to date have structures which are derived from the fluorite (CaF<sub>2</sub>) type. In the fluorite structure, the high fluoride ion motion has been attributed to the presence of Frenkel defects, i.e. vacancies on the anionic sublattice and an equal number of anions in interstitial positions at the center of the F<sub>8</sub> cubes not containing a metal ion [1]. The fluoride ion mobility occurs by ion jumps between interstitials and vacancies, involving simultaneous displacement of anions towards the positive electrode and anion vacancies towards the negative electrode. In addition, the fluorite structure undergoes a diffuse phase transition at high temperature (T<sub>c</sub>) called "superionic transition." At T<sub>c</sub>, well below the melting point (T<sub>m</sub>), the conductivity increases to a value similar to that of a molten ionic salt, and the anionic sublattice is considered as being molten [2]. The concept of "sublattice melting" has been supported by X-ray and neutron diffractions, which show considerable disorder on the anionic sublattice, with F<sup>-</sup> occupancy factors below unity and strong anharmonic thermal vibrations [3-5].

It has been shown that the presence of a lone pair carrier metal or semi-metal, such as Sn(II) or Bi(III), in structures related to the fluorite type, enhances the fluoride ion mobility by several orders of magnitude and leads to lower activation energies [6-7].

The goal of the present study is to investigate if the Frenkel defect model is consistent with: (i) the trend of the conductivities of the  $\text{MF}_2$  fluorides crystallizing in the fluorite type structure, and (ii) the very high conductivities of the  $\text{MSnF}_4$  materials.

## STRUCTURES OF THE FLUORITE TYPE AND OF $\text{MSnF}_4$

The fluorite type structure is found for the  $\text{MF}_2$  fluorides where M is a large metal ( $\text{M} = \text{Ca}, \text{Sr}, \text{Ba}, \text{Cd}, \text{Hg}$  and  $\text{Eu}$ ). The lattice is face centered cubic (fcc), the space group is  $\text{Fm}\bar{3}\text{m}$  (No. 225) and the ions are located in the following Wyckoff sites:  $\text{Ca}^{2+}$  in 1a (0,0,0) and  $\text{F}^-$  in 3c ( $1/4, 1/4, 1/4$  and  $3/4, 3/4, 3/4$ ) (fig. 1)[8]. The fluoride ions form a primitive cubic sublattice, with the edge of the  $\text{F}_8$  cubes being half the edge of the unit-cell. The metal ions are located in the center of the  $\text{F}_8$  cubes, and thus have a  $\text{MF}_8$  cubic coordination, whereas the fluoride ions have a  $\text{FM}_4$  tetrahedral coordination (fig. 2). Figure 3a shows a projection of the structure of  $\text{BaF}_2$  in the  $(\vec{a}, \vec{c})$  plane. Only the ions located at heights  $y = -1/4$  to  $+1/4$  are shown. The figure shows that only half of the  $\text{F}_8$  cubes have a metal ion in their center, with filled and empty cubes alternating along the three axes of the unit-cell.

The structure of  $\text{MSnF}_4$  ( $\alpha$ - $\text{PbSnF}_4$  type) is related to the fluorite type (fig. 3b). The unit-cell of  $\text{MSnF}_4$  ( $a_\alpha, b_\alpha, c_\alpha$ ) is obtained from the unit-cell of the fluorite type ( $a_F, b_F, c_F$ ) by rotating the  $\vec{a}$  and  $\vec{b}$  axes  $45^\circ$  in the  $(\vec{a}, \vec{b})$  plane ( $a_\alpha = b_\alpha = a_F \sqrt{2}/2$ ) and by doubling the  $\vec{c}$  axis ( $c_\alpha = 2c_F$ ). The rotation of  $\vec{a}$  and  $\vec{b}$  is due to the tetragonal distortion and loss of the F Bravais lattice, whereas the doubling of  $c$  results from the order between M and Sn layers along the  $\vec{c}$  axis [9, 10]. The space group is  $\text{P4/nmm}$  (No. 129). Figure 3 shows the main differences compared to the fluorite type [11, 12]:

- (i) The metals are ordered along  $\vec{c}$  (Ba Ba Sn Sn Ba Ba ...);
- (ii) The layer of fluoride ions which should be present between two adjacent tin layers has disappeared and is replaced by a layer of lone pairs of electrons located on the adjacent tin layers. Thus, unlike  $\text{MF}_2$ ,  $\text{MSnF}_4$  has a layered structure;
- (iii) The fluoride ions from the layer that has disappeared have moved to adjacent empty  $\text{F}_8$  cubes and form axial bonds to tin. This has two important consequences:
  - the coordination of tin is  $\text{SnF}_5\text{E}$  distorted octahedral, where E, the tin(II) lone pair, occupies one of the tin hybridized orbitals ( $\text{sp}^3\text{d}^2$ ), and the coordination of the other metal M is 8+4 (distorted  $\text{F}_8$  cube, plus 4 longer distances);
  - there is no more empty  $\text{F}_8$  cubes like in the fluorite type structure. All are occupied by fluorine axially coordinated to tin.

## CONDUCTIVITY OF $\text{MF}_2$ AND $\text{MSnF}_4$

Conductivity trends: Figure 4a shows the conductivity and the activation energy for  $\text{MF}_2$  and  $\text{MSnF}_4$  at  $350^\circ\text{C}$  versus the ionic radius of the metal. No general trend is

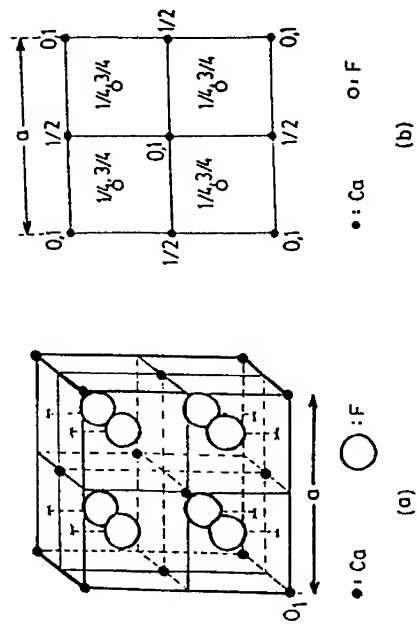


Figure 1: The fluorite type structure: (a) 3D view;

(b) projection onto the (a,b) plane.

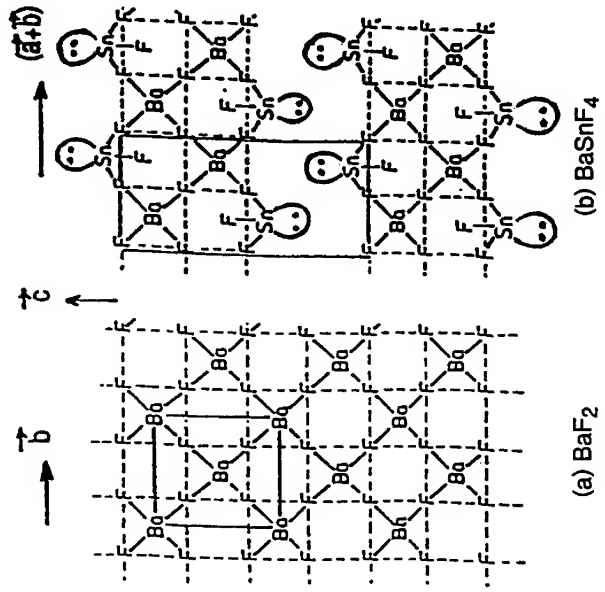


Figure 3: Projection of a layer (one  $MF_8$  cube thick) in: (a)  $BaF_2$ , (b)  $BaSnF_4$ .

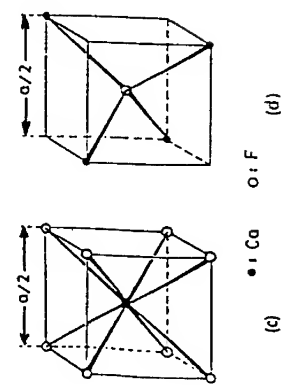


Figure 2: Coordination of the metal and the anion in the fluorite type structure.

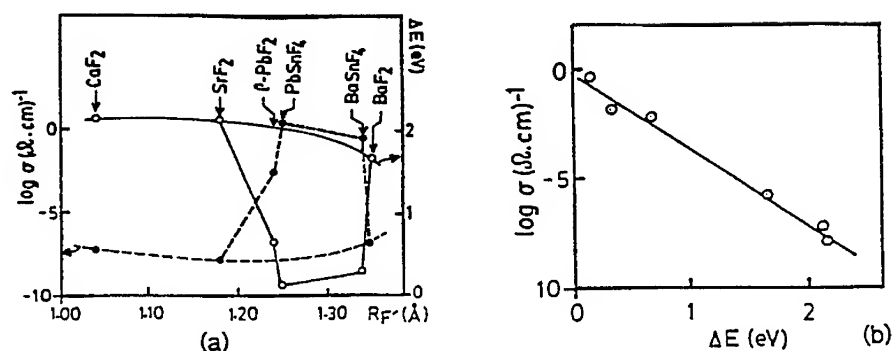


Figure 4: (a) Conductivity and activation energy of  $\text{MF}_2$  and  $\text{MSnF}_4$  versus the radius of the metal ion  $\text{M}^{2+}$ ; (b) conductivity versus activation energy.

observed, however, the materials can be divided into three general categories: (i)  $\text{MF}_2$  for "hard core" alkaline earths (Ca, Sr and Ba) have the lowest conductivities and the highest activation energies, (ii)  $\text{MSnF}_4$  ( $\text{M} = \text{Pb}$  and  $\text{Ba}$ ) have the highest conductivities and lowest activation energies, and  $\text{MF}_2$  for "soft"  $\text{Pb}^{2+}$  ion ( $\beta\text{-PbF}_2$ ) has a conductivity and an activation energy between the two other kinds. The symmetry between the conductivity and activation energy curves is striking: the conductivity varies linearly with the activation energy (fig. 4b). This is not surprising, since the lower the activation energy, the less energy is required to make the ions jump from one site to another, the easier it is for the ions to move, and therefore the more of them will move, and it will result a higher conductivity.

#### Failure of the Frenkel defect model to explain the conductivity of $\text{MF}_2$ and $\text{MSnF}_4$ :

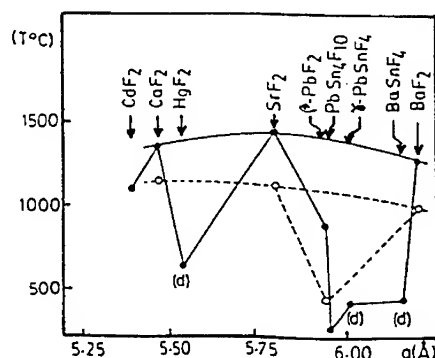
The high conductivity of the  $\text{MF}_2$  fluorite type has been accounted for by Frenkel defects, i.e. the fact that half of the  $\text{F}_8$  cubes in the fluorite structure are empty and therefore are potential vacant sites for fluoride ion interstitials. However, in order for a fluoride ion to fit comfortably in the middle of an  $\text{F}_8$  cube, the cube must be large enough. The radius of the interstitial sites is 1.04  $\text{\AA}$  in  $\text{CaF}_2$ , 1.18  $\text{\AA}$  in  $\text{SrF}_2$ , 1.24  $\text{\AA}$  in  $\beta\text{-PbF}_2$  and 1.35  $\text{\AA}$  in  $\text{BaF}_2$ , compared to the ionic radius of  $\text{F}^-$  (1.34  $\text{\AA}$ ). Obviously, the vacant sites in  $\text{CaF}_2$  and  $\text{SrF}_2$  are much too small to take an interstitial fluoride ion without considerable local distortion. On the other hand, they are perfectly well suited in  $\text{BaF}_2$ , therefore one could expect the conductivity of  $\text{BaF}_2$  to be much higher than that of  $\text{CaF}_2$  and  $\text{SrF}_2$ , and its activation energy to be much lower. Figure 4a shows this is not the case. The Frenkel defect mechanism fails to explain why  $\text{BaF}_2$  is not significantly a better conductor than  $\text{CaF}_2$  and  $\beta\text{-PbF}_2$ . The conductivity of  $\text{MSnF}_4$  is several orders of magnitude higher than the corresponding



MF<sub>2</sub>, and the activation energy is much lower. However, figure 3b shows that, although the MSnF<sub>4</sub> structure is closely related to the MF<sub>2</sub> fluorite type, there is no empty F<sub>8</sub> cubes in MSnF<sub>4</sub>, since all the F<sub>8</sub> cubes not containing a metal ion contain a fluorine atom axially covalently bonded to tin. Therefore, the Frenkel defect mechanism using a large number of F<sub>8</sub> cubes does not explain the much enhanced conductivity of MSnF<sub>4</sub>.

The role of soft M<sup>2+</sup> ions and covalently bonded metals: Figure 5 shows the temperature T<sub>C</sub> of the superionic transition and T<sub>m</sub> of melting for the MF<sub>2</sub> fluorite type and MSnF<sub>4</sub>. These temperatures are higher for hard core metals, i.e. for the

Figure 5: Superionic transition temperature (open circles and dashed lines) and melting point (closed circles and solid lines) for MF<sub>2</sub> and MSnF<sub>4</sub>.



poorest conductors. Therefore, an essential factor seems to be the strength of the lattice, i.e. the softer the lattice, the higher the conductivity. This is perhaps because it is easier for the mobile ions to create local temporary lattice distortions while jumping from one site to another. The hard core ions give very strong ionic lattices, and therefore are poor conductors. For lead(II), which also has a non-hybridized lone pair on the 6s orbital, and therefore is somewhat polarizable, the lattice is softer, and it results in a higher conductivity. Incorporation of low melting SnF<sub>2</sub> (T<sub>m</sub> = 215°C) in the fluorite type MF<sub>2</sub> gives the MSnF<sub>4</sub> structure. Its very high conductivity is most likely due to weaker Sn-F bonds, which softens the lattice. In addition, the combination of polarizable Pb<sup>2+</sup> and soft SnF<sub>2</sub> gives the highest performance fluoride ion conductor, PbSnF<sub>4</sub>, which has a higher conductivity than BaSnF<sub>4</sub> [7].

## CONCLUSION

Although the Frenkel defect mechanism is in agreement with the higher fluoride ion conductivity of the fluorite type, compared to compact structures, it fails to explain the

trend of conductivity versus the ionic radius of the metal ion in  $\text{MF}_2$  fluorite structures, and it does not account for the very high conductivity of  $\text{MSnF}_4$ . The polarizability of  $\text{Pb}^{2+}$  and the presence of soft  $\text{SnF}_2$  are the major factors that boost the fluoride ion mobility. The softening of the solid lattice creates a large number of vacancies on the fluorine sites bonded to tin. The resulting interstitial fluorine atoms cannot be located by neutron diffraction and are probably responsible for the very high conductivity [11, 12]. It must be pointed out that the combination of  $\text{SnF}_2$  and a structure related to the fluorite type is necessary to achieve very high conductivities, since the conductivity of pure  $\text{SnF}_2$ , which has a molecular structure, is similar to that of  $\beta\text{-PbF}_2$ , therefore much lower than that of  $\text{MSnF}_4$ , although much higher than for the hard core  $\text{MF}_2$  fluorite type [13]. It is ironic that the most efficient way to enhance the ionic conductivity of the fluorite type, which is a property typical of ionic structures is to combine it with a molecular compound.

## REFERENCES

1. J. Schoonman, *Solid State Ionics* **1**, 121 (1980).
2. A.V. Chadwick, *Solid State Ionics* **8**, 209 (1983).
3. S.M. Shapiro and F. Reidinger, in *Physics of Superionic Conductors*, edited by M.B. Salamon (Springer, Berlin, 1979), p. 45.
4. M.H. Dickens, W. Hayes, C. Smith and M.T. Hutchings, in *Fast Ion Transport in Solids*, edited by P. Vashishta, J.N. Mundy and G.K. Shenoy (North-Holland, Amsterdam, 1979), p. 225.
5. K. Koto, H. Schultz and R.A. Huggins, *Solid State Ionics* **1**, 355 (1980); **3/4**, 381 (1981).
6. C. Lucat, A. Rhandour, J.M. Reau, J. Portier and P. Hagenmuller, *J. Solid State Chem.* **29**, 373 (1979).
7. G. Denes, T. Birchall, M. Sayer and M.F. Bell, *Solid State Ionics* **13**, 213 (1984).
8. R.W.G. Wyckoff, *Crystal Structures*, 2nd ed., Vol. 1 (Interscience Publishers, New York, 1963), pp. 239-244.
9. G. Denes, J. Pannetier and J. Lucas, *C. R. Acad. Sc. Paris, Series C* **280**, 831 (1975).
10. J. Pannetier, G. Denes and J. Lucas, *Mat. Res. Bull.* **14**, 627 (1979).
11. T. Birchall, G. Denes, K. Ruebenbauer and J. Pannetier, *Hyperfine Interact.* **29**, 1331 (1986).
12. G. Denes, Y.H. Yu, T. Tyliszczak and A.P. Hitchcock, *J. Solid State Chem.* **91**, 1 (1991).
13. D. Ansel, J. Debuigne, G. Denes, J. Pannetier and J. Lucas, *Ber. Bunsenges. Phys. Chem.* **82**, 376 (1978).
14. G. Denes, in *Proceedings of the Second Nassau Mossbauer Conference*, edited by C.I. Wynter and E.E. Alp (W.C. Brown Publishers, 1994), pp. 109-135.

## POINT DEFECTS AND CATION DIFFUSION IN COBALTOUS OXIDE

SANJEEV AGGARWAL AND RÜDIGER DIECKMANN

Cornell University, Department of Materials Science and Engineering, Ithaca NY 14853

### ABSTRACT

The deviation from stoichiometry,  $\Delta$ , in  $\text{Co}_{1-\Delta}\text{O}$  was measured in-situ as a function of oxygen activity at temperatures between 1000 and 1400 °C, using a high resolution microbalance. The experiments were conducted over the entire  $\text{Co}_{1-\Delta}\text{O}$  phase stability region at atmospheric pressure. The experimental results were analyzed with regard to the point defect structure and also in comparison with mass and charge transport data. Contrary to prior belief, it was found that the average mobility of the cationic defects and holes varied with their respective concentration.

### INTRODUCTION

Cobaltous oxide, a metal deficient p-type semiconductor, has been of interest for some time to various research groups. A literature survey reveals that most previous investigations [1-6] on the non-stoichiometry of cobaltous oxide were limited to high oxygen activities. Using coulometric titration, Sockel and Schmalzried [7] studied the deviation from stoichiometry in cobaltous oxide at 1200 °C over its entire phase stability range at 1 atm total pressure. Unfortunately, their data at low oxygen activity,  $a_{\text{O}_2}$  ( $= P_{\text{O}_2}/P^\circ$ ;  $P^\circ = 1$  bar), are questionable. Hölscher and Schmalzried [8] measured the non-stoichiometry of  $\text{Co}_{1-\Delta}\text{O}$  over the entire stability range at 1000 and 1100 °C. However, they made large corrections at low oxygen activities to obtain their data set. Thus, a comprehensive and reliable data set on the non-stoichiometry of cobaltous oxide was not available in the literature when we initiated a new experimental study of this subject a few years ago. Experimental data and a preliminary analysis were published in [9].

Despite the lack of a quantitative description of  $\Delta$ , the point defect structure of  $\text{Co}_{1-\Delta}\text{O}$  has been under discussion for a long time. In the literature there is general agreement that the oxygen sublattice can be assumed to be close to ideal because of the size difference between the larger oxygen ion and the smaller cobalt ion. The deviation from stoichiometry in  $\text{Co}_{1-\Delta}\text{O}$  is attributed to cationic defects charge compensated by holes. Many investigators have attempted to assign a point defect structure to  $\text{Co}_{1-\Delta}\text{O}$  based on measured non-stoichiometry and transport data as a function of temperature and oxygen partial pressure. Various point defect structures have been proposed depending on the assumptions made.

In 1977, Dieckmann [10] quantitatively modelled the then available experimental non-stoichiometry, electrical conductivity and cation tracer diffusion data on cobaltous oxide.

He described the observed non-stoichiometry on the basis of an ideal solution of holes and differently charged cation vacancies, i.e., of  $(V_{Co^{2+}})''$ ,  $(V_{Co^{2+}})'$  and  $(V_{Co^{2+}})^X$ . The superscript “'” denotes a negative charge and “X” a neutral state. According to the model, at low  $a_{O_2}$  doubly charged cation vacancies prevail, while singly charged and neutral vacancies significantly contribute to  $\Delta$  at high oxygen activities. Another approach also discussed in Ref. [10] uses the Debye-Hückel theory to take into account the electrostatic interaction between charged defects, and limits the modelling to doubly charged cation vacancies and holes as defects. In 1989 Nowotny and Rekas [11-13] reviewed the different types of modelling discussed above and also considered the existence of various defect clusters. However, their articles are inconclusive. Finally, several theoretical studies exist which predict the presence of defect clusters [14-17] based on defect energy calculations.

In the past, the lack of reliable experimental data for  $\Delta$  in  $Co_{1-\Delta}O$  at low oxygen activities gave researchers some freedom in the interpretation of the defect structure and in data fitting. Our experimental study of  $\Delta$  in  $Co_{1-\Delta}O$  was intended to fill this gap and provides an extensive and reliable data base over the entire phase stability range at 1 atm total pressure at temperatures between 1000 and 1400 °C. A figure summarizing the experimental data was published in Ref. [9]. Since unequivocal conclusions with regard to the defect structure of  $Co_{1-\Delta}O$  cannot be made using these data without additional information, no attempt was made so far to model this defect structure based on different types of defects. Instead, an empirical expression was developed which allows to quantitatively describe  $\Delta$  as a function of temperature and oxygen activity.

## EXPERIMENTS

### Sample Preparation

Polycrystalline and single crystal samples were used for our thermogravimetric measurements. The polycrystalline samples were prepared starting with high purity  $Co_3O_4$  powder. This powder was cold-pressed and reduced to  $Co_{1-\Delta}O$  at 800 °C in a nitrogen atmosphere ( $a_{O_2} \sim 10^{-4}$ ). The samples obtained in this way were porous allowing for a fast reequilibration after oxygen activity changes. The single crystalline samples used were grown several years ago by the Verneuil technique at Argonne National Laboratory.

### Thermogravimetric Measurements

Thermogravimetric studies were conducted at temperatures between 1000 to 1400 °C by the successor of the microbalance described in [18]. The resolution and noise level of the microbalance used in this study are of the order of  $1 \cdot 10^{-6}$  g at high temperatures and flowing gases. Oxygen activities were established using  $CO/CO_2$  and  $O_2/CO_2$  gas mixtures of different compositions and monitored with electrochemical cells using a zirconia-based electrolyte. All oxygen activity jumps were performed relative to

a reference oxygen activity, and the mass changes,  $\Delta m$ , occurring after these jumps were recorded. Finally, the values recorded for  $\Delta m$  were used to calculate values for changes in  $\Delta$ ,  $\delta\Delta$ .

## RESULTS

The measured relative mass changes,  $\Delta m$ , were converted to relative changes in  $\Delta$ ,  $\delta\Delta$ , using Eqn. (1):

$$\delta\Delta = \frac{\Delta m}{n_{\text{Co}} \cdot M_{\text{O}}} \quad (1)$$

where  $n_{\text{Co}}$  is the number of moles of Co and  $M_{\text{O}}$  is the atomic weight of oxygen. The values obtained for  $\delta\Delta$  at 1200 °C in the polycrystalline samples and in the single crystals studied are shown in Fig. 1 as a function of oxygen activity relative to  $\Delta$  at the Co/CoO equilibrium. Between 1000 and 1400 °C the  $\delta\Delta$ -values measured in single crystalline samples match exactly with those for polycrystalline samples. The solid line drawn through the points shown in Fig. 1 stems from a fit to the following empirical equation:

$$\delta\Delta = \Delta - \Delta_{\text{Ref}} = X \cdot a_{\text{O}_2}^{\alpha} + Y \cdot a_{\text{O}_2}^{\beta} - \Delta_{\text{Ref}} \quad (2)$$

where  $\Delta_{\text{Ref}}$  is the  $\Delta$  at the reference point selected for a set of measurements.  $X$  and  $Y$  are Arrhenius-type functions of the temperature and  $\alpha = 1/6$  and  $\beta = 0.40$ . As mentioned above, the data shown in Fig. 1 are displayed relative to  $\Delta$  at the Co/CoO equilibrium,  $\Delta_{\text{Co/CoO}}$ . The value  $\Delta_{\text{Co/CoO}}$  is obtained by fitting the experimental data to Eq. (2). A more detailed discussion of the derivation of Eq. (2) and data fitting procedure will be published shortly [19].

## DISCUSSION

A comparison of the  $\Delta$ -values determined in this study combined with results from earlier studies available in the literature was made in Ref. [9]. In general, our data are in good agreement with literature data at high oxygen activities. At lower oxygen activities this is not the case. However, the relative changes in  $\Delta$  that can be derived from the data sets reported by Sockel and Schmalzried [7] and by Hölscher and Schmalzried [8] are very similar to our results. Therefore, their  $\delta\Delta$ -data can be converted to absolute values for  $\Delta$  that are compatible with our  $\Delta$ -values by choosing a different  $\Delta_{\text{Ref}}$  than

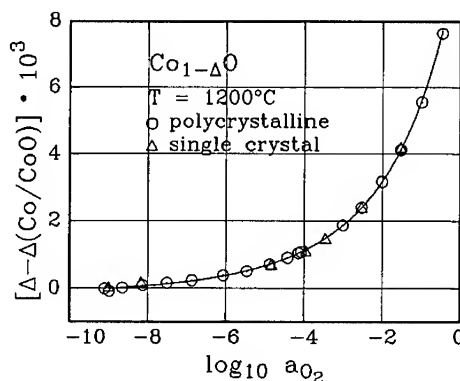


Fig. 1:  $\delta\Delta$  versus  $\log a_{\text{O}_2}$  at 1200 °C for single- and polycrystalline  $\text{Co}_{1-\Delta}\text{O}$

those used in Refs. [7] and [8]. The experimental data suggest that  $\text{Co}_{1-\Delta}\text{O}$  has a cation deficit over its entire stability range between 1000 and 1400 °C at 1 atm total pressure and that a cation excess does not occur at low  $a_{\text{O}_2}$ .

Data for the cobalt tracer diffusion coefficient,  $D_{\text{Co}}^*$ , in  $\text{Co}_{1-\Delta}\text{O}$  measured at 1310 °C, see Ref. [10], were compared with  $\Delta$  values from this study, after interpolation to 1310 °C, see Fig. 2. If the mean mobility of all cationic defects is considered to be independent of composition,  $\Delta$  and  $D_{\text{Co}}^*$  should vary identically with oxygen activity. This is not the case. Fig. 2 shows that the tracer diffusion coefficient increases faster with oxygen activity than the deviation from stoichiometry. The tracer diffusion coefficient is given by:

$$D_{\text{Co}}^* = \frac{1}{6} \cdot a_{\text{Co}}^2 \cdot f_{\text{Co}} \cdot \Gamma_{\text{Co}} \cdot x_{\text{def}}, \quad (3)$$

where  $1/6$  is the geometrical factor,  $a_{\text{Co}}$  is the elementary jump length,  $f_{\text{Co}}$  is the correlation factor,  $\Gamma_{\text{Co}}$  is an elementary jump frequency and  $x_{\text{def}}$  is the molar defect concentration. For  $\text{Co}_{1-\Delta}\text{O}$ :

$$x_{\text{def}} = \frac{\Delta}{1 - \Delta} \approx \Delta. \quad (4)$$

If one assumes that the diffusion of Co occurs via only one type of defect, then:

$$\frac{D_{\text{Co}}^*}{\Delta} = \frac{1}{6} \cdot a_{\text{Co}}^2 \cdot f_{\text{Co}} \cdot \Gamma_{\text{Co}}. \quad (5)$$

The right hand side of Eqn. (5), if constant, would lead in a  $\log D_{\text{Co}}^*/\Delta$  vs  $\log a_{\text{O}_2}$  plot to a line parallel to the  $\log a_{\text{O}_2}$  axis. Fig. 3 is such a plot and shows clearly a positive slope. If Co should diffuse by only one type of defect, this would imply that one or more of the quantities on the right hand side of Eq. (5) are composition dependent. A significant variation in  $a_{\text{Co}}$  can be excluded based on a study by Faber [20] which suggests that the lattice parameter decreases only slightly with increasing  $\Delta$ . It is also unlikely that  $f_{\text{Co}}$  varies much. Therefore the elementary jump frequency,  $\Gamma_{\text{Co}}$ , must vary with composition. This frequency can be expressed as follows:

$$\Gamma_{\text{Co}} = \Gamma_{\text{av}}^0 \cdot \exp\left(-\frac{E_{\text{app}}}{k \cdot T}\right), \quad (6)$$

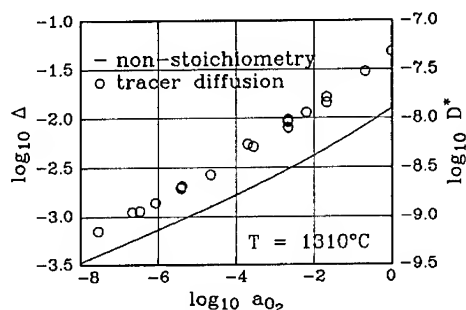


Fig.2: Comparison of the  $a_{\text{O}_2}$  dependence of  $D_{\text{Co}}^*$  and of interpolated values of  $\Delta$  at 1310 °C.

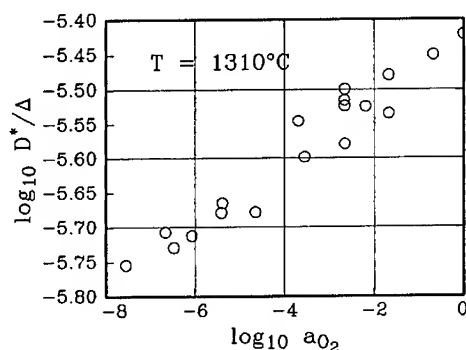


Fig. 3:  $\log D_{\text{Co}}^*/\Delta$  versus  $\log a_{\text{O}_2}$  at 1310 °C.

where  $E_{app}$  is the activation energy for the diffusion of the cationic defects and  $\Gamma_{av}^{\circ}$  is a pre-exponential factor. Substitution into Eq. (5) leads to:

$$\frac{D_{Co}^*}{\Delta} = \left[ \frac{1}{6} \cdot a_{Co}^2 \cdot f_{Co} \cdot \Gamma_{av}^{\circ} \right] \cdot \exp\left(-\frac{E_{app}}{k \cdot T}\right) = A \cdot \exp\left(-\frac{E_{app}}{k \cdot T}\right), \quad (7)$$

where A is a pre-exponential term summarizing the content of the rectangular bracket.

The activation energy,  $E_{app}$ , was calculated for different, fixed values of  $\Delta$ . Therefore, any change of the ratio  $D_{Co}^*/\Delta$  with composition is solely due to a change in the mean jump frequency. The  $D_{Co}^*$  vs T behavior was investigated at different values of  $\Delta$ . The slope and intercept of a  $\log D_{Co}^*$  vs  $T^{-1}$  plot yields values for  $E_{app}$  and A, respectively. Fig. 4 shows the values determined for  $E_{app}$  at different values of  $\Delta$ . Within the range of  $\Delta$  considered,  $E_{app}$  decreases by  $\sim 10\%$  with increasing  $\Delta$ . The pre-exponential term is not expected to vary significantly with  $\Delta$  if the diffusion of Co occurs by only one type of defect. However, as shown in Fig. 5, the A-values change almost by a factor of 1.5 in the range of  $\Delta$  considered here. Since the correlation factor is not expected to vary significantly with  $\Delta$  and the lattice parameter does not change significantly, then the jump frequency must change with  $\Delta$ . Though the pre-exponential term, A, and the exponential term influence the value of the ratio  $D_{Co}^*/\Delta$  as a function of  $\Delta$  in opposite ways, the exponential term must be prevailing to account for the increase of  $D_{Co}^*/\Delta$  with  $a_{O_2}$  shown in Fig. 2.

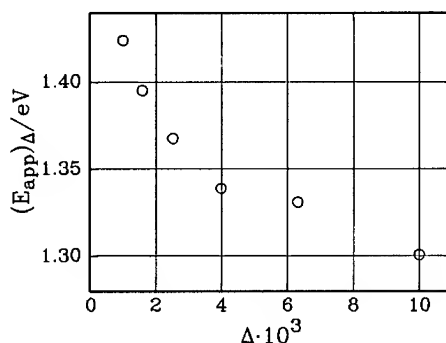


Fig. 4:  $E_{app}$  for the diffusion of cations versus  $\Delta$  in  $Co_{1-\Delta}O$ .

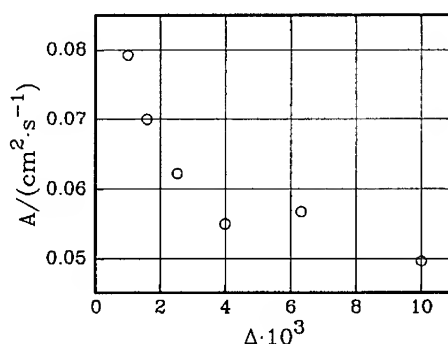


Fig. 5: A-values for the diffusion of Co versus  $\Delta$  in  $Co_{1-\Delta}O$ .

A comparison between the electrical conductivity,  $\sigma$ , which is commonly assumed to be dominated by holes, and the deviation from stoichiometry shows that the hole mobility also decreases with  $\Delta$  [19]. It turns out that it is impossible to model the observed oxygen activity dependences of  $\Delta$ ,  $D^*$ , and  $\sigma$  in terms of differently charged cation vacancies and holes, all with composition-independent mobilities. From the currently available experimental data, it is impossible to draw unequivocal conclusions about the exact nature of the cationic defects present in  $Co_{1-\Delta}O$ .

## CONCLUSIONS

A comparison between new non-stoichiometry and cation tracer diffusion data for  $\text{Co}_{1-\Delta}\text{O}$  suggests that if Co ions diffuse via only one type of point defect, the activation energy for motion,  $E_{\text{app}}$ , and the jump frequency,  $\Gamma_{\text{av}}^{\circ}$ , are functions of  $\Delta$ , contrary to common belief. Consequently, the mean mobility of the cationic defects is not independent of  $\Delta$ ; rather it increases with increasing  $\Delta$ . It is still unclear why the ratio of the cobalt tracer diffusion coefficient and the deviation from stoichiometry,  $D_{\text{Co}}^*/\Delta$ , increases with  $\Delta$ . It could be that more than one type of cationic defects is present and contributes to the diffusion of Co, similar as discussed in earlier publications. Changes in their individual contributions to  $\Delta$  with oxygen activity as well as different jump frequencies could be responsible for the trends observed in  $D_{\text{Co}}^*/\Delta$ .

## ACKNOWLEDGEMENTS

We would like to acknowledge the U.S. Department of Energy for support of this work under grant DE-FG02-88ER45357. Furthermore, we thank the Cornell Materials Science Center (supported by the National Science Foundation under Award No. DMR-9121654) for the use of its facilities.

## REFERENCES

- [1] R. E. Carter and F. D. Richardson, *Trans. AIME*, **200**, 1244 (1954).
- [2] I. Bransky and J. M. Wimmer, *J. Phys. Chem. Solids*, **33**, 801 (1972).
- [3] B. Fisher and D. S. Tannhauser, *J. Chem. Phys.*, **44** (4), 1663 (1966).
- [4] N. G. Eror and J. B. Wagner, JR., *J. Phys. Chem. Solids*, **29** 1597 (1968).
- [5] E. Fryt, *Oxid. Met.*, **10** (5), 311 (1976).
- [6] B. Fisher and J.B. Wagner Jr., *J. Appl. Phys.*, **38** (10), 3838 (1967).
- [7] H.-G. Sockel and H. Schmalzried, *Ber. Bunsenges. Phys. Chem.*, **72** (7), 745 (1968).
- [8] U. Hölscher and H. Schmalzried, *Z. Phys. Chem. NF*, **39** 69 (1984).
- [9] S. Aggarwal and R. Dieckmann, *Ceram. Trans.*, **24**, 23 (1991).
- [10] R. Dieckmann, *Z. Phys. Chem. NF*, **107** 189 (1977).
- [11] J. Nowotny and M. Rekas, *J. Am. Ceram. Soc.*, **72** (7), 1199 (1989).
- [12] J. Nowotny and M. Rekas, *J. Am. Ceram. Soc.*, **72** (7), 1207 (1989).
- [13] J. Nowotny and M. Rekas, *J. Am. Ceram. Soc.*, **72** (7), 1215 (1989).
- [14] C.R.A. Catlow and A.M. Stoneham, *J. Am. Ceram. Soc.*, **64** (4), 234 (1981).
- [15] R.W. Grimes, A.B. Anderson and A.H. Heuer, *J. Phys. Chem. Solids*, **48** (1), 45 (1987).
- [16] S.M. Tomlinson, C.R.A. Catlow and J.H. Harding, *J. Phys. Chem. Solids*, **51** (6), 477 (1990).
- [17] P.K. Khowash and D.E. Ellis, *Phys. Rev. B*, **36** (6), 3394 (1987).
- [18] M. Keller and R. Dieckmann, *Ber. Bunsenges. Phys. Chem.*, **89** (8), 883 (1985).
- [19] S. Aggarwal R. Dieckmann and F. Morin, (to be published)
- [20] J. Faber, Jr. and R.L. Hitterman, (1987) (unpublished).

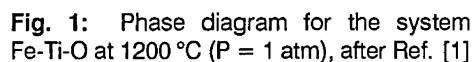


$$(\text{Fe,Ti})_{3-\delta}\text{O}_4$$

Cornell University, Department of Materials Science and Engineering, Bard Hall, Ithaca, NY 14853-1501

Cation diffusion in the spinel solid solution  $(\text{Fe}_{1-x}\text{Ti}_x)_{3-\delta}\text{O}_4$  ( $0 \leq x \leq 0.3$ ) was investigated at 1200 °C as a function of oxygen activity,  $a_{\text{O}_2}$ , and cationic composition,  $x$ . At different cationic compositions, cation tracer diffusion coefficients,  $D_{\text{Me}}^*$ , of  $\text{Me} = \text{Fe}$  and  $\text{Ti}$  were measured as a function of oxygen activity. Plots of  $\log D_{\text{Me}}^*$  vs.  $\log a_{\text{O}_2}$  show V-shaped curves, indicating that different types of point defects prevail at high and low oxygen activities. Thermogravimetric experiments were conducted, using a high resolution microbalance, to determine the deviation from stoichiometry in  $(\text{Fe}_{1-x}\text{Ti}_x)_{3-\delta}\text{O}_4$  at 1200 °C.  $\delta$  versus  $\log a_{\text{O}_2}$  curves are S-shaped. An analysis of the oxygen activity dependences of the cation diffusion coefficients and the deviation from stoichiometry with regard to the point defect structure suggests that at high oxygen activities cation vacancies are the predominant defects governing the deviation from stoichiometry and the diffusion of cations. At low oxygen activities, and at small values of  $x$ , cation interstitials determine the deviation from stoichiometry, while they dominate for  $0 \leq x \leq 0.3$  in the cation diffusion.

This study is part of a more general investigation of the relationships between non-stoichiometry and transport of matter and charge in transition-metal containing spinels. Predominantly, cation tracer diffusion data and deviations from stoichiometry were measured as a function of oxygen activity,  $a_{O_2}$  ( $= P_{O_2}/P^\circ$ ;  $P^\circ = 1$  bar), in quasi-binary and quasi-ternary spinel solid solutions of the type  $(Me, Fe)_{3-\delta}O_4$  ( $Me = Co, Mn$ ). Recently, these studies were extended to  $Me = Cr$  and  $Ti$ . This article focusses on the magnetite-ulvöspinel solid solution  $(Fe_{1-x}Ti_x)_{3-\delta}O_4$ . In the Earths science



community, this solid solution has received considerable attention due to its importance in mineralogical, petrological and paleomagnetic fields. Titaniferous magnetite ores are also a source of iron, though less attractive than nontitaniferous materials. For our investigations we chose the temperature of 1200 °C because of experimental suitability and to enable a comparison with results of previous studies for Me = Co and Mn. A phase diagram for the Fe-Ti-O system at 1200 °C is shown in Fig. 1. This figure is based on a diagram reported in Ref. [1] which is questionable with regard to the stability field of  $\alpha$ -oxide, a matter not of interest here. From Fig. 1 it follows that the width of the oxygen activity range in which  $\delta$  and  $D_{Me}^*$  can be investigated strongly decreases with increasing Ti-content.

The current knowledge of the point defect equilibria of magnetite,  $Fe_{3-\delta}O_4$ , [2] suggests that cation vacancies and cation interstitials should be the majority point defects in  $(Fe_{1-x}Ti_x)_{3-\delta}O_4$ . Based on the defect chemistry of magnetite, it is expected that the deviation from stoichiometry in magnetite-ulvöspinel solid solutions will closely follow the expression

$$\delta = [V_{Me}]^o \cdot a_{O_2}^{2/3} - [Me_i]^o \cdot a_{O_2}^{-2/3}, \quad (1)$$

where  $[V_{Me}]^o$  and  $[Me_i]^o$  are concentrations of cation vacancies and cation interstitials, respectively, normalized to  $a_{O_2} = 1$ . The type of oxygen activity dependence shown in Eq. (1) has been experimentally proven to hold for the deviation from stoichiometry,  $\delta$ , in  $Fe_{3-\delta}O_4$  [2],  $Mn_{3-\delta}O_4$  [3],  $(Fe,Mn)_{3-\delta}O_4$  [4],  $(Co,Mn)_{3-\delta}O_4$  [5],  $(Co,Fe)_{3-\delta}O_4$  [6] and  $(Fe,Co,Mn)_{3-\delta}O_4$  [7].

In this article, first results of our ongoing study of the nonstoichiometry and the diffusion of Fe and Ti for  $T = 1200$  °C are reported. Measurements at other temperatures are currently underway.

## EXPERIMENTS

### Sample Preparation

Polycrystalline samples of  $(Ti_xFe_{1-x})_{3-\delta}O_4$  ( $0 \leq x \leq 0.3$ ) were prepared starting with high purity powders of  $Fe_2O_3$  and  $TiO_2$ . These powders were mixed in appropriate molar ratios, cold-pressed into rods and then sintered at 1300 °C under different controlled atmospheres (selected based on phase stability information) for 5 days to form the spinel phase. To obtain dense samples, a prerequisite for successful tracer diffusion experiments, another processing step was needed. The sintered rods were crushed into powders again using a mortar and pestle and further reduced to micron size powders using a jet mill. These powders were then cold-pressed into rods with a diameter of  $\sim 8$  mm and sintered at 1300 °C, again under controlled atmospheres, for another 5 days. X-ray diffraction was used to confirm the spinel phase and the absence of other phases. 1 mm thick slices were cut from these rods for the tracer diffusion and thermogravimetric measurements.

## Thermogravimetric Measurements

Thermogravimetric studies were conducted at 1200 °C by the successor of the microbalance described in [8]. The resolution and noise level of the microbalance used are of the order of  $1 \cdot 10^{-6}$  g at high temperatures with flowing gases. The oxygen activities were established using different ratios of CO/CO<sub>2</sub> mixed with N<sub>2</sub> in a ratio of 1:9. The oxygen activities were monitored using electrochemical cells with a zirconia-based electrolyte. A reference oxygen activity was used and all oxygen activity jumps were performed relative to this activity and the mass changes,  $\Delta m$ , were recorded. From the  $\Delta m$ -values the corresponding changes in the deviation from stoichiometry were calculated.

## Tracer Diffusion Experiments

Cation tracer diffusion coefficients of Fe and Ti in  $(\text{Fe}_{1-x}\text{Ti}_x)_{3-\delta}\text{O}_4$  were measured simultaneously using the radioactive isotopes Fe-59 and Ti-44. Prior to performing the diffusion experiments, each sample was pre-annealed at a selected oxygen activity to establish the equilibrium point defect concentrations. The sample was then mounted on a stainless steel disk, and, using diamond tools, ground plane-parallel. Finally, it was polished mirror-like on one side. The radioactive tracers, in form of aqueous solutions of chlorides, were applied on the polished side of the sample using syringes in small-sized spots. Afterwards, heating at 200 °C for an hour was used to remove water from the samples. Then a diffusion anneal was performed under the same conditions used for pre-annealing.

The residual activity method was used to determine the diffusion coefficients. The radioactive isotope Ti-44 (half-life:  $10^3$  years) decays into Sc-44 (half-life: 3.9 h) emitting  $\gamma$ -rays with an energy of 1.16 MeV [9]. Fe-59 (half life: 45 d) decays under the emission of  $\gamma$ -rays with energies of 1.10 MeV and 1.29 MeV [9]. A detailed description of the set-up and procedure used in our diffusion experiments is given in [7]. After the diffusion anneal the sample was mounted on a stainless steel disk. To ensure that we did not detect  $\gamma$ -rays from the decay of any Sc-44 that was present during the diffusion anneal, we waited for at least 10 half lives of Sc-44 before measuring diffusion profiles. A typical penetration profile is shown in Fig. 2. At all compositions and oxygen activities investigated at 1200 °C, the depth of the penetration profile of Ti is much shorter than that of Fe, indicating that Fe diffuses much faster than Ti.

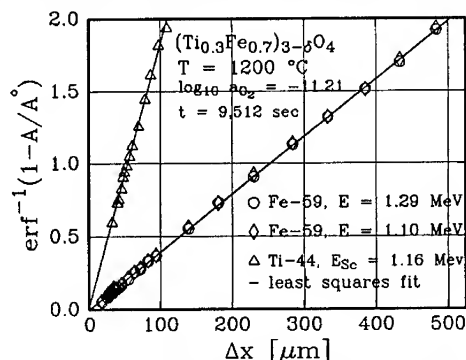


Fig 2: Typical penetration profiles of Fe-59 and Ti-44 obtained from a cation tracer diffusion experiment in  $(\text{Fe}_{1-x}\text{Ti}_x)_{3-\delta}\text{O}_4$ .

## RESULTS AND DISCUSSION

### Thermogravimetry

The measured relative mass changes  $\Delta m$  were converted to  $\Delta\delta$  using the following equation:

$$\Delta\delta = \delta - \delta^\circ$$

$$= \left[ \frac{9 M_{Me}}{4 M_O} + 3 \right] \cdot \frac{\Delta m}{m^\circ}, \quad (2)$$

where  $M_{Me} = x \cdot M_{Ti} + (1-x) \cdot M_{Fe}$ ;  $M_O$  is the atomic weight of oxygen,  $m^\circ$  the mass of the sample used and  $\delta^\circ$  the deviation from stoichiometry at the reference oxygen activity (+ in Fig. 3). Then the  $\Delta\delta$ -values derived for each set of measurements were fit to Eq. (1), leading to absolute values of  $\delta$  and data for

$[V_{Me}]^\circ$  and  $[Me_i]^\circ$ . As an example, experimental data for  $x = 0.1$  and  $T = 1200^\circ\text{C}$  fitted in this way were plotted as a function of oxygen activity in Fig. 3. The solid line shown in addition to the individual data points corresponds to the fit to Eqn. 1. In principle, the solid line is S-shaped. However, the branch at low oxygen activities is not very pronounced and becomes even less prominent with increasing  $x$ . The high oxygen activity branch of the curve is attributed to the presence of cation vacancies as majority defects, and the low oxygen branch to cation interstitials, similar to magnetite [2].

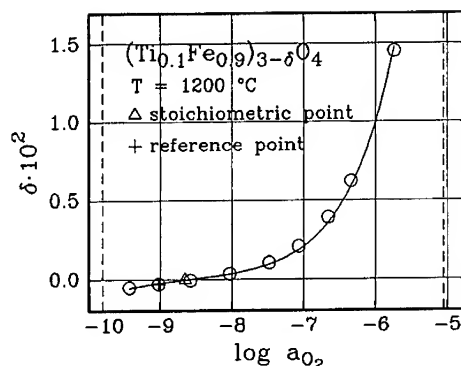


Fig. 3:  $\delta$  in  $(\text{Fe}_{0.9}\text{Ti}_{0.1})_{3-\delta}\text{O}_4$  at  $1200^\circ\text{C}$  as a function of oxygen activity.

### Tracer Diffusion

Values for cation tracer diffusion coefficients were obtained using the expression:

$$\frac{A}{A^\circ} = 1 - \operatorname{erf} \left( \frac{\Delta x}{2\sqrt{D_{Me}^* \cdot t}} \right). \quad (3)$$

This equation can be obtained by integration of the solution of Fick's second law for a very thin film of tracer applied to a sheet of material with infinite thickness.  $A$  is the activity (counts per time) measured when material of the thickness  $\Delta x$  has been removed, i.e., a residual activity, and  $A^\circ$  is this activity before removal of any material.  $D_{Me}^*$  is the tracer diffusion coefficient and  $t$  the diffusion time. It is worth noting that Eqn. (3) is based on the assumption that the absorption of emitted  $\gamma$ -rays in the samples can be neglected; this is true for our case.

The set of  $D_{Me}^*$ -values determined for  $Me = \text{Fe}$  and  $\text{Ti}$  and  $x = 0.1$  at  $1200^\circ\text{C}$  is shown as a function of oxygen activity in Fig. 4. The solid lines drawn through the data points correspond to Eqn. (4) which can be derived by combining diffusion theory with

point defect thermodynamics.

$$D_{Me}^* = D_{Me[V]}^0 \cdot a_{O_2}^{2/3} + D_{Me[I]}^0 \cdot a_{O_2}^{-2/3}, \quad (4)$$

where  $D_{Me[V]}^0$  and  $D_{Me[I]}^0$  are normalized partial tracer diffusion coefficients for diffusion via vacancies and interstitials, respectively. The normalization is to  $a_{O_2} = 1$ . As shown in Fig. 4, the data fall on V-shaped curves. The lines shown were generated by fitting the experimental data to Eq. (4). The observed oxygen activity dependence suggests that at high oxygen activities cations diffuse via cation vacancies and that at low oxygen activities cations diffuse via cation interstitials.

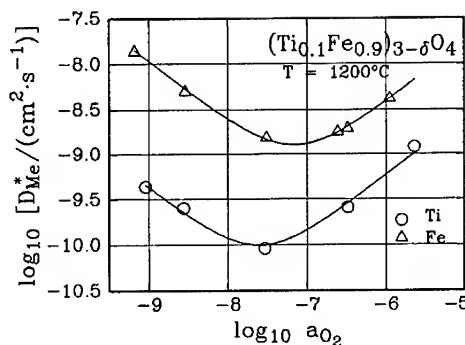


Fig 4:  $D_{Me}^*$  versus  $\log a_{O_2}$  in  $(Fe_{0.9}Ti_{0.1})_{3-\delta}O_4$  at 1200 °C.

A comparison of the data shown in Figs. (3) and (4) shows that although the concentrations of cation interstitials are small, these defects contribute very strongly to the diffusion of Fe and Ti in  $(Fe_{1-x}Ti_x)_{3-\delta}O_4$ . This suggests that the mobilities of cations diffusing via cation interstitials is significantly larger than diffusing via cation vacancies. The fact that the oxygen activities of the minima in the diffusion coefficient isotherms are larger than the oxygen activity where  $\delta = 0$  (inflection point in Fig. 3) is a consequence of these differences in mobility.

The oxygen activity where  $\delta = 0$ , i.e., the spinel is stoichiometric, can be obtained from Eqn. (1) by setting  $\delta = 0$ ; it is given by:

$$a_{O_2}^0 = \left[ \frac{[Me_I]^0}{[V_{Me}]^0} \right]^{3/4}. \quad (5)$$

The corresponding point for  $x = 0.1$  is denoted in Fig. 3 by a triangle.

The values of the constants  $[V_{Me}]^0$  and  $[Me_I]^0$ , see Eq. (1), depend to some extent on the cation distribution among tetrahedral and octahedral sites, because they contain contributions of differently coordinated cation vacancies and of cation interstitials. At constant total pressure, this cation distribution changes with temperature and cationic composition. Unfortunately, the cation distribution data available from the literature were measured on quenched samples, see, for example, Refs. [10] and [11]. A study [12] on the cation distribution in cobalt ferrite has shown cation distributions can be very significantly influenced by quenching rates. Therefore, the in situ cation distribution in  $(Fe_{1-x}Ti_x)_{3-\delta}O_4$  must be considered as unknown. This prevents currently a more detailed analysis of the nonstoichiometry and the cation diffusion in magnetite-ulvöspinel solid solutions.

## SUMMARY

Preliminary results for the non-stoichiometry and cation tracer diffusion in the spinel solid solution  $(\text{Fe}_{1-x}\text{Ti}_x)_{3-2x}\text{O}_4$  as a function of oxygen activity were presented. Data for other temperatures and other cationic compositions will be published in the near future. An analysis of the oxygen activity dependences of the deviation from stoichiometry and the tracer diffusion coefficients of Fe and Ti with regard to point defects suggests that at high oxygen activities cation vacancies are the majority defects and cations diffuse there via them, while at low oxygen activities cation interstitials strongly influence the nonstoichiometry and dominate the cation diffusion. At  $x = 0.1$  the mobilities of cations diffusing via interstitials are larger than those of cations diffusing via cation vacancies.

## ACKNOWLEDGEMENTS

We would like to acknowledge the U.S. Department of Energy for supporting this work under Grant DE-FG02-88ER45357. Furthermore, we thank the Cornell Materials Science Center (supported by the National Science Foundation under Award No. DMR-9121654) for the use of its facilities.

## REFERENCES

- [1] A.H. Webster and N.F.H. Bright, *J. Amer. Ceram. Soc.*, **44** (3), 110 (1961).
- [2] R. Dieckmann, *Ber. Bunsenges. Phys. Chem.*, **86** (2), 112 (1982).
- [3] M. Keller and R. Dieckmann, *Ber. Bunsenges. Phys. Chem.*, **89** (10), 1095 (1985).
- [4] P. Franke and R. Dieckmann, (unpublished).
- [5] F.-H. Lu and R. Dieckmann, *Solid State Ionics*, **67**, 145 (1993).
- [6] F.-H. Lu, S. Tinkler and R. Dieckmann, *Solid State Ionics*, **62**, 39 (1993).
- [7] F.-H. Lu and R. Dieckmann, *Solid State Ionics*, **53-56**, 290 (1992).
- [8] M. Keller and R. Dieckmann, *Ber. Bunsenges. Phys. Chem.*, **89** (8), 883 (1985).
- [9] B.J. Wilson, Ed., *The Radiochemical Manual*, The Radiochemical Center, Amersham, 1966.
- [10] W. O'Reilly, *Rock and Mineral Magnetism*, Blackie & Son. Ltd., Glasgow and London, 1984.
- [11] S.K. Banerjee, W. O'Reilly, T.C. Gibb and N.N. Greenwood, *J. Phys. Chem. Solids*, **28**, 1323 (1967).
- [12] M.R. De Guire, G. Kalonji and R.C. O'Handley, *J. Amer. Ceram. Soc.*, **73** (10), 3002 (1990).

# NONSTOICHIOMETRY AND POINT DEFECT STRUCTURE OF OLIVINES, $(\text{Fe}_x\text{Mg}_{1-x})_2\text{SiO}_4$

TSE-LUN TSAI AND R. DIECKMANN

Cornell University, Department of Materials Science and Engineering, Ithaca, NY 14853

## ABSTRACT

A thermogravimetric study was conducted on synthetic olivines  $(\text{Fe}_x\text{Mg}_{1-x})_2\text{SiO}_4$ , prepared either by a conventional ceramic method or a sol-gel method, to determine the nonstoichiometry and the point defect structure. Measurements were carried out as a function of oxygen activity and cationic composition at elevated temperatures. To avoid the dissolution of transition metal components of the silicate into noble metal containers, commonly used in previous investigations, quartz containers were used. The analysis of the point defect structure of olivines based on the new experimental results is presented.

## INTRODUCTION

Olivines are very important minerals because they are the major components in the upper earth's mantle. The chemical formula of olivines can be represented by the formula  $(\text{Fe}_x\text{Mg}_{1-x})_2\text{SiO}_4$ , where  $0 \leq x \leq 1$ . Some of the physical and chemical properties of olivines are related to point defects. The systematic investigation of the point defect structure and defect-related transport properties of olivines can provide a better understanding of these materials and therefore of the upper mantle.

At present, the basic knowledge on the point defect structure of olivines is still far from complete. Most of the data available in the literature are unreliable. Among these, the nonstoichiometry data obtained by thermogravimetric measurements by Nakamura and Schmalzried<sup>1</sup> are believed to be the most accurate. Unfortunately, noble metal containers were used and samples were in direct contact with these containers during the thermogravimetric measurements. The possible dissolution of the transition metal component Fe into the noble metal container was ignored. As pointed out, for example, by Dieckmann<sup>2</sup>, the degree of the dissolution of transition metal components of oxides into noble metals is oxygen activity dependent and cannot be ignored in thermogravimetric measurements, especially if performed at low oxygen activities. Therefore, the nonstoichiometry data published by Nakamura and Schmalzried<sup>1</sup> and the point defect modelling performed by them are to some extent questionable.

To obtain a better understanding of the nonstoichiometry and point defect structure of olivines, a systematic study of the nonstoichiometry of olivines was performed as a function of oxygen activity, cationic composition and temperature on high purity polycrystalline samples. To avoid the problem of using noble metal containers, special sample holders made of quartz and alumina were used in the thermogravimetric experi-

ments. In this article, results from new nonstoichiometry measurements as a function of oxygen activity and cationic composition at 1130 °C are presented. Possible point defect models compatible with these results are discussed. Furthermore, possible reasons for errors in the nonstoichiometry data published previously are given.

## EXPERIMENTAL PROCEDURES

### A. Sample preparation

Polycrystalline samples were prepared either by a modified sol-gel method or by a conventional ceramic method. The sol-gel method has been described in detail elsewhere<sup>3</sup>. For the conventional ceramic method, appropriate amounts of the starting materials  $\text{Fe}_2\text{O}_3$  (Johnson Matthey, 99.999%),  $\text{MgO}$  (Strem Chemicals, Inc., 99.999%), and  $\text{SiO}_2$  (Strem Chemicals, Inc., 99.999%) were wet-mixed with isopropanol (Fisher, electronic grade) and Teflon® media. After ball-milling for 3 h, the solvent was evaporated by heating at  $\sim 100$  °C. The resulting powder was hydrostatically pressed into a cylindrical rod and sintered at 1100 °C to 1350 °C, depending on the composition, for several days. The compositions of the samples prepared for this investigation were  $x = 1.0, 0.9, 0.8, 0.5, 0.3$ , and  $0.2$ .

Fig. 1 is based on data published by Nitsan<sup>4</sup> and shows the thermodynamic stabilities of olivine phases with different iron content. The upper curves (OSM) define the stability limits for olivines with  $x = 1.0, 0.5$  and  $0.2$  at high oxygen activities,  $a_{\text{O}_2}$  ( $= P_{\text{O}_2}/P^\circ$  with  $P^\circ = 1$  bar), and the lower curves (OSI) define the stability limits for these olivines at lower oxygen activities. The different olivine phases are stable within the oxygen activity ranges between these limits. During sintering, the oxygen activities were established by  $\text{CO}/\text{CO}_2$  gas mixtures with different ratios. To avoid carbon deposition, these  $\text{CO}/\text{CO}_2$  gas mixtures were diluted with  $\text{N}_2$  with a ratio of 1:9. Prior to the thermogravimetric measurements, all samples were examined by X-ray diffraction with a Scintag X-ray diffractometer. Some of the samples were further characterized with an electron microprobe (JOEL 733). Within the resolution of the analytical techniques secondary phases were not observed in the samples.

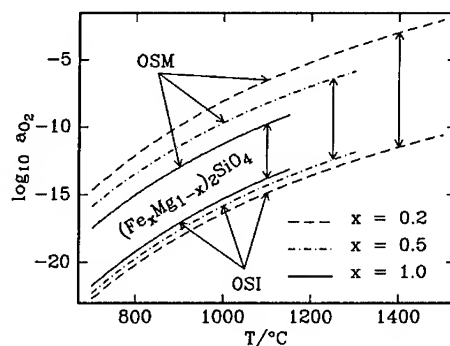


Fig. 1: Temperature dependence of the thermodynamic stability of olivines,  $(\text{Fe}_x\text{Mg}_{1-x})_2\text{SiO}_4$ , according to Nitsan<sup>4</sup>.

### B. Thermogravimetric measurements

The instrument used in the performed in-situ thermogravimetric measurements is a very sensitive, symmetric thermobalance; its resolution and noise level is about  $1 \mu\text{g}$  in



flowing gases at high temperatures. Oxygen activities were monitored by EMF cells. The experimental conditions in this investigation were similar to those in the study made by Nakamura and Schmalzried<sup>1</sup>. The major difference is that sample holders in our study were made of alumina and quartz, instead of Pt-30%Rh crucibles as used by Nakamura and Schmalzried. Several samples of identical composition, with an overall mass between 1 and 2 grams, were placed in a sample holder with an appropriate amount of quartz as a counterweight on the counterbalance holder. During the experiments only the bottom of the sample was in direct contact with quartz. Therefore, the contact between quartz and the stack of samples is minimal and reactions between the samples and the sample holder can be ignored. Mass change measurements were performed as a function of oxygen activity at 1130 °C within the stability fields of the olivines investigated. The oxygen activities were established by mixing CO and CO<sub>2</sub> with different ratios and diluting CO/CO<sub>2</sub> mixtures with N<sub>2</sub> in a ratio 1:9. The total pressure was kept at ~ 0.55 atm to minimize the noise. Mass changes were determined by performing oxygen activity jumps from a reference oxygen activity (given by a CO/CO<sub>2</sub> mixture with a mixing ratio 20/80) to different oxygen activities and backward. The resulting mass changes were recorded and used to calculate changes in the deviation from stoichiometry.

## RESULTS AND DISCUSSION

The experimentally observed mass changes  $\Delta m$  are shown in  $\Delta m$  vs.  $\log_{10} a_{O_2}$  plots for  $(Fe_xMg_{1-x})_2SiO_4$  with  $x = 1.0$  and 0.5 at 1130 °C in Figs. 2a and 2b. For comparison, the experimental data published by Nakamura and Schmalzried<sup>1</sup> are also shown. The details of the experimental results will be described elsewhere<sup>5</sup>. In this article, the deviation from stoichiometry  $\delta$  refers the formula  $(Fe_xMg_{1-x})_2SiO_{4+\delta}$ . Mass changes can be converted into relative changes of the deviation from stoichiometry by using the following relation:

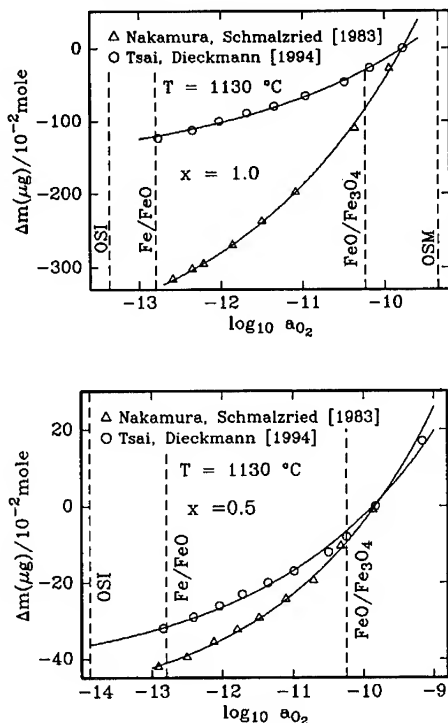


Fig. 2: Plots of experimentally observed mass changes  $\Delta m$  vs.  $\log_{10} a_{O_2}$  for  $10^{-2}$  mole of  $(Fe_xMg_{1-x})_2SiO_4$  at  $T = 1130$  °C, in comparison with data from Ref. 1: (a)  $x = 1.0$  and (b)  $x = 0.5$ .

$$\Delta\delta = \frac{M_{OL}}{M_O \cdot m_{OL}} \cdot \Delta m \quad (1)$$

where  $m_{OL}$ ,  $M_{OL}$ , and  $M_O$  are the actual mass of the olivine sample, the molecular weight of olivine, and the atomic weight of oxygen, respectively. The approach used to convert  $\Delta\delta$  into  $\delta$  was discussed earlier in the literature<sup>6</sup>. By assuming that only one type of majority point defects predominates in the oxygen activity range studied, absolute values for  $\delta$  can be derived by fitting experimental data to the expression

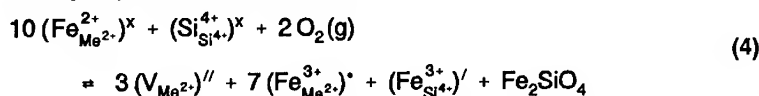
$$\delta = K_2 \cdot a_{O_2}^{1/n} = \Delta\delta + \delta^0 \quad (2)$$

where  $\delta^0$  is the deviation from stoichiometry at the reference oxygen activity. The resulting  $\log_{10} \delta$  vs.  $\log_{10} a_{O_2}$  plots are shown in Fig. 3. It is found that all experimental data for  $\Delta\delta$  can be fit best with  $n = 5.5$  (see Fig. 3) and slightly worse with  $n = 6$ ; these values of  $n$  are somewhat different from the  $n$ -values reported in the literature. Defect models compatible with  $n = 5.5$  and  $n = 6$  will be discussed below.

When, at high temperature, within the stability range of an olivine, the oxygen partial pressure is increased an oxygen uptake occurs. Because the Si:Fe:Mg ratio remains constant this excess oxygen must be incorporated into the lattice. This may happen (i) in  $SiO_4$  tetrahedra or (ii) interstitially. For case (i) the oxygen incorporation requires that some Mg or Fe cations change their coordination, i.e., move to a tetrahedral  $Si^{4+}$  site. For local charge compensation reasons the cations most likely to do this are the  $Fe^{3+}$  ions. The defects active in this case are  $(V_{Me^{2+}})''$ ,  $(Fe_{Si^{4+}}^{3+})'$  and  $(Fe_{Me^{2+}}^{3+2+})^*$ . The electroneutrality condition is

$$2[(V_{Me^{2+}})'] + [(Fe_{Si^{4+}}^{3+})'] = [(Fe_{Me^{2+}}^{3+2+})^*] \quad (3)$$

The component activity dependent defect equilibrium is



This leads to the following expression for the equilibrium constant of reaction (4)

$$K_4 = \frac{a_{Fe_2SiO_4} \cdot [(V_{Me^{2+}})']^3 \cdot [(Fe_{Si^{4+}}^{3+})'] \cdot [(Fe_{Me^{2+}}^{3+2+})^*]^7}{[(Fe_{Me^{2+}}^{2+})^x]^{10} \cdot [(Si_{Si^{4+}}^{4+})^x] \cdot a_{O_2}^2} \quad (5)$$

With the assumption that  $a_{Fe_2SiO_4}$  in an olivine with constant  $x$  does not change significantly with  $\delta$ , it follows for the oxygen activity dependence of  $\delta$ :

$$\delta = \frac{4}{3} [(V_{Me^{2+}})'] = \frac{4}{7} [(Fe_{Me^{2+}}^{3+})^*] = 4 [(Fe_{Si^{4+}}^{3+})'] \propto a_{O_2}^{1/5.5} \quad (6)$$

The excellent description of the experimental nonstoichiometry data by the fit performed with an oxygen activity dependence of  $d \log \delta / d \log a_{O_2} = 1 / 5.5$  suggests that the

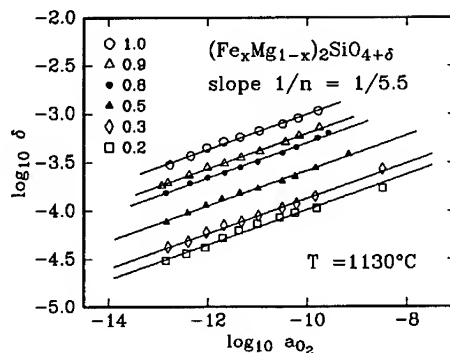
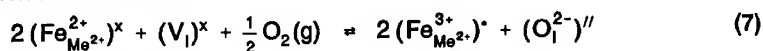


Fig. 3:  $\log_{10} \delta$  vs.  $\log a_{O_2}$  plots for  $x = 1.0$  and  $0.5$  at  $1130^\circ C$ .

majority point defects in the region studied are very likely  $(V_{Me^{2+}})''$ ,  $(Fe_{Si^{4+}}^{3+})'$  and  $(Fe_{Me^{2+}}^{3+2+})^\bullet$ .

However, as mentioned before, it is also possible to fit the experimental data to an oxygen activity dependence of  $d \log \delta / d \log a_{O_2} = 1/6$ . Such a dependence is obtained if one assumes that the oxygen taken up by olivine is accommodated as interstitial oxygen. In this case (ii) the majority point defects are  $(Fe_{Me^{2+}}^{3+2+})^\bullet$  and  $(O_i^{2-})''$ . The defect formation reaction in this case is



The electroneutrality condition reads

$$[(Fe_{Me^{2+}}^{3+})^\bullet] = 2[(O_i^{2-})''] \quad (8)$$

Finally, for the oxygen activity of the deviation from stoichiometry one obtains

$$\delta = [(O_i^{2-})''] \propto a_{O_2}^{1/6} \quad (9)$$

Both  $n = 5.5$  and  $n = 6$  are in very good agreement with the experimental results. Although the fit with  $n = 5.5$  is slightly better than with  $n = 6$ , it is impossible to make an unequivocal conclusion which defect model is physically more appropriate based on the nonstoichiometry data alone. Therefore, we have initiated systematic studies of the iron tracer diffusion and the electrical conductivity on very pure, synthetic olivine single crystals which are in progress. In that work, transport of matter and charge is studied as a function of crystal orientation, oxygen activity, cationic composition and temperature.

As shown in Figs. 2a and 2b, the mass changes of olivines measured in this study are at all compositions smaller than those published by Nakamura and Schmalzried<sup>1</sup>. One possible reason for the larger mass changes observed by these authors may be the non-negligible oxygen activity dependent dissolution of Fe from olivines into the noble metal containers used in their thermogravimetric work. This dissolution may lead to an additional mass change when the oxygen activity is increased and therefore to erroneous nonstoichiometry data. Large additional mass changes may occur if an olivine sample is not phase pure and contains secondary phases, sometimes due to their small concentrations undetectable by X-ray diffraction. For example, we have observed larger mass changes if a small excess of silica was present at  $1.0 > x \geq 0.2$ . Additional mass changes may also occur if other secondary phases are present, for example, iron oxide. Fig. 4 shows a comparison of mass changes observed for a single phase olivine with  $x = 0.5$  and an olivine sample with same composition containing a small amount of excess iron oxide that was undetectable X-ray diffraction. The abrupt mass change observed at  $\log_{10} a_{O_2} = -12.7$ ,

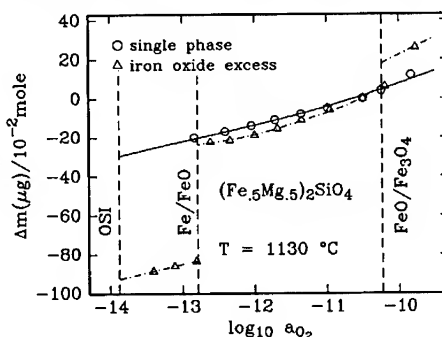


Fig. 4: Comparison of mass changes observed for a single phase olivine with  $x = 0.5$  and a sample with  $x = 0.5$  containing excess iron oxide.

which corresponds to the Fe/FeO phase equilibrium, indicates the presence of the wüstite phase (FeO). The abrupt mass change is caused by the reduction of FeO to Fe. The concentration of FeO present in the sample, calculated from the experimental data, is around  $3.5 \cdot 10^{-2}$  mole %, which is hardly detectable by X-ray diffraction. In the case of the presence of wüstite in olivine samples, the observed mass change is the sum of mass changes caused by nonstoichiometry changes in olivine and wüstite. According to the literature, the relative changes in the nonstoichiometry of wüstite are several orders of magnitude larger than those of olivines. Consequently, even the presence of a very small amount of excess iron oxide can change experimental results significantly.

## CONCLUSIONS

New data have been determined for the deviation from stoichiometry  $\delta$  in olivines,  $(\text{Fe}_x\text{Mg}_{1-x})_2\text{SiO}_{4+\delta}$ , at 1130 °C as a function of oxygen activity,  $a_{\text{O}_2}$ , and composition,  $x$ , by thermogravimetry.  $\delta$  is a measure of point defect concentrations. The experimental results for  $\delta$  for the cationic compositions  $x = 1.0$  and  $0.5$  are well fit with an oxygen activity dependence  $d \log \delta / d \log a_{\text{O}_2}$  of  $1 / 5.5$ , suggesting that the majority defects are cation vacancies, ferric ions on silicon sites, and ferric ions on cationic sites. However, the results can also be fit with an oxygen activity dependence of  $1 / 6$ , suggesting that the majority point defects could also be oxygen interstitials and ferric ions on cationic sites. Based on nonstoichiometry data alone no unequivocal conclusion is possible on the type of majority defects present. Further investigations are needed to determine the type of the predominant defect species.

Errors in nonstoichiometry data published previously are likely caused by the dissolution of Fe from olivine samples into noble metal containers and/or by the presence of secondary phases. The presence of secondary phases, especially of iron oxide, can change experimental results significantly.

## ACKNOWLEDGEMENTS

The authors wish to acknowledge the National Science Foundation for supporting this study through the Cornell Materials Science Center under Grant DMR-8818558.

## REFERENCES

- [1] A. Nakamura and H. Schmalzried, *Phys. Chem. Minerals* **10**, 27 (1983).
- [2] R. Dieckmann, *Solid State Ionics* **45**, 271 (1991).
- [3] T.-L. Tsai, D.A. Robinson, and R. Dieckmann, *J. Mat. Syn. Proc.* **1**, 395 (1993).
- [4] U. Nitsan, *J. Geophys. Res.* **79**, 706 (1974).
- [5] T.-L. Tsai and R. Dieckmann, to be published.
- [6] C. Greskovich and H. Schmalzried, *J. Phys. Chem. Solids* **31**, 639 (1970).

# POINT DEFECTS AND CATION TRACER DIFFUSION IN $(\text{Cr}_x\text{Fe}_{1-x})_{3-\delta}\text{O}_4$ SPINELS

J. TÖPFER, R. DIECKMANN

Department of Materials Science and Engineering, Cornell University, Ithaca, NY 14853-1501, USA

## ABSTRACT

The cation diffusion in the spinel solid solution  $(\text{Cr}_x\text{Fe}_{1-x})_{3-\delta}\text{O}_4$  ( $0 \leq x \leq 0.5$ ) was experimentally investigated at 1200 °C as a function of oxygen activity,  $a_{\text{O}_2}$  ( $= P_{\text{O}_2}/P^\circ$  with  $P^\circ = 1$  bar) and cationic composition,  $x$ . Cation tracer diffusion coefficients,  $D_{\text{Me}}$ , of  $\text{Me} = \text{Co}, \text{Cr}, \text{Fe}$  and  $\text{Mn}$ , were determined using the radioactive isotopes Co-60, Cr-51, Fe-59 and Mn-54. For each cationic composition V-shaped  $\log D_{\text{Me}}^*$  vs.  $\log a_{\text{O}_2}$  plots were obtained. The observed oxygen activity dependences indicate that the cation diffusion is determined by different point defect species prevailing at high and low oxygen activities, respectively. The observed oxygen activity dependences, in comparison with considerations based on point defect thermodynamics, suggest that cations diffuse via cation vacancies at high  $a_{\text{O}_2}$ , while at low  $a_{\text{O}_2}$  cation interstitials prevail in the cation diffusion. In addition, new experimental data for the deviation from stoichiometry  $\delta$  in  $(\text{Cr}_x\text{Fe}_{1-x})_{3-\delta}\text{O}_4$  are presented and discussed.

## INTRODUCTION

Spinel of the system Cr-Fe-O are of technological importance (steel industry, Cr-containing refractories, oxidation of Cr-Fe alloys, etc.) as well as geochemical (e.g., natural chromite deposits) and basic scientific interest. Although the investigation of phase relations in the system Fe-Cr-O at high temperatures has attracted considerable effort, systematic studies on the defect chemistry of spinels of the solid solution  $(\text{Cr}_x\text{Fe}_{1-x})_{3-\delta}\text{O}_4$  and on the diffusion of matter in these materials are still lacking. For the model compound  $\text{Fe}_3\text{O}_4$ , end member of the investigated solid solution ( $x = 0$ ), data on the deviation from stoichiometry, the influence of the defect chemistry on physical properties (e.g., electrical conductivity), and cation diffusion are available in the literature [1-3]. When replacing Fe by Cr one expects a change in the point defect concentrations and cation tracer diffusion coefficients because defect formation energies and mobilities of defects and ions are in general composition dependent. In this study, the tracer diffusion coefficients of Fe, Co, Mn and Cr were measured at 1200 °C as a function of oxygen activity and cationic composition. From the oxygen activity dependence of the diffusion data the

type of point defects governing the cation diffusion process can be derived. Moreover, measurements of the deviation from stoichiometry,  $\delta$ , as a function of the oxygen activity allow the determination of the type and concentration of point defects present. A defect model for the spinel solid solution, combining the results of tracer diffusion studies and nonstoichiometry measurements, will be presented and discussed.

## EXPERIMENTAL

### Sample Preparation

The samples were prepared starting from a mixture of  $\text{Fe}_2\text{O}_3$  and  $\text{Cr}_2\text{O}_3$  powders. After ball milling these powders they were pressed isostatically to small cylinders and sintered at 1300 °C for two days in a nitrogen atmosphere with  $a_{\text{O}_2} \sim 10^{-4}$ . Next, the samples were crushed in a steel mortar, and the grain size of the resulting powder was further reduced using a jet mill. After isostatic pressing the cylinders were sintered at 1300 °C for one week in the nitrogen atmosphere denoted above. After sintering the cylinders were cut into small discs. X-ray diffraction confirmed that the samples were single-phase after sintering.

### Tracer Diffusion Experiments

The tracer diffusion coefficients  $D_{\text{Me}}^*$  of the cations Fe, Co and Mn were measured simultaneously using the radioactive isotopes Fe-59 (1.29 MeV), Co-60 (1.33 MeV) and Mn-54 (0.83 MeV), which emit  $\gamma$ -rays with the energies given in brackets. Before each diffusion run the samples were pre-annealed at the conditions for the subsequent diffusion experiment in order to establish the equilibrium point defect concentrations. The oxygen activity stability limits for the different compositions were taken from the phase diagram of the system Fe-Cr-O at 1200 °C [4] shown in Fig. 1. The analysis of the diffusion was performed with the residual activity method. The analytical expression for the data evaluation has been derived from the solution of the diffusion equation for the case of a thin film and reads:

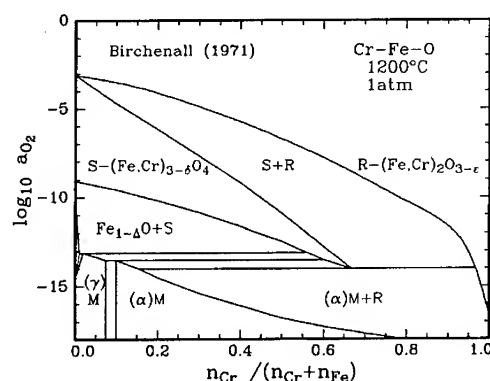


Fig. 1: Phase diagram of the system Fe-Cr-O at 1200 °C according to Birchenall [4].

at 1200 °C [4] shown in Fig. 1. The analysis of the diffusion was performed with the residual activity method. The analytical expression for the data evaluation has been derived from the solution of the diffusion equation for the case of a thin film and reads:

$$\frac{A}{A^0} = 1 - \operatorname{erf} \left( \frac{\Delta x}{2\sqrt{D \cdot t}} \right) \quad (1)$$

Tracer diffusion coefficients of Cr were determined using the isotope Cr-51 (0.32 MeV). Because of the significantly slower diffusion of the Cr tracer ions it was necessary to perform a second diffusion run. The diffusion times were much longer; the resulting penetration depths were only 30 - 40  $\mu\text{m}$ . Fig. 2 shows, as an example, a set of diffusion profiles for  $x = 0.1$ .

#### Nonstoichiometry Measurements

The point defect equilibria causing the deviation from stoichiometry in  $(\text{Cr}_x\text{Fe}_{1-x})_{3-\delta}\text{O}_4$  were investigated, both qualitatively and quantitatively, by thermogravimetric measurements at 1200 °C. A high resolution microbalance (noise level 1  $\mu\text{g}$ , for details see [1]) was used to measure the in-situ mass change in the sample under controlled oxygen activities that were established by  $\text{CO}/\text{CO}_2/\text{N}_2$  gas mixtures. The deviation from stoichiometry, associated with the release or uptake of oxygen, was measured by performing jumps from a reference oxygen activity (+ in Fig. 6) to different oxygen activities. The recorded mass changes were used to calculate changes in the deviation from stoichiometry.

## RESULTS

The results of the cation diffusion studies are shown in Figs. 3-5 for the compositions  $x = 0, 0.1$ , and 0.33. The obtained tracer diffusion coefficients are plotted as function of the oxygen activity. Values of  $D_{\text{Me}}^*$  for  $\text{Me} = \text{Fe}, \text{Co}$  and  $\text{Mn}$  for  $x = 0$  were taken from Ref. [5] and the Cr tracer diffusion coefficients were compared to data from Ref. [3]. The values of  $D_{\text{Me}}^*$  for  $x = 0$  obtained in this study agree very

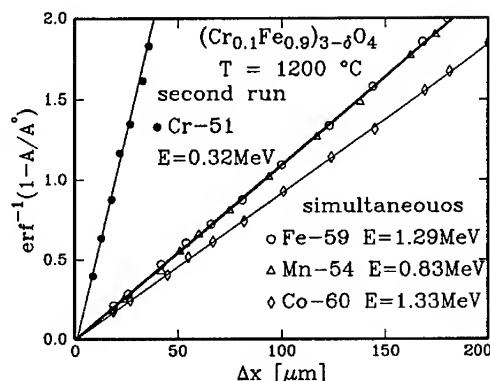


**Fig. 2:** Example of diffusion profiles for  $(\text{Cr}_{0.1}\text{Fe}_{0.9})_{3-\delta}\text{O}_4$  at  $T = 1200\text{ }^\circ\text{C}$ , a) simultaneous measurement of Fe-59, Mn-54, Co-60:  $\log a_{\text{O}_2} = -9.16$ ,  $t = 2623\text{ s}$ , b) measurement of Cr-51 in a second step:  $\log a_{\text{O}_2} = -8.86$ ,  $t = 308743\text{ s}$ .

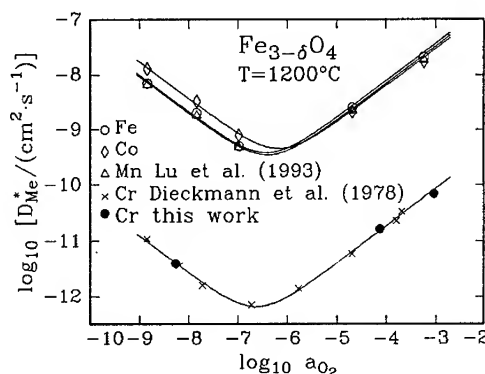


**Fig. 3:** Cation tracer diffusion coefficients of Fe, Co, Mn and Cr for  $x = 0$  at 1200 °C.

well with the earlier reported data points.

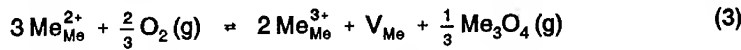
Results of the nonstoichiometry measurements,  $\delta$ , are shown as a function of oxygen activity for  $x = 0.1$  in Fig. 6. The mass changes measured in the thermobalance were transformed into changes of the nonstoichiometry  $\delta$  by using the following equation:

$$\Delta \delta = \frac{\Delta m}{m^0} \cdot \left( \frac{9 M_{Me}}{4 M_O} + 3 \right) \quad (2)$$

$m^0$  is the initial mass of the sample and  $M_{Me}$  refers to the mean molar mass of the cations.

## DISCUSSION

The defect formation equilibria which have been shown to be valid in  $Fe_3O_4$  [1-3] are expected to be similar for the solid solution  $(Cr_x Fe_{1-x})_3O_4$ . The anionic sublattice is assumed to be perfect and not to take part in defect formation processes. The formation of cation vacancies may be described by the following reaction:



Hence, the vacancy concentration can be expressed as:

$$[V_{Me}] = \frac{K_V}{4} \cdot a_{O_2}^{2/3} = [M]^0 \cdot a_{O_2}^{2/3} \quad (4)$$

Cation interstitials are formed via Frenkel defect formation



leading to an oxygen activity dependence of the interstitial concentration of the form

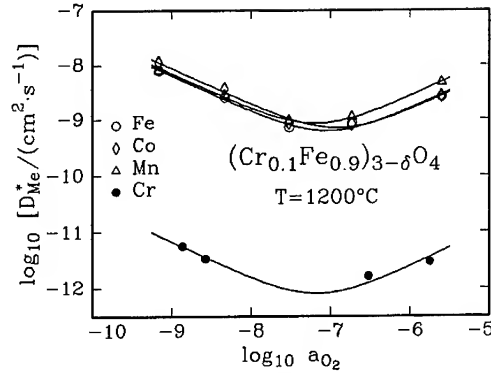


Fig. 4: Cation tracer diffusion coefficients of Fe, Co, Mn and Cr for  $x = 0.1$  at 1200 °C.

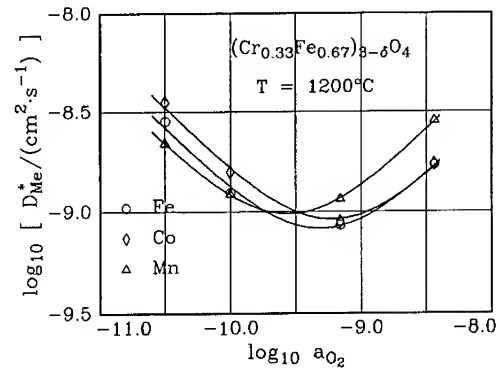


Fig. 5: Cation tracer diffusion coefficients of Fe, Co, Mn for  $x = 0.33$  at 1200 °C.



$$[Me_i^{n+}] = [I]^o \cdot a_{O_2}^{-2/3} \quad (6)$$

Taking into account both defect formation reactions, the deviation from stoichiometry can be written as

$$\begin{aligned} \delta &= [V_{Me}] - [Me_i^{n+}] \\ &= [V]^o \cdot a_{O_2}^{2/3} - [I]^o \cdot a_{O_2}^{-2/3} \end{aligned} \quad (7)$$

$[V]^o$  and  $[I]^o$  are normalized cation vacancy and interstitial concentrations, respectively. The oxygen activity dependence of the tracer diffusion coefficient was derived in Ref. [3] as

$$D_{Me}^* = D_{Me[V]}^* + D_{Me[I]}^* = D_{Me[V]}^o \cdot a_{O_2}^{2/3} - D_{Me[I]}^o \cdot a_{O_2}^{-2/3}, \quad (8)$$

$D_{Me[V]}^o$  and  $D_{Me[I]}^o$  being normalized partial cation tracer diffusion coefficients of the cation diffusion via vacancies and interstitials; they are normalized to  $a_{O_2} = 1$ . The experimentally determined values of the individual tracer diffusion coefficients were fitted as a function of the oxygen activity according to Eq. (8). V-shaped curves were obtained for the tracer diffusion coefficients, see Figs. 3-5. The slope  $d \log D_{Me}^* / d \log a_{O_2}$  is  $2/3$  in the higher oxygen activity range, indicating that cation vacancies are dominant in the cation diffusion. At lower oxygen activities the slope is equal to  $-2/3$ . This means that interstitials prevail in the diffusion of cations at low oxygen activities. At the minimum of the  $\log D_{Me}^*$  vs.  $\log a_{O_2}$  curves cation vacancies and cation interstitials contribute equally to the cation diffusion. The results of the measurements of the nonstoichiometry were plotted according to Eq. (7). As an example one plot for  $x = 0.1$  is shown in Fig. 6. The obtained plot for  $\delta$  versus  $\log a_{O_2}$  is S-shaped indicating cation vacancies to be the dominant defects at higher oxygen activities while at lower oxygen activities cation interstitials are the majority point defects. These findings confirm the interpretation of the diffusion results. Moreover, the results show that, in principle, the same defect formation processes as for  $Fe_3O_4$  hold in this solid solution (at least in the composition range investigated). Finally, the inflection point of the S-shaped curve in Fig. 6 (●) is at  $\delta = 0$ .

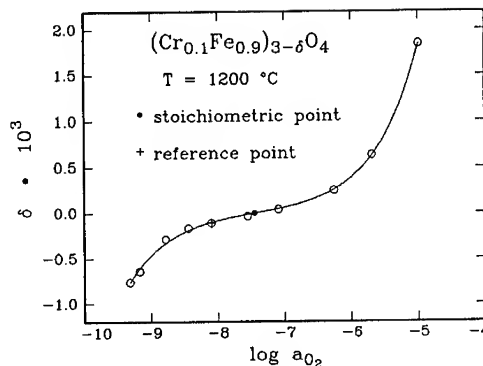


Fig. 6: Deviation from stoichiometry vs. oxygen activity for  $x = 0.1$  at  $1200^\circ\text{C}$ .

## ACKNOWLEDGEMENTS

We would like to thank the U.S. Department of Energy for support of this work under Grant No. DE-FG02-88ER45357. One of the authors (J. T.) is grateful for a scholarship of the Deutsche Forschungsgemeinschaft. Furthermore, we thank the Cornell Materials

Science Center (supported by the National Science Foundation under Award No. DMR-9121654) for the use of its facilities.

## REFERENCES

- [1] R. Dieckmann, Ber. Bunsenges. Phys. Chem. **86**, 112 (1982).
- [2] R. Dieckmann, C.A. Witt and T.O. Mason, Ber. Bunsenges. Phys. Chem. **87**, 495 (1983).
- [3] R. Dieckmann, T.O. Mason, J.D. Hodge and H. Schmalzried, Ber. Bunsenges. Phys. Chem. **82**, 778 (1978).
- [4] C.E. Birchenall, Oxidation of Metals and Alloys, ASM Monographs, Metals Park 1971, p. 193.
- [5] F.H. Lu, S. Tinkler and R. Dieckmann, Solid State Ionics **62**, 39 (1993).

## CALCULATION OF DEFECT FORMATION ENERGY FROM THE THERMAL EXPANSION DATA FOR LEAD FLUORIDE

BRENDA J. SCHULER\*, T. S. AURORA\*<sup>A</sup>, D. O. PEDERSON\*\*<sup>B</sup>, S. M. DAY\*\*\*<sup>C</sup>

\*Philadelphia College of Pharmacy and Science, Philadelphia, PA 19104

\*\*University of Arkansas, Fayetteville, AR 72701

\*\*\*Miami University, Oxford, OH 45056

### ABSTRACT

Lead fluoride is a superionic conductor with the fluorite structure. Results of the measurement of linear thermal expansion of lead fluoride (reported earlier in literature) showed a large increase in the thermal expansion coefficient near 700 K where the ionic conductivity has been shown to exhibit a sharp increase. It is believed that thermally-generated defects in a crystal lattice affect the thermal expansion coefficient. This idea was applied in the present analysis to calculate the defect formation energy ( $E_f$ ) by using the literature values of the coefficient of thermal expansion. It was assumed that the thermal expansion in excess of that produced due to the lattice anharmonicity ( $\Delta\alpha$ ) is proportional to the concentration of defects ( $n$ ). With this assumption, one may write:  $\Delta\alpha = c n_0 \exp(-E_f/kT)$ , where  $c$  is a constant. For lead fluoride, a plot of  $\ln(\Delta\alpha)$  versus  $(1/T)$  yielded  $E_f = 0.56$  eV which is lower than the literature values. The assumptions in this analysis and the discrepancy in the result are discussed.

### INTRODUCTION

Lead fluoride ( $\text{PbF}_2$ ) is a crystal with the fluorite structure. It is a material characterized by a stable structure, melting point above 1000 K, and an absence of crystallographic phase transitions at atmospheric pressures and room temperatures [1]. It is optically transparent and finds applications in optical components [2]. It becomes highly ion-conducting above 710 K where it is believed to undergo a diffuse transition [3]. Measurements of the temperature coefficients of linear thermal expansion of lead fluoride indicate a large increase near the temperature where the ionic conductivity increases rapidly [4-6]. A similar decrease in the attenuation coefficient of ultrasonic waves was observed near 715 K [7], and it was attributed to the sample undergoing superionic phase transition.

### THEORY

Using the data obtained by x-ray scattering experiment, Cartz [8] demonstrated that there existed "some kind" of law of corresponding states for the metals. It was found that the data for the thermal expansion of metals, after suitable normalization, followed a "common curve". Pathak and Vasavada [9, 10] found considerable deviation from the "common curve" behavior when thermal expansion measurements were extended to higher temperatures in alkali halides. At higher temperatures, the coefficient of thermal expansion ( $\alpha$ ) was found to be larger than its

values ( $\alpha_{anh}$ ) expected from lattice anharmonicity effects. This departure was attributed to the formation of defects in the alkali halide crystal lattices. By assuming that the excess thermal expansion  $\Delta\alpha$  ( $= \alpha - \alpha_{anh}$ ) was proportional to the concentration of lattice defects ( $n$ ), defect formation energy was calculated. With this assumption,

$$\Delta\alpha = c n, \quad (1)$$

where  $c$  is a constant. The defect concentration ( $n$ ) varies with temperature as

$$n = n_0 e^{-E_f/kT}, \quad (2)$$

where  $k$  is the Boltzmann constant and  $E_f$  is the defect formation energy. Combining equations (1) and (2), and taking logarithm, it follows that

$$\ln(\Delta\alpha) = \ln(c n_0) - E_f/(kT), \quad (3)$$

If  $E_f$  is assumed to be independent of temperature, a plot of  $\ln(\Delta\alpha)$  as a function of  $(1/T)$  will yield a straight line having a slope of  $(-E_f/k)$ . This yields an activation energy  $E_f = -k(\text{slope})$ .

## DATA ANALYSIS

The experimental data [6] being analyzed is shown in Figure 1. The solid line is a linear fit to the data points between 354 K and 549 K and represented by

$$\alpha (10^{-6}/K) = 24.13 + (0.02648) T. \quad (4)$$

This line is the assumed variation of the coefficient of expansion due to the lattice anharmonicity before the concentration of defects becomes significant. The excess thermal expansion ( $\Delta\alpha$ ) is the difference in the extrapolated values of expansion (solid line) and the actual experimental data shown in Figure 1, and is shown in Figure 2. Only the data below the transition point ( $\sim 705$  K) is analyzed by this method.

Figure 3 shows a plot of the natural logarithm of the excess expansion (shown in Figure 2) as a function of the inverse temperature. The activation energy,  $E_f$ , was calculated from the slope of a linear fit through the points shown in Figure 3.  $E_f$  was found to be 0.56 eV over the range 560 - 705 K.

## DISCUSSION

Table I shows the literature values of  $E_f$  for lead fluoride over several temperature ranges. The value of  $E_f$  found in the present analysis is seen to be lower than the literature values for temperatures below the phase transition ( $\sim 705$  K). This discrepancy may be partly due to the scatter in the thermal expansion data used in this work. In addition, the assumption that the activation energy is independent of temperature may not be valid in this case [12].

It has also been suggested that the thermal expansion may have more complex dependence on the defect concentration than that assumed (equation 1) in this work [11]. When a "common curve" behavior was studied for lead fluoride, calcium fluoride, and barium fluoride, the departure from it was very large near the transition temperature. This analysis worked for the alkali halides because these materials are not superionic conductors and the defect concentration remains at the ppm level at elevated temperatures. On the other hand, the defect concentration in superionic conductors, such as lead fluoride, is very large in the conducting regime and the formation energy decreases with temperature (Table I). Therefore, the simple analysis of Pathak and Vasavada [9, 10] may not be applicable in the case of superionic lead fluoride.

A similar analysis of the data above 705 K, yielded  $E_f = -1.9$  eV. A negative activation energy is not physically meaningful. Therefore, one must exercise caution in using this method for obtaining activation energies. The conductivity data is well established, and leads to a more reliable determination of defect concentration and formation energies.

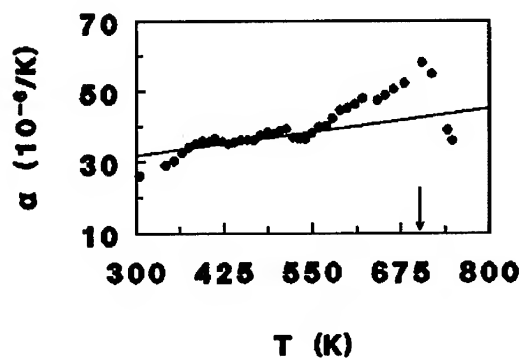


**Figure 1.** Coefficient of thermal expansion as a function of temperature. The solid line is a linear fit through the data up to 549 K. The arrow indicates the temperature corresponding to the transition to the superionic state.

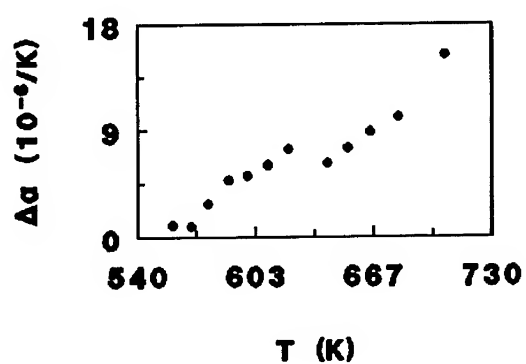


Figure 2. The excess thermal expansion as a function of temperature.

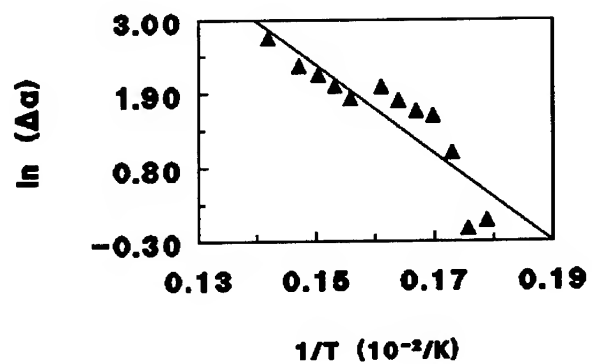


Figure 3. Natural log of the excess thermal expansion as a function of the inverse temperature. The line is a linear fit through the data.

**Table I. Literature values of the activation energy,  $E_r$ , of lead fluoride.**

Region (K)	Technique	$E_r$ (eV)	Reference
390-550	conductivity	0.75	13
	conductivity	0.59	14
	conductivity	0.66	15
	conductivity	0.75	16
	conductivity	0.73	17
	conductivity	0.67	18
	conductivity	0.65	19
	conductivity	0.70	20
	dielectric loss	0.72	21
	nmr	0.74	22
	nmr	0.73	23
	nmr	0.70	24
550-720	conductivity	1.12	13
	conductivity	1.10	14
	conductivity	1.15	15
	conductivity	0.92	16
	conductivity	1.03	17
	conductivity	0.88	19
	conductivity	1.05	20
	nmr	1.00	22
	dielectric loss	0.99	14
720 -	thermal expansion	0.56	This work
	conductivity	0.25	16
	conductivity	0.30	19
	nmr	0.20	21

#### ACKNOWLEDGMENTS

The authors (TSA, BJS) would like to thank Philadelphia College of Pharmacy and Science for research support, and Dr. R. P. Marande for his encouragement.

## REFERENCES

- A. Author for all correspondence.
1. *Crystals with the Fluorite Structure*, edited by W. Hayes (Clarendon, Oxford, 1974), p 111.
2. R. J. Harris, G. T. Johnston, G. A. Kepple, P. C. Krok and H. Mukai, *Appl. Opt.* **16**, 436 (1977).
3. J. B. Boyce and B. A. Huberman, *Phys. Rep.* **51**, 189 (1979).
4. R. B. Roberts and G. K. White, *J. Phys. C* **19**, 7167 (1986).
5. G. K. White, *J. Phys. C* **13**, 4905 (1980).
6. T. S. Aurora, D. O. Pederson and S. M. Day, *Phys. Rev B* **41**, 9647 (1990).
7. M. O. Manasreh, D. O. Pederson and T. S. Aurora, *Mat. Res. Soc. Symp. Proc.* **135**, 309 (1989).
8. L. Cartz, *Proc. Phys. Soc. (London) B* **68**, 957 (1955).
9. P. D. Pathak and N. G. Vasavada, *J. Phys. C* **3**, L44 (1970).
10. P. D. Pathak and N. G. Vasavada, *J. Phys. C* **3**, L77 (1970).
11. J. Oberschmidt, *Phys. Rev. B* **23**, 5038 (1981).
12. T. S. Aurora, Ph.D. dissertation, University of Arkansas, 1983.
13. J. M. Oberschmidt and D. Lazarus, *Phys. Rev. B* **21**, 2952 (1980).
14. S. Palchoudhuri and G. K. Bichlie, *Solid State Comm* **69**, 271 (1989).
15. J. H. Kennedy, R. Miles, and J. Hunter, *J. Electrochem. Soc.* **120**, 1441 (1973).
16. A. Azimi, V. M. Carr, A. V. Chadwick, F. G. Kirkwood, and R. Saghafian, *J. Phys. Chem. Solids* **45**, 23 (1984).
17. G. A. Samara, *J. Phys. Chem. Solids* **40**, 509 (1979).
18. R. W. Boone and J. Schoonman, *J. Electrochem. Soc.* **124**, 28 (1977).
19. R. Benz, *Z. Phys. Chem. (Frankfurt)* **95**, 25 (1975).
20. J. Schoonman, G. J. Dirksen, and G. Blasse, *J. Solid State Chem.* **7**, 245 (1973).
21. G. A. Samara, *Phys. Rev. B* **13**, 4529 (1976).
22. J. B. Boyce, J. C. Mikkelsen, Jr. and M. O'Keefe, *Solid State Comm.* **21**, 955 (1977).
23. T. Y. Hwang, M. Englesberg, and I. J. Lowe, *Chem. Phys. Lett.* **30**, 303 (1975).
24. R. E. Gordon and J. H. Strange, *J. Phys. C* **11**, 3212 (1978).



---

## PART V

---

### **Solid Electrolytes**

## IMPROVED OXIDE ION ELECTROLYTES

MAN FENG AND JOHN B. GOODENOUGH

Center for Materials Science and Engineering, ETC 9.102,  
The University of Texas at Austin, Austin, TX 78712-1063

### ABSTRACT

Systematic experiments on anion-deficient  $\text{ABO}_{3-\delta}$  perovskites are reviewed with a view to the development of a strategy for the design of improved oxide-ion electrolytes.  $\text{Ba}_{0.6}\text{La}_{0.4}\text{InO}_{2.7}$  is shown to be competitive with the best yttria-stabilized zirconia and  $\text{La}_{0.9}\text{Sr}_{0.1}\text{Ga}_{0.8}\text{Mg}_{0.2}\text{O}_{2.85}$  to be a superior oxide-ion electrolyte suitable for fuel-cell applications.

### INTRODUCTION

An electrolyte is an ionic conductor and an electronic insulator. Solid oxide-ion electrolytes are used in both open-circuit and power applications; sensors represent the former and fuel cells the latter. In both types of application, the electrolyte is in the form of a thin membrane in order to minimize the internal resistance

$$R = L / \sigma_o A \quad (1)$$

of the device, where  $L$  is the thickness of the membrane of area  $A$  and  $\sigma_o$  is the oxide-ion conductivity. One measure of the quality of an oxide-ion electrolyte material is the magnitude of  $\sigma_o$ , another is the ease of its fabrication as a thin, large-area membrane. For power applications, a  $\sigma_o > 10^{-2}$  S/cm at the operating temperature  $T_{op}$  is generally needed, and one goal of the designer of an oxide-ion electrolyte is a lowering of  $T_{op}$ .

The oxide-ion conduction through the electrolyte is designed to match the electron transfer associated with chemical processes occurring at the two surfaces of the membrane. Any electronic conduction through the membrane reduces the efficiency of the device, so another measure of the quality of the electrolyte is the transport number, which is defined as the ratio of the conductivity of the working ion (the oxide ion in our case) to the total conductivity  $\sigma = \sigma_o + \sigma_e \dots$  of the membrane:

$$t_o = \sigma_o / \sigma \quad (2)$$

where  $\sigma_e$  is the electronic conductivity. A  $t_o \approx 1$  is desired. Where the membrane must operate at high temperatures in an oxidizing atmosphere on one side and a reducing atmosphere on the other, as in a fuel cell, this requirement constrains the choice of material to an electronic insulator with a large energy gap  $E_g$ . The electrolyte must have its energy-gap "window" matched to the chemical reactants providing electron transfer at the surfaces of the electrolyte membrane; i.e. the bottom of the conduction band must be above the HOMO of the reductant and the top of the valence band must be below the LUMO of the oxidant. Since oxide-ion electrolytes are oxides, this constraint is normally satisfied for fuel-cell applications where  $E_g$  is large enough to retain a  $t_o \approx 1$  at  $T_{op}$ .

Anion conduction occurs within a fixed cation array. Faraday<sup>1</sup> first discovered fast anion conduction in  $\text{PbF}_2$ , which has the fluorite structure with a fixed face-centered-cubic  $\text{Pb}^{2+}$  ion array within which the  $\text{F}^-$  ions are mobile at high temperatures. The oxide-ion electrolytes used commercially today consist of zirconia stabilized in the oxygen-deficient fluorite structure by addition of  $\text{CaO}$ ,  $\text{Y}_2\text{O}_3$  or  $\text{Ln}_2\text{O}_3$  ( $\text{Ln}$  = rare earth). These oxides require a  $T_{op} \geq 1000^\circ\text{C}$  not only because the phenomenological oxide-ion conductivity,

$$\sigma_o = (A/T) \exp(-E_a/kT) \quad (3)$$

contains an activation energy  $E_a \approx 1.0$  eV, but also because  $\sigma_o$  deteriorates with time (ages) if maintained at temperatures  $700 < T < 1000^\circ\text{C}$ . At a  $T_{op} \approx 1000^\circ\text{C}$ , chemical reactions between the electrolyte and the metallic-oxide cathode have plagued fuel-cell development. Clearly a superior oxide-ion electrolyte is needed.

Any search for an improved oxide-ion electrolyte begins with the choice of an alternate fixed cation array within which the oxide ions can move. We report here on experiments with anion-deficient perovskites  $\text{ABO}_{3-\delta}$ ; these perovskites contain a CsCl-type array of the A and B cations. In cubic  $\text{ABO}_3$  perovskites, the B cations occupy the octahedral sites of an array of corner-sharing oxygen octahedra and the larger A cations have twelvefold oxygen coordination. In the fluorite structure, each cation is coordinated by 8 anions.

## PHENOMENOLOGY

The oxide ions move diffusely through the cation sublattice, so the oxide-ion mobility is given by the Nernst-Einstein relation

$$\mu_o = qD/kT \quad (4)$$

where  $q = -2e$  is the charge carried by an  $\text{O}^{2-}$  ion and the diffusion coefficient  $D = D_o \exp(-\Delta G_m/kT)$  contains the motional free energy  $\Delta G_m = \Delta H_m - T\Delta S_m$ . If the creation of mobile oxide ions requires an activation energy  $\Delta H_i$ , then

$$E_a = \Delta H_m + (1/2)\Delta H_i \quad (5)$$

in Equation (3). As has been pointed out elsewhere<sup>2</sup>, vacancy ordering in a stoichiometric anion-deficient compound creates a

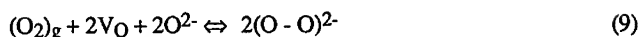
$$\Delta H_i = \Delta H_g(0) - c\varepsilon \quad (6)$$

where  $c = n/N$  is the fraction of energetically equivalent sites occupied by the mobile ions and  $\varepsilon$  is a measure of the decrease in the splitting  $\Delta H_g$  between ordered vacancies and similar occupied sites due to excitation of mobile ions into the vacancy array. Complete disorder collapses the splitting  $\Delta H_g$ , and the strong positive feedback built into Equation (6) can lead to a first-order order-disorder transition at a temperature  $T_t$ . Short-range order persisting above  $T_t$  may prevent complete collapse of  $\Delta H_g$  on traversing  $T_t$ , but measurement of  $E_a$  above  $T_t$  provides an upper limit of the motional enthalpy  $\Delta H_m$ . This procedure was used<sup>3</sup> to determine a  $\Delta H_m < 0.6$  eV in the stoichiometric perovskite  $\text{Ba}_2\text{In}_2\text{O}_5$ ; an  $E_a \approx 0.6$  eV would be small enough to give a  $\sigma_o > 10^{-2}$  S/cm at a  $T_{op} = 500^\circ\text{C}$ . A first-order transition at  $T_t \approx 930^\circ\text{C}$  prevents use of  $\text{Ba}_2\text{In}_2\text{O}_5$  as a solid electrolyte, and a doping strategy was employed to suppress the first-order transition.

Substitution of an aliovalent cation for either  $\text{Ba}^{2+}$  or  $\text{In}^{3+}$  in  $\text{Ba}_2\text{In}_2\text{O}_5$  not only disorders -- at least at long-range -- the oxygen vacancies, it also introduces point centers that trap by  $\Delta H_i$  mobile ions introduced into the vacancy array. Consequently Equation (5) contains a

$$\Delta H_i = \Delta H_t + \Delta H_g \quad (7)$$

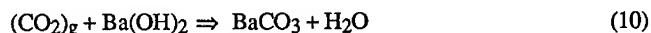
that is not negligible even though the change from long-range to short-range order sharply reduces the effective  $\Delta H_i$ . Moreover, disordering of the oxygen vacancies makes the vacancies more accessible to water or oxygen from the atmosphere via the reactions



where  $\text{V}_\text{O}$  is a bulk oxygen vacancy. Such reactions are always associated with surface oxygen vacancies on oxides,<sup>4</sup> and migration of  $\text{H}^+ + \text{OH}^-$  ions into the bulk is relatively easy where thermodynamics would stabilize occupancy of the vacancies under the condition that overall charge neutrality is preserved. Strategies for aliovalent cation substitution to suppress long-range vacancy ordering must avoid the introduction of neutral oxygen species into the bulk.

## RESULTS

Oxide-ion conduction in cubic perovskites was first studied by Steele *et al*<sup>5</sup> and by Takahashi and Iwahara;<sup>6</sup> later studies<sup>7</sup> encountered proton conduction at lower temperatures in oxygen-deficient  $\text{A} = \text{Ba}$  or  $\text{Sr}$  perovskites containing  $\text{B} = \text{Zr}$ ,  $\text{Ce}$ , or  $\text{Hf}$  partially substituted by trivalent ions, and the absorption of water by the disordered vacancies in the system  $\text{BaIn}_{1-x}\text{Zr}_x\text{O}_{2.5+0.5x}$  was clearly demonstrated.<sup>8</sup> An attempt to substitute  $\text{Y}$  for  $\text{In}$  in  $\text{Ba}_2\text{In}_2\text{O}_5$  led to the compound  $\text{Ba}_3\text{Y}_4\text{O}_9$ , which could be stabilized at room temperature by quenching from high temperature; but this compound was found to decompose to  $\text{BaCO}_3$  and  $\text{Y}_2\text{O}_3$  via the intermediate composite consisting of a  $\text{Ba}(\text{OH})_2 + \text{BaCO}_3$  mixture in  $\text{Y}_2\text{O}_3$ ; above the melting temperature of the mixture, the melt was immobilized by the  $\text{Y}_2\text{O}_3$  and gave a remarkable protonic conductivity that deteriorated as the reaction



proceeded to completion.<sup>9</sup>

These data suggested to one of us<sup>8</sup> that  $\text{B}$  cations that are unstable in less than sixfold oxygen coordination attract water from the environment into neighboring anion vacancies even where anions are available to them from the neighborhood of a  $\text{B}$  cation such as  $\text{In}^{3+}$  that is stable in fourfold or sixfold coordination. If this were the only reason for water absorption, then substitution of  $\text{In}^{3+}$  by a ferroelectric ion like  $\text{Nb}^{5+}$  or  $\text{Ti}^{4+}$  in  $\text{Ba}_2\text{In}_2\text{O}_5$  could be expected to suppress long-range vacancy ordering without the accompanying absorption of water. However, substitution of  $\text{Nb}$ ,  $\text{Ti}$ , or  $\text{Sn}$  for  $\text{In}$  in  $\text{Ba}_2\text{In}_2\text{O}_5$  resulted in water absorption below  $500^\circ\text{C}$  just as in the case of the substitution of  $\text{In}$  by  $\text{Zr}$ .<sup>10</sup>

Fig. 1 shows an Arrhenius plot of the total conductivity of  $\text{Ba}_2\text{In}_{2-x}\text{Ti}_x\text{O}_{5+0.5x}$  for several  $\text{Ti}$  concentrations, and Fig. 2 shows the evolution with indium concentration of the cubic-perovskite lattice constants. The change in slope of the  $\log \sigma$  vs  $1/T$  curve reflects a change from predominantly protonic to predominantly oxide-ion conduction as water is lost at higher temperatures. Such behavior is typical of perovskites containing absorbed water at lower temperatures.<sup>11</sup> The deviation from Végard's law in this system, Fig. 2, reflects a decreasing water content with decreasing lattice parameter, as is also evident from the larger low-temperature protonic conduction for  $x = 0.4$ .

From these data we concluded that coordination of the large  $\text{Ba}^{2+}$  ion in less than twelvefold oxygen coordination must also play a significant role in the attraction of water to the oxygen vacancies provided the lattice parameter exceeds a critical size. Two experiments were performed to test this conclusion.

First, we performed thermogravimetric analysis (TGA) on  $\text{Ba}_2\text{In}_2\text{O}_5$  with a scanning rate of  $2^\circ\text{C}/\text{min}$  in both dry air and wet nitrogen. In this compound, only  $\text{In}^{3+}$  ions stable in either octahedral or tetrahedral oxygen coordination are found on the  $\text{B}$  sites. Nevertheless Fig. 3 shows there is absorption of water into the oxide-ion vacancies below  $300^\circ\text{C}$ .

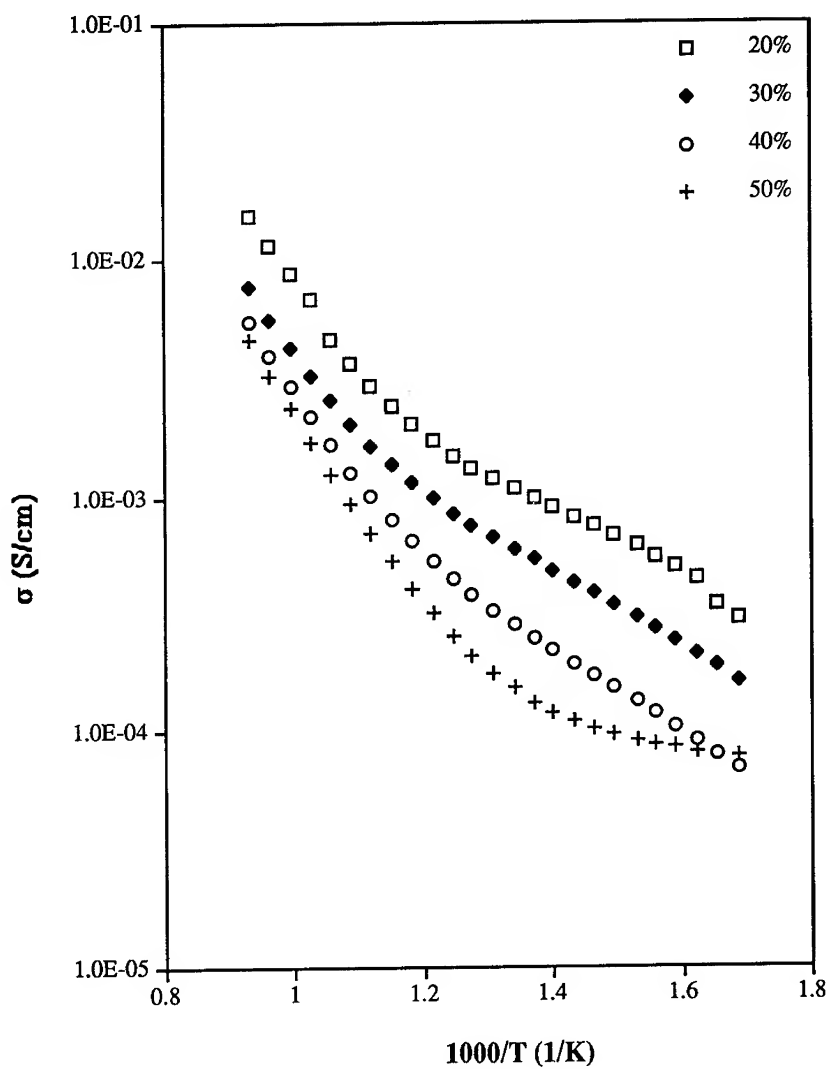


Fig. 1: Conductivity of Ti-doped Ba<sub>2</sub>In<sub>2</sub>O<sub>5</sub> for various Ti concentrations.

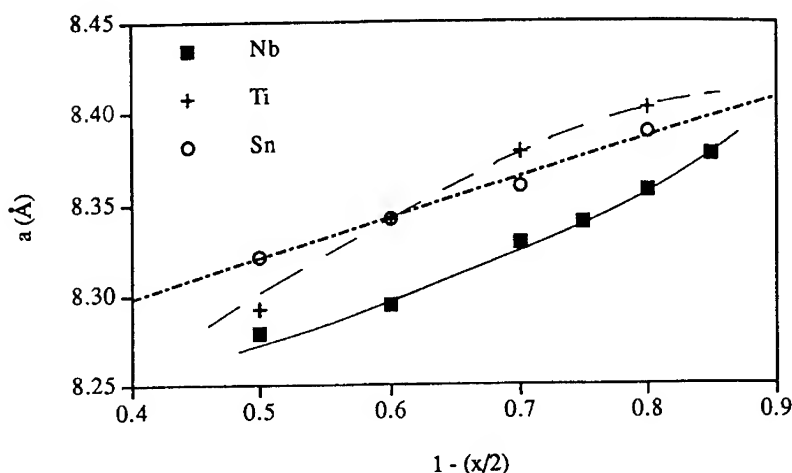


Fig. 2: Lattice constants of doped  $\text{Ba}_2\text{In}_2\text{O}_5$  vs. the concentration of indium.

Second, the smaller  $\text{La}^{3+}$  ion was substituted for  $\text{Ba}^{2+}$  to disorder the vacancies and also reduce the cubic lattice parameter.<sup>12</sup> A cubic solid solution was found in the range  $0.2 \leq x \leq 0.4$ , and the amount of water absorbed decreased with decreasing lattice parameter; no water absorption was detected in  $\text{Ba}_{0.6}\text{La}_{0.4}\text{InO}_{2.7}$ .

Fig. 4 compares the Arrhenius plot for  $\text{Ba}_2\text{In}_2\text{O}_5$  with those for  $\text{Ba}_2\text{In}_{1.6}\text{M}_{0.4}\text{O}_{5+\delta}$ ,  $\text{M} = \text{Ti}, \text{Nb}, \text{or Sn}$ . Water absorption can be seen to be less of a problem with the more acidic  $\text{Sn}^{4+}$  ion than with  $\text{Ti}^{4+}$  substitution. The highest oxide-ion conductivity can also be seen to occur in  $\text{Ba}_{0.6}\text{La}_{0.4}\text{InO}_{2.7}$ , but a relatively high activation energy indicates that the  $\Delta H_i$  of Equation (7) remains significant. It would appear that considerable short-range order is retained below  $1000^\circ\text{C}$ , and the observation of a deterioration of the conductivity with time at  $800^\circ\text{C}$  (an aging phenomenon like that found in yttria-stabilized zirconia) supports this deduction.

The compound  $\text{Ba}_2\text{In}_2\text{O}_5$  was initially chosen for study not only to obtain a measure of  $\Delta H_m$  above an anticipated long-range order-disorder transition ( $T_1 \approx 930^\circ\text{C}$  in  $\text{Ba}_2\text{In}_2\text{O}_5$ ), but also because the large sizes of the  $\text{Ba}^{2+}$  and  $\text{In}^{3+}$  ions provide a relatively large "bottleneck" triangular interface, bounded by two A and one B cation, through which an oxide ion must jump to go from one equivalent site to another. A larger interface was expected to give a smaller  $\Delta H_m$ . On the other hand, an easier back transfer of electrons to the cations might reduce the effective size of the mobile anion on traversing the interface. A more covalent matrix might also reduce the energy gained by local ordering of the vacancies, thereby suppressing the aging phenomenon if not also the contribution of  $\Delta H_g$  to the  $\Delta H_i$  of Equation (7). Therefore it was decided to explore next perovskites having La as the A atom.

The  $\text{La}^{3+}$  ion is stable in less than twelvefold oxygen coordination, so reduction of its coordination in an anion-deficient perovskite from 12 to 11, or even 10, should not cause a problem with water absorption. Bond-length matching requires a smaller B cation than  $\text{In}^{3+}$  if  $\text{A} = \text{La}$  is used. We wished to retain a main-group B cation stable in both octahedral and tetrahedral coordination. Therefore we chose  $\text{LaGaO}_3$  as a parent perovskite to be made anion deficient by aliovalent cation substitution.<sup>12</sup>

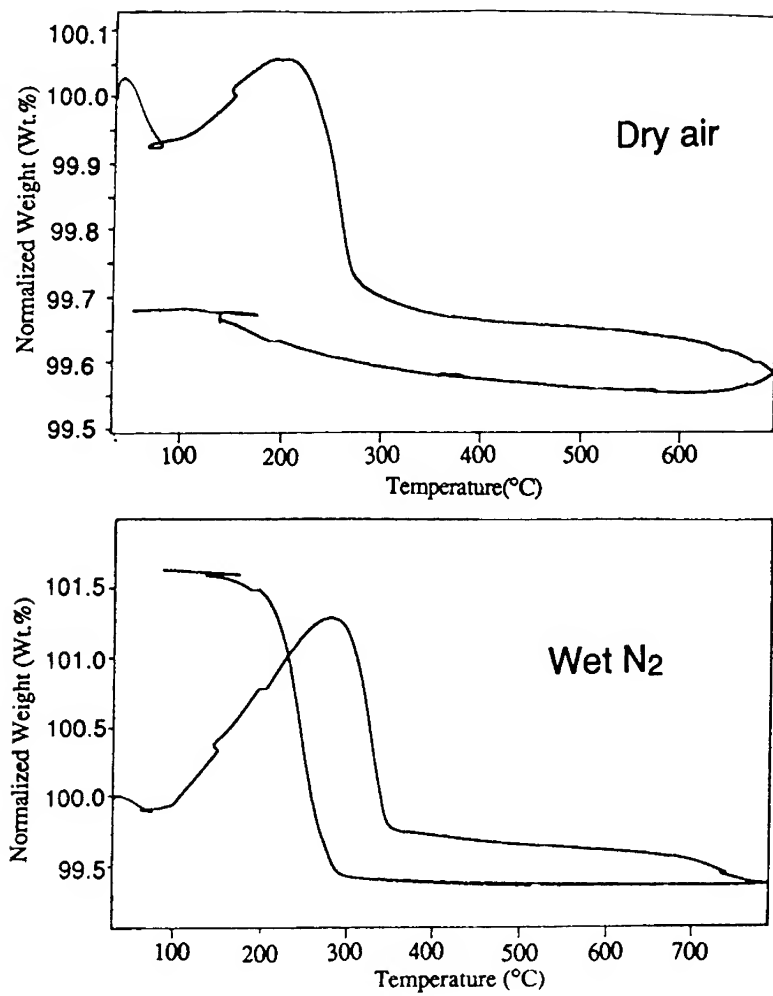


Fig. 3: TGA on  $\text{Ba}_2\text{In}_2\text{O}_5$ ; the top measurement is performed in dry air, the bottom one in wet nitrogen.

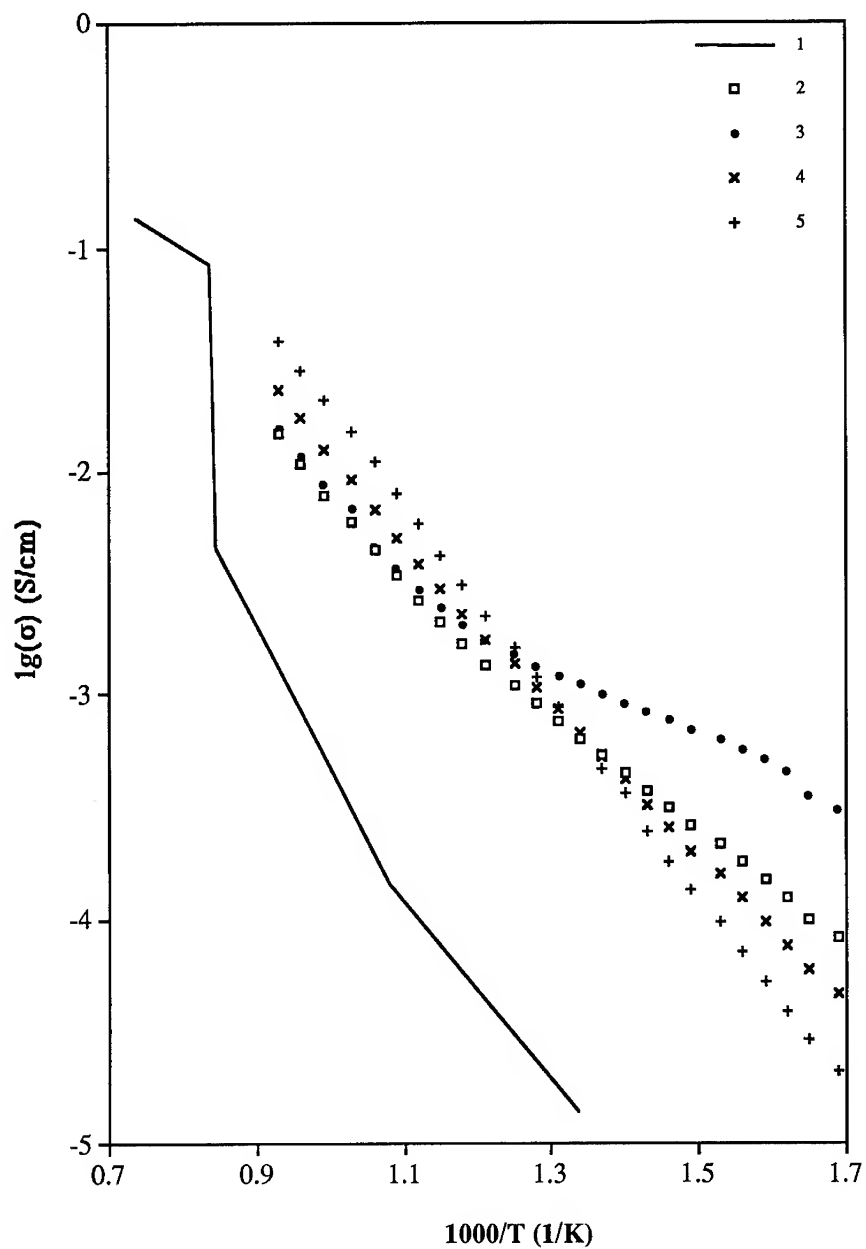


Fig. 4: Conductivity of Ba<sub>2</sub>In<sub>2</sub>O<sub>5</sub> and its doped materials: 1 - Ba<sub>2</sub>In<sub>2</sub>O<sub>5</sub>; 2 - Ba<sub>2</sub>In<sub>1.6</sub>Nb<sub>0.4</sub>O<sub>5.4</sub>; 3 - Ba<sub>2</sub>In<sub>1.6</sub>Ti<sub>0.4</sub>O<sub>5.2</sub>; 4 - Ba<sub>2</sub>In<sub>1.6</sub>Sn<sub>0.4</sub>O<sub>5.2</sub>; 5 - Ba<sub>0.6</sub>La<sub>0.4</sub>InO<sub>2.7</sub>.



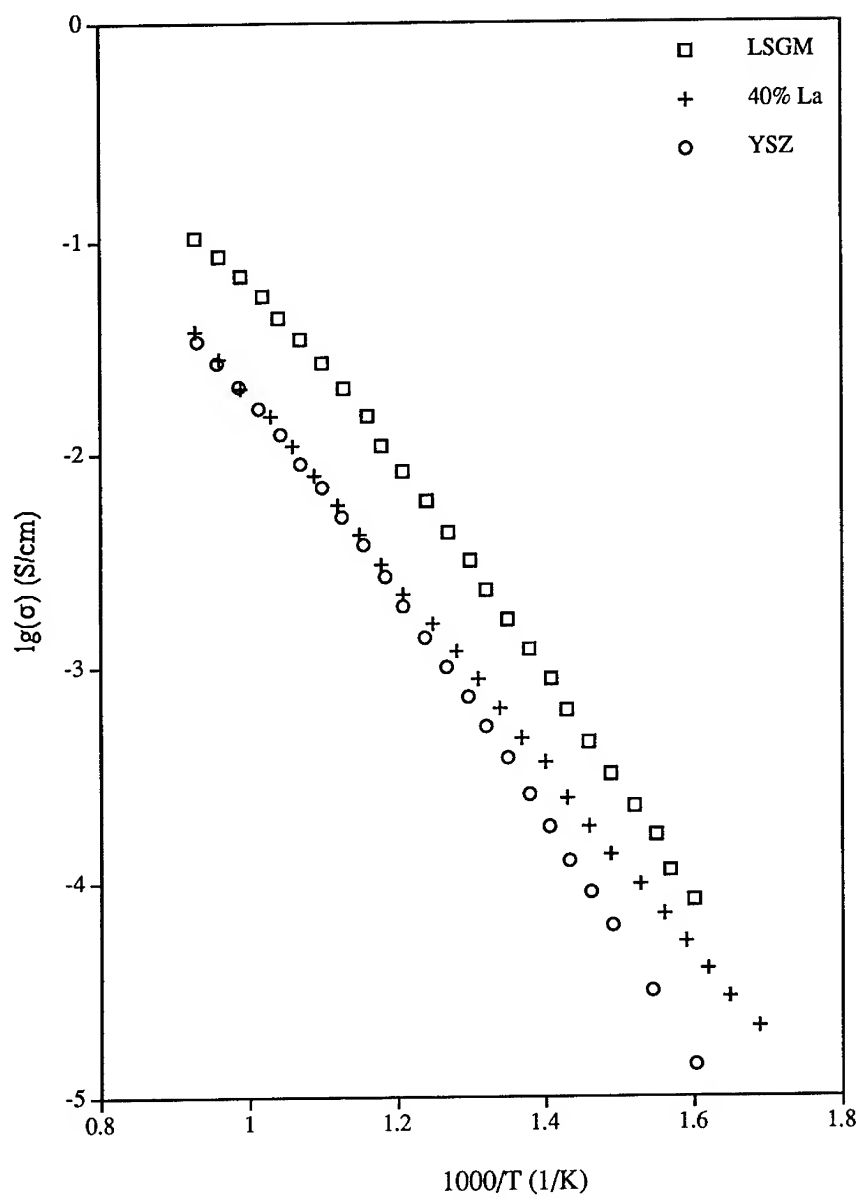


Fig. 5: Conductivity of LSGM compared to  $\text{Ba}_{0.6}\text{La}_{0.4}\text{InO}_{2.5+\delta}$ , and 9% yttria-stabilized zirconia.

Aliovalent doping of  $\text{LaGaO}_3$  was also explored independently by two other groups;<sup>13, 14</sup> our results are in good agreement. Of the alkaline earths,  $\text{Sr}^{2+}$  has the best size match to  $\text{La}^{3+}$ ; nevertheless only a limited concentration of Sr can be substituted for La in  $\text{La}_{1-x}\text{Sr}_x\text{GaO}_{3-0.5x}$ . In order to retain B cations stable in both octahedral and tetrahedral sites, we chose  $\text{Zn}^{2+}$  and  $\text{Mg}^{2+}$  as the main-group ions to be substituted for  $\text{Ga}^{3+}$ . We were unable to substitute Zn for Ga with conventional synthetic procedures; so we can only report results for  $\text{La}_{1-x}\text{Sr}_x\text{Ga}_{1-y}\text{Mg}_y\text{O}_{3-0.5(x+y)}$ .

The best oxide-ion conductivity was found for  $x = 0.1$  and  $y = 0.2$  in  $\text{La}_{0.9}\text{Sr}_{0.1}\text{Ga}_{0.8}\text{Mg}_{0.2}\text{O}_{2.85}$ ; we refer to this compound as LSGM. Our LSGM was single-phase to x-ray powder diffraction with a cubic lattice constant  $a = 3.911 \text{ \AA}$ . A sintered density as high as 99.7% was achieved upon heating milled powders at  $1450^\circ\text{C}$  for two days. Impedance spectroscopy indicated only a small grain-boundary contribution to the total resistance. Water absorption is not a problem. Fig. 5 compares the bulk conductivity of LSGM with that of  $\text{Ba}_{0.6}\text{La}_{0.4}\text{InO}_{2.7}$  and 9% yttria-stabilized zirconia (YSZ). The activation energy and the pre-exponential factor of LSGM are 1.07 eV and  $24.8 \times 10^6 \text{ K}\cdot\text{S}/\text{cm}$ , respectively, as compared to 0.98 eV and  $1.1 \times 10^6 \text{ K}\cdot\text{S}/\text{cm}$  for YSZ. The larger effective activation energy and pre-exponential factor in LSGM suggest the approach of an order-disorder transition, as does the change of slope of  $\log \sigma$  vs  $1/T$  at high temperatures. However, any order is short-range, and the order-disorder transition is therefore smooth. The approach to disorder of the short-range ordering at high temperatures not only enhances  $\sigma_0$ , it also suppresses the aging phenomenon. We found no deterioration of  $\sigma_0$  with time on operating a pellet at  $650^\circ\text{C}$  for more than 140 hours. These advantageous features make LSGM the leading candidate for the ceramic membrane of a high-temperature fuel cell operating at a  $T_{\text{op}}$  of  $600 - 800^\circ\text{C}$ . Moreover, we used thermomechanical analysis (TMA) to obtain a thermal expansion coefficient of  $1.0 \times 10^{-5} \text{ K}^{-1}$ , which is close to that of YSZ. With a lower  $T_{\text{op}}$ , we anticipate the problems of chemical reactions with a metallic  $\text{La}_{1-x}\text{Sr}_x\text{MnO}_3$  cathode will not be a problem, but this conjecture has yet to be tested experimentally.

## CONCLUSIONS

Anion-deficient, cubic  $\text{ABO}_{3-8}$  perovskites can be competitive oxide-ion electrolytes. Use of the large, electropositive cations  $\text{Ba}^{2+}$  or  $\text{Sr}^{2+}$  as A cations, especially in the presence of larger and more electropositive (basic) B cations, is plagued by the absorption of water into the anion vacancies. Even  $\text{Ba}_2\text{In}_2\text{O}_5$ , which contains only  $\text{In}^{3+}$  ions stable in either octahedral or tetrahedral sites, absorbs water below  $300^\circ\text{C}$  to destroy the long-range anion-vacancy ordering of the brownmillerite structure. However, substitution of  $\text{La}^{3+}$  for  $\text{Ba}^{2+}$  in  $\text{Ba}_{2-x}\text{La}_x\text{In}_2\text{O}_{5+0.5x}$  suppresses the absorption of water, and  $\text{Ba}_{0.6}\text{La}_{0.4}\text{O}_{2.7}$  is a cubic, anion-deficient perovskite having an oxide-ion conductivity as good as the best yttria-stabilized zirconia. In both materials aging occurs below  $1000^\circ\text{C}$  as a result of a local segregation of the dopant that traps out mobile anion vacancies. On the other hand,  $\text{La}_{0.9}\text{Sr}_{0.1}\text{Ga}_{0.8}\text{Mg}_{0.2}\text{O}_{2.85}$  has been found to be a superior oxide-ion electrolyte that does not appear to age and is relatively easy to fabricate into a dense membrane. However, Ga is a relatively expensive element, and further work on oxygen-deficient perovskites would appear to be warranted.

## ACKNOWLEDGMENT

The financial support of the Texas Advanced Research Program, the Robert A. Welch Foundation, Houston, Texas, and K. H. Wong Education Foundation Ltd., Hong Kong is gratefully acknowledged.

## REFERENCES

1. M. Faraday, *Experimental Researches in Electricity*, (Taylor and Francis, London 1839) Art. 1339.
2. J.B. Goodenough, *Proc. Roy. Soc. London* **A393**, 215 (1984)
3. J.B. Goodenough, J.E. Ruiz-Diaz, and Y.S. Zhen, *Solid State Ionics* **44**, 21 (1990)
4. W.A. England, M.E. Cross, A. Hamnett, P.J. Wiseman, and John B. Goodenough, *Solid State Ionics* **1**, 231 (1980)
5. B.C.H. Steele, B.E. Powell, and P.M.R. Moody, *Proc. Brit. Ceram. Soc.* **5**, 87 (1968)
6. T. Takahashi and H. Iwahara, *Energy Conversion* **11**, 105 (1971)
7. M. Iwahara, *Solid State Ionics* **28-30**, 573 (1988)
8. A. Manthiram, J. F. Kuo, and J. B. Goodenough, *Solid State Ionics* **62**, 225 (1993); J. B. Goodenough, A. Manthiram, and J. F. Kuo, *Materials Chemistry and Physics* **35**, 221 (1993)
9. Man Feng and J. B. Goodenough, *Solid State Ionics* **68**, 269 (1994)
10. Man Feng and J.B. Goodenough, (this volume)
11. H. Iwahara, T. Yajima, and M. Ushida, *Solid State Ionics* **70/71**, 267 (1994)
12. Man Feng and J.B. Goodenough, *Eur. J. Solid State Inorg. Chem.* **31**, 663 (1994)
13. A.V. Strelkov, A.R. Kaul, and Yu. D. Tretyakov, *Solid State Ionics*, *Proc. Int. Conf. on Advanced Materials* (May, 1991) eds M. Balkanski, T. Takehashi, and H.L. Tuller (Elsevier, Amsterdam, 1992) p. 605
14. T. Ishihara, M. Matsuda, and Y Takita, *J. Am. Chem. Soc.* **116**, 3801 (1994)

## PEROVSKITES AS OXIDE-ION ELECTROLYTES

MAN FENG\* AND JOHN B. GOODENOUGH\*\*

\*Department of Physics, RLM 5.208, the University of Texas at Austin, Austin, TX 78712

\*\*Center for Material Science and Engineering, ETC 9.102, the University of Texas at Austin, Austin, TX 78712

### ABSTRACT

Substitution of Nb, Ti, or Sn for In and of La for Ba was used to obtain cubic, anion-deficient perovskites  $\text{ABO}_{3-\delta}$ . Neither the ferroelectric character of  $\text{Nb}^{5+}$  and  $\text{Ti}^{4+}$ , nor the more acidic character of  $\text{Sn}^{4+}$  suppressed water absorption into the anion vacancies at temperatures  $T < 500^\circ\text{C}$ . However, the smaller  $\text{La}^{3+}$  ion in  $\text{Ba}_{1-x}\text{La}_x\text{O}_{2.5+0.5x}$  did suppress the absorption of water for  $x = 0.4$ , and  $\text{Ba}_{0.6}\text{La}_{0.4}\text{InO}_{2.7}$  is competitive with yttria-stabilized zirconia as an oxide-ion electrolyte.

### Introduction

Recent experimental work<sup>1-8</sup> has shown that oxygen-deficient  $\text{ABO}_{3-\delta}$  perovskites are good oxide-ion electrolytes provided the oxygen vacancies are disordered and the A and B cations are, respectively, stable in less than twelvefold and sixfold anion coordination. For example, with A = Ba or Sr and some of B = Zr, Ce, Hf, Ln, or Y (Ln = rare earth), an oxygen-deficient perovskite is not stable in air; water and/or oxygen from air enter the oxygen vacancies. Absorbed water introduces mobile protons; absorbed oxygen oxidizes the oxygen array.

$\text{Ba}_2\text{In}_2\text{O}_5$  was found<sup>1</sup> to be a fast oxide-ion conductor above a first-order phase transition from the vacancy-ordered brownmillerite structure to a cubic structure at  $T_t \approx 930^\circ\text{C}$ . In the cubic phase, the long-range vacancy ordering of brownmillerite is lost, but considerable short-range order persists<sup>3</sup>. The energy gap  $\Delta H_g = \Delta H_g(0) - \epsilon c$  between the vacancy sites and the occupied sites of the brownmillerite phase decreases with the fractional occupancy  $c$  of the vacancy sites by thermally excited oxygen atoms:

$$c \sim \exp(-\Delta H_g/kT). \quad (1)$$

The strong positive feedback in the decrease of  $\Delta H_g$  as the temperature increases results in a first-order collapse of the phenomenological activation energy

$$E_a = \Delta H_m + \Delta H_g, \quad (2)$$

as the temperature increases to  $T_t \approx 930^\circ\text{C}$ ; a measured  $E_a$  above  $T_t$  gives an upper limit  $\Delta H_m < 0.6$  eV for the motional enthalpy of the oxide ion in the cubic perovskite phase, which is small enough to give a  $\sigma_O > 10^{-2}$  S/cm at a  $T_{op} \approx 500^\circ\text{C}$ .

Aliovalent substitution for Ba or In is an obvious strategy for the suppression of long-range ordering of the oxygen vacancies in  $\text{Ba}_2\text{In}_2\text{O}_5$ . The compound  $\text{Ba}_3\text{In}_2\text{MO}_8$  with  $M = \text{Zr, Ce, or Hf}$  were first investigated as  $\text{Ca}_3\text{Fe}_2\text{TiO}_8$  is reported<sup>9</sup> to have a vacancy ordering that gives tetrahedral coordination of the B cations in every third (0 0 1) B-O layer; it was anticipated<sup>1</sup> that the  $M^{4+}$  cations would have a sufficient preference for octahedral coordination to pull oxygen into neighboring vacancies from the octahedrally coordinated  $\text{In}^{3+}$  ions, and indeed a high ionic conductivity was observed below  $400^\circ\text{C}$ . However, a subsequent study<sup>4</sup> showed that the low-

temperature ionic conductivity was predominantly protonic; disordering of the vacancies is accompanied by absorption of water and/or oxygen from the atmosphere via the reactions



where  $\text{V}_\text{O}$  is a bulk oxygen vacancy. Loss of water and excess oxygen occurs above 400°C, and above 550°C the conductivity is dominated by oxide-ion conduction.

A preliminary conclusion from this study was that ions stable in fourfold and sixfold anion coordination, *e.g.*  $\text{In}^{3+}$  or  $\text{Ga}^{3+}$ , would stabilize oxygen vacancies that do not attract water and/or oxygen from the atmosphere whereas the introduction of cations that are not stable in less than sixfold oxygen coordination would attract water into the oxygen vacancies of an oxygen-deficient perovskite. The present study was undertaken to test this hypothesis.

We have investigated substitution of  $\text{Ti}^{4+}$  or  $\text{Nb}^{5+}$  for  $\text{In}^{3+}$  as these cations are stable in 5+1 oxygen coordination; moreover, it was hoped that dynamic cation displacements within an octahedral site would facilitate oxide-ion mobility, thereby lowering the motional enthalpy  $\Delta H_\text{m}$  of Equation (2). Substitution of  $\text{Sn}^{4+}$  was tried because it is more acidic than  $\text{Zr}^{4+}$ ,  $\text{Ce}^{4+}$  and  $\text{Hf}^{4+}$ . Protonic conduction persisted at low temperatures with all three cation substitutions; in fact, it was found even in the end member  $\text{Ba}_2\text{In}_2\text{O}_5$ . Therefore, substitution of a smaller  $\text{La}^{3+}$  ion for  $\text{Ba}^{2+}$  was investigated; this substitution suppresses both the absorption of water and long-range ordering of the oxygen vacancies.

### Experimental Procedures

Samples were prepared by standard ceramic procedures from stoichiometric mixtures of  $\text{BaCO}_3$ ,  $\text{In}_2\text{O}_3$  and dopant metal oxides of better than 99.9% purity from Alpha and Aldrich. Overnight heating of the mixture at 820°C prevented loss of indium oxide;  $\text{In}_2\text{O}_3$  sublimes above 850°C. The temperature of the furnace was raised to 960°C to decompose the carbonates; solid-state reaction was carried out at 1100°C. Pulverized powders of the reaction product were pressed into pellets and sintered above 1400°C to complete the reaction. The single-phase cubic material thus obtained was then micronised in a milling machine with agate balls; the resulting fine powders were pressed into cylindrical pellets and heated at 1430°C to 1440°C for about two days. After sintering, the furnace was cooled slowly in steps of less than 50°C to 550°C before quenching in ambient atmosphere. Powder X-ray diffraction confirmed that all samples remained cubic and single-phase. Commercial synthetic silicon powder was used as the internal standard for determination of the lattice parameters.

The bulk conductivity  $\sigma$  of each sample was measured in air with a complex-impedance analyzer from 320°C to 800°C. The ac signal amplitude was set at 40 mV and the measuring frequency ranged from 5 Hz to 13 MHz. The two ends of the cylindrical pellets were carefully sanded flat before their mass density was measured by a gas pycnometer. Silver paste was painted on both faces after measurement of the pellet geometric dimensions. Unlike the stabilized zirconias, the barium indates can be sintered into dense pellets at about 1400°C without either a sintering aid or hot pressing. As in the case of modified bismuth sesquioxides, no grain-boundary semicircle was found at any temperature  $320 < T < 800^\circ\text{C}$  in the complex-impedance plots, which indicates that grain-boundary processes were giving no significant contribution to the total resistance.

### Results

Quenching samples from 550°C prevented any significant water absorption in the room temperature products. Table I gives the diffraction lines of  $\text{Ba}_2\text{InTiO}_{5.5}$  below 82° in 2 $\theta$ . The

Table I: d-spacing from X-ray powder diffraction for  $\text{Ba}_2\text{InTiO}_{5.5}$  ( $a = 8.292 \pm 0.003 \text{ \AA}$ ).

$2\theta$	$d \text{ (\AA)}$	$I \text{ (\%)}$	$(h \ k \ l)$	$\Delta d \text{ (\AA)}$
21.390	4.151	2.3	2 0 0	0.0048
30.466	2.932	100	2 2 0	0.0001
37.552	2.393	10.0	2 2 2	-0.0004
43.622	2.073	33.2	4 0 0	0.0003
49.117	1.853	2.7	4 2 0	-0.0008
54.160	1.692	63.2	4 2 2	-0.0005
63.406	1.466	21.9	4 4 0	0.0000
71.955	1.311	22.7	6 2 0	0.0002
76.094	1.250	3.1	6 2 2	-0.0002
80.100	1.197	6.6	4 4 4	0.0003

lines indexed as (2 0 0), (4 2 0), and (6 2 2) were not present in the diffraction patterns of samples with smaller concentrations of B-site dopant Ti, Sn or Nb. In the systems  $\text{BaIn}_{1-x}\text{M}_x\text{O}_{2.5+\lambda x}$ , where  $\lambda = 0.5$  for  $\text{M} = \text{Ti}$  or  $\text{Sn}$  and  $\lambda = 1.0$  for  $\text{M} = \text{Nb}$ , the lattice parameters decreased linearly with  $x$  as expected since  $\text{In}^{3+}$  is the larger B cation; in each system a continuous solid solution was obtained.

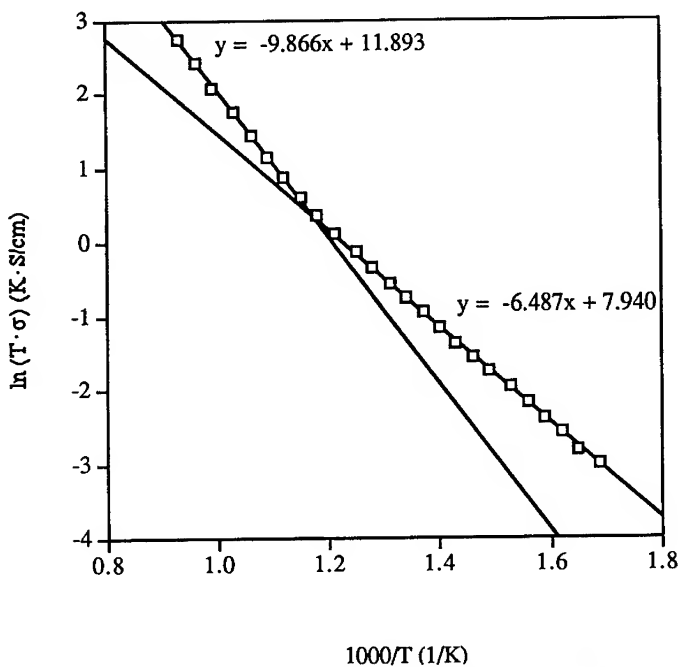


Fig. 1: Arrhenius plot for  $\text{Ba}_2\text{In}_{1.6}\text{Nb}_{0.4}\text{O}_{5.4}$  on cooling from  $800^\circ\text{C}$ .

Doping suppresses the first-order order-disorder transition at  $T_1 \approx 930^\circ\text{C}$ . On first heating, the measured  $\ln(\sigma \cdot T)$  vs.  $1/T$  curves exhibit a shoulder near  $550^\circ\text{C}$  that disappears on cycling in the temperature range of measurable conductivity. Therefore we use the data obtained on cooling runs for the following discussion. The conductivity measured on cooling is consistently lower than that on heating, particularly below  $550^\circ\text{C}$ .

Fig. 1 shows a plot of  $\ln(\sigma \cdot T)$  vs.  $1/T$  for nominal  $\text{Ba}_2\text{In}_{1.6}\text{Nb}_{0.4}\text{O}_{5.4}$  taken on cooling from  $800^\circ\text{C}$  to  $320^\circ\text{C}$ ; it is representative of the samples investigated. The lines are the least-squares fit to the data. Such an appearance of the Arrhenius plot is typical of doped perovskites with proton conduction dominating at lower temperatures and oxide-ion conduction at higher ( $T > 550^\circ\text{C}$ ) temperatures<sup>10</sup>. Compared to  $\text{Ba}_2\text{In}_2\text{O}_5$ , the oxide-ion conductivity of the doped samples is over one order of magnitude higher at temperatures  $T \leq 800^\circ\text{C}$ .

The low-temperature proton conduction is magnified in pellets with poor microstructure. For example, pellets formed from ground powders of Nb-doped  $\text{Ba}_2\text{In}_2\text{O}_5$  sintered at  $1450^\circ\text{C}$  gave higher protonic conduction than those formed from micronised powders even though the crystal structures of the bulk powders were identical. As illustrated in Fig. 2, the impedance spectra obtained for coarse powders at moderate ( $100 < T < 400^\circ\text{C}$ ) temperatures exhibited a small semicircle at the high end of the frequency range to the left of the bulk semicircle. This semicircle reduces to a sector of arc with increasing temperature and a shifted left end of the bulk semicircle, which can be easily misinterpreted as the concurrence of conventional bulk and grain-boundary contributions rather than of an intergranular and a bulk contribution.

Variation of the Cole-Cole plot with changing microstructure eliminates electronic conduction as a major contributor to the total low-temperature conductivity. Although the total resistance of our pellets was too high below  $200^\circ\text{C}$  to allow measurement of the low-temperature transport number for a specific ion by the concentration-cell method, nevertheless the circumstantial evidence for proton conduction is compelling. Cycling of a sample between  $100$  and  $400^\circ\text{C}$  gave a stable, long-term enhanced conductivity; but heating above  $400^\circ\text{C}$  resulted in a lower conductivity that took days at room temperature to recover to its initial value. Thermogravimetric

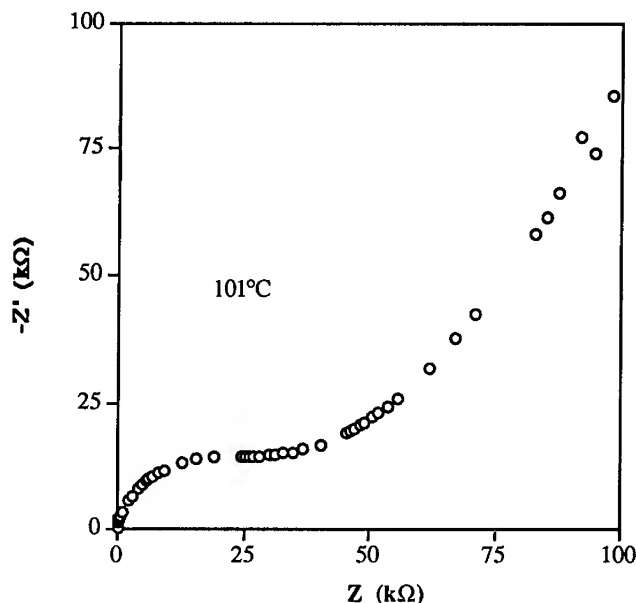


Fig. 2: Cole-Cole plot at  $101^\circ\text{C}$  for  $\text{Ba}_2\text{In}_{1.6}\text{Nb}_{0.4}\text{O}_{5.4}$  sintered from coarse powder.

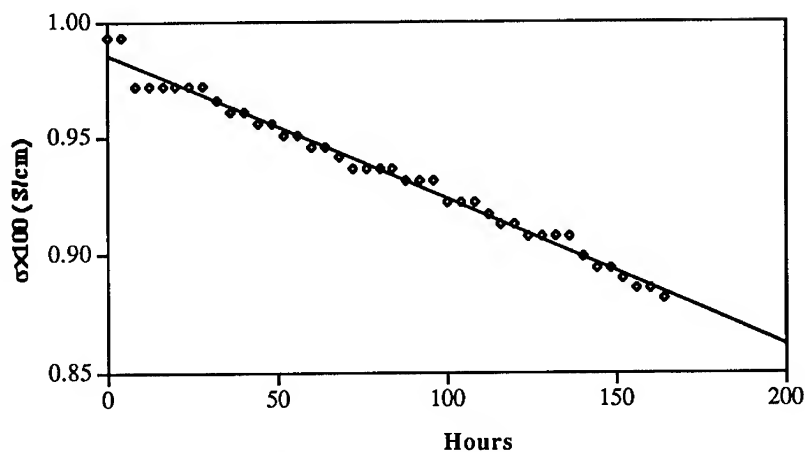


Fig. 3: Conductivity of  $\text{Ba}_2\text{In}_{1.6}\text{Nb}_{0.4}\text{O}_{5.4}$  as a function of time at  $750^\circ\text{C}$ .

analysis in moist and dry air and nitrogen atmospheres showed water loss above  $400^\circ\text{C}$  required a similar time to be reabsorbed at lower temperatures.

The low-temperature intergranular conductivity determined from the small, high-frequency semicircle of Fig. 2 is  $\sim 10^{-4}$  S/cm for  $100 < T < 200^\circ\text{C}$ ; this value is similar to that reported earlier<sup>1</sup> for low-temperature  $\text{Ba}_3\text{In}_2\text{ZrO}_8$ . The data are consistent with proton conduction in intergranular water that is enhanced by a more open microstructure.

To check for aging of the oxide-ion conduction, a pellet of  $\text{Ba}_2\text{In}_{1.6}\text{Nb}_{0.4}\text{O}_{5.4}$  was kept at  $750^\circ\text{C}$  for 160 hours during which time its conductivity was measured every 4 hours. The results of this test are plotted in Fig. 3. The long-term decrease in conductivity is linear in time although small fluctuations are apparent. Such deterioration implies atomic segregation and trapping out of the mobile vacancies.

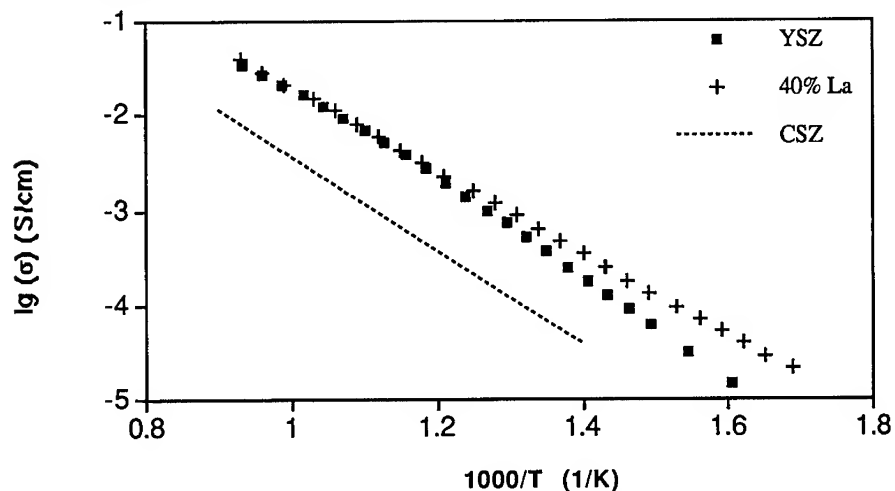


Fig. 4: Conductivity of  $\text{Ba}_{0.6}\text{La}_{0.4}\text{InO}_{2.7}$ , 9% yttria-stabilized zirconia, and 13% calcia-stabilized zirconia.



We also found that  $\text{Ba}_2\text{In}_2\text{O}_5$  absorbs water below  $300^\circ\text{C}$ , which shows that the  $\text{Ba}^{2+}$  ion in less than twelvefold oxygen coordination attracts water to anion vacancies even where the vacancies are stabilized by long-range order in the presence of  $\text{In}^{3+}$  ions stable in either fourfold or sixfold anion conduction. The absorption of water into the vacancies makes the room-temperature structure indeterminate; it no longer has the brownmillerite structure. To suppress the absorption of water into anion vacancies by  $\text{Ba}^{2+}$  ions as well as the long-range ordering of the vacancies, we turned to the substitution of La for Ba.

Solid solution in the system  $\text{Ba}_{1-x}\text{La}_x\text{InO}_{2.5+0.5x}$  was obtained in a cubic perovskite phase over the limited range  $0.2 \leq x \leq 0.4$ . Low-temperature proton conduction persists through  $x = 0.3$ ; it is not evident for the limiting composition  $x = 0.4$ . The water intake decreases with decreasing vacancy concentration and decreasing lattice parameter. By  $x = 0.4$ , the percolation limit for oxygen vacancies neighboring  $\text{La}^{3+}$  ions is exceeded, and only oxide-ion conduction is observed to lowest temperatures. Fig. 4 compares the plot of  $\log(\sigma)$  vs.  $1/T$  for  $\text{Ba}_{0.6}\text{La}_{0.4}\text{InO}_{2.7}$  with that for 13% calcia-stabilized zirconia (dotted line) and 9% yttria-stabilized zirconia. Densification of the  $\text{Ba}_{0.6}\text{La}_{0.4}\text{InO}_{2.7}$  sample was sufficient to eliminate any measurable grain-boundary contribution. The conductivity of stabilized zirconia is determined from the bulk semicircle on the Cole-Cole plot. The oxide-ion conductivities in the two samples are comparable. Yttria stabilized zirconia is known to age below  $1000^\circ\text{C}$ ; a test for aging of  $\text{Ba}_{0.6}\text{La}_{0.4}\text{InO}_{2.7}$  showed similar behavior.

## Conclusions

Aliovalent cation substitution at either the A or the B sites of  $\text{Ba}_2\text{In}_2\text{O}_5$  suppresses long-range ordering of the oxygen vacancies and enhances the oxide-ion conductivity in the range  $550 < T < 930^\circ\text{C}$ . However, water is absorbed at lower temperatures so long as the A sites all contain  $\text{Ba}^{2+}$  ions.

Low-temperature protonic conduction is enhanced in pellets formed from coarser powders; these samples have poorer microstructures and appear to absorb water into the intergranular space as well as into the bulk structure. Proton conduction in the intergranular space appears to resemble that occurring in a pressed particle hydrate<sup>11</sup>.

Substitution of  $\text{La}^{3+}$  for  $\text{Ba}^{2+}$  suppresses both long-range order of the oxygen vacancies and water absorption. The oxide-ion conductivity of  $\text{Ba}_{0.6}\text{La}_{0.4}\text{InO}_{2.7}$  is comparable to the best yttria-stabilized zirconia and is more easily prepared as a dense ceramic.

We thank the Texas Advanced Research Program, the Robert A. Welch Foundation, Houston, Texas, and the K. H. Wong Education Foundation Ltd., Hong Kong for financial support.

## References

1. John. B. Goodenough, J. E. Ruiz-Diaz, and Y. S. Zhen, *Solid State Ionics* **44**, 21 (1990).
2. A. F. Sammells, R. L. Cook, J. H. White, J. J. Osborne and R. C. MacDuff, *Solid State Ionics* **52**, 111 (1992).
3. T. R. S. Prasanna and A. Navrotsky, *J. Mater. Res.* **8**, 1484 (1993).
4. A. Manthiram, J. F. Kuo, and John. B. Goodenough, *Solid State Ionics* **62**, 225 (1993).
5. M. Schwartz, B. F. Link and A. F. Sammells, *J. Electrochem. Soc.* **40**, L62 (1993).
6. S. Adler, S. Russek, J. Reimer, M. Fendorf, A. Stacy, Q. Huang, A. Santoro, J. Lynn, J. Baltisberger and U. Werner, *Solid State Ionics* **68**, 193 (1994).
7. J. K. Thomas, K. R. Kendall and H. zur Loye, *Solid State Ionics* **70/71**, 225 (1994).
8. I. Kontoulis, Ch. P. Ftikos and B. C. H. Steele, *Materials Sci. & Eng.* **B22**, 313 (1994).
9. J. Rodrigues-Carvajal, M. Vallet-Regi, and J. M. G. Calbet, *Mat. Res. Bull.* **24**, 423 (1989).
10. H. Iwahara, T. Yajima and H. Ushida, *Solid State Ionics* **70/71**, 267 (1994).
11. W. A. England, M. E. Cross, A. Hamnett, P. J. Wiseman, and J. B. Goodenough, *Solid State Ionics* **1**, 231 (1980).

## ELECTROCHEMICAL STUDIES OF PEROVSKITE MIXED CONDUCTORS

Eric L. Brosha, Brandon W. Chung, and Fernando H. Garzon.  
Electronic and Electrochemical Materials and Devices Group  
Los Alamos National Laboratory, Los Alamos, N.M. 87545

Research into the growth of high-quality single crystal thin films of high transition temperature ( $T_c$ ) superconductors have stimulated interest in other perovskite metal oxides with a variety of physical properties.<sup>1</sup> Thin films of perovskite materials are among the major focal research areas for optical, sensor, electronic, and superconducting applications.<sup>1</sup> Two lanthanum-based oxygen/electronic conducting perovskite oxides of particular interest for high temperature fuel cell electrodes and interconnects and for other electrochemical applications such as oxygen separation devices are  $\text{La}_{1-x}\text{Sr}_x\text{MnO}_{3-y}$  and  $\text{La}_{1-x}\text{Sr}_x\text{CoO}_{3-y}$ . The La-based perovskites are valuable for these technologies because they reduce interfacial resistances by eliminating the need for a three phase contact area (gas, metal electrode, electrolyte).<sup>2</sup> In addition, these oxides may also serve a valuable role as novel catalysts or catalytic supports; however, little is known about what catalytic properties they may possess.

Fundamental study of the electrochemical, diffusional oxygen transport, and surface catalytic properties of these materials can be greatly simplified if the complications associated with the presence of grain boundaries and multiple crystallite orientations can be avoided. Therefore, single crystals of these La-based perovskites become highly desirable. In this work, we report the structural and electrical properties of highly oriented thin films of  $\text{La}_{0.84}\text{Sr}_{0.16}\text{MnO}_3$  thin films grown on single crystal yttrium stabilized zirconia (YSZ) substrates. In addition, we have demonstrated growing, *in situ*, epitaxial multilayer perovskite/fluorite/perovskite configurations for fundamental fuel cell modeling.

### Experimental

We have deposited films by using a 90° off-axis radio-frequency (RF) magnetron sputtering<sup>3,4</sup> technique from a single 2-inch-diameter, hot-pressed stoichiometric target of  $\text{La}_{0.84}\text{Sr}_{0.16}\text{MnO}_3$  (purchased from SSC) on YSZ (200)-oriented substrates. We also deposited  $\text{La}_{0.8}\text{Sr}_{0.2}\text{MnO}_3$  in a multilayer configuration on epitaxial YSZ on  $\text{SrTiO}_3$  (100). In a typical deposition, a  $1\text{cm}^2$  substrate was fastened to a heater box using silver paint, and the substrate heater temperature was measured using thermocouple and/or IR camera. The substrate heater was maintained at a temperature of 650°C-700°C. All of the depositions were carried out at an RF power of 100W. Typical total pressures were between 40 and 42 mTorr (60% argon and 40% oxygen). After the depositions, the chamber was flooded with pure oxygen to a pressure of 5 Torr, then the films were allowed to cool to room temperature.

For each of the films, x-ray diffraction (XRD) data was taken for structure and texture analysis. The XRD measurements were made with a Siemens D5000 diffractometer fitted with a  $\text{CuK}\alpha$  source. We used Rutherford Backscattering spectroscopy (RBS) to study the composition and deposition rate of films. Scanning tunneling microscopy (STM) was used to image the free surfaces of the oriented films for studies of surface microstructures. A Schlumberger 1260 frequency response analyzer was used to obtain AC impedance spectroscopy data.

## Results and Discussion

Figures 1a and b are XRD patterns for a  $\text{La}_{0.84}\text{Sr}_{0.16}\text{MO}_3$  (LSMO) sputtered thin films. In Figure 1a, the principal orientation is rhombohedral  $[-110]$ ; however, a small amount ( $<1\%$ ) of  $[110]$  orientation is present. By varying temperature, heater position, and  $\text{Ar}/\text{O}_2$  pressure, it was also possible to obtain a principal  $[110]$  orientation, Figure 1b, or a mixture of both orientations. Figures 2a and 2b are XRD patterns of the rocking curve of the  $(110)$  reflection and the phi-scan of the  $(341)$  reflection for the film in Figure 1a. The FWHM of the rocking curve is  $1.84^\circ$ . These data indicate that the sputtered LSMO films exhibit a high degree of crystallinity and biaxial texturing on the  $[100]$  YSZ substrate.

The surface microstructures of the LSMO depositions were examined by STM. The images indicated an island growth mechanism with plateaus present within the islands. Most significantly, LSMO films sputtered on YSZ single crystals revealed a typical root-mean-square roughness of 17 to  $40\text{\AA}$ .

The capability of growing smooth oriented thin films is necessary in order to grow oxide materials in multilayer configurations.<sup>5</sup> One useful configuration, for fundamental electrochemical device modeling, is a LSMO/YSZ multilayer grown *in situ* on  $\text{SrTiO}_3$ . Figure 3 is an XRD trace of such a multilayer film. A  $5000\text{\AA}$  thick  $[200]$  oriented YSZ film was first grown on  $[100]$   $\text{SrTiO}_3$  followed by a  $2500\text{\AA}$  thick  $[110]$ -pseudocubic oriented LSMO film on the YSZ layer. The excellent epitaxy, evident in this XRD trace, shows that an all single-crystal thin-film fuel-cell model can be fabricated for fundamental electrochemical study.

For electrical AC response characterization, an  $8000\text{\AA}$ -thick oriented LSMO film was grown on single crystal YSZ substrate; for comparison, a 1 micron thick polycrystalline LSMO film was prepared by sputtering onto a  $1\text{ cm}^2$  polycrystalline tetragonal zirconia substrate. For both the single crystal and polycrystalline samples, a small  $2\text{ mm}^2$  platinum electrode was then sputtered onto the LSMO film and a platinum counter electrode was sputtered to completely cover the zirconia side. Platinum wire was bonded to the electrodes and both substrates were placed into a furnace under flowing oxygen. Figures 4a and b are AC impedance data taken under polarizing and non-polarizing conditions for the two LSMO films at the conditions of 1 atm  $\text{PO}_2$

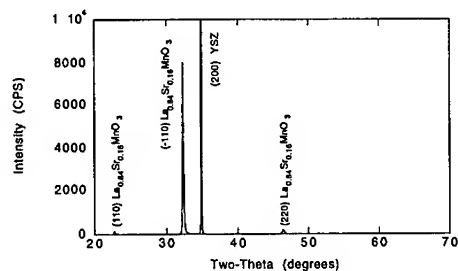


Figure 1a. XRD pattern of a principal [-110] oriented  $\text{La}_{0.84}\text{Sr}_{0.16}\text{MnO}_3$  thin film grown on YSZ [100].

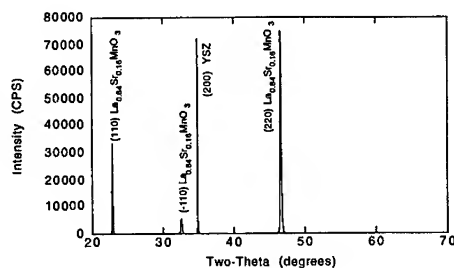


Figure 1b. XRD pattern of a principal [110] oriented  $\text{La}_{0.84}\text{Sr}_{0.16}\text{MnO}_3$  thin film grown on YSZ [100].

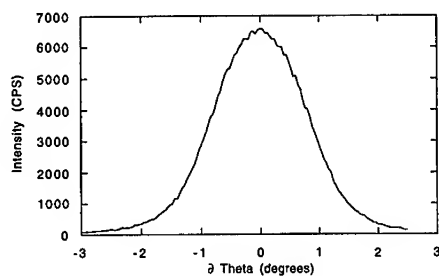


Figure 2a. XRD rocking curve of the (110) reflection of a  $\text{La}_{0.84}\text{Sr}_{0.16}\text{MnO}_3$  thin film grown on YSZ [100].

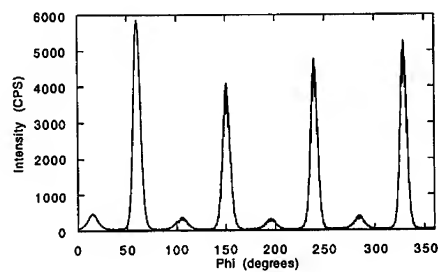


Figure 2b. XRD phi-scan of the (341) reflection of a  $\text{La}_{0.84}\text{Sr}_{0.16}\text{MnO}_3$  thin film grown on YSZ [100].

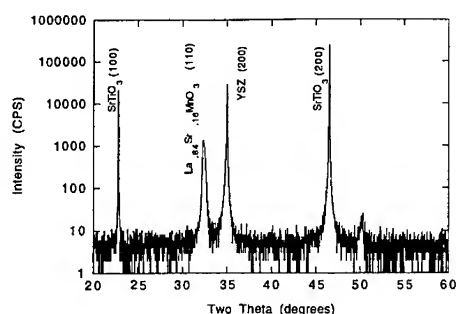


Figure 3. XRD pattern of a  $\text{La}_{0.84}\text{Sr}_{0.16}\text{MnO}_3$  [110] / YSZ [100] /  $\text{SrTiO}_3$  multilayer stack configuration.

and 500°C. Figure 5 is the current-voltage data for the two films taken at these same conditions. XRD analysis indicated that heating the single crystal films above 600°C would lead to recrystallization. The frequency range for these measurements was 1MHz to 100mHz with an amplitude of 50mV. The equivalent circuit used to model the data is shown in each figure as well. Although, for this work, the system remains underdetermined, we do see a simplification in the equivalent circuit for the oriented LSMO film vis à vis the polycrystalline film. Also, while clear trends are present in the resistive components of the single-crystal data, with respect to applied polarization, these trends are not observed in the polycrystalline sample. This preliminary data tends to suggest that the presence of grain boundaries in the film/substrate dominate the electrochemical response.

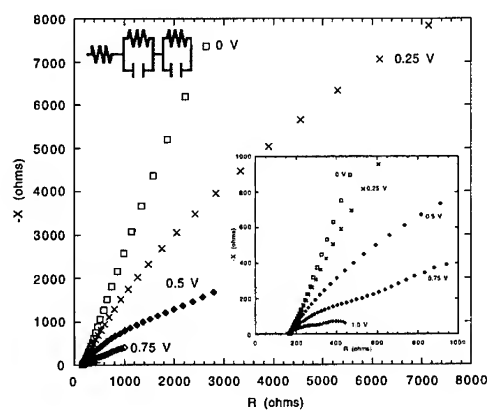


Figure 4a. AC impedance characterization, 1MHz-0.1Hz and 50 mV amplitude, of an oriented  $\text{La}_{0.84}\text{Sr}_{0.16}\text{MnO}_3$  [110] thin film grown on Y-ZrO<sub>2</sub> [100]. AC data was taken under polarizing and non-polarizing conditions at 1 atm PO<sub>2</sub> and 500°C. Frequency decreases from left to right. Inset: expanded view. Top: equivalent circuit used to model this data.

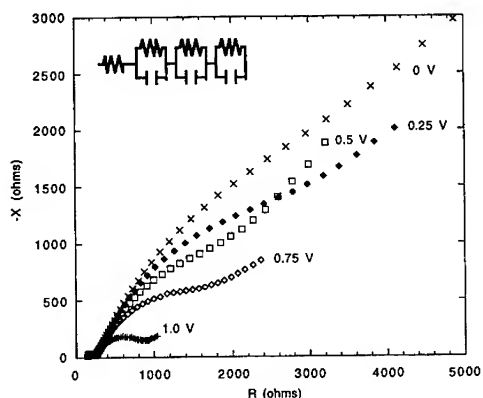
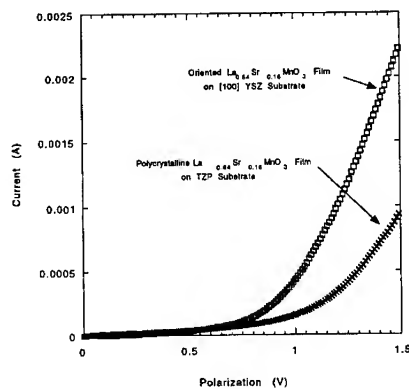


Figure 4b. AC impedance characterization, 1MHz-0.1Hz and 50 mV amplitude, of a polycrystalline  $\text{La}_{0.84}\text{Sr}_{0.16}\text{MnO}_3$  thin film sputtered on TZP. AC data was taken under polarizing and non-polarizing conditions at 1 atm  $\text{PO}_2$  and  $500^\circ\text{C}$ . Frequency decreases from left to right. Top: equivalent circuit used to model this data.

Figure 5. IV sweep of a polycrystalline  $\text{La}_{0.84}\text{Sr}_{0.16}\text{MnO}_3$  film on TZP and of an oriented  $\text{La}_{0.84}\text{Sr}_{0.16}\text{MnO}_3$  film grown on [100] YSZ. Scan conditions were  $500^\circ\text{C}$  and 1 atm  $\text{P}(\text{O}_2)$ .



## Conclusions

We have demonstrated that high quality, fully dense, and smooth thin films of  $\text{La}_{0.84}\text{Sr}_{0.16}\text{MnO}_{3-y}$  can be grown on single crystal YSZ substrates via off axis RF magnetron sputtering. In addition, epitaxial, multilayer perovskite/fluorite/perovskite configurations can be grown *in situ*. Preliminary AC impedance analysis indicates that these films may be utilized to simplify equivalent circuit modeling for fundamental electrochemical study of working fuel cell devices.

## Acknowledgments

We would like to thank Marilyn Hawley and Prabhat Tiwari of the Superconductor Technology Center, Los Alamos National Laboratory, for the STM and RBS data cited in this work.

## REFERENCES

- <sup>1</sup>J. T. Cheung, P. E. D. Morgan, D. H. Lowndes, X. Y. Zheng, and J. Breen. Appl. Phys. Lett. **62**, 2045 (1993); and references therein.
- <sup>2</sup>N.Q. Minh. J. Am. Ceram. Soc., 76, 563 (1993); and references therein.
- <sup>3</sup>C. B. Eom, J. Z. Sun, K. Yamamoto, A. F. Marshall, K. E. Luther, S. S. Laderman, and T. H. Geballe, Appl. Phys. Lett. **53**, 595 (1988).
- <sup>4</sup>C. B. Eom, J. Z. Sun, B. M. Lairson, S. K. Streiffer, A. F. Marshall, K. Yamamoto, S. M. Anlage, J. C. Bravman, T. H. Geballe, S. S. Laderman, R. C. Taber, and R. D. Jacowitz, Physica C, **171**, 354 (1990).
- <sup>5</sup>R.J. Houlton, D.W. Reagor, M.E. Hawley, K.N. Springer, Q.X. Jia, C.B. Mombourquette, F.H. Garzon, and X.D. Wu to be published in the IEEE Transactions on Applied Superconductivity Proceedings of the Applied Superconductivity Conference - Boston MA., October 1994.

**$\text{Bi}_2\text{Sr}_2\text{M}'_2\text{M}''\text{O}_{11.5}$  [(M' = Nb, Ta) and (M'' = Al, Ga)], SYNTHESIS AND CHARACTERIZATION OF OXYGEN-DEFICIENT AURIVILLIUS PHASES**

KURT R. KENDALL, CARLOS J. NAVAS, AND HANS-CONRAD ZUR LOYE,  
Department of Chemistry, Massachusetts Institute of Technology, Cambridge, MA 02139

**ABSTRACT**

Oxygen-deficient layered bismuth oxides,  $\text{Bi}_2\text{Sr}_2\text{M}'_2\text{M}''\text{O}_{11.5}$  [(M' = Nb, Ta) and (M'' = Al, Ga)] were synthesized. Powder X-ray diffraction and transmission electron microscopy were used to characterize the new materials' structures. The ionic conductivity was measured using impedance spectroscopy which indicated the existence of multiple conductive states in the new oxygen-deficient materials. Arrhenius plots of the conductivity showed discontinuities which were attributed to transitions between different conductive states. At 800 °C,  $\text{Bi}_2\text{Sr}_2\text{Nb}_2\text{GaO}_{11.5}$  and  $\text{Bi}_2\text{Sr}_2\text{Nb}_2\text{AlO}_{11.5}$ , have ionic conductivities of  $2.0 \times 10^{-2}$  S/cm and  $1.2 \times 10^{-2}$  S/cm, respectively. Differential thermal analysis showed phase transitions in the oxygen-deficient materials. These transitions occurred at temperatures similar to those at which discontinuities were observed in the Arrhenius plots of the conductivity and are attributed to oxygen vacancy order/disorder transitions. The transference number was calculated for some of the samples by measuring both the EMF and the conductivity as a function of oxygen partial pressure. Under atmospheric conditions the new materials are predominantly ionic conductors.

**INTRODUCTION**

New ionic electrolytes, specifically oxygen ion conductors, are being explored for possible replacement of existing materials. Applications where oxygen ion electrolytes can be used include sensors, batteries, fuel cells, and catalysts.[1,2] To increase the future commercialization of devices using these materials, the operating temperatures of oxygen electrolytes need to be decreased.[3]

A key factor in designing new oxygen ion conductors is maximizing the number of oxygen vacancies. Oxygen ion conduction in solids occurs as oxygen anions hop from an occupied lattice site to an unoccupied site;[4] thus, increasing the number of vacancies will lead to higher ionic conductivities. Without a large number of vacancies, the oxygen ion conductivity is expected to be limited.

The oxygen vacancies can either be extrinsically introduced through the use of dopants, or can be an intrinsic part of the structure, as is the case with the high temperature phase of bismuth oxide.[5]  $\text{Bi}_2\text{O}_3$  undergoes a phase change at 730 °C from a monoclinic  $\alpha$ -phase to a cubic defect fluorite phase,  $\sigma\text{-Bi}_2\text{O}_3$ , where 1/4 of the anion sites are vacant. The conductivity jumps several orders of magnitude when this transition occurs. Attempts to stabilize this highly conductive phase to room temperature have met with only limited success.[6]



The most successful oxygen ion conductor in terms of commercialization is stabilized zirconia.[7] The vacancies are extrinsically induced by doping with either yttrium or calcium, and at 1000 °C the conductivity is approximately  $1 \times 10^{-1}$  S/cm. As the temperature is decreased, however, the conductivity decreases rapidly, so that devices that use stabilized zirconias tend to operate at high temperatures.

Our research group has tried to design low-temperature oxygen ion conductors by modifying Aurivillius phases so that oxygen vacancies are incorporated into the structure. Aurivillius phases are layered materials with alternating bismuth oxide and perovskite layers.[8] By introducing oxygen-deficient perovskite layers into the perovskite region of the structure, we have been able to obtain oxygen ion conductors that appear to have multiple conducting phases. We have previously reported on the structural characterization by powder X-ray diffraction of the new modified Aurivillius phases, as well as on the measurement of the conductivity using impedance spectroscopy.[9,10] In this paper we report preliminary TEM results confirming the existence of the layered structure as well as conductivity and EMF data indicating that the conductivity is predominantly ionic under atmospheric conditions.

## EXPERIMENTAL PROCEDURES

All materials were synthesized using traditional solid state techniques. The oxides or carbonates were mechanically combined, pressed into pellets, and heated several times to 800 °C and then later to 1100 °C for three days. Between heatings, the pellets were reground, then pressed into new pellets. The materials were characterized by powder X-ray diffraction (XRD), differential thermal analysis (DTA), thermogravimetric analysis (TGA), and high resolution transmission electron microscopy (TEM). XRD was performed on a Rigaku RU300 diffractometer with Cu  $K_{\alpha}$  radiation and DTA-TGA measurements were made using a TA Instruments SDT 2960. TEM measurements were performed on a Topcon 002b microscope operating at 200 kV and on a Hitachi H-9000NAR microscope operating at 300 kV.[11]

Conductivity measurements were made on sintered pellets using a Solartron 1260 Impedance/Gain-Phase analyzer coupled with a PC computer over the frequency range of 1 Hz to 5 MHz. The temperature was cycled between 300 and 975 °C several times. To ascertain the degree of ionic conductivity, the conductivity and EMF were measured as a function of oxygen partial pressure.

The various oxygen partial pressures were obtained by employing different mixtures of argon and oxygen. Partial pressures ranged from 1 to  $10^{-6}$  atm of oxygen. The EMF measurements were made by exposing opposite faces of a sintered pellet to two gases (oxygen-argon mixture/ air). The gases were kept apart by ceramic seals; however, there were indications that some gas may have leaked through the seals. This had a detrimental effect on the EMF measurements at low  $pO_2$  ( $<10^{-4}$  atm)

## RESULTS AND DISCUSSION

### Structure

The materials synthesized by our group are derivatives of the Aurivillius phases,  $\text{Bi}_2\text{A}_{n-1}\text{M}_n\text{O}_{3n+3}$ . They consist of alternating square pyramidal bismuth oxide and  $n$  octahedral perovskite layers ( $n = 1$  to 5).[12] For example,  $\text{Bi}_2\text{VO}_{5.5}$ ,  $\text{Bi}_2\text{SrNb}_2\text{O}_9$ , and  $\text{Bi}_4\text{BaTi}_4\text{O}_{15}$  have  $n = 1, 2$ , and 4 octahedral layers, respectively. The parent structure for the oxygen deficient materials reported in this paper was  $\text{Bi}_2\text{Sr}_2\text{M}'_2\text{TiO}_{12}$ , ( $\text{M}' = \text{Nb}, \text{Ta}$ ). The oxygen vacancies were introduced by replacing titanium by either aluminum or gallium.

Powder X-ray diffraction data indicated that the oxygen-deficient materials,  $\text{Bi}_2\text{Sr}_2\text{M}'_2\text{M}''\text{O}_{11.5}$  [ $(\text{M}' = \text{Nb}, \text{Ta})$  and  $(\text{M}'' = \text{Al}, \text{Ga})$ ], could be indexed to a pseudo-tetragonal unit cell with lattice constants (Table 1) in agreement with the non-deficient parent structures,  $\text{Bi}_2\text{Sr}_2\text{M}'_2\text{TiO}_{12}$ , ( $\text{M}' = \text{Nb}, \text{Ta}$ ). Because of the way in which the perovskite layers stack with the bismuth oxide layers, the  $c$  parameter represents the distance between two bismuth oxide/perovskite layers. Figure 1 shows a TEM picture of the  $ac$  plane of  $\text{Bi}_2\text{Sr}_2\text{Nb}_2\text{GaO}_{11.5}$ , where the distance between each successive bismuth oxide layer is approximately  $16.7(2) \text{ \AA}$ . If this is doubled, the value of

Table 1: Lattice constants

Compounds	$a \text{ (\AA)}$	$c \text{ (\AA)}$
$\text{Bi}_2\text{Sr}_2\text{Nb}_2\text{AlO}_{11.5}$	3.907(1)	33.24(1)
$\text{Bi}_2\text{Sr}_2\text{Nb}_2\text{GaO}_{11.5}$	3.913(1)	33.29(1)
$\text{Bi}_2\text{Sr}_2\text{Ta}_2\text{GaO}_{11.5}$	3.909(1)	33.20(1)
$\text{Bi}_2\text{Sr}_2\text{Ta}_2\text{AlO}_{11.5}$	3.904(1)	33.08(1)
$\text{Bi}_2\text{Sr}_2\text{Nb}_2\text{TiO}_{12}$	3.892(1)	33.18(1)
$\text{Bi}_2\text{Sr}_2\text{Ta}_2\text{TiO}_{12}$	3.893(1)	33.13(1)

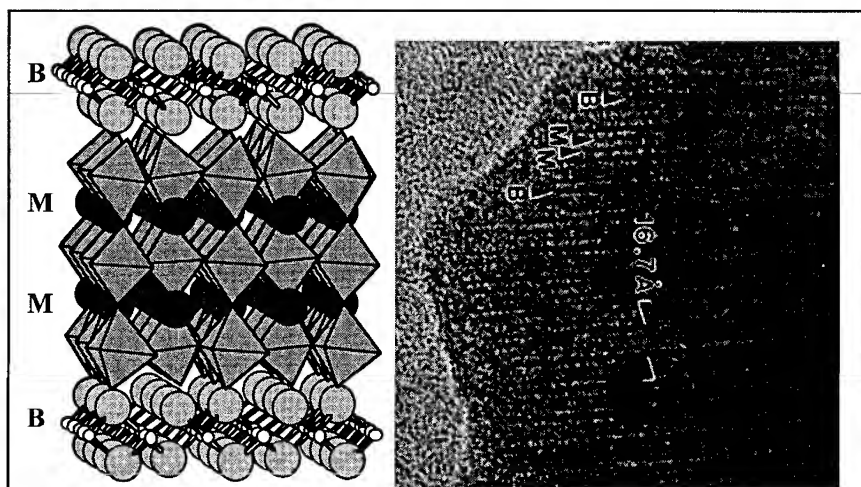


Figure 1: Three layer Aurivillius phase and TEM picture of  $\text{Bi}_2\text{Sr}_2\text{Nb}_2\text{GaO}_{11.5}$ . The distance between bismuth oxide layers ( $16.7(2) \text{ \AA}$ ) agrees with distance calculated from powder X-ray diffraction data ( $16.65 \text{ \AA}$ )

33.4 Å is the same as the *c* lattice constant determined from the powder X-ray diffraction data within experimental error. Figure 1 also contains a graphical representation of the Aurivillius phase showing the associated features of the structure for comparison with the TEM data.

### Conductivity

The conductivity was measured using impedance spectroscopy and indicated the existence of three separate conductive regions. An extensive description of the conductivity behavior for all of the oxygen-deficient materials, as well as the two reference Aurivillius phases,  $\text{Bi}_2\text{Sr}_2\text{M}'_2\text{TiO}_{12}$ , ( $\text{M}' = \text{Nb}, \text{Ta}$ ), can be found in a previous paper.[9] An

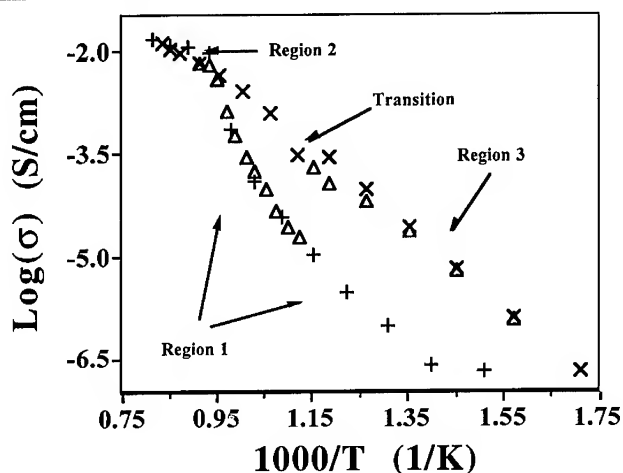


Figure 2: Arrhenius plot of conductivity for  $\text{Bi}_2\text{Sr}_2\text{Ta}_2\text{GaO}_{11.5}$ . The data represents the conductivity for (+) initial heating, ( $\Delta$ ) cooling, and (X) second heating cycle. Three different conductive regions are observed, with an abrupt transition occurring between the third region and the first region during the second heating cycle.

Arrhenius plot of the conductivity of  $\text{Bi}_2\text{Sr}_2\text{Ta}_2\text{GaO}_{11.5}$  is shown in Figure 2, and is representative of all the oxygen-deficient materials. During the initial heating cycle, the oxygen-deficient phases were in the lower conductive state (Figure 2: Region 1), which exhibited non-linear behavior in the Arrhenius plot. Between 700 and 800 °C, the oxygen-deficient phases showed a large jump in their conductivity. Above 800 °C (Figure 2: Region 2), the Arrhenius plots were linear and had activation energies of  $\approx 0.4$  eV.

Upon cooling, a discontinuity was observed in the Arrhenius plot around 800 °C, where the activation energies, as calculated from the Arrhenius plots, increased to around 1.2 eV (1.4 eV for  $\text{Bi}_2\text{Sr}_2\text{Ta}_2\text{AlO}_{11.5}$ ). This third conductive state (Figure 2: Region 3) remained stable down to at least 300 °C. The second heating cycle was started when the

resistances increased beyond the resolution of our impedance analyzer. Around 600 °C, both  $\text{Bi}_2\text{Sr}_2\text{Ta}_2\text{GaO}_{11.5}$  and  $\text{Bi}_2\text{Sr}_2\text{Nb}_2\text{GaO}_{11.5}$  showed a sharp decrease in conductivity (Figure 2: Transition) as the temperature was increased. In the case of  $\text{Bi}_2\text{Sr}_2\text{Ta}_2\text{GaO}_{11.5}$ , the conductivity dropped by more than a factor of ten over a temperature interval of less than 10 °C. These two oxygen-deficient materials appear to undergo a phase change from the conductive state in Region 3 to the conductive state in Region 1. For reasons not fully understood, the two oxygen-deficient materials containing aluminum instead of gallium do not show a similar drop in conductivity during the second heating cycle.

The multiple conductive states in the oxygen-deficient materials are believed to be due to order/disorder transitions in the oxygen vacancies. To better understand these transitions DTA-TGA measurements were performed on all of the samples. With the exception of  $\text{Bi}_2\text{Sr}_2\text{Ta}_2\text{AlO}_{11.5}$ , all of the oxygen deficient materials exhibited phase transitions between 750 and 825 °C. The transitions were not observed in the two reference Aurivillius phases.

#### Transference Numbers

Because of the possibility of electronic conduction, the EMF and the conductivity as a function of oxygen partial pressure were measured for  $p\text{O}_2$  varying from 1 to  $10^{-6}$  atm. Figure 3 shows the  $p\text{O}_2$  dependence of the conductivity for  $\text{Bi}_2\text{Sr}_2\text{Nb}_2\text{GaO}_{11.5}$ ,  $\text{Bi}_2\text{Sr}_2\text{Nb}_2\text{AlO}_{11.5}$ , and  $\text{Bi}_2\text{Sr}_2\text{Ta}_2\text{GaO}_{11.5}$ . The linearity of all of the  $p\text{O}_2$  plots indicates that either the conductivity is predominantly ionic ( $t_{\text{ion}} \approx 1$ ) or the materials are electronic conductors changing from n-type conduction to p-type conduction.[13] To distinguish

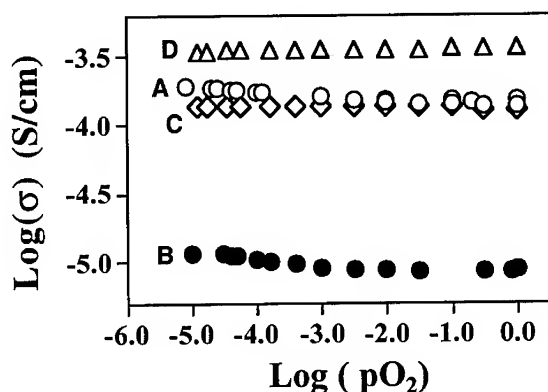


Figure 3: Partial pressure of oxygen dependency of the conductivity for  $\text{Bi}_2\text{Sr}_2\text{Nb}_2\text{GaO}_{11.5}$  at 720 °C (A) and 620 °C (B),  $\text{Bi}_2\text{Sr}_2\text{Ta}_2\text{GaO}_{11.5}$  at 720 °C (C), and  $\text{Bi}_2\text{Sr}_2\text{Nb}_2\text{AlO}_{11.5}$  at 600 °C (D). The conductivity data for  $\text{Bi}_2\text{Sr}_2\text{Nb}_2\text{GaO}_{11.5}$  and  $\text{Bi}_2\text{Sr}_2\text{Ta}_2\text{GaO}_{11.5}$  were obtained from Region 1 (see Figure 2), while the data for  $\text{Bi}_2\text{Sr}_2\text{Nb}_2\text{AlO}_{11.5}$  was obtained from Region 3.

which is the case, EMF measurements were performed on  $\text{Bi}_2\text{Sr}_2\text{Nb}_2\text{GaO}_{11.5}$  and  $\text{Bi}_2\text{Sr}_2\text{Nb}_2\text{AlO}_{11.5}$ . The data indicated that down to  $10^{-3}$  atm,  $t_{\text{ion}} \approx 1$ . At lower  $p\text{O}_2$ ,  $t_{\text{ion}}$  begins to decrease; however, because of the difficulty in maintaining tight seals and because of the  $p\text{O}_2$  dependency data, we believe that these materials are predominately ionic conductors down to  $10^{-6}$  atm of oxygen.

## CONCLUSION

The synthesis and characterization of  $\text{Bi}_2\text{Sr}_2\text{M}'_2\text{M}''\text{O}_{11.5}$  [ $\text{M}' = \text{Nb, Ta}$ ] and [ $\text{M}'' = \text{Al, Ga}$ ] has resulted in the discovery of a new class of oxygen ion conductors. TEM data along with powder X-ray diffraction data confirms that these materials form the expected three-layer Aurivillius phases. Conductivity data indicates that the oxygen deficient materials undergo structural changes that directly affect the conductivity of the sample. The oxygen vacancies in the perovskite layers are believed to undergo an order/disorder transition which greatly increases the ionic conductivity. The transference number for several of the new materials was measured and demonstrated that the conductivity is predominantly ionic down to  $10^{-6}$  atm of oxygen.

## ACKNOWLEDGMENTS

This work was funded by the National Science Foundation through grant number DMR9200688. The authors wish to thank Mark Fendorf for his help with the TEM data.

## REFERENCES

1. N. Q. Minh, *J. Am. Ceram. Soc.* **76**, 563 (1993).
2. R. Di Cosimo, J. D. Burrington, R. K. Grasselli, *J. Catal.* **102**, 234 (1986).
3. P. Hagenmuller, in *Superionic Solids and Solid Electrolytes* A. L. Laskar, S. Chandra, Eds. (Academic Press, New York, 1989) p. 679.
4. I. Riess, in *Science and Technology of Fast Ion Conductors* H. L. Tuller, M. Balkanski, Eds. (Plenum Press, New York, 1987) p. 23.
5. T. Kudo, K. Fueki, *Solid State Ionics* (VCH Publishers, New York, 1990)
6. T. Takahashi, H. Iwahara, T. Esaka, *J. Electrochem. Soc.* **124**, 1563 (1977).
7. B. C. H. Steele, *J. Power Sources* **49**, 1 (1994).
8. B. Aurivillius, *Arkiv. Kemi.* **1**, 463 (1949).
9. K. R. Kendall, J. K. Thomas, H. C. zur Loye, *Chem. Mater.*, In Press (1994).
10. K. R. Kendall, J. K. Thomas, H.-C. zur Loye, *Solid State Ionics* **70/71**, 221 (1994).
11. M. Fendorf, U.C. Berkeley, Portions of the TEM work were performed at the National Center for Electron Microscopy, Lawrence Berkeley Laboratory, a facility funded by the Director, Office of Energy Research, Office of Basic Energy Sciences, Materials Science Division of the U.S. Department of Energy under Contract Number DE-AC03-76SF00098 (1994).
12. E. C. Subbarao, *J. Am. Ceram. Soc.* **45**, 166 (1962).
13. H. L. Tuller, P. K. Moon, *Mater. Sci. Eng. B-Solid State M.* **B1**, 171 (1988).

## CATION CONDUCTIVITY IN MIXED SULFATE-BASED AND MIXED IODIDE-BASED SOLIDS WITH PHASE TRANSITIONS

E. A. SECCO

Department of Chemistry, St. Francis Xavier University, Antigonish, Nova Scotia, CANADA B2G 2W5

### ABSTRACT

The ac electrical conductivity versus temperature dependence of solids undergoing phase transitions incorporating various guest ions, viz isovalent cations and anions, ions with different ionic radius, ions with different polarizability, in  $\text{Na}_2\text{SO}_4$ -based,  $\text{Ag}_2\text{SO}_4$ -based,  $\text{Li}_2\text{SO}_4$ -based and  $\text{UO}_2\text{SO}_4$ -based compositions along with  $\text{M}_x\text{Tl}_{(1-x)}\text{I}$  compositions for  $1 \leq x \leq 0.13$ , whose  $\text{M} = \text{K}, \text{Rb}, \text{Cs}$ , are reported. An overview is given of the interplay of various factors, structural and non-structural, with their contribution limits impacting on locking-in the fast cation conductivity phase and the interpretation of fast-ion conductivity in the context of a percolation-type of ion transport mechanism.

### INTRODUCTION

Fast-ion conduction in solids is considered a paradigm for a structure-property relation. The sharp jump in ionic conductivity, factor  $\sim 10^4$ , accompanying the structural change at the phase transition is consistent with this relation. It suggests a promising strategy to retain fast-ion conductivity at room temperature would be, therefore, to preserve or lock-in the high-temperature high-conductivity structure. In this behavior the qualitative resemblance of the sharp jump in the logarithm  $\sigma T$  versus  $T^{-1}$  plot for these solids, e.g. alkali sulfates,  $\text{Ag}_2\text{SO}_4$ ,  $\text{AgTlSO}_4$ ,  $\text{AgI}$ ,  $\text{TlI}$ ,  $\text{Li}_2\text{MCl}_4$  spinels, to the site percolation probability function, i.e.  $P(p)$  plot (1,2), suggests the percolation model for ion transport. The  $P$  versus  $p$  describes the function  $P(p)$  where  $P$  is the percolation probability or the fraction of the structure taken up by the percolation path and  $p$  represents the probability that a neighboring site is unblocked or the probability of intersite connectivity to an activated hopping ion. That is, at the phase transition or the structural percolation threshold the number of intersite channel connectivities or the percolation probability in the network structure increases sharply, giving rise to the observed sudden jump in ion conductivity. This paper presents an overview of the interplay of various factors, with their contribution limits, impacting on the enhancement of ion conductivity and on locking-in the fast-ion conductivity structure along with our effort to fit these results to the percolation model of ion transport.

### EXPERIMENTAL PROCEDURE

All compounds used were of stated purity  $> 99.9\%$  except  $\text{UO}_2\text{SO}_4 \cdot 3\text{H}_2\text{O}$ ,  $96\%$ . The requisite well-ground mixed compositions were fused in a Pt or porcelain crucible 50-60 min. Checks on after-melted sample weights showed negligible weight loss  $< 0.02\%$ , indicating the sample maintained its original composition.

The ac electrical conductivity measurements were done using the two terminal method already described (3,4). The samples, both compressed ground-fused particle and uncompressed solidified fused mass crystalline and glass state products, were 1-2 mm thick and up to  $75 \text{ mm}^2$  in area. Each sample with both surfaces touched with graphite (DAG #154

Acheson) was maintained by a spring-loaded support between stainless-steel leads using two polished Pt discs as electrodes contained in a stainless steel conductivity cell. The conductivity was measured under reduced pressure ( $\sim 10^{-3}$  Torr) at frequencies 0.1, 1, 10, 100 kHz with heating and cooling rate of  $\sim 1^\circ \text{ min}^{-1}$ . Early measurements were made by the null method using a GR 1608-A impedance bridge with manual recording and by continuous automatic recording with a GenRad 1688 LC Digibridge interfaced to Apple IIe microcomputer and Epson PX-85 printer. Recent measurements were by continuous automatic recording with SRS (Stanford Research Systems) Model SR 720 LCR meter interfaced to a 386 SX/25 2MB microcomputer operating at 16 MHz and Panasonic KX-P1123 24 PIN Multi-mode printer. Temperature was monitored by standardized chromel-alumel thermocouple with a digital multimeter (Keithley or Hewlett-Packard).

Phase transitions were determined using differential scanning calorimetry (DSC) accessory on a DuPont 1090B Thermal Analyzer equipped with disk memory and data analyzer.

## RESULTS AND DISCUSSION

Ionic transport in a condensed phase occurs by a process of activated hopping of vibrating ions of charge  $q$  with frequency  $\nu$  surmounting the potential energy barrier between two equivalent sites separated by distance  $\lambda$  under a directional force of an applied electric field. The dependence of solid state ionic conductivity on temperature usually follows the Arrhenius-type expression

$$\sigma T = \sigma_0 \exp\left(-\frac{Q_c}{RT}\right) \quad (1)$$

where  $Q_c$  is the apparent activation energy for ionic conductivity and  $T(K)$  the temperature. The details in the derivation of Eq. (1) from fundamental relationships and its limits have already been given (5). The plot of  $\ln(\sigma T)$  versus  $T(K)^{-1}$  yields the value of  $Q_c$  from the slope.

### Sulfate-based Systems

Typical  $\sigma$ - $T$  plots illustrating the effect of some guest ions on ion conductivity and phase transitions in  $\text{Na}_2\text{SO}_4$  were reported earlier (4,5). Figs. 1 and 2 show the enhanced conductivity by the larger radius  $\text{Rb}^+$  and  $\text{MoO}_4^{2-}$ , respectively. The conductivity jumps observed with  $\text{Rb}^+$  correlate with the solid-solid phase transitions in  $\text{Na}_2\text{SO}_4$ - $\text{Rb}_2\text{SO}_4$  phase diagram (6,7). The presence of  $\text{MoO}_4^{2-}$  stabilizes the high temperature hexagonal structure of  $\text{Na}_2\text{SO}_4$ -I in the composition  $\text{Na}_2(\text{SO}_4)_{0.5}(\text{MoO}_4)_{0.5}$ . This phase stabilization is effected by  $\text{Na}_2\text{MoO}_4$  being isomorphous with  $\text{Na}_2\text{SO}_4$ -I,  $P6_3/mmc$ , indicating ease of anion substitution in their respective sublattices and the structural control manifested by the larger radius isovalent  $\text{MoO}_4^{2-}$  in the larger lattice volume phase of  $\text{Na}_2\text{SO}_4$ -I.

Log  $\sigma$ - $T$ -composition isotherms for  $\text{Na}_2\text{SO}_4$ - $\text{Rb}_2\text{SO}_4$  and  $\text{Ag}_2\text{SO}_4$ - $\text{Rb}_2\text{SO}_4$  systems are given in Fig. 3 (6) and the same isotherm for  $\text{Na}_2\text{SO}_4$ - $\text{Na}_2\text{MoO}_4$  is given in Fig. 4(6). The positive conductivity-composition effect by the incorporation of isovalent guest ions impacts on the structural and non-structural contributing factors. Furthermore, the drop in activation energy  $Q_c$  to  $45 \pm 4$  kJ/mole from  $55 \pm 5$  kJ/mole in pure  $\text{Na}_2\text{SO}_4$  for ion conductivity in the same hexagonal structure of binary composition containing the larger radius isovalent ion indicated a greater facility for ion mobility in an expanded lattice of more "free" volume. The increases in  $\sigma$  value by factor  $10^2$ - $10^3$  at both ends of the system composition at  $282^\circ\text{C}$

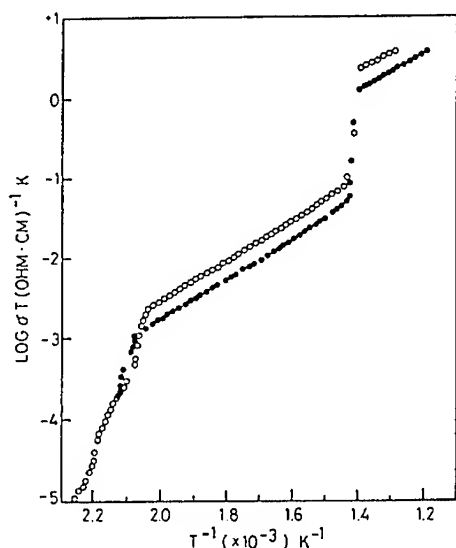


Fig. 1. Plots of  $\log \sigma T$  versus  $TK^{-1}$  of  $Na_2SO_4$ - $Rb_2SO_4$  in mole ratios 1:2 (●) and 2:1 (○).

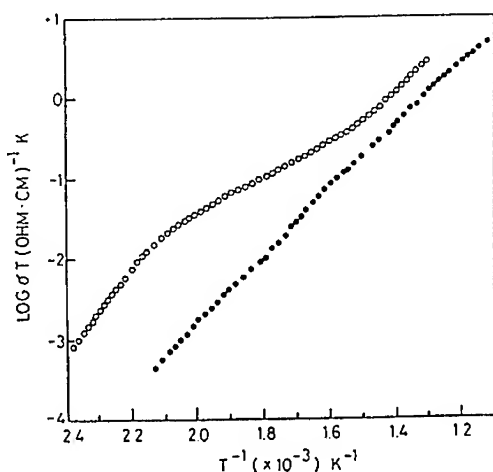


Fig. 2. Plots of  $\log \sigma T$  versus  $TK^{-1}$  of  $Na_2SO_4$ - $Na_2MoO_4$  in mole ratios 1:1 (●) and 4:1 (○).

and in the 50-70 mole % interval at 527°C, Fig. 3, are somewhat unexpected on the basis that the fraction of mobile charge carriers,  $Na^+$  or  $Ag^+$ , decreases proportionately with their respective decrease in system composition. It appears that the decrease in system composition is more than compensated by a higher concentration of activated mobile ions effected by "lattice loosening" along with facility of ion mobility provided by "free" volume. On the other hand we observe  $\sigma$  increase at the  $Na_2SO_4$ -rich end of  $Na_2SO_4$ - $Na_2MoO_4$  system, Fig. 4, followed by a drop in  $\sigma$  at the 50 mole % composition where the high-temperature hexagonal structure is stabilized. Again this  $\sigma$  drop is unexpected since the system composition of  $Na^+$  is constant and the "free" volume increases with increasing  $MoO_4^{2-}$  presence. This behavior strongly suggests a lower concentration of activated mobile ions effected by "lattice tightening" as a result of stronger  $Na^+$  and  $MoO_4^{2-}$  interaction or bonding.

Computer simulation studies on glasses have shown that higher densities generally gave lower conductivities, as the "free" volume and space for ionic mobility are reduced (8). The existence of  $Na_4UO_2(SO_4)_3$ , tetrasodium uranyl sulfate, in both crystal and glass phase provided an opportunity to compare mobility in these phases with ~7% extra volume in the glass phase. Fig. 5 shows heat and cool plots of  $\log \sigma T$  versus  $TK^{-1}$  for  $Na_4UO_2(SO_4)_3$ : A, glass sample and E, crystalline sample (3). Plot E shows a slight incline near 325°C which correlates with the crystalline  $\alpha \rightarrow \beta$  transition (9). The rise in conductivity immediately

preceding the glass devitrification drop is attributed to structural relaxation and expansion. Recent studies on glass and crystalline solids of  $Na_2MoO_4$ - $UO_2SO_4$  system report similar behavior of structural relaxation and expansion prior to devitrification (10), Fig. 6. The three major discontinuities or peaks in the  $\log \sigma T$  versus  $TK^{-1}$  plots at temperatures 324, 372,



426°C correlate with the exotherms at 336, 385, 428°C on the DSC heating trace. The three conductivity peaks and exotherms indicate three intermediate statically disordered solid states. This structural relaxation step leading to the glass-product transformation provides insight into

the phase transition molecular rearrangement and confirms the ionic conductivity as a useful probe in monitoring the molecular dynamics prior to and during phase transitions.

With  $V \propto 1/P$  the contribution of structure "free" volume to ionic conductivity was investigated directly using hydrostatic pressure on  $\text{Na}_2\text{SO}_4$ . The observed inverse dependence of conductivity on pressure and the increase in activation energy with pressure are consistent with lattice compression impeding the transport of  $\text{Na}^+$  ions (11). The conductivity-free volume correlation was also reported by Jiang and Weller on studies of (Ag, Na)-halide sodalites and -nitrite sodalites (12,13).

Our efforts to probe the factors affecting fast-ion conductivity were extended by incorporating the smaller radius  $\text{Li}^+$  ion into alkali sulfate analogs and  $\text{Ag}_2\text{SO}_4$  and also other monovalent ions, viz  $\text{Na}^+$ ,  $\text{K}^+$ ,  $\text{Rb}^+$ ,  $\text{Cs}^+$ ,  $\text{Ag}^+$ ,  $\text{Tl}^+$  in  $\text{Li}_2\text{SO}_4$  and  $\text{Ag}_2\text{SO}_4$  (14). Isotherms of conductivity versus ionic radius for the compositions studied are presented in Fig. 7. The compositions include the specific cation  $M^+$  in its undoped parent, i.e.

$\text{Li}^+$  in  $\text{Li}_2\text{SO}_4$ ,  $\text{Na}^+$  in  $\text{Na}_2\text{SO}_4$ , etc. plot a, 10 mole %  $\text{Li}^+$  in host  $\text{M}_2\text{SO}_4$ , i.e.  $\text{Li}_{0.20}\text{Na}_{1.80}\text{SO}_4$ , etc. plot b, 10 mole % given guest cation  $M^+$  in host  $\text{Li}_2\text{SO}_4$ , i.e.  $\text{M}_{0.20}\text{Li}_{1.80}\text{SO}_4$ , etc. plot c, 10 mole % given guest cation  $M^+$  ion host  $\text{Ag}_2\text{SO}_4$ , i.e.  $\text{Li}_{0.20}\text{Ag}_{1.80}\text{SO}_4$ , etc. plot d. Plot b, viz  $\text{Li}^+$  in  $\text{M}_2\text{SO}_4$  shows higher conductivity relative to pure  $\text{M}_2\text{SO}_4$  attributed to the higher mobility of the smaller radius  $\text{Li}^+$  in the lattice. In plot c, while the conductivity is lower than its host  $\text{Li}_2\text{SO}_4$  attributed to

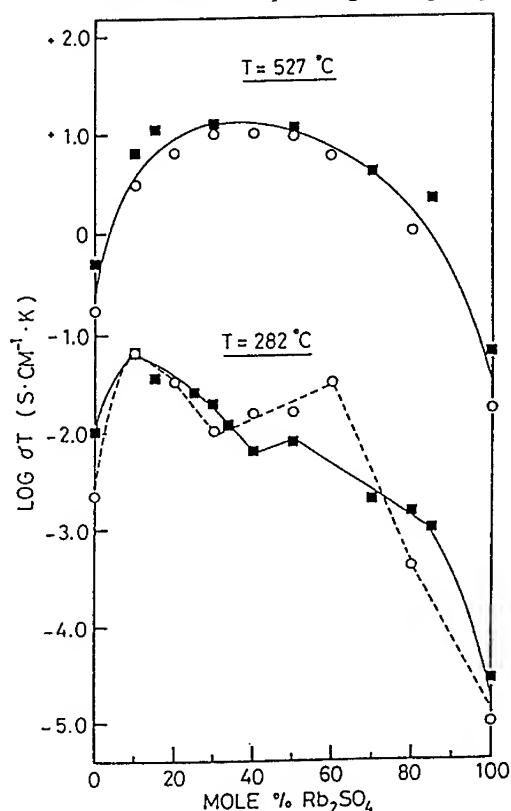


Fig. 3. Isotherm plots of  $\log \sigma T$  versus mole %  $\text{Rb}_2\text{SO}_4$  in  $\text{Ag}_2\text{SO}_4$  (■) and in  $\text{Na}_2\text{SO}_4$  (○).

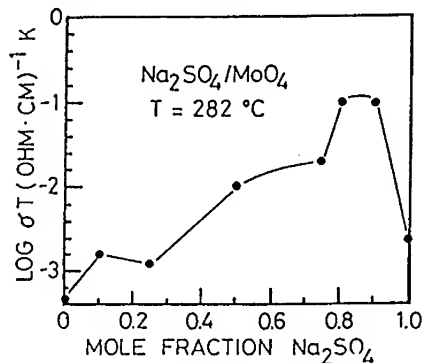


Fig. 4. Isotherm plot of  $\log \sigma T$  versus mole fraction  $\text{Na}_2\text{MoO}_4$  in  $\text{Na}_2\text{SO}_4$ .

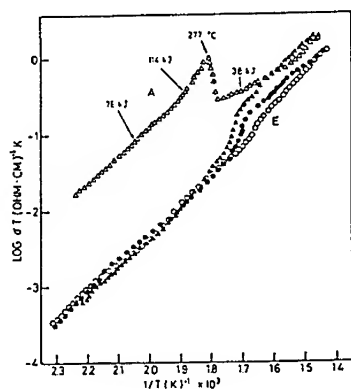


Fig. 5. Plots of  $\log \sigma T$  versus  $TK^{-1}$  for  $Na_4UO_2(SO_4)_3$ : A, glass sample ( $\Delta$  heat,  $\blacktriangle$  cool); E, crystalline sample ( $\circ$  heat,  $\bullet$  cool).

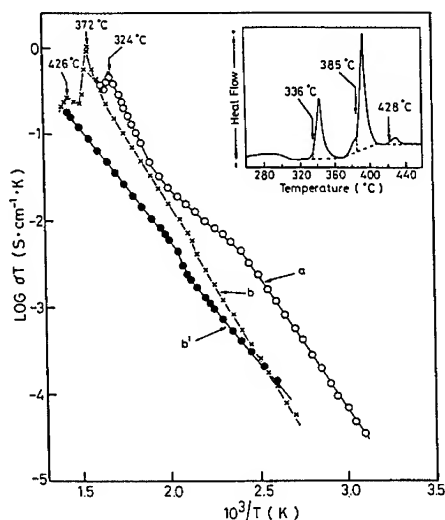


Fig. 6.  $\log \sigma T$  versus  $T^{-1}$  plot for compressed ground glass of molar composition 0.63  $Na_2MoO_4:0.37UO_2SO_4$ : (a) first heat of compressed disc, (b) second heating of disc, (b') cooling sample from (b). Insert is DSC heating trace for uncompressed glass sample. [Ref. (10)].

the lower concentration of the activated more mobile  $Li^+$  ion, the conductivity is higher relative to plot b consistent with enhanced mobility accompanying lattice expansion effect with larger guest-ion presence. The most outstanding feature is the distinct behavior of the guest-ion  $Ag^+$  in  $Li_2SO_4$ , plot c, and all the guest ions in  $Ag_2SO_4$ -based compositions, i.e. plot d relative to plots a, b, and c. The higher mobility of the smaller  $Li^+$  giving higher conductivity in the hexagonal structure of  $\alpha$ - $Ag_2SO_4$  is expected but the equally high conductivity for 10 mole %  $Ag^+$  in  $Li_2SO_4$  in an abnormal deviation from the trend in plot c is surprising. While undoped  $Ag_2SO_4$  shows the highest conductivity undoped  $Tl_2SO_4$  is second highest relative to undoped  $Na_2SO_4$ ,  $K_2SO_4$ ,  $Rb_2SO_4$ ,  $Cs_2SO_4$ .

Notwithstanding the high correlation established between conductivity, structure and "free" volume the question arises as to the basis for higher ionic conductivities in  $Ag_2SO_4$  and  $Tl_2SO_4$  relative to  $Na_2SO_4$  in the same

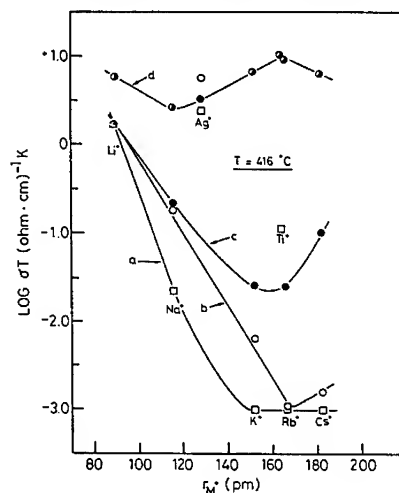


Fig. 7. Isotherm plots of  $\log \sigma T$  versus  $r_{M^+}$ , ionic radius of cation  $M^+$ : (a)  $M^+$  in its undoped parent  $M_2SO_4$ , (b) 10 mole %  $Li^+$  in host  $M_2SO_4$ , (c) 10 mole %  $M^+$  in host  $Li_2SO_4$ , (d) 10 mole %  $M^+$  in host  $Ag_2SO_4$  [Ref. (14)].

skeletal framework of hexagonal structure, space group  $P6_3/mmc$ , where  $r_{Ag^+} = 129$  pm and  $r_{Tl^+} = 164$  pm relative to  $r_{Na^+} = 116$  pm for C.N. = 6 (15) and  $m_{Ag^+} = 108$  and  $m_{Tl^+} = 204$  relative to  $m_{Na^+} = 23$ . Recently, Wuensch (16) showed in the analysis of fast cation conductivity in  $Ag^+$  and  $Cu^+$  halides relative to their  $Na^+$  and  $Li^+$  analogs that bonding characteristics and concentration of mobile ions in a given compound or composition can override the geometry of the anion array. One visualizes the activation energy for cation mobility to be a composite of three energies of ion interaction effects, i.e.  $Q_c = E_c + E_s + E_r$ , with  $E_c$  the coulombic attraction energy between cation and its anion surroundings,  $E_s$  the strain energy for cation passage through the bottleneck, and  $E_r$  the mobile ion-ion repulsion

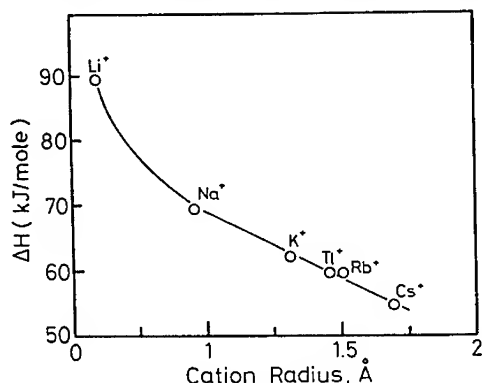


Fig. 8. Activation energies  $\Delta H$  for alkali ion conduction in zeolite versus cation radius [Refs. (19,20)].

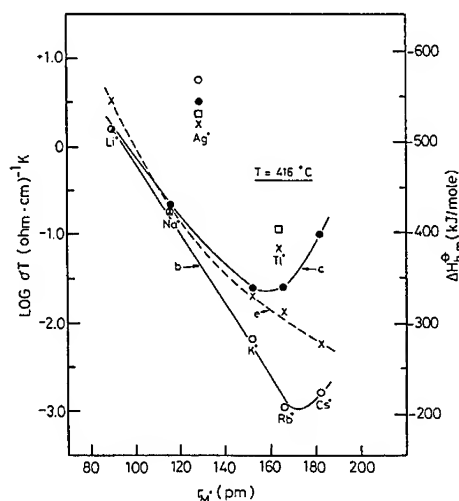


Fig. 9. Plot of standard molar enthalpy of hydration  $\Delta H_{h,m}^0$  versus cation radius for alkali ions (e) along with values for  $Ag^+$  and  $Tl^+$  and conductivity data taken from Fig. 7 [Ref. (14)].

Cation conductivity in zeolites is greater than in most other crystals, viz.  $NaCl$ ,  $KCl$ , etc. due to their internal channel structure and the diffusion coefficient/ionic conductivity for  $Na^+$  in hydrated Faujasite is  $10^4$  times greater than its anhydrous analog at room temperature (18). Furthermore, the activation energy for cation conduction in hydrated zeolite is inversely dependent on ionic radius for monovalent ions (19,20), Fig. 8. In Fig. 9 we plot the dependence of the standard molar enthalpy of hydration  $\Delta H_{h,m}^0$  on ionic radius, plot e, along with plots b and c and data for  $Ag^+$  and  $Tl^+$  from Fig. 7. The parallel behavior of plot e with plots b and c plus the distinct departure from this trend by  $Ag^+$  and  $Tl^+$  suggest an ion-ion interaction effect, most likely cation-anion. The electron configuration, the polarizing power and the polarizability of the cation relative to the common anion  $SO_4^{2-}$  in the sulfate analogs loom most probable. That is, two ions of the same charge and approximate size, one with an  $(n-1)d^xns^0$  electronic configuration will be more polarizing than a cation with a noble gas configuration  $(n-1)s^2(n-1)p^6ns^0$ . Using acid-base terminology where hard electrostatic interactions involving  $Li^+$ ,  $Na^+$ ,  $K^+$  with  $SO_4^{2-}$  and soft covalent interactions  $Ag^+$  or  $Cu^+$  with  $SO_4^{2-}$  one might speculate that weaker bonding between the  $d^{10}$  ions and the  $SO_4^{2-}$  sublattice permits a greater ease of mobility relative to  $s^2p^6$  alkali ions.

This interpretation suggests  $Tl^{+}5d^{10}6s^2$  being intermediate between the two configurations would show intermediate conductivity behavior as is observed.

#### TlI-based compositions

The chemistry for  $Tl^{+}$  bears some resemblance to that of  $Ag^{+}$  (21) and to the alkali metals especially  $Rb^{+}$  (22).  $TlI$  was chosen along with  $RbI$  for a parallel study with  $AgI$ . Yellow  $TlI$  transforms at  $175^{\circ}C$  to a red cubic form accompanied by a 3% reduction in volume paralleling the decrease in volume of 6% for  $AgI$  at its phase transition  $147^{\circ}C$ . While there is a significant jump in conductivity at each phase transition the conductivity jump-free volume correlation obviously does not hold for  $AgI$  and  $TlI$ . The presence of 20 mole %  $Rb^{+}$  in  $AgI$  in the form of the compound  $RbAg_4I_5$  preserves the high conductivity of  $\alpha$ - $AgI$  at room temperature. These features along with  $r_{Tl^{+}} \approx r_{Rb^{+}}$  prompted us to investigate the effect of  $Rb^{+}$  in  $TlI$  with the similar aim of stabilizing or preserving the high conductivity phase of  $TlI$  at room temperature.

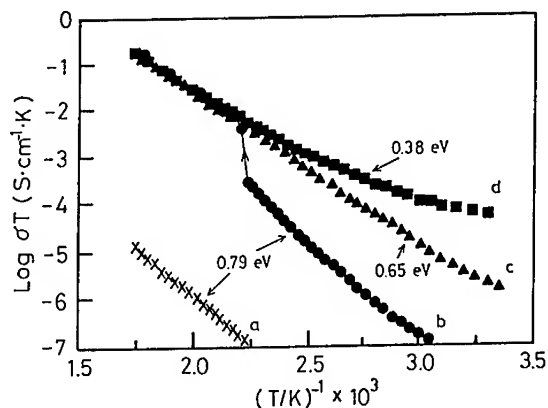


Fig. 10. Plots of  $\log \sigma T$  versus  $T^{-1}$  of (a)  $RbI$ , (b)  $TlI$ , (c)  $Rb_{0.10}Tl_{0.90}I$ , (d)  $Rb_{0.05}Tl_{0.95}I$  [Ref. (23)].

Fig. 10 gives the conductivity-temperature dependence for  $RbI$ (a),  $TlI$ (b),  $Rb_{0.10}Tl_{0.90}I$ (c), and  $Rb_{0.05}Tl_{0.95}I$ (d) for heat mode only, where each sample was annealed uncompressed quenched solidified fused mass (23). The absence of the  $\beta \rightarrow \alpha$  conductivity jump in (c) and (d) is consistent with its endotherm absence in DSC traces and the presence of the red  $\alpha$ - $TlI$  structure as confirmed by X-ray diffraction. The same high conductivity for  $Rb_{0.05}Tl_{0.95}I$  as for  $\alpha$ - $TlI$  is preserved in the cool mode for the temperature interval  $300-30^{\circ}C$ . The locking-

in of the cubic  $\alpha$ -phase in  $Rb_{0.05}Tl_{0.95}I$  was interpreted in terms of a chemical ion-ion interaction effect. From simple ion-ion interaction considerations we visualize bonding between the more electropositive  $Rb^{+}$  and  $I^{-}$  to be stronger than that between  $Tl^{+}$  and  $I^{-}$  in the solid. This stronger bonding, paralleling that of cubic  $TlCl$  and  $TlBr$ , can effect a structural contraction sufficient to stabilize the cubic structure of  $TlI$ .

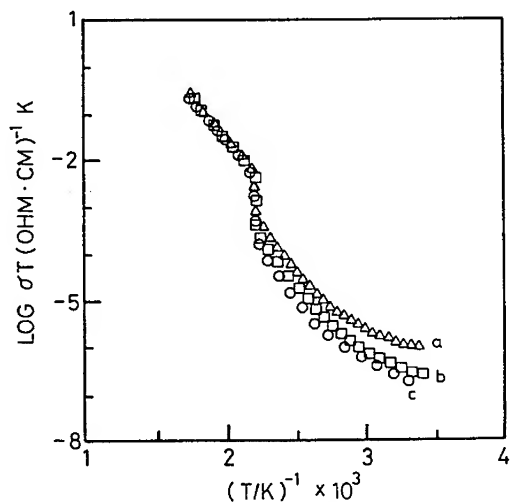


Fig. 11. Heat mode plots of  $\log \sigma T$  versus  $T^{-1}$  for  $K_xTl_{(1-x)}I$ : (a)  $x = 0.05$ , (b)  $x = 0.075$ , (c)  $x = 0.10$ .

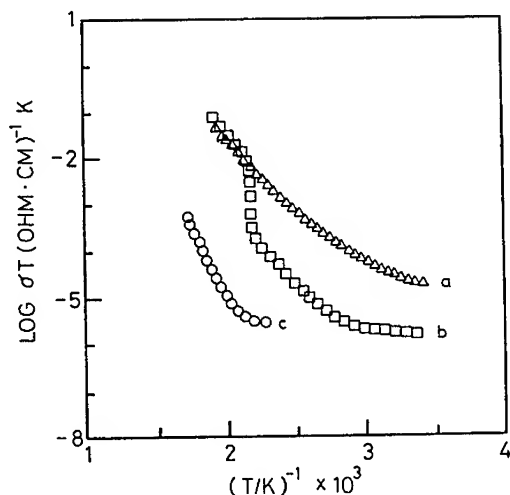


Fig. 12. Heat mode plots of  $\log \sigma T$  versus  $T^{-1}$  for  $Cs_xTl_{(1-x)}I$ : (a)  $x = 0.075$ , (b)  $x = 0.05$ , (c)  $x = 1.0$ , pure CsI.

With the  $\sim 3\%$  volume reduction required to stabilize the cubic  $\alpha$ -TlI we pursued this aspect via two avenues, viz a physical one with a smaller radius guest ion,  $K^+$ , and the chemical one with a more electropositive and larger radius guest ion,  $Cs^+$ . The conductivity-temperature plots for  $K_xTl_{(1-x)}I$  and  $Cs_xTl_{(1-x)}I$  on heating are given in Figs. 11 and 12, respectively. The  $\beta \rightleftharpoons \alpha$  phase transition identified with TlI is confirmed by the conductivity jump for all compositions of  $K_xTl_{(1-x)}I$  studied and  $Cs_{0.05}Tl_{0.95}I$ . The conductivity jump is absent for  $Cs_{0.075}Tl_{0.925}I$  which is stabilized in the cubic  $\alpha$ -phase in agreement with DSC trace and X-ray diffraction pattern.

The effectiveness of the larger radius and more electropositive  $Cs^+$  ion over the smaller radius  $K^+$  ion in stabilizing the high temperature cubic  $\alpha$ -TlI structure to room temperature indicates the primary and dominant role of the chemical effect over the physical effect in structural volume reduction. The higher percentage of  $Cs^+$  relative to  $Rb^+$ , viz 7.5% versus 5%, is interpreted as a requirement to compensate for the larger  $Cs^+$  ionic radius. Any suggestion to rationalize the stabilization of  $\alpha$ -TlI by invoking the isomorphic structure of CsI with  $\alpha$ -TlI, i.e. space group Pm3m, would not be consistent with RbI whose space group Fm3m produces the same result. In summary the outer electron configuration of  $Rb^+$ , i.e.  $3d^{10}4s^2p^6$  or of  $Cs^+$ , i.e.  $4d^{10}5s^2p^6$  relative to that of  $Tl^+$ , i.e.  $4f^{14}5d^{10}6s^2$

or of  $K^+$ , i.e.  $3s^2p^64s$  is more effective in reducing lattice volume as a mode of preserving the CsCl-type structure of  $\alpha$ -TlI in common with the room temperature structure of  $TlCl$  and  $TlBr$  than any contribution by the smaller ionic radius of  $K^+$ ,  $r_{K^+} = 152$  pm relative to that of  $Tl^+$ ,  $r_{Tl^+} = 164$  pm.

## ACKNOWLEDGEMENTS

This research program has received support from the National Research Council of Canada, the Natural Sciences and Engineering Research Council of Canada and the University Council for Research. I am indebted to Anita Sharma for allowing me to present her unpublished results.

## REFERENCES

1. J. M. Ziman, Models of Disorder (Cambridge University Press, Cambridge, 1979), Chap. 9.
2. R. Zallen, The Physics of Amorphous Solids (John Wiley & Sons, New York, 1983), Chap. 4.
3. U. M. Gundusharma and E. A. Secco, *Appl. Phys.* **A51**, 7 (1990).
4. M. D. Leblanc, U. M. Gundusharma and E. A. Secco, *Solid State Ionics* **20**, 61 (1986).
5. E. A. Secco, *Mat. Res. Soc. Symp. Proc.* **293**, 379 (1993).
6. U. M. Gundusharma and E. A. Secco, *Can. J. Chem.* **65**, 1205 (1987).
7. V. E. Plyushchev, R. G. Samsuseva and I. F. Poletaev, *Zh. Neorgan. Khim.* **7**, 860 (1962); *Russ. J. Inorg. Chem. (Engl. Transl.)* 445 (1962).
8. C. A. Angell, *Solid State Ionics* **9/10**, 3 (1983); **18/19**, 72 (1986).
9. P. I. Fedorov, *Zh. Neorg. Khim.* **11**, 2176 (1966); *Russ. J. Inorg. Chem. (Engl. Transl.)* **11**, 1168 (1966).
10. P-N. Huang and E. A. Secco, *solid State Ionics* (in press 1994); 9th International Conference on Solid State Ionics, The Hague, The Netherlands, September 12-17, 1993.
11. R. A. Secco and E. A. Secco, *J. Phys. Chem. Solids* **53**, 749 (1992).
12. M. R. M. Jiang and M. T. Weller, *J. Chem. Soc. Faraday Trans.* **87**, 3787 (1991).
13. M. R. M. Jiang and M. T. Weller, *Solid State Ionics* **46**, 341 (1991).
14. E. A. Secco, *Solid State Ionics* **68**, 213 (1994).
15. R. D. Shannon, *Acta Crystallogr.* **A32**, 751 (1976).
16. B. Wuensch in Solid State Ionics of International Conference on Advanced Materials, edited by M. Balkanski, T. Takahashi and H. L. Tuller (Elsevier Science Publishers, Amsterdam, 1992) p. 291.
17. Z. Zhang, S. Anderson, H. Eckert and J. H. Kennedy, *J. Electrochem. Soc.* **139**, 469 (1992).
18. R. M. Barrer, *Proc. Brit. Ceram. Soc.* **1**, 145 (1964).
19. D. W. Breck, *J. Chem. Educ.* **41**, 678 (1964).
20. J. G. Cohn in Kinetics of Reactions in Ionic Systems, Vol 4 of Materials Science Research, edited by T. J. Gray and V. D. Frechette (Plenum, New York, 1967) p. 12.
21. F. A. Cotton and G. Wilkinson, Advanced Inorganic Chemistry 3rd ed. (Interscience, New York, 1972) p. 280.
22. N. N. Greenwood and A. Earnshaw, Chemistry of the Elements (Pergamon, New York, 1984) p. 255.
23. P-N. Huang and E. A. Secco, *J. Solid State Chem.* **103**, 314 (1993).

## ELECTRICAL CONDUCTIVITY IN $(\text{Gd}_{1-x}\text{Ca}_x)_2\text{Sn}_2\text{O}_{7\pm\delta}$ PYROCHLORE SYSTEM

Tae-Hwan Yu and Harry L. Tuller

Department of Materials Science and Engineering, Crystal Physics and Electro-Ceramics Laboratory,  
Massachusetts Institute of Technology, Cambridge, MA 02139, USA

### ABSTRACT

Electrical conductivity measurements were performed on  $\text{Gd}_2\text{Sn}_2\text{O}_7$  as a function of temperature,  $\text{Po}_2$  and Ca doping concentration. An effective frenkel constant and oxygen vacancy mobility were derived. The high level of intrinsic anion disorder found in this study is consistent with expectations based on the cation radius ratio ( $r_A/r_B$ ) which was earlier found to be important in determining anion disorder in  $\text{A}_2\text{B}_2\text{O}_7$  pyrochlore compounds [1]. The magnitude of the ionic conductivity in  $\text{Gd}_2\text{Sn}_2\text{O}_7$  was found to be depressed relative to  $\text{Gd}_2(\text{Ti}_{1-x}\text{Zr}_x)_2\text{O}_7$  based systems due to a high oxygen vacancy migration energy.

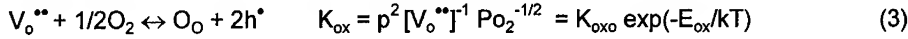
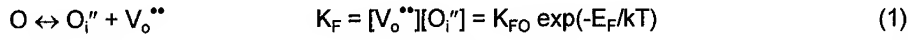
### INTRODUCTION

A number of pyrochlore compounds ( $\text{A}_2\text{B}_2\text{O}_7$ ) exhibit high oxygen ion conductivities when they have the appropriate degree of anion disorder [1,2]. Moon and Tuller demonstrated that the ionic conductivity increases in  $\text{Gd}_2(\text{Ti}_{1-x}\text{Zr}_x)_2\text{O}_7$  (GZT) as Zr substitutes for Ti due to increasing anion disorder. This appears to be coupled to the decrease in the average B to A cation radius ratio which, in the limit, leads to full disordering to the defect fluorite structure  $(\text{A,B})_4\text{O}_7$  [1,3]. When  $x > 0.4$  in GZT, for example, it becomes an intrinsic ionic conductor with ionic conductivity  $\sim 10^{-2}$  S/cm at 1000 °C [1]. The systematic disordering of both the cation and anion sublattices with increasing  $x$  has also been confirmed by neutron scattering in the closely related pyrochlore system  $\text{Yi}_2(\text{Ti}_{1-x}\text{Zr}_x)_2\text{O}_7$ . [4].

In this paper, we report, for the first time, results of an investigation of the electrical properties of  $\text{Gd}_2\text{Sn}_2\text{O}_7$  (GS) as a function of  $\text{Po}_2$ , temperature and Ca doping concentration. Since the ionic radius of  $\text{Sn}^{4+}$  is between that of  $\text{Zr}^{4+}$  and  $\text{Ti}^{4+}$  [3], it is of interest to examine whether disorder in GS is comparable to that in  $\text{Gd}_2(\text{Ti}_{0.2}\text{Zr}_{0.8})_2\text{O}_7$  which has the same average B site cation radius as GS.

## THEORY

For the pyrochlore GZT, the conductivity data conform to a defect model in which oxygen interstitials and/or acceptor dopants compensate the oxygen vacancies [1,2]. The defect chemistry of GS, using standard defect notation, can be described by a number of quasi-chemical reactions relating to intrinsic anion frenkel disorder, oxidation, and intrinsic electron-hole generation.



Electroneutrality requires a balance of charged species. This is represented by

$$2[V_o^{**}] + p + [D^*] = [A'] + n + 2[O_i''] \quad (4)$$

in which  $A'$  and  $D^*$  represent singly ionized acceptors and donors. Combining Eq. (1)-(4) and solving for  $[V_o^{**}]$  yields

$$[V_o^{**}] = 0.25 [1 + (I^2 + 16K_F)^{1/2}] = R \quad (5)$$

$$n = K_e (K_{ox} R)^{-1/2} P_{O_2}^{-1/4} \quad (6)$$

$$p = (K_{ox} R)^{1/2} P_{O_2}^{+1/4} \quad (7)$$

where  $I = [A'] - [D^*]$  is the net acceptor concentration. The ionic conductivity can be obtained by multiplying Eq. (5) by its effective charge ( $2e$ ) and mobility ( $\mu_i$ ).

$$\log \sigma_i = \log \{ 0.5 [1 + (I^2 + 16K_F)^{1/2}] e \mu_i \} \quad (8)$$

Multiplying each of the mobile charge carriers ( $V_o^{**}$ ,  $e'$ ,  $h^*$ ) by their mobilities and summing the three terms gives an expression for the total conductivity [1,2].

$$\sigma_{tot} = \sigma_i + \sigma_e + \sigma_h = A + B(P_{O_2})^{-1/4} + C(P_{O_2})^{1/4} \quad (9)$$



## EXPERIMENTAL PROCEDURES

Powder samples were prepared by the Pechini liquid mix technique with compositions  $(\text{Gd}_{1-x}\text{Ca}_x)_2\text{Sn}_2\text{O}_{7\pm\delta}$  ( $x=0, 0.01, 0.03, 0.1$ ) [5]. Based on earlier studies of Ca doped  $\text{Gd}_2\text{Ti}_2\text{O}_7$  (GT) [2], we expect that Ca substitutes for Gd in GS thereby forming a singly ionized acceptor ( $\text{Ca}_{\text{Gd}}'$ ). The powders were die pressed at 4 Kpsi and isopressed at 40 Kpsi and then sintered at 1550 °C for 16 h. X-ray diffraction data confirms that GS forms the pyrochlore phase with superlattice peaks which distinguish the pyrochlore from the defect fluorite phase [3].

The sintered samples were prepared as either bars with four probe configuration or discs with two probe configuration. Impedance spectroscopy measurements were performed with an HP4192A impedance analyzer to separate bulk, grain boundary and electrode conductivities. Two and four probe DC conductivity measurements were performed with an HP4140b picoammeter and Keithley 188 nanovoltmeter. Measurements were made over the temperature range of 800 °C - 1050 °C with 50 °C increments over the  $\text{Po}_2$  range from  $1\text{-}10^{-15}$  atm. Exposure to more reducing atmospheres resulted in decomposition of the phase as evidenced by a sharp decrease in conductivity.

## RESULTS

The  $\text{Po}_2$ -dependence of the total conductivity of undoped GS is shown in Fig. 1 for a number of isotherms. The solid curves represent the least square fits of the data to Eq. (9). P type conduction is observed at high  $\text{Po}_2$  followed by a  $\text{Po}_2$ -independent plateau which is attributed to ionic conduction. Compared with GZT, undoped GS has an ionic conductivity lower by two orders of magnitude than that of GZT ( $x>0.4$ ) [1]. GS specimens doped with Ca show a similar dependence of the total conductivity on  $\text{Po}_2$ . The ionic component of the total conductivity, extracted from the  $\log \sigma$  vs.  $\log \text{Po}_2$  data for each of these compositions with the aid of Eq. (9), are shown plotted versus reciprocal temperature in Fig. 2. Note that while the specimens with  $x=0.02$  and  $x=0.05$  show only small increases in conductivity over undoped GS, the specimen with  $x=0.1$  exhibits an ionic conductivity approximately 12 times greater in magnitude. The derived activation energies, which range from 1.42 ~1.51 eV, are approximately double those found for ionic conduction in GZT [1,2].

The isothermal composition dependence of the ionic conductivity of GS on Ca content is shown plotted in Fig. 3. These data were first fit to Eq. (8) in an attempt to extract values for  $K_F$  and  $\mu_i$ . The fit was found to be unsatisfactory particularly with regard to replicating the expected curvature. Since Eq. (8) is based on a model which assumes non-interacting defects [6], we suspect results for the specimen with  $x=0.1$  to deviate most strongly from these simplifying assumptions. The solid curves in Fig. 3, therefore, represents the best fits of Eq. (8) to only the first three compositions. Extrapolation of this curve to  $x=0.1$  shows it to underestimate the measured

conductivity. Figures 4 and 5 represent the derived value of  $K_F$  and  $\mu_i$  at each of the isotherms and the best fits through these data result in the following expressions.

$$K_F = 1.55 \times 10^{41} \exp(-0.11 \pm 0.06 \text{ eV}/kT) \text{ cm}^{-6}$$

$$\mu_i = 2.33 \exp(-1.44 \pm 0.02 \text{ eV}/kT) \text{ cm}^2/\text{V-sec}$$

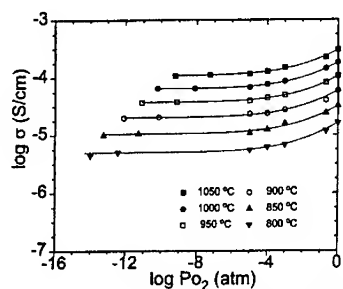


Fig. 1  $\log \sigma_1$  vs.  $\log P_{O_2}$  for  $Gd_2Sn_2O_7$  at temperature from 800 °C to 1050 °C. The lines represent the least squares fits to Eq. (9).

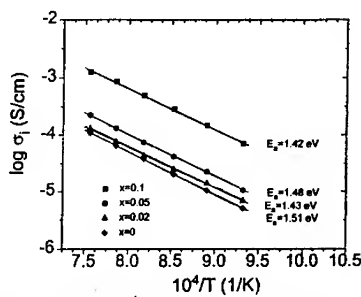


Fig. 2  $\log \sigma_1$  vs.  $10^4/T$  for  $(Gd_{1-x}Ca_x)_2Sn_2O_{7\pm\delta}$ .

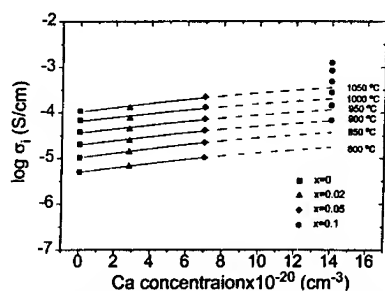


Fig. 3  $\log \sigma_1$  vs.  $[Ca_{Gd}]$  concentration for  $(Gd_{1-x}Ca_x)_2Sn_2O_{7\pm\delta}$ . The lines are the least squares fits of Eq.(8). to the data limited to  $x=0, 0.02$  and  $0.05$

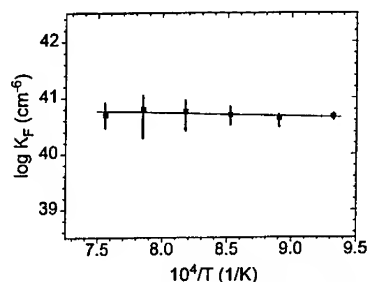


Fig. 4 Calculated values for the frenkel constant in  $Gd_2Sn_2O_7$  as a function of  $1/T$

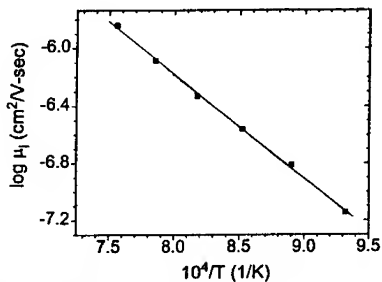


Fig. 5 Calculated values of the oxygen vacancy mobility in  $Gd_2Sn_2O_7$  as a function of  $1/T$

## DISCUSSION

From a lattice constant comparison [3],  $\text{Gd}_2(\text{Ti}_{0.2}\text{Zr}_{0.8})_2\text{O}_7$  has the same average B site cation radius as GS. The question arises whether a given  $r_A/r_B$  ratio generates the same degree of intrinsic anion disorder in both GZT and GS. It has been estimated from the pre-exponential term  $\sigma_0$  that the oxygen vacancy density is  $\sim 0.3\%$  in  $\text{Gd}_2(\text{Ti}_{0.2}\text{Zr}_{0.8})_2\text{O}_7$  [1] (Our re-analysis points to a somewhat higher value of  $\sim 0.85\%$ ). The high value of  $4.23 \times 10^{41} \text{ cm}^{-6}$  obtained for the frenkel constant at  $1000^\circ\text{C}$  proves that GS is intrinsically highly disordered. From Eq. (1), an oxygen vacancy density of  $0.94\%$  is obtained, which is in very good agreement with that estimated for  $\text{Gd}_2(\text{Ti}_{0.2}\text{Zr}_{0.8})_2\text{O}_7$ . The frenkel defect energy of  $0.11 \pm 0.06 \text{ eV}$  calculated from the GS data follows the decreasing trend in  $E_F$  with increasing  $x$  in GZT, i.e.  $0.44 \text{ eV}$  in  $\text{Gd}_2(\text{Zr}_{0.25}\text{Ti}_{0.75})_2\text{O}_7$  and  $0.24 \text{ eV}$  in  $\text{Gd}_2(\text{Zr}_{0.3}\text{Ti}_{0.7})_2\text{O}_7$  [1,7]. Therefore we may conclude that the high level of intrinsic anion disorder in GS is consistent with expectations. We have also found that defect model described in Eq. (8) breaks down at  $x$  values  $> 0.05$  for which we find that  $\sigma_i$  ( $x=0.1$ ) is higher than predictions. This suggests that either  $K_F$  or  $\mu_i$  increases as the Ca doping level increases.

The ionic conductivity of GS, on the other hand, is considerably lower than that of  $\text{Gd}_2(\text{Ti}_{0.2}\text{Zr}_{0.8})_2\text{O}_7$  presumably due to a much lower oxygen vacancy mobility. The oxygen vacancy migration energy of  $1.44 \text{ eV}$  in GS is almost twice that in GZT [1,2]. One possible source is the more covalent nature of Sn-O bonding than Zr-O, Ti-O bonding. It has been calculated that there is significant covalent bonding between Sn and O in  $\text{SnO}_2$  [8]. The lower conductivity in GS than GZT indicates the possible importance of the local bonding on mobility. In contrast, disorder appears to be more clearly tied to the relative size of the ions.

As shown in Fig. 1, Clear p-type conduction has been observed in GS up to  $\text{Po}_2 = 10^{-4} \text{ atm}$  range with a  $1/4$  slope dependence of  $\log \sigma$  on  $\log \text{Po}_2$ .  $\text{SnO}_2$  is known to be difficult to oxidize with a calculated oxidation energy of  $5.53 \text{ eV}$  [9]. P-type conduction in GS indicates that the highly disordered state in GS accommodates oxygen easily in contrast to  $\text{SnO}_2$  which exhibits low intrinsic disorder. The activation energies measured for p type conduction in Ca:GS range from  $1.03\sim 1.41 \text{ eV}$  which are similar to that in GZT [6]. The p-type conduction was often difficult to determine in GZT due to the higher ionic conduction which serves to mask the p-type conduction in GZT.

## CONCLUSION

Electrical measurements were made on the pyrochlore compound  $\text{Gd}_2\text{Sn}_2\text{O}_7$  doped with different level of Ca. The results were fit to a defect model based on the superposition of intrinsic anion frenkel defects and acceptor impurities. The value of the frenkel constant  $K_F$  suggests substantial ( $\sim 1\%$  of oxygen sites) intrinsic anion disorder in this system thereby confirming that the cation radius ratio ( $r_A/r_B$ ) is an important factor determining anion disorder in  $\text{A}_2\text{B}_2\text{O}_7$  pyrochlore compounds.

However, the ionic conductivity was found to be lower than expected due to low oxygen vacancy mobilities.

## ACKNOWLEDGMENT

This work has been supported by the Department of Energy, Division of Materials Science, Office of Basic Energy Research under grant # DE-FG02-86ER45261.

## REFERENCE

- [1]. P.K. Moon and H.L. Tuller, in Solid State Ionics, edited by G. Nazri, R.A. Huggins, and D.F. Shriver (Mater. Res. Soc. Proc. **135**, Pittsburgh, PA, 1986) pp. 199-206
- [2]. S.A. Kramer, M. Spears and H.L. Tuller, Solid State Ionics **72**, 59-66 (1994)
- [3]. M.A. Subramanian, G. Aravamudan and G.V. Subba Rao, Progress in Solid State Chemistry **15**, 55-143 (1983)
- [4]. C. Heremans, B.J. Wuensch, J.K. Stalick and E. Prince, in Solid State Ionics III, edited by G. Nazri, J. Tarascon and M. Armand (Mater. Res. Soc. Proc. **293**, Pittsburgh, PA, 1993) pp. 349-354
- [5]. M.P. Pechini, U.S. Patent No. 3,330,697 (1967)
- [6]. P.K. Moon, Ph.D. Thesis, Massachusetts Institute of Technology, 1988
- [7]. S.A. Kramer and H.L. Tuller, in Ceramics Today - Tomorrow's Ceramics, edited by P. Vincenzini (Elsevier Science Publishers, New York 1991), pp. 2211-2218
- [8]. A. Svane and E. Antoncik, J. Phys. Chem. Solids **48**, 171-180 (1987)
- [9]. C.M. Freeman and C.R.A. Catlow, J. Sol. State Chem. **85**, 65-75 (1990)

## OXYGEN PERMEABILITY OF STRONTIUM-DOPED $\text{LaCoO}_{3-\delta}$ PEROVSKITES

RENÉ H. E. VAN DOORN, H. KRUIDHOF, H.J.M. BOUWMEESTER AND  
A.J. BURGGRAAF

University of Twente, Fac. of Chemical Technology Department of Inorganic Chemistry and  
Material Science, P.O.Box 217, NL-7500 AE Enschede, The Netherlands

### ABSTRACT

Oxygen permeation rates are reported for 2 mm thick  $\text{La}_{1-x}\text{Sr}_x\text{CoO}_{3-\delta}$  ( $0 \leq x \leq 0.8$ ) in the temperature range  $700 \leq T \leq 1100^\circ\text{C}$  and oxygen partial pressure range  $7.0 \times 10^{-3} - 1.0 \times 10^5$  Pa. With the exception of  $x = 0.6$  permeation rates increase with an increase in Sr doping level. The oxygen permeation can be described by Wagner theory. An anomaly is observed in the oxygen permeation between  $750 - 775^\circ\text{C}$ , which is attributed to an order-disorder transition. It is further shown that the partial pressure at the low partial pressure side of the membrane has an important influence on the permeation rate. The (calculated) ionic conductivities and oxygen vacancy diffusion coefficients are among the highest reported in literature.

### INTRODUCTION

Perovskite type of oxides ( $\text{ABO}_3$ ) are currently receiving great interest as possible membranes for oxygen separation. Although the work of Teraoka *et al.*<sup>1,2</sup> already indicated high permeabilities for oxygen in earthalkaline-doped lanthanide cobaltites, not much is known on the influence of the Sr-doping level on the oxygen permeation level through  $\text{La}_{1-x}\text{Sr}_x\text{CoO}_{3-\delta}$ . Kruidhof *et al.*<sup>3</sup> showed that ordering phenomena in  $\text{SrCoO}_{3-\delta}$ -based perovskites might play an important role on the oxygen permeation, whereas Adler *et al.*<sup>4</sup> showed by  $^{17}\text{O}$ -NMR that the local structure is of extreme importance for the ionic conductivity.

In this paper, we wish to report first results on the oxygen permeation as a function of Sr-doping level, a detailed description of the results will be the subject of a forthcoming paper<sup>5</sup>.

### THEORY

By applying a  $p_{\text{O}_2}$ -gradient across a mixed-conducting dense ceramic membrane, semipermeable to oxygen, oxygen will be driven from the high  $p_{\text{O}_2}$ -side ( $p'_{\text{O}_2}$ ) to the low  $p_{\text{O}_2}$ -side ( $p''_{\text{O}_2}$ ). This process is facilitated by the joint diffusion of oxygen anions and electrons, or associated lattice defects, which compensate each other electrically as required by local charge neutrality. The oxygen flux through these dense membranes can be described by Wagner's theory of oxide growth on metals<sup>6</sup>:

$$j_{O_2} = \frac{RT}{4^2 F^2 L_{Mem}} \int_{a_{O_2}''}^{a_{O_2}'} t_{ion} t_{el} \sigma_{total} d \ln(a_{O_2}) \quad (1)$$

with  $j_{O_2}$  the oxygen permeation flux ( $\text{mol cm}^{-2} \text{s}^{-1}$ ),  $F$  Faraday's constant,  $L_{mem}$  the membrane thickness (cm),  $t_{ion}$ ,  $t_{el}$  the ionic and electronic transference numbers of the total conductivity ( $\sigma_{total}$  in  $\text{S cm}^{-1}$ ) respectively. The boundaries of integration are the oxygen activities at the high and low partial pressure side. Other symbols have their usual meaning.

Since for  $\text{La}_{1-x}\text{Sr}_x\text{CoO}_{3-\delta}$   $t_{el}$  is close to unity<sup>1</sup>, the permeation rate is determined by the ionic conductivity ( $\sigma_{ion}$ ). This ionic conductivity is purely anionic. Assuming a simple vacancy diffusion mechanism, the ionic conductivity, based on the Nernst-Einstein relation, is given by:

$$\sigma_{ion} = \frac{\delta z_i^2 D_v F^2}{V_M RT} \quad (2)$$

with  $\delta$  the vacancy concentration,  $z_i$  the valance charge of the anions ( $=2$ ),  $D_v$  the oxygen vacancy diffusion coefficient and  $V_m$  the molar volume. For the small gradients applied in this study, the oxygen non-stoichiometry can be modelled by a power-law in  $p_{O_2}$ <sup>7</sup>. Assuming ideal gas-behaviour, inserting eq. (2) into eq. (1) and the power-law for  $\delta$ , eq. (1) can be rewritten to:

$$j_{O_2} = \frac{D_v \delta^o}{4 n L_{Mem} V_M} (p_{O_2}'^n - p_{O_2}''^n) \quad (3)$$

which is equivalent with:

$$j_{O_2} = \frac{RT}{n 4^2 F^2 L_{Mem}} \sigma_{ion}^o (p_{O_2}'^n - p_{O_2}''^n) \quad (4)$$

with  $n$  the order with respect to oxygen and the superscript  $o$  denoting properties at a  $p_{O_2}$  of unity.

## EXPERIMENTAL METHODS

Powders were made by decomposition of metal-EDTA complexes as described elsewhere<sup>8</sup>. After calcination powders were isostatically pressed and sintered at about 1100 °C resulting in densities of 94 % or more of their theoretical value. Calcined powders were examined by XRD using Ni-filtered  $\text{CuK}\alpha$  radiation (Philips PW1710). A selected composition was examined by means of electron diffraction (Philips CM30 HR30 (S)TEM at 300 kV). Prior to permeation experiments, the rods obtained were sliced to disk-shaped samples 12 or 15 mm in diameter and a thickness of 2 mm. Both sides were polished with 1000 MESH SiC. Oxygen permeabilities were determined using a set-up similar to the one described by Bouwmeester *et al.*<sup>9</sup>, which allows the simultaneous measurement of oxygen permeated through the sample *and* possibly occurring leakage through either the sample or the seal. Permeation rates were normalised with respect to the surface area exposed to the lower partial pressure side. As feed gas a mixture of oxygen and nitrogen (mostly technical air) at 100 ml(STP)  $\text{min}^{-1}$  was used. By means of a zirconia-based sensor depletion of the feed gas was checked and found not to occur. He (UCAR 4.2) at 5 or 10 ml(STP)  $\text{min}^{-1}$  was used as sweep gas. For calculations CISTR conditions were assumed. Oxygen

non-stoichiometry has been determined using the phenomenological model of Mizusaki *et al.*<sup>7</sup> for  $0 \leq x \leq 0.7$ .

## RESULTS AND DISCUSSION

### X-Ray analysis

XRD results revealed the perovskite structure for all samples. For  $x \geq 0.5$  the cubic perovskite phase was observed, whereas for  $x < 0.5$  a rhombohedral distortion of the ideal cubic structure was observed. According to Petrov and Kofstad<sup>10</sup> all compositions above 800 °C have the cubic perovskite phase.

### Oxygen permeation

In Fig. 1 the oxygen permeation Arrheniusplots are given for  $\text{La}_{1-x}\text{Sr}_x\text{CoO}_{3.5}$  in an Air-He gradient. Due to experimental problems such as a too low permeation rate ( $x = 0$ ) and cracking of the seal, it was not possible to measure all the compositions in the same temperature region.

As is clear from Fig. 1, the activation energy decreases with an increase in  $x$ . Since the driving force for oxygen permeation ( $\nabla\mu_{\text{O}_2}$ ) decreases at increased Sr-doping level and increasing temperature, the gradient for permeation is not the same for different temperatures. This phenomena manifests itself in convex curvatures of the Arrheniusplots, which is most pronounced at high temperature and large  $x$ . Therefore, only apparent activation energies can be determined ranging from  $206 \pm 6 \text{ kJ mol}^{-1}$  ( $x = 0$ ) until  $38 \pm 5 \text{ kJ mol}^{-1}$  ( $x = 0.8$ ). Experiments with a fixed gradient, so adjusted helium sweep rate, did not show the curvature and showed activation energies which were up to two times higher for  $x = 0.7$ .

In Fig. 2 an overview of oxygen permeation rates as a function of  $x$  under an Air-He gradient is shown. Except for  $x = 0.6$  the permeation rate increases with increasing Sr-doping level, as is expected on basis of defect chemistry. An explanation

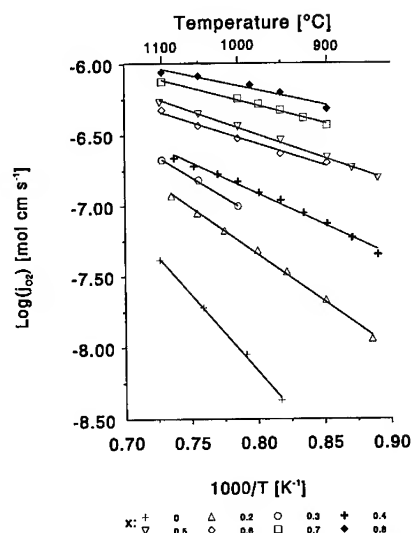


Fig. 1 Arrheniusplot for  $\text{La}_{1-x}\text{Sr}_x\text{CoO}_{3.5}$ .

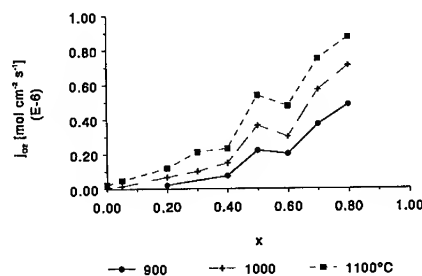


Fig. 2 Oxygen permeation rates as a function of Sr-doping for  $\text{La}_{1-x}\text{Sr}_x\text{CoO}_{3.5}$ .

for this behaviour is given at the end of the results section.

### Calculated ionic conductivities

In Fig. 3 a typical result of the variation of the high oxygen partial pressure ( $p'_{O_2}$ ) on the oxygen permeation flux is shown. As can be seen, the result can be fairly well fitted to eq. (4). An overview of the so determined ionic conductivities ( $\sigma_{ion}$ ) as a function of composition is given in Fig. 4. Included in this figure are the orders with respect to oxygen ( $n$ ) as determined from the variation of  $p'_{O_2}$  and the results of non-stoichiometry as a function of  $p_{O_2}$  after Mizusaki *et al.*<sup>7</sup> ( $n_{Mizus}$ ). For  $x \leq 0.6$  an excellent agreement is obtained for the oxygen non-stoichiometry results. However, for larger  $x$ -values this agreement vanishes. This might be (partly) due to limitation by surface exchange.

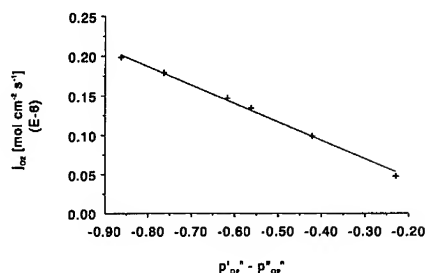


Fig. 3  $p_{O_2}$ -dependency for  $x = 0.4$  ( $n = -0.186$ ) at  $T = 1000$  °C.

Since only a limited number of oxygen ionic conductivities has been presented in literature, it is difficult to compare our values with those of others. The calculated ionic conductivities for  $x = 0.2$  and  $0.5$  of Sekido<sup>12</sup> ( $1 \times 10^{-2}$  and  $4.5 \times 10^{-2}$  S  $cm^{-1}$  respectively) are lower than ours, whereas those determined by Shuk *et al.*<sup>13</sup> for  $x = 0.4$  and  $0.5$  ( $1$  and  $5$  S  $cm^{-1}$ ) are higher. Our values for  $x = 0.4 - 0.6$  are lower than those of Itoh *et al.*<sup>14</sup> ( $0.05 - 0.3$  S  $cm^{-1}$ ), who also used oxygen permeation data to determine ionic conductivities. These last authors assumed, however, an incorrect  $\ln(\frac{p'}{p''})$ -dependency for their calculations, which over estimates the value for the ionic conductivity.

The oxygen diffusion coefficients calculated by means of eq. (3) showed values in the range of  $1 - 5 \times 10^{-5}$   $cm^2 s^{-1}$ , depending on temperature and composition. These values are among the highest reported in literature, not only for  $La_{1-x}Sr_xCoO_{3-\delta}$  but also for YSZ and  $\delta$ - $Bi_2O_3$ .

### Ordering processes

In Fig. 5 the Arrheniusplot is shown for  $La_{0.5}Sr_{0.5}CoO_{3-\delta}$  under an Air-He gradient in the temperature range  $700 - 1100$  °C. An anomaly is observed around  $750 - 775$  °C. Similar anomalies have been observed for  $x = 0.4, 0.6, 0.7$  and  $0.8$ . These anomalies might be caused by the occurrence of

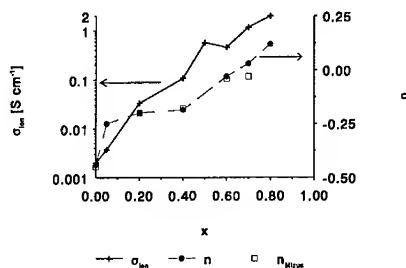


Fig. 4 Ionic conductivities determined from oxygen permeation at  $1000$  °C and order with respect to oxygen.



oxygen vacancy order-disorder transitions as were reported to occur for *e.g.*  $\text{La}_{0.5}\text{Sr}_{0.5}\text{CoO}_{3-\delta}$  by Kirchnerov and Hibbert<sup>13,16</sup>. In literature there are indications that ordering phenomena might play a role on the oxygen permeation rate through perovskites<sup>3,4,17</sup>. An indication for the occurrence of a phase transition, below 775 °C, is the occurrence of long stabilisation times for the oxygen permeation rates after sealing and cooling to temperatures below 775 °C. During this stabilisation time the permeation rate dropped considerably. When after this stabilisation time the temperature was increased above 775 °C long stabilisation times were encountered, during which the permeation increased. Further increase of temperature now resulted in fast stabilisation times.

Further evidence for the occurrence of oxygen vacancy ordering is shown in Fig. 6, where a SAED pattern for  $\text{La}_{0.3}\text{Sr}_{0.7}\text{CoO}_{3-\delta}$  annealed for 15 h at 650 °C under air is shown ( $\delta$  estimated 0.17). As can be seen, extra diffraction spots are present. Since in the XRD-pattern no indications for a superstructure are present, these diffraction spots are attributable to an ordering in the oxygen lattice. A more extensive discussion of these results will be published elsewhere<sup>18</sup>.

The higher permeation rates for  $x = 0.5$  as compared with  $x = 0.6$ , might also be due to ordering. However, in this case a  $\text{La}^{3+}/\text{Sr}^{2+}$  cation ordering, as suggested by Gai and Rao<sup>11</sup>, for this composition should occur. Due to this cation ordering, an ordering in the  $\text{Co}^{3+}/\text{Co}^{4+}$  structure occurs, which might lead to high conductivity pathways, as was also suggested by Adler *et al.*<sup>4</sup> for *e.g.*  $\text{La}_{0.6}\text{Sr}_{0.4}\text{Co}_{0.8}\text{Cu}_{0.2}\text{O}_y$  and  $\text{La}_{0.5}\text{Ba}_{0.5}\text{Co}_{0.7}\text{Cu}_{0.3}\text{O}_y$ .

## CONCLUSIONS

Isothermal oxygen permeation rates through 2 mm thick gas-tight  $\text{La}_{1-x}\text{Sr}_x\text{CoO}_{3-\delta}$  disks ( $0 \leq x \leq 0.8$ ) and  $700 \leq T \leq 1100$  °C are reported. For  $x = 0.5$  permeation rates were higher than for  $x = 0.6$ , which might be due to long range oxygen vacancy ordering, leading to preferential diffusion paths. The permeation results could be modelled using Wagner theory, indicating bulk diffusion limitation. The  $p_{\text{O}_2}$ -dependencies show for  $x \leq 0.6$

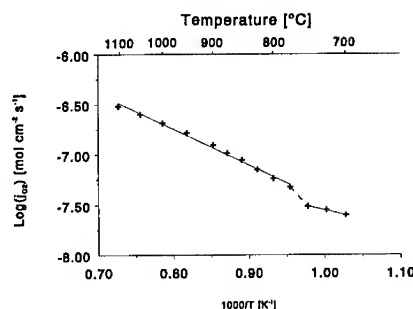


Fig. 5 Arrheniusplot for  $\text{La}_{0.5}\text{Sr}_{0.5}\text{CoO}_{3-\delta}$ .

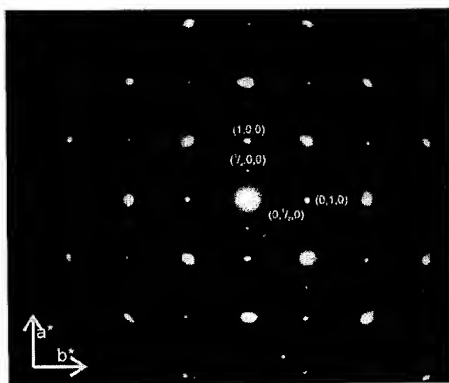


Fig. 6 SAED pattern of  $\text{La}_{0.3}\text{Sr}_{0.7}\text{CoO}_{3-\delta}$  aligned along  $[0,0,1]$ , annealed in air for 15 hours at 650 °C, showing a  $2a \times 2a$  superstructure.

good agreement with oxygen non-stoichiometry data of Mizusaki *et al.*<sup>7</sup>. For  $x = 0.7$  a discrepancy was found, which might indicate (partial) surface exchange limitation. The partial pressure at the lower pressure side proved to be of importance for the overall permeation rate. The thermal history of the sample is of importance due to possible occurring order-disorder transitions. This ordering of oxygen vacancies has been observed for  $x = 0.7$  by means of SAED.

The calculated ionic conductivities at 1000 °C and  $p_{O_2} = 1.0 \times 10^5$  Pa varies from  $2.0 \times 10^{-3}$  S cm<sup>-1</sup> for  $x = 0$  to  $2.0$  S cm<sup>-1</sup> for  $x = 0.8$ . Oxygen vacancy diffusion coefficients are among the largest reported in literature.

#### ACKNOWLEDGEMENTS

Mr. A. Nijmeijer is gratefully acknowledged for his help in the preparation of the samples and his help in performing permeation experiments.

#### LITERATURE CITED

- [1] Y. Teraoka, H.M. Zhang, K. Okamoto and N. Yamazoe, *Mat. Res. Bull.*, **23**, 51 (1988).
- [2] Y. Teraoka, T. Nobunaga, K. Okamoto, N. Miura and N. Yamazoe, *Solid State Ionics*, **48**, 207 (1991).
- [3] H. Kruidhof, H.J.M. Bouwmeester, R.H.E. van Doorn and A.J. Burggraaf, *Solid State Ionics*, **63 - 65**, 816 (1993).
- [4] S. Adler, S. Russek, J. Reimer, M. Fendorf, A. Stacy, Q. Huang, A. Santoro, J. Lynn, J. Baltisberger and U. Werner, *Solid State Ionics*, **68[3&4]**, 193 (1994).
- [5] R.H.E. van Doorn, H. Kruidhof, A. Nijmeijer, H.J.M. Bouwmeester and A.J. Burggraaf, *to be Submitted to J. Electrochem. Soc.*
- [6] C. Wagner, *Z. Phys. Chem.*, **B21**, 25 (1933).
- [7] J. Mizusaki, Y. Mima, S. Yamauchi, K. Fueki and H. Tagawa, *J. Solid State Chem.*, **80**, 102 (1989).
- [8] R.H.E. van Doorn, H. Kruidhof, L. Winnubst, H.J.M. Bouwmeester and A.J. Burggraaf, *Submitted to J. Amer. Ceram. Soc.*
- [9] H.J.M. Bouwmeester, H. Kruidhof, A.J. Burggraaf and P.J. Gellings, *Solid State Ionics*, **53 - 56**, 460 (1992).
- [10] A.N. Petrov and P. Kofstad, *Proc. 3<sup>rd</sup> Int. Symp. on Solid Oxide Fuel Cells*, 220 (1993).
- [11] P.L. Gai and C.N.R. Rao, *Mat. Res. Bull.*, **10**, 787 (1975).
- [12] S. Sekido, H. Tachibana, Y. Yamamura and T. Kambara, *Solid State Ionics*, **37**, 253 (1990).
- [13] P. Shuk, V. Charton and V. Samochval, *Mat. Science Forum*, **76**, 161 (1991).
- [14] N. Itoh, T. Kato, K. Uchida and K. Haraya, *J. Membrane Science*, **92**, 239 (1994).
- [15] J. Kirchnerova and D.B. Hibbert, *J. Mat. Science*, **28**, 5800 (1993).
- [16] J. Kirchnerova and D.B. Hibbert, *Mat. Res. Bull.*, **25**, 585 (1990).
- [17] C.-Y. Tsai, Y.H. Ma, W.R. Moser and A.G. Dixon, *Preprint Proc. 3<sup>rd</sup> Int. Symp. Inorganic Membranes (ICIM'3)*, (1994).
- [18] R.H.E. van Doorn, H.J.M. Bouwmeester and A.J. Burggraaf *to be published*.

## OXYGEN PERMEATION STUDIES OF $\text{SrCo}_{0.8}\text{Fe}_{0.2}\text{O}_{3-\delta}$

Y. L. YANG, T. H. LEE, L. QIU, L. LIU AND A. J. JACOBSON  
Department of Chemistry and Texas Center for Superconductivity University of Houston,  
Houston, TX 77204-5641

### ABSTRACT

Oxygen permeation fluxes through dense  $\text{SrCo}_{0.8}\text{Fe}_{0.2}\text{O}_{3-\delta}$  discs have been measured in the temperature range of 620-920 °C under various oxygen partial pressure gradients. The permeation results are compared with the previous measurements. Below 800 °C, the apparent activation energy for the overall permeation is  $22 \pm 4$  kcal/mol. The permeation results are discussed in light of the phase diagram of  $\text{SrCo}_{0.8}\text{Fe}_{0.2}\text{O}_{3-\delta}$ . Based on experiments in which the membrane thickness is varied, we propose that the surface exchange process is the rate-limiting step in the overall permeation reaction. Preliminary catalytic studies of methane partial oxidation in a membrane reactor are reported.

### INTRODUCTION

Dense oxygen-permeating membranes made of mixed electronic-ionic conducting oxides are of considerable interest for novel oxygen separation and membrane catalysis processes.<sup>1-5</sup> Catalytic reactors built from these membranes have potential applications in oxidation processes such as direct syngas generation.<sup>3-5</sup> Oxygen permeation in mixed conducting oxides involves the interplay between the oxygen gas-solid surface exchange kinetics, bulk transport of oxygen ions, and the defect chemistry. The permeation mechanism depends on the specific material and on the temperature and partial pressures of oxygen on either side of the membrane and in general is not well understood.

Teraoka *et al.*<sup>6-8</sup> initiated oxygen permeation studies on the  $(\text{La,Sr})(\text{Co,Fe})\text{O}_{3-\delta}$  series of perovskite oxides. Measurements of the total and ionic conductivities under controlled atmospheres<sup>6,9</sup> and temperature-programmed desorption were also reported.<sup>9-11</sup> The highest oxygen permeation fluxes were found in  $\text{SrCo}_{0.8}\text{Fe}_{0.2}\text{O}_{3-\delta}$ . Selected materials in this series were later re-examined using thermogravimetry, differential scanning calorimetry, and oxygen permeation flux measurements.<sup>12</sup> Gellings and Bouwmeester<sup>1</sup> reported preliminary results of  $\text{SrCo}_{0.8}\text{Fe}_{0.2}\text{O}_{3-\delta}$  surface exchange kinetics. Nisancioglu and Gür<sup>13</sup> measured the conductivity and the non-stoichiometry of  $\text{SrCo}_{0.8}\text{Fe}_{0.2}\text{O}_{3-\delta}$ . Liu *et al.*<sup>14</sup> have recently determined the phase diagram of  $\text{SrCo}_{0.8}\text{Fe}_{0.2}\text{O}_{3-\delta}$  by thermogravimetric analysis. The oxygen permeation fluxes through dense membranes of  $\text{SrCo}_{0.8}\text{Fe}_{0.2}\text{O}_{3-\delta}$  were recently measured at various experimental conditions and the results compared with the previous data obtained by Teraoka *et al.*<sup>6-8</sup> and Kruidhof *et al.*<sup>12</sup> In this paper, the oxygen permeation fluxes obtained by the different groups are reviewed and discussed in relation to the relative contributions of the surface exchange kinetics and the bulk transport to the overall permeation rate. The existing experimental data regarding the ionic conductivity,<sup>6-8, 10, 13</sup> and surface exchange kinetics<sup>1</sup> are also discussed. Preliminary catalytic studies of the partial oxidation of methane using a  $\text{SrCo}_{0.8}\text{Fe}_{0.2}\text{O}_{3-\delta}$  membrane as both an oxygen separator and catalyst are also described.

### EXPERIMENTAL

The detailed synthesis, phase diagram and structural characterization of  $\text{SrCo}_{0.8}\text{Fe}_{0.2}\text{O}_{3-\delta}$  are presented elsewhere.<sup>14</sup> The  $\text{SrCo}_{0.8}\text{Fe}_{0.2}\text{O}_{3-\delta}$  powder was ball-milled for 48 h and then pressed into membranes of various thicknesses. The membranes were sintered in air at 1160 °C for 5 h with a heating and cooling rate of 2 °C/min. The measured disc density was typically

>94% of theoretical density assuming the cubic perovskite unit cell dimensions.<sup>18</sup> Both sides of the sintered discs were ground using 600 grit SiC polishing paper, and further polished to a 6  $\mu\text{m}$  finish using diamond paste.

The oxygen permeation measurements were made in the apparatus previously described.<sup>15</sup> From the measured oxygen concentrations and the flow rate of the helium sweep gas, the total oxygen permeation rates (mol/s) were calculated. Any small oxygen leakages due to pin-holes or cracks can be monitored and corrected by the corresponding nitrogen concentrations. The permeation fluxes (mol/cm<sup>2</sup>s) are calculated by dividing the permeation rates by the effective permeating area of the discs. Oxygen and nitrogen mixtures were used to regulate the oxygen partial pressure at oxygen-rich side. At each temperature, the oxygen permeation flux was periodically measured until a constant flux is obtained. The permeation fluxes reported below therefore are steady state fluxes. For catalytic studies, 5% methane in helium was used in place of helium on the oxygen-lean side of the membrane. The products were analyzed using an Amtek 3000 gas chromatograph with thermal conductivity and field ionization detectors.

## RESULTS AND DISCUSSION

The variation of the measured permeation flux with temperature range is shown in Figure 1. Simulated air (20% O<sub>2</sub> in N<sub>2</sub> balance) was used on the oxygen rich side. Previous measurements are also plotted for comparison. Our data are generally larger by a factor of 5 than those of Kruidhof *et al.*<sup>12</sup> but smaller by a factor of 5 than those of Teraoka *et al.*<sup>6-8</sup> Differences in the details of the experimental procedures used by the different groups may account for the discrepancies. Direct comparisons of separate measurement are difficult to make because the oxygen partial pressure gradients under which the permeation experiments were conducted may be different due to differences in membrane area and sweep rates. Kruidhof *et al.*<sup>12</sup> have suggested that different preparation methods may result in different microstructure and texture of a dense disc thereby affecting the permeation flux. We have also observed that if ambient air is used on the oxygen rich side, the permeation fluxes are lower presumably due to the influence of minor amounts of CO<sub>2</sub>. The difference between our data that used synthetic air and the results of

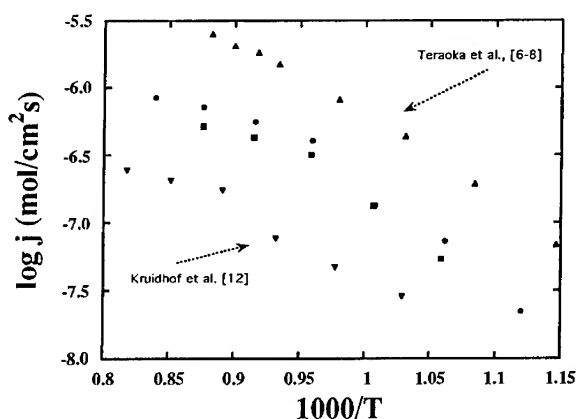


Figure 1. A comparison of oxygen permeation data for SrCo<sub>0.80</sub>Fe<sub>0.20</sub>O<sub>3- $\delta$</sub>  membranes. Kruidhof *et al.*<sup>12</sup> using ambient air may be due to this effect. As far as other experimental details are concerned, we have found that the glass seals<sup>12</sup> readily react with SrCo<sub>0.80</sub>Fe<sub>0.20</sub>O<sub>3- $\delta$</sub>  at high temperature and therefore, may change the surface composition of a permeating disc. Oxygen

permeation through the silver seals used by Teraoka *et al.*,<sup>6-8</sup> may have contributed significantly to their measured fluxes. Silver is known to permeate oxygen in this temperature range.<sup>16,17</sup>

A general descriptive picture of the permeation process can be developed from the  $\text{SrCo}_{0.80}\text{Fe}_{0.20}\text{O}_{3-\delta}$  phase diagram determined by Liu *et al.*<sup>14</sup> The phase diagram is shown in Figure 2 and is similar to that of  $\text{SrFeO}_{3-\delta}$ .<sup>8</sup> In the temperature range where the permeation measurements were made, the phase diagram is composed of three regions—cubic perovskite, orthorhombic brownmillerite and a two phase region. The perovskite phase is thermodynamically stable at higher oxygen partial pressures ( $>0.1$  atm) and higher temperatures. The brownmillerite phase exists over only a narrow region with  $\delta \sim 0.5$ . The two phase region exists at lower oxygen partial pressures ( $<0.1$  atm) and at temperatures below  $770^\circ\text{C}$ . Under a constant oxygen partial pressure, the perovskite phase loses oxygen as the temperature rises. Therefore, the permeating membrane may vary its composition depending upon the temperature and the oxygen partial pressures on each side. For example, when the oxygen partial pressure gradient is between  $0.20$  and  $10^{-4}$  atm, the membrane is in the perovskite phase on the oxygen-rich side and brownmillerite on the oxygen-lean side with a two phase region separating them. Above the brownmillerite-perovskite phase transition temperature ( $770^\circ\text{C}$ ), the whole disc is composed of the perovskite phase over a wide range of oxygen partial pressure gradients. The brownmillerite-perovskite phase transition temperature coincides with the slope change observed around  $800^\circ\text{C}$  in the flux curve in Figure 1. The slope change in the permeation flux curve was previously noted by Kruidhof *et al.*,<sup>12</sup> but not by Teraoka *et al.*<sup>6-8</sup> Kruidhof *et al.*<sup>12</sup> related this change in activation energy to an order-disorder transition of the oxygen vacancies.

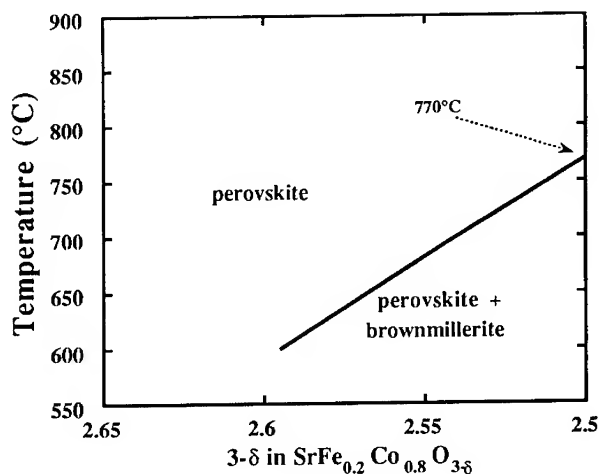


Figure 2. A schematic phase diagram for  $\text{SrCo}_{0.80}\text{Fe}_{0.20}\text{O}_{3-\delta}$ .

A key question in permeation studies is to determine the rate-limiting step. The most direct test is to measure the variation of the permeation fluxes with membrane thickness. If the permeation is limited by the bulk diffusion, then the permeation flux should depend on the thickness. Results of thickness variation experiments are shown in Figure 3. The data clearly show that the permeation flux at a fixed temperature is independent of the disc thickness. However, we are not able to determine whether one or both of the two surfaces limit the permeation rate. The exchange kinetics could be different at both sides of the disc, because the surface structures and compositions are expected to be different on each side due to the dependence of the bulk composition on temperature and partial oxygen pressure. In general, different oxygen pressure regimes may result in different surface kinetic behaviors. From Figure

3, an apparent activation energy of  $22 \pm 4$  kcal/mol was obtained for the overall oxygen permeation below the phase transition temperature. This value is far smaller than the reported activation energy of 50 kcal/mol<sup>13</sup> for the bulk chemical diffusion of the oxygen ions in a comparable temperature range. Such a difference may suggest indirectly that the bulk-diffusion is not the rate-limiting step.

A quantitative comparison can be made using the available experimental data on the bulk transport, the surface exchange kinetics, and the oxygen permeation flux in  $\text{SrCo}_{0.80}\text{Fe}_{0.20}\text{O}_{3-\delta}$ .

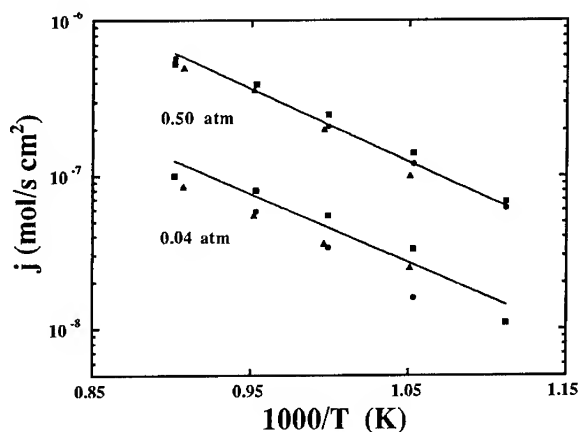


Figure 3 Oxygen permeation as a function of membrane thickness. The symbols refer to disks with thicknesses of 1, 2.7 and 5.5 mm and the labels to  $p_{\text{O}_2}^{\text{rich}}$ .

At 700 °C, the measured oxygen permeation flux of  $1 \times 10^{-7}$  mol/cm<sup>2</sup>s is very close to the oxygen surface exchange rate of  $1.2 \times 10^{-7}$  mol/cm<sup>2</sup>s measured by Gellings and Bouwmeester,<sup>1a</sup> consistent with surface exchange being the rate-limiting step. A theoretical permeation flux limited by the bulk transport can be calculated assuming  $\sigma_e \gg \sigma_i$  in the Wagner equation and using an oxygen partial pressure gradient of  $p_{\text{O}_2}^{\text{rich}} = 0.20$  atm and  $p_{\text{O}_2}^{\text{lean}} = 8.9 \times 10^{-3}$  atm. The diffusion-controlled limit is approximately  $4.6 \times 10^{-10}$  mol/cm<sup>2</sup>s if an ionic conductivity  $\sigma_i$  of approximately  $10^{-4}$  S/cm<sup>13</sup> at 700 °C is used suggesting a bulk transport limitation. At 800 °C, two different ionic conductivity values have been reported 1 S/cm<sup>9</sup> and  $10^{-3}$  S/cm.<sup>13</sup> The diffusion controlled limits are estimated to be  $1.6 \times 10^{-6}$  mol/cm<sup>2</sup>s and  $1.6 \times 10^{-9}$  mol/cm<sup>2</sup>s. A comparison with the permeation flux of  $5.3 \times 10^{-7}$  mol/cm<sup>2</sup>s at 800 °C, indicates that the ionic conductivity data of Teraoka *et al.*<sup>14</sup> favor the surface-controlled mechanism, while data of Nisancioglu and Gür<sup>13</sup> favor the diffusion-controlled mechanism. Such conflicting experimental results reflect the difficulties in studying mixed conducting oxides with large electronic contributions to the total conductivity. To clarify inconsistencies between various experimental approaches, further comprehensive studies of the ionic transport properties of  $\text{SrCo}_{0.80}\text{Fe}_{0.20}\text{O}_{3-\delta}$  are clearly needed.

Some preliminary results on methane oxidation are presented in Figure 4. These data were obtained with 5% methane in helium at a flow rate of 40ml/min in the temperature range 715°C to 820°C. The methane conversion rate increases from roughly 20% at 715°C to 35% at 815°C, consistent with the increase in the oxygen permeation rate over this temperature range. The variation of the methane to oxygen ratio due to the changes in the oxygen flux is indicated by the numbers labelling the conversion points. The CO selectivity at these conditions is ~ 90% and is independent of temperature. The only other product observed is CO<sub>2</sub>. Because of the low oxygen partial pressures (roughly 1%) at the methane side, the data cannot be compared with

selectivities and conversions obtained using  $\text{SrCo}_{0.80}\text{Fe}_{0.20}\text{O}_{3-\delta}$  as a catalyst in a co-feed flow reactor at higher oxygen partial pressures. Instead, the data are compared with equilibrium calculations assuming that CO,  $\text{CO}_2$ ,  $\text{H}_2$  and  $\text{H}_2\text{O}$  were the only products of the methane oxidation. Reactions involving carbon formation were excluded. The calculations were carried out using a software package from Outokumpu Research and are also shown in Figure 4. The results reproduce the observed conversions and indicated that complete selectivity to CO would be expected at equilibrium for this range of conditions. The small amount of  $\text{CO}_2$  observed in the experiment is most likely due to a small  $\text{O}_2$  leak through the membrane. More recent data for a similar membrane with a negligible leak rate gave a much higher selectivity to CO.

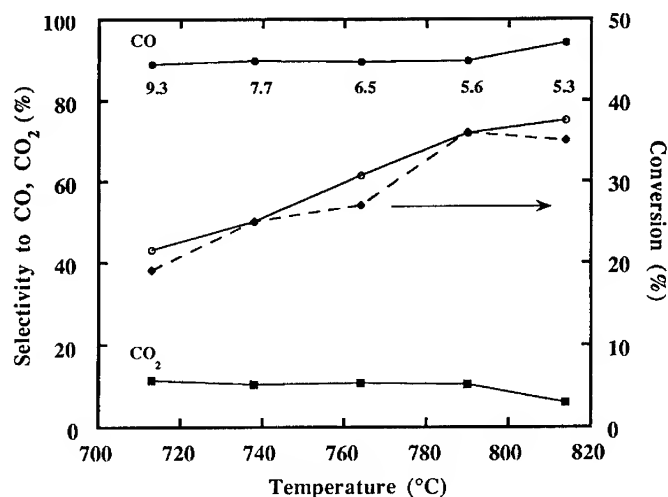


Figure 4 Methane partial oxidation data for a  $\text{SrCo}_{0.80}\text{Fe}_{0.20}\text{O}_{3-\delta}$  membrane. The numbers are the  $\text{CH}_4/\text{O}_2$  ratios at the various temperatures. The open circles are the calculated conversion values; the  $\text{CO}$  selectivity is calculated to be 100% for these conditions.

In conclusion, the oxygen permeation fluxes have been measured over a wide temperature range under various oxygen partial pressure gradients. Below 800 °C, an apparent activation energy of  $22 \pm 4$  kcal/mol was obtained. The permeation data are discussed in light of the phase diagram of  $\text{SrCo}_{0.80}\text{Fe}_{0.20}\text{O}_{3-\delta}$  compared with the previous measurements. Based on disc thickness variation experiments, we propose that the rate-limiting step in the overall permeation is the surface exchange process. We report the preliminary studies on methane partial oxidation using the permeating membrane as oxygen separator and catalyst. High selectivity of CO in the oxidation products was found.

#### ACKNOWLEDGMENT

We thank the Robert A. Welch Foundation and Los Alamos National Laboratory for financial support of this work.

#### REFERENCES

1. P.J. Gellings and H.J.M. Bouwmeester, *Catalysis Today* **12**, (1992) 1.

2. H. Iwahara, in *Solid State Ionic Devices*, ed. B.V.R. Chowdari and S. Radhakrishna, World Scientific, Singapore, 1988, p.309.
3. J. Zaman and A. Chakma, *J. Membrane Sci.* **92**, (1994) 1.
4. G. Saracco and V. Specchia, *Catal. Rev.—Sci. Eng.* **36**, (1994) 305.
5. T.J. Mazanec, in *The Activation of Dioxygen and Homogeneous Catalytic Oxidation*, ed. D.H.R. Barton *et al.*, Plenum Press, New York, 1993, p.85.
6. Y. Teraoka, T. Nobunaga, K. Okamoto, N. Miura and N. Yamazoe, *Solid State Ionics* **48**, (1991) 207.
7. Y. Teraoka, T. Nobunaga and N. Yamazoe, *Chem. Lett.*, (1988) 503.
8. Y. Teraoka, H. Zhang, S. Furukawa and N. Yamazoe, *Chem. Lett.*, (1985) 1743.
9. Y. Teraoka, *et al.*, *Mat. Res. Bull.* **23**, (1988) 51.
10. Y. Teraoka, *et al.*, *Chem. Lett.*, (1981) 1767.
11. Y. Teraoka *et al.*, *Chem. Lett.* (1985) 1367.
12. H. Kruidhof, H.J.M. Bouwmeester, R.H.E.v. Doorn, and A.J. Burggraaf, *Solid State Ionics* **63/65**, (1993) 816.
13. K. Nisancioglu and T.M. Gür, *Proc. 3rd Int. Sym. Solid Oxide Fuel Cells*, ed.S.C. Singhal and H. Iwahara, Electrochemical Society, Remington, New Jersey, 1994.
14. L.-M. Liu, L. Qiu, T. H. Lee, Y. L. Yang, and A. J. Jacobson to be published.
15. L. Qiu, T. H. Lee, L.-M. Liu, Y. L. Yang and A. J. Jacobson, *Solid State Ionics* submitted
16. I. Kontoulis and B.C.H. Steele, *Solid State Ionics* **47**, (1991) 317.
17. H. Rickert, *Electrochemistry of Solids—an Introduction*, Springer, Berlin, 192, p168.
18. Y. Takeda, K. Kanno, T. Takada, O. Yamamoto, M. Takano, N. Nakayama and Y. Bando, *J. Solid State Chem.* **63**, (1988) 237.



## A STUDY OF THE ELECTROCATALYTIC PROPERTIES OF $\text{SrCo}_{0.8}\text{Fe}_{0.2}\text{O}_{3-\delta}$ BY IMPEDANCE SPECTROSCOPY

AI QUOC PHAM AND ALLAN J. JACOBSON

University of Houston, Department of Chemistry and Texas Center for Superconductivity,  
Houston, TX 77204-5641

### ABSTRACT:

The electrocatalytic behavior of the mixed electron - ion conductor  $\text{SrCo}_{0.8}\text{Fe}_{0.2}\text{O}_{3-\delta}$ , in the form of an electrode on YSZ, has been studied using impedance spectroscopy at low frequencies. The results suggest that the electrode process is dominated by the surface exchange at high temperatures and by the bulk oxygen diffusion at lower temperatures. No limiting current was observed in  $I$ - $V$  measurements. The electrode polarization decreased with increasing current density. The creation of additional oxygen vacancies in the electrode material is suggested to account for the better performance at the higher current densities.

### INTRODUCTION:

Mixed ionic-electronic conductors have attracted much attention because of their potential applications as membranes for gas separation and cathodes for solid oxide fuel cells (SOFCs). For most purely electronically conducting electrodes such as platinum, the charge transfer reaction takes place only at the triple phase boundary (air/electrode/electrolyte). With a mixed conducting electrode, the charge transfer occurs over the whole electrode surface because both oxygen ions and electrons are mobile. The cathodic polarization losses should consequently be reduced. However, limited experimental evidence demonstrating the superiority of mixed conductors over conventional metal electrodes is available. The oxide  $(\text{La},\text{Sr})\text{MnO}_3$  is widely used as a cathode material for SOFCs but is not a good example of a mixed conductor because its ionic conductivity is low at typical cathode oxygen partial pressures. The diffusion coefficient has been found to be small,<sup>1</sup> consistent with the very small oxygen non stoichiometry even at  $p_{\text{O}_2} \geq 10^{-8}$  atm.<sup>2</sup> Consequently, the electrode performance is very dependent on the extent of the three phase boundary and the electrode structure.<sup>3</sup> Hammouche *et al.* have suggested that mixed conduction may occur but only at high cathodic polarization.<sup>4,5</sup> Other mixed conductors with high ionic conductivity, such as  $(\text{La},\text{Sr})\text{CoO}_{3-\delta}$ , have been reported to have small overpotentials for oxygen reduction in comparison to platinum electrodes.<sup>6</sup>

In this paper, the electrode behavior of the mixed conductor  $\text{SrCo}_{0.8}\text{Fe}_{0.2}\text{O}_{3-\delta}$  has been studied using impedance spectroscopy at low frequencies. We have chosen  $\text{SrCo}_{0.8}\text{Fe}_{0.2}\text{O}_{3-\delta}$  because this mixed conductor has been shown to exhibit a very high oxygen permeation rate and oxide ion conductivity.<sup>7</sup>

### EXPERIMENTAL

$\text{SrCo}_{0.8}\text{Fe}_{0.2}\text{O}_{3-x}$  was synthesized using the coprecipitation method.<sup>8</sup> Electrolyte discs were prepared by pressing powders of yttrium stabilized zirconia (YSZ 8% from Tosho) and sintering at 1500°C for 6h. The final diameters and thicknesses of the discs were 0.25" and 0.06" respectively.  $\text{SrCo}_{0.8}\text{Fe}_{0.2}\text{O}_{3-\delta}$  powder was dispersed in polyethylene glycol and painted on

YSZ pellets. The pellets with electrodes were heated in an oven at 200°C to remove the organic solvent, then heated at 1200°C for 3 h.

Sample purity was checked by X-ray diffraction using a Scintag XDS2000 diffractometer. Impedance measurements were performed using a Solartron 1260. The applied voltage amplitude when not specified, was 50mV. Measurements were made in the temperature range 700-1000°C in different atmospheres using predried mixtures of nitrogen and oxygen. The impedance data were fitted using Boukamp's 'Equivrt' program.<sup>9</sup>

## RESULTS AND DISCUSSION

### Impedance spectroscopy

The impedance spectra of the electrode were found to be strongly dependent on the thermal history of the sample. Slow transformation kinetics between the perovskite and brownmillerite phases of  $\text{SrCo}_{0.8}\text{Fe}_{0.2}\text{O}_{3-\delta}$  have been observed by Kruidhof *et al.* in permeation experiments<sup>10</sup> and by Liu *et al.* in thermogravimetric measurements.<sup>11</sup> To minimize this effect, measurement were made on cooling from 1000°C, after annealing for 2h at the specific atmosphere and temperature of the measurement. Longer annealing times at temperatures higher than 1000°C were not possible because  $\text{SrCo}_{0.8}\text{Fe}_{0.2}\text{O}_{3-\delta}$  reacts significantly with the solid electrolyte YSZ.

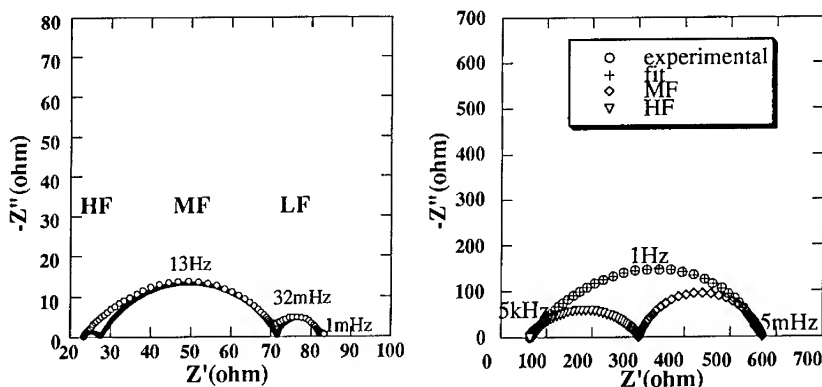


Figure 1. Impedance data for an  $\text{SrCo}_{0.8}\text{Fe}_{0.2}\text{O}_{3-\delta}$  electrode at (a) 950°C and (b) 750°C.

Impedance spectra recorded in 0.6% oxygen are shown in Figure 1. At temperatures above 700°C, the bulk and grain boundary semi-circles are no longer present and the total resistance is determined at the high frequency intercept with the real axis. The observed frequency response in Figure 1 is due to electrode processes. At 950°C, three arcs are present (Figure 1a). The high (HF) and medium (MF) frequency arcs overlap strongly but the low frequency (LF) arc is well separated. The overall electrode resistance is dominated by the MF arc. At lower temperatures, for example at 750°C (Figure 1b), the LF arc is no longer present while the HF and MF arcs become similar in size. A fourth arc was observed under some conditions at the tail of the high frequency arc but was too small to be studied. The impedance spectra corresponding to the electrode reactions were analyzed with an equivalent circuit

comprising a series of parallel  $R_iQ_i$  elements ( $i = \text{HF, MF, LF}$ ). The total electrode resistance is defined as the sum of all the components.

Figure 2 shows the Arrhenius plot of the normalized resistance of the three components together with the total electrode resistance measured in 0.6% oxygen. The low frequency resistance ( $R_{\text{LF}}$ ) decreases with decreasing temperatures. This small "negative" activation energy of 0.34 eV, together with the fact that  $R_{\text{LF}}$  also decreases with increasing oxygen partial pressure, strongly suggest that  $R_{\text{LF}}$  is due to an adsorption process.

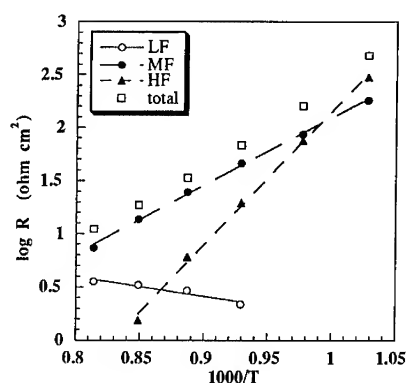


Figure 2 Arrhenius plot of the contributions to the total electrode resistance at 0.6%  $\text{O}_2$ .

The resistances,  $R_{\text{HF}}$  and  $R_{\text{LF}}$  have activation energies of 2.5 eV and 1.27 eV, respectively. The two Arrhenius plots cross over at 740°C. Above 740°C,  $R_{\text{MF}}$  is the major component of the total resistance while below this temperature,  $R_{\text{HF}}$  is more important. A change in the slope in the Arrhenius plot of the total resistance versus  $1/T$  is a consequence of the cross-over between the two regimes. The data obtained at  $p_{\text{O}_2} = 0.2$  or 1.0 atm were more difficult to analyze. The HF and MF semi-circles overlap strongly exhibiting similar resistances. The  $R_{\text{HF}}$  and  $R_{\text{MF}}$  Arrhenius plots again cross at high temperature, ~ 820°C somewhat higher than observed in the 0.6% data. Compared to data recorded in 0.6% oxygen,  $R_{\text{MF}}$  decreases by about half an order of magnitude while  $R_{\text{HF}}$  is almost unchanged. Studies of the oxygen exchange and of the permeation properties of cobaltite materials have shown that the bulk oxygen diffusion coefficient is very high and that the surface exchange appears to be the limiting step.<sup>1,12,13</sup> The activation energy for the surface exchange process is usually lower than that for the bulk diffusion coefficient.<sup>12</sup> Therefore,  $R_{\text{MF}}$  and  $R_{\text{HF}}$  can be tentatively attributed to the surface exchange polarization and the concentration polarization due to the bulk diffusion of the oxygen species to the solid electrolyte/electrode interface.

Some reported permeation data for  $\text{SrCo}_{0.8}\text{Fe}_{0.2}\text{O}_{3.8}$  also show a change in the activation energy of the permeation flux, sometimes with a discontinuity, in a similar temperature range where the changes in the electrode resistance are observed.<sup>10</sup> In permeation experiments, the change has been associated with the transformation of the ordered brownmillerite structure to the disordered perovskite phase.<sup>10</sup> However according to the phase diagram, no transition should be observed above 770°C whatever the atmosphere.<sup>11</sup> Because of the slow transformation kinetics some residue of the brownmillerite phase may remain at high temperatures, explaining the small peak observed in Kruidhof's DSC experiment performed in air.<sup>10</sup> In the present experiments the sample was cooled from above 770°C and none of the brownmillerite phase should remain. The activation energy change is therefore not due to the order-disorder transition. The change in the slope of the electrode resistance with temperature is due to the balance between the surface exchange and the diffusion processes that have different activation energies.

### *I-V* characteristics of $\text{SrCo}_{0.8}\text{Fe}_{0.2}\text{O}_{3-\delta}$ electrodes on a YSZ electrolyte

Impedance spectroscopy can be used to obtain the *I-V* characteristics of a cell.<sup>14</sup> Although the method can not give a value for the dc current density, the qualitative behavior can be determined. Figure 3 shows the *I-V* characteristics of silver electrodes on a YSZ pellet.<sup>14</sup> With increasing amplitude of the applied voltage, the Ag electrode resistance was found to be first unchanged up to 0.3V and then increased linearly with V up to a second threshold beyond which it decreased rapidly. The resulting *I-V* characteristics of the whole cell with *I* defined as the ratio between the applied voltage amplitude and the total resistance (electrode+electrolyte), shows three different regions. The first region corresponds to ohmic behavior of the electrode. The second consists of an almost horizontal plateau indicating the presence of a limiting current density. The third section with a rapid increase of the current density corresponds to the decomposition of the solid electrolyte. This *I-V* curve is characteristic of a metal electrode with oxygen diffusion as a limiting step. The qualitative behavior is similar to the *I-V* characteristics obtained using dc currents.<sup>15</sup> The advantage of the ac method is that it shows which process is affected by the increasing current density.<sup>14</sup>

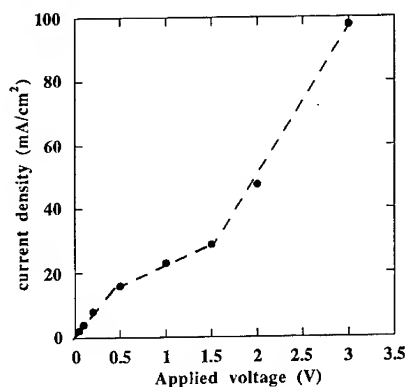


Figure 3. *I-V* characteristics of a silver electrode in air at 660°C.

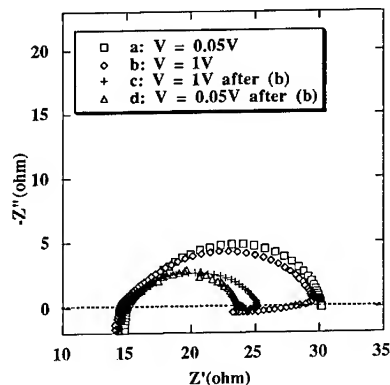


Figure 4. Impedance spectra of a  $\text{SrCo}_{0.8}\text{Fe}_{0.2}\text{O}_{3-\delta}$  electrode under different conditions.

The same technique has been used to study  $\text{SrCo}_{0.8}\text{Fe}_{0.2}\text{O}_{3-\delta}$  electrodes at an oxygen partial pressure of 1 atm. When the applied voltage increases, the electrode resistance remains constant up to a threshold, 0.3V in oxygen at 949°C for example. Beyond this value, the electrode impedance data show an inductive loop at the low frequency end (Figure 4, plot b). Such an inductive loop has been reported for  $\text{La}_{0.5}\text{Sr}_{0.5}\text{MnO}_3$  under high polarization but the interpretation is not clear.<sup>5</sup> After a certain time, the impedance does not change further although the frequency sweep continues, indicating that a steady state is reached. The measurement was then stopped and a second frequency sweep started immediately under the same conditions. The impedance data show a significantly smaller resistance and the low frequency plot of the spectrum intercepts the real axis at the point close to the last point of the previous measurement (Figure 4, plot c). The non-reproducibility indicates that the electrode has undergone a composition change under the applied voltage. It has been suggested that at high voltage, oxygen vacancies are created in the electrode, the ionic conduction increases and the electrode performance improves. If the second measurement made at a much lower applied voltage (50mV), in the ohmic region, the electrode resistance is also smaller, but increases with time (Figure 4, plot d). After a few hours, the electrode resistance recovers its initial value (Figure 4, plot a). The reversibility of the electrode change further supports the above hypothesis, the electrode is reoxidized when the high voltage is removed. The inductive loop observed during the first measurement can simply arise from a non-steady state process and reflects the reduction occurring at the electrodes. In air, the same phenomenon is observed. The influence of the voltage amplitude on the electrode is smaller, consistent with a smaller range for the oxygen content change.

The  $I$ - $V$  characteristic of the cell in 1atm oxygen with  $\text{SrCo}_{0.8}\text{Fe}_{0.2}\text{O}_{3-\delta}$  electrodes is shown in Figure 5. At low voltage, an ohmic behavior is observed. Above 0.3V, the current increases with increasing voltage but no limiting current is observed up to the decomposition voltage of YSZ. Figure 6 shows the Arrhenius plots of the electrode resistance measured at 1.5V. Compared to the reference data recorded in the ohmic region (50mV), the electrode resistance is lower and the activation energy has significantly decreased.

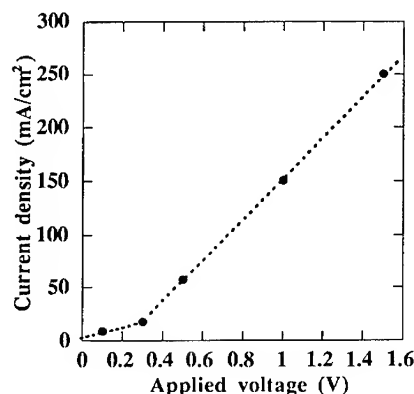


Figure 5.  $I$ - $V$  data for  $\text{SrCo}_{0.8}\text{Fe}_{0.2}\text{O}_{3-\delta}$  electrode in 1atm  $\text{O}_2$

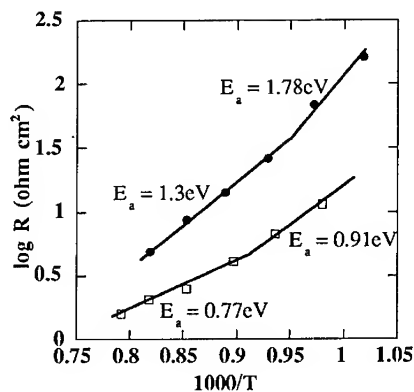


Figure 6. Electrode resistances at 1.5V and 50mV.

The above results clearly show the important advantages of mixed conductors over normal metal electrodes. The presence of ionic conductivity improves significantly the electrode performance especially under high current densities. Similar measurements have been made for  $\text{La}_{0.7}\text{Sr}_{0.3}\text{MnO}_3$ . The ohmic region is much more important, in this case and the inductive loop was observed only for voltages higher than 2V, close to the decomposition value of the solid

electrolyte. The difference in performance of lanthanum strontium manganate at high current densities is due to its smaller range of oxygen non-stoichiometry over a comparable range of oxygen partial pressures.<sup>16</sup>

## CONCLUSION:

Impedance spectroscopy has been used to study the electrocatalytic properties of  $\text{SrCo}_{0.8}\text{Fe}_{0.2}\text{O}_{3-\delta}$  electrodes on a YSZ electrolyte. The results suggest that the electrode process is dominated by the surface exchange at high temperatures and by polarization due to the bulk diffusion at low temperatures. Impedance spectroscopy has been used to obtain the qualitative  $I$ - $V$  characteristics of the  $\text{SrCo}_{0.8}\text{Fe}_{0.2}\text{O}_{3-\delta}$  electrode. The results demonstrate the superiority of mixed conductors over normal metal electrodes. No limiting current is observed with increasing applied voltage and a better electrode performance is obtained at high current densities. The creation of additional oxygen vacancies at high current densities is thought to be responsible for the better performance and that the ionic conduction in mixed conductors does participate in the electrode process.

Although  $\text{SrCo}_{0.8}\text{Fe}_{0.2}\text{O}_{3-\delta}$  performs well as an electrocatalytic material, it cannot be used as an electrode material in SOFCs because of its low mechanical stability and high chemical reactivity when used with YSZ solid electrolytes. Further studies of other oxides containing mixed valence transition metal cations that can be reduced without phase decomposition and which are more compatible with YSZ are in progress.

We thank the R. A. Welch Foundation for partial support of this work.

## REFERENCES

1. S. Carter, A. Selcuk, R. J. Charter, J. Kajda, J. A. Kilner and B. C. H. Steele, *Solid State Ionics* **53-56**, 597 (1992).
2. J. Mizusaki, H. Tagawa, K. Naraya and T. Sasamoto, *Solid State Ionics* **49**, 111 (1991).
3. J. Mizusaki, H. Tagawa, K. Tsuneyoshi and A. Sawata, *J. Electrochem. Soc.*, **138**, 1867 (1991).
4. A. Hammouche, E. Siebert, A. Hammou and M. Kleitz, *J. Electrochem. Soc.* **138**, 1212 (1991).
5. B. Gharbage, T. Panier and A. Hammou, *J. Electrochem. Soc.* **141**, 2118 (1994).
6. T. Inoue, K. Eguchi, T. Setoguchi and H. Arai, *Solid State Ionics* **40-41**, 407 (1990).
7. Y. Teraoka, H.M. Zhang, S. Furukawa and N. Yamazoe, *Chem. Letters* 1743 (1985).
8. D. W. Johnson, Jr., P. Gallagher, F. Schrey and W.W. Rhodes, *Ceram. Bulletin* **55**, 520 (1976).
9. B. A. Boukamp, *Solid State Ionics* **20**, 31 (1986).
10. H. Kruidhof, H. J. M. Bouwmesster, R. H. E. V. Doorn and A. J. Burggraaf, *Solid State Ionics* **63-65**, 816 (1993).
11. L. M. Liu, T. H. Lee, Y. L. Yang, and A.J. Jacobson to be published
12. I. C. Fullarton, J. A. Kilner, B. C. H. Steele and P. H. Middleton, *Proceedings of the Second International Symposium on Ionic and Mixed Conducting Ceramics*, Eds. by T. A. Ramanarayanan, W. L. Worrell and H. L. Tuller, The Electrochemical Society, Pennington, NJ 1994, pp. 9-26.
13. L. Qiu, T. H. Lee, L. M. Liu, Y. L. Yang, and A. J. Jacobson, submitted for publication.
14. A. Q. Pham and A. J. Jacobson, *J. Electrochem. Soc.* submitted for publication.
15. T. H. Etsell and S. N. Flengas, *J. Electrochem. Soc.* **118**, 1890 (1971).
16. A.Q. Pham and A.J. Jacobson unpublished.

## PROCESSING AND ELECTROCHEMICAL PROPERTIES OF MIXED CONDUCTING $\text{La}_{1-x}\text{A}_x\text{Co}_{1-y}\text{Fe}_y\text{O}_{3-\delta}$ (A=Sr, Ca)

W. J. WEBER, J. W. STEVENSON, T. R. ARMSTRONG, L. R. PEDERSON, AND  
J. J. KINGSLEY

Pacific Northwest Laboratory, P.O. Box 999, Richland, WA 99352, USA

### ABSTRACT

Powder compositions in the series  $\text{La}_{1-x}\text{A}_x\text{Co}_{1-y}\text{Fe}_y\text{O}_{3-\delta}$  (A=Sr, Ca) have been prepared by a combustion synthesis method. Sintering of pressed powders produced high-density test specimens with the perovskite structure. The specimens exhibited high electrical conductivities with appreciable oxygen-ion conductivity that increased with Co content for the compositions studied. Oxygen permeation studies showed a significant flux of oxygen that increased with temperature for specimens in a  $\text{P}(\text{O}_2)$  gradient with no applied field. Thermogravimetric studies of the  $\text{La}_{1-x}\text{Sr}_x\text{Co}_{0.2}\text{Fe}_{0.8}\text{O}_{3-\delta}$  system indicated a reversible mass loss with increasing temperature that increased with Sr content.

### INTRODUCTION

Mixed ionic-electronic conductors exhibit appreciable ionic and electronic conductivities at elevated temperatures. Mixed-conducting oxides with high oxygen-ion conductivity are promising candidate materials for a wide range of attractive applications, such as cathodes for solid oxide fuel cells, oxygen-separation membranes, catalytic materials, and oxygen sensors [1,2]. The utilization of mixed conducting oxides in these applications will require a detailed understanding of processing behavior as well as electrical properties, oxygen stoichiometry, and phase stability as a function of temperature, oxygen partial pressure, and composition.

Oxides with the  $\text{ABO}_3$  perovskite-type structure are an important class of electroceramics that are receiving increased attention. The perovskite-type oxide,  $\text{LaCoO}_3$ , exhibits very high p-type electronic conductivity [3]. Recent studies [4-11] have demonstrated that the substitution of acceptor dopants onto the A or B sites of  $\text{LaCoO}_3$  can introduce high concentrations of oxygen vacancies that give rise to oxygen-ion conductivity. Perovskites in the  $\text{La}_{1-x}\text{Sr}_x\text{Co}_{1-y}\text{Fe}_y\text{O}_{3-\delta}$  system have received particular attention recently due to their high oxygen-ion conductivity [4-9]. Although the ionic transference number may be quite small ( $<0.01$ ), the magnitude of the ionic conductivity can be quite large. At  $800^\circ\text{C}$ , the oxygen ion conductivity of  $\text{La}_{0.8}\text{Sr}_{0.2}\text{Co}_{0.8}\text{Fe}_{0.2}\text{O}_{3-\delta}$  is reported to be an order of magnitude higher than for yttria-stabilized zirconia [4,5]. One of the important issues regarding compositions in these systems is structural stability.

In this study, compositions in the series  $\text{La}_{1-x}\text{A}_x\text{Co}_{1-y}\text{Fe}_y\text{O}_{3-\delta}$  (A=Sr, Ca) with the perovskite structure were prepared by a combustion synthesis method. Phase development and densification of dry pressed samples were studied by X-ray diffraction and SEM analyses. Electrochemical properties were determined by electrical conductivity measurements, oxygen permeation studies, and thermogravimetric analysis.

### EXPERIMENTAL PROCEDURES

Sample powders of the general composition,  $\text{La}_{1-x}\text{A}_x\text{Co}_{1-y}\text{Fe}_y\text{O}_{3-\delta}$ , where A = Sr and Ca,

were synthesized using a glycine-nitrate process [12]. In this process, metal nitrate solutions were mixed in appropriate proportions, then glycine was added as a fuel and complexant. This glycine-nitrate mixture was heated until combustion occurred, producing a fine ash powder of the desired stoichiometry. These fine powders were calcined in air at 850°C for 12 hours. The powders were then passed through a 200-mesh sieve and pressed into rectangular bars for conductivity measurements or discs for permeation measurements. The powders were uniaxially pressed at 10,000 psi and subsequently cold isostatically pressed at 20,000 psi. The samples were sintered in air for 2 to 4 hours at temperatures ranging from 1150 to 1250°C. Bulk densities of the sintered specimens, which were measured using an immersion technique in ethanol, were 90-95% of the theoretical density.

Electrical conductivities were measured in air using a four-probe, pulsed dc technique on specimens in the form of rectangular bars, nominally 3 mm by 3 mm by 38 mm. Specimens were positioned in a resistance-heated furnace with Pt knife-edge contacts, set at predetermined distances, and Pt lead wires. The contacts were coated with Pt paste to reduce contact resistance, and the temperature of each specimen was measured with two calibrated Pt-Pt10%Rh thermocouples in contact with the specimens. The electrical conductivity instrumentation and temperature measurements were computer interfaced for automated data collection and storage. Measurements were made both on heating and cooling over the temperature range from 25 to 1200°C.

Thermogravimetric analysis (TGA) was carried out over the temperature range from 25 to 1250°C using a Cahn Model TG-171 instrument. Measurements were performed with an air atmosphere on single-phase powders that were calcined at 850°C. The rate of heating during the measurements was 5°C/min, and the rate of cooling was 2°C/min.

Oxygen permeation measurements were carried out using disc specimens (2.5 mm thick and 25 mm diameter). Each specimen was sealed in an alumina cell with gold gaskets. During the measurements, one side was exposed to a stream of O<sub>2</sub> (1 atm), while the other side was exposed to a N<sub>2</sub> stream. The oxygen/nitrogen P(O<sub>2</sub>) gradient (~10) across the specimen provided a driving force for oxygen transport from the oxygen side to the nitrogen side. Due to the mixed conductivity in these perovskite systems, the specimens responded to the P(O<sub>2</sub>) gradient by spontaneously reducing O<sub>2</sub> to anionic oxygen at the high P(O<sub>2</sub>) surface, transporting the anionic oxygen through the material via an oxygen-vacancy mechanism, and oxidizing the anionic oxygen to O<sub>2</sub> at the low P(O<sub>2</sub>) side. The passive (i.e., no applied electric field) flux of oxygen through the specimens was measured as a function of temperature with a mass spectrometer.

## RESULTS AND DISCUSSION

### *X-ray diffraction*

X-ray diffraction analysis showed that all compositions in the La<sub>1-x</sub>Sr<sub>x</sub>Co<sub>1-y</sub>Fe<sub>y</sub>O<sub>3-δ</sub> system were phase-pure perovskites, while compositions in the La<sub>1-x</sub>Ca<sub>x</sub>Co<sub>1-y</sub>Fe<sub>y</sub>O<sub>3-δ</sub> were 95% phase-pure perovskites. Compositions sintered in air with high Sr content exhibited high densities; however, the sintered specimens tended to be extensively microcracked. Processing techniques that successfully reduce the microcracking will be reported at a later date.

### *Electrical conductivity*

The dependence of electrical conductivity,  $\sigma$ , on absolute temperature,  $T$ , for specimens in the La<sub>1-x</sub>Sr<sub>x</sub>Co<sub>1-y</sub>Fe<sub>y</sub>O<sub>3-δ</sub> and the La<sub>1-x</sub>Ca<sub>x</sub>Co<sub>1-y</sub>Fe<sub>y</sub>O<sub>3-δ</sub> systems is shown in Figs. 1 and 2,



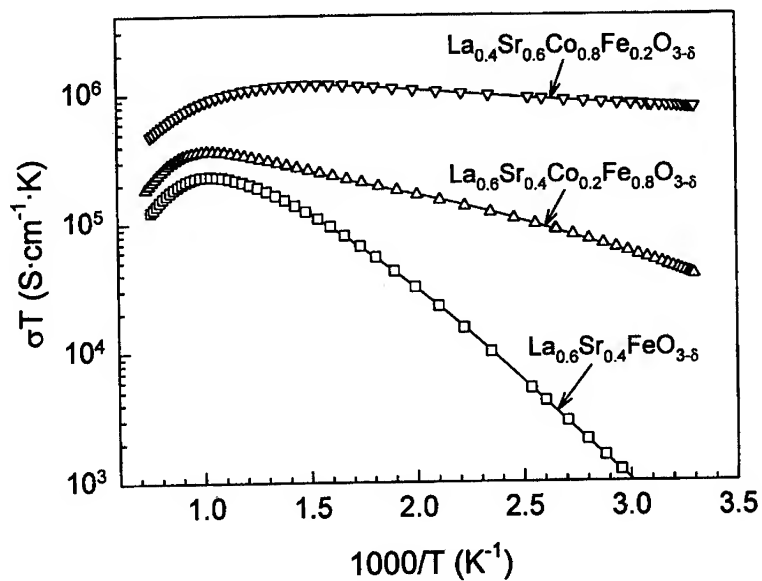


Fig. 1.  $\text{Log}(\sigma T)$  versus  $1/T$  for compositions in the  $\text{La}_{1-x}\text{Sr}_x\text{Co}_{1-y}\text{Fe}_y\text{O}_{3-\delta}$  system.

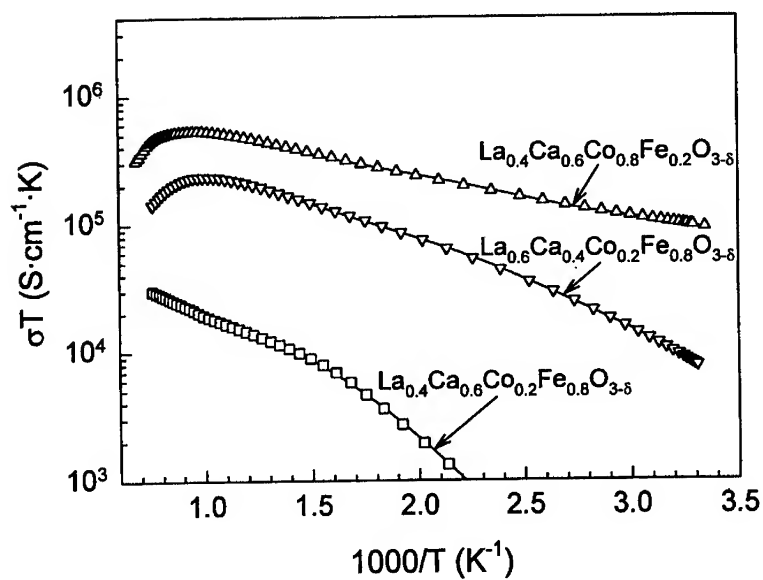


Fig. 2.  $\text{Log}(\sigma T)$  versus  $1/T$  for compositions in the  $\text{La}_{1-x}\text{Ca}_x\text{Co}_{1-y}\text{Fe}_y\text{O}_{3-\delta}$  system.

respectively. At lower temperatures,  $\sigma T$  follows the behavior expected for small polaron conduction in these materials that is given by the expression [13,14]:

$$\sigma T = C \exp(-E_a/kT) \quad (1)$$

where the pre-exponential  $C$  is both a charge carrier and material dependent constant,  $E_a$  is the activation energy, and  $k$  is the Boltzmann constant. Activation energies measured below 650°C are less than 0.2 eV, consistent with a small polaron hopping mechanism. The highest conductivities are observed in the high-Co, high-(Sr,Ca) specimens,  $\text{La}_{0.4}(\text{Sr,Ca})_{0.6}\text{Co}_{0.8}\text{Fe}_{0.2}\text{O}_{3-\delta}$ . The decrease in conductivity at temperatures above about 900°C can be attributed to a decrease in electronic charge carriers as a result of oxygen loss observed by TGA (below). This decrease in electron holes is described by the defect equation:



Thus, the decrease in oxygen stoichiometry with increasing temperature decreases the concentration of the dominant charge carriers (electron holes) and increases the concentration of ionic charge carriers (oxygen vacancies), which results in an increased oxygen-ion conductivity (oxygen permeation rate), as discussed below.

#### *Thermogravimetric analysis*

The TGA results for specimens in the  $\text{La}_{1-x}\text{Sr}_x\text{Co}_{0.2}\text{Fe}_{0.8}\text{O}_{3-\delta}$  system are shown in Fig. 3. The decrease in mass from oxygen loss increases with increasing temperature and with Sr content. The most stable compound of this group,  $\text{La}_{0.6}\text{Sr}_{0.4}\text{Co}_{0.2}\text{Fe}_{0.8}\text{O}_{3-\delta}$ , has the lowest Sr content. The mass loss from oxygen creates additional vacancies in the lattice, which increases the oxygen-ion conductivity and decreases the small polaron concentration. Continued TGA measurements as a function of oxygen partial pressure are in progress, and analysis of additional compositions is planned, particularly those corresponding to the electrical conductivity data in Figs. 1 and 2.

#### *Oxygen permeation*

The passive rates of oxygen permeation through 2.5 mm thick disc specimens of  $\text{La}_{0.6}\text{Sr}_{0.4}\text{Co}_{0.2}\text{Fe}_{0.8}\text{O}_{3-\delta}$  and  $\text{La}_{0.4}\text{Sr}_{0.6}\text{Co}_{0.2}\text{Fe}_{0.8}\text{O}_{3-\delta}$  in an oxygen/nitrogen  $\text{P}(\text{O}_2)$  gradient of  $\sim 10$  are shown in Fig. 4 as a function of temperature. The steep temperature gradient is due to the thermally-activated diffusion of oxygen and an increase in the concentration of oxygen vacancies at elevated temperatures. From the flux measurements, it is possible to calculate the oxygen-ion conductivity. At 900°C, the ionic conductivities are 0.194 and 0.499  $\text{S}\cdot\text{cm}^{-1}$  for  $\text{La}_{0.6}\text{Sr}_{0.4}\text{Co}_{0.2}\text{Fe}_{0.8}\text{O}_{3-\delta}$  and  $\text{La}_{0.4}\text{Sr}_{0.6}\text{Co}_{0.2}\text{Fe}_{0.8}\text{O}_{3-\delta}$ , respectively. Based on the ionic conductivity and the total electrical conductivity (Fig. 1), the ionic transference number for  $\text{La}_{0.6}\text{Sr}_{0.4}\text{Co}_{0.2}\text{Fe}_{0.8}\text{O}_{3-\delta}$  at 900°C is  $7.7 \times 10^{-4}$ , which is similar to that found by others [8]. The ionic conductivities deduced from Fig. 4 indicate an increasing ionic conductivity with temperature, in agreement with the results of others [5,8]. Consequently, the decrease in total electrical conductivity observed in Fig. 1 is due to a decrease in electronic conductivity (i.e., a decrease in the electronic carrier concentration).

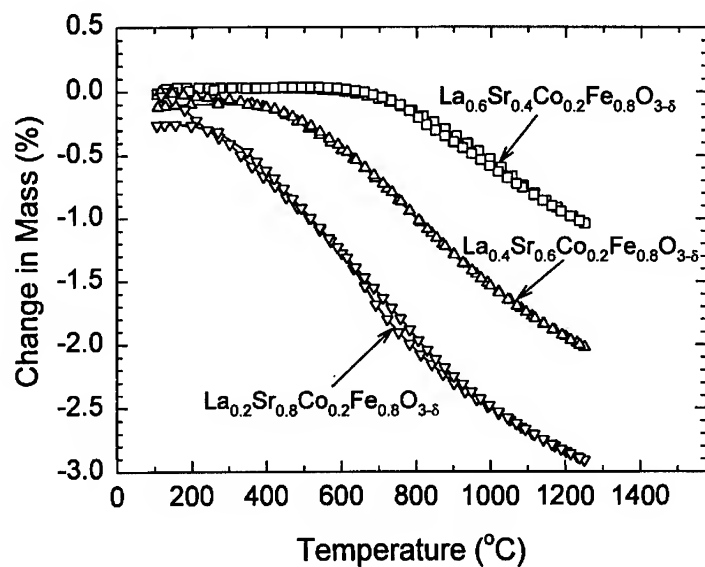


Fig. 3. TGA results for specimens in the  $\text{La}_{1-x}\text{Sr}_x\text{Co}_{0.2}\text{Fe}_{0.8}\text{O}_{3-\delta}$  system.

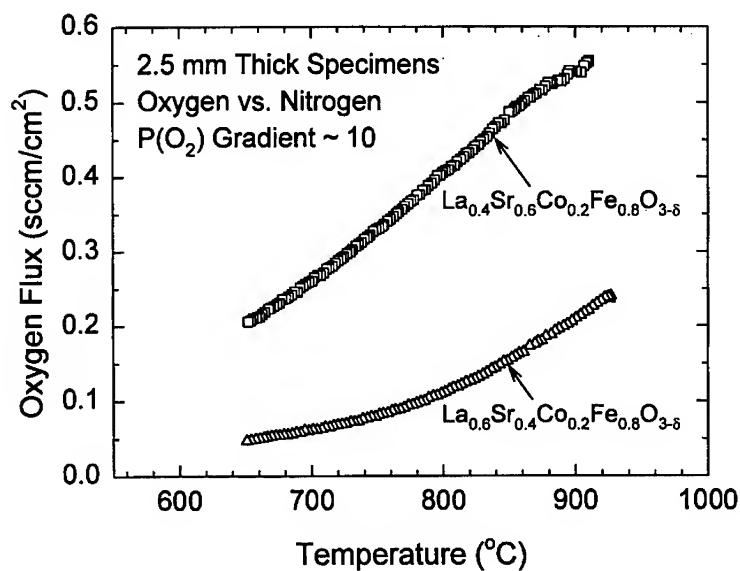


Fig. 4. Passive oxygen flux through  $\text{La}_{0.6}\text{Sr}_{0.4}\text{Co}_{0.2}\text{Fe}_{0.8}\text{O}_{1-\delta}$  in a gradient established by oxygen versus nitrogen.

## ACKNOWLEDGEMENTS

The authors gratefully acknowledge R. W. Stephens for technical assistance with the electrical conductivity and oxygen permeation measurements and D. E. McCready for the X-ray diffraction analysis. This research was supported by the Office of Fossil Energy, U. S. Department of Energy under Contract DE-AC06-76RLO 1830.

## REFERENCES

- [1] A.R. West, *J. Mater. Chem.* **1** [2] 157 (1991).
- [2] W.J. Weber, H.L. Tuller, T.O. Mason, and A.N. Cormack, *Mater. Sci. and Engr.* **B18**, 52 (1993).
- [3] P.M. Raccach and J.B. Goodenough, *Phys. Rev.* **3**, 932 (1967).
- [4] Y. Teraoka, H.M. Zhang, K. Okamoto, and N. Yamazoe, *Mater. Res. Bull.* **23**, 51 (1988).
- [5] Y. Teraoka, T. Nobunga, K. Okamoto, N. Miura, and N. Yamazoe, *Solid State Ionics* **48**, 207 (1991).
- [6] S. Sekido, H. Tachibana, Y. Yamamura, and T. Kambara, *Solid State Ionics* **37**, 253 (1990).
- [7] W.L. Worrell, *Solid State Ionics* **52**, 147 (1992).
- [8] H.U. Anderson and C.C. Chen, in *Ionic and Mixed Conducting Ceramics*, edited by T.A. Ramanarayanan, W.L. Worrell, and H.L. Tuller (The Electrochemical Society, Pennington, NJ, 1994) pp. 376-383.
- [9] T.R. Armstrong, J.L. Bates, G.W. Coffey, J.J. Kingsley, L.R. Pederson, J.W. Stevenson, W.J. Weber, and G.E. Youngblood, in *Proc. of the Eighth Annual Conf. on Fossil Energy Materials*, CONF-9405143, edited by N.C. Cole and R.R. Judkins (National Technical Information Service, Springfield VA, 1994) pp. 89-96.
- [10] H. Nagamoto, I. Mochida, K. Kagotani, and H. Inoue, *J. Mater. Res.* **8** [12] 3158 (1993).
- [11] Y. Denos, F. Morin, and G. Trudel, in *Ionic and Mixed Conducting Ceramics*, edited by T.A. Ramanarayanan, W.L. Worrell, and H.L. Tuller (The Electrochemical Society, Pennington, NJ, 1994) pp. 150-158.
- [12] L.A. Chick, L.R. Pederson, G.D. Maupin, J.L. Bates, L.E. Thomas, and G.J. Exarhos, *Mater. Lett.* **10** [1,2] 6 (1990).
- [13] I.G. Austin and N.F. Mott, *Adv. Phys.* **18**, 41 (1969).
- [14] J.M. Wimmer and I. Bransky, in *Electrical Conductivity in Ceramics and Glasses, Part A, Ch. 4*, edited by N.M. Tallan (Marcel Dekker, New York, 1974) pp. 269-311.

## STRUCTURAL, ELECTRICAL AND OPTICAL PROPERTIES OF LASER DEPOSITED THIN FILMS OF $\text{SrCo}_{0.8}\text{Fe}_{0.2}\text{O}_{3-\delta}$

C. ZHANG\* H. DENG\*, J. VARON\*, B. ABELES\*, Y. YANG\*\*, A.Q. PHAM\*\* AND  
A.J. JACOBSON\*\*

\*Exxon Research and Engineering Co, Annandale NJ

\*\*Department Of Chemistry and Texas Center of Superconductivity, U of Houston,  
TX 77204-5641

### ABSTRACT

Thin film  $\text{SrCo}_{0.8}\text{Fe}_{0.2}\text{O}_{3-\delta}$  were made by pulse laser deposition. The electrical conductivity is thermally activated in the temperature 25-500 °C with an activation energy of 0.17-0.19 eV and is temperature independent from 500-800 °C. The optical absorption shows characteristic features which are interpreted qualitatively in terms of a simple band structure diagram.

### INTRODUCTION

Perovskite oxides can tolerate large departure from the ideal stoichiometry  $\text{ABO}_3$ . Oxygen ion deficiency can be achieved by aliovalent doping, which can result in a large oxygen ion and electronic conductivities. Such materials, referred to as mixed ionic-electronic conductors, are used as active elements in membranes and fuel cells. The perovskite  $\text{SrCo}_{0.8}\text{Fe}_{0.2}\text{O}_{3-\delta}$  has received a great deal of attention<sup>1,2</sup> because of its high oxygen ion diffusion coefficient. For fundamental understanding as well as device application it is desirable to study this material in thin film form. Thin films can be prepared with near ideal density, highly orientated and with high crystalline perfection and they are well suited for spectroscopic studies. In this work we describe the preparation of  $\text{SrCo}_{0.8}\text{Fe}_{0.2}\text{O}_{3-\delta}$  films by pulse laser deposition and we report on their structural, electrical and optical properties.

### FILM PREPARATION AND STRUCTURE

The laser targets, 1 inch in diameter and 1/4 inch thick, were made by sintering  $\text{SrCo}_{0.8}\text{Fe}_{0.2}\text{O}_{3-\delta}$  powder<sup>3</sup>. Two different targets were made: target 1 was heated at 1°C/min to 1100°C, held there for 12h and cooled at 1°C/min; target 2 was heated at 1°C/min to 1160°C, held there for 60h and cooled at 1°C/min. The targets were mounted in a vacuum system with base pressure  $10^{-6}$  Torr. The pressure during deposition was maintained at 70 mTorr of  $\text{O}_2$ . The films were deposited with a 246 nm laser, Lambda Physics LPX300i. The laser beam, focused by a quartz lens, was incident on the target through a quartz window at a 45° angle of incidence. The laser power density incident on the target was 1 J/cm<sup>2</sup> over an area of 2x6 mm<sup>2</sup>, the pulse width was 30 ns and repetition rate was 20 Hz. Silica or single crystal MgO substrates were cemented with silver paste on a heater which was 3.5 inch from the target surface. The films reported here were deposited at 600 °C in the thickness range 0.05-1 µm. The deposition rates depended on the sintering conditions of the targets. Target 1 yielded a deposition rate of 0.06Å/pulse while target 2 yielded a deposition rate, under the same deposition conditions, of 0.02Å/pulse. This difference in deposition rates between the two targets is likely due to a higher density of target 2.

2 yielded a deposition rate, under the same deposition conditions, of 0.02A/pulse. This difference in deposition rates between the two targets is likely due to a higher density of the target 2.

The composition of the films determined by EDX was found to be unchanged from that of the target. The X-ray diffraction spectrum in Fig.1 shows that the films are highly oriented. In Fig.2, SEM shows that the average grain size is 700A in a 500A thick film and increases to about 1500A for films 3000A thick. No difference was found in the structure of films made from targets 1 and 2.

## ELECTRICAL CONDUCTIVITY

Electrical conductivity  $\sigma$  was measured in the plane of the films at dc and ac (0.1-10<sup>5</sup> Hz), in air ambient in the temperature range 22-800 °C. Platinum current electrodes were deposited on the films by RF sputtering. The sample was heated up to 800 °C at a rate of 6 °C/min and held at that temperature for 30 min before taking the data. Then it was cooled at the rate of 6 °C/min to the next lower temperature, and data was taken after waiting for 30 min for equilibrium. The temperature dependence of  $\sigma$  of two films 3000A thick, on MgO substrates, deposited from targets 1 and 2, is shown in Fig.3. The conductivities of the two films do not differ significantly from one another. Over the entire temperature range the ac conductivity was frequency independent and equal to the dc conductivity, indicating that the conductivity is primarily electronic. The measured conductivity is thermally activated in the temperature range 22-500 °C, with an activation energy of 0.17-0.19 eV and from 500-800 °C it becomes essentially temperature independent.

We first discuss the mechanism for electronic and ionic transport in the perovskites. In general the cations can appear in the valence states A<sup>1+</sup>B<sup>5+</sup>O<sub>3</sub>, A<sup>2+</sup>B<sup>4+</sup>O<sub>3</sub> and A<sup>3+</sup>B<sup>3+</sup>O<sub>3</sub>. Defects can be introduced by aliovalent doping. By substituting on the A site the divalent rare earth Sr, oxygen vacancies are created simultaneously for charge compensation so that a fraction of the B ions, cobalt this case, are in the tetravalent states i.e. Sr<sup>2+</sup>Co<sup>3+</sup>(Co<sup>4+</sup>)O<sub>3- $\delta$</sub> . This results in p-type electronic conductivity, while the oxide ion conduction is via oxygen vacancies. The larger  $\delta$ , the larger the ionic conductivity will be. A small amount of Fe is added to SrCoO<sub>3- $\delta$</sub>  in order to stabilize the cubic structure<sup>4</sup>. The Fe<sup>3+</sup> ion stabilizes the lattice because it has a larger ionic radius than Co<sup>3+</sup>. The ionization energy to produce Fe<sup>4+</sup> is 3.5 eV larger than that for<sup>5</sup> Co<sup>4+</sup> so Fe ions are mainly in their Fe<sup>3+</sup> valence states.

Because the electrical conductivity of SrCo<sub>0.8</sub>Fe<sub>0.2</sub>O<sub>3- $\delta$</sub>  is thermally activated, it falls into the category of charge transfer perovskites<sup>6</sup>. The holes are localized on the B<sup>4+</sup> sites and hop via oxygen 2p states to the neighboring B<sup>3+</sup>:



In order to satisfy the charge neutrality condition when there are  $\delta$  oxygen vacancies per unit cell, there must be (2 $\delta$ ) B<sup>3+</sup> ions and (1-2 $\delta$ ) B<sup>4+</sup> ions. In the limit of small vacancy concentration ( $\delta \ll 3$ ), the conductivity  $\sigma$  is proportional to the product of the probabilities of the valences B<sup>4+</sup> and B<sup>3+</sup> and the concentration of O<sup>2-</sup>:

$$\sigma \propto (1-2\delta)(3-\delta)2\delta e^{-E_a/kT} \quad (2)$$

where  $E_a$  is the activation energy for the transfer process.

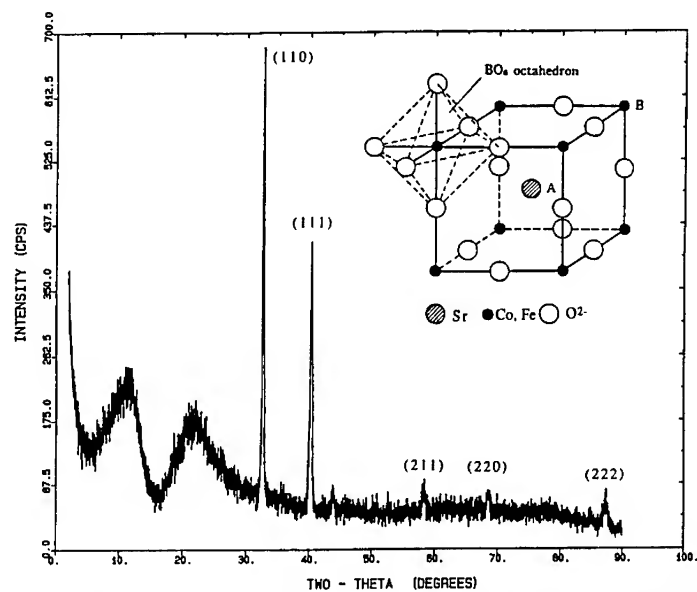


Fig.1: X-ray diffraction of  $\text{SrCo}_{0.8}\text{Fe}_{0.2}\text{O}_{3-\delta}$  film deposited on silica substrate at 600 °C. The insert is the structure of  $\text{ABO}_3$  perovskite.

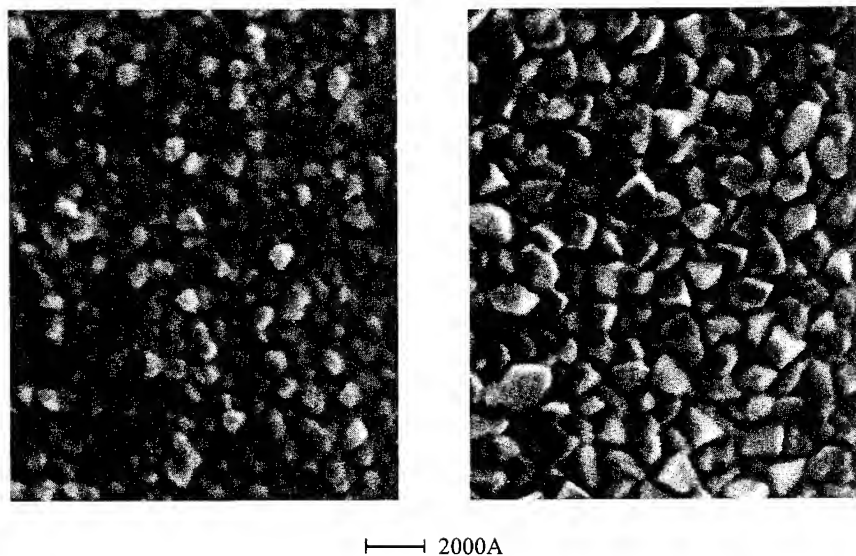


Fig.2: SEM photographs of  $\text{SrCo}_{0.8}\text{Fe}_{0.2}\text{O}_{3-\delta}$  films deposited on  $\text{MgO}$  substrates at 600 °C with thicknesses of 500 Å (left) and 1400 Å (right).

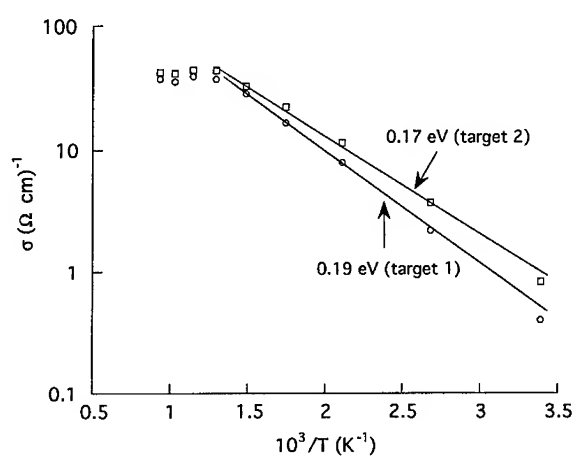


Fig.3: Electrical conductivity  $\sigma$  of  $\text{SrCo}_{0.8}\text{Fe}_{0.2}\text{O}_{3-\delta}$  as a function of reciprocal temperature

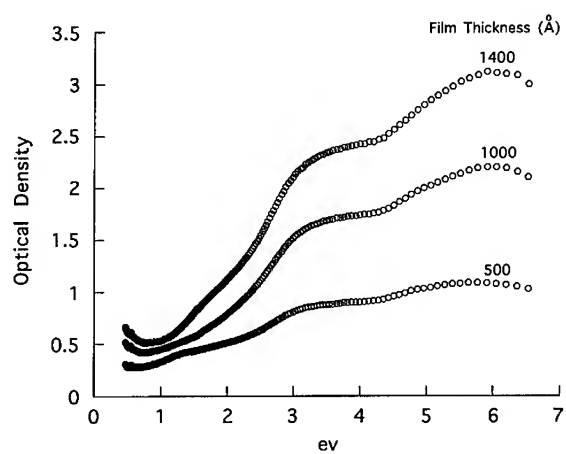


Fig.4: Optical density spectra of  $\text{SrCo}_{0.8}\text{Fe}_{0.2}\text{O}_{3-\delta}$  thin films.



We associate the observed activation energy in Fig.3 with the hopping process given by Eq(1). The saturation of  $\sigma$  above 500 °C may be due to small changes in  $\delta$  at the high temperature, since the pre-exponential factor is quite sensitive to the value of  $\delta$  near  $\delta=0.4$ . Below 500 °C any changes in  $\delta$  would be too slow to be observed on the time scale of our experiment so that there  $\delta$  is essentially constant with temperature.

## OPTICAL PROPERTIES

Optical transmission measurements were made on a Cary spectrophotometer in the range 0.5 eV to 6.5 eV. In Fig.4 we show the optical density for three films with different thicknesses deposited on silica, all made with target 2. All three films exhibit similar features, a steep rise between 2-3 eV, a shoulder between 3-4 eV and a peak near 6eV. The optical absorption coefficient  $\alpha$  plotted in Fig.5 was derived from the difference in the optical densities OD of the 1400Å and the 1000Å films:

$$\alpha = (OD_1 - OD_2) / \Delta l \quad (3)$$

where  $\Delta l$  is the difference in the thickness of the two films. This procedure eliminates, to a good approximation, the effect of reflection from the film-air and film-substrate interfaces.

In order to interpret qualitatively the optical spectra we consider the band structure of  $SrCo_{0.8}Fe_{0.2}O_{3-\delta}$ . The 3d electrons of the transition metals, which are in octahedral coordination, are strongly localized and form narrow bands. Because of the crystalline field of the six oxygen ion octahedron, the 3d states split into two levels. A high energy band  $e_g$  corresponding to  $d_{z^2}$ ,  $d_{x^2-y^2}$  electron orbitals and low energy band  $t_{2g}$  corresponding to  $d_{xy}$ ,  $d_{xz}$ ,  $d_{yz}$ . Outer s and p electrons form extended bands and can be treated by means of one-electron theory.

A pseudoparticle density of states diagram is shown in Fig.6. The partially filled  $3d^5$  band corresponds to  $t_{2g}$ . The empty  $3d^{5*}$  band is due to the  $e_g$  states and the multiplet splitting of d levels. The 2p electrons of the oxygen form an extended filled band and the 4s electrons of the transition-metals form an extended empty band.

We associate the steep rise in the absorption in the range 2-3 eV with the strong allowed electric dipole transition from the filled 2p band to the empty  $3d^{5*}$  band. The rise in absorption between 4-6 eV we associate with the transition  $2p-4s$  and  $3d^{5*}-4s$ . The later transition may be suppressed somewhat because of the forbidden nature of  $3d-4s$  electric dipole transition, but covalency of the s electrons with the anion 2p wave function overcomes the selection rule to a large extent<sup>7</sup>. The  $3d^5-3d^{5*}$  and  $2p-3d^5$  transitions are expected to be weak. In Fig.5 we show schematically the different contributions to the absorption. The absorption at low energy is due to the water absorption peak centered at 0.4 eV<sup>8</sup>.

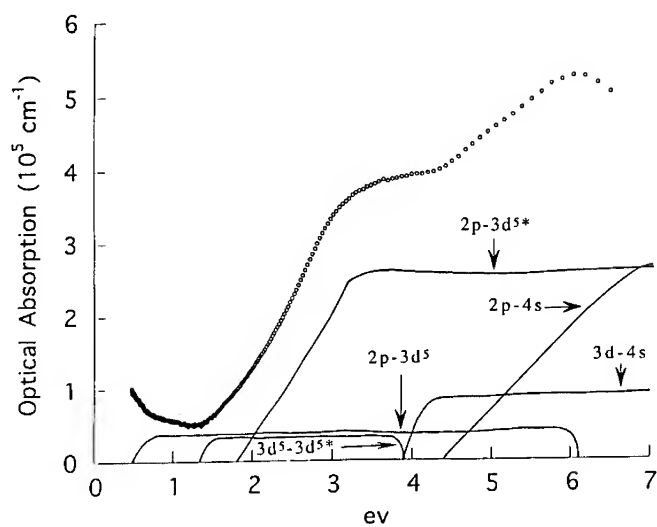


Fig.5: Optical absorptions derived from Eq(3) and data in Fig.4 and schematic representation of absorption process.

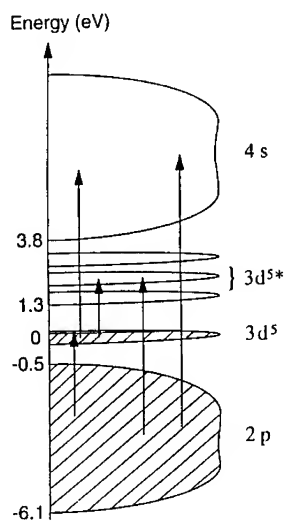


Fig.6: Band structure of  $\text{SrCo}_{0.8}\text{Fe}_{0.2}\text{O}_3$ , shaded areas are the filled states.

#### REFERENCES:

1. Y. Teraoka and H.M. Zhang, Chem. Lett. 1743 (1985)
2. H. Kruidhof, H. J. M. Bouwmeester, R. H. E. v. Doorn and A. J. Burggraaf, Solid State Ionics **63-65**, 816(1993)
3. A. Q. Pham and A.J. Jacobson, these proceedings.
4. N. Yamazoe and Y. Teraoka, Catalysis Today **8**, 175 (1990)
5. CRC Handbook of Chem. & Phys. p E-63, CRC Press, Inc. 1984
6. J. B. Torrance, P. Lacorro, C. Asavaroengchai and R. M. Metzger, J. of Solid State Chemistry **90**, 168(1991)
7. J. B. Goodenough, Magnetism and the Chemical Bond, Interscience New York, 1963
8. A. P. Bradford, G. Hass and M. McFarland, Applied Optics **11**, 2242 (1972)

## MEASUREMENT OF PARTIAL CONDUCTIVITIES IN MIXED CONDUCTORS USING BLOCKING ELECTRODES

AI QUOC PHAM AND ALLAN J. JACOBSON

University of Houston, Department of Chemistry and Texas Center for Superconductivity,  
Houston, TX 77204-5641.

### ABSTRACT

The blocking electrode method commonly used for the determination of the partial conductivities in a mixed ionic-electronic conductor has been suspected by several authors to give incorrect results in some cases. Experimental evidence illustrating the limitations of this method are presented. The resistance of three pellets of YSZ, the middle one playing the role of a "mixed" conductor, was studied by ac impedance spectroscopy. The imperfect contacts on a microscopic scale formed at the interface between the blocking electrodes and the sample were shown to give rise to additional resistances which cannot be separated from the total bulk resistance. The method was also used to study the conductivity of gold metal. Despite the presence of the ionically blocking electrodes an electronic current is observed. This electronic leakage current is due to the interaction with the gaseous environment, the mixed conductor playing the role of an electrode for the conversion of oxygen ions to electrons.

### INTRODUCTION

The Hebb-Wagner polarization method, <sup>1,2</sup> called sometimes the blocking electrode method, is the most commonly used technique for the characterization of the partial conductivities in mixed ionic-electronic conductors (MIEC). According to this method, appropriate blocking electrodes are used to block one type of conduction, ionic or electronic. Originally, the Hebb-Wagner method was devised to measure the partial conductivity in non oxide mixed conductors under dc polarization and gave reliable results. Later the method was extended to oxygen ion mixed conductors using both dc and ac polarizations. <sup>3-5</sup> This extension is not straightforward because of the possible interference of oxygen gas in the surrounding atmosphere and the values of ionic conductivity determined from such measurements are rather uncertain. Often, very wide discrepancies in the conductivity data for the same material, have been reported. An example is the case of the superconductor  $\text{YBa}_2\text{Cu}_3\text{O}_{7-\delta}$ . <sup>6</sup> A very high activation energy of 2.2 eV and a very high ionic conductivity of 1 S/cm at 500°C have been reported by Carrillo-Cabrera *et al.* <sup>5</sup> On the other hand, Vischjager *et al.* have reported an activation energy of 1.23 eV and a much lower conductivity,  $2 \cdot 10^{-4}$  S/cm. <sup>4</sup> The discrepancies have been analyzed by Irvine *et al.* <sup>6</sup> Actually, the results depend on the ways the Hebb-Wagner method is applied, as illustrated by Anderson *et al.* for the example of the mixed conductor  $(\text{La,Sr})(\text{Co,Fe})\text{O}_3$ . <sup>7</sup>

Some problems associated with the Hebb-Wagner polarization method have already been suggested. In particular, the electronic current is not completely blocked by the blocking electrodes and the measured conductivity includes an electronic leakage current. <sup>8,9</sup> Several problems have been discussed in detail theoretically by Riess *et al.* <sup>9</sup> However, experimental evidence for the occurrence of the electronic leakage current and its impact on the measured

ionic conductivity is not known. The purpose of this paper is to clarify experimentally the origin of the problems associated with the Hebb-Wagner method using ac impedance spectroscopy. Materials with known conductivities are used and the only unknown parameter is the blocking electrode/mixed conductor interface.

### The interface blocking electrode/mixed conductor:

Yttria stabilized zirconia powder (YSZ 8% from Tokai) was pressed into pellets and sintered at 1500°C for 6 hours. The sintered pellets were 6.4mm diameter and of variable thickness:  $t$ ,  $t/2$ ,  $t/3$  ( $t = 3.6\text{mm}$ ). Platinum paint was used to make the electrodes. Three cells were studied:

cell#1	Pt(O <sub>2</sub> ) / YSZ / Pt(O <sub>2</sub> )
cell#2	Pt(O <sub>2</sub> ) / YSZ / YSZ / Pt(O <sub>2</sub> )
cell#3	Pt(O <sub>2</sub> ) / YSZ / YSZ / YSZ / Pt(O <sub>2</sub> )

Cell#1 is a single pellet of thickness  $t$  and serves as a reference. Cell#2 is composed of two pellets of thickness  $t/2$  each. The two pellets are pressed mechanically together using a spring loading mechanism. The only difference between cell#1 and cell#2 is the presence of the interface. Cell#3 is composed of three pellets of thickness  $t/3$  each. Compared to cell#1, cell#3 has two YSZ/YSZ interfaces. Cell#3 has the standard configuration for a blocking electrode experiment in ac polarization, the middle pellet acting as a mixed conductor with good ionic conductivity and poor electronic conductivity (ionic transference number  $t_i = 1$ ). The two pellets with the platinum paint on the outer side play the role of the blocking electrodes.

During the first heating from room temperature, the impedance plots for cell#2 and cell#3 were very complex, presenting many overlapping semi-circles. Both cells were then heated to 900°C overnight to improve the interfacial contact and measurements were then made on cooling. The different semicircles were better resolved after this heat treatment. Cell#1 did not show any difference on heating or cooling.

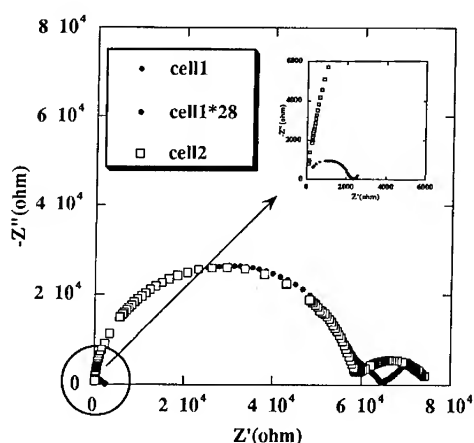


Figure 1. Impedance spectra for cell#1 and cell#2 in air at 493°C. The insert is an enlargement of the data for cell#1.

Figure 1 shows a typical impedance diagram for cell#1 and cell#2. At the same temperature, the resistance of cell#1 is about 28 times smaller than the resistance of cell#2, despite the same total thickness. The impedance plot of cell#1 was enlarged by a factor of 28 (by multiplying both  $Z'$  and  $Z''$ ) to match the bulk resistances of the two cells (left semi-circles). No difference in the shapes of the high frequency semi-circles that are usually attributed to the bulk conduction process, are observed. The much larger semi-circle observed for cell#2 could arise from a large interface resistance that overshadows the bulk resistance of the YSZ pellets. However, the capacitance value of 18pF (21pF for cell#1), in the range typical of a bulk process suggests a different interpretation. Taking into account the roughness of the pellet surface, the real contact area is expected to be smaller than the pellet area ( $A$ ), and consequently there is a reduction of the effective area of the interface. Since  $R = l/\sigma A$ , a smaller  $A$  induces an apparently higher resistance. Therefore, the presence of the interface YSZ/YSZ introduces an apparent difference in the measured bulk resistance. This observation appears surprising since the bulk resistance should be independent of the presence of the interface. Ignoring the true interfacial area and assuming the geometric area of the pellet leads to an underestimate of the bulk conductivity. Reducing the roughness of the pellet surfaces by polishing was found to increase the contact area (smaller resistance) without completely suppressing the problem.

The larger bulk semi-circle when the interface is present can lead to misinterpretation of the impedance diagram. When measurements are made on unknown materials, the increase in resistance is attributed to the ionic conductivity of the measured sample. The above experiment shows that part of this increase is due to the reduction of the interface area. It is then difficult to clearly identify different components on the impedance diagram.

The plots of the conductivity versus  $1000/T$  calculated from the measured resistances, assuming the geometric pellet area, are shown in Figure 2. The activation energy is very similar for cell#1 and cell#2 (1eV), confirming the above interpretation (assuming a constant contact area in the measured temperature range, 400-800 °C).

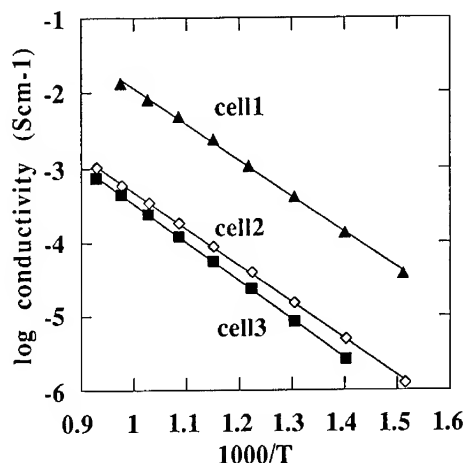


Figure 2. Arrhenius plot of the conductivity for cells #1, #2 and #3.

The impedance diagrams show significant differences in the intermediate frequency range. For cell#1, a small semi-circle overlapping with the bulk semi-circle attributed to the grain boundary conduction is observed. For cell#2, a much larger and well separated depressed semi-circle is observed. Since both cells contain pellets prepared from the same starting material

under the same conditions, this depressed semi-circle cannot be due to grain boundary effects but is attributed to the interface contribution. The capacitance of 69nF is however in the characteristic range for grain boundary conduction. This suggests that the interface YSZ/YSZ after the "sintering step" presents characteristics similar to a grain boundary but with two orders of magnitude higher resistance.

Cell#3 presents similar characteristics to cell#2. The difference between the bulk resistance of cell#3 and cell#1 is two times higher than the difference between the resistances of cell#2 and cell#1 (Figure 2), consistent with the presence of the two interfaces in cell#3, and further supporting the above interpretation. The same activation energy for the conductivity is observed. Since cell#3 has the same configuration as a blocking electrode experiment but with YSZ as a mixed conductor, it is apparent that, neglect of the unknown interface contact area will result in an incorrect determination of the ionic conductivity of the mixed conductor.

In a similar study of the YSZ/YSZ interface effect, Fabry *et al.*<sup>10</sup> gave a different interpretation. A large extra semi-circle was also observed in their impedance data and was attributed to the interfacial resistance, not to the geometric reduction of the contact area at the interface. The different interpretations may arise from the fact that we have attempted to "sinter" the interface by annealing at high temperatures before all measurements.

At the YSZ/YSZ interface, oxygen ions can be transferred either by direct transfer of ions or by conversion of oxygen ions to adsorbed oxygen atoms or molecules which are then converted back to oxygen ions on the other side of the interface.<sup>10</sup> In the latter case the surface of the YSZ pellet plays the role of an electrode. Consistent with Fabry's observation,<sup>10</sup> we have observed that the interface semi-circle is independent of the oxygen partial pressure, suggesting a direct transfer of oxygen ions.

#### The electronic leakage current.

When the mixed conductor is a good ionic conductor with  $t_i$  close to 1, there is a direct transfer of the oxygen ions at the interface. For the extreme opposite case where the electronic transference number  $t_e$  is close to one, such a mechanism may no longer be valid. To study this case, a good electronic conductor with negligible oxygen ion conductivity is required. Gold metal is a good candidate since gold does not dissolve oxygen and is a poor electrode. Gold metal also has the advantage of being malleable, minimizing the problem of the contact area.

Two cells were studied:

Cell#4:	Pt(O <sub>2</sub> ) / YSZ / Au <sub>foil</sub> / YSZ / Pt(O <sub>2</sub> )
Cell#5 :	Au(O <sub>2</sub> ) / YSZ / Au(O <sub>2</sub> ).

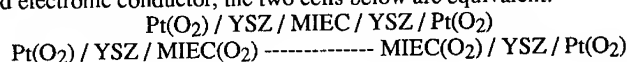
Cell#4 was assembled by sandwiching a piece of gold foil between two pellets of YSZ each of thickness  $t/2$ . The cell was then heated with applied pressure at 1030°C, close to the melting point of gold to "sinter" the interface. The reference cell#5 consists of a pellet of YSZ of thickness  $t$  with gold electrodes (obtained by painting gold paste and annealing at 800°C for 1 h).

The impedance diagram corresponding to the bulk resistance is similar for both cells over the whole temperature range. An example of data measured at 649°C in air is shown in Figure 3. At this temperature, the bulk and grain boundary semi-circles are no longer present. The total (bulk+grain boundary) resistance is determined at the high frequency intercept with the real axis. The observed depressed semi-circles for both cells are due to electrode process as suggested by the capacitance values of 50μF and 20μF for cells#4 and #5, respectively.

The similarity of the high frequency part of the impedance diagram for both cells, in spite of the presence of gold foil for cell#5, clearly shows that there is an electronic current through the gold foil despite the presence of the blocking electrodes.

Further examination of the impedance diagram suggests that the electronic leakage is possible because gold plays the role of an electrode. The two outer electrodes of cell#4 are

made with platinum paint which has much lower resistance than the observed value. Therefore the depressed semi circle observed for cell#4 in Figure 3 can be attributed to the gold foil. Its similarity in shape with the signal observed for cell#5 which has gold electrodes, suggests that the oxygen ions from the blocking electrode  $\text{Pt}(\text{O}_2)$  / YSZ are converted to electrons (and oxygen atoms or molecules) at the interface YSZ / Au<sub>foil</sub>. The reverse phenomena occurs when the electrons arrive at the other interface. The difference in size between the two semi-circles is probably due to the non porous gold foil compared to the gold paste electrodes of the reference cell. For a good electronic conductor, the two cells below are equivalent:



Consequently, for a good ionic conductor with poor electronic conductivity,  $t_i = 1$  (e.g. YSZ), direct transfer of oxygen ions occurs at the interface. In the case of a good electronic conductor with poor ionic conductivity,  $t_e = 1$  (e.g. gold), oxygen ions are converted to electrons and adsorbed oxygen atoms or molecules. For intermediate cases, both processes can take place simultaneously making the interpretation of the data difficult.

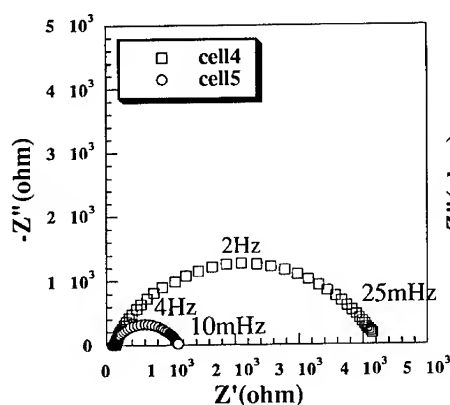


Figure 3. Impedance spectra for cells #4 and #5 in air at 649°C.

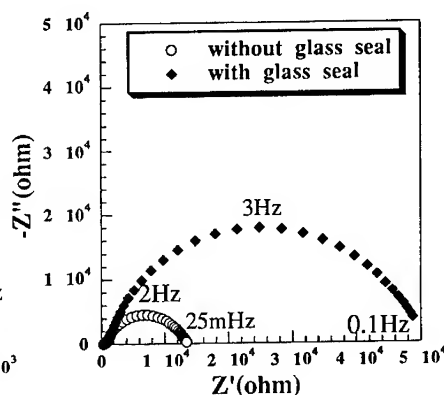


Figure 4. Impedance spectra for cell #4 with and without a glass seal.

Since the electronic leakage current arises for oxide systems because of the interaction with the gaseous environment, sealing the cell using a glass has been suggested to prevent this leakage.<sup>11</sup> The impedance plots of cell#4 (with gold foil) with and without a glass seal are shown in Figure 4. No difference is apparent in the bulk resistance, suggesting that the electrodes are still not blocking. The semi-circle attributed to the electrode process increases significantly in size after glass sealing. The same phenomenon is observed when measurement for cell#4 without a glass seal were made in nitrogen instead of in air. The effect of sealing the interface appears to correspond to a decrease in the oxygen partial pressure. Sealing makes the electrode processes involving oxygen slower but they still occur. Presumably sufficient gaseous or adsorbed species are still present because of remaining pores at the interface and between the interface and the glass seal. Although sealing the interface may enhance the direct ion transfer, it may not completely eliminate the electronic leakage current. For a good electronic conductor, the conversion of oxygen ions to electrons is still the predominant process.



## CONCLUSION

For oxide ion mixed conductors, the Hebb-Wagner polarization method has been shown to be subject to two distinct problems:

- because of the roughness of the pellet surface, the contact area between two pressed pellets is much smaller than the geometric area. This reduction at the interface leads to an error in the calculation of the ionic conductivity. Polishing the surfaces can lower this area difference but it is difficult to suppress it completely. The problem is also minimized in the case of soft and/or malleable materials, for example the mixed conductor, silver sulfide, studied in the original Hebb-Wagner experiments.

- for mixed conductors with good ionic conductivity, a direct transfer of oxygen ions occurs at the interface. For good electronic conductors, the most favorable process is the conversion of oxygen ions to electrons. Because of the interaction with the gaseous environment, despite the presence of the blocking electrodes, electrons are the predominant current carriers in mixed conductors. This feature is specific to oxide materials. For non-oxide conductors, the environment is not expected to effect the interface.

This study has been made using ac techniques to separate and identify the different processes involved in transport. The main conclusions also apply to dc measurements. The failure of the Hebb-Wagner polarization method for oxides is due to the assumption that the interface is ideal. A new method for the determination of the partial conductivities has been proposed by Riess.<sup>12</sup>

Since mixed conductors will find application primarily as electrodes in, for example, fuel cells, an alternative approach is to study directly their electrocatalytic properties as electrodes using ac impedance spectroscopy at low frequencies.<sup>13</sup> Such measurements do not give the ionic conductivity of the mixed conductor directly but can give many insights on the different processes occurring, the rate limiting steps and the overall electrode performance.

We thank the Robert A. Welch Foundation for partial support of this work.

## REFERENCES

1. M. H. Hebb, J. Chem. Phys. **20**, 185 (1952).
2. C. Wagner, Z. Electrochem. **60**, 4 (1956).
3. Y. Teraoka, H. M. Zhang, K. Okamoto and N. Yamazoe, Mat. Res. Bull. **23**, 51 (1988).
4. D. J. Vischjager, A. A. van Zomeren, J. Schoonman, Solid State Ionics **40/41**, 810 (1990).
5. W. Carrillo-Cabrera, H-D. Wiemhofer and W. Gopel, Solid State Ionics **32/33**, 1172 (1989).
6. J. T. S. Irvine, J. G. Fletcher, A. R. West, J.A. Labrincha and F.M.B. Marques in Proceedings of the 14th International Symposium on Materials Science, eds. F. W. Poulsen, J. J. Bentzen, T. Jacobsen, E. Skou and M. J. L. Ostergard, Riso 1993 pp. 263-268.
7. H.U. Anderson, C. Chou, L. Tai and M. M. Nasrallah in Proceedings of the Second International Symposium on Ionic and Mixed Conducting Ceramics, eds. T. A. Ramanarayanan, W. L. Worrell and H. L. Tuller, The Electrochemical Society, Pennington, NJ 1994 pp. 376-387.
8. I. Kontoulis and B. C. H. Steele, Solid State Ionics **47**, 317 (1991).
9. I. Riess in Proceedings of the Second International Symposium on Ionic and Mixed Conducting Ceramics, eds. T. A. Ramanarayanan, W. L. Worrell and H. L. Tuller, The Electrochemical Society, Pennington, NJ 1994 pp. 286-306.
10. P. Fabry, E. Schouler and M. Kleitz, Electrochimica Acta. **23**, 539 (1978).
11. J. Maier, P. Murugaraj, G. Pfundter and W. Sitte, Ber. Buns. Phys. Chem. **93**, 1350 (1989).
12. I. Riess, Solid State Ionics **44**, 207 (1991).
13. A.Q. Pham and A.J. Jacobson (to be published).

## DIFFUSION-REACTION IN MIXED IONIC ELECTRONIC CONDUCTOR SOLID OXIDE MEMBRANES WITH POROUS ELECTRODES

HUIMING DENG, MINYAU ZHOU AND BENJAMIN ABELES  
Exxon Research and Engineering Co. Annandale NJ 08801

### ABSTRACT

We solve the transport equations for diffusion-reaction, in the limit of a small  $O_2$  pressure gradient, in a mixed oxygen ion-electronic conductor (MIEC) solid oxide membrane consisting of a porous anode and cathode separated by a thin dense layer. The enhancement in ion current due to the porous electrodes calculated for MIEC perovskites is of order 100 for electrode surface area of  $10^6 \text{ cm}^2/\text{cm}^3$ .

### INTRODUCTION

Fuel cells and electrocatalytic membranes in general consist of a porous cathode and anode separated by a non-porous layer. The purpose of the non-porous layer is to block the direct passage of gas molecules between the electrodes. In this work we focus on oxygen ion conducting solid oxide membranes in which the electrodes as well as the dense blocking layer are mixed ionic electronic conductors (MIEC). In the application of membranes as chemical reactors or for separation of gases, a critical question is the upper limit of ion current that can be achieved for a given pressure drop across the membrane. The ion current in a dense membrane, in the absence of porous electrodes, can be increased by reducing the thickness of the membrane until its thickness  $L$  is less than  $L_d$ , where  $L_d = D_{IE}/K$ ,  $D_{IE}$  is the ambipolar diffusion coefficient in the MIEC and  $K$  is the surface exchange coefficient<sup>1,2</sup>. The maximum achievable current  $I_i(s)$  in the limit  $L \ll L_d$  is given by:

$$I_i(s) = Kc_i \frac{\Delta\mu_g}{RT} \quad (1)$$

where  $c_i$  is the oxygen ion concentration in the solid,  $\Delta\mu_g = (\mu'_g - \mu''_g)/4$  and  $\mu'_g$  and  $\mu''_g$  are the chemical potentials of the gas at the high pressure and low pressure sides of the membrane respectively. Any further increase in the ion current can be achieved only by making use of porous electrodes to increase the effective surface area for chemical reaction. In a previous paper<sup>3</sup> we derived the length scales that govern diffusion-reaction in membranes with porous electrodes based on the assumption that the rate limiting step in the ion current is due to ionic diffusion and surface reaction. In that limit the gas pressures in the two electrodes are assumed to be uniform and equal to the inlet and outlet pressures respectively, so that the entire pressure drop is across the non-porous layer. In this paper we extend the model to the case where there can be a significant gas pressure drop in the pores.

## MODEL

Our model is based on the following set of assumptions: (1) The membrane, of total thickness  $L$ , consists of a porous cathode and anode with identical properties, separated by a thin non-porous layer at  $x=0$  whose thickness is small enough so that the drop in chemical potential across it can be neglected (2) The chemical potential drop across the membrane is small compared to  $RT$ . This allows us to neglect the variation in material parameters of the membrane with variation in chemical potential and linearize the transport equations. (3) As a result of the chemical reaction at the gas-pore wall interface,  $(1/2)O_2 + 2e \rightleftharpoons O^{2-}$ , the chemical reaction current density of ions,  $i$  is given by:

$$i = Kc_i \left( \frac{1}{2} \mu_g - \mu \right) / RT \quad (2)$$

and the corresponding chemical reaction current of the electrons is  $-2i$ . Here  $\mu = \mu_i - 2\mu_e$  is defined as the ambipolar chemical potential and  $\mu_g$ ,  $\mu_i$  and  $\mu_e$  are the chemical potentials of the gas, the ions and the electrons. (4) The pore structure is characterized by the volume fraction of the solid,  $(1-\phi)$ , pore wall surface area per unit volume,  $S$ , and tortuosity of the solid phase,  $\tau_s$ . (5) The pore dimensions are much smaller than the thickness  $L$  of the membrane. This allows us to treat the porous membrane as an effective medium and to neglect variations in chemical potential in the plane of the membrane. The transport equations are then one-dimensional with the gas molecule, ion and electron currents flowing parallel to the direction of the pressure gradient. The ion and electron current densities  $I_i$  and  $I_e$  can then be expressed as:

$$I_i = -\frac{1-\phi}{\tau_s} \frac{D_i c_i}{RT} \left( \frac{d\mu_i}{dx} + 2FE \right) \quad (3)$$

$$I_e = -\frac{1-\phi}{\tau_s} \frac{D_e c_e}{RT} \left( \frac{d\mu_e}{dx} + FE \right) \quad (4)$$

where  $E$  is the electric field, and  $D_i$ ,  $D_e$  and  $c_i$ ,  $c_e$  are the ion and electron diffusion coefficients and concentrations and  $F$  is the Faraday constant.

Eliminating  $E$  between Eqs(3) and (4) we obtain:

$$\frac{I_i}{D_i c_i} - \frac{2I_e}{D_e c_e} = -\frac{1-\phi}{\tau_s} \frac{1}{RT} \frac{d\mu}{dx} \quad (5)$$

The spatial dependence of  $I_i$  and  $I_e$  is determined by the chemical reaction current:

$$\frac{dI_i}{dx} = iS \quad (6)$$

$$\frac{dI_e}{dx} = -2iS \quad (7)$$

Eliminating  $i$  between Eqs(6) and (7) and integrating we obtain:

$$2I_i(x) + I_e(x) = I_0 \quad (8)$$

where, in order to satisfy continuity of current at the two interfaces,  $x = \pm L/2$ , the integration constant  $I_0$  is set equal to the external current. In the case of the membrane with no external load resistor,  $I_0 = 0$ .

From Eqs(5) and (8) we obtain:

$$I_i = -\frac{1-\phi}{\tau_s} \frac{D_{IE} c_i}{RT} \frac{d\mu}{dx} \quad (9)$$

where the ambipolar diffusion coefficient  $D_{IE}$ :

$$D_{IE} = D_i / (1 + \frac{\sigma_i}{\sigma_e}), \quad (10)$$

$\sigma_i$  and  $\sigma_e$  are the ionic and electronic conductivities and we have made use of the Nernst-Einstein relations  $D_i c_i = \sigma_i RT / 4F^2$  and  $D_e c_e = \sigma_e RT / F^2$ .

Substituting Eq(9) in Eq(6), and neglecting the second order term  $(d\mu/dx)(dc_i/dx)$ , yields a second order linear differential equation for  $\mu$ :

$$\frac{d^2 \mu}{dx^2} = \frac{1}{L_p^2} (\mu - \frac{1}{2} \mu_g) \quad (11)$$

where the length scale  $L_p$  is given by:

$$L_p = \sqrt{\frac{L_d(1-\phi)}{S\tau_s}}. \quad (12)$$

The variation in the chemical potential of the gas in the pores is determined by the diffusion equation:

$$-\frac{\phi}{\tau} \frac{D_g c_g}{RT} \frac{d^2 \mu_g}{dx^2} = -\frac{1}{2} iS \quad (13)$$

where  $D_g$  is the diffusion coefficient of the gas in the pores and  $\tau$  is the tortuosity of the pore space. Substituting Eq(2) in Eq(13) we have:

$$\frac{d^2\mu_g}{dx^2} = \frac{1}{L_g^2} (\mu_g - 2\mu) \quad (14)$$

where the length scale  $L_g$  is given by:

$$L_g = 2 \sqrt{\frac{\tau_s}{\tau} \frac{\phi}{1-\phi} \frac{D_g c_g}{D_{IE} c_i}} L_p \quad (15)$$

Eqs(11) and (14) are simultaneous linear second order differential equations. The general solution in the region  $0 < x < L/2$ , obtained by diagonalizing the Eqs. (9) and (14), is given by:

$$\mu - \mu_0 = (g_{11}e^{-x/L_m} + g_{12}e^{x/L_m})\Psi_{11} + (g_{21}x + g_{22})\Psi_{12} - \Delta\mu_g \quad (16)$$

$$\mu_g - \mu_g'' = (g_{11}e^{-x/L_m} + g_{12}e^{x/L_m})\Psi_{21} + (g_{21}x + g_{22})\Psi_{22} \quad (17)$$

where  $\mu_0 = (\mu'_g + \mu''_g)/4$  and  $L_m$  is given by the relation:

$$\frac{1}{L_m^2} = \frac{1}{L_p^2} + \frac{1}{L_g^2} \quad (18)$$

$\Psi_{11}$ ,  $\Psi_{12}$  and  $\Psi_{21}$ ,  $\Psi_{22}$  are components of the eigenvectors ensuing from the diagonalization of Eqs(11) and (14) and  $g_{11}$ ,  $g_{12}$ ,  $g_{21}$ ,  $g_{22}$ , are integration constants determined from the boundary conditions:

$$\mu = \mu_0 \quad \text{at} \quad x=0 \quad (19)$$

$$-\frac{1-\phi}{\tau_s} D_{IE} \frac{c_i}{RT} \frac{d\mu}{dx} = (1-\phi) \frac{K c_i}{RT} \left[ \mu - \frac{1}{2} \mu_g'' \right] \quad \text{at} \quad x=L/2. \quad (20)$$

$$-\frac{\phi}{\tau} \frac{D_g c_g}{RT} \frac{d\mu_g}{dx} = 0 \quad \text{at} \quad x=0 \quad (21)$$

$$\mu_g = \mu_g'' \quad \text{at} \quad x=L/2 \quad (22)$$

Eq(20) equates the ion current  $I_i$  to the chemical reaction current  $i$  at the  $x=L/2$  electrode-gas interface. Equation(21) expresses the condition that the dense layer at the center of the membrane blocks the gas flow and Eq(22) equates the chemical potential of the gas at boundary to that of the gas at the low pressure side of the membrane. As a consequence of the symmetry of the

membrane the solution in the range  $-L/2 < x < 0$  is given by:  $\mu(-x) - \mu_0 = -\mu(x) + \mu_0$  and  $\mu_g(-x) - \mu_0 = -\mu_g(x) + \mu_0$ .

## DISCUSSION

By specifying the material parameters  $L_d$ ,  $D_{IE}$ , the parameters characterizing the porous structure  $D_g$ ,  $S$ ,  $\tau_s$  and  $\phi$  and the gas pressure  $P$ , we can evaluate numerically the chemical potentials and ion current derived in the previous section. We model the porous MIEC electrodes by a simple cubic array of consolidated spherical grains of radius  $r$ , with unit cell of length  $2(r-\delta)$ . The ratio  $\delta/r$  characterizes the degree of consolidation of the grains. Assuming  $\delta/r=0.1$ , which corresponds to a well consolidated grain structure, the simple cubic model yields  $S=2.2(1-\phi)/r$ ,  $1-\phi=0.69$  and  $\tau_s=1.16$ . For  $D_g$  we use the relation:

$$D_g = \frac{1}{3} v_{th} \lambda \quad (23)$$

where  $v_{th}$  is the thermal velocity of the molecules,  $\lambda$  is the molecular mean free path in the pores,  $1/\lambda = 1/\lambda_{th} + 1/1.5r$  and  $\lambda_{th}$  is the molecular thermal mean free path.

For a wide variety of MIEC perovskites in the temperature range 700-900 °C,  $L_d$  lies in the range<sup>2</sup> 50 to 500  $\mu\text{m}$ . In the following we use the value  $L_d=100 \mu\text{m}$ . For  $D_{IE}$  we use the value  $5 \times 10^{-7} \text{ cm}^2/\text{sec}$  which is the upper bound for observed oxygen diffusion coefficients in perovskites. For the  $\text{O}_2$  pressure we take  $P=1$  and 0.01 atm and for the temperature, 1000K.

In Fig.1 we plot the spatial dependence of the chemical potential  $\mu$  and  $\mu_g$  calculated from Eqs(16) and (17) for a membrane with  $L=4\mu\text{m}$  and  $S=10^6 \text{ cm}^{-1}$ . We note the profound effect the ratio  $L_p/L_g$  has on the behavior of  $\mu$  and  $\mu_g$ . For  $P=1\text{atm}$ ,  $L_p/L_g \ll 1$  and most of the drop in  $\mu_g$  is across the non-porous layer. We note that since the total ion flux is proportional to the area between  $\mu_g$  and  $\mu$  most of the contribution to the ion flux comes from the region  $3L_p$  at the center of the membrane. On the other hand for  $P=0.01\text{atm}$ ,  $L_p/L_g > 1$ , there is an appreciable drop in  $\mu_g$  over the porous electrodes and most of the contribution to the ion flux comes from the regions near the outer interfaces of the membrane.

$I_i(0)$ , which is equal to the total oxygen flux through the membrane, is plotted normalized by  $I_i^{(S)}$  in Fig.2 as a function of the normalized membrane thickness  $L/L_m$  for different values of  $S$ . The normalized flux  $I_i(0)/I_i^{(S)}$  peaks because at low  $L/L_m$  the effective surface area of the electrodes is low, while at large values of  $L/L_m$ , the loss in chemical potential due to pressure drop on the electrodes becomes significant. The enhancement in ion current is reduced at low values of  $P$  because the gas pressure drop on the electrodes becomes more significant, as can be seen in Fig.1.

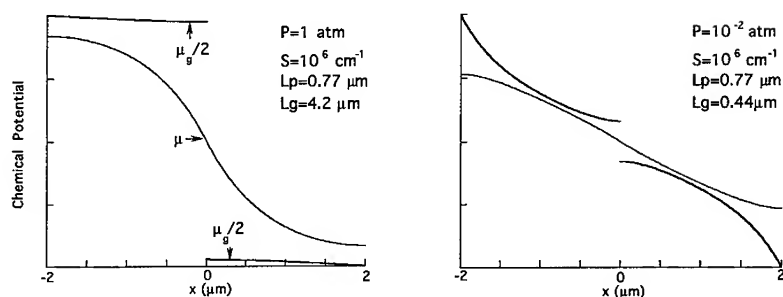


Fig. 1: Spatial dependence of chemical potentials  $\mu$  and  $\mu_g$  for a membrane with  $L=4\mu\text{m}$ ,  $S=10^6 \text{ cm}^{-1}$ ,  $L_d=100\mu\text{m}$ ,  $1-\phi=0.69$ , and  $\tau_s=1.16$ , calculated from Eqs(16) and (17) for  $P=1$  and  $0.01$  atm.

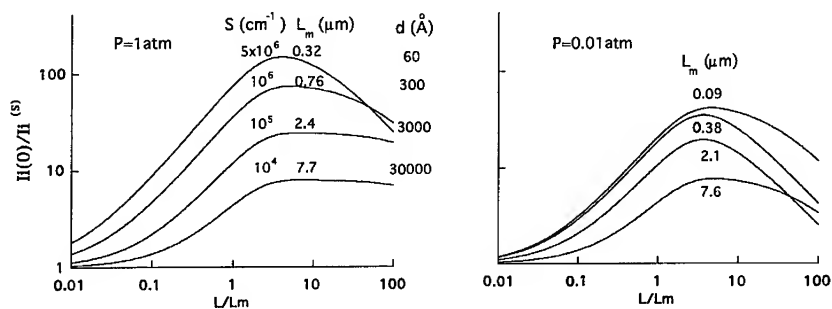


Fig.2: Normalized ion flux  $I_i(0)/I_i(S)$  as a function of the normalized membrane thickness,  $L/L_m$ , for a membrane with  $L_d=100\mu\text{m}$ ,  $1-\phi=0.69$ ,  $\tau_s=1.16$ , calculated from Eqs(1), (9) and (16) for different values of  $S$  at  $P=1$  and  $0.01$  atm.

#### REFERENCES:

1. S. Carter, A. Selcuk, R.J. Chater, J. Kajda, J.A. Kilner, B.C.H. Steele, Solid State Ionics, **53-56**, 597 (1992)
2. H.J.M. Bouwmeester, H. Kruidhof and A.J. Burggraaf, Solid State Ionics **72**, 185 (1994)
3. H.Deng, M.Zhou and B. Abeles, Solid State Ionics **74**, 75 (1994)

## STUDY OF AC CONDUCTIVITY IN DILUTE $\text{CeO}_2\text{:Y}^{3+}$ CERAMICS

A.V. VAYSLEYB, B.S. LIM, AND A.S. NOWICK

Columbia University, School of Mines, Materials Science Division, New York, NY 10027

### ABSTRACT

The ac conductivity was studied for different compositions of  $\text{CeO}_2$  ceramics, undoped and doped with  $\text{Y}^{3+}$  ions in the composition range 1 to 12 atomic %Y over the temperature range from 50 K to 500 K. It was observed that in temperature range 300-400 K, the ac conductivity (as well as the real part of the dielectric constant,  $\epsilon'$ , ) follows the universal power-law frequency dependence with exponent  $s \approx 0.63$ . No systematic variation of  $s$ , either with temperature or with dopant concentration, was observed, although for nominally "pure"  $\text{CeO}_2$  no power-law regime was observed. The features of the ac behavior were explained on the basis of a percolation approach.

### 1. Introduction

Many highly disordered solids, such as amorphous semiconductors, glasses, polymers and heavily doped ionic crystals which have been studied in the course more than two decades[1-4] exhibit a power-law frequency dependence of ac conductivity over several decades in the frequency. Because of the wide range of materials with both electronic and ionic conductivities that show it, this behavior was called "universal"[5]. As was shown by Almond and West [6] usually the experimental ac conductivity data can be represent as a sum of two terms as follows

$$\sigma(\omega) = \sigma(0) \cdot [1 + (\omega\tau)^s], \quad (1)$$

where  $\sigma(0)$  is the low frequency or dc conductivity,  $\omega$  is angular frequency and  $s$  is an exponent falling in the range  $0 < s < 1$ . The quantity  $\tau$  is an appropriate relaxation time, which can be written of the Arrhenius form  $\tau = \tau_0 \cdot \exp(E_\tau / kT)$  with the energy of relaxation  $E_\tau$ , that is usually close to the activation energy of the dc conductivity  $E_\sigma$ , and with the quantity  $\tau_0$ , that may be anticipated to be equal to the reciprocal value of the characteristic phonon frequency  $\nu_{ph} \approx 10^{13}$  Hz. The imaginary part of the dielectric constant,  $\epsilon''$ , is defined as

$$\epsilon'' = [\sigma(\omega) - \sigma(0)] / \omega \epsilon_0 \propto (\omega\tau)^{s-1}, \quad (2)$$

where  $\epsilon_0$  is the permittivity of free space. Correspondingly, as a consequence of the well-known Kramers-Kronig relation applied to Eq. (2), the real part of the dielectric constant  $\epsilon'$  varies with frequency as

$$\epsilon' - \epsilon_\infty \propto (\omega\tau)^{s-1}, \quad (3)$$

where  $\epsilon_\infty$  is the value at very high frequencies. The fractional energy loss,  $\tan\delta$ , with the aid of Eqs. (2), (3) can be written of the form [5] :

$$\tan\delta = \epsilon'' / (\epsilon' - \epsilon_\infty) = \cot(s \cdot \pi / 2) \quad (4)$$



There has been a much theoretical and experimental activity attempting to understand Eqs. (1)-(4). Some authors assume that the ac conductivity in this range can be described with Eq (1), where  $s = s(T)$  is a monotonous decreasing function of temperature,  $T$  [1,2,7], while Nowick et al.[8, 9] claim that this behavior can be described with the constant exponent  $s \approx 0.6$ , in an elevated temperature region which they called the "Jonscher regime". Thus, one of the key questions for understanding of the conductivity mechanism, is the temperature dependence of  $s$ .

It is generally accepted that the origin of a universal power-law frequency dependent behavior is either in structural or electric-field disorder (Coulomb potential) [10, 11], but so far it is not quite clear what kind of quantitative criterion can be used to determine the appropriate degree of disorder. Disorder materials are usually created by the introduction of impurities. In particular, in ionic crystals, introduction of aliovalent impurities leads to the creation of point defects which are responsible for the conductivity. Thus, the second key question is: "What is the lowest level of impurity concentration that is required for ac universal behavior?" In this connection, the question of the concentration dependence of the  $s$  exponent should also be considered.

While many of the experimental investigations on ac conductivity of ionically conducting materials have been on glasses and other highly disordered materials, a small amount of work has been focused on the simpler crystalline materials which have been widely studied previously for their dc conductivity [8, 9]. The advantage of studying of such materials is that the conductivity mechanisms are much better understood than in the case of glasses.

To obtain answers to the two questions mentioned above, in the present paper we will thoroughly examine the well-studied system of  $\text{CeO}_2$  doped with aliovalent  $\text{Y}^{3+}$  cations [12]. In this case doubly positive-charged oxygen vacancies  $\text{V}_\text{O}^{\bullet\bullet}$  appear to compensate the negative charge of aliovalent dopant cations. The oxygen vacancy concentration is half that of the  $\text{Y}^{3+}$  ion concentration. The objective our work is to study these materials in the range from dilute solid solutions to high concentrations of dopants. The experimental method is described in [8, 9].

## 2. Results and Discussion

The various compositions of  $\text{Y}^{3+}$ -doped  $\text{CeO}_2$  ceramics (from 1 to 12 mole %  $\text{Y}^{3+}$ ) that have been studied are listed in Table 1. In Fig. 1 a typical example of the frequency dependencies

Table 1. Pertinent data for crystalline materials studied in the temperature range from 300 to 500 K.

Material	$E_\sigma$ [eV]	$E_\tau$ [eV]	$s$	$\tau_0^{-1}$ [s]
$\text{CeO}_2$ : 1% $\text{Y}^{3+}$	0.84	0.86	0.63	$4.8 \times 10^{14}$
$\text{CeO}_2$ : 2% $\text{Y}^{3+}$	0.79	0.816	0.63	$4.8 \times 10^{14}$
$\text{CeO}_2$ : 4% $\text{Y}^{3+}$	0.77	0.80	0.63	$1.7 \times 10^{15}$
$\text{CeO}_2$ : 8% $\text{Y}^{3+}$	0.79	0.80	0.63	$2.0 \times 10^{15}$
$\text{CeO}_2$ : 12% $\text{Y}^{3+}$	0.87	0.88	0.64	$3.5 \times 10^{15}$
$\text{CeO}_2$ : undoped	0.83	—	—	—

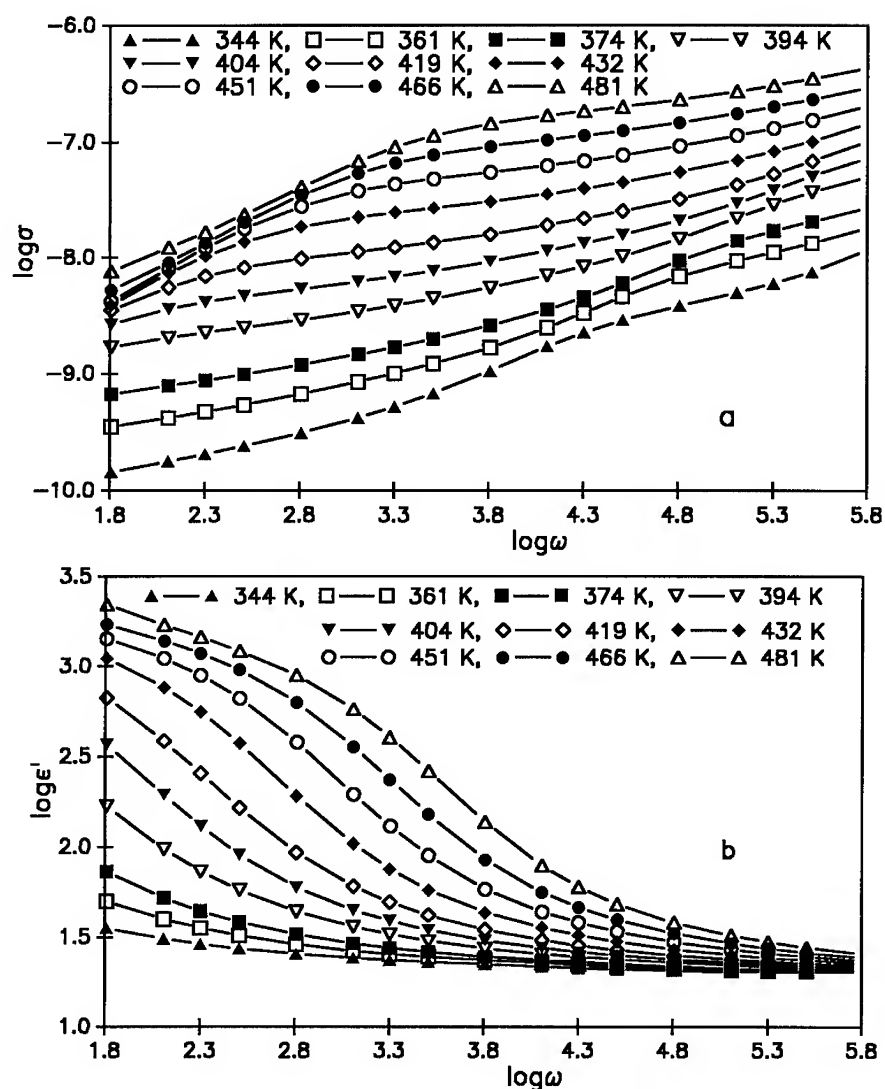


Fig. 1. The frequency dependence for  $\text{CeO}_2 : 1\% \text{Y}^{3+}$ : a – the ac conductivity, b – the real part of the dielectric constant

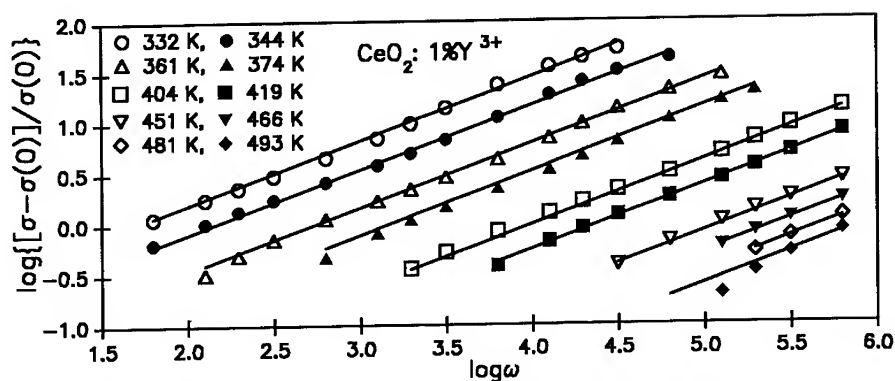


Fig. 2. The frequency dependence of  $[\sigma - \sigma(0)]/\sigma(0)$ . The experimental data are presented by symbols, and the power-law fit is represented by solid lines.

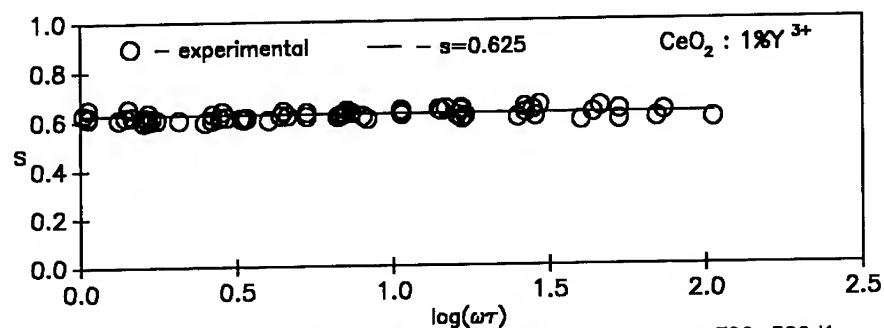


Fig. 3. The frequency and temperature dependence of  $s$  in the range 300–500 K.

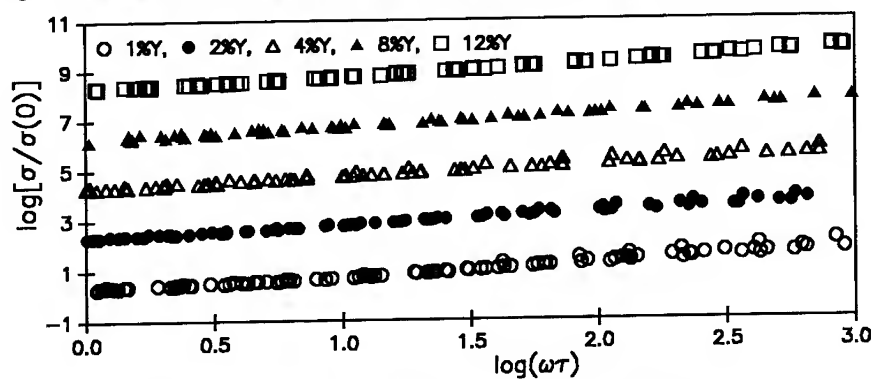


Fig. 4. The master curves of the reduced conductivity  $\sigma/\sigma(0)$  vs.  $\omega\tau$  in log-log scale for 5 compositions of  $\text{CeO}_2$  ceramics. The curves are shifted for clarity.

of the ac conductivity and of the real part of the dielectric constant,  $\epsilon'$ , for dilute solid solution  $\text{CeO}_2 : 1\% \text{Y}^{3+}$  over the temperature range from  $\sim 300$  to  $500$  K are presented on a log-log scale. At the highest temperatures,  $\sigma(\omega)$  shows a flat (frequency-independent) region, representing the dc conductivity,  $\sigma(0)$ , although there is some drop off at low frequencies due to electrode blocking effects; it is also seen from the sharp increase at low frequencies of the  $\epsilon'$  data (Fig. 1b). At the lowest temperatures, the dc region has moved off of the scale of available frequencies, so that conductance readings take the form of Eq. (1). In order to obtain the  $s$  exponent we have plotted  $\log\{[\sigma(\omega) - \sigma(0)]/\sigma(0)\}$  versus  $\log \omega$  as shown in Fig. 2. Similar analysis using Eq. (3) allows us to find the  $s$  value from the capacitance data. The average values of exponents obtained are equal to  $s = 0.629$  and  $0.628$ , from conductance and capacitance data, respectively. In Fig. 3 we plot  $s$  value of  $\text{CeO}_2 : 1\% \text{Y}^{3+}$  vs.  $\log(\omega\tau)$  as function both temperature and frequency as obtained from of Eq. (4). Further, as shown in Table 1, over the full range of dopant concentrations the value of the exponent  $s$  is equal to  $0.63$ – $0.64$ . Table 1 also presents the activation energies  $E_\sigma$  obtained from the dc conductivity, and  $E_\tau$  obtained from the quantity  $\tau$  in Eq. (1). It is seen that the difference  $\Delta E = E_\tau - E_\sigma$  is  $\sim 0.03$  eV, in good agreement with previous work [8, 9]. However the magnitudes of  $\tau_0^{-1}$  values are surprising since they exceed expected phonon frequency  $\nu_{\text{ph}}$  by one or two orders of magnitude. In contrast to these results, we have studied the ac conductivity of "undoped" ceramic sample (with possible aliovalent impurity concentration less than  $0.01 - 0.1\%$ ) and found no power-law behavior with frequency.

In fig. 4 the ac conductivity curves for various temperatures normalized to  $\sigma(0)$  and plotted against  $\omega\tau$  are shown to produce a single master curve for each composition. Such scaling behavior means that the ac conductivity depends on frequency and temperature as product of two functions, one of which  $\sigma(0)$ , is only a temperature dependent function, while the another one,  $f(\omega\tau)$ , is a function of frequency and temperature simultaneously (consistent with Eq. (1)).

All the studied cerium oxide ceramics doped with aliovalent  $\text{Y}^{+3}$  cations (beginning from  $1\%$  and up to  $12\%$ ) follow the universal power-law frequency behavior with  $s \approx 0.63$ . Thus, we have verified the result claimed earlier by Nowick et al. [8, 9], that for ionically conducting glasses and crystalline materials,  $s$  can be considered as a constant in this regime.

There are many theories to explain the power-law conductivity behavior, such as the "jump relaxation" model [3] (in the strong electrolyte approximation), the "coupling model" [13] or the "diffusion controlled relaxation" model [14], but none of them explains why  $s \approx 0.63$  and does not vary with the temperature or the concentration of impurities. For an appropriate dopant concentration the absence of concentration dependence of  $s$  suggests that a critical (threshold) phenomenon takes place in these ranges temperatures and frequencies. On the other hand the absence of a power-law region for undoped  $\text{CeO}_2$  ceramic emphasizes that this ac relaxation behavior can only take place when carriers are present in sufficient concentration for there to be interactions between them. For this reason we developed a percolation approach on the basis of the Efros and Shklovskii's scaling hypothesis [15] for binary systems, consisting of randomly distributed metallic inclusions in a dielectric matrix. The model can be generalized to involve clusters of more highly conducting regions surrounded by poorly conducting regions. Such a structure may occur through fluctuations and need not involve a second phase. This model predicts an explicit value of  $0.62$  for  $s$  [15], obtained from the analysis of computer experiments [16]. In the low frequency approximation near the percolation threshold we can represent the effective ac conductivity of such a system approximately as sum of a dc part and a frequency dispersive part in the form of Eq. (1). In this equation  $\sigma(0) = \sigma_h^0 (\sigma_p^0 / \sigma_h^0)^s$  and

$\tau \propto \epsilon_s / \sigma_p$ , where  $\sigma_h^0$  and  $\sigma_p^0$  are the dc conductivities of highly and poorly conducting regions, respectively, and  $\epsilon_s$  is the static limit of the dielectric constant of the medium. The difference between relaxation and activation energies,  $\Delta E \equiv E_\tau - E_\sigma = (1-s) \cdot (E_p - E_h) > 0$ , also follows from such approach and has a simple meaning, in that  $E_h$  and  $E_p = E_\tau$  are the activation energies in highly and poorly conducting regions, respectively. Eq.(1) is a valid in this approach under the following restrictions

$$\omega_p \ll \omega \ll \omega_h, \text{ and } n_0 \gg (\pi^2 / v_c) \cdot [\epsilon_s kT / (2e)^2]^3, \quad (5)$$

where  $\omega_p \propto \sigma_p^0 / \epsilon_s$ ,  $\omega_h \propto \sigma_h^0 / \epsilon_s$ ,  $n_0$  is a number of carriers which can jump per unit volume,  $e$  is electron charge, and  $v_c = 0.29$  is the critical volume fraction [11]. For  $Y^{+3}$ -doped  $CeO_2$  ceramics we obtained  $n_0 \gg 8 \times 10^{18}$ , corresponding to 0.03 mole % which is in a good agreement with the absence of ac relaxation for the undoped sample. Note that Eq. (4) can be rewritten as a ratio of the Coulomb repulsive energy  $W$  between moving vacancies to their kinetic energy  $kT$  in the form  $(W/kT) \gg 1$ . The latter inequality implies that repulsive Coulomb energy of mobile carriers forbids more than one particle to occupy the same position. The present percolation approach is consistent with the atomistic approach [3] and with computer simulations [10] that show how disorder and Coulomb interaction result in frequency dispersive conductivity behavior. It should also be pointed out, as seen from Eq. (5), materials with a small dielectric constant maintain ac relaxation behavior to a lower concentration than those with a high dielectric constant. We will show elsewhere (for  $CaTiO_3$ ) that this prediction appears to be valid.

#### Acknowledgment

We are grateful to the U.S. Department of Energy for support of this work.

#### References

1. A.R. Long, Adv. Phys. **31**, 553 (1982).
2. S.R. Elliott, Solid State Ionics **90/91**, 27 (1994).
3. K. Funke, Prog. in Sol. State Chem. **22**, 111 (1993).
4. C.A. Angel, Chem. Rev. **90**, 523 (1990).
5. A.K. Jonscher, Dielectric Relaxation in Solids (Chelsea Dielectrics, London 1983).
6. D.P. Almond, G.K. Duncan and A.R. West, Solid State Ionics **8**, 159 (1983).
7. A. Hunt, J. Phys.: Condens. Matter **4**, 5371 (1992).
8. W.K. Lee, B.S. Lim, J. F. Liu, and A.S. Nowick, Solid State Ionics **53-56**, 831 (1992).
9. A.S. Nowick, B. Lim, and A.V. Vaysleyb, J. Non-Cryst. Solids **172-174**, 1243 (1994).
10. P. Maas, J. Peterson, A. Bunde, and W. Dieterich, Phys. Rev. Lett. **66**, 52 (1991).
11. B.I. Shklovskii, and A.L. Efros, Electronic Properties of Doped Semiconductors, (Springer-Verlag, Berlin 1984).
12. A.S. Nowick, in Diffusion in Crystalline Solids, edited by G.E. Murch and A.S. Nowick (Academic Press Inc., Orlando, 1984) pp. 143-188.
13. K.L. Ngai, Comments Solid State Phys. **9**, 127 (1979); **9**, 141 (1980).
14. S.R. Elliott, Solid State Ionics, **27**, 131 (1988).
15. A.L. Efros, and B.I. Shklovskii, Phys. Stat. Sol. **B76**, 475 (1976).
16. I. Webman, J. Jortner, and M.H. Cohen, Phys. Rev. **B11**, 2885 (1975).

## WATER UPTAKE AND CONDUCTION IN STRONTIUM YTTERBIUM CERATE

G. W. COFFEY\*, L. R. PEDERSON\*\*, AND W. J. WEBER\*\*

\*Washington State University at Tri-Cities, Richland, Washington 99352 USA

\*\*Pacific Northwest Laboratory, P. O. Box 999, Richland, Washington 99352 USA

### ABSTRACT

Water uptake and conduction have been studied in  $\text{SrYb}_{0.05}\text{Ce}_{0.95}\text{O}_{3.8}$ , a composition known to conduct protons, oxygen ions, and electrons, depending on temperature and environment. Water uptake kinetics evaluated by thermogravimetry occurred in two distinct stages: a rapid, initial weight gain ( $0.39 \pm 0.09$  eV, attributed to grain boundary and near surface hydration) followed by a much slower uptake ( $2.8 \pm 0.4$  eV, attributed to hydration of the bulk grains). From cyclic voltammetry and mass spectrometry measurements for a cell exposed to asymmetric conditions, currents and activation energies for electronic, oxygen ion, and proton conduction were determined. The activation energy for electronic conduction,  $0.90 \pm 0.09$  eV, is believed to be artificially high due to the increase in electron carrier concentration with increased temperature. The activation energy for oxygen ion conduction ( $0.97 \pm 0.10$  eV) agrees well with other oxygen conductors. Proton conduction appeared to follow two different mechanisms: a low temperature process characterized by an activation energy of  $0.42 \pm 0.04$  eV, and a high temperature process, characterized by an activation energy of  $1.38 \pm 0.13$  eV. A possible explanation is that proton conduction at low temperatures is dominated by grain boundaries and is dominated by bulk conduction at higher temperatures.

### INTRODUCTION

Hydrogen may be incorporated into some perovskite-type oxides as defects, where they can be ionized and be caused to migrate [1-3]. The best proton-conducting oxides, ytterbium-doped strontium cerate and neodymium-doped barium cerate, have proton conductivities of approximately 0.01 S/cm at 800°C. Such conductivities make them potentially useful as solid electrolytes in solid oxide fuel cells, as hydrogen sensors, as hydrogen pumps, and as steam electrolyzers to produce hydrogen from water [3, 4]. Because these oxides exhibit mixed electron and proton conductivity at elevated temperatures, they may be used as a passive membrane in a membrane reactor to upgrade methane to ethane and other higher hydrocarbons [5].

These perovskite-type metal oxides are host to several types of point defects, and thus support multiple transport mechanisms [2]. At low temperatures, proton hopping between oxide ions is believed to be the dominant conduction mechanism [3]. Oxygen ion and electron migration are known to occur at high temperatures [6-8]. It has also been proposed that hydrogen is carried by negatively charged hydroxyl ions rather than by protons [9]. Difficulties in preparing these materials without interconnected porosity has complicated transport mechanism determinations.

This study focused on water uptake and conductivity in  $\text{SrYb}_{0.05}\text{Ce}_{0.95}\text{O}_{3.8}$  as a function of temperature and environment. This level of ytterbium doping has been shown previously to give the highest overall conductivity [8]. Water uptake kinetics and quantities were measured by thermogravimetry in fully dense samples. Proton, oxygen ion, and electronic contributions to the overall conductivity were determined using gas concentration cells and cyclic voltammetry techniques. Hydrogen and oxygen fluxes in cyclic voltammetry experiments were additionally determined by mass spectrometry.

### EXPERIMENTAL PROCEDURES

#### *Sample Preparation and Characterization*

Fine and homogeneous  $\text{SrYb}_{0.05}\text{Ce}_{0.95}\text{O}_{3.8}$  powders were prepared by calcination of combustion-derived precursors [10, 11]. An aqueous solution containing strontium acetate, ceric ammonium nitrate, ytterbium nitrate, and glycine was decomposed at approximately 250°C in air in a 316 stainless steel container. This process yielded a fine and voluminous ash. This material was then calcined at temperatures <950°C for several hours, uniaxially and isostatically pressed into

discs and bars, and sintered to greater than 98% of full density at 1500°C for 12 hours.

#### *Measurement Techniques*

The kinetics and extent of water uptake by fully dense  $\text{SrYb}_{0.05}\text{Ce}_{0.95}\text{O}_{3-\delta}$  samples was determined by thermogravimetry using a Cahn Model 171 Thermogravimetric Analyzer (TGA). Prior to performing water uptake measurements, the cerate samples were dried in the TGA at 1300°C in flowing dry air. The sample temperature was then changed to the desired value (from 600 to 1100°C) and held in flowing dry air until the equilibrium oxygen stoichiometry had been re-established. A desired partial pressure of water was then introduced with air as the carrier, and sample weight gain monitored.

Discs of  $\text{SrYb}_{0.05}\text{Ce}_{0.95}\text{O}_{3-\delta}$ , approximately 2.5 mm thick and 25 mm in diameter, were sealed in an alumina cell with gold gaskets. Porous platinum electrodes were previously applied to each surface. The seals were verified to be helium leak-tight using quadrupole mass spectrometry. Pt-Pt,10%Rh thermocouples provided local temperature measurements on each side of the samples as well as electrical leads for cyclic voltammetry and emf measurements. Gas fluxes (hydrogen, oxygen, or water) were monitored by mass spectrometry, using a stainless steel capillary tube to sample the gas stream.

Cyclic voltammetry measurements were performed using a Princeton Applied Research Model 173 Potentiostat/Galvanostat and a Princeton Applied Research Model 175 Universal Programmer. Voltage sweeps were made in the  $\pm 1.25$  volt range at 2 mV/s in the temperature range 300 to 900°C. To estimate the electronic component to total conductivity, wet nitrogen was swept by the "source" side of the sample while dry nitrogen was the carrier gas on the opposite side. Current/voltage responses in the  $\pm 0.5$  volt range were linear; non-linear responses at higher voltages corresponded to water decomposition to hydrogen and oxygen. Similarly, wet oxygen versus nitrogen and wet 4% hydrogen in argon versus nitrogen were used to estimate oxygen and hydrogen conductivities, respectively.

## RESULTS AND DISCUSSION

#### *Water Uptake Measurements*

Water uptake by  $\text{SrYb}_{0.05}\text{Ce}_{0.95}\text{O}_{3-\delta}$  typically followed a two-stage process, as is shown in Figure 1 at 800°C. The first, rapid uptake stage is attributed to hydration of the grain boundaries and near surface regions, whereas the much slower, long-term hydration is attributed to hydration of the bulk grains, which averaged 15  $\mu\text{m}$  in diameter in the present samples. Below approximately 700°C, times required to reach full hydration of the bulk sample were prohibitively long (>days). In previous studies of water uptake by similar compositions, complete hydration of the bulk was reported to be reached within a few hours even for temperatures below 600°C [12]. To fully remove water from the sample following each hydration experiment in the present study, it was necessary to heat to 1300°C in dry, flowing air for at least 24 hours.

Concomitant with the introduction of water vapor to the air sweep gas, the overall conductivity of  $\text{SrYb}_{0.05}\text{Ce}_{0.95}\text{O}_{3-\delta}$  decreased, as determined by the four-probe method. These results are also included in Figure 1. The overall conductivity in air at 800°C in this material is known to have significant contributions from oxygen ions [6-8]. Oxygen vacancies, however, are consumed in a reaction with water vapor to yield defects capable of conducting protons [1-3], but resulting in a lowering of the oxygen conductivity. Hydration of the grain boundaries and near surface regions would yield a partially resistive shell around each grain, consistent with the trends given in Figure 1.

Activation energies were determined for both stages of water uptake by the perovskite. For the early stage of water uptake, which is attributed to grain boundary and near surface hydration, an activation energy of  $9 \pm 2$  kcal/mole ( $0.39 \pm 0.09$  eV) was found. The second stage of hydration yielded a much higher activation energy:  $64 \pm 9$  kcal/mole ( $2.8 \pm 0.4$  eV), which is attributed to bulk hydration. Clearly, two substantially different processes contribute to the overall hydration of this material.

#### *Cyclic Voltammetry Measurements*

Cyclic voltammetry measurements performed with different choices of gas streams on each side of a  $\text{SrYb}_{0.05}\text{Ce}_{0.95}\text{O}_{3-\delta}$  sample allowed an estimate of currents carried by electrons, protons,

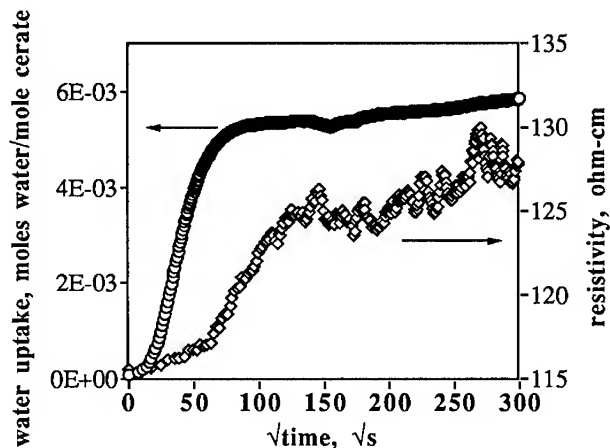


Figure 1. Water uptake and four-probe conductivity results obtained at 800°C for an initially dry sample exposed to a wet air stream (23 mm Hg water partial pressure).

and oxygen ions to be made over a range of temperatures. Cyclic voltammetry measurements are summarized in Figure 2 a-d. Simultaneous mass spectrometry measurements provided an independent means to determine mass fluxes through the sample as a function of applied voltage, temperature, and environment. In general, the agreement between mass fluxes determined by mass spectrometry and those calculated from current/voltage responses was very good.

Electron contributions to conduction in  $\text{SrYb}_{0.05}\text{Ce}_{0.95}\text{O}_{3-\delta}$  were calculated from the slope of current versus voltage responses when nitrogen streams were applied to both sides of the sample. Linear responses were obtained in the voltage range of  $\pm 0.5$  volts in the temperature range 300 to 900°C, as shown in Figure 2a. Water electrolysis was apparent outside that voltage range at the highest temperatures, leading to transport of hydrogen or oxygen ions in addition to the electronic current, depending on the sign of the voltage. Concurrent fluxes of hydrogen or oxygen were observed by mass spectrometry. Results corresponding to 900°C in Figure 2a are unusual in that the electronic current would appear to be less than at lower temperatures. Some water decomposition at 900°C is likely even in the  $\pm 0.5$  volt range, which would provide oxygen and hydrogen for transport. The electron current could be offset by a proton flux in the same direction or by an oxygen ion flux in the opposite direction. Passive electron/proton fluxes in this composition and advantages for use in a membrane reactor have been discussed previously [5].

Proton currents were determined from current/voltage responses where a stream of 4% hydrogen in argon was applied on one side of the ceramic and a nitrogen stream was applied to the other side. Similarly, oxygen currents were determined using an air stream on one side and nitrogen on the other. Results for 4% hydrogen versus nitrogen and for air versus nitrogen are given in Figure 2b and 2c, respectively. Electronic currents were subtracted from the overall current versus voltage curves in both cases. Asymmetric responses were obtained, as expected. Higher currents were found when a negative voltage was applied with hydrogen on the source side; a positive voltage gave higher currents with oxygen on the source side. With 4% hydrogen on the source side and air on the opposite side, shown in Figure 2c, the cerate supported proton, oxygen ion, and electron currents simultaneously. This arrangement is similar to that used in a solid oxide fuel cell [13].

Activation energies were calculated for electron, oxygen ion, and proton transport as a function of temperature from cyclic voltammetry and mass spectrometry data. These results are given in Figures 3a, 3b, and 3c for electronic, oxygen ion, and proton transport, respectively. The activation energy for electronic transport was found to be  $20.7 \pm 2.0$  kcal/mole ( $0.90 \pm 0.09$  eV). From electron hole transport in  $\text{BaSm}_{0.1}\text{Ce}_{0.9}\text{O}_{3-\delta}$  reported by Iwahara et al. [4], an apparent activation energy of 26 kcal/mole (1.1 eV) can be calculated, similar to present results. Such higher than expected activation energies for electronic conduction probably reflect the creation of additional carriers ( $\text{Ce}^{4+}/\text{Ce}^{3+}$  equilibrium) with increased temperature as well as increased mobility. The activation energy for oxygen ion conduction was found to be  $22.4 \pm 2.3$  kcal/mole



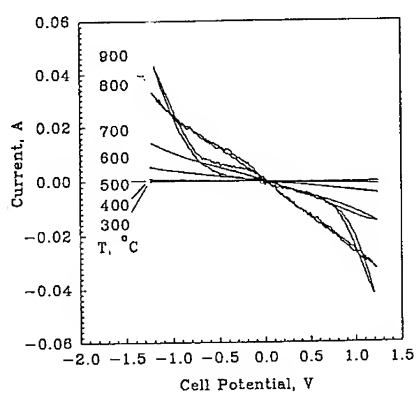


Figure 2a. Current/voltage curves at various temperatures for wet nitrogen versus nitrogen.

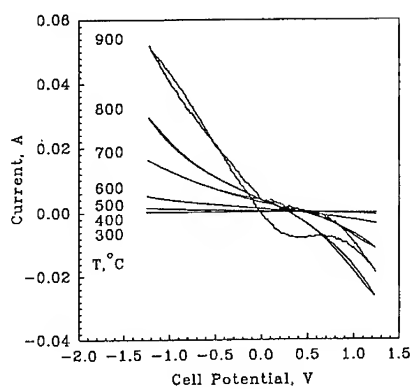


Figure 2b. Current/voltage curves for 4% hydrogen in argon (wet) versus nitrogen.

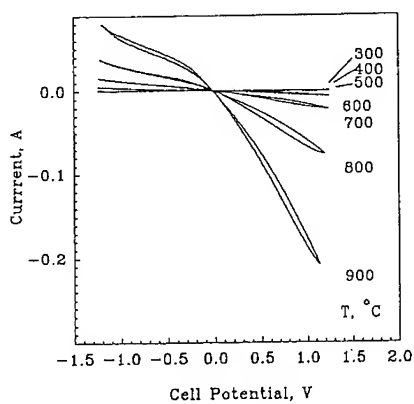


Figure 2c. Current/voltage curves for wet air versus nitrogen.

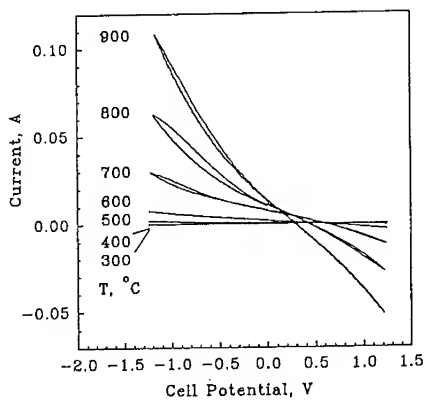


Figure 2d. Current/voltage curves for 4% hydrogen in argon (wet) versus air.

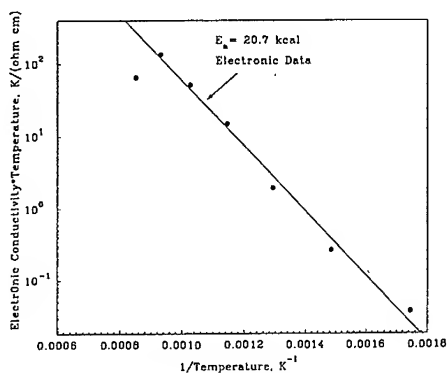


Figure 3a. Electronic conductivity versus reciprocal temperature.

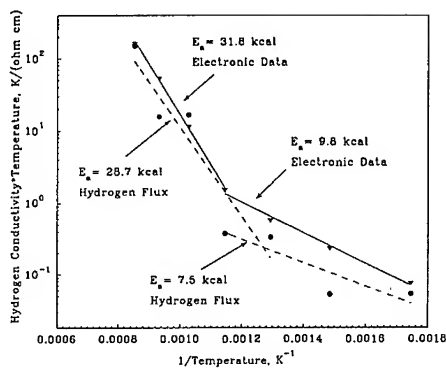


Figure 3b. Hydrogen ion conductivity versus reciprocal temperature determined from current/voltage curves and by direct measure of molecular hydrogen flux by mass spectrometry.

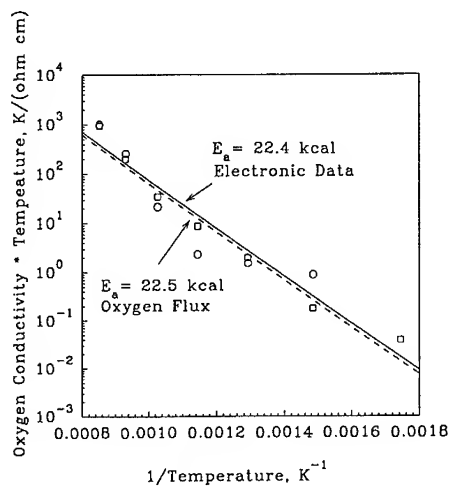


Figure 3c. Oxygen ion conductivity versus reciprocal temperature determined from current/voltage curves and by direct measure of molecular oxygen flux by mass spectrometry.

( $0.97 \pm 0.10$  eV), in good agreement with results for cerates [4] and other oxygen conductors such as yttria-stabilized zirconia [14]. Currents calculated from oxygen fluxes determined by mass spectrometry were in good agreement with those determined from current/voltage curves (see Figure 3b). Activation energies for oxygen ion conduction determined from the two methods likewise were in good agreement.

Results for hydrogen conduction (see Figure 3c) appear to show two different regimes. At low temperatures (300 to 600°C), an activation energy of  $9.8 \pm 1.0$  kcal/mole ( $0.42 \pm 0.04$  eV) was obtained from current/voltage responses, whereas at higher temperatures (600 to 900°C), an activation energy of  $32 \pm 3$  kcal/mole ( $1.38 \pm 0.13$  eV) was found. Hydrogen fluxes determined by mass spectrometry were in fairly good agreement with those calculated from current/voltage curves. One possible explanation is that proton currents at low temperatures are dominated by grain boundaries, while those at high temperatures are due to bulk conduction. A grain boundary component in proton currents in barium cerate compositions has been previously reported, attributed to a separate grain boundary phase [15]. In the strontium ytterbium cerates, however, no microscopic evidence for a grain boundary phase or segregation could be found.

#### ACKNOWLEDGEMENTS

The authors gratefully acknowledge R. W. Stephens for technical assistance in performing transport measurements, D. E. McCready for performing x-ray diffraction analyses, N. T. Saenz for preparing specimens for microscopy, J. E. Coleman for SEM analyses, and J. J. Kingsley for preparing cerate powders. Research was supported by the Advanced Research and Technology Development Materials Program, Office of Fossil Energy, U. S. Department of Energy. Pacific Northwest Laboratory is operated for the U. S. Department of Energy by Battelle Memorial Institute under Contract DE-AC06-76RLO 1830.

#### REFERENCES

- [1] T. Norby, *Solid State Ionics* **40/41** 857 (1990).
- [2] N. Bonanos, *Solid State Ionics* **53-56** 967 (1992).
- [3] H. Iwahara, *Solid State Ionics* **28-30** 573 (1988).
- [4] H. Iwahara, T. Yajima, T. Hibino, and H. Ushida, *J. Electrochem. Soc.* **140** [6] 1687 (1993).
- [5] S. Hamakawa, T. Hibino, and H. Iwahara, *J. Electrochem. Soc.* **141** [7] 1720 (1994).
- [6] T. Yajima, H. Iwahara, and H. Uchida, *Solid State Ionics* **47** 117 (1991).
- [7] N. Bonanos, B. Ellis, and M. N. Mahmood, *Solid State Ionics* **44** 305 (1991).
- [8] T. Scherban and A. S. Nowick, *Solid State Ionics* **35** 189 (1989).
- [9] R. L. Cook and A. F. Sammells, *Solid State Ionics* **45** 311 (1991).
- [10] L. A. Chick, L. R. Pederson, G. D. Maupin, J. L. Bates, L. E. Thomas, and G. J. Exarhos, *Materials Letters* **10** 6 (1990).
- [11] T. R. Armstrong, J. L. Bates, G. W. Coffey, J. J. Kingsley, L. R. Pederson, J. W. Stevenson, W. J. Weber, and G. E. Youngblood, *Proc. 8th Annual Conf. on Fossil Energy Materials*, CONF-9405143, Oak Ridge National Laboratory, Oak Ridge, Tennessee (1994) p. 89.
- [12] H. Iwahara, *Solid State Ionics* **52** 99 (1992).
- [13] H. Iwahara, T. Yajima, T. Hibino, and H. Ushida, *J. Electrochem. Soc.* **140** [6] 1687 (1993).
- [14] H. L. Tuller, in *Ceramic Materials for Electronics*, ed. R. C. Buchanon, Marcel Dekker, New York (1986) p. 425.
- [15] K. D. Kreuer, E. Schonherr, and J. Maier, *Proc. 14th Int. Symp. Materials Science*, eds. F. W. Poulson, J. J. Bentzen, T. Jacobsen, E. Skou, and M. L. J. Ostergard, Riso National Laboratory, Roskilde, Denmark (1993) p. 297.

## MICROSTRUCTURE-CONDUCTIVITY RELATIONSHIPS IN SOLID ANISOTROPIC IONICALLY CONDUCTING MATERIALS

E. BUTCHEREIT, J. SCHOONMAN, H. W. ZANDBERGEN\*, C. LUTZ-ELSNER\*\*, M. SCHREIBER\*\*, and P. WANG\*\*

Laboratory for Applied Inorganic Chemistry, Delft University of Technology, P.O. Box 5045, 2600 GA Delft, The Netherlands

\*Laboratory of Materials Science, Delft University of Technology, Rotterdamseweg 137, 2628 AL Delft, The Netherlands

\*\*Materials Research Laboratory, Daimler Benz AG, Wilhelm-Runge-Straße 11, 89081 Ulm, Germany

### ABSTRACT

In a randomly oriented polycrystalline ionically conducting material the total conductivity is reduced by the lengthening of the effective conduction pathway which is determined by the microstructure. It is, therefore, desirable to develop a better understanding of the relationship between the conductivity and the microstructure of the ceramic material.

This work focused on the quantification of the various contributions to the overall conductivity. Na- $\beta$ " alumina ceramics with different microstructures but the same chemical composition were used as samples. Conductivity data were obtained by impedance spectroscopy measurements (IS) carried out in a temperature range from 350 to -30 °C at frequencies from 1 Hz to 500 KHz. An attempt has been made to calculate distinct geometric factors for the specific values of the grain and grain boundary contribution. These were inferred from the sample geometry, Laser Scanning Microscope (LSM) pictures, microstructural observations by image analysis, Transmission Electron Microscope (TEM) pictures, and considerations of the current pathways in the anisotropically conducting ceramic.

### INTRODUCTION

With the application of complex plane analysis of AC impedance spectroscopy measurements on solid ion conductors, which had been first introduced by Bauerle in 1969 [1] it became possible to separate grain and grain boundary contributions to the total resistivity of a sample. Nevertheless, to compare the resistivities measured for different samples the absolute values obtained from impedance spectroscopy measurements need to be normalized. In the case of the grain contribution this can in a first approximation be done by multiplying the measured values for the grain resistivity by the macroscopic area over length factor given by the sample geometry. For two-dimensional conductors the pathway length for the Na-ion migration is longer than in ceramics with isotropic crystals. A tortuosity factor of 3/2 should be used to correct the measured values as suggested by Armstrong et al. [2].

In the case of the grain boundary contribution a normalization of the measured resistivities is more difficult, since the volume fraction of grain boundaries, and hence, the current pathway length across or along the grain boundaries changes dependent on the microstructure of the ceramic, and may not be simply approximated by the sample geometry.

The aim of this work is the quantification of the grain and grain boundary contributions to the overall conductivity. For this purpose, four ceramics with different microstructures but the same chemical composition were investigated. Laser Scanning Microscope (LSM) pictures of the

samples served as starting pictures for image analysis, which was used to characterize the ceramic microstructures. TEM investigations were performed of the grain boundary zone of the different microstructures. The total resistivity as well as the grain and grain boundary contributions were determined using impedance spectroscopy (IS).

## EXPERIMENTAL ASPECTS

### Sample preparation

Four samples with different microstructures were used for the investigations. Sample CEO was a commercially available Na- $\beta$  alumina with a chemical composition of 90.40 wt%  $\text{Al}_2\text{O}_3$ , 8.85 wt%  $\text{Na}_2\text{O}$ , and 0.75 wt%  $\text{Li}_2\text{O}$ . The other samples were prepared from a commercially available powder of the same nominal composition which consisted mainly of  $\alpha$ - $\text{Al}_2\text{O}_3$  and Na-aluminate, as could be confirmed by X-ray diffraction measurements (XRD).

The mean particle size of 0.61  $\mu\text{m}$  has been determined using a laser beam particle sizer Model Galai CIS.

Prior to sintering, all powder samples were predensified by uniaxial pressing at 40 MPa and subsequent isostatic pressing at 200 MPa. The green bodies were then sintered in air. In order to obtain different microstructures, the sintering conditions were varied as follows:

6413:	$\xrightarrow{2^\circ/\text{min}}$	$\rightarrow 600^\circ\text{C}, 1.5\text{h}$	$\xrightarrow{4^\circ/\text{min}}$	$\rightarrow 1250^\circ\text{C}$	$\xrightarrow{15^\circ/\text{min}}$	$\rightarrow 1620^\circ\text{C}, 15\text{min}$
6428:	$\xrightarrow{2^\circ/\text{min}}$	$\rightarrow 600^\circ\text{C}, 1.5\text{h}$	$\xrightarrow{4^\circ/\text{min}}$	$\rightarrow 1250^\circ\text{C}$	$\xrightarrow{15^\circ/\text{min}}$	$\rightarrow 1650^\circ\text{C}, 15\text{min}$
6432:	$\xrightarrow{2^\circ/\text{min}}$	$\rightarrow 600^\circ\text{C}, 1.5\text{h}$	$\xrightarrow{5^\circ/\text{min}}$	$\rightarrow 1500^\circ\text{C}$	$\xrightarrow{2^\circ/\text{min}}$	$\rightarrow 1585^\circ\text{C}, 15\text{min}$

### Sample preparation for LSM, IS, and TEM investigations

The samples which were used for the investigations in the Laser Scanning Microscope (LSM) were polished on one side to 1  $\mu\text{m}$  using successive grades of diamond paste. Since Na- $\beta$  alumina is sensitive to water [3], a lubricant based on ethanol was used. After each polishing step, the samples were thoroughly cleaned in an ultrasonic bath with isopropanol. After polishing, the samples were thermally etched at 1400  $^\circ\text{C}$  for 20 minutes. To enhance the reflection of the sample surface in the microscope, a 10 nm thick Au layer was sputtered onto the polished surfaces. LSM investigations were carried out using a ZEISS Laser Scanning Microscope.

Samples used for the impedance spectroscopy measurements were polished in the same way but on two opposite surfaces. After polishing, these samples were dried in an Ar atmosphere at 500  $^\circ\text{C}$  for at least 10 hours to remove residual moisture before ion blocking Al electrodes were deposited on the polished surfaces by evaporation in a Leybold evaporation equipment Model L560. Impedance measurements were carried out in the frequency range from 1 Hz to 500 kHz using a Zahner IM5e at temperatures from 350 to -30  $^\circ\text{C}$  in a dry Ar atmosphere. The Argon was dried by passing it over  $\text{P}_2\text{O}_5$ -powder.

The samples used for the TEM investigations were first polished to a final thickness of about 100 nm before they were ion milled for about 10 hours. Using ion milling creates holes in the thin ceramic material. In the neighbourhood of the holes the samples are then thin enough to carry out High Resolution TEM investigations. A Philips TEM Model CM30 was used.

## RESULTS AND DISCUSSION

### Laser Scanning Microscopy

For microstructure analysis pictures were taken of the samples using the Laser Scanning Microscope in the confocal mode. In order to compare the results of the image analysis the different microstructures had to be photographed at the same magnification. This is difficult to do when grain sizes in the range of  $< 1\text{ }\mu\text{m}$  to several  $100\text{ }\mu\text{m}$  are present. With the magnification of about 1000 a representative picture of the microstructure could be obtained, in which grains of about  $2\text{ }\mu\text{m}$  could still be resolved.

The automated image analysis requires a picture of the microstructure with maximum contrast between the features of interest, which is then converted into a binary picture using the threshold functions supplied by the image analysis software program. Comparisons of SEM and LSM pictures of the ceramic microstructures showed that the latter had a better contrast between grains and grain boundaries.

The microstructures of the four samples are shown in Figure 1. The microstructure of sample CE0 may be described as a duplex structure in which large grains form a network, and small crystals fill the wedges. Compared to the other samples, the content of crystals smaller than  $1\text{ }\mu\text{m}$  is significantly higher. In contrast, the other samples do not have a duplex structure but are built up by crystals of a rather broad grain size distribution.

### Image analysis

Image analysis programs offer the opportunity to measure certain geometric features which may be used to characterize microstructures such as the grain size distribution, shape factors of crystals, and aspect ratios. In order to be able to use time-saving automated measuring procedures binary pictures of the microstructures in which the grains are white and the grain boundaries are black or vice versa have to be provided. If the contrast in the original greyscale picture is high enough i.e. if there is a definite assignment of certain greylevels to certain features in the microstructure, an easy conversion into a binary picture using threshold functions or so-called watershed algorithms is possible. The threshold functions work in a way that all greyvalues in a given picture which are below a chosen threshold value are set as black, all others as white. Comparisons between LSM and SEM pictures of thermally and chemically etched samples showed that a maximum contrast between grains and grain boundaries could be achieved using LSM pictures of thermally etched samples. Nevertheless, dark structures in the grains, which had about the same greyvalue as most of the grain boundaries, and light parts of the latter made an application of thresholding functions impossible. Therefore, the grain boundaries were traced with a black pencil and the black and white pictures obtained this way were photo scanned into the computer. Crystals smaller than about  $1\text{ }\mu\text{m}$  were painted black, and treated as a different phase.

In order to obtain reasonable results from the image analysis a sufficiently large number of grains has to be measured. In this work, ten pictures with together 800 to 1200 grains larger than about  $1\text{ }\mu\text{m}$  were taken of each sample.

The most obvious difference between CE0 and the other samples was the large amount of small grains in the microstructure. The determination of the area fraction of black features which includes both, grain boundaries and small grains, gave values of 30% of small grains for CE0 compared to about 15 % for the other samples. This reflects the impression one obtains when first looking at the microstructure. For the calculation of the grain size distribution, the shape

factor and the maximum chord-to-average chord ratio, the small grains shown in black were neglected and only the white grains larger than about  $1\text{ }\mu\text{m}$  were examined.

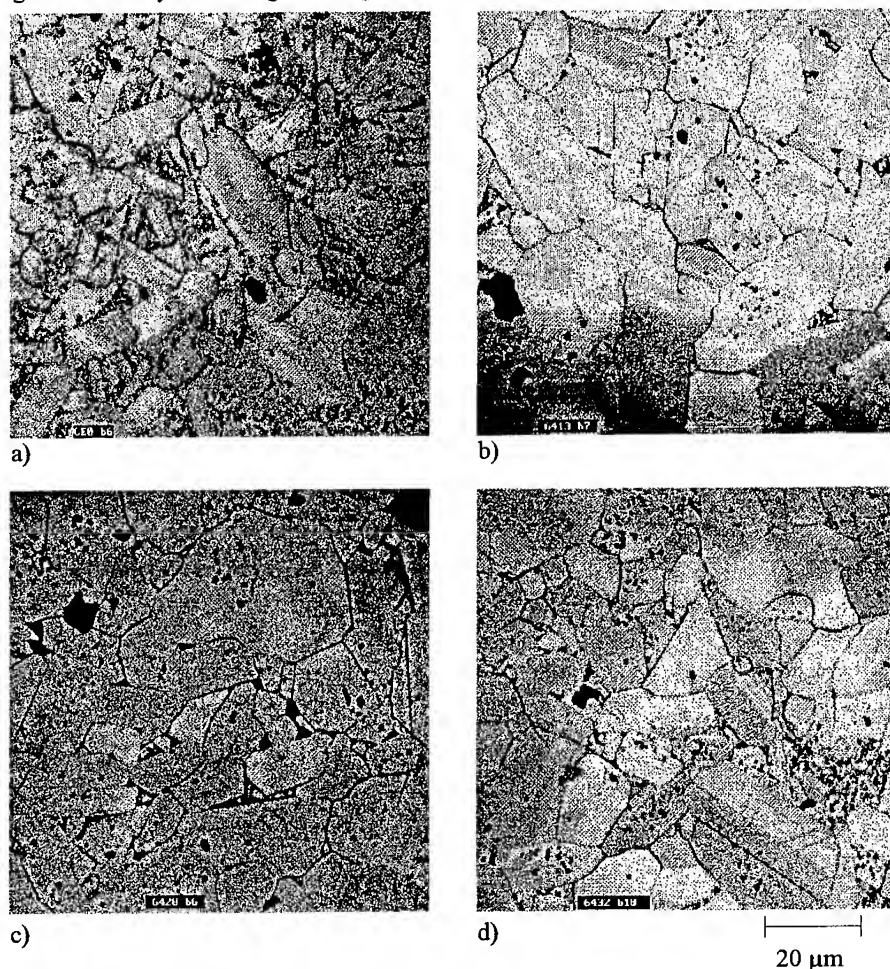


Fig. 1: Polished and etched microstructures of the samples a) CE0, b) 6413, c) 6428, and d) 6432.

The grain size distribution in the four samples is presented in Figure 2. All microstructures show a bimodal distribution with maxima at areas ranging from  $1$  to  $10\text{ }\mu\text{m}^2$  and  $100$  to  $200\text{ }\mu\text{m}^2$ . In the CE0 material the percentage of small grains is considerably higher than in all other samples. Sample 6432 which was sintered at the lowest temperature shows less pronounced maxima indicating that a more uniform grain growth has taken place.

In the evaluation of the grain size distribution only the areas of the crystals are considered. To obtain information about the grain shapes, the shape factor and the maximum chord-to-average chord ratio ( $\text{MaxChord}/\text{AvChord}$ ) have to be calculated.

The shape factor can be calculated from two measured values. It is defined as

$$\text{shape factor} = 4\pi \cdot \text{area} / \text{perimeter}^2 \quad (1)$$

and gives 1 for spheres. Rectangular grains show decreasing values with increasing length to width ratios. Another parameter which provides information about the grain shape is the maximum chord-to-average chord ratio. The maximum chord length is defined as the maximum straight line which can be drawn in a crystal, and, therefore, gives the maximum elongation of a crystal independent on the orientation of the grain in the ceramic. The average chord can be calculated by deviding the area of the grain by the maximum chord, and give an average width. The ratio MaxChord/AvChord is larger the more elongated the crystals are. The distribution of both factors is given in Figures 3 and 4. Separate diagrams are given for area ranges of 1 to 10, 10 to 100, and exceeding 100  $\mu\text{m}^2$ .

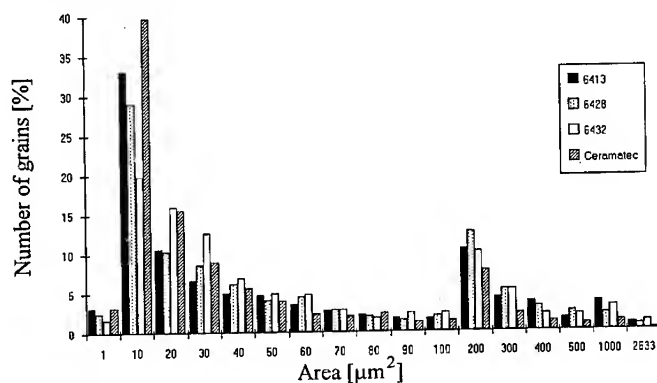


Fig. 2: Grain size distribution in the four samples. The grains smaller than about 2  $\mu\text{m}$  were treated as a second phase and are neglected in this diagram.

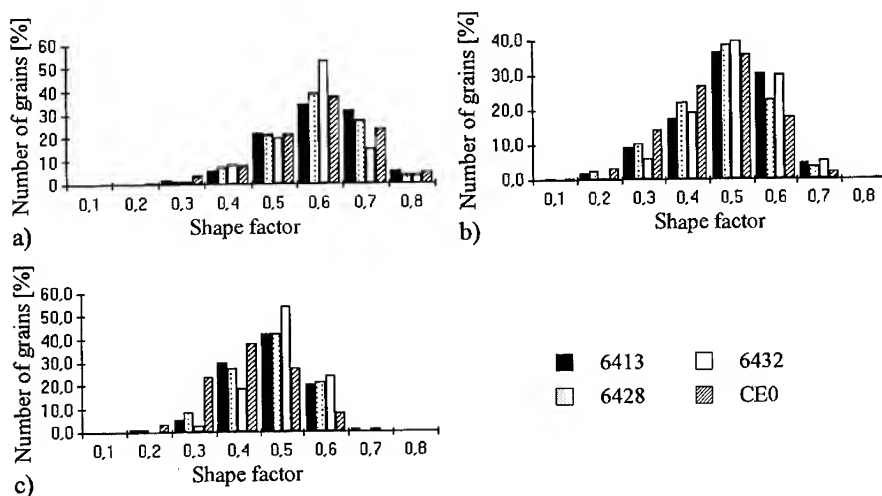


Fig. 3: Shape factor distribution in the area ranges a) 1-10  $\mu\text{m}^2$ , b) 10-100  $\mu\text{m}^2$ , and c) 100-2633  $\mu\text{m}^2$ .



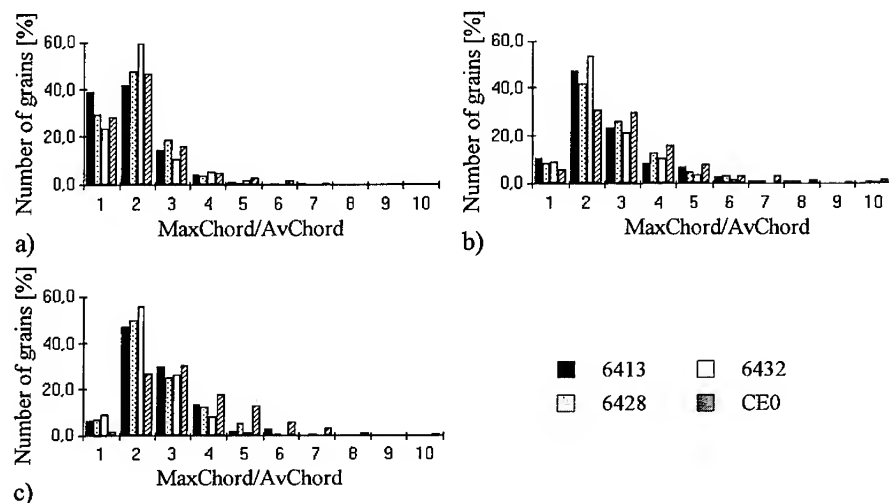


Fig. 4: Distribution of the maximum chord-to-average chord ratio in the area ranges a) 1-10  $\mu\text{m}^2$ , b) 10-100  $\mu\text{m}^2$ , and c) 100-2633  $\mu\text{m}^2$ .

The CE0 material shows a higher percentage of grains with small shape factors and large MaxChord/AvChord ratios in the area ranges 10-100 and larger than 100  $\mu\text{m}^2$ . This indicates that there is a higher amount of large and elongated crystals in this sample compared to the others.

In all considerations it was neglected that the crystals in a ceramic are generally not rectangularly shaped. Therefore, the diagrams can only show a trend.

#### Transmission Electron Microscopy

High Resolution TEM investigations of samples CE0 and 6413 were carried out to examine the grain boundaries of the different microstructures. The results are shown in Figures 5 and 6.

The grain boundaries used for the investigations were chosen in such a way that the a-c-plane of at least one of the two neighbouring crystals was perpendicular to the incident electron beam. In this orientation, a pattern of black and white lines can be observed which can be attributed to the stacking arrangement of the so-called spinel blocks and conduction layers in the Na- $\beta$ " alumina structure. A definite attribution of the black and white lines to the two structure elements can not be made, but from the crystal structure it is obvious that the thinner line must be attributed to the conduction layers (white lines in Fig. 6a-c and 7b, and black line in Fig. 7a). Each unit cell of Na- $\beta$ " alumina with a lattice constant in c-direction of about 34 Å contains three conduction slabs. As can be seen best in Figure 6a, which has been taken at the highest magnification, the stacking arrangement observed in these TEM pictures indeed repeats after three conduction slabs. The dark spots in every fourth line are at the same position.

The grain boundary structures in samples CE0 and 6413 are rather similar. An amorphous grain boundary phase or disturbed layer could not be observed. The disordered region which can be observed in Figure 6b is due to the fact that the spur of the grain boundary in the depth was not perfectly parallel to the incident electron beam. Imaging of the overlapping crystal lattices of the two neighbouring differently oriented crystals results in a apparently disturbed layer.

Both samples show a variety of different orientations of neighbouring grains. In most cases, angles between the conduction slabs of two neighbouring crystals ranging from nearly zero (see Fig. 6b) to 70 or 80° (see Fig. 5a and b) are observed. In all these cases, an easy hopping of Na-ions from one grain into the other can be expected. Nevertheless, due to the random orientation of the grains in the ceramic, a certain percentage of grains is oriented in such a way that the conduction layers of the two neighbouring crystals are perpendicular to each other (see Fig. 5c). These grain boundaries will be blocking for the Na-ion migration.

In sample CE0 it is important to note that no difference between grain boundaries between two large grains and grain boundaries between two small grains could be seen (see Figs. 5a-c and 5d, respectively).

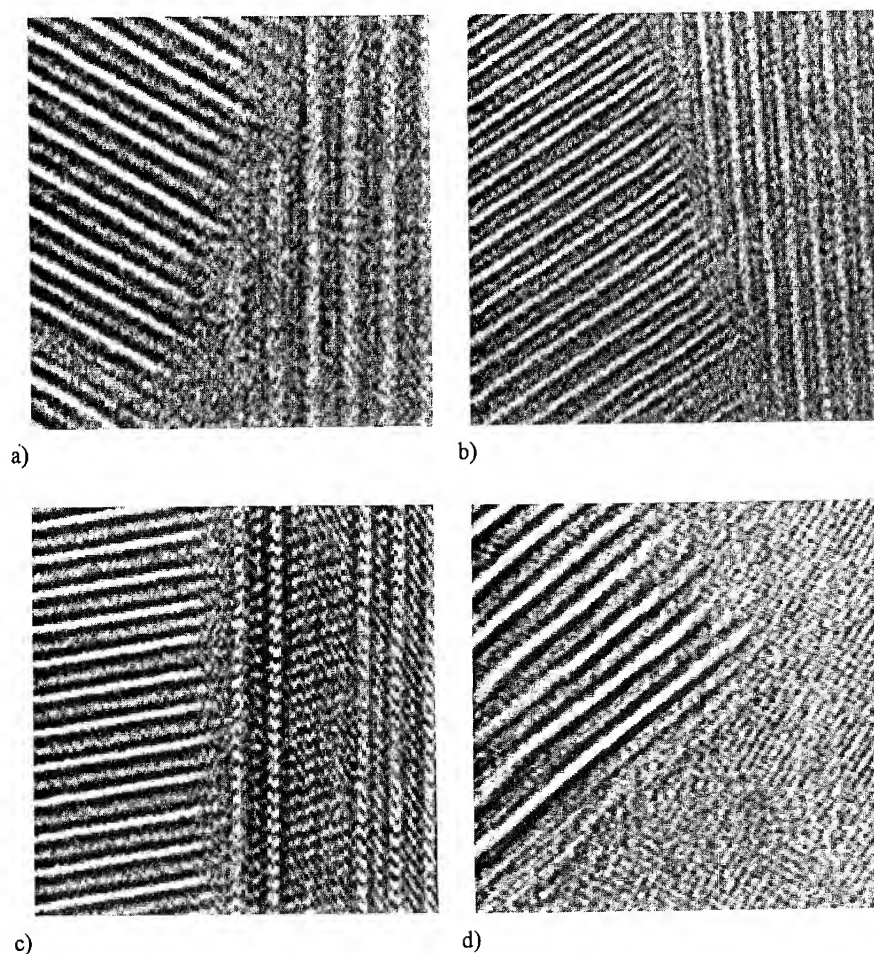


Fig. 5: Grain boundaries in sample CE0 a)- c) between two large grains, and d) between two small grains

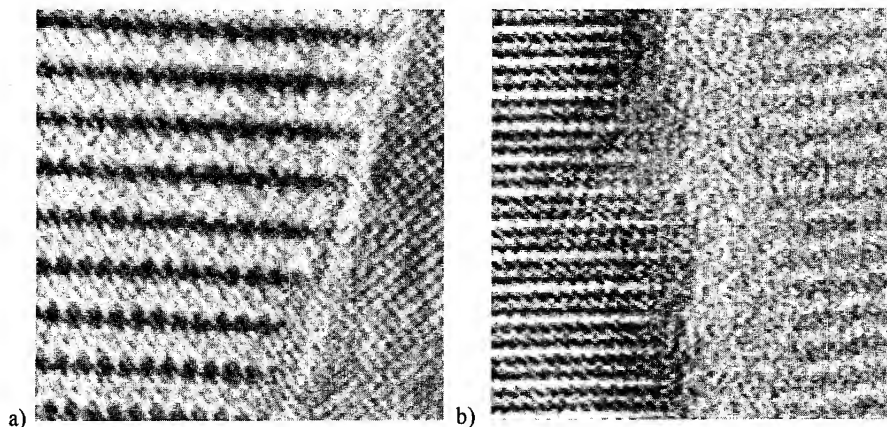


Fig. 6: Grain boundaries in sample 6413.

#### AC Impedance Spectroscopy

The behaviour of a polycrystalline ionically conducting ceramic in the AC-field measured with blocking electrodes is often described [4] using the equivalent circuit shown in Figure 7.

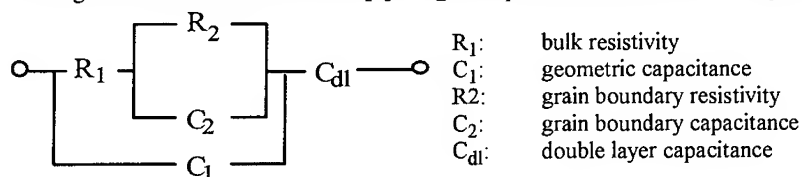


Fig. 7: Equivalent circuit used to describe the impedance behaviour of polycrystalline ion conductors measured with blocking electrodes.

The resulting ideal complex impedance spectrum shown in Figure 8 consists of two semicircles at high and medium frequencies which are due to the grain and grain boundary contributions to the total resistivity. Moreover, at the low frequencies a  $90^\circ$  spur is expected for the response of the electrode/electrolyte interface [5]. The total resistivity  $R_{tot} = R_1 + R_2$  can be determined by extrapolation of the low frequency line to the real axis. Either the high frequency intercept of the first, or the low frequency intercept of the second semicircle with the real axis can be used to determine  $R_1$ .

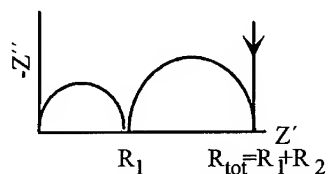


Fig. 8: Ideal impedance spectrum of a ceramic ion conductor measured with ion blocking electrodes.

Figure 9 shows the impedance spectra of the four samples at 30 °C.

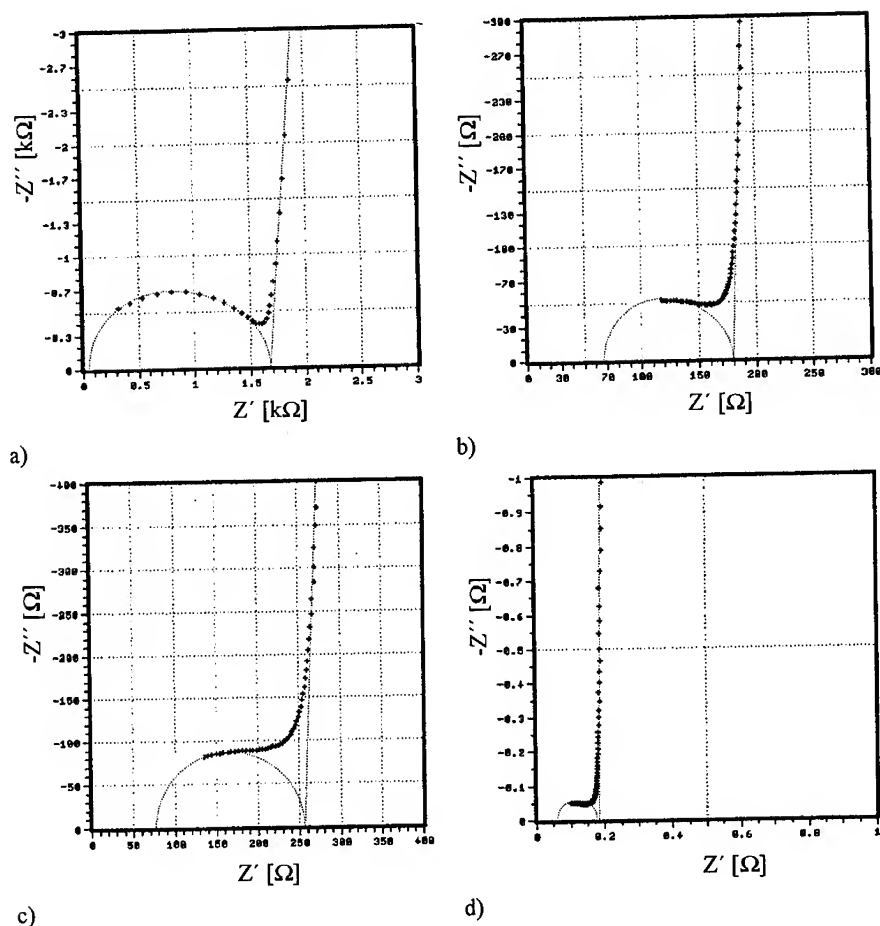


Fig. 9: Impedance spectra of the samples a) CE0, b) 6413, c) 6428, and d) 6432 at 30 °C. The graphical extrapolation of the semicircles to the real axis is given by the dashed lines.

As can be seen, the spectra of all samples show part of a semicircle at the highest measured frequencies, and a nearly 90° spur at low frequencies. The graphical extrapolation of the semicircle to the real axis is given by the dashed lines. All samples but CE0 give intercepts at positive  $Z'$ -values, indicating that a second semicircle at higher frequencies exists which can not be resolved because of the limited frequency range. The graphical extrapolation of the semicircle in the spectrum of sample CE0 does not give a clear intercept at a positive  $Z'$ -value. This could either indicate that the grain semicircle is rather small compared to the grain boundary semicircle and therefore can not be resolved or that one semicircle indeed passes the origin and actually consists of two overlapping arcs. In this case, the relaxation times for the grain and grain boundary conductivity, and hence the specific resistivities and dielectric constants for both

contributions have to be very similar. To find out which case may apply, first the total resistivities measured for the four samples have to be compared. They were derived by graphical extrapolation of the low frequency line to the real axis. Fig. 10 shows the Arrhenius plot of the total conductivities. For the calculation of the specific conductivities the geometric factor of the samples  $A/l$  was used.

In all diagrams a change in the activation energy over the temperature range investigated can be observed. While both the high and low temperature activation energies of samples 6213, 6428, and 6432 are rather similar sample CE0 shows a higher activation energy at low temperatures. Moreover, the temperature at which the change in  $E_a$  is observed is lower for sample CE0. Comparing the total conductivities measured for the samples, CE0 with the highest amount of small crystals shows the highest conductivity over the entire temperature range. This is in contrast to the idea that the low conductivity values of polycrystalline Na- $\beta$ " alumina compared to single crystals are to a large extent due to the contribution of the less conductive grain boundaries [7]. In this case, the finest grained ceramic or the one with the largest amount of small crystals should exhibit the highest total resistivity as has been shown by VIRKAR et al.[8].

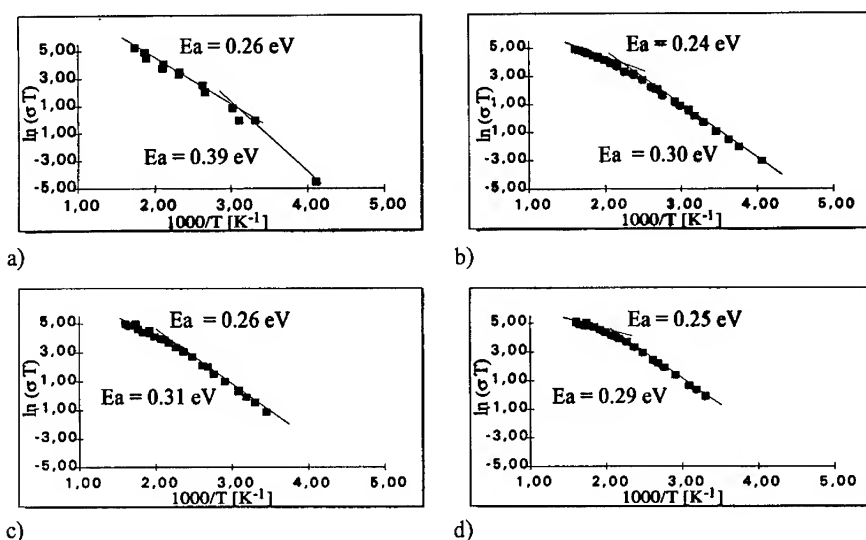


Fig. 10: Arrhenius plot of the total conductivities of the samples a) CE0, b) 6413, c) 6428, and d) 6432. The activation energies are given in eV.

To determine the exact grain and grain boundary contributions, an equivalent circuit somewhat different from the one shown in Figure 8 was used to fit the measured data using a software supplied by Zahner. Constant Phase Elements (CPE) instead of simple capacities were used for the fitting procedures since all semicircles were slightly depressed. To describe the electrode/electrolyte interface behaviour more appropriately a double layer resistivity was added in parallel to the double layer capacitance.

The starting values of  $R_1$ ,  $R_2$ ,  $CPE_1$ ,  $R_{dl}$  and  $C_{dl}$  were derived from the measured spectra.  $CPE_{geo}$  was calculated using  $\epsilon=30$  as had been suggested by Hunter [9]. It turned out that the impedance spectra of samples 6413, 6428, and 6432 could be fitted well using the modified

equivalent circuit. The results obtained for sample 6413, for which a series of low temperature data were available, are exemplified in Figure 11.

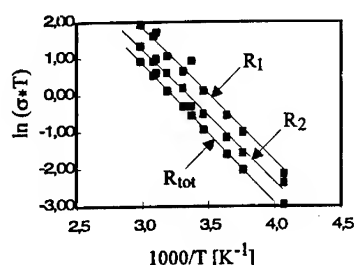


Fig. 11 Arrhenius plot for the grain and grain boundary contribution to the total conductivity in the temperature range 70 to -30 °C.

As can be seen from Figure 11, the activation energies for the grain and grain boundary contribution are similar in the temperature range from 50 to -30 °C. This indicates that the conduction mechanisms for grain and grain boundary conduction are similar. Considering the grain boundaries this appears to be reasonable. For sample CE0 the data obtained from fitting were too inaccurate to obtain reasonable results.

## CONCLUSIONS

Based on comparisons of the results from microscopic investigations and conductivity measurements of samples CE0 and 6413 which have the same chemical composition but different microstructures, a model for the Na-ion conduction in both ceramics is proposed:

AC impedance spectroscopy measurements of both samples yield distinct differences in the impedance spectra. While for sample 6413 two semicircles could be resolved at low temperatures, indicating that there are two contributions to the total resistivity, only one semicircle was observed for sample CE0.

High Resolution TEM investigations were carried out to see whether this difference in the impedance spectra could be explained by different grain boundary structures. It could be shown that both samples have similar grain boundaries with neighbouring grains interconnected without any evidence of an amorphous film or trapped impurities in between. A variety of different orientations of neighbouring grains is observed in both samples. In most of the cases the orientation of the conduction slabs is such that an easy hopping of Na-ions from one grain into the other can be assumed. The specific resistivity for the migration across such a grain boundary will be similar to the specific resistivity for the migration in grains and substantial polarization effects are not likely to occur. Therefore, a resolution of distinct grain and grain boundary semicircles will be impossible provided that all grains are suitably orientated.

In every non-textured Na-β" alumina ceramic, however, a certain percentage of grains will be orientated in such a way that the conduction slabs of two neighbouring grains are perpendicular to each other. These boundaries will be blocking for the Na-ion migration and a transport along grain boundaries to the next suitably orientated crystal will be necessary. The specific resistivity for this process will be different from that of the grain conduction, and polarization effects are probable to occur giving rise to an additional grain boundary capacitance. A resolution of two semicircles should, therefore, be possible.

The phenomena described so far, hold true for both samples. Therefore, the differences in the impedance spectra have to be due to the different microstructures.

Sample CE0 shows a duplex structure in which large grains form a network and small grains fill the wedges. In contrast, the microstructure of sample 6413 is built up by crystals with a rather broad grain size distribution. The most obvious difference, however, is the much higher content of grains smaller than about 1  $\mu\text{m}$  in sample CE0, which makes up about 30 % of the total area compared to about 15 % in sample 6413.

Considering the pathways for Na-ions in both microstructures, distinct differences can be found. In sample 6413, it is very likely that the Na-ions will - after passing a number of suitably oriented grains - meet a blocking grain boundary where an easy hopping into the next crystal is not possible. Since the grains are fairly large migration along grain boundaries over a rather long distance has to occur. This will then give rise to the second semicircle which is found in the impedance spectrum of sample 6413.

A different situation occurs in sample CE0. Na-ions which approach a blocking grain boundary between two large grains may easily find smaller grains in the neighbourhood having orientations, which allow the easy hopping across the grain boundary. Since there is a large amount of small crystals, the probability to find one with a suitable orientation is very high. Therefore, a migration along grain boundaries will not be necessary in this kind of microstructure. Polarization effects are then of minor importance and a resolution of a distinct grain boundary contribution in the impedance spectrum will not be observed.

Provided, that the grain boundaries are free of amorphous phases or trapped impurities, an easy hopping of Na-ions from one grain into the other across the grain boundaries can take place if the grains are suitably oriented. Since hopping of Na-ions across grain boundaries adds a very minor contribution to the total resistivity, compared to migration of Na-ions along grain boundaries, fine grained ceramics with a high probability for non-blocking orientations of neighbouring crystals are likely to show better specific conductivities than coarse grained ceramics. In addition, fine grained ceramics can also provide improved mechanical properties.

## LITERATURE

1. J.E. Bauerle, *J. Phys. Chem. Solids* **30**, 2657 (1969).
2. R.D. Armstrong, T. Dickinson, and P.M. Willis, *Electroanal. Chem.* **53**, 389 (1974)
3. R.D. Armstrong and D.P. Sellick, *Electrochim. Acta* **25**, 1199 (1980)
4. M Wasiucionek, J. Garbarczyk, and W. Jakubowski, *Solid State Ionics* **7**, 283 (1982)
5. W.I. Archer, R.D. Armstrong, D.P. Sellick, W.J. Budgen, and J.H. Duncan, *J. Mater. Sci.* **53**, 389 (1974)
6. E. Lilley and J.E. Strutt, *Phys. Status Solidi* **54**, 639 (1979)
7. G.C. Farrington, *J. Electrochem. Soc.* **123**, 1213 (1976)
8. A.V. Virkar, G.R. Miller, and R.S. Gordon, *J. Amer. Ceram. Soc.* **61**, 250 (1978)
9. C.C. Hunter, M.D. Ingram, and A.R. West, *J. Mater. Sci. Letters* **1**, 522 (1982)

## IONIC CONDUCTIVITIES OF LITHIUM PHOSPHORUS OXYNITRIDE GLASSES, POLYCRYSTALS AND THIN FILMS

B. WANG, J. B. BATES, B. C. CHAKOUMAKOS, B. C. SALES, B. S. KWAK, R. A. ZUHR  
Solid State Division, Oak Ridge National Laboratory, Oak Ridge, TN 37831, USA

AND

J. D. ROBERTSON  
Department of Chemistry, University of Kentucky, Lexington, KY 40502, USA

### ABSTRACT

Various lithium phosphorus oxynitrides have been prepared in the form of glasses, polycrystals, and thin films. The structures of these compounds were investigated by X-ray and neutron diffraction, X-ray photoelectron spectroscopy (XPS), and high-performance liquid chromatography (HPLC). The ac impedance measurements indicate a significant improvement of ionic conductivity as the result of incorporation of nitrogen into the structure. In the case of polycrystalline  $\text{Li}_{2.88}\text{PO}_{3.73}\text{N}_{0.14}$  with the  $\gamma\text{-Li}_3\text{PO}_4$  structure, the conductivity increased by several orders of magnitude on small addition of nitrogen. The highest conductivities in the bulk glasses and thin films were found to be  $3.0 \times 10^{-7}$  and  $8.9 \times 10^{-7} \text{ S}\cdot\text{cm}^{-1}$  at  $25^\circ\text{C}$ , respectively.

### INTRODUCTION

Recent work in this Laboratory shows that the addition of nitrogen into the structure of amorphous lithium phosphate thin films deposited by sputtering  $\text{Li}_3\text{PO}_4$  in  $\text{N}_2$  increases the lithium ionic conductivity by a factor of about 40 [1, 2]. More importantly, the lithium phosphorus oxynitride electrolyte is stable in contact with metallic lithium at high potentials enabling the development of rechargeable thin film lithium batteries [3]. To systematically study the ionic conductivities in the lithium phosphorus oxynitride system and the effect of increase in nitrogen and lithium concentration on the ionic conductivity of the thin films, we have synthesized various lithium phosphorus oxynitrides in the forms of glasses, polycrystals, and thin films. In this paper, we report the structures and ionic conductivities of these lithium phosphorus oxynitride materials.

### EXPERIMENTAL PROCEDURES

#### Synthesis

#### *Glasses*

Lithium phosphorus oxynitride glasses were prepared by remelting a base glass at  $775^\circ\text{C}$  for several days in flowing anhydrous ammonia. The base glass was chosen to contain the highest lithium content that can form a phosphate glass by the conventional melt-quench technique [4, 5].



The glass was prepared from  $\text{Li}_2\text{CO}_3$  and  $\text{NH}_4\text{H}_2\text{PO}_4$  by melt-quench at  $800^\circ\text{C}$  in the air. About 2 g of powder of the base glass contained in an alumina boat lined with graphite foil was sealed inside a quartz tube. After remelting in ammonia at high temperature, the samples were furnace cooled to room temperature to avoid bubble formation in the sample.

### *Polycrystals*

A material of a single crystalline phase was obtained by a solid-state reaction between  $\text{Li}_3\text{N}$  and  $\text{LiPO}_3$  at a molar ratio of 2/3:1. The solid state reaction was carried out by heating the mixture at  $600^\circ\text{C}$  for 24 hours under a flowing  $\text{N}_2$  atmosphere inside a sealed stainless steel furnace liner. Samples of  $\gamma\text{-Li}_3\text{PO}_4$  were prepared by heating  $\text{Li}_3\text{PO}_4$  (Alfa, 99%) at  $800^\circ\text{C}$  for 24 hours and cooling slowly to room temperature.

### *Thin Films*

The lithium phosphorus oxynitride films were deposited by planar rf magnetron sputtering of single lithium phosphorus oxynitride targets in  $\text{N}_2$ . Two targets were prepared by cold pressing and sintering powders of (1)  $5/3\text{Li}_3\text{N} + \text{LiPO}_3$  and (2)  $\text{Li}_3\text{N} + \text{Li}_3\text{PO}_4$  at  $600^\circ\text{C}$  for 24 hours. After processing, the target measured 1' in diameter by about 3 mm thick. The details of the deposition and the array of substrates were described earlier [1]. The thickness of the films measured by a profilometer ranged between 0.5 to  $1.0\ \mu\text{m}$ .

### Characterization

#### *Chemical Analysis*

Chemical analyses of the glasses were performed by an independent laboratory using various techniques. The nitrogen content was determined by the Kjeldahl method, phosphorus by plasma emission spectroscopy, and lithium by atomic absorption spectroscopy. The oxygen stoichiometry was determined by difference assuming charge balance. The nitrogen content in the polycrystals was estimated from the total weight gain in flowing  $\text{O}_2$  during a thermal gravimetric analysis (TGA) measurement performed in a Perkin-Elmer TGS-2 system. The films compositions were determined using proton-induced  $\gamma$ -ray emission analysis (PIGE) to obtain Li/P ratio and by Rutherford backscattering spectrometry (RBS) to obtain the N/P ratio [1,2].

#### *Structural Determination*

Powder X-ray diffraction (PXRD) measurements were made with a Scintag diffractometer equipped with a high-purity Ge detector using  $\text{Cu K}\alpha$  radiation. Neutron diffraction data for the polycrystal sample were collected using the HB4 powder diffractometer at the High-Flux Isotope Reactor at ORNL. A full description of the instrument design and experimental details are given elsewhere [6, 7]. The structural refinements were made using the computer program GSAS [8], which employs the Rietveld method [9]. High-performance liquid chromatography (HPLC) was

used to determine the distribution of phosphate anions in the samples. X-ray photoelectron spectroscopy (XPS) was used to measure the core levels of Li, P, N and O in the oxynitrides with a PHI 5000 ESCA system using 1487 eV Al  $K\alpha$  X-rays as the excitation source.

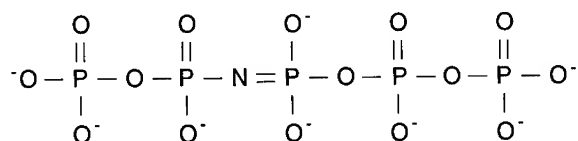
### *Ionic Conductivity Measurements*

Impedance measurements were made at frequencies from 0.1 Hz to 10 MHz using frequency response analyzers (a Solartron 1250 and a Hewlett-Packard 3577A), with signals of 10 to 50 mV p-p applied to the samples. For these measurements, the glass samples were cut into thin plates, and the fine powder of polycrystals was cold pressed into a pellet then sintered at 500°C in flowing N<sub>2</sub> (oxynitride) or in air ( $\gamma$ -Li<sub>3</sub>PO<sub>4</sub>). Metal contacts (Pt or Au) about 2000 Å thick were deposited onto the faces of the glass plates and the polycrystal pellets by sputtering. The samples were sandwiched between Pt plates and pressed against a heater block inside a small vacuum chamber and a thermocouple attached to the heater block near the sample. The portion of the film for the ionic conductivity measurement was deposited over a 2500 Å thick Au contact on a Coors ADS 996 alumina substrate. Afterward, a top Au contact was deposited over the film at 90° to the bottom electrode forming a metal/film/metal sandwich structure. High purity argon was circulated through the chamber during the impedance measurements which were made at 10 and 20°C increments from 25° to 300°C with increasing and decreasing temperatures.

## RESULTS AND DISCUSSION

### Glasses

The N<sub>1s</sub> spectrum was resolved into two components, the doubly coordinated nitrogen -N= at 398.4 eV and triply coordinated nitrogen -N< at 399.8 eV based on the proposed assignments in other studies of oxynitride glasses [10] (Fig. 1). The larger area of -N< peak indicates the relatively higher concentration of -N< in the glass structure. The weak peak at 403.3 eV is probably due to O-N=O groups [11]. Chromatograms of the glass samples are shown in Fig. 2. The position and area under each peak indicates, respectively, the chain length (denoted by  $P_n = P_n O_{3n+1}^{(n+2)-}$ ) and the relative amount of phosphorus associated with a given phosphate anion. The significant changes in the phosphate anion distribution after nitrogen incorporation into the glass are immediately apparent in the chromatograms. The possible origins of the additional peaks (indicated by the arrows) in the chromatogram of the nitrated sample are phosphate anions which are linked together by -N= thus forming mixed anions such as:



The assignment of the new peaks is also based on the topological and electronic similarity between these -N= linked phosphate anion chains and the normal phosphate anion chains. While distinct

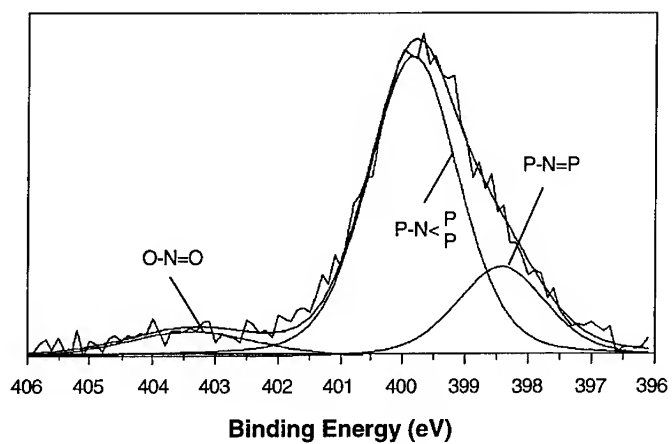


Fig. 1  $N_{1s}$  XPS spectrum of lithium phosphorus oxynitride glass.

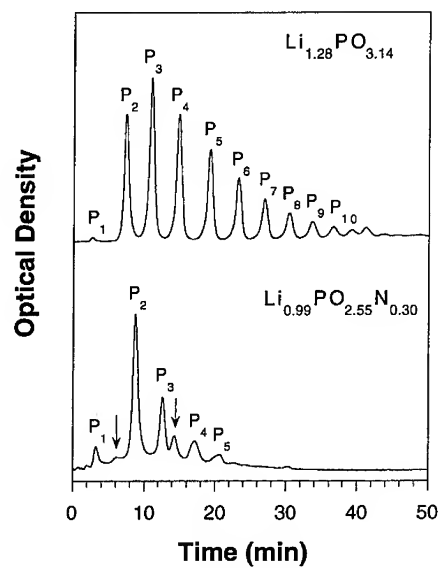


Fig. 2 Chromatograms of  $Li_{1.28}PO_{3.14}$  and  $Li_{0.99}PO_{2.55}N_{0.30}$  glasses. The arrows indicate the mixed phosphate anions linked together by  $-N=$ .

peaks due to the branched  $\text{P-N} \begin{smallmatrix} \text{P} \\ \text{P} \end{smallmatrix}$  phosphate anions may not be detected by HPLC, these anions may be responsible for the increased background particularly obvious in Fig. 2. The lack of suitable crystalline standards containing either  $\text{-N=}$  or  $\text{-N<}$  linked anions, however, makes it impossible to rule out  $\text{-N<}$  anions as the source of some of the unidentified chromatogram peaks. The nitrogen incorporation into the glass also reduces the fraction of longer phosphate chains that are detected by the HPLC measurement. This does not mean that longer chains are not formed. It is likely, however, that many of the longer phosphate chains linked by  $\text{-N<}$  are not detectable by the HPLC. The overall result of nitridation is the polymerization of the glass structure through the nitrogen cross-linking in  $\text{P-N} \begin{smallmatrix} \text{P} \\ \text{P} \end{smallmatrix}$  and  $\text{P-N=P}$ .

The conductivity data for the lithium phosphorus oxynitride glasses are shown in Fig. 3. The results indicate that the increase of ionic conductivity after nitridation is due to the decrease in activation energy. The increase in ionic conductivity in the nitrated samples can be attributed to the structural changes as the result of nitrogen incorporation into the glass. Analogous to the "mixed anion effect" in which the formation of cross-linking macromolecular structure by two or more different glass formers increases ionic conductivity [1, 12 - 13], nitrogen incorporation into lithium phosphate glasses increases structural cross-linking and leads to an increase in ionic conductivity. The increase of ionic conductivity in the nitrated samples can also be attributed to the decreasing electrostatic energy after nitridation as proposed by Unuma *et al.* [14]. Based on the Anderson-Stuart model [15], Unuma *et al.* suggested that the increase of ionic conductivity by a

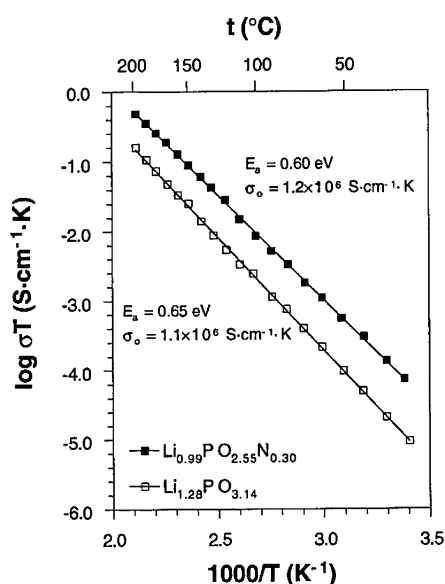


Fig. 3 Temperature dependence of the ionic conductivity of  $\text{Li}_{1.28}\text{PO}_{3.14}$  and  $\text{Li}_{0.99}\text{PO}_{2.55}\text{N}_{0.30}$  glasses.

decrease of activation energy is due to the decreasing electrostatic energy when P-O bonds are replaced by more covalent P-N bonds in the alkali silicate oxynitride glasses [14].

### Polycrystals

It was found that the X-ray diffraction powder pattern for the synthesized polycrystalline lithium phosphorus oxynitride was similar to that of  $\gamma\text{-Li}_3\text{PO}_4$  [16]. The structure of  $\gamma\text{-Li}_3\text{PO}_4$  is built up by corner sharing of the lithium and phosphate tetrahedra (Fig. 4). Each oxygen is shared by three  $\text{LiO}_4$  tetrahedra and one  $\text{PO}_4$  tetrahedron. The observed, calculated, and the difference neutron powder diffraction profiles of  $\gamma\text{-Li}_3\text{PO}_4$  and the oxynitride sample are presented in Fig. 5. The neutron data refinement indicates that  $\text{Li} \leftrightarrow \text{P}$  disorder is present in the oxynitride sample  $\text{Li}_{2.88}\text{PO}_{3.73}\text{N}_{0.14}$ . Although the neutron diffraction data do not clearly indicate which of the oxygen sites are occupied by nitrogen due to the low nitrogen content in the sample, it is expected that one oxygen vacancy is created for every two nitrogen atoms incorporated into the structure in order to maintain charge balance. The chromatogram of  $\text{Li}_{2.88}\text{PO}_{3.73}\text{N}_{0.14}$  contains additional features in addition to the orthophosphate anions ( $\text{P}_1$ ) [7]. The major feature is the shoulder under the  $\text{P}_1$  peak which is probably due to nitrogen substituted phosphate tetrahedra  $\text{PO}_3\text{N}$ . The other weak peaks are possibly due to phosphate anions linked together by  $-\text{N}=$  apparently due to the some  $\text{Li} \leftrightarrow \text{P}$  disorder in the structure.

The introduction of a small amount of nitrogen into the structure of  $\gamma\text{-Li}_3\text{PO}_4$  increases the conductivity by several orders of magnitude as shown in Fig. 6. A comparison of the values of  $E_a$  and  $\sigma_0$  suggests that the higher conductivity of  $\text{Li}_{2.88}\text{PO}_{3.73}\text{N}_{0.14}$  is due to a lower activation energy. In the  $\gamma\text{-Li}_3\text{PO}_4$  structure, the  $\text{Li}^+$  ions occupy tetrahedral sites in a framework structure formed by the P and O [17 - 19], and all of the Li sites are fully occupied. On the other hand, in  $\text{Li}_{2.88}\text{PO}_{3.73}\text{N}_{0.14}$ , a large concentration of vacancies at the Li-sites (4.00%) and the anion-sites (3.25%) were created as the result of the substitution of nitrogen for oxygen. In addition, the replacement of smaller  $\text{O}^{2-}$  ions with larger  $\text{N}^{3-}$  ions increases the size of the small bottleneck through which the lithium ions must pass in  $\gamma\text{-Li}_3\text{PO}_4$  [20] as evidenced by the increase of  $a$  and  $b$  unit-cell parameters from the refinement. This also lowers the activation energy.

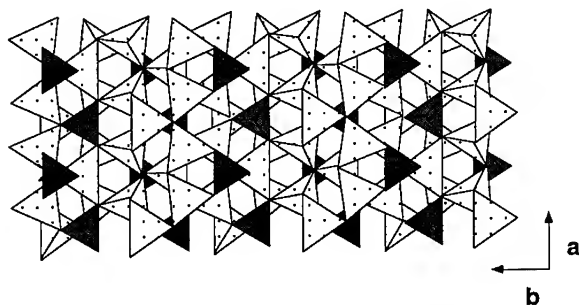


Fig. 4 Polyhedral crystal structure projection of the (001) view of  $\gamma\text{-Li}_3\text{PO}_4$ . The darker shaded tetrahedra are  $\text{PO}_4$  and the lighter shaded tetrahedra are  $\text{LiO}_4$ .

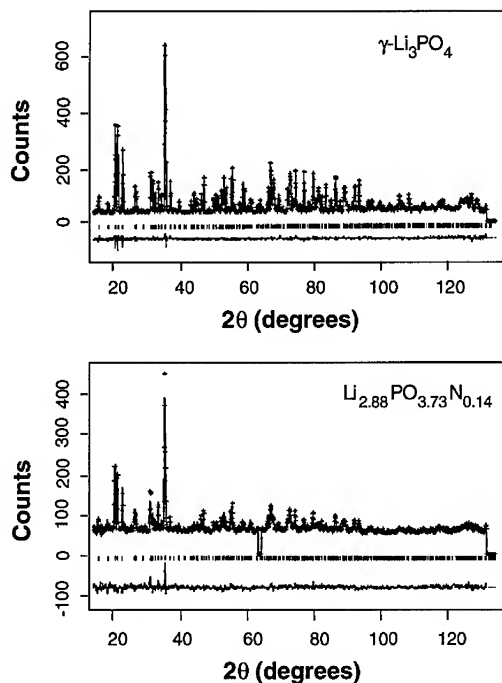


Fig. 5 Observed, calculated, and difference neutron diffraction profiles for  $\gamma\text{-Li}_3\text{PO}_4$  and  $\text{Li}_{2.88}\text{PO}_{3.73}\text{N}_{0.14}$ . The observed data are indicated by +, and the calculated profile is the continuous solid line in the same field. The short vertical lines below the profiles mark the positions of all possible Bragg reflections, and the bottom curve is the difference between the observed and calculated intensity.

### Thin films

The X-ray diffraction measurements indicate that all the thin films are amorphous. Based on the PIGE measurements of the Li/P ratios and RBS measurements of the N/P ratios, the compositions of the films are given by  $\text{Li}_{5.80}\text{PO}_{4.77}\text{N}_{0.42}$  and  $\text{Li}_{1.15}\text{PO}_{1.96}\text{N}_{0.74}$  for the film deposited from the  $\text{Li}_3\text{N} + \text{Li}_3\text{PO}_4$  target and the film deposited from the  $5/3\text{Li}_3\text{N} + \text{LiPO}_3$  target, respectively. An example of an RBS spectrum is shown on Fig. 7. The solid circles are the calculated backscattering from the computer simulation. The lithia-deficiency in the film deposited from the  $5/3\text{Li}_3\text{N} + \text{LiPO}_3$  target is due to the  $\text{LiPO}_3$  portion in the target, since the films deposited from a single  $\text{LiPO}_3$  target were also lithia-deficient as a result of the redistribution of  $\text{Li}_2\text{O}$  on the target surface and consequent loss of  $\text{Li}_2\text{O}$  during sputtering [21].

The chromatogram of the  $\text{Li}_{5.80}\text{PO}_{4.77}\text{N}_{0.42}$  film shown in Fig. 8 indicates that orthophosphate anions ( $\text{P}_i$ ) is the major phosphate anions in the structure due to the high lithium concentration in the sample. The  $\text{Li}_{1.15}\text{PO}_{1.96}\text{N}_{0.74}$  film contains both shorter and longer phosphate anions because of its lower lithium concentration. Similar to the glass sample, the  $-\text{N}=\text{N}-$

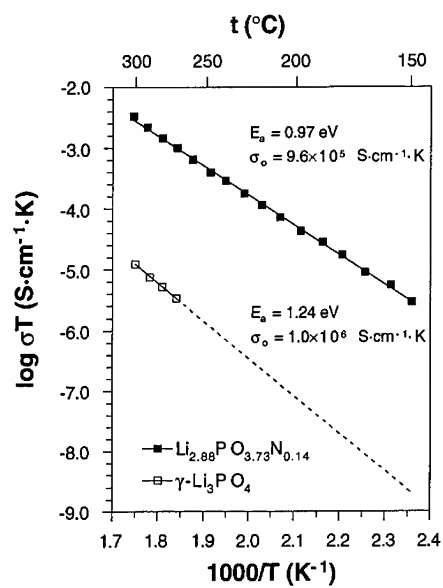


Fig. 6 Temperature dependence of the ionic conductivity of  $\gamma$ - $\text{Li}_3\text{PO}_4$  and  $\text{Li}_{2.88}\text{PO}_{3.73}\text{N}_{0.14}$  polycrystals.

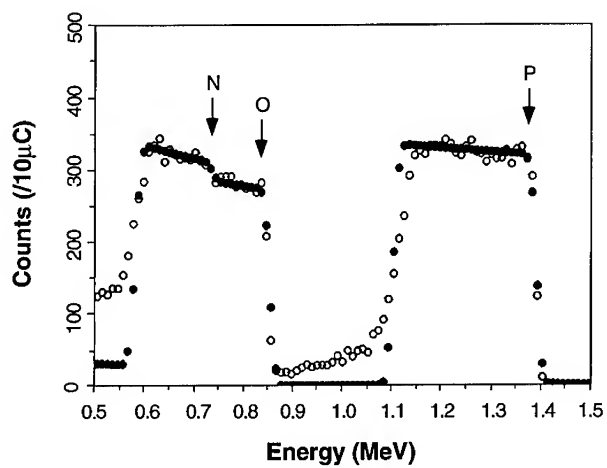


Fig. 7 RBS spectrum for thin film  $\text{Li}_{5.80}\text{PO}_{4.77}\text{N}_{0.42}$ . Solid circles are the calculated backscattering from the computer simulation.

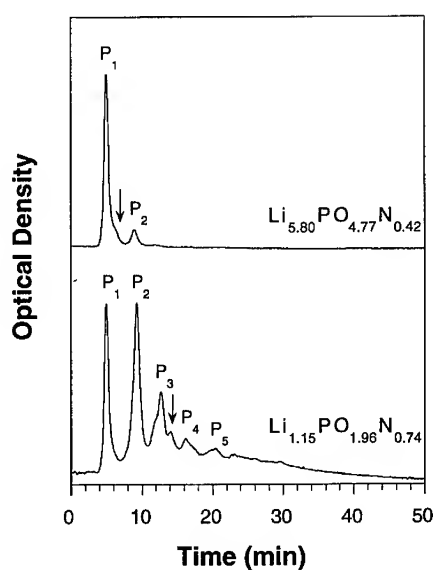


Fig. 8 Chromatograms of  $\text{Li}_{5.80}\text{PO}_{4.77}\text{N}_{0.42}$  and  $\text{Li}_{1.15}\text{PO}_{1.96}\text{N}_{0.74}$  thin films. The arrows indicate the mixed phosphate anions linked together by  $-\text{N}=\text{P}-$ .

linked phosphate anions (indicated by the arrows) were also observed in both films. The high background in the chromatogram of the  $\text{Li}_{1.15}\text{PO}_{1.96}\text{N}_{0.74}$  film can be attributed to the high concentration of branched  $\text{P}-\text{N}-\text{P}$  phosphate anions in the structure.

Graphs of the temperature dependence of the ionic conductivity of the thin films are shown in Fig. 9. Both graphs show a curvature at the relative high temperature. The low temperature data can be fit with the Arrhenius equation  $\sigma T = \sigma_0 \exp(-E_a/RT)$  while the high temperature data can be fit with the equation  $\sigma = \sigma_0' \exp[-E_a/R(T-T_0)]$ . In the latter,  $T_0$  is the ideal vitreous transition temperature which is much lower than the vitreous transition temperature  $T_g$  [22]. The lower  $T_0$  of the  $\text{Li}_{5.80}\text{PO}_{4.77}\text{N}_{0.42}$  film is apparently due to the high lithium concentration in the sample. Above the  $T_g$ , the movement of  $\text{Li}^+$  ions is facilitated by cooperative movement of the anionic macromolecular chains. The lower conductivity of the  $\text{Li}_{1.15}\text{PO}_{1.96}\text{N}_{0.74}$  film is apparently due to its low lithium content although it has the higher nitrogen content. The conductivity of the  $\text{Li}_{5.80}\text{PO}_{4.77}\text{N}_{0.42}$  film is slightly lower than that of the previously studied lithium oxynitride films deposited by sputtering single  $\text{Li}_3\text{PO}_4$  targets in  $\text{N}_2$  [1, 2], although the  $\text{Li}_{5.80}\text{PO}_{4.77}\text{N}_{0.42}$  film has the higher lithium concentration. This is probably due to the partial crystallization which was not detected by the X-ray diffraction. Analogous to the glasses, the high ionic conductivity in the thin films is attributed to the increase in structural cross-linking by  $-\text{N}=\text{P}-$  and  $-\text{N}-\text{P}-$  [1, 2].



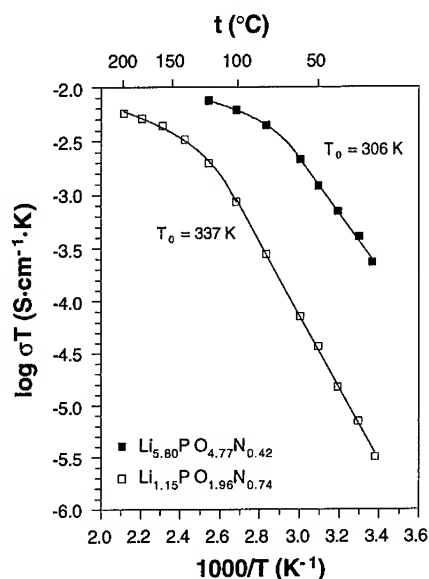


Fig. 9 Temperature dependence of the ionic conductivity of  $\text{Li}_{5.80}\text{PO}_{4.77}\text{N}_{0.42}$  and  $\text{Li}_{1.15}\text{PO}_{1.96}\text{N}_{0.74}$  thin films.

#### Comparison of the ionic conductivities of glasses, polycrystals and thin films

The calculated activation energies  $E_a$ , the preexponential factors  $\sigma_0$  in the Arrhenius equation  $\sigma T = \sigma_0 \exp(-E_a/RT)$ , and the conductivities for the glasses, polycrystals, and thin films are listed in Table 1. Although nitrogen incorporation into the lithium phosphate structure increases the ionic conductivities in all three forms, the origin for this enhancement is different: the increase in cross-linking is attributed to the increase of ionic conductivity in the glasses and thin films, whereas the creation of vacancies and the increase in cell volumes is attributed to in the increase in ionic conductivity of the single phase polycrystalline  $\text{Li}_{2.88}\text{PO}_{3.73}\text{N}_{0.14}$  with the  $\gamma\text{-Li}_3\text{PO}_4$  structure.

As shown in Table 1, the ionic conductivity of the  $\text{Li}_{1.15}\text{PO}_{1.96}\text{N}_{0.74}$  thin film is one order of magnitude lower than the glass sample with the similar composition ( $\text{Li}_{0.99}\text{PO}_{2.55}\text{N}_{0.30}$ ). The film has larger activation energy and preexponential factor than that of the glass (Table 1). The large differences between the thin film and bulk glass conductivities can be attributed to the difference in the sample preparation process. Based on the weak electrolyte model Pradel *et al.* [5] suggest that the increase in long-range disorder in a glass with increased cooling rate causes a decrease in activation energy and preexponential factor. Compared to the glass formation by the melt-quench method, the film formation is a process that corresponds to a very slow cooling of a melt [1] and leads to a lower ionic conductivity.

Table 1. Comparison of conductivity at 25°C and activation energy for glass, polycrystals and thin film lithium phosphorus oxynitride materials.

Sample	$\sigma_{25^\circ\text{C}}$ (S·cm <sup>-1</sup> )	$E_a$ (eV)	$\sigma_0$ (S·cm <sup>-1</sup> ·K)
<b>Glasses</b>			
Li <sub>1.28</sub> PO <sub>3.14</sub>	$4.6 \times 10^{-8}$	0.65	$1.1 \times 10^6$
Li <sub>0.99</sub> PO <sub>2.55</sub> N <sub>0.30</sub>	$3.0 \times 10^{-7}$	0.60	$1.2 \times 10^6$
<b>Polycrystals</b>			
$\gamma$ -Li <sub>3</sub> PO <sub>4</sub>	$4.2 \times 10^{-18\text{a}}$	1.24	$1.0 \times 10^6$
Li <sub>2.88</sub> PO <sub>3.73</sub> N <sub>0.14</sub>	$1.4 \times 10^{-13\text{a}}$	0.97	$9.6 \times 10^5$
<b>Thin Films</b>			
Li <sub>1.15</sub> PO <sub>1.96</sub> N <sub>0.74</sub>	$1.4 \times 10^{-8}$	0.69 <sup>b)</sup>	$1.8 \times 10^{6\text{b)}$
Li <sub>5.80</sub> PO <sub>4.77</sub> N <sub>0.42</sub>	$8.9 \times 10^{-7}$	0.51 <sup>c)</sup>	$1.1 \times 10^{5\text{c)}$

a) Extrapolated data.

b) Least-square fit between 25°C - 100°C.

c) Least-square fit between 25°C - 60°C.

## CONCLUSIONS

Nitrogen incorporation into the structure increases the ionic conductivities of lithium phosphate glasses, polycrystals and thin films. The increase in ionic conductivity in the glasses and thin films is due to an increase in structural cross-linking. The ionic conductivity of polycrystalline Li<sub>2.88</sub>PO<sub>3.73</sub>N<sub>0.14</sub> is several orders of magnitude higher than that of  $\gamma$ -Li<sub>3</sub>PO<sub>4</sub> due to a lower activation energy which is attributed to the Li-site and anion-site vacancies and the expanded *a* and *b* cell dimensions. Among these materials, the amorphous lithium phosphorus oxynitride thin film, Li<sub>5.80</sub>PO<sub>4.77</sub>N<sub>0.42</sub>, deposited by sputtering Li<sub>3</sub>N + Li<sub>3</sub>PO<sub>4</sub> target in N<sub>2</sub> has the highest ionic conductivity ( $\sigma_{25^\circ\text{C}} \sim 8.9 \times 10^{-7}$  S·cm<sup>-1</sup>).

## ACKNOWLEDGMENTS

The authors thank Dr. N. J. Dudney for her critical reading of the manuscript and Mr. C. F. Luck for his help in thin film deposition. This research was sponsored by the Division of Materials Sciences, U. S. Department of Energy under contract No. DE-AC05-84OR21400 with Martin Marietta Energy Systems, Inc. The DOE sponsored appointment of BW and BSK to the Oak Ridge National Laboratory Postdoctoral Research Program which is administered by the Oak Ridge Institute for Science and Education.

## REFERENCES

1. J. B. Bates, N. J. Dudney, G. R. Gruzalski, R. A. Zuhr, A. Choudhury, C. F. Luck and

- J. D. Robertson, *Solid State Ionics* **53/56**, 647 (1992).
2. J. B. Bates, G. R. Gruzalski, N. J. Dudney and C. F. Luck, *Proc. 35th Power Sources Symp.*, p. 337 (1992).
3. J. B. Bates, N. J. Dudney, G. R. Gruzalski, C. F. Luck, X-H. Yu and S. D. Jones, *Solid State Tech.*, July, 59 (1993).
4. M. Doreau, A. Abou el Anouar and G. Robert, *Mat. Res. Bul.* **15**, 285 (1980).
5. A. Pradel, T. Pagnier and M. Ribes, *Solid State Ionics* **17**, 147 (1985).
6. B. C. Chakoumakos, J. A. Fernandez-baca and L. A. Boatner, *J. Solid State Chem.* **103**, 105 (1993).
7. B. Wang, B. C. Chakoumakos, B. C. Sales, B. S. Kwak, J. B. Bates, *J. Solid State Chem.*, in press.
8. A. C. Larson and R. B. Von Dreele, GSAS -- General Structure Analysis System, Rept. LA-UR-86-748, Los Alamos National Laboratory, Los Alamos, NM 87545, 1990.
9. H. M. Rietveld, *J. Appl. Crystallogr.* **2**, 65 (1969).
10. R. Marchand, D. Agliz, L. Boukbir, A. Quemerais, *J. Non-Cryst. Solids* **103**, 35 (1988).
11. C. D. Wagner, W. M. Riggs, L. E. Davis and J. F. Moulder, In Handbook of X-ray Photoelectron Spectroscopy; edited by G. E. Muilenberg (Perkin-Elmer Corporation: Eden Prairie, MN, 1979).
12. B. Carette, M. Ribes and J. L. Souquet, *Solid State Ionics* **9/10**, 735 (1983).
13. M. Tatsumisago, K. Yoneda, N. Machida and T. Minami, *J. Non-Cryst. Solids* **95/96**, 857 (1987).
14. H. Unuma, K. Komori and S. Saka, *J. Non-Cryst. Solids* **95/96**, 913 (1987).
15. O. L. Anderson and D. A. Stuart, *J. Am. Ceram. Soc.* **37**, 573 (1954).
16. H. E. Swanson, M. C. Morris, E. H. Evans and L. Ulmer, *Natl. Bur. Stand. (U. S.) Monogr.* **25**, 39 (1964).
17. C. Keffer, A. Mighell, F. Mauer, H. Swanson and S. Block, *Inorg. Chem.* **6**, 119 (1969).
18. W. H. Baur, *Inorg. Nucl. Chem. Lett.* **16**, 525 (1980).
19. J. Zemmann, *Acta Cryst.* **13**, 863 (1960).
20. H. Y-P. Hong, *Mat. Res. Bull.* **13**, 117 (1978).
21. N. J. Dudney, J. B. Bates and J. D. Robertson, *J. Vac. Sci. Technol.* **A11**, 377 (1993).
22. A. Pradel and M. Ribes, *Mat. Sci. Eng.* **B3**, 45 (1989).

## STRUCTURAL CHEMISTRY OF ALKALINE EARTH HEXA-ALUMINATES

JAE-GWAN PARK AND A. N. CORMACK

New York State College of Ceramics at Alfred University, Alfred, NY 14802, U.S.A.

### ABSTRACT

Computer-based atomistic simulation techniques have been used to investigate the crystal chemistry and phase relationships in alkaline earth hexa-aluminates. The lattice energies for hexa-aluminate-related structural models are calculated and successfully predict that barium prefers the  $\beta$ -alumina-type structures with charge-balancing defects, whilst calcium or strontium prefers the ideal magnetoplumbite structure. In the case of magnesium, it is predicted that it does not prefer a hexa-aluminate structure.

### INTRODUCTION

Hexa-aluminates commonly refer to hexagonal polyaluminates having a structure related to that of  $\beta$ -alumina ( $\beta$ , ideal formula  $\text{NaAl}_{11}\text{O}_{17}$ ) and magnetoplumbite (MP, ideal formula  $\text{SrAl}_{12}\text{O}_{19}$ ). The two parent structures,  $\beta$  and MP, are similar, characterized by hexagonal symmetry of space group  $\text{P6}_3/\text{mmc}$ . They are composed of spinel-structured blocks and mirror planes containing large cations. Each spinel block consists of four close-packed oxygen layers with aluminum ions in both octahedral and tetrahedral sites. The major difference between the two lies in the interspinel layer structures, which are loose-packed in  $\beta$  but close-packed in MP.

Experimental observations show that among the divalent alkaline earths, whilst Ca or Sr forms the ideal MP structure, Ba, however, is found to form two nonstoichiometric phases based on the  $\beta$  structure<sup>1-6</sup>. In the case of Mg, it does not form a hexa-aluminate phase.

In this paper, we aim to elucidate the fundamental reasons for the diverse structural chemistry through a systematic understanding of the structural stability and crystal chemistry, by using atomistic simulation techniques.

### COMPUTATIONAL TECHNIQUES

The lattice simulation techniques employed in this work have been described in a number of previous works for a wide range of ceramic oxides (see, for example, reference 7). In brief, the simulations are formulated within the framework of the Born model which treats the ionic solid as a collection of point ions with short range forces acting between them. The lattice interactions, as defined through interatomic pair potentials, are calculated explicitly and ions are relaxed to zero force using a second derivative Newton-Raphson minimization procedure. Details of the procedure have been outlined by Cormack<sup>8</sup>. The electronic polarization effects of the lattice are taken into account by means of the Dick-Overhauser shell model<sup>9</sup>. The interatomic potentials and shell model parameters used in this study are taken from the compilation of Lewis and Catlow<sup>10</sup>. The validity of these "empirically fitted" potential parameters in the simulation of hexa-aluminates is fully discussed in one of our recent works<sup>11</sup>.

### STRUCTURE MODELS FOR SIMULATION

The structure models for perfect lattice simulation, which are necessary to investigate the relative stabilities of related phases of hexa-aluminates, are described as follows. Structural analogues of a particular model have the same input structure as the original model except for the replacement of the alkaline earths. The  $\beta$  structure used, as a reference point for the input models, is an idealized modification of the structure of sodium  $\beta$ -alumina reported by Peters *et*

*al.*<sup>12</sup>: the large cation and the oxygen in the mirror plane are assumed to be only at the 2d BR (Beevers-Ross) site and at the 2c site, respectively.

### **Magnetoplumbite, MP**

The input model structure for simulation of the magnetoplumbites is the x-ray structure reported by Lindop *et al.*<sup>13</sup> for strontium magnetoplumbite.

### **Hexa-aluminate phase I, $\beta(I)$**

The input structures for simulation of the two non-stoichiometric  $\beta$ -type hexa-aluminate phases,  $\beta(I)$  and  $\beta(II)$ , are based on the structure models proposed for Ba hexa-aluminates. The crystal structure of Ba- $\beta(I)$  is well characterised in the two independent studies<sup>14, 15</sup>. In the proposed structure, there are two kinds of half unit cell: one is a perfect half cell having the ideal  $\beta$  structure, and the other is a defect half cell containing a Ba vacancy and a so-called Reidingen defect, a string of point defects running parallel to the *c* axis:  $V_{Al}-Al_i-O_i-Al_i-V_{Al}$  in Kroger-Vink notation. The ratio of the perfect to the defect cell is three to one, for charge neutrality reasons. A random distribution of the two half cells was inferred from the lack of superstructure reflections. An input structure model for this phase is generated assuming that it has a superstructure based on a  $2a \times 2a \times c$  quadruple cell of  $\beta$ . The superstructure cell, the formula of which becomes  $Ba_6Al_{18}O_{138}$ , contains eight half cells of  $\beta$ , among which six are the perfect and two are the defect cells. The two defect half cells may be distributed in various ways within the supercell. Our simulation results<sup>16</sup>, however, showed that the lattice energy of the supercell was almost independent of the distribution of the defects, explaining the absence of a superstructure in  $\beta(I)$ . In this study, therefore, one input model is commonly examined for the  $\beta(I)$  analogues of other alkaline earths.

### **Hexa-aluminate phase II, $\beta(II)$**

For Ba- $\beta(II)$ , on the other hand, the diffraction evidence suggests a  $\sqrt{3}a \times \sqrt{3}a \times c$  triple superstructure of  $\beta$ , and at least three different structure models have been proposed<sup>17-19</sup>. Our simulation study<sup>16</sup> on the defect structure of this phase revealed that, of the various models, that of Iyi *et al.*<sup>18</sup> was both energetically most favorable and structurally most compatible with experimental results. In their structure model, there are two kinds of basic cell: one is a perfect cell having the ideal  $\beta$  structure, and the other is a defect cell which contains the excess barium of this phase. There are two main features to this defect cell. One is the presence of three Reidingen defects located around a Ba vacancy in a mirror plane (the other mirror plane has the ideal  $\beta$  structure). The second feature is the existence of Ba interstitials within the spinel blocks. This interstitial Ba site requires removal of an aluminum ion and an oxygen ion in the spinel block, becoming coordinated by twelve oxygens. Charge neutrality requires a ratio of two perfect cells to one defect cell, with an ordered distribution to give the triple supercell structure. The formula of the supercell becomes  $Ba_7Al_{64}O_{103}$ . The input model for simulation of this  $\beta(II)$  is generated in a  $\sqrt{3}a \times \sqrt{3}a \times c$  supercell of  $\beta$ , in consideration of all the defects described above.

## **RESULTS AND DISCUSSION**

### **Equilibrated crystal structures**

#### ***1) Magnetoplumbites, MP:***

The calculated crystal structures of the models for MP's are given in Table I, in which the experimental x-ray structures<sup>13, 20</sup> of Sr and Ca MP's are also given for comparison. We can see

that the x-ray and the equilibrated structures of Ca and Sr MP's are in good agreement concerning both crystal symmetry and atomic coordinates. The success of these calculations in reproducing the complex MP structures allowed us to continue the calculations for other models.

Table I. Calculated crystal structures of models for the magnetoplumbites. Experimental structural parameters of Ca and Sr MPs are given in parentheses for comparison.

Ca-MP			Sr-MP			Ba-MP			Mg-MP		
a = 5.6435 (5.564)			a = 5.6581 (5.562)			a = 5.6793			a = 5.6297		
c = 21.5446 (21.892)			c = 21.6676 (21.972)			c = 21.8927			c = 21.3723		
c/a = 3.818 (3.935)			c/a = 3.829 (3.950)			c/a = 3.855			c/a = 3.796		
P6 <sub>3</sub> /mmc			P6 <sub>3</sub> /mmc			P6 <sub>3</sub> mc			P6 <sub>3</sub> /mmc		
Atom	Site	Coordinates	Atom	Site	Coordinates	Atom	Site	Coordinates	Atom	Site	Coordinates
Ca	2d	x 0.6667 (0.6667) z 0.2500 (0.2500)	Sr	2d	x 0.6667 (0.6667) z 0.2500 (0.2500)	Ba	2b	x 0.6667 z 0.2500	Mg	2d	x 0.6667 z 0.2500
Al(1)	2a	x 0.0000 (0.0000) z 0.0000 (0.0000)	Al(1)	2a	x 0.0000 (0.0000) z 0.0000 (0.0000)	Al(1)	2a	x 0.0000 z 0.0000	Al(1)	2a	x 0.0000 z 0.0000
Al(2)	2b	x 0.0000 (0.0000) z 0.2500 (0.2500)	Al(2)	2b	x 0.0000 (0.0000) z 0.2500 (0.2500)	Al(2)	2a	x 0.0000 z 0.2424	Al(2)	2b	x 0.0000 z 0.2500
Al(3)	4f	x 0.3333 (0.3333) z 0.0307 (0.0280)	Al(3)	4f	x 0.3333 (0.3333) z 0.0311 (0.0276)	Al(3)	2b	x 0.3333 z 0.0319	Al(3)	4f	x 0.3333 z 0.0301
						Al(3')	2b	x 0.3333 z 0.4688			
Al(4)	12k	x 0.1683 (0.1687) z 0.8912 (0.8911)	Al(4)	12k	x 0.1681 (0.1685) z 0.8923 (0.8918)	Al(4)	6c	x 0.1679 z 0.8941	Al(4)	12k	x 0.1685 z 0.8897
						Al(4')	6c	x 0.8315 z 0.1061			
Al(5)	4f	x 0.3333 (0.3333) z 0.1890 (0.1904)	Al(5)	4f	x 0.3333 (0.3333) z 0.1883 (0.1903)	Al(5)	2b	x 0.3333 z 0.1871	Al(5)	4f	x 0.3333 z 0.1899
						Al(5')	2b	x 0.3333 z 0.3127			
O(1)	4e	x 0.0000 (0.0000) z 0.1481 (0.1501)	O(1)	4e	x 0.0000 (0.0000) z 0.1474 (0.1481)	O(1)	2a	x 0.0000 z 0.1479	O(1)	4e	x 0.0000 z 0.1488
						O(1')	2a	x 0.0000 z 0.8578			
O(2)	4f	x 0.3333 (0.3333) z 0.9465 (0.9445)	O(2)	4f	x 0.3333 (0.3333) z 0.9471 (0.9462)	O(2)	2b	x 0.3333 z 0.9482	O(2)	4f	x 0.3333 z 0.9458
						O(2')	2b	x 0.3333 z 0.5528			
O(3)	6h	x 0.1827 (0.1806) z 0.2500 (0.2500)	O(3)	6h	x 0.1829 (0.1822) z 0.2500 (0.2500)	O(3)	6c	x 0.1827 z 0.2487	O(3)	6h	x 0.1824 z 0.2500
O(4)	12k	x 0.1547 (0.1549) z 0.0524 (0.0524)	O(4)	12k	x 0.1543 (0.1552) z 0.0520 (0.0523)	O(4)	6c	x 0.1534 z 0.0522	O(4)	12k	x 0.1552 z 0.0529
						O(4')	6c	x 0.8452 z 0.4499			
O(5)	12k	x 0.5021 (0.5036) z 0.1462 (0.1501)	O(5)	12k	x 0.5006 (0.5025) z 0.1444 (0.1476)	O(5)	6c	x 0.4990 z 0.1421	O(5)	12k	x 0.5043 z 0.1487
						O(5')	6c	x 0.5013 z 0.8580			

An interesting and important feature in the equilibrated structures is that, whilst Mg-, Ca-, and Sr-MP maintain the ideal symmetry P6<sub>3</sub>/mmc, Ba-MP loses the mirror plane symmetry perpendicular to the c axis, resulting in P6<sub>3</sub>mc symmetry. The barium, aluminum (Al(2)), and three oxygen ions (O(3)) in the mirror plane of the MP structure can be no longer in a plane but in a slab. This is due to the fact that the large ionic size of barium ion does not allow the coplanar arrangement of those ions, in conjunction with the atomic arrangement in the spinel block layers. This intrinsically low symmetry of Ba-MP may be closely related to its instability. In the case of Mg, in spite of relatively small ionic radius, it seems to form an ideal mirror plane arrangement and thus a stable MP structure, from the symmetry viewpoint. This is not the case, however, from the energetical viewpoint, as discussed in a later section.

It is noteworthy that the values of c/a of the equilibrated structures increase with increasing ionic radius of the alkaline earth ion. This increase is mainly due to an increase in the c parameter. This structural behavior, which is also found in the equilibrated structures of the  $\beta$ -type compounds,  $\beta$ (I) and  $\beta$ (II), in following sections, is similar to that observed in the  $\beta$ -aluminas of various monovalent cations<sup>21</sup>. The c/a ratio may be used as a criterion for determining the structural type of hexa-aluminates:  $\beta$ -type compounds usually have the ratios of about 4.02, whereas MP-type ones about 3.94<sup>21-23</sup>.

## 2) Hexa-aluminate phase I, $\beta(I)$ :

The equilibrated structures of Ba- $\beta(I)$  and its Sr, Ca, and Mg analogues do not have an exact hexagonal structure, but a pseudo-hexagonal one, as shown in Table II. The space group symmetries and corresponding cell parameters of the exact symmetry cells of the equilibrated  $\beta(I)$ 's are also given in the table.

Table II. The cell parameters of the equilibrated pseudo-hexagonal supercells and their exact symmetry cells for Ba- $\beta(I)$  and its analogues. (Units: Å and degree)

Model	Pseudo-hexagonal cell			Exact symmetry cell				Axes relations
	a' $\alpha'$	b' $\beta'$	c' $\gamma'$	a" $\alpha''$	b" $\beta''$	c" $\gamma''$	Space group	
Ba- $\beta(I)$	11.2510 90.0000	11.2510 90.0000	22.7539 118.4421	11.5149 90.0000	19.3326 90.0000	22.7539 90.0000	Cmcm	a' + b'; -a' + b'; c'
Sr- $\beta(I)$	11.2440 90.0000	11.2440 90.0000	22.5505 118.4483	11.5066 90.0000	19.3211 90.0000	22.5505 90.0000	Cmcm	a' + b'; -a' + b'; c'
Ca- $\beta(I)$	11.2475 90.0000	11.2475 90.0000	22.3679 118.4670	22.3679 90.0000	19.3291 90.0000	11.5071 90.0000	Ama2	c'; -a' + b'; a' + b'
Mg- $\beta(I)$	11.2255 89.7383	11.2255 89.7383	22.2598 118.3279	11.5080 90.0000	19.2773 90.5105	22.2598 90.0000	C1c1	a' + b'; -a' + b'; c'

In the equilibrated structures of Ba-, Sr-, and Ca- $\beta(I)$ , though most of the  $\beta$ -type structural features, including the mirror plane symmetry perpendicular to the c axis, are maintained, the interaxial angles  $\gamma$  deviate slightly from 120°, resulting in orthorhombic structures. These pseudo-hexagonal structures, however, seem to result from the assumption of a superstructure which is lacking in the real system, rather than being inherent properties. If the random distribution of the defect half cells throughout the crystal is taken into account (by, for example, using a bigger supercell in the calculations), the angle  $\gamma$  may have the hexagonal value, and accordingly the structure may have a hexagonal symmetry. A structural feature worthy of notice is that the alkaline earth ion is equilibrated to the ideal cation site in the mirror plane only in the Ba- $\beta(I)$ , but not in the Ca and Sr analogues. In the equilibrated structure of Mg- $\beta(I)$ , on the other hand, the atomic arrangement in the interspinel layer is much disturbed; it loses the mirror plane symmetry and acquires a monoclinic structure.

## 3) Hexa-aluminate phase II, $\beta(II)$ :

The space group symmetries and lattice parameters of the equilibrated supercells of the models for Ba- $\beta(II)$  and its analogues are shown in Table III. The equilibrated structure and symmetry (P62m) of Ba- $\beta(II)$  are consistent with those observed for Ba(20% Pb)- $\beta(II)$  by Iyi *et al.*<sup>18</sup> The detailed discussion on this is given in reference 16.

As can be seen in Table III, the Sr analogue forms an isostructure with Ba- $\beta(II)$ . In these structures, the perfect interspinel layers maintain the ideal  $\beta$  structure, whilst the defect mirror plane regions undergo some structural relaxations from the ideal  $\beta$ -type structure: Both the interstitial oxygens at the mO (mid-oxygen) sites around the Ba vacancy and the oxygens at the ideal 2c sites in the defect mirror plane are relaxed towards the adjacent aBR (anti-Beevers-Ross) sites, due to the repulsion between them, still, however, maintaining the symmetry.

On the other hand, the Ca analogue is equilibrated to a pseudo-hexagonal (exactly, an orthorhombic) structure due to the slight deviation of the interaxial angle  $\gamma$  from 120°. The perfect interspinel layer, though maintaining the mirror plane symmetry perpendicular to the c axis, is equilibrated to a relaxed structure, unlike the layer in Ba- or Sr- $\beta(II)$ ; the Ca and O ions are slightly off-positioned from the ideal 2d and 2c sites, respectively. It suggests that the atomic arrangement of the ideal  $\beta$  structure is not suitable for Ca, due to its smaller size than Ba

or Sr. The equilibrated structure in the defect mirror plane region is isostructural with that of Ba- $\beta$ (II).

Table III. The cell parameters of the equilibrated (pseudo-)hexagonal supercells and their exact symmetry cells for Ba- $\beta$ (II) and its analogues. (Units: Å and degree).

Model	(Pseudo-)Hexagonal cell			Exact symmetry cell				Space group	Axes relations
	a' $\alpha'$	b' $\beta'$	c' $\gamma'$	a'' $\alpha''$	b'' $\beta''$	c'' $\gamma''$			
Ba- $\beta$ (II)	9.8835 90.0000	9.8835 90.0000	22.9701 120.0000	9.8835 90.0000	9.8835 90.0000	22.9701 120.0000		P6 <sub>2</sub> m	a'; b'; c' (origin shifting)
Sr- $\beta$ (II)	9.8607 90.0000	9.8607 90.0000	22.7280 120.0000	9.8607 90.0000	9.8607 90.0000	22.7280 120.0000		P6 <sub>2</sub> m	a'; b'; c' (origin shifting)
Ca- $\beta$ (II)	9.8680 90.0000	9.8680 90.0000	22.5632 120.3667	22.5632 90.0000	17.1234 90.0000	9.8133 90.0000		Amm2	c'; -a' + b'; a' + b'
Mg- $\beta$ (II)	9.8406 91.4719	9.8328 89.2650	22.3977 119.9746	9.8328 90.0000	17.0487 91.4719	22.3977 90.0000		C1m1	a' + b'; -a' + b'; c'

In the case of the Mg analogue, while the defect mirror plane region is almost isostructural with others, the perfect mirror plane region undergoes substantial structural disturbances which lead the distortion of the whole structure to a monoclinic cell.

#### Structural stabilities of hexa-aluminates in terms of lattice energies

The equilibrated lattice energies of the models for alkaline earth magnetoplumbite hexa-aluminates are listed in Table IV, being compared with sums of lattice energies of the two-phase mixtures---a binary oxide mixture and a  $\beta$ -type two-phase mixture---which are equivalent in composition to the magnetoplumbites.

Table IV. Calculated lattice energies of magnetoplumbites, being compared with the sums of those of compositionally equivalent two-phase mixtures. Values are in eV per formula unit. ( $\beta$ (I) =  $M_6Al_{88}O_{138}$ ,  $\beta$ (II) =  $M_7Al_{64}O_{103}$ )

M	Binary oxides mixture 2MO + 12Al <sub>2</sub> O <sub>3</sub>	Magnetoplumbite M <sub>2</sub> Al <sub>24</sub> O <sub>38</sub>	$\beta$ -type two-phase mixture (1/5.8) $\beta$ (I) + (0.8/5.8) $\beta$ (II)
Ba	-1967.98	-1968.08	<b>-1969.87</b>
Sr	-1972.86	<b>-1975.24</b>	-1973.83
Ca	-1977.41	<b>-1979.23</b>	-1976.52
Mg	<b>-1986.29</b>	-1983.43	-1981.28

As can be seen in the table, the calculated lattice energies predict the diverse structural behavior between alkaline earths with respect to the formation of hexa-aluminates, being consistent with experimental observations: whereas Ba prefers the nonstoichiometric  $\beta$ -type structures, Sr and Ca prefer the ideal MP structure, and Mg does not adopt any hexa-aluminate structure, from the energetical point of view. In the case of Mg, the sum of lattice energies of the spinel and aluminum oxide mixture (2MgAl<sub>2</sub>O<sub>4</sub> + 10Al<sub>2</sub>O<sub>3</sub>) is calculated to be -1989.25 eV per the formula unit, indicating the stability of spinel phase. It has been revealed by experiments and simulations that, as in the spinel, Mg prefers the inner spinel block tetrahedral site in hexa-aluminates<sup>24, 25</sup>. The tetrahedral site preference of Mg in aluminates does not permit the formation of an MP or a  $\beta$ -type structure, but a spinel which is the only intermediate



compound between MgO and Al<sub>2</sub>O<sub>3</sub>. This is clearly confirmed by our calculations.

It can be pointed out that the thermodynamic instabilities of the analogues for a stable form are connected with the structural disturbances or the lowering of crystal symmetry in their structures, as mentioned in earlier sections.

## SUMMARY

We have examined the crystal chemistry and phase stabilities in alkaline earth hexa-aluminates by using atomistic simulation methods. Our calculations clearly show that unlike Ca or Sr counterparts, Ba hexa-aluminate is not stable in the MP structure but will form a two-phase mixture with  $\beta$ -type structures. It is also shown that Mg does not form a hexa-aluminate structure. These predictions, consistent with experiments, allow us to investigate further the complex defect and structural chemistries in various hexa-aluminates.

## ACKNOWLEDGMENTS

The U. S. Department of Energy, Office of Basic Energy Sciences is thanked for financial support (Grant # DE-FG02-91ER45451). Some of the calculations reported here were performed at the Cornell National Supercomputer Facility, which is funded in part by New York State, National Science Foundation and IBM Corporation.

## REFERENCES

1. F. Haberey, G. Oehlschlegel, and K. Sahl, *Ber. Dtsch. Keram. Ges.*, **54**, 373 (1977).
2. S. Kimura, E. Bannai, and I. Shindo, *Mater. Res. Bull.*, **17**, 209 (1982).
3. P.E.D. Morgan and T.M. Shaw, *Mater. Res. Bull.*, **18**, 539 (1983).
4. N. Iyi, S. Takekawa, Y. Bando, and S. Kimura, *J. Solid State Chem.*, **47**, 34 (1983).
5. N. Yamamoto and M. O'Keeffe, *Acta Cryst. B*, **40**, 21 (1984).
6. B.M.J. Smets and J.G. Verlijsdonk, *Mat. Res. Bull.*, **21**, 1305 (1986).
7. C.R.A. Catlow and W.C. Mackrodt, in *Computer Simulation of Solids*, edited by C.R.A. Catlow and W.C. Mackrodt (Springer-Verlag, Berlin, 1982) p. 3.
8. A.N. Cormack, *Solid State Ionics*, **8**, 187 (1983).
9. B.G. Dick and A.W. Overhauser, *Phys. Rev.*, **112**, 90 (1958).
10. G.V. Lewis and C.R.A. Catlow, *J. Phys. C: Solid State Phys.*, **18**, 1149 (1985).
11. J.-G. Park and A.N. Cormack, submitted to *Phil. Mag. B*.
12. C.R. Peters, M. Bettman, J.W. Moore, and M.D. Glick, *Acta Cryst.*, **B**, **27**, 1826 (1971).
13. A.J. Lindop, C. Matthews, and D.W. Goodwin, *Acta Cryst.*, **B**, **31**, 2940 (1975).
14. F.P.F. van Vekel, H.W. Zandbergen, G.C. Verschoor, and D.J.W. IJdo, *Acta Cryst.*, **C**, **40**, 1124 (1984).
15. N. Iyi, Z. Inoue, S. Takekawa, and S. Kimura, *J. Solid State Chem.*, **52**, 66 (1984).
16. J.-G. Park and A.N. Cormack, submitted to the *J. Solid State Chem.*
17. H.W. Zandbergen, F.C. Mijlthoff, D.J.W. IJdo, and G. van Tendeloo, *Mater. Res. Bull.*, **19**, 1443 (1984).
18. N. Iyi, Z. Inoue, S. Takekawa, and S. Kimura, *J. Solid State Chem.*, **60**, 41 (1985); N. Iyi, Y. Bando, S. Takekawa, Y. Kitami, and S. Kimura, *ibid.*, **64**, 220 (1986).
19. T.R. Wagner and M. O'Keeffe, *J. Solid State Chem.*, **73**, 19 (1988).
20. K. Kato and H. Saalfeld, *Neues Jahrb. Mineral. Abh.*, **109**, 192 (1968).
21. J.M.P.J. Verstegen and A.L.N. Stevels, *J. Lumin.*, **9**, 406 (1974).
22. A.L.N. Stevels and A.D.M. Schrama-de Pauw, *J. Electrochem. Soc.; Solid-State Science and Technology*, **123**, 691 (1976).
23. P.E.D. Morgan and J.A. Miles, *J. Am. Ceram. Soc.*, **69**, C157-C159 (1986).
24. J.O. Thomas and G.C. Farrington, *Acta Cryst.*, **B**, **39**, 227 (1983).
25. L. Xie and A.N. Cormack, *Materials Letters*, **9**, 474 (1990).

## STRAIN DRIVEN TWO-DIMENSIONAL PHASE TRANSITION IN $\text{PbSnF}_4$ SUPERIONIC CONDUCTOR

GEORGES DENES, M.C. MADAMBA AND J.M. PARRIS

Concordia University, Laboratory of Solid State Chemistry and Mössbauer Spectroscopy, Laboratories for Inorganic Materials, Department of Chemistry and Biochemistry, 1455 De Maisonneuve Blvd. W., Montreal, Quebec, H3G 1M8, Canada

### ABSTRACT

When a minor amount of HF is added to the  $\text{SnF}_2$  reacted with lead nitrate in aqueous solutions to prepare  $\text{PbSnF}_4$ , a phase transition from tetragonal  $\alpha\text{-PbSnF}_4$  to orthorhombic  $\alpha\text{-PbSnF}_4$  takes place. The transition is essentially bidimensional and takes place in the  $(\vec{a}, \vec{b})$  plane of the unit-cell. The compactness of the structure increases at the transition. No essential structural change occurs: the transition is most likely displacive and it is driven by bidimensional nonuniform strain acting along the  $\vec{a}$  and  $\vec{b}$  axes of the unit-cell. This transition is similar to ferroic transitions (in this case, paraelastic  $\rightarrow$  ferroelastic). No detectable change of chemical composition occurs at the transition, and the reason why the presence of HF in the reaction mixture causes the transition remains unknown.

### INTRODUCTION

Tetragonal  $\alpha\text{-PbSnF}_4$  was first prepared in 1967 by Donaldson and Senior, by adding an aqueous solution of lead nitrate to a solution of  $\text{SnF}_2$  [1]. In 1975, Denes et al. confirmed the method of preparation and the tetragonal symmetry for  $\text{PbSnF}_4$  prepared either from aqueous solutions or by direct reaction of  $\text{SnF}_2$  and  $\text{PbF}_2$  at 250 °C [2]. High temperature phases tetragonal  $\beta\text{-PbSnF}_4$  and cubic  $\gamma\text{-PbSnF}_4$  have also been discovered [3]. The structures of all the polymorphic forms of  $\text{PbSnF}_4$  are derived from the  $\beta\text{-PbF}_2$  fluorite-type structures, either by tetragonal distortions due to ordering between Pb and Sn (in  $\alpha\text{-}$  and  $\beta\text{-PbSnF}_4$ ), or by local site distortions only, when Pb and Sn are fully disordered and the cubic unit-cell type of  $\beta\text{-PbF}_2$  is preserved (in  $\gamma\text{-PbSnF}_4$ ) [4-6]. In all structures of  $\text{PbSnF}_4$ , the tin(II) non-bonded electron pair (lone pair) is stereoactive, whereas that of lead(II) is non-stereoactive [7]. The structure of  $\text{BaSnF}_4$ , isostructural to  $\alpha\text{-PbSnF}_4$ , is shown on figure 1.  $\text{PbSnF}_4$  is the highest performance fluoride ion conductor [8]. This makes it a good candidate for applications in solid state batteries and sensors. Recently, it was used for the construction of an amperometric oxygen sensor [9].

Reau et al. claimed that  $\text{PbSnF}_4$  prepared by the aqueous route is orthorhombic instead of tetragonal [3]. Then, Perez et al. revised the claim to monoclinic [3]. Our earlier attempts to identify an orthorhombic or a monoclinic distortion produced only

tetragonal  $\alpha$ -PbSnF<sub>4</sub> [2-5]. Now, we have discovered the reason for this apparent discrepancy between the results of different groups: both tetragonal and orthorhombic PbSnF<sub>4</sub> can be obtained by reaction in aqueous solutions, depending on preparation conditions: addition of HF to the solution of SnF<sub>2</sub> gives the orthorhombic phase (o-PbSnF<sub>4</sub>), whereas in the absence of HF, the tetragonal phase ( $\alpha$ -PbSnF<sub>4</sub>) is obtained. An X-ray diffraction study of the  $\alpha \rightarrow$  o-PbSnF<sub>4</sub> phase transition upon addition of HF to the reaction mixture is presented here.

## EXPERIMENTAL

All reactions were carried out by adding dropwise a 1.7M aqueous solution of Pb(NO<sub>3</sub>)<sub>2</sub> to a 1.5M fresh aqueous (pure H<sub>2</sub>O or aqueous HF) solution of SnF<sub>2</sub> upon stirring. The volumes of the two solutions were chosen to give an overall Pb/Sn ratio of 0.2. The ratio of the volume of 40% aqueous HF to the total volume of the SnF<sub>2</sub> aqueous solution was varied from 0 to 0.57. The reactions were carried out in air at ambient temperature in a polythene beaker. A white precipitate formed immediately on contact between the two solutions. Then, the precipitate was filtered, washed several times with water and allowed to dry in air at room temperature.

X-ray diffraction was performed on a Philips X-ray powder diffractometer that has been automated with the SIE112 Sietronics system. Background subtraction and peak search were carried out by use of the SIE112 software. The absolute angular values were calibrated with a SiO<sub>2</sub> external standard sample and additional control of peak position and linewidth were performed by using KCl as an internal standard.

## RESULTS AND DISCUSSION

### Bidimensionality of the transition

The X-ray powder diffraction patterns of  $\alpha$ -PbSnF<sub>4</sub> and o-PbSnF<sub>4</sub> are shown on figure 2. The Bragg peaks observed for  $\alpha$ -PbSnF<sub>4</sub> are characteristic of a large tetragonal distortion ( $c/a = 0.956$  in  $\beta$ -PbF<sub>2</sub> axes, compared to 1 in cubic) as can be seen by the splitting of the (200) peak of  $\beta$ -PbF<sub>2</sub> to (110) and (004). The changes of the Miller indices relative to  $\beta$ -PbF<sub>2</sub> are due to: (i) the 45° rotation of the  $\vec{a}$  and  $\vec{b}$  axes in the  $(\vec{a}, \vec{b})$  plane, which is due to the loss of the F Bravais lattice (e.g. (200) of  $\beta$ -PbF<sub>2</sub> gives (110)), and (ii) the doubling of the  $\vec{c}$  axis (e.g. (002) of  $\beta$ -PbF<sub>2</sub> gives (004)) due to Pb/Sn ordering along the  $\vec{c}$  axis. In addition, the loss of the F Bravais lattice, the tetragonal distortion and the doubling of  $c$  also gives rise to new peaks at low angles (e.g. (001 and (002)).

The diffraction pattern of o-PbSnF<sub>4</sub> is very similar to that of the  $\alpha$ -phase. The main difference is the splitting of some peaks, which are characteristic of a further symmetry loss. These changes are in agreement with the results of Reau et al., and

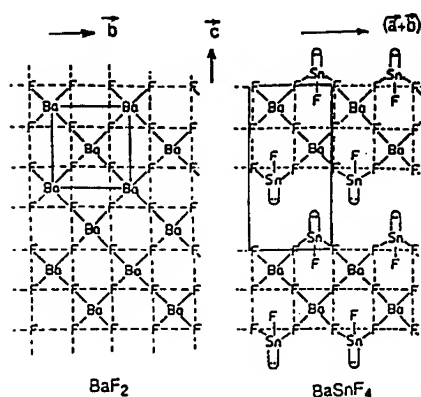


Figure 1: Projection of the structures of  $\text{BaF}_2$  (isostructural to  $\beta\text{-PbF}_2$ ) and  $\text{BaSnF}_4$  (isostructural to  $\alpha\text{-PbSnF}_4$ ) in the  $(\vec{b}, \vec{c})$  plane ( $\beta\text{-PbF}_2$  axes).

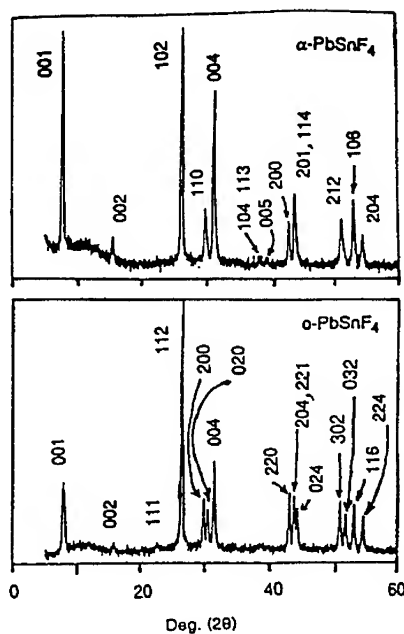


Figure 2: X-ray powder diffraction patterns of  $\alpha\text{-PbSnF}_4$  and  $\text{o-PbSnF}_4$ .

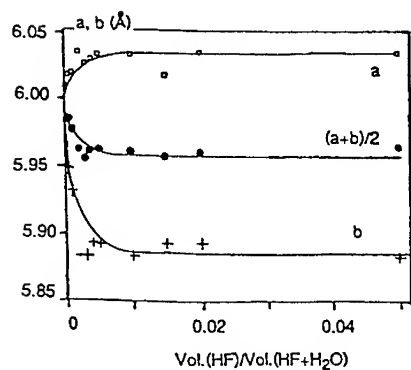


Figure 3: Unit-cell parameters  $a$  and  $b$  (in orthorhombic axes) versus  $\text{Vol.}(\text{HF})/\text{Vol.}(\text{HF}+\text{H}_2\text{O})$

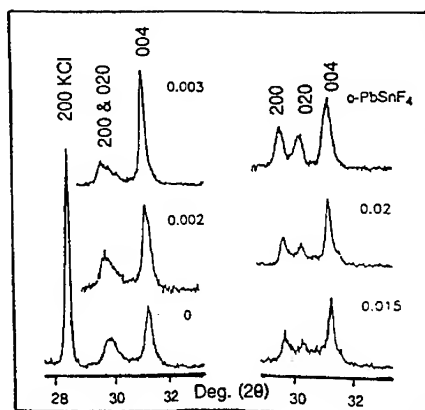


Figure 4: Profile of the  $(110)_\alpha \rightarrow (200)_o$  and  $(020)_o$  peaks versus  $\text{Vol.}(\text{HF})/\text{Vol.}(\text{HF}+\text{H}_2\text{O})$

can be fully justified in an orthorhombic unit-cell [3]. There is no need to add a further symmetry break to monoclinic as suggested by Perez et al. [3]. The unit-cell parameters of the two phases of  $\text{PbSnF}_4$  are compared to those of  $\beta\text{-PbF}_2$  in Table I.

Table I: Unit-cell parameters of  $\beta\text{-PbF}_2$ ,  $\alpha\text{-PbSnF}_4$  and  $\text{o-PbSnF}_4$  (Note: all unit-cell parameters have been converted to the  $\beta\text{-PbF}_2$  unit-cell axes for computing ratios of unit-cells and percentage changes).

	$\beta\text{-PbF}_2$	$\alpha\text{-PbSnF}_4$		$\text{o-PbSnF}_4$		
	Unit-cell	Unit-cell	% change from $\beta\text{-PbF}_2$	Unit-cell	% change from	
					$\beta\text{-PbF}_2$	$\alpha\text{-PbSnF}_4$
a ( $\text{\AA}$ )	5.940	4.220	0.69	6.009	1.16	0.69
b ( $\text{\AA}$ )	5.940	4.220	0.69	5.885	-0.93	-1.39
c ( $\text{\AA}$ )	5.940	11.415	-3.91	11.409	-3.96	-0.05
V ( $\text{\AA}^3$ )	209.6	203.3	-3.01	403.5	-3.75	-0.77
c/a	1.000	0.956	-	0.949	-	-
c/b	1.000	0.956	-	0.969	-	-
b/a	1.000	1.000	-	0.979	-	-

Table I shows that the  $\alpha \rightarrow \text{o-PbSnF}_4$  is mostly a bidimensional phase transition taking place in the  $(\vec{a}, \vec{b})$  plane of the unit-cell. Indeed, a increases by 0.69% and b decreases by 1.39 %, whereas the change of c (0.05% decrease) is very minor. The slight shrinkage along  $\vec{c}$  is undoubtedly due to a more efficient stacking of the layers (see fig. 1), which is made possible by the shifts of the atoms within the layers when the tetragonal symmetry is broken.

#### Stress induced transition in the $(\vec{a}, \vec{b})$ plane

The  $\alpha \rightarrow \text{o-PbSnF}_4$  transition is a continuous transition: it starts with the use of a very minor amount of HF (for a  $\text{HF}/(\text{HF}+\text{H}_2\text{O})$  volume ratio of the  $\text{SnF}_2$  solution used for the synthesis as low as 0.001). The orthorhombic splitting keeps increasing up to a volume ratio of ca. 0.005, when constant unit-cell parameters are reached (fig. 3). The values given in Table I are those found at full splitting.

Figure 4 shows the evolution of the profile of the (110) peak of  $\alpha\text{-PbSnF}_4$  versus the ratio  $\text{Vol.}(\text{HF})/\text{Vol.}(\text{HF}+\text{H}_2\text{O})$  as it splits to give the (200) and (020) peaks of o-

PbSnF<sub>4</sub>. For tetragonal  $\alpha$ -PbSnF<sub>4</sub>, when no HF is used, the (110) peak is broadened, compared to the (200) peak of the KCl internal standard. This broadening increases asymmetrically towards higher angles and is observed for a volume ratio as low as 0.002. At a volume ratio of 0.015, the (200) and (020) peaks of o-PbSnF<sub>4</sub> have started emerging, however, there is still much background underneath, and for a volume ratio of 0.02, the two peaks are now much cleaner, and for 0.57, much of this background has disappeared.

Line broadening is usually due to the small size of the particles in the direction perpendicular to the family of planes responsible for the peak. The moderate broadening of the (004) peak could be due to the small thickness of platelet-like crystallites, which is explained by the cleavage originating in the lack of bonding between sheets and high repulsions due to adjacent layers of lone pairs facing each other on adjacent sheets. However, the plane of the sheets are polymerized and contain strong metal-fluorine bonds, which give rise to large surface platelets (several millimeters edge) parallel to the  $(\vec{a}, \vec{b})$  plane of the unit-cell, therefore, broadening of the (110) peak of  $\alpha$ -PbSnF<sub>4</sub> cannot be due to the small size of the crystallites in the [110] direction. The reason for line broadening is nonuniform stress (uniform stress gives line shift without broadening) [10].

It results that  $\alpha$ -PbSnF<sub>4</sub> is stressed in the  $(\vec{a}, \vec{b})$  plane, that is the atoms would rather shift away from the tetragonal Wyckoff sites, however, they are held in by symmetry. When HF is used in the reaction, this stress increases, and it starts overcoming the symmetry constraints, at which point, orthorhombic splitting occurs in the highly stressed structure. As the amount of HF is increased further, the stability of the orthorhombic phase increases, and thus the stress decreases. For large amounts of HF, the orthorhombic structure is very stable and most of the stress has disappeared.

## CONCLUSION

Tetragonal  $\alpha$ -PbSnF<sub>4</sub>, stressed in the  $(\vec{a}, \vec{b})$  plane, is obtained when an aqueous solution of Pb(NO<sub>3</sub>)<sub>2</sub> is added to an aqueous solution of SnF<sub>2</sub>. If the solution of SnF<sub>2</sub> contains a very minor amount of HF, the stress increases. For larger amounts of HF, orthorhombic o-PbSnF<sub>4</sub> is obtained, and the stress decreases when the amount of HF used increases. The  $\alpha \rightarrow$  o-PbSnF<sub>4</sub> phase transition is a continuous transition, nearly purely bidimensional, taking place in the  $(\vec{a}, \vec{b})$  plane, and is driven by a large amount of stress acting in the same plane.  $\alpha$ -PbSnF<sub>4</sub> crystallizes "uncomfortably" in tetragonal, and is on the verge of distorting to orthorhombic. For unknown reasons, the presence of HF in the SnF<sub>2</sub> solution used for the reaction provides the mean for overcoming the tetragonal symmetry constraints. Within experimental precision, there is no change of chemical composition occurring at the transition. The transition is complex and proceeds according to the following steps, when the amount of HF used increases (the limits of each step are diffuse):

1. No HF: Stressed  $\alpha$ -PbSnF<sub>4</sub>;
2. HF/(HF+H<sub>2</sub>O) = 0 to 0.001: Stress increases;

3.  $\text{HF}/(\text{HF}+\text{H}_2\text{O}) = 0.001$  to  $0.005$ : Stress and orthorhombic splitting increase;  
 4.  $\text{HF}/(\text{HF}+\text{H}_2\text{O}) > 0.005$ : orthorhombic splitting is constant, stress decreases slowly.  
 The highly stressed region can be called a "transitional phase", which is found between the stressed tetragonal and the low stress orthorhombic. It is an intermediate phase, where an average of the  $\vec{a}$  and  $\vec{b}$  directions are observed, because these directions are becoming unequivalent, but are not sufficiently unequivalent yet to make the atomic positions stabilize in the orthorhombic Wyckoff sites. This instability generates a large amount of stress, which smears out the difference between the two directions. This makes the  $\alpha \rightarrow \text{o-PbSnF}_4$  transition similar to ferroic transitions (paraelastic  $\rightarrow$  ferroelastic), which take place upon cooling or increasing pressure. Like ferroic transitions, this is certainly also a displacive transition, although no structure of  $\text{o-PbSnF}_4$  is available to confirm it.

## REFERENCES

1. J.D. Donaldson and B.J. Senior, J. Chem. Soc. (A), **1967**, 1821.
2. G. Denes, J. Pannetier and J. Lucas, C. R. Acad. Sc. (Paris), Ser. C **280**, 831 (1975).
3. J.M. Reau, C. Lucat, J. Portier and P. Hagenmuller, Mat. Res. Bull. **13**, 877 (1978); J. Pannetier, G. Denes and J. Lucas, *ibid.*, **14**, 627 (1979); G. Perez, S. Vilminot, W. Granier, L. Cot, C. Lucat, J.M. Reau, J. Portier and P. Hagenmuller, *ibid.* **15**, 587 (1980).
4. G. Denes, T. Birchall, M. Sayer and M.F. Bell, Solid State Ionics **13**, 213 (1984).
5. T. Birchall, G. Denes, K. Ruebenbauer and J. Pannetier; J. Chem. Soc., Dalton Tr. **1981**, 2296; Hyperfine Interact. **29**, 1331 (1986).
6. G. Denes, Y.H. Yu, T. Tyliczszak and A.P. Hitchcock, J. Solid State Chem. **91**, 1 (1991); **104**, 239 (1993).
7. G. Denes, in Proceedings of the Second Nassau Mossbauer Conference, edited by C.I. Wynter and E.E. Alp (W.C. Brown Publishers, 1994), pp. 109-135.
8. J.M. Reau, C. Lucat, J. Portier, P. Hagenmuller, L. Cot and S. Vilminot, Mat. Res. Bull. **13**, 877 (1978); R. Kanno, S. Nakamura, K. Ohno and Y. Kawamoto, *ibid.*, **26**, 1111 (1991).
9. A. Wakagi and J. Kuwano, J. Mater. Chem. **41**, 973, (1994).
10. B.D. Cullity, Elements of X-ray Diffraction, 2nd ed. (Addiso-Wesley, Reading (1959), pp. 263-269, 444-453).

## ELECTRICAL CONDUCTIVITY AND RAMAN STUDIES OF $B_2O_3$ - $Na_2O$ - $NaI$ GLASS SYSTEMS

BYOUNG-KOO CHOI, KYOUNG-HEE SHIN AND HYO-KYOUNG LEE  
Department of science education, Dankook University, Yongsan, Seoul  
140-714, Korea

### ABSTRACT

Glasses of  $B_2O_3$ - $Na_2O$ - $NaI_2$  have been prepared over a wide range of compositions on the basis of a fixed O/B ratio and a fixed Na/B ratio, respectively. Raman spectra and the ionic conductivity have been measured to elucidate the role of the iodide. In the fixed O/B ratio, a drastic increase of the conductivity with the addition of iodide is observed. The conductivity results are found to be consistent with the Raman results. In the fixed Na/B ratio, the substitution of iodide does not influence significantly the glass structure as well as the ionic conductivity.

### INTRODUCTION

The ionic conductivity of alkali haloborate glasses has drawn significant interest for a considerable period of time. Extensive work has been performed on the physical properties of  $B_2O_3$ - $Li_2O$ - $LiX$  ( $X = F, Cl, Br, I$ ) glass systems [1-3]. Upon the addition of a modifier such as  $Li_2O$ , some fraction of the  $Li_2O$  dissociates, releasing free lithium ions and thus considerably increasing the ion conductivity of the glass. A further increase in the conductivity is achieved by adding a dopant such as  $LiX$ .

The Raman study of  $B_2O_3$ - $Li_2O$ - $LiX$  ( $X = Cl, Br$ ) glasses indicate that the spectra of the binary lithium borate glasses and ternary glasses are identical for glasses containing the same amount of  $Li_2O/B_2O_3$  [2,4,5]. It reveals that the glass structure depends on the O/B ratio and not on the halide content. In contrast, recent Raman study of lithium borate glasses shows that binary and ternary systems with constant O/B ratios do not exhibit identical boron-oxygen network due to interactions between the network and the anions of the doping salt [6]. In the Raman studies of ternary haloborate glasses, it has been frequently mentioned that fluorine participates in network formation forming  $BO_3F$  and  $BO_2F_2$  units, while chlorine and bromine enter interstitial positions [6-9]. In contrast, NMR study shows that fluorine and chlorine enter the network interstitially and so do not participate in network formation [10]. However, it was pointed out that the ambiguity on the network modifying property of halogens in the haloborate glasses might be caused by the lack of ability of experimental technique to identify specific polyborate units which correspond to intermediate range order [11].

The present work deals with Raman spectroscopic studies on a series of compositions in the  $B_2O_3$ - $Na_2O$ - $NaI_2$  glass systems, prepared on the basis of a fixed O/B ratio and a fixed Na/B ratio, respectively. Ionic conductivity investigations are also described and discussed with respect to structural modifications by the



introduction of iodide.

## EXPERIMENTAL

Glass samples were prepared by conventional glass melting and quenching techniques. Starting materials for the glasses were anhydrous reagent grade  $B_2O_3$ ,  $Na_2CO_3$  and NaI. They were mixed thoroughly and melted at 950°C for 30 minutes in air by using a covered platinum crucible to produce completely fused homogeneous melts. Wet chemical analysis indicated that the NaI contents do not deviate appreciably from the nominal concentrations.

The complex impedances were determined by means of a HP model 4192A LF impedance analyzer. The sample under investigation was mounted in an oven with platinum electrodes. Most of the measurements were performed with heating and cooling rates of 1°C/min with average measuring intervals 1°C. The complex impedance measured in the frequency range between 100 Hz and 1 MHz allowed us to obtain the direct current conductivity of the bulk glass by means of the usual impedance analysis.

The Raman spectrum was excited with 100 mW of 488.0 nm Argon laser light. The Stokes Raman light scattered was analyzed in the frequency-shifted range 10–1600  $cm^{-1}$  with a Jovin-Yvon U1000 double monochromator at a spectral resolution of 3  $cm^{-1}$ .

## RESULTS AND DISCUSSION

According to former observations, boron oxide glass is formed of an infinite network of boroxol groups  $B_3O_3$ , which forms a planar ring [3,12–14]. The spectrum of  $B_2O_3$  glass is dominated by a narrow, strongly polarized, intense band at 806  $cm^{-1}$ , which is assigned to the symmetric breathing vibration of the boroxol rings. In the binary glass of  $B_2O_3-xNa_2O$ , the 806  $cm^{-1}$  band reduces in intensity and a new band develops at 770  $cm^{-1}$  due to the increase of the fraction of 4-coordinated boron atoms. When x is increased further, there appears a progressive depolymerization of the borate network, through the formation of non-bridging oxygen(NBO)-containing borate units such as the metaborate rings and the pyroborates [3,13,14].

Figure 1 shows Raman spectrum of  $B_2O_3-xNa_2O-yNa_2I_2$  glass systems with x = 0.25 and 0.43, respectively. In the binary  $B_2O_3-0.25Na_2O$  glass, the line at 805  $cm^{-1}$  corresponding to the vibration of the boroxol ring is still present. When x = 0.25, most pronounced feature with the addition of NaI is the disappearance of the 805  $cm^{-1}$  band and the appearance of a shoulder at about 720  $cm^{-1}$  on the 770  $cm^{-1}$  band along with the decrease of frequency of the 770  $cm^{-1}$  band. It reveals that addition of iodide causes to increase the fraction of four-coordinated boron-atoms. The changes of the shape of the  $BO_4$  band suggest that iodine enters interstitial positions which produce braking of B-O-B links and formation of  $BO_4$  units, as was mentioned frequently in the haloborate glasses [6–9].

When x = 0.43, we observe the increase of the intensity of the band attributed to the vibrations of groups with NBO atoms at 960 and 1480  $cm^{-1}$  [13]. It reveals  $BO_4$  units are transformed into  $BO_3$  triangles and  $BO_3$  units with NBO atoms such as metaborate or ditriborate groups, indicating a decrease of the linkage of the

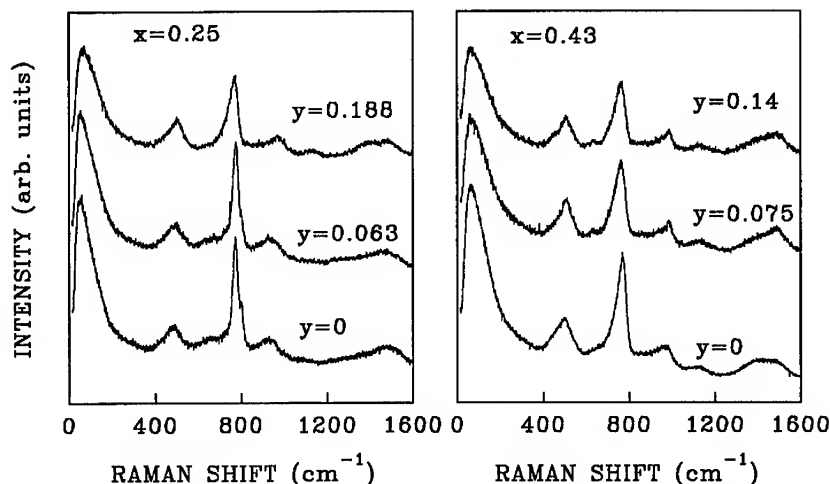


Fig.1 Raman spectra of  $B_2O_3$ - $xNa_2O$ - $yNa_2I_2$  glasses with fixed O/B ratios.

network and the expansion of the network. In addition, a new band at  $630\text{ cm}^{-1}$  appears with the addition of iodide, which is assigned to the ring-breathing vibration of ring-type metaborate units [15].

The ionic conductivity is measured for the glasses of same compositions to compare with the Raman results. Figure 2 shows the variation of the ionic conductivity at  $150^\circ\text{C}$  as a function of relative concentrations of  $Na_2I_2/Na_2O$ . Iodide additions result in drastic and non-linear increases in logarithmic conductivity, which cannot be accounted for by the increased number of charge carriers only. It is considered that the main reason for the large enhancement of the ionic conductivities is due to the structural modifications upon adding large iodine ions, which expands the lattice and modifies glass network, broadening the path windows and weakening also the Na-O bonds. It seems that migration rather than carrier concentration dominates the transport process.

For higher value of  $x$ , the conductivity increases more slowly with the iodine doping level. At low oxide contents, the number of

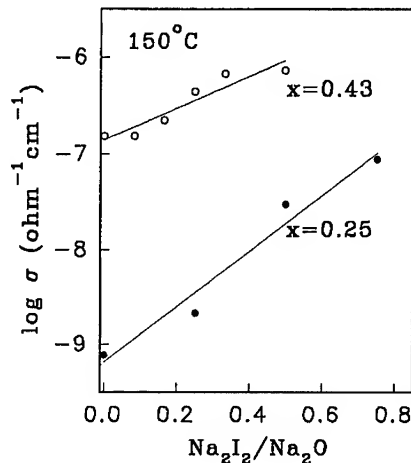


Fig.2 Conductivity vs. iodide addition for  $B_2O_3$ - $xNa_2O$ - $yNa_2I_2$  glasses with fixed O/B ratios.

$\text{BO}_4$  groups increases with the addition of  $\text{NaI}$ . The  $\text{BO}_4$  units may be considered as negative ions with a large ionic radius which provide binding sites with a small bridging energy for the mobile lithium ions [6]. The increase of the ionic conductivity comes from the increase of the number of  $\text{BO}_4$  units and of the number of free sodium ions. At higher oxide contents, there appear  $\text{BO}_3$  units with the formation of negatively charged NBO atoms which trap the free sodium ions and, therefore, the conductivity is less sensitive to the addition of the doping salt.

Next we examine the glass systems on the basis of a fixed  $\text{Na/B}$  content, where the compositions of the glasses are controlled such that the sodium ion concentration is fixed even as the iodide replaces the oxide. The effects of replacing  $\text{Na}_2\text{O}$  with  $\text{Na}_2\text{I}_2$  on the ionic conductivities are shown in Fig. 3 for the glasses of  $\text{B}_2\text{O}_3-x\text{Na}_2\text{O}-y\text{Na}_2\text{I}_2$  with  $x+y=0.25$  and  $0.43$ . The conductivity decreases slightly upon the iodide substitution level. Raman spectrum of Fig. 4 shows that the glass structure does not change significantly upon the substitution of iodide. It appears reasonable to suggest that the similarity in conductivity stems from a basic similarity in glass structure when the glasses are compared on the basis of identical  $\text{Na/B}$  ratios.

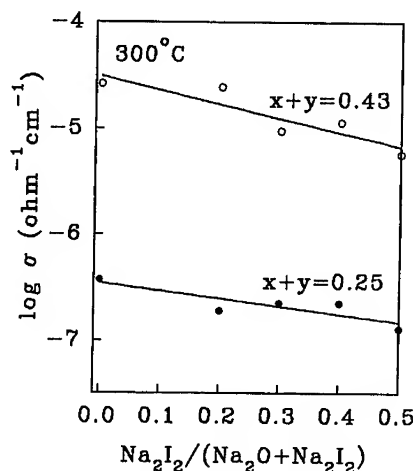


Fig.3 Conductivity vs. iodide substitution for  $\text{B}_2\text{O}_3-x\text{Na}_2\text{O}-y\text{Na}_2\text{I}_2$  glasses with fixed  $\text{Na/B}$  ratios.

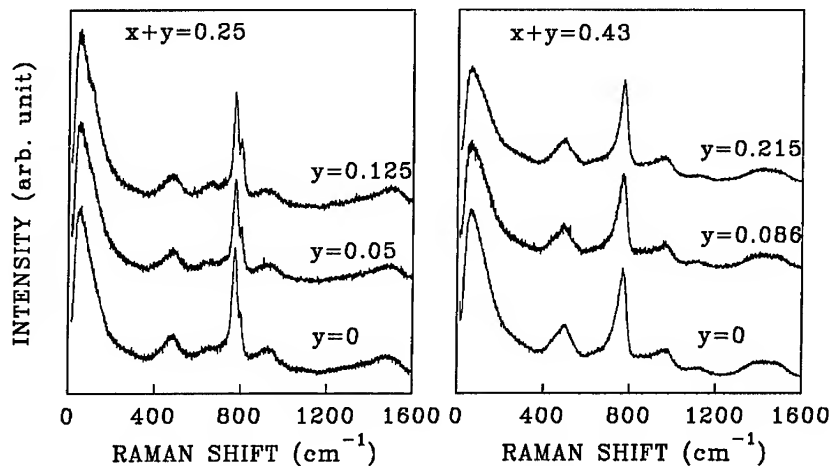


Fig.4 Raman spectra of  $\text{B}_2\text{O}_3-x\text{Na}_2\text{O}-y\text{Na}_2\text{I}_2$  glasses with fixed  $\text{Na/B}$  ratios.

In the conductivity studies of alkali haloborate glasses with fixed O/B ratios, a general observation is that introduction of dopants results in substantial enhancement of ionic conductivity [1,2,11]. In contrast with these general observations, recent results indicate that fluorine doping to the lithium fluoroborate glass [16] and iodine doping to the potassium diborate glass [17] result in a drop in conductivity. In the sodium haloborate glasses with fixed Na/B ratios, it has been reported recently a small decrease of conductivity with the substitution of NaF [18] and, on the other hand, a large increase of conductivity with the substitution of NaCl [17]. These results, including our results, reveal that there is a great deal of dissimilarity in the role of halogens in the borate glasses according to the species of both the doping salts and the oxide modifiers.

#### CONCLUSIONS

In the fixed O/B ratio, the addition of iodide has a drastic effect on the glass network structure and the enhancement of the ionic conductivity. At lower oxide content, the modification of the glass structure with the addition of NaI is characterized with the disappearance of boroxol rings and the increase of  $\text{BO}_4$  units. At the higher oxide content, with the addition of NaI,  $\text{BO}_4$  units are transformed into  $\text{BO}_3$  triangles and  $\text{BO}_3$  with NBO atoms, indicating a decrease of the linkage of the network. Iodide substitutions to the sodium borate glass with fixed Na/B ratios do not influence significantly the ionic conductivity as well as the network structures.

#### Acknowledgement

This paper was supported by NON DIRECTED RESEARCH FUND, Korea Research Foundation, 1993.

#### REFERENCES

1. H.L. Tuller, D.P. Button and D.R. Uhlmann, *J. Non-Cryst. Solids*, **40**, 93 (1980).
2. A. Levasseur, J.C. Brethous, J.M. Reau, M. Couzi and P. Hagemuller, *Solid State Ionics*, **1**, 177 (1980).
3. M. Balkanski, R.F. Wallis, J. Deppe and M. Massot, *Mat. Sci. Eng. B*, **12**, 281 (1992) and references therein.
4. M. Irion and M. Couzi, A. Levasseur, J.M. Reau and J.C. Brethous, *J. Solid St. Chem.* **31**, 285 (1980).
5. W. Soppe, J. Kleerebezem and H.W. Hartog, *J. Non-Cryst. Sol.* **93**, 142 (1987).
6. M. Massot, E. Haro, M. Oueslati and M. Balkanski, in *Solid State Ionics*, edited by G. Nazri, R.A. Huggins and D.F. Shriver (Mater. Res. Soc. Proc. **135**, Pittsburgh, PA, 1989) pp. 207-217.
7. Y. Wang, A. Osaka, Y. Miura and K. Takahashi, *J. Non-Cryst. Solids*, **95&96**, 571 (1987).
8. D.E. Turcotte, W.M. Risen Jr. and E.I. Kamitos, *Solid State Commun.* **51**, 313 (1984).

9. G.D. Chryssikos, E.J. Kamitos and M.A. Karakassides, *Phys. Chem. Glasses*, **30**, 243, 1989.
10. A.E. Geissberger, F. Bucholtz and P.J. Bray, *J. Non-Cryst. Solids*, **49**, 117 (1982).
11. D.P. Button, R.P. Tandon, C. King, M.H. Velez and D.R. Tuller, *J. Non-Cryst. Solids*, **49**, 129 (1982).
12. W.L. Konijnendijk and J.M. Stevels, *J. Non-Cryst. Solids*, **18**, 307 (1975).
13. E.L. Kamitos, G.D. Chryssikos, *J. Molecular Structure*, **247**, 1 (1991).
14. B.N. Meera and J. Ramakrishna, *J. Non-Cryst. Solids*, **159**, 1 (1993) and references therein.
15. T.W. Bril, *Philips Res. Rep. Suppl. No. 2*, 111 (1976).
16. Y. Wang, A. Osaka, Y. Miura and K. Takahashi, *J. Mater. Res.* **2**, 606 (1987).
17. F.A. Fusco, H.L. Tuller and D.P. Button, *Materials Sci. and Eng. B*, **13**, 157 (1992).
18. J.E. Shelby and R.L. Ortolano, *Phys. Chem. Glasses*, **31**, 25 (1990).

## SPECTROFLUORIMETRIC CHARACTERIZATION OF AN IONIC CONDUCTOR: SODIUM SULFATE HIGH-TEMPERATURE PHASES DOPED WITH EUROPIUM(III)

LOWELL R. MATTHEWS,\* EDWARD T. KNOBBE,\*† GAMINI DHARMASENA,\*\* RENÉE COLE,\*\* AND ROGER FRECH\*\*†

\*Department of Chemistry and Center for Laser Research, Oklahoma State University, Stillwater, Oklahoma, 74078-0447

\*\*University of Oklahoma, Department of Chemistry, Norman, Oklahoma, 73019

### ABSTRACT

The highest-temperature polymorph of sodium sulfate, (I), has significant orientational disorder in its structure which allows it to readily accept substitution by di- and trivalent cations. Although  $\text{Na}_2\text{SO}_4$  (I) exhibits reasonable ionic conductivity, it cannot be quenched to room temperature without changing phase. However, aliovalent solid solutions of (I) can be quenched to RT and resultant cation vacancies promote conduction via  $\text{Na}^+$  migration. The closely related but more ordered phase  $\text{Na}_2\text{SO}_4$  (III) can also form aliovalent solid solutions which can be quenched to RT.

The europium(III) ion is an extremely sensitive and useful probe of its immediate local environment. The presence, location, and intensity of its fluorescence transitions (particularly the  $^5D_0 \rightarrow ^7F_{0-2}$  emissions) can provide detailed information about the symmetry, nature, and multiplicity of the individual  $\text{Eu}^{3+}$  site which cannot be gained from X-ray or neutron diffraction techniques.

Our research (supported by the National Science Foundation and the State of Oklahoma) involves the structural characterization of two europium-doped sodium sulfate phases via fluorescence spectroscopy.

### INTRODUCTION

Sodium sulfate (I), stable from 237°C–883°C,<sup>1</sup> is a modest ionic conductor; its conductivity ( $\sigma$ ) is  $1.1 \times 10^{-5}$  S/cm at 250°C.<sup>2</sup> This value can be increased by two orders of magnitude by doping (I) with aliovalent cations; for example, (I) doped with 4 mol %  $\text{La}_2(\text{SO}_4)_3$  has  $\sigma = 1.08 \times 10^{-3}$  S/cm at 290°C (equal to that of pure phase (I) at 500°C).<sup>3</sup>  $\text{Na}_2\text{SO}_4$  (I) has much orientational disorder in its structure which allows it to readily accept substitution by aliovalent cations,<sup>4</sup> including trivalent rare-earth ions.<sup>1,3</sup> Doping (I) increases  $\sigma$  by creating vacancies and extends its thermodynamic stability region to much lower temperatures.<sup>5</sup> When cooled towards room temperature (RT), pure  $\text{Na}_2\text{SO}_4$  (I) changes to the orthorhombic phase (III), stable from 200°–235°C and metastable at RT.<sup>4,6</sup> Aliovalent solid solutions of (I) cool to RT *without* changing phase because dopant-induced disorder favors the phase (I) structure; stabilization occurs over a 200°C range and can be effected by as little as 1.2 mol %  $\text{Y}_2(\text{SO}_4)_3$ . At lower dopant levels (< 1 mol %), phase (III) also forms aliovalent solid solutions stabilized to RT.<sup>1</sup> This paper reports the incorporation of europium(III), an ion chosen for its unique spectroscopic properties, into  $\text{Na}_2\text{SO}_4$  (I) and (III).

The  $\text{Eu}^{3+}$  ion is an extremely sensitive probe of its local environment because its fluorescence, particularly that of the  $^5D_0 \rightarrow ^7F_{0-2}$  emissions (abbreviated  $E_{0-2}$ ), strongly depends upon the character of the  $\text{Eu}^{3+}$  site. It has been used to probe inner-sphere coordination in both solution<sup>7</sup> and the solid state.<sup>8</sup> Bünzli and Pradervand used  $\text{Eu}^{3+}$  fluorescence spectroscopy to identify three chemically different  $\text{Eu}^{3+}$  sites in a crown ether system.<sup>9</sup> In the present study,  $\text{Eu}^{3+}$  fluorescence spectroscopy provides additional structural characterization for two europium-doped sodium sulfate phases, (I) and (III), both stabilized to at least room temperature. Spectra of europium(III) chloride are included as references.

† Contact authors.

## EXPERIMENTAL METHODS

$\text{EuCl}_3 \cdot 6\text{H}_2\text{O}$  was obtained from Pfaltz & Bauer and used directly. The Eu-doped  $\text{Na}_2\text{SO}_4$  samples, (I): $\text{Eu}^{3+}$  (3.0 mol %) and (III): $\text{Eu}^{3+}$  (0.8 mol %), were prepared via the method previously reported,<sup>1</sup> namely, by melting the appropriate amounts of  $\text{Eu}_2(\text{SO}_4)_3 \cdot 8\text{H}_2\text{O}$  and  $\text{Na}_2\text{SO}_4$  (both at  $\geq 99\%$  purity) at  $950^\circ\text{C}$  for 6 h, cooling to  $700^\circ\text{C}$  for 3 h, and finally cooling to RT over 6 h. Continuous-wave luminescence (emission and excitation) spectra, software-corrected, were obtained using a Spex Industries Model F112 spectrofluorimeter. Ionic conductivity measurements were conducted using the techniques previously reported.<sup>1</sup>

## DISCUSSION OF RESULTS

The  $\sigma$  of the Eu-doped sodium sulfates (Fig. 1) demonstrates a change in phase behavior. Ionic conductivity has a complex temperature dependence expressed as:

$$\ln \sigma T = \ln \sigma_0 - \frac{Q_c}{RT} = -\left(\frac{Q_c}{R}\right)\left(\frac{1}{T}\right) + \ln \sigma_0 \quad (1)$$

where, after Mundy,<sup>10</sup>  $\sigma_0$  is the pre-exponential term,  $Q_c$  is the ionic-motion activation energy,  $R$  is the gas constant, and  $T$  is the absolute temperature. A plot of  $\ln \sigma T$  v.  $1/T$  (Fig. 1) can provide  $Q_c$  and  $\sigma_0$  values and also highlights phase changes, which appear as slope discontinuities.<sup>10</sup> In Figure 1, such discontinuities exist in pure  $\text{Na}_2\text{SO}_4$  (476–535 K) and in 0.8% Eu (485–526 K). The (V)–(III) and (III)–(I) phase transitions should occur at 473 K and 508 K, respectively.<sup>6</sup> The discontinuity covers both phase transitions in pure  $\text{Na}_2\text{SO}_4$ . Since 0.8% Eu is already in phase (III), the discontinuity marks the (III)–(I) transition. Additional evidence for identification of these phases is found in the  $Q_c$  and  $\sigma_0$  values (Table 1). The  $Q_c$  values for all three samples at  $T > 500$  K (especially  $T > 580$  K) are very close to one another (see Fig. 1), consistent with all three samples existing in phase (I) at these temperatures. The  $Q_c$  values for those samples predicted to be in phase (V) (pure  $\text{Na}_2\text{SO}_4$  at  $T < 500$  K) and in phase (III) (0.8% Eu at  $T < 500$  K) are significantly different from the  $Q_c$  expected for phase (I).

The  $\sigma$  values at the lowest comparable temperatures are  $1.56 \times 10^{-9}$  S/cm for pure  $\text{Na}_2\text{SO}_4$  (V) at  $102^\circ\text{C}$ ,  $5.02 \times 10^{-9}$  S/cm for 0.8% Eu (III) at  $103^\circ\text{C}$ , and  $2.78 \times 10^{-7}$  S/cm for 3.0% Eu (I) at  $102^\circ\text{C}$ . The value of 3.0% Eu is nearly 200 times greater than that of pure (V), but at this temperature it is four orders of magnitude below the superionic threshold. Near  $290^\circ\text{C}$ , where  $\sigma = 1.08 \times 10^{-3}$  S/cm for (I)+4%  $\text{La}_2(\text{SO}_4)_3$ ,<sup>3</sup> for 3.0% Eu at  $308^\circ\text{C}$   $\sigma = 3.80 \times 10^{-4}$  S/cm, fully 35% of the value of La-doped (I) and a factor of only 2.6 below the superionic threshold.

Figures 2–5 and Table 2 display the room-temperature ( $\approx 290$  K) europium(III) fluorescence spectra and spectral data used to conduct spectrofluorimetric characterization of the Eu-doped sodium sulfates, 0.8% Eu and 3.0% Eu, and the stoichiometric reference,  $\text{EuCl}_3 \cdot 6\text{H}_2\text{O}$ .

Virtually all of the features visible in the emission spectra (Figs. 2–4) arise from radiative emissions from the  $\text{Eu}^{3+} {}^5D_0$  level ( $17,300 \text{ cm}^{-1}$  above the  ${}^7F_0$  ground state) to the first five  $J$  levels of the  ${}^7F$  manifold. The features visible in the excitation spectra (Fig. 5) arise from those absorptive transitions from the  ${}^7F_0$  ground state which

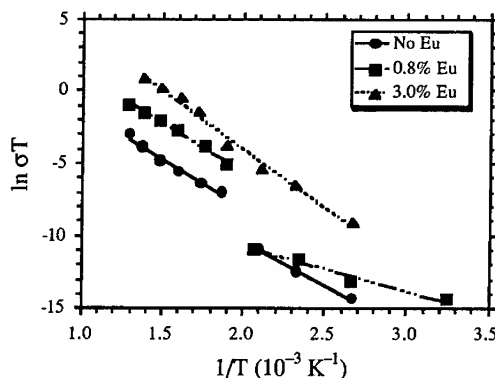


FIGURE 1: Ionic conductivities of pure and Eu-doped  $\text{Na}_2\text{SO}_4$ , fitted by linear regression.

TABLE 1

Eu Dopant Level	$Q_c$ (J/mol)	$\sigma_0$ (S cm <sup>-1</sup> K)	Corr
None, $T > 500$ K	57.5	$2.84 \times 10^2$	-0.989
None, $T < 500$ K	49.0	$3.82 \times 10^0$	-0.998
0.8% Eu, $T > 500$ K	55.4	$2.27 \times 10^3$	-0.997
0.8% Eu, $T < 500$ K	25.3	$9.09 \times 10^{-3}$	-0.986
3.0% Eu	67.1	$1.76 \times 10^5$	-0.994
3.0% Eu, $T > 580$ K	56.2	$2.74 \times 10^4$	-0.992

TABLE 1: Values of  $Q_c$  (the ion-migration activation energy),  $\sigma_0$  (the pre-exponential constant), and the linear regression correlation factor for pure and Eu-doped Na<sub>2</sub>SO<sub>4</sub> as functions of dopant level and temperature, obtained from the data in Figure 1.

populate the  $^5D_0$  emitting level either directly or by internal conversion. Excited states include the  $^5D_0$ ,  $^5D_1$ ,  $^5D_2$ ,  $^5L_6$ ,  $^5G_{4-6}$ ,  $^5D_4$ , and  $^5H_6$ , with excitation bands centered near 580, 530, 465, 395, 380, 360, and 320 nm, respectively; the strongest transition is the  $^7F_0 \rightarrow ^5L_6$ .<sup>11</sup> The excitation spectra show a relative enhancement of the  $^7F_0 \rightarrow ^5L_6$  and diminution of the  $^7F_0 \rightarrow ^5H_6$  absorption transitions in the sodium sulfates.

Because the  $^5D$  and  $^7F$  terms of Eu<sup>3+</sup> both arise from its  $4f^6$  electronic configuration, transitions between them are forbidden by the Laporte rule for electric-dipole (ED) interactions and therefore appear only when magnetic-dipole (MD) interactions or external perturbations, particularly those which introduce static and/or vibrational asymmetry into the ligand field, partially relax the rule.<sup>12</sup> Because the  $E_{0-2}$  transitions, in particular, arise from different interactions, their responses to perturbations differ significantly; these differences in behavior can then be used to characterize the Eu<sup>3+</sup> ion's local ligand field.

Of the five  $E_J$  transitions, only  $E_1$  is purely MD; its intensity is relatively insensitive to the ligand field.<sup>8</sup> In those environments which possess inversion symmetry (*e.g.* aqueous solution or [Eu(NO<sub>3</sub>)<sub>6</sub>]<sup>3-</sup>), the MD  $E_1$  transition dominates the spectrum and the other four ED features are insignificant.<sup>9, 13</sup> In contrast, the  $E_2$  transition operates by a forced ED mechanism and is "hypersensitive," a property observed in those transitions which nominally obey the selection rules for electric quadrupole (EQ) radiation (chiefly,  $\Delta J = 2$ ) but which can have intensities much greater than those attributable to the EQ mechanism. Hypersensitive transitions are most intense when an asymmetric electronic distribution within the rare-earth ion is produced by the external electric fields present in environments of low symmetry (classes  $C_s$ ,  $C_n$ , and  $C_{nv}$ ).<sup>14</sup> An absolute increase of the integrated intensity ( $S$ ) of  $E_2$  and a relative increase of  $S(E_2)$  to  $S(E_1)$  (the  $\eta_{21}$  ratio) is a strong indicator of the lowering of symmetry, particularly the removal of inversion symmetry,<sup>7</sup> and the increasing of chemical bond strength between Eu<sup>3+</sup> and its surroundings.<sup>13</sup>

The "superforbidden"  $E_0$  transition gains a weak MD oscillator strength in fields of low symmetry (again, classes  $C_s$ ,  $C_n$ , and  $C_{nv}$ ). Because it is a transition between  $J = 0$  states, it is completely nondegenerate and has no internal structure or Stark splitting. The other four transitions have  $2J + 1$  Stark components, some of which may be degenerate depending upon field symmetry. Therefore, any band structure or significant broadening of the  $E_0$  line arises from Eu<sup>3+</sup> ions in energetically different sites.<sup>15</sup>

The emission spectra of 0.8% Eu and 3.0% Eu (Fig. 2) resemble each other much more strongly than they resemble that of EuCl<sub>3</sub>·6H<sub>2</sub>O, primarily due to differences in crystal structure as discussed below. In particular, both have higher maximum emission intensities ( $I$ ) and all four  $E_J$  transitions have significantly wider bandwidths. While their intensities are relatively high, however, their  $E_1$  and  $E_2$  bands' Stark components are poorly resolved, effectively resulting in broad singlet peaks with a high-energy shoulder. If these two effects were to arise from chemically identical Eu<sup>3+</sup> ions, there would be a contradiction—Stark degeneracy arises from high symmetry, which is associated with low emission intensity, particularly of  $E_2$ . Because the  $E_2$



intensity is high and  $E_0$  is present, the broadening of the  $E_J$  bands must be inhomogeneous, caused by two or more chemically distinct  $\text{Eu}^{3+}$  sites.<sup>9, 15</sup>

$\text{EuCl}_3 \cdot 6\text{H}_2\text{O}$  was chosen as a reference compound because it was readily available and provides an  $\text{Eu}^{3+}$  environment of relatively low symmetry in which all five  $E_J$  transitions are visible at RT. Its monoclinic crystal structure is composed of  $[\text{Eu}(\text{H}_2\text{O})_6\text{Cl}_2]^+$  ions arranged in a strongly distorted cube of  $C_{2h}$  symmetry and isolated  $\text{Cl}^-$  ions.<sup>16</sup> At RT, vibrational deviations from inversion symmetry allow a weak  $E_0$  transition. The number of Stark components of its  $E_1$ ,  $E_2$ , and  $E_4$  transitions points to a basic symmetry different from that of 0.8% Eu and 3.0% Eu due to the differences between the monoclinic structure of europium chloride and the orthorhombic or roughly hexagonal structures of the Eu-doped sodium sulfates.

The detailed pictures of the  $E_2$  (Fig. 3) and  $E_{0-1}$  (Fig. 4) emission regions were obtained by decreasing the spectral data interval and the emission monochromator bandpass in order to narrow the peak bandwidths. In Fig. 3, the poor resolution in 0.8% Eu and 3.0% Eu is a strong indicator of multiple nonequivalent  $\text{Eu}^{3+}$  sites. In Fig. 4, the three  $E_1$  Stark components of  $\text{EuCl}_3 \cdot 6\text{H}_2\text{O}$  at 588, 591 and 592 nm are clearly visible, along with a very sharp  $E_0$  peak and two small peaks which probably arise from the weak  $^5D_1 \rightarrow ^7F_3$  emission.<sup>17</sup> Again, the poor resolution in  $E_1$  of 0.8% Eu and 3.0% Eu is a strong indicator of multiple nonequivalent  $\text{Eu}^{3+}$  sites, as is the large bandwidth of  $E_0$ . The doublet structure of  $E_0$  in 0.8% Eu points to two significantly different  $\text{Eu}^{3+}$  sites; in fact, the  $\text{Na}_I$  and  $\text{Na}_{II}$  sites in  $\text{Na}_2\text{SO}_4$  (III) have different symmetries ( $C_{2v}$  and  $C_{2h}$ ).<sup>6</sup> The  $\text{Na}_I$  and  $\text{Na}_{II}$  sites in (I) are also quite different:  $\text{Na}_I$  has four close, two intermediate, and four distant O neighbors at 252, 280, and 300 pm, respectively;  $\text{Na}_{II}$  is surrounded by six close and rather equidistant O atoms, 231–240 pm. However, the  $E_0$  band of 3.0% Eu, while fairly wide, does not have the doublet structure of 0.8% Eu; therefore, in (I) the

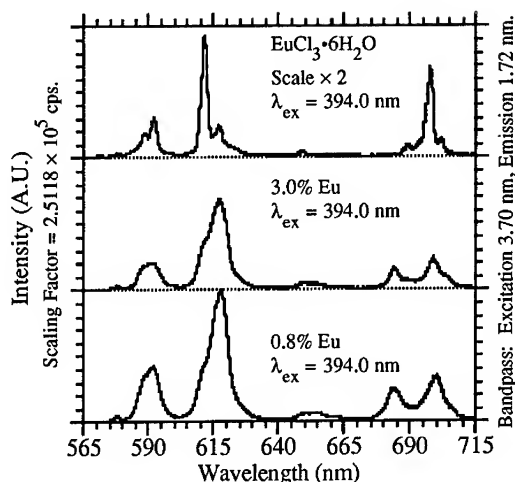


FIGURE 2: Full RT emission spectra of 0.8% Eu, 3.0% Eu, and  $\text{EuCl}_3 \cdot 6\text{H}_2\text{O}$ , normalized and scaled to 0.8% Eu. The europium chloride spectrum has been multiplied by 2 for clarity.

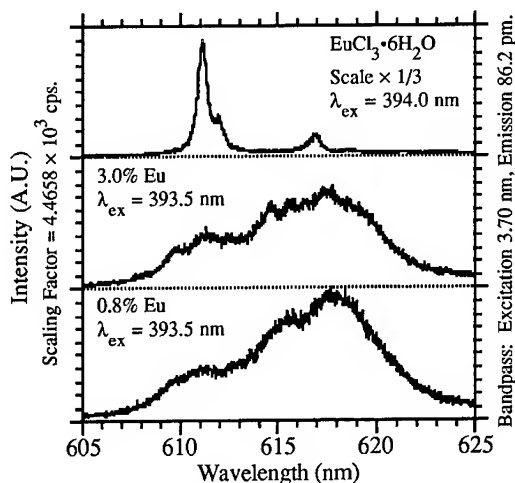


FIGURE 3: Detailed RT emission spectra of 0.8% Eu, 3.0% Eu, and  $\text{EuCl}_3 \cdot 6\text{H}_2\text{O}$ , focusing on the  $E_2$  region, normalized and scaled to 0.8% Eu. The europium chloride spectra has been divided by 3.

$\text{Eu}^{3+}$  ion must preferentially substitute into the larger  $\text{Na}_\text{I}$  site, but the strong orientational disorder in (I) makes individual  $\text{Na}_\text{I}$  sites sufficiently nonequivalent as to cause inhomogeneous line broadening.<sup>4</sup>

Table 2 displays parameters evaluated from the emission spectral data, of which the most important for determination of the  $\text{Eu}^{3+}$  local environment is the ratio of the intensities of the most prominent and sensitive ED transition,  $E_2$ , to the relatively insensitive MD transition,  $E_1$ , defined by the expression  $\eta_{21} \equiv S(E_2)/S(E_1)$ ; they are the boldface values in Table 2. The rule is simply stated: higher values of  $\eta_{21}$  are associated with lowered symmetry and increased bond strength between  $\text{Eu}^{3+}$  and its neighbors.<sup>7, 13</sup> The  $\eta_{21}$  values increase in the order  $\text{EuCl}_3 \cdot 6\text{H}_2\text{O} < 0.8\% \text{ Eu} < 3.0\% \text{ Eu}$ , confirming the trends discussed earlier. It may be noted that  $\text{EuCl}_3 \cdot 6\text{H}_2\text{O}$  has a higher local symmetry than do the europium-doped sodium sulfates, even though the sodium sulfates have crystal structures of nominally higher symmetry. Most significantly, the  $\eta_{21}$  values increase from 0.8% Eu to 3.0% Eu in accordance with the expected increase of disorder and hence asymmetry in going from (III) to (I).

## CONCLUSIONS

Two high-temperature polymorphs of sodium sulfate, (I) and (III), of which at least (I) is potentially a good ionic conductor, have been stabilized to room temperature through the incorporation of  $\text{Eu}^{3+}$  ions, which were chosen because they are capable of stabilizing the phases (as are many other di-, tri-, and tetravalent ions), and because the unique spectroscopic properties of  $\text{Eu}^{3+}$  make it a useful probe of its local environment. Measurements of the phases' ionic conductivities have demonstrated both the increases in ionic conductivity which accompany doping with aliovalent cations and the concomitant formation of cation vacancies which promotes  $\text{Na}^+$  ion migration, and also the existence of the predicted phases and their transitions in the predicted temperatures regions. The ionic conductivity of 3.0% Eu is sufficiently high that it almost meets the threshold requirements for superionic con-

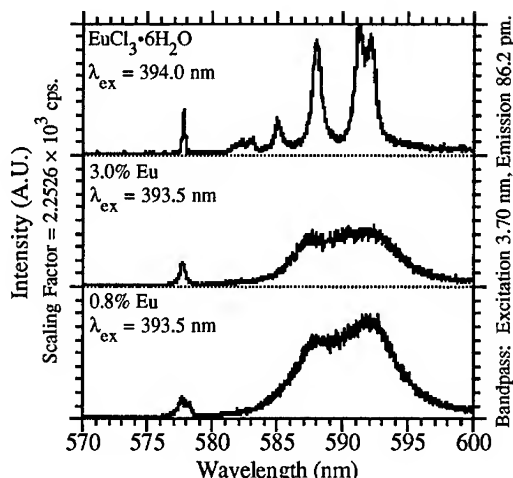


FIGURE 4: Detailed RT emission spectra of 0.8% Eu, 3.0% Eu, and  $\text{EuCl}_3 \cdot 6\text{H}_2\text{O}$ , focusing on the  $E_0$ - $E_1$  emission region, scaled to  $\text{EuCl}_3 \cdot 6\text{H}_2\text{O}$ .

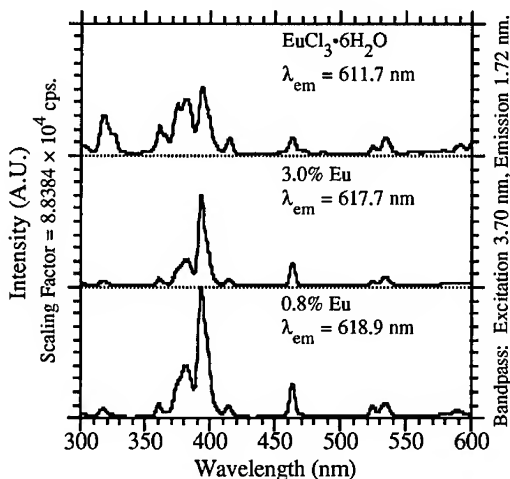


FIGURE 5: Full RT excitation spectra of 0.8% Eu, 3.0% Eu, and  $\text{EuCl}_3 \cdot 6\text{H}_2\text{O}$ , viewed at the  $E_2$  emission, scaled to 0.8% Eu.

ductors. Finally, a series of detailed spectroscopic measurements using europium(III) fluorescence as a probe of the local  $\text{Eu}^{3+}$  ion environment has confirmed the structural predictions of previous researchers' X-ray analyses in showing an increase in disorder between phases (III) and (I) and a change in preference for particular  $\text{Na}^+$  crystal sites with the changing crystal structure.

TABLE 2

	0.8% Eu	3.0% Eu	Chloride
$S(E_0)$	0.135	0.085	0.048
$S(E_1)$	4.015	2.047	1.000
$S(E_2)$	10.421	7.295	2.346
$\eta_{21}$	<b>2.596</b>	<b>3.564</b>	<b>2.346</b>
FWHM $E_0$	2.9	2.9	3.2

TABLE 2: RT parameters for  $\text{Eu}^{3+}$   $E_{0-2}$  emissions in 0.8% Eu, 3.0% Eu, and  $\text{EuCl}_3 \cdot 6\text{H}_2\text{O}$ : integrated emission intensity  $S$ , normalized to  $E_1$  of  $\text{EuCl}_3 \cdot 6\text{H}_2\text{O}$ ;  $E_2:E_1$  intensity ratio,  $\eta_{21} = S(E_2)/S(E_1)$ ; and  $E_0$  peak Full Width at Half Maximum (nm). The data interval and bandpass were 0.1 and 1.72 nm, respectively.

## REFERENCES

1. G. Dharmasena and R. Frech, *J. Chem. Phys.* **99**, 8929 (1993).
2. M. A. Careem and B. E. Mellander, *Solid State Ionics* **15**, 327 (1985).
3. G. Prakash and K. Shahi, *Solid State Ionics* **23**, 151 (1987).
4. W. Eysel, H. H. Höfer, K. L. Keester, and Th. Hahn, *Acta Cryst.* **B41**, 5 (1985).
5. (a) H. H. Höfer, W. Eysel, and U. von Alpen, *J. Solid State Chem.* **36**, 365 (1981). (b) H. H. Höfer, U. von Alpen, and W. Eysel, *Acta Cryst.* **A34**, S358 (1978).
6. B. N. Mehrotra, *Z. Kristallogr.* **155**, 159 (1981).
7. M. J. Lochhead, P. R. Wamsley, and K. L. Bray, *Inorg. Chem.*, in press.
8. S. J. L. Ribeiro, R. S. Hiratsuka, A. M. G. Massabni, M. R. Davolos, C. V. Santilli, and S. H. Pulcinelli, *J. Non-Cryst. Solids* **147 & 148**, 162 (1992).
9. J.-C. G. Büinzli and G.-O. Pradervand, *J. Chem. Phys.* **85**, 2489 (1986).
10. J. N. Mundy, in *Fast Ion Transport in Solids: Electrodes and Electrolytes*, edited by P. Vashishta, J. N. Mundy, and G. K. Shenoy (Elsevier North Holland, Inc., Amsterdam, 1979), p. 159.
11. W. T. Carnall, P. R. Fields, and K. Rajnak, *J. Chem. Phys.* **49**, 4412 (1968).
12. (a) B. R. Judd, *Phys. Rev.* **127**, 750 (1962). (b) G. S. Ofelt, *J. Chem. Phys.* **37**, 511 (1962). (c) Robert D. Peacock, *Struct. Bond. (Berlin)* **22**, 83 (1975).
13. R. Reisfeld, V. Chernyak, M. Eyal, and C. K. Jørgensen, in *The Second International School on Excited States of Transition Elements*, edited by W. Strek, W. Ryba-Romanowski, J. Legendziewicz, and B. Jezowska-Trzebiatowska (World Scientific Publishing Co. Pte. Ltd., Singapore, 1992), p. 247.
14. B. R. Judd, *J. Chem. Phys.* **44**, 839 (1966).
15. R. Campostrini, G. Carturan, M. Ferrari, M. Montagna, and O. Pilla, *J. Mater. Res.* **7**, 745 (1992).
16. N. K. Bel'skii and Yu. T. Struchkov, *Kristallografiya (Sov. Phys., Cryst.)* **10**, 21 (Russian) or 15 (English) (1965).
17. C. Brecher, H. Samelson, and A. Lempicki, in *Optical Properties of Ions in Crystals*, edited by H. M. Crosswhite and H. W. Moos (Interscience Publishers Division of John Wiley & Sons, Inc., New York, 1967), p. 73.

## SYNTHESIS, CHARACTERIZATION AND ELECTROCHEMICAL STUDY OF THE SOLID SOLUTION $\text{Li}_x\text{Na}_{0.875-\delta}\text{Fe}_{0.875}\text{Ti}_{1.125}\text{O}_4$ ( $0 \leq \delta \leq 0.4$ , $x \geq 0$ )

ALOIS KUHN, F. GARCIA-ALVARADO, E. MORAN and M.A. ALARIO-FRANCO  
Departamento de Química Inorgánica, Facultad de Ciencias Químicas, Universidad Complutense,  
28040 Madrid, Spain.

### ABSTRACT

The calcium ferrite type structure of  $\text{Na}_{0.875}\text{Fe}_{0.875}\text{Ti}_{1.125}\text{O}_4$  [1] has double tunnels which are occupied by double rows of sodium atoms running along the b-axis. We have partially removed sodium from this compound at moderate temperatures with different oxidizing agents. Electrochemical studies show that the resulting materials,  $\text{Na}_{0.875-\delta}\text{Fe}_{0.875}\text{Ti}_{1.125}\text{O}_4$  ( $0 \leq \delta \leq 0.4$ ), can reversibly intercalate lithium at potentials between 3.8 and 1 volt. At the lowest voltages, a compound containing  $\sim 0.5$  lithium per formula is formed. By chemical reaction of  $\text{Na}_{0.875}\text{Fe}_{0.875}\text{Ti}_{1.125}\text{O}_4$  with n-butyllithium, the maximum lithium content also corresponds to  $\text{Li}_{0.5}\text{Na}_{0.875}\text{Fe}_{0.875}\text{Ti}_{1.125}\text{O}_4$ . This suggests that many more than the one eighth of the empty sodium sites, per unit cell, of the parent phase are now being occupied by lithium.

### INTRODUCTION

$\text{Na}_{0.875}\text{Fe}_{0.875}\text{Ti}_{1.125}\text{O}_4$  is a member of the multiple rutile-chain family. The basic structural unit, as in  $\text{NaFeTiO}_4$  [2] and other isomorphous calcium ferrites [3, 4] is a pair of edge-shared octahedra which extends infinitely in the b-direction. These double blocks are further condensed by edge sharing, giving a distorted Z-shaped quadruple-rutile ribbon, which extends infinitely in the b direction. These are corner-joined to four other Z-shaped ribbons leaving double tunnels between them. These "double barrelled" tunnels are occupied by double rows of sodium atoms (Fig. 1), with a 12.5% vacancies.

The  $\text{CaFe}_2\text{O}_4$ -type oxides show a broad extent of non-stoichiometry in the occupancy of the tunnels. Results of electrical measurements in  $\text{Na}_{0.875}\text{Fe}_{0.875}\text{Ti}_{1.125}\text{O}_4$  gave evidence for a one-dimensional sodium mobility along the b-axis with a low activation process [5]. This agrees with the high anisotropic thermal factor reported for the  $\text{Na}^+$  cation [1]. We have tried to take advantage of the high mobility of these ions to partially remove them from the structure. In this work we present the synthesis and characterization of a new sodium deficient solid solution  $\text{Na}_{0.875-\delta}\text{Fe}_{0.875}\text{Ti}_{1.125}\text{O}_4$  ( $0 \leq \delta \leq 0.4$ ). These new compounds showing non-stoichiometric occupancy of the "double-barrelled" tunnels, that can also be formulated as  $\text{Na}_{0.875-\delta}(\text{Fe}^{\text{III}}_{0.875-\delta}\text{Fe}^{\text{IV}}_{\delta})\text{Ti}_{1.125}\text{O}_4$  ( $0 \leq \delta \leq 0.4$ ), have been used as a host for a lithium intercalation reaction; the corresponding results are also presented in this paper.

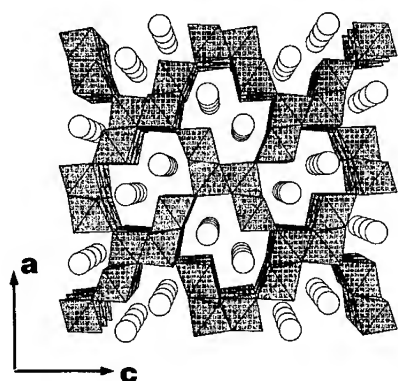


Fig. 1: Schematic representation of the  $\text{Na}_{0.875}\text{Fe}_{0.875}\text{Ti}_{1.125}\text{O}_4$  structure showing the double tunnels running along the b-direction.

## EXPERIMENTAL

The synthesis of  $\text{Na}_{0.875}\text{Fe}_{0.875}\text{Ti}_{1.125}\text{O}_4$  was performed as described previously [1]. Powder preparations were made by heating in air finely ground mixtures of sodium carbonate and the appropriate amounts of  $\text{Fe}_2\text{O}_3$  and  $\text{TiO}_2$  (rutile). A progressive heating from 600°C to 1000°C was made to ensure the decarbonation of  $\text{Na}_2\text{CO}_3$ . Intermediate regrinding, after quenching in air, and reheating to the maximum temperature were done to ensure the completion of the reaction.

X-Ray powder diffractograms, recorded in a Siemens D-5000 diffractometer using  $\text{CuK}\alpha$  radiation and silicon as internal standard, were used for the determination of the cell parameters and structural characterization. The oxidized samples were protected against moisture during the XRD

measurements by using an aluminium sample holder covered with a beryllium window, which was loaded under an argon atmosphere. For Rietveld analysis, intensity data were recorded at slow scan rates over a  $2\theta$  range from 10 to 80°.

The partial removal of sodium from  $\text{Na}_{0.875}\text{Fe}_{0.875}\text{Ti}_{1.125}\text{O}_4$  was achieved at room temperature and by heating and stirring under reflux 300-500 mg of the starting material in a solution of dry acetonitrile (b.p.: 81°C) containing 25% excess of an oxidizing agent for 24 h. [6]. After reaction, the resulting powder was filtered, washed with dry acetonitrile and dried under vacuum. The following oxidizing agents were used: iodine ( $\text{I}_2$ ), bromine ( $\text{Br}_2$ ) and nitrosonium tetrafluoroborate ( $\text{NO}_2\text{BF}_4$ ).

The molar ratio of the metals was determined by means of inductive coupled plasma spectroscopy (ICP) using a JY-70 plus instrument. The calibration was performed with standard solutions of each metal.

Electrochemical lithium insertions and removals were performed in Swagelok test cells [7] using metallic lithium as the anode. The cathodes were prepared from 20-30 mg of the above sodium iron titanium oxide, mixed with 10% conducting carbon black and 1% by weight of ethylene propylene diene terpolymer (EPDTP) and then pressed into 8 mm diameter pellets. The electrolyte used was a 1M solution of  $\text{LiClO}_4$  in a solution of ethylene carbonate (EC) and diethoxyethane (DEE) in a 50:50 volume ratio [8]. The samples were assembled in an argon atmosphere and glass paper was used as separator between the electrodes. A current density of  $\pm 50 \mu\text{A}$  was used to cycle the cell between the range 3.8-1 V.

## RESULTS AND DISCUSSION

### 1.- Chemical removal of sodium. Synthesis of oxidized phases

Table I shows the compositions obtained along with the oxidant and the experimental conditions employed in each case. The ICP results showed that in the samples with lowest sodium content, the maximum concentration would correspond to the formula  $\text{Na}_{0.47}\text{Fe}_{0.875}\text{Ti}_{1.125}\text{O}_4$ . Note that the amount of sodium remaining in the material decreases with the increasing strength of the oxidizing agent. In addition, we observed a change from the original brown color, passing through reddish brown to black, indicating that a gradual change in properties is probably occurring, as the sodium content decreases. The complete removal of sodium from the structure has not yet been possible, even at longer times under those conditions.

Table I. Oxidation conditions and resulting compositions after sodium extraction from  $\text{Na}_{0.875}\text{Fe}_{0.875}\text{Ti}_{1.125}\text{O}_4$ .

Oxidant	$E^0$ vs. $\text{Li/Li}^+$	Temp. ( $^{\circ}\text{C}$ )	Composition
-	-	-	$\text{Na}_{0.875}\text{Fe}_{0.875}\text{Ti}_{1.125}\text{O}_4$
$\text{I}_2$	+3.5	R.T.*	$\text{Na}_{0.87}\text{Fe}_{0.875}\text{Ti}_{1.125}\text{O}_4$
$\text{Br}_2$	+ 4.1	R.T.*	$\text{Na}_{0.87}\text{Fe}_{0.875}\text{Ti}_{1.125}\text{O}_4$
$\text{Br}_2$	+4.1	81**	$\text{Na}_{0.85}\text{Fe}_{0.875}\text{Ti}_{1.125}\text{O}_4$
$\text{NO}_2^+$	+5.1	81**	$\text{Na}_{0.64}\text{Fe}_{0.875}\text{Ti}_{1.125}\text{O}_4$
$\text{NO}_2^+$ , twice	+5.1	81**	$\text{Na}_{0.51}\text{Fe}_{0.875}\text{Ti}_{1.125}\text{O}_4$
$\text{NO}_2^+$ , three times	+5.1	81**	$\text{Na}_{0.47}\text{Fe}_{0.875}\text{Ti}_{1.125}\text{O}_4$

\*:  $\sim 20^{\circ}\text{C}$ , \*\*: b.p. of acetonitrile ( $81^{\circ}\text{C}$ )

### 2.- Structural characterization

X-ray diffraction patterns can be indexed on the basis of the orthorhombic cell given by Reid *et al.* [1] (space group  $\text{Pnma}$ ). The evolution of refined cell parameters  $a$ ,  $b$ ,  $c$  and the unit cell volume with the sodium content are represented on Figure 2. The  $a$  lattice parameter linearly increases, by  $0.076 \text{ \AA}$ , with decreasing sodium content, reaching a maximum value at  $x=0.405$ . On the contrary, over the same composition range the  $b$  lattice parameter smoothly decreases, by  $0.027 \text{ \AA}$ . The  $c$  lattice parameter initially increases by  $0.022 \text{ \AA}$  with a decreasing sodium

content from 0.875 to 0.64 and then decreases on further sodium extraction from 0.64 to 0.47, by 0.035 Å. The combination of the three effects leads to a very slight decrease of the unit cell volume, by 0.67 Å<sup>3</sup>, practically within the standard deviation.

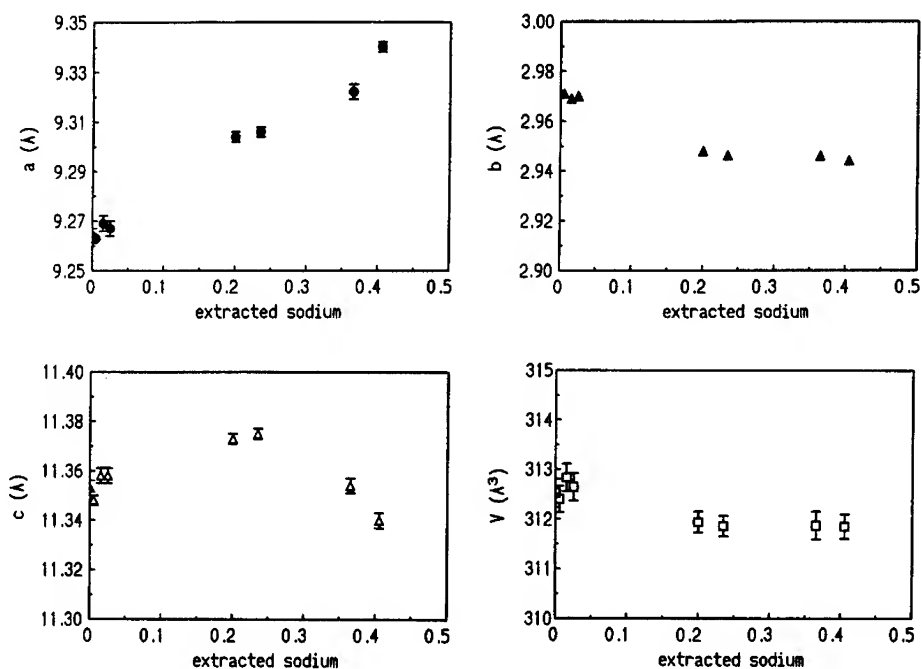


Fig. 2: Evolution of the refined cell parameters and the unit cell volume with the amount of extracted sodium,  $\delta$  in  $\text{Na}_{0.875-\delta}\text{Fe}_{0.875}\text{Ti}_{1.125}\text{O}_4$ .

### 3.- Electrochemical intercalation of lithium

A typical voltage-composition curve in the range 3.5 - 1.0 V of a cell using  $\text{Na}_{0.875}\text{Fe}_{0.875}\text{Ti}_{1.125}\text{O}_4$  (labeled  $\delta=0$ ) as the positive electrode is shown in Fig. 3. (top). As can be seen, the parent phase can effectively intercalate a relative high quantity of lithium. At 1 volt, the lithium content corresponding to  $x=0.45$  is reached. Nevertheless, the corresponding composition is likely to correspond to a mixture of phases. Just one region can be assigned to a solid solution of phases  $\text{Li}_x\text{Na}_{0.875}\text{Fe}_{0.875}\text{Ti}_{1.125}\text{O}_4$  ( $0.12 \leq x \leq 0.25$ ). This is labeled as A in Fig. 3 (top) and appears between ~2.13 and ~1.69 V. The total quantity of lithium indicates that more than the, one eighth, normally empty sodium tunnels are being filled by lithium. In fact, lithium seems to occupy different sites from those of sodium. It can be seen

ions can be removed from the structure, showing a certain irreversibility of the insertion reaction. For the oxidized sample  $\text{Na}_{0.64}\text{Fe}_{0.875}\text{Ti}_{1.125}\text{O}_4$  (labeled  $\delta=0.235$ ), the appearance of

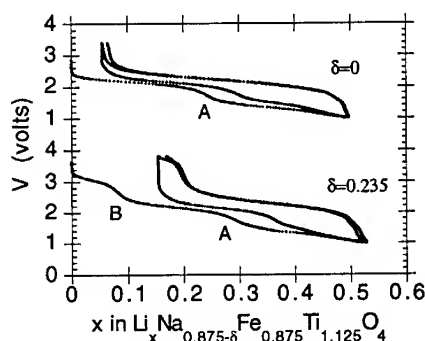


Fig. 3: Voltage-composition curves corresponding to samples of the series  $\text{Na}_{0.875-\delta}\text{Fe}_{0.875}\text{Ti}_{1.125}\text{O}_4$  with  $\delta=0$  and  $\delta=0.235$

a new solid solution region at higher voltages ( $> 2.5\text{V}$ ) with  $0.06 \leq x \leq 0.11$  (Fig. 3, bottom), denoted B, can be observed. With decreasing sodium content a broadening of the B region was observed, suggesting that lithium occupies the sites left by sodium. Further lithium insertion at lower voltages ( $< 2.5\text{V}$ ) leads to the formation of the same solid solution region as seen in Fig. 3 (top).

Each sodium atom in the double tunnels has a prismatic sixfold coordination to its nearest oxygen neighbours. It then seems that, looking for a lower coordination, lithium will shift somewhat from the tunnel center. Neutron diffraction is in progress to ascertain this point. These lithium ions would then be responsible for the irreversibility of the insertion process.

On the other hand, the smooth lithium intercalation may be hindered somewhat by the sodium atoms remaining in the structure, because the amount of inserted lithium, although being higher than the initially empty 1/8 sodium positions, does not reach that of extracted sodium.

A voltammogram of the first and second reduction/oxidation cycles of  $\text{Na}_{0.875}\text{Fe}_{0.875}\text{Ti}_{1.125}\text{O}_4$  (labeled  $\delta=0$ ) is shown in Fig. 4 (left). The existence range of the solid solution  $\text{Li}_x\text{Na}_{0.875-\delta}\text{Fe}_{0.875}\text{Ti}_{1.125}\text{O}_4$  ( $0.12 \leq x \leq 0.25$ ), above called A, is established between the reductive maximum at 2.13 V, corresponding to the beginning of the solid solution, and a minimum at 1.69 V marking its end.

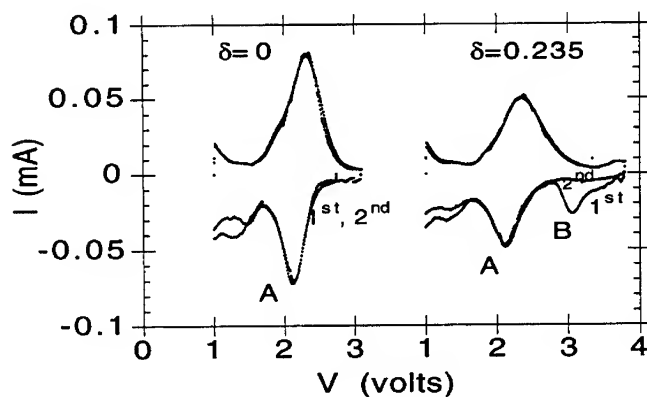


Fig. 4: Voltammograms corresponding to samples of the series  $\text{Na}_{0.875-\delta}\text{Fe}_{0.875}\text{Ti}_{1.125}\text{O}_4$  with  $\delta=0$  and  $\delta=0.235$ .



The reversibility of the insertion process is observed when cycling. In comparison, the oxidized sample  $\text{Na}_{0.64}\text{Fe}_{0.875}\text{Ti}_{1.125}\text{O}_4$  (Fig. 4, right) shows an additional peak during the first reduction cycle at 3 V, corresponding to the formation of a further solid solution region, denoted B, as mentioned above. The lithium here inserted can not be deintercalated on further oxidation; that means irreversibility (to be seen by the absence of the peak on oxidation). In the second and later cycles only the lower voltage peak appears, the same as in the non-oxidized sample, characteristic of the reversible intercalation process.

It then seems that there are two different lithium insertion processes. The first takes place reversibly in a voltage range between 2.15 - 1.7 V, and is observed in all the samples up to quite high lithium content, suggesting that lithium occupies different sites of those of sodium atoms in the double tunnel structure. On the other hand, the change in the sodium content of the positive electrode material leads to a further significant difference during lithium intercalation. These extra lithiums are inserted irreversibly in the positions, originally occupied by sodium atoms at a 3 V voltage range, where they could easily be "trapped".

## REFERENCES

- [1] W.G. Mumme and A.F. Reid, *Acta Cryst.* **B24**, 625-630 (1968).
- [2] A. F. Reid, A.D. Wadsley and M.J. Sienko, *Inorg. Chem.* **7**, 1, 112-118 (1956).
- [3] B.F. Decker and J.S. Kasper, *Acta Cryst.* **10**, 332-337 (1957).
- [4] P.M. Hill, H.S. Peiser and J.R. Rait, *Acta Cryst.* **9**, 981-986 (1956).
- [5] F. Archaimbault and J. Choisnet, *J. Solid State Chem.* **90**, 216-227 (1991).
- [6] F. García-Alvarado, J.M. Tarascon and B. Wilkens, *J. Electrochem. Soc.* **139**, 11, 3206-3214 (1992).
- [7] J.M. Tarascon, *ibid.* **139**, 11, 2089 (1985).
- [8] D. Guyomard and J. M. Tarascon, *ibid.*, **139**, 937 (1992).

## MONITORING OF PROCESS OF ION TRANSPORT IN NONSTOICHIOMETRIC FLUORIDES WITH THE $\text{LaF}_3$ STRUCTURE

NIKOLAY I. SOROKIN AND BORIS P. SOBOLEV  
Institute of Crystallography, Russian Academy of Sciences,  
Leninsky prospect 59, Moscow 117333, Russia

### ABSTRACT

Fluoride compounds with the tysonite ( $\text{LaF}_3$ - type) crystal structure form an important class of materials which find diverse technological applications as fast ionic conductors. The results of investigations of the ionic conductivity process within tysonite structured  $\text{R}_{1-x}\text{M}_x\text{F}_{3-x}$  single crystals (R=rare earths and M=alkali-rare earths) are presented using various techniques of electrical response spectroscopy. Influence of isomorphic substitutions of iso- and heterovalent cations on ion transport parameters was studied. By monitoring the composition of nonstoichiometric  $\text{R}_{1-x}\text{M}_x\text{F}_{3-x}$  crystals we can vary fluorine-ion conductivity within the range  $10^{-7}$  -  $10^{-4}$  S/cm at 293 K and  $10^{-4}$  -  $10^{-2}$  S/cm at 500 K. The studied nonstoichiometric crystals with the  $\text{LaF}_3$ -structure are promising solid electrolytes which can be used in chemical sensors and fluorine generators.

### INTRODUCTION

At high temperatures compounds with the tysonite and fluorite structure exhibit a superionic conductivity phenomenon associated with an extensive disorder of the anion sublattice. In recent years the research interest in tysonite and fluorite structured compounds has been extended to include doped compounds (or nonstoichiometric fluorides). The most typical products of high-temperature chemical interactions of fluorides of 24 metals (Na, Ca, Sr, Ba, Cd, Pb, Sc, Y, La and 13 Lanthanides, Zr, Hf) in  $\text{MF}_m\text{-RF}_n$  systems are iso- and heterovalent solid solutions. A large number of solid solutions with a variable number of atoms per unit cell (nonstoichiometric phases) crystallize in two basic  $\text{LaF}_3$ - and  $\text{CaF}_2$ -structures in  $\text{MF}_m\text{-RF}_n$  systems. These phases exhibit the maximum stoichiometry perturbations among the known ionic crystals.

At the beginning of the eighties a research program on solid state ionics of fluorides in binary  $\text{MF}_m\text{-RF}_n$  systems was undertaken at the Institute of Crystallography. The practical aim of the program is the searching for and preparing of new multicomponent fluoride materials for modern electrochemical applications. At the present time part of the program, namely, a study of fluorite structured materials in  $\text{MF}_2\text{-RF}_3$  systems, has been mainly completed. The results of that stage are summarised in the reviews [1].

This paper summarises the preliminary results of ionic conductivity measurements of nonstoichiometric fluorides with the tysonite structure. The following criteria of the choice of

fluorides as components of tysonite nonstoichiometric phases were used: 1) a high isomorphic capacity of the raw materials, and 2) a possibility to prepare these phases in the single crystalline form. In the course of investigations of ionic transport in polycrystalline samples difficulties are encountered due to grain boundaries. A total of 18 chemical elements, which form 45  $\text{MF}_2\text{-RF}_3$  systems ( $\text{M}=\text{Ca}, \text{Sr}, \text{Ba}$  and  $\text{R}=\text{La}, \text{Ce}, \text{Pr}, \text{Nd}, \text{Sm}, \text{Eu}, \text{Gd}, \text{Tb}, \text{Dy}, \text{Ho}, \text{Er}, \text{Tm}, \text{Yb}, \text{Lu}, \text{Y}$ ) meet the above requirements. The limiting deviation of  $\text{R}_{1-x}\text{M}_x\text{F}_{3-x}$  solid solutions from the stoichiometric  $\text{RF}_3$  composition is 33 mol.%  $\text{MF}_2$  difluoride or the  $\text{MR}_2\text{F}_8$  composition. We were concerned with the following problems at this stage of research: 1) a study of the influence of isomorphic iso- and heterovalent substitutions in the tysonite structural type on the parameters of ion transport, and 2) a search for chemical compositions of crystals with optimum electrolytical and technological parameters.

## EXPERIMENTAL

Single crystals of nonstoichiometric fluorides were grown from melt by the Stockbarger technique. A special feature of the growth technique was a directed crystallization with the employment of fluorinating atmosphere. This allowed us to avoid unwanted effects of pyrohydrolysis and to obtain single crystals 10 mm in diameter and 30 mm in length. Multicellular graphite crucibles were used, their depression rate was 3 mm/h. The crystals were found to belong to the tysonite structural type by X-ray diffraction technique. The qualitative chemical analysis of solid solutions was performed by X-ray fluorescence analysis. The deviations of the composition of the single crystals under study from starting mixture compositions was less than  $\pm 1$  mol %.

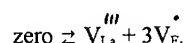
Electrical conductivity of the fluoride crystals was determined by the complex impedance technique. The conductometry set-up is described in [1]. Impedance measurements were made on electrochemical cells with graphite electrodes in the range of frequencies  $10^{-1}$ - $10^6$  Hz and temperatures 293-800 K. The values of electric conductivity obtained by dc voltammetry show that the contribution of the electronic component of conductivity ( $\sigma_e < 10^{-8}$  S/m at 293 K) can be neglected. Anionic conductivity of crystal was determined from the impedance or admittance curves of the electrochemical cells with graphite electrodes.

## RESULTS AND DISCUSSION

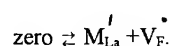
The tysonite structural type originates from the trifluoride  $\text{LaF}_3$ . This compound exhibits fluorine-ion superionic conductivity. The conductivity in  $\text{LaF}_3$  attains  $4 \cdot 10^{-6}$  S/cm and  $3 \cdot 10^{-4}$  S/cm at 293 K and 500 K, respectively.  $\text{LaF}_3$  crystals belong to the trigonal crystal system, sp. gr.  $\text{P3c1}$ . The tysonite lattice contains three types of structurally inequivalent fluorine atoms  $\text{F}_1$ ,  $\text{F}_2$  and  $\text{F}_3$  in the ratio 6:2:1.  $\text{F}_1$  atom sites are located on the three-fold axes.

Electric conductivity of tysonite,  $\text{LaF}_3$ , is due to migration motion of fluorine anions, according to the vacancy mechanism. Fluorine vacancies are ion current carriers in tysonite structures. The number of fluorine vacancies in tysonite structured crystals can be increased in

two ways. Upon heating, the concentration of thermal fluorine vacancies in a pure  $\text{LaF}_3$  crystal, formed according to the Shottky mechanism, is higher (in the Kroger-Vink notation)



At the same time, incorporation a lower valency  $M^{2+}$  cations into tysonite matrix of  $\text{LaF}_3$  gives rise to the formation of fluorine vacancies due to impurities



At the doping level of 1 mol% of  $\text{MF}_2$  difluoride the concentration of  $V_{\text{F}}$  vacancies which result from chemical substitutions, is higher by several orders of magnitude than the number of intrinsic thermal fluorine vacancies.

As the temperature rises, there occurs an exchange of charge carriers between various fluorine systems, which form an anion sublattice in the structure of lanthanum trifluoride. The anionic conductivity of  $\text{R}_{1-x}\text{M}_x\text{F}_{3-x}$  solid solutions is due to impurities, that is why the dependence  $\sigma(T)$  is defined by the temperature dependence of the mobility of fluorine vacancies

$$\mu_v = (\mu_0/T) \exp(-\Delta H_{m,v}/kT),$$

where  $\Delta H_{m,v}$  is the activation enthalpy of migration of fluorine vacancies. The nature of the enthalpy  $\Delta H_{m,v}$  is associated with the clearing of potential barriers by fluorine ions which move by hops over the structural sites of the anion sublattice.

#### Isovalent isomorphous substitutions

We have studied the effect of the dimensional factor (cation radii) on the anion transport characteristics in crystals with the tysonite-type structure in the temperature range from the melting point to room temperature [2]. With this aim, we have measured the electrolytic properties of  $\text{LaF}_3$ ,  $\text{NdF}_3$  and  $\text{La}_{1-x}\text{Pr}_x\text{F}_3$  with  $x=0.25, 0.50$  and  $0.75$ . Isovalent cationic substitutions change the geometric sizes of the lattice.

Figure 1 shows the dependence of anionic conductivity on the average radius ( $r_c$ ) of cations for the compounds of constant and variable compositions. The analysis of the published data indicates that in the family of tysonite structured  $\text{RF}_3$  fluorides the maximum conductivity is observed for  $\text{CeF}_3$ . Figure 1 shows that the curve  $\sigma=f(r_c)$  has a maximum at  $r_c=1.270\text{--}1.285 \text{ \AA}$  (it should be noted that  $r_{\text{Ce}^{3+}}=1.283 \text{ \AA}$ ). We found that  $\sigma(\text{La}_{0.25}\text{Pr}_{0.75}\text{F}_3) / \sigma(\text{LaF}_3) = 2.5$  at 500 K.

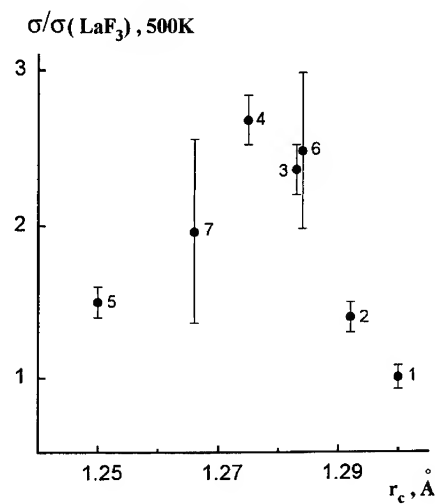


Fig. 1. Isothermal conductivity at 500K as a function of  $r_c$  for single crystals: (1)  $\text{LaF}_3$ , (2)  $\text{La}_{0.75}\text{Pr}_{0.25}\text{F}_3$ , (3)  $\text{La}_{0.5}\text{Pr}_{0.5}\text{F}_3$ , (4)  $\text{La}_{0.25}\text{Pr}_{0.75}\text{F}_3$ , (5)  $\text{NdF}_3$ , (6)  $\text{CeF}_3$ , and (7)  $\text{PrF}_3$ . References for the data on  $\text{CeF}_3$  and  $\text{PrF}_3$  are given in paper [ 2 ].

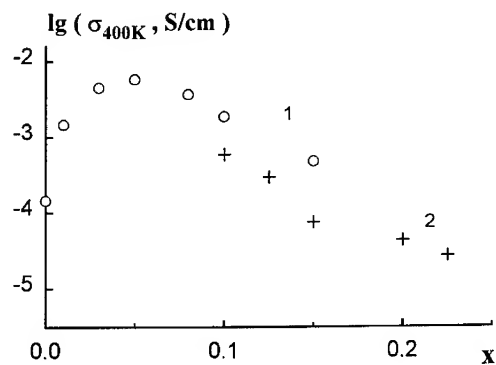


Fig.2 . Concentration dependence of  $\sigma$  at 400K for  $\text{La}_{1-x}\text{Sr}_x\text{F}_{3-x}$  (1) and  $\text{Gd}_{1-x}\text{Sr}_x\text{F}_{3-x}$  (2) .

### Heterovalent isomorphic substitutions

Heterovalent cationic substitutions give rise change of the geometry of the lattice, as well as to the formation of lattice defects (fluorine vacancies). We have studied the effect of the heterovalent cation substitutions on the anion transport characteristics in  $\text{La}_{1-x}\text{Sr}_x\text{F}_{3-x}$  ( $0 < x \leq 0.15$ ) and  $\text{La}_{1-x}\text{Gd}_x\text{F}_{3-x}$  ( $0.10 \leq x \leq 0.225$ ) solid solution [3,4]. An abrupt change at  $T_c = 420\text{--}450\text{ K}$  on the dependencies  $\sigma(T)$  for  $\text{La}_{1-x}\text{Sr}_x\text{F}_{3-x}$  crystals is observed. This discontinuity divides them into two sections. The correlation  $\Delta H_{m,v}(T < T_c) > \Delta H_{m,v}(T > T_c)$  is fulfilled for activation enthalpies of the migration. No discontinuity was found on the  $\sigma(T)$  curves in the range of  $340\text{--}630\text{ K}$  for  $\text{Gd}_{1-x}\text{Sr}_x\text{F}_{3-x}$  crystals.

Figure 2 shows concentration dependencies of ionic conductivity in these solid solutions. At concentration  $x_m = 0.05$  the  $\sigma(x)$  curves for  $\text{La}_{1-x}\text{Sr}_x\text{F}_{3-x}$  exhibit a maximum in the range of  $T < T_c$ , which is smoothed upon a transition to the temperature range of  $T > T_c$ . With an increase of  $\text{SrF}_2$  content in the  $\text{GdF}_3$  matrix from 10 mol% to 22.5 mol% the anionic conductivity decreases. These specific features of the  $\sigma(x, T)$  dependences can be explained in terms of the model of the hopping motion of charge carriers over various structural sites, with an account of effects of cluster formation, percolation phenomenon and ion-ion interaction of charge carriers [3].

In the range of  $x > x_m$  the mobility of fluorine vacancies decreases due to ion-ion interactions, with an increase in the concentration of  $\text{M}^{2+}$  cations, along with an increase of the concentration of charge carriers. Presumably, in concentrated solid solutions some fluorine vacancies can be located near  $\text{Sr}^{2+}$  ions and they form associates of defects, similar to clusters in fluorite structured concentrated solid solutions [1]. These vacancies are not involved in the ion transport process. A competitive influence of the above factors on the electric transport makes  $\sigma$  the largest at  $x_m = 0.05$ .

We have also studied anion transport in  $\text{R}_{0.95}\text{M}_{0.05}\text{F}_{2.95}$  crystals ( $\text{R} = \text{La, Ce, Pr, Nd}$  and  $\text{M} = \text{Ca, Sr, Ba}$ ). For these crystals the values of the conductivity hardly depend on the chemical composition and exceed the value of  $\sigma$  pure tysonite matrix by two orders of magnitude.

### CONCLUSIONS

The performed study of nonstoichiometric fluorides with the tysonite structure suggests practical recommendations for the choice of single crystalline solid electrolytes with monitored fluorine-ion conductivity within  $6 \cdot 10^{-7}\text{--}10^{-4}\text{ S/cm}$  at  $293\text{ K}$  and  $10^{-4}\text{--}3 \cdot 10^{-2}\text{ S/cm}$  at  $500\text{ K}$ .

Nonstoichiometric fluorides are a new family of fluorine-ion conductors. Anionic conductivity of fluorite-type  $\text{M}_{1-x}\text{R}_x\text{F}_{2+x}$  and tysonite-type  $\text{R}_{1-x}\text{M}_x\text{F}_{3-x}$  solid solutions extends within 12 orders of magnitude from  $10^{-14}\text{ S/cm}$  to  $10^{-2}\text{ S/cm}$  at  $500\text{ K}$ . These crystals were used for the development of chemical sensors for fluorine in gaseous media and as fluorine generators for industrial applications [5].

Our further intentions include detailed studies of the mechanism of fast ion transport in nonstoichiometric fluorides with the tysonite structure in preliminarily tested single crystals using X-ray diffraction, nuclear magnetic resonance of  $^{19}\text{F}$  nuclei, IR-spectroscopy and other techniques.

Here we confine ourselves to a discussion of the properties of single crystals. However, other fluoride materials, such as composites, glasses, ceramics and thin films are of special interest for chemistry and physics of superionic multicomponent fluoride materials. Studies of all these materials are performed at the Lab. of Physico-Chemical Analysis of the Institute of Crystallography (Moscow).

## REFERENCES

1. A.K. Ivanov-Shitz, N.I. Sorokin, P.P. Fedorov, and B.P. Sobolev, *Solid State Ionics* **31**, 253 (1989); **31**, 269 (1989)
2. N.I. Sorokin and B.P. Sobolev, *Kristallografiya* **39**, 114 (1994) [*Crystallography Reports* **39**, 101 (1994)]
3. N.I. Sorokin and B.P. Sobolev, *Kristallografiya* (in press, 1994) [*Crystallography Reports* (in press, 1994)]
4. N.I. Sorokin, E.A. Krivandina, D.N. Kuranov, Z.I. Zhmurova, and B.P. Sobolev, *Kristallografiya* (in press, 1995) [*Crystallography Reports* (in press, 1995)]
5. E.F. Sudakova, E.Ya. Alksnis, R.S. Perlovskii, E.A. Krivandina, and B.P. Sobolev, 1992 MRS Fall Meeting, Symposium on Solid State Ionics, Boston, MA, 1992, p.160

## ACKNOWLEDGEMENT

The authors wish to thank Drs. E.A. Krivandina and Z.I. Zhmurova for assistance in growing crystals. This study has been sponsored by the Russian Foundation of Fundamental Investigations (Project 94-0345-74) and by the International Science Foundation (Travel Grant 4425/22).

---

## PART VI

---

### **Polymer Electrolytes and Electrodes**



## NEW CONCEPTS IN PRIMARY AND RECHARGEABLE SOLID STATE LITHIUM POLYMER BATTERIES

GIANNI APPETECCHI, FAUSTO CROCE, FURIO GERACE, STEFANIA PANERO, STEFANO PASSERINI, ERALDO SPILA AND BRUNO SCROSATI  
Dipartimento di Chimica, Università 'La Sapienza' 00185 Rome, Italy

### ABSTRACT

The properties of some examples of new classes of highly conducting ionic membranes are described and evaluated in terms of applications in new-design electrochemical devices.

### INTRODUCTION

In view of improvements in the powering systems of consumer electronic devices and of the launch of long-range, commercial electric vehicles, large attention is presently devoted to lithium polymer batteries<sup>1</sup>. Indeed, today various are the R&D projects devoted to the progress of this type of batteries with the involvement of many prestigious academic and industrial laboratories. Such an outstanding effort is motivated by the fact that these batteries, in addition to a high energy content which is a general attribute of all lithium batteries, offer the benefit of an all-plastic, modulable-design configuration which instead is specific of the polymer systems.

The most crucial component of the lithium polymer batteries is the electrolyte, namely the membrane which acts both as the electrode separator and as the ionic medium. Following the initial development which considered complexes between a poly(ethylene oxide) host and a lithium salt, many other approaches, mainly directed to the enhancement of the ionic conductivity, have been pursued in the recent years. The results is that a large variety of electrolytic membranes are presently available. However, it is not yet fully clear which is the effective impact that these new and exotic polymer electrolytes may exert on the progress and the development of the lithium battery technology. Therefore, in this paper, after describing the properties of some examples of new classes of membranes, we attempt to evaluate their applicability and to suggest to which type of devices they can be profitably addressed.

### EXPERIMENTAL

The gel electrolyte membranes were prepared by immobilizing selected lithium salt solutions in a poly(acrylonitrile) PAN or in a poly(methyl methacrylate) PMMA matrix. The details of the synthesis procedure were reported in previous works<sup>2-4</sup>. For simplicity sake, the membranes are hereafter indicated by writing in sequence the selected lithium salt, the liquid solvent (or solvent mixture) and the immobilizing polymer. For instance, the notation LiClO<sub>4</sub>-EC-PC-PAN refers to a membrane formed by immobilizing a lithium perchlorate ethylene carbonate-propylene carbonate solution of in a poly(acrylonitrile) matrix.

All the electrolyte membranes were characterized using standard electrochemical equipment, such as impedance spectroscopy for transport properties and stability towards the lithium metal electrode, and cyclic voltammetry for electrode reversibility and cell cyclability.

The lithium rechargeable batteries were assembled in an environmentally controlled dry box by pressing into appropriate cases a sequence formed by the metal disk anode, the electrolyte membrane and the film cathode. The latter was alternatively a lithium cobalt oxide<sup>5</sup>, LiCoO<sub>2</sub> or poly(pyrrole)<sup>6</sup>, pPy. The thin-film, primary batteries were fabricated in a laminated structure which included the lithium metal anode strip, the electrolyte membrane and the M<sub>x</sub>YO<sub>4</sub> (M=As,Cu; X=W,Cr) cathode<sup>7</sup>. The rocking chair batteries were assembled using a

graphite (Lonza KS 44)-PMMA blend film, the electrolyte membrane, and a  $\text{LiMn}_2\text{O}_4$ -C-PMMA composite cathode film. The solid-state supercapacitors were based on two polypyrrole film electrode at different doping levels, separated by a thin electrolyte membrane.

The batteries and the supercapacitors were evaluated using standard electrochemical instrumentations.

## RESULTS AND DISCUSSION

### 1. Electrochemical properties of ionic membranes.

Among the various approaches followed to obtain ionically conducting membranes, the most popular and successful has been that involving the immobilization of liquid lithium salt solutions in a polymer matrix. The trapping procedure varies from case to case and includes crosslinking or gelification. Historically, gel-type membranes, formed by trapping liquid solutions into poly(acrylonitrile) PAN or poly(methylmethacrylate) PMMA, were first proposed in 1975 by Feuilade and Perche<sup>8</sup>. However, their relevance in the lithium battery field was fully recognized only recently following the work of Abraham and co-workers<sup>9,10</sup>, Scrosati and co-workers<sup>2,5</sup>, Halpert and co-workers<sup>11</sup> and Tarascon and co-workers<sup>12</sup>. A detailed investigation of the transport and the electrochemical properties of a large variety of these membranes has been carried out in our laboratory. Figure 1 illustrates the Arrhenius plots of some typical examples. The high ionic conductivity, which approaches that of the liquids (Figure 1 also shows for comparison reason the Arrhenius plot of a common liquid solution) is certainly the most distinctive and appealing feature of these membranes, often called "hybrid electrolytes"<sup>13</sup> or with the more inventive term of "gelionics"<sup>14</sup>. Furthermore, as determined in previous works<sup>2,4</sup> and summarized in Table 1, the fast ionic transport is accompanied by a series of other important properties, such as high lithium ion transference number and wide electrochemical stability.

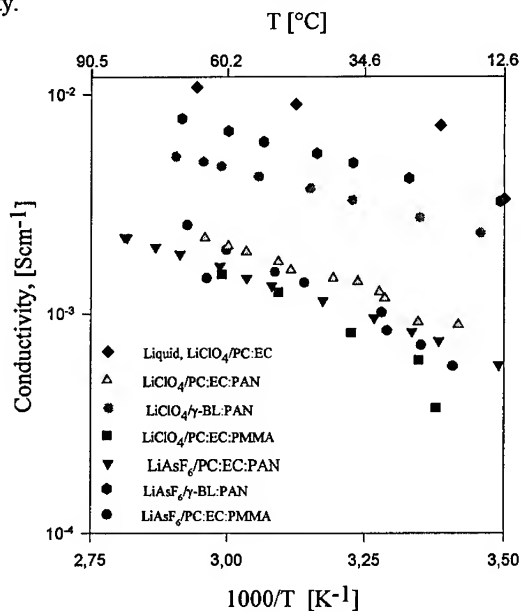


Figure 1.  
Arrhenius plots of various PAN- and PMMA-based gel-type membranes. The plot of the  $\text{LiClO}_4$ -PC/EC liquid solution is also reported for comparison purposes.  
PC = Propylene carbonate;  
EC = ethylene carbonate;  
BL =  $\gamma$ -butyrolactone.

Table 1- Electrochemical properties gelionic membranes at 25°C.

electrolyte	composition (mole ratio)	conductivity $10^3 \text{ Scm}^{-1}$	lithium transfer number	anodic stability (V vs.Li)
LiClO <sub>4</sub> -EC-PC-PAN	4.5-56.5-23-16	1.1	0.5-0.6	4.9
LiAsF <sub>6</sub> -EC-PC-PAN	4.5-56.5-23-16	0.9	0.6-0.7	4.3
LiN(CF <sub>3</sub> SO <sub>2</sub> ) <sub>2</sub> -EC-PC-PAN	4.5-56.5-23-16	1.0	0.7-0.8	4.6
LiClO <sub>4</sub> -BL-PAN	4.5-79.5-16	2.8	0.5-0.6	5.0
LiAsF <sub>6</sub> -BL-PAN	4.5-79.5-16	4.1	0.6-0.7	4.6
LiN(CF <sub>3</sub> SO <sub>2</sub> ) <sub>2</sub> -EC-BL-PAN	4.5-56.5-23-16	2.6	0.6	4.7
LiClO <sub>4</sub> -EC-PC-PMMA	4.5-46.5-19-30	0.7	0.4	4.6
LiAsF <sub>6</sub> -EC-PC-PMMA	4.5-46.5-19-30	0.8	0.6	4.8
LiN(CF <sub>3</sub> SO <sub>2</sub> ) <sub>2</sub> -EC-PC-PMMA	4.5-46.5-19-30	0.7	0.7	4.9

## 2. Lithium polymer batteries

From the results described in the previous session one may reasonably conclude that, at least in terms of transport characteristics, the progress on the electrolyte side has been outstanding and therefore, that a large variety of ionically conducting membranes are potentially available for use as separators in low-resistance, thin-film lithium batteries. To confirm this prevision, we have assembled and tested various cells having different nature and composition. Same typical examples are:

cell# 1:

Li/LiAsF<sub>6</sub>-EC-PC-PAN/LiCoO<sub>2</sub> (1)

cell # 2:

Li/LiClO<sub>4</sub>-EC-PC-PAN/poly(pyrrole) (2)

Typical room temperature charge-discharge cycles for the two cells, shown in figures 2 and 3, respectively, suggest that the gel-type membranes are in principle suitable for lithium battery applications.

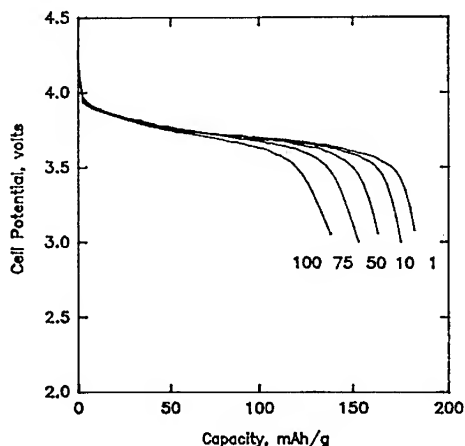


Figure 2. Voltage profile of a Li/LiAsF<sub>6</sub>-EC-PC-PAN/LiCoO<sub>4</sub> battery cycled at room temperature and at 0.25 mA cm<sup>-2</sup> rate. (From reference 5)

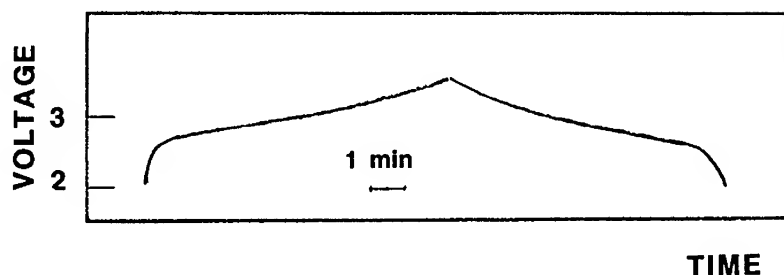


Figure 3- Voltage profile of a Li/LiClO<sub>4</sub>-EC-PC-PAN/pPy battery cycled at room temperature at 0.1 mA cm<sup>-2</sup> rate Ppy=Poly(pyrrole). (From reference 6).

### 3. The lithium electrode interface

The performance of the batteries described in the previous session, although remarkable in the initial stage of operation, tends to decay upon cycling. Typically, a high fraction of the theoretical capacity is delivered at the initial cycles after which a consistent decline in capacity occurs.

The phenomenon is common to all the lithium batteries examined in our laboratory, as well as, although at different extents, to the most of those reported in the literature. Obviously, this is a major problem which may affect the reliability of the batteries, thus limiting their practical development. Quite likely, kinetics problems related to the degradation of the lithium electrode interface, may be responsible for the cell failures. Infact, results obtained in our <sup>2,15</sup> and in other <sup>10</sup> laboratories, have clearly demonstrated that the lithium electrode undergoes serious passivation phenomena when in contact with the new generation, gel-type membranes. This is not surprising since these gels contain materials which are very aggressive towards lithium. As well known, uncontrolled passivation phenomena affect the cyclability of the lithium electrode (and thus, of the entire battery) and may eventually lead to a serious safety hazard.

Therefore, it appears of paramount importance to fully control the chemical and the electrochemical reactions occurring at the interface, and this requires a clear understanding of the nature and the morphology of the passivation film growing on the lithium electrode when in contact with a given electrolyte membrane. With the aim of achieving this important goal, we have developed a model of the lithium interface based on detailed impedance analyses<sup>5</sup>. According to this model which is illustrated in Figure 4, upon contact with the electrolyte lithium experiences an initial passivation reaction with the formation of a compact layer which grows directly on the metal surface (or on a native film). On prolonged contact time, the passivation phenomena give rise to an additional, porous layer, whose nature and morphology probably depend upon the type of solvent, the type and amount of impurities and upon other unpredictable causes (e.g. direct reaction with the host polymer and physical separation of the anode from the gel electrolyte). As long as this additional layer remains porous, the rise in the interfacial resistance is limited; however, with extended contact time, the layer becomes progressively denser to finally collapse on the electrode interface with a consequent sharp rise in the interfacial resistance. Therefore, the model of Figure 4 suggests that is the second thick layer the one which mostly affects the lithium electrode performance and hence, that studies should be directed to inhibit its formation and growth. One approach in this direction is the selection of electrolytes based on components which are expected to be the less aggressive towards the lithium metal. A second approach is the addition to the electrolyte of materials

which may act as impurity-getters, namely of substances capable of trapping the impurities, so preventing their flow to the interface.

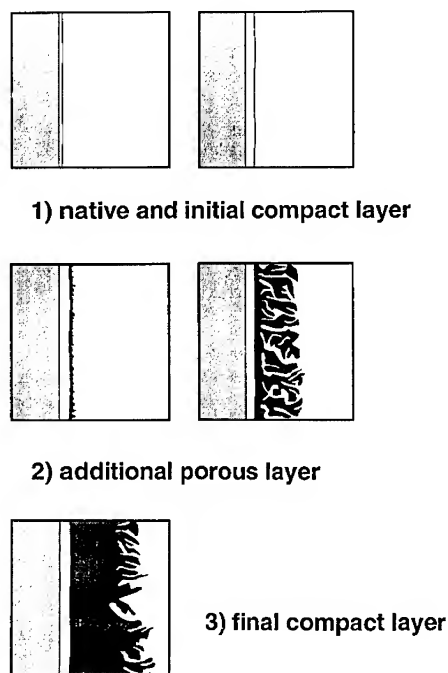


Figure 4- Model of the passivation phenomena occurring at the lithium electrode/gel-type membrane interface. (From reference 5).

Ceramic fillers like  $\gamma$ -lithium al uminate or zeolites, are expected<sup>16-18</sup> to satisfactorily fulfill this action. These expectations are confirmed by practical results; in fact, addition of zeolites to the  $\text{LiClO}_4\text{-EC-PC-PAN}$  membrane considerably alleviates the passivation of the lithium electrode as shown in Figure 5 which compares the trend of the interfacial resistance of a Li electrode in contact with the  $\text{LiClO}_4\text{-EC-PC-PAN}$  membrane and with the same membrane added with zeolite.

The beneficial effect of the ceramic fillers on the response of the interface is further confirmed by the induced improvements in the lithium cycling efficiency which increases from 72% in the plain  $\text{LiClO}_4\text{-EC-PC-PAN}$  membrane electrolyte to a value of 85% for a cell using a composite ( $\text{LiClO}_4\text{-EC-PC-PAN}+10$  weight percent zeolite) membrane. Further improvements can also be obtained when substituting poly(acrylonitrile) with poly(methyl methacrylate) as the polymer component<sup>2</sup>. However, although encouraging, these improvements are still not sufficient for practical purposes. In fact, for assuring acceptable applicability, the lithium cycling efficiency should fall between 97 and 99% and, at the present stage of knowledge, it is difficult to foresee that such values can be achieved in cells using the above discussed gel-membranes.

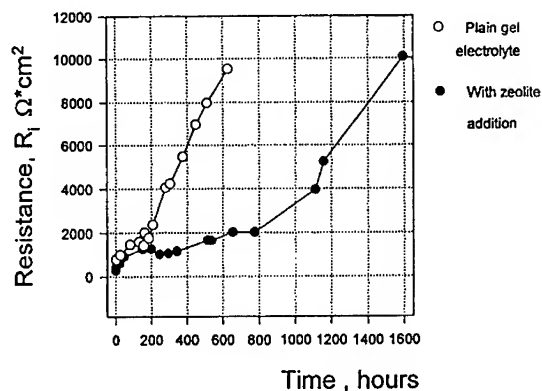
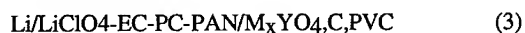


Figure 5- Time evolution of the interfacial resistance of the lithium electrode in a plain (-o-) and in a zeolite-added (-●-)  $\text{LiClO}_4\text{-PC-EC-PAN}$  membrane. Data obtained by impedance analysis.(From Reference 6).

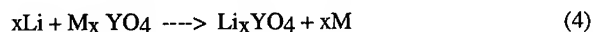
In conclusion, concern should be taken when proposing new electrolytes for applications in electrochemical devices. If the envised application is in lithium batteries, beside transport properties, electrode compatibility should additionally be chosen among the most crucial selection requisites. The results here discussed suggest that gel-type electrolyte membranes, and quite likely the majority of the wet polymer electrolytes which generally contain aggressive liquid components, do not fulfill the requirements for applications in long-life, rechargeable, lithium metal batteries. If one wants to successfully exploit the outstanding transport properties of these electrolytes, alternative types, yet technologically important, devices should be considered. These include primary thin layer batteries, rocking-chair batteries and supercapacitors.

#### 4. Primary thin film lithium batteries

Batteries of the type:



have been fabricated in a laminated structure which includes a lithium metal anode strip, a gel-type electrolytic membrane and a cathode layer <sup>7</sup>. The latter was formed by blending a mixture of  $\text{M}_x\text{YO}_4$  ( $\text{M} = \text{Ag, Cu}$ ;  $\text{Y} = \text{W, Cr}$ ), carbon and poly(vinylchloride) PVC. The important feature of these batteries is that the main discharge process:



is a displacement reaction which produces the  $\text{Li}_x\text{YO}_4$  salt and the  $\text{M}$  ( $\text{M} = \text{Ag, Cu}$ ) metal. Since this reaction involves two-phases, the voltage remains constant until completion of the discharge. Furthermore, the continuous production of finely dispersed metal assures a good electronic contact throughout the entire cathode mass and this consistently reduces ohmic polarization during discharge. All this reflects in a remarkable performance, as clearly shown in

figures 6 and 7 which illustrates typical continuous and pulse discharge curves, respectively, of two types of  $\text{Li/MxYO}_4$  batteries. The exceptional flatness of the discharge curves and the fast recovery after the pulse are two specific features of these batteries. Due to these important characteristics, the batteries appear particularly suitable for the consumer electronic market, such as smart credit cards, small calculators and similar products.

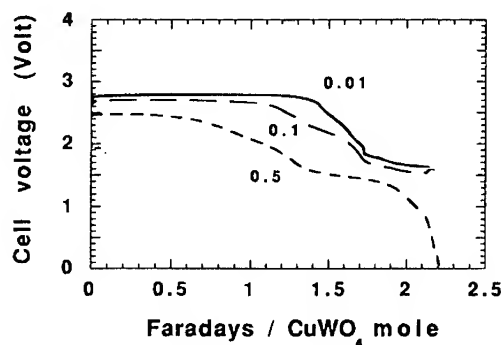


Figure 6- Typical discharge curves at the Li-CuWO<sub>4</sub> thin-film polymer battery at room temperature and at various rates given in mA cm<sup>-2</sup>. (From reference 7)

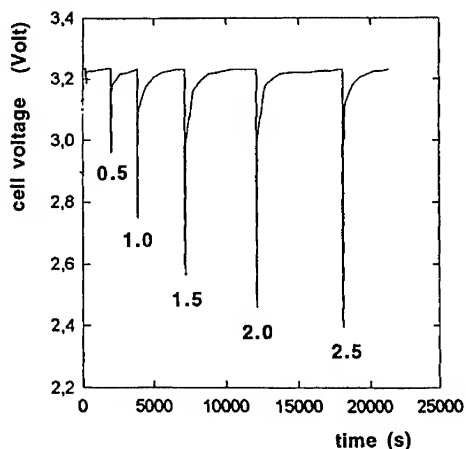


Figure 7- Pulse (30s) discharge at various current rates (given in mA cm<sup>-2</sup>) of the Li/Ag<sub>2</sub>CrO<sub>4</sub> thin film polymer battery.

##### 5. Laminated rocking chair batteries

As well known, the most common configuration of rocking chair batteries uses lithiated carbon,  $\text{Li}_x\text{C}_6$ , as the negative electrode, a lithium metal oxide  $\text{LiMO}_2$  ( $\text{M}=\text{Co}, \text{Ni}$ ) or

$\text{LiMn}_2\text{O}_4$ , as the positive electrode and liquid organic solutions as the electrolyte<sup>19-21</sup>. Due to the high oxidizing character of the selected cathode, these batteries may suffer from electrolyte decomposition upon cycling. Therefore, the replacement of the liquid electrolyte with a solid, thin-layer, Li-ion conducting membrane would be highly beneficial in terms of performance, especially if this membrane has a high ionic conductivity and a wide electrochemical stability window. The gelionic membranes above discussed seem to fulfill these conditions and thus, they appear to be compatible with the  $\text{Li}_x\text{C}_6/\text{LiMO}_2$  couples. To confirm this prevision, we have considered the cell:



having the electrodes fabricated by blending both the graphite (Lonza KS 44) and the lithium manganese oxide with PMMA and carbon. Preliminary results confirm the feasibility of the rocking chair concept in the laminated structure. Such a feasibility has also been shown in other laboratories<sup>9,12</sup> and the development of laminated lithium ion polymer batteries is actively in progress. It may also be pointed out that in addition to carbon, other lithium ion anodes have been successfully used in gel electrolyte rocking chair batteries. Particular interest is the behavior of transition metal sulphides, such as titanium-disulphide<sup>22</sup>.

## 6. Solid state supercapacitors

The applicability of the gel-type membranes for the development of new-design, laminated supercapacitors, has been tested by considering the system:



where  $\text{pPy}^{+++}$  and  $\text{pPy}^+$  are heavily and lightly, respectively, p-doped poly(pyrrole) electrodes. Thus, this system works as a supercapacitor of the redox type<sup>23</sup> where the usual liquid electrolyte is replaced by one of the above discussed ionic membranes. Figure 8 shows a cyclic voltammetry of the capacitor and Figure 9 a series of galvanostatic discharge curves. Although in a very preliminary form, the results suggest a good response and thus that the laminated configuration may be further exploited and optimized for the fabrication of capacitors of practical importance.

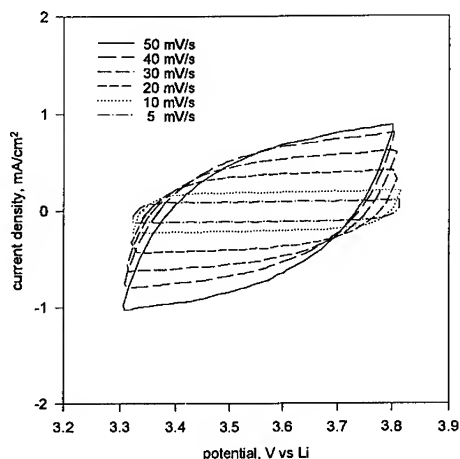


Figure 8-Cyclic voltammetry of a  $\text{pPy}^{+++}/\text{LiClO}_4\text{-EC-PC-PMMA}/\text{pPy}^+$  laminated redox capacitor at room temperature and at various scan rates.



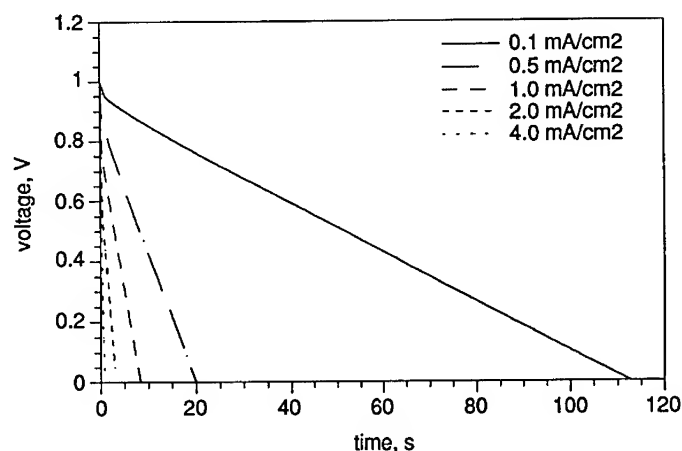


Figure 9- Discharge curves of a  $\text{pPy}^{++}/\text{LiClO}_4\text{-EC-PC-PMMA/pPy}^+$  laminated redox capacitor at room temperature and at various rates.

## 7. Conclusions

The properties and the behavior of the gel-type membranes here discussed are directly related to their particular configuration. In fact, these membranes contain loosely trapped liquid electrolyte solutions and thus, they are usually considered as hybrid or wet-like systems. Due to this particular structure, the ionic transport approaches that of the liquid phase and this accounts for the very high conductivity. On the other hand, the syneresis of the liquid component, which is an unavoidable consequence of the two-phase configuration, is very detrimental in terms of the stability towards the lithium metal electrode due to fast corrosion effects. This makes problematic the use of the membranes for rechargeable, long-life lithium batteries. On the contrary, the wetting action may be very useful in the case of devices based on non-metal, high-surface electrodes. In fact, in these cases the dispersion of the liquid electrolyte may assure the formation of the necessary protecting layer (carbon rocking-chair anodes) or the intimate interfacial contact (redox capacitor electrodes). Indeed, the preliminary results obtained in our laboratory and particularly those reported by others<sup>9-12</sup> on operating devices, seem to confirm the unique and important impact that the gel membranes may exert to the progress of laminated, advanced electrochemical power sources.

## Acknowledgements

This work has been in part supported by the US Air Office of Scientific Research, EOARD, under contracts SPC-92.4003 and SPC-93-4033.

## References

1. Applications of Electroactive Polymers, Ed. B. Scrosati (Chapman & Hall Pu., London, 1993) p. 182.
2. G. Appetecchi, F. Croce, G. Dautzenberg, S. Passerini, B. Scrosati *Electrochim. Acta*, **39**, 2187, (1994) .
3. G. Dautzenberg, F. Croce, S. Passerini, B. Scrosati, *Chem. Mat.* **6**, 538(1994) .
4. G.B. Appetecchi, F. Croce and B. Scrosati, *Electrochim Acta*, in press.
5. F. Croce, B. Scrosati and M. Salomon, in Proceedings of the 36th Power Sources Conferences, Cherry Hill, N.J. June 1994, p. 57.
6. S. Kakuka, T. Momma, T. Osaka, G.B. Appetecchi and B. Scrosati, *J. Electrochem. Soc.*, in press.
7. S. Passerini, S. Loutzky, B. Scrosati *J. Electrochem. Soc.* **141**, L80 (1994) .
8. G. Feullade and Ph. Perche, *J. Appl. Electrochem.*, **5**, 63(1975) .
9. K.M. Abraham, in Applications of Electroactive Polymers, Edited by B. Scrosati (Chapman & Hall Pu., London, 1993) p.75.
10. K.M. Abraham and M. Alamgir, *J. Power Sources*, **44**, 195(1993) .
11. G. Nagajubramanian, A.I. Attia and G. Halpert, *J. Appl. Electrochem.* **24**, 298(1994) :
12. C. Schmutz, J.M. Tarascon, A.S. Gordz, P.C. Warren and F.K. Shokoohi, Electrochem. Soc. Meeting, Miami, Florida, Oct. 9-14, 1994 abstr. n. 109.
13. C. Arbizzani, M. Mastragostino, L. Meneghello, X. Andrieu and T. Vicedo, in Mat. Res. Soc. Symp. Proceedings, Vol. **293**, 169 (1993) .
14. B. Scrosati, in Solid State Ionic Materials, edited by B.V.R. Chowdari et.al. (World Sci Pu. Singapore, 1994) p. 111.
15. F. Croce and B. Scrosati, *J. Power Sources*, **44**, 9 (1993) .
16. F. Croce, B. Scrosati, *Polym. Adv. Techn.*, **4**, 198 (1993) .
17. M. Borghini, M. Mastragostino, S. Passerini and B. Scrosati, *J. Electrochem. Soc.*, submitted.
18. S. Slane and M. Salomon (1994), in course of publication.
19. T. Nagura and K. Kazawa, *Prog. Batt. Solar Cells*, **9**, 203 (1990) .
20. B. Scrosati, *J. Electrochem. Soc.* **139**, 2776 (1992) .
21. J.M. Tarascon and D. Guyomard, *J. Electrochem. Soc.*, **139**, 937 (1992) .
22. S. Passerini, S. Loutzy, and B. Scrosati, *J. Electrochem. Soc.*, **141**, L80 (1994).
23. A. Rudge, J. Davey, I. Raistrick and S. Gottesfeld, *J. Power Sources*, **47**, 89 (1994).

## NON-CRYSTALLIZING MOLTEN SALT AND IONIC RUBBER ELECTROLYTES WITH WIDE ELECTROCHEMICAL WINDOWS

K. XU AND C. A. ANGELL

Dept. of Chemistry, Arizona State University, Tempe, AZ 85287, USA

### ABSTRACT

New realizations of the type of ambient temperature lithium ion conducting electrolyte introduced at this symposium two years ago are given and a 5 volt electrochemical window, absent from the earlier examples, is demonstrated. The new systems satisfy the criteria for "ionic oils" though their conductivities,  $\sim 10^{-3} \text{ S cm}^{-1}$ , are smaller than desirable.

### INTRODUCTION

Two years ago at this symposium we made the first announcement of a new class of solid electrolytes, designated "polymer-in-salt-electrolytes," or "ionic rubbers." These materials have potential applications in cells because of their combination of high cationic conductivity and rubbery compliance. The latter is due to the presence of a small amount of high molecular weight polymer dissolved in a liquid salt mixture. While the original formulations had impressive conductivities they suffered from problems of recrystallization over long periods at ambient temperature, and in addition they showed rather poor chemical and electrochemical stabilities. In the interim, some of these problems have been resolved and we report here some results on new systems which are much closer to being practical realizations of the "ionic rubber" electrolyte concept.

The new materials depend to a large extent on the synthesis of variants of the anion trifluoromethane sulfonimide, which was first utilized in conventional salt-in-polymer electrolytes by Armand.<sup>(1)</sup> In work being reported elsewhere<sup>(2)</sup> we describe the synthesis of several anions of the imide type with lower molecular weights than the above: the lithium salts of these anions seem incapable of crystallization. The salts have higher glass transition temperatures than expected, and the lithium ions are strongly coupled to the anion, hence the new imides themselves have poor conductivities at ambient temperature. However both properties change favorably when the salt is complexed with  $\text{AlCl}_3$ . Further enhancement of the conductivity by the addition of lithium tetrachloroaluminate results in systems which, while apparently incapable of crystallization, have conductivities above  $10^{-4} \text{ S cm}^{-1}$ . Such systems also prove to have very wide electrochemical windows and to support reversible deposition of lithium in cyclic voltammetry experiments. These findings suggest that practical realizations of the ionic rubber concept are close at hand.

## EXPERIMENTAL

The new imides, dichlorosulfonimide  $[N(CISO_2)_2]^-$  and chlorofluorosulfonimide  $[ClSO_2-N-SO_2F]^-$  anions, were synthesized as acids by procedures being described elsewhere,<sup>(2)</sup> and converted to lithium salts by reaction with lithium hydride. Their behavior individually, in  $AlCl_3$ -complexed form, and in mixtures with lithium aluminum chloride, was investigated.

Glass transition temperatures and liquidus temperatures (where measurable) were determined using differential scanning calorimetry. DC conductivities were determined by complex impedance analysis of data obtained using an automated Hewlett-Packard Model HP4192A Frequency Impedance Analyzer, and dip-type cells with platinum wire electrodes. The electrochemical characteristics were determined using an EG&G Princeton Applied Research potentiostat/galvanostat Model 273, and a three platinum electrode cell. Scans were conducted at different scan speeds, but are reported only for the scan speed 20 mV/s.

## RESULTS

As described in more detail elsewhere,<sup>(2)</sup> the lithium salts of the imide anions referred to in the previous section are very resistant to crystallization, hence no melting points can be reported. The glass transition temperatures of these two salts, unfortunately for the present purposes, are either at (25°C, chlorofluoro case) or above (~35°C, dichloro case) room temperature. Since the lithium cations in imides, notwithstanding the low anion basicities, are strongly coupled to the anions, the ambient electrical conductivities are immeasurably low.

In order to obtain an electrolyte which conducts under ambient conditions, both the glass transition temperature and the coupling of the lithium cation to the imide anion must be reduced. This may be achieved by preparing the one-to-one adduct of the imide with the Lewis acid  $AlCl_3$ . The new anions are thus unsymmetrical variants of the  $AlCl_4^-$  anion. These new salts also show no tendency to crystallize at room temperature despite glass transition temperatures which now fall well below room temperature.  $T_g$  for the dichloro-anion-based salt is found to be -21°C while that for the mixed fluorochloro-imide-based salt is even lower at -35°C.

The conductivity of the chlorofluorosulfonimide chloroaluminate salt, which is more fluid than the dichloro analog at ambient temperature, is shown in Arrhenius form in Fig. 1. It is only  $10^{-5.7}$  S  $cm^{-1}$  at 25°C, which is disappointing considering its low  $T_g$  value.

The phase behavior of mixtures of this salt with lithium tetrachloroaluminate, is shown in Fig. 2. It is noticed that crystallization can only be observed in the lithium tetrachloroaluminate-rich half of the phase diagram. Furthermore, by a short extrapolation of the liquidus line, this melt would evidently be thermodynamically stable with respect to  $LiAlCl_4$  crystallization at room temperature for all compositions containing less than 50% of the tetrachloroaluminate. The glass transition temperatures are included in the diagram, and it can be estimated that the crystallization of the tetrachloroaluminate would become intrinsically impossible ( $T_{liquidus} < T_g$ ) for  $X_{LiAlCl_4} < \sim 0.4$ .

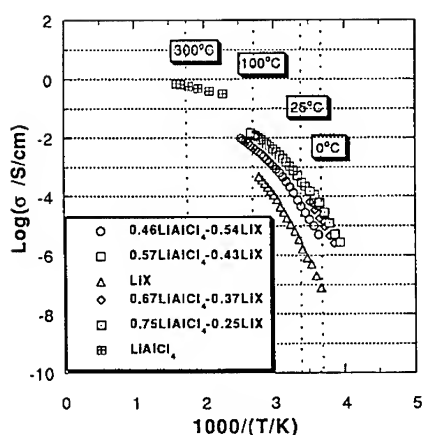


Fig. 1. DC conductivities of several melts of this study as indicated in figure legend. shown in Arrhenius form. X in the legend represents the fluorochlorosulfonimidetrichloroaluminate anion.

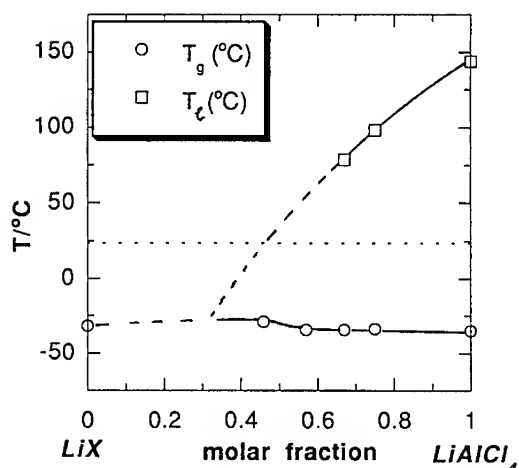


Fig. 2. Partial phase diagram for the binary system lithium chlorofluoro sulfonimidetrichloroaluminate +  $\text{LiAlCl}_4$ , showing wide uncrystallizable region, and also glass transition temperatures.

The conductivities of selected compositions in this binary system are included in the Arrhenius plot, Fig. 1, and are also displayed as isotherms vs mole fraction of  $\text{LiAlCl}_4$  in Fig. 3. At mole fraction 0.57 of  $\text{LiAlCl}_4$  the ambient temperature conductivity reaches  $10^{-3.3} \text{ S/cm}$ . This composition will crystallize slowly on standing at room temperature, but at the 1:1 composition, a conductivity of  $10^{-3.9} \text{ S cm}^{-1}$  is achieved in the absence of any crystallization at all. The isothermal conductivities show a jump in the vicinity of the 1:1 composition, the structural origin of which is not obvious. The data obtained at higher temperatures are compatible with extrapolations of  $\text{LiAlCl}_4$  conductivity data extrapolated below the melting point according to the Arrhenius plot given by Weppner and Huggins.<sup>(3)</sup>

Finally, in Fig. 4 we demonstrate the electrochemical stability of the 0.57 $\text{LiAlCl}_4$  binary solution using a cyclic voltammogram conducted at 20 mv/s. We note that the Li deposition and stripping parts of the plot superimpose, and remark that area assessments indicate almost complete reversibility of the process. There is no sign of Al deposition, suggesting that  $\text{Al}^{3+}$  is kinetically protected against electron transfer (hence reduction) by its stable complex environment. The temperature up to which this favorable situation obtains has not yet been determined.

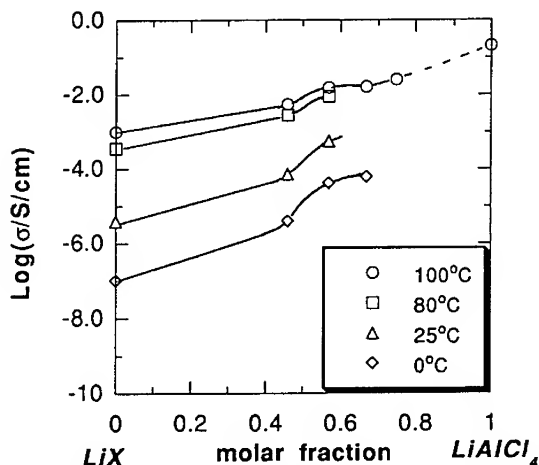


Fig. 3. Conductivity isotherms for binary solutions in the system of Fig. 2. X is defined in Fig. 1 caption.

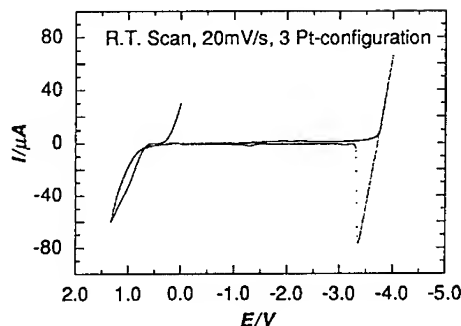


Fig. 4. Cyclic voltammograms on the binary melt of the above system containing 57%  $\text{LiAlCl}_4$  showing voltage window of  $\sim 5\text{V}$ , and reversible lithium deposition and stripping.

## DISCUSSION

### Crystallization Characteristics

The reason for the welcome reluctance of the two new imides to crystallize is at this time unclear. Elemental analysis yields compositions in close accord with calculated values hence the stability against crystallization is presumably intrinsic rather than impurity-induced. Since lithium trifluoromethanesulfonimide melts at  $236^\circ\text{C}$ , it seems unlikely that the new imides could have melting points below their glass transition temperatures and therefore in principle they should be capable of being crystallized even if the nucleation event is very improbable. Efforts to crystallize them will be made in the future in order to gain information on the relation between structure and melting point.

In previous studies we have noted that when a lithium salt in which the anion can act as a Lewis base is reacted with the strong acid  $\text{AlCl}_3$ , the 1:1 adduct which forms either fails to crystallize or has a melting point sharply lower than that of the original salt. The best known case is that of  $\text{LiAlCl}_4$  itself<sup>(3)</sup> in which the complex melting point is  $145^\circ\text{C}$  compared with the melting point  $605^\circ\text{C}$  for  $\text{LiCl}$  itself. This effect is more pronounced when the new ligand yields an unsymmetrical chloroaluminate anion and usually gives rise to crystallization temperatures so low relative to the melt viscosity that the nucleation kinetics are greatly retarded and glassforming ability results. If the initial lithium salt is resistant to crystallization, due to low melting point, as in the case of the imides synthesized for this study, then the additional melting point lowering associated with the addition of the strongly interacting  $\text{AlCl}_3$  should render crystallization impossible. While the possibility of higher melting adducts cannot be ruled out, it seems probable that "the barely stable compound" principle<sup>(4)</sup> should apply to the present system and that the melting point of the 1:1 adduct, lithium chlorofluorosulfonamidetrichloroaluminate, should

be extremely low and perhaps impossible to determine in principle. The latter obtains if the liquid can be shown to be thermodynamically stable at its glass transition temperature, as has been documented in isolated cases.<sup>(5)</sup>

Assuming that the melting point of the adduct has at least been pushed to below ambient temperature (even the simple tetrahaloaluminate  $\text{LiAlCl}_3\text{I}$  melts as low as  $80^\circ\text{C}$ ),<sup>(6)</sup> then we can claim to have prepared a real lithium "ionic oil", or ambient-uncrystallizable lithium ionic liquid. Supposing that even this compound were to have a melting point, then this melting point would be further depressed by the addition of a second component,  $\text{LiAlCl}_4$ , in the binary system illustrated in Fig. 2. The claim that melts in that system containing less than 0.4 mole fraction of  $\text{LiAlCl}_4$  are uncrystallizable, is probably a strong one, though the jog in the glass transition temperature near the 1:1 composition hints at some structural peculiarity which may indicate an ordering of anions, and a possible crystalline compound may form. A binary system in which the second component is  $\text{LiAlCl}_3\text{I}$  or a comparable mixed haloaluminate would presumably become uncrystallizable with respect to this component at higher tetrahaloaluminate content, and such systems may be advantageous.

It is worth noting the relation of this type of system to the two component ice + sugar, or ice + protein systems discussed by Slade and Levine.<sup>(7)</sup> In these systems the key feature is the uncrystallizability of one component in a binary system without binary compounds. In the resulting pseudo-phase diagram the eutectic temperature and eutectic composition are replaced by a pseudo fixed point called  $T_g'$ , where the solution composition is  $X'$  in the uncrystallizable component. At  $T_g'$  the liquidus temperature for the crystallizable component reaches the glass transition temperature of the binary solution. Then, for reasons of vanishing crystal growth rates, no further crystallization (hence no further melting point lowering) is possible. Following this line of thought we identify the composition 70% imidetrichloroaluminate as  $X'$  and  $T_g'$  as  $-36^\circ\text{C}$ , though this depends on the absence of a 1:1 crystal form.

### Conductivity

The conductivity of the first ambient temperature-uncrystallizable solution, according to the above discussion, is  $\sim 1 \times 10^{-4} \text{ S cm}^{-1}$ . While this is not as high as desirable it is certainly an improvement on the best single ion conducting polymer system reported to date.<sup>(8)</sup> We hope to improve it considerably in future work. Rubberization requires incorporation of a small amount of an  $\text{AlCl}_3$ -resistant high molecular weight polymer which will be described in a future publication.

### Electrochemical Stability

Finally we turn to the question of electrochemical stability. The stability of these liquids against aluminum deposition was unexpected. While the reversible deposition of lithium from molten tetrachloroaluminates has been reported before<sup>(9)</sup> it has only been possible in the case of melts containing both excess chloride ion and additions of  $\text{HCl}$ . The mechanism by which the  $\text{Al}^{3+}$  is protected has not been determined. Our liquids have no excess chloride and no  $\text{HCl}$  and in any case the drop in activity of  $\text{AlCl}_3$  across the  $[\text{Cl}^-]:[\text{Al}^{3+}] = 4.0$  point is very much smaller than in the case of the organic cation tetrachloroaluminates studied previously. Therefore it seems unlikely that thermodynamic stabilization of the aluminate is playing an important role in our phenomenology. More probable is the role of the high

viscosity in our system at the temperature of the experiment. We conjecture that a critical requirement for electron transfer to the aluminum at the electrode surface is the transient exposure of the  $\text{Al}^{3+}$  center to the electrode electrons during a ligand exchange, i.e. the  $\text{AlX}_4^-$  complex lifetime is involved.

Although little formal study of the problem has been made it seems reasonable to suppose that in a glassforming melt such a ligand rearrangement is severely restricted in probability by the requirement that all such processes be cooperative in nature. For instance, ligand exchange around a cobalt ion in an ionic melt has been observed to have essentially the same time scale as that of the structural relaxation of the melt taken as a whole.<sup>(10)</sup> If the complex has a special stability which discourages ligand exchange, as in the case of chloroaluminates, then it seems that such exchanges would occur very much *less* frequently than the rearrangements of other particles around them, i.e. than the structural relaxation time. By this argument the probability of ligand exchange around  $\text{Al}^{3+}$  under conditions in which even the structural relaxation time is approaching the long values characteristic of the glass transition, would become extremely small. Clearly, then, the success of our electrolyte in resisting Al deposition is critically dependent on our success in ensuring that motion of the lithium ion can occur independently of its environment, since it is this decoupling factor which permits us to have a high conductivity in the presence of a high viscosity.

The possibility of using low glass transition temperature, high conductivity, chloroaluminated lithium salt melts in lithium rechargeable batteries which is raised by the above line of thought, and supported by the observations of Fig. 4, must be regarded as a serendipitous byproduct of our search for the decoupled cation, high conductivity, low temperature liquid electrolytes. We hope to report vindications of the concept in future papers in which these electrolytes are incorporated into electrochemical cells.

#### ACKNOWLEDGEMENTS

This work was supported by the Department of Energy under Grant No. DEFG0393ER14378.

#### REFERENCES

1. M. Armand, W. Gorecki, and R. Andreani, Proc. 2nd. Int. Conf. Pol. Electrolytes, Sienna, Italy, p. 614-16. (1990).
2. K. Xu and C. A. Angell, to be submitted to *Inorganic Chemistry*.
3. W. Weppner and R. A. Huggins, J. Electrochem. Soc., 124, 35, (1977).
4. C. A. Angell, M. Videa, and K. Xu (to be published).
5. G. Vuillard, Ann. Chim. (Paris), 2, 233, (1957).
6. Changliu Liu and C. A. Angell, unpublished work.
7. L. Slade, H. Levine, and J. W. Finley in *Protein Quality and Effects of Processing*, edited by R.D. Phillips and J. W. Finley (Marcel Dekker Inc., New York, 1989).
8. J-V. Sanchez, F. Alloin, D. Benrabah, and C. Roux, (this volume)
9. T. L. Riechel and J. S. Wilkes, J. Electrochem. Soc., 139, 4 (1989).
10. R. Bohmer and C. A. Angell, J. Phys. Chem., 96, 9089, (1992).



## ELECTRICAL PROPERTIES OF HIGH ION CONDUCTIVE POLYMER COMPLEXES CONTAINING ROOM TEMPERATURE MOLTEN SALT

NORIO AOSHIMA, MASAHIRO RIKUKAWA, KOHEI SANUI, NAOYA OGATA  
Sophia University, Department of Chemistry, 7-1 Kioi-cho, Chiyoda-ku, Tokyo, 102, Japan

### ABSTRACT

New ion conductive polymers were obtained by dissolving polycations into room temperature molten salt consisting of methyltriethylammonium chloride (MEACl) and aluminium chloride ( $\text{AlCl}_3$ ). These complexes formed viscoelastic solids when the polycation content was increased more than 4 unit mol%. The ionic conductivity of polycation complexes was in the range of  $10^{-4}$ – $10^{-3} \text{ Scm}^{-1}$  at room temperature and were affected by their composition, types of polycations, and counter anion species.

### INTRODUCTION

Ion conductive polymers with light weight and excellent processability have been attracting many attentions for their potential technological applications as organic solid electrolytes for use in batteries. Ion conductive polymers in "salt in polymer systems" have been studied most intensively [1,2], where the polymer serves as a solvent for an inorganic salt, and the transport of charge carrier ions, generated by the dissociation of organic salts, is associated with the segmental motion of the polymer. Since  $T_g$  of the ion conductive polymers rises with increasing salt concentrations due to the interaction between the polymer segments and carrier ions, the ionic conductivity have limited to the values about  $10^{-5}$ – $10^{-4} \text{ Scm}^{-1}$ . Consequently, the simultaneous increases of carrier ion and mobility are inconsistent.

It is known that molten salts are formed by mixing ammonium compounds and aluminium chloride. The molten salts are ionic liquids and consist of only ions, and these materials have high ionic conductivity of about  $10^{-3}$ – $10^{-2} \text{ Scm}^{-1}$  at moderate temperatures.

This study deals with the preparation and the electrical properties of new ion conductive polymer complexes composed of room temperature molten salts and polycations. (Figure 1) [3] The molten salt was obtained by mixing MEACl and  $\text{AlCl}_3$  with a 1 / 2 (MEACl /  $\text{AlCl}_3$ ) mole ratio, and the conductivity of molten salt was about  $3 \times 10^{-3} \text{ Scm}^{-1}$ . Novel ion conductive polymer complexes were prepared by dissolving polycations into the MEACl /  $\text{AlCl}_3$  molten salt. The polycations used in this study are containing ammonium, pyridinium, phosphonium, or sulfonium salt unit in these main or side chains.

### EXPERIMENTAL

#### Preparation of room temperature molten salt

Room temperature molten salts were obtained by mixing MEACl and  $\text{AlCl}_3$  in an argon-filled drybox. MEACl was recrystallized twice from ethanol / ethyl acetate.  $\text{AlCl}_3$  was purified by sublimation method as follows: in the argon-filled drybox, crude  $\text{AlCl}_3$ , aluminium wires, and a small amount of sodium chloride were put into a glass tube, and were dried in vacuum at  $80^\circ\text{C}$ . Then the tube was cooled down to room temperature and sealed completely. This tube was heated up gradually from room temperature to  $195^\circ\text{C}$  step by step and kept at  $195^\circ\text{C}$  for 12 hours. At last the tube was pulled up very slowly at a rate of  $1.0 \text{ cmh}^{-1}$ .

	Ammonium type	Pyridinium type	Sulfonium type Phosphonium type
Main chain type	$\left[ \begin{array}{c} (\text{Br}^-) \quad (\text{Br}^-) \\ \text{Cl}^- \quad \text{CH}_3 \quad \text{Cl}^- \quad \text{CH}_3 \\   \quad   \\ (\text{CH}_2)_3 \text{N}^+ (\text{CH}_2)_6 \text{N}^+ \\   \quad   \\ \text{CH}_3 \quad \text{CH}_3 \end{array} \right]_n$ <p><b>PBCL, (PBBr)</b></p>	$\left[ \begin{array}{c} (\text{Br}^-) \quad (\text{Br}^-) \\ \text{Cl}^- \quad \text{Cl}^- \\   \quad   \\ \text{H}_2\text{C}-\text{N}^+ \text{---} \text{C}_5\text{H}_4 \text{---} \text{N}^+ \text{---} \text{CH}_2 \\   \quad   \\ \text{CH}_3 \quad \text{CH}_3 \end{array} \right]_n$ <p><b>PMVCl, (PMVBr)</b></p>	$\left[ \begin{array}{c} \text{I}^- \quad \text{I}^- \\   \quad   \\ (\text{CH}_2)_4 \text{S}^+ (\text{CH}_2)_6 \text{S}^+ \\   \quad   \\ \text{CH}_3 \quad \text{CH}_3 \end{array} \right]_n$ <p><b>PSI</b></p>
Side chain type	$\left[ \begin{array}{c} \text{CHCH}_2 \\   \\ \text{C}_6\text{H}_4 \\   \\ \text{CH}_2 \\   \\ \text{H}_3\text{C}-\text{N}^+-\text{CH}_3 \\   \\ \text{CH}_3 \end{array} \right]_n$ <p><b>PBACl</b></p>	$\left[ \begin{array}{c} \text{CHCH}_2 \\   \\ \text{C}_5\text{H}_4\text{N}^+ \\   \\ (\text{CH}_2)_3 \\   \\ \text{CH}_3 \end{array} \right]_n$ <p><b>PPyCl, PPyBr</b></p>	$\left[ \begin{array}{c} \text{CHCH}_2 \\   \\ \text{C}_6\text{H}_4 \\   \\ \text{CH}_2 \\   \\ \text{P}^+ (\text{C}_6\text{H}_5)_3 \end{array} \right]_n$ <p><b>PBPCl</b></p>

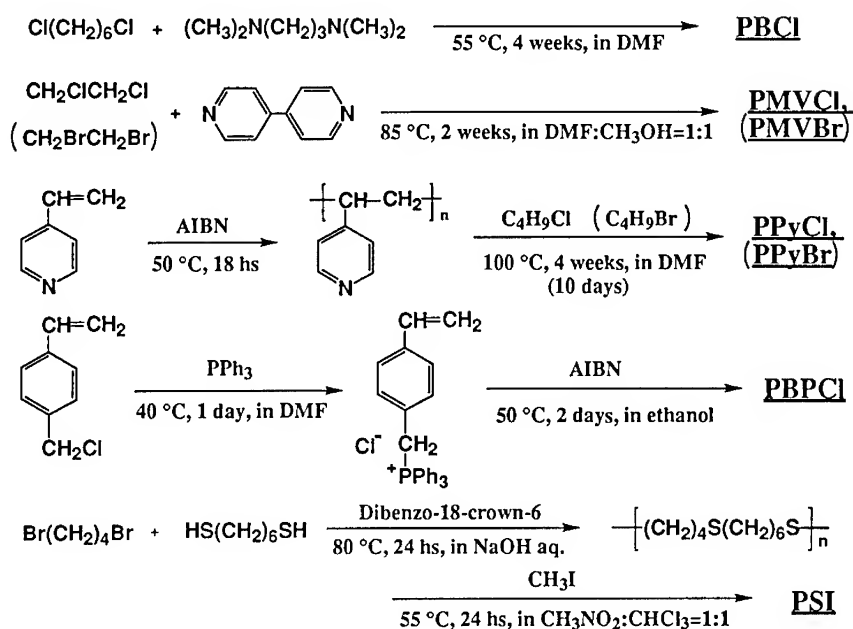
Figure 1 Structure of polycations.

#### Synthesis of room temperature molten salt / polycation complexes

The polymer complexes were prepared as described below. After heating room temperature molten salt to about 150 °C, the polycation was added into the molten salt with stirring. The polycations were dissolved completely in the room temperature molten salt, then these complexes were cooled down to room temperature. Homogeneous viscoelastic solids were obtained.

The polycations used for preparation of complexes with the room temperature molten salt were poly(*N,N,N',N'*-tetramethyl-*N*-trimethylenehexamethylenediammonium dichloride) (or its bromide compound) (PBCL or PBBr), poly(vinylbenzyl-*N,N*-dimethylammonium chloride) (PBACl), poly[methylviologen chloride (bromide)] (PMVCl or PMVBr), poly[4-vinyl-1-butylpyridinium chloride (bromide)] (PPyCl or PPyBr), poly[triphenyl(4-vinylbenzyl) phosphonium chloride] (PBPCl), and poly(*S,S'*-dimethyl-*S*-tetramethylenehexamethylene disulfonium diiodide) (PSI).

PBBr and PBACl were used after purification by reprecipitation. PBCL were prepared by using Menshutkin reaction between 1,6-dichlorohexane and *N,N,N',N'*-tetramethyl propanediamine. Polymerization of MVCl (PMVBr) was carried out by condensation polymerization of 1,2-dichloroethane (1,2-dibromoethane) and 4,4'-bipyridine. PPyCl (PPyBr) was synthesized by quaternization of poly(4-vinylpyridine). PBPCl was obtained by radical polymerization of triphenyl(4-vinylbenzyl)ammonium chloride which is prepared by reaction of *p*-chloromethylstyrene and triphenylphosphine. PSI was prepared by alkylation of sulfur atom of the condensation polymer with iodomethane. (Scheme 1)



Scheme 1 Syntheses of polycations.

### Measurements

Conductivity of the room temperature molten salt consisting of MEACl and AlCl<sub>3</sub> was measured by using a conductivity meter (Horiba, DS-7) with a pair of platinum-black electrode. The ionic conductivities of polymer complexes were determined with AC impedance analysis with blocking platinum electrodes. The complexes were sandwiched between a couple of platinum disks with Teflon ring spacers and packed in a sealed cell with stainless terminals. These measurements were carried out over the temperature range from -60 to 40 °C and the frequency range from 5 to 13 MHz by using an impedance analyzer (YHP, 4192A) under computer control (NEC, PC9801-VX).

### RESULTS AND DISCUSSION

Figure 2 displays the melting points (a) and ionic conductivity (b) as a function of the mole percent of AlCl<sub>3</sub> in MEACl / AlCl<sub>3</sub> molten salts. The mixtures were ionic liquids at room temperature over the AlCl<sub>3</sub> composition range from 60 to 75 mol%, although both MEACl and AlCl<sub>3</sub> were crystalline solids at room temperature. The highest conductivity of 4.1×10<sup>-3</sup> S cm<sup>-1</sup> was achieved at 70 mol% AlCl<sub>3</sub>.

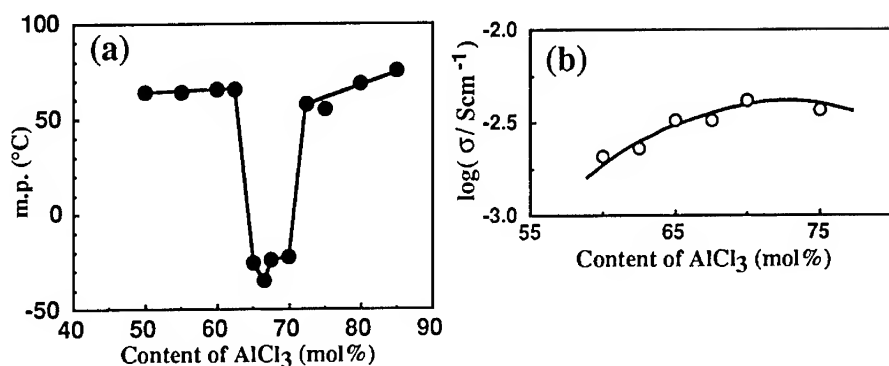


Figure 2 Melting points (a) and ionic conductivity of molten salts (MEACl / AlCl<sub>3</sub>) at 25°C (b).

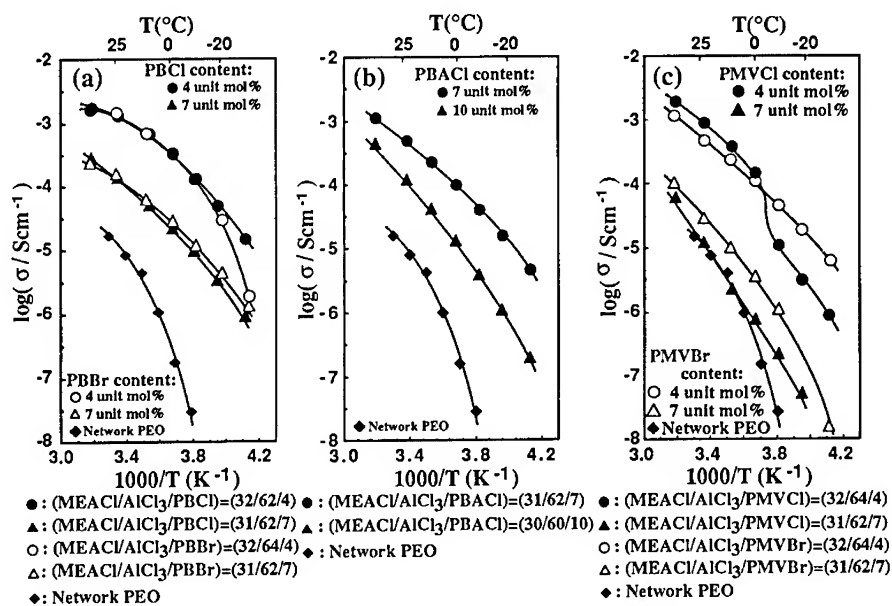


Figure 3 Temperature dependence of ionic conductivity for molten salt / PBCl, PBBr (a), molten salt / PBACl (b), and molten salt / PMVCl, PMVBr (c).

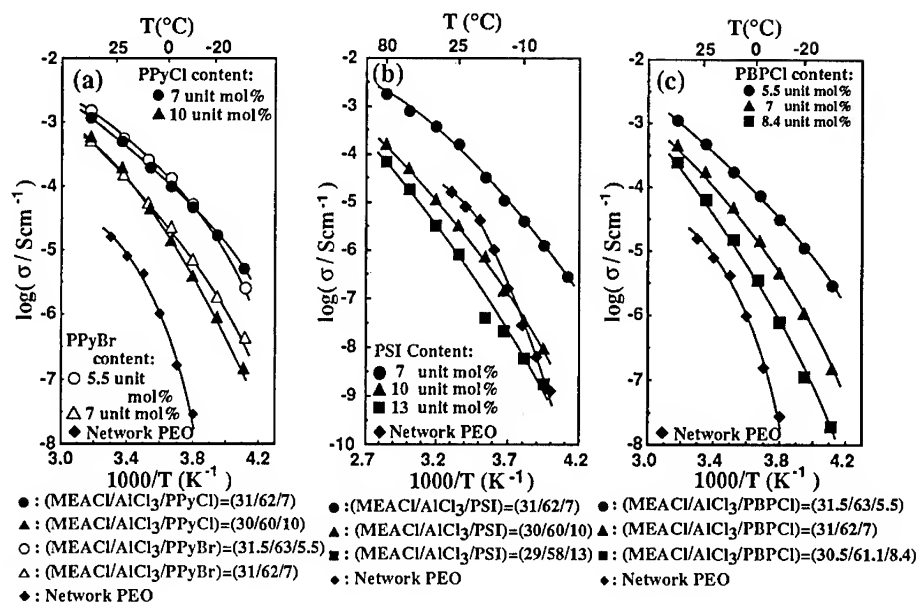


Figure 4 Temperature dependence of ionic conductivity for molten salt / PPyCl, PPyBr (a), molten salt / PSI (b), and molten salt / PBPCl (c).

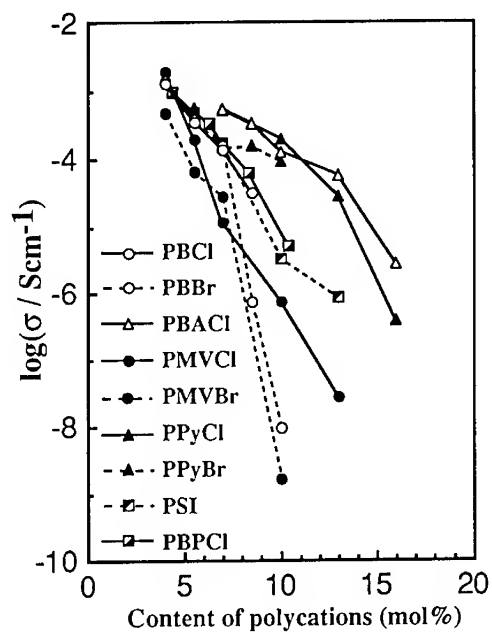
The polycation complexes formed homogeneous and viscoelastic solids at room temperature when the polycation mole fractions were more than 4 unit mol%.

Figure 3 and 4 show Arrhenius plots of ionic conductivity for polymer complexes with various compositions. The polymer complexes exhibited much higher conductivity than polyether-based polymer electrolytes by a factor of  $10^2$  to  $10^3$  and low temperature dependence especially in low temperatures below  $0^{\circ}\text{C}$ . The ion conductivity of polymer complexes increased with increasing mole fraction of molten salt. These results indicate that all of polycations including onium salt enable to form homogeneous complexes with MEACl / AlCl<sub>3</sub> molten salt and the transport of carrier ions is not associated with the segmental motion of polycations.

Ionic conductivity of polycation complexes at room temperature as a function of unit mol% of polycations is presented in Figure 5. It is found that the polymer complexes with oniumcations in side chains have higher ion conductivity than that of main chain types such as PBCl and PMVCl. The complexes with chloride ions as the counter ions showed higher ionic conductivity compared with that of bromide ions such as PMVBr and PPyBr. These results were caused of small ionic radii of counter anion and the flexibility of polycations due to the pendant structure.

## CONCLUSION

New ion conductive polymers consisting of the onium polycation and room temperature molten salt were synthesized. These complexes formed homogeneous and viscoelastic solid at the polycation content of more than 4 unit mol%. The ionic conductivity of these polymer complexes was ten times as high as that of polyether-based polymer electrolytes, and was affected by such factors as the composition, types of polycations, and counter anions. These polycation complexes are quite promising materials as a new polymer electrolyte because of higher ionic conductivity and film forming property.



**Figure 5** Relationship between content of polycations and ionic conductivity for molten salt / polycation complexes.

## REFERENCES

1. Polymer Electrolyte Reviews I, edited by J.R. MacCallum and C.A. Vincent, (Elsevier, London, 1987).
2. M.B.Armand, J.M.Chabagno, and M.J.Duclot, in Fast Ion Transport in Solids, edited by P.Vashishta, J.N.Mundy and G.K.Shenoy, (Elsevier, Amsterdam, 1979), p.131.
3. M.Watanabe, S.Yamada, K.Sanui, N.Ogata, J.Chem.Soc., Chem. Commun., 929 (1993).

## CHARACTERIZATION OF PLASTICIZED POLYETHER-URETHANE SOLID POLYMER ELECTROLYTES

M. Forsyth<sup>1</sup>, P. Meakin<sup>2</sup>, D. R. MacFarlane<sup>2</sup>, and A. J. Hill<sup>3†</sup>,

<sup>1</sup>Department of Materials Engineering, Monash University, Clayton, Victoria, Australia 3168

<sup>2</sup>Department of Chemistry, Monash University, Clayton, Victoria, Australia 3168

<sup>3</sup>Faculty of Engineering, Monash University, Clayton, Victoria, Australia 3168

† To whom correspondence should be addressed.

### ABSTRACT

The effect of plasticizer addition on the density, conductivity, glass transition, and free volume behavior of salt containing polyether-urethanes has been examined. The addition of up to 1.5 molal LiClO<sub>4</sub> salt results in an effective crosslinking of the polyether-urethane chains due to the Li<sup>+</sup> coordination with the oxygens of the host polymer. This crosslinking decreases inter- and intra-chain separation and reduces polymer chain mobility as illustrated by increased density and T<sub>g</sub>, decreased free volume, and, at salt concentrations greater than 0.6 molal, decreased conductivity. The addition of approximately 30 wt % tetraglyme plasticizer to the 1 molal LiClO<sub>4</sub>/host polymer complex is shown to counter the effective crosslinking resulting in a decreased T<sub>g</sub> to a value equal to that of the pure host polymer, increased conductivity, and increased average free volume cavity size to a value equal to that of the pure host polymer. However, the relative number of free volume cavities in the plasticized host polymer/salt complex remains fewer than that of the pure host polymer over the concentration range of plasticizer studied, and in a similar manner the density remains greater than that of the pure host polymer. The room temperature conductivity, free volume, and density behavior in conjunction with the T<sub>g</sub> results suggest that the plasticizer addition leads to Li<sup>+</sup> coordination with the oxygens of the plasticizer chains as well as increased mobility of the host polymer chains.

### INTRODUCTION

The solubility of the salt in the host polymer of the solid polymer electrolyte (SPE) is necessary for the distribution of ions in the polymer. The dissociation of the salt and distribution of ions can lead to a reasonable charge carrier density and conductivity. Host polymer chain mobility also is important to conductivity, and it has been shown that the strong coordination of some ions with the host polymer structure results in limited chain mobility and hence restricted conductivity [1]. The LiClO<sub>4</sub>/polyether-urethane system has been shown to be one such SPE for which the restricted chain mobility with increasing salt concentration can outweigh the increase in charge carrier density resulting in a decrease in conductivity [2]. Previous results using NMR [3] have shown that the use of plasticizers in a NaCF<sub>3</sub>SO<sub>3</sub>/polyether-urethane system can increase the host polymer chain mobility and the conductivity. Hence plasticizers present a possible solution to the problem of reduced conductivity in SPE's caused by ion coordination with the host polymer chains. The action of the plasticizer on parameters, other than host polymer chain mobility, which may affect conductivity has not been thoroughly examined. The subject of this work is an investigation of the action of the plasticizer in the LiClO<sub>4</sub>/polyether-urethane system on the glass transition temperature, T<sub>g</sub>, and on the room temperature density, free volume, and conductivity of the polymer/salt complex.

### Positron Annihilation Lifetime Spectroscopy

The free volume measurement in the present study is provided by the positron annihilation lifetime spectroscopy (PALS) technique. The orthoPositronium (oPs) pickoff annihilation lifetime,  $\tau_3$ , in polymers is inversely proportional to the overlap of the wavefunction of the oPs with that of

electrons in the surrounding cavity wall [4]. There is some discrepancy as to whether the cavities are pre-existing free volume cavities or holes formed by the oPs probe [5]. In either case, the value of  $\tau_3$  reflects a quantity related to free volume, whether it is the mean free volume cavity radius of pre-existing intra- and inter-chain cavities or the hole energy or cohesive energy of the polymer. Reviews of the PALS probe of free volume in polymers can be found elsewhere [6,7]. Reports correlating  $\tau_3$  and polymeric free volume calculated by the Bondi group contribution method are convincing as are the correlations between  $\tau_3$  and gas diffusivity in glassy and rubbery polymers [5,8]. Hence the interpretation of the oPs pickoff lifetime  $\tau_3$  as a measure of the mean free volume cavity radius appears reasonable. The number of annihilations taking place with a mean lifetime of  $\tau_3$  is given by the intensity quantity  $I_3$ . The intensity  $I_3$  is a function of the positronium (Ps) formation probability and the number of sites available for oPs localization. The quantity  $I_3$  is often related to the relative number of free volume cavities in the volume of polymer probed and has been shown to be sensitive to degree of crystallinity, physical aging, and external pressure in glassy polymers [6,9,10].

Relationships have been developed to relate  $\tau_3$  to a spherical cavity radius and to relate a function of  $\tau_3$  and  $I_3$  to free volume fraction [7-9,10]. Typical values of radii calculated for polymers and molecular liquids range from 0.2 nm to 0.4 nm whilst typical values of free volume fraction vary from approximately 1% to 10%. The free volume measured by PALS is both static (interstitial) and dynamic (fluctuating in time). The ratio of static to dynamic free volume is temperature dependent, and at temperatures far above the glass transition temperature,  $T_g$ , the polymer mobility is such that dynamic free volume dominates. The annihilation rate of oPs is  $10^9$  Hz hence molecular motions occurring at frequencies  $> 10^9$  Hz occupy the dynamic free volume for the lifetime of the oPs. Hence the relative number of annihilations taking place with a lifetime of  $\tau_3$  can be reduced due to the increasing fraction of dynamic free volume. The PALS data in the present work are interpreted as reflecting the mean free volume cavity size ( $\tau_3$ ) and the relative number of free volume cavities in the volume probed ( $I_3$ ); however, oPs probes a fraction of the total free volume (that fraction is related to the size of the probe and hence its lifetime [7,10]), thus the reported values reflect only that free volume fraction accessible to the oPs probe. Fortunately the range of free volume cavity radii probed by oPs in most polymers (0.2 nm to 0.4 nm) is similar to typical interatomic distances in polymers (0.2 nm to 0.6 nm).

The relationship between free volume and ionic conductivity in SPE's has been eloquently reviewed by Ratner [11]. Measurement of free volume variation in SPE's, as well as measurement of related properties such as density and  $T_g$  as functions of plasticizer concentration, should help build an understanding of the role of free volume in conductivity.

## EXPERIMENTAL

A series of samples was prepared by dissolving between 0.5 molal (M) and 1.5 M  $\text{LiClO}_4$  (Aldrich) in a trihydroxy poly (ethylene oxide-co-propylene oxide) copolymer (molecular weight  $5000 \text{ g mol}^{-1}$ ) (abbreviated as 3PEG), stirring at  $80^\circ\text{C}$  for 2 hrs, followed by crosslinking at  $40^\circ\text{C}$  with hexamethylene diisocyanate (HDI) using a Thorcat 535 catalyst. A second series of samples was prepared by mixing 3PEG with variable concentrations of tetraglyme (vacuum distilled over sodium) before crosslinking. A third series of 1 M  $\text{LiClO}_4$ /3PEG polymer electrolytes with varying wt % tetraglyme also was prepared.

Samples were sealed in aluminium DSC pans, quenched in liquid nitrogen and then transferred to a Perkin Elmer DSC7 cold head. Glass transition temperatures were measured at heating rates of  $10^\circ\text{C min}^{-1}$  and were recorded to an accuracy of  $\pm 1^\circ\text{C}$ . Conductivity measurements were performed at room temperature using a Wayne-Kerr Bridge operating at 1592 Hz. Density measurements were performed at room temperature using the Archimedeian method



with propane-2-ol (density =  $0.7869 \text{ g cm}^{-3}$ ). Results are the mean value of five measurements with an accuracy of  $\pm 0.0035 \text{ g cm}^{-3}$ .

PALS measurements were made using an automated EG&G Ortec fast-fast coincidence system with a  $^{22}\text{Na}$  resolution of 250 picoseconds. The equipment and samples were thermally stabilised at  $22 \pm 0.5^\circ\text{C}$ . The  $^{22}\text{NaCl}$  source was a 2 mm diameter spot source of  $25 \mu\text{Ci}$  sandwiched between two  $2.54 \mu\text{m}$  titanium foil sheets. Data were collected at  $22^\circ\text{C}$  on 2 mm thick cast polymer sheets and analysed using the PFPOSFIT program. The shortest lifetime was fixed at 125 ps characteristic of pPs self-annihilation. Five spectra of 30,000 peak counts were collected for each sample, and error bars are population standard deviations of these results. The PALS parameters (lifetimes and intensities) for these polymers did not change as a function of contact time with the source. The source gave a two lifetime (166 ps, 98.2%, and 450 ps, 1.8%) best fit to 99.99% pure annealed and chemically polished aluminium samples. No source correction was used in the analysis.

## RESULTS AND DISCUSSION

Figures 1-5 present the variation in  $T_g$ , free volume, density, and conductivity in the pure homopolymer 3PEG as functions of  $\text{LiClO}_4$  salt concentration. As mentioned in the Introduction, it is postulated that the addition of salt causes  $\text{Li}^+$  coordination with the oxygens of the polyether-urethane chains resulting in an effective crosslinking. This crosslinking is shown to increase  $T_g$  (Figure 1) and decrease the mean size (related to  $\tau_3$ ) and relative number (related to  $I_3$ ) of free volume cavities in the polymer (Figures 2 and 3). The density of the  $\text{LiClO}_4$  salt is  $2.428 \text{ g cm}^{-3}$ , hence the increase in density shown in Figure 4 does not reflect the additive increase due to the salt concentration. The first 0.5 M addition of salt causes the largest incremental density increase postulated to be due to the  $\text{Li}^+$  coordination with the polymer chains which decreases inter- and intra-chain spacing. The conductivity data in Figure 5 show an increase for 0.6 M addition of salt. The initial increase in charge carriers causes this increasing conductivity; however, further increase in charge carrier density does not increase conductivity because the charge carriers have reduced mobility. The effective crosslinking of the chains restricts polymer mobility and hence charge carrier mobility such that the conductivity decreases (Figure 5). It is interesting to note that thermal energy does not reverse the effective crosslinking as illustrated by the reduced conductivity and free volume measured at temperatures over  $80^\circ\text{C}$  above  $T_g$ . Recently Stevens et al. [12] also have observed a decrease in  $\tau_3$  and  $I_3$  with increasing  $\text{NaCF}_3\text{SO}_3$  concentration in polypropylene glycol measured over a similar temperature range above  $T_g$  as that used in the present study.

The effect of tetraglyme plasticizer (a low molecular weight polyether analogue) addition to the pure 3PEG homopolymer was investigated in order to be able to distinguish the differences in behavior of the host polymer/salt complex from the pure host polymer. Theories of plasticization attribute the decrease in stiffness and  $T_g$  on plasticizer addition to the interruption of polymer-polymer bonding in favour of weaker plasticizer-polymer bonding. The free volume theory of plasticization [13] predicts an increase in the total free volume of the system due to the plasticizer action of interrupting inter- and intra-chain bonding of the host polymer. The plasticizer and polymer, however, must be compatible for mixing, and strong interactions between the polymer and plasticizer can reduce free volume leading to antiplasticization [14]. Previous PALS studies of plasticization and antiplasticization have reported either a decrease or no change in the amount of free volume below  $T_g$  due to the addition of plasticizer [15,16].

Figures 6-10 compare the response of pure 3PEG to the response of the host polymer/salt complex with increasing plasticizer concentration. Approximately 30 wt % addition of tetraglyme is needed to decrease the  $T_g$  of the host polymer/salt complex to that of the pure host polymer (Figure 6). Similarly, an addition of 30 wt % tetraglyme increases the value of  $\tau_3$  (indicative of mean free volume cavity radius) to that of the pure host polymer (Figure 7). The increase in cavity

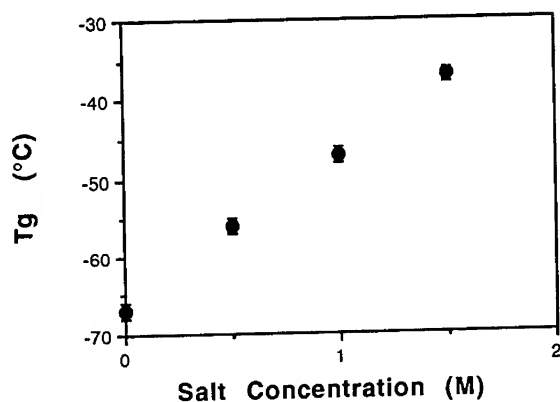


Fig. 1 Glass transition temperature as a function of  $\text{LiClO}_4$  concentration in pure 3PEG.

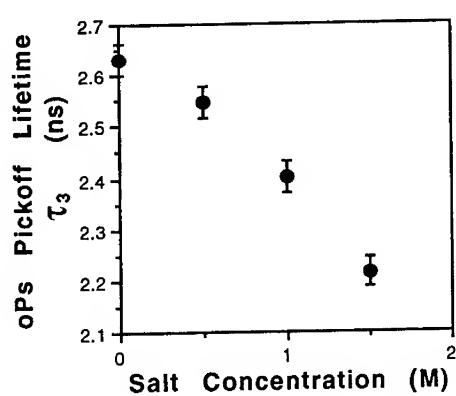


Fig. 2 oPs lifetime  $\tau_3$  as a function of  $\text{LiClO}_4$  concentration in pure 3PEG.

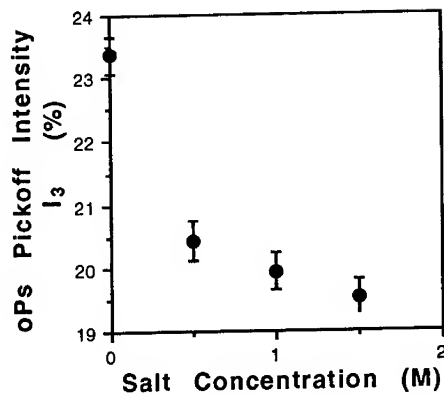


Fig. 3 oPs intensity  $I_3$  as a function of  $\text{LiClO}_4$  concentration in pure 3PEG.

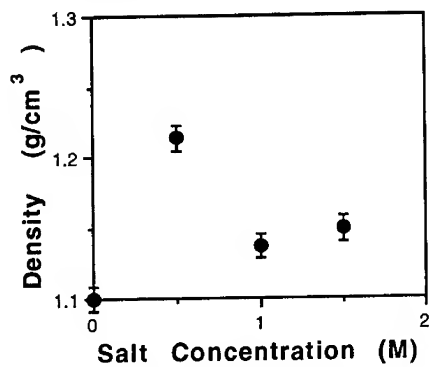


Fig. 4 Density as a function of  $\text{LiClO}_4$  concentration in pure 3PEG.

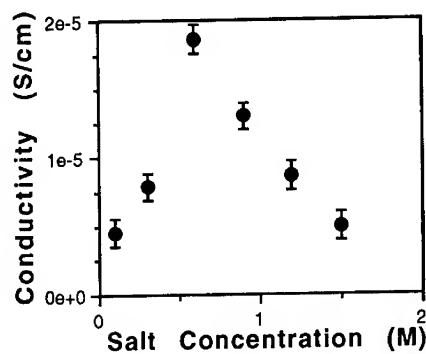


Fig. 5 Conductivity as a function of  $\text{LiClO}_4$  concentration in pure 3PEG.

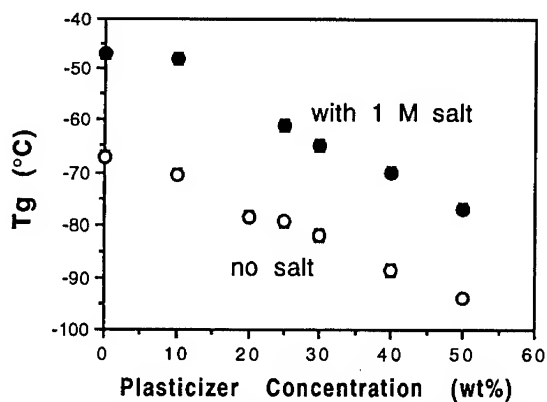


Fig. 6 Glass transition temperature as a function of tetraglyme concentration.

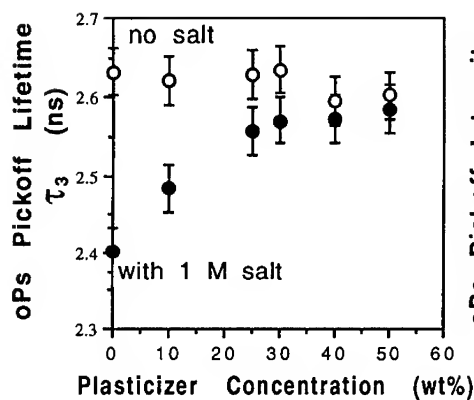


Fig. 7 oPs lifetime  $\tau_3$  as a function of tetraglyme concentration.

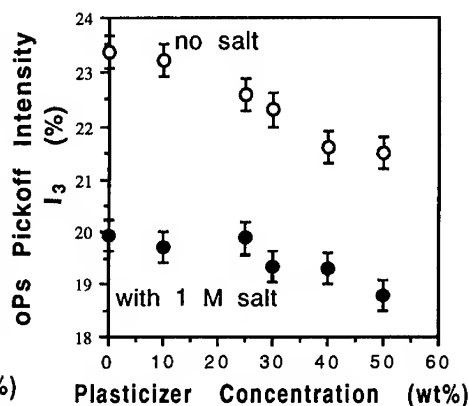


Fig. 8 oPs intensity  $I_3$  as a function of tetraglyme concentration.

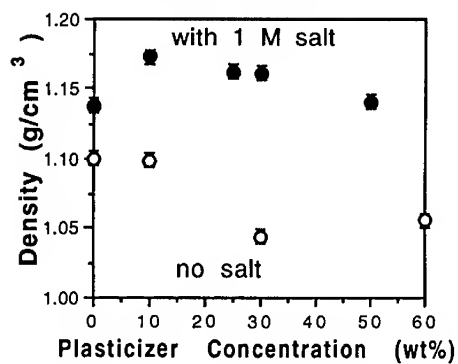


Fig. 9 Density as a function of tetraglyme concentration.

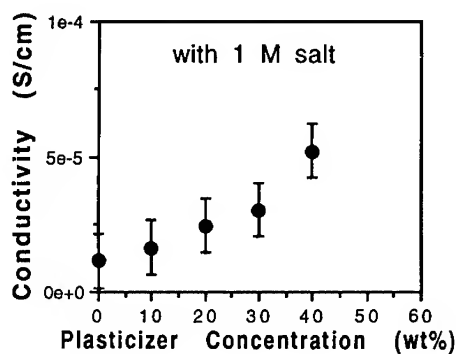


Fig. 10 Conductivity as a function of tetraglyme concentration.

size is not a result of plasticization of the polymer, since tetraglyme does not increase  $\tau_3$  when added to pure 3PEG. Therefore, an interaction between tetraglyme and  $\text{Li}^+$  ions is proposed that reduces the number of 3PEG- $\text{Li}^+$ -3PEG crosslinks allowing greater main chain mobility and increasing the chain separation. The plasticized host polymer salt complex is thought to be heterogeneous on a micro-scale and composed of  $\text{Li}^+$  coordinated regions, where the mobility of the plasticizer and host polymer are restricted, and non-coordinated regions, where the plasticizer acts to increase the main chain mobility.

The relative number of free volume cavities remains decreased in the host polymer/salt complex with the addition of plasticizer (Figure 8). The plasticizer competes with the host polymer for interaction with the  $\text{Li}^+$  ions, hence coordinated regions (plasticizer and host polymer) are still present, and the number of free volume sites in the volume probed remains decreased. The mean free volume cavity size increases because of an increase in the fraction of larger cavities on addition of the plasticizer and because of the increased separation between previously crosslinked chains; however, the number of cavities in the volume probed remains decreased because the tetraglyme becomes coordinated. The density results in Figure 9 support the previous statements by showing that the density of the host polymer/salt complex remains greater than that of the pure 3PEG with increasing plasticizer concentration over the range studied. The density of pure tetraglyme plasticizer is  $1.009 \text{ g cm}^{-3}$ . Finally, the conductivity (Figure 10) increases with increasing plasticizer concentration in the host polymer/salt complex due to the combined effects of the plasticizer competing with the host polymer for interaction with the salt and increasing the host polymer chain mobility.

This study has illustrated that the free volume available for ionic transport can be decoupled from the free volume as measured by density. The ability of the PALS probe of free volume to monitor relative cavity size and number has helped link the dynamic free volume available for ionic transport with the action of the plasticizer in the host polymer/salt complex.

## REFERENCES

1. M. Watanabe and N. Ogata, *British Polymer Journal*, **20**, 181 (1988).
2. M. Forsyth, P. Meakin, D. R. MacFarlane, and A. J. Hill, *J. Phys. Condensed Matter*, submitted Dec. 1994.
3. M. Forsyth, P. Meakin, D. R. MacFarlane, G. Bulmer, and M. Reid, *J. Mater. Chem.*, **4**, 1149 (1994).
4. W. Brandt, S. Berko, and W. Walker, *Phys. Rev.*, **120**, 1289 (1960).
5. Y. Kobayashi, K. Haraya, Y. Kamiya, S. Hattori, *Bull. Chem. Soc. Jpn*, **65**, 160 (1992).
6. J. R. Stevens, *Methods of Experimental Phys.*, **16A**, 371 (1980).
7. Y. C. Jean, *Microchem J.*, **42**, 72 (1990).
8. K. Okamoto, K. Tanaka, M. Katsube, H. Kita, O. Sueoka, and Y. Ito, *Polymer J.*, **25**, 275 (1993).
9. Y. Kobayashi, W. Zheng, E. F. Meyer, J. D. McGervey, A. M. Jamieson, and R. Simha, *Macromolecules*, **22**, 2802 (1989).
10. J. E. Kluin, Z. Yu, S. Vleeshouwers, J. D. McGervey, A. M. Jamieson, R. Simha, and K. Sommer, *Macromolecules*, **26**, 1853 (1993).
11. M. Ratner, in *Polymer Electrolyte Reviews*, J. R. MacCallum and C. A. Vincent, Eds., Elsevier, London, 1987.
12. J. R. Stevens, S. H. Chung, P. Horoyski, and K. R. Jeffrey, *J. Non-Cryst. Solids*, **172-174**, 1207, (1994).
13. A. K. Doolittle, *The Technology of Solvents and Plasticisers*, Wiley, New York, 1954.
14. Y. Maeda and D. R. Paul, *J. Polym. Sci. B*, **25**, 1005 (1987).
15. R. J. Elwell and R. A. Pethrick, *Eur. Polym. J.*, **26**, 853 (1990).
16. T. Okada, S. Nishijima, Y. Honda, and Y. Kobayashi, *J. de Physique IV, Colloque C4*, **3**, 291 (1993).

## IONIC ASSOCIATION OF LITHIUM TRIFLATE IN GLYMES, MODEL SOLVENTS, AND HIGH MOLECULAR WEIGHT POLY(ETHYLENE OXIDE)

R. FRECH\*, W. HUANG\*, and M. A. K. L. DISSANAYAKE\*\*

\*University of Oklahoma, Department of Chemistry, 620 Parrington Oval, Norman, OK 73019

\*\*University of Peradeniya, Department of Physics, Sri Lanka.

### ABSTRACT

Ionic association in lithium trifluoromethanesulfonate (triflate) dissolved in glymes, glycols, model solvents, and high molecular weight poly(ethylene oxide) is studied by analysis of vibrational band structure. Surprisingly, the  $\text{CF}_3$  symmetric deformation mode is shown to be the most accurate measure of ionic association and the reasons for this are discussed. The nature of various associated lithium triflate species as deduced from *ab initio* calculations is supported by spectral data presented here. A weak interaction of the triflate anion with certain solvent molecules containing an alcohol OH group is observed. Finally the temperature dependence of ionic association in a complex of lithium triflate and high molecular weight poly(ethylene oxide) is described.

### Introduction

Polymer electrolytes are an important class of fast ion conductors whose technological potential has attracted intense scientific interest. These materials are polymers with a heteroatom such as oxygen, nitrogen or sulfur, into which a metal salt is dissolved. Ionic association in the resulting polymer-salt complex plays a major role in controlling the ionic conductivity. One of the most useful methods of studying the composition and structure of the associated species is vibrational spectroscopy. In the usual application of this technique, the metal salt contains a polyatomic anion whose intramolecular vibrational modes are used to examine ionic association according to the following:

1. Multiple bands in the spectral region of a non-degenerate mode signal the presence of the anion in different vibrational potential energy environments. These environments can be attributed to different kinds of cation-anion interactions, e.g. "free" ions, ion pairs, ion triples, etc.

2. Ionic association almost always lowers the symmetry of the anion potential energy environment, leading to the lifting of the degeneracy of a degenerate mode. The resulting splitting of a degenerate band into several components is a strong indication of ionic association, and the frequency separation of the split components indicates the strength of the interaction.
3. Ab initio calculations of normal mode frequencies and intensities for various model structures of the associated species can be compared with the corresponding experimental spectroscopic data. Such a comparison often supports the existence of a particular associated species or a specific cation-anion coordination.

Very early work examined ionic association in PEO complexes with  $\text{NaBH}_4$  and  $\text{NaBF}_4$ <sup>1</sup>. Cation-anion interactions have been studied in polyethers complexed with lithium<sup>2,3</sup> and sodium<sup>4</sup> perchlorate, lithium<sup>5</sup>, sodium<sup>5,6</sup>, and potassium<sup>5</sup> thiocyanate, and lithium fluoroborate<sup>7</sup>. However the most widely studied anion is trifluoromethanesulfonate (triflate),  $\text{CF}_3\text{SO}_3^-$ , since several of its intramolecular modes are particularly sensitive to interactions with cations and solvent molecules. Earlier work by Torell established the presence of "free" ions, cation-anion pairs, and aggregate ions<sup>8,9</sup>. Many additional studies followed, examining the effect of temperature<sup>10,11</sup>, salt concentration<sup>11-13</sup>, polymer chain length<sup>14,15</sup> and the nature of the polymer end group<sup>14,15</sup>. Most of the earlier studies utilized poly(propylene oxide) to avoid problems of crystallization and compound formation present in high molecular weight poly(ethylene oxide), PEO. Recent studies have been extended to low molecular weight oligomers of PEO capped with OH groups or  $\text{OCH}_3$ <sup>14</sup>. Ionic association in divalent and trivalent salt systems has also been examined<sup>16-21</sup>. In addition, studies of ionic association of triflate salts in model solvents such as acetone and acetonitrile have provided useful insight<sup>22</sup>.

## Experimental

Lithium triflate, "LiTf," (Aldrich, 97%), sodium triflate, "NaTf," (Aldrich, 98%), potassium triflate, "KTf," (Alfa, 98%) ammonium triflate, " $\text{NH}_4\text{Tf}$ ," (Aldrich, 99%) and tetra-n-butylammonium triflate, "TbaTf," (Aldrich, 99%) salts were dried separately in a vacuum oven under a  $10^{-2}$  Torr vacuum at elevated temperatures (100~130 °C) for no less than 24 hours and allowed to cool in a desiccator before use. The low molecular weight solvents used in this study were acetonitrile (Mallinckrodt, HPLC grade), acetone (CMS Inc., 99.5%), ethanol (Midwest Grain Products, absolute), methanol (Mallinckrodt, absolute),

2-propanol (Baker, 99.9%), tetrahydrofuran, (Mallinckrodt, 99.9%), triethylene oxide dimethyl ether, "triglyme," (Aldrich, 99%) and deionized water. Poly(ethylene oxide) with an average MW=4,000,000 was obtained from Aldrich. The triglyme-salt solutions were prepared to give a ratio of 20 ether oxygens to one cation. The other solutions of LiTf and TbaTf in the low molecular solvents were prepared at a ratio of 20 solvent molecules per cation, except for TbaTf which is only slightly soluble in water. The high molecular weight PEO-LiTf films were made by casting a thin layer of viscous solution (PEO + LiTf + acetonitrile) onto a Teflon plate and subsequently removing the acetonitrile solvent at 80 °C under a  $10^{-2}$  Torr vacuum. All non-aqueous solutions were prepared in a dry box filled with nitrogen gas; the detailed preparation procedure was described in Reference 23.

Raman scattering spectra from samples contained in a glass capillary were recorded in a standard right angle scattering geometry at room temperature using a system previously described <sup>6</sup>. Infrared spectra were collected using a Nicolet 200 SXV or a Bio-Rad FTS Fourier Transform Infrared Spectrometer at 2  $\text{cm}^{-1}$  spectral resolution. Barium fluoride or silver bromide IR windows were used in a variety of standard liquid cells for both liquid and solid sample spectra.

*Ab initio* molecular-orbital calculations of the free triflate ion and its several lithium ion pairs and aggregates were performed using program GAMESS <sup>24</sup> at the HF/3-21+G\* and HF/6-31+G augmented with polarization functions (d-type orbitals) on the sulfur atom of the triflate ion. The geometries of the calculated triflate ion, its lithium ion pairs and aggregates were fully optimized using the method of Baker <sup>25</sup> in Cartesian coordinates subject to a  $C_{3v}$  or a  $C_s$  symmetry constraint. Analytical first and numerical second derivatives were used for the calculation of force constants and harmonic frequencies. Contamination from the contributions of translational and rotational "modes" to the vibrational frequencies was removed by transforming the force constants from Cartesian coordinates to internal coordinate and back to Cartesian coordinates.

#### Ionic association from the $\nu_s(\text{SO}_3)$ mode and the $\delta_s(\text{CF}_3)$ mode

As previously noted in the work of Torell and others, the  $\nu_s(\text{SO}_3)$  region is particularly sensitive to the presence of ionic association. However, unequivocal evidence of ionic association may also be noted in the symmetric  $\text{CF}_3$  deformation mode,  $\delta_s(\text{CF}_3)$  <sup>15</sup> and a comparison of these two regions is a bit surprising. Figure 1 shows the Raman scattering data for a number of triflate salts complexed with  $\text{CH}_3(\text{OCH}_2\text{CH}_2)_3\text{OCH}_3$  (triglyme) in the  $\nu_s(\text{SO}_3)$  region.

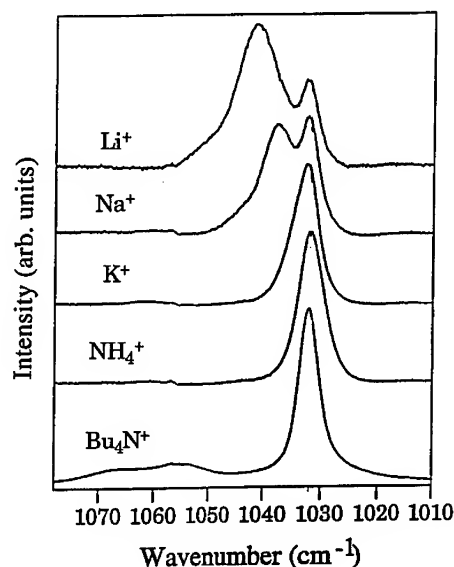


Figure 1. Raman scattering spectra of triglyme-triflate salt solutions in the  $\nu_s(\text{SO}_3)$  region. The ether oxygen:cation ratio in each solution is 20:1. The triglyme bands have been removed by spectral subtraction.

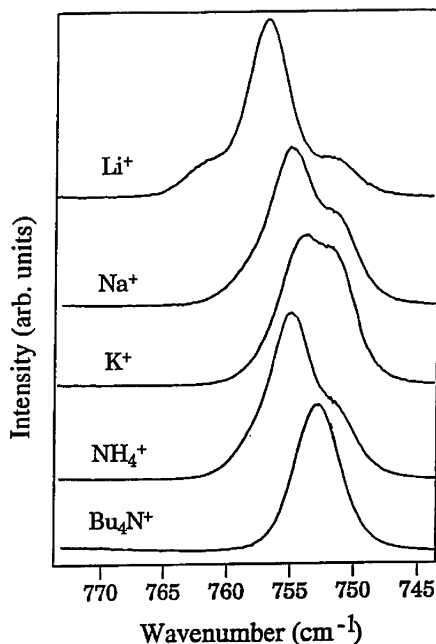


Figure 2. Raman scattering spectra of triglyme-triflate salt solutions in the  $\delta_s(\text{CF}_3)$  region. The ether oxygen:cation ratio in each solution is 20:1. The triglyme bands have been removed by spectral subtraction.

The single band at  $1032\text{ cm}^{-1}$  in the potassium, ammonium and tetrabutylammonium (Tba) salt complexes would suggest that only the "free" ion is present, while a second band at higher frequency in the sodium and lithium salts indicates the presence of ion pairs, since the frequency of this band depends on the nature of the cation. However a comparison of these data with the Raman scattering spectra in the  $\delta_s(\text{CF}_3)$  region in Figure 2 gives a different picture. Only the spectrum of the Tba triflate solution has a single band. In the ammonium and potassium triflate solutions there is now an ion pair band which is more intense than the "free" ion band. There is an ion pair band and a "free" ion band in the lithium and sodium triflate solutions evident in both spectral regions, however in the sodium triflate solution the ion pair band is more intense than the "free" ion band in the  $\delta_s(\text{CF}_3)$  region. The conclusion to be drawn from the  $\delta_s(\text{CF}_3)$  spectral region is that there is significant ionic



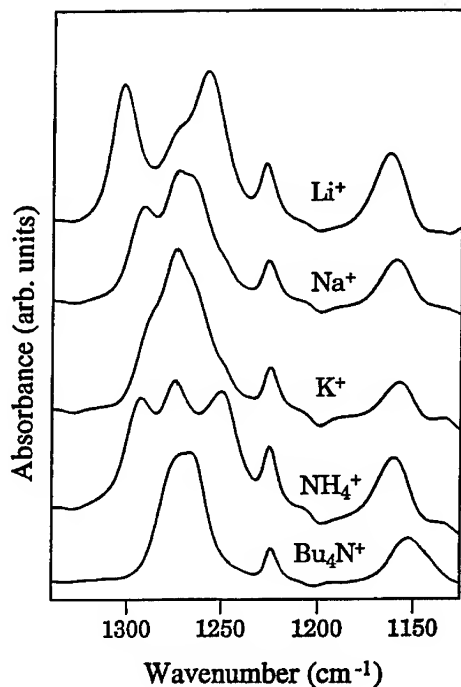


Figure 3. Infrared transmission spectra of triglyme-triflate salt solutions in the  $\nu_{as}(\text{SO}_3)$  region. The ether oxygen:cation ratio in each solution is 20:1. The triglyme bands have been removed by spectral subtraction.

association in all solutions except Tba. This conclusion is supported by the data in Figure 3, which shows infrared spectra of the antisymmetric  $\text{SO}_3$  stretching mode,  $\nu_{as}(\text{SO}_3)$ . The splitting of this band in the spectra of all solutions with the single exception of Tba is unequivocal and argues that the  $\delta_s(\text{CF}_3)$  region is a more reliable indication of ionic association than the  $\nu_s(\text{SO}_3)$  region. We will return to this point in a later section.

#### Solvent Effects

Figure 4 shows the Raman scattering spectra of lithium triflate in ethylene oxide trimers which are OH-capped and  $\text{OCH}_3$ -capped, and compares these spectra to the spectrum of Tba triflate in an ethylene oxide trimer which is  $\text{OCH}_3$ -capped. This comparison is motivated by the bulky nature of the cation in the Tba triflate, which minimizes cation-anion interactions and provide a close approximation to a "free" triflate anion. The upper spectrum of the figure primarily consists of a single band at  $1032\text{ cm}^{-1}$ , which by comparison with the lower spectrum of Tba triflate, would argue that most triflate ions exist as "free" ion in the solution of lithium triflate in OH-capped trimer. However Figure 5

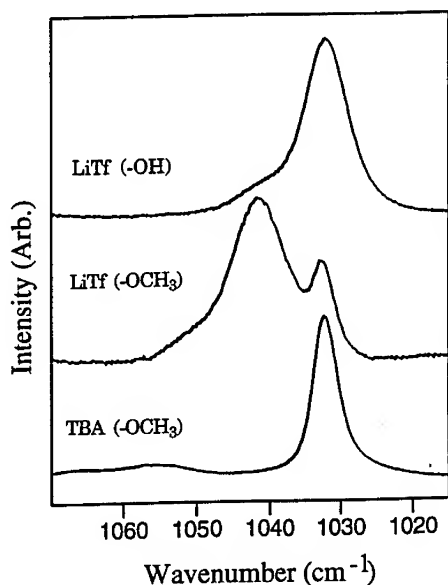


Figure 4. Raman scattering spectra of ethylene oxide trimer-triflate salt solutions in the  $\nu_s(\text{SO}_3)$  region. LiTf (-OH) is lithium triflate in OH-capped ethylene oxide trimer, LiTf (-OCH<sub>3</sub>) is lithium triflate in triglyme, and TBA (-OCH<sub>3</sub>) is tetrabutylammonium triflate in triglyme. The ether oxygen:cation ratio in each solution is 20:1. The trimer bands have been removed by spectral subtraction.

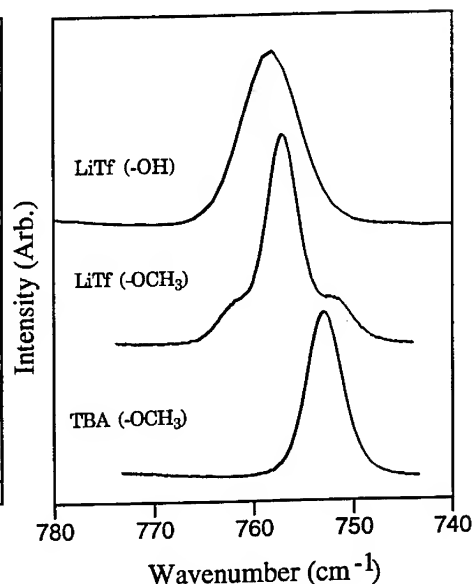


Figure 5. Raman scattering spectra of ethylene oxide trimer-triflate salt solutions in the  $\delta_s(\text{CF}_3)$  region. The labeling of the figure and the concentrations are the same as in Figure 4. The trimer bands have been removed by spectral subtraction.

shows comparable data in the  $\delta_s(\text{CF}_3)$  region. Here a comparison of the upper curve for lithium triflate in the OH-capped trimer with the Tba triflate spectrum clearly shows that there is some sort of association occurring in the lithium triflate solution. These data suggest that a solvent-anion interaction is present in the OH-capped trimer solution which competes with the cation-anion interaction.

The possible interaction of a solvent molecule with the triflate anion may be further investigated by examining ionic association data for a series of solvents

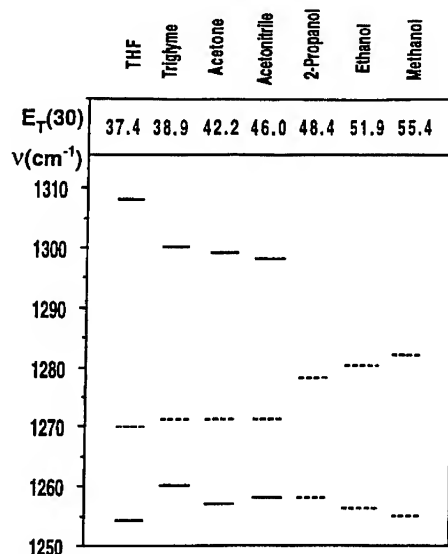


Figure 6. Frequencies ( $\text{cm}^{-1}$ ) of  $\nu_{as}(\text{SO}_3)$  in various solvents. Solid line indicate LiTf and dashed lines indicate TbaTf solutions.

with a selected range of properties. Frequency data for the antisymmetric  $\text{SO}_3$  stretching mode,  $\nu_{as}(\text{SO}_3)$ , are shown in Figure 6 for a variety of solvents plotted as a function of  $E_T(30)$ , the electron pair acceptance polarity index<sup>26</sup>. This index is a solvatochromic method of measuring the electrophilic nature of the solvent, where increasing values of  $E_T(30)$  indicate an increasing electron-accepting ability of the solvent. The solid lines indicate solutions of lithium triflate, and the dashed lines indicate solutions of tetrabutylammonium triflate. As previously noted, ionic association in the latter is minimized, due to the bulky nature of the cation which protects the positive charge. Therefore the tetrabutylammonium triflate data describe the behavior of "free" anions in the various solvents. From the figure there appears to be two distinct regimes of behavior. In solvents with a low  $E_T(30)$  value (THF through acetonitrile) the large splitting of  $\nu_{as}(\text{SO}_3)$  in the lithium triflate solutions indicate a strong cation-anion interaction, while the relatively constant value of the single band at about  $1271 \text{ cm}^{-1}$  in the Tba triflate solutions indicates a weak anion-solvent interaction. In the alcohol solutions, with relatively large  $E_T(30)$  values, the band splittings in the lithium triflate solutions cannot be resolved and appear as a very broad band. However there is a distinct splitting of  $\nu_{as}(\text{SO}_3)$  in the Tba triflate-alcohol solutions. This splitting is not as large as that observed in the lithium triflate solutions with low  $E_T(30)$  solvents, and is consistent with a specific anion-solvent interaction, most probably the formation of a hydrogen bond between the hydrogen atom of the OH group in the alcohol and an oxygen atom of the triflate anion. Therefore even in the absence of any significant

cation-anion interaction, the anion may experience a weak interaction with a solvent molecule and is not truly free.

#### The $\delta_s(\text{CF}_3)$ mode as a measure of ionic association

Recent *ab initio* calculations of the normal mode frequencies of the triflate ion, lithium triflate ion pairs<sup>27,28</sup> and more highly associated lithium triflate species<sup>28</sup> have provided some insight into the reasons for the greater sensitivity of the  $\delta_s(\text{CF}_3)$  mode to ionic association relative to the other CF modes. The sensitivity arises in part because the mode assigned as a  $\delta_s(\text{CF}_3)$  mode is actually a mixture of  $\text{CF}_3$  symmetric deformation and CF stretching. The formation of a cation-anion pair (or more highly associated species) is accompanied by a redistribution of charge, affecting the various force constants of the triflate ion. The net effect of this charge redistribution on the various component force constants contributing to the frequency of the  $\delta_s(\text{CF}_3)$  mode is summarized in Figure 7 and compared to analogous calculations for other selected intramolecular modes. Here it is clear that the frequency of the  $\delta_s(\text{CF}_3)$  mode is relatively as sensitive to the presence of ionic association as the frequency of the  $\nu_s(\text{SO}_3)$  mode. However there is no solvent interaction at the  $\text{CF}_3$  of the anion; therefore the  $\delta_s(\text{CF}_3)$  mode shows primarily the effects of ionic association whereas the  $\nu_s(\text{SO}_3)$  mode is affected by interactions with both the cation and the solvent molecules. The *ab initio* calculations further show that complex interactions can shift the  $\nu_s(\text{SO}_3)$  mode to lower frequencies as well as higher frequencies, while the  $\delta_s(\text{CF}_3)$  mode is only shifted to higher frequencies by all interactions considered in the calculation<sup>28</sup>.

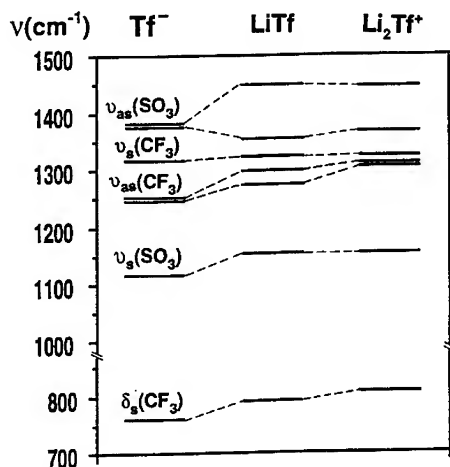


Figure 7. Calculated frequencies ( $\text{cm}^{-1}$ ) of selected modes of lithium triflate species. The calculations are discussed in the text.

These calculations also argue that the more highly associated lithium triflate species is a  $[\text{Li}_2\text{Tf}]^+$  triple ion<sup>25</sup>. Experimental support for this assignment can be found in the frequency shifts of lithium, sodium, and potassium triflate in triglyme solutions at an O:M ration of 20:1. These data are summarized in Table 1. Three bands are resolved, and the relative contribution of each band to the total integrated intensity is shown in parentheses following the frequency of the band center. The frequency differences between the "free" ion band, band 1, and the other two bands are shown as  $\Delta\nu_{1j}$ , where  $j=2,3$ . It is important to notice that the frequency differences of band 3 caused by cation substitution are almost twice as large as those for band 2. This suggests that the number of cations coordinating with each triflate anion for band 3 is double that of band 2, consistent with the assignment of band 3 to a  $[\text{Li}_2\text{Tf}]^+$  triple ion.

Table I. Band center frequencies in  $\text{cm}^{-1}$ , relative integrated band intensities (in parentheses), and frequency differences of lithium, sodium, and potassium triflate in triglyme (O:M = 20:1).

	Band 1	Band 2	$\Delta\nu_{12}$	Band 3	$\Delta\nu_{13}$
LiTf	1033 (23)	1042 (66)	9	1051 (11)	18
NaTf	1033 (44)	1038 (39)	5	1044 (17)	11
KTf	1033 (74)	1035 (20)	2	1039 (6)	6

#### High Molecular Weight Poly(ethylene oxide)-Lithium Triflate Complexes

The infrared spectra of a film of poly(ethylene oxide) complexed with lithium triflate at an ether oxygen:cation ratio of 5:1 are shown in Figure 8 for the  $\delta_s(\text{CF}_3)$  spectral region over a temperature range of 38 to 190 °C. Raman scattering spectra in the same region yield similar results and are not shown. According to the published phase diagram<sup>29</sup>, at room temperature there are two phases present, crystalline PEO and a compound which can be represented as  $(\text{PEO})_3\text{LiTf}$ <sup>30</sup>. A systematic study of the temperature dependence of all bands shows that as the complex is heated, the crystalline PEO is observed to melt, while the compound persists to the liquidus point in accord with the phase diagram. The ionic association of the triflate anion as deduced from the frequency of the  $\delta_s(\text{CF}_3)$  mode is consistent with a  $[\text{Li}_2\text{Tf}]^+$  species, which is the bridged structure seen in the x-ray study of the  $(\text{PEO})_3\text{LiTf}$  compound<sup>30</sup>. It is particularly interesting that there is no trace of a "free" triflate anion at any temperature, an observation which has consequences for the mechanism of ionic conduction in this material.

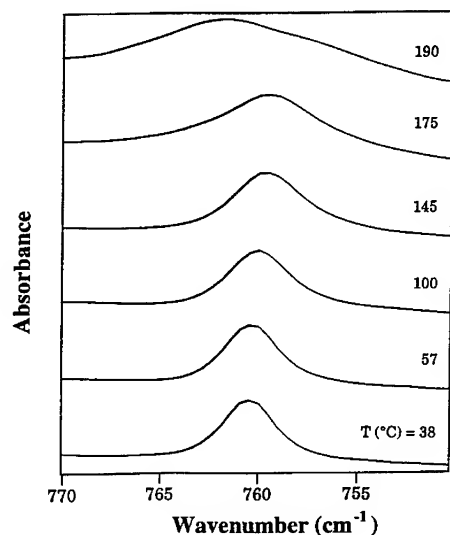


Figure 8. Infrared transmission spectra in the  $\delta_s(\text{CF}_3)$  region of high molecular weight PEO complexed with LiTf (EO:M=5:1) from 38 to 190 °C.

## Conclusions

Raman scattering and infrared transmission spectra are used to study ionic association of lithium triflate in glymes, glycols, model solvents and high molecular weight poly(ethylene oxide). Spectral data from other triflate salt solutions, primarily tetrabutylammonium triflate, are also useful in characterizing the associated species. Although ionic association is studied by analysis of vibrational band structure in the  $\text{SO}_3$  antisymmetric stretching mode, the  $\text{SO}_3$  symmetric stretching mode and the  $\text{CF}_3$  symmetric deformation mode, the latter is shown to be the most accurate measure of ionic interactions. The electronic redistribution in the triflate anion following an interaction with a cation is responsible for the sensitivity of this mode, although the  $\text{CF}_3$  group itself plays no role in any interaction of the anion with a cation. In solvents with an alcoholic OH group, a weak hydrogen-bonding interaction with the triflate  $\text{SO}_3$  group is observed.

The temperature dependence of ionic association in a complex of lithium triflate and high molecular weight poly(ethylene oxide) is described. The temperature-dependent spectrum of the complex can be understood from the phase diagram. At all temperatures there is no indication of "free" triflate anions.

### Acknowledgements

This work was partially supported by funds from the National Science Foundation EPSCoR Advanced Development Program (Grant No. EHR-9108771) and the American Chemical Society (Grant No ACS-PRF 25481-AC7P).

### References

1. R. Dupon, L. Papke, M. A. Ratner, D. H. Whitmore and D. F. Shriver, J. Am. Chem. Soc. **104**, 6247 (1982).
2. S. Schantz, L. M. Torell, and J. R. Stevens, J. Appl. Phys. **64**, 2038 (1988).
3. M. Kakihana, S. Schantz, L. M. Torell, and L. Börjesson, Mat. Res. Symp. Proc. **351**, 135 (1989).
4. S. Schantz and L. M. Torell, Solid State Ionics **60**, 47 1(1993).
5. J. P. Manning, R. Frech and E. Hwang, Polymer **31**, 2245 (1990).
6. R. Frech, J. P. Manning, and B. Black, Polymer **60**, 1785 (1989).
7. R. Frech and J. P. Manning, Electrochim. Acta **37**, 1499 (1992).
8. L.M. Torell and S. Schantz in *Polymer Electrolyte Reviews 1*; edited by J. R. MacCallum and C. A. Vincent (Elsevier Applied Science: London, 1989) p. 1.
9. S. Schantz, J. Sadahl and L. Börjesson, L.M. Torell and J. R. Stevens, Solid State Ionics **128-30**, 1047 (1988).
10. S. Schantz, L.W. Torell and J.R. Stevens, J. Chem. Phys. **94**, 6862 (1991).
11. J. Manning and R. Frech, Polymer **33**, 6862 (1992).
12. S. Schantz, J. Chem. Phys. **94**, 6296 (1991).
13. S. Schantz and L.M. Torell Solid State Ionics, **60**, 47 (1993).
14. G. Peterson, P. Jacobsson and L.M. Torell, Electrochim. Acta **37**, 1495 (1992).
15. W. Huang and R. Frech, Polymer **35**, 235 (1994).
16. Å. Wendsjö, J. Lindgren, J. O. Thomas and G. C. Farrington, Solid State Ionics, **53-56**, 1077 (1992).
17. Å. Wendsjö, J. Lindgren and C. Paluszkievicz, Electrochim. Acta **37**, 1689 (1992).
18. A. Berson and J. Lindgren, Solid State Ionics **60**, 31 (1993).
19. Å. Wendsjö, . O. Thomas and J. Lindgren, Polymer **34**, 2243 (1993).
20. G. Petersen, L.M. Torell, S. Panero, B. Scrosati, C.J. da Silva and M. Smith Solid State Ionics, **60**, 55 (1993).
21. R. Frech and W. Huang, Solid State Ionics **66**, 183 (1993).
22. R. Frech and W. Huang, J. Sol. Chem. **23**, 469 (1994).
23. W. Huang, Ph.D. Dissertation, The University of Oklahoma, Norman, OK, (1994).

- 
24. M.W. Schmidt, K.K. Baldridge, J.A. Boatz, J.H. Jensen, S. Koseki, M.S. Gordon, K.A. Nguyen, T.L Windus and S.T. Elbert, QCPE Bull. **10**, 52 (1990).
  25. J. Baker, J. Comput. Chem. **7**, 385 (1986).
  26. U. Mayer, in *Ions and Molecules*, edited by N. Tanaka, H. Ohtake, and R. Tamamushi (Elsevier, Amsterdam, 1983).
  27. S.P. Gejji, K. Hermansson, J. Tegenfeldt and J. Lindgren, J. Phys. Chem. **97**, 11402 (1993).
  28. W. Huang, R. Frech and R.A. Wheeler, J. Phys. Chem. **98**, 100 (1994).
  29. C. D. Robitaille and D. Fauteux, J. Electrochem. Soc. **133**, 315 (1986).
  30. P. Lightfoot, M. A. Mehta and P. G. Bruce, Science **262**, 883 (1993).



## CONDUCTIVITY IN POLY(ETHYLENE OXIDE) COMPLEXED WITH MIXED ALKALI METAL SALTS

BYOUNG-KOO CHOI AND YOUNG-WAN KIM

Department of science education, Dankook University, Yongsan, Seoul 140-714, Korea

### ABSTRACT

Conductivity has been measured for mixed alkali systems of  $\text{Li}_x\text{Na}_{1-x}\text{ClO}_4(\text{PEO})_n$  with  $n = 6, 16$  and  $40$ , and a mixed anion system of  $\text{LiCl}_x\text{I}_{1-x}(\text{PEO})_{16}$  complexes with varying concentrations of  $x$ . In the  $\text{Li}_x\text{Na}_{1-x}\text{ClO}_4(\text{PEO})_n$  complexes, it shows no unusual conductivity behavior. In the  $\text{LiCl}_x\text{I}_{1-x}(\text{PEO})_{16}$  complexes, the conductivity shows positive deviation from additivity in the mixed-anion region and the mixed-anion effect is also observed in the semicrystalline-to-amorphous transition temperature.

### INTRODUCTION

The mixed alkali effect (MAE) refers to deviation from additivity in isotherms of physical properties that are related to alkali transport such as conductivity, dielectric loss and viscosity. Most commonly observed manifestation of the MAE is the strong minimum observed in the ionic conductivity of various glasses and the  $\beta$ -alumina families [1-3]. Unlike the MAE, the mixed-anion effect shows a small maximum of conductivity in the mixed anion region, and few papers have been published on this subject [4,5]. However, little work on the mixed salt effect of polymer electrolytes has been conducted.

An unusual enhancement in conductivity in PEO-based electrolytes was first reported by Moryoussef et al. [6]. They observed a noticeable enhancement of conductivity due to mixing of either cations or anions. It was suggested that this was due to a plastifying effect which favors the formation of an amorphous phase at the expense of the crystalline phase. Several systems of mixed cations, mixed anions and both mixed cations and anions have been studied, but most studies have been confined to compositions in which the ratio of salt(I)/salt(II) is 50/50 mole fraction [6-10]. Recently, Yang et al. reported the variation of conductivity with mixed salt ratio [11]. They observed a significant conductivity enhancement in the  $[x\text{ZnBr}_2 + (1-x)\text{LiBr}](\text{PEO})_{16}$  complexes, but no unusual conductivity behavior in  $[x\text{Mg}(\text{ClO}_4)_2 + (1-x)\text{LiClO}_4](\text{PEO})_{16}$  complexes. The MAE and the mixed-anion effect observed in ionically conducting glasses are considered not to be applicable consistently in polymer electrolytes.

In this paper we present conductivity data on mixed alkali systems of  $\text{Li}_x\text{Na}_{1-x}\text{ClO}_4(\text{PEO})_n$  with  $n = 6, 16$  and  $40$  and a mixed-anion system of  $\text{LiCl}_x\text{I}_{1-x}(\text{PEO})_{16}$  complexes, which were prepared with varying concentrations of  $x$ .

## EXPERIMENTAL

The complexes were prepared by dissolving predetermined amounts of PEO (Aldrich, MW  $2 \times 10^6$ ) and alkali salts in acetonitrile. This solution was stirred at room temperature for approximately 24h. Films were cast on a Teflon plate by evaporating solvent in dried air for 24h and further dried under vacuum at room temperature for 24h. Finally, the samples were dried under vacuum at  $110^\circ\text{C}$  for a minimum of 48h. After complete solvent evaporation, polymer films of thickness ranging between 50 and  $150\ \mu\text{m}$  were obtained. Sample films were sandwiched between two stainless steel electrodes of the same diameter. The mounted sample of a polymer electrolyte film was kept under a mechanical pressure of  $2\ \text{kg/cm}^2$  and dried under vacuum at  $120^\circ\text{C}$  for 3 hours within the cell and cooled to room temperature. Conductivity measurements were recorded at  $1^\circ\text{C}$  interval from 10 to  $150^\circ\text{C}$  at heating and cooling rates of  $0.5^\circ\text{C/min}$ . All the conductivity data of this work represented average values of  $\sigma$  for at least two different samples of each electrolyte.

The complex impedances were determined by means of a HP model 4192A LF impedance analyzer. The complex impedance measured in the frequency range from 100 Hz to 1 MHz allowed us to obtain the direct current conductivity by means of the usual impedance analysis.

## RESULTS AND DISCUSSION

The results of conductivity measurements for the family of  $\text{LiClO}_4(\text{PEO})_n$  and  $\text{NaClO}_4(\text{PEO})_n$  complexes with  $n = 6, 16$  and  $40$  are shown in Fig. 1. More dilute samples,  $n = 16$  and  $40$ , show a clear transition to higher conductivities around  $60^\circ\text{C}$ , the temperature at which pure PEO melts. This transition is suppressed at higher salt concentration ( $n = 6$ ). The data for lithium perchlorate mixtures with PEO are comparable to results previously reported for this material [12]. It has been observed that the conductivity of  $\text{LiClO}_4(\text{PEO})_n$  complexes initially increases with increasing total metal ion concentration, reaches a maximum at an  $\text{EO/Li}^+$  ratio over the range 12-20, and then decreases as the concentration is further increased. In the high temperature range above  $60^\circ\text{C}$ , the  $\log \sigma$  against reciprocal temperature are well described by the Arrhenius equation and the activation energies of two PEO/salt systems are nearly same for the same PEO/salt ratio. However, the high temperature value of the conductivity of  $\text{NaClO}_4(\text{PEO})_n$  is slightly higher than that of  $\text{LiClO}_4(\text{PEO})_n$  for the same composition  $n$ . It has been known that conductivities tend to be higher for the heavier alkali ions for a given stoichiometry [13]. It reveals that cations having larger ionic radii would have weaker interaction with either oxygens in the polymer backbone resulting in higher ionic conductivity.

Conductivity data of mixed  $\text{Li}_{1-x}\text{Na}_x\text{ClO}_4(\text{PEO})_n$  complexes at  $100^\circ\text{C}$  for  $\text{EO/M}^+$  ratios of  $n = 6, 16$  and  $40$  with varying  $\text{Li}^+/\text{Na}^+$  ratios are shown in Fig. 2. Data for conductivity versus mole fraction of sodium ion at constant values of  $\text{EO/M}^+$  are found not to deviate from additivity for all values of  $\text{EO/M}^+$  ratios. It reveals independent migration of both  $\text{Li}^+$  and  $\text{Na}^+$  ions. Though an increase

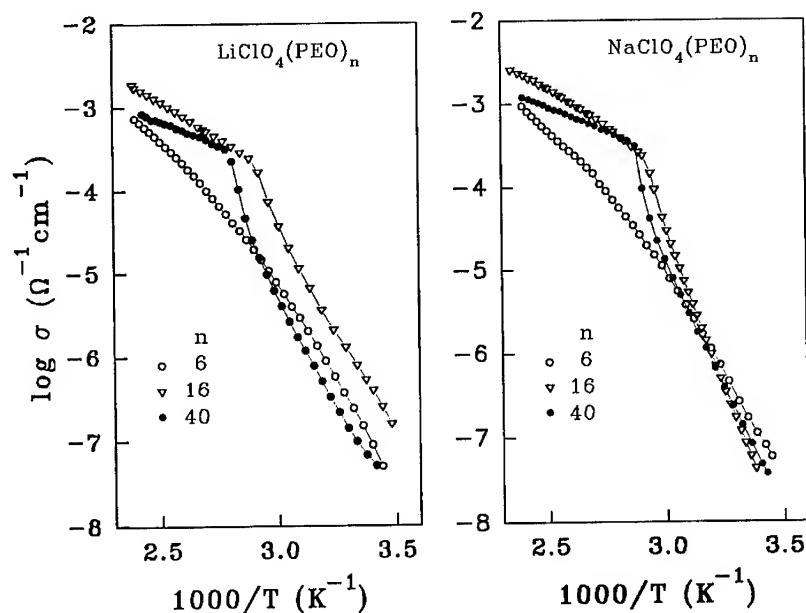


Fig.1 Temperature dependence of conductivity for  $\text{LiClO}_4(\text{PEO})_n$  and  $\text{NaClO}_4(\text{PEO})_n$  complexes with variable mole ratios of  $\text{EO}/\text{M}^+$ .

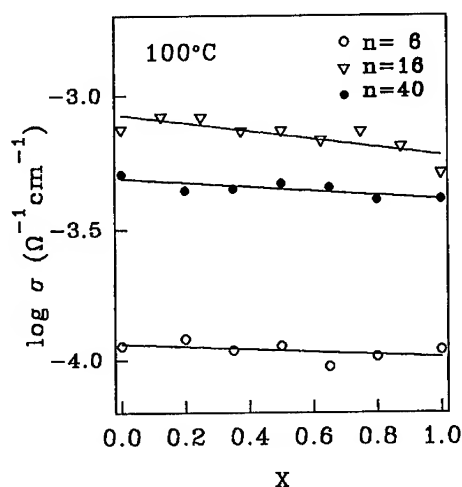


Fig.2 Compositional dependencies of conductivity at  $100^\circ\text{C}$  for  $\text{Li}_x\text{Na}_{1-x}\text{ClO}_4(\text{PEO})_n$  complexes.

of amorphous phase upon mixing salts has been suggested in several  $\text{PEO}/\text{mixed-salt}$  complexes [6, 9, 10], morphological changes as well as changes in ion aggregation with varying  $\text{Li}^+/\text{Na}^+$  ratios are not expected to occur in the  $\text{Li}_x\text{Na}_{1-x}\text{ClO}_4(\text{PEO})_n$  complexes.

Parallel studies were carried out with mixed-anion complexes of the type,  $\text{LiCl}_x\text{I}_{1-x}(\text{PEO})_{16}$ . Figure 3 shows the results of conductivity measurements with  $x = 0, 0.5, 1$ . The conductivity values obtained for  $\text{LiCl}(\text{PEO})_{16}$  complexes are several times lower than those of  $\text{LiI}(\text{PEO})_{16}$  for all temperatures. The smaller anions  $\text{Cl}^-$  exert stronger electrostatic interactions on cations than do  $\text{I}^-$  ions, resulting in lower ionic conductivity. Figure 4

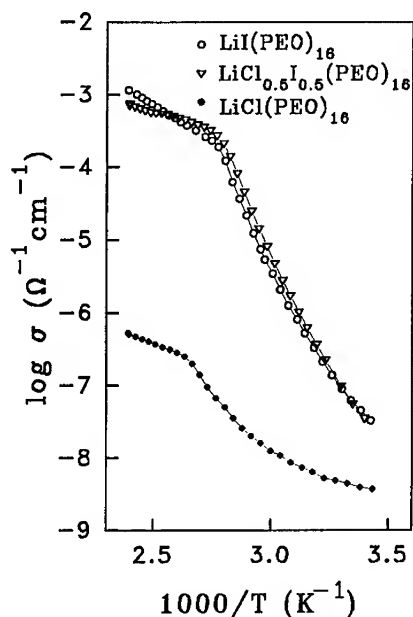


Fig.3 Temperature dependence of conductivity for mixed  $\text{LiCl}_x\text{I}_{1-x}(\text{PEO})_{16}$  complexes.

shows a small mixed-anion effect of  $\text{LiCl}_x\text{I}_{1-x}(\text{PEO})_{16}$  complexes, where the conductivity shows positive deviation from additivity in the mixed-anion region. The mixed anion effect is also observed in the semicrystalline-to-amorphous transition temperature. Thermal hysteresis is always observed between the cooling and heating cycle due to the low rate of phase transition process of PEO, especially for samples of low salt contents. The transition temperatures of Fig. 4 were taken in the cooling cycle, since they were defined better than those of the heating cycle.

In the several PEO/mixed-salt complexes, an unusual conductivity enhancement upon the mixing of cations or anions occurs [6-11]. In contrast, a few mixed complexes show a conductivity minimum [14,15] and the other few mixed complexes, including our results, show gradual

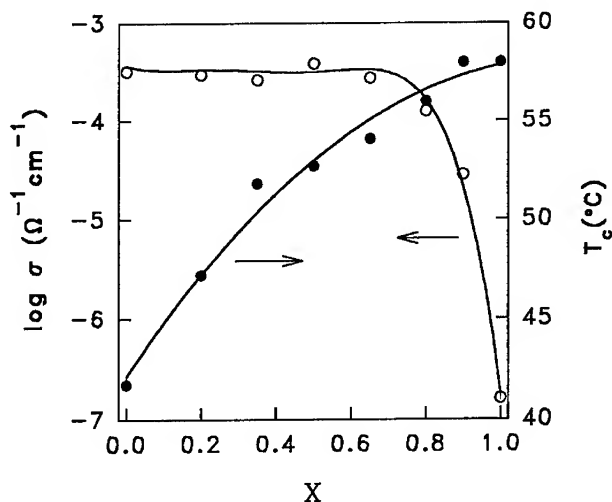


Fig.4 Compositional dependencies of conductivity at 100°C and transition temperature for mixed  $\text{LiCl}_x\text{I}_{1-x}(\text{PEO})_{16}$  complexes.

conductivity change between two systems [7,11]. It seems there are no general rules for the MAE in the PEO/salt complexes. However, the most commonly observed manifestation of the MAE, observed typically in ionically conducting glasses, is that the conductivity in mixed alkali glasses can be a factor  $10^4$  or  $10^5$  less than in the single alkali glasses. Such large departures from additivity clearly constitute a major failure of the principle of independent migration of ions. Hence it is properly to be expected that various mechanisms governing the MAE in ion conductive glasses are not applicable to the understanding of ionic transport mechanism of PEO/mixed-salt complexes. More work is needed to establish their general characteristics and the principal factors that determine their properties.

## CONCLUSIONS

In the  $\text{Li}_x\text{Na}_{1-x}\text{ClO}_4(\text{PEO})_n$  mixed complexes, the conductivity of the mixed-salt complexes changes linearly between that of two pure PEO-salt complexes. In the  $\text{LiClI}_{1-x}(\text{PEO})_{16}$  complexes, the conductivity shows a small positive deviation from additivity in the mixed-anion region. It seems no general results on the mixed-alkali and mixed-anion effect in polymer electrolytes, since the restricted number of investigations give rather conflicting results and little is known about the temperature dependence of ion-ion associations in polymer electrolytes. More systematic work is needed to be done before any general conclusions on the mixed salt effect of PEO/salt complexes.

## Acknowledgement

This work was supported by the Korea Science and Engineering Foundation (KOSEF) through the SRC of Excellence Program.

## REFERENCES

1. J.O. Isard, *J. Non-Cryst. Solids*, **1**, 235 (1969).
2. D.E. Day, *J. Non-Cryst. Solids*, **21**, 343 (1976).
3. H. Sato, *Solid State Ionics*, **40/41**, 725 (1990).
4. B. Carette, M. Ribes and J.L. Souquet, *Solid State Ionics* **9/10**, 735 (1983).
5. T. Minami, *J. Non-Cryst. Solids*, **73**, 273 (1985).
6. A. Moryoussef, M. Bonnat, M. Fouletier and P. Hicter, in *Proc. 6th RISO Int. Symp. Metallurgy and Materials Science*, edited by F.W. Poulsen, N.H. Andersen, K. Clausen, S. Skaarup and O.T. Sorensen (Roskilde, The Hague 1985), p. 335.
7. R. Dupon, B.L. Papke, M.A. Ratner, D.A. Whitmore and D.F. Shriver, *J. Am. Chem. Soc.* **104**, 6247 (1982).
8. I.E. Kelly, J.R. Owen and B.C.H. Steele, *J. Power Sources*, **14**, 13 (1985).
9. J.R. MacCallum, A.S. Tomlin, D.P. Tunstall and C.A. Vincent, *Br. Polym. J.* **20**, 203 (1988).
10. D.P. Tunstall, A.S. Tomlin, F.M. Gray, J.R. MacCallum and C.A. Vincent, *J. Phys. Condens. Matter*, **1**, 4035 (1989).

11. H. Yang and G.C. Farrington, *J. Polym. Sci. B*, **31**, 157 (1993).
12. C.D. Robitaille and D. Fauteux, *J. Electrochem. Soc.* **133**, 315 (1986).
13. E.A. Rietman, M.L. Kaplan and R.J. Cava, *Solid State Ionics*, **25**, 41 (1986).
14. G. Li, Q. Yang, B. Fang, C. Hu and S. Ying, in Recent Advances in Fast Ion Conducting Materials and Devices, edited by B.V.R. Chowdari, Q. Liu and L. Chen (World Scientific, Singapore, 1990), p. 295.
15. D. Teeters, M. Wong and C.L. Straub, *Solid State Ionics*, **53-56**, 1083 (1992).

## POLYMER BLENDS BASED ON POLY(ETHYLENE OXIDE) AS MATRICES OF SOLID STATE IONICS

ANNA I. SUVOROVA AND IRINA S. TUJKOVA  
Urals State University, Lenin St.51, 620083, Yekaterinburg, Russia

### ABSTRACT

The equilibrium sorption, inverse gas chromatography (dynamic sorption), optic microscopy, X-ray diffraction and visible light scattering methods were used to investigate the structure of poly(ethylene oxide) (PEO) blended with poly(vinylacetate) and poly(siloxanes) as matrices of polymer solid electrolytes. It was shown that the melting point ( $T_m$ ) and the degree of crystallinity in such PEO-blends were lower than in pure PEO. The Gibbs energy of mixing and the compatibility parameter ( $\chi_{12}$ ) were obtained for PEO-blends. In the vicinity of  $T_m$  all the systems were thermodynamically compatible, however at the ambient temperature they were microheterogeneous and compatible only in the narrow range of PEO-modifier contents. This must be taken into consideration while creating solid polymer electrolytes based on polymer blend matrices.

### INTRODUCTION

A considerable interest has been attracted at last decade to the development of solid polymer electrolytes with high ionic conductivity at ambient temperature. Though these materials are macroscopically solid the ionic transport is facilitated by the segmental motion of the polymer. In poly(ethylene oxide) (PEO) which possesses a high crystallinity this motion takes place only in amorphous part of polymer structure. Polymer crystallinity can be decreased by different ways. One of them is the preparation of polymer blends based on poly(ethylene oxide).

Recently it was reported about the preparation of the novel polymer electrolytes formed on PEO blended with poly(vinylacetate) (PVA) [1,2], poly(2-vinylpyridine) [3] and lithium perchlorate. The conductivity of such systems at the different  $\text{LiClO}_4$  content exhibits a value  $10^{-5} - 10^{-6} \text{ S cm}^{-1}$  at room temperature. Besides, these blends have a desirable mechanical properties. It must be mentioned that such data on solid polymer electrolytes obtained by blending of two high molecular weight polymer and  $\text{LiClO}_4$  are rare. It appears that a central and unsolved problem in the field of polymer blend electrolytes is compatibility of components in such systems and its influence on the structure of the polymer matrix. The study deals with investigation of the compatibility and structure of PEO-PVA and PEO-poly(siloxane) blends.

### EXPERIMENTAL

The materials which were used in this investigations were commercial PEO ( $M = 5 \cdot 10^6$ ) and PVA ( $M = 2 \cdot 10^6$ ); poly(dimethylsiloxane) (PDMS,  $M = 1,2 \cdot 10^5$ ) and poly(methylphenylsiloxane)

(PMPS,  $M = 5,7 \cdot 10^5$ ) which were supplied by the Institute of Synthetic Rubber (St-Petersburg). The polymer blends of the desirable concentrations were prepared by casting from the 2% solution of the components in  $\text{CHCl}_3$  onto mirror glass substrate. The solvent was evaporated at the temperature of  $25^\circ\text{C}$ , the blends were dried in vacuum at  $40^\circ\text{C}$  for at least one day. All samples were thin films (50-70  $\mu\text{m}$ ) and stored in a desiccator.

The melting point ( $T_m$ ) of the samples was determined with the help of a microscope with cross Nicol prisms (type POLAM) and from the temperature dependence of the light scattering intensity (LS) of the He-Ne laser light with the wave length equal to 638 nm. The LS investigations were performed at constant angle of scattering ( $12,5^\circ$ ).

The inverse gas chromatography (IGC) was used to determine  $T_m$ , the degree of crystallinity (K) and compatibility parameter  $\chi_{12}$  of polymer blends. In the IGC method  $\text{CHCl}_3$  and  $\text{CCL}_4$  were used as sorbates. The degree of crystallinity (K) was determined also by X-ray diffraction. The PEO-blend films were analyzed with BSW-22 diffractometer (30 kV, 20 mA,  $\Theta = 0,5^\circ/\text{min}$ ) using  $\text{K}\alpha$  Cu radiation.

From the equilibrium sorption of the  $\text{CHCl}_3$  vapor the depression of the solvent vapor pressure over each polymer and their blends was determined. The sorption measurements were carried out at the constant temperature of  $25^\circ\text{C}$ . The Gibbs mixing energy ( $\Delta G_x$ ) of the components in blends can be calculated using the thermodynamic cycle by the equation:

$$\Delta G_x = \Delta G_{bl} - (\omega_1 \Delta G_1 + \omega_2 \Delta G_2) \quad (1)$$

where  $\Delta G_{bl}$ ,  $\Delta G_1$ ,  $\Delta G_2$  are the Gibbs energies of mixing of blend (bl), PEO -modifier (1), PEO (2) with  $\text{CHCl}_3$ ;  $\omega_1$ ,  $\omega_2$  are weight fractions of the components in the films [4].

## RESULTS AND DISCUSSION

Figure 1 shows the temperature of the melting point PEO versus the content of modifier in various PEO blends. By the use of different methods the beginning (LS, IGC) and the end (microscopy) of the melting process have been noted. The amorphous component (PVA, PDMS, PMPS) decreases  $T_m$  of PEO, but this decreasing is insignificant because the high crystallinity of PEO hinders the penetration of the modifier segments into PEO-phase. Nevertheless the degree of crystallinity (K). PEO is diminished in blends.

Figure 2 illustrates K changes with the content of amorphous modifier in blends. This effect is a result of the definite type interaction of the components in blends, while degree of the crystallinity (K) is depressed larger than additive value, which can be calculated as a result dilution of the crystalline phase PEO by amorphous component. The K value, which was determined from X-ray diffraction, is larger than K obtained by the IGC and microscopy methods. It is a characteristic feature of the crystalline structure of the blends at the ambient temperature. The other methods (IGC, microscopy) are giving the value of K in the vicinity of the melting point. The data of  $T_m$  of PEO blends (Figure 1) were used to calculate the interaction parameter  $\chi_{12}$  by means of equation:

$$\frac{1}{T_m} - \frac{1}{T_0} = \frac{RV_2}{\Delta H V_1} \chi_{12} (1 - \varphi_2)^2 \quad (2),$$



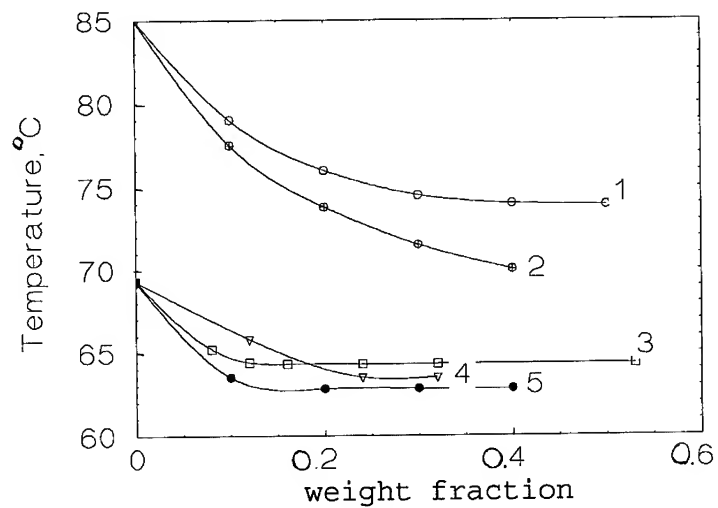


Figure 1. PEO-blends melting points  $T_m$  versus modifier concentration  $\omega_1$  :  
 ○ PVA, □ PDMS, ▽ PMPS, determined by LS (1), microscopy (2) IGC methods (3-5).

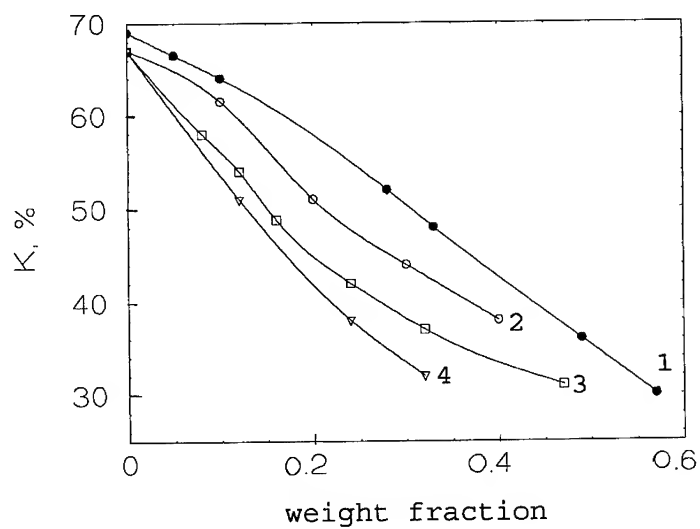


Figure 2. Concentration dependence of the crystallinity degree  $K$  in PEO- blends determined by X-ray diffraction (1) and JGS (2-4) methods. □ PVA, ○ PDMS, ▽ PMPS.

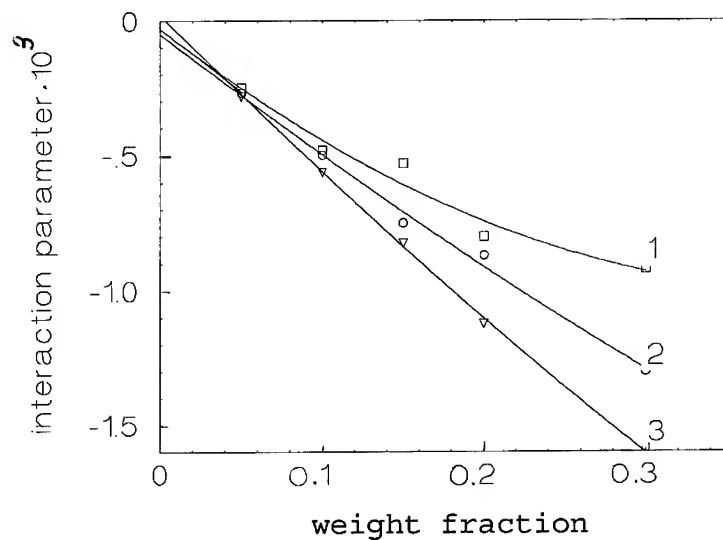


Figure 3. Dependence of the interaction parameter  $\chi_{12}$  on the modifier contents  $\omega_1$  in PEO. 1-PDMS, 2-PVA, 3-PMPS.

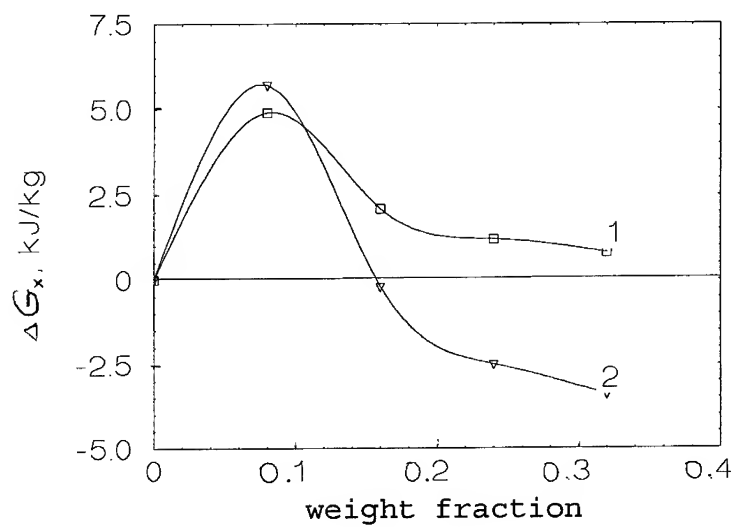


Figure 4. Concentrational dependence of the Gibbs energy of mixing in PEO-PDMS (1) and PEO-PMPS (2) systems.

where  $T_0$ ,  $T_m$  are melting points of PEO and its blends;  $V_2$ ,  $V_1$  are molar volume of the repeated links of PEO and modifier;  $\Delta H$  is enthalpy of fusion of PEO;  $\phi_2$  is its volume fraction [5].

The interaction parameter  $\chi_{12}$  as a function of the content of PEO modifier in the blends is shown on Figure 3. Near the melting point parameter  $\chi_{12} < 0$  and all the components are compatible. The compatibility increases in the row PMPS-PVA-PDMS. However, as it is presented on Figure 1, at the room temperature all the systems are microheterogeneous as they correspond to the contents under the "liquidus line". The compatibility in such systems was determined by the sorption of the  $\text{CHCl}_3$  vapor by PEO and its blends at  $25^\circ\text{C}$ . Then, using eqs. (1), the Gibbs energy of mixing ( $\Delta G_X$ ) was calculated. Figure 4 illustrates the dependence of  $\Delta G_X$  on the modifier content in PEO-polysiloxane blends. Only the PEO-PMPS systems are thermodynamically compatible:  $\Delta G_X < 0$  if the content of amorphous component (PMPS) is more than 12 mass. %.

Thus, Figures 3,4 show that the systems are compatible at high temperatures (in vicinity of  $T_m$ ) and incompatible at the ambient temperature. In the such microheterogeneous blends the second polymer penetrates only in amorphous part of PEO structure. It means, that in the creation of new solid polymer electrolytes the compatibility of the components in blends must be taken into consideration because it determines their stability at the used conditions.

## REFERENCES

1. K. Orihara, H.Yonekura, *Macromol.Sci.Chem.*,27,1217 (1990).
2. A.L.Krugliashov, I.Ye.Animitza, O.V.Bushkova, V.M.Zshukovsky, A.I.Suvorova, International Symposium on "Systems with the Fast Ionic Transport", Warszawa, 10-14 May, 1994, P. 12.
3. J.Li, E.A.Mintz, I.M.Khan, *Chem.Mater.*,4,1131 (1992).
4. A.A.Tager, T.I.Scholohovich, J.S.Bessonov, *Europ. Polym. J.* 11,231,(1975).
5. T.Nishi, T.T.Wang, *Macromolecules*,8, 909 (1975).

## XAFS STUDIES OF POLYMER ELECTROLYTES

H M N BANDARA\*, R G LINFORD, R J LATHAM AND W S SCHLINDWEIN  
Department of Chemistry, De Montfort University  
The Gateway, Leicester LE1 9BH, England.

\*On leave from the University of Peradeniya, Sri Lanka

### ABSTRACT

Because of the procedures associated with the deconvolution of the data present in an EXAFS spectrum, the experimental XAFS spectra also include both the edge and XANES regions. It is possible to obtain additional structural and chemical information from the data associated with these regions of the XAFS spectrum and in this work we have re-examined the XAFS spectra for a series of polymer electrolytes. These spectra were originally recorded for EXAFS analysis. The XANES spectra for  $\text{PEO}_n\text{:CaBr}_2$  electrolytes confirm that the behaviour of calcium polymer electrolytes appears to be very different from that of other divalent based electrolytes. We have also examined the edge features for  $\text{PEO}_6\text{:NiBr}_2$  samples which were subject to different thermal histories and evidence for phase separation is presented.

### INTRODUCTION

Polymer electrolytes are potentially useful in a range of applications including power sources, electrochromics and sensors<sup>1</sup>. To guide the materials scientist, it is important to maximise our knowledge and understanding of the relationships between performance parameters such as conductivity and the structural characteristics of the material.

Polymer electrolytes and glasses differ from crystalline solid electrolytes such as the  $\beta$ -aluminas, modified silver/copper iodides etc., in that they do not possess long range order in the amorphous conducting regions. Unlike glasses, in polymer electrolytes the matrix surrounding the mobile species is flexible and co-ordination changes with time, a situation that justifies the description "immobile solvent". For sensor and other applications there is a diverse range of candidate conducting species, some of which exhibit co-ordination and redox effects.

Diffraction techniques<sup>2</sup> have an important but incomplete role to play in elucidating the features of structural interest within polymer electrolytes. Spectroscopic and scattering techniques have provided powerful insights about aspects of their chemical behaviour. X-ray absorption spectroscopy, and in particular the generic XAFS (X-ray absorption fine structure) accesses both local structure and chemical information, providing a useful adjunct to more conventional techniques.

## Background to XAFS

Although it is possible to use equipment based on rotating anode configurations, XAFS experiments are normally performed at a high intensity source such as synchrotron storage ring.

There are three regions of importance in an experimental XAFS spectrum:-

1. The edge region. This contains the absorption edge (usually K or  $L_{III}$ ) and immediately adjacent pre- and post-edge features.
2. The NEXAFS or XANES region in which several types of information are convoluted. This is usually associated with the region up to about 50 eV ( $3.6 \text{ \AA}^{-1}$ ) above the edge.
3. The EXAFS region which follows the XANES region and continues up to about 1000 eV ( $16 \text{ \AA}^{-1}$ ) beyond the edge.

A XAFS spectrum for a polymer electrolyte is shown in figure 1a. Features in region A can give indications of valence state and internal electronic transitions. The shift in the absolute position of the edge can, under certain circumstances, be informative. Region B contains the convoluted XANES information<sup>3, 4</sup>. One component of this arises from interference between the outgoing photoelectron wave, caused by the interaction between the X-ray photon and the K or  $L_{III}$  shell of the target atom, and the backscattered wave from second and third nearest neighbours to the target species. A second component, similar in cause, is the multiple reflection from first nearest neighbours. These two components are difficult to separate and analyse in a rigorous manner. In addition there may be significant chemical effects similar to those observed in the edge-region which it may be possible to ascribe to individual chemical states within a system. Such an approach has been used to detect the presence of Cr(VI) in electrolyte solutions<sup>5</sup>. Region C contains information arising from backscattering by first nearest neighbours. Reasonably precise nearest neighbour distances,  $r$ , ( $\pm 0.01 \text{ \AA}$ ) can be obtained together with an indication of the number of nearest neighbours,  $N$ , ( $\pm 10\text{-}20\%$ ). EXAFS results for a number of polymer electrolyte systems have previously been reported<sup>6-19</sup>.

In order to extract values of  $N$  and  $r$  from a raw EXAFS spectrum such as that shown in figure 1a, it is necessary to perform the following data treatment steps:-

1. Calibration of the spectrum with respect to the notional position of the edge and removal of experimental glitches. The precise position of the X-ray beam from the synchrotron ring and the energy calibration from the monochromator change slightly between beam refills. This limits the comparative information that can be obtained between systems studied during different beam shifts.
2. Background subtraction to reveal the EXAFS features. Not only does this require the obvious step of extrapolating a smooth curve through the post-edge region but also it is necessary to compensate for the existence of the edge itself by extrapolation of the pre-edge region.

A consequence of this procedure is that EXAFS data sets contain the additional information pertaining to the edge and XANES regions. The result of the background subtraction is to produce a spectrum of the type shown in figure 1b.

3. Fast Fourier transformation of this produces the radial distribution function shown as the bold line in figure 1c. The fit of this with respect to a trial local structure is refined by iteration of both the k-space background subtracted spectrum and its Fourier transform. The adjusted parameters in addition to  $r$  and  $N$  include  $\Delta E_0$ , the adjustment on the notional edge position and  $\sigma^2$ , the Debye-Waller factor which has both static and thermal contributions. The Debye-Waller factor is correlated with  $N$  which accounts for the uncertainty in numbers of nearest neighbours, and  $\Delta E_0$  is correlated with  $r$ . The iteration procedure caters for a range of trial local structures, such as that which produces the dotted lines in figures 1b and 1c. For example, one can compare the fit indices for single and multi shell oxygen nearest neighbours in a polymer electrolyte.

#### Data Sets

It can be seen from the above that data sets for EXAFS spectra contain edge and XANES information. We have therefore re-examined our earlier EXAFS data sets in order to seek further information on this range of systems. Whereas it is possible to draw broad comparative conclusions between data from systems examined at different times, it is not possible to draw firm conclusions from small (1-2 eV) shifts in absolute edge position because of calibration difficulties.

In this paper we report results for:-

- (a)  $\text{PEO}_n\text{:CaBr}_2$  where  $n = 4, 8, 12$ ;
- (b)  $\text{PEO}_8\text{:MBr}_2$  where  $M$  is Co, Ni, Cu, Zn, for spectra of samples, prepared by our normal procedures, taken at room temperature;
- (c)  $\text{PEO}_8\text{:NiBr}_2$  prepared under different regimes and/or with spectra obtained at different temperatures.

#### **EXPERIMENTAL**

The XAFS spectra re-examined in this work were obtained at the Synchrotron Radiation Source, Daresbury Laboratory, UK, during allocations of beam time in the period 1986-1994. All spectra were obtained in transmission mode on station 7.1, with the exception of those for the calcium K-edge. The beam energy was 1.98 GeV with a typical average stored ring current of 150 mA from a high brightness lattice configuration. Data were acquired using argon filled ion chambers and a Si (111) double crystal monochromator with 50% harmonic rejection. The calcium K-edge spectra were obtained on station 8.1 in transmission mode with argon filled ion chambers. These older data were obtained before the installation of the high brightness lattice at a beam energy of 1.8 GeV and with a ring storage current in the range 100-300 mA (but less focused). On this station the monochromator utilises bent Si (111) crystals with harmonic rejection.

Polymer electrolyte samples were prepared as described for the previously published EXAFS results, namely as described in reference 20 for  $\text{PEO}_8\text{:MBr}_2$  ( $M$  is Co, Ni, Cu, Zn) and reference 17 for remaining nickel based electrolytes. For the  $\text{PEO}_n\text{:CaBr}_2$  samples, the EXAFS results have not been previously reported. The samples were prepared in a manner analogous to that described for  $\text{PEO}_4\text{:CaI}_2$  in reference 6.

## RESULTS AND DISCUSSION

### Anomalous Behaviour of Calcium Systems

Detailed examination of the edge and XANES regions of the spectrum for  $\text{PEO}_8\text{CaBr}_2$  shown in figure 1d reveals features which can be compared with those obtained from the guideline compounds  $\text{CaBr}_2$  and  $\text{CaO}$ . For example, as shown in figure 2 having aligned the spectra to a  $1s \rightarrow 3d$  feature at 4036 eV, smooth peaks, i and ii, can be seen in both the polymer electrolyte and  $\text{CaO}$  spectra. In addition, a sharp peak, iii, is present in the spectra of both the electrolyte and  $\text{CaBr}_2$ .

Consequently it can be inferred that there is a significant interaction between calcium and oxygen. By comparison there are no common features in the room temperature XANES of  $\text{PEO}_8\text{MBr}_2$  (where M is Co, Ni, Cu, Zn) that resemble those in the appropriate oxide, although strong similarity to the spectrum of the parent bromide is observed. Thus, the calcium XANES results appear to be somewhat anomalous. The EXAFS region of the XAFS spectrum for  $\text{PEO}_8\text{CaBr}_2$  shown in figure 1a together with those for  $\text{PEO}_n\text{CaBr}_2$  ( $n = 4, 12$ ) have been analysed using the procedure described in the introduction. The results are presented in table 1. It can be seen that, in comparison with other divalent systems,  $\text{Ca}^{2+}$  is surrounded by an unusually large number of oxygen nearest neighbours. The unusual behaviour of calcium-based polymer electrolytes is clearly revealed in both the XANES and EXAFS regions. It is not possible from these results alone to state with confidence whether this behaviour results from the innate characteristics of the calcium ion in polymer electrolyte systems, or the presence of adventitious water as previously noted for analogous systems<sup>6</sup>.

### Phase Separation in Nickel Systems

Many polymer electrolyte systems display phase separation as the temperature increases<sup>1</sup>. Polymer electrolytes based on nickel bromide have been reported to exhibit unusual characteristics<sup>20</sup>, although phase separation was not considered as an explanation at that stage. Careful examination of the nickel EXAFS spectra of  $\text{PEO}_8\text{NiBr}_2$  taken at room temperature<sup>17</sup>, revealed the same Ni-Ni distance, 3.6 Å, as found in the present  $\text{NiBr}_2$ . Also, the Debye-Waller factor for the neighbouring oxygens was substantially different for samples run at room temperature and 170°C whereas that for nearest neighbour bromines remained essentially the same. On the basis of the Ni-Ni distance and the Debye-Waller factor considerations, the possibility of phase separation was tentatively suggested.

Independent evidence on the basis of both polarising and atomic force microscopy of specially prepared very thin films, to be presented elsewhere<sup>21</sup>, has clearly shown that phase separation occurs in Ni films that have been subjected to heating to 140°C at some point in their thermal history. In this work we have therefore examined the XANES spectra for six Ni systems:-

1.  $\text{NiBr}_2$  guideline (model) compound : Daresbury SRS data set R26870, station 7.1.
2.  $\text{NiO}$  guideline (model) compound : Daresbury SRS data set R26868, station 7.1
3.  $\text{PEO}_8\text{NiBr}_2$  (PENN). This sample, prepared in Philadelphia and kindly supplied by Professor G C Farrington was initially dried by heating to 140°C for a prolonged period under vacuum<sup>20</sup> and the XAFS spectrum was then run at room temperature. Daresbury SRS data set R26889, station 7.1.

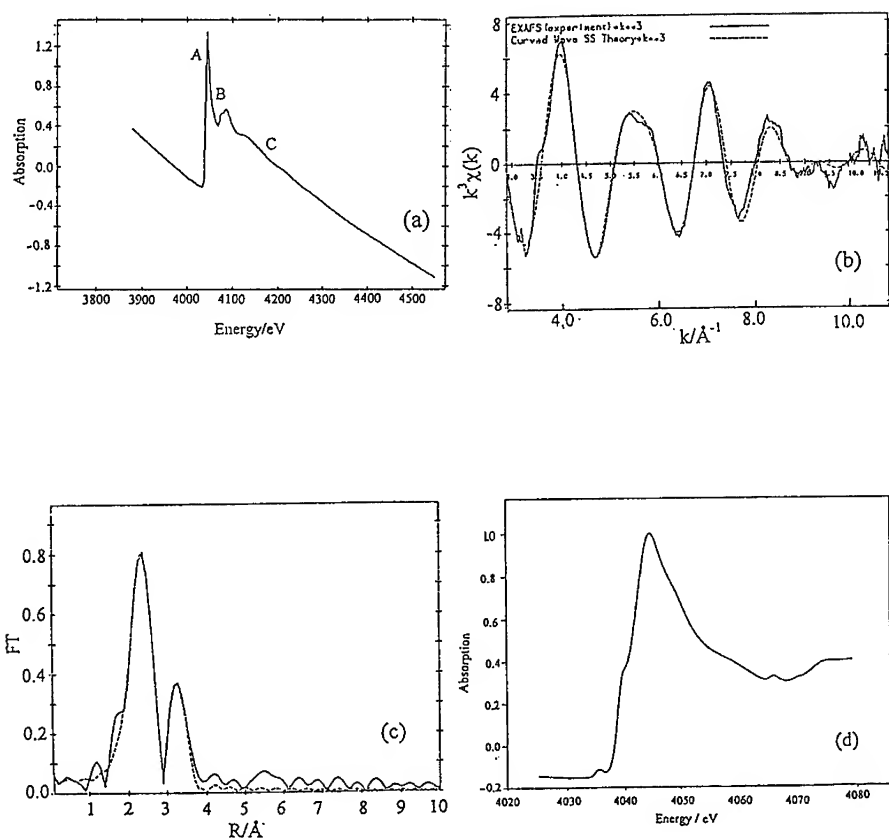


Figure 1. Examination of the XAFS spectrum for  $\text{PEO}_8:\text{CaBr}_2$  polymer electrolyte films.

- 1a. Raw XAFS data showing regions A, B and C;
- 1b. Background subtracted EXAFS spectrum;
- 1c. Fourier transform of spectrum in 1b. In both 1b and 1c the solid lines are the experimental data and the dotted lines are theoretical fits using curved wave theory;
- 1d. Expanded edge and XANES regions for the XAFS spectrum in 1a.



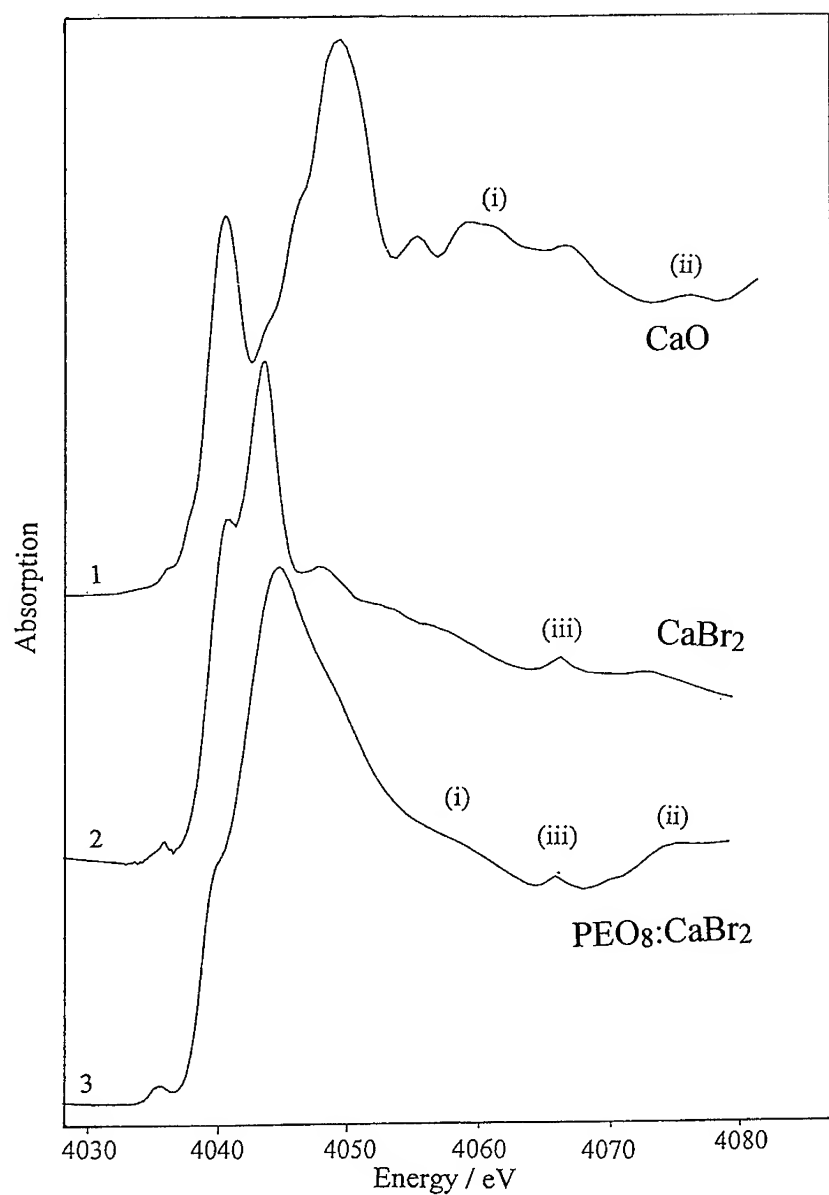


Figure 2. A comparison of the edge and XANES regions in the XAFS spectra of PEO<sub>8</sub>:CaBr<sub>2</sub> polymer electrolyte, CaO and CaBr<sub>2</sub> guideline compounds.

4.  $\text{PEO}_8\text{:NiBr}_2$  (170°C, DMU). This sample was initially dried by heating to 50°C under vacuum using the D50 procedure described in reference 21 and the spectrum was run at 170°C. Daresbury SRS data set R27821, station 7.1. This sample was similar to that used to produce the spectrum given in reference 17 but more data points in the edge and XANES regions were obtained.
5.  $\text{PEO}_8\text{:NiBr}_2$  (D140, DMU). This sample was made at Leicester using the Philadelphia methodology as for sample 3. Daresbury SRS data set R13142, station 7.1 (n.b. data set numbers were reset to zero in 1991).
6.  $\text{PEO}_8\text{:NiBr}_2$  (D50, DMU). This was prepared as for sample 4 and run at room temperature. Daresbury SRS data set R12115, station 7.1.

The edge and XANES spectra for these six samples are shown in figure 3. The energy scale has been adjusted so that the small pre-edge feature associated with the NiO guideline compound forms the reference point at 8316 eV. Whereas the features of interest in the calcium system were to be found in the XANES region, the edge itself is particularly informative for this range of nickel samples.

For the nickel bromide guideline compound there are two edge peaks at 8327 and 8332 eV. The lower energy peak is echoed in the strong shoulders in the spectra for samples 4 and 5, and a discernable shoulder in spectrum 3. This feature is completely absent from spectrum 6. Because XAFS spectra are inevitably spacially averaged as a result of the relatively large beam dimensions (1 mm x 10 mm), this shoulder can be regarded as indicative of the presence of phase separated nickel bromide. This is consistent with the morphological and EXAFS evidence previously described.

The absence of phase separated nickel bromide in the D50 sample and its presence in all samples that have been subjected to heating above 140°C in their thermal history supports an earlier suggestion<sup>22</sup> that the use of elevated temperatures for drying has a substantial effect on the final morphology of the film.

Of the samples run at room temperature, that prepared in Leicester (sample 5) has a more evident shoulder than the Philadelphia sample (3). The latter was prepared several months before XAFS examination and storage conditions were inevitably less stringently controlled than for the Leicester sample which was directly transferred from the vacuum area to special sealed holders<sup>7</sup>. It is possible that the irregularities in the leading edge of the D140 sample are connected with the evolution of phase separation process.

In the leading-edge region of the spectra, between the pre-edge feature used for alignment and the first  $\text{NiBr}_2$  edge peak, there is a small shoulder for NiO which can also be discerned in the D50 spectrum but not in the spectra of the other samples. This is consistent with a stronger association between Ni and O in the non-phase-separated sample.

Similarly, in the XANES region, there is a small broad peak at 8368 eV in  $\text{NiBr}_2$  and in the 'phase separated' set of samples, which is absent in the NiO and D50 samples whereas the latter have a broad peak at 8382 eV which is not present in the  $\text{NiBr}_2$ -related set.

EXAFS results from these samples are reported in table 2. It should be noted that the data fit previously reported in reference 17 for samples 3 and 5, shows a peak at about 3.6 Å which was tentatively ascribed to nickel-nickel interactions. The results in table 2 show that for these samples the peak can now be unambiguously ascribed to such interactions.

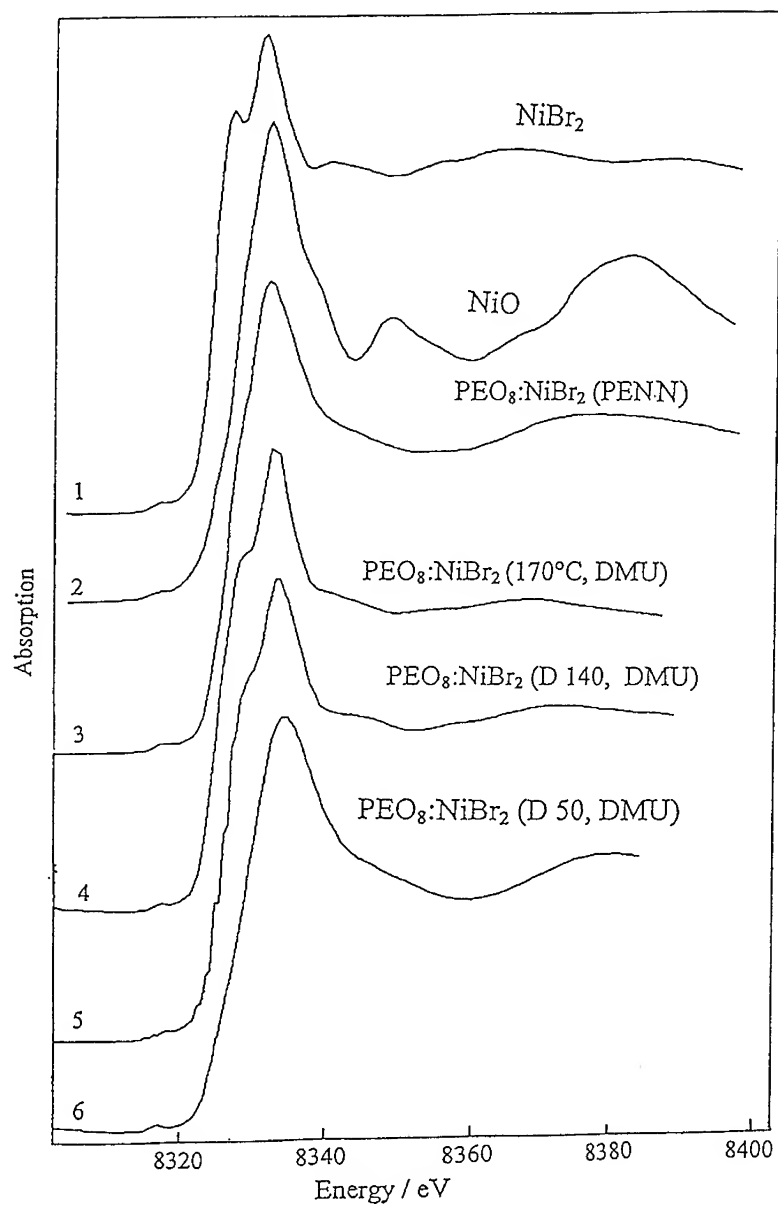


Figure 3. A comparison of the edge features associated with the XAFS spectra of  $\text{PEO}_8\text{:NiBr}_2$  polymer electrolytes subjected to different thermal history,  $\text{NiO}$  and  $\text{NiBr}_2$  guideline compounds.

Table 1 - EXAFS results of CaO, CaBr<sub>2</sub> and PEO<sub>8</sub>:CaBr<sub>2</sub> polymer electrolytes

Sample	NNA	N	r	$\sigma^2$	E <sub>0</sub>	R
CaO	O	5.1	2.38	0.018	6.89	56.50
	Ca	8.4	3.37	0.014		
CaBr <sub>2</sub> *	Br	6.9	2.88	0.024	6.54	45.85
PEO <sub>4</sub> :CaBr <sub>2</sub>	O	7.3	2.40	0.028	11.82	32.03
	Br	1.7	2.83	0.021		
	Ca	1.9	3.38	0.020		
PEO <sub>8</sub> :CaBr <sub>2</sub>	O	9.2	2.41	0.030	10.95	20.97
	Br	2.0	2.78	0.039		
	Ca	2.0	3.35	0.018		
PEO <sub>12</sub> :CaBr <sub>2</sub>	O	9.1	2.38	0.024	12.50	35.96
	Br	1.0	2.83	0.026		
	Ca	2.8	3.36	0.029		

Table 2 - EXAFS results of NiO, NiBr<sub>2</sub> and PEO<sub>8</sub>:NiBr<sub>2</sub> polymer electrolytes

M	NNA	N	r	$\sigma^2$	E <sub>0</sub>	R
NiO	O	6.4	2.05	0.009	15.40	58.37
	Ni	13.0	2.92	0.012		
NiBr <sub>2</sub>	Br	4.5	2.50	0.012	8.70	27.75
	Ni	7.6	3.62	0.025		
PENN 170°C	Br	3.9	2.45	0.020	14.09	34.03
	Ni	9.2	3.58	0.058		
DMU D140°C	Br	4.4	2.50	0.018	11.20	27.40
	Ni	6.1	3.66	0.035		
PENN (RT)	O	3.0	2.11	0.021	11.48	35.06
	Br	3.0	2.47	0.019		
	Ni	4.9	2.67	0.042		
DMU (RT)	O	5.8	2.12	0.027	17.92	23.71
	Br	4.5	2.40	0.022		

NNA = nearest neighbour atom; N = co-ordination number; r = Inter-atomic distance/Å

$\sigma^2$  = Debye-Waller factor/Å<sup>2</sup>, E<sub>0</sub> = edge displacement/eV; R = residual

\* Only bromine nearest neighbours are shown because of combination of the effects of light backscattering neighbours (Ca) and experimental difficulties.

These EXAFS spectra therefore support the suggestions made on the basis of edge and XANES information that phase separation occurs in samples 3, 4 and 5 but not in sample 6.

## CONCLUSIONS

1. Edge and XANES X-ray spectra can be used to provide structural inferences that can complement evidence drawn from EXAFS and other spectra, and morphological techniques.
2. The full XAFS spectra of calcium-based polymer electrolytes support the suggestion that these systems display a greater cation-oxygen association than is found for polymer electrolytes based on Co, Ni, Cu and Zn.
3. The XAFS spectra for  $\text{PEO}_8\text{:NiBr}_2$  polymer electrolytes prepared and examined under different conditions show that the thermal history has a pronounced effect on the local structure<sup>22</sup>. In this work we have observed changes in EXAFS edge features which can be associated with phase separation in samples that have been subjected to heating above 140°C at some point in their history.

## ACKNOWLEDGEMENTS

The former UK SERC are thanked for the following grants of beam time at the SRS, Daresbury Laboratory: GR/C/89472; GR/E.50070; GR/F/21695; BAP 22/262.

HMNB wishes to thank the EEC International Scientific Co-operation Initiative for the Marie Curie Fellowship contract number CI 1\*-CT93-0197. Duracell UK and the CNPq, Brazil are thanked for support.

## REFERENCES

1. P G Bruce and C A Vincent, J. Chem. Soc. Faraday Trans., **89**, 3187 (1993).
2. P Lightfoot, M A Mehta and P G Bruce, Science, **262**, 883 (1993).
3. X Q Yang, J Chen, T A Skotheim, Y Okamoto and M L Den Boer, in Second International Symposium on Polymer Electrolytes, ed. B Scrosati, Elsevier Applied Science, London and New York, 17 (1989).
4. M F Toney and J McBreen, Interface, **2(1)**, 22 (1993).
5. A J Davenport, Interface, **2(3)**, 37 (1993).
6. K C Andrews, M Cole, B R Dobson, R J Latham, R G Linford and H M Williams, Solid State Ionics, **28-30**, 929 (1988).

7. M Cole, M H Sheldon, M D Glasse, R J Latham and R G Linford, *Applied Physics A*, **49**, 249 (1989).
8. M Cole, R J Latham, R G Linford, W S Schlindwein and M Sheldon, in *Mat. Res. Soc. Symp. Proc.*, **135** : Solid State Ionics, ed. G.Nazri, R A Huggins and D F Shriver, MRS, Pittsburgh, USA, 383 (1989).
9. R J Latham, R G Linford and W S Schlindwein, *J. Chem. Soc., Faraday Discussions*, **88**, 103 (1989).
10. M Cole, R J Latham, R G Linford and M H Sheldon in *Mat. Res. Soc. Proc. : Solid State Ionics*, ed. G Nazri, R A Huggins and D F Shriver, MRS Pittsburgh, USA, **210**, 263 (1991).
11. A G Einset, R J Latham, R G Linford and R A J Pynenburg, *J. Electrochem. Soc.*, **138**, 1569 (1991).
12. R T Edwards, R J Latham, R G Linford and R A J Pynenburg, in *X-ray Absorption Fine Structure*, ed. S S Hasnain, Ellis Horwood, London, 390 (1991).
13. R J Latham, R G Linford, R A J Pynenburg and W S Schlindwein, in *Mat. Res. Soc. Proc. : Solid State Ionics*, ed. G Nazri, R A Huggins and D F Shriver, MRS Pittsburgh, USA, **210**, 273 (1991).
14. R J Latham, R G Linford, R A J Pynenburg and W S Schlindwein, *Electrochem. Soc. Softbound Proc.*, **92-1**, 227 (1992).
15. M D Glasse, R J Latham, R G Linford and R A J Pynenburg, *Solid State Ionics*, **53**, 1111 (1992).
16. R J Latham, R G Linford, R A J Pynenburg and W S Schlindwein, *Electrochim. Acta.*, **37(9)**, 1529 (1992).
17. R J Latham, R G Linford, R A J Pynenburg, W S Schlindwein, G C Farrington, *J. Chem. Soc. Faraday Trans.*, **89(2)**, 349 (1993).
18. R J Latham, R G Linford and R A J Pynenburg, *Solid State Ionics*, **60**, 105, (1993).
19. R J Latham, R G Linford, R A J Pynenburg and W S Schlindwein, *J. Electrochem. Soc.*, **140(4)**, 1056 (1993).
20. R Huq and G C Farrington, *J. Electrochem. Soc.*, **135**, 524 (1988).
21. H M N Bandara, R J Latham, R G Linford and W S Schlindwein, *J. Electrochem. Soc.*, to be submitted.
22. M D Glasse, R G Linford and W Schlindwein, in *Second International Symposium on Polymer Electrolytes*, ed. B Scrosati, Elsevier Applied Science, London and New York, 203 (1989).

## XAS STUDIES OF PEO BASED POLYMER ELECTROLYTES

J. MCBREEN\*, X. Q. YANG\*, H. S. LEE\* AND Y. OKAMOTO\*\*

\*Brookhaven National Laboratory, Upton, NY 11973

\*\*Polytechnic University, Brooklyn, NY 11201

### ABSTRACT

X-ray absorption spectroscopy (XAS) has been very useful in elucidation the structure of polymer electrolytes, in particular ion-ion and ion-polymer interactions. Several examples are discussed. One is the use of XAS to study the effect of temperature on ion pairing. The other is the elucidation of the mixed cation effect on electrolyte conductivity. Several investigations have indicated abnormally high oxygen coordination numbers for cations. These are discussed.

### INTRODUCTION

X-ray absorption spectroscopy (XAS) is an ideal method for *in situ* studies of electrochemical systems because both the probe and signal are penetrating x-rays. The technique yields both structural and chemical information. A great advantage is that XAS is element specific, and this permits investigation of the chemical environment of minor constituent elements in a composite material. For instance, it is possible to study the chemical environment of a mixed salt system by tuning the beam energy to the specific absorption edge. The element specific nature of the probe make it ideal for the study of dilute salt systems. Since XAS probes only short range order it can provide structural information on amorphous materials, liquids, gases, adsorbed monolayers, as well as hydrated ions and complexes in aqueous solution or polymer electrolytes. Because of this XAS is finding application in an enormous variety of problems in solid state ionic systems. XAS has been invaluable in the study of ion conducting polymers, where the ion conducting phase is amorphous.

The main disadvantage of XAS is that it is an averaging technique. With x-ray diffraction it is possible to distinguish the contribution of various phases. However, the XAS spectrum for an element that exist in different phases is a composite of the spectra for the individual phases. This often makes analysis of the EXAFS difficult or even impossible. In the case where there are two phases present, such as a polymer electrolyte at room temperature, it is possible to analyze the XANES spectra in terms of a combination of the spectra of the individual phases. This treatment is analogous to that used for analysis of UV/visible spectra for redox processes in solution. Another disadvantage is the impossibility of doing XAS on lithium because of the low absorption energy (54.7 eV). *Ex situ* measurements can be done on elements as light as carbon in vacuum (K edge energy = 284 eV). The lightest element on which *in situ* measurements have been done is sulfur (K edge energy = 2472 eV). Other disadvantages are the need for a synchrotron source and the tedious nature of the analysis of the EXAFS data.

Chadwick has reviewed XAS studies of ionically conducting solids including polymer electrolytes (1). The review covers extensive EXAFS studies related to solid state ionics such as inorganic ionic conductors including AgI, rare earth doped alkaline earth fluorides, cubic stabilized zirconia, rare earth doped bismuth oxide and mixed fluorides. The early work on Rb salt/poly(ethylene oxide) complexes is also reviewed. XAS studies of polymer electrolytes continues to be an active area of research because the conducting phase is amorphous. Most of the work has been done by Linford and his co-workers at De Montfort University, in Leicester, and by the Polymer Group at Brookhaven National Laboratory. Since it is impossible to do XAS at the Li K edge the work has been done on polymer complexes of potassium, rubidium, calcium, nickel, cobalt and zinc salts.

Most polymer electrolytes are based on lithium salts dissolved in poly(ethylene oxide) (PEO). There is an excellent review of progress in the field, up to 1990, by Grey (2). As in any other electrolyte the conductivity depends on the number of charge carriers and their mobility. The mobility has been correlated with segmental motion of the polymer chains. Conductivity also depends on ion pairing, coulombic interactions among ionic carriers and interactions of the ions with the host polymer. Little is known about the nature of the charge carriers and the conduction mechanism. The dielectric constant of the polymers is typically 4-8. As a result there is formation of ion pairs, triplets and higher aggregates. Ion pairing and aggregate formation has been confirmed both by infrared and Raman spectroscopy (3,4). A number of surprising phenomena have been found. One is that the transport number for lithium in the polymer electrolyte is very low. Bruce *et al.* have found transference numbers for lithium of 0.06 using the Hittorf method (5). This has important implications regarding the utilization of cathode materials in lithium polymer electrolyte batteries (6). Another unusual phenomenon is an increase in ion pairing with increasing temperature. This has been confirmed by physicochemical measurements such as deviations from the Walden rule in low molecular weight polymer complexes (7). Raman spectroscopy also indicates an increase in ion pairing with temperature (8). It has also been found that the conductivity of mixed cation systems is often higher than that found for the corresponding single salt systems. All of these unusual phenomena are due ion-ion and ion-polymer interactions. XAS is a very useful technique for elucidating these phenomena.

## APPLICATIONS OF XAS TO POLYMER ELECTROLYTES

### Temperature Effects on Ion Pairing

Ion pairing is an important problem in ionic conducting polymers, since it is directly related to number of charge carriers, one of the parameters that govern the conductivity. There is strong evidence from Raman spectroscopy that in some cases ion pairing in polymer electrolytes can increase with increasing temperature. Torell and her co-workers have carried out Raman studies of the symmetric stretching modes of the anions of  $\text{NaCF}_3\text{SO}_3$  and  $\text{LiClO}_4$  dissolved in poly(propylene glycol) and confirmed that ion pairing increased with increasing temperature (9,10). With XAS it is possible to probe the environment around the cation and study ion pairing effects. It is much more convenient to do XAS measurements on thin polymer films than to do Raman studies. Yang and co-workers have carried out several XAS studies on potassium salt/PEO complexes as a function of temperature (11-13). Recently they studied a



potassium salt in a modified carbonate solvent and in a PEO polymer that contained the carbonate as a plasticizer (13). By using reference systems such as aqueous potassium salt solutions and potassium crown ether complexes they found a correlation between ion pairing and the degree of white line splitting in the XAS spectra. The white line peak at the potassium K edge is related to electron transitions of  $1s$  into empty  $4p$  states. If the potassium ion is in a symmetrical environment such as in a crown ether or is coordinated with PEO the  $p$  states are either degenerate, or close to being degenerate, and the white line is a single peak, or broad peak with no significant features. Ion pairing will lift the degeneracy of the  $p$  states and the white line will be split. Pairing with a sulfonic acid group would probably yield a  $C_{3v}$  symmetry and the  $p$  states would be split in two. This accounts for the two peaks that are observed for the salt. From the development of the two peaks they concluded that the degree of ion pairing increases with increasing temperature (25-110°C) in both systems. Figure 1 shows the results obtained in the polymer. The effect was reversible in that the systems reverted to the same state on cooling to ambient temperature. The XAS results complement the Raman studies lend further proof of the increase in ion association at higher temperatures. Since XAS is an averaging technique, the effect of increasing temperature on ion pairing has to be substantial to yield such large effects on the XAS. Similar effects were seen earlier in KI/PEO complexes (11,12). There they found that the salt was dissociated in dilute solutions ( $KI(PEO)_{20}$ ). In concentrated solutions ( $KI(PEO)_4$ ) there was evidence for ion pairing. In the case of  $KI(PEO)_8$  the ion pairing was negligible. However, on going to 100°C there was evidence of ion pairing.

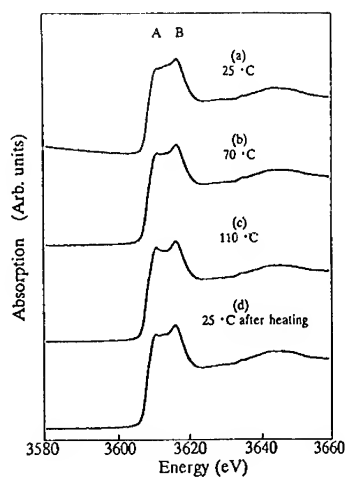


Fig. 1 Effect of temperature on the potassium XANES for a potassium salt/PEO/modified carbonate plasticizer film with a weight ratio of 100/80/40; (a) 25°C, (b) 70°C, (c) 110°C and (d) spectrum obtained on cooling from 110°C to 25°C. The potassium salt was di-potassium N,N'-Jeffamine dipropylene sulfonate (JDPS) (13).

## The Mixed Cation Effect

The conductivity of poly(ethylene oxide) (PEO) based electrolytes can be modified by several methods such as the use of salts with a low lattice energy, modification of the polymer host to increase segmental motion, incorporation of polar plasticizers and by the addition of a second salt (14,15). The latter is known as the mixed cation effect. Examples are  $[0.5\text{Ca}(\text{CF}_3\text{SO}_3)_2 + 0.5\text{Mg}(\text{CF}_3\text{SO}_3)_2](\text{PEO})_{15}$  and  $[\text{xCoBr}_2 + (1-\text{x})\text{LiBr}](\text{PEO})_{16}$ . In the case of  $[\text{xCaBr}_2 + (1-\text{x})\text{ZnBr}_2]$  and  $[\text{xCaI}_2 + (1-\text{x})\text{ZnI}_2]$  the conductivity is lowered (14). In some cases there is no mixed cation effect such as in  $[\text{xKSCN} + (1-\text{x})\text{NaSCN}](\text{PPO})_{9,6}$  or in mixtures of  $\text{ZnBr}_2$  and  $\text{LiBr}$  in PEO. The most remarkable effects have been observed in PEO-based polymer electrolytes containing mixed  $\text{CoBr}_2/\text{LiBr}$  salts (15). Large increases in the conductivity were observed in the mixed salt-polymer complexes. The maximum effect was observed with a  $\text{CoBr}_2:\text{LiBr}$  ratio of 0.45:0.55. The effect was also strongly dependent on the thermal history of the polymer complex. The mechanism of the mixed cation effect is not known. One possibility is that the effect is due to complex formation. It is also possible that the second salt modifies the polymer segmental motion and the ion mobility. McBreen and co-workers have carried out an XAS study at the Co K edge on  $\text{CoBr}_2(\text{PEO})_{16}$  and  $[0.45\text{CoBr}_2 + 0.55\text{LiBr}](\text{PEO})_{16}$  at  $25^\circ\text{C}$  (16).

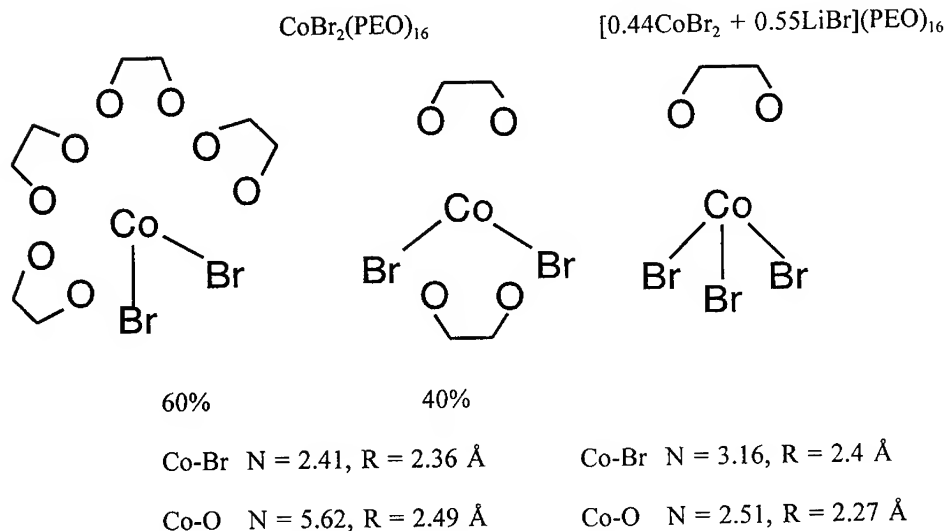
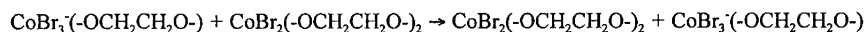


Fig. 2 Models that fit EXAFS data for  $\text{CoBr}_2(\text{PEO})_{16}$  and  $[0.45\text{CoBr}_2 + 0.55\text{LiBr}](\text{PEO})_{16}$  at  $25^\circ\text{C}$ . The calculated coordination numbers and bond distances are also shown.

Figure 2 shows models that fit the EXAFS data. In the case of  $\text{CoBr}_2(\text{PEO})_{16}$  the results could be fitted to a model consisting of a 60:40 mixture of octahedral and tetrahedral complex of largely undissociated  $\text{CoBr}_2$ . The large amount of oxygens can only be accommodated by assuming that five membered  $-\text{OCH}_2\text{CH}_2\text{O}-$  chelate rings occupy single coordination sites. In the case of  $[0.45\text{CoBr}_2 + 0.55\text{LiBr}](\text{PEO})_{16}$  a model consisting of pseudo-tetrahedral  $\text{CoBr}_3^-$  complexes, with a single five membered  $-\text{OCH}_2\text{CH}_2\text{O}-$  chelate ring occupying one apex of the tetrahedron, fits the data. Mendolia and Farrington reported on a study of  $\text{CoBr}/\text{LiBr}$  mixtures in a polytetramethylene glycol (PTMG) solvent and found similar results (17). In polyethylene glycol (PEG) they found that the formation of higher Co-Br complexes was facilitated by the ease which the bidentate  $-\text{OCH}_2\text{CH}_2\text{O}-$  units in PEG could chelate with the Co. They attributed this to the stability of the five-membered chelate ring of the bidentate  $-\text{OCH}_2\text{CH}_2\text{O}-$  ligand. The increased conductivity of the mixed salt PEO complex may be due to a conductivity mechanism based on hopping of  $\text{Br}^-$  ions by the following reaction



The reduced crosslinking of the polymer in the mixed salt may also play a role.

#### High Oxygen Coordination numbers in PEO

Linford and co-workers, in some early XAS work, reported very high oxygen coordination numbers ( $\sim 10$ ) for  $\text{Ca}^{++}$  in PEO (19). At first this was looked upon with some skepticism. However, there is a growing body of evidence that very high oxygen coordination numbers can occur in PEO. On the basis of a concentration study and FTIR spectroscopy of lanthanide triflate salts in PEO, Berenson and Lindgren concluded that in the case of  $\text{La}_3\text{CF}_3\text{SO}_3$  the  $\text{La}^{+++}$  was coordinated with 12 oxygens (20). Recently, McBreen and co-workers have done XAS studies at the Rb K edge on  $[0.8\text{ZnBr}_2 + 0.2\text{RbBr}](\text{PEO})_{12}$  and at the Zn K edge on  $[0.2\text{ZnBr}_2 + 0.8\text{RbBr}](\text{PEO})_{12}$  (21). It is well known that  $\text{RbBr}$  is not soluble in PEO. Mixing with  $\text{ZnBr}_2$  promotes the dissolution of  $\text{RbBr}$ . The results of Zn XAS indicate that the  $\text{RbBr}$  acts as a bromide ion donor and forms  $\text{ZnBr}_4^{2-}$  complexes. Analysis of the EXAFS at the Rb K edge yield an oxygen coordination number of 10 and a bond distance of 2.91 Å. The Rb XANES indicate a highly symmetrical environment for the  $\text{Rb}^+$  ions, such as  $T_h$  or  $O_h$  symmetry. In the case of octahedral symmetry if each  $-\text{OCH}_2\text{CH}_2\text{O}-$  five membered ring occupied a single coordination site, this would yield a total oxygen coordination of 12. Similarly tetrahedral coordination would yield a coordination number of 8. Given the uncertainty for determination of coordination numbers from EXAFS either symmetry is a possibility. These results together with the results presented above for  $\text{CoBr}_2(\text{PEO})_{16}$  indicate that very high oxygen coordination numbers are possible in PEO. It also points out the unique properties of PEO as a solvating polymer. These unique properties apparently accrue from the nature of the  $-\text{OCH}_2\text{CH}_2\text{O}-$  five membered ring.

## ACKNOWLEDGEMENTS

The authors gratefully acknowledge support of the U.S. Department of Energy, Division of Materials Sciences, under Contract Number DE-FG05-89ER45384 for its role in development and operation of Beam Line X-11 at the National Synchrotron Light Source (NSLS). The NSLS is supported by the Department of Energy, Division of Materials Sciences under Contract Number DE-AC02-76CH00016. The experimental work was supported by the Department of Energy Division of Materials Chemistry.

## REFERENCES

1. A. V. Chadwick, in Applications of Synchrotron Radiation, eds. C. R. A. Catlow and G. N. Greaves (Blackie & Son Ltd., Glasgow, 1990), pp.171-200.
2. F. M. Grey, Solid Polymer Electrolytes (VCH Press, New York, 1991).
3. S. Schantz, *J. Chem. Phys.* **94**, 6296 (1991).
4. A. Bernson and J. Lindgren, *Solid State Ionics* **60**, 37 (1993).
5. P. G. Bruce, M. T. Hardgrave and C. A. Vincent, *Solid State Ionics* **53-56**, 1087 (1992).
6. T. F. Fuller, M. Doyle and J. Newman, *J. Electrochem. Soc.* **141**, 1 (1994).
7. M. G. McLin and C. A. Angell, *J. Phys. Chem.* **95**, 9464 (1991).
8. L. M. Torell, P. Jacobsson, D. Sidebottom and G. Petersen, *Solid State Ionics* **53-56**, 1037 (1992).
9. S. Schantz, L. M. Torell, and J. R. Stevens, *J. Chem. Phys.* **94**, 6862 (1991).
10. M. Kakihana, S. Schantz and L. M. Torell, *J. Chem. Phys.* **92**, 6271 (1992).
11. X. Q. Yang, J. Chen, C. S. Harris, T. A. Skotheim, M. L. den Boer, H. Mei, Y. Okamoto and J. Kirkland, *Mol. Cryst. Liq. Cryst.* **160**, 89 (1988).
12. X. Q. Yang, J. Chen, C. S. Harris, T. A. Skotheim, Y. Okamoto, J. Kirkland and M. L. den Boer, *Phys. Rev.* **B40**, 7948 (1989).
13. X. Q. Yang, H. S. Lee, J. McBreen, Z. S. Xu, T. A. Skotheim, Y. Okamoto and F. Lu, *J. Chem. Phys.* **101**, 3230 (1994).
14. R. J. Latham, R. G. Linford, R. A. J. Pynenburg and W. S. Schlindwein, *Electrochimica Acta* **37**, 1529 (1992).
15. B. V. R. Chowdari, R. Huq and G. C. Farrington, *Solid State Ionics* **57**, 49 (1992).
16. J. McBreen, X. Q. Yang, H. S. Lee and Y. Okamoto, *Electrochim. Acta*, (1994) (submitted).
17. M. S. Mendolia and G. C. Farrington, *Electrochim. Acta* **37**, 1695 (1992).
19. K. C. Andrews, M. Cole, R. J. Latham, R. G. Linford, H. M. Williams and B. R. Dobson, *Solid State Ionics* **28/30**, 929 (1988).
20. A. Bernson and J. Lindgren, *Solid State Ionics* **60**, 31 (1993).
21. J. McBreen, X. Q. Yang, H. S. Lee and Y. Okamoto, *J. Electrochem. Soc.*, (1994) (accepted).

## POLYANILINE: INFLUENCE OF POLYMERIZATION CURRENT DENSITY

STEEN SKAARUP\*, L.M.W.K. GUNARATNE\*, KELD WEST\*\*  
and BIRGIT ZACHAU-CHRISTIANSEN\*\*

\*Physics Department, \*\*Department of Physical Chemistry  
Technical University of Denmark, DK-2800 Lyngby, Denmark.

### ABSTRACT

Polyaniline has been synthesized in propylene carbonate by galvanostatic electrochemical polymerization at current densities between 16 and 1000  $\mu\text{A}/\text{cm}^2$ . Earlier results for polypyrrole have shown that low and high current density films have different properties: The films synthesized at low current density have a higher conjugation length and a more regular structure. The corresponding effect in PANI has been investigated by cyclic voltammetry and UV/visible spectroscopy. Simultaneous measurement of cyclic voltammograms and the absorption of selected spectral lines is used because of the complex nature of the PANI system which involves several redox systems as well as forms differing in the degree of protonation and morphology.

The main result is that the method of galvanostatic synthesis at low current densities ( $\sim 16 \mu\text{A}/\text{cm}^2$ ) produces polyaniline polymers of different, more conjugated and more regular structure than those prepared at higher current densities. The standard method of *in situ* layer-by-layer polymerization of conducting polymers during cyclic voltammetry often results in uncontrolled and unmeasured current densities of 0.5-2  $\text{mA}/\text{cm}^2$  which produces a film that probably has a less regular structure containing more deviations from ideality.

### INTRODUCTION

The discovery about 20 years ago of highly enhanced electronic conductivity in doped polyacetylene [1,2] initiated a new field of materials science. The expansion of this field of research was driven both by the important new theoretical aspects of organic compounds with conductivities approaching or surpassing that of Cu and by the many practical application envisioned in devices such as sensors [3], battery electrodes [4] and electrochromic coatings [5].

Most electronically conducting polymers are insulators in the pure state, but become conducting when doped with counterions, corresponding to reduction or oxidation of the conjugated organic polymer backbone. The conductivity can increase by many orders of magnitude at dopant levels of only a few atom percent by the introduction of novel conducting species such as solitons, polarons and bipolarons [6]. The doping process can be reversible, and this crucial role of the presence and motion of counterions means that electronically conducting polymers are interesting from the point of view of solid state ionics. The doping mechanism is different from that in inorganic semiconductors, since the ions are not substituted into fixed positions in a crystal lattice, but are loosely or strongly associated with more or less well-defined sites along the one-dimensional polymer chain. The motion of ions between these positions and the electrolyte is an analogy to the intercalation or insertion of alkali metal ions in inorganic sulphides and oxides [7], and the same experimental methods and partly the same theoretical framework can be applied.

The high mobility of electronic species along the chains is possible because of the delocalization of the  $\pi$ -bonds. This delocalization is at a maximum when adjacent monomer units are all co-planar and undisturbed by chemical defects or by physical imperfections such as different chain lengths, side chains and kinks caused by folding. All deviations from the ideal and one-dimensional structure will tend to lower the effective conjugation length - e.g. the number of alternating single/double bond pairs participating in the delocalization. The conjugation length can be highly sample dependent, because of different methods of preparation and experimental conditions. Nominally identical samples from different sources can therefore have dissimilar properties - this is the reason for the lack of consensus about even well studied polymer systems.

Initial work on polypyrrole centered on trying to produce polymer films close to the ideal "intrinsic" form, in order to resolve the dependence on sample history. This in theory corresponds to infinite conjugation length, but in practice, the properties converge between 10 and at most 100. For polypyrrole, the crucial parameter turned out to be the current density during electrochemical polymerization [8]. When the current density during synthesis was varied from 60 to 4000  $\mu\text{A}/\text{cm}^2$ , a sequence of polymers with differing properties are formed. They can be characterized by their very different cyclic voltammograms, as well as the changes in optical absorption [9]. It turned out that polymerization at low current densities produced a polymer which is highly conjugated. This form, which is able to incorporate about 0.15 counterions extra per monomer unit and which recent results indicate may have a higher degree of crystallinity and a higher conductivity [10], has been used as a reference material in the investigation of the effect of using different counterions and solvent electrolytes on the properties [11].

The present work presents results from an investigation using the same methods and concepts on polyaniline (PANI), which is at present the conducting polymer with the most favorable technological prospects. The polyaniline system is more complicated than that of polypyrrole, both because of the presence of more than one redox process, and because the basic amine group is able to add protons, making the properties depend on both the acidity and the oxidation potential [12,13].

The proposed states of PANI is shown in figure 1. The leucoemeraldine state is fully reduced and contains only amine ( $\text{sp}^3$ ) nitrogens and benzenoid rings. On oxidation, the number of imine ( $\text{sp}^2$ ) nitrogens and quinoid rings become larger. An oxidation state can be represented by containing the fraction  $y$  of amine, and  $1-y$  of imine nitrogens.  $y=0, 0.5$  and  $1$  then corresponds to leucoemeraldine, emeraldine and pernigraniline [14]. The numbers are idealized, limiting values, which are not fully reached in actual samples. Depending on the acidity of the solvent, the species will be in the neutral, basic form or protonated to some degree. The electronic conductivity of the states vary from being insulators to about  $100 \Omega^{-1}\text{cm}^{-1}$ , with emeraldine salt being the most important conducting state (the positive charges are balanced by negative counterions associated with the chain).

## EXPERIMENTAL

Because of the sensitivity to sample history, it is necessary to separate the two processes of synthesis and characterization in order to work with a well-defined system. The usual method of gradually building the film layer-by-layer during cyclic voltammetry has the disadvantage of using an uncontrolled (and often high) current density determined by the reaction itself. The polymers were formed galvanostatically using current densities from 16 to 1000  $\mu\text{A}/\text{cm}^2$ .

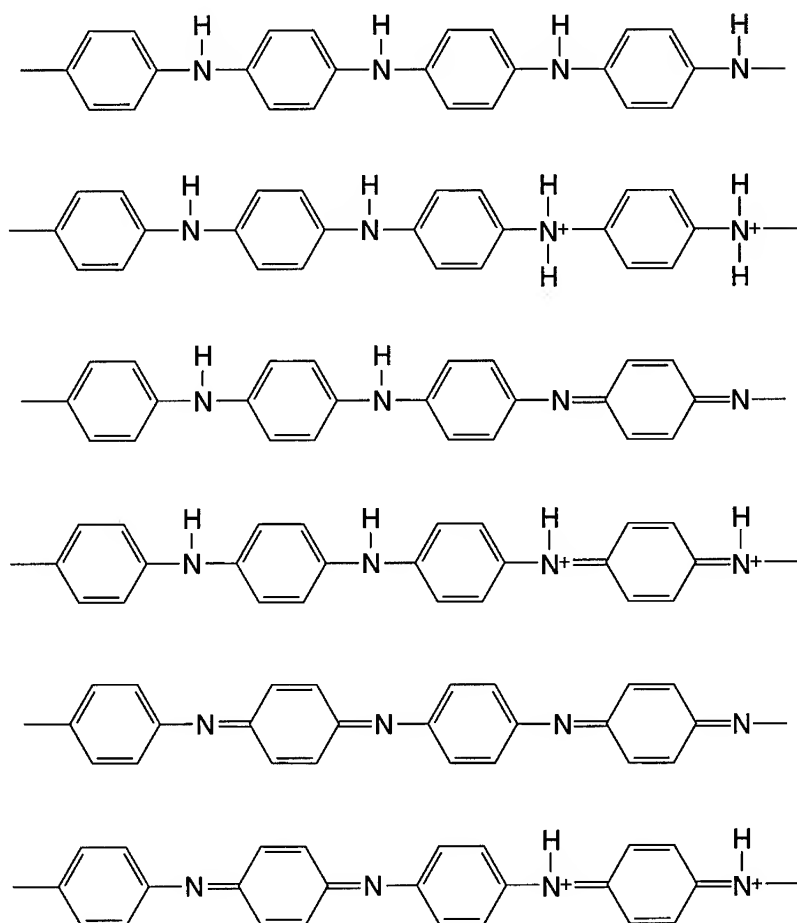


Figure 1. Possible PANI oxidation and protonation states. From top: Leucoemeraldine base, leucoemeraldine salt, emeraldine base, emeraldine salt, pernigraniline, pernigraniline salt.

The potential during synthesis was 3.8 V relative to a lithium reference electrode. Because PANI is known to be electrochemically active only if polymerized in the presence of acid, all films used the same synthesis solution: 0.5 M aniline monomer (freshly distilled), 2.0 M  $\text{CF}_3\text{COOH}$  and 1.0 M  $\text{LiClO}_4$  in propylene carbonate (PC). Water must be excluded rigorously. The film thickness (usually 0.5  $\mu\text{m}$ ) was regulated by the time of reaction, and calculated by assuming that 240  $\text{mC}/\text{cm}^2$  corresponds to a 1  $\mu\text{m}$  film - as for polypyrrole [15]. The value

is only approximate because of the dependence on oxidation and protonation state. The films were thoroughly rinsed after formation in monomer-free solution. The solution contained salt alone or salt plus acid, depending on whether a neutral or acid system was needed.

The rinsed samples deposited on 0.5 mm diameter Pt wires were characterized by cyclic voltammetry at rates down to 0.5 mV/s. The electrolyte solution was 0.5 M LiClO<sub>4</sub> in PC with 0.5 M CF<sub>3</sub>COOH also added in acid systems. Li is used as reference electrode - 2.92 V vs Li is equivalent to 0 V vs *sce*. Other samples were deposited on transparent ITO-glass electrodes, and UV/visible spectra in the range 285-900 nm (4.35-1.38 eV) were recorded as a function of potential in a teflon cell. Because of the many possible processes and changes of morphology with time in PANI, the absorptions at selected wavelengths were also followed in a setup allowing the simultaneous measurement of absorption and cyclic voltammogram [16].

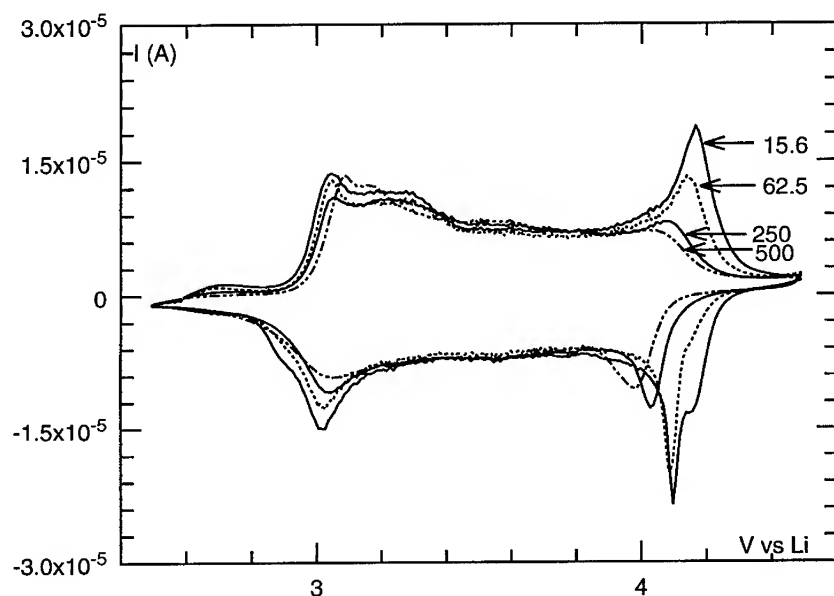


Figure 2. Cyclic voltammograms (5 mV/s) of polyaniline films in 0.5 M LiClO<sub>4</sub> in PC. Current densities during synthesis ( $\mu\text{A}/\text{cm}^2$ ) indicated.

## RESULTS AND DISCUSSION

### Current Density Dependence

Figure 2 shows voltammograms in neutral solution for four films differing only in current density during electrochemical polymerization. For reasons discussed later, the sweep shown is not the first sweep after synthesis, but the traces reached after a few cycles. The results show the same effect earlier observed for polypyrrole: The low current modifications display more, and more sharply defined, capacity peaks, and a higher total capacity. The shapes of, and the



differences between the sweeps are quite reproducible, also with respect to minor features such as the shoulder in the cathodic trace at 4.2 V. This points to a similar important role of low current density in producing a film with a degree of structural order of the chains and the ions.

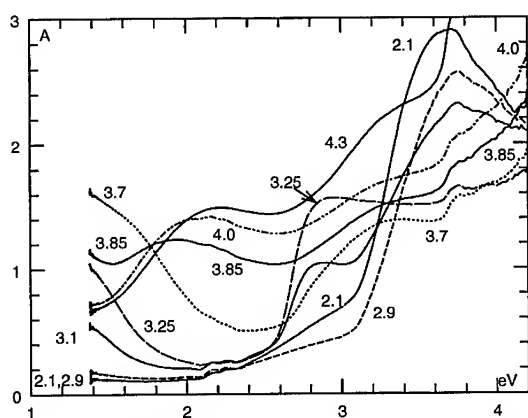


Figure 3. Absorption spectra as a function of oxidation state in neutral solution of an LC PANI film synthesized at  $15.6 \mu\text{A}/\text{cm}^2$ . Potential vs Li marked on curves.

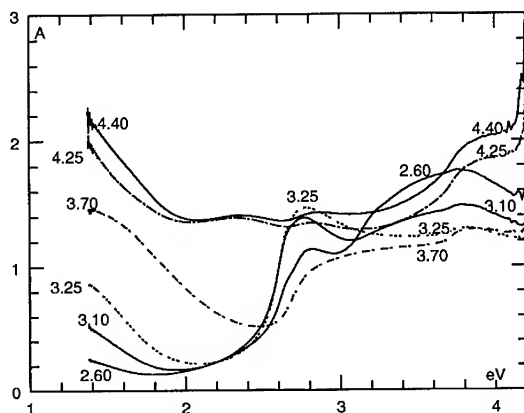


Figure 4. Absorption spectra as a function of oxidation state in neutral solution of an HC PANI film synthesized at  $250 \mu\text{A}/\text{cm}^2$ . Potential vs Li marked on curves.

The absorption spectra of two types of films can be compared in figures 3 and 4, and display significant differences: The low current density (LC) form has a much cleaner spectrum in the fully reduced, leucoemeraldine form (below  $\sim 3$  V vs Li). The spectrum has only one strong absorption at 3.7 eV (335 nm). The peak is assigned to the  $\pi$ - $\pi^*$  transition ( $\sim$ band gap) and is expected to have a lower value for systems with a high degree of conjugation. A recent

systematic study of the optical properties of PANI [17] obtained 3.94 eV for the transition in aqueous solution, others have measured a value of 4.07 eV [18]. The lower energy observed for the LC sample indicates a higher conjugation length. This conclusion is strengthened by the fact that films polymerized at intermediate current densities ( $64 \mu\text{A}/\text{cm}^2$  - spectrum not shown) has the peak at 3.9 eV corresponding to less effective conjugation. The HC form (figure 4) has an extra absorbance at 2.8 eV, and a very broad  $\pi$ - $\pi^*$  transition. Both the presence of the extra peak and the broadening, which implies a distribution of band gap energies, point to a less well-defined structure of the HC modification. On further oxidation, there is a gradual decrease in  $\pi$ - $\pi^*$  intensity, while two new peaks at  $\sim 1.4$  and 2.9 eV grow. These are associated with polaron bands in the emeraldine oxidation state, and the 2.9 eV peak has its maximum at 3.25 V vs Li before being displaced towards higher energies and lower intensity. In the fully oxidized, pernigraniline state, the lowest absorbance is shifted to 2.2 eV, while a strong peak above the 4.2 eV limit grows. The observations are in agreement with the energy level diagram given by Huang and MacDiarmid in reference 17, but the non-aqueous solution in this work makes it possible to reach higher oxidation potentials.

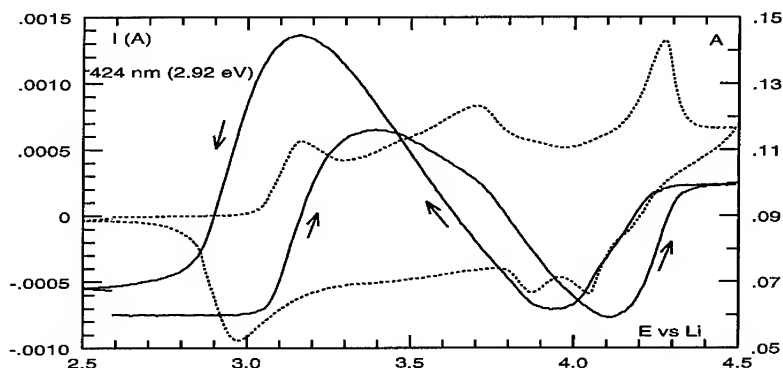


Figure 5. LC PANI film in neutral solution. Current (dashed) and absorbance of 2.92 band (full line - arrows indicate increasing or decreasing voltage) vs potential.

In order to follow the changes in absorbance more closely, simultaneous cyclic voltammograms and absorbances of the prominent peaks were obtained. Figure 5 shows the results for the 2.9 eV band of the LC form in neutral solution. The peaks in the cyclic voltammogram are broader than those of figure 1, probably because of the difficulty of achieving a homogeneous reaction over the full area in the optical cell of several  $\text{cm}^2$ . There is at least one extra peak present at 3.7 V vs Li. This complexity is reflected in the change of absorbance: The 2.9 eV band increases with the first current peak at (maximum at 3.15 V), and decreases after it. The rate of decrease changes as the middle peak is passed. The absorbance at this frequency then increases again at the last oxidation peak at 4.3 V. The close correlation between the two types of experiment underscores the usefulness of the simultaneous measurement. The absorbance is interpreted as involving two separate transition processes - each associated with one of the two main redox pairs.

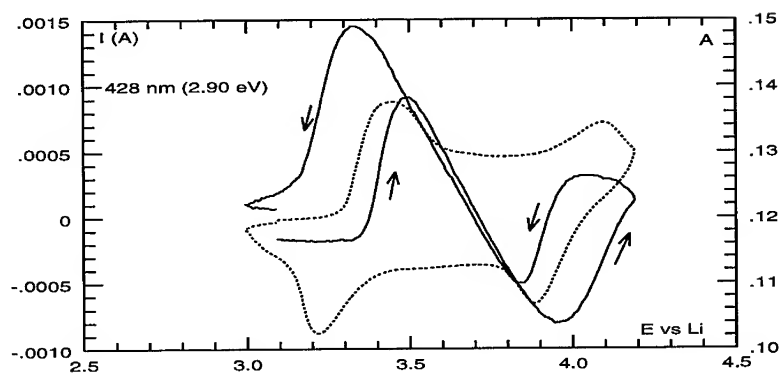


Figure 6. LC PANI film in acid solution: 0.5 M  $\text{CF}_3\text{COOH}$  + 0.5 M  $\text{LiClO}_4$  in PC. Current (dashed) and absorbance of 2.90 eV band (full line) vs potential.

#### Acidity Dependence

The simultaneous measurement of the 2.9 eV absorbance and the cyclic voltammogram is shown in figure 6 for a low current density film, but cycled with  $\text{CF}_3\text{COOH}$  also added to the solution. The main difference is the contraction of the voltage range of electrochemical activity from about 1.4 to 0.9 V. This is caused about equally by the displacement of the first oxidation peak towards higher potentials, and the second towards lower. This first shift can be explained by the imine nitrogens of emeraldine being much weaker bases than the amine nitrogens of leucoemeraldine. The acidic form of emeraldine is therefore relatively less stable and requires stronger oxidation. In aqueous systems, the first peak is shifted in the same direction as in this work, but the second peak is reported to move towards higher potentials in acid [12], in contrast to our results. The acidic voltammogram is less complex and consists of only the two main redox pairs.

#### Time and Potential Dependent Effects.

It is known that the electrochemical properties of conducting polymers depend on its redox history [19]. Figure 7 shows the pronounced difference between the first and second voltage cycles observed for galvanostatically synthesized PANI. Both oxidation peaks show differences that are reproducible between samples. The change in the second peak is especially marked: The amplitude of the first sweep being much larger than that of the second. In order to investigate the influence of oxidation potential on this effect, a sample was cycled to chosen potentials in the midrange before passing the second peak at 4.2 V. Figure 8 shows that the change in the first redox pair at 3.1 and 3.4 V is induced already by the first oxidation to only 3.6 V. The amplitude of the second redox pair at 4.2 V is, however unchanged by the two first oxidations, and retains its large value typical of a "first" cycle until after third cycle to 4.4 V. The change

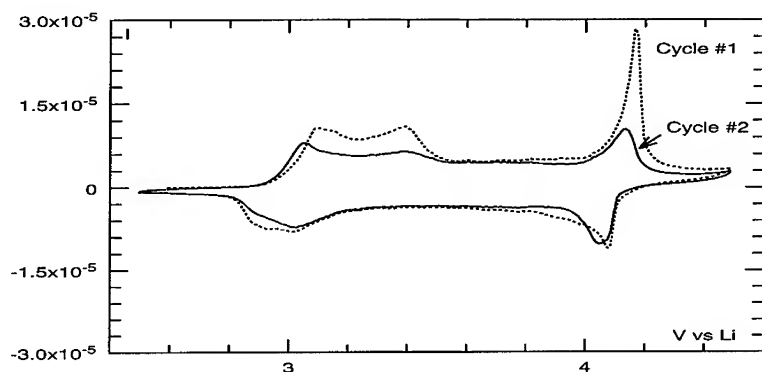


Figure 7. Comparison of first and second cycles (2.5-4.4 V vs Li) of a PANI film polymerized at  $500 \mu\text{A}/\text{cm}^2$ .

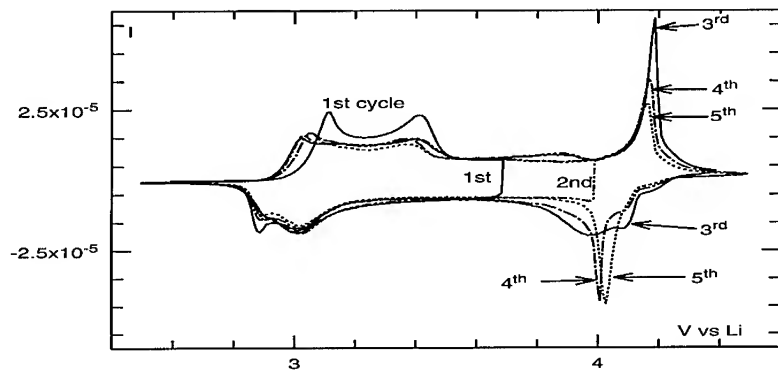


Figure 8. PANI film cycled to two lower voltages in the first and second cycles before a full cycle (to 4.4 V vs Li) in the third and later cycles.

is apparently caused either by passing the capacity peak or by the absolute value of the maximum potential.

Figure 9 shows an attempt to distinguish between these two possibilities: A film has been cycled to 4.20 V, which is right after the position of the narrow peak. The results show that the strong, narrow peak shape is retained even though the corresponding redox process is almost finished at this potential. The change in the material seems to be caused by being oxidized to a high potential rather than being caused directly by the second redox process.

The changes observed on oxidation may be related to chemical processes, or to morphological changes caused by chain coiling [20], perhaps effected by interchain hydrogen bonds [21].

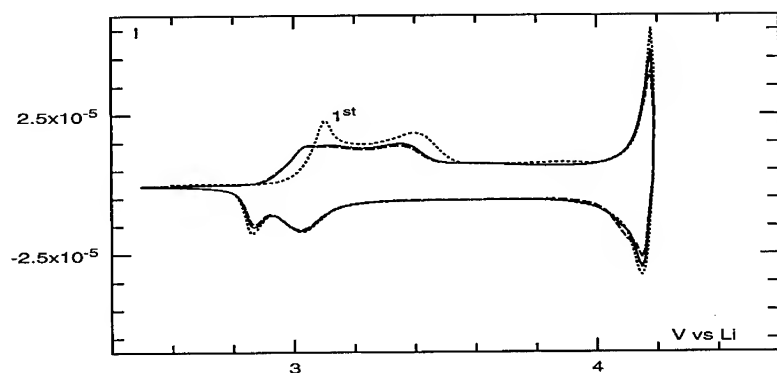


Figure 9. PANI film cycled repeatedly to just after the second redox process: 4.20 V vs Li.

## CONCLUSION

The most important result is that the galvanostatic polymerization of polyaniline at low current densities (down to  $16 \mu\text{A}/\text{cm}^2$ ) produces films (LC form) which have a more regular structure, and which can incorporate counterions at more well-defined sites. The low value of the  $\pi$ - $\pi^*$  transition (3.7 eV vs literature values of 3.9-4.1 eV) points to a higher degree of conjugation for the low current density modification. The cleaner spectrum of the reduced LC form could also be of interest in the application as color-changing electrochromic films. These conclusions are similar to those found for the polypyrrole system. The experimental methods used cannot distinguish between the effects of better chemical perfection and more regular physical packing of chains. The different types of PANI produced by varying the current density during synthesis reflect the complexity of the material and is similar to the earlier described difference between two classes of emeraldine, depending on the method of preparation [22,23]. The goal is that the well-defined LC polymer can function as a reference material in the investigation of the influence of solvent, counterions and cycling conditions.

The detailed shapes and positions of the peaks in cyclic voltammograms can be used to follow the changes in morphology induced by time or electrochemical history.

## ACKNOWLEDGEMENTS

L.M.W.K. Gunaratne thanks the International Program in the Physical Sciences, Uppsala, Sweden for a fellowship to visit the Technical University of Denmark.

## REFERENCES

1. T. Ito, H. Shirakawa and S. Ikeda, *J. Polym. Science* **12**, 11 (1974).
2. P.J. Nigrey, A.G. MacDiarmid and A.J. Heeger, *J. Chem. Soc., Chem. Comm.* **1979**, 594.
3. G. Gustafsson, I. Lundström, B. Liedberg, C.R. Wu, O. Inganäs and O. Wennerström, *Synth. Met.* **31**, 163 (1989).
4. D. Naegle and R. Bittihn, *Solid State Ionics* **28-30**, 983 (1988).
5. P.J.S. Foot and R. Simon, *J. Phys. D: Appl. Phys.* **22**, 1598 (1989).
6. M. Aldissi, *J. Mater. Educ.* **9**, 333 (1987).
7. S. Skaarup, M. Careem and K. West, in *Solid State Ionics - Materials and Applications*, edited by B.V.R. Chowdari, S. Chandra, Shri Singh and P.C. Srivasta (World Scientific, Singapore, 1992) p. 219.
8. K. West, T. Jacobsen, B. Zachau-Christiansen, M. A. Careem and S. Skaarup, *Synth. Met.* **55-57**, 1412 (1993).
9. S. Skaarup, K. West, B. Zachau-Christiansen and M.A. Careem, in *Solid State Ionics III*, edited by G.-A. Nazri, J.-M. Tarascon and M. Armand (*Mater. Res. Soc. Proc.* **293**, Pittsburgh PA, 1993) pp. 141-152.
10. P. Dyreklev *et al* (to be published).
11. S. Skaarup, K. West, B. Zachau-Christiansen, M.A. Careem and G.K.R. Senadeera, *Solid State Ionics* **72**, 108 (1994).
12. E.M. Geniés, A. Boyle, M. Lapkowski and C. Tsintavis, *Synth. Met.* **36**, 139 (1990).
13. E.M. Geniés and M. Lapkowski, *J. Electroanal. Chem.* **220**, 67 (1987).
14. W.R. Salaneck, I. Lundstrom, W.S. Huang and A.G. MacDiarmid, *Synth. Met.* **13**, 291 (1986).
15. A.F. Diaz and J.I. Castillo, *J. Chem. Soc., Chem. Comm.* **1980**, 397.
16. S. Skaarup, L.M.W.K. Gunaratne, K. West and B. Zachau-Christiansen, in *Solid State Ionic Materials*, edited by B.V.R. Chowdari, M. Yahaya, I.A. Talib and M.M. Salleh (World Scientific, Singapore, 1994) p. 439.
17. W.S. Huang and A.G. MacDiarmid, *Polymer* **34**, 1833 (1993).
18. T. Kobayashi, H. Yoneyama and H. Tamura, *J. Electroanal. Chem.* **177**, 281 (1984).
19. C. Odin and M. Nechtschein, *Synth. Met.* **55-57**, 1281 (1993).
20. E.E. Havinga, M.M. Bouman, E.W. Meijer, A. Pomp and M.M.J. Simenon, *Synth. Met.* **66**, 93 (1994).
21. P.H. Colomban, A. Gruger, A. Novak and A. Régis, *J. Mol. Struct.* **317**, 261 (1994).
22. M.E. Jozefowicz, A.J. Epstein and X. Tang, *Synth. Met.* **46**, 337 (1992).
23. J.P. Pouget, M. Laridjani, M.E. Jozefowicz, A.J. Epstein, E.M. Scherr and A.G. MacDiarmid, *Synth. Met.* **51**, 95 (1992).

# INTERLAYER INTERACTIONS IN SELF-ASSEMBLED POLY(PHENYLENE VINYLENE) MULTILAYER HETEROSTRUCTURES, IMPLICATIONS FOR LIGHT-EMITTING AND PHOTORECTIFYING DIODES

A.C. FOU, O. ONITSUKA, M. FERREIRA, AND M.F. RUBNER  
Massachusetts Institute of Technology, Bldg. 13-5016, Cambridge, MA 02139.

B.R. HSIEH  
Xerox Corporation, Webster Research Center, Webster, NY 14580.

## ABSTRACT

Layer-by-layer molecular self-assembly has been used to fabricate multilayer heterostructures containing poly(phenylene vinylene) (PPV) and a variety of polyanions. These ultrathin films exhibit widely different photoluminescence intensities and peak positions (emission color) depending on the polyanion used. The characteristics of light-emitting devices based on such films are described. This represents the first demonstration of working organic light-emitting diodes, the active layer of which consists of ultrathin, self-assembled films of between 130 - 500 Å.

## INTRODUCTION

Thin films of organic materials have been studied extensively for their potential as the active components of devices such as light-emitting diodes. Of the polymeric class of visible light emitters, none has been more widely studied than poly(phenylene vinylene) and its derivatives [e.g. 1-3]. Improvements in the material itself and in device parameters have led to respectable device characteristics such as lifetime, light output, and efficiency. In this paper, we present the first successful light-emitting devices based on ultrathin multilayer heterostructures of PPV fabricated via layer-by-layer molecular self-assembly.

Layer-by-layer molecular self-assembly is a unique process whereby single layers of polymers can be deposited in a highly controlled manner onto the surface of a substrate. Our previous work has shown that self-assembly can be used to manipulate a wide variety of conjugated and non-conjugated polyions into multilayer thin films with molecular-level control [4-5]. This is done simply by dipping a substrate alternately into a solution containing a polyanion and another containing a polycation. Each layer is attracted to the surface by electrostatic interactions; some of the charges are bound to the previous layer while the rest are left "dangling," ready to attract the next layer of the oppositely charged polyion. As long as the alternating sequence between polycations and polyanions is continued, any number of components can be self-assembled into a complex, multilayer heterostructure. By providing molecular-level control over single layers of material, self-assembly uniquely provides the ability to design and fabricate supermolecular architectures not easily achievable by traditional thin film processing methods such as spin-coating, Langmuir Blodgett thin film transfer, electrochemical deposition, or vacuum deposition. As will be seen, the quality of the self-assembled films and the versatility of the process significantly improve the variety of useful organic thin film devices that can be fabricated.

## EXPERIMENTAL PROCEDURE

Thin film heterostructures of PPV and various polyanions were fabricated via molecular self-assembly using the following solutions. The PPV sulfonium precursor (PPV-p) solution was used as provided by Dr. Bing R. Hsieh [3]. The pH was measured to be 2.5. The solution of polyethyleneimine (PEI) was 0.1 vol% in water, diluted from the original 30 vol% solution from

Polysciences by adding ultrapure Millipore water; the resultant pH was 6.5. The solutions of 0.1 M polymethacrylic acid (PMA) and 0.1 M poly(styrene-4-sulfonate) (SPS) were prepared by dissolving the powder (99% Aldrich) in Millipore water and adjusting the pH to 4.5 by adding a few drops of hydrochloric acid. Sodium chloride is optionally added for ionic strength adjustment. It is generally known that increasing the ionic strength of the solution results in thicker layers being deposited. The solutions of other polyanions were 0.001 M poly(thiophene-3-acetic acid) (PTAA), 0.001 M sulfonated polyaniline (SPAN), 0.001 M poly(N,N'-bis(p,p'-oxydiphenylene)pyromellitimide) (PMDA-ODA), or 0.001 M sulfonated fullerenes (S-C<sub>60</sub>) [6]. The reported concentrations for all of the above polyions are based on the molecular weight of the repeat unit containing one charged functional group.

The fabrication of simple two-component (binary) multilayer films via molecular self-assembly begins by pretreating cleaned microscope slides in the PEI solution for 15 minutes. The layer of PEI promotes the adhesion of the film to the substrate. Then the substrate is immersed in the solution of a polyanion (designated as the "counterpolymer") for 10 minutes, rinsed in a stream of Millipore water, and dried in a stream of filtered, compressed air. The substrate is then dipped into the solution containing the positively charged sulfonium precursor of PPV for 10 minutes, rinsed, and dried. This sequence of alternating dips into the polyanion and the PPV-p is repeated until the desired number of bilayers (pair of polyanion and PPV-p layers) are built up. The sample is then dried overnight with fresh desiccant in a nitrogen atmosphere and then dried overnight under dynamic vacuum (100 mTorr). The subsequent thermal conversion of the PPV-p to the conjugated, light-emitting form of PPV involves heating the samples from room temperature to 180°C over a 4 hour period, holding the temperature at 180°C for 4 hours, and then allowing them to cool back down to room temperature over another 4 hour period, all under dynamic vacuum. Longer conversion times were found to result in lower photoluminescence intensities. The photoluminescence spectra were measured with a SPEX 312 scanning spectrophotometer using an excitation wavelength of 360 nm.

The fabrication of LEDs based on self-assembled films of PPV is as follows [7]. A substrate patterned with lines of ITO (2 mm width, 1500 - 2000 Å thick) is immersed in the PEI solution for 15 minutes and then in the SPS or PMA solution for 10 minutes. Then self-assembly of the PPV-p with either SPS or PMA is commenced. Samples containing between 10 - 50 bilayers of PPV/SPS or PPV/PMA were built up, dried, and thermally converted as above. Aluminum top electrodes of around 1500 Å were thermally evaporated onto the sample through a mask to give 2 mm wide lines perpendicular to the ITO lines. The intersections of the aluminum lines and the ITO lines defined the active device areas of 2 mm x 2 mm each. Gold wire leads were attached with silver paste to the ends of the ITO lines and aluminum lines away from the active device areas; each "pixel" could then be individually addressed by connecting the appropriate leads. The samples were transferred into a nitrogen glove box, with as little exposure to air as possible. Current-voltage characteristics were measured simultaneously with emission intensity measurements using a Hewlett-Packard variable voltage source with digital multimeter and a calibrated silicon photodiode. No corrections were made for the losses due to absorption, reflections, or waveguiding effects of the ITO and glass substrate. Electroluminescence spectra were measured in air with an Oriel Instaspec 250 multichannel analyzer.

## RESULTS AND DISCUSSION

Figure 1 below shows that the layer-by-layer self-assembly of the PPV precursor (PPV-p) and a variety of polyanions results in a linear deposition characteristic; that is, with each dip, a reproducible amount of PPV was deposited. The linear deposition was traced out by plotting the absorbance of the film after each dip of the conjugated polyanion. The remarkable consistency in deposition even among many samples is a hallmark of the self-assembly technique. The different slopes seen in the figure are due to the different deposition characteristics of PPV-p with a particular polyanion; the larger the slope, the larger the amount deposited per dip. It is clear that PPV-p can be self-assembled in a highly controlled manner with a wide variety of polyanions.



Figure 2 shows the UV-visible absorbance of several binary PPV/polyanion systems. The spectra are offset for clarity. The important feature to note is that despite the widely different polyanions incorporated into the film, the chemical form of the PPV after thermal conversion is very nearly the same. The differences in the positions of the maxima in the absorption spectra shown ( $< 20$  nm) are attributed to the inherent variability in the thermal conversion process. As will become apparent later, the small differences in the form of the PPV cannot account for the significant differences in the photoluminescence spectra of the various PPV systems. In the majority of the cases, the absorption spectra are identical among the samples used in "side-by-side" comparisons. This indicates that there are no ground state interactions between the PPV and the polyanion present in the multilayer heterostructure film, that the PPV is of the same conjugation length and chemical form, and that the differences in the photoluminescence are due to some type of excited state interactions.

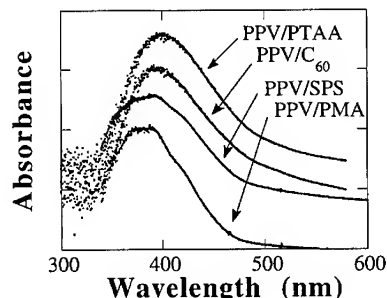
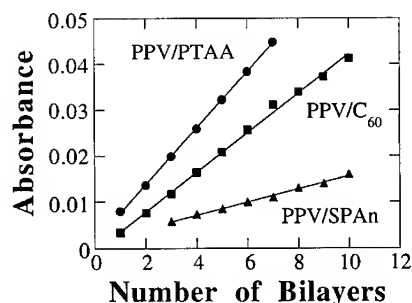


**Figure 1:** Linear Deposition of PPV/polyanion Via Layer-by-Layer Molecular Self-Assembly

**Figure 2:** Absorbance of Various PPV Self-Assembled Films (spectra offset for clarity)

From the photoluminescence spectra of the simple two-component films, it was found that the intensity, shape, and position of the photoluminescence emission peaks of PPV depend strongly on the identity of the complementary polyanion. It is thought that the intermolecular interactions between the PPV and the polyanion in adjacent layers give rise to these phenomena. For example, as shown in Figure 3, a binary heterostructure of PPV and PMA exhibits intense blue-green light after thermal conversion while a PPV/SPS system emits a much weaker orange light. In other binary systems of PPV and conjugated polyanions such as PTAA, C<sub>60</sub>, SPAn, or PMDA-ODA, the luminescence is essentially completely quenched. In some cases like C<sub>60</sub>, which is known to be a strong electron acceptor, this quenching effect is thought to be due to a photoinduced charge transfer from the excited PPV to the polyanion, followed by nonradiative decay in the polyanion. This suggests that the fluorescence of the PPV may be further tuned by modification of the counterpolymers by functionalization with electron-withdrawing or electron-donating groups. By subjecting the samples to identical drying and thermal histories, the inherent variability in the thermal conversion process was avoided; the absorbance and therefore the chemical form and conjugation length of the PPV are the same among the samples used in the "side-by-side" comparisons. The variation in the photoluminescence must then be due to some excited state interaction, the nature and extent of which depends on the identity of the counterpolymer assembled with the PPV. Figure 4 shows that there may even be variability in the photoluminescence of a single binary system such as PPV/SPS; the intensities of the photoluminescence have been normalized to show that the peak positions for the two different PPV/SPS systems can shift by as much as 100 nm. The photoluminescence spectrum of pure PPV

deposited by the spin-coating technique was also included in the figure for comparison. A complete understanding of the intermolecular interactions in these self-assembled, multilayer heterostructure films will make it possible to deliberately tailor the color and intensity of the photoluminescence of PPV by designing and fabricating complex supermolecular architectures via self-assembly.

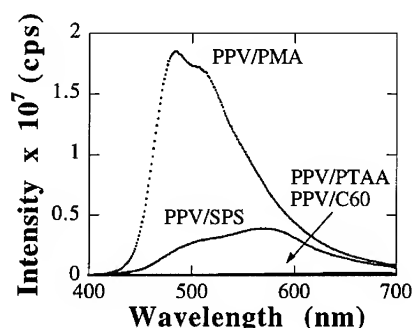


**Figure 3:** PPV Photoluminescence of Binary PPV/polyanion Heterostructures

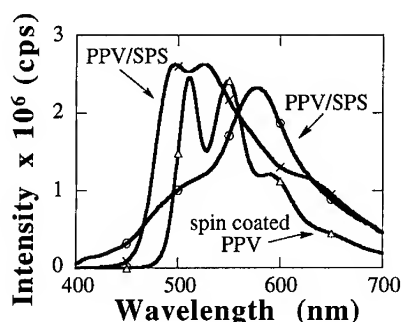


**Figure 4:** Normalized Photoluminescence of Two Types of PPV/SPS and spin coated PPV

In the quenched systems, the luminescence intensity can be deliberately re-established by separating the PPV layers from the quenching polyanion layers; this is done by inserting a few inert "spacer" layers between the PPV and the quenching agent. These layers mediate and eliminate the quenching interactions between the PPV and the counterpolymer. When the PPV is fully isolated from the quenching agent, the resulting photoluminescence intensity corresponds to that of a binary PPV film of similar thickness containing no quenching agents. This is particularly significant since it clearly indicates that the layered structure of the PPV and polyanion multilayer film is preserved even after the thermal treatment for the conversion of the PPV. The insertion of 3 - 5 "spacer" bilayers (depending on the binary system) will result in a heterostructure film with a completely un-quenched photoluminescence intensity. There is also evidence in the binary PPV/polyanion systems that there is some degree of self-quenching between PPV layers. This is borne out by the fact that when inert spacer layers are inserted between each PPV/polyanion bilayer, the photoluminescence intensity increases incrementally. Further, self-assembled PPV films of around 100 Å have been shown to give equal or greater photoluminescence intensity than much thicker spin-coated films of between 1000 - 2000 Å; this suggests that the isolation of PPV into individual layers leads to less self-quenching and brighter photoluminescence. Although further study is needed to determine the exact amount of interpenetration between layers, it is clear from the photoluminescence studies that the layered structure is preserved to some degree. Lastly, the heterostructures built in this "un-quenching" study typically consisted of three or more different components. These multilayer, multicomponent heterostructures are typically difficult to fabricate using traditional thin film processing techniques. Layer-by-layer molecular self-assembly, on the other hand, has uniquely provided the means to manipulate individual layers of a wide variety of polymers into complex, multicomponent films, making this study possible.

Light-emitting devices based on the simple binary heterostructures of PPV/PMA and PPV/SPS were fabricated and characterized. It is remarkable to note that films as thin as 130 Å could be successfully used as the active layers of the LEDs. Although pinholes and defects have plagued other traditional thin film processing techniques in the fabrication of ultrathin films for devices, they are not problematic for the devices discussed here, even with the thinnest self-

assembled films. Figure 5 shows the current and light versus voltage plot of a 390 Å film of PPV/PMA. The I-V characteristic is neither ohmic nor traditionally rectifying; rather it is symmetric, with an exponential rise in current at virtually the same voltage in both the forward and reverse bias regimes. Additionally, the light emission intensity is also symmetrical. The color, intensity, and stability of the light emission in reverse bias are essentially the same as that in forward bias, suggesting that AC operation may also be possible. Although it is not completely clear at this point, the symmetric nature of the current and light versus voltage characteristics is thought to be due to phenomena related to the extremely small thicknesses of the films studied. Indeed, more traditionally rectifying (Schottky-type) current versus voltage plots have been widely published for PPV LEDs [e.g. 1-3]; but those curves are based on much thicker spin-coated films. We too have reproducibly generated "traditional" I-V and light versus voltage curves with spin-coated PPV devices as shown in Figure 6. The light intensity typically maps out with the current; that is, the light intensity rises exponentially as the current rises exponentially. The voltage at the beginning of the exponential rise in current and light is designated as the "turn-on" voltage since it corresponds to the point at which the unaided eye can first see visible light emission in a darkened room.

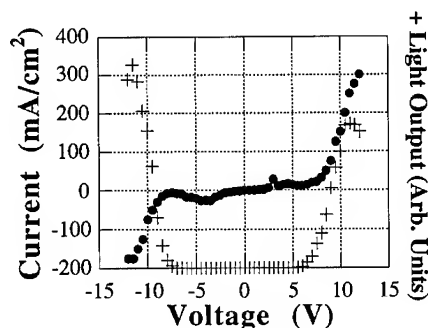


**Figure 5:** Current and Light versus Voltage  
(390 Å Self-Assembled PPV/PMA Film)

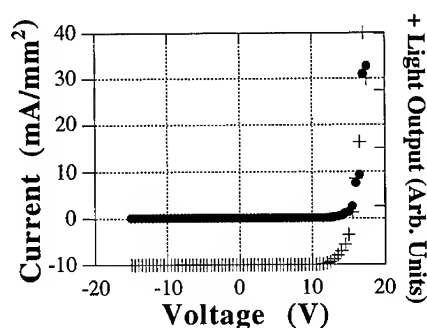


**Figure 6:** Current and Light versus Voltage  
(940 Å Spin Coated PPV Film)

Molecular self-assembly makes it possible to study another aspect of the device characteristics, the variation of the turn-on voltage with the thickness of the active layer film. The precise control over single layers and thicknesses afforded by self-assembly makes it possible to vary the thickness of these active layer films on the order of angstroms. Previous work by Parker [8] has elegantly demonstrated that the external turn-on voltages vary directly with the thickness of the film. This implies that there exists a singular electric field at which the exponential rise in current will occur; the value of this field is determined by the band-offsets at the cathode and anode. The smaller offset determines the identity of the majority carrier in the film and the magnitude of the larger offset determines the efficiency of the device. A tunneling mechanism based on the assumption of a band model is proposed [8]. The preliminary observations on the self-assembled films are consistent with the above model. According to this model, devices based on the same cathode and anode materials (in this case aluminum and ITO, respectively) will exhibit a singular turn-on field but different turn-on voltages depending on the thickness of the active layer.

Finally, the self-assembled PPV devices exhibited respectable lifetimes of over 100 hours, in some cases, under constant voltage operation in a nitrogen atmosphere. The devices were held at 0.5 V above the turn-on voltage, with light emission clearly visible to the unaided eye in a

darkened room. The electroluminescence color was chalky green to the eye, corresponding to a broad peak centered at 530 nm. There are two possible mechanisms by which burn-out typically occurred. The first is labeled "punch-through," in which the current is observed to jump rapidly with a corresponding drop in light intensity. It is likely that short circuit channels are formed through the ultrathin film, perhaps by the electromigration of aluminum under the influence of the large fields (typically 1 - 5 MV/cm). The second possible breakdown mechanism occurs when the aluminum electrodes spark and vaporize at high voltages (high fields), with the sudden loss of current. The use of thicker aluminum electrodes (around 1500 Å) has virtually eliminated the instances of this burn-out mechanism. As pointed out earlier, it is remarkable that these ultrathin films of as little as 130 Å can be used for hours under constant DC operation at such enormous fields. The quality of the self-assembled films makes this possible. The ability of self-assembly to deposit high quality ultrathin films onto substrates of various sizes, geometries, and surface chemistries will likely allow the fabrication of large-area, light-emitting devices on a variety of substrates, a feat not easily achieved by conventional thin film processing techniques. Further studies are underway to improve the efficiency, light intensity, and stability of these devices. More complex heterostructure devices containing carrier injection and transport layers are being investigated towards this end.

## CONCLUSION

We have shown that molecular self-assembly uniquely provides the ability to design and fabricate complex multilayer heterostructures. The interlayer interactions achievable in self-assembled, multicomponent heterostructures can be exploited to tune the color and intensity of the photoluminescence of PPV. Further, the molecular level control over single layers of material afforded by self-assembly has allowed us to build working light-emitting devices from extremely thin films of as little as 130 Å and thus access a thickness regime never before accessible by conventional thin film processing techniques. Layer-by-layer molecular self-assembly is a versatile and powerful technique that greatly expands the horizons of possibility in the arena of organic thin film devices.

## ACKNOWLEDGMENTS

The authors wish to acknowledge the contributions of Michael J. Whitney and Douglas W. Howie to the photoluminescence studies. Partial support for this work was provided by the National Science Foundation, TDK Corporation, and the Center of Materials Science and Engineering at MIT.

## REFERENCES

1. J.H. Burroughes, D.D.C. Bradley, A.R. Brown, R.N. Marks, K. Mackey, R. H. Friend, P.L. Burn, and A.B. Holmes, *Nature*, **347**, p. 539, (1990).
2. D. Braun and A.J. Heeger, *Appl. Phys. Lett.*, **58**, p. 1982, (1991).
3. B.R. Hsieh, H. Antoniadis, M.A. Abkowitz, and M. Stolka, *Polymer Preprints*, **33** (2), p. 414, (1992), and references therein.
4. M. Ferreira, J.H. Cheung, M.F. Rubner, *Thin Solid Films*, **244**, p.806, (1994).
5. J.H. Cheung, A.C. Fou, M.F. Rubner., *Thin Solid Films*, **224**, p.985, (1994); and *Polymer Preprints*, **34** (2), (1993).
6. M. Ferreira, M.F. Rubner, B.R. Hsieh, *MRS Proceedings, Symposium Q*, **328**, p.119, (1994) and references therein.
7. A.C. Fou, O. Onitsuka, M.F. Rubner, B.R. Hsieh, to be published.
8. I.D. Parker, *J. Appl. Phys.*, **75** (3), p. 1656-1666, 1 Feb 1994.

## PREPARATION AND CHARACTERIZATION OF POLYANILINE-PALLADIUM COMPOSITE FILMS

HONGSHI LI, D. R. BAER, M. H. ENGELHARD, J. JANATA AND M. JOSOWICZ

Environmental Molecular Sciences Laboratory  
Pacific Northwest Laboratory\*  
Richland, Washington 99352, U.S.A.

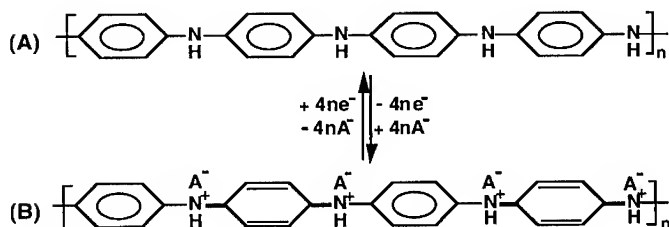
### ABSTRACT

Electrosynthesized polyaniline (PANi) can be chemically functionalized by incorporation of palladium clusters. The functionalization of electrochemically, freshly prepared and dried PANi film occurs spontaneously during the relaxation process. This process is carried out in sulfuric acid containing palladium salt. The material properties of the new composite PANi-Pd film were investigated by applying electrochemical, UV-visible spectroscopic and surface microscopy techniques. The PANi-Pd composite materials behaved electrochemically different than PANi film alone or Pd film deposited electrochemically. This finding is particularly important for developing layers for chemical sensors, electrocatalysis or supercapacitors applications.

### INTRODUCTION

The development of the chemistry of metal clusters and aggregates in conducting polymers has led to interesting applications in the field of chemical gas sensors<sup>1-2</sup> and electrocatalysis<sup>3-4</sup>, owing to the high reactivity and to the specificity that those materials towards various molecules/ systems.

It is known that the general formula of PANi is based on an alternate structure of *p*-phenylene-imine-*p*-phenylene-amine. The redox state of the polymer can be rearranged chemically or electrochemically from that of the fully reduced leucoemeraldine (LM, yellow), through that of the half-oxidized emeraldine (EM, green), to that of the fully oxidized pernigraniline (PNA, blue). Such structural transition is accompanied by electron transfer and a protonation/ deprotonation process. Therefore, the polymer matrix offers a possibility for reducing metal ions which diffuse from the surrounding salt containing electrolyte into the PANi film. In this paper we describe the non-polarized method which is called chemical relaxation process for preparing PANi-Pd composite materials. The obtained results can be interpreted by the change of the redox state of the  $\text{Pd}^{2+}$  to  $\text{Pd}^0$  inside the reduced PANi film which in turn becomes oxidized.



Scheme 1 Schematic illustration of structure transition in PANi chains:  
(A) fully reduced yellow film, (B) conducting green film.

\* Pacific Northwest Laboratory is a multiprogram national laboratory operated by Battelle Memorial Institute for the U.S. Department of Energy under Contract No. DE-AC06-76RLO#1830.

## EXPERIMENTAL SECTION

The incorporation of Pd species into a PANi film by relaxation process has been detailed in our previous publication<sup>5</sup>. The UV-visible absorption spectra were recorded on a Varian Cary 5 spectrometer and the spectra were acquired with an IBM/AT 286 computer. The atomic force microscopy experiments were performed with a Digital Instruments Nanoscope II AFM, Nano-probe cantilevers (integral Si<sub>3</sub>N<sub>4</sub> tips, 100- $\mu$ m legs, 0.58N/m spring constant), and the "D" piezoelectric scan head (14696-nm x-y range) have been used.

## RESULTS AND DISCUSSION

It is known that the redox state of PANi can be easily controlled by the potential sweep technique during electrosynthesis. The electropolymerization is stopped in this work at -0.1 V, at which the polymer corresponds to a fully reduced state. A relaxation process will occur when such dry, freshly prepared PANi film is immersed in H<sub>2</sub>SO<sub>4</sub> which was also used as the background electrolyte during the PANi electrosynthesis. Due to the presence of sulfuric acid changes in the redistribution of  $\pi$ - $\pi^*$  electrons and protonation doping within the imine and amine groups occur within the polymer chains. Figure 1 illustrates changes in the UV-vis absorption spectra of a freshly prepared PANi film upon immersion in 1.0-M H<sub>2</sub>SO<sub>4</sub> solution as a function relaxation time. A significant change between dry and wet film has been first observed. Only one dominant absorption band near 320 nm (4.0 eV) can be seen in a dry condition which corresponds to  $\pi$ - $\pi^*$  transition (curve *a*), indicating that the PANi film stays in an isolated state (yellow, reduced). Immersion of the dry film in 1.0-M H<sub>2</sub>SO<sub>4</sub> solution introduces immediately an appearance of two absorption bands near 420 nm (3.0 eV) and 800 nm (1.5 eV) (curve *b*). Finally, these two absorption bands become really important and definitive after 180 minutes (curve *e*). That is reflected in the presence of two absorption bands near 420 and 800 nm which are assigned to polarons<sup>6-8</sup>.

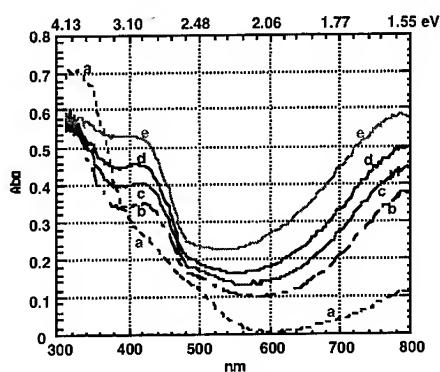


Fig.1 UV-vis absorption spectra of PANi film upon immersion in 1.0M H<sub>2</sub>SO<sub>4</sub>: (a) fresh dry film, (b) in H<sub>2</sub>SO<sub>4</sub> solution for 0min, (c) for 15min, (d) for 60min, (e) for 3h.

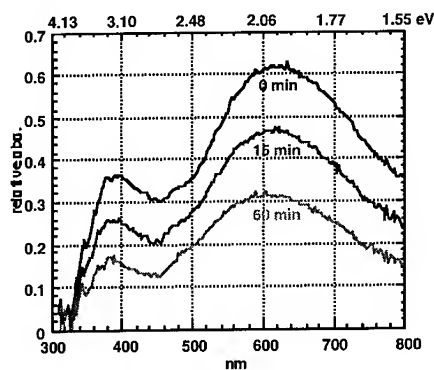


Fig.2 Normalization of UV-vis absorption spectra from Figure 1.  
relative absorption =  $(A_{3h} - A_t) / A_{3h}$ .

A normalization method has been used for treating UV-vis data that is shown in Fig. 2. Two important bands near 390 nm (3.2 eV) and 610 nm (2.0 eV) appear after the treatment. The band at 3.2 eV indicates the separation between the valence band and the antibonding polaron level of the polaronic state<sup>9</sup>. The transition around the 2.0 eV indicates the ongoing protonation doping. At high protonation level this transition disappears<sup>10</sup>. From the protonating doping, formation of semiquinone radical ions results which contributes to the change of the redox state of the PANi from reduced to half-oxidized.

The UV-visible absorption spectra recorded during relaxation process of PANi films in the  $\text{PdSO}_4/\text{H}_2\text{SO}_4$  system behaves the same way as described above for the  $\text{H}_2\text{SO}_4$  solution only. It means, that the relaxation process of PANi film is not influenced by the presence of  $\text{Pd}^{2+}$  ions. The absorption spectra changes of  $\text{PdSO}_4/\text{H}_2\text{SO}_4$  solution with progressing relaxation time have also been recorded (not presented in this paper). The  $\text{PdSO}_4$  salt in  $\text{H}_2\text{SO}_4$  solution exhibits an intensive absorption peak at 230 nm (5.39 eV) and a small broad band near to 395 nm (3.14 eV). If the PANi film is placed in this solution the  $\text{Pd}^{2+}$  peak at 230 nm decreases with relaxation time of the polymer. That indicates a loss of  $\text{Pd}^{2+}$  species in the solution and their incorporation in the PANi matrix.

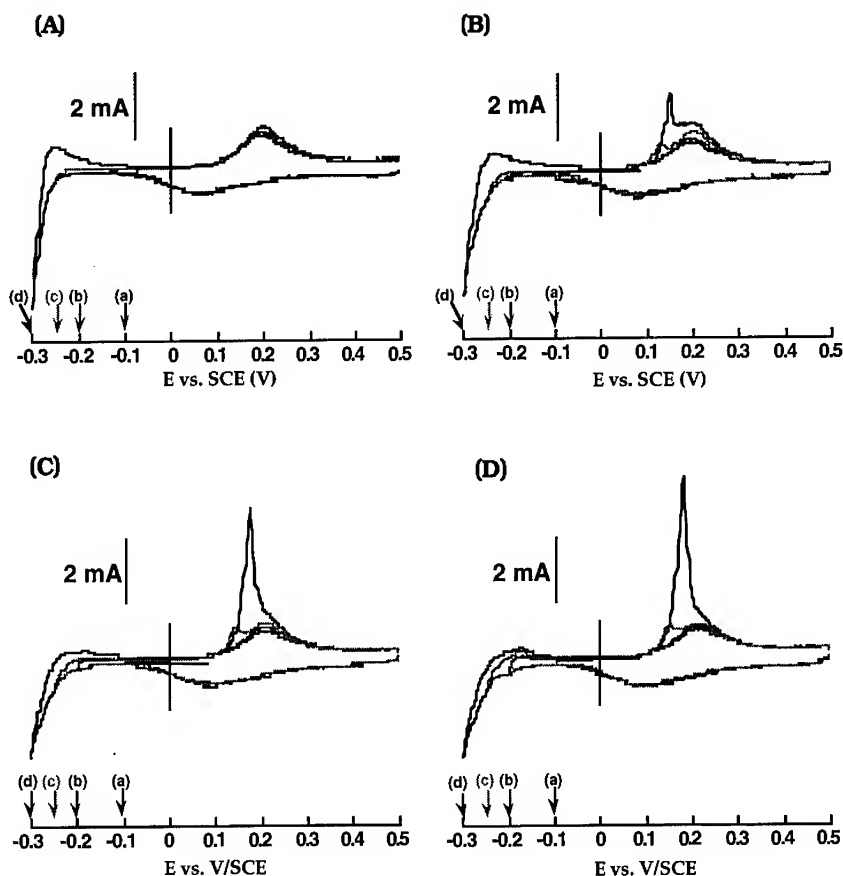


Figure 3. Cyclic voltammograms of PANi and PANi-Pd film recorded in 1.0-M  $\text{H}_2\text{SO}_4$  solution with 50 mV/s scan rate from open cell potential limits to : (a) -0.10, (b) -0.20, (c) -0.25, (d) -0.30 V/SCE.

- (A) PANi film alone,
- (B) PANi-Pd film, carried by relaxing the PANi film for 0.5h,
- (C) PANi-Pd film, carried by relaxing the PANi film for 17h,
- (D) PANi-Pd film, carried by relaxing the PANi film for 65h.

The incorporation of Pd particles in the PANi film can be tested electrochemically in acid solution due to the affinity of proton/hydrogen to Pd clusters. Figure 3 shows the cyclic voltammograms of PANi film alone (Fig. 3A) and after relaxation in  $\text{PdSO}_4/\text{H}_2\text{SO}_4$  solution for different relaxation time period (Fig. 3). In case of PANi film alone, a broad oxidation peak that appears at approximately +0.20 V and a broad reduction peak at +0.10 V represent respectively the normal deprotonation/protonation of the polymer. Extension of the scanning potential to -0.30 V leads to an appearance of a hydrogen evolution current and an irreversible peak at -0.26 V that corresponds to the hydrogen desorption. After a short relaxation in  $\text{PdSO}_4/\text{H}_2\text{SO}_4$  solution (30 min, Fig. 3B), the cyclic voltammogram in cathodic region behaves the same as that in the case of PANi alone. An additional sharp peak at +0.13 V appears during the anodic sweep when cathodic extension is beyond -0.25V. It has been interpreted by a similar peak in that potential region as oxidation of hydrogen which, as produced at negative potentials, has been trapped in the polymer network<sup>11</sup>. Long time relaxation of PANi in Pd solution produces an important growth for this sharp additional peak (17h and 65h, Fig. 3C and D), indicating that the relaxation process and formation of Pd clusters in the bulk are controlled by the diffusion of the Pd species into the PANi film. Furthermore, a couple of redox peaks at -0.2V ( $E_{\text{pc}}$ ) and -0.17V ( $E_{\text{pa}}$ ) are observed which can be interpreted by the result from the reversible adsorption and desorption of hydrogen on Pd particles that have been incorporated into the bulk of PANi film<sup>5</sup>.

Finally, the AFM photomicrographs of PANi film alone and PANi-Pd composite film are shown in Figure 4. The palladium particles of spherical shape are distributed homogeneously on the surface of the polymer film, the average cluster size is approximately 300 nm which can be compared with our TEM results. The metallic state of the palladium nanostructures in the PANi matrix has been determined by XPS photoelectron spectroscopy<sup>5</sup>. Transmission electron microscope (TEM) results (not presented in this paper) confirm a 3D structure of homogeneously distributed clusters in PANi film.

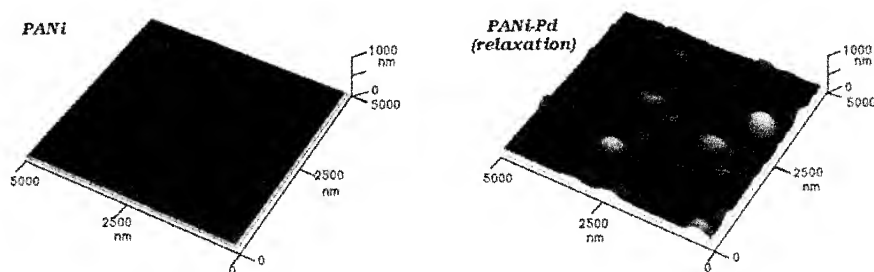


Figure 4. Atomic force microscope images of PANi and PANi-Pd composite film. The PANi-Pd composite film was carried by relaxing the PANi film in 1.0-M  $\text{H}_2\text{SO}_4$  solution containing  $5 \times 10^{-4}$  M  $\text{PdSO}_4$  for 17h.

## CONCLUSIONS

Palladium particles can be incorporated as a 3D array in electrosynthesized PANi film by a chemical relaxation process. Immersion of a freshly prepared and dried PANi film into  $\text{PdSO}_4/\text{H}_2\text{SO}_4$  solution introduces three effects: (1) the protonic doping, (2) the change of redox states of the polymer chains and consequently (3) incorporation of Pd ions from solution into the bulk of the polymer film. The reorganization of the polymer structure offer an opportunity for reducing the diffusing  $\text{Pd}^{2+}$  species into the PANi matrix to  $\text{Pd}^0$  clusters. We have shown that the resulting composite materials behaved electrochemically differently than the PANi film alone or Pd film deposited electrochemically.



## REFERENCES

1. J. Langmaier and J. Janata; *Analytical Chemistry*, 64, 523 (1992).
2. J. Li, D. Petelenz and J. Janata; *Electroanalysis*, 5 (1993) 791.
3. K.M. Kost, D.E. Bartak, B. Kazee and T. Kuwana; *Anal. Chem.*, 60 (1988) 2379.
4. A. Yassar, J. Roncali and F. Garnier, *J. Electroanal. Chem.*, 255 (1988) 53.
5. HongShi Li, M. Josowicz, M. Engelhard, D.R. Baer and J. Janata; *J. Electrochem. Soc.*, (paper accepted for publication).
6. W.W. Focke, G.E. Wnek and Y. Wei; *J. Phys. Chem.*, 91 (1987) 5813.
7. A. Watanabe, K. Mori, Y. Iwasaki, Y. Nakamura and S. Niizuma; *Macromolecules*, 20 (1987) 1793.
8. A.J. Epstein, J.M. Ginder, F. Zuo, R. Bigelow, H.S. Woo, D.B. Tanner, A.F. Richter, W.S. Huang and A.G. MacDiarmid; *Synth. Met.*, 18 (1987) 303.
9. T. Ohsawa, T. Kabata, O. Kimura, K. Yoshino; *Synth. Met.*, 29 (1989) E203.
10. Jiang Yue, Z.H. Wang, K.R. Cromack, A.J. Epstein, A.G. MacDiarmid; *J. Am. Chem. Soc.*, 113 (1991) 2665.
11. A. Leone, W. Marino and B.R. Scharifker; *J. Electrochem. Soc.*, 139 (1992) 438.

## ACKNOWLEDGMENT

The authors wish to thank Dr. Bruckner-Lea Cynthia for AFM analysis and Dr. Larry Thomas for TEM analysis.

## MOLECULAR LAYER PROCESSING OF POLYANILINE VIA THE USE OF HYDROGEN BONDING INTERACTIONS

WILLIAM B. STOCKTON AND MICHAEL F. RUBNER

Department of Materials Science and Engineering  
Massachusetts Institute of Technology, Cambridge, MA 02139.

### ABSTRACT

Molecular layer-by-layer build-up on a variety of substrates is demonstrated for doped polyaniline (PAn) alternating with non-ionic water soluble polymers. The adsorption is enabled by the strong interchain interactions with PAn, such as hydrogen bonding. Multilayer build-up has been demonstrated with four distinctly different non-ionic water soluble polymers: poly(vinyl pyrrolidone) (PVP), poly(vinyl alcohol) (PVA), poly(acrylamide) (PAAm), and poly(ethylene oxide) (PEO). Thus, non-ionic water soluble polymers containing a wide variety of functional groups such as amide, hydroxyl or ether groups can be used to successfully fabricate multilayer thin films with polyaniline. FTIR spectroscopy measurements show the PAn to be hydrogen bonded in these multilayer films. Conductivities for multilayer films are on the order of 1-4 S/cm for films doped with methane sulfonic acid. Conductivities on the order of 0.1 S/cm can be achieved for a *single* mixed layer self-assembled from a mixed solution of PAn/PVP or PAn/PAAm.

Understanding the structure of such systems and the mechanism of adsorption is important for controllably manipulating the films on the molecular level. Processing parameters considered include solution concentrations, pH conditions, ionic strength, and adsorption times. The extent of monolayer coverage, the film uniformity, interfacial diffuseness, and the mechanism of adsorption in molecular level assemblies are addressed.

### 1. INTRODUCTION

We have recently demonstrated that electrically conducting multilayer thin film assemblies of doped conjugated polymers can be fabricated quite simply by adsorption from aqueous solutions [1, 2]. In the case of doped PAn, a positively charged polymer, multilayer build-up of alternating layers of polycations and polyanions was accomplished by means of electrostatic forces. The approach presented in this paper is to form thin film molecular assemblies of both doped and undoped PAn with strongly interacting non-ionic "counter-polymers." The thin film assemblies are formed by means of layer-by-layer self-assembly, a technique developed in our research group for conjugated polymers. The advantages are the relative ease of the technique combined with the quality of deposited films. Since deposition from aqueous solutions is generally more desirable, the formation of stable aqueous solutions in the concentration range of interest is quite important. Depending on the conditions, PAn can be coaxed into a solution that is 90-95% water, thus it is well suited for self-assembly.

In the work presented in this paper, we exploit the strong interchain interactions between PAn and several non-ionic water soluble polymers. Preliminary results suggest that it is primarily hydrogen bonding that enables this molecular layer-by-layer build-up. The films consist of alternating layers of PAn with one of several other strongly interacting polymers. We believe that this is the first demonstration of polymer-polymer multilayer build-up of a rigid conjugated polymer (PAn) with a flexible, non-ionic water soluble polymer [3]. The layer thickness can be controlled by the processing conditions such as solution concentration, pH, and ionic strength, as well as the adsorption time. It is this ability to controllably form thin electroactive films capable of adhering to a variety of surfaces that renders this technique so useful. Broad areas of interest include transparent electrodes, anti-static coatings, EMI shielding, surface modification, and sensors, just to name a few. Understanding the structure of such systems and the mechanism of adsorption are important for controllably manipulating the films on the molecular level.

## 2. EXPERIMENTAL

The self-assembly technique for PAn is described in detail in [2, 4], and outlined briefly here. The basis for the technique involves coating substrates with layers of polymers by means of spontaneous adsorption from aqueous solutions. Multilayers are built up by dipping the substrate alternately from one solution to the next.

PAn was synthesized chemically by the direct oxidation of aniline by slowly adding an equimolar amount of ammonium persulfate (dissolved in 1 M HCl) to freshly distilled aniline, also dissolved in 1 M HCl (similar to the method described in [5]). Based on results from many similar syntheses [6, 7], the molecular weight ( $M_n$ ) is estimated to be 20-25K g/mole with a polydispersity of about 2.5. PAn was dissolved in either N-methyl pyrrolidone (NMP) or dimethyl acetamide (DMAc) at 20 mg/ml by first stirring overnight, then sonicating the solution for about 8-10 hours. The 0.01 M (molar in terms of two aniline repeat units) PAn dipping solution was prepared by slowly adding one part (by volume) of the filtered PAn solution (in DMAc or NMP) in with 9 parts water with the pH adjusted to about 3.0-3.5 with methane sulfonic acid (MeSA). The pH was then quickly lowered to 2.5-2.6 by adding drops of concentrated MeSA. Care must be taken to not go below pH=2.5 or above pH=3.5 to avoid precipitating the doped PAn. The solution was filtered through a 0.45  $\mu$ m filter just before use.

In forming the other dipping solutions, all polymers were used as-received (polydisperse), and dissolved in water to form 0.01 M solutions, molar in terms of one repeat unit. There was no pH adjustment, except for the sulfonated polystyrene (SPS) solutions, which were adjusted to pH=2.6 with MeSA. The solutions were all filtered through a 0.2  $\mu$ m filter. The structures and MWs of these polymers are shown in Figure 1.

### Water Soluble Polymers

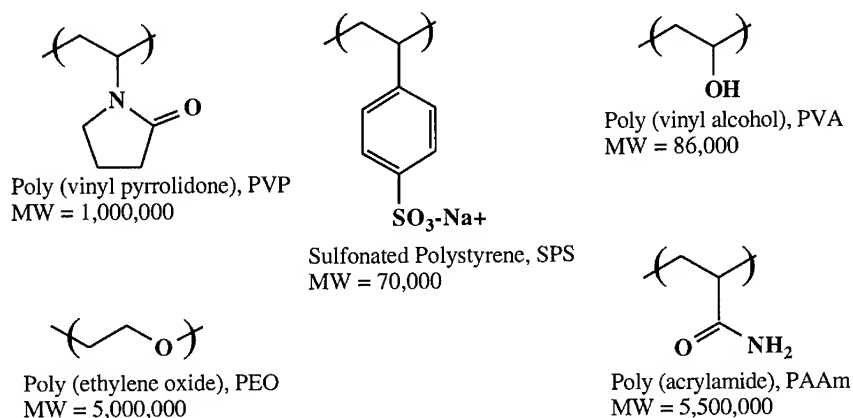


Figure 1. Water soluble polymers and their molecular weights, as used in this work.

The films were deposited on a variety of substrates, including glass, plastics, metal, and silicon. Adhesion could be enhanced by surface treatment of the substrate. Glass slides and silicon wafers were rendered charged by surface treatment. This treatment is described in [2]; briefly, it involves acid cleaning and hydroxylating the glass or silicon, then silanizing with an amine-terminated trifunctional silane, protonating to give the surface a positive charge, then covering with a monolayer of sulfonated polystyrene (by immersion into a SPS solution) to give the surface a negative charge. The layer-by-layer build-up is then started by immersion of the "treated" slides into the PAn solution for 15 minutes, followed by rinsing with water at pH=2.5 (MeSA), then drying with a compressed air jet. A 15 minute dip time is used because

we have shown that 90-95% of the equilibrium thickness occurs in the first 15 minutes. The films were then immersed in the non-ionic polymer solution for 15 minutes, followed by rinsing with neutral water, and compressed air drying. From there, layers were simply alternated between PAn and the non-ionic polymer. The resulting films were only lightly doped; they must be immersed in a 1 M MeSA solution to fully dope, followed by a quick rinse in 1 M HCl to remove residual surface MeSA.

Layer-by-layer build-up was monitored by visible and infrared spectroscopy. Visible light absorption spectra were taken directly from coated glass slides using an Oriel 250 mm spectrophotometer. IR spectra were taken on films built up on ZnSe plates, using a Nicolet 510P FTIR. The spectra were taken between each bilayer after dedoping the films by rinsing with 0.1 M ammonium hydroxide. This was to ensure a uniform electronic state in all films for direct comparison of absorption spectra. Atomic force microscopy (AFM) was performed using a Digital Instruments Nanoscope III operating in tapping mode. The film thicknesses were measured by both profilometry (using a Sloan Dektak 8000) and by ellipsometry (for films on reflective surfaces, using a Gaertner three wavelength ellipsometer). All conductivities of fully doped films were measured in air by the van der Pauw four corner probe method.

### 3. RESULTS AND DISCUSSION

The multilayer deposition can be monitored by either visible or infrared spectroscopy, where absorbance per bilayer is measured. Figure 2 shows the excitonic absorption for dedoped PAn at 630 nm as a function of the number of bilayers deposited for six different systems. The linearity of the absorbance at 630 nm indicates uniform multilayer build-up for all of these systems. Each bilayer is delivering approximately the same amount of PAn, with the exception of the first bilayer. Since all of these films were deposited on SPS-treated glass, the first bilayer is effectively a PAn/SPS bilayer. Thus, the thickness of the first bilayer should be closer to that of the PAn/SPS system. There is also some uncertainty as to the extent of coverage of the first bilayer. Properties such as conductivity and surface hydrophilicity (as determined by contact angle) indicate that the first bilayer behaves differently than the subsequent layers, suggesting non-uniform coverage.

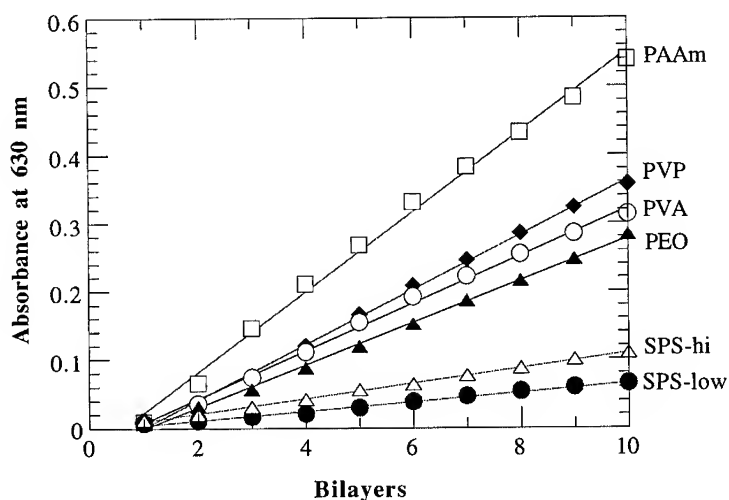


Figure 2. Absorbance at 630 nm vs. number of bilayers for several PAn bilayer systems: PAAm - poly(acrylamide), PVP - poly(vinyl pyrrolidone), PVA - poly(vinyl alcohol), PEO - poly(ethylene oxide), SPS - sulfonated polystyrene (low - low MW, hi - high MW).

Some of the properties of these multilayer films are outlined in Table 1. Listed are the polymers displayed in Figure 2 and their MWs (all are polydisperse). All solution concentrations were 0.01 M, as defined in the experimental section. This concentration is well below the calculated critical overlap concentration in all cases. Thus, adsorption is from non-overlapping chains in solution. It is possible, however, that there is some extent of nano-aggregation in the PAn solution, since it is in water, a non-solvent. Lower concentration PAn ( $10^{-4}$  M) delivers smoother (as determined by AFM), yet thinner, films. These thinner films also have higher dichroic ratios, measured using polarized light. This indicates a preferred in-plane chain orientation, more so than in films adsorbed from the higher concentrations ( $10^{-2}$  M). This results from the more favorable conditions for chain elongation on the surface due to decreased competition for surface sites. Detailed AFM and dichroism results are to be published.

Table 1. Systems alternating with PAn at pH=2.6. All polymer solutions at  $10^{-2}$  M.

1. Polymer System w/ PAn	2. Overall Thickness (Å)	3. Bi-layers	4. Å per bilayer	5. pH	6. $\sigma$ (S/cm)	7. Absorb. (630 nm) /bilayer	8. Est. vol% PAn
PAAm (5,500,000)	1260	10	126	5.8	3.6	0.0540	55
PVP (1,000,000)	785	10	78	6.1	2.5	0.0357	59
PEO (5,000,000)	720	10	72	6.7	2.2	0.0282	51
PVA (86,000)	650	10	65	6.1	2.9	0.0313	62
SPS-low [4] (70,000)	575	16	36	2.6	0.5-1.0	0.0067	24
SPS-hi (500,000)	340	10	34	2.6	0.4	0.0109	41

Included in Table 1 are the average film thicknesses for multilayer films (column 2), measured by profilometry, and the corresponding average thickness per bilayer (column 4). The non-ionic polymer solution pH is listed in column 5. Results show that the film thickness can depend on this value, depending on the particular system. Conductivities ( $\sigma$ , column 6) are measured for fully doped films (doped with MeSA). These samples showed about an order of magnitude drop in conductivity after one year stored in air. The absorbance (at 630 nm) per bilayer is listed for dedoped films (column 7). An approximate vol% PAn is listed in the last column. This is calculated using the estimated value of  $\epsilon$ , the extinction coefficient at 630 nm, of approx.  $14000 \text{ (M-cm)}^{-1}$  for dedoped PAn (where a mole is defined for two aniline repeat units) [4]. Assuming a density of  $1 \text{ g/cm}^3$  for the films, and using Beer's law relating absorbance to concentration, the absorbance/unit thickness is  $7.74 \times 10^{-4}/\text{\AA}$ . Using this value and the absorbance per bilayer value (column 7), the contribution of PAn per bilayer is estimated. The volume% PAn (column 8) is simply this PAn contribution divided by the overall thickness.

It is evident (from Figure 2) that although each deposited bilayer is approximately the same thickness for a given PAn bilayer system, there is a wide range of bilayer thicknesses depending on the particular system. In fact, the ionic system, SPS, delivers the thinnest bilayers, while the non-ionic polymers show up to seven times the visible light absorbance per bilayer. In comparing two similar MW systems at the same concentration, SPS (ionic, MW=70K) to PVA (non-ionic, MW=86K), the non-ionic polymer still shows over four times the absorbance per bilayer. There are other factors affecting the deposition and resulting properties, however, such as molecular weight, solution pH, and concentration. It has been observed that thinner layers are deposited from less concentrated solutions. As seen in Table 1, PAAm delivered a much thicker bilayer than PEO, of comparable MW. Each system behaves

slightly differently, as also evident by the large disparity in MW between PVA and PEO, yet both deliver comparable thicknesses and conductivities. The pH of the non-ionic polymer solution can affect a polymer's ability to hydrogen bond, as seen with PVP. Thicker films are delivered from a neutral pH range (about 4-7) than a low pH (about 2.5). It is expected that high pHs would completely prevent multilayer build-up by preventing hydrogen bonding. Similar pH effects were seen with PVP and PEO adsorption onto glass capillaries [8, 9].

Conductivity and film thickness as a function of the number of bilayers deposited were also measured for a PAN/PVP system. After only two bilayers, the film was already within an order of magnitude of its ultimate conductivity. This corresponds to a film thickness of about 75 Å. The first bilayer is quite thin (< 30 Å) likely due to both incomplete coverage and the fact that it is effectively a bilayer of PAN/SPS rather than PAN/PVP. The incomplete coverage is suggested by the extremely low conductivity ( $<10^{-5}$  S/cm, the limit of our measuring capabilities). The second layer fills in more, with total coverage coming by the third bilayer. After three bilayers, the film is approximately 150 Å thick, and has almost reached its eventual conductivity. Each successive bilayer delivers about 80 Å, the average bilayer thickness. Beyond three bilayers, there is little subsequent increase in conductivity, suggesting complete coverage by the third bilayer.

Preliminary results show that a single mixed layer of PAN and either PVP or PAAM can be deposited from a mixed solution. The significance is that a conducting layer is deposited with a single "dip." The single layer conductivity is 0.1 S/cm for both films, only about an order of magnitude lower than the eventual conductivity for multilayer films. These are highly transparent coatings, only about 50-60 Å thick.

The actual extent of interaction between any two layers can be monitored to some extent by the presence of hydrogen bonds, as measured by FTIR. Coleman and Painter have used such an approach for determining the extent of hydrogen bonding in polyurethanes [10] and for determining the extent of phase separation in H-bonding polymer blends [11, 12]. The energy of the N-H stretch (of PAN), and the carbonyl C=O stretch (in PVP) both depend on whether they are H-bonded or not, thus these two absorbance peaks can be monitored as a function of their environment. Because PAAM and PVA both H-bond with themselves, it is more difficult to determine whether the H-bonds are inter- or intra- molecular. PEO is also more difficult since there is not a strong energy shift for a free ether linkage compared to a H-bonded one [12].

The presence of hydrogen bonding is evident in the IR spectra shown in Figure 3 for the PAN/PVP system. The N-H stretch of PAN in its dedoped state (not charged) appears at 3382  $\text{cm}^{-1}$ . In a multilayer system with PVP, there is a new lower energy peak at 3304  $\text{cm}^{-1}$ , corresponding to a hydrogen bonded N-H. There is a fraction of these hydrogens that remains free, as evident by the continued presence of the peak at 3382  $\text{cm}^{-1}$ . This same peak shift was seen in PAN/PEO multilayer films. Also shown for comparison is the blended system; a film of approximately 50/50 PAN/PVP cast from a mixed solution in NMP. The PAN/PVP blend also shows the shifted peak, here at 3315  $\text{cm}^{-1}$ , evidence of some extent of hydrogen bonding. This implies significant phase mixing in this blend. A PAN/PEO blend (not shown) shows no such shift, thus has few hydrogen bonding interactions, suggesting a phase separated system. Observing these blends under a light microscope at 1000x confirms the phase separated structure of the PEO blend, and the phase mixed structure of the PVP blend.

Investigations have been made into the ability of charged polymers to adhere to non-ionic polymers, and vice versa. PEO and PVP, in solutions at both low pH (2.6) and "neutral" pH (4.5-6.5), will build multilayer systems with PAN, with slightly better build-up in the neutral pH. Multilayer build-up has also been demonstrated with PAN and PVP where the PAN layer was completely dedoped (thus electrostatically neutral) after deposition, but before deposition of the PVP layer. PEO and PVP will not build up multilayers with SPS, a polyanion, in this pH range (2.5-6.5), nor poly(allyl amine), a polycation at low pH (2-3). The implication is that there are very strong specific interactions with PAN not related to ionic charges, since these water soluble polymers (PVP, PEO, etc.) will not interact with other charged polymers, either positive or negative, in a manner that allows multilayer self-assembly.

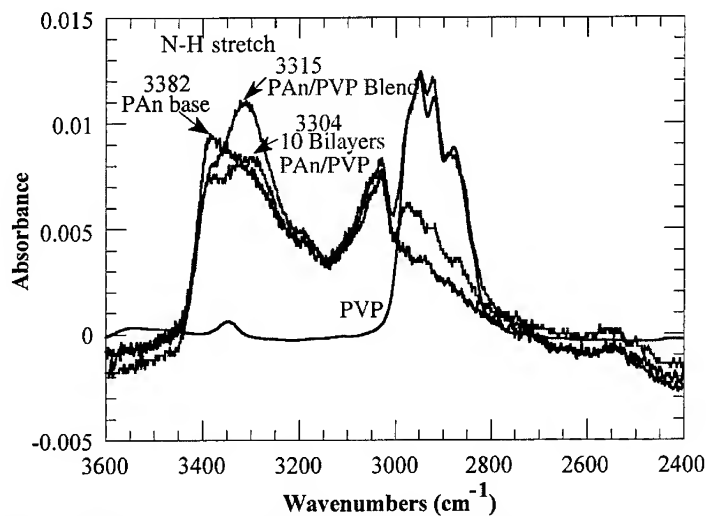


Figure 3. FTIR spectra of the N-H stretch region of PAn/PVP systems.

It might be expected that multilayer build-up would be possible with most any hydrogen bonding pairs, such as PVP with PVA, or PAAm with PVP, PVA, or PEO. Preliminary results show, however, that none of these four systems forms multilayer films, as determined by IR spectroscopy. This suggests that there are additional specific interactions between PAn and these water-soluble polymers, or that the hydrogen bonding is not of as strong of a nature between PAAm and PVA, for example, as it is between PAn and PVA or PAAm.

## ACKNOWLEDGMENTS

The authors thank the NSF and the MIT Center for Materials Science for partial funding for this work. Also thanks to Wade Samec, an undergraduate working in our lab, for tremendous help with sample preparation and characterization.

## REFERENCES

1. M. Ferreira, J.H. Cheung, and M.F. Rubner, *Thin Solid Films*, **244**, 806 (1994).
2. J.H. Cheung, A.C. Fou, M.F. Rubner, *Thin Solid Films*, **244**, 985 (1994).
3. W.B. Stockton and M.F. Rubner, *ACS Polymer Preprints*, **35** (1), 319 (1994).
4. J.H. Cheung, Ph.D. Thesis, MIT, 1993.
5. J.-C. Chiang and A.G. MacDiarmid, *Synth. Met.*, **13**, 193 (1986).
6. C.-H. Hsu, P.M. Peacock, R.B. Flippen, S.K. Manohar, and A.G. MacDiarmid, *Synthetic Metals*, **60**, 233 (1993).
7. E.J. Oh, Y. Min, J.M. Wiesinger, S.K. Manohar, E.M. Scherr, P.J. Prest, A.G. MacDiarmid, and A.J. Epstein, *Synthetic Metals*, **55-57**, 977 (1993).
8. M.A. Cohen Stuart and H. Tamai, *Macromolecules*, **21**, 1863 (1988).
9. M.A. Cohen Stuart and H. Tamai, *Langmuir*, **4**, 1184 (1988).
10. M.M. Coleman, K.H. Lee, D.J. Skrovanek, and P.C. Painter, *Macromolecules*, **19**, 2149 (1986).
11. M.M. Coleman, Y. Xu, and P.C. Painter, *Macromolecules*, **27**, 127 (1994).
12. C. Le Menestrel, D.E. Bhagwagar, P.C. Painter, M.M. Coleman, and J.F. Graf, *Macromolecules*, **25**, 7101 (1992).

---

## PART VII

---

### **Ionic Devices**



## THE Li-ION TECHNOLOGY: ITS EVOLUTION FROM LIQUID TO PLASTIC

J.M. TARASCON, C. SCHMUTZ, A.S. GOZDZ, P.C. WARREN, AND F.K. SHOKOOHI  
*Bellcore, 331 Newman Springs Road, Red Bank, NJ, 07701*

### ABSTRACT

In 1992, Bellcore researchers demonstrated the feasibility of a liquid-electrolyte Li-ion system based on the  $\text{Li}_{1+x}\text{Mn}_2\text{O}_4/\text{C}$  redox couple which presents cost and environmental advantages over the  $\text{LiCoO}_2/\text{C}$  system. However, neither of these systems are free of the risk of electrolyte leakage. To address this problem, we investigated various means of trapping the liquid electrolyte in a polymer matrix and developed the first practical plastic Li-ion battery. In this paper we compare the performance and scalability of this technology to those of its liquid Li-ion counterpart. Based on the "hybrid polymer" concept, this battery exhibits excellent cycle life (more than 2500 cycles) and good rate capabilities (the battery can deliver 95% of its total capacity at a 1C discharge rate). This technology is compatible with various positive ( $\text{LiMn}_2\text{O}_4$ ,  $\text{LiCoO}_2$  and  $\text{LiNiO}_2$ ) and negative (carbon, graphite) electrode materials.

### INTRODUCTION

The rechargeable liquid-electrolyte Li-ion batteries, which were introduced commercially by Sony<sup>1</sup> in 1990, are presently well accepted in the market place. However, their manufacturing cannot meet the present demand dictated by a growing portable electronics market. Among the existing commercial rechargeable battery technologies, the Li-ion battery technology is the most suitable for the portable electronic market due to its light weight and large volumetric and gravimetric energy densities. As portable electronics devices become smaller, thin and flexible batteries are urgently needed. Today's liquid-electrolyte Li-ion technology is limited to only rigid cylindrical or prismatic cell shapes. Rechargeable polymer Li batteries<sup>2</sup> possess the required shape flexibility, but after twenty years of research and development, the rechargeable polymer lithium battery technology is still incapable of functioning efficiently at room temperature because of the lack of polymer electrolytes with sufficient ionic conductivity.

Midway between the rechargeable lithium batteries that use liquid and pure polymer electrolytes are those using hybrid electrolytes, e.g., polymers swollen in liquid electrolytes. They combine the advantages of both liquid (high power rate) and polymer electrolyte batteries (no electrolyte leakage, easier scalability) batteries. While enjoying a true renaissance during the last several years, the hybrid electrolyte concept was demonstrated by Feuillade et al.<sup>3</sup> as early as 1974. In addition, it should be remembered that the primary dry alkaline cells also contain a liquid electrolyte which is immobilized in an elastic matrix. The principle of electrolyte immobilization has also been applied to the recently popularized rechargeable lead-acid batteries known as VRLA's (valve-regulated lead-acid batteries) in which the

electrolyte is either in the form of a gel or is absorbed in a silica-mat separator. During the last several years, this concept has been widely applied in the field of rechargeable Li batteries to prepare solid polymer electrolyte batteries in which the electrolyte is trapped in a appropriate polymer matrix. Hybrid polymer electrolyte films are usually made by dissolving a polymer matrix<sup>4</sup> in a low-boiling solvent (acetonitrile, THF, etc ..) together with a non-aqueous Li-salt electrolyte. The most popular polymer matrices are PEO and its derivatives; PAN, MEEP, etc... Depending on the voltage range, a variety of liquid electrolytes have been reported, PC-EC/Li-based salts being the most popular. The resulting viscous solution is then cast to give usually tacky films that may be stabilized by either chemical or physical cross-linking. All the above processes must be carried out in a completely moisture-free atmosphere, resulting in high processing costs.

We have successfully addressed this issue through several proprietary processing steps and developed the first reliable and practical rechargeable Li-ion plastic battery. Here, we report the processing and performance of Bellcore's new plastic Li-ion battery<sup>5-6</sup>. Except for the activation step, this battery can be fabricated in an uncontrolled environment; its performance compares favorably with its liquid Li-ion counterpart while in addition offering safety, scaleability, shape flexibility, and cost advantages.

## EXPERIMENTAL

In order to describe our plastic battery it is important to recall that a plastic is commonly defined as a combination of a polymer matrix with various additives and components, such as other polymers, plasticizers, fillers, pigments, stabilizers, and so on. The familiar spiral phone cord, for example, is made of a plastic that consists of about 50% polymer (PVC), the remainder being liquid plasticizers, and other additives. In this plastic material the liquid is so well trapped that the cord looks and feels dry. However, the partial vapor pressure of the "immobilized" liquid in a plastic matrix is similar to that of pure liquid. Bellcore's plastic electrolyte fits the above definition, with the Li-based liquid electrolyte acting as the plasticizer of the polymer matrix in both electrodes and the separator/electrolyte.

### *a) Choice of the polymer matrix*

When designing a plastic, the choice of the polymer and additives depends on the targeted application. Obviously, the plastic used for the phone cord is different from that needed for our battery. However, the basic concept in terms of polymer-liquid compatibility established by the plastics community is still valid. A suitable polymer for plastic battery should be 1) commercially available, 2) abundant and low-cost, 3) electrochemically stable over a wide range of potential (0 to 5V vs. Li/Li<sup>+</sup>), 4) should have a high melting temperature and low creep before reaching its melting point, 5) good mechanical properties and 6) be able to absorb a large amount of liquid electrolyte to ensure high ionic conductivity. Each of the above requirements is necessary, but not sufficient in itself, thus the problem in selecting the suitable polymer matrix. However, the possibility of adding fillers, stabilizers etc. to the plastic relieve some of the constraints placed on the polymer matrix.

The first step toward developing a plastic-based battery was to select a polymer that would have the properties described above, while being easy to process. Fluorinated polymers were previously rejected in rechargeable Li batteries because of an interfacial reaction between Li and fluorine resulting in the formation of LiF. In the Li-ion technology, the Li metal negative electrode is substituted by a carbon-based negative electrode, thus a pure Li metal is not present, eliminating the possibility of decomposing fluorine-based polymers at the Li interface. The use of poly(vinylidene fluoride) (PVDF) as a binder in the carbon-based negative electrodes in commercial Li-ion cells that can be cycled more than 2000 times confirms the above expectation. The electrochemical stability of fluorinated polymers over the 0 to 5V (vs. Li/Li<sup>+</sup>) potential range being already experimentally established in liquid Li-ion batteries, we decided to investigate further their ability to swell in liquid electrolyte.

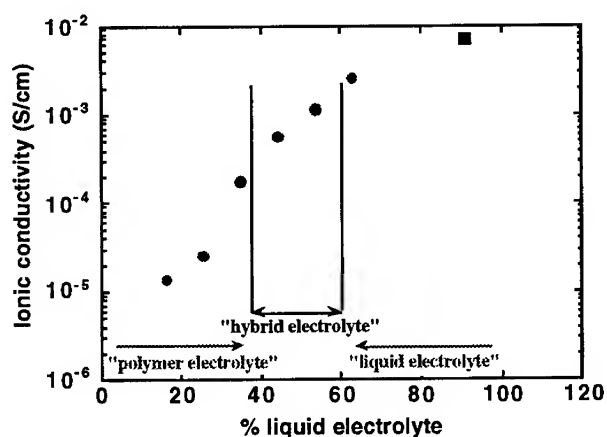


**Figure 1.** Ionic conductivity of hybrid electrolyte films based on P(VDF-12%HFP) and 1M LiPF<sub>6</sub> in EC/PC

PVDF homopolymer does not swell appreciably in liquid electrolytes based on carbonate esters, but we found that the presence of hexafluoropropylene (HFP) in PVDF (the well-known PVDF-HFP copolymers commercialized by Atochem under the Kynar trademark) increases their electrolyte uptake<sup>7-8</sup>. The amount of electrolyte uptake by a polymer matrix is a function of polymer crystallinity. Copolymers with a large fraction of amorphous phase (e.g., high HFP content) form highly swollen, tacky materials (Viton), while copolymers with a high content of crystalline phase (e.g., low HFP content), swell poorly.

We selected the HFP content in PVDF-HFP copolymers to achieve sufficient ionic conductivity. The optimum swelling of PVDF-HFP copolymers

in liquid electrolytes was found for HFP content from 8 to 15%. In this case, the polymer matrix can absorb up to 60% of liquid electrolyte while maintaining good mechanical/elastic properties and ionic conductivity (0.4 mS/cm). The ionic conductivity of the plastic matrix turns out to be directly related to the amount of trapped liquid electrolyte as shown in Figure 1. However, the ionic conductivity of 0.4 mS/cm at room temperature is not sufficient to obtain good battery performance in terms of power rate over a wide range of temperatures. By modifying our plastic material, we were able to prepare plastic electrolyte films with ionic conductivities up to 3 mS per cm, compared to 2.5mS/cm for the liquid electrolyte 1M LiClO<sub>4</sub> in EC-PC(50-50) .

Plastic electrolyte films are mechanically stable up to temperatures of about 100°C (Figure. 3, Ref 8) and show good elastic and mechanical properties with little evidence of polymer softening prior the melting temperature.

#### ***b) Assembly of the plastic cell***

A rechargeable Li-ion cell was assembled from 5 components: a copper current collector, a carbon-based negative electrode, a plastic electrolyte separator, a positive electrode, and an aluminium current collector. The positive electrode was prepared by mixing a lithium transition metal oxide powder (LiMn<sub>2</sub>O<sub>4</sub>, LiCoO<sub>2</sub> or LiNiO<sub>2</sub>) , conductive carbon and the PVDF-HFP polymer to produce, either by solvent casting or hot melt processing, a plastic electrode film. Similarly, a plastic negative electrode was prepared from petroleum coke or graphite as the negative active ingredient. The battery laminate was constructed by first hot laminating the positive and negative electrodes with the aluminium and copper grids, respectively, to produce two laminated electrodes. The plastic separator was then placed between the positive and negative electrode laminates and the three layers were fed together through a heated double-roll laminator to produce the single battery cell laminate. The advantage of this process is that it produces a battery which is free of a macroscopic interface, since the same plastic matrix is present throughout all three layers of the battery. A schematic representation of such a cell is given in Figure 2. It can be regarded as a plastic electrolyte matrix with Li-based oxide particles embedded on one side and carbon particles embedded on the other.

The resulting single-laminate cell which can be fabricated in an uncontrolled environment may be cut using a razor blade into two or more parts for duplicate experiments. Each part is then activated by a proprietary process, inserted into a metal-plastic laminate bag and sealed to produce the plastic Li-ion cell. Our research laboratory prototype Li-ion plastic cells are flat, with a surface area of about 25cm<sup>2</sup> and a thickness of 500 microns. The cells were tested using either a Mac-Pile system (Bio Logic, Claix, France) or a Moli Cycler (Moli energy Ltd., Vancouver, Canada) operating in a galvanostatic mode.

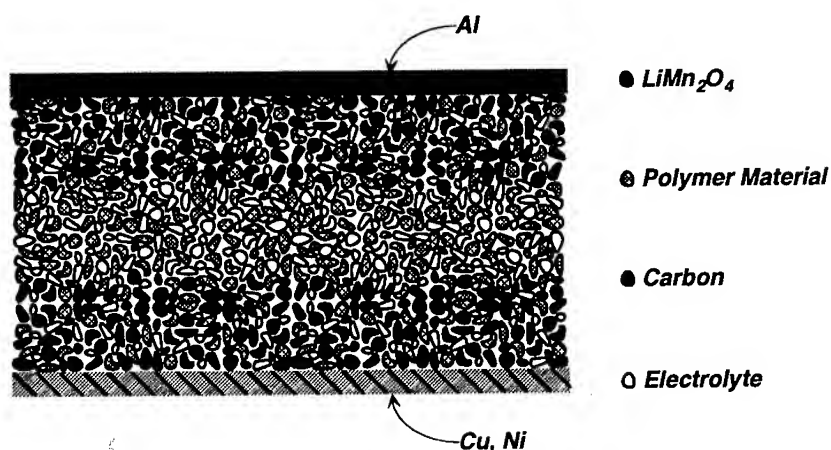


**Figure 2.** Schematic view of an Li-ion battery based on the common plasticized electrode binder and hybrid electrolyte.

## RESULTS AND DISCUSSION

The performance of Li-ion plastic cells is discussed below. The cells exhibit excellent cycle-life (more than 3000 cycles were obtained at 25°C; Fig. 2) and excellent power rate (the cells can deliver 95% of their total energy in less than one hour, similar to their liquid electrolyte Li-ion counterparts; Fig. 3). The main reason for such behavior appears to be the lack of a macroscopic interface within our Li-ion plastic cells, and the high ionic conductivity of the plastic electrolyte.

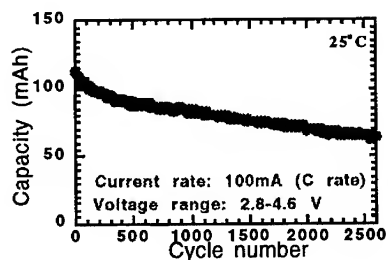


**Figure 3.** Capacity vs. cycle number at 25°C for a Li-ion plastic cell based on LiMn<sub>2</sub>O<sub>4</sub> as the positive electrode

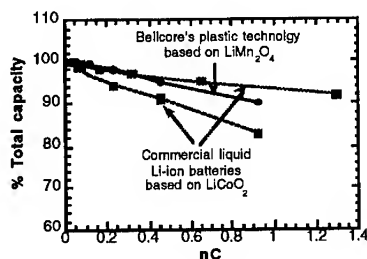


**Figure 4.** The power rate of Bellcore Li-ion plastic cell is compared to commercial liquid Li-ion cells

It should be emphasized that the polymer used in these plastic, rechargeable, lithium-ion batteries is neutral vs. a number of active materials used in both electrodes. Figure 5 shows that plastic batteries can incorporate various cathode materials, such as  $\text{LiCoO}_2$ ,  $\text{LiNiO}_2$ , and  $\text{LiMn}_2\text{O}_4$ , and various anode materials: coke or graphite, as well as various liquid electrolyte compositions, while their performance remains unaffected (Fig. 4). In short, all the know-how accumulated in the case of the liquid Li-ion battery technology can be directly implemented in the plastic battery technology.

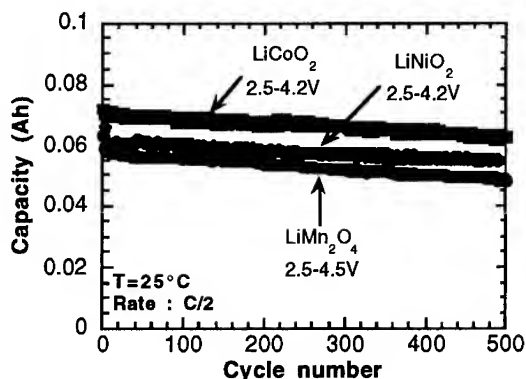


**Figure 5.** Capacity vs. cycle number for Li-ion plastic cells using  $\text{LiMn}_2\text{O}_4$ ,  $\text{LiCoO}_2$  or  $\text{LiNiO}_2$  as the positive electrode materials.

To be practical a battery has to operate efficiently over a wide temperature range,  $-20^\circ\text{C}$  to  $60^\circ\text{C}$ . A permanent concern with respect to polymer lithium batteries has been their limited power rate at low temperatures. Figure 6 dispels this skepticism. At  $-20^\circ\text{C}$ , the plastic cell can deliver 80% of its capacity down to a voltage of 2.5V at a C/5 rate, similar to what is achieved with liquid Li-ion cells. Specific capacities of 2 and 1.8 mAh/cm<sup>2</sup> can be obtained at  $-20^\circ\text{C}$  at power rates of C/16 and C/5, respectively.

At the upper range of temperatures needed for practical applications, battery cycle life (capacity fading) and storage performance usually raise more concerns than power rate. The behavior of the plastic cells at  $55^\circ\text{C}$  is shown in Fig. 7 for Li-ion plastic cells using either  $\text{LiMn}_2\text{O}_4$ ,  $\text{LiCoO}_2$  as the positive electrode materials. More than 500 cycles have been completed so far; the experiment is still in progress. In Figure 8, we compare the capacity fading of a Li-ion plastic cell based on  $\text{LiMn}_2\text{O}_4$  with a commercial Liquid Li-ion cell based on  $\text{LiCoO}_2$  as the positive electrode. The capacity fading for the plastic and liquid cells is similar.

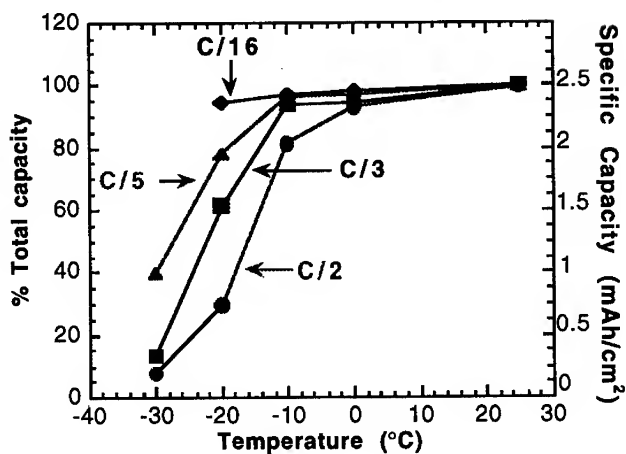


**Figure 6a.** The capacity and specific capacity for a Li plastic cell is shown as a function of temperature for various power rates

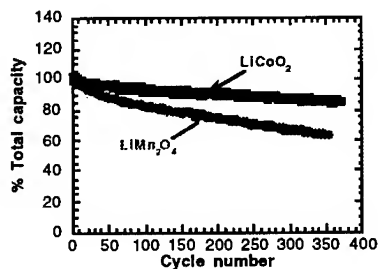


**Figure 7.** Capacity vs. cycle number at 55°C for Li-ion plastic cells using either LiMn₂O₄ or LiCoO₂ as the positive

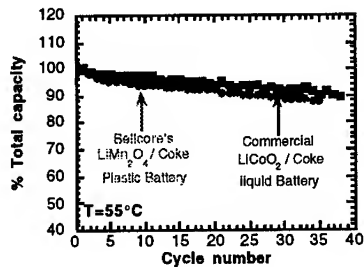


**Figure 8.** Comparison of the capacity fading upon cycling between a plastic and a liquid Li-ion cell at 55°C

The room temperature self-discharge for Li-ion plastic cells, based on either LiMn₂O₄ or LiCoO₂ as the positive electrode materials are shown in Figures 9 and 10. In these experiments, the LiMn₂O₄ and LiCoO₂-based cells were charged to 4.5V and 4.2V, respectively. The cells were then placed at rest for 50 days and their voltages were monitored (Fig. 9). Afterwards, the cells were discharged down to 2V and recharged to their initial voltage 4.5V and 4.2V (Fig. 10). This sequence was repeated. Figure 10 shows the variation of the discharge/charge voltage of the cell prior to placing at rest and after two successive rests of 50 days each. From these curves, one can deduce the amount

of total self-discharge (reversible and irreversible) for each cell after the two subsequent self-discharge cycles; the results are summarized in figure 11.

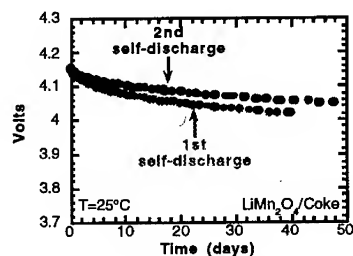


**Figure 9.** The voltage decay of a Li-ion plastic cell at rest for 50 days.

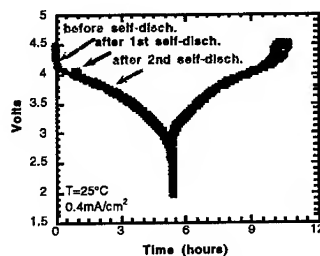


**Figure 10.** The charge/discharge voltage traces for a Li-ion plastic cell prior and after being placed at rest.

For the  $\text{LiMn}_2\text{O}_4/\text{C}$  plastic cell we measured a 16% self-discharge in fifty days, 7% of which were irreversible. After the subsequent 50 days rest, a self-discharge of 8% was measured, 4% of which was irreversible. Similar results were obtained for the  $\text{LiCoO}_2$ -based plastic cells. These results indicate that the part of irreversible loss during storage at room temperature decreases considerably during subsequent storage cycles at room temperature. These cells are still being studied. In parallel, we have initiated a similar study of the magnitude of self-discharge for batteries stored for 50 days at  $55^\circ\text{C}$ . These results will be reported elsewhere.

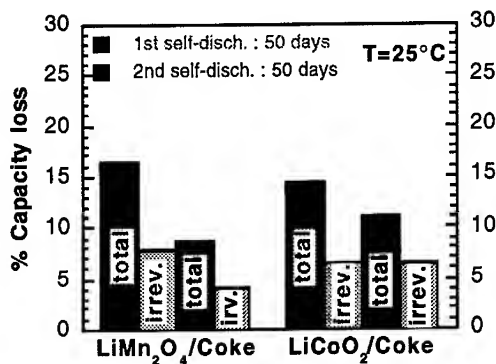


**Figure 11.** The irreversible and reversible capacity losses for a  $\text{LiMn}_2\text{O}_4$ -based Li-ion plastic cell placed at rest for two subsequent periods of fifty days is compared to that of a  $\text{LiCoO}_2$ -based Li-ion plastic cell under similar conditions.



An important figure of merit in evaluating a new technology is its scaleability. Large size prototypes, single module or bimodule cells, in which the single battery laminate was bent at 180°, were also built. The cycleability as well as the power rate for such cells are similar to those of single cells, independent of either a flat or bent configuration.

In summary, we used a fluorinated copolymer matrix to trap the liquid electrolyte used in liquid Li-ion batteries and to produce the first practical Li-ion plastic battery. Such a battery, based on lithium-ion chemistry, is unique in that the entire battery is composed of a plasticized polymer ("plastic") laminate. It works exactly like liquid-electrolyte Li-ion batteries, i.e., lithium ions are shuttled back and forth between the anode and the cathode as the battery is charged and discharged. The plastic electrolyte feature of such a battery allows one to avoid the problem of liquid leakage should the hermetic seal break. Such a battery compares favorably in terms of gravimetric or volumetric energy density, cycle life, power rate and self-discharge to its liquid counterparts, while having enhanced safety characteristics, higher shape flexibility (the plastic laminate sheet can be folded, rolled or stacked in ways limited only by the designer's creativity), greater scaleability and lower cost.

## REFERENCES

- [1] T. Nagaura and K. Tazawa, *Prog. Batteries Sol. Cells*, 9, 20(1990).
- [2] M. Armand, J.M. Chabagno et M.J. Duclot, "Fast ion transport in solids", P. Vashista, J.M. Mundy et G.K. Shenoy (Eds), North Holland, New York, p.131(1979).
- [3] G. Feuillade, Ph. Perche, Jr. of *Applied Electrochemistry*, 5, 63 (1975).
- [4] M. Alamgir and K.M. Abraham, Chapter 3 in *Lithium Batteries*, New Materials, Developments and Perspectives, Vol. 5 in *Industrial Chemistry Library*, G. Pistoia, Ed., Elsevier, New York (1994).
- [5] A.S. Gozdz, C. Schmutz, J.M. Tarascon, U.S. Patent 5,296,318.
- [6] C. Schmutz, J.M. Tarascon, A.S. Gozdz, P.C. Warren and F.K. Shokoohi, Paper 109 presented at the Symposium of the 186th Electrochemical Society meeting, Miami, Florida, Oct. 13-18 (1994).
- [7] T. Gozdz, J.M. Tarascon, C. Schmutz, P.C. Warren O.S. Gebizlioglu, and F.K. Shokoohi, Paper 117 presented at the Rechargeable Lithium and Lithium-ion (RCT) Batteries Symposium of the 186th Electrochemical Society meeting, Miami, Florida, Oct. 13-18 (1994).
- [8] T. Gozdz, J.M. Tarascon, O.S. Gebizlioglu, C. Schmutz, P.C. Warren, and F.K. Shokoohi, Paper to be presented at the 10th Annual Battery Conference on Applications and Advances, Long Beach, California, January 10-15 (1995).

## PERFORMANCE OF POLYMER-BASED SUPERCAPACITORS

CATIA ARBIZZANI<sup>o</sup>, MARINA MASTRAGOSTINO<sup>o</sup> AND LUCA MENEGHELLO<sup>\*o</sup>

<sup>o</sup>University of Bologna, Dept. of Chemistry "G. Ciamician", via F. Selmi 2, 40126 Bologna, Italy

<sup>\*</sup>University of Pavia, Dept. of Physical Chemistry, viale Taramelli 16, 27100 Pavia, Italy

### ABSTRACT

Supercapacitors are now attracting much attention as an electric vehicle power source. The present study focuses on redox supercapacitors with electronically conducting polymers as electrode materials. Performance data of a symmetric supercapacitor based on p-doped poly(pyrrole), of an unsymmetric supercapacitor based on p-doped poly(pyrrole) and poly(3-methylthiophene), and of a symmetric supercapacitor based on p- and n-doped poly(dithieno[3,4-b:3',4'-d]thiophene) are here compared.

### INTRODUCTION

Supercapacitors are attracting much attention as devices complementary to batteries for applications requiring high operating power levels. The hybrid systems (batteries and supercapacitors) being proposed for electric vehicle propulsion are an application which has been stimulating the research to develop high performance devices. Two types of supercapacitor, with different modes of energy storage, are currently under study: i) *double-layer supercapacitors*, in which capacitance is electrostatic in origin and the electrode materials are high-area Faradaically inactive carbon powders; high performance devices of this type are already on the market; ii) *redox supercapacitors*, in which Faradaic charge transfer takes place as in a battery; in these devices capacitance arises from Faradaic reactions and is known as pseudocapacitance [1].

Electronically conducting polymers (ECPs) represent an interesting class of electrode materials for redox supercapacitors because the kinetics of the electrochemical charge-discharge processes - known as doping-undoping - are generally fast, the charge is stored through the volume of the material and they can be produced at lower cost than noble metal oxides, which have also been used in redox supercapacitors. Heretofore much attention has been devoted to the use of the ECPs in electrochemical devices, i.e. as cathode-active materials in rechargeable batteries and as electrochromic materials in variable light transmission devices, and their use in redox supercapacitors is a recently suggested application.

The versatility of the ECPs enables different redox supercapacitor configurations, as already stressed by Rudge et al. who in ref [2] report three schemes with an increasing charge storage capacity and operating potential range from type to type: (I) a symmetric supercapacitor based on a p-doped ECP, (II) a unsymmetric supercapacitor based on two p-doped ECPs which are dopable over different potential ranges, and (III) a symmetric supercapacitor with a p- and n-doped ECP. Configuration III is the most promising in terms of energy and power density but these advantages are offset by the difficulty of obtaining polymers which can be n-doped in an efficient way. There are numerous reports in the literature on p-doped heterocyclic polymers but very few on the n-doped conducting forms. Reversible n-doping of conventional conjugated polymers has been observed only with alkylammonium salts and very negative potentials are generally required so that the stability of the n-doped form is strongly dependent on the solvent's properties [3].

The present paper reports experimental data of our ongoing investigations into the three types of polymer-based supercapacitors with liquid organic electrolytes. Types I and II were tested in propylene carbonate (PC) - LiClO<sub>4</sub> using conventional ECPs, i.e. poly(pyrrole) (pPy)

for I and pPy and poly(3-methylthiophene) (pMeT) for II, whereas type III was tested in PC-tetraethylammonium tetrafluoroborate (TEABF<sub>4</sub>) using the poly(dithieno[3,4-b:3',4'-d]thiophene) (pDTT), a new ECP specially designed with narrow energy gap between valence and conduction bands[4]. The charge injection of both sign (p and n doping) in pDTT is possible inside the electrochemical stability window of PC - TEABF<sub>4</sub> [5]. On the basis of these preliminary results, a rating of power and energy density performance of the three devices is reported and the values are compared to the requisites set for electric vehicle supercapacitors by the U.S. Department of Energy (DOE).

## EXPERIMENTAL

Polymer films were galvanostatically grown on carbon paper electrode (Toray Industries, Inc., Japan) by monomer oxidation as follows:

pPy at  $I=10 \text{ mA cm}^{-2}$  in acetonitrile (ACN)-0.5 M LiClO<sub>4</sub>-0.6M Py;

pMeT at  $I=5 \text{ mA cm}^{-2}$  in ACN-0.5 M LiClO<sub>4</sub>-0.1M MeT;

pDTT at  $I=1 \text{ mA cm}^{-2}$  in ACN-0.1 M TEABF<sub>4</sub>-0.015M DTT [5].

The carbon paper substrates had an actual area thrice that of the geometrical area and in all calculations the latter was used. All electrode potential values reported in this paper are referred to Ag (a quasi reference electrode).

The supercapacitor prototypes were assembled by facing the two polymer electrodes at 2 mm distance using a Teflon spacer. For type I a pPy electrode potentiostatically charged at 0.8 V was coupled with a discharged one; for type II a pMeT electrode potentiostatically charged at 1.0 V was coupled with a discharged pPy one, and two pDTT discharged electrodes were coupled for type III.

A 273A PAR potentiostat/galvanostat and a 1255 HF Solartron frequency response analyzer were used for electrochemical characterization. All measurements were performed in a Labmaster 130 MBraun dry-box (oxygen and water content less than 1 ppm).

During supercapacitor cyclic voltage sweep (VS), there is no electrode potential control as there is during single electrode cyclic voltammetry (CV), but we verified by a reference electrode that the electrode potentials were in the polymer doping domains.

## RESULTS AND DISCUSSION

ECP-based supercapacitors will provide significantly improved performance over double-layer capacitors only if thick polymer films can be doped in an efficient way; here polymer films electrosynthesized with  $2.5 \text{ C cm}^{-2}$  were used in all supercapacitor configurations.

The symmetric supercapacitor (I) involves in the fully charged state one pPy electrode in fully p-doped state and the other in the undoped state, whereas in the completely discharged supercapacitor both electrodes are at a half-p-doped state. Hence, only one-half of the total p-doping charge of pPy (figure 1a shows the pPy electrode's CV at  $10 \text{ mV s}^{-1}$ ) can be delivered and stored by the operating device.

The unsymmetric supercapacitor (II) based on pPy and pMeT, p-dopable polymers over different potential ranges (figure 1b shows the CVs of the two polymers at  $10 \text{ mV s}^{-1}$ ), involves in the completely charged state the pMeT in the fully p-doped state and the pPy in the undoped state, whereas when it is discharged both pMeT and pPy electrodes are partially p-doped. The charge involved in this type of supercapacitor is related to the potential difference between the domains of p-doping of the two polymers.

The symmetric device (III) based on p- and n-dopable pDTT inside the electrochemical stability window of the PC-TEABF<sub>4</sub>, as shown in figure 1c, involves in the fully discharged supercapacitor both pDTT electrodes in the undoped state, whereas in the charged state one pDTT electrode is p-doped and the other n-doped. The advantages of this latter configuration are that all the doping charge can be released by the operating supercapacitor and that it is

delivered at high potential because of the separation between p-doping and n-doping potential domains. This configuration is thus the most promising in terms of power and energy.

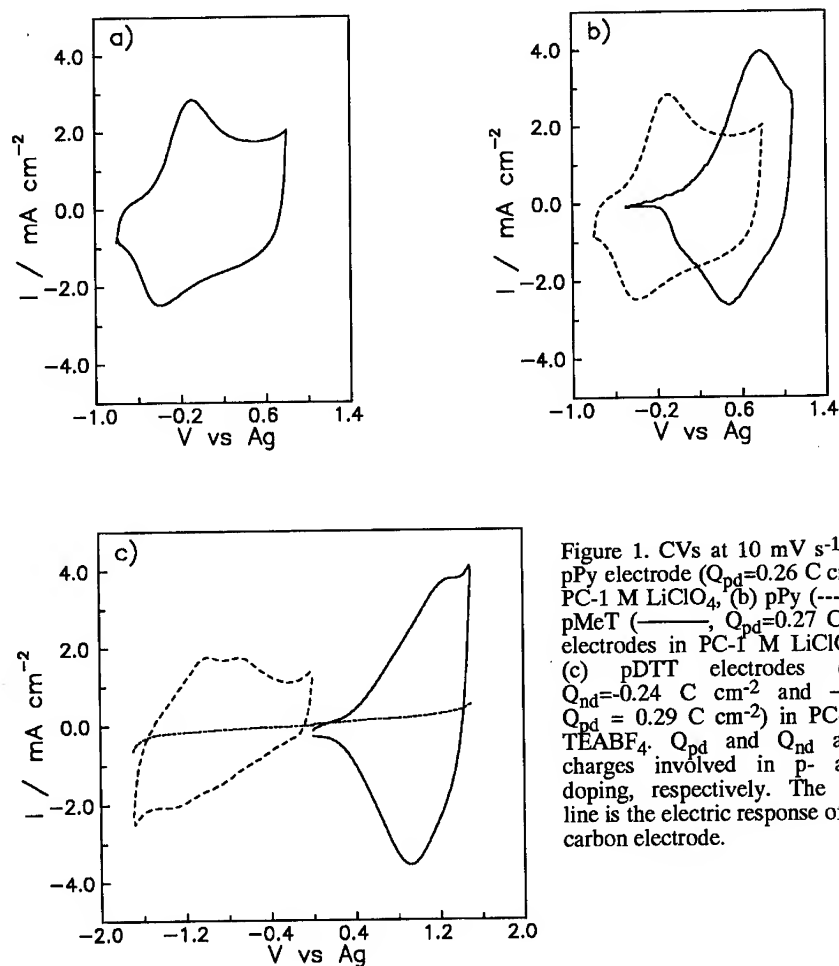


Figure 1. CVs at  $10 \text{ mV s}^{-1}$  of (a) pPy electrode ( $Q_{\text{pd}}=0.26 \text{ C cm}^{-2}$ ) in PC-1 M  $\text{LiClO}_4$ , (b) pPy (-----) and pMeT (—,  $Q_{\text{pd}}=0.27 \text{ C cm}^{-2}$ ) electrodes in PC-1 M  $\text{LiClO}_4$  and (c) pDTT electrodes (-----,  $Q_{\text{pd}}=0.24 \text{ C cm}^{-2}$  and —,  $Q_{\text{pd}}=0.29 \text{ C cm}^{-2}$ ) in PC-0.2 M  $\text{TEABF}_4$ .  $Q_{\text{pd}}$  and  $Q_{\text{nd}}$  are the charges involved in p- and n-doping, respectively. The dashed line is the electric response of a bare carbon electrode.

Figure 2 shows the VSs of the three supercapacitor types at different sweep rates scaled by dividing by the scan rate to enable the direct evaluation of device capacitances. The electric responses of types I and II, unlike that of III, resemble a circuit's having a capacitor in series with a resistor. These patterns are sweep rate dependent but the amount of stored-delivered charge at fast sweep rate is still high enough to be of practical interest. At high sweep rates the experimental time scale approaches the circuit time constant, and hence the total resistance value of these supercapacitors is low but not low enough to make the curves coalesce towards a square shape.

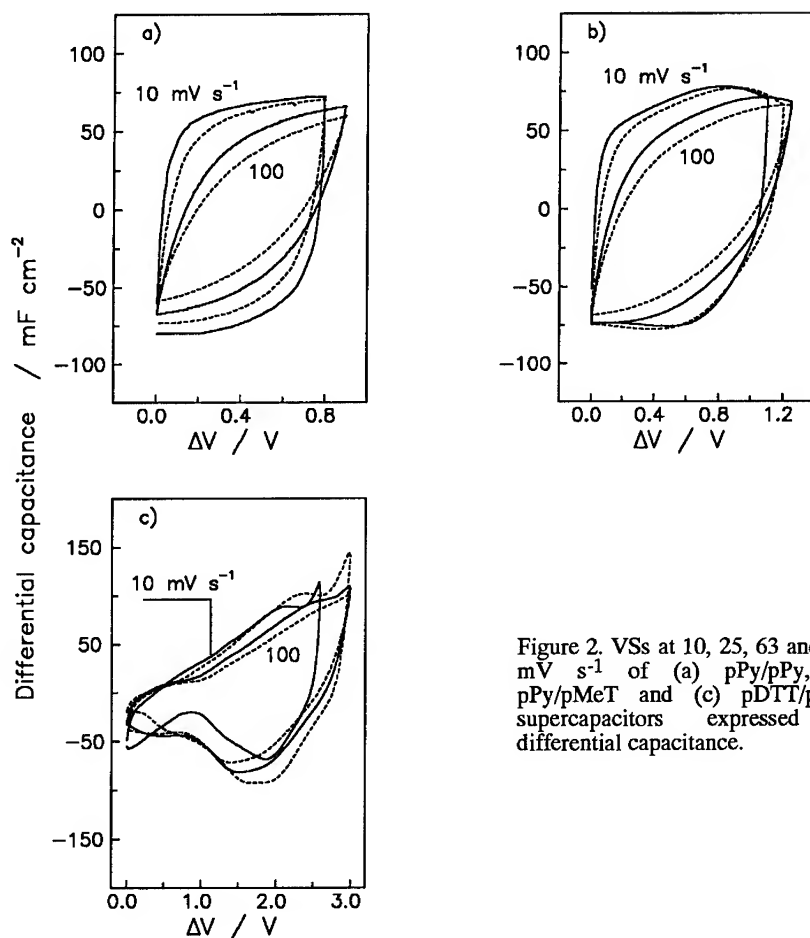


Figure 2. VSs at 10, 25, 63 and 100  $\text{mV s}^{-1}$  of (a) pPy/pPy, (b) pPy/pMeT and (c) pDTT/pDTT supercapacitors expressed as differential capacitance.

We tested the performance of these devices under galvanostatic discharge conditions and figure 3 displays the discharge curves at increased current density up to  $16 \text{ mA cm}^{-2}$ . The pPy/pPy, pPy/pMeT and pDTT/pDTT supercapacitors were charged at 1.1, 1.15 and 3 V with  $0.11$ ,  $0.12$  and  $0.23 \text{ C cm}^{-2}$ , respectively. Figure 3 shows that pDTT/pDTT supercapacitor performs best in terms of energy and power values.

The stored-delivered charge (coulombic efficiency values about 100%) by supercapacitor III during repeated galvanostatic cycles at  $8 \text{ mA cm}^{-2}$  between 0 and 3 V was also tested and the data reported in figure 4 demonstrate the cycling stability of this device. Repeated galvanostatic cycles at different current densities are in progress to test the stability of all three supercapacitors over a longer cycle number.

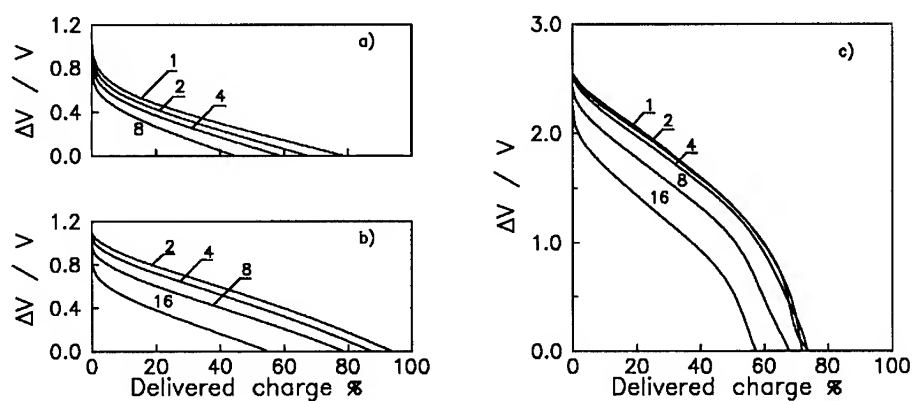


Figure 3. Galvanostatic discharge curves at different current densities ( $\text{mA cm}^{-2}$ ) of (a) pPy/pPy (stored charge  $0.11 \text{ C cm}^{-2}$ ), (b) pPy/pMeT (stored charge  $0.12 \text{ C cm}^{-2}$ ) and (c) pDTT/pDTT (stored charge  $0.23 \text{ C cm}^{-2}$ ) supercapacitors.

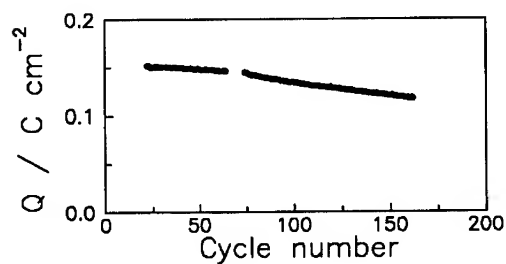


Figure 4. Stored-delivered charge by the pDTT/pDTT supercapacitor during repeated galvanostatic cycles at  $8 \text{ mA cm}^{-2}$  between 0 and 3 V.

A.c. impedance spectroscopy was used to get a measure of the resistance associated with the charging-discharging processes, and impedance experiments were performed on either the single polymer electrode (3-electrode mode) or the supercapacitor (2-electrode mode). Figure 5 shows impedance spectra in 3-electrode mode of partially doped polymers (p and n-doped) at potential values for which the circuit parameters become almost constant. The spectra were analyzed on the basis of a modified Randles circuit using a fitting procedure [6] based on two separate subcircuits for data in the high and the low frequency regions. To account for deviation from ideal behaviour, the capacitance and the Warburg impedance were replaced by a constant-phase element (CPE) with the impedance  $Z_{\text{CPE}} = Y_0^{-1}(j\omega)^{-\eta}$ .

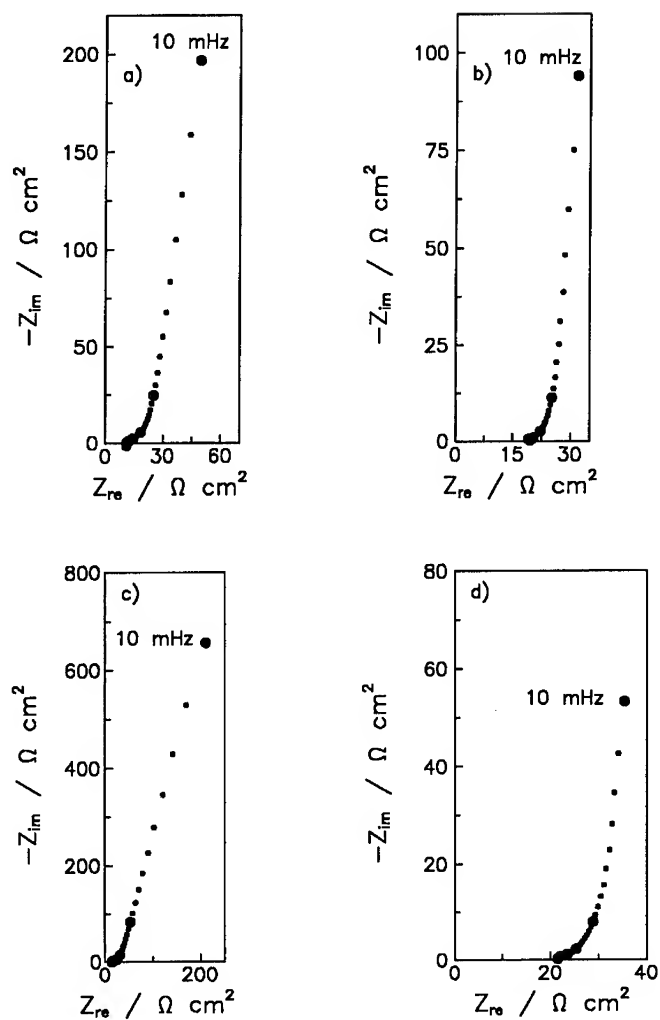


Figure 5. Impedance spectra (3-electrode mode) from 10 kHz to 10 mHz of (a) p-doped pPy at 0.4 V vs Ag, (b) p-doped pMeT at 0.8 V vs Ag, (c) n-doped pDTT at -1.2 V vs Ag and (d) pDTT at 0.8 V vs Ag.

Some resulting parameters are summarized in table 1:  $R_{\Omega}$  (electrolyte resistance between the reference and working electrode),  $R_{ct}$  (charge transfer resistance),  $R_L$  (resistance representing the dissipative part of the finite diffusion process of the counterions in the

polymer), and  $Y_{OL}$  and  $n$  values, which are representative of the limit capacitance. Table 1 shows that the charge transfer resistances are low, as is the energy dissipation for diffusion processes, which is in the order of  $pMeT \approx pDTT(p) < pPy < pDTT(n)$ ; an important part of the total resistance is due to the  $R_{\Omega}$  values. Impedance spectra of the supercapacitors in the two-electrode mode also evinced that the main part of the internal resistance is due to the electrolyte resistance. Hence, improved power data are expected with optimized design of these supercapacitors, in which very thin layers of electrolyte will be used.

Table 1. Refined parameters from impedance spectra of figure 5.

	E V vs Ag	$R_{\Omega}$ $\Omega cm^2$	$R_{ct}$ $\Omega cm^2$	$R_L$ $\Omega cm^2$	$Y_{OL}$ $mF cm^{-2} s^{n-1}$	$n_L$
pPy	0.4	11	0.5	10	62	0.91
pMet	0.8	18	1.3	5	144	0.94
pDTT(n)	-1.2	13*		27	18	0.90
pDTT(p)	0.8	21	3.1	4	227	0.90

\*  $R_{\Omega} + R_{ct}$

The results of the supercapacitor discharge curves were used to evaluate the performance of these polymer-based supercapacitors in terms of energy and power density. The data, which take into account only the weight of the active polymers, are reported in a Ragone plot in figure 6. Given that the mid-term requisites fixed by the DOE for supercapacitor modules are  $E > 5 \text{ Wh kg}^{-1}$  and  $P > 500 \text{ W kg}^{-1}$ , figure 6 indicates that these polymer-based supercapacitors are high-performance devices.

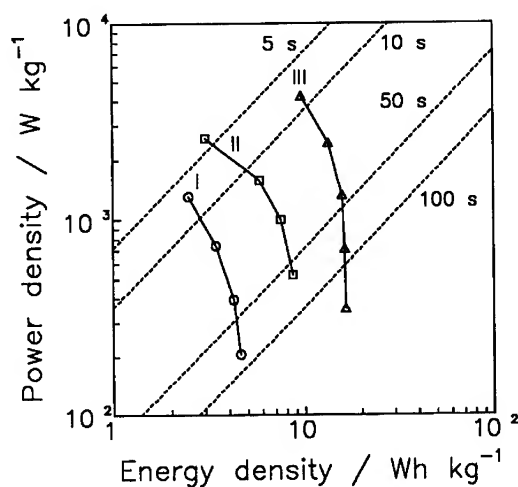


Figure 6. Ragone plot of pPy/pPy (I), pPy/pMeT (II) and pDTT/pDTT (III) supercapacitors. The dotted lines show the discharge time scale.



## CONCLUSIONS

Our data, even if preliminary, clearly demonstrate the reliability of all three schemes of polymer supercapacitors. Improved performance of the tested devices should be achieved by optimizing their design and using polymer films grown on high-area carbon paper with an electropolymerization charge greater than  $2.5 \text{ C cm}^{-2}$ , and work is in progress. Type III, particularly for its high operating potential, is a very promising supercapacitor; given that the impedance measurements showed that its performance is controlled by the n-doping process, our future research will address the optimization of pDTT preparation and the development of new, truly efficient n-dopable polymer materials.

## ACKNOWLEDGEMENTS

We would like to thank Dr. M. Catellani, Istituto di Chimica delle Macromolecole, CNR, Milan (Italy) for kindly providing DTT and CNR, Progetto Strategico *Batterie leggere per auto elettriche. Supercapacitori redox* for financial support.

## REFERENCES

1. B.E. Conway, Proc. Electrochem Soc., **93-23**, 15 (1993)
2. A. Rudge, J. Davey, S. Gottesfeld and J.P. Ferraris, Proc. Electrochem. Soc., **93-23**, 74 (1993)
3. M. Mastragostino, L. Soddu, Electrochim. Acta, **35**, 463 (1990)
4. A. Bolognesi, M. Catellani, S. Destri R. Zamboni and C. Taliani, J. Chem. Soc., Chem. Comm., 246 (1988)
5. C. Arbizzani, M. Catellani, M. Mastragostino and C. Mingazzini, Electrochim. Acta, submitted
6. M. Mastragostino, L. Meneghello and P. Ferloni, Electrochim. Acta, to be submitted

## SENSORS FOR ACID-BASE-ACTIVE GASES

JOACHIM MAIER\*, MICHAEL HOLZINGER\*, AND WERNER SITTE\*\*

\*Max-Planck-Institut für Festkörperforschung, Heisenbergstr. 1, 70569 Stuttgart, Germany

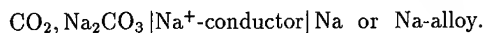
\*\*Institut für Physikalische und Theoretische Chemie, Technische Universität Graz, Rechbauerstraße 12, A-8010 Graz, Austria

### ABSTRACT

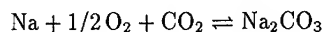
The theoretical background for potentiometric and conductometric (bulk and surface) sensors is briefly discussed with regard to the usual application, viz. the detection of redox-active gases, and the importance of understanding chemical diffusion is stressed in this context. It is then shown how the analogous concept applied to acid-base interactions leads to powerful possibilities to measure partial pressures of acid-base active gases such as CO<sub>2</sub>, NH<sub>3</sub> and H<sub>2</sub>O. Two examples of novel sensor principles are discussed: i) The response of the surface ionic conductivity of AgCl or CaF<sub>2</sub> upon changes of partial pressures of (Lewis) basic or acid gases can be used to sense NH<sub>3</sub> and BF<sub>3</sub>. ii) In the major part of the paper it is shown how the deliberate use of overall acid-base cell reactions in potentiometric arrangements leads to a fast and precise CO<sub>2</sub>-sensor. For this purpose, open reference electrodes based on Na<sub>2</sub>Ti<sub>6</sub>O<sub>13</sub> or Na<sub>2</sub>SnO<sub>3</sub> have been constructed. Owing to the criteria developed in the text the whole cell can be exposed to a CO<sub>2</sub> and O<sub>2</sub> containing atmosphere without the necessity of sealing. Detailed results are given.

### INTRODUCTION

Chemical sensor principles given in the literature are almost exclusively relying on redox interactions. Oxygen concentration cells using a ZrO<sub>2</sub>(Y<sub>2</sub>O<sub>3</sub>) electrolyte are typical examples of potentiometric sensors of this type. Conductometric sensors normally make use of changes of the electronic bulk (e.g. O<sub>2</sub>/SrTiO<sub>3</sub>) or surface conduction (O<sub>2</sub> or CO/SnO<sub>2</sub>) upon partial pressure changes of redox-active gases such as oxygen or carbon monoxide. Even in the case of gases which act primarily in an acid-base active way these principles have been maintained. An example are CO<sub>2</sub> sensors of the type [1]



Here the cell reaction is clearly a redox reaction, namely



and as a consequence the signal is dependent on the oxygen partial pressure. Since the reference electrode must be carefully protected against both O<sub>2</sub> and CO<sub>2</sub>, the materials problems are tremendous. The discussion in the section "Chemical Sensors for Acid-Base-Active Gases II" shows that this is an unnecessary fundamental and technical complication. Below it is pointed out how a systematic translation of sensor-principles relevant for redox-active gases to the acid-base situation can be used to design appropriate sensing modes for

gases such as CO<sub>2</sub> or NH<sub>3</sub>.

## CHEMICAL SENSORS FOR REDOX-ACTIVE GASES

### Potentiometric Sensors

A redox-active gas in the following denoted by E<sub>2</sub> (elemental gas) undergoes a redox-reaction of the form ( $n \leq 0$ )



with the equilibrium condition ( $\mu$  and  $\tilde{\mu}$ : chemical and electrochemical potentials, respectively)

$$\frac{1}{2}\mu_{E_2} + n\tilde{\mu}_{e^-} = \tilde{\mu}_{E^{n-}}. \quad (2a)$$

Referring to the same locus ( $\phi = \text{const}$ ) it may be simplified to

$$\frac{1}{2}\mu_{E_2} + n\mu_{e^-} = \mu_{E^{n-}}. \quad (2b)$$

A potentiometric sensor is an electrochemical cell the overall reaction of which contains the species E to be detected. Since the solid electrolyte is ionically conducting  $\nabla\tilde{\mu}_{E^{n-}} = 0$ . However, the gradient of the electrochemical potential of the electrons is non-zero and, due to Eq. (2), proportional to  $\nabla\mu_E$ . Integration yields the cell voltage as a function of  $\mu_E$ :

$$E \propto \Delta\tilde{\mu}_{e^-} \propto \Delta\mu_E \propto \Delta \ln P_{E_2}. \quad (3)$$

The summing up of the electrode reactions yields the cell reaction plus the difference of  $\tilde{\mu}$ -values of the electrons and of the transferred ion between anode and cathode. In terms of the electrochemical potentials, the last difference vanishes and the first yields the cell voltage such that (R: chemical overall reaction)

$$\frac{1}{2}E_2 \propto \Delta_R G = \alpha \ln P_{E_2} + \beta. \quad (4)$$

Eq. (4) is more useful than Eq. (3) since it also highlights the possibility of having other ions than E<sup>n-</sup> as the dominant ionic species in the solid electrolyte, which is directly obvious by coupling other equilibria to Eq. (3). This is a well-known result, in particular from liquid electrochemistry where the conducting ion is frequently not identical to the ion dominant in the electrode reactions. There is no difficulty as long as a thermodynamical convertibility (e.g. solubility) is guaranteed.

Examples of potentiometric sensors for O<sub>2</sub> are cells of the types



or Ag-activity cells (or Cl-activity cells) of the type



An additional electrolyte such as  $\text{Ag}_2\text{O}-\beta\text{-Al}_2\text{O}_3$  as proposed in the literature is not necessary.

### Bulk Conductometric Sensors

If  $\text{E}_2$  is dissolved completely in a given material, it changes by virtue of Eq. (1) the electronic and ionic defect concentrations and thus the respective partial conductivities. In the bulk the condition of electroneutrality is fulfilled. If the defects are dilute, we can write down ideal mass action laws and we obtain sectional solutions for the defect concentration in the form of power laws:

Thus

$$\ln \sigma = \alpha \ln P_{\text{E}_2} + \beta. \quad (5)$$

In Eq. (5) the prefactor  $\alpha$  which is very important for the sensitivity depends on the defect chemistry. For oxides such as  $\text{SrTiO}_3$  or  $\text{SnO}_2$  ( $\text{E}_2 = \text{O}_2$ ) at high temperatures  $|\alpha| = 1/4$  for an acceptor doped situation and  $1/6$  for an intrinsic situation. ( $\alpha = 0$  for a donor doped situation);  $\alpha$  can even be as high as  $1/2$  in  $\text{YBa}_2\text{Cu}_3\text{O}_6$  [2]. This type of conductivity sensors can be used at high temperatures, and competes, if thin film materials are used, with  $\lambda$ -sensors in cars.

### Surface Conductometric Sensors

At low temperatures the diffusivity or the reaction rate at the surface may not be high enough for the gaseous species to be introduced into the sample. Adsorbed species, however, also exert a conductivity effect. Oxygen, e.g. ( $\text{E}_2 = \text{O}_2$ ), adsorbed on a material such as  $\text{SnO}_2$  at room temperature traps electrons out of the boundary region; as a consequence in the n-type conductor depletion layers appear with increased surface resistance. Reducing gases such as  $\text{H}_2$  or  $\text{CO}$  have the opposite effect on n-conductors or the same on p-conductors [3]. As shown in Ref. [4], however, ionic defect concentrations may also play an important role with regard to the effect.

For a quantitative treatment we start from Eq. (2a). In phase and contact equilibrium both  $\nabla \mu_{\text{E}}$  and  $\nabla \tilde{\mu}_{\text{e}^-}$  are zero but  $\nabla \mu_{\text{e}^-}$  is non-zero constituting space charge regions. It holds e.g. for the conduction electrons ( $c_{\text{n}}$  = concentration of conduction electrons)

$$\nabla \ln c_{\text{n}} \propto \nabla (\tilde{\mu}_{\text{e}^-} - \tilde{\mu}_{\text{n}}^{\circ}) \propto \nabla (\text{E}_{\text{F}} - \text{E}_{\text{CB}}) \quad (6)$$

( $\text{E}_{\text{F}}$  (or  $\tilde{\mu}_{\text{e}^-}$ ),  $\text{E}_{\text{CB}}$  (or  $\tilde{\mu}_{\text{n}}^{\circ}$ ) : Fermi-level, conduction band edge). In addition the Poisson-equation no longer reduces to the equation of local electroneutrality. Generally speaking the extent of the effect is governed by the "degree of influence" [5]

$$\vartheta = \frac{(c_0/c_{\infty})^{1/2} - 1}{(c_0/c_{\infty})^{1/2} + 1} \quad (7)$$

and the Debye-length  $\lambda \propto c_{\infty}^{-1/2}$  ( $c_0$ : boundary value in the space charge layer,  $c_{\infty}$ : bulk value). In the case of an accumulation effect, the excess parallel conductance is given by

[5,6]

$$\Delta Y^{\parallel} = (2\lambda)(2c_{\infty})uF\vartheta/(1 - \vartheta) \quad (8)$$

and in the case of a depletion effect the excess perpendicular resistance by [6,7]

$$\Delta Z^{\perp} = -(2\lambda)2(c_{\infty}uF)^{-1}\vartheta/(1 + \vartheta). \quad (9)$$

(u: mobility)

Under simplified conditions again a linear relationship of the form [8]

$$\ln(\Delta\sigma^{\parallel,\perp}) \simeq \alpha^{\parallel,\perp} \ln P_{E_2} + \beta^{\parallel,\perp} \quad (10)$$

holds with  $\alpha^{\parallel}, \alpha^{\perp}; \beta^{\parallel}, \beta^{\perp}$  not necessarily being equal. The exact evaluation of the  $\ln \Delta\sigma$  vs.  $\ln P_{E_2}$  relationship is a problem of the defect chemistry in boundary regions which is at present under more detailed investigation. In the case of ZnO or SnO<sub>2</sub> it could be shown that  $\alpha^{\parallel,\perp}$  is roughly half the bulk value at high T, thus being 1/8 rather than 1/4 [8].

#### Kinetic Problems

The kinetics of the chemical sensors is determined by the rate constants at the interfaces as well as by the chemical diffusion coefficients. In the case of SrTiO<sub>3</sub> bulk conductivity sensors the chemical diffusion coefficient of oxygen determines the response time at high temperatures and/or thick samples, whereas the response time at low T and/or thin films is determined by the effective rate constants. Recently these parameters could be precisely measured in situ by an optical absorption technique [9]. (The effective rate constant determined by tracer techniques is not necessarily identical with the desired rate constants for oxygen incorporation!) In the surface conductivity sensing mode the response time is given by the rate constants of the interfacial reactions whereas the chemical diffusion coefficient is a decisive parameter for the drift. In the case of potentiometric sensors again the electrode reaction kinetics determines the response time whereas the chemical diffusion problem plays a role for gas leakage. The same optical technique could also be applied to YSZ and in both cases it could be shown that the interpretation of  $\tilde{D}$  demands the inclusion of internal redox reactions in the form of impurity or self-trapping of carriers in the thermodynamic factor [10]. In turn this enables to tune the  $\tilde{D}$ -values. E.g., in the case of bulk conductivity sensors, the material should be as free as possible of redox-active impurities whereas in the case of boundary sensors impurity trapping is favorable. The knowledge of the oxygen incorporation kinetics also allows one to optimize the electrode materials [9].

#### CHEMICAL SENSORS FOR ACID-BASE-ACTIVE GASES I: SURFACE CONDUCTIVITY SENSORS USING IONIC CONDUCTORS

In the present paper the term acid-base interaction of a species Y means by analogy to Eq. (1), the interaction with ions rather than with electrons [11] according to



with the equilibrium condition

$$\mu_Y + \tilde{\mu}_{E^{n-}} = \tilde{\mu}_{YE^{n-}}. \quad (12a)$$

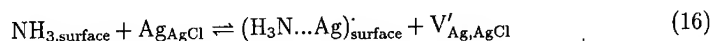
If the electrical potential is the same for all species involved (i.e. bulk or same locus) Eq. (12a) simplifies to

$$\mu_Y + \mu_{E^{n-}} = \mu_{YE^{n-}}. \quad (12b)$$

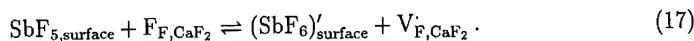
Examples are



It is obvious that the principle discussed in the subsection "Surface Conductometric Sensors" can be generalized to acid-base interactions by measuring the surface conductivity of ionic conductors. Two examples to be mentioned in this context are the conductivity changes of AgCl due to changes in the  $\text{NH}_3$  (or  $(\text{CN})_2$ ) partial pressure [12] as well as the analogous effect of  $\text{SbF}_5$  or  $\text{BF}_3$  [13] on  $\text{CaF}_2$ . The relevant defect reactions are:



and



In such cases vacancy enriched space charge regions appear. Figure 1 displays the relevant situation. The theoretical background is discussed in detail in the literature [6]. Again the

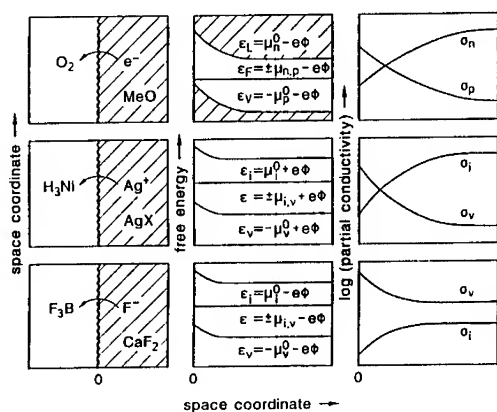


Figure 1: Center and bottom: Level bending and conductivity effects of acid-base active gases in contact to ionically conducting materials ( $\text{AgCl}$ :  $i = \text{Ag}_i'$ ,  $v = V'_{\text{Ag}}$ ;  $\text{CaF}_2$ :  $i = F_i'$ ,  $v = V_F'$ ). Top: Electronic analogue for redox active gases.

interaction of the ions can be discussed in terms of the "degree of influence" (Eq. (7) [5]). The band bending has to be replaced by a level bending (see Fig. 1). Under simplified conditions again an equation of the form

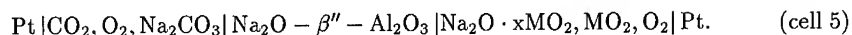
$$\ln \Delta \sigma^{\parallel, \perp} = \alpha^{\parallel, \perp} \ln P_Y + \beta^{\parallel, \perp} \quad (18)$$

can be derived. In the case of  $\text{AgCl}$  the measurements must be performed at elevated temperatures above the existence range of possible  $\text{AgCl-NH}_3$  compounds. The pressure dependence of the  $\sigma$ -response in the case of a polycrystalline film is more complicated and

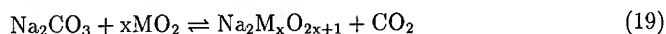
involves microstructural effects (see Ref. [12]). In this field a large variety of possibilities opens for the construction of new chemical sensors. Especially the use of proton conductors should render possible the detection of Brønsted-acid-base gases.

## CHEMICAL SENSORS FOR ACID-BASE-ACTIVE GASES II: POTENTIOMETRIC SENSORS WITH OPEN REFERENCE ELECTRODES

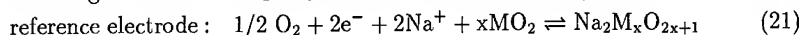
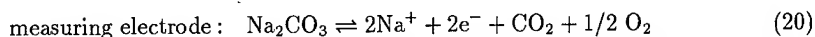
As long as electronic electrodes are used, the electrode reactions are certainly redox-reactions. However, the overall cell reaction can be made a pure acid-base interaction [11,14]. Following these considerations a potentiometric sensor for gaseous  $\text{CO}_2$  can be designed as follows:



The sodium oxide activity on the measuring electrode is determined by the partial pressure of  $\text{CO}_2$  (in contact with  $\text{Na}_2\text{CO}_3$ ), on the reference side it is fixed by the two phase mixture  $\text{Na}_2\text{O} \cdot x\text{MO}_2 (= \text{Na}_2\text{M}_x\text{O}_{2x+1})/\text{MO}_2$ . The cell reaction



can be regarded as an acid-base-interaction of the basic  $\text{Na}_2\text{CO}_3$  reacting with the acidic  $\text{MO}_2$  to form  $\text{Na}_2\text{M}_x\text{O}_{2x+1}$  and  $\text{CO}_2$ . Although  $\text{O}_2$  is participating in the electrode reactions:



its influence cancels on both sides, and therefore does not appear in the overall cell reaction. The emf of the cell is given by

$$E = E^\circ - \frac{RT}{2F} \ln \left( \frac{p_{\text{CO}_2}}{p^\circ} \right) \quad (22)$$

with

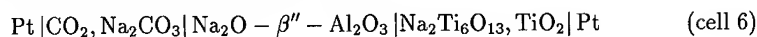
$$E^\circ = -\frac{\Delta_R G^\circ}{2F}. \quad (23)$$

The sensor signal is independent of the partial pressure of  $\text{O}_2$  as long as it is the same on both electrodes. This is one necessary condition for being able to expose the galvanic cell to the atmosphere to be measured without sealing the reference electrode. In order to guarantee that  $\text{CO}_2$  does not react with the reference electrode (this is the second requirement) the condition

$$\Delta_R G = \Delta_R G^\circ + RT \ln \left( \frac{p_{\text{CO}_2}}{p^\circ} \right) \leq 0 \quad (24)$$

( $\Delta_R G$  being the Gibbs energy of the cell reaction) must be fulfilled in the temperature and  $\text{CO}_2$ -partial pressure range chosen. The oxide  $\text{MO}_2$  must be sufficiently acidic in order to keep  $\Delta_R G$  negative. In addition, the component  $\text{Na}_2\text{M}_x\text{O}_{2x+1}$  must be stable against  $\text{MO}_2$ . Besides, phase compatibility of  $\text{Na}_2\text{M}_x\text{O}_{2x+1}$  and  $\text{MO}_2$  with the solid electrolyte has to be ensured.

The systems  $\text{Na}_2\text{Ti}_6\text{O}_{13}/\text{TiO}_2$  and  $\text{Na}_2\text{SnO}_3/\text{SnO}_2$  were found to fulfil all these conditions and were incorporated into the galvanic cells as



and

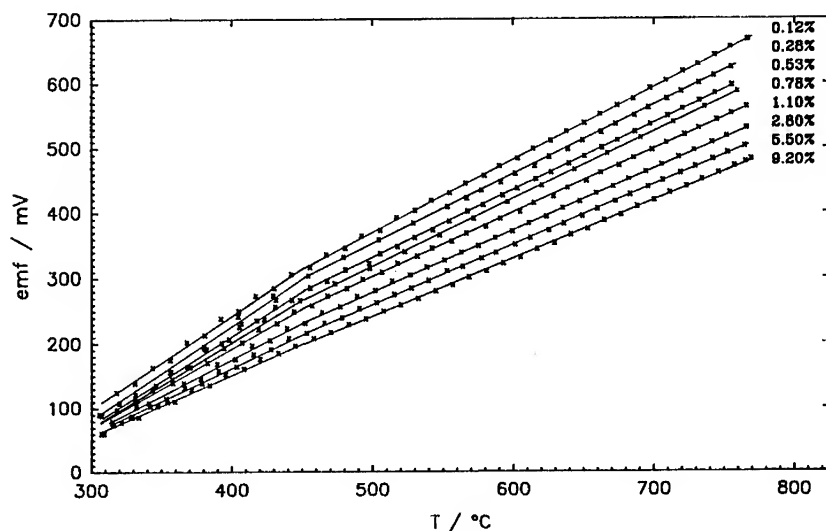
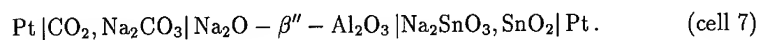


Figure 2: Temperature dependence of the sensor-signal of cell 6 for various partial pressures of  $\text{CO}_2$ .

Because of the thermodynamically well-defined state of the electrodes, the emf-signals obtained from cell 6 and cell 7 are stable and reproducible without any sealing. The potentiometric sensors were tested in the temperature range between 300 and 780°C,  $\text{CO}_2$ -partial pressures ranging from 0.1 to 9.2%.

Figure 2 shows the temperature dependence of the emf of cell 6 for various  $\text{CO}_2$ -partial pressures. The emf vs.  $T$  characteristic is very linear. There is an evident change of the slope at 450°C, which is due to the monoclinic/hexagonal phase transition of  $\text{Na}_2\text{CO}_3$  at this temperature.

The emf was also measured as a function of the  $\text{CO}_2$ -partial pressure at various temperatures. The emf vs.  $\ln p_{\text{CO}_2}$ -plot is shown in Fig. 3. The slopes of the straight lines are compared with those calculated from the Nernst-equation (22). The good agreement of experimental and theoretical values confirms the assumption of a 2-electron-process.

The advantages of cell 6 are not only the stable, reproducible and  $p_{\text{O}_2}$ -independent emf-signals following the Nernst-equation, but also its very fast response. (Cell 7 is slightly more sluggish but still very fast.)



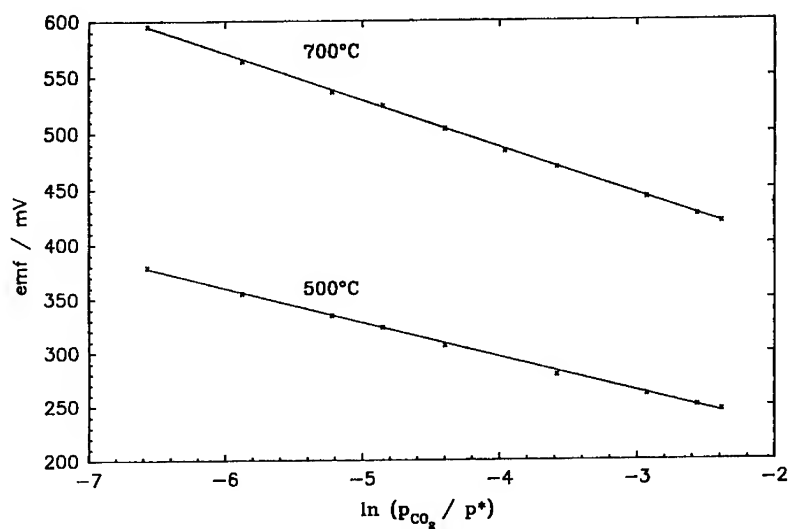


Figure 3: Emf response of cell 6 for various temperatures. The slopes of the experimental straight lines are equivalent to the theoretical values calculated from the Nernst-equation for a two-electron process ( $n = 2.0$ ).

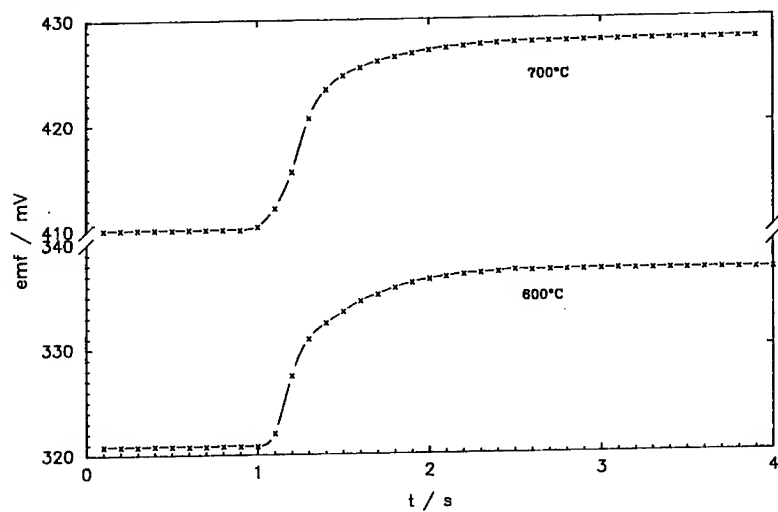


Figure 4: Response times of the sensor signal of cell 6 during a change of the CO<sub>2</sub> partial pressure from 90 to 60 mbar for two temperatures.

Figure 4 shows the emf response during a sudden change of the CO<sub>2</sub>-partial pressure (achieved by fast evacuation of the gas chamber) for various temperatures. Response times are in the range of 1-2 seconds, without any optimization in this respect and may possibly be further improved.

### CHEMICAL SENSORS FOR ACID-BASE-ACTIVE GASES III: BULK CONDUCTIVITY SENSORS

Clearly the analogue to the subsection "Bulk-conductometric Sensors" is the incorporation of the (complex) gaseous species Y in the bulk. Various perovskites, e.g., offer the possibility to dissolve H<sub>2</sub>O, and consequently have been proposed as humidity sensors [15]. The incorporation reaction can be written as the formation of internal OH-groups:



The resulting change of the proton conductivity can be measured. Again mass action laws lead to:

$$\ln \sigma = \alpha \ln P_Y + \beta \quad (26)$$

As long as  $[\text{V}_{\text{O}}^{\bullet\bullet}]$  is constant Sievert's law is fulfilled and  $\alpha = 1/2$ . Generally, the diffusion of complex species is slow and demands thin films. The chemical water diffusion demands a counter-diffusion of  $\text{V}_{\text{O}}^{\bullet\bullet}$  and  $\text{H}_i^{\bullet}$  (i.e.  $\text{OH}_{\text{O}}^{\bullet}$  defects). The values for BaCeO<sub>3</sub> (Gd<sub>2</sub>O<sub>3</sub>) have been measured in Ref. [16]. In the same way the dissolution of NH<sub>3</sub> may be considered in related materials. Owing to the complexity of the gases and the expected kinetic restrictions, surface conductivity sensors (as described in the section before the previous one) should be more favorable.

### CONCLUSIONS

It is shown that a systematic use of acid-base properties leads to new perspectives in the field of chemical sensors especially for those gases that cannot be easily or at least selectively detected by redox reactions. In particular: i) A fast and simple CO<sub>2</sub> sensor is designed and verified in this context, which can be exposed in its entirety to the ambient atmosphere without sealing and which is not affected by pO<sub>2</sub>; ii) the use of ionic conductors in the case of surface-conductometric sensors opens new possibilities for the detection of acid-base-active gases. A case is made for NH<sub>3</sub>, (CN)<sub>2</sub>, BF<sub>3</sub> and SbF<sub>5</sub>.

### References

1. J. Liu, W. Weppner, Solid State Chem. **76**, 311 (1990); H. Schettler, J. Liu, W. Weppner, R.A. Huggins, Appl. Phys. A, **57**, 31 (1993).
2. J. Maier, P. Murugaraj, G. Pfundtner, W. Sitte, Ber. Bunsenges. Phys. Chem. **93**, 1359 (1989); J. Maier, H.L. Tuller, Phys. Rev. B, **47**, (13), 8105-8110 (1993).
3. W. Göpel, Progr. Surface Sci. **20**, 1 (1986).

4. W. Göpel, J. Maier, K. Schierbaum, and H.-D. Wiemhöfer, *Solid State Ionics*, **32/33**, 440 (1989).
5. J. Maier, *J. Phys. Chem. Solids*, **46**, 309 (1985).
6. J. Maier in *Recent Trends in Superionic Solids and Solid Electrolytes*, edited by S. Chandra, A. Laskar (Academic Press, New York, 1989) p. 137.
7. J. Maier, *Ber. Bunsenges. Phys. Chem.* **90**, 26 (1986).
8. J. Maier, *Solid State Ionics*, **32/33**, 727 (1989).
9. T. Bieger, J. Maier, and R. Waser, *Ber. Bunsenges. Phys. Chem.* **97** (9), 1098-1104 (1993); I. Denk, W. Münch, J. Maier, in preparation.
10. T. Bieger, H. Yugami, N. Nicoloso, J. Maier, and R. Waser, *Solid State Ionics*, **72**, 41 (1994).
11. J. Maier, *Solid State Ionics*, **62** (1,2), 105-111 (1993).
12. J. Maier, U. Lauer, *Ber. Bunsenges. Phys. Chem.* **94**, 973 (1990).
13. Y. Saito, K. Hariharan and J. Maier, *Proc. 4th Int. Symp. on Syst. with Fast Ionic Transport*, in press.
14. J. Maier, M. Holzinger, W. Sitte, *Solid State Ionics*, in press.
15. H. Iwahara, H. Uchida and J. Kondo, *J. Appl. Electrochem.* **13**, 365 (1983).
16. K.-D. Kreuer, E. Schönherr, and J. Maier, *Solid State Ionics*, **70/71**, 278 (1994).

## VAPOR DEPOSITION OF THIN-FILM Y-DOPED $\text{ZrO}_2$ FOR ELECTROCHEMICAL DEVICE APPLICATIONS

Brandon W. Chung, Eric L. Brosha, David R. Brown, and Fernando H. Garzon.  
Los Alamos National Laboratory, Los Alamos, N.M. 87545

### ABSTRACT

The growth of high-quality, pin-hole free, yttrium doped  $\text{ZrO}_2$  thin films is of great interest for a variety of electrochemical applications such as fuel cells and oxygen gas separation devices. In the work, we have grown polycrystalline thin films of yttrium doped  $\text{ZrO}_2$  on thick porous  $\text{Al}_2\text{O}_3$  substrates in multilayer  $\text{La}_{1-x}\text{Sr}_x\text{MEO}_3/\text{YSZ}/\text{La}_{1-x}\text{Sr}_x\text{MEO}_3$  (ME = Mn, Co) configurations using a combination of single-target RF magnetron sputtering and electron beam physical vapor deposition techniques. The structure and morphology of these films have been studied using X-ray diffraction, and Scanning Electron Microscopy techniques. The ionic conductivity of the thin films has been measured using AC impedance analysis.

### INTRODUCTION

Solid oxide electrolytes based on yttria-stabilized zirconia (YSZ) is widely used in applications such as oxygen sensors, solid oxide fuel cells, oxygen pumps, electrocatalytic reactors, and electrochemically driven oxygen separation membranes. However, bulk YSZ is used in these applications. This requires high operating temperatures in order to minimize ohmic loss. One alternative of overcoming this problem is to use a thin film of the electrolyte. The thin films of YSZ would exhibit lower resistance and hence greater oxygen flux at similar temperatures, enabling their use at reduced operating temperatures. Thus, there has been increased recent interest in thin films of stabilized zirconia [1-4]. In order to make thin-film solid oxide electrolyte applicable, it is necessary to establish a method for forming thin films on porous substrates.

In this study, we report the structure, morphology, and conductivity of the thin films of  $\text{La}_{1-x}\text{Sr}_x\text{MEO}_3/\text{YSZ}/\text{La}_{1-x}\text{Sr}_x\text{MEO}_3$  (ME = Mn, Co) deposited on porous alumina substrates.

### EXPERIMENTAL

We have deposited  $\text{La}_{0.8}\text{Sr}_{0.2}\text{CoO}_3$  and  $\text{La}_{0.84}\text{Sr}_{0.16}\text{MnO}_3$  films by using  $90^\circ$  off-axis radio-frequency (RF) magnetron sputtering [5] from a single 2-inch-diameter, hot-pressed stoichiometric target (purchased from Seattle Specialty Ceramics) on porous alumina substrates (purchased from Coors Ceramics with approximate porosity of 20%).

The substrate heater was maintained at a temperature of 700°C during the deposition of La-based perovskite oxides. All of the depositions of perovskites were carried out at an RF power of 100W with total pressure of 40 mTorr (75% argon and 25 % oxygen). The electron beam physical vapor deposition technique was used to produce thin films of yttria-stabilized zirconia (YSZ) on  $\text{La}_{1-x}\text{Sr}_x\text{MEO}_3$  (ME = Mn, Co) layers. All the depositions were carried out with  $\text{ZrO}_2$  doped with 7.3 mole percent yttrium (purchased from International Advanced Materials) at a substrate temperature of 800°C. The top layer of La-based perovskite oxides were produced using the same condition as the bottom layer to form a single cell. Figure 1 shows the top view of the cell observed with an optical microscope. The cells were demonstrated to be open circuit at room temperature.

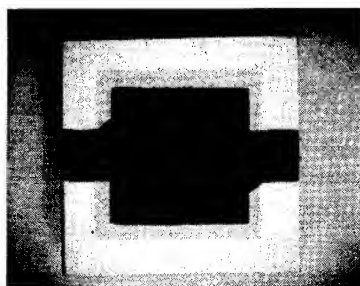


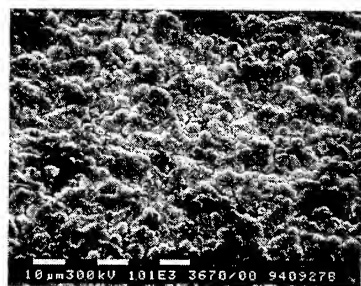
Figure 1. The top view of the multilayer device (1cm  $\times$  1cm)

We employed X-ray diffraction and Scanning Electron Microscopy techniques to study the structure and morphology of these films. The ionic conductivity of the YSZ thin films has been measured using AC impedance analysis using Solartron 1260 Frequency Response Analyzer in the frequency range between 0.1 Hz and 1 MHz.

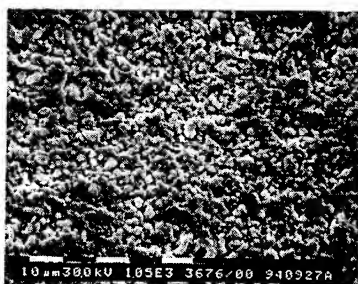
## RESULTS AND DISCUSSION

The thickness and stoichiometry of La-based perovskite oxides were obtained using Rutherford backscattering spectroscopy (RBS). The thickness of the perovskite oxides was between 16 and 18  $\mu\text{m}$  (deposition rate of 2000  $\text{\AA}/\text{hour}$ ). The compositions of the films were revealed to be close to the nominal values. The thickness of deposited YSZ was between 14 and 15  $\mu\text{m}$  as determined by profilometer. Using energy dispersive spectroscopy (EDS), the yttrium concentration in zirconia was found to be 6.5 mole percent.

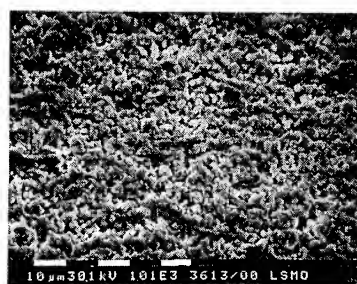
Fig. 2 shows a representative scanning electron micrograph of the deposited layers. The yttria-stabilized zirconia (YSZ) was shown to grow with similar surface morphology without visible pinholes on both  $\text{La}_{0.8}\text{Sr}_{0.2}\text{CoO}_3$  and  $\text{La}_{0.84}\text{Sr}_{0.16}\text{MnO}_3$  layers. However, the surface morphology of La-based perovskite oxide layers were found to be different. The  $\text{La}_{0.8}\text{Sr}_{0.2}\text{CoO}_3$  films were more dense and granular than the  $\text{La}_{0.84}\text{Sr}_{0.16}\text{MnO}_3$  films.



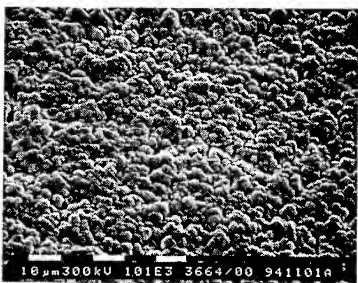
(a)



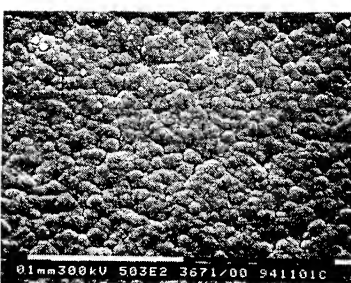
(b)



(c)



(d)



(e)

Figure 2. SEM micrograph of (a) YSZ layer, (b)  $\text{La}_{0.84}\text{Sr}_{0.16}\text{MnO}_3$  on  $\text{Al}_2\text{O}_3$ , (c)  $\text{La}_{0.84}\text{Sr}_{0.16}\text{MnO}_3$  on YSZ, (d)  $\text{La}_{0.8}\text{Sr}_{0.2}\text{CoO}_3$  on  $\text{Al}_2\text{O}_3$ , and (e)  $\text{La}_{0.8}\text{Sr}_{0.2}\text{CoO}_3$  on YSZ.

The x-ray diffraction patterns of a multilayer  $\text{La}_{1-x}\text{Sr}_x\text{MEO}_3/\text{YSZ}/\text{La}_{1-x}\text{Sr}_x\text{MEO}_3$  (ME = Mn, Co) depositions are shown in fig. 3. The diffraction patterns of yttrium doped zirconia layers on  $\text{La}_{0.84}\text{Sr}_{0.16}\text{MnO}_3$  and  $\text{La}_{0.8}\text{Sr}_{0.2}\text{CoO}_3$  were both assigned to cubic zirconia. The X-ray diffraction analysis indicates that  $\text{La}_{0.8}\text{Sr}_{0.2}\text{CoO}_3$  films are grown with rhombohedral structure while  $\text{La}_{0.84}\text{Sr}_{0.16}\text{MnO}_3$  films are shown to grow with cubic perovskite structure. However, after the AC impedance measurements at various

temperature, the x-ray diffraction pattern of  $\text{La}_{0.84}\text{Sr}_{0.16}\text{MnO}_3$  shows splitting of (111) peak indicating crystallographic transition to rhombohedral perovskite structure. Table I shows parameters obtained from x-ray analyses.

Table I. Structural parameters for YSZ thin film

	after deposition	after measurement
YSZ/ $\text{La}_{0.84}\text{Sr}_{0.16}\text{MnO}_3$	5.05 Å	5.08 Å
YSZ/ $\text{La}_{0.8}\text{Sr}_{0.2}\text{CoO}_3$	5.08 Å	5.09 Å

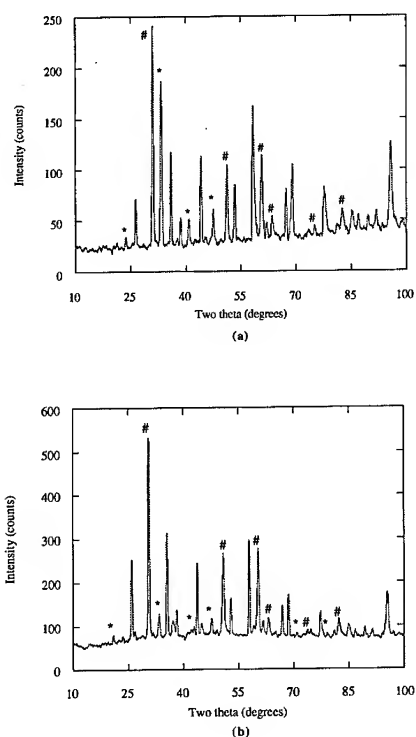


Figure 3. X-ray diffraction patterns of multilayers. (a)  $\text{La}_{0.84}\text{Sr}_{0.16}\text{MnO}_3/\text{YSZ}/\text{La}_{0.84}\text{Sr}_{0.16}\text{MnO}_3$ ; (b)  $\text{La}_{0.8}\text{Sr}_{0.2}\text{CoO}_3/\text{YSZ}/\text{La}_{0.8}\text{Sr}_{0.2}\text{CoO}_3$ . \* =  $\text{La}_{1-x}\text{Sr}_x\text{MEO}_3$  (ME=Mn, Co), # = YSZ.

The AC impedance measurements were done under open circuit condition on multilayers. The real and imaginary parts of the complex impedance are plotted in the complex plane and shown in Fig. 4 in the temperature range between 300°C and 800°C.

The AC impedance data were interpreted using an equivalent circuit model shown in figure 4. The offset from the origin is indicative of the presence of a purely resistive path at high frequency. The equivalent circuit is tentatively proposed to represent a simple model that simulates the experimentally observed frequency dispersion in fig. 4. It is comprised of a resistance at high frequency in series with parallel combinations of resistance, constant phase angle capacitive elements, and Warburg [6] impedances. The resistance at high frequency may be associated with the total YSZ electrolyte resistance. The total YSZ electrolyte conductivity obtained from the complex plane is shown in Fig. 5.

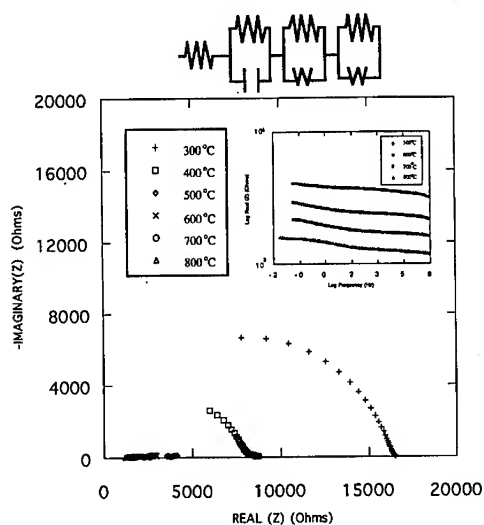


Figure 4. Frequency dispersion characteristic for  $\text{La}_{0.84}\text{Sr}_{0.16}\text{MnO}_3/\text{YSZ}/\text{La}_{0.84}\text{Sr}_{0.16}\text{MnO}_3$  multilayer with a proposed equivalent circuit model

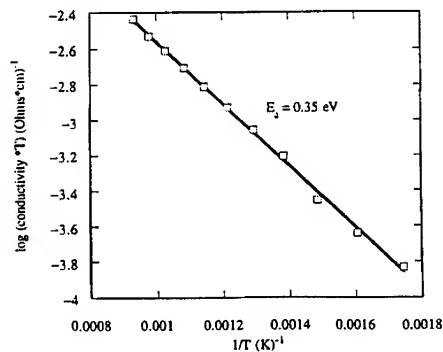


Figure 5. Arrhenius plot for the conductivity of YSZ thin film electrolyte.



## CONCLUSION

We have demonstrated that highly dense, pin-hole free, thin films of yttria-stabilized zirconia can be formed on thick porous  $\text{Al}_2\text{O}_3$  substrates in multilayer  $\text{La}_{1-x}\text{Sr}_x\text{MEO}_3/\text{YSZ}/\text{La}_{1-x}\text{Sr}_x\text{MEO}_3$  ( $\text{ME} = \text{Mn}, \text{Co}$ ) configurations using RF magnetron and electron beam physical vapor deposition techniques. The structure and morphology of each layer of these films have been studied. Cracks and pinholes were not detected with a scanning electron microscope. The ionic conductivity of the film of YSZ showed low activation energy of 0.35eV.

## REFERENCES

1. A. Negishi, K. Nozaki, and T. Ozawa, *Solid State Ionics*, **3/4**, 443 (1981)
2. E. T. Kim, J. W. Lee, S. H. Lee, and S. G. Yoon, *J. Electrochem. Soc.*, **140**, 2625 (1993)
3. H. Yamane and T. Hirai, *J. Crystal Growth*, **94**, 880 (1989)
4. U. B. Pal and S. C. Singhal, *J. Electrochem. Soc.*, **137**, 2937 (1990)
5. E. B. Eom, J. Z. Sun, K. Yamamoto, A. F. Marshall, K. E. Luther, S. S. Laderman, and T. H. Geballe, *Appl. Phys. Lett.*, **53**, 595 (1988)
6. E. Warburg, *Ann. Physik*, **67**, 493 (1899)

## IONIC CURRENT INDUCED MIGRATION OF A HOT SPOT IN $\text{GdBa}_2\text{Cu}_3\text{O}_{7-\delta}$ CERAMICS

T. OKAMOTO, B. HUYBRECHTS AND M. TAKATA

Nagaoka University of Technology, Nagaoka, Niigata, 940-21, Japan

### ABSTRACT

An electric field sensitive moving hot spot appeared when a dc voltage over 5 V was applied at room temperature to  $\text{GdBa}_2\text{Cu}_3\text{O}_{7-\delta}$  ceramic thin rods under oxygen partial pressures ranging from 0.05 to 1.00 atm (5 kPa to 100 kPa). The spot moved to the negative electrode, and the direction of movement could be reversed time after time by switching the positive and negative electrode. This is believed to be caused by electric field movement of oxygen ions, thereby generating an ionic current. The total current after the appearance of the hot spot was independent of the applied voltage for every oxygen partial pressure,  $P_{\text{O}_2}$ . However the current and spot velocity increased significantly with increasing  $P_{\text{O}_2}$ . By the best of the authors's knowledge this is the first report on the influence of the  $P_{\text{O}_2}$  on the moving hot spot. The potential use of this phenomenon as an oxygen sensor will be shown.

### INTRODUCTION

When a dc voltage above a critical value is applied to a  $\text{GdBa}_2\text{Cu}_3\text{O}_{7-\delta}$  ceramic thin rod, a visible distinct hot region, further referred to as hot spot, appears on the sample and moves towards the negative electrode as the authors already reported before [1]. Figure 1 shows a sequence photograph at 3 minute intervals after the appearance of the hot spot when a dc voltage of 9 V was applied to a sample in static air. The plus and minus marks show the direction of the applied voltage. The spot moved towards the negative electrode, and when the voltage direction was turned the other way, the spot reversed its movement towards the negative electrode. From the dependence of the spot size and the applied voltage, the resistivity in static air of the cold region was found to be  $0.015 \Omega\text{cm}$ , while the resistivity of the hot spot was  $0.205 \Omega\text{cm}$  [2]. Using these data and the resistivity-temperature characteristic, a temperature of about  $900^\circ\text{C}$  is found for the hot spot in

dc 9 V

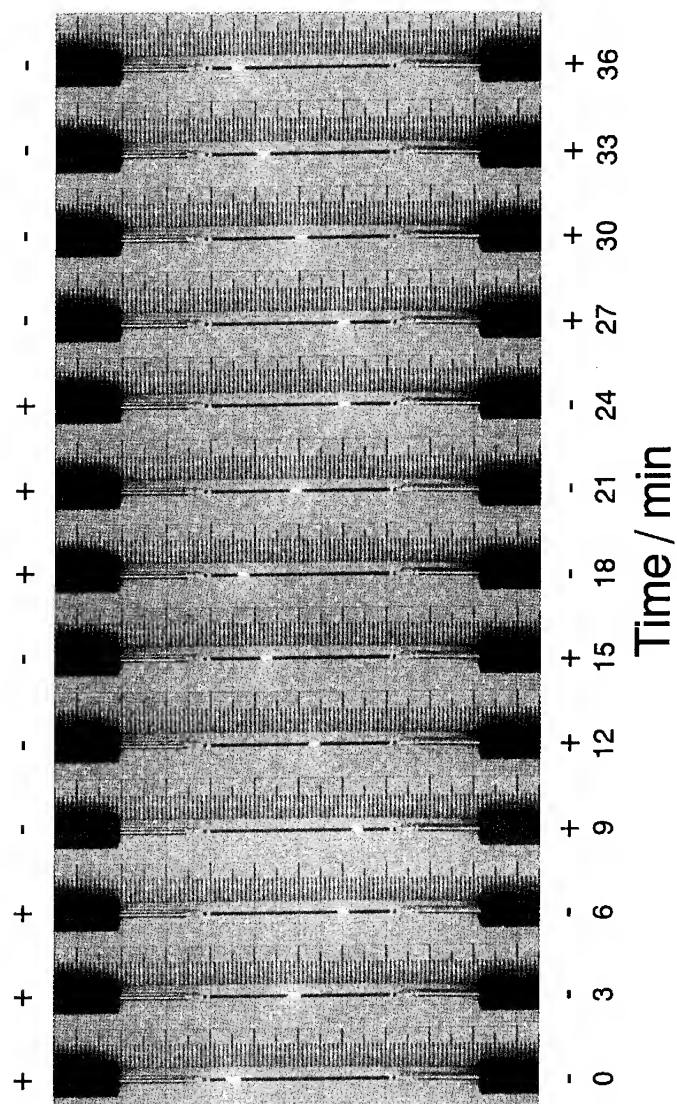


Fig. 1. Sequence photograph after applying a dc 9 V to the sample. The pictures are taken at 3 minute intervals. It is clear that the hot spot moves towards the negative electrode. The movement reversed itself each time when the polarity was reversed.

static air [2].

For  $\text{MBa}_2\text{Cu}_3\text{O}_{7-\delta}$  (where M is a rare earth metal), the appearance of the hot spot is related to the steep increase in resistivity above a temperature  $T^*$  [3-9]. It is for example well known that the resistivity in air of  $\text{YBa}_2\text{Cu}_3\text{O}_{7-\delta}$  steeply increases above 400 °C due to the loss of oxygen [4-6]. Also the resistivity in air of  $\text{GdBa}_2\text{Cu}_3\text{O}_{7-\delta}$  increases steeply above 400°C [2].

When a voltage is applied over the sample, the sample heats up by joule heating, see Fig. 2. If there is an area in the sample with a slightly higher resistance, due to some inhomogeneity in composition, density or section area of the sample, the electric field over that area will be higher than over the rest of the sample. Therefore the temperature of this area reaches  $T^*$ , faster than the rest of the sample. The voltage will further concentrate over that part due to the steep increase in resistivity caused by the release of oxygen. Finally the sample has a distinct hot region which is clearly visible, while the rest of the sample is much colder. The temperature of the hot and cold region can be obtained by the heat balance of the sample:

$$C \frac{dT}{dt} = i^2 R - W(T) - \frac{d}{dx} \lambda \frac{dT}{dx} \quad (1)$$

where C is the heat capacity, i the current, R the resistance,  $\lambda$  the heat conductivity, and  $W(T)$  the heat dissipated to the environment. When the system is in equilibrium, and if we assume each region is at a constant uniform temperature, the heat balance can be written as

$$i^2 R = W(T) \quad (2)$$

Figure 3 shows schematically the joule heat and the dissipated heat as a function of the temperature. It can be seen that there are 3 temperatures for which the generated joule heat balances the heat dissipated to the environment, namely  $T_1$ ,  $T_2$  and  $T_3$ . The temperature  $T_3$  is however unstable. Assume for example there is a slight increase in temperature in the region at temperature  $T_3$ . The produced heat is then larger than the dissipated heat and the temperature increases until  $T_2$ . If we assume a slight decrease in temperature, the temperature decreases further, because the generated heat is smaller than the dissipated heat.

The migration of the hot spot is believed to be related to the oxygen movement in the hot spot. The oxygen ions in the hot spot move easily due to the high temperature and high concentration of oxygen vacancies, see Fig. 4. When oxygen

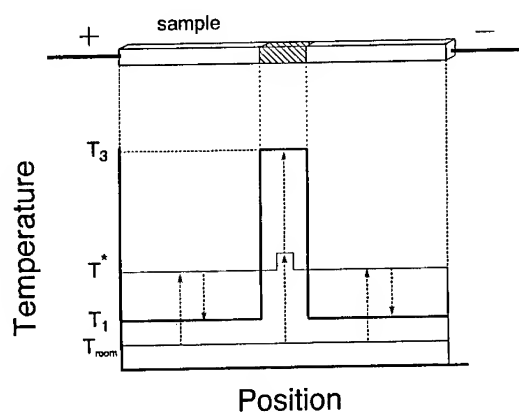


Fig. 2. A schematic representation of the appearance of the hot spot. When the voltage is applied to the sample, the sample heats up. However when there is an area for which the resistivity is slightly higher, the temperature will be higher in that area because the voltage concentrates over that area. When the temperature is in the neighborhood of  $T^*$ , the temperature of the area with a slightly higher resistivity will be higher than  $T^*$ . Therefore the resistivity will further increase, resulting in a further increase in temperature. The system will equilibrate at temperature  $T_1$  and  $T_3$  as shown in Fig. 3.

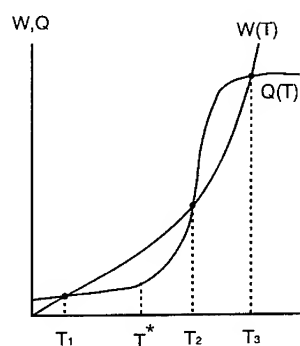


Fig. 3. Graphical representation of the generated joule heat and the dissipated heat as a function of temperature for the sample in equilibrium. When the sample is in equilibrium the generated heat and the dissipated heat must balance each other. This can only at three different temperatures,  $T_1$ ,  $T_2$  and  $T_3$ . The temperature  $T_2$  is however unstable.

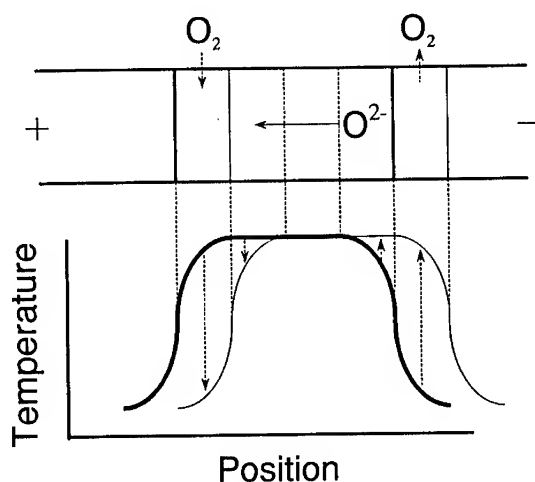


Fig. 4. Schematic representation of the movement of the hot spot. After the hot spot appeared oxygen ions move from the negative side towards the positive side. The resistivity increases therefore on the negative side. Consequently the temperature increases, oxygen is released on that side, and the resistivity increases further. The spot moves therefore to the negative electrode.

ions move to the positive potential side of the hot spot, the resistivity increases on the negative side and decreases on the positive side. The generated heat is therefore larger on the negative side than on the positive side, consequently the temperature of the spot decreases at the positive side and increases at the negative side. Because the system tries to stay in equilibrium, oxygen will diffuse into the sample at the positive side which will further decrease the resistivity and the temperature. At the side of the positive electrode oxygen will be released from the sample, hence the resistivity and the temperature will increase. Consequently, the spot will move to the negative electrode.

Although this phenomenon has been reported before [1,10–12], the influence of the oxygen partial pressure ( $P_{O_2}$ ) has not yet been clearly reported. This paper describes the influence of the  $P_{O_2}$  on the characteristics of this phenomenon and shows that this phenomenon can be used for oxygen sensing.

## EXPERIMENTAL

The  $\text{GdBa}_2\text{Cu}_3\text{O}_{7-\delta}$  samples were prepared by conventional solid-state reaction. The details are described elsewhere [1]. The obtained samples had a 56% theoretical density. Figure 5 shows a scanning electron microscope (SEM) photograph of the as sintered sample. Samples were cut in rectangular shape ( $0.65 \text{ mm} \times 0.65 \text{ mm} \times 46.5 \text{ mm}$ ) and the outer edges were electroded by using Ag paste. Although the voltage was applied at the electrodes at the outer edges, it was measured between two Ag-paste electrodes positioned 40 mm apart. This was done to avoid any influence of the contact resistance. Figure 6 shows the experimental set up for the measurement. The dc voltage was applied using a regulated dc power supply, while the sample was kept under a controlled  $\text{O}_2/\text{N}_2$  gas mixture at room temperature. The  $P_{\text{O}_2}$  was controlled by changing the flow rate of the oxygen and nitrogen. The total flow rate was kept constant at 1.0 l/min, and the total pressure was 1.0 atm (100 kPa). The current, velocity, and spot size as a function of the voltage were obtained by increasing the voltage over the sample with 0.10 V every 6 seconds. The  $P_{\text{O}_2}$  was constant during this measurement. The measurements were done without changing the polarity, and for every  $P_{\text{O}_2}$  a new sample was used. The examined  $P_{\text{O}_2}$  range was 0.05 to 1.00 atm (5 kPa – 100 kPa).

## RESULTS AND DISCUSSION

Figure 7 shows the dc voltage dependence of the current under various  $P_{\text{O}_2}$ . After the voltage reached a critical value in the range of 5 V to 6 V, a hot spot appeared on the sample for each  $P_{\text{O}_2}$ . When the hot spot appeared, the current decreased abruptly. The current was almost constant after the appearance of the hot spot. Figure 8 shows the dc voltage dependence of the spot size under various  $P_{\text{O}_2}$ . The spot size increased linearly with increasing voltage. The constant current characteristic shown in Fig. 7 is related to the linear increase in spot size or in other words to the linear increase in the length of the high resistivity region.

Figure 9 shows the  $P_{\text{O}_2}$  dependence of the current at 8 V as derived from Fig. 7. The current increases with increasing  $P_{\text{O}_2}$ . A possible explanation for this result is as follows. When the  $P_{\text{O}_2}$  is increased, it is known that  $\delta$  decreases[9]. Consequently the hole and carrier density increases, resulting in an increase in current.

Figure 10 shows the  $P_{\text{O}_2}$  dependence of the spot velocity at 8 V. These data were obtained from the spot migration observed during the current-voltage

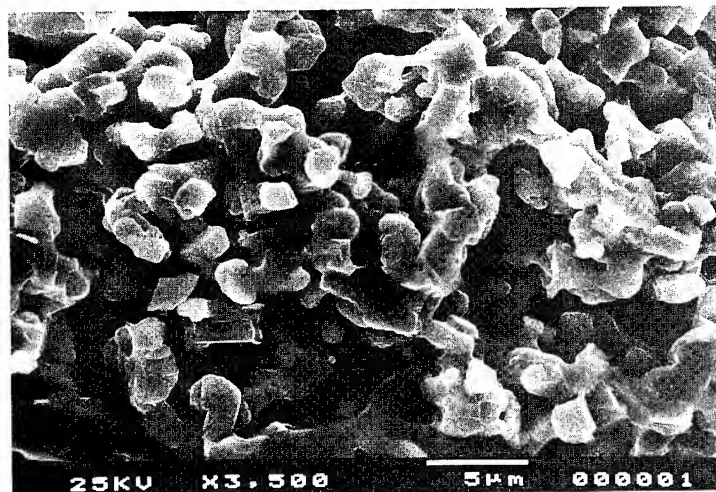


Fig. 5. SEM photograph of fractured surface of the as sintered  $\text{GdBa}_2\text{Cu}_3\text{O}_{7-\delta}$  sample showing the porous structure. The density is about 56 % of the theoretical density.

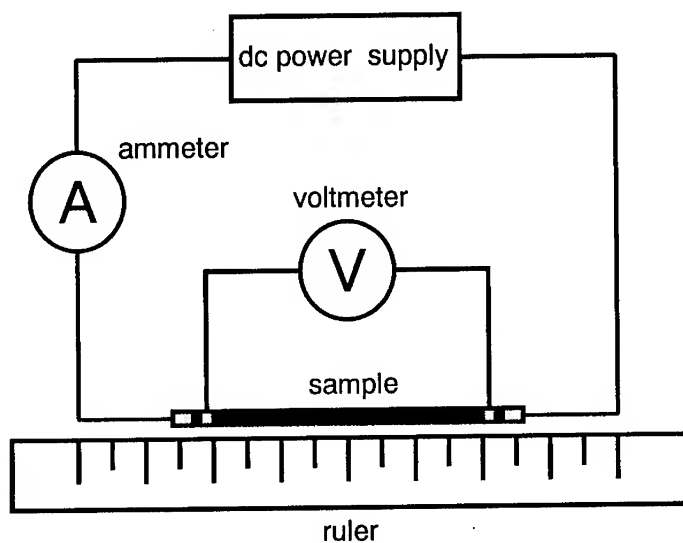


Fig. 6. Experimental setup for the measurement of the current, velocity, and spot size. Although the voltage was applied at the electrodes at the outer edges, it was measured between two Ag-paste electrodes positioned 40 mm apart in order to avoid influence of the contact resistance at the electrodes.



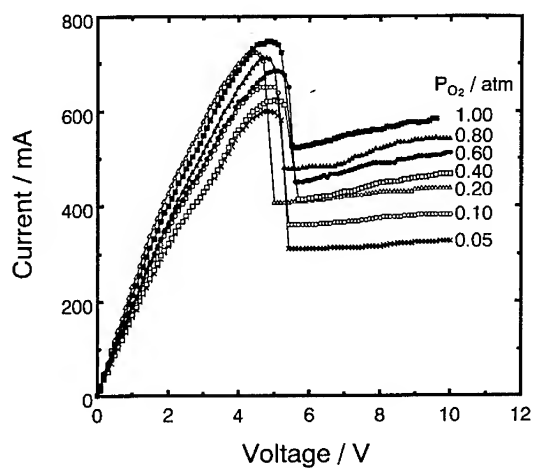


Fig. 7. Current voltage characteristic for several  $P_{O_2}$ . The voltage was increased every 6 seconds with 0.1 V. At around a voltage of 5 V, the spot appeared and the current dropped abruptly. The current was almost constant after the hot spot appeared.

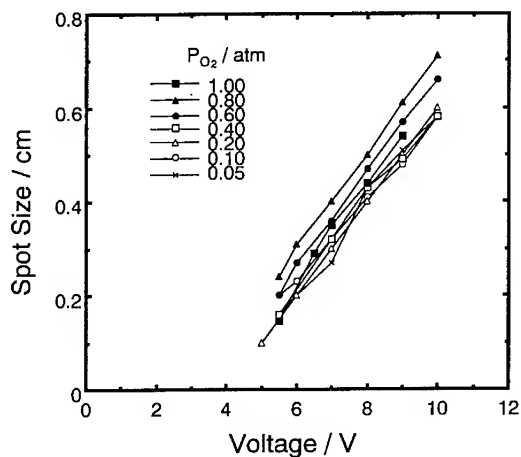


Fig. 8. Voltage dependence of the spot size. The spot size increased linearly with increasing voltage, which explains why the current is independent of the voltage.

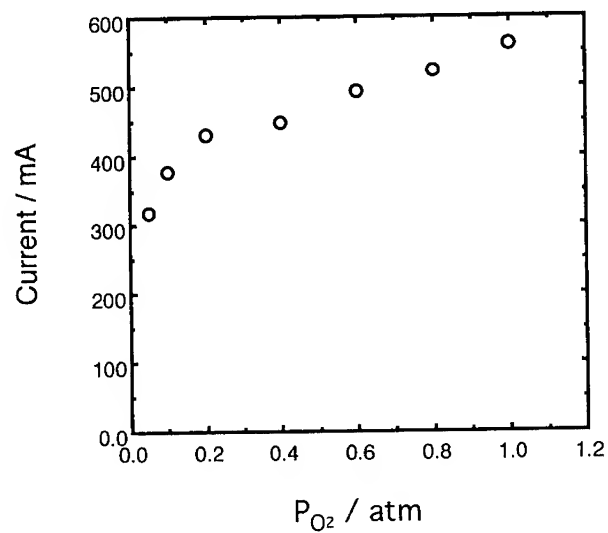


Fig. 9. The current after the hot spot appeared as a function of the  $P_{O_2}$ . The current increased with increasing  $P_{O_2}$ . This characteristic might be used to construct a very simple oxygen sensor.

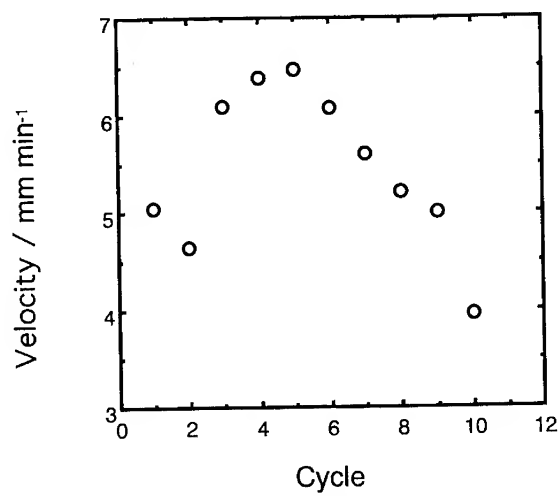


Fig. 10.  $P_{O_2}$  dependence of the spot velocity. The spot velocity increased with increasing  $P_{O_2}$ . This result is believed to be due to changes in the oxygen migration.

measurements. The spot velocity also increases with increasing  $P_{O_2}$ . This suggests that the diffusion of oxygen becomes faster with increasing  $P_{O_2}$ , which in its turn suggest an increase in temperature of the hot spot.

## CONCLUSIONS

It is found that the current after the hot spot appear is very sensitive to the oxygen partial pressure in the atmosphere, but independent of the applied voltage. The current in a  $P_{O_2}$  of 0.05 atm (5 kPa) was almost two times smaller than for a  $P_{O_2}$  of 1.00 atm (100 kPa). It is suggested that this might lead to a very simple oxygen sensor. It is also found that the spot velocity increased with increasing oxygen partial pressure in the atmosphere. It is believed that this is related to changes in the oxygen migration in the hot spot.

## REFERENCES

1. T. Okamoto, B. Huybrechts and M. Takata, *Jpn. J. Appl. Phys.* **33**, L1212 (1994).
2. T. Okamoto, B. Huybrechts and M. Takata, *J. Am. Ceram. Soc.* (submitted)
3. J. Nowotny, M. Rekas and W. Weppner, *J. Am. Ceram. Soc.* **73**, 1040 (1990).
4. V. A. M. Brabers et al., *Mater. Res. Bull.* **23**, 197 (1988).
5. A. T. Fiory et al., *Phys. Rev. B*, **36**, 7262 (1987).
6. T. K. Chaki and M. Rubinstein, *Phy. Rev. B*, **36**, 7259 (1987).
7. W. Carrillo-Cabrera, H. D. Wiemhofer and W. Gopel, *Solid State Ionics*, **32/33**, 1172 (1989).
8. M. V. Patrakeev, I. A. Leonidov and V. L. Kozhenikov, *Physica C*, **210**, 213 (1993).
9. K. Kishio et al., *Jpn. J. Appl. Phys.* **26**, L1228 (1987).
10. G. I. Abramov et al., *Fiz. Tverd. Tela (Leningrad)*, **27**, 2250 (1985) [*Sov. Phys. Solid State*, **27**, 1350 (1985)].
11. Y. A. Osip'yan et al., *Pis.'mzh. Eksp. Teor. Fiz.* **47**, 257 (1988) [*JETP Lett.* **47**, 310 (1988)].
12. E. Yanmaz, I. R. Harris and J. S. Abell, *J. of Alloys and compounds*, **185**, 311 (1992).

## FABRICATION OF $V_2O_5$ THIN FILMS AND THEIR ELECTROCHEMICAL PROPERTIES IN LITHIUM MICROBATTERIES

C. JULIEN, A. GORENSTEIN\*, A. KHELFA, J.P. GUESDON AND I. IVANOV\*\*  
Laboratoire de Physique des Solides, associé au CNRS, Université Pierre et Marie Curie  
4 place Jussieu, 75252 Paris Cedex 05, France

### ABSTRACT

Thin films of  $V_2O_5$  were prepared using the flash-evaporation technique. Amorphous and polycrystalline samples were characterized by X-ray diffraction, Raman spectroscopy and XPS analysis. The electrical properties of the samples were determined. The effect of either deposition parameters or post-deposition treatments, i.e., annealing in various atmospheres and at different temperatures, on transport properties are presented.

Electrochemical characteristics are evaluated in  $V_2O_5/LiClO_4\text{-PC}/Li$  microbatteries. The discharge curves present several voltage plateaus, similar to those already observed in cells with bulk  $V_2O_5$  cathodes. Kinetics of lithium intercalation have been investigated as a function of the growth conditions of  $V_2O_5$  films. Chemical diffusion coefficient and enhancement factor are calculated as a function of the degree of lithium intercalation. All the results are compared with previous reported results for bulk vanadium oxides. The relationship between the crystallinity of the films and their electrochemical features is also discussed.

### 1. INTRODUCTION

A number of vanadium-oxide phases, with different stoichiometries and crystal structures have been proposed as host materials for lithium insertion, with potential applications in secondary batteries.<sup>1,2</sup> Among these vanadium oxides, bulk  $V_2O_5$  is the most studied material due to the high voltage and the good reversibility. During electrochemical discharge, the shape of the voltage vs. composition curve for bulk  $Li_xV_2O_5$  shows various plateaus, which has been attributed to the formation of several phases:  $\alpha$ -phase ( $x < 0.1$ ),  $\epsilon$ -phase ( $0.35 < x < 0.5$ ) and  $\delta$ -phase ( $0.9 < x < 1$ ). More recently, it has been shown that for higher intercalation levels, new phases are formed with good cycling behaviour.<sup>3</sup>

Thin films of  $V_2O_5$ , in contrast to bulk materials, are much less studied in spite of the growing interest in the development of microbatteries.<sup>4</sup> The performance of a thin-film cathode is strongly dependent on its physical and chemical characteristics, and it is well known that these characteristics are linked to the growth technique and growth parameters. Vanadium pentoxide films can be prepared by a variety of methods, including sol-gel synthesis,<sup>5</sup> sputtering deposition,<sup>6</sup> and flash evaporation,<sup>7</sup> leading to materials with different crystallinities and stoichiometric deviations.

In this work, thin films of  $V_2O_5$  were prepared using the flash evaporation technique, which has been pointed out to preserve the stoichiometry of the original powder material. Amorphous and polycrystalline samples are obtained by changing either the deposition parameters or by performing the post-deposition treatment. The samples were characterized by X-ray diffraction, XPS (X-ray Photoelectron Spectroscopy) and Raman spectroscopy. The electrical properties are determined. Electrochemical characteristics are evaluated in a non-aqueous  $Li^+$  electrolyte and the kinetics of lithium intercalation have been investigated as a function of the growth conditions of  $V_2O_5$  films.

\*Permanent address: Physics Institute, UNICAMP, CP6165, CEP13081 Campinas SP, Brazil.

\*\*Permanent address: Solid State Physics Dept., Sofia University, 1126 Sofia, Bulgaria.

## 2. EXPERIMENTAL

The thin films were prepared by flash evaporation of polycrystalline  $V_2O_5$  powder (99.99% Alpha-Ventron). In this method, the powder falls at a controlled rate on a pre-heated crucible and immediately evaporates, minimizing the decomposition of the source material. Molybdenum crucibles at about 920°C were used. The films were grown at a rate of 0.4 nm s<sup>-1</sup>, in a vacuum of below 10<sup>-3</sup> Pa. Either (111) oriented Si (Raman experiments), Au contacts/glass (electrical measurements) or ITO/glass (optical and electrochemical experiments) were used as substrates. The substrate temperature,  $T_s$ , was controlled by means of a thermocouple. Samples of geometric area 1x1 cm<sup>2</sup> and 0.5  $\mu$ m thick were obtained. Annealing in Ar or O<sub>2</sub> atmosphere was also performed for some samples.

X-ray diffraction was carried out using a Philips diffractometer equipped with a molybdenum source ( $\lambda=1.788$  Å). XPS measurements were performed using an ISA-Riber (model Mac-2) electron spectrometer and a Mg-K $\alpha$  (1253.6 eV) X-ray source. The Raman spectra were obtained in the quasi backscattering geometry. A 514.5 nm Ar-ion laser line, a Jobin-Yvon U1000 double-monochromator with holographic gratings and a computer-controlled photon-counting system were used. The power excitation was 10 mW. The spectra presented here are the average of 12 scans recorded with a spectral resolution of 4 cm<sup>-1</sup>.

For the electrochemical experiments, Li foil was used both as the counter and the reference electrode. The electrolyte was 1M LiClO<sub>4</sub> in propylene carbonate. Both salt and solvent were previously dried by conventional means. The electrochemical cells were prepared and maintained during experiments in a dry box (purified Ar atmosphere) containing less than 2 ppm of water.

## 3. FILM CHARACTERIZATION

Figure 1 presents the X-ray diffractograms for as-grown samples deposited at  $T_s=25^\circ\text{C}$  (Fig. 1a) and films annealed in either air (Fig. 1b) or oxygen atmosphere (Fig. 1c). The as-deposited films have the typical color of  $V_2O_5$  (yellow-orange) and are amorphous in nature, while annealing promotes crystallization. Films annealed in O<sub>2</sub> present a polycrystalline structure, with preferential orientation about the (001) plane.

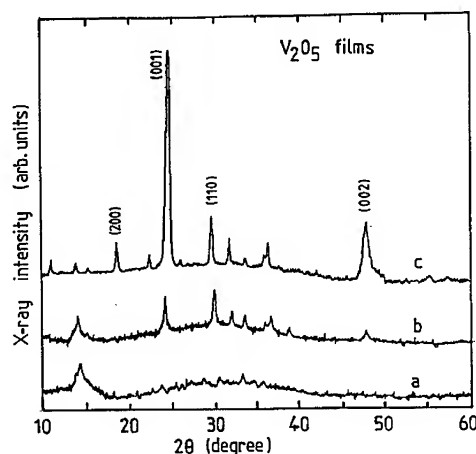


Fig. 1. X-ray diffractograms of flash-evaporated  $V_2O_5$  films at  $T_s=25^\circ\text{C}$ : (a) as-deposited, (b) annealed at 375°C for 7 h in air and (c) annealed at 375°C for 7 h in O<sub>2</sub>.

The appearance of the (001) reflection indicates a regular stacking of imperfect ab planes with the c-direction perpendicular to the substrate plane. The same preferential orientation has been observed in thermally evaporated and annealed  $V_2O_5$  films.<sup>8</sup>

The composition of the films has been investigated using X-ray photoelectron spectroscopy. The XPS spectrum displays peaks attributed to the  $O_{1s}$ ,  $V_{2p_{1/2}}$  and  $V_{2p_{3/2}}$  located at 529, 523 and 516 eV, respectively (Fig. 2). The ratio between the peak intensity of  $O_{1s}$  and  $V_{2p_{3/2}}$  is 1.23, which corresponds well to the value measured for  $V_2O_5$  crystal.<sup>9</sup>

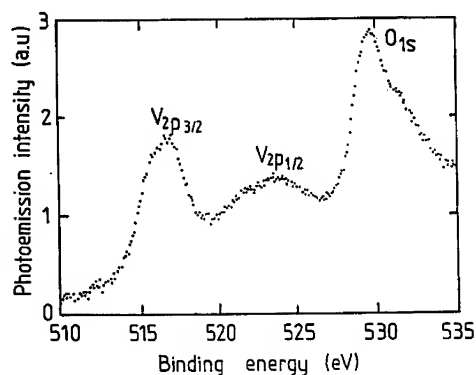


Fig. 2. XPS spectrum of flash-evaporated  $V_2O_5$  films at  $T_s=25^\circ\text{C}$ .

$V_2O_5$  crystallizes in the orthorhombic system. The layered-like structure is build up from distorted trigonal bipyramidal coordination polyhedra of O atoms around V atoms, which share edges to form  $(V_2O_4)_n$  zigzag double chains along the (001) direction and are cross-linked along the (100) direction through shared corners. The Raman scattering (RS) spectra of the  $V_2O_5$  flash-evaporated films are shown in Fig. 3.

Films deposited at room temperature are rather amorphous, but the spectrum (curve a) shows some peaks that are also present in the sample grown at higher temperature and in the annealed sample as shown in curves (b) and (c), respectively. These results indicate some short-range order and the layered structure for the as-grown film. Films grown at  $T_s=250^\circ\text{C}$  are polycrystalline and exhibit a well-resolved spectrum (curve b).

The RS spectrum of a film grown at ambient temperature and annealed in  $O_2$  (curve c) shows that the structural disorder disappears and the spectrum becomes similar to that of the  $V_2O_5$  polycrystalline phase. In the RS spectra the internal modes, which lie in the high-frequency region can be described in terms of stretching and bending of V-O bonds.<sup>10</sup> The external modes can be viewed as relative motions of the units with respect to each others (translations and librations); some of the translations give rise to rigid-layer modes. Normally, they lie in the low-frequency region because each unit is considerably heavier than the building atoms, while the restoring force is of the same order of magnitude. Three rigid-layer modes can be distinguished (Fig. 3) at 105, 146 and  $199\text{ cm}^{-1}$ . The high-frequency mode at  $993\text{ cm}^{-1}$  corresponds to the stretching of the shortest V-O bond. It has been shown<sup>11</sup> that the structural reconstruction in the films results in (1) a decrease of the broad band, which corresponds to the phonon density-of-states in amorphous material (Fig. 3a), (2) the appearance of well-resolved rigid layer modes located in the vicinity of  $146\text{ cm}^{-1}$  (Fig. 3c), and (3) the decreased of the broad peak, which is an infrared-active mode, appearing in the RS spectrum at  $830\text{ cm}^{-1}$  in a disordered material. So, the spectra in Fig. 3 (curves b and c) indicate that higher substrate temperature and/or annealing promote reconstruction of the  $V_2O_5$  lattice.

Lithium-intercalated samples were prepared by immersion of the film in *n*-butyl lithium.<sup>12</sup> The RS spectrum of a lithiated sample is shown in Fig. 4 (curve b). The effect of the lithium intercalation on the vibrational spectra is three-fold: (1) a frequency shift of the normal modes of the  $V_2O_5$  lattice, (2) the large increase of infrared-active mode, and (3) the appearance of new modes located at 805 and 1060  $cm^{-1}$ . The rigid-layer mode at 147  $cm^{-1}$  is the most affected band in the lithiated sample. Its frequency shift indicates an increase of the restoring force for this type of vibration, due to the increase in the inter-layer distance as a consequence of lithium intercalation. The new modes should be assigned to longitudinal and transverse intercalation mode, in which the lithium atoms in the van der Waals gap vibrate strongly against the host material, i.e. the terminal-oxygen atoms as first neighbors.<sup>13</sup>

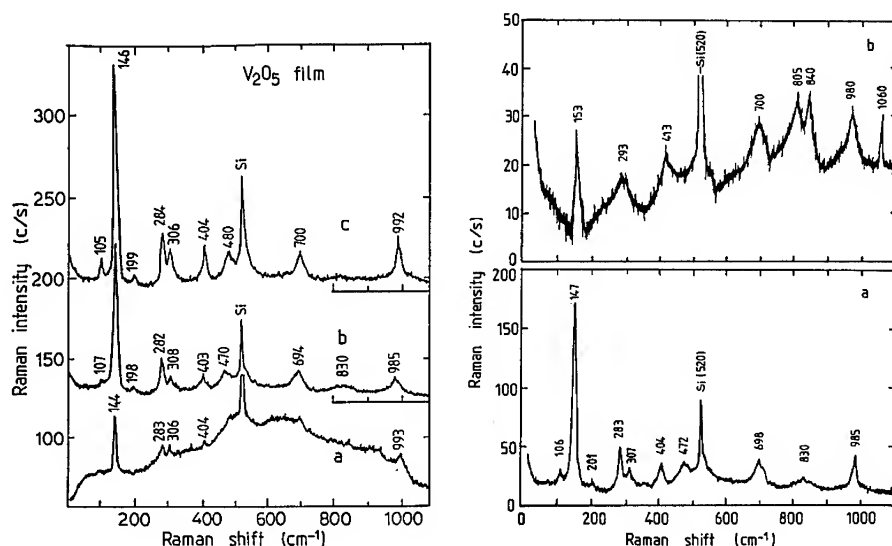


Fig. 3. Raman scattering spectra of flash-evaporated  $V_2O_5$  films grown on Si substrate maintained at (a, c)  $T_g=25^\circ C$  and (b)  $T_g=250^\circ C$ . Curve (c) is the spectrum of an annealed film in  $O_2$  at  $300^\circ C$  for 60 h.

Fig. 4. Raman scattering spectra of (a) pure  $V_2O_5$  film and (b) lithium-intercalated  $V_2O_5$  film. Films were grown on (111) oriented Si substrate maintained at  $T_g=250^\circ C$  and annealed at  $300^\circ C$  in argon atmosphere for 48 h.

It is well known that  $V_2O_5$  can be non-stoichiometric.  $V^{4+}$  ions can be produced as a consequence of the formation of oxygen vacancies. Small polarons are formed around these ions, due to the highly polar structure of this oxide. Thermally activated electronic hopping between  $V^{4+}$  and  $V^{5+}$  states is responsible for the electric transport. Also, it has been pointed out that the amount of  $V^{4+}$  ions in  $V_2O_5$  films is indicated by the color of the film.<sup>14</sup> As mentioned above, films deposited at room temperature are yellow-orange, which is an indication of the low  $V^{4+}$  content. Films grown at higher substrate temperature and/or annealed in Ar are green-black, which indicates a higher  $V^{4+}$  content. The temperature dependence of the electrical conductivity of the  $V_2O_5$  films is shown in Fig. 5. The conductivity curves are typical of a small polaron hopping mechanism. The activation energies of the high-temperature regime are listed in Table 1.

The decrease in activation energy and the increase in conductivity have been suggested by Murawski et al.<sup>14</sup> They are due to the decrease in the quenching rate of evaporated films, which is the difference between the powder sublimation temperature and the substrate temperature during the growth. The highly quenched films (grown at  $T_s=25^\circ\text{C}$ ) have the lowest conductivity and the highest activation energy, due either to the disorder or to the lowest  $\text{V}^{4+}$  concentration for these films in accordance to the Mott's model.<sup>15</sup> The highest conductivity values are obtained for annealed samples.

Table 1.  
Activation energy of the electrical conductivity for flash-evaporated  $\text{V}_2\text{O}_5$  films grown with different conditions.

Substrate temperature ( $^\circ\text{C}$ )	Annealing	Activation energy (meV)
25	-	433
250	-	188
25	Ar	126
250	Ar	136
25	$\text{O}_2$	199
250	$\text{O}_2$	150

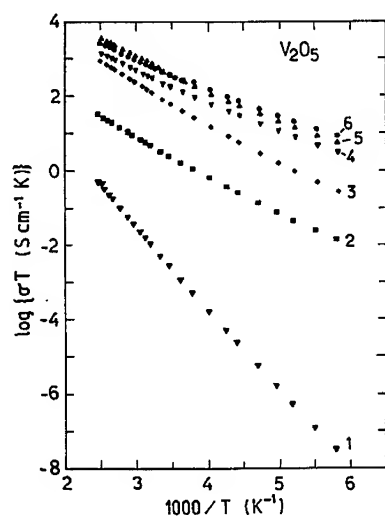


Fig. 5. Temperature dependence of the electrical conductivity of the  $\text{V}_2\text{O}_5$  films grown in various conditions. With  $T_s=25^\circ\text{C}$ : (1) as-grown, (3) annealed in  $\text{O}_2$ , and (4) annealed in Ar. With  $T_s=250^\circ\text{C}$ : (2) as-grown, (5) annealed in  $\text{O}_2$ , and (6) annealed in Ar. The annealing process was performed at  $300^\circ\text{C}$  for 60 h.

#### 4. ELECTROCHEMICAL STUDIES

Bulk vanadium pentoxide, when used as a cathode material in lithium rechargeable batteries, has a theoretical energy density of about  $500 \text{ W h kg}^{-1}$ , being one of the most important material for this type of battery. The electrochemical behaviour of flash-evaporated  $\text{V}_2\text{O}_5$  thin films were



analyzed using aprotic  $\text{Li}^+$ -containing electrolyte cells, as described in the experimental section. Figure 6 shows the discharge curves for films grown at different substrate temperatures. Polycrystalline  $\text{V}_2\text{O}_5$  films (grown at  $T_s=250^\circ\text{C}$ ) present the typical plateaus already observed in bulk materials. Amorphous  $\text{V}_2\text{O}_5$  films show a monotonically decreasing curve. For both cathodes, the cell voltage is higher than 2.0 V for a lithium uptake of  $x=2.5$ , showing up that the performance of thin-film cathodes can be as promising as that of the bulk material. The monotonically decreasing curve for amorphous film has been already observed for other materials and has been associated to a preponderant entropic term in the thermodynamic voltage expression.<sup>16</sup> The films can uptake about 3 Li at a discharge potential down to 1.2 V. The capacity of a cell using a  $\text{V}_2\text{O}_5$  film grown at  $T_s=250^\circ\text{C}$  (Fig. 6) is  $90 \text{ A h kg}^{-1}$ , which is close to the value measured for bulk materials. The charging curve shown in Fig. 7 presents some hysteresis, probably linked to the different kinetics on charge-discharge behaviour of thin films.

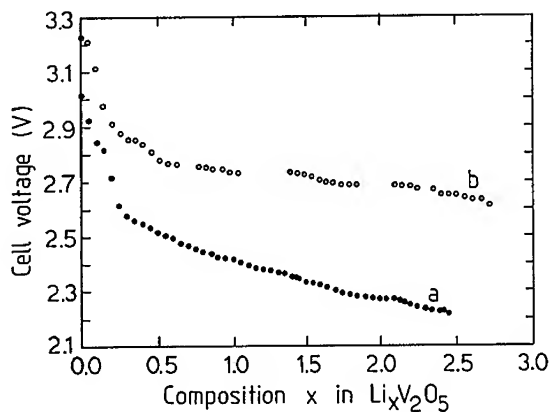


Fig. 6. Discharge curves as a function of the degree of lithium insertion in  $\text{Li}_x\text{V}_2\text{O}_5$  films. (a) grown at  $T_s=25^\circ\text{C}$  and (b) grown at  $T_s=250^\circ\text{C}$ .

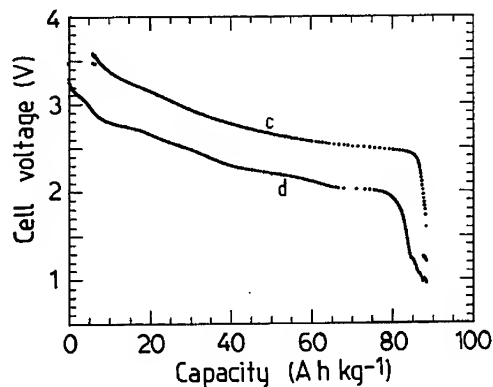


Fig. 7. Charge-discharge curve as a function of cell capacity recorded with a current density  $15 \mu\text{A cm}^{-2}$  using a thin-film cathode grown at  $T_s=250^\circ\text{C}$ .

The kinetic parameters of Li-insertion in the  $\text{Li}_x\text{V}_2\text{O}_5$  films, i.e. the chemical diffusion coefficient and the enhancement factor (thermodynamic factor), were evaluated during the relaxation period of the discharge, following the method of Honders et al.<sup>17</sup> In an intercalation compound, the chemical diffusion coefficient  $D^*$  is given by  $D^*=D_0W$ , where  $D_0$  is the component diffusion coefficient and  $W$  is the thermodynamic factor. The chemical diffusion coefficient is  $3 \times 10^{-13} \text{ cm}^2 \text{ s}^{-1}$  at the beginning of the intercalation process, and slightly decreases in the range  $0 < x < 3$ . For comparison, we remark that Baudry et al.<sup>18</sup> found a diffusion coefficient of  $2.5 \times 10^{-12} \text{ cm}^2 \text{ s}^{-1}$  in thermally evaporated  $\text{V}_2\text{O}_5$  thin films and Bates et al.<sup>19</sup> reported diffusion coefficients varying between  $4 \times 10^{-15}$  and  $2.6 \times 10^{-12} \text{ cm}^2 \text{ s}^{-1}$  for sputtered  $\text{V}_2\text{O}_5$  films. The low diffusion coefficient values are also attributed to the undefined conduction paths between grains of the films. The potential barriers are more important in the inter-grain and the  $\text{Li}^+$  ions may be trapped by structural defects. The thermodynamic factor,  $W$ , has an increasing value up to  $x=1$ , and then assumes a nearly constant value up to the maximum lithium insertion content (Fig. 9).

The differences between materials of low and high crystallinity, as far as the microstructural and macrostructural aspects are concerned have been pointed out by Pereira-Ramos et al.<sup>16</sup> At the macroscopic level, materials of low crystallinity obtained by evaporation techniques are formed by small particles, i.e., the crystallites of the film. These influence thermodynamics and kinetics as observed in the electrochemical behaviour of the studied  $\text{V}_2\text{O}_5$  thin-films cells. When the microscopic level is taken into account, several factors distinguish poorly crystalline from highly crystalline materials: (1) The degree of long-range order is reduced. The presence of very small crystallites reduces the probability that a diffusing ion impinges a channel in the  $\text{V}_2\text{O}_5$  host structure. (2) The polyhedra constituting the unit cell may have some flexibility in the absence of a long-range order. (3) The site energies may not be the same as for the crystalline analogs, as a consequence of the different level of symmetry of the basic polyhedra. (4) The number of sites available for an intercalating ion may also not be the same. (5) In microcrystallite-based compounds, pathways for ion diffusion are shorter.

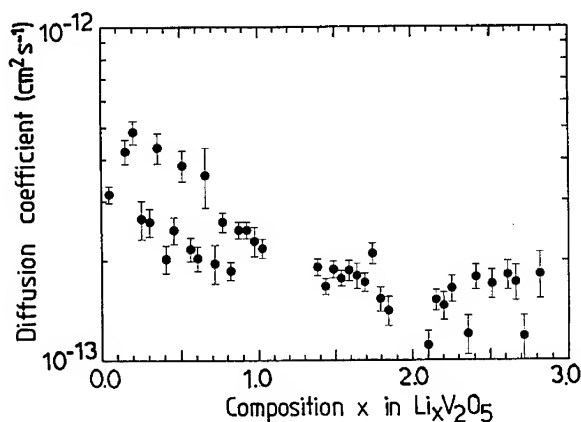


Fig. 8. Chemical diffusion coefficient of  $\text{Li}^+$ -ions as a function of the degree of insertion in films cathode grown at  $T_s=250^\circ\text{C}$ . The error bars come from the fitting procedure.

The microscopic features above listed determine substantial differences between cathodes of quite different crystallinity in terms of thermodynamic and kinetic properties. A striking difference in the compositional variation of the cell voltage is observed for the two classes. Crystalline  $\text{V}_2\text{O}_5$  and thin-films  $\text{V}_2\text{O}_5$  cathodes show remarkable differences. It is typical of the well-crystallized cathodes to show plateaus and knees, while amorphous materials have sloping curves with more gradual changes of cell voltage with composition.

From the Gibbs-Helmholtz equation, the cell voltage is given by  $V = F^{-1}(\Delta H - T\Delta S)$ . One observes that both an enthalpic and an entropic term contribute to the shape of the emf vs. composition curve. The enthalpic contribution,  $\Delta H$ , mainly comes from changes in the electrochemical potential, interactions among  $\text{Li}^+$ -ions residing in neighboring sites and energy required to modify the structure, e.g. volume expansion.<sup>20</sup> The entropic contribution is indicative of major structure reorganizations, such as two-phase formation or structure destruction.<sup>21</sup>

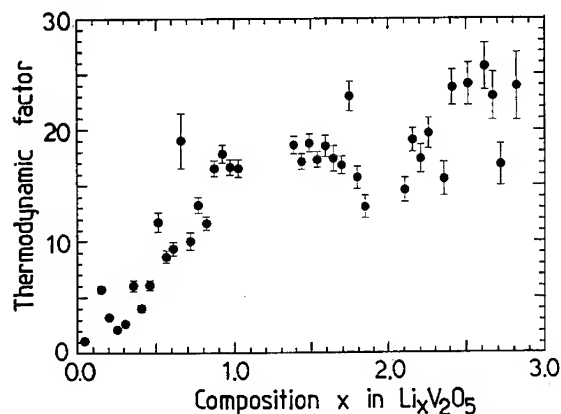


Fig. 9. Thermodynamic factor as a function of the degree of insertion in films cathode grown at  $T_s=250^\circ\text{C}$ . The error bars come from the fitting procedure.

The absence of sudden change in the cell voltage for low-crystallinity materials such as  $\text{V}_2\text{O}_5$  films denotes a reduced entropic contribution, in term referable to the lack of the long-range order. Conversely, the gradual variation of the cell voltage with composition seems to stem from a gradual change in the enthalpic term. Instead, the unit cell possibly undergoes a modification which allows intercalation of  $\text{Li}^+$ -ions in more sites than permitted by the crystalline forms due to the flexibility of the polyhedra constituting the unit cell of the film in an environment having a limited range order. This seems connected to changing interactions among intercalated  $\text{Li}^+$ -ions and from an energy term related to minor modifications in the microstructure of  $\text{V}_2\text{O}_5$  films.

As a result, it seems that the morphology of the film plays an important role on the lithium intercalation reaction in  $\text{V}_2\text{O}_5$  films. Concerning the various interactions occurring in these intercalated systems, one can notice that (1) poorly crystalline  $\text{V}_2\text{O}_5$  cathode does not show evidence of constant repulsion forces among inserted neighboring ions, (2) the interaction between intercalated ions and the host material seems to be more important for the low intercalation values, (3) the intercalation reaction may be related with the density of the film, and (4) the presence of impurities should be considered due to the probability for a blocking effect of the ion diffusion by impurities.

## 5. CONCLUDING REMARKS

$\text{V}_2\text{O}_5$  thin films were grown using a flash-evaporation method in which the control of the deposition rate promotes the film stoichiometry. The thin film structure, composition, optical and electrical properties have been investigated as functions of deposition conditions and post-treatment which play important roles in the physical and chemical characteristics of the material. As a result, a  $\text{V}_2\text{O}_5$  film grown at  $T_s=250^\circ\text{C}$  and heat-treated in argon atmosphere at moderate temperature has a polycrystalline structure and exhibits a high electrical conductivity.

The electrochemical behaviour of  $V_2O_5$  films during the lithium insertion in the host structure is linked to their structural characteristics. The kinetically accessible discharge range amounts to  $0 \leq x \leq 3$  for the Li insertion in  $Li_xV_2O_5$  active cathode films at a discharge potential down to 2.1 V. A capacity of  $90 \text{ A h kg}^{-1}$  has been measured during the first discharge of a cell using a  $V_2O_5$  film flash-evaporated at  $250^\circ\text{C}$ . In  $V_2O_5$  films deposited on substrate at  $250^\circ\text{C}$ , the chemical diffusion coefficient of  $\text{Li}^+$ -ions is about  $10^{-13} \text{ cm}^2 \text{ s}^{-1}$  and remains nearly stable in the entire intercalation range.

However, it is difficult to clearly establish relationships between factors such as crystallinity, stoichiometry and discharge capability. It seems that the morphology of the film plays an important role on the lithium intercalation reaction. Work is in the course to better understand all these points. Nevertheless, it is interesting to point out that  $V_2O_5$  films can be successfully used in solid-state microbatteries using either polymeric or glassy electrolyte with large values of specific storage capacity.

## REFERENCES

1. K. West, B. Zachau-Christiansen, M.J. Ostergard and T. Jacobsen, *J. Power Sources* **20**, 165 (1987).
2. C. Delmas, in *Lithium Batteries, New Materials, Development and Perspectives*, edited by G. Pistoia (Elsevier, Amsterdam, 1994), p. 457.
3. J.M. Cocciantelli, M. Menetrier, C. Delmas, J.P. Doumerc, M. Pouchard and P. Hagenmuller, *Solid State Ionics* **50**, 99 (1992).
4. C. Julien, in *Lithium Batteries, New Materials, Development and Perspectives*, edited by G. Pistoia (Elsevier, Amsterdam, 1994), p. 167.
5. J. Livage, *Chem. Mater.* **3**, 578 (1991).
6. K. West, B. Zachau-Christiansen, S.V. Skaarup and F.W. Poulsen, *Solid State Ionics* **57**, 41 (1987).
7. L. Murawski, C. Gledel, C. Sanchez, J. Livage and J.P. Audiere, *J. Non-Cryst. Solids* **89**, 98 (1987).
8. A.M. Abo-El-Soud, B. Mansour and L.I. Soliman, *Thin Solid Films* **247**, 140 (1994).
9. Y. Fujita, K. Miyazaki and C. Tatsuyama, *Jpn. J. Appl. Phys.* **29**, L1708 (1990).
10. L. Abello, E. Husson, Y. Repelin and G. Lucazeau, *Spectrochim. Acta A* **39**, 641 (1983).
11. C. Julien, J.P. Guesdon, A. Gorenstein, A. Khelfa and I. Ivanov, *Thin Solid Films* (to be appeared).
12. M.S. Whittingham and M.B. Dines, *J. Electrochem. Soc.* **124**, 1387 (1977).
13. C. Julien, I. Ivanov and A. Gorenstein, unpublished data.
14. C. Sanchez, J. Livage, J.P. Audiere and A. Madi, *J. Non-Cryst. Solids* **65**, 285 (1984).
15. N.F. Mott, *Adv. Phys.* **16**, 49 (1967).
16. J.P. Pereira-Ramos, N. Baffier and G. Pistoia, in *Lithium Batteries, New Materials, Development and Perspectives*, edited by G. Pistoia (Elsevier, Amsterdam, 1994), p. 281.
17. A. Honders, J.M. Der Kinderen, A.H. Van Heeren, J.H.W. De Wit and G.H.J. Broers, *Solid State Ionics* **15**, 265 (1985).
18. P. Baudry, M.A. Aegerter, D. Deroo and B. Valla, *J. Electrochem. Soc.* **138**, 460 (1991).
19. J.B. Bates, G.R. Gruzalski, N.J. Dudney, C.F. Luck and X.H. Yu, *Solid State Ionics* **70-71**, 619 (1994).
20. A.S. Nagelberg and W.L. Worrell, *J. Solid State Chem.* **38**, 321 (1981).
21. J.P. Pereira-Ramos, R. Messina, C. Piolet and J. Devynck, *Electrochim. Acta* **33**, 1003 (1988).

## EFFECT OF THE CRYSTALLINITY OF $V_6O_{13}$ FILMS ON THE ELECTROCHEMICAL BEHAVIOR OF LITHIUM MICROBATTERIES

A. GORENSTEIN\*, A. KHELFA, J.P. GUESDON AND C. JULIEN\*\*

Laboratoire de Physique des Solides, associé au CNRS, Université Pierre et Marie Curie  
4 place Jussieu, 75252 Paris Cedex 05, France.

### ABSTRACT

Electrochemical characteristics of  $Li/V_6O_{13}$  microbatteries are evaluated in relation with the crystallinity and morphology of thin-film cathodes. Thin films of  $V_6O_{13}$  were prepared using the flash evaporation technique. Amorphous and polycrystalline samples were characterized by X-Ray diffraction, Raman spectroscopy and conductivity measurements. The effect of either deposition parameters or post-deposition treatment are presented in this work. Thermodynamics and kinetics of lithium insertion were studied in  $V_6O_{13}$  thin films obtained with various growth conditions. Discharge curves present different types of behavior depending on the cathode morphology. Diffusion coefficients and enhancement factors were calculated as a function of the degree of lithium intercalation.

### 1. INTRODUCTION

Vanadium oxides have potential use, particularly in thin-film form, for a wide variety of applications involving high energy density lithium microbatteries [1] and electrochromic devices [2]. However, these applications depend on the techniques used to grow films and performances are related with crystallinity and morphology of the films [3].  $V_6O_{13}$  is by far the most important lower oxide deduced from  $V_2O_5$ . The use of  $V_6O_{13}$  as an intercalation cathode material for rechargeable lithium batteries has been widely studied since it was first reported by Murphy et al. [4-5]. At room temperature,  $V_6O_{13}$  reversibly incorporates lithium ions to give a bronze with the limiting composition  $Li_8V_6O_{13}$  [6].

$V_6O_{13}$  is a black material with a monoclinic symmetry. Its structure is formed from a double shearing of the  $ReO_3$  structure and it is intermediate in composition between  $VO_2$  and  $V_2O_5$ . In this family,  $V_3O_7$  and  $V_4O_9$  appear to have an intermediate structure between that of  $V_6O_{13}$  and  $V_2O_5$ . It has been confirmed [7-9] that the structure of  $V_6O_{13}$  consists of alternating double and single zigzag chains of corner-shared distorted  $VO_6$  octahedra. The three-dimensional framework of  $V_6O_{13}$  contains channels extending in the (010) direction. It has never been reported that a thin-film of  $V_6O_{13}$  has been obtained, because of the oxygen deficient structure if compared to the  $V_2O_5$ . Nevertheless, it has been demonstrated that flash-evaporated films of vanadium pentoxide are more homogeneous and exhibit higher properties than others [10]. This advantage of the flash-evaporation technique has been used to grow  $V_6O_{13}$  films. Our goal is to fabricate lithium microbatteries having  $V_6O_{13}$  insertion cathodes.

The purpose of this work is to investigate the relationship between growth conditions and the film properties of flash-evaporated  $V_6O_{13}$ . We report the structural, optical, and electrical properties of these films.

### 2. EXPERIMENTAL

Flash-evaporated  $V_6O_{13}$  films were grown using finely powdered  $V_6O_{13}$  prepared by thermal decomposition of  $NH_4VO_3$  (Ventron). This powdered substance was placed in a rotary furnace purged with ultra pure argon (5 liters/minute). The rotary blade inside the furnace was set at 40 revolutions per minute. The furnace temperature was raised to 150°C and maintained for 2 h, then

\*Permanent address: Physics Institute, Universidade Estadual de Campinas, CP6165, Campinas SP Brazil.

\*\*Corresponding author.

raised to 400°C and maintained for 4 h, and finally raised to 550°C and maintained for 1 h. The samples were then quenched to room temperature and transferred into a glove box filled with argon. The dark blue sample formed in this process had a particle size in the range 5–8  $\mu\text{m}$ .

The flash-evaporation method allows the control of the deposition rate and avoids any decomposition of the starting material before evaporation. Different varieties of samples were obtained by changing the substrate temperature and the annealing process conditions. Various substrates were used: silica glass coated with ITO, silica glass with thin gold coating, and (111) oriented silicon wafer. Polycrystalline  $\text{V}_6\text{O}_{13}$  films have been obtained by a thermal treatment at 300°C in argon for 60 h. Films of dimensions 1x1  $\text{cm}^2$  were prepared using tantalum masks and molybdenum boat in a vacuum of below  $10^{-3}$  Pa. In the flash evaporation technique the source substances were powdered and evaporated from a home-made system described elsewhere [11], in which the controlled boat temperature was about 920°C. The substrate temperature,  $T_s$ , is controlled by means of an iron-constantan thermocouple with an accuracy of  $\pm 2^\circ\text{C}$ . Stoichiometric  $\text{V}_6\text{O}_{13}$  films were grown using a special design of the crucible. In this apparatus the  $\text{V}_6\text{O}_{13}$  powder falls into the heated crucible at a speed of  $0.25 \mu\text{g s}^{-1}$ . The rate at which the powder is provided is a crucial parameter for the growth of  $\text{V}_6\text{O}_{13}$  films because of the tendency of oxygen loss during the film formation. This optimized value allows an evaporation rate of about  $0.4 \text{ nm s}^{-1}$  for  $\text{V}_6\text{O}_{13}$  films. The thickness of all the samples is about  $0.5 \mu\text{m}$ .

### 3. FILM CHARACTERIZATION

The film structure of  $\text{V}_6\text{O}_{13}$  films was determined by X-ray diffraction (XRD) and Raman scattering (RS) experiments. Figure 1 displays the X-ray diffraction diagrams of flash-evaporated  $\text{V}_6\text{O}_{13}$  films (curves a and b) compared with the X-ray pattern of the used  $\text{V}_6\text{O}_{13}$  powder (curve c). It is shown that a film grown at  $T_s=25^\circ\text{C}$  is amorphous (Fig. 1a) whereas the effect of thermal annealing temperature,  $T_a$ , is clearly observed on the structural XRD analysis. When annealed at  $T_a=300^\circ\text{C}$  in argon atmosphere for 60 h,  $\text{V}_6\text{O}_{13}$  films are formed with a rather polycrystalline structure and we observed appreciable changes in the XRD diagram (Fig. 1b). This XRD diagram exhibits the (00l) Bragg peaks which indicate that the film orientation occurs preferentially parallel to the chains. The chains are linked together into single and double sheets of octahedra parallel to the (001) plane. Thus, the XRD patterns of annealed films reveal no trace of phases other than  $\text{V}_6\text{O}_{13}$  and Bragg peaks can be indexed in the monoclinic structure in good agreement with previous reports on crystalline phases [7–9]. It was shown that the plane of easy cleavage is the (001) plane. The orientation of the mirror plane of the film and consequently the direction of the monoclinic axis are parallel to the substrate plane. There is no trace of the  $\text{V}_2\text{O}_5$  phase in the XRD patterns.

Figure 2 shows the Raman scattering (RS) spectra of  $\text{V}_6\text{O}_{13}$  films (curves a–c) compared with the RS spectrum of  $\text{V}_6\text{O}_{13}$  crystal (curve d). Flash-evaporated  $\text{V}_6\text{O}_{13}$  films were deposited on (111) oriented silicon wafers maintained in the temperature range 25–250°C. The RS spectrum of as-deposited  $\text{V}_6\text{O}_{13}$  films grown at either  $T_s=25^\circ\text{C}$  or  $T_s=250^\circ\text{C}$  (Fig. 2a) are amorphous-like, whereas films grown at  $T_s=25^\circ\text{C}$  and heat-treated at 300°C in either Ar (Fig. 2b) or  $\text{O}_2$  atmosphere (Fig. 2c) for 60 h have a polycrystalline structure and exhibit well-resolved Raman lines. The quantitative Raman efficiency of the films may be related with the unique silicon Raman line located at  $520 \text{ cm}^{-1}$ .

The RS spectrum of  $\text{V}_6\text{O}_{13}$  can be discussed in terms of internal and external modes [12–17]. The highest stretching frequency at  $990 \text{ cm}^{-1}$  is attributed to the shortest ( $1.65 \text{ \AA}$ ) V–O bond. The next highest stretching frequency at  $685 \text{ cm}^{-1}$  is assigned to the intermediate bridging V–O bond. The 510 and  $407 \text{ cm}^{-1}$  bands are attributed to a V–O–V stretching modes, consistent with the medium-range order [13]. The mode at  $280 \text{ cm}^{-1}$  is a V–O–V bending mode, and the bands at 300, 193, 139 and  $94 \text{ cm}^{-1}$  are the external modes. Considering the RS spectra shown in Fig. 2, it is clear that the morphology of the  $\text{V}_6\text{O}_{13}$  films has changed upon annealing treatment. Here, the modification of the crystallinity of the  $\text{V}_6\text{O}_{13}$  films deduced from Raman measurements can be discussed using the shape and frequency of two groups of peaks located at low-frequency, i.e., in the vicinity of  $139 \text{ cm}^{-1}$ , and in the high-frequency range, i.e., the bands at 840 and  $990 \text{ cm}^{-1}$ . The RS spectrum of an as-grown film (Fig. 2a) consists of three broad bands located at 160, 330 and  $920 \text{ cm}^{-1}$  whereas the RS spectra of annealed films (Fig. 2b and 2c) display common features with the spectrum of the crystalline phase. The peak located at  $152 \text{ cm}^{-1}$ , which

appears at  $139\text{ cm}^{-1}$  in crystal, can be viewed as a distorted low-frequency mode of  $\text{V}_6\text{O}_{13}$ .

These results suggest a simple mechanism for the influence of the substrate temperature on the film stoichiometry. If we take into account that oxygen is lighter than vanadium we can suppose that the desorption leads to a higher loss of oxygen than of vanadium. Then it follows that the stoichiometry in the film will be poorer in oxygen than in the source material. This depletion in oxygen should be enhanced if the substrate temperature is higher than room temperature. So, one can expect that the film grown at  $T_s=250^\circ\text{C}$  will be oxygen-deficient if compared to the film grown at  $T_s=25^\circ\text{C}$ . However, if the annealing is performed in  $\text{O}_2$  atmosphere then the lacking oxygen can be taken from the atmosphere and the formation of oxygen-rich oxides will be favoured.

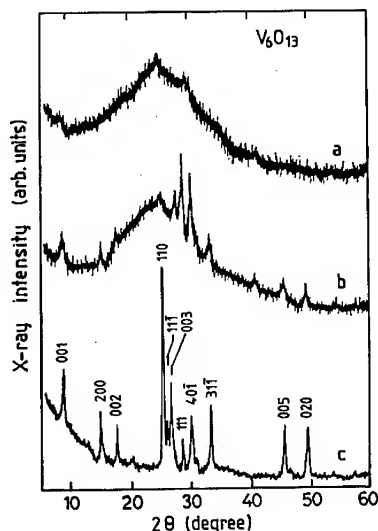


Fig. 1. X-ray diagrams of (a) as-deposited  $\text{V}_6\text{O}_{13}$  film at  $T_s=25^\circ\text{C}$ , (b) annealed film at  $T_s=300^\circ\text{C}$  for 60 h in Ar atmosphere, and (c)  $\text{V}_6\text{O}_{13}$  powder.

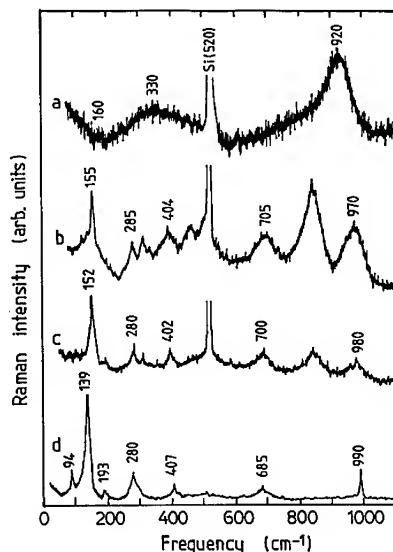


Fig. 2. Raman scattering spectra of (a-c)  $\text{V}_6\text{O}_{13}$  flash-evaporated films and (d)  $\text{V}_6\text{O}_{13}$  crystal. Films were deposited on (111) oriented silicon substrate: (a) as-grown film at  $T_s=250^\circ\text{C}$ , (b)  $T_s=25^\circ\text{C}$  and annealed in Ar, and (c)  $T_s=25^\circ\text{C}$  and annealed  $\text{O}_2$  atmosphere.

If one accepts the hypothesis of preferable desorption of oxygen during growth and its dependence on the substrate temperature as proposed above, then the following phenomena should be observed. (1) It is well known that the conduction in  $\text{V}_6\text{O}_{13}$  is mainly due to the presence of  $\text{V}^{4+}$  ions. The conductivity of oxygen-deficient films grown at high substrate temperature should be higher because in general vanadium oxides with smaller O/V ratio have higher conductivity [20]. This behavior has been identified in  $\text{V}_2\text{O}_5$  films as a consequence of the quenching rate, which is the difference in temperature between the melt and the substrate [22-23]. A decrease of the quenching rate produces an increased conductivity and a decreased activation energy. (2) If samples are annealed in oxygen atmosphere one should expect oxidation of the films and formation of vanadium oxides with higher O/V ratio, that is  $\text{V}_6\text{O}_{13}$ . Obviously, a crystallization effect should also be expected on annealing, which should promote an increase of conductivity.

The results of the electrical conductivity measurements in the  $\text{V}_6\text{O}_{13}$  films grown at both temperatures and annealed in  $\text{O}_2$  and Ar atmosphere are shown in Table I and Fig. 3. The conductivity of films grown at  $T_s=25^\circ\text{C}$  was too low to be measured. The electrical conductivity at

room temperature of an as-grown film at  $T_s=250^\circ\text{C}$  is about  $2 \times 10^{-5} \text{ S cm}^{-1}$  with an activation energy  $E_a=0.38 \text{ eV}$ , whereas the conductivity of a film annealed in Ar is four orders of magnitude higher with similar activation energy. These results can be compared with the electrical conductivities of  $\text{V}_6\text{O}_{13}$  single crystals. It has been reported [18] that stoichiometric  $\text{V}_6\text{O}_{13}$  has a conductivity  $\sigma \approx 10^{-2} \text{ S cm}^{-1}$  at room temperature whereas for  $\text{V}_6\text{O}_{13.27}$  is a little less than  $1 \text{ S cm}^{-1}$  [19]. The values of the activation energies are also consistent with those reported for  $\text{V}_6\text{O}_{13}$  crystals [20-21]. The excess oxygen creates disorder in the mixed valence  $\text{V}_6\text{O}_{13}$  which has been shown to be a bipolaronic conductor. It is noteworthy that the activation energy in film deposited at  $T_s=25^\circ\text{C}$  corresponds to about  $E_a=E_g/2$  measured by absorption experiments.

Table I. Room temperature electrical conductivity and activation energy of  $\text{V}_6\text{O}_{13}$  films grown and heat treated using different conditions.

$T_s$ ( $^\circ\text{C}$ )	Annealing	$\sigma$ (S/cm)	$E_a$ (meV)
250	-	$3 \times 10^{-5}$	380
25	Ar	$2 \times 10^{-5}$	266
25	$\text{O}_2$	$3 \times 10^{-2}$	250
250	$\text{O}_2$	$5 \times 10^{-2}$	250
250	Ar	$3 \times 10^{-1}$	191

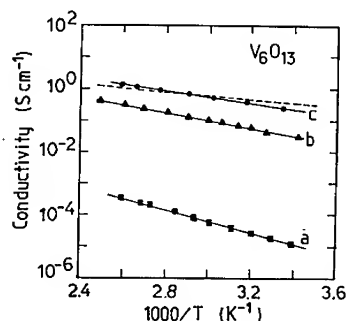


Fig. 3. Arrhenius plots of the electrical conductivity of  $\text{V}_6\text{O}_{13}$  films obtained in various conditions. (a) as-grown at  $T_s=250^\circ\text{C}$ , (b) grown at  $T_s=250^\circ\text{C}$  and annealed in  $\text{O}_2$ , and (c) grown at  $T_s=250^\circ\text{C}$  and annealed in Ar. The dashed line represents the electrical conductivity of a  $\text{V}_6\text{O}_{13}$  crystal.

#### 4. ELECTROCHEMICAL STUDIES

The electrochemical properties of a series of four films prepared at different conditions are shown in Figs. 4 and 5. These figures illustrate the discharge curves as a function of degree of lithium insertion,  $x$ , for  $\text{Li}/\text{V}_6\text{O}_{13}$  microbatteries using active cathode films grown at  $T_s=250^\circ\text{C}$  and  $T_s=25^\circ\text{C}$  (as-deposited and annealed in Ar atmosphere), respectively. These discharge measurements have been carried out using a current density  $5 \mu\text{A cm}^{-2}$ . The measured cell voltages are in the range 3.3-2.5 V. The general trends of these results are: (i) The cell voltage decreases continuously with the degree of Li insertion in the host lattice of  $\text{V}_6\text{O}_{13}$  films. (ii) There are some notable differences between the behavior of these films and crystalline  $\text{V}_6\text{O}_{13}$ . Crystalline  $\text{V}_6\text{O}_{13}$  has been thoroughly characterized as electrode material in lithium cells [6,24]. During the first discharge several plateaus are seen, reflecting the sequential filling of inequivalent sites in the cavities of the  $\text{V}_6\text{O}_{13}$  structure. (iii) Above  $x=1.2$  the voltage of the thin-film cell is higher than the voltage of the crystalline cell. (iv) About  $6e^-$  per V atom may be transferred in the host material, with voltage above 2.5 V. (v) The cell voltages for microbatteries using films deposited at  $T_s=250^\circ\text{C}$  are higher (more than 100 mV) than for cells using films deposited at room temperature. (vi) A plateau appears at about 3 V in the discharge curve of a cell with a film deposited at  $T_s=250^\circ\text{C}$  and annealed at  $300^\circ\text{C}$ . (vii) Above  $x=1.2$ , the  $\text{Li}^+$ -ion insertion in  $\text{V}_6\text{O}_{13}$  forms a homogeneous compound, the discharge curves indicate that the material remains in a single phase even for high degree of lithium intercalation.



It is obviously observed the influence of the substrate temperature on the electrochemical behavior of the active cathode films. A film grown at  $T_s=250^\circ\text{C}$  displays a steadily discharge curve in the range  $0 \leq x \leq 6$  whereas the cell voltage for a film grown at  $T_s=25^\circ\text{C}$  decreases more rapidly as the  $\text{Li}^+$ -ions are inserted in the host material. Furthermore, we observe the appearance of a voltage plateau for the film annealed at  $300^\circ\text{C}$  but the different phases recorded during the discharge of a cell with crystalline  $\text{V}_6\text{O}_{13}$  are not observed in these experiments. This behavior can be attributed to the difference in the electronic band structure. Here, there are localized states situated in the band-gap and their density varies with the film crystallinity giving rise to different electrochemical features. This assumption has been confirmed by different measurements of the films. The structure of flash-evaporated  $\text{V}_6\text{O}_{13}$  films observed by Raman scattering experiments shows that some distortions exist even in the well-reconstructed lattice. The frequency shift of the V-O bond stretching modes and the existence of the disorder-band near  $830\text{ cm}^{-1}$  which remains in films grown at  $250^\circ\text{C}$  and annealed in argon come to illustrate the medium-range disorder in polycrystalline  $\text{V}_6\text{O}_{13}$  films. The increase in the indirect gap with increasing substrate temperature may also be attributed to the change in V-V distance [23]. The distorted structure of  $\text{V}_6\text{O}_{13}$  films induces modification in the electronic band structure which should appear in the 3d-subband system [15]. Consequently, a slight shift of the subband gives rise to an increase in indirect electronic density of states, and this is in agreement with the electrochemical features of  $\text{V}_6\text{O}_{13}$  film cells.

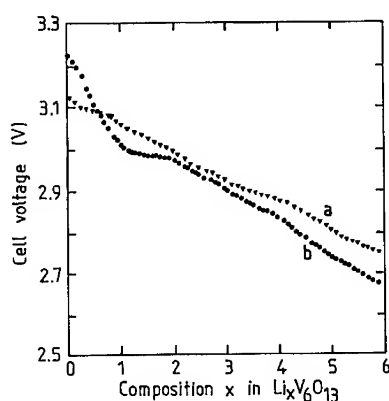


Fig. 4. Discharge curves as a function of the degree of lithium insertion for  $\text{Li}/\text{V}_6\text{O}_{13}$  thin-film microbatteries. Active cathode films were grown with different conditions. (a)  $T_s=250^\circ\text{C}$ , as deposited; (b)  $T_s=250^\circ\text{C}$ , annealed in Ar.

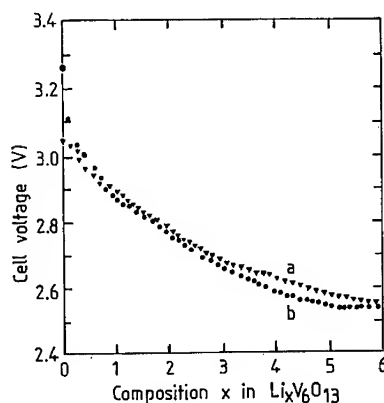


Fig. 5. Discharge curves as a function of the degree of lithium insertion for  $\text{Li}/\text{V}_6\text{O}_{13}$  thin-film microbatteries. Active cathode films were grown with different conditions. (a)  $T_s=25^\circ\text{C}$ , as deposited; (b)  $T_s=25^\circ\text{C}$ , annealed in Ar.

Figures 6 and 7 illustrate the chemical diffusion coefficients of  $\text{Li}^+$ -ions as a function of degree of lithium insertion in  $\text{Li}_x\text{V}_6\text{O}_{13}$  films. For films grown at either  $T_s=25^\circ\text{C}$  or  $T_s=250^\circ\text{C}$  the diffusion coefficient remains constant over the compositional range  $0 \leq x \leq 2$  with a mean value of about  $10^{-13}\text{ cm}^2\text{ s}^{-1}$  and then decreases abruptly with increasing the lithium insertion. The best results are obtained for film grown at  $T_s=25^\circ\text{C}$  and annealed at  $300^\circ\text{C}$  in argon atmosphere. This film exhibits a constant diffusion coefficient  $10^{-13}\text{ cm}^2\text{ s}^{-1}$ . This value is about five orders of magnitude lower than the values obtained for the stoichiometric crystalline phase. West et al. [24] have measured a chemical diffusion coefficient of  $9 \times 10^{-9}\text{ cm}^2\text{ s}^{-1}$  using complex impedance measurements. This is reasonable. In other systems, such as in  $\text{Li}_x\text{InSe}$  [25] and  $\text{LiMn}_2\text{O}_4$  [26] the same result has been obtained. As the diffusion path for lithium ions passes through the cavities, occupation of the pyramidal sites will change the diffusion coefficients in polycrystalline

film grown at  $T_s=250^\circ\text{C}$ . The difference between oxide prepared in crystalline form and the film could thus be ascribed to differences in crystal perfection, i.e., static disorder or short chains with undistorted cavities.

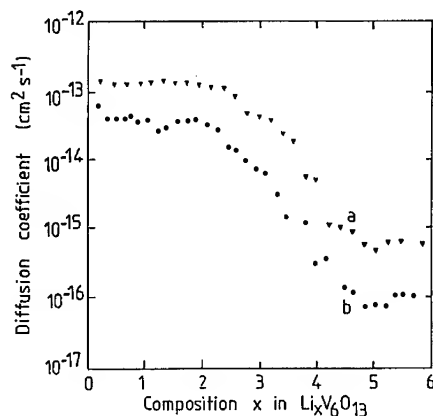


Fig. 6. Chemical diffusion coefficient of  $\text{Li}^+$  ions in  $\text{Li}_x\text{V}_6\text{O}_{13}$  films as a function of the degree of lithium insertion. The growth conditions are those mentioned in Fig. 4.

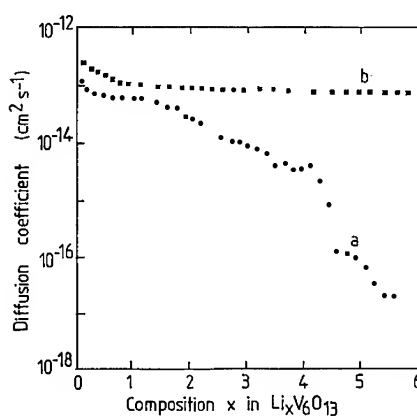


Fig. 7. Chemical diffusion coefficient of  $\text{Li}^+$  ions in  $\text{Li}_x\text{V}_6\text{O}_{13}$  films as a function of the degree of lithium insertion. The growth conditions are those mentioned in Fig. 5.

Considering the abrupt decrease of the chemical diffusion coefficient of  $\text{Li}^+$ -ions in polycrystalline  $\text{Li}_x\text{V}_6\text{O}_{13}$  films, it is noteworthy that, in  $\text{V}_6\text{O}_{13}$ , the  $\text{Li}^+$  conduction is believed to be virtually one-dimensional, with lithium ions residing in double channels of interconnected cavities [30]. The low diffusion coefficient values are attributed to the undefined conduction paths between grains of the films. The potential barriers are more important in the inter-grain and the  $\text{Li}^+$ -ions may be trapped by structural defects. The differences between materials of low and high crystallinity, as far as the microstructural and macrostructural aspects are concerned have been pointed out by Pereira-Ramos et al. [27]. At the macroscopic level, materials of low crystallinity obtained by evaporation techniques are formed by small particles, i.e., the crystallites of the film. These influence thermodynamics and kinetics as observed in the electrochemical behavior of the studied  $\text{V}_6\text{O}_{13}$  thin-films cells, which may be related with the density of the material.

## 5. CONCLUSION

It has been demonstrated for the first time that  $\text{V}_6\text{O}_{13}$  films can be prepared using the flash-evaporation technique. The structural properties of  $\text{V}_6\text{O}_{13}$  films were determined by X-ray diffraction and Raman scattering experiments. Similar results were obtained from both techniques. It is shown that a film grown at  $T_s=25^\circ\text{C}$  is amorphous whereas the effect of thermal annealing temperature,  $T_a$ , forms a polycrystalline structure.

The results of the electrical conductivity measurements in the  $\text{V}_6\text{O}_{13}$  films grown at different substrate temperatures show that the behavior can be identified as a consequence of the quenching rate, which is the difference in temperature between the melt and the substrate. A decrease of the quenching rate produces an increased conductivity and a decreased activation energy. The activation energy in film deposited at  $T_s=25^\circ\text{C}$  corresponds to about  $E_a=E_g/2$  measured by absorption experiments.

This work has clearly shown the influence of the growth conditions of  $\text{V}_6\text{O}_{13}$  thin films on their electrochemical behavior during the lithium insertion in the host structure. The kinetically accessible discharge range amounts to  $0 \leq x \leq 6$  for the Li insertion in  $\text{Li}_x\text{V}_6\text{O}_{13}$  active cathode films.

The choice of a  $V_6O_{13}$  flash-evaporated film in solid-state microbatteries depends on its utilization. Two types of films can be prepared. A film deposited on substrate at 250°C delivers high-voltage utilization but the low diffusion coefficient will be a current density limitation. A film grown at room temperature presents higher and constant diffusion coefficient but delivers lower voltage than the former. In  $V_6O_{13}$  films deposited on substrate at 25°C and annealed at 300°C in argon atmosphere, the diffusion coefficient  $10^{-13} \text{ cm}^2 \text{ s}^{-1}$  remains stable in the entire intercalation range.

### Acknowledgments

The authors wish to thank Dr. G.A. Nazri who provided crystalline stoichiometric  $V_6O_{13}$ . One of us (A.G) is grateful for the financial support from CNPq (Brazil).

### REFERENCES

1. C. Julien and G.A. Nazri, Solid State Batteries: Materials Design and Optimization (Kluwer, Boston, 1994).
2. Y. Fujita, K. Miyazaki and C. Tatsuyama, *Jpn. J. Appl. Phys.* **24**, 1082 (1985).
3. C. Julien, A. Khelifa, J.P. Guesdon and A. Gorenstein, *Appl. Phys. A* **78**, 173 (1994).
4. D.W. Murphy and P.A. Christian, *Science* **205**, 651 (1979).
5. D.W. Murphy, P.A. Christian, F.J. DiSalvo and J.N. Carides, *J. Electrochem. Soc.* **126**, 497 (1979).
6. K. West, B. Zachau-Christiansen and T. Jacobsen, *Electrochim. Acta* **28**, 1829 (1983).
7. F. Aeibi, *Helv. Chim. Acta* **31**, 8 (1948).
8. K.A. Wilhelmi, K. Waltersson and L. Kihlborg, *Acta Chem. Scand.* **25**, 2675 (1971).
9. P.D. Dernier, *Mat. Res. Bull.* **9** (1974) 955.
10. L. Murawski, C. Gledel, C. Sanchez, J. Livage and J.P. Audiere, *J. Non-Cryst. Solids* **89**, 98 (1987).
11. C. Julien, A. Khelifa, N. Benramdane, J.P. Guesdon, P. Dwonkowski, I. Samaras and M. Balkanski, *Mater. Sci. Eng. B* **23**, 105 (1994).
12. I.R. Beattie and T.R. Gilson, *J. Chem. Soc. A* 2322 (1969).
13. L. Abello, E. Husson, Y. Repelin and G. Lucazeau, *Spectrochim. Acta A* **39**, 641 (1983).
14. F.D. Hardcastle and I.E. Wachs, *J. Phys. Chem.* **95**, 5031 (1991).
15. W. Van Hove, P. Clauws and J. Vennik, *Solid State Commun.* **23**, 11 (1980).
16. P. Clauws and J. Vennik, *Phys. Status Solidi (b)* **69**, 491 (1975).
17. C. Sanchez, J. Livage and G. Lucazeau, *J. Raman Spectr.* **12**, 68 (1982).
18. C. Julien, L. El-Farh, M. Balkanski, G.A. Nazri and O.M. Hussain, *Appl. Surf. Sci.* **65-66**, 325 (1993).
19. M. Bose, *Phys. Rev. B* **46**, 7542 (1992).
20. S. Kachi, T. Takada and K. Kosuge, *J. Phys. Soc. Japan* **18**, 1839 (1963).
21. H. Okinaka, K. Nagasawa, K. Kosuge, Y. Bando and S. Kachi, *J. Phys. Soc. Jpn* **29**, 245 (1970).
22. C. Sanchez, J. Livage, J.P. Audiere and A. Madi, *J. Non-Cryst. Solids* **65**, 285 (1984).
23. A.M. Abo-El-Soud, B. Mansour and L.I. Soliman, *Thin Solid Films* **247**, 140 (1994).
24. K. West, B. Zachau-Christiansen, T. Jacobsen and S. Atlung, *J. Power Sources* **14**, 235 (1985).
25. C. Julien, I. Samaras, M. Tsakiri, P. Dzwonkowski and M. Balkanski, *Mater. Sci. Eng. B* **3**, 25 (1989).
26. C. Liquan and J. Schoonman, *Solid State Ionics* **67**, 17 (1994).
27. J.P. Pereira-Ramos, N. Baffier and G. Pistoia, in Lithium Batteries, New Materials, Development and Perspectives, edited by G. Pistoia (Elsevier, Amsterdam, 1994), p. 281.

## ELECTROCHROMISM AND PHOTOCROMISM OF WO<sub>3</sub> THIN FILMS

C. LEFROU, O. MARROT, F. GAROT,

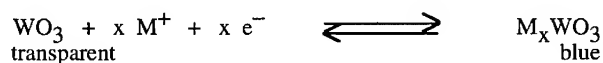
Saint-Gobain Recherche, 39 quai Lucien Lefranc, 93 303 Aubervilliers Cedex, France.

### ABSTRACT

A photochromic effect is observed in WO<sub>3</sub>-based electrochromic devices with an ion-conducting polymer as electrolyte. Upon exposure to sun light, the electrochromic cells become blue. This is due to a change of color of the WO<sub>3</sub> electrode. The photoeffect on this layer is due to a simultaneous insertion reaction (reduction) of the WO<sub>3</sub> material and a photooxidation of water contained in the polymer. It is reversible and therefore not destructive for the complete device. The study of the transmittance and rest potential as a function of the time of exposure to light shows that a steady state is reached in c.a. 10 hours. The addition of U.V.-cut filters changes the reached steady-state, indicating that the photochromic effect is dependent upon the structure of the WO<sub>3</sub> material.

### 1. INTRODUCTION

Almost all the electrochromic devices that have been investigated up to now use WO<sub>3</sub> as cathodic electrochromic material. The simultaneous insertion of cations like H<sup>+</sup> or Li<sup>+</sup> and electrons in a WO<sub>3</sub> thin film causes a color change from transparent to dark blue according to :



A major requirement for electrochromic devices in outdoor applications is stability under solar irradiation. WO<sub>3</sub>, however, is also a photochromic material : in presence of oxidizable species (like water, ethanol, chloride anions,...cf [1,2]), exposure to light will induce a photoelectrochemical insertion in WO<sub>3</sub> thin films, which become blue.

This work reports results about the effect of illumination of a WO<sub>3</sub> thin film in contact with a polymer electrolyte, as used in complete electrochromic devices. Analysis of the phenomena and its possible effects on complete electrochromic devices will be discussed.

### 2. EXPERIMENTAL

Two types of devices were used for this study. The first one is an electrochromic half-cell, consisting of a three-layered structure between two glass substrates :

transparent electron-conducting layer /  $\text{WO}_3$  / ion-conducting polymer.

In the second one, an additionnal transparent electron-conducting layer was used as a counter-electrode :

transparent electron-conducting layer /  $\text{WO}_3$  / ion conducting polymer / transparent electron-conducting layer.

The transparent electron-conducting layer was  $\text{SnO}_2:\text{F}$  with a sheet resistance of  $10 \Omega / \text{square}$ . The ion-conducting polymer was a  $\text{PEO}-\text{H}_3\text{PO}_4$  complex. The  $\text{WO}_3$  layer was deposited by planar DC magnetron sputtering from a tungsten target in an argon / oxygen plasma. The thickness of this amorphous layer was about 310 nm.

The two xenon lamps that were used in the experiment had quartz and borosilicate filters and a power of 0.55 and  $0.2 \text{ W/m}^2 \cdot \text{nm}$  at 340 nm respectively. Two kinds of U.V.-cut filters could be added for varying the spectrum in the U.V. region : filter 385 (respectively 410) will absorb, with  $A > 99\%$ , all the wavelengths below 385 nm (respectively 410 nm), that is, energies above 3.2 eV (respectively 3.0 eV).

### 3. COLORIMETRIC EVOLUTION

Exposure to light of half-cells induces a color change from transparent to bluish. Figure 1 shows the evolution of the normal transmittance of the half-cell exposed without any U.V.-cut filter.

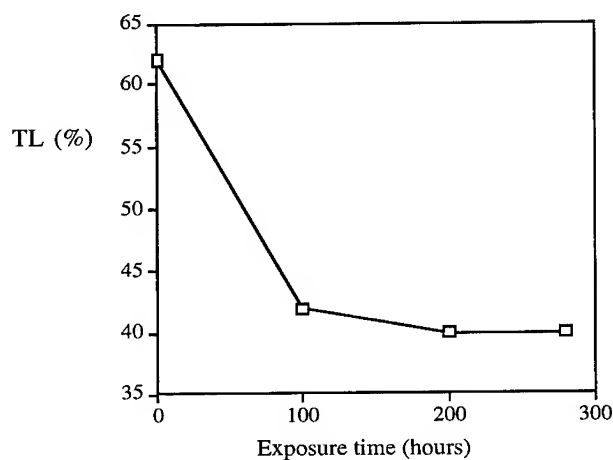


Figure 1 : transmittance of a half-cell exposed without U.V.-cut filter to a light source of  $0.55 \text{ W/m}^2 \cdot \text{nm}$  at 340 nm.

In another experiment, a  $\text{WO}_3$  layer deposited on  $\text{SnO}_2\text{:F}$  coated glass and with no polymer overcoat was exposed directly to light and did not become blue.

Two important results could be drawn from these experiments :

- \* a photochromic effect on the  $\text{WO}_3$  layer is observed when the layer is in contact with the electrolyte ; that is, in the cell configuration,
- \* a steady state is reached after several hours.

In order to study the influence of the light spectrum in the U.V. region, the same experiment was carried out with half-cells protected with a U.V.-cut filter. A color effect was also observed. The coloration was, however, weaker than in the previous experiment, as shown in table 1.

	before test			after 200 h		
	TL (%)	$\lambda_d$ (nm)	pe (%)	$\Delta\text{TL}$ (%)	$\Delta\lambda_d$ (nm)	$\Delta\text{pe}$ (%)
without filter	62	575	11,5	- 22	- 76	- 8,7
filter 385	72	574	8,1	- 14	- 64	- 6,7
filter 410	65	574	10,2	- 11	- 24	- 7,5

Table 1 : effect of U.V.-cut filter addition on half-cells color evolution after 200 hours of light exposure.

TL is the normal transmittance ,  $\lambda_d$  is the dominant wavelengh, pe is the purity.

We have shown that the photochromic effect we observed in the electrochromic half-cells depends upon the spectrum of the light source. In all cases a steady state was reached after several hours.

#### 4. EVOLUTION OF THE REST POTENTIAL

The opening of blue cells after exposure showed that the blue color is due to the  $\text{WO}_3$  layer. Cyclic voltammetry of the blue layer dipped in an aqueous electrolyte showed that the coloration was reversible and that the layer was not deteriorated. This blue color is, therefore, related to an electron + cation insertion; that is, the coloration reaction occuring in the standard operation of an electrochromic device. It has been shown that the change from a non inserted layer to a partially-inserted layer corresponds to a significant evolution of the layer thermodynamic potential [3]. Therefore, one could take advantage of this characteristic to follow the layer state of insertion during the exposure.

In order to monitor the  $\text{WO}_3$  layer potential during exposure to light, a set of electrochromic cells using  $\text{SnO}_2\text{:F}$  were manufactured. Neglecting the influence of light on the potential of the transparent electron-conducting layer, the change of the cell rest potential is equal to the variation of the  $\text{WO}_3$  layer potential ; that is, its state of insertion.

Figure 2 shows the evolution of the rest potential of a cell with  $\text{SnO}_2\text{:F}$  as a counter-electrode during a light exposure without U.V.-cut filter.

This experiment is consistent with the previous one and confirms the existence of a steady state. Curve fitting by an exponential shows a time constant of about 10 hours for reaching this steady state, which corresponds to a change of transmittance from 73 % to 51 % and a total charge insertion of  $3.8 \text{ mC.cm}^{-2}$ .

The same experiment with an U.V.-cut filter (filter 385) shows the same kinetics parameters (time constant of 10 hours) but the steady state will be different : the transmittance goes from 74 % to 70 % and the total inserted charge is  $0.8 \text{ mC.cm}^{-2}$ .

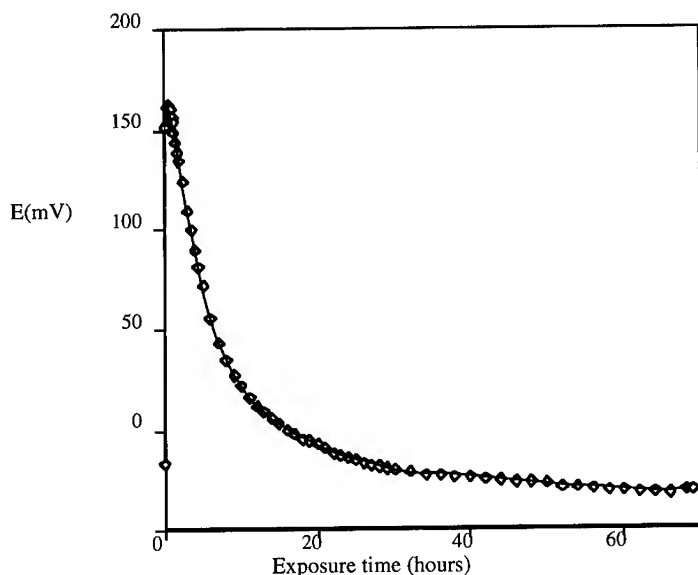
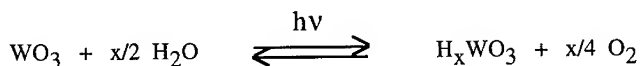


Figure 2 : rest potential of a cell with  $\text{SnO}_2\text{:F}$  as counter-electrode exposed without U.V.-cut filter to a light source of  $0.2 \text{ W/m}^2\text{.nm}$  at  $340 \text{ nm}$ .

## 5. DISCUSSION

As  $\text{WO}_3$  is a n-type semi-conductor material [1,4-6], the only possible photoelectrochemical reactions are photooxidation effects : the apparent oxidation potential under illumination is smaller than in dark. In the system, the  $\text{WO}_3$  layer is in contact with a polymer and the most probable oxidizable species is water. With illumination, the apparent potential of oxidation of water (producing oxygen) is smaller and a battery situation is reached between oxidation of water and reduction of  $\text{WO}_3$  (i.e. insertion) :



In our experiments, the steady state corresponds to about  $2 \text{ mC.cm}^{-2}$ . To reach this results by the above reaction, about 10 ppm of water is needed : this value is by far less than the water content of the polymer in the system. The reaction produces oxygen at the interface ; however, the corresponding bulk concentration in the polymer is  $5.10^{-4} \text{ mol.L}^{-1}$ , which is too low to cause the formation of bubbles (none was observed in the experiments).

One can explain that the system reaches a steady state, considering that the potentials change during the photoelectrochemical reaction. Producing oxygen, the potential of  $\text{H}_2\text{O} / \text{O}_2$  increases a little and on the other hand the progressive insertion of the  $\text{WO}_3$  layer causes a decrease of the potential of  $\text{H}_x\text{WO}_3 / \text{WO}_3$ . Progressively the battery current, therefore, decreases and tends to zero, indicating that a steady state is reached.

The influence of the light source spectrum (additional filters) on the steady state is not easy to understand. With a perfect semi-conductor, energy levels higher than the gap energy would not be more efficient than the gap energy. Only a binary behavior should therefore be expected : if  $E > E(\text{gap})$  a photochromic effect is observed, and if  $E < E(\text{gap})$  there is no effect of illumination. In the previous experiment, a progressive effect is observed. A possible explanation may be the amorphous structure of the  $\text{WO}_3$  layer, for which localised states could exist and therefore the gap would not be well defined. This assumption is confirmed by the analysis of the optical absorption spectrum (cf figure 3) of the same material deposited on a silica substrate :

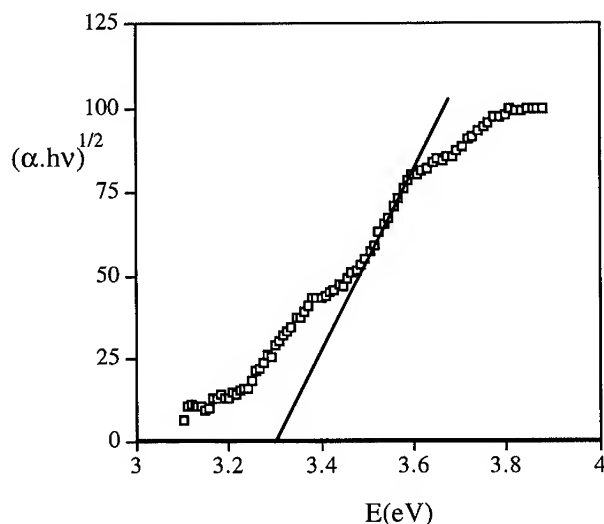
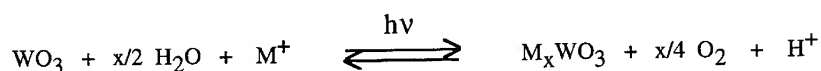


Figure 3 : Determination of gap energy with the absorption spectrum of a  $\text{WO}_3$  amorphous layer on a silica substrate.



## 6. CONCLUSIONS

In the configuration of complete electrochromic devices, one could observe a photoelectrochemical effect with the insertion of WO<sub>3</sub> layer and photooxydation of some traces of water. This effect was studied in protonic devices but is also observed in lithium devices :



In a complete device this photochromic effect is not destructive in short times because it is reversible (the WO<sub>3</sub> layer could be desinserted), limited (a steady state is rapidly reached) and the oxygen production is not sufficient to produce bubbles. Upon long exposure time, however, this will cause progressively an increase of the total charge in the complete system which could be destructive.

For outdoor applications, it is important to lower the photochromic effect in electrochromic devices. One way to do this is to lower dramatically the water concentration at the WO<sub>3</sub> / polymer interface. Another way, which seems more suitable, according to the literature [1,4-6], is to work on the structure of the WO<sub>3</sub> material in order to lower the gap energy and the number of localised states.

## 7. REFERENCES

- [1] J.Desilvestro, M.Grätzel, J. Electroanal. Chem. **238**, 129 (1987).
- [2] M.Nagasu, N.Koshida, J. Appl. Phys. **71**, 398 (1992).
- [3] M.Rezrazi, B.Vuillemin, O.Bohnke, J. Electrochem. Soc. **138**, 2770 (1991).
- [4] W.Gissler, R.Memming, J. Electrochem. Soc. **124**, 1710 (1977).
- [5] W.Erbs, J.Desivestro, E.Borgarello, M.Grätzel, J. Phys. Chem. **88**, 4001 (1984).
- [6] P.Judenstein, A.Chemseddine, C.Sanchez, J. Chim. Phys. **89**, 1469 (1992).

## HIGH RATE DEPOSITION OF NICKEL OXIDE ELECTROCHROMIC THIN FILMS BY REACTIVE DC MAGNETRON SPUTTERING

Kazuki YOSHIMURA, T. MIKI and S. TANEMURA  
Multifunctional Material Science Department  
National Industrial Research Institute of Nagoya, Nagoya, 462 JAPAN

### ABSTRACT

Nickel oxide electrochromic thin films were prepared by reactive DC magnetron sputtering. As-deposited optical property and electrochromic behavior strongly depended on the target operation mode and the substrate temperature. In the condition of low oxygen flow ratio (~1%), the deposition rate can be raised up to 40 nm/min at the power of 60 W. The sample with the deposition rate of 30 nm/min exhibited the best electrochromic performance when the substrate temperature was kept to 200°C-300°C during sputtering. The integrated luminous transmittance of the best sample could be controlled from 6.6% to 82.3%.

### INTRODUCTION

Electrochromic nickel oxide films can be prepared by several techniques such as electrodeposition [1,2], sol-gel processing [3], vacuum evaporation [4], electron beam deposition [5-6] and sputter deposition [7-12]. Among these techniques a reactive DC sputtering is considered to have advantages in the lower target and instrument costs and higher deposition rate than RF sputtering.

Generally reactive sputtering with a metal target is often faced with following difficulties [13]. One is a deposition rate reduction due to the presence of reactive gas. The other one is formation of compound at a target surface caused by a reaction with induced gas. The second phenomena is called 'poisoning' of target and sometimes bad reproducibility of film formation is caused.

To resolve these problems, we prepared nickel oxide thin films by reactive DC magnetron sputtering under various conditions and identified the preparation method with the high deposition rate and the good reproducibility.

### EXPERIMENTAL

Nickel oxide films were prepared by reactive DC magnetron sputtering with a water-cooled metallic nickel target (50 mm in diameter, 99.9% purity). Argon and Oxygen gases were introduced through separate mass flow controllers. Total pressure was fixed to 3 Pa. Oxygen flow ratio to argon gas was changed from 1% to 100%.

The substrates were 11×11×1 mm glass plates with a conductive coating of ITO (Indium-Tin Oxide) having a sheet resistance of 10  $\Omega/\text{cm}^2$ . They were mounted on the substrate holder which can be heated up to 800°C in an oxygen containing atmosphere using a SiC ceramic heater. Substrate temperature was monitored using the calibrated reading of a W/Re thermocouple in contact with the surface of the substrate holder. The discharge power was set at a value in the 5 - 60 W interval.

Deposition rate and thickness were monitored in real time with a quartz oscillator thickness and rate monitor whose reading was calibrated by the post-deposition measurement using a noncontact surface profilometer model.

After the evacuation down to  $5 \times 10^{-4}$  Pa by a turbomolecular pump, the first pre-sputtering was performed for 5 minutes by pure argon atmosphere to remove the oxidized layer of the target. Argon and oxygen gas were then introduced to the chamber and the second presputtering was carried out for 5 minutes. After these procedure, actual deposition was started by opening the shutter.

The spectral transmittance and reflectance of as-deposited films were measured by HITACHI U3400 spectrometer. After electrochemical treatment using a cyclic voltammetry technique, sample in colored state and bleached state were investigated by *in situ* visible transmittance measurements.

## RESULTS AND DISCUSSION

### Deposition rate

Because the deposition rate dependence on oxygen flow rate and induced power is the most important factor in the reactive sputtering system, we firstly studied the detailed relationship among these three parameters.

Figure 1 shows the measured deposition rate of unheated samples as a function of the oxygen flow ratio and the sputtering power. The 3-dimensional mesh was plotted using polynomial functions to fit the measured data by a least mean square approximation. Before every measurement nickel target was presputtered by pure Ar atmosphere to prevent poisoning effect. Substrate temperature has minor effect on the deposition rate and this curve can be applied for heated samples.

It is well known that there are two operation modes in reactive sputtering: metallic mode and compound mode [14]. Between two modes there is narrow transition region. Fig.1 shows that in the case of nickel target the deposition rate dependence on oxygen flow is different from that of other target. The deposition rate at constant power of 60W decreases slightly with increasing oxygen flow in the flow ratio range of more than 30%. This range corresponds to compound mode. But at oxygen flow ratio of less than 30% the deposition rate decreases rapidly with decrease of oxygen flow. This range may correspond to transition region. It is characteristic for nickel target that no metallic mode was observed in the oxygen flow ratio from 1% to 100% and transition region is much wider than other targets. The boundary between transition region and compound mode is displayed by the solid line in Fig. 1. It should be remarked that on-set oxygen flow ratio to compound mode depend on induced power. It decreases with decrease of power. In compound mode the maximum deposition rate is about 7 nm/min at 60W. But in transition region the deposition rate can be raised up to 40 nm/min at the same power.

In compound mode the sputtered nickel target was deep blue in appearance, while the sputtered target looked metallic gold in transition region. In our experiment every time before the deposition, presputtering using pure Ar atmosphere was performed to remove oxidized layer being checked to show silver metallic surface of nickel target. These procedure is important to prevent poisoning and to get the reproducible results.

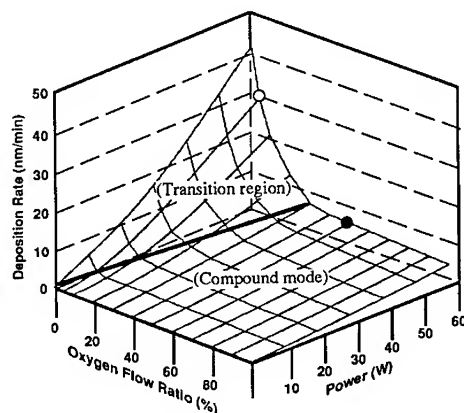


Figure 1

3-dimensional plot of deposition rate vs. oxygen flow ratio and induced power.

Table I. Sample preparation conditions.

	Oxygen flow ratio (%)	Deposition rate (nm/min)	Substrate temperature (°C)
Sample A	5	30	60
Sample B	50	5	70
Sample C	5	30	200
Sample D	50	5	200
Sample E	5	30	400
Sample F	50	5	400

#### Optical Transmittance

The optical properties of as-deposited samples showed strong dependence on the deposition rate and the substrate temperature. In this paper we selected typical 6 conditions which are specified in Table I and show the results of characterizations. Samples A, C & E were sputtered in transition region and had high deposition rate, while samples B, D & F were sputtered in compound mode and had low deposition rate. In Fig. 1 each condition is displayed by open circle in transition region and filled circle in compound mode, respectively. Samples A and B were grown on unheated substrates. All samples had the same thickness of about 100 nm for comparison.

Measured spectral transmittance of as-deposited samples are summarized in Fig. 2. Integrated solar transmittance  $T(\text{sol})$  and integrated luminous transmittance  $T(\text{lum})$  [5] were calculated from spectra in Fig. 2. Results are given on the 1st and the 2nd columns of Table II, respectively.

In unheated conditions the transmittance of as-deposited samples sputtered in compound mode is small and have dark brown color. While the transmittance of unheated samples sputtered in transition region depend on the deposition rate. The sample with higher deposition rate has higher solar and luminous transmittance. The samples with the deposition rate more than 20 nm/min look pale gray.

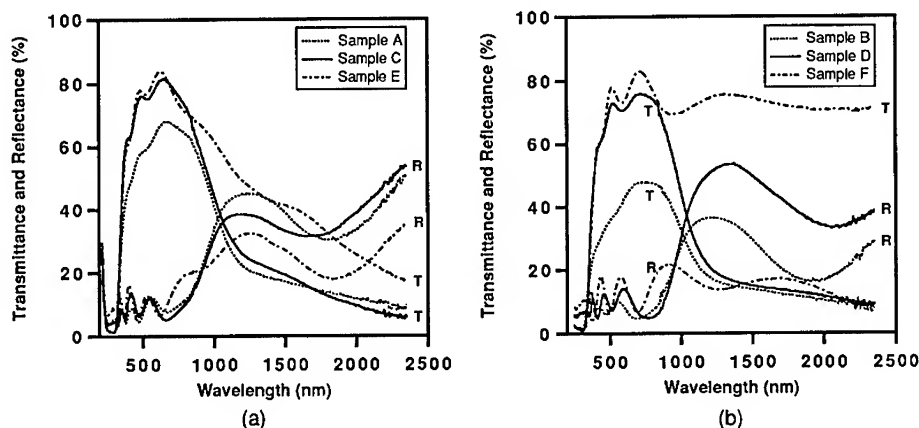


Figure 2 Spectral transmittance (T) and reflectance (R) of as-deposited samples: (a) sputtered in transition region with the deposition rate of 30 nm/min, (b) sputtered in compound mode with the deposition rate of 5 nm/min.

As seen in Fig. 2 the transmittance of sample B sputtered in compound mode is much smaller than that of sample A sputtered in transition region. Integrated solar and luminous transmittance of sample B are also smaller than samples A. It means sample B is already colored in as-deposited state. It has been reported that as-deposited films by sputtering have dark brown color [6-8]. But our results show the sample sputtered in transition region with high deposition rate are pale gray in appearance and more transparent.

In heated conditions the difference of transmittance between the samples in compound mode and the samples in transition region is smaller. Though the transmittance of samples C is slightly larger than sample D, both samples look pale gray.

Solar and luminous transmittance of samples E & F are very high and both samples look almost transparent. Transmittance of sample E in near infrared region is larger than that of samples with lower substrate temperatures (samples A-D). Optical property of sample F is quite different from other samples. Its transmittance is high and reflectance is low in all measured region.

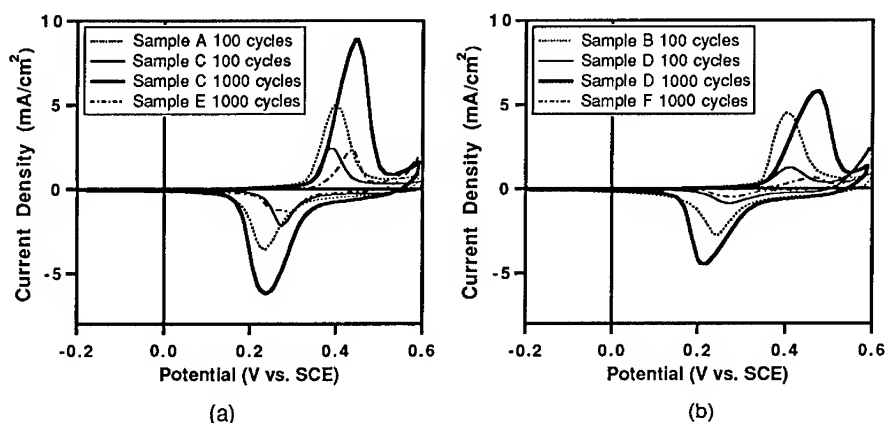


Figure 3 Cyclic Voltammograms of samples: (a) sputtered in transition region with the deposition rate of 30 nm/min, (b) sputtered in compound mode with the deposition rate of 5 nm/min.

#### Cyclic voltammetry

Electrochemical properties of the sputtered nickel oxide films were studied by cyclic voltammetry. Deposited films were cycled using a triangular waveform in 1N KOH solution with a standard three-electrode configuration consisting of the sample as the working electrode, a conventional saturated calomel electrode (SCE) and a Pt counter electrode.

Figure 3 presents the cyclic voltammetric curves of samples. The cyclic potential range was set from -0.2 to +0.6 V at a scan rate of 20 mV/s. The working area of the sample was 0.7 cm<sup>2</sup>. All potentials are reported with respect to SCE.

These results show that their electrochromic properties have a strong dependence on the substrate temperature rather than the deposition rate. In samples A & B an anodic peak occurs at 0.4 V and the cathodic peak occurs at 0.24 V after 100 cycles. Each sample shows almost no peak at the first scan. But after aging the anodic and cathodic peaks increased in size, and the anodic peak position shifted to the positive side and the cathodic peak position shifted to the negative side respectively. After 150 cycles samples A & B show degradation and peak current decrease. Moreover after 500 cycles a part of the films peeled off in both samples.

Anodic and cathodic peak currents of samples C & D are not so large compared with samples A & B after 100 cycles. But these peaks constantly increase up to 800 cycles. After 1000 cycles

very large peak current are established for samples C & D. Peak current of sample C is 20% larger than sample D.

Reported deposition rate of nickel oxide films by sputtering were low level, maximum 5 nm/min. Svensson *et al.* reported the sample with the deposition rate of more than 6 nm/min showed significant degradation after 50 cycles [7]. It has been also reported that the annealed sample showed degradation of electrochromic performance [8]. But we found that after enough aging the samples with substrate temperature of 200°C shows good electrochromism although the sample has the deposition rate as high as 30 nm/min.

Anodic and cathodic peak current of samples E & F were very small even after 1000 cycles. Especially peak current of sample F is only 10% of sample D.

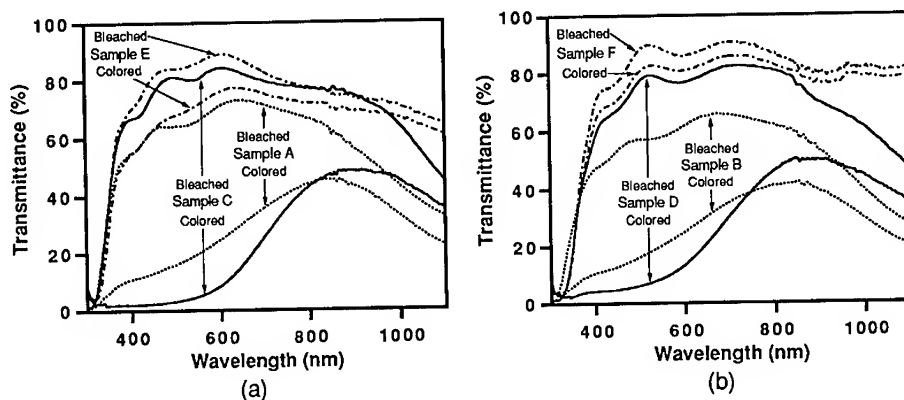


Figure 4 *In situ* spectral transmittance in fully bleached state and fully colored state: (a) sputtered in transition region with the deposition rate of 30 nm/min, (b) sputtered in compound mode with the deposition rate of 5 nm/min. Samples A & B are after 100 cycles. Samples C-F are after 1000 cycles.

#### *in situ* Optical Property

After cyclic voltammetry we measured *in situ* optical transmittance. Electrochemical cell contained a 1N KOH electrolyte was attached to optical spectrometer. Normal visible transmittances were measured after fully coloring and fully bleaching. These *in situ* spectral transmittance are shown in Fig. 4. Transmittance of samples A & B were measured after 100 cycles. That of other samples were measured after 1000 cycles. Integrated luminous transmittance in colored state and bleached state calculated from the spectra in Fig. 4 are listed on the 3rd and the 4th columns of Table II respectively.

Sample C & D shows excellent electrochromism. Especially optical modulation range of sample C is quite wide. Its integrated luminous transmittance can be varied continuously and reversibly between 6.6% and 82.3%.

Electrochromism of samples A & B are better than sample C & D after 100 cycles. But as mentioned previously they show strong degradation after 500 cycles. Samples E & F are always almost transparent.

The electrochromic performance of samples with the substrate temperature of 300°C was quite similar to that of samples of 200°C. Optical modulation range of samples with the deposition rate of 40 nm/min was narrower than that of the sample with the rate of 30 nm/min. The best electrochromic performance were obtained for samples with substrate temperature of 200 - 300 °C and deposition rate of 30 nm/min.

Table II. Integrated solar and luminous transmittance.

	As-deposited		After cyclic voltammetry	
	T(sol) (%)	T(lum) (%)	T(lum) (%) (bleached)	T(lum) (%) (colored)
Sample A	47.7	64.9	67.9	21.7
Sample B	33.2	39.7	59.4	21.8
Sample C	56.7	77.1	82.3	6.6
Sample D	53.2	71.4	77.6	10.7
Sample E	64.4	79.6	85.0	72.8
Sample F	72.7	74.9	87.6	81.5

## CONCLUSIONS

In the reactive DC sputtering of metal nickel target, target operation mode is classified into transition region and compound mode. In compound mode as-deposited unheated films looks dark brown, while in transition region as-deposited films looks pale gray and deposition rate can be raised up to 40 nm/min.

The electrochromic behavior of sputtered films strongly depended on the substrate temperature during sputtering. The sputtered films which had the deposition rate of 30 nm/min with substrate temperature of 200°C-300°C showed excellent electrochromism after several hundred voltammetric cycles. The integrated luminous transmittance could be varied from 6.6% up to 82.3% for the best sample.

## REFERENCES

1. P. C. Yu and C. M. Lampert, *Solar Energy Mater.* **25**, 301 (1992).
2. M. Fantini and A. Gorenstein, *Solar Energy Materials* **16**, 487 (1987).
3. T. Miki, K. Yoshimura, Y. Tai, M. Tazawa, P. Jin and S. Tanemura, in *Proc. ISES Solar World Congress, Budapest 1993* (Hungarian Energy Society, Hungary, 1993) Vol. 2, pp. 304.
4. C. Ottermann, A. Temmink and K. Bange, in *Proc. Optical Materials Technology for Energy Efficiency and Solar Energy Conversion IX, The Hague* (SPIE, Washington, 1990) pp. 111.
5. N. R. Lynam and H. R. Habibi, in *Optical Materials Technology for Energy Efficiency and Solar Energy Conversion VII: Hamburg* (SPIE, Washington, 1988) pp. 63.
6. A. Agrawal, H. R. Habibi, R. K. Agrawal, J. P. Cronin, D. M. Roberts, R. Caron-Popowich and C. M. Lampert, *Thin Solid Films* **221**, 239 (1992).
7. J. S. E. M. Svensson and C. G. Granqvist, *Appl. Phys. Lett.* **49**, 1566 (1986).
8. S. Yamada, T. Yoshioka, M. Miyashita, K. Urabe and M. Kitao: *J. Appl. Phys.* **63**, 2116 (1988).
9. W. Estrada, A. M. Andersson and C. G. Granqvist, *J. Appl. Phys.* **64**, 3678 (1988).
10. R. S. Conell, D. A. Corrigan and B. R. Powell, *Solar Energy Mater.* **25**, 301 (1992).
11. D. A. Wruck and M. Rubin, *J. Electrochem. Soc.* **140**, 1097 (1993).
12. A. M. Anderson, W. Estrada and C. G. Granqvist, in *Optical Materials Technology for Energy Efficiency and Solar Energy Conversion IX, The Hague* (SPIE, Washington, 1990) pp. 96.
13. J. A. Thornton, *Deposition Technologies for Films and Coatings*, edited by R. F. Bunshah (Noyes, Park Ridge, 1982) pp.170.
14. E. Kusano, *J. Appl. Phys.* **73**, 8565 (1993).

## THIN FILM FUEL CELLS

V.E.J. VAN DIETEN, J.P. DEKKER, AND J. SCHOONMAN

Laboratory for Applied Inorganic Chemistry, Delft University of Technology,  
Julianalaan 136, 2628 BL Delft, The Netherlands

### ABSTRACT

In recent years there has been an enormous increase in the application of thin film technologies in the fabrication of solid state electrochemical devices. Devices in which thin film components are utilized are, *e.g.* solid oxide fuel cells (SOFCs), thin film rechargeable batteries, and chemical gas sensors. Chemical vapour deposition (CVD) is one of the synthesis techniques for the fabrication of thin film components for solid state electrochemical devices. This paper will focus on the application of novel CVD techniques for the fabrication of the thin film components of one of these devices, *i.e.* the solid oxide fuel cell. A new SOFC design concept which uses only one gas phase synthesis method will be presented.

### INTRODUCTION

A solid oxide fuel cell is a device for the generation of direct-current electric power. An advantage fuel cells have over most conventional forms of power generation is that they are not Carnot limited. While many other modes of power generation involve the thermodynamic inefficient conversion of heat to mechanical energy, fuel cells convert the free energy of a chemical reaction directly into electrical energy. Therefore, high fuel efficiency and potentially very large power density (W/kg) are possible<sup>1-3</sup>. A SOFC consists of a gastight oxygen ion conducting solid electrolyte, a porous oxygen electrode (cathode), and a porous fuel electrode (anode). The solid electrolyte has to be gastight in order to prevent direct combustion of the fuel. The electrodes have to be porous in order to allow easy gas transport to the electrode-electrolyte interface. Charge transfer reactions take place at the ternary interface gas-electrode-electrolyte. SOFCs operate at high temperatures (>800°C), which has a favourable effect on the reaction kinetics at the ternary interface and mass transfer through the electrolyte. The fast kinetics eliminate the necessity of using expensive noble metal catalysts. To form a power generator, several elementary cells have to be connected parallel or in series, using an appropriate interconnection material. The interconnection material connects the anode of one cell with the cathode of the next. Therefore, it has to be gastight in order to prevent direct combustion of the fuel.

Because of the high operation temperature of SOFCs, and because SOFCs are ceramic devices, the materials used for the various components have to fulfil stringent requirements depending on their primary function. Furthermore, the materials need to be chemically compatible, and need to have a comparable thermal expansion coefficient (TEC) with neighbouring components. The requirements for the individual components are summarized in Table I.

A variety of configurations is now being considered for the SOFC. These include tubular, monolithic, and planar concepts<sup>1-3</sup>. There is a continuous search for component materials



which can fulfil all the requirements presented in Table I at process temperatures as low as possible. The research and development of SOFCs has led to the "state-of-the-art" materials, and fabrication techniques listed in Table II.

Table I. General cell component requirements at operating temperature<sup>4</sup>.

Requirement	Anode	Cathode	Electrolyte	Interconnect
High ionic conductivity	preferable	preferable	essential	detrimental
High electronic conductivity	essential	essential	detrimental	essential
Chemical and TEC compatibility	electrolyte/interconnect	electrolyte/interconnect	anode/cathode	anode/cathode
Chemical stability	reducing environment	oxidizing environment	reducing/oxidizing environment	reducing/oxidizing environment
Catalytic activity	essential	essential	--	--
Microstructure	porous	porous	impervious	impervious

The performance of a SOFC can be improved by using materials with superior electrical properties or by minimizing the thickness of the cell components. Both methods will lead to a reduction of the ohmic polarization losses. In recent years there has been an increased interest in the use of thin film components in SOFCs. Because all components are solid state materials, advanced thin film technology can be applied for the synthesis of fuel cell components, or complete fuel cells. For the planar and monolithic SOFC designs all components can be produced by tape casting and subsequent sintering. However, the advantages of synthesizing the cell components by a CVD process are that, in general, lower process temperatures are required than with sintering, and that thinner films can be produced. In principle, all thin film components of the SOFC can be fabricated using the conventional CVD technique.

Table II. "State-of-the-art" materials, and fabrication techniques for SOFC components<sup>5</sup>.

component	material	fabrication technique
electrolyte	YSZ (8 - 10 mol%)	Electrochemical Vapour Deposition, tape casting
interconnect	$\text{LaCr}_{1-x}\text{Mg}_x\text{O}_3$	Electrochemical Vapour Deposition, tape casting
cathode	$\text{La}_{1-x}\text{Sr}_x\text{MnO}_3$	slurry coating, tape casting
anode	Ni-YSZ cermet	slurry coating, tape casting

However, the gas impervious components, *i.e.* the electrolyte and interconnect, have to be deposited onto the porous electrodes. With conventional CVD it is difficult to deposit pinhole-free layers on porous substrates. Therefore, this technique as such is not well suited for the production of these components. For the production of the solid electrolyte and the interconnect Westinghouse Electric Corporation has developed a special form of CVD called electrochemical vapour deposition (EVD), which has become the key technology for the production of these components for the tubular concept SOFC<sup>6,7</sup>. Advantages of this technique are that thin dense films, typically a few microns, of uniform thickness can be deposited on porous substrates, and that the technique is not restricted to flat substrates. The EVD process is similar to the chemical vapour infiltration (CVI) process using a counter reactant flow. Depending on the design of the SOFC, the CVI process itself might also be an applicable synthesis method. Other CVD techniques are expected to be suitable as well for the production of SOFC components. In principle, particle-precipitation-aided CVD (PP-CVD) can be a suitable method for the synthesis of the components of a SOFC, as it has been proven that PP-CVD is a suitable method for the synthesis of thin layers of ceramics with controlled porosity<sup>8,9</sup>, and for the synthesis of gas impervious films on porous substrates.

First, the principles of the EVD, CVI, and PP-CVD processes will be discussed briefly, and some of the aspects which are illustrative for these CVD processes will be highlighted. Finally, a new SOFC design concept will be presented, using only one gas phase synthesis method.

## CHEMICAL VAPOUR DEPOSITION TECHNIQUES

CVD is a process for the synthesis of solid products by chemical reactions between gaseous reactants. With CVD, ceramics and refractory metals are formed at moderate reaction temperatures. The reaction temperature lies well below the melting point of the product. The materials can be synthesized in the form of coatings, powders, or formed solid products<sup>10-13</sup>.

EVD<sup>6,7,14-19</sup> and PP-CVD<sup>8,9,20,21</sup> are modifications of the conventional CVD process of which the names refer to the type of chemical process involved. CVI is the CVD process for the densification of a porous preform to make a matrix composite material. In the field of fabrication of thin films of SOFC components EVD is a key technology, whereas CVI and PP-CVD are, in principle, suitable techniques. The principles of these processes will be briefly discussed below.

### Electrochemical Vapour Deposition

EVD is a modified form of CVD, developed by Westinghouse, which utilizes a chemical potential gradient to grow thin, gas impervious layers of either electronically, or ionically conducting metal oxides on porous substrates<sup>6,7,14-19</sup>. The primary application of EVD to date has been in the fabrication of the solid electrolyte YSZ, and the interconnection material magnesium-doped lanthanum chromium oxide as used in SOFCs.

The steps involved in the EVD process are shown in Figure 1. A porous substrate separates the reactant metal chloride vapours from a mixture of oxygen (O<sub>2</sub>) and steam (H<sub>2</sub>O). The first step in film formation involves pore closure by a normal CVD-type

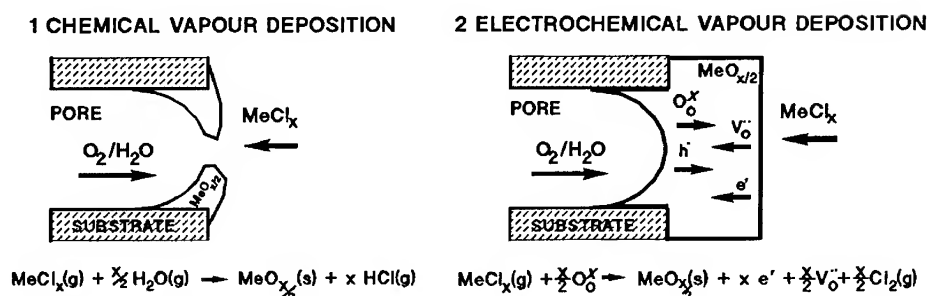


Figure 1. Schematic representation of the principle of the EVD process.

reaction between the reactant metal chloride and steam (or oxygen). Once pore closure is complete, the reactants are no longer in direct contact. Film growth then proceeds by oxygen ion diffusion through the film owing to the presence of a large oxygen chemical potential gradient across the deposited film. In this step oxygen ion vacancies and electrons formed at the metal chloride side diffuse through the thin metal oxide layer to the oxygen-rich side. This results in a net flux of oxygen to the metal chloride side, where the oxygen reacts with the metal chloride vapour to form the metal oxide product.

The pore closure step is very important in determining the ultimate properties of the deposited film. Ideally, the pore plugging layer (CVD layer) should form on the substrate surface at the metal chloride side, and barely penetrate the substrate pores, be thin, and as close to the composition of the EVD layer as possible.

During the EVD process on a porous substrate the overall film growth can be limited by a) gas diffusion in the substrate pores, b) surface kinetics on either side of the film, or c) solid state diffusion in the growing film. When the rate of film growth is controlled by solid state diffusion, the kinetics are similar to the Wagner oxidation of metals, and the film growth rate is inversely proportional to the oxide thickness<sup>22,23</sup>,

$$\frac{dL}{dt} = \frac{K_0}{L} \quad (1)$$

where  $L$  is the film thickness and  $K_0$  the parabolic growth rate constant.

The diffusion processes which can take place during EVD growth are shown in Figure 1. The large oxygen partial pressure gradient across the growing film results in a flux of oxygen ions. Oxygen ion diffusion is only possible if at the same time a counter diffusion of a species with the same charge or a parallel diffusion of a species with opposite charge occurs to preserve electroneutrality.

#### Chemical Vapour Infiltration

In CVI a porous preform is densified with a solid deposit to produce a ceramic composite with high toughness and strength. CVI is mainly used for the production of special products for the automotive and aerospace industry<sup>24</sup>. The main difference between CVI and EVD is that in CVI deposition of a solid should occur in the pores of a preform, whereas in EVD

deposition should occur on the porous preform. Furthermore, in the CVI process the reactants are fed to the same side of the preform, instead of to the opposite sides, as in the EVD process.

If the CVI process is performed in a hot wall reactor, the process is referred to as the Isothermal CVI (ICVI) process. The CVI process can be divided into two classes depending on process conditions and its application, *i.e.* CVI processes using long process times of up to 500 hours for the synthesis of dense composites, and CVI processes using relatively short process times of less than 10 hours for the surface modification of porous systems.

A well known CVI process using long process times is the densification of porous fibre preforms to produce ceramic composites with high toughness and strength<sup>25-29</sup>. In general, these long process times are necessary for full densification of the porous preform. The search for improved densification using short process times has resulted in the development of different reactor geometries. For example, a forced flow through the substrate will result in shorter process times because of the higher deposition rates, and a temperature gradient opposite to the reactant flux in the porous preform will result in a higher final density. A combination of these two processes has resulted in the development of the ORNL (Oak Ridge National Laboratory) CVI process<sup>30,31</sup>. It has been reported that these modifications of the CVI process shorten the process time considerably.

The CVI process using relatively short process times can be used to modify the internal surface of a porous preform with only a thin deposit. For example, a bundle of fibres can be coated with a thin layer for the protection of the individual fibres. In this case, each fibre has to be coated with a thin chemically inert layer, without interconnecting the fibres in the bundle<sup>32</sup>. This process can also be used for the modification of ceramic membranes<sup>33</sup>, or for the improvement of the mechanical strength of sintered porous metals<sup>34</sup> and ceramics<sup>35</sup>. Furthermore, the CVI process using relatively short process times is promising as a novel synthesis method for catalyst materials<sup>36</sup>.

Mathematical modelling of the process can give a better understanding of the influence of the individual process parameters on the deposition characteristics such as final porosity and deposition profiles in the pores. The model should describe the change in pore geometry due to the deposition of a solid in the pores, and as a result, the change in diffusion rate of the reactants in the pores during the process. The conditions for optimal experimental circumstances for the CVI process can only be deduced from a CVI model if it describes the mass transfer in a realistic pore network, and if a correct kinetic expression is implemented. In recent years, starting with the work of Van den Brekel *et al.*<sup>37</sup>, quite a number of reports have been published on the modelling of the CVI process<sup>26,33,38-44</sup>.

#### Particle-Precipitation-Aided Chemical Vapour Deposition

In general, powder formation in the gas phase in a CVD process should be avoided, because this will considerably deplete the reactants necessary for the heterogeneous (CVD) reaction, leading to a non-uniform film thickness. In addition, powder formed in the gas phase can diffuse towards the substrate and deposit onto the surface. Often this will lead to an undesirable microstructure of the film. However, under certain experimental conditions powder formation can be used to our advantage. The hot-wall CVD process can be modified to control the microstructure of the layer by a controlled deposition of the particles on the substrate. In Particle Precipitation aided CVD (PP-CVD) an aerosol is formed at elevated temperatures, and the particles are precipitated on the substrate by introducing an external force for particle deposition, such as thermophoresis,

electrophoresis, or forced flow. Particle precipitation on the substrate will result in a loose powder deposit with a poor mechanical stability. In order to obtain a coherent layer, the powder should be sintered, or a heterogeneous reaction should occur simultaneously to interconnect the individual particles. Thus, the PP-CVD process consists of three steps, *i.e.* particle formation, particle precipitation, and interconnection or sintering of the particles, as illustrated in Figure 2.

The PP-CVD process was introduced by the group of Komiyama<sup>20,45-48</sup>. Using this technique, they synthesized titania ( $\text{TiO}_2$ )<sup>45,46</sup>, zirconia ( $\text{ZrO}_2$ )<sup>56</sup>, and aluminium nitride ( $\text{AlN}$ )<sup>47,48</sup>. The driving force for particle deposition was thermophoresis. Dense to highly porous layers were obtained depending on the experimental conditions. The microstructure of the layers seemed to be determined by a combination of particle deposition, sintering, and heterogeneous reaction.

Dekker *et al.* have investigated the synthesis of titanium nitride ( $\text{TiN}$ ) by the PP-CVD process<sup>9,21</sup>. Because  $\text{TiN}$  has a poor sinterability, a heterogeneous reaction is necessary to interconnect the precipitated particles. Hence, the reactant mixture used in the PP-CVD process has to serve as a source for powder formation as well as for the heterogeneous reaction. In principle, two separate reaction mechanisms, *i.e.* one for the homogeneous, powder formation, reaction and one for the heterogeneous reaction, which can occur at the same reaction temperature and reactor pressure should be used. In principle, a variety of compounds, such as nitrides, oxides, carbides, and metals can be deposited using this technique.

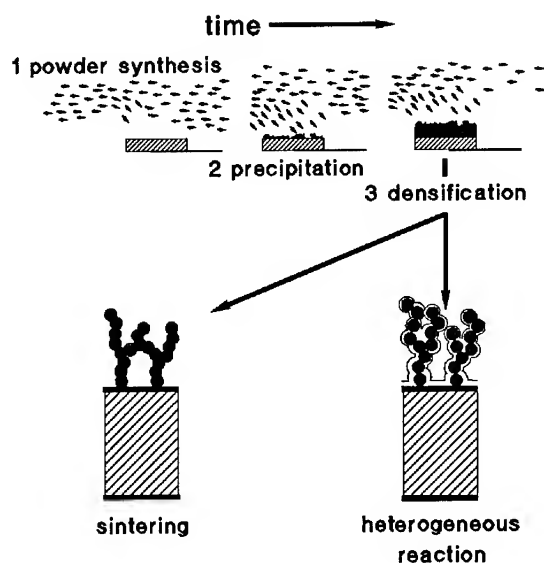
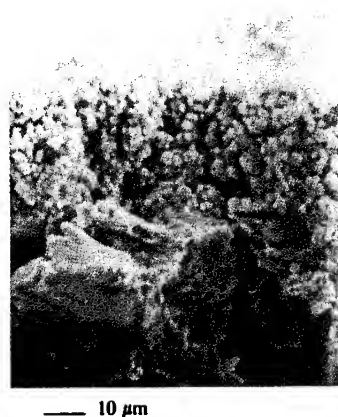


Figure 2. The principle of the PP-CVD process

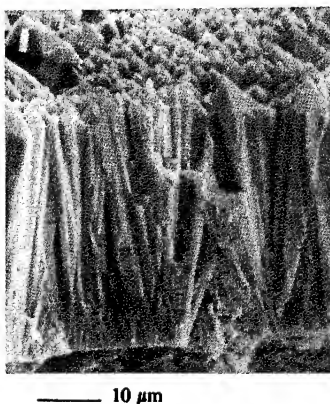
In principle, PP-CVD might be a suitable technique for the synthesis of all components of a SOFC, as it has been demonstrated that it is possible to obtain layers with controlled porosity and good mechanical strength, and that also dense layers can be formed on porous supports, as is shown in Figure 3.



a)



b)



c)

Figure 3. SEM micrographs of cross sections of TiN layers deposited using the PP-CVD technique. a) Porous layer typical for layers grown at intermediate temperature gradients in the gas phase, and low reaction temperatures; b) porous layer typical for layers grown at intermediate temperature gradients in the gas phase, and high reaction temperatures; c) dense layer typical for layers grown without cooling the substrate.

## SOFC FABRICATION USING NOVEL CVD TECHNIQUES

### PP-CVD

In theory the PP-CVD technique can be used to produce all components of a single SOFC, as discussed above. Hence, it should be possible to form all SOFC components in one process step, using one CVD technique, by only altering the reactant supply and reaction conditions. This production method has the following advantages over the conventional way of producing a complete SOFC:

- less temperature cycles during production; hence, less risk of mechanical failure of the components;
- if produced at operating temperature, the SOFC will be stress-free during operation;
- thin film components are produced, so ohmic polarization losses will be minimal;
- no contamination of the interfaces between the components.

As mentioned before, to obtain uniform coherent layers two separate reaction mechanisms are required under the same experimental conditions. There should be a homogeneous reaction in the gas phase as well as a heterogeneous reaction. Thus, for the successful deposition of a SOFC component by the PP-CVD process knowledge of the heterogeneous CVD reaction and of the aerosol synthesis of the material is essential. Unfortunately, this information is scarce or proprietary. However, some general conditions concerning the chemistry of the PP-CVD process can be presented.

For the formation of metal oxides by CVD metal chlorides and oxidant vapours, *e.g.*  $\text{H}_2\text{O}$ ,  $\text{O}_2$ , or carbon dioxide/hydrogen ( $\text{CO}_2/\text{H}_2$ ) can be used as reactants. In general, a reaction at a high temperature between metal chloride vapour and  $\text{H}_2\text{O}$  results in powder formation. A  $\text{CO}_2/\text{H}_2$  mixture is usually used as oxidant source for the formation of a metal oxide film<sup>49,50</sup>. It is believed that this mixture generates a low concentration of  $\text{H}_2\text{O}$ . Usually, this formation takes place at the CVD surface, which will favour the formation of metal oxide at the surface by a heterogeneous reaction. Because oxygen is less reactive than steam, it might be possible that oxidation of the metal chlorides with oxygen can only take place by a heterogeneous reaction. Thus, a reactant input mixture of  $\text{MeCl}_x$ ,  $\text{H}_2\text{O}$ , and  $\text{CO}_2/\text{H}_2$  or  $\text{O}_2$ , where  $\text{CO}_2/\text{H}_2$  or  $\text{O}_2$  are in excess of the  $\text{MeCl}_x$ , and the  $\text{MeCl}_x$  is in excess of the  $\text{H}_2\text{O}$ , will result in powder formation as well as a heterogeneous reaction.

Until now, all materials deposited by means of PP-CVD are binary compounds. However, the SOFC cathode material and interconnection material are perovskite oxides, which are ternary compounds. Because there are few reports on powder synthesis of perovskite oxides in the gas phase, we have started to investigate the possibility to synthesize a perovskite oxide aerosol by gas-to-particle conversion, *i.e.* the first step in the PP-CVD process. We have investigated the formation of the perovskite oxide yttrium chromium oxide ( $\text{YCrO}_3$ ) from the gas phase using yttrium trichloride ( $\text{YCl}_3$ ), chromium trichloride ( $\text{CrCl}_3$ ), and  $\text{H}_2\text{O}$  and/or  $\text{O}_2$  as precursors under conditions expected to be typical for the formation of the material by heterogeneous reaction, which is essential in the PP-CVD process. The reaction temperature was kept constant at about 1283 K, while the ratio of the reactants was varied. The experimental details are reported elsewhere<sup>51</sup>.  $\text{YCrO}_3$  is chosen instead of  $\text{LaCrO}_3$ , which is commonly used as interconnection material in a SOFC (Table II), for practical reasons. It is easier to obtain the necessary high gas phase concentrations of  $\text{YCl}_3$  than of  $\text{LaCl}_3$ , because  $\text{LaCl}_3$  is much less volatile than  $\text{YCl}_3$ .  $\text{YCrO}_3$  is isostructural with  $\text{LaCrO}_3$  and has almost the same electrical and thermal properties as  $\text{LaCrO}_3$ <sup>52</sup>.

In experiments where only oxygen, and no steam, was present no powder was formed, but only deposition on the reactor wall by a heterogeneous reaction could be observed. This indicates that the reactivity of the gas mixture without steam is not high enough to induce nucleation in the gas phase, and that oxygen may be a suitable reactant for heterogeneous CVD of  $\text{YCrO}_3$ . In experiments where steam was present powder was formed. Hence, for powder formation the presence of steam is necessary.

XRD analysis of the powders revealed that it is possible to synthesize the perovskite oxide  $\text{YCrO}_3$  from the gas phase, using metal chlorides, and steam and oxygen as precursors. At the reaction conditions chosen,  $\text{Cr}_2\text{O}_3$ , or mixtures of  $\text{Cr}_2\text{O}_3$  and  $\text{YCrO}_3$  are formed. Formation of single phase  $\text{YCrO}_3$  is inhibited by either thermodynamic or kinetic limitations. Thermodynamic equilibrium equations could elucidate this problem. In case of thermodynamic limitations, experimental conditions have to be chosen such that  $\text{YCrO}_3$  is the only stable solid species. In case of kinetic limitations, it is possible that, although according to thermodynamic equilibrium calculations only one solid phase is stable, e.g.  $\text{YCrO}_3$ , other solid phases, e.g.  $\text{Cr}_2\text{O}_3$ , are formed. Then, it is more difficult to obtain the optimal reaction conditions.

In combination with these calculations, further experiments need to be performed in order to determine the range of reaction conditions, in which single phase  $\text{YCrO}_3$  powder is formed. If these conditions are known, it is useful to determine the conditions for the heterogeneous formation of  $\text{YCrO}_3$  in separate experiments, using experimental conditions within the range necessary for the homogeneous reaction to take place. Then, it might be possible to choose reaction conditions such that the homogeneous and heterogeneous reactions occur simultaneously, which is a necessity in the PP-CVD process, for the formation of films of perovskite oxides with controlled morphology.

#### New SOFC Design Using CVI Techniques

The configurations considered for a SOFC include tubular, planar, and monolithic concepts<sup>1-3</sup>. Virtually all configurations are based on a multi-layer laminate of the active cell components (cathode-electrolyte-anode). Depending on the cell concept a separate porous support (cathode or interconnect) gives the cell the necessary mechanical stability. A different design concept by Dekker<sup>4</sup> using only one gas phase synthesis method will be described here. This new concept has not the characteristic laminate structure, and the electrolyte material gives the cell its mechanical stability. A schematic representation of the individual process steps in the production of this fuel cell is given in Figure 4. A porous body of an arbitrary shape of the electrolyte material is used as preform (0 in Figure 4). This preform is partially densified with the electrolyte material by CVI. During densification it is intended that there is only pore plugging in the middle of the porous body (1 in Figure 4). As a result an electrolyte is formed consisting of two porous compartments separated by an impermeable deposit of the electrolyte material. Consequently, the electrodes have to be deposited into the two separate porous compartments by CVI (2 and 3 in Figure 4). In this case, pore plugging should be avoided. The result will be the formation of one fuel cell. The proposed production method can be applied for the tubular concept as well as for the planar concept. If a planar concept is used the interconnect can be similar as the electrolyte (A and B in Figure 4). A schematic representation of a complete cell using planar porous supports is given in Figure 5.



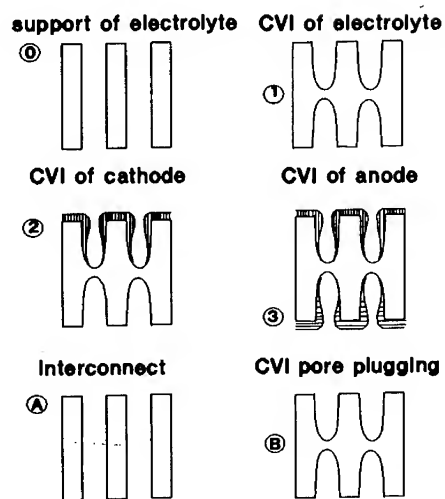


Figure 4. A schematic representation of the synthesis route for the production of a fuel cell by CVD. 0) Porous preform of electrolyte material; 1) pore closure in the middle of the preform; 2) deposition of a thin cathode layer; 3) deposition of a thin anode layer; A) porous preform of the interconnect; B) pore closure in the middle of the preform.

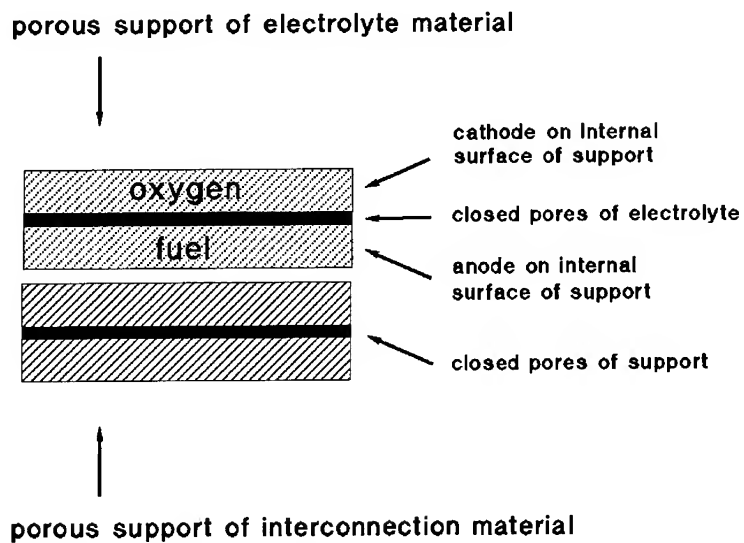


Figure 5. Schematic representation of a planar SOFC fabricated using only CVD techniques.

This production method offers several advantages over conventional production techniques. The temperature required for CVI is lower than for sintering of the component materials. This reduces thermal stresses, and the chance of undesirable interface reactions between the individual cell components. The number of thermal cycles during synthesis can be reduced to one, because, in principle, the three CVI production steps can be performed in one reactor. In addition, the accessible electrode/electrolyte surface area is higher than for the conventional planar or tubular concepts with a laminated structure. It is expected that the mechanical stability of such a cell is good, because the mechanical strength is determined by the tough YSZ electrolyte. The realisation of this proposed fuel cell relies entirely on knowledge of the kinetic laws of the reactant mixtures for the synthesis of the individual cell components, because the dependence of the growth rate with respect to the reactant concentrations, in combination with the mass transport into the pore network will determine the mass distribution of the deposit. The implications of the desired mass distribution for the individual cell components will be discussed next.

For the production of the electrolyte the densification should occur from the inside to the outside of the porous preform until there is pore plugging in the middle of the preform. A preferential pore closure in the middle of a porous preform is only possible if the CVD reaction rate of the electrolyte has a negative order dependence with respect to at least one reactant concentration. In addition, this reactant may not be present in excess with respect to the other reactants. For example,  $\text{YCl}_3$ ,  $\text{ZrCl}_4$ , and  $\text{CO}_2/\text{H}_2$  can be used for CVD of YSZ. The reaction mechanism responsible for the growth of YSZ using these reactants is not known. However, some  $\text{ZrO}_2$ -CVD experiments implicitly indicate that the growth rate has a negative order dependence on one of the reactant concentrations<sup>50</sup>. Such an order dependence favours pore filling from the inside to the outside<sup>44</sup>.

CVD of the perovskite oxide  $\text{La}_{1-x}\text{Sr}_x\text{MnO}_{3\pm\delta}$  has not been reported in literature. However, the formation of a doped perovskite oxide should be possible at high reaction temperatures using gaseous oxygen containing species and metal halides. The thickness of the deposit in the porous preform should be as thin as possible in order to reduce the oxygen ion transfer resistance through the cathode layer. On the other hand, the deposit should be as thick as possible to reduce polarization in the electrode material.

CVI of nickel oxide (NiO) can be used for the production of the anode material. After deposition of NiO the CVI layer can easily be reduced leaving a porous nickel electrode layer on the internal surface of the support. Such an electrode has a large accessible ternary (electrode-electrolyte-gas) interface area. Optionally, the electrode surface can be immobilized by an additional EVD process for the deposition of YSZ to prevent sintering of the Ni during cell operation<sup>1,3</sup>. NiO can be formed using nickel tetracarbonyl ( $\text{Ni}(\text{CO})_4$ ) and  $\text{O}_2$ <sup>53</sup>.

## CONCLUSIONS

An outlook has been given with respect to the potential application of novel CVD techniques for the fabrication of solid oxide fuel cells. It has been shown that relative new CVD techniques, e.g. CVI, EVD, and PP-CVD, offer new possibilities in the field of SOFC production, and that these techniques are a valuable contribution to the already available more conventional synthesis routes.

## REFERENCES

1. A. Hammou, *Advances in Electrochemical Science and Engineering*, **2**, 87 (1992).
2. K. Kinoshita, F.R. McLarnon, and E.J. Cairns, *DOE Report DOE/METC-88/6096* (U.S. Department of Energy-METC, Morgantown, 1988), p. 87.
3. N.Q. Minh, *J. Am. Ceram. Soc.*, **76**, 563 (1993).
4. J.P. Dekker, Ph.D. Thesis, Delft University of Technology, Delft, 1994, Ch. 8.
5. S.C. Singhal, in *Proc. 2nd Int. Symp. on SOFCs*, edited by F. Grosz, P. Zegers, S.C. Singhal, and O. Yamamoto (CEC, Luxembourg, 1991), p. 25.
6. A.O. Isenberg, in *Proc. Symp. Electrode Materials and Processes for Energy Conversion and Storage*, edited by J.D.E. McIntyre, S. Srinivasan, and F.G. Will (The Electrochemical Society, Pennington, NJ, 1977), p. 572.
7. U.B. Pal and S.C. Singhal, *J. Electrochem. Soc.*, **137**, 2937 (1990).
8. J.P. Dekker, P.J. van der Put, H.J. Veringa, and J. Schoonman, *J. Am. Ceram. Soc.*, submitted (1994).
9. J.P. Dekker, P.J. van der Put, H.J. Veringa, and J. Schoonman, *Aerosol Sci. and Technol.*, **19**, 549 (1993).
10. F.S. Galasso, *Chemical Vapour Deposited Materials* (CRC Press Inc., Boca Raton, FL, 1992).
11. K.E. Spear, *Pure Appl. Chem.*, **54**, 1297 (1982).
12. C.H.J. van den Brekel, *Philips Res. Repts.*, **32**, 118 (1977).
13. C.H.J. van den Brekel and J. Bloem, *Philips Res. Repts.*, **32**, 134 (1977).
14. M.F. Carolan and J.N. Michaels, *Solid State Ionics*, **37**, 189 (1990).
15. J.P. Dekker, N.J. Kiwiet, and J. Schoonman, in *Solid Oxide Fuel Cells*, edited by S.C. Singhal (The Electrochemical Society, Pennington, NJ, 1989), p. 57.
16. N.J. Kiwiet and J. Schoonman, in *Proc. 25th Int. Soc. Energy Conv. Eng. Conf.*, edited by P.A. Nelson *et al.* (AIChE, Vol. 3, New York, NY, 1990), p. 240.
17. J. Schoonman, J.P. Dekker, J.W. Broers, and N.J. Kiwiet, *Solid State Ionics*, **46**, 299 (1991).
18. Y.S. Lin, L.G.J. de Haart, K.J. de Vries, and A.J. Burggraaf, *J. Electrochem. Soc.*, **137**, 3960 (1990).
19. Y.S. Lin, Ph.D. Thesis, University of Twente, Enschede, 1991, Ch. 6.
20. H. Komiyama, T. Osawa, Y. Shimogaki, N. Wakita, M. Mianamiyama, and T. Ueoka, in *Proc. 10th Int. Conf. Chemical Vapor Deposition*, edited by G.W. Cullen and J.M. Blocher Jr. (Vol. 87-7, The Electrochemical Society, Pennington, NJ, 1987), p. 1119.
21. J.P. Dekker, P.J. van der Put, H.J. Veringa and J. Schoonman, in *Ceramics Adding the Value*, AUSTCERAM 92, edited by M.J. Bannister (Vol. 1, CSIRO Publications, Melbourne, 1992), p. 787.
22. C. Wagner, *Z. Physik. Chem.*, **B21**, 25 (1933).
23. P. Kofstad, *High Temperature Corrosion* (Elsevier Applied Science Publishers LTD, Amsterdam, 1988), Ch. 6.
24. J.D. Buckley, *Am. Ceram. Soc. Bull.*, **67**, 364 (1988).
25. E. Fitzner and R. Gadow, *Am. Ceram. Soc. Bull.*, **65**, 326 (1986).
26. J.Y. Rossignol, J.M. Quenisset, and R. Naslain, *Composites*, **18**, 135 (1987).
27. P. Reagan, M.F. Ross, and F.N. Huffman, *Adv. Ceram. Mater.*, **3**, 198 (1988).
28. R.D. Veltri, D.A. Condit, and F.S. Galasso, *J. Am. Ceram. Soc.*, **72**, 478 (1989).
29. E. Fitzner, W. Remmele, and G. Schoch, in *J. de Physique, Coll. C5*, (suppl. J. de Physique II, 1989), C5-209.

30. A.J. Caputo and W.J. Lackey, *Ceram. Eng. Sci. Proc.*, **5**, 654 (1984).
31. T.D. Gulden, J.L. Kaae, and K.P. Norton, in *Proc. 11th Int. Conf. Chemical Vapor Deposition*, edited by K.E. Spear and G.W. Cullen (Vol. 90-12, The Electrochemical Society, Pennington, NJ, 1990), p. 546.
32. E. Fitzer, in *J. de Physique IV, Coll. C2* (suppl. J. de Physique II, 1991), Vol. 1, C2-509.
33. Y.S. Lin and A.J. Burggraaf, *Chem. Eng. Sci.*, **46**, 3067 (1991).
34. M. Shiroyama, Japanese Patent, JP 61-207282, (1986).
35. J.P. Dekker, P.J. van der Put, H.J. Veringa, and J. Schoonman, in *Proc. Int. Ceram. Conf., AUSTCERAM 92*, edited by M.J. Bannister (Vol. 2, CSIRO Publications, Melbourne, 1992), p. 712.
36. M. Izaka and H. Komiyama, in *Proc. 11th Int. Conf. Chemical Vapor Deposition*, edited by K.E. Spear and G.W. Cullen (Vol. 90-12, The Electrochemical Society, Pennington, NJ, 1990), p. 596.
37. C.H.J. van den Brekel, R.M.M. Fonville, P.J.M. van der Straten, and G. Verspui, in *Proc. 8th Int. Conf. Chemical Vapor Deposition*, edited by J.M. Blocher Jr. *et al.* (Vol. 81-7, The Electrochemical Society, Pennington, NJ, 1980), p. 142.
38. N.H. Tai and T.W. Chou, *Mat. Res. Soc. Symp. Proc.*, **120**, 185 (1988).
39. N.H. Tai and T.W. Chou, *J. Am. Ceram. Soc.*, **73**, 414 (1989).
40. Y.S. Lin, in *Proc. 11th Int. Conf. Chemical Vapor Deposition*, edited by K.E. Spear and G.W. Cullen (Vol. 90-12, The Electrochemical Society, Pennington, NJ, 1990), p. 532.
41. S.M. Gupte and J.A. Tsamopoulos, *J. Electrochem. Soc.*, **136**, 555 (1989).
42. R. Moene, J.P. Dekker, M. Makkee, J. Schoonman, and J.A. Moulijn, *J. Electrochem. Soc.*, **141**, 282 (1994).
43. R. Fedou, F. Langlais, and R. Naslain, in *Proc. 11th Int. Conf. Chemical Vapor Deposition*, edited by K.E. Spear and G.W. Cullen (Vol. 90-12, The Electrochemical Society, Pennington, NJ, 1990), p. 513.
44. J.P. Dekker, P.J. van der Put, H.J. Veringa, and J. Schoonman, *J. Electrochem. Soc.*, **141**, 787 (1994).
45. Y. Shimogaki and H. Komiyama, in *New Materials Processing*, World Congress III of Chemical Engineering (Tokyo, Japan, 1986), p. 258.
46. H. Komiyama, European Patent, EP 0186 910 A1 (1985).
47. T. Osawa and H. Komiyama, in *New Materials Processing*, World Congress III of Chemical Engineering (Tokyo, Japan, 1986), p. 250.
48. H. Komiyama and T. Osawa, *Jpn. J. Appl. Phys.*, **24**, L795 (1985).
49. R. Funk, H. Schachner, C. Triquet, M. Kornmann, and B. Lux, in *Proc. 5th Int. Conf. Chemical Vapor Deposition*, edited by J.M. Blocher Jr. (Vol. 75-2, The Electrochemical Society, Princeton, NJ, 1975), p.469.
50. E. Sipp, F. Langlais, and R. Naslain, *J. of Alloys and Compounds*, **186**, 65 (1992); **186**, 77 (1992).
51. V.E.J. van Dieten, J.P. Dekker, E.J. Hurkmans, and J. Schoonman, *Aerosol Sci. and Technol.*, **19**, 562 (1993).
52. G.F. Carini II, H.U. Anderson, D.M. Sparlin, and M.M. Nasrallah, *Solid State Ionics*, **49**, 233 (1991).
53. H.O. Pierson, *Handbook of Chemical Vapor Deposition (CVD)* (Noyes Publications, Park Ridge, NJ, 1992).

## THIN-FILM ELECTROLYTES FOR REDUCED TEMPERATURE SOLID OXIDE FUEL CELLS

STEVEN J. VISCO\*, LI-SHUN WANG\*\*, SELMAR SOUZA\*, AND LUTGARD C. DE JONGHE\*

\*Materials Science Division, Lawrence Berkeley Laboratory, Berkeley, CA 94720

\*\*Optical Coatings Laboratory, Inc., 2789 Northpoint Parkway, Santa Rosa, CA 95407-7397

### ABSTRACT

Solid oxide fuel cells produce electricity at very high efficiency and have very low to negligible emissions, making them an attractive option for power generation for electric utilities. However, conventional SOFC's are operated at 1000 °C or more in order to attain reasonable power density. The high operating temperature of SOFC's leads to complex materials problems which have been difficult to solve in a cost-effective manner. Accordingly, there is much interest in reducing the operating temperature of SOFC's while still maintaining the power densities achieved at high temperatures. There are several approaches to reduced temperature operation including alternative solid electrolytes having higher ionic conductivity than yttria stabilized zirconia, thin solid electrolyte membranes, and improved electrode materials. Given the proven reliability of zirconia-based electrolytes (YSZ) in long-term SOFC tests, the use of stabilized zirconia electrolytes in reduced temperature fuel cells is a logical choice. In order to avoid compromising power density at intermediate temperatures, the thickness of the YSZ electrolyte must be reduced from that in conventional cells (100 to 200  $\mu\text{m}$ ) to approximately 4 to 10  $\mu\text{m}$ . There are a number of approaches for depositing thin ceramic films onto porous supports including chemical vapor deposition/electrochemical vapor deposition, sol-gel deposition, sputter deposition, etc. In this paper we describe an inexpensive approach involving the use of colloidal dispersions of polycrystalline electrolyte for depositing 4 to 10  $\mu\text{m}$  electrolyte films onto porous electrode supports in a single deposition step. This technique leads to highly dense, conductive, electrolyte films which exhibit near theoretical open circuit voltages in  $\text{H}_2/\text{air}$  fuel cells. These electrolyte films exhibit bulk ionic conductivity, and may see application in reduced temperature SOFC's, gas separation membranes, and fast response sensors.

### 1. INTRODUCTION

Materials problems associated with operating electrochemical devices at temperatures of 1000 °C or more have limited the development of solid oxide fuel cells. The technical complexity and associated costs of fabricating fuel cell stacks require that these devices operate reliably for 30,000 or more hours. This places great demands on the mechanical and chemical stability of materials used in high temperature fuel cells. For these reasons, several research groups are pursuing the development solid oxide fuel cells that can operate at reduced temperatures, e.g. 700 to 850 °C. Clearly, as the temperature of the fuel cell is lowered, resistive losses across the solid electrolyte increase and overpotentials at the air and fuel electrode are similarly magnified. Still, the lower temperature of operation allows for a wider choice of electrode materials as well as decreasing the problem of electrode sintering. Approaches to minimize resistive losses across the electrolyte have included replacing the yttria stabilized zirconia electrolyte (YSZ) with alternative electrolytes having higher ionic conductivity, and/or reducing the thickness of the ceramic electrolyte from 100 - 200 microns to a few microns.

There are several reported methods for fabricating thin electrolyte films including electrochemical vapor deposition (EVD), sputter deposition, sol-gel film processing, and recently tape-calendaring of ceramic filled plastic tapes. Among the various thin-film techniques, the sol-gel and bilayer extrusion techniques are probably the most cost effective approaches. Although it has been shown in this laboratory and others that sol-gel deposition of ceramic films can be accomplished on porous substrates, the upper limit to thickness for a single coating step is typically 0.5 microns. Electrolytes of these dimensions have a high probability of pinholes and rarely demonstrate acceptable open circuit voltages in completed fuel cells. Furthermore, when the film thickness approaches the grain boundary thickness, the film becomes inherently unstable at temperature. Accordingly, in order to deposit practical electrolytes on porous substrates ( $> 2 \mu\text{m}$ ), multiple sol-gel coatings are required. The necessity of building up multiple sol-gel coatings in order to achieve adequate electrolyte performance clearly increases the processing time which may diminish the attractiveness of the sol-gel approach. Thus, we modified our approach to allow deposition of dense, pinhole-free, electrolyte films of 2 microns or more in thickness with a single pass. Fuel cells fabricated with these new films exhibit close to theoretical open circuit voltage, and high current densities.

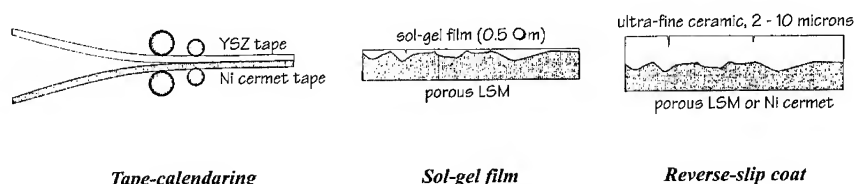


Fig. 1 Some of the approaches used to fabricate thin-film electrolyte fuel cells.

The performance of thin-film fuel single-cells can rival that observed for high temperatures SOFC's. This has been demonstrated by the work of Nguyen Q. Minh at Allied Signal<sup>1</sup>, Scott Barnett at Northwestern University<sup>2</sup>, and by our group at Lawrence Berkeley Laboratory<sup>3</sup>. It is not known at this time whether the high performance of thin-film single SOFC's will be realized in multi-cell stacks, and whether thin-film cells will exhibit long life operation. A goal of reduced temperature operation of SOFC's is to decrease the cost of the multi-cell stack while still delivering high performance and long life. A perceived means of achieving this goal is through the use of metal interconnects. This remains to be shown for thin-film fuel cell stacks, and is clearly a priority in the evolution of thin-film SOFC technology.

## 2. BACKGROUND

Initial work in our group on electrolyte membranes utilized metal alkoxide chemistry as a route to thin ceramic films<sup>4</sup>. First, zirconium alkoxide films were applied to continuous substrates either by spin or dip-coating techniques. In order to avoid cracking of the hydrolyzed alkoxide thin films, the metal alkoxides were first reacted with chelating agents such as diethanolamine. In this way, 1-dimensional polymeric chain structures are favored upon water hydrolysis of the chelated alkoxide, imparting elastomeric properties to the hydrolyzed film, allowing it to relieve stress on drying. This technique was quite successful, allowing us to routinely coat a variety of continuous substrates (Pt, Ni, Si,  $\text{SiO}_2$ , etc.) with dense crack-free films at firing temperatures below  $700^\circ\text{C}$ . It was found that an upper limit of approximately 0.5

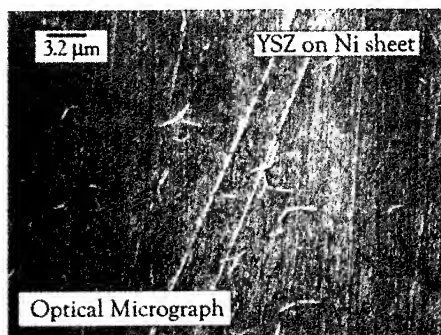


Fig. 2 Metal alkoxide sol-gel film on Ni sheet

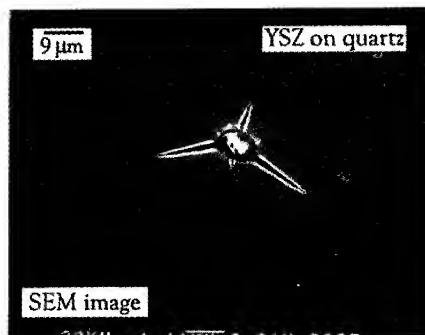


Fig. 3 Sol-gel film on quartz substrate

The second phase of the alkoxide work involved demonstration of the feasibility of applying dense, crack-free, coatings on porous substrates. In order to achieve that goal, model substrates were employed. The substrates chosen were Anotec™ alumina membranes; ceramic filters of well defined porosity. Chelated metal alkoxide solutions were spun onto ceramic membranes having pore sizes of 0.2, 0.1, and 0.02 microns. Thin, crack-free films of yttria stabilized zirconia (YSZ) were successfully deposited onto the porous ceramic membranes<sup>4</sup>. To our knowledge, this was the first time a dense ceramic electrolyte was successfully deposited from solution onto a porous substrate. Interestingly, it was observed that the critical thickness above which cracking occurred was reduced to 0.2 microns. Also, the critical pore size above which the films could not bridge the pore was found to be approximately 0.02 microns. In other words, high quality YSZ thin films were obtained for Anotec membranes having 0.02 micron pores, but for membranes with larger pore sizes, open porosity films were obtained.

Since the research on film coating of Anotec membranes showed that very fine surface pore sizes were necessary for successful deposition of high quality YSZ films from alkoxide solutions, fabrication of suitable electrode structures was attempted. An established technology for ultrafiltration (CeraVer membranes) involves sol-gel coating of graded porosity alumina tubes to yield pore sizes on the order of 40 to 200 Å. Similarly, if planar Ni/YSZ cermets or perovskite electrodes could be graded to a fine surface pore size, the above metal alkoxide procedure for YSZ thin-film deposition could be utilized to generate a fuel cell structure. Graded LaSrMnO<sub>3</sub> substrates were successfully fabricated using sedimentation casting and filtration casting. YSZ films were applied to the electrodes by dip-coating with the metal alkoxide solutions. Although continuous films were observed locally on the substrate, surface defects such as large pores, gave rise to pinholes in the film. Since it appeared unlikely that graded porosity electrodes could be fabricated defect-free, a slightly different technique was employed to coat the electrode. In order to raise the viscosity of the coating solution the metal alkoxide solutions were replaced by chelated glycine-nitrate solutions. Metal nitrates were dissolved in aqueous glycine solutions, and concentrated with heat to yield highly viscous solutions. These solutions were cast onto release sheets, allowed to dry to tacky films, and then transferred to the porous LSM substrates. The tape-transfer technique allowed us to coat virtually any porous substrate in a single step. The fired films were continuous and adherent. However, a critical thickness of about 0.5 μm was still observed. This was expected to present practical difficulties since surface topography of the porous LSM substrate exhibited variations of greater than 0.5 μm. The YSZ/LSM bilayers were subsequently coated with Ni/YSZ paint,

observed. This was expected to present practical difficulties since surface topography of the porous LSM substrate exhibited variations of greater than 0.5  $\mu\text{m}$ . The YSZ/LSM bilayers were subsequently coated with Ni/YSZ paint, and fuel cells were constructed. Low open circuit voltages were observed for the thin-layer fuel cells. Most likely, this was due to short-circuiting of the cell by surface defects penetrating the thin YSZ films. Two possible solutions to this problem were envisaged. The YSZ film thickness could be increased by using multiple tape-transfer coating, however, this would increase the complexity of the process, and the cost. Therefore, a different approach was taken, which proved to be highly successful.

### 3. APPROACH

The technical approach used in this work involved the use of colloidal dispersions of metal oxides to coat porous substrates with thin, fully dense, electrolyte films. In order to deposit YSZ films on the order of 4 to 10 microns in a single step, a technique of reverse slip-coating was employed. Ceramic powders were calcined at various heating schedules in order to tailor the shrinkage profiles of electrode substrates. Porous anode or cathode substrates were then pre-fired to strengthen the electrode structures. Colloidal dispersions of 0.18  $\mu\text{m}$  YSZ powders were prepared and found to be stable for several days. Porous electrode substrates were then immersed in the colloidal dispersion, removed, and allowed to dry. The green bilayers were subsequently fired, yielding dense, pinhole free YSZ films of 4 to 10  $\mu\text{m}$  on the porous electrode supports. Films could be successfully deposited onto porous cathodes or cermet anodes. Fuel cell structures were completed by screen printing of the complementary electrode onto the bilayer, and mounting of the single cell onto a zirconia tube. Single-cell fuel cells exhibited near theoretical OCV's and high power densities. The approach is quite general and allows us to deposit fully dense YSZ thin films 4 to 10  $\mu\text{m}$  on a variety of porous substrates in a single step.

### 4. COLLOIDAL YSZ ROUTES TO HIGH QUALITY THIN-FILM ON POROUS SUBSTRATES

In this approach a solution of colloidal YSZ particles is deposited on a partially sintered porous anode or cathode structure. The colloidal YSZ film is deposited in a single step onto the substrate and attains a final thickness of approximately 4 to 10  $\mu\text{m}$  after sintering. In order to avoid cracking of the YSZ thin film due to stresses built up by the 2-D confinement of the sintering film, the substrate is pre-fired to the extent that the shrinkage of the substrate matches the shrinkage profile of the YSZ thin film. In this way, the film is under compression rather than tension while sintering, and highly dense, crack-free films having thicknesses of 4 to 10  $\mu\text{m}$  can be deposited in a single step onto porous substrates. This approach has been very successful. Furthermore, it does not require the use of graded porosity substrates, and consequently substrate preparation is straightforward. The YSZ films deposited in this way lead to near theoretical open circuit voltages and high power densities in single cell fuel cells.

#### 4.1 Experimental: colloidal YSZ

##### 4.1.1 NiO-YSZ anode substrate processing:

YSZ (Tosoh) was pre-calcined at 1200  $^{\circ}\text{C}$  for 4 hours and attritor milled for 1 hour. NiO powder (J.T. Baker) was attritor milled for 1 hour. The milled NiO and YSZ powders were mixed with corn starch in isopropanol or acetone and attritor milled for an additional 3 hours in isopropanol. The powders were mixed approximately as 40 wt% NiO, 40 wt% YSZ, and 10 wt% corn starch. After milling, the anode powders were collected and mixed with approximately 3



wt% binder, and 1 wt% dispersant in isopropanol. The mixture was well stirred on a magnetic stirring plate until the solvent had evaporated and then the powder were sifted using a 100  $\mu\text{m}$  sieve. The anode powders were then compacted under uniaxial pressure in a 1" die at a pressure of 4000 lbs. Green anode disks were subsequently fired at 950  $^{\circ}\text{C}$  for 10 hours to coarsen the microstructure.

#### 4.1.2 LSM-YSZ cathode substrate processing:

$\text{La}_{0.85}\text{Sr}_{0.15}\text{MnO}_3$  powders were made by the glycine-nitrate process as described earlier. LSM and YSZ were mixed in a ratio of 50/50 wt% with 3% binder and 1% dispersant in isopropanol. The mixture was stirred on a magnetic stir plate until the solvent evaporated. The LSM powder was then passed through a 100  $\mu\text{m}$  sieve. The LSM powder was then pressed uniaxially at 4000 lbs. in a 1" diameter die. The green LSM disks were then coarsened at 1250  $^{\circ}\text{C}$  for 2 hours. For the case where LSM was applied to a Ni-cermet/YSZ bilayer, the sieved LSM/YSZ powders were mixed with ethylene glycol to form a paste.

#### 4.1.3 YSZ thin-film coating

High quality YSZ powders (Tosoh) were mixed in distilled water and sonicated with a high intensity ultrasonic probe for 15 minutes. The solution was allowed to settle for 1 hour to allow the large particles to sediment out. The supernatant was decanted, placed in a large diameter evaporating dish, and allowed to dry. The finer particles deposited on the outer edges of the evaporating dish. These particles were collected, redispersed in isopropanol, and sonicated with the ultrasonic probe. This formed a very stable colloidal dispersion of fine YSZ particles suitable for casting thin films. YSZ thin films could be obtained either by dip-coating or direct casting onto the porous substrate.

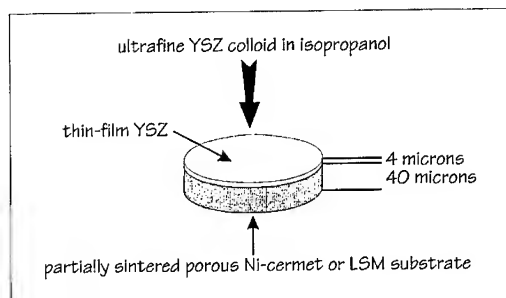


Fig. 4 Schematic representation of colloidal deposition of YSZ on porous substrates

The electrolyte/electrode bilayer is fired below 1350  $^{\circ}\text{C}$  in the case for YSZ/LSM to avoid reactions at the interface that would degrade fuel cell performance. For the Ni-cermet/YSZ bilayer, the structure is fired at 1400  $^{\circ}\text{C}$  for approximately 1 hour to achieve full density of the YSZ thin-film. After the bilayer is fired at the appropriate temperature, the corresponding anode or cathode is screen printed onto the bilayer and refired at 1250  $^{\circ}\text{C}$  for about 1 hour.

#### 4.1.4 Current collector

Platinum mesh was bonded to the anode and cathode surfaces using platinum paste. Two leads were spot-welded to each Pt mesh current collector to compensate for ohmic drop from the

galvanostat to the fuel cell. The current collectors were then fired onto the electrode surfaces at 700 °C for 1 hour.

#### 4.1.5 Seals

Ceramic seals were used to bond the fuel cell/current collector structure to a zirconia or alumina tube.

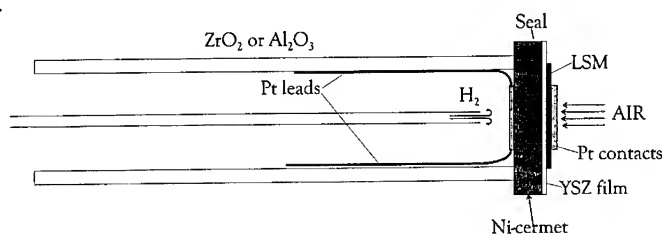


Fig. 5 Schematic of thin-film fuel cell test apparatus.

Although glass seals were also successful, the ceramic seals were far easier to fabricate, and did not appear to compromise fuel cell performance. The seals between the Ni-cermet and alumina tube was accomplished with a thin layer of Aremco 571 and this seal was encapsulated by a thick Aremco 516 (zirconia based) cement seal. The seals were cured as the fuel cell structure was brought to temperature for testing.

#### 4.1.6 Impedance Spectroscopy Analysis

Impedance analysis of thin YSZ films, bilayers, and fuel cells based on them was accomplished with a Shlumberger Solartron 1260 Frequency Response Analyzer. Measurements to date were obtained with a two probe setup. Since the porous Ni-cermet was completely covered by the thin YSZ film, the use of 2 reference electrodes for 4-probe impedance analysis is not possible. Instead, 3-probe testing is used to accurately determine the YSZ/LSM interfacial impedance.

#### 4.1.7 Fuel Cell Testing

Humidified hydrogen (4% H<sub>2</sub>O) was supplied to the Ni-cermet anode at a rate of 0.5 cm. Oxygen was supplied to the cathode by ambient air. Initially, fuel cells were operated galvanostatically with 2-wire connections to cell. However, ohmic drop across the leads must be separately measured and corrected for in the fuel cell performance curves. The cell was then fabricated using a 4-wire construction, allowing 2 wires for power, and 2 wires for sensing. On cell heat-up, argon gas is supplied to the anode. Once the cell has thermally equilibrated at the operating temperature of 700 to 800 °C, the anode gas is switched to H<sub>2</sub> and the NiO/YSZ anode is reduced to the Ni-cermet.

### 4.2 Results

#### 4.2.1 LSM/YSZ and Ni-cermet/YSZ bilayers

In order to deposit thin YSZ films on the order of 4 to 10 μm in a single step without cracking, it was imperative to control the shrinkage profile of the porous substrate to match that of the film. As can be seen in the shrinkage profiles for YSZ and LSM, both materials exhibit

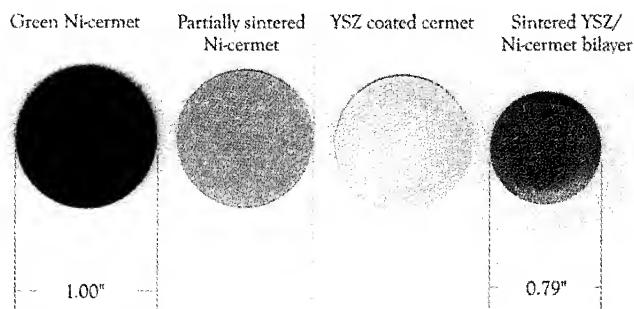


**Fig. 6 Optical image of Ni-cermet, coated cermet, and sintered electrode/electrolyte bilayer.**

It is desirable to have slightly more shrinkage of the substrate relative to the film, in order to put the film in compression. In some cases this would actually heal visible cracks that occurred after drying of the sol film and prior to densification. Control of the substrate sintering profile was accomplished through careful calcination of the glycine-nitrate derived powders. Typically a bimodal distribution of coarsened powders was used to control shrinkage. For the case of Ni-cermet substrates, systematic control of particle size and mixing was necessary to create a highly porous and homogeneous substrate suitable for coating. In the absence of careful control of substrate fabrication, single-step deposition would not close the surface porosity of the substrate and several coatings were necessary. Since it is highly desirable to achieve one-step deposition, control of substrate homogeneity is important. Furthermore, it is expected that control of cermet morphology will be critical in achieving desired electrochemical and mechanical properties of the bilayer structure and will govern fuel cell performance. Fortunately, control of particle size and cermet homogeneity is not an expensive proposition, but rather requires systematic investigation of the process parameters controlling these properties. This was accomplished in our case by methodical studies of the effects of attritor milling of as-received and as-synthesized metal oxide powders, and binder/dispersant concentrations, on the morphology of the substrate as determined by optical and scanning electron microscopy (SEM). The relationship between morphology and thin-film quality was determined in a similar fashion. Finally, the relationship between substrate morphology and fuel cell performance was examined, and is part of the ongoing research program.

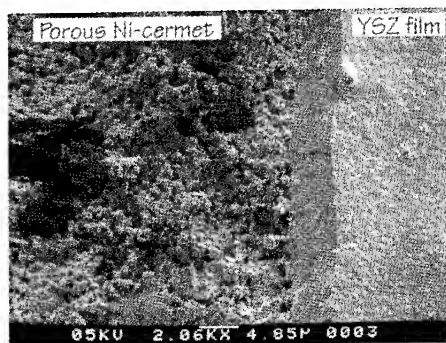


Fig. 7 SEM micrograph of thin YSZ film on porous Ni-cermet

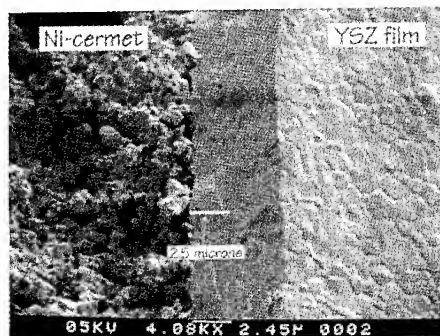


Fig. 8 Higher magnification SEM micrograph of Ni-cermet/YSZ bilayer structure

Successful deposition of fully dense, 4 to 10  $\mu\text{m}$  thick, YSZ films has been routinely achieved on highly porous LSM and Ni-YSZ cermets. As stated above, the quality of the film was largely determined by the quality of the substrate. Subtle changes in particle size as a result of changes in attritor milling and/or coarsening schedule were shown to adversely affect the homogeneity of the compact and lead to poor film quality on deposition. Conversely, by controlling process parameters carefully, high quality substrates are routinely obtained. Accordingly, single-step deposition of crack-free YSZ is relatively simple on such substrates. The high degree of homogeneity of the LSM and Ni-cermet substrates also leads to good mechanical strength and good adhesion of the YSZ film to the substrate. Although thin YSZ films could be deposited on either porous LSM or Ni-YSZ cermets, the reactivity of the LSM/YSZ interface reported in numerous studies implies that the Ni-cermet is probably more desirable as a substrate. This is clearly supported by the diffraction patterns shown in Fig. 9 and Fig. 10. In the case where a LSM/YSZ bilayer was sintered at 1325  $^{\circ}\text{C}$  there was no indication of second phase formation, however, at 1350  $^{\circ}\text{C}$  the reaction of LSM and YSZ is clearly evidenced by the appearance of  $\text{La}_2\text{Zr}_2\text{O}_7$  in the xray diffraction pattern (Fig. 10).

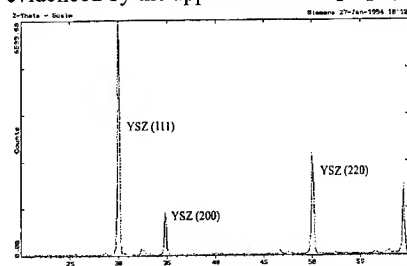


Fig. 9 Thin YSZ film sintered on LSM substrate at 1325  $^{\circ}\text{C}$  for 1 hour.

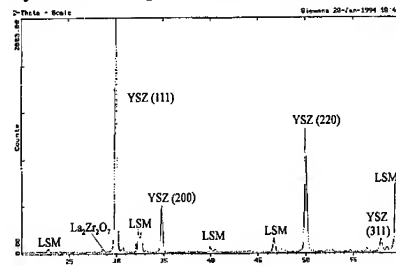


Fig. 10 Thin YSZ electrolyte film sintered onto LSM substrate at 1350  $^{\circ}\text{C}$  for 1 hour.

#### 4.2.2 Electrical Properties of bilayers

Although partially sintered porous LSM substrates were easily coated with a dense crack-free YSZ film using this approach, the LSM/YSZ interfacial impedance was found to be larger than for Ni-cermet coated substrates. When LSM/YSZ bilayers were sintered at 1325  $^{\circ}\text{C}$ , acceptable interfacial properties were obtained, however, by raising the sintering temperature

acceptable interfacial properties were obtained, however, by raising the sintering temperature merely 25 °C the appearance of  $\text{La}_2\text{Zr}_2\text{O}_7$  (above) could be detected in the xray diffraction data, and bilayer impedance was compromised. The instability of this interface at elevated temperatures is yet another reason to reduce the operating temperature of fuel cells based on these materials. Whether deposited onto porous Ni-cermets or LSM substrates, the ionic conductivity of the YSZ thin film as well as the activation energy for conduction matched that of bulk YSZ. In light of the temperature at which the thin-film electrolytes are fired, it is not surprising that binder burnout is complete, and the thin-film materials attain bulk properties.

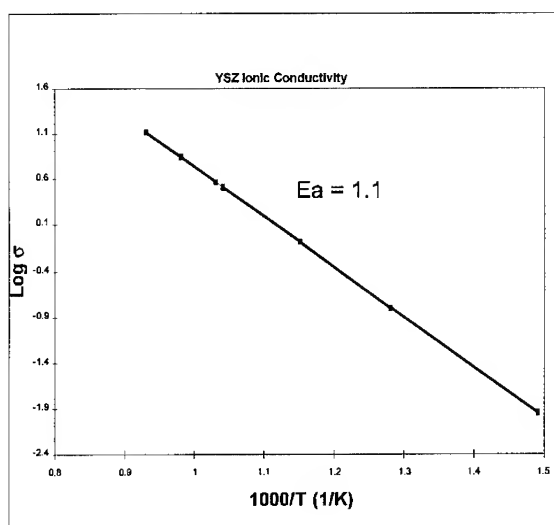


Fig. 11 Ionic conductivity of thin-film YSZ as a function of temperature.

Although the resistance of the electrolyte has been greatly reduced by limiting the thickness of this component to a few microns, the performance of the bilayer structures and fuel cells based on them depends critically on the nature of the electrode/electrolyte interface and its stability over time at the operating temperature of the device. To determine interfacial impedance of the LSM/YSZ bilayer, Pt leads were attached to the structure with Pt paste, and the impedance of the device was determined over the frequency range of 0.01 Hz to 65 kHz. The interfacial impedance of this device was found to be approximately  $3.2 \Omega \text{ cm}^2$ . The impedance response was also determined for a fuel cell where a Ni/YSZ cermet was applied to the electrolyte face of the LSM/YSZ bilayer. The impedance spectrum can be seen in Fig. 12 below. The total impedance for this fuel cell was approximately  $8 \Omega \text{ cm}^2$ , of which  $1.8 \Omega \text{ cm}^2$  was lead resistance, and  $6.2 \Omega \text{ cm}^2$  was interfacial contact resistance ( $3.2 \Omega \text{ cm}^2$  for LSM/YSZ and  $3.0 \Omega \text{ cm}^2$  for Ni-cermet/YSZ). The interfacial impedances clearly dominate the electrical response of this fuel cell, and must be reduced. The cathode in this fuel cell was porous LSM. The interfacial impedance could be improved through the inclusion of YSZ in the cathode formulation. Several groups have claimed that the use of LSM/YSZ cathodes not only reduce the interfacial impedance at the (LSM/YSZ)/YSZ interface, but also improve the long-term stability of this interface. This is due presumably to spreading the LSM/YSZ reaction layer out over a large surface area, as opposed limiting the reaction layer to the electrode/electrolyte interface where it

interface where it presents a large series resistance. The current/voltage profile of this fuel cell is presented in the next section.

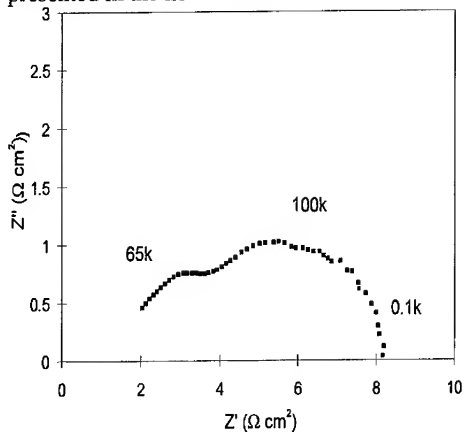


Fig. 12 Impedance spectra for LSM/YSZ bilayer

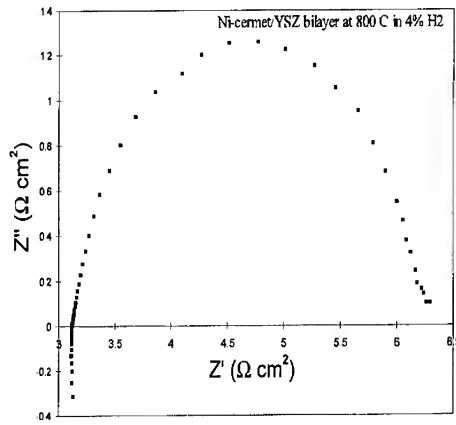


Fig. 13 Impedance spectrum for Ni-cermet/YSZ bilayer.

The AC response of a Ni-YSZ/YSZ cermet is shown in Fig. 13. The interfacial impedance of the cermet is approximately  $3.0 \Omega \text{ cm}^2$ . One would expect this impedance to be significantly smaller than that observed for the LSM/YSZ cermet. It has been suggested that if hydrogen reduction of the NiO-YSZ/YSZ bilayer is not done carefully, deterioration of the Ni-YSZ/YSZ interface results. Consequently, the Ni-cermets are presently being brought to temperature under argon, and then reduced at  $800^\circ\text{C}$  with hydrogen. Impedance spectroscopy has not yet been performed on these samples.

#### 4.2.3 Fuel Cell Testing and Evaluation

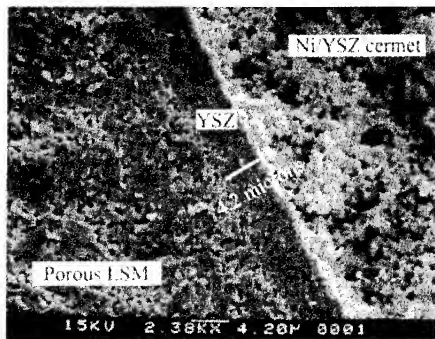


Fig. 14 SEM micrograph of fracture cross-section of thin-film fuel cell.

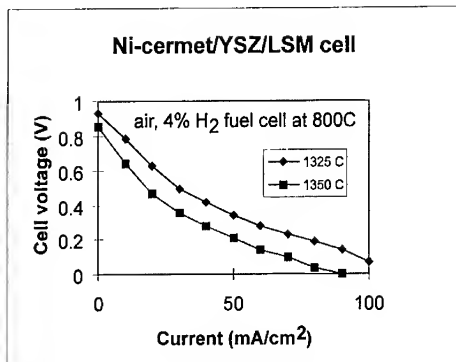


Fig. 15 Current-voltage profile for thin-film LSM/YSZ bilayer-based fuel cell.

Thin-film fuel cells were constructed as described in the experimental section. The completed cells were then slowly brought to temperature and the NiO electrode reduced to Ni metal *in situ*. As expected, the performance of the fuel cells based on LSM/YSZ bilayers was fair, but not outstanding. The cell exhibited near theoretical OCV, but exhibited a steeply sloping voltage/current profile with a short circuit current of approximately 100 mA/cm<sup>2</sup>. This was most likely due to the presence of a reaction layer during firing of the bilayer, as detected in the xray, and impedance spectroscopy. The performance of the Ni-cermet/YSZ/LSM cell based on a LSM/YSZ bilayer is shown in Fig. 15. As would be expected, the cell fabricated from a LSM/YSZ bilayer fired at 1350 °C performed worse than the cell where the bilayer was fired at 1325 °C. This correlates well with the xray observation of La<sub>2</sub>Zr<sub>2</sub>O<sub>7</sub> for bilayers formed at 1350 °C.

Although high quality porous LSM substrates had proven to be relatively simple to fabricate and coat, the instability of the interface at temperatures above 1350 °C prompted us to focus efforts towards fabrication of highly homogeneous porous NiO/YSZ substrates. This effort was successful, and enabled routine coating of these substrates with 4 to 10 micron thick, fully dense YSZ. These cells easily outperformed cells based on LSM/YSZ bilayers. Fig. 16 and Fig. 17 below shows the performance of one such fuel cell.

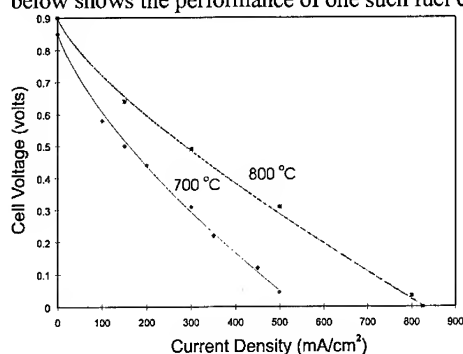


Fig. 16 Current-voltage profile for Ni-cermet/YSZ bilayer fuel cell with LSM cathode

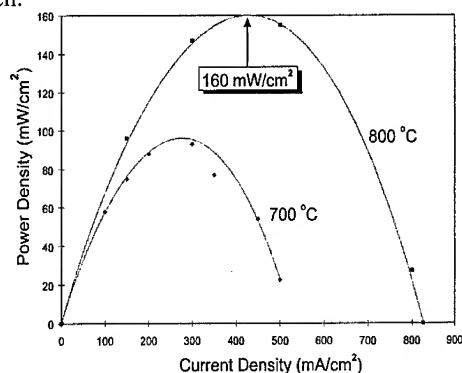


Fig. 17 Power-current profile for Ni-cermet/YSZ thin-film bilayer fuel cell with LSM cathode.

As can be seen from the current/voltage curves, at 800 °C the fuel cell based on a Ni-cermet/YSZ thin film electrolyte demonstrated short circuit currents of approximately 820 mA/cm<sup>2</sup>. The power output for this cell is shown in Fig. 17. The cell attained an output of approximately 160 mW/cm<sup>2</sup> at 800 °C. It is quite likely that the cell performance exceeded that shown Fig. 18 and Fig. 19, since the temperature of operation was taken using the furnace controller thermocouple. Hydrogen was supplied directly to the Ni-cermet anode without pre-heating of the gas, and consequently it is possible that the anode was appreciably cooled by the fuel gas. The fuel cell test apparatus has been redesigned with a thermocouple at the Ni-cermet surface to monitor the actual operating temperature of the cell. In any event, the output shown in the figures above represents a minimum for the thin-film based cells.

The open circuit voltage of the thin-film electrolyte cell in Fig. 16 is about 100 mV less than theoretical. In order to realize maximum efficiency and power output of the fuel cell, this loss must be eliminated. The slight depression of cell voltage may be due to either a leak in cell seals, the presence of pinholes in the thin-film electrolyte, or both factors. Improvement of cell sealing has been accomplished recently through the use of a dual layer seal. The presence of

pinholes has been detected in some sintered bilayers by penetration of a low viscosity organic solvent. This has been corrected by further improvements in the Ni-cermet preparation, and by increasing the solids loading in the colloidal YSZ coating solution.

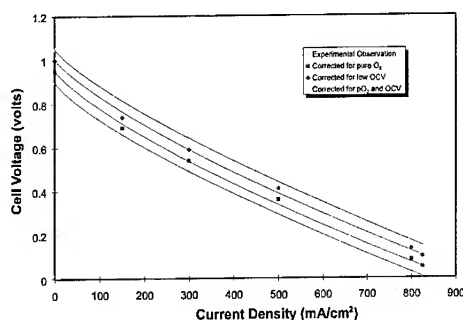


Fig. 18 Estimated thin-film fuel cell I-V curves corrected for leaks, etc.

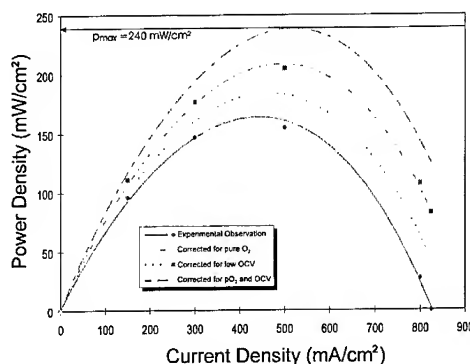


Fig. 19 Estimated thin-film power densities corrected for leaks, etc.

The performance of the Ni-YSZ/YSZ bilayer based fuel cells can be roughly corrected for the depressed OCV and for higher  $O_2$  concentrations than were used experimentally. The oxygen atmosphere corrections were estimated from published data for actual fuel cell performance<sup>5</sup> as a function of  $pO_2$ . As can be seen from the above figures, maximum power densities of  $240 \text{ mW/cm}^2$  at  $800^\circ\text{C}$  should be attainable. It is expected that these results will be verified shortly with the improved Ni-cermet bilayers, and the redesigned fuel cell test apparatus.

## 5. CONCLUSIONS

A highly successful thin-film deposition procedure was developed through systematic elucidation of the shrinkage profiles for thin-film electrolytes and the porous electrode substrates to be coated. Colloidal dispersions of submicron polycrystalline electrolyte powders were used as the coating solutions. Partially sintered porous substrates (anodes or cathodes) were coated with the colloidal dispersions, and the resulting bilayers were co-fired to yield fully dense, crack-free electrolyte films of 4 to  $5 \mu\text{m}$  in thickness in a single depositions step. In order to avoid reaction of the YSZ with LSM at the co-firing temperature, Ni-cermets were typically used as the porous substrate. The thin electrolyte films exhibited ionic conductivities of the bulk material.

LSM cathodes were screen-printed on the Ni-cermet/YSZ electrolyte bilayers and fired to yield single cell thin-film devices. Upon mounting into fuel cell test rigs, the thin-film cells were tested in  $H_2$ /air environments at the intermediate temperatures of 700 to  $800^\circ\text{C}$ . The cells exhibited near theoretical open circuit voltages, and high power densities under load. Importantly, the goal of using thin-film techniques to reduce the operating temperature of SOFC's while maintaining excellent performance was realized.

Thin-film electrolytes of the order of 4 to  $10 \mu\text{m}$  can be deposited on highly porous substrates in a single deposition step. The electrolytes are fully dense and crack-free, and exhibit ionic conductivity comparable to bulk material. The colloidal sol approach is a generic means of depositing thin-films and was found to work equally well for porous LSM or Ni-YSZ substrates. The quality of the deposited film depends largely on the homogeneity of the porous substrate, and careful matching of film and substrate sintering profiles. In this way the electrolyte film is



allowed to shrink in 3 dimensions as it sinters to full density. It was found that even in the case of poor films where visible cracking could be seen prior to the final firing, the substrate shrinkage would heal the cracks and high quality electrolyte films were obtained. It was observed that for the case where LSM substrates were coated with YSZ, a  $\text{La}_2\text{Zr}_2\text{O}_7$  film could be observed in the xray if the sintering temperature exceeded 1350 °C. The presence of this film is deleterious to fuel cell performance, and for this reason it was decided that a preferable avenue was to coat Ni-YSZ substrates with thin electrolyte films. Impedance spectroscopy of the Ni-YSZ/YSZ bilayer showed a lower interfacial impedance relative to the LSM/YSZ bilayer. Furthermore, performance of the Ni-YSZ/YSZ thin-film fuel cell was far improved relative to the performance seen when LSM was used as a substrate for film deposition. The Ni-YSZ/YSZ/LSM fuel cell exhibited power densities of approximately 160 mW/cm<sup>2</sup> at 800 °C. It is expected that power densities well over 240 mW/cm<sup>2</sup> will be demonstrated shortly.

#### References

- <sup>1</sup> N. Minh, J. Am. Ceram. Soc. 76, 563 (1993).
- <sup>2</sup> L. S. Wang and S. A. Barnett, J. Electrochem. Soc. 139, L89 (1992).
- <sup>3</sup> L. Wang, S. J. Visco, L. C. De Jonghe, EPRI/GRI Fuel Cell Workshop, Atlanta, Georgia, 1994.
- <sup>4</sup> T. Kueper, S. J. Visco, and L. C. De Jonghe, Solid State Ionics 52, 251 (1992).
- <sup>5</sup> K. Tsuneyoshi, K. Mori, A. Sawata, J. Mizusaki, and H. Tagawa, Solid State Ionics 35, 263 (1989).

**NANOSTRUCTURED ORGANIC/INORGANIC FILMS FROM  
POLY (D-LYSINE HYDROBROMIDE) OR POLY(N-METHYL-4-VINYL PYRIDINIUM  
BROMIDE) AND HECTORITE**

ELAINE R. KLEINFELD AND GREGORY S. FERGUSON\*  
Department of Chemistry, Lehigh University, Bethlehem, PA 18015

**ABSTRACT**

Establishing the generality of any new preparative method is important for its future usefulness in applications of interest. In this paper, we build on results reported earlier for the formation of nanostructured ultrathin films from macromolecular precursors (a particular cationic polyelectrolyte and inorganic sheet silicate) by demonstrating that the method can readily be adapted to different polymers and more complex adsorption schemes. In particular, we used ellipsometry to monitor the regular growth of films incorporating poly(D-lysine hydrobromide) or poly(N-methyl-4-vinylpyridinium bromide) (PMVP) and hectorite. For the PMVP/ hectorite films, X-ray diffraction confirmed the presence of structural order by revealing a lattice spacing of 1.5 nm.

**INTRODUCTION**

Multilayered films offer potential for applications in such diverse fields as optics,<sup>1,2,3</sup> microelectronics,<sup>4</sup> and molecular sensing,<sup>5</sup> as long as their thickness and structure can be precisely controlled. Methods that rely on vapor-phase transport of precursors or component materials, however, have limited applicability for the formation of films containing complex organic molecules of low volatility. Molecular self-assembly offers promise for the convenient preparation of such films under ambient conditions.<sup>6</sup> These films can be formed one layer at a time so that the film thickness can be precisely controlled, and careful choice of precursors allows the formation of films with designed properties. Approaches to the self-assembly of multilayered films from monomeric precursors have included adsorption/ activation of silanes,<sup>7</sup> alternate treatments with organic phosphonates and di- or tetravalent metal compounds,<sup>8</sup> and alternate treatments with an  $\alpha,\omega$ -mercaptoalkanoic acid and copper ions.<sup>9</sup> In both metal-phosphonate<sup>1</sup> and silane systems,<sup>2</sup> films have been prepared in which polar alignment of the constituent chromophores imparted second-order nonlinear optical activity. Self-assembled multilayered films have also been evaluated for use in microelectronics<sup>10</sup> and molecular sensing.<sup>5</sup>

The adsorption of films from macromolecular precursors by ion exchange has also been reported. For example, Decher et al. reported formation of ultrathin films on flat substrates by alternate adsorption of various polycations and polyanions [e.g., poly(styrene sulfonate) and poly(allylamine hydrochloride)].<sup>11</sup> These films were smooth and uniform, as evidenced by X-ray reflectivity, though interpenetration of the cationic and anionic polymer chains reduced the degree of structural order in the direction normal to the substrate surface.<sup>12</sup> Rubner et al.<sup>13</sup> recently used this technique with sulfonated polystyrene and p-doped conducting polymers, such as polyaniline or polypyrrole, to form conducting films with potential usefulness as antistatic coatings, and Cooper et al.<sup>14</sup> prepared multilayers from polypeptides and various chromophores.

We have reported the formation of ordered organic/inorganic multilayers to thicknesses greater than 0.2  $\mu\text{m}$  by alternate adsorption of the cationic polyelectrolyte poly(diallyldimethylammonium chloride) (PDDA) and the anionic sheet silicate hectorite.<sup>15</sup> This technique offers certain advantages over other methods for multilayer formation: the ion-exchange process by which the films form is rapid, and, as a result, thick films can be formed in short periods of time. Due to the high aspect ratio of the silicate sheets<sup>16</sup> and the tendency of these sheets to align parallel to one another, the films possess order in the direction normal to the substrate surface at the angstrom level (lattice spacing  $\sim 15$  Å). This level of nanoscale order is unprecedented among films formed on flat substrates by adsorption from solutions. Furthermore, interpenetration of a polymer chain with an adjacent hectorite sheet is not possible.

The ion-exchange mechanism of adsorption of the components in the multilayered films (i.e., the reliance upon Coulombic interactions rather than upon formation of covalent bonds) suggests that there should be great flexibility with respect to the choice of the polymer and sheet mineral.<sup>17</sup> The ability to vary systematically the structure of the polymer in these multilayers may allow the rational design of films having properties of interest—for example, in chiral sensing<sup>5,18</sup> or nonlinear optical applications.<sup>1,2,19</sup> An approach for the preparation of films active for chiral sensing would be incorporation of a polymer with a chiral backbone or chiral substituents into the composite film. Likewise, incorporation of a polymer having a polarizable backbone or substituents would create the possibility of forming composite films with second- or third-order nonlinear optical activity. As model polymers to initiate these studies, we chose poly(D-lysine hydrobromide) and poly(*N*-methyl-4-vinylpyridinium bromide) (PMVP).

## EXPERIMENTAL METHODS AND RESULTS

A multilayered film was formed by alternate adsorption of poly(D-lysine hydrobromide) [5% (w/w), aqueous] and Laponite RD, a synthetic hectorite [0.2%

(w/w), aqueous] under conditions described previously.<sup>15,20,21</sup> Briefly, in each step, the aqueous adsorbate solution or suspension was dripped onto the substrate, rinsed with water after ~5 s, and dried with a stream of nitrogen. Treatment with both components, polymer and then silicate, is defined as one adsorption cycle. The growth in film thickness was monitored ellipsometrically (Rudolph Auto-EL III, assuming a refractive index of 1.5) and is shown in Figure 1. Thicknesses after individual steps in the first five cycles are shown; the thickness grew approximately 4 Å in the lysine-adsorption steps and 10 Å in the hectorite-adsorption steps.

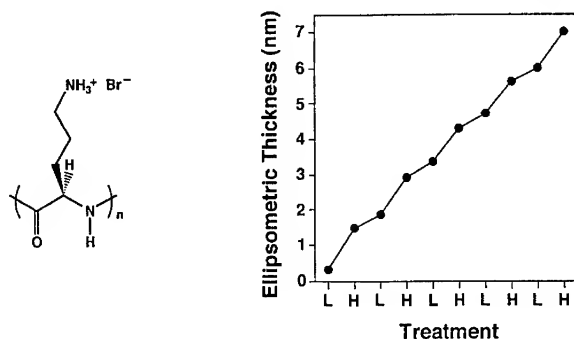


**Figure 1.** Structure of poly(D-lysine hydrobromide) and growth in thickness of a polylysine/hectorite composite film with each treatment in the first five adsorption cycles (L = polylysine; H = hectorite).

Figure 2 shows the growth in thickness of multilayers formed from poly(*N*-methyl-4-vinylpyridinium bromide) (PMVP) [10% (w/w), aqueous] and Laponite RD [0.2% (w/w), aqueous] as a function of the number of adsorption cycles (again assuming a refractive index of 1.5).<sup>22</sup> X-ray photoelectron spectroscopy (Scienta ESCA-300) of a sample formed by 25 complete adsorption cycles on silicon/silicon dioxide revealed the presence of carbon, nitrogen, and bromine from the polymer, and silicon, magnesium, and oxygen from the hectorite. The presence of bromine and the apparent absence of monovalent cations associated with the hectorite (lithium and sodium) suggest that the polymer is present in excess of the cation exchange capacity of the clay.

The linearity of the data in Figures 1 and 2 indicates that the adsorption process is regular and could be continued indefinitely to produce films of precisely controllable thickness; however, these data provide *no* information concerning the structure of the films. X-ray diffraction, in contrast, can provide structural information. Figure 3 shows the X-ray diffractogram (Philips APD 3720) of a sample formed by 46 adsorption cycles of PMVP and hectorite on the native oxide of silicon. The peak at  $5.8 \pm 0.2^\circ 2\theta$  is assigned as the (001) reflection of the PMVP/hectorite lattice; it indicates a d-spacing of  $15.2 \pm 0.5 \text{ Å}$ . The two peaks centered around  $18^\circ$  and  $27^\circ 2\theta$  are sufficiently broad and weak that they are difficult to assign

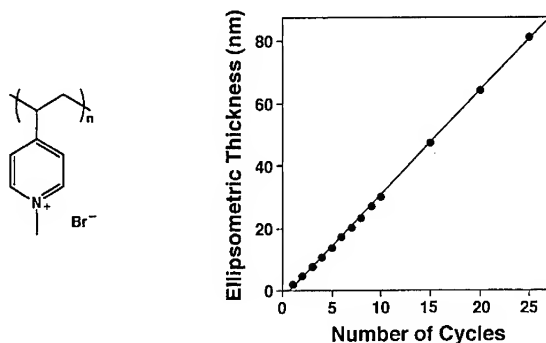


**Figure 2.** Structure of poly(*N*-methyl-4-vinylpyridinium bromide) and growth in thickness of a PMVP/hectorite composite film during 25 complete adsorption cycles.

unambiguously, though they may be due to higher-order reflections of the PMVP/hectorite lattice. The lattice spacing given by the (001) reflection suggests that the hectorite sheets, which are 9.6 Å in thickness, are separated by layers of polymer roughly 5.6 Å in thickness. These values are similar to those for PDDA/hectorite films, in which the hectorite sheets are separated by PDDA layers roughly 4.9 Å in thickness.<sup>15</sup>

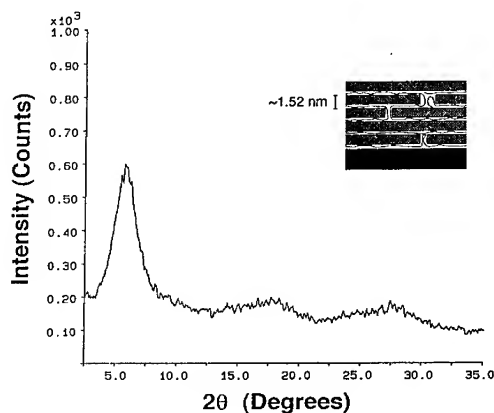


**Figure 3.** X-ray diffraction pattern of a sample prepared by the adsorption of 46 cycles of PMVP and hectorite onto a silicon wafer.

We have also prepared multilayers with more complex structures incorporating both PDDA and PMVP. Figure 4 shows the ellipsometric growth of a film formed by adsorbing these components in the order PDDA/hectorite/PMVP/hectorite.<sup>23</sup> Again, the thickness increased in a regular fashion.

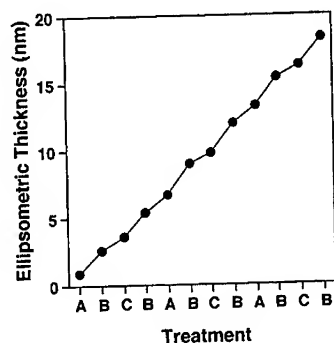


**Figure 4.** Ellipsometric growth of a film formed by sequential adsorptions of components in the order PDDA/hectorite/PMVP/hectorite (A = PDDA; B = hectorite; C = PMVP).

## SUMMARY/CONCLUSIONS

Alternate adsorption of a cationic polyelectrolyte and anionic sheet silicate onto Si/SiO<sub>2</sub> offers a versatile synthetic method for the stepwise formation of nanostructured ultrathin films. Not only can films be adsorbed with an unprecedented level of order in the direction normal to the substrate, as demonstrated previously,<sup>15</sup> but the use of Coulombic interactions rather than covalent interactions allows flexibility in film composition and structure. Specifically, we have found that regular film growth occurs in two-step adsorption cycles involving polylysine and hectorite, or PMVP and hectorite, as well as in a four-step adsorption cycle involving PMVP, PDPA, and hectorite. The successful use of polylysine to form multilayered films demonstrates that protonated polycations (as opposed to quaternary ammonium cations) can be used to form multilayered films with hectorite. While ellipsometry provided evidence of regular growth, X-ray diffraction confirmed the presence of structural order in the PMVP/hectorite system.<sup>24</sup> The flexibility of this preparative method enhances its potential for the formation of films with structures and properties of interest.

## ACKNOWLEDGEMENTS

We thank Lehigh University for support of the Scienta ESCA-300 facility. E.R.K. gratefully acknowledges an AT&T Bell Laboratories Ph.D. Scholarship.

## REFERENCES

1. H.E. Katz, G. Scheller, T.M. Putvinski, M.L. Schilling, W.L. Wilson, C.E.D. Chidsey, *Science* **254**, 1485 (1991).
2. D. Li, M.A. Ratner, T.J. Marks, C. Zhang, J. Yang, G.K. Wong, *J. Am. Chem. Soc.* **112**, 7389 (1990).
3. C.L. Nagendra and G.K.M. Thutupalli, *Applied Optics* **27**, 2320 (1988); P. Dhez, *Thin Solid Films* **175**, 151 (1989).
4. F. Kaneko, M. Shibata, Y. Inaba, S. Kobayashi, *Thin Solid Films* **179**, 121 (1989).
5. L.C. Brousseau, K. Aoki, M.E. Garcia, G. Cao, T.E. Mallouk, in *Multifunctional Mesoporous Inorganic Solids*, edited by C.A.C. Sequeira and M.J. Hudson (Kluwer Academic Publishers, Boston, 1993), pp. 225-236.
6. A. Ulman, *An Introduction to Ultrathin Organic Films: From Langmuir-Blodgett to Self-Assembly*. (Academic Press, Boston, MA, 1991.)
7. L. Netzer, R. Iscovici, J. Sagiv, *Thin Solid Films* **99**, 235 (1983).
8. G. Cao, H.-G. Hong, T.E. Mallouk, *Acc. Chem. Res.* **25**, 420 (1992). H.C. Yang, K. Aoki, H.-G. Hong, D.D. Sackett, M.F. Arendt, S.-L. Yau, C.M. Bell, T.E. Mallouk, *J. Am. Chem. Soc.* **115**, 11855 (1993).
9. S.D. Evans, A. Ulman, K.E. Goppert-Berarducci, L.J. Gerenser, *J. Am. Chem. Soc.* **113**, 5866 (1991).
10. H.E. Katz, M.L. Schilling, *Chem. Mater.* **5**, 1162 (1993); L.J. Kepley, D.D. Sackett, C.M. Bell, T.E. Mallouk, *Thin Solid Films* **208**, 132 (1992).
11. Y. Lvov, H. Haas, G. Decher, H. Möhwald, A. Kalachev, *J. Phys. Chem.* **97**, 12835 (1993), and references therein.
12. J. Schmitt, T. Grunewald, G. Decher, P.S. Pershan, K. Kjaer, M. Lösche, *Macromolecules* **26**, 7058 (1993).
13. J.H. Cheung, A.F. Fou, M.F. Rubner, *Thin Solid Films* **244**, 985 (1994).
14. T.M. Cooper, A.L. Campbell, C. Noffsinger, J. Gunther-Greer, R.L. Crane, and W. Wade Adams, in *Molecularly Designed Ultrafine/Nanostructured Materials*, edited by K.E. Gonsalves, G.-M. Chow, D.D. Xiao, and R.C. Cammarata (*Mat. Res. Soc. Symp. Proc.* **351**, San Francisco, CA, 1994) pp. 239-244.
15. E.R. Kleinfeld and G.S. Ferguson, *Science* **265**, 370 (1994).
16. The silicate sheets are 9.6 Å in thickness and approximately 300 Å in diameter.
17. Evidence for regular growth of thin films by alternate adsorption of polyanions such as  $\alpha$ -Zr(HPO<sub>4</sub>)<sub>2</sub> and Ti<sub>2</sub>NbO<sub>7</sub><sup>-</sup> and polycations such as polyallylamine and cytochrome c has recently been reported; see: S.W. Keller, H.-N. Kim, T.E. Mallouk, *J. Am. Chem. Soc.* **116**, 8817 (1994).
18. Y. Nakamura, A. Yamagishi, S. Matumoto, K. Tohkubo, Y. Ohtu, M. Yamaguchi, *J. Chromatography* **482**, 165 (1989).
19. P.G. Lacroix, R. Clément, K. Nakatani, J. Zyss, I. Ledoux, *Science* **263**, 658 (1994).
20. Substrates for these adsorptions were pre-treated by performing two adsorption cycles using a 5% (w/w) solution of PDDA and a 0.2% w/w hectorite suspension under conditions described previously (see reference 15). The substrates were primed in this way to provide a hectorite-coated substrate so that we could focus on multilayer formation independently from the issue of the affinity of the particular polymer for the native oxide on the silicon wafer.
21. Poly(D-lysine hydrobromide) was obtained from Sigma; Laponite RD was obtained from Laporte Industries Limited.
22. Poly(N-methyl-4-vinylpyridinium bromide) was obtained from Polysciences.
23. G. Decher, Y. Lvov, J. Schmitt, *Thin Solid Films* **244**, 772 (1994).
24. We have not yet attempted to obtain XRD patterns of the other structures discussed in this paper.

## ELECTRICAL PROPERTIES OF DONOR AND ACCEPTOR DOPED $\text{Gd}_2\text{Ti}_2\text{O}_7$

\*  
IGOR KOSACKI AND HARRY L. TULLER

Crystal Physics and Electro-Ceramics Laboratory ,  
Department of Materials Science & Engineering ,Massachusetts Institute of Technology ,  
Cambridge , MA 02139 , USA

The results of electrical conductivity measurements on Nb , W , and Mn-doped  $\text{Gd}_2\text{Ti}_2\text{O}_7$  are presented. A correlation between electrical conductivity , the oxygen partial pressure and type of dopants has been obtained. The source of the different  $\text{P}_{\text{O}_2}$  dependence for Mn-doped material is discussed.

### 1. INTRODUCTION

Mixed ionic and electronic conduction , MIEC , plays an important role in a number of phenomena of interest to the operation of solid state electrochemical devices including electrode kinetics , permeation and bulk redox kinetics. Among the better oxygen ion conductors , MIEC has been investigated at least to some extent in  $\text{CeO}_2$  and  $\text{ThO}_2$  and in stabilized zirconia. The flexibility in controlling MIEC in these materials is , however , limited by the binary nature of these systems [1,2].

In recent years , we have demonstrated that MIEC can be controlled over wide limits in the pyrochlore oxides described by compositions  $\text{Gd}_2(\text{Zr}_x\text{Ti}_{1-x})_2\text{O}_7$  (GZT) and  $\text{Y}_2(\text{Zr}_x\text{Ti}_{1-x})_2\text{O}_7$  (YZT) by control of both the parameter  $x$  and by doping with altermvalent ions. At one extreme , it is possible to obtain an excellent electrolyte by acceptor doping the end-member  $\text{Gd}_2\text{Ti}_2\text{O}_7$  (GT) with Ca [3] or by selecting  $x > 0.4$  in GZT [4,5]. On the other extreme , we find reduced or donor doped GT to exhibit predominantly a  $\text{P}_{\text{O}_2}$ -dependent semiconducting behavior [6]. This has been, for example , recently examined in relation to potential sensor applications [7].

In the present work , we examine the influence of potentially multi-valent donors and acceptors on the electronic properties of  $\text{Gd}_2\text{Ti}_2\text{O}_7$ . These might be expected to have interesting effects on both electronic and ionic carriers given their ability to both influence the redox behavior and serve as the potential source for impurity-band conduction.

Comparing the ionic radii and valence electron configurations , we expect that  $\text{W}^{5+}$  (5d electrons) could be a more effective donor than  $\text{Nb}^{4+}$  (4d electrons). This is indeed confirmed as we show below. Further , given that W is a column VI element , we could expect that  $\text{W}^{6+}$  may also exist leading , in conjunction with  $\text{W}^{5+}$  , to the possibility of polaron conduction via a hopping process. The same may be said for  $\text{Mn}^{3+}/\text{Mn}^{4+}$  which may act as an acceptor rather than a donor.

In the current work , the results of the conductivity measurements on Nb , W and Mn-doped  $\text{Gd}_2\text{Ti}_2\text{O}_7$  as a function of temperature and oxygen partial pressure are presented. The aim of this paper is the study the influence of Nb , W and Mn dopants on the electrical properties of  $\text{Gd}_2\text{Ti}_2\text{O}_7$  and to find the correlation between the conductivity and stoichiometry in this material. Confirmation of the polaron transport model in W and Mn-doped  $\text{Gd}_2\text{Ti}_2\text{O}_7$  is also an objective.

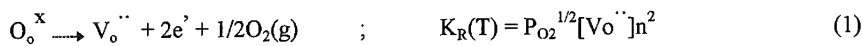
\* Permanent address: Radom Technical University , ul.Malczewskiego 29 , 26-600 Radom , Poland.



Results of the electrical conductivity measurements are analyzed with the aid of a defect model.

## 2. DEFECT MODEL

The electrical properties of titanate-based pyrochlores can be described by defect models in which the acceptor and donor impurities are compensated by oxygen vacancies or oxygen interstitials respectively [6,8]. The key reactions include the redox and frenkel reaction , dopant ionization , e-h generation and the electroneutrality equation:



The parameters  $K_R(\text{T})$ ,  $K_F(\text{T})$ ,  $K_M(\text{T})$  and  $K_e(\text{T})$  are the equilibrium constants with the standard exponential form  $K_i(\text{T}) = K_i^0 \exp(-E_i/kT)$  [3,8,9].

### 2.1 Donors with fixed valence:

The defect equilibria of donor-doped  $\text{Gd}_2\text{Ti}_2\text{O}_7$  have been discussed in [6,7]. Here we briefly summarize the relevant conclusions. In the case of donor-doped pyrochlores , we expect that , at high  $P_{\text{O}_2}$  , charge compensation occurs by the formation of oxygen interstitials  $[\text{D}'] = 2[\text{O}_\text{i}^{\prime\prime}]$ . For intermediate  $P_{\text{O}_2}$  , the electron concentration is determined by the donor ionization processes ,  $n = [\text{D}']$  and for low  $P_{\text{O}_2}$  we assume electron compensation of the charge carriers generated in the reduction reaction (1) ,  $n = 2[\text{V}_\text{o}^{\cdot\cdot}]$ . Combining equations (1-4) with the above simplified neutrality relations , we can obtain the solutions for the electron conductivity in each  $P_{\text{O}_2}$  region [6]:

$$\sigma_e \sim P_{\text{O}_2}^{-r} \quad (6)$$

where:  $r = 1/6$  for low  $P_{\text{O}_2}$   
 $r = 0$  for intermediate  $P_{\text{O}_2}$   
 $r = 1/4$  for high  $P_{\text{O}_2}$

In this model , all donors are assumed to be ionized at high  $P_{\text{O}_2}$ .

The measurements of conductivity as a function of oxygen partial pressure provide a means of identifying the defect regimes relevant to a set of equilibrium conditions-temperature,  $P_{O_2}$  and dopant concentration. The  $P_{O_2}$  independent region ( $r=0$ ), limited by donor ionization, provides an opportunity to derive the donor ionization energy, a key defect parameter.

## 2.2 Impurities with variable valence:

If impurities are present in two or more ionization states such as  $[Mn_{Ti}^x]$  and  $[Mn_{Ti}']$ , conduction can take place by the transfer of electrons from a lower to a higher valence state. This process is determined by the concentration of the respective Mn charge states and also by the overlap between the electron wave functions at nearby states. The hopping contribution to the total conductivity is described by [3,10,11]:

$$\sigma_H = ve^2 a^2 / kT [Mn]_{total}^{-1} [Mn_{Ti}'] [Mn_{Ti}^x] \exp(-2\alpha a) \exp(-E_h/kT) \quad (7)$$

where  $a$  is the site spacing,  $v$  is the electron jump frequency,  $\alpha$  is the electron tunneling probability and  $E_h$  is the effective hopping energy.

Assuming, as a first approximation, that the hopping energy and tunneling factor are  $P_{O_2}$  independent, the polaron conductivity becomes a function of  $[Mn_{Ti}']$  and  $[Mn_{Ti}^x]$  which are  $P_{O_2}$  dependent. For  $[Mn_{Ti}'] = [Mn_{Ti}^x]$ , the conductivity is predicted to attain a maximum. Therefore, a plot of  $\ln \sigma_{max}$  vs  $1/T$  should give the hopping energy  $E_h$ .

## 3. EXPERIMENTAL

Powders of  $Gd_2Ti_2O_7$  doped with 1%Nb, 2%W and 2%Mn (on a Ti site fraction percent basis) were prepared by the Pechini "liquid-mix" technique [12], pressed into pellets at 40,000 psi and sintered at 1600°C for 16 hours achieving pyrochlore structures with 93% theoretical density. Two probe AC impedance measurements were performed with an HP 4192a impedance analyzer over the frequency range 5HZ-13MHz and temperature range of 600 to 1000°C. Oxygen partial pressures were controlled by use of Ar/O<sub>2</sub> and CO/CO<sub>2</sub> gas mixtures. Sputtered platinum films were used as electrodes.

## 4. RESULTS AND DISCUSSION

Equilibrium electrical conductivity data obtained for Nb and W-doped  $Gd_2Ti_2O_7$  as a function of  $P_{O_2}$  are presented in Figs.1 and 2. For 1%Nb, the conductivity follows a  $P_{O_2}^{-1/4}$  dependence at high  $P_{O_2}$ , while at low  $P_{O_2}$ , the dependence changes from  $P_{O_2}^{-1/2}$  to  $P_{O_2}^{-1/6}$  for low and high temperatures respectively, with the steeper slope likely due to defect association at the lower temperatures. The  $P_{O_2}$ -independent behavior at intermediate  $P_{O_2}$  is expected for the condition  $n=[Nb_{Ti}]$ . A similar plateau is observed in the data of W-doped  $Gd_2Ti_2O_7$  (Fig.2). The ionization energies have been determined by examining the Arrhenius plots of the conductivities

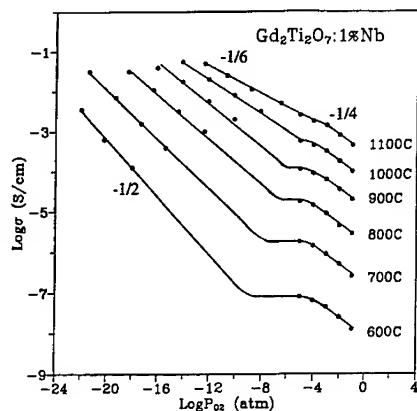


Fig.1 The electrical conductivity of  $\text{Gd}_2\text{Ti}_2\text{O}_7\text{:Nb}$  as a function of  $P_{\text{O}_2}$ .

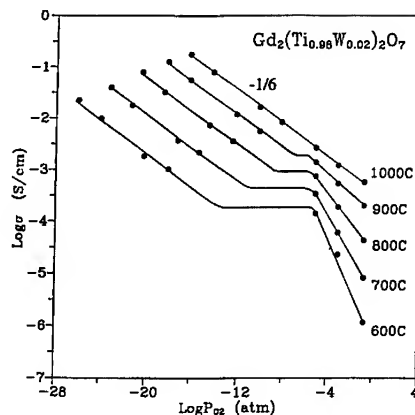


Fig.2 The electrical conductivity of  $\text{Gd}_2\text{Ti}_2\text{O}_7\text{:W}$  as a function of  $P_{\text{O}_2}$ .

obtained for intermediate  $P_{\text{O}_2}$ s (Fig.3). Ionization energies of 1.95eV and 0.82eV were obtained for 1%Nb and 2%W-doped  $\text{Gd}_2\text{Ti}_2\text{O}_7$  respectively. This suggests that Nb and W form deep donors in these pyrochlores. The introduction of W into  $\text{Gd}_2\text{Ti}_2\text{O}_7$ , however, increases the low temperature conductivity by about 3 orders of magnitude as compared with the Nb-dopant. This can be important from the application point of view. Additional measurements are necessary to separate out ionization from hopping terms in the measured activation energies.

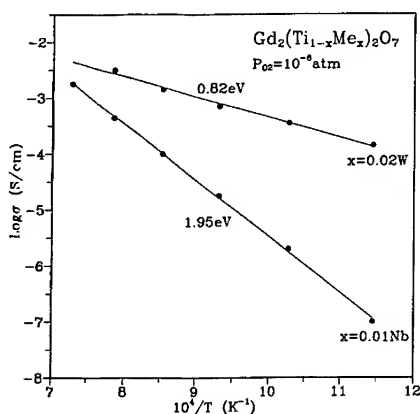


Fig.3 Temperature dependence of electron conductivity in Nb and W-doped  $\text{Gd}_2\text{Ti}_2\text{O}_7$  at intermediate  $P_{\text{O}_2}$ .

The observation of only a single activation energy in both Nb and W-doped  $\text{Gd}_2\text{Ti}_2\text{O}_7$  suggests that these elements remain predominantly in the single ionization state of +5 with the +6 state remaining unimportant.

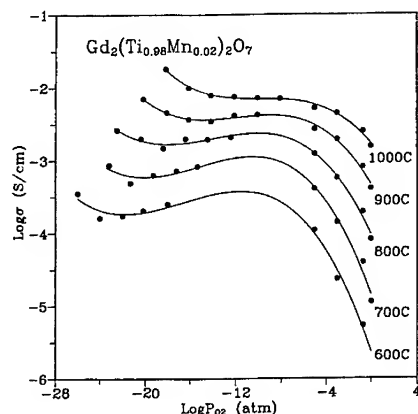


Fig.4 The electrical conductivity of  $\text{Gd}_2\text{Ti}_2\text{O}_7\text{:Mn}$  as a function of  $P_{\text{O}_2}$ .

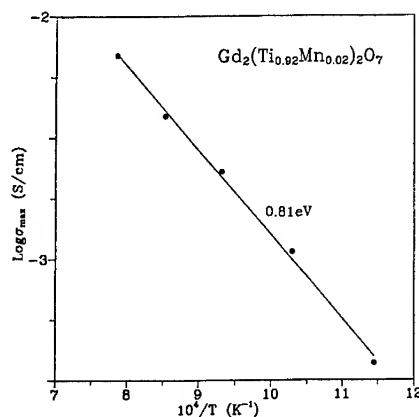


Fig.5 Temperature dependence of the peak conductivity for  $\text{Gd}_2\text{Ti}_2\text{O}_7\text{:Mn}$ .

Qualitatively different behavior has been observed for 2%Mn-doped  $\text{Gd}_2\text{Ti}_2\text{O}_7$  as we can see in Fig.4. The observed maximum of conductivity at intermediate  $P_{\text{O}_2}$  suggests polaron transport. The peak conductivity, believed to be electronic, corresponds to the condition  $[\text{Mn}_{\text{Ti}}^{\cdot}]=[\text{Mn}_{\text{Ti}}^{\cdot\cdot}]=[\text{Mn}]_{\text{tot}}/2$ . However, this interpretation should be confirmed by transference measurements. From the behavior of the peak in electrical conductivity (Fig.4), it is possible to determine the electron hopping energy. The peak conductivity plotted vs  $1/T$  for 2%Mn-doped  $\text{Gd}_2\text{Ti}_2\text{O}_7$  is presented in Fig.5 and gives an energy of 0.81eV. This value is relatively high when compared, for example, with the hopping energy of 0.4eV or 0.2eV observed for  $\text{CeO}_{2-x}$  [9,13] and  $\text{Y}_2\text{Ti}_2\text{O}_7$  [14] respectively.

The influence of the different Mn valence states on the electrical conductivity has recently been studied in  $\text{BaTiO}_3$  [15]. No maximum in conductivity was observed. There the authors find that the condition  $[\text{Mn}^{3+}]=[\text{Mn}^{4+}]$  occurs at  $P_{\text{O}_2}$ 's above those accessible experimentally. Furthermore, they do not suggest impurity band hopping possibly due to the low Mn solubility limits detected, ca 1% [15]. Mn-doped  $\text{Gd}_2\text{Ti}_2\text{O}_7$ , on the other hand, is an interesting example of a material where we can change the ratio between Mn valence states by oxygen partial pressure and observe the polaron hopping conductivity.

## 5. CONCLUSIONS

The electrical properties of Nb, W and Mn-doped have been investigated as a function of temperature and oxygen partial pressure. In contrast to expectations, Nb was found to form deep donor levels on the order of  $\sim 2\text{eV}$  below the conduction band. While W is a more effective donor with an ionization energy of 0.82eV, it still lies quite deep within the gap. The same value of conductivity at high temperature of  $2 \times 10^{-3}$  S/cm has been determined for both Nb and W-impurities; but at low temperatures, W-doped sample show conductivity levels three orders of magnitude higher as compared with Nb-doped  $\text{Gd}_2\text{Ti}_2\text{O}_7$ .

A quite different  $P_{O_2}$  behavior of electrical conductivity has been observed for 2%Mn-doped  $Gd_2Ti_2O_7$ . This can be described by a hopping mechanism with activation energy of 0.81eV for electron hopping between  $Mn^{3+}$  and  $Mn^{4+}$ .

#### ACKNOWLEDGMENT

Partial support for this program is gratefully acknowledged from the Basic Energy Sciences Division of the U.S. Department of Energy under contract #DE-FG02-86ER45261 and The DOW Chemical Company.

#### REFERENCES

1. H.H. Fujimoto and H.L. Tuller, in Fast Ion Transport in Solids, eds. P. Vashishta, J.N. Mundy and G.K. Shenoy (North-Holland, Amsterdam, 1979) pp.649.
2. H.L. Tuller, in Non-Stoichiometric Oxides, ed. O.T. Sorensen (Academic Press, New York, 1981) pp.271.
3. S. Kramer, M. Spears and H.L. Tuller, Solid State Ionics, 72,59(1994).
4. P.K. Moon and H.L. Tuller, in Solid State Ionics, Proc. Symp. Vol.135, Boston, MA, eds. G. Nazri, R.R. Huggins and D.F. Shriver (Mater. Res. Soc., Pittsburg, PA, 1990) p.149.
5. P.K. Moon and H.L. Tuller, Solid State Ionics, 28-30,470(1988).
6. I. Kosacki, S. Kramer and H.L. Tuller, Proc. 4th Intl. Symp. on Systems with Fast Ion Transport, eds. W. Bogusz, W. Jakubowski and F. Krok (Trans Tech Publ. 1994) in print.
7. I. Kosacki and H.L. Tuller, Sensors and Actuators, 1994, in print.
8. H.L. Tuller and P.K. Moon, Mater. Sci. Eng. B1,171(1988)
9. H.L. Tuller, Solid State Ionics, 52,135(1992).
10. M. Sayer and A. Mansingh, Phys. Rev. B6,4629(1972).
11. I.G. Austin and N.F. Mott, Adv. Phys.19,41(1969).
12. M.P. Pechini, U.S. Patent #3,330,697(1967).
13. T.G. Stratton and H.L. Tuller, J. Chem. Soc. Faraday Trans.2,83,1143(1987).
14. D. Goldschmidt and H.L. Tuller, Phys. Rev. B34,5558(1986).
15. S. Osawa, A. Furuzawa and N. Fijikawa, J. Am. Ceram. Soc.76,1191(1993).

## Author Index

- Abeles, Benjamin, 401, 415  
 Aggarwal, Sanjeev, 301, 307  
 Alario-Franco, M.A., 131, 481  
 Amarilla, J.M., 87  
 Angell, C.A., 505  
 Anne, M., 39  
 Aoshima, Norio, 511  
 Appetecchi, Gianni, 495  
 Arbizzani, Catia, 605  
 Armstrong, T.R., 395  
 Arntz, F.O., 137  
 Aurora, T.S., 325  
  
 Bach, S., 191  
 Baer, D.R., 581  
 Baffier, N., 179, 191  
 Bandara, H.M.N., 547  
 Barker, J., 201  
 Bates, J.B., 445  
 Beaudoin, B., 107  
 Bloch, D., 39  
 Bohnke, O., 125  
 Bouwmeester, H.J.M., 377  
 Bridou, F., 125  
 Broscha, Eric L., 349, 623  
 Brown, David R., 623  
 Burggraaf, A.J., 377  
 Butchereit, E., 433  
  
 Cao, X., 59  
 Chabre, Yves, 97  
 Chakoumakos, B.C., 445  
 Chaput, F., 211  
 Choi, Byoung-Koo, 469, 535  
 Chung, Brandon W., 349, 623  
 Clauson, S.L., 149  
 Coffey, G.W., 427  
 Cole, Renée, 475  
 Cormack, A.N., 457  
 Corno, J., 125  
 Cramer, C., 233  
 Croce, Fausto, 495  
  
 Dahn, J.R., 69  
 Davidson, P., 179  
 Day, S.M., 325  
 De Jonghe, Lutgard C., 683  
 de Kock, A., 17  
 de la Cruz, A. Martinez, 131  
 Dekker, J.P., 669  
 Delahaye-Vidal, A., 107  
 Delmas, C., 81  
 den Boer, M., 29, 59  
 Denes, Georges, 295, 463  
 Deng, Huiming, 401, 415  
 Deschamps, M., 165  
 Dharmasena, Gamini, 475  
 Dieckmann, Rüdiger, 301, 307, 313, 319  
 Dieterich, W., 225  
  
 Dissanayake, M.A.K.L., 523  
 Du, Yang, 289  
 Dunn, B., 211  
  
 Engelhard, M.H., 581  
  
 Farcy, J., 191  
 Farrington, G.C., 211  
 Fauteux, D., 29  
 Feng, Man, 333, 343  
 Ferg, E., 17  
 Ferguson, Gregory S., 697  
 Ferreira, M., 575  
 Figlarz, M., 107  
 Forsyth, M., 517  
 Fou, A.C., 575  
 Frech, Roger, 475, 523  
 Funke, K., 233  
  
 Garcia-Alvarado, F., 131, 481  
 Garot, F., 657  
 Garzon, Fernando H., 349, 623  
 Gerace, Furio, 495  
 Goldner, R.B., 137  
 Goodenough, John B., 333, 343  
 Gorenstein, A., 125, 639, 649  
 Gozdz, A.S., 595  
 Graeber, R., 233  
 Greenbaum, S.G., 29, 59  
 Guérard, Daniel, 155  
 Guerlou-Demourgues, L., 81  
 Guesdon, J.P., 639, 649  
 Gummow, R.J., 17  
 Gunaratne, L.M.W.K., 565  
 Guyomard, D., 47  
  
 Haas, T.E., 137  
 Hill, A.J., 517  
 Holzinger, Michael, 613  
 Hsieh, B.R., 575  
 Huang, W., 523  
 Huggins, Robert A., 3  
 Huybrechts, B., 629  
  
 Ingram, M.D., 233  
 Ivanov, I., 639  
  
 Jacobson, Allan J., 383, 389, 401, 409  
 Jamin, T., 107  
 Janata, J., 581  
 Josowicz, M., 581  
 Julien, C., 119, 125, 639, 649  
  
 Katz, B., 211  
 Kendall, Kurt R., 355  
 Khelfa, A., 639, 649  
 Kim, Young-Wan, 535  
 Kingsley, J.J., 395  
 Klein, J.D., 149

- Kleinfeld, Elaine R., 697  
Knobbe, Edward T., 475  
Knödler, D., 225  
Koksang, R., 201  
Kosacki, Igor, 703  
Kostov, S., 59  
Kruidhof, H., 377  
Kuhn, Alois, 481  
Kwak, B.S., 445
- Latham, R.J., 547  
Le Cras, F., 39, 87  
Lee, H.S., 559  
Lee, Hyo-Kyoung, 469  
Lee, T.H., 383  
Lefrou, C., 657  
Leroux, F., 47  
Li, Hongshi, 581  
Li, W., 69  
Lim, B.S., 421  
Lin, H.W., 59  
Linford, R.G., 547  
Liu, L., 383  
Liu, T.Y., 137  
Liu, W., 211  
Livage, J., 179  
Loneragan, Mark C., 245  
Lutz-Elsner, C., 433
- Maaza, M., 125  
MacFarlane, D.R., 517  
MacLean, L.A.H., 87  
Madamba, M.C., 463  
Maier, Joachim, 613  
Marrot, O., 657  
Massucco, A., 29  
Mastragostino, Marina, 605  
Matthews, Lowell R., 475  
McBreen, J., 559  
McLin, M., 29  
Meakin, P., 517  
Meneghello, Luca, 605  
Miki, T., 663  
Moran, E., 131, 481
- Nalimova, Vera A., 155  
Navas, Carlos J., 355  
Nitzan, Abraham, 245  
Nowick, A.S., 289, 421
- Ogata, Naoya, 511  
Okamoto, T., 629  
Okamoto, Y., 559  
Olsen, I.I., 201  
Onitsuka, O., 575  
Ouyang, B., 29, 59
- Panero, Stefania, 495  
Pannetier, Jean, 97  
Pardo, B., 125  
Park, Jae-Gwan, 457  
Parris, J.M., 463  
Passerini, Stefano, 495
- Pederson, D.O., 325  
Pederson, L.R., 395, 427  
Pendzig, P., 225  
Pereira-Ramos, J.P., 179, 191  
Pham, Ai Quoc, 389, 401, 409  
Piffard, Y., 47  
Poinsignon, C., 87  
Portemer, F., 107  
Pynenburg, R., 201
- Qiu, L., 383
- Ratner, Mark A., 245  
Rikukawa, Masahiro, 511  
Robertson, J.D., 445  
Roger, G., 125  
Root, J.H., 69  
Rubner, Michael F., 575, 587  
Rybakov, K.I., 263
- Saatkamp, T., 233  
Sac-Epee, N., 107  
Saidi, M.Y., 201  
Sales, B.C., 445  
Salloux, K., 211  
Sanui, Kohei, 511  
Schlindwein, W.S., 547  
Schmutz, C., 595  
Schoonman, J., 433, 669  
Schreiber, M., 433  
Schuler, Brenda J., 325  
Scrosati, Bruno, 495  
Secco, E.A., 361  
Sella, C., 125  
Semenov, V.E., 263  
Shi, J., 29  
Shin, Kyoung-Hee, 469  
Shokoohi, F.K., 595  
Shriver, Duward F., 245  
Sitte, Werner, 613  
Skaarup, Steen, 201, 565  
Slane, S., 59  
Slaven, S., 137  
Sobolev, Boris P., 487  
Sorokin, Nikolay, 487  
Souza, Selmar, 683  
Spears, Marlene A., 271  
Spila, Eraldo, 495  
Stevenson, J.W., 395  
Stockton, William B., 587  
Strobel, P., 39, 87  
Suvorova, Anna I., 541
- Takata, M., 629  
Tanemura, S., 663  
Tarascon, J.M., 595  
Tedjar, F., 87  
Thackeray, M.M., 17  
Töpfer, J., 319  
Torres-Martinez, Leticia M., 131  
Tsai, Tse-Lun, 313  
Tujkova, Irina S., 541  
Tuller, Harry L., 271, 371, 703

Van Dieten, V.E.J., 669  
Van Doorn, René H.E., 377  
Varon, J., 401  
Vaysleyb, A.V., 421  
Visco, Steven J., 683

Wang, B., 445  
Wang, Li-Shun, 683  
Wang, P., 433  
Warren, P.C., 595  
Weber, W.J., 395, 427  
West, Keld, 201, 585  
Wilmer, D., 233

Xu, K., 505

Yang, X.Q., 559  
Yang, Y., 401  
Yang, Y.L., 383  
Yazami, R., 165  
Yebka, B., 119  
Yoshimura, Kazuki, 663  
Yu, Tae-Hwan, 371

Zachau-Christiansen, Birgit, 201, 565  
Zandbergen, H.W., 433  
Zerigian, P., 137  
Zhang, C., 401  
Zhou, Minyau, 415  
Zuhr, R.A., 445  
Zur Loye, Hans-Conrad, 355



## Subject Index

- ab initio calculation, 523
- acid-base-active gas sensor, 613
- aerogel vanadium oxide, 211
- alkali haloborate, 469
- alkaline earth hexa-aluminates, 457
- ambipolar diffusion, 415
- atomic simulation, 457
- Aurivillius phases oxide, 355
- bismuth oxide, layered, 355
- blocking electrodes, 409
- bulk
  - conduction in oxides, 427
  - oxygen diffusion, 389
- carbon anode, 137
- carbon-lithium system, 165
- carbonaceous lithium anode, 165
- cation
  - diffusion, 301
  - in spinel, 319
  - tracer diffusion, 319
  - vacancies, 475
- ceramics  $\text{CeO}_2\cdot\text{Y}^{3+}$ , 421
- chemical
  - diffusion
    - ( $\text{LiWO}_3$ ), 125
    - constant, 137
    - vapor deposition, 669
- Chemie douce, 191
- combustion synthesis, 395
- composition-phase diagram, 39
- conductive polymer, 511
- conductivity,
  - AC, 225, 401, 421, 433, 623
  - Aurivillius oxides, 355
  - exponents, 225
  - fluorite  $\text{MF}_2$ , 295
  - glass electrolyte, 445
  - iodide-based, 361
  - mixed
    - conductors, 409
    - sulfate based, 361
  - modeling, 245
  - of glass electrolyte, 469
  - pyrochlore system, 371
  - spectra, 233
- correlated local motion, 225
- crystal-phase relationships, 457
- cyclic voltammetry, 427
  - $\text{IrO}_x$ , 149
- DC Magnetron deposition, 663
- defect
  - formation energy, 325
  - modeling, 271
  - spinel, 39
- diffusion
  - coefficient, 649
    - $\text{LiMoO}_3$ , 119
    - perovskite, 377
  - reaction, 415
- Diffusivity  $\text{LiWO}_3$ , 125
- dispersive transport, 225
- dynamic
  - response, 3
  - sorption, 541
- dynamically disordered hopping, 245
- effective frankel constant, 371
- electrocatalytic of mixed conductors, 389
- electrochemical methods, 3
- electrochromic
  - $\text{IrO}_x$ , 149
  - nickel oxide, 663
- electrochromism, 657
- energy of mixing polymers, 541
- enhancement factor, 649
- fast-ion conductivity, 361
- flash evaporation, 639
- fluorescence transition, 475
- fluorite structure, 325
  - $\text{MSnF}_4$ , 295
- free volume behavior, 517
- Frenkel defect model, 295
- FTIR spectroscopy, 587
- fuel
  - cell electrolyte, 333
  - cells, 669, 683
- $\text{GdBa}_2\text{Cu}_{3-x}$  ceramics, 629
- gel  $\text{LiV}_3\text{O}_8$ , 201
- GIC, 155
- glass
  - electrolyte, 445
  - transition, 517
- graphite-donor species, 155
- graphite intercalation, 155
- impedance spectroscopy, 389
- induced
  - electromotive force, 263
  - migration, 629
- insertion
  - compounds, 17, 39
  - reaction, 3
- intercalation chemistry, 155
- ion
  - association, 523
  - conducting materials, 433
  - insertion vanadium oxide, 211
  - mobility, 301
  - transport in  $\text{LaF}_3$ , 487
- ion-polymer interaction, 559

- ionic
  - conductivity, 325
  - in tysonite, 487
  - current induced migration, 629
  - oils, 505
  - rubber, 505
- isotope effect, 289
- jump relaxation model, 233
- laser deposition thin films, 401
- lattice
  - gas model, 225
  - simulation technique, 457
- layered
  - double hydroxides, 81
  - manganese oxide, 47
- Li-ion battery, 595
- Li-Mn-O systems, 39
- Li/WO<sub>3</sub> cells, 125
- LiC<sub>2</sub>, MC<sub>4</sub>, LiC<sub>6</sub>, 155
- LiCoO<sub>2</sub>,
  - cathode, 137
  - EPR, 59
  - MAS, 59
  - NEXAFS, 59
- light-emitting diodes, 575
- LiMn<sub>2</sub>O<sub>4</sub>, 29
- LiNiO<sub>2</sub>, 165
- liquid crystal, 179
- Lithium 7-NMR, 59
- lithium aqueous battery, 59
  - batteries, 179, 191, 445, 495
  - cobalt oxide, 59
  - conducting glass, 233
  - insertion,
    - LiMoO<sub>3</sub>, 119
    - W<sub>18</sub>O<sub>49</sub>, 131
  - intercalation, 59, 649
- ion
  - battery, 29
  - technology, 595
  - manganese oxide, 59
  - phosphorus oxynitride, 445
  - triflate in glymes, 523
- lithium-ion cells, 165
- LiV<sub>3</sub>O<sub>8</sub> cathode, 201
- magetite-ulvospinel, 307
- manganese
  - oxide
    - gamma, 97
    - Groutellite, 97
    - MD, 97
    - natural, 87
    - phases, 97
    - ramsdellite, 87
    - structure defects, 97
    - substituted Ni(OH)<sub>2</sub>, 81
- mass
  - spectroscopy, 427
  - transport theory, 263
- materials design, 271
- membranes, perovskite oxides, 377
- methane oxidation, 383
- microbattery, 639
- microstructure-conductivity, 433
- MIEC, 409
  - perovskite, 415
- mixed
  - alkali salt in polymer, 535
  - anion effect, 535
  - conductors, 415
- molten salt, 511
- Monte Carlo simulations, 225
- multilayer
  - heterostructure polymer, 575
  - polymer, 587
- N-butyllithium W<sub>18</sub>O<sub>49</sub> system, 131
- Na- beta" alumina, 233, 433
- Ni hydroxide dissolution, 107
- Ni/Cd cells, 81, 107
- Ni/H<sub>2</sub> cells, 107
- nickel
  - hydroxide crystal chemistry, 81
  - oxide, 663
- non-exponential relaxation, 225
- non-stoichiometry oxides, 481
- olivines, 313
- optical
  - properties, 410
  - transmittance IrO<sub>x</sub>, 149
- order-disorder transition, 355, 377
- Oswald Ripening, 107
- oxide
  - electrolytes, 333
  - membrane, 415
  - permeability, 377
  - permeation, 383, 395
  - sensor, 629
  - vacancies, 355, 371, 377, 389
- oxide-ion electrolytes, 343
- partial conductivity, 409
- PbSnF<sub>4</sub>, 463
- PEO modifier, 541
- PEO-
  - CaBr<sub>2</sub> systems, 547
  - NiBr<sub>2</sub> systems, 547
- perovskite
  - anion deficient, 333
  - La-based, 349
  - mixed conductors, 349
  - oxides, 343, 377, 401
  - type compounds, 289
- phase transition, 361, 463
- phase-composition relations, 39
- photochromism, 657
- plastic li-ion batteries, 595
- plasticiser effect, 517
- PMMA, 495
- point defect, 289, 301, 313, 319
- poly(3-methylthiophene), 605
- poly(acrylonitrile), PAN, 495

- poly(dithieno[3,4-b:3',4'-d]thiophene, 605
- poly(pyrrole), 605
- polyaniline, 565
  - cyclic voltammetry, 565
  - hydrogen bonding, 587
  - UV-Vis spectroscopy, 565
- polyaniline-palladium, 581
- polyether-urethane plasticized, 517
- polyethylene oxide, 523, 541
- polymer
  - blend electrolyte, 541
  - electrolyte, 165, 495, 517, 547
  - modeling, 245
  - XAS, 559
  - in salt electrolyte, 505
  - supercapacitors, 605
- polyphenylene vinylene, 575
- ponderomotive force, 263
- positron annihilation, 517
- potentiometric, 87
- power-law exponents, 233
- proton insertion, 98
- protonic conduction, 289
- pulse application, 3
- Raman spectroscopy, 469, 649
  - MoO<sub>3</sub>, 119
- Rancieite, 47
- redox-active gases, 613
- rocking-chair cells, 17
- roughness effect, WO<sub>3</sub>, 125
- rutile chain family oxide, 481
- self-assembled films, 575
- sensor, 487, 613
- sensors,
  - conductometric, 613
  - potentiometric, 613
- single crystal, 349
- sodium sulfate doped Eu(III), 475
- sol-gel, 179, 313, 683
  - intercalation, 191
- solid oxide fuel cells, 669, 683
- spectrofluorimetry, 475
- spinel, cation diffusion, 307
- spinel oxide, 29
- spray drying, 201
- strain driven transition, 463
- supercapacitor, 605
- superion conductor, 463
- synthesis
  - manganese oxide, 47
  - oxide, 481
  - W<sub>18</sub>O<sub>49</sub>, 131
- TEM, LSM, 433
- TGA, 165, 201, 313
- thermal expansion, lead fluoride, 325
- thin film, 349, 401, 445, 623
  - battery, 137
  - electrolyte, 683
  - fuel cells, 669
  - IrO<sub>x</sub>, 149
  - lithium batteries, 445
  - nickel oxide, 663
  - WO<sub>3</sub>, 125
- tracer diffusion, 307
- transition metal
  - oxide gels, 179
  - oxides, 17
- Uv-vis spectroscopy polyaniline, 581
- V<sub>2</sub>O<sub>5</sub> sol-gel, 191
- vanadium
  - oxide, 211, 639
  - V<sub>6</sub>O<sub>13</sub>, 649
  - xerogels, 211
  - pentoxide gels, 179
- vapor deposition, 137, 623
- vehicle traction, 3
- water uptake oxides, 427
- WO<sub>3</sub>, 657
- x-ray
  - and neutron diffraction, 475
  - diffraction, 623, 649
  - grazing angle, 125
  - MoO<sub>3</sub>, 119
  - XPS glass, 445
- XAFS polymer, 547
- XANES polymer electrolyte, 547
- xerogel
  - V<sub>2</sub>O<sub>5</sub>, 191
  - vanadium oxide, 211
- yttria-stabilized zirconia, 333
- YSZ conductivity, 409
- zirconia based electrolytes, 683
- ZrO<sub>2</sub>-Y doped, 623